Polymer 52 (2011) v–xvi

Contents lists available at ScienceDirect

Polymer

journal homepage: www.elsevier.com/locate/polymer

Polymer Vol. 52, No. 3, 3 February 2011

Contents

POLYMER COMMUNICATIONS

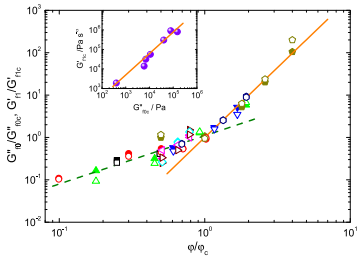

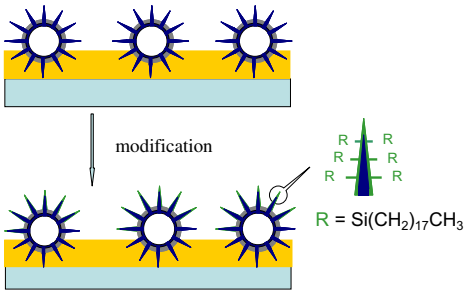

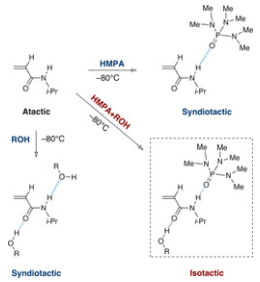

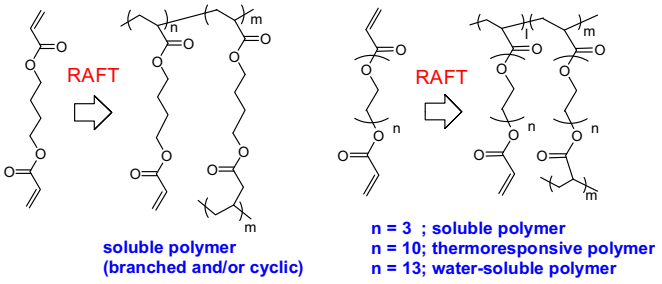

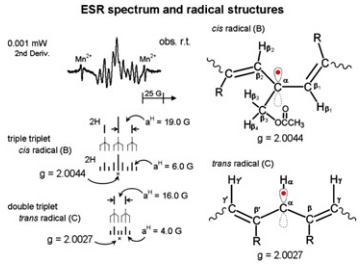

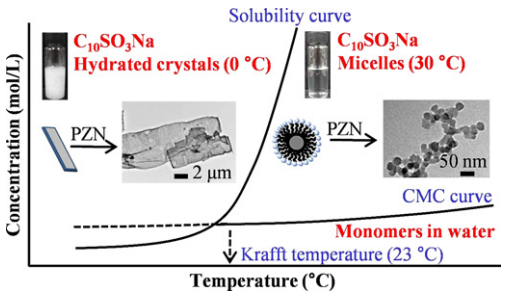

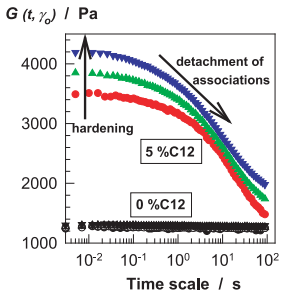

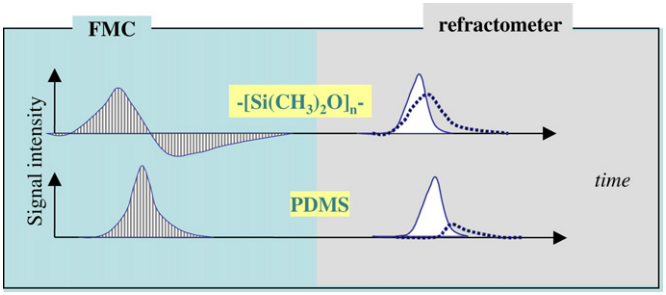

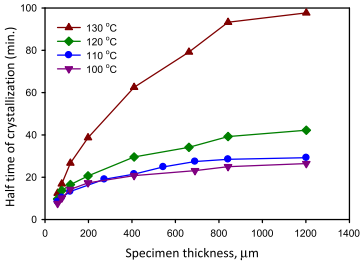

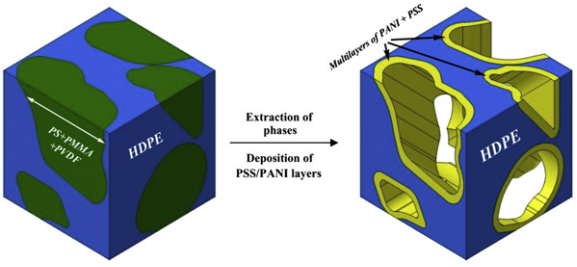

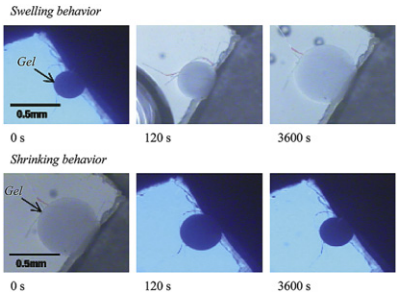

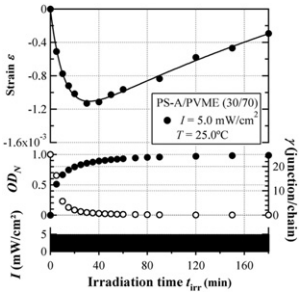

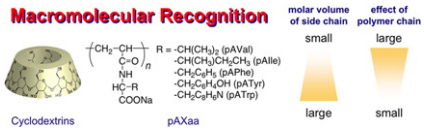

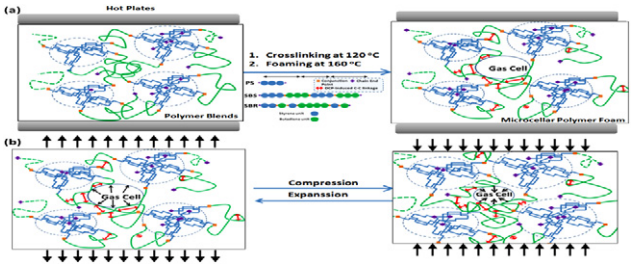

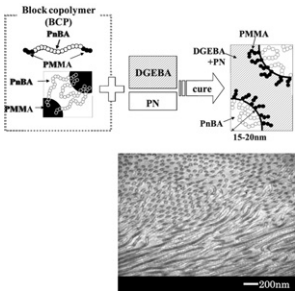

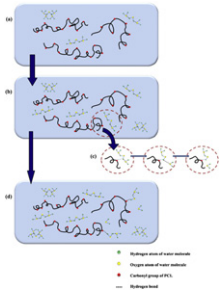

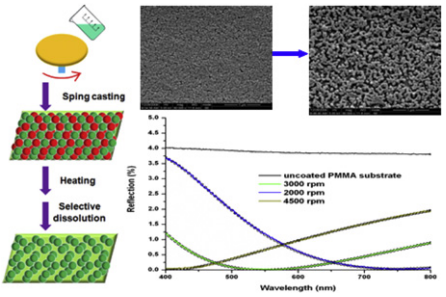

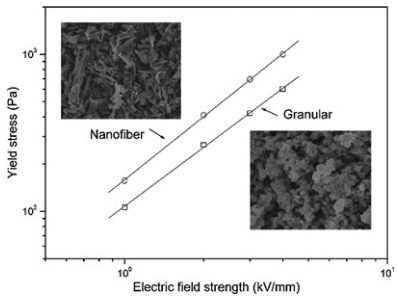

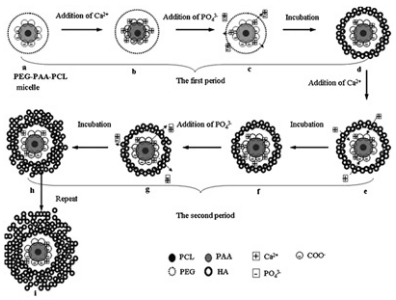

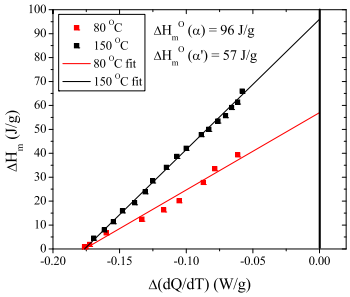

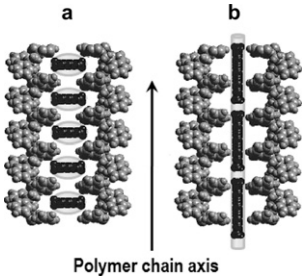

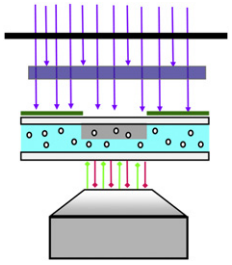

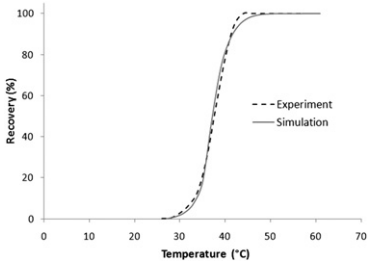

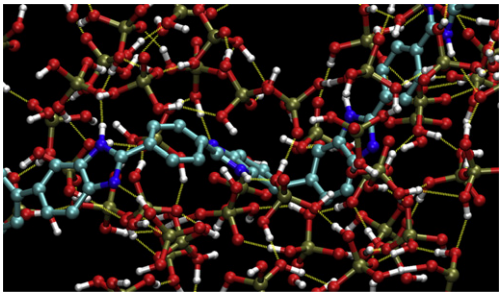

OTHER CONTENT

*Corresponding author

Abstracted/indexed in: AGRICOLA, Beilstein, BIOSIS Previews, CAB Abstracts, Chemical Abstracts. Current Contents: Life Sciences, Current Contents: Physical, Chemical and Earth Sciences, Current Contents Search, Derwent Drug File, Ei compendex, EMBASE/Excerpta Medica, Medline, PASCAL, Research Alert, Science Citation Index, SciSearch. Also covered in the abstract and citation database SCOPUS®. Full text available on ScienceDirect®

ELSEVIER

ISSN 0032-3861

Author Index

Polymer 52 (2011) 593–596

Contents lists available at ScienceDirect

Polymer

journal homepage: www.elsevier.com/locate/polymer

Polymer Communication

Application of two phase model to linear viscoelasticity of reinforced rubbers

Yihu Song*, Qiang Zheng

Key Laboratory of Macromolecular Synthesis and Functionalization of Ministry of Education, Department of Polymer Science and Engineering, Zhejiang University, Hangzhou 310027, China

ARTICLE INFO

Article history:
Received 9 July 2010
Received in revised form
15 October 2010
Accepted 22 December 2010
Available online 30 December 2010

Keywords:
Rubbers
Fillers
Linear viscoelasticity

ABSTRACT

A two phase model proposed for accounting for linear viscoelasticity of polymer nanocomposite melts [14] is applied to rubbers filled with nanoclay and conventional fillers (carbon black and silica) to probe mechanisms of the fluid- and the solid-like behaviors beyond the terminal flow region. This model shows strong applicability in linear rheology beyond terminal region for a variation of filled rubbers. Characteristic moduli of the "filler phase" from different filled rubbers could collapse onto a master curve, which reveals a jamming transition with increasing filler concentration across the percolation threshold. The strain amplification effect and reduced characteristic moduli of the "filler phase" are discussed within the framework of the cluster–cluster aggregation model.

1. Introduction

Most usage of rubbers would be impossible without reinforcement using conventional fillers such as carbon black (CB) and silica. Layered silicates are now used as promising reinforcement for rubbers [1,2]. Filling universally leads to a decrease in loss factor tan δ and increases in storage modulus $G'(\omega)$, loss modulus $G''(\omega)$, absolute complex modulus $|G^*(\omega)|$ and absolute complex viscosity $|\eta^*(\omega)|$ while the viscoelastic response is mainly altered in the low-frequency (ω) zone. A fluid-to-solid transition characterized as a modulus plateau in the low-ω zone exclusively appears with increasing filler volume fraction ϕ above percolation limit ϕ_c. The plateau appears at surprisingly low filler concentrations in nanofilled rubbers [3,4]. The origination of the fluid-to-solid transition has been arbitrarily ascribed to formation of physical jamming or percolation particle network [3,5], transient network or entrapped entanglements due to polymer adsorption on the filler surface [6–10], and the restriction of polymer relaxations by the filler [4,10,11]. The solid-like rheology of nanocomposites has also been ascribed to the strong interfacial interaction [4], the reduced thermal fluctuations of individual polymers on confinement [12], or strong frictional interactions between clay layers rather than confinement effects [13].

We have proposed a two phase model for accounting for the linear dynamic rheology of nanofilled polymer melts and disclosed a common principle for both the fluid- and the solid-like behaviors [14]. Our approach was essentially derived from a microrheological model based on fractal concept [15] and from the widely accepted concept of strain amplification related to hydrodynamic effects [16]. The particle–particle and the polymer–particle interactions, which have been included into phenomenological [17–22] and molecular models [23,24], or the possible interfacial (glassy) layers around the fillers proposed for accounting for the high level of stress between fillers [25–27], are included in the "filler phase". Interconnected particle aggregates as contorted rigid rods are able to respond to small deformations. The microrheological model reveals that the elastic contribution of elastically rigid interaggregate chains is very weakly dependent on ω while the viscous component is approximately independent of ω [15]. The viscoelasticity of the "filler phase" can be expressed as

$$G_f^*(\omega) = G'_{f1}\omega^{\alpha} + iG''_{f0} \tag{1}$$

Here, α is an exponent, G'_{f1} represents elastic contribution of the "filler phase" at $\omega = 1$ rad s^{-1} and G''_{f0} is a constant representing the viscous contribution of the "filler phase". The presence of the "filler phase" does not influence the polymer dynamics in the bulk phase far away from the filler while the complex modulus of the pure matrix $G_m^*(\omega)$ is enlarged to $A_f G_m^*(\omega)$ in the suspensions [28]. Here, A_f is strain amplification factor related to concentration and structure of the filler as well as the filler-polymer affinity. Both the filler and the polymer contribute independently to modulus; the total rheological response is the sum of the two independent contributions

$$G^*(\omega) = A_f G_m^*(\omega) + G_f^*(\omega) \tag{2}$$

* Corresponding author. Fax: +86 571 8793075.
E-mail address: s_yh0411@zju.edu.cn (Y. Song).

0032-3861/$ – see front matter © 2010 Elsevier Ltd. All rights reserved.
doi:10.1016/j.polymer.2010.12.047

The proposed model was successfully applied to linear viscoelasticity in the terminal flow region of a variety of filled polymer melts [14]. Here we shall further examine its applicability to the linear rheology beyond the terminal region for filled rubbers (rheology of the matrixes deviating from typical terminal flow characterized by $G'_m(\omega) \sim \omega^2$ and $G''_m(\omega) \sim \omega^1$). Another purpose of this article is to examine the difference in reinforcement in rubbers filled with nanoclay and conventional fillers (CB and silica) by analyzing viscoelastic functions $G'(\omega)$, $G''(\omega)$, $|G^*(\omega)|$, $|\eta^*(\omega)|$ and tan δ as a function of ω.

2. Results and discussion

The systems under consideration include nanoclay filled ethylene-propylene diene terpolymer (EPDM) [29], nitrile rubber (NBR) [30], and maleated ethylene-propylene rubber (EPR) [31], CB filled EPDM [29,32] and polyisobutylene (PIB) terpolymer [33], as well as silica filled EPDM [29]. Linear rheological data of the systems under consideration were taken from the published reports and are analyzed in the framework of the two phase model. Fig. 1 shows time–temperature superposed linear viscoelastic master curves for nanoclay filled NBR [30] and CB filled PIB [33] in a wide ω range spanning more than 5 orders of magnitude [34]. Phenomenological, rubbers filled with nanoclay exhibit linear

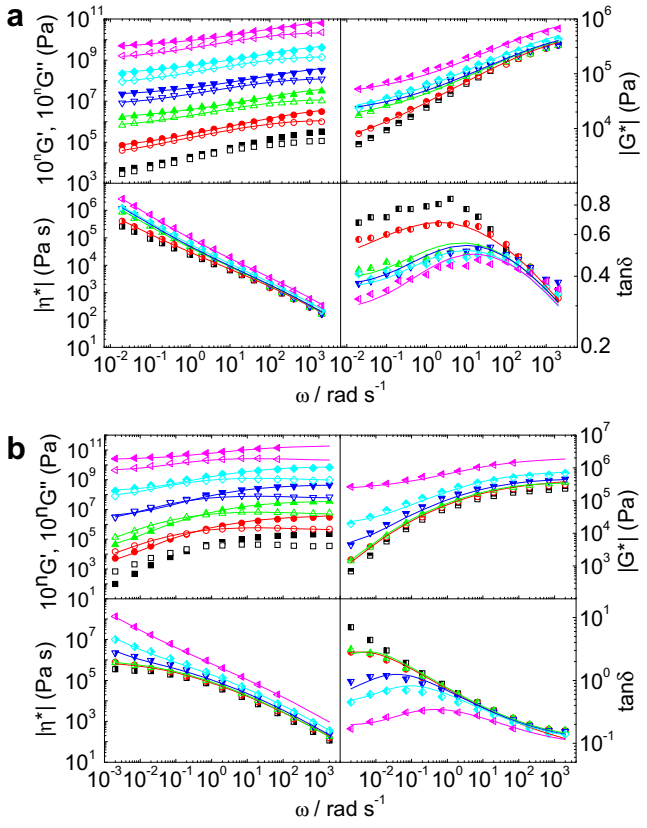

Fig. 1. Fluid-to-solid transition in filled rubbers. (a) Time–temperature superposed linear viscoelastic master curves of G' (filled symbols), G'' (open symbols), $|G^*|$ (upper-half filled symbols), $|\eta^*|$ (right-half filled symbols) and tan δ (left-half filled symbols) as a function of ω at 120 °C for silicate nanosheets filled NBR with $\phi = 0$ (squares), $\phi = 0.007$ (circles), $\phi = 0.021$ (up-triangles), $\phi = 0.050$ (down-triangles), $\phi = 0.058$ (diamonds), and $\phi = 0.071$ (left-triangles). The G' and G'' data for silicate nanosheets filled NBR were taken from Chung et al. [30]. (b) Viscoelastic master curves at 120 °C for CB filled PIB terpolymer with $\phi = 0$ (squares), $\phi = 0.025$ (circles), $\phi = 0.050$ (up-triangles), $\phi = 0.090$ (down-triangles), $\phi = 0.13$ (diamonds), and $\phi = 0.20$ (left-triangles). The G' and tan δ data for CB filled PIB were taken from Yurekli et al. [33]. The solid lines are drawn according to Eq. (2).

dynamic rheology similar to those filled with conventional fillers. Filling ineluctably leads to the fluid-to-solid transition characterized by the gradually diminished ω-dependences of $G'(\omega,\varphi)$, $G''(\omega,\varphi)$ and $|G^*(\omega,\phi)|$ with increasing ϕ. NBR exhibits rheology far away from terminal flow region, as depicted by $G'_m(\omega) > G''_m(\omega)$ and the tan δ peak. Consequently, $G'(\omega,\varphi)$ and $G''(\omega,\varphi)$ curves of nanoclay filled NBR do not form any crossover and the tan δ peak shifts gradually toward high frequencies upon filling. PIB exhibits a rheological behavior of $G'_m(\omega) \sim \omega^{1.81}$ and $G''_m(\omega) \sim \omega^{0.81}$ with one modulus crossover point at $\omega = 0.71$ rad s^{-1}. The tan δ curve adopts a minus slope. Filling PIB with CB up $\phi = 0.050$ leads the modulus crossover point to shift to $\omega = 0.36$ rad s^{-1}. At $\phi = 0.090$, the modulus crossover disappears and the filled rubber is characterized by $G'_m(\omega) \approx G''_m(\omega)$ at $\omega < 0.42$ rad s^{-1}. The highly filled rubbers behave solid-like as $G'(\omega,\varphi) > G''(\omega,\varphi)$. Increasing ϕ leads to the formation of a tan δ peak that shifts to high frequencies.

Eq. (1) was used to fit the data in Fig. 1 with the fitting procedure described elsewhere [14]. The best fitted results shown as solid curves in Fig. 1 well describe the viscoelasticity of nanoclay filled NBR and CB filled PIB despite of the subtle rheological differences between the two systems. Eq. (1) is also applicable to the linear rheologies of nanoclay filled EPDM [29] and maleated EPR, CB filled EPDM and PIB terpolymer as well as silica filled EPDM. The wide applicability of Eq. (1) indicates that the two phase model can be extended to the non-terminal linear rheology of filled polymer melts. The main implication is the same as our previous study [14], that is, the fluid- and the solid-like rheologies in filled rubbers follow the same mechanism and the presence of nanosheet or conventional fillers may not significantly influence the dynamics of the bulky rubbery chains responsible for the suspension viscoelasticity.

The parameters A_f, G'_{f1}, G''_{f0} and α reflect the structural differences underlying the common reinforcement mechanism. As shown in Fig. 2a, when A_f is plotted as a function of reduced filler volume fraction ϕ/ϕ_c, all the data from different filled rubbers collapse to a single master curve. Here, ϕ_c is percolation threshold. In the case of fractal clusters, the Huber–Vilgis expression allows relating A_f to filler particle size a, cluster size ξ, fractal dimension d_f, and anomalous diffusion exponent d_w of filler clusters [35–37].

$$A_f = 1 + C'(\xi/a)^{d_w - d_f}\varphi^{2/3-d_f} \tag{3}$$

Here, C' is a constant. Eq. (3) as a strictly monotone increasing function can be modified to

$$A_f = 1 + C(\varphi/\varphi_c)^{2/3-d_f} \tag{4}$$

with $C = C'(\xi/a)^{d_w-d_f}\varphi_c^{2/3-d_f}$. Eq. (4) was used to fit the collapsed data in Fig. 2a using least square fitting method. The fitted fractal dimension value of $d_f = 1.83 \pm 0.04$ is in agreement with the theoretical value predicated for self-similar clusters [37,38]. The d_f value is the same as that previously determined in filled polymers in the terminal flow region [14]. As shown in Fig. 2b, plotting scaled characteristic moduli, G'_{f1}/G'_{f1c} and G''_{f0}/G''_{f0c}, as a function of ϕ/ϕ_c demonstrates data superposition for different filled rubbers. Here, G'_{f1c} and G''_{f0c} are the elastic and viscous contributions of the filler phase at ϕ_c. The scaled characteristic moduli are described by

$$G''_{f0}/G''_{f0c} = G'_{f1}/G'_{f1c} = (\varphi/\varphi_c)^x \tag{5}$$

with $x = 1.14 \pm 0.11$ at $\phi < \phi_c$ and $x = 3.50 \pm 0.12$ at $\phi > \phi_c$, respectively, which indicates a jamming transition at ϕ_c [39,40]. The x value at $\phi > \phi_c$ accords with the theoretical value predicted for elastically effective cluster backbone in the diffusion-controlled cluster–cluster aggregation (CCA) model [41–44]. Inset in Fig. 2b suggests a scaling law for characteristic moduli at ϕ_c

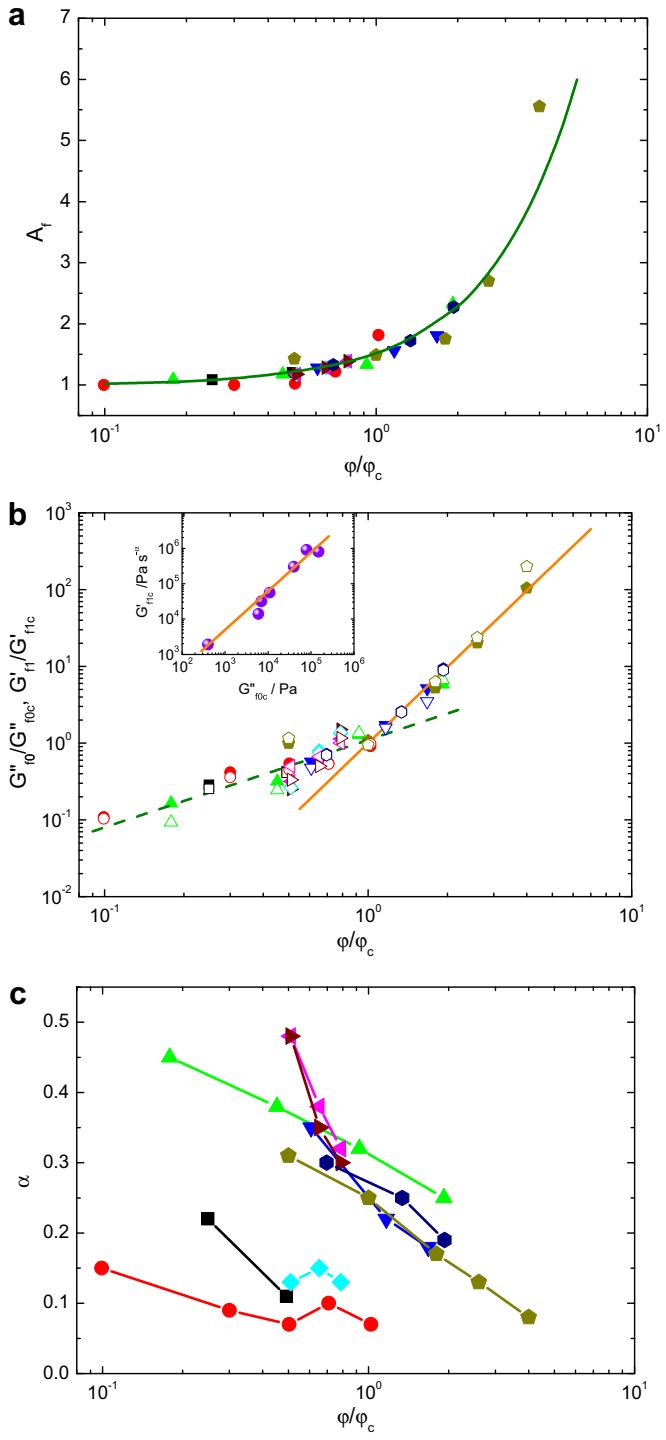

Fig. 2. Model parameters. (a) A_f (solid symbols) as a function of scaled filler volume fraction ϕ/ϕ_c for different composites: nanoclay filled NBR [30] (circles, 120 °C), EPDM [29] (squares, 100 °C) and maleated EPR [31] (up-triangles, 170 °C), CB filled EPDM [29,32] (diamonds, 50 °C, down-triangles and left-triangles 100 °C, right-triangles, 150 °C) and PIB terpolymer [33] (pentagons, 120 °C), as well as silica filled EPDM [29] (hexagons, 100 °C). (b) G'_{f1}/G'_{f1c} (solid symbols) and G''_{f0}/G''_{f0c} (hollow symbols) as a function of ϕ/ϕ_c. Inset, G'_{f1c} as a function of G''_{f0c} (solid circles). (c) α (solid symbols) as a function of ϕ/ϕ_c. The solid curve in part (a) is drawn according to Eq. (4), the lines in part (b) are drawn according to Eq. (5), and the line in inset of part (b) is drawn according to Eq. (6).

$$G'_{f1c} = A\left(G''_{f0c}\right)^{y} \tag{6}$$

with a constant $A = 1.43 \pm 0.20$ and an exponent $y = 1.13 \pm 0.08$. Jamming transition is usually adopted to account for the rheological variation of filled polymers. The scaled plot in Fig. 2b suggests that the jamming transition does occur in the filler phase with increasing ϕ across ϕ_c and this transition shares a common scaling characteristic in rubbers of different polarities filled with fillers of different topologies.

Fig. 2c discloses a general tendency that α decreases with increasing ϕ/ϕ_c, suggesting that the filler phase develops a more and more elastic structure with increasing ϕ. It is worth noting that the α values as a function of ϕ/ϕ_c are close to each other for CB and silica filled rubbers except for CB filled EPDM at 50 °C that shows very small α values due to the presence of crystalline fraction in the matrix. The α values of clay filled maleated EPR are close to the CB and silica filled rubbers. In fact, clay is present as intercalated tactoids alongside delaminated platelets in maleated EPR, according to transmission electron microscope (TEM) examination of the elastomer-based nanocomposites [31]. The α values of clay filled EPDM and NBR are considerably lower than the other compounds due to the well dispersion of the silicate nanosheets. The fine dispersion of clay in NBR has been observed using high-resolution TEM [30]. Interactions between the well dispersed silicate nanosheets and the absorbed polymer chains leads to formation of nanosized cage structures that effectively slower overall relaxation rate and widen distribution of relaxation times of polymers participating in the "filler phase" [45,46]. The low α value of clay filled EPDM is consistent with variation of average relaxation time of the nanocomposites estimated by analyzing $G'(\omega)$ using the empirical Havriliak–Negami (HN) distribution function [30].

There are two populations of polymer chains with distinct dynamics in filled melts; a small fraction of solid-like chains with either no perceptible relaxation time or with relaxation times beyond the experimental range and a large fraction of bulk chains [47]. The population of slow chains is not responsible for the long time solid-like character of the filled rubbers [13,48] while it actually influences the viscoelasticity of the filler phase that becomes essentially elastic with α approaching zero at ϕ high enough. Either nanoclay or conventional fillers might impose on segmental relaxation of chain in the thin absorbed shell close to the fillers [20,49,50] to form bound and occluded polymers [51] and even a glassy lay [52–55]. The absorbed shell leads to the formation of filler clusters and an increase in effective filler volume fraction, which has been taken into consideration in the CCA model [35–37]. The strong interfacial interaction and the presence of geometrical confinement slow down the relaxation of the occluded polymers, which explains the small α value in rubbers filled with nanosheet rather than conventional fillers.

3. Conclusion

In summary, the two phase model could well account for linear viscoelasticity of reinforced rubbers beyond the terminal flow region. A common jamming transition is revealed from the collapsed data of reduced characteristic moduli G'_{f1}/G'_{f1c} and G''_{f0}/G''_{f0c} as a function of ϕ/ϕ_c. The strain amplification effect and characteristic moduli of the filler phase could be well understood within the framework of the CCA model.

References

[1] Sengupta R, Chakraborty S, Bandyopadhyay S, Dasgupta S, Mukhopadhyay R, Auddy K, et al. Polym Eng Sci 2007;47:1956–74.
[2] Karger-Kocsis J, Wu CM. Polym Eng Sci 2004;44:1083–93.

[3] Ren JX, Silva AS, Krishnamoorti R. Macromolecules 2000;33:3739–46.
[4] Ray SS, Okamoto M. Prog Polym Sci 2003;28:1539–641.
[5] Li L, Masuda T. Polym Eng Sci 1990;30:841–7.
[6] Aranguren MI, Mora E, DeGroot JV, Macosko CW. J Rheol 1992;36:1165–82.
[7] Sternstein SS, Zhu AJ. Macromolecules 2002;35:7262–73.
[8] Osman MA, Atallah A. Polymer 2006;47:2357–68.
[9] Sarvestani AS, Jabbari E. Macromol Theor Simul 2007;16:378–85.
[10] Krishnamoorti R, Giannelis EP. Macromolecules 1997;30:4097–102.
[11] Wu DF, Wu L, Zhang M. J Polym Sci Pol Phys 2007;45:2239–51.
[12] Claessens MMAE, Tharmann R, Kroy K, Bausch AR. Nat Phys 2006;2:186–9.
[13] Galgali G, Ramesh C, Lele A. Macromolecules 2001;34:852–8.
[14] Song Y, Zheng Q. Polymer 2010;51:3262–8.
[15] Wolthers W, vandenEnde D, Breedveld V, Duits MHG, Potanin AA, Wientjes RHW, et al. Phys Rev E 1997;56:5726–33.
[16] Mullins L, Tobin NR. J Appl Polym Sci 1965;9:2993–3009.
[17] Leonov AI. J Rheol 1990;34:1039–68.
[18] Mujumdar A, Beris AN, Metzner AB. J Non-Newton Fluid 2002;102:157–78.
[19] Havet G, Isayev AI. Rheol Acta 2001;40:570–81.
[20] Simhambhatla M, Leonov AI. Rheol Acta 1995;34:329–38.
[21] Kagarise C, Koelling KW, Wang YR, Bechtel SE. Rheol Acta 2008;47:1061–76.
[22] Wang YR, Xu JH, Bechtel SE, Koelling KW. Rheol Acta 2006;45:919–41.
[23] Sarvestani AS, Picu CR. Rheol Acta 2005;45:132–41.
[24] Sarvestani AS, Picu CR. Polymer 2004;45:7779–90.
[25] Merabia S, Sotta P, Long DR. Macromolecules 2008;41:8252–66.
[26] Berriot J, Montes H, Lequeux F, Long D, Sotta P. Macromolecules 2002;35:9756–62.
[27] Montes H, Lequeux F, Berriot J. Macromolecules 2003;36:8107–18.
[28] Pryamitsyn V, Ganesan V. Macromolecules 2006;39:844–56.
[29] Tan H, Isayev AI. J Appl Polym Sci 2008;109:767–74.
[30] Chung JW, Han SJ, Kwak SY. Compos Sci Technol 2008;68:1555–61.
[31] Austin JR, Kontopoulou M. Polym Eng Sci 2006;46:1491–501.
[32] Osanaiye GJ. J Appl Polym Sci 1996;59:567–75.
[33] Yurekli K, Krishnamoorti R, Tse MF, Mcelrath KO, Tsou AH, Wang HC. J Polym Sci Polym Phys 2001;39:256–75.
[34] Song Y, Zheng Q, Cao Q. J Rheol 2009;53:1379–88.
[35] Huber G, Vilgis TA. Kaut Gummi Kunstst 1999;52:102–7.
[36] Heinrich G, Kluppel M, Vilgis TA. Curr Opin Solid State Mater Sci 2002; 6:195–203.
[37] Kluppel M. Adv Polym Sci 2003;164:1–86.
[38] Cassagnau P. Polymer 2003;44:2455–62.
[39] Trappe V, Prasad V, Cipelletti L, Segre PN, Weitz DA. Nature 2001;411:772–5.
[40] Cipelletti L, Ramos L. Curr Opin Colloid Interface Sci 2002;7:228–34.
[41] Witten TA, Rubinstein M, Colby RH. J de Phys II France 1993;3:367–83.
[42] Kluppel M, Schuster RH, Heinrich G. Rubber Chem Technol 1997;70:243–55.
[43] Kluppel M, Heinrich G. Rubber Chem Technol 1995;68:623–51.
[44] Kluppel N. Macromol Symp 2003;194:39–45.
[45] Mijovic J, Lee HK, Kenny J, Mays J. Macromolecules 2006;39:2172–82.
[46] Lu HB, Nutt S. Macromolecules 2003;36:4010–6.
[47] Krishnamoorti R, Yurekli K. Curr Opin Colloid Interface Sci 2001;6:464–70.
[48] Solomon MJ, Almusallam AS, Seefeldt KF, Somwangthanaroj A, Varadan P. Macromolecules 2001;34:1864–72.
[49] Lee KJ, Lee DK, Kim YW, Choe WS, Kim JH. J Polym Sci Polym Phys 2007; 45:2232–8.
[50] Robertson CG, Roland CM. Rubber Chem Technol 2008;81:506–22.
[51] Bogoslovov RB, Roland CM, Ellis AR, Randall AM, Robertson CG. Macromolecules 2008;41:1289–96.
[52] Yim A, Chahal RS, St. Pierre LE. J. Colloid Interface Sci 1973;43:583–90.
[53] Landry CJT, Coltrain BK, Landry MR, Fitzgerald JJ, Long VK. Macromolecules 1993;26:3702–12.
[54] Tsagaropoulos G, Eisenberg A. Macromolecules 1995;28:396–8.
[55] Tsagaropoulos G, Eisenberg A. Macromolecules 1995;28:6067–77.

Polymer 52 (2011) 597–601

Contents lists available at ScienceDirect

Polymer

journal homepage: www.elsevier.com/locate/polymer

Polymer Communication

Papillae mimetic hairy composite spheres towards lotus leaf effect coatings

Zhaokai Meng, Qian Wang*, Xiaozhong Qu, Chengliang Zhang, Jiaoli Li, Jiguang Liu, Zhenzhong Yang*

State Key Laboratory of Polymer Physics and Chemistry, Institute of Chemistry, Chinese Academy of Sciences, Beijing 100190, China

ARTICLE INFO

Article history:
Received 20 October 2010
Received in revised form
9 December 2010
Accepted 13 December 2010
Available online 21 December 2010

Keywords:
Hairy sphere
Composite
Superhydrophobic coating

ABSTRACT

An effective approach is proposed to fabricate a robust superhydrophobic coating constructed from hairy composite spheres. The hairy spheres mimic structure of the papillae on the surface of lotus leaf. The synthesis is based on template method and the corresponding PANi hairy spheres are prepared by polymerization induced diffusion growth via nanosized channels of a polymer cage. The composite spheres become more robust by coating a layer of inorganic materials onto the PANi hairy spheres. By using a middle adhesive layer of epoxy resin, the hairy spheres can be tightly attached to the substrate. The superhydrophobic coating is achieved with a contact angle of 159.9 ± 1.9° and tilt angle below 2° by a post hydrophobic modification with octadecyltrichlorosilane. Such coating is robust enough to resist water flushing and organic solvents. This method can be scaled up for almost all kinds of substrates.

1. Introduction

Wettability is an important property of solid surfaces, which is controlled by both chemical composition and topographic feature [1–4]. For example, the superhydrophobic performance of a lotus leaf arises from hydrophobic micron-sized papillae units on the leaf surface [5]. Onto each papilla, there exist nanosized protruded pillars, which make the papilla look like hairy sphere. Recently, superhydrophobic surfaces have gained increasing interests due to their promising applications [6–8]. Inspired by the unique structure of a lotus leaf, many elegant methods have been proposed to construct superhydrophobic coatings [9–21]. Among those methods, coating from papilla mimetic spheres onto desired substrates is easy and direct [15–18]. However, most of the coatings are lack of sufficient adhesion strength against water flushing. It has been reported that epoxy resin is effective to adhere particles onto different substrates including glass, polymers and metals [16,19]. After being cured, it can offer desirable mechanical strength for the superhydrophobic coatings. Another key concern is to increase strength and stability of the hairy spheres, since most papilla mimetic spheres are organic thus can not survive from harsh conditions like solvents bath, physical friction, and etc. Fortunately, it has been revealed in our previous work that the stability of the spheres can be greatly enhanced after incorporation of inorganic materials within the organic spheres [22–25].

Herein, we introduce the construction of a robust superhydrophobic coating from hairy composite spheres, as illustrated in Scheme 1. The hairy composite spheres offer both the micro- and nanodual structures to mimic papillae of a lotus leaf. The hairy polyaniline/silica composite spheres spread onto the pretreated glass substrate with a layer of curable epoxy resin and diethylenetriamine. At high temperature, the epoxy resin layer firstly becomes fluidic and the hairy spheres are partially embedded inside the epoxy resin matrix. During the progressively cross linking procedure of the epoxy resin, both silica and polyaniline can participate in the reaction. Therefore, the hairy spheres are strongly bound onto the surface forming a lotus leaf like coating. The exposed surface of the hairy spheres is modified with octadecyltrichlorosilane, and finally the corresponding superhydrophobic coating is generated. The contact angle of a water droplet of 3 μL on this superhydrophobic coating is 159.9°, while the tilt angle is as low as 1°. The superhydrophobicity can be well preserved even after being flushed with water at high speed.

2. Experimental

2.1. Materials

Polystyrene hollow spheres were obtained from Rhom & Haas Company. The aniline monomer (from Beijing Chemical Reagents Company) was distilled under reduced pressure before use. Octadecyltrichlorosilane was purchased from Acros Organics Company. Epoxy resin F46 was supplied by the Shanghai Resin Factory and used as received. Ferric chloride, HCl, and other reagents were

* Corresponding authors. Fax: +86 10 62559373.
E-mail addresses: wangqian@iccas.ac.cn (Q. Wang), yangzz@iccas.ac.cn (Z. Yang).

0032-3861/$ – see front matter © 2010 Elsevier Ltd. All rights reserved.
doi:10.1016/j.polymer.2010.12.020

purchased from Beijing Chemical Reagents Company and used without further treatment.

2.2. Synthesis of hairy spheres and coating formation thereby

2.2.1. PANi/PS hairy spheres

PANi/PS hairy spheres were synthesized by oxidative polymerization induced diffusion through transverse channels of the polystyrene hollow spheres [26]. In a typical procedure, 3.6 ml of aniline was added to 30 ml of HCl (2 M) aqueous solution at room temperature under stirring to yield a uniform solution. Then 20 mg of the dried polystyrene hollow spheres was added into the solution. The above mixture was then kept at room temperature for 24 h to ensure the aniline to diffuse into the polystyrene hollow spheres via the transverse channels within the shell. After centrifugation to remove the excess aniline, the spheres were dispersed into 100 ml of $FeCl_3$ (0.2 M) aqueous solution to allow the oxidative polymerization of PANi under stirring at room temperature. The resultant dark green hairy PANi/PS spheres were washed with water.

2.2.2. Hairy silica/PANi/PS composite spheres

Freeze-dried PANi/PS hairy sphere (50 mg) was dispersed in 20 ml of tetraethoxysilane (TEOS) sol (according to the typical formulation, water: ethanol: HCl (2 M): TEOS, 1:5:0.15:6, w:w:w:w), and a sol–gel process was carried out under stirring at 70 °C for 24 h. Finally, the hairy silica/PANi/PS composite spheres were obtained by centrifugation and wash with ethanol.

2.2.3. Hairy titania/PANi/PS composite spheres

After freeze-dried PANi/PS hairy sphere (50 mg) was dispersed in ethanol (5 ml), 0.02 ml of water was added into the dispersion. 0.2 ml of tetrabutyltitanate (TBT)/ethanol mixture (1:1, vol:vol) was dropped into the above dispersion under stirring for 2 h to allow a sol–gel reaction. Hairy titania/PANi/PS composite spheres were obtained by centrifugation and wash with ethanol.

2.2.4. Superhydrophobic coating

A crosslinkable epoxy resin layer was coated on a glass substrate. After 0.5 g of F46 and 0.05 g of diethylenetriamine was dissolved in 2 g of acetone, a thin film was coated onto a glass substrate by spin coating. After acetone was evaporated, a dispersion of the hairy spheres in ethanol was spread onto the epoxy resin film. Upon heating to 60 °C for 6 h, the epoxy layer progressively crosslinked and the hairy spheres were partially incorporated inside the film. By sonication in ethanol, free hairy spheres were removed from the composite coating. The composite coating was immersed in a solution of 0.1 g of octadecyltrichlorosilane and 5 ml of hexane at room temperature for 12 h. After being flushed with hexane and ethanol, the lotus leaf mimetic superhydrophobic coating was generated.

2.3. Characterization

The structure and morphology of the spheres were characterized by transmission electron microscope (JEOL 100CX instrument operated at an accelerating voltage of 100 kV) and scanning electron microscope (SEM) (HITACHI S-4300 instrument operated at an accelerating voltage of 15 kV). TEM samples were prepared by dispersing a drop of the sample dispersed in ethanol onto a copper grid coated with a carbon support film. The SEM samples were prepared by vacuum sputtering Pt onto the dried samples at room temperature. The infrared spectra were recorded on a BRUKER EQUINOX 55FT-IR with samples pressed with KBr. A Perkin–Elmer TGA-7 was used to determine the inorganic content of the composite hairy spheres at a ramp rate of 10 °C/min under nitrogen atmosphere. The contact angle and the tilt angle were measured on an OCA20 system (DataPhysics, Germany) at ambient temperature. The liquid droplet was 3 μl.

3. Results and discussion

The PANi/PS hairy spheres were synthesized accordingly [26]. The PS cage (Fig. 1a) has an average diameter of 433 nm and a smooth shell of 60 nm. The polymer cage is composed of a polystyrene shell and a thin poly(methyl methacrylate)-poly(methacrylic acid) (PMMA-PMA) hydrophilic inner layer and transverse channels [23]. Monomer aniline was loaded inside the cavity of the hollow spheres. Upon addition of oxidative initiator outside the spheres in the aqueous phase, polymerization took place at the outermost surface of the hollow spheres forming PANi on the surface of the spheres. While the diffusion/polymerization coupling proceeded, the nanoparticles grew along the diffusion direction forming longer hairs progressively [26]. The composition of the hairy spheres was confirmed by FT-IR. After the oxidative polymerization of ANi, the peaks of PANi appear (Fig. S1). The characteristic bands at 1589 and 1503 cm^{-1} are assigned to quinoid and benzenoid rings of PANi, respectively. The bonds at 1307 cm^{-1} (C–N stretching), 1144 cm^{-1} (C=N stretching), and 826 cm^{-1} are identical to the emeraldine salt form of PANi [27,28].

The morphological evolution was systematically characterized. The hairy structure can be controlled by the polymerization time and the concentration of the aniline. At a given aniline concentration, the outermost surface of the hollow spheres becomes coarse after polymerization for 1 h. Some small protuberances appear on the surface of the polymer cage (Fig. 1b). After polymerization for 3 h, hairy PANi gets distinct (Fig. 1c). Some hairs protrude out of the polymer cage, with a size of about 30–50 nm long and several-10 nm in diameter. After 6 h, the hairs grow up longer than 80 nm, and about more than 20 nm in diameter (Fig. 1d). Some hairy spheres start to slightly aggregate at the PANi hair. With further prolonging the polymerization time, for example 24 h, the hairs do not show further change. No PANi free particles are found in the serum. This indicates that almost all aniline has polymerized to form the nanosized pillars. On the other hand, varying the concentration of aniline creates different morphologies of the hairy structure. When the content of aniline increases from 1.8 ml to 3.6 ml, the polyaniline hair becomes longer from 50 nm (Fig. 1e) to 100 nm long (Fig. 1f). All the spheres are dispersible in water. With further increasing the aniline concentration to a very high level for example 7.2 ml, the polyaniline hair becomes so long that some hairs start to interconnect among the spheres (Fig. 1g). This is

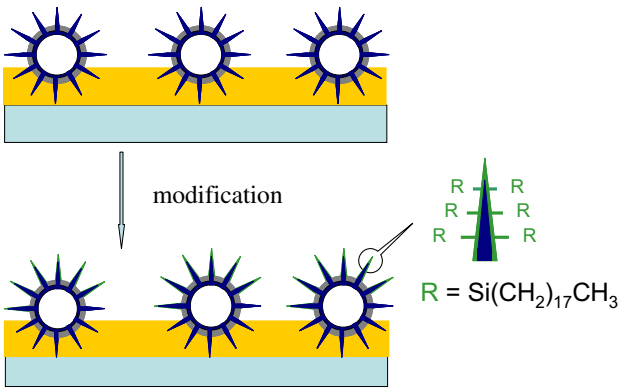

Scheme 1. Schematic construction of a superhydrophobic coating from hairy composite spheres. See the context for more detailed descriptions.

consistent with heavy aggregation between the spheres from the dispersion.

The long PANi nanosized hairs are soft and can not persist their protruded shape especially for long hairs after drying. In order to mimic the papilla structure of lotus leaf, the strength of the hair has to be improved so as to fix the hairy structure. An efficient strategy is to coat a layer of inorganic materials onto the PANi surface. PANi can catalyze a sol–gel process of either tetraethoxysilane (TEOS) or tetrabutyltitanate (TBT) and can induce a favorable growth of the inorganic materials thereby [25]. The resultant silica/PANi/PS composite spheres remain the hairy structure (Fig. 2a); moreover, they are dispersible without aggregation. After the organic components are selectively removed by calcination at 450 °C in air, the silica hairy structure is well preserved (Fig. 2b).

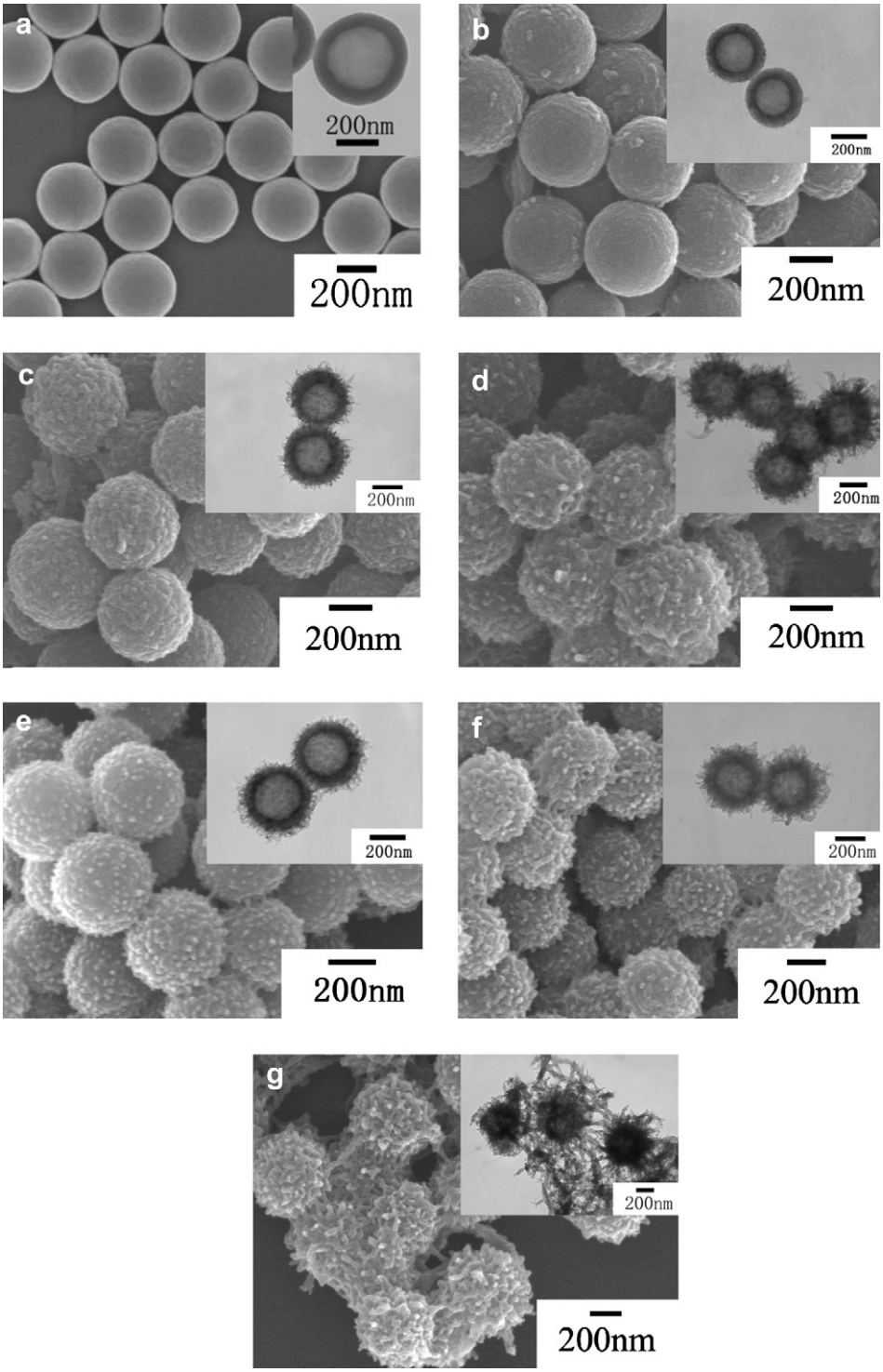

Fig. 1. Morphological evolution of the hairy spheres. a) the polystyrene (PS) hollow spheres; b–d) hairy PANi/PS spheres prepared at different polymerization time (3.6 ml of aniline dissolved in 30 ml of HCl (2 M) aqueous solution): b) 1 h, c) 3 h, and d) 6 h; e–g) the PANi/PS hairy spheres polymerized for 24 h but at different monomer concentration: e) 1.8 ml aniline/30 ml of HCl (1 M) aqueous solution, f) 3.6 ml of aniline/30 ml HCl (2 M) aqueous solution, g) 7.2 ml of aniline/30 ml of HCl (4 M) aqueous solution.

This indicates that silica forms a continuous phase onto the sphere surface. The hairy silica/PANi/PS composite spheres are then washed with toluene to remove the PS component. The left hollow sphere contour with hairy structure is well preserved (Fig. 2c). Removal of PS from the composite spheres is confirmed by TGA results (Fig. S2). In contrast, spherical contour of the hairy PANi/PS spheres is greatly broken and the hairy structure is lost when they were treated with toluene (Fig. 2d). The presence of silica helps the spheres to tolerate solvents. Similarly, hairy titania/PANi/PS composite spheres were synthesized (Fig. 2e). After being calcined at 450 °C in air, hollow titania spheres were derived (Fig. 2f), indicating titania forms a continuous network onto the sphere surface. The inorganic content was measured about 16.2 wt-% (Fig. S2).

Epoxy resin F46 is a commercial resin which can offer satisfactory mechanical strength after being cured, which can resist almost all the organic solvents. Therefore it is used as an adhesive layer to connect the hairy spheres and the substrates. Meanwhile, PANi and the inorganic materials can participate the curing of the epoxy resin. After being heated, the epoxy resin became fluidic and the hairy spheres were partially embedded inside the epoxy resin. As prolonging the time, the cross linking reaction completed and the embedded spheres were tightly bound onto the substrate. The excess unbound hairy spheres were removed from the substrate by sonication, and the lotus leaf mimetic coating was left to be exposed (Fig. 3a). Epoxy resin and PANi are both hydrophilic, so that the coating is hydrophilic. CA of the water droplets on such coating is 75.6 ± 1.3° (Fig. 3b). The amine group of PANi can react with octadecyltrichlorosilane. After the coating was treated by octadecyltrichlorosilane, the hydrophilic coating becomes hydrophobic. CA of water droplets on the modified coating is much larger (159.9 ± 1.9°, see Fig. 3c). More important, the tilt angle is rather small (1°). It is quite difficult for water droplets to rest on the surface, which means that the coating becomes superhydrophobic. Such composite coating is robust enough to resist water flushing at high speed, for example, 1 m/s. During the treatment, a trace of hydrochloric acid was released. In this case, polyaniline is doped, and the color of the coating changes from blue to green. The nanostructure of the particles plays an important role in constructing superhydrophobic coating. The contact angle of water droplets on the coating constructed by PS particles without PANi hairs after being subsequently modified with silane is 129.3 ± 1.2°.

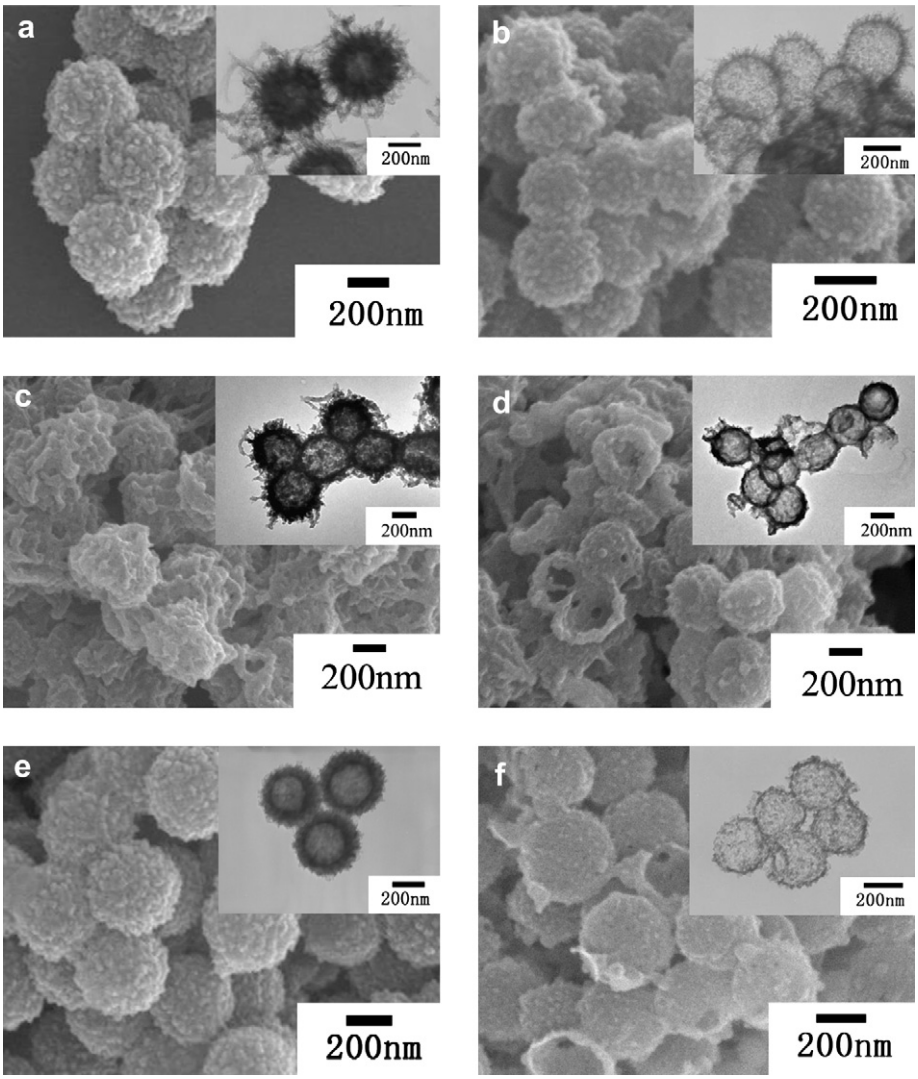

Fig. 2. Morphologies of some representative hairy composite spheres. a, b) the hairy silica/PANi/PS composite spheres before and after being calcined at 450 °C in air for 2 h; c) the hairy silica/PANi/PS composite spheres after being treated with toluene; d) the hairy PANi/PS composite spheres after being treated with toluene; e, f) the hairy titanic/PANi/PS composite spheres before and after being calcined at 450 °C in air for 2 h.

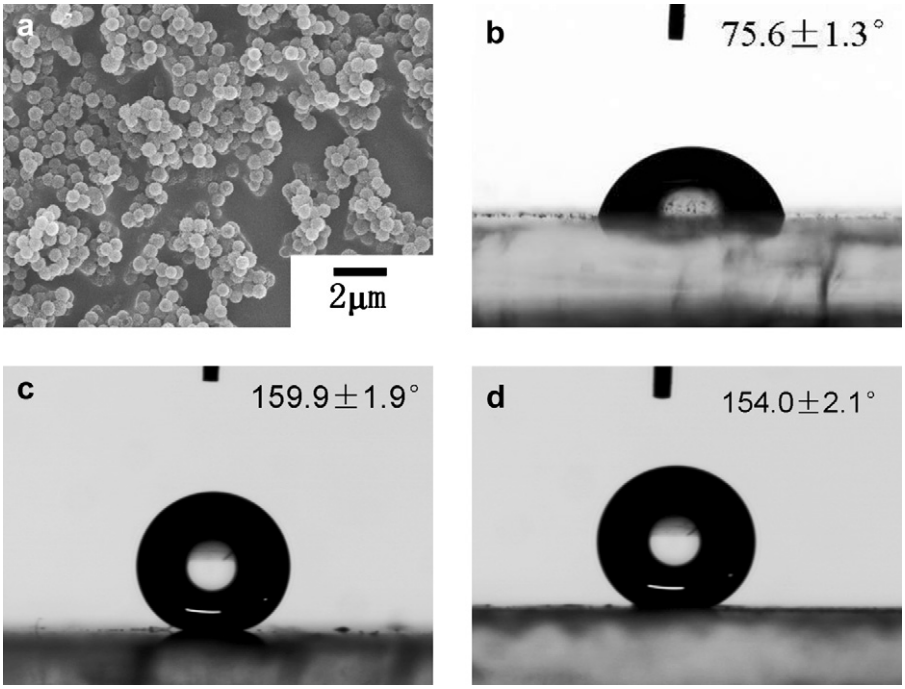

Fig. 3. a) SEM image of the coating formed by the hairy PANi/PS spheres; b–d) water droplets of 3 μl on three representative coatings: b) the as-prepared coating; c) the coating (b) after being modified with octadecyltrichlorosilane; d) the coating formed by hairy silica/PANi/PS spheres and after being modified with octadecyltrichlorosilane.

The contact angle of water droplets on the coating constructed by the composite spheres with shorter hairs (prepared in 1.8 ml aniline/30 ml of HCl (1 M) aqueous solution) is less than 150°. Moreover, water can not roll off this coating until a tilt angle 20°. Both coatings are not superhydrophobic. However, the superhydrophobicity lost upon treatment with solvents, for example toluene. This is consistent with the observed structural lose of the hairy spheres upon treatment with toluene. Similarly, using the hairy silica/PANi composite spheres instead of PANi/PS spheres, a superhydrophobic coating could also form with a CA of 154.0 ± 2.1° and tilt angle about 1° (Fig. 3d). What's more important is that the superhydrophobicity of the coating can be well preserved even upon treatment with toluene. We have chosen other representative substrates such as aluminum and ceramic besides glass. Our idea works for the substrates. It is understandable that epoxy resin can strongly adhere with the substrates and the hairy particles, therefore the particles can be strongly bound with the substrates [16].

4. Conclusion

We have constructed robust hairy polymer/inorganic composite spheres, which possess improved strength and stability resistant to organic solvents. These hairy spheres with both nanosized hairs onto micron-sized spheres surface mimic unique structure of papillae on lotus leaf. By coating such hairy spheres onto substrates in the presence of crosslinkable epoxy resin layer, a robust superhydrophobic coating is generated after further modification with silanes. The contact angle of water droplets on this coating is 159.9 ± 1.9°, and the tilt angle is below 2°. This method is easy and direct, which can be carried out onto almost all substrates on large scale.

Acknowledgements

We thank Dr. Mu Yang for discussion about the hairy spheres characterization. This work was supported by the NSF of China (50733004, 20720102041), and the Chinese Academy of Sciences (KJCX2-YW-H20).

Appendix. Supplementary material

The supplementary data associated with this article can be found in the on-line version at doi:10.1016/j.polymer.2010.12.020

References

[1] Gau H, Herminghaus S, Lenz P, Lipowsky R. Science 1999;283:46–9.
[2] Lenz P. Adv Mater 1999;11:1531–4.
[3] Hui M, Blunt MJ. J Phys Chem B 2000;104:3833–45.
[4] Barthlott W, Neinhuis C. Planta 1997;202:1–8.
[5] Feng L, Li S, Li Y, Li H, Zhang L, Zhai J, et al. Adv Mater 2002;14:1857–60.
[6] Chen W, Fadeev Y, Heieh MC, Jner D, Youngblood J, McCarthy TJ. Langmuir 1999;15:3395–9.
[7] Youngblood JP, McCarthy TJ. Macromolecules 1999;32:6800–6.
[8] Lafuma A, Quéré D. Nat Mater 2003;2:457–60.
[9] Liu K, Yao X, Jiang L. Chem Soc Rev 2010;39:3240–55.
[10] Zhang X, Shi F, Niu J, Jiang Y, Wang Z. J Mater Chem 2008;18:621–33.
[11] Sun T, Feng L, Gao X, Jiang L. Acc Chem Res 2005;38:644–52.
[12] Li X, Reinhoudt D, Crego-Calama M. Chem Soc Rev 2007;36:1350–68.
[13] Roach P, Shirtcliffe NJ, Newton MI. Soft Matter 2008;4:224–40.
[14] Feng X, Jiang L. Adv Mater 2006;18:3063–78.
[15] Zhu Y, Hu D, Wan M, Jiang L, Wei Y. Adv Mater 2007;19:2092–6.
[16] Ming W, Wu D, Benthem RV, With GD. Nano Lett 2005;5:2298–301.
[17] Zhang G, Wang D, Gu Z, Möhwald H. Langmuir 2005;21:9143–8.
[18] Koch K, Bhusham B, Jung YC, Barthlott W. Soft Matter 2009;5:1386–93.
[19] Wang Q, Li J, Zhang C, Qu X, Liu J, Yang Z. J Mater Chem 2010;20:3211–5.
[20] Cho D, Zhou H, Chou Y, Audus D, Joo YL. Polymer 2010;51:6005–12.
[21] Zheng J, He A, Li J, Xu J, Han CC. Polymer 2006;47:7095–102.
[22] Yang M, Ma J, Zhang C, Yang Z, Lu Y. Angew Chem Int Ed 2005;44:6727–30.
[23] Yang M, Ma J, Niu Z, Dong X, Xu H, Meng Z, et al. Adv Funct Mater 2005;15:1523–8.
[24] Yang Z, Niu Z, Lu Y, Hu Z, Han CC. Angew Chem Int Ed 2003;42:1943–5.
[25] Niu Z, Yang Z, Hu Z, Lu Y, Han CC. Adv Funct Mater 2003;13:949–54.
[26] Yang M, Yao X, Wang G, Ding H. Coll Surf A 2008;324:113–6.
[27] MacDiarmid AG, Chiang JC, Halpern M, Huang WS, Mu SL, Somasiri NLD, et al. Mol Cryst Liq Cryst 1985;121:173–80.
[28] Asturias GE, MacDiarmid AG, McCall RP, Epstein AJ. Synth Met 1989;29:157–62.

Polymer 52 (2011) 602–605

Contents lists available at ScienceDirect

Polymer

journal homepage: www.elsevier.com/locate/polymer

Polymer Communication

Porous polyethylene spheres with nanofiber structure from Ziegler-Natta catalyst supported on porous polymer particles

Lei Jinhua [a,b], Li Dongliang [a,b], Wang Honghua [a], Zhou Guangyuan [a,*]

[a] Key Laboratory of Polymer Ecomaterials, Changchun Institute of Applied Chemistry, Chinese Academy of Sciences, Changchun, Jilin 130022, China
[b] Graduate University of Chinese Academy of Sciences, Beijing 100049, China

ARTICLE INFO

Article history:
Received 26 September 2010
Received in revised form
10 November 2010
Accepted 7 December 2010
Available online 14 December 2010

Keywords:
Porous polymer support
Extrusion polymerization
Porous polyethylene sphere

ABSTRACT

Porous polyethylene with nanofiber structure in the form of discrete, freeflowing, micron-sized spheres was formed in high activity by ethylene polymerization with porous polymer supported Ziegler-Natta catalyst. Such versatile porous support catalyst played as a template in two levels. One level is the whole support beads, which resulted in the porous polyethylene spheres. Another level is the porous structure in the support beads, which played as a nanoreactor and resulted in the nanofiber structure in the polyethylene spheres.

Nature has provided us with many examples of organic and polymer reactions in confined reaction environments [1]. For example, in the biosynthesis of highly crystalline cellulose fibers by the bacterium *Acetobacter xylinum*, cellulose synthase in a cellular membrane forms fine elementary fibrils of cellulose. They are then assembled into macrofibrils and fibers by extrusion through nanopores arranged in the cellular membrane [2]. During the past two decades there has been increasing interest in the development of nanoscopic reactors to replicate these natural systems and many successful nanoreactors were developed [3–8]. Aida developed a nanoreactor for ethylene polymerization named mesoporous silica fiber-supported titanocene and produced crystalline polymers with a fibrous morphology [9]. However, such mesoporous silica fiber-supported catalyst showed a poor ethylene polymerization activity. This can be ascribed to catalyst deactivation caused by reactive surfaces of such acidic supports [10]. To cope with such problem, we have focused our attention on silica-free supports designed for chemical versatility and rugged physical properties to best exploit state-of-the-art catalysts. We report here a porous polymer-based support technology that not only yields supported catalyst more active than that of Aida's but also generates porous polyethylene with nanofiber structure in the form of discrete, free flowing, micron-sized spheres that grow in proportion to the polymerization time. We proposed a conceptual scheme for the growth of porous polyethylene spheres with nanofiber structure by porous polymer support-assisted extrusion polymerization (Scheme 1).

On the basis of above ideas, first we employed seeded polymerization to produce monodisperse cyano-functionalized porous polymeric beads poly(St-*co*-DVB-*co*-AN) (P for short) [11]. Scanning electron microscopy (SEM) showed that the overall condition of the particles (Fig. 1A) was excellent, all the particles displayed porous spherical shape and uniformity in size. Such porous particles have a tri-modal pore structure of interconnected macropores, mesopores and micropores, and have a high surface area in the dry state, typically in the range of 100–280 $m^2 g^{-1}$, measured by N_2 sorption and application of the BET (Brunauer–Emmett–Teller) theory (see Electronic Supplementary Material).

As we know, the reported activities of polymer supported Ziegler-Natta catalysts were in general lower than those of $MgCl_2$-supported catalysts [12–15]. One way to cope with this problem is to modify polymer support with magnesium compound [16–19]. Herewith, we modified the monodisperse cyano-functionalized porous polymeric beads with an excess of CH_3MgCl. Subsequently, the modified polymer supports were used for supporting $TiCl_4$ (Scheme 2). The mechanism of each step can be proved by the results of FT-IR and XPS [20] of the porous support (P), modified support (MP) and the supported catalyst (TMP) (see Electronic Supplementary Material). Both of the two reactions were carried out under the protection of N_2 and using toluene as solvent. The content of Ti was estimated to be 1.64 mmol Ti/g beads by inductively coupled plasma atomic emission spectroscopy (ICP-AES).

* Corresponding author.
E-mail address: gyzhou@ciac.jl.cn (Z. Guangyuan).

0032-3861/$ – see front matter © 2010 Elsevier Ltd. All rights reserved.
doi:10.1016/j.polymer.2010.12.012

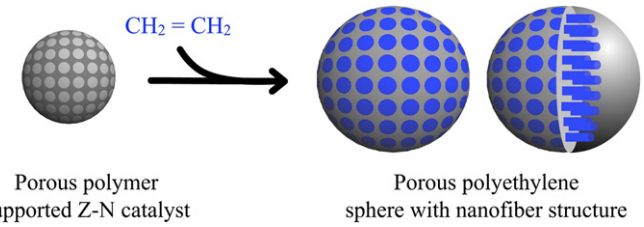

Scheme 1. Conceptual scheme for the growth of porous polyethylene spheres with nanofiber structure by porous polymer support-assisted extrusion polymerization.

Finally, the porous polymer supported Ziegler-Natta catalyst was tested for ethylene polymerization activity by treatment with triisobutyl aluminium (TIBA) and ethylene gas. The ethylene uptake curve for a typical polymerization (in a 1 L autoclave, catalyst: 40 mg, $T = 60$ °C, $P_{C2H4} = 5$ atm, Al/Ti (mol/mol) = 300) (Fig. 1B) indicates that there is only a slight loss in activity during the course of the reaction. The ethylene consumption rate after 2 h is ~75% of its initial value. This result attests to the prolonged active life of the catalyst bead [10].

The supported catalysts display excellent activity for the slurry-phase polymerization of ethylene (Table 1). Typical activities are in the range of 100–200 g PE/mmol Ti h atm (Table 1). Gel permeation chromatography (GPC) analysis of the product polymer revealed weight-average molecular weights (M_w) in the range of 100,000 to 200,000, which are much lower than that of Aida's [9], and with typical polydispersities of 2–3, which are much narrower than that of polyethylene catalyzed by a ordinary silica-supported titanium catalyst [21]. Thermal analysis of the PE by differential scanning calorimetry (DSC) under unconstrained conditions showed an endotherm (T_{m1}) in the range of 141–145 °C. In the second stage of heating, such a high-temperature endotherm was no longer observed, whereas a peak (T_{m2}) was observed at a lower temperature in the range of 135–138 °C. These results are quiet similar to that of Aida's except for the endotherm at 159 °C in the first stage of heating observed by Aida, which was proved to be additional signal of aluminum by Turunen [22]. The ^{13}C nuclear magnetic resonance (NMR) spectrum of the PE in 1,2-dichlorobenzene-C_6D_6 at 130 °C showed a single CH_2 signal at d 30.1 ppm [23], which indicates a linear sequence of the repeating ethylene units without any branch structures.

The bulk morphology of the product polymer is quite good (Fig. 1C). From the photo of polyethylene we can see that the product is isolated as discrete, free flowing beads. The bulk density of the product polymer is in the range of 0.25–0.40 g/ml. A regular spherical shape is the ideal result in industrial-scale polymerizations, where particles of very small or highly variable sizes or those that have grossly irregular shapes interfere with the efficiency and general operation of the reactor [10].

Significantly, from the SEM images of the overall (Fig. 1D and E) and the cross-section (Fig. 1F) of the product we can find that the product is isolated in the form of discrete porous spherical beads of micron dimension, with a distribution of sizes similar to that of the

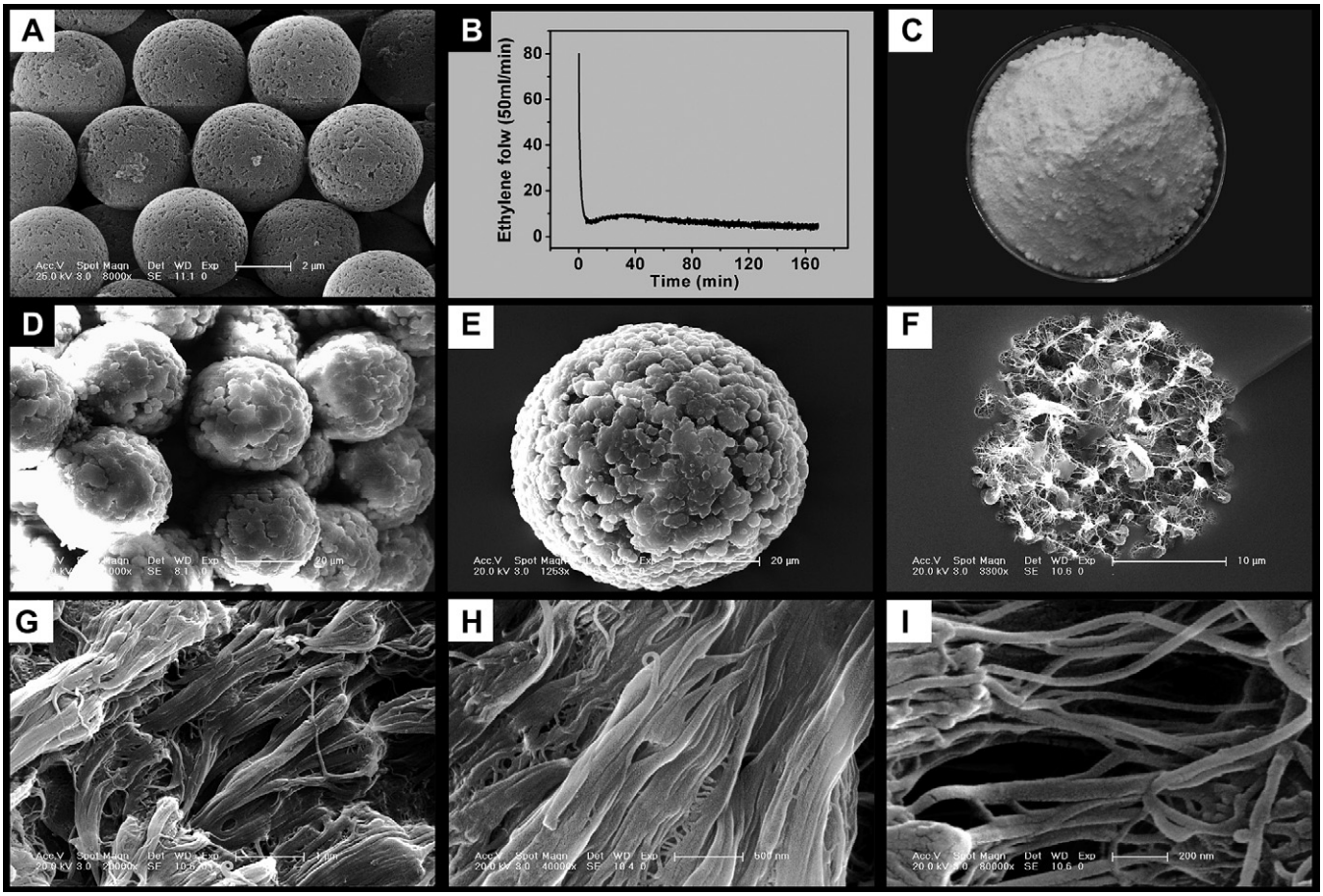

Fig. 1. (A) SEM image of poly(St-*co*-DVB-*co*-AN). (B) Ethylene consumption versus polymerization time for a representative polymerization run. (C) A photo of polyethylene powder obtained from a typical polymerization. (D and E) SEM images of a typical product bead. (F) Cross-section morphology of a typical product bead. (G to I) Internal fibrous morphology of a typical product bead.

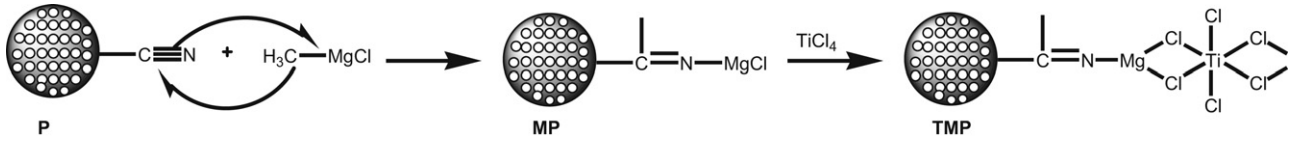

Scheme 2. Sequential functionalization of monodisperse cyano-functionalized porous polymeric beads with (i) CH_3MgCl, (ii) $TiCl_4$.

Table 1
Results of ethylene polymerization and DSC and GPC analysis of polyethylene.

Polymerization conditions[a]						Polymerization results			DSC results		GPC results	
Run	Catalyst bead (mg)	Al/Ti (mol/mol)	T/°C	P/atm	t/min	Yield/g	Act.[b]	Bulk density in g/ml	T_{m1}[c]/°C	T_{m2}[d]/°C	M_w[e]	PDI
1*	35	100	50	5	30	12.8	89	0.29	141.8	136.9	170,000	2.7
2	33	100	50	5	30	12.4	91	0.31	143.2	137.9	122,700	2.5
3	10	300	50	10	30	10.4	127	0.28	141.3	136.0	116,300	2.3
4	10	300	50	5	60	13.4	164	0.34	142.7	135.9	128,300	2.3
5#	43	300	60	5	120	160.6	229	0.40	145.0	137.0	125,400	2.3

[a] Polymerization condition: in a 0.1 L autoclave, 60 ml hexane (*in toluene; #in a 1 L autoclave, 500 ml hexane).
[b] Catalyst activity is measured in g (mmol Zr)$^{-1}$ h^{-1} (atm ethylene)$^{-1}$.
[c] first melt of DSC scan.
[d] Second melt of DSC scan.
[e] Weight-average molecular weight (M_w): g (mol PE)$^{-1}$.

starting poly(St-*co*-DVB-*co*-AN) beads. This finding implies that each polymer particle results from the polymerization of an individual catalytic bead [10]. The size of the product beads depends on the reaction time; beads produced by longer reaction time exhibited correspondingly greater radii. The size of the product beads can even be calculated from the ethylene uptake curve. All these results lead to the considerable proof of the formation of polyethylenes on porous polymer supported catalyst beads and no leaching of catalyst from the support into solution occurred. To confirm that, the analysis of Ti content of hexane solution part after aging the catalyst at 50 °C for 1h was performed by ICP [24]. It was found that no Ti was detected in the hexane medium, which gave a proof of no leaching of the catalyst in this polymerization system.

The most exciting result is that the product polymers were filled with polyethylene nanofibers throughout the whole sphere which can be observed by further magnifying the cross-section of the product bead (Fig. 1G–I). This reminds us of extrusion polymerization proposed by Aida ten years ago [9]. That is to say, the chain growth can be restrained by the pores existed in porous polymer support in a certain direction as the mesoporous silica fiber used by Aida. The difference between two supports is the uniformity of pore structure, which is disordered in poly(St-*co*-DVB-*co*-AN) and ordered in mesoporous silica fiber. This difference resulted in the difference uniformity and orderliness of the obtained fibers. Nevertheless, the generation mechanism of nanofibers should be similar to each other. Taking into account the overall morphology of product polymer, the porous polymer support played as a template in two levels. One level is the whole support beads [25], which resulted in the porous polyethylene spheres. Another level is the porous structure in the support beads, which played as a nanoreactor and resulted in the nanofiber structure in the polyethylene spheres. On the basis of above ideas, we proposed a conceptual scheme for the growth of porous polyethylene spheres with nanofiber structure by porous polymer support-assisted extrusion polymerization (Scheme 1). From the conceptual scheme we can image what had happened in the polymerization. The catalyst sites distributed throughout the whole support beads began to catalyze ethylene when the ethylene gas was led in. With the continuous chain growth the catalyst beads became bigger gradually because of the expansion existed in the catalyst beads and external growth by the active sites in the outer surface. It is easy to know that the catalyst beads must be broken by the expansion exist in the catalyst beads, although the product beads maintained a whole sphere structure all the time. That is to say the porous polymer support is not as firm as mesoporous silica fiber. And this soft polymer support will further result in quick chain termination. That is why the molecular weights of our product polymer are much lower than that of the Aida's. In fact, as far as we know, the reason why the molecular weight of polymer catalyzed by polymer supported catalyst is often lower than that of polymer catalyzed by inorganic supported catalyst can partially be ascribed to the lower firmness of the polymer supports than that of the inorganic materials. This should be an urgently desirable problem to be solved in polymer supports.

The fragile support will result in another problem, why the expanding, and probably also fragmenting polymer substrate should confine the PE to form nanofibers with diameter of 20–80 nm, mainly of 30–50 nm? The reason is that our porous support has a hierarchical pore structure (See Electronic Supplementary Material, Fig. S2). We all know that larger pores have bigger pore surface area than the smaller ones, and will be located with more active sites. This will further lead to a result that the larger pores fragment easily during ethylene polymerization. So it is reasonable to conclude that the smaller pores in the support mainly served as nanoreactor, while the larger pores in the support mainly provided prerequisites for disintegrating and expansion of PE microspheres.

An appealing feature of this polymer supported catalyst is its versatility. Functional versatility is expressed in the ability to obtain directly micron-size porous polyethylene spheres with nanofiber structure. The present method, using poly(St-*co*-DVB-*co*-AN) as a support, may be widely applied to other catalyst system because of the little destructive interaction and the easily to be functioned merit of the polymer support. Moreover, the use of polymer support of different architectures as templates for polymerization is expected to provide common polymers with some new bulk properties.

Acknowledgments

This work was supported by The National Natural Science Foundation of China for project No. 20934006.

Appendix. Supplementary material

Experimental procedures and spectral data. This material is available free of charge via the Internet at http://pubs.acs.org.

References

[1] Vriezema DM, Aragones MC, Elemans J, Cornelissen J, Rowan AE, Nolte RJM. Chem Rev 2005;105:1445–89.
[2] Nevell TP. Cellulose chemistry and its applications. New York: Halsted; 1985 [chapter 2].
[3] Monteiro MJ. Macromolecules 2010;43:1159–68.
[4] Vriezema DM, Garcia PML, Oltra NS, Hatzakis NS, Kuiper SM, Nolte RJM, et al. Angew Chem Int Edit 2007;46:7378–82.
[5] Milliron DJ, Caldwell MA, Wong HSP. Nano Lett 2007;7:3504–7.
[6] Li J, Zeng HC. Angew Chem Int Ed 2005;44:4342–5.
[7] Han BH, Polarz S, Antonietti M. Chem Mater 2001;13:3915–9.
[8] Stein A, Melde BJ, Schroden RC. Adv Mater 2000;12:1403–19.
[9] Kageyama K, Tamazawa J, Aida T. Science 1999;285:2113–5.
[10] Roscoe SB, Frechet JMJ, Walzer JF, Dias AJ. Science 1998;280:270–3.
[11] Nam JB, Ryu JH, Kim JW, Chang IS, Suh KD. Polymer 2005;46:8956–63.
[12] Kaur S, Singh G, Gupta VK. J Polym Sci Pol Chem 2008;46:7299–309.
[13] Mori H, Ohnishi K, Terano M. Macromol Rapid Commun 1996;17:25–9.
[14] Mteza SB, Hsu CC, Bacon DW. J.Polym Sci Pol Chem 1996;34:1693–702.
[15] Bochkin AM, Pomogailo AD, Dyachkovskii FS. React Polym 1988;9:99–107.
[16] Huang R, Malizia F, Pennini G, Koning CE, Chadwick JC. Macromol Rapid Commun 2008;29:1732–8.
[17] Sobota P. Polym-Plast Technol 1989;28:493–510.
[18] Karol FJ. Catal Rev 1984;26:557–95.
[19] Soga K, Ohnishi R, Doi Y. Polym Bull 1983;9:299–304.
[20] da Silva AA, Alves MDM, dos Santos JHZ. J Appl Polym Sci 2008;109: 1675–83.
[21] Pullukat TJ, Hoff RE. Catal Rev 1999;41:389–428.
[22] Turunen JPJ, Haukka M, Pakkanen TT. J Appl Polym Sci 2004;93:1812–5.
[23] Galland GB, de Souza RF, Mauler RS, Nunes FF. Macromolecules 1999; 32:1620–5.
[24] Musikabhumma K, Uozumi T, Sano T, Soga K. Macromol Rapid Commun 2000; 21:675–9.
[25] Mackie P, Berger MN, Grieveso BM, Lawson DJ. Polym Sci Pol Lett 1967; 5:493–4.

Polymer 52 (2011) 606–616

Contents lists available at ScienceDirect

Polymer

journal homepage: www.elsevier.com/locate/polymer

Functional biohybrid materials synthesized via surface-initiated MADIX/RAFT polymerization from renewable natural wood fiber: Grafting of polymer as non leaching preservative

Damien Tastet [a,b], Maud Save [a,b,*,1], Fatima Charrier [c], Bertrand Charrier [c], Jean-Bernard Ledeuil [a,d], Jean-Charles Dupin [a,d], Laurent Billon [a,b,*]

[a] IPREM, UMR 5254, CNRS, Université de Pau et des Pays de L'Adour, Technopole Helioparc, 2 Avenue P. Angot, 64053 Pau Cedex 9, France
[b] Equipe de Physique et Chimie des Polymères (EPCP), IPREM, CNRS, UPPA, 64053, France
[c] Sylvadour, IUT des Pays de l'Adour, Université de Pau et des Pays de L'Adour, 40 004 Mont de Marsan Cedex, France
[d] Equipe de Chimie Physique (ECP), IPREM, CNRS, UPPA, France

ARTICLE INFO

Article history:
Received 9 November 2010
Received in revised form
20 December 2010
Accepted 21 December 2010
Available online 30 December 2010

Keywords:
Controlled radical polymerization
Wood fibers
Surface modification

ABSTRACT

Crude wood fibers represent a wide class of renewable resources. The surface modification of such materials via covalent grafting of polymer offers new surface properties with non-leaching coating. The grafting of the polymer chains was achieved by surface-initiated controlled radical polymerization through a grafted xanthate chain transfer agent. Macromolecular design via interchange of xanthate (MADIX) technique was chosen to graft poly(vinyl acetate), polystyrene, poly(*n*-butyl acrylate) and poly (4-vinylbenzyl chloride)-polystyrene amphiphilic cationic copolymers. Water contact angle measurements highlighted the hydrophobization of the wood fiber surface with a nanoscaled polymer monolayer indicating the appropriate coverage of the fiber. X-ray photoelectron spectroscopy showed the successful grafting of the polymer after drastic washing procedure. The quaternization of the grafted polystyrene-*co*-poly(4-vinyl benzyl chloride) copolymers with tertiary amine allows the introduction of biocide quaternary ammonium functions while preserving the hydrophobic character of the modified wood fiber when introducing a long alkyl chain in the statistical copolymer. Finally, the cationic copolymer was subjected to *Coniophora Puteana* to evaluate its propensity to limit the fungi expansion.

1. Introduction

Surface treatment of renewable resources is known to improve the characteristic values of biocomposites by introducing new surface properties [1,2] or by favoring dispersion in a polymeric matrix [3]. In the context of wood development, we are concerned with tuning the surface properties of natural wood fibers by grafting polymer chains from the fiber surface. We aim to covalently attach the polymer in order to prevent any leaching of the coating, an important issue for environmental concerns. The grafting of hydrophobic polymer chains will contribute to the preservation of the wood fibers against external stress (humidity, fungi…) and the introduction of additional biocidal functions inside the polymer chains should bring benefit to the coating.

Surface-initiated controlled radical polymerization (SI-CRP) has proved to be a powerful method to graft polymer chains from a wide variety of surfaces (for example, silica nanoparticles [4], silicon wafer [5], ordered mesoporous silica [6,7], metallic surface [8], magnetic nanoparticles [9], carbon nanotubes [10,11], and polymer films [12,13]). The combination of "grafting from" and controlled radical polymerization techniques produces grafted polymer chains with controlled length exhibiting a high grafting density thanks to the simultaneous growth of polymer chains from the surface [14,15]. Since the first SI-CRP performed from a polysaccharide [16], many studies were devoted to SI-CRP of various polymers from pure cellulose fibers or Whatman filter paper as substrates, either by atom transfer radical polymerization (ATRP) [1,2,17–23] or by reversible addition fragmentation transfer (RAFT) [24–29] process through dithiobenzoate-based chain transfer agents. Recent reviews devoted to the modification of polysaccharide through controlled radical polymerization grafting highlights the interest of such strategy to generate high performance biohybrid materials [30,31].

* Corresponding authors. Equipe de Physique et Chimie des Polymères (EPCP), IPREM, CNRS, UPPA, 64053, France.
E-mail addresses: maud.save@univ-pau.fr (M. Save), laurent.billon@univ-pau.fr (L. Billon).
[1] Tel.: +33 540175014.

0032-3861/$ – see front matter © 2011 Elsevier Ltd. All rights reserved.
doi:10.1016/j.polymer.2010.12.046

Herein, we present the surface modification of renewable raw wood fibers still containing cellulose and lignin derivatives. The polymer grafting is performed by SI-CRP through macromolecular design via interchange of xanthate (MADIX) process [32,33]. MADIX process is based on a reversible addition fragmentation transfer equilibrium involving xanthate agents, less colored species that dithiobenzoate-based chain transfer agents. Xanthates proved to be efficient chain transfer agents (CTA) to control the polymerization of a wide class of vinylic monomers such as styrenic [34,35], alkyl acrylates [36] and especially vinyl esters [37–42]. Indeed, xanthates are the only appropriate CTA to control the RAFT polymerization of vinyl acetate [37–42]. For the purpose of this work, the wood fibers are derivatized to introduce the chain transfer agent via the R-group [43] (see Scheme 1). The radicals are then created on the surface of the wood fibers by transfer reactions [44], which allows the growing of the polymer chains from the fiber surface. The straightforward attachment of the xanthate agent was performed in two simple steps using low cost commercially available reagents. The intermediate alkyl bromide was not used for ATRP polymerization to avoid both the use of amine-based ligands and the additional purification step for copper catalyst removal. For all the above mentioned reasons, MADIX polymerization was chosen for the present study for the surface-initiated polymerization of the selected styrenic, acrylic and vinyl ester monomers. Only one study previously reported the MADIX polymerization of VAc initiated from a soluble polysaccharide backbone (hydroxypropyl cellulose) using a xanthate agent grafted via the Z group [42].

The present work is devoted to the grafting of poly(vinyl acetate) (PVAc), poly(butyl acrylate) (P*n*BA), polystyrene (PS) and cationic amphiphilic PS-based copolymers from the raw wood fibers. P*n*BA and PVAc rise interest for their adhesive properties [45,46] whereas PS and cationic amphiphilic copolymers are known respectively for their hydrophobic character and biocide activity. The macromolecular features of the free chains are explored to assess the level of polymerization control. The fiber surface is analyzed by X-ray photoelectron spectroscopy to prove the success of the chemical surface modification. Finally, the properties of the polymer-grafted wood fibers are investigated in terms of wettability and the effect of the synthesized cationic polymer onto a fungi growing is studied. To the best of our knowledge, this is the first report of grafting polymer chains by controlled radical polymerization initiated from natural wood fibers which were not submitted to the delignification process.

2. Experimental section

2.1. Materials

Vinyl acetate (VAc, Sigma Aldrich, 99%), styrene (St, Sigma Aldrich, 99%) and 4-vinylbenzyl chloride (VBC, Sigma Aldrich, 90%) were purified through an inhibitor removal column (Sigma Aldrich). Pyridine (ABCR, 99%), acetone (Xilab, reagent grade) and toluene (Sigma Aldrich, 99.7%) were dried with molecular sieves (Aldrich, 4 Å pore diameter). 2,2′-azobis(isobutyronitrile) (AIBN, Acros, 99%), ethyl-2-bromopropionate (EBP, Fluka, 98%), 2-bromo-propionyl

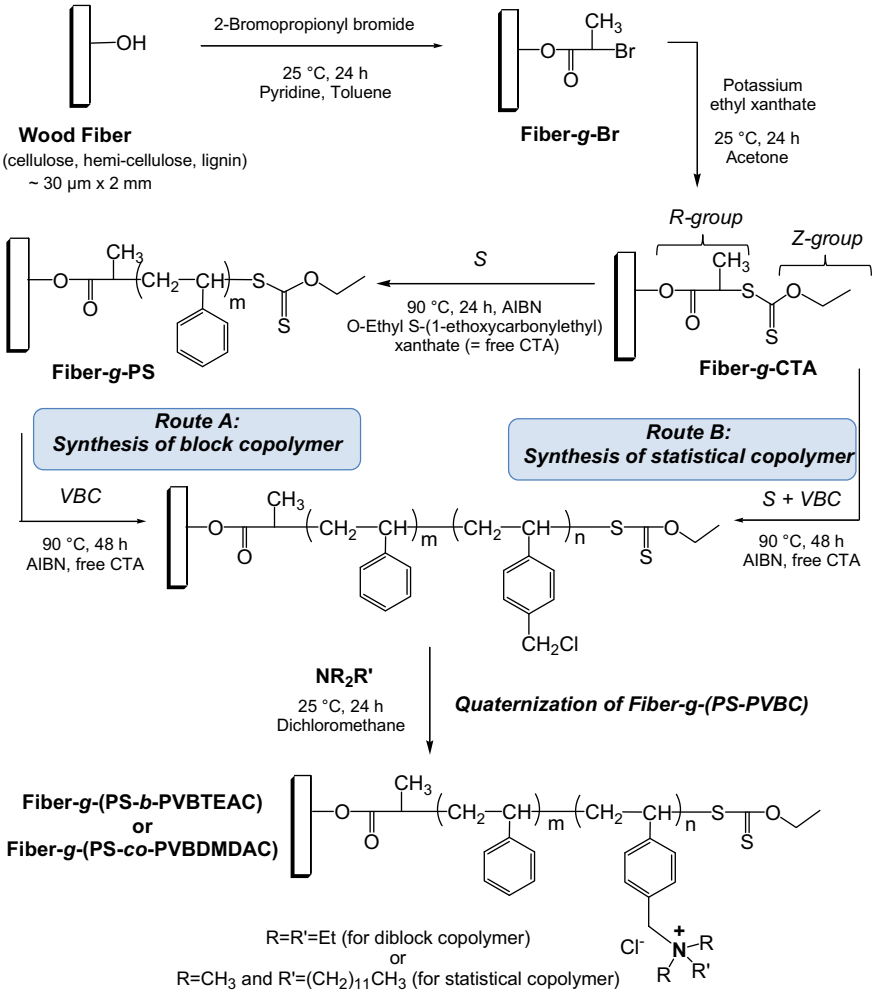

Scheme 1. General scheme for the synthesis of polymer grafted wood fibers by surface-initiated MADIX/RAFT polymerization.

bromide (BrPBr, ABCR, 97%), *O*-ethyl xanthic acid potassium salt (ABCR, 98%), triethylamine (Sigma Aldrich, 99%), *N*,*N*′-dimethyldodecylamine (ABCR, 90%), malt (Biokar Diagnostics, Bacteriological Malt Extract), agar–agar (Merck, Microbiological use) were used as received. Pinus Maritimus natural fibers (Finsa Mediland) were used as wood fibers with average size of 20–40 μm of diameter × 2–3 mm length (see optical microscopy in Supplementary data, Fig. SI-1). The fibers were approximately composed of 75 wt-% of cellulose and hemicelluloses and 25 wt-% of lignin. The crude wood fibers were washed by Soxhlet extraction with successively acetone, methylene chloride and methanol and dried at room temperature.

2.2. Synthesis

2.2.1. Synthesis of O-ethyl S-(1-ethoxycarbonylethyl) xanthate as chain transfer agent (CTA)

The synthesis of the molecular chain transfer agent was adapted from the procedure described in reference [38]. The bromide precursor (EBP, 3 g, 1.6×10^{-2} mol) was diluted in acetone (25 mL) previously dried with molecular sieves and stirred with a 1.5-fold excess of *O*-ethyl xanthic acid potassium salt (4 g, 2.5×10^{-2} mol) for 24 h at room temperature. The suspended salts were filtered off and washed several times with chloroform. The yellow solid was recovered after evaporation of the solvent under vacuum.

^{1}H NMR: 7.26 (s, CDCl3), 4.64 (q, 2H, −C(=S)−O−C*H*$_2$−R), 4.38 (q, 1H, −C(=O)−C*H*−S−), 4.19 (q, 2H, −C(=O)−O−C*H*$_2$−R), 1.58 (d, 3H, −C(=O)−CH(C*H*$_3$)−S−), 1.41 (t, 3H, −C(=S)−O−CH$_2$−C*H*$_3$), 1.28 (t, 3H, −C(=O)−O−CH$_2$−C*H*$_3$). Yield: 85%.

2.2.2. Synthesis of bromide grafted fibers (Fiber-g-Br)

Pine fibers (6.6 g) were immersed into a basic aqueous solution (NaOH 2 M) for 24 h at room temperature. The fibers were first repeatedly washed by Soxhlet extraction with methanol until neutral pH, then dried and kept at room temperature. The pretreated fibers (4.11 g) were then immersed in toluene (280 mL) containing pyridine (12.4 mL, 0.153 mol). The 2-bromo-propionyl bromide (5.5 mL, 0.052 mol) was added dropwise to the heterogeneous mixture kept at 0 °C in a water/ice bath for 1 h. The temperature was raised to room temperature and the reaction proceeded for 23 h. Fibers are cleaned of the yellowish precipitate by rinsing them by Soxhlet extraction with methanol for 10 h (30 cycles). The obtained Fiber-*g*-Br were dried and kept at room temperature. The results of elemental analysis are reported in Supplementary data.

2.2.3. Immobilization of xanthate onto wood fibers (Fiber-g-CTA)

The Fiber-*g*-CTA were obtained by mixing Fiber-*g*-Br (3.9 g) with *O*-ethyl xanthic acid potassium salt in a large excess (0.63 g, 3.9 mmol) in dry acetone. The mixture was stirred at room temperature overnight and the Fiber-*g*-CTA were washed by soxhlet extraction with methanol for 10 h (30 cycles). The results of elemental analysis are reported in Supplementary data.

2.3. Polymerization

2.3.1. Free-radical polymerization of styrene in the presence of crude wood fibers

The effect of the presence of crude fibers on the free-radical polymerization of styrene was here investigated as follows: PS was synthesized in bulk, using AIBN as initiator (with concentrations between 0 and 0.04 mol L^{-1}), in presence or absence of pretreated wood fibers (1 wt-% versus the monomer). The solution was degassed by nitrogen bubbling for 20 min at 0 °C. The sealed flask was immersed into a thermostated oil bath and the polymerization was carried out at 90 °C for 6 h. At the end, a part of the crude solution was withdrawn and poured into deuterated chloroform for proton NMR analysis in order to determine the final monomer conversion (see more details in Supplementary data).

2.3.2. Grafting of PS, PVAc, PBA and PS-stat-PVBC statistical copolymer via surface-initiated MADIX polymerization from Fiber-g-CTA

All the experiments were carried out with a similar procedure and the following example concerns the experiment 4 of Table 2. The Fiber-*g*-CTA (0.51 g, 1 wt-% versus the monomer) were mixed with styrene (50 g, 0.418 mol), *O*-Ethyl S-(1-ethoxycarbonylethyl) xanthate (0.72 g, 3.2×10^{-3} mol) and AIBN (0.051 g, 3.1×10^{-4} mol). The flask was sealed with a rubber septum, degassed by nitrogen bubbling for 30 min at 0 °C and immersed into an oil bath at 90 °C. The reaction was stopped after 24 h by cooling the flask in an ice bath and the contents were exposed to air. A part of the crude solution was withdrawn to measure the monomer conversion by proton NMR (see Supplementary data). The rest of the mixture was solubilized in THF and the Fiber-*g*-PS were separated from the free chains by soxhlet extraction with methylene chloride for 10 h (50 cycles). The free PS chains were precipitated into methanol and characterized by SEC.

2.3.3. Chain extension of VBC via surface-initiated MADIX polymerization from Fiber-g-PS

The Fiber-*g*-PS (0.2 g, 1 wt-% versus the monomer) were mixed with vinylbenzyl chloride (20 g, 0.13 mol), *O*-Ethyl S-(1-ethoxycarbonylethyl) xanthate (0.073 g, 3.2×10^{-4} mol) and AIBN (0.012 g, 7.2×10^{-5} mol). The flask was sealed with a rubber septum, degassed by nitrogen bubbling for 20 min at 0 °C and immersed into an oil bath at 90 °C for 48 h. The monomer conversion was calculated by proton NMR of the crude solution (see Supplementary data). The Fiber-*g*-(PS-*b*-PVBC) were washed as described for PS grafted fibers and the free PVBC chains were precipitated into methanol before SEC analysis.

2.4. Aging experiments

The Fiber-*g*-PS (expt 4, Table 2) were placed in an oven at 40 °C with 80% of relative humidity for 3 months. The Fiber-*g*-PS were thoroughly washed by soxhlet extraction using dichloromethane for 10 h and dried before contact angle measurement.

2.5. Quaternization of PS-b-PVBC, PS-stat-PVBC, Fiber-g-(PS-b-PVBC) and Fiber-g-(PS-stat-PVBC)

The quaternization of PS-PVBC free chains was performed according to the recipe described in reference [47]. The quaternization of both Fiber-*g*-(PS-*b*-VBC) (0.1 g) and Fiber-*g*-(PS-*stat*-VBC) (0.1 g) was performed in methylene chloride at room temperature for 24 h, respectively with a large excess of triethylamine (1.65 g, 1.6×10^{-2} mol) and dimethyldodecylamine (0.27 g, 1.3×10^{-3} mol) to obtain Fiber-*g*-(PS-*b*-VBTEAC) and Fiber-*g*-(PS-*stat*-PVBDMDAC) (with VBTEAC for vinylbenzyltriethylammonium chloride and VBDMDAC for vinylbenzyldimethyldocecylammonium chloride). After modification these two types of fibers were washed by soxhlet extraction with methanol for 10 h (30 cycles) and dried at room temperature.

2.6. Study of fungi growing

Tests of durability were carried out using radial growth of the *Coniophora puteana* reference fungi sown on different culture media. Culture media were prepared in Petri dishes. In each nutritive medium, made up from a malt-agar mixture (40 g of malt and

20 g of agar–agar dissolved in 1 L of distilled water), the PVBTEAC polymer was introduced at different concentrations (0.5, 1 and 2 wt-% with regard to the medium weight). These concentrations were selected according to traditional tests on wood biocides (EN 350 and EN 113). After medium sterilization for 20 min at 120 °C in an autoclave, the medium was poured into different Petri dishes (five replicates at each concentration) and a small sample of *C. puteana* was introduced in the center of each Petri sample. Then samples were placed at 25 °C and 70% of relative humidity for 20 days. The fungi growth surface area was measured during the test for each polymer concentration as presented in Fig. 9.

2.7. Instrumentation

2.7.1. Nuclear Magnetic Resonance (NMR) spectroscopy

Proton NMR spectra were recorded in deuterated chloroform as solvent using a Brüker 400 MHz spectrometer at 25 °C.

2.7.2. Size Exclusion Chromatography (SEC)

The free polymer chains were analyzed at 30 °C with THF as eluent at a flow rate of 1 mL min^{-1}. The SEC system was equipped with three Waters Styragel columns HR 0.5, 2, 4 working in series (separation range 1×10^2–3×10^6 g mol^{-1}) and a refractive index detector ERC 7515-A. Number-average molar molecular weight (M_n) and dispersity (M_w/M_n) of polymers were calculated from a calibration derived from PS standards. For PVAc and PBA the M_n value was corrected according to the Mark–Houwink parameters of PS and PVAc or PBA in THF at 25 °C ($K_{PS} = 14.1 \times 10^{-5}$ dL g^{-1}, $\alpha_{PS} = 0.70$; $K_{PVAc} = 16 \times 10^{-5}$ dL g^{-1}, $\alpha_{PVAc} = 0.70$, $K_{PBA} = 12.2 \times 10^{-5}$ dL g^{-1} and $\alpha_{PBA} = 0.70$) [48–50]. All polymers samples were prepared at 1–5 g L^{-1} concentrations and filtered through PVDF 0.45 μm filters.

2.7.3. Optical microscopy

Pictures were taken in reflection with a Leica DM/LM microscope equipped with × 20 optic and a Leica DFC280 video camera. The regular image treatments were performed with the Image Manager IM50 software.

2.7.4. Scanning electron microscopy (SEM)

The surface morphology of the fiber samples was observed, after gold metallization, by SEM using HIROX SH-3000 microscope, operated at an accelerating voltage of 15 kV.

2.7.5. Fourier Transform Infrared (FTIR)

Spectra were recorded in transmission, from KBr pellets at room temperature, using a NICOLET Magna-IR560 Fourier Transform Infrared Spectrometer.

2.7.6. Elemental analysis (EA)

Samples were analyzed for C, N, Br, S and Cl content by the Service Central d'Analyse of the Centre National de la Recherche Scientifique in Solaize (France).

2.7.7. Static contact angle (CA) measurements

Measurements were conducted on a TECLIS Tracker instrument equipped with a 55 mm Telecentric camera using 5 μL droplets of deionized water. The fiber pellets of 10–40 mg (or double-layer pellets–Fig. 6) were prepared by pressing the fibers (or two pellets for Fig. 6) at 4 tons using a press. The water contact angles were determined on the pictures recorded at various interval times using the Windrop 1.9 software.

2.7.8. X-ray photoelectron spectroscopy (XPS)

XPS measurements were performed on a Thermo K-alpha spectrometer with a hemispherical analyzer and a microfocussed (analysis area was *ca.* 400 μm^2) monochromatized radiation (AlKα, 1486.6 eV) operating at 72 W under a residual pressure of 1×10^{-9} mbar. The pass energy was set to 20 eV. Charge effects were compensated by the use of a dual beam charge neutralization system (low energy electrons and Ar + ions) which had the unique ability to provide consistent charge compensation. All the neutralizer parameters remained constant during analysis and allow ones to find a 285.0 eV C1s binding energy for adventitious carbon. Spectra were mathematically fitted with Casa XPS software using a least squares algorithm and a non-linear baseline. The fitting peaks of the experimental curves were defined by a combination of Gaussian (70%) and Lorentzian (30%) distributions.

3. Results and discussion

3.1. Effect of the crude wood fibers on free-radical polymerization of styrene

The crude wood fibers used for this study contain roughly 25% of lignin and 75% of cellulose and hemicelluloses. Lignin is known to present complex tridimensional polyphenolic structures which depend on the origin of vegetable source [51]. Deffieux et al. [52] studied the effect of model lignin derivatives on radical polymerization processes. It was shown that lignin derivatives can act as both inhibitor and chain transfer agent for free radical polymerization of methyl methacrylate [52]. Therefore, we investigated the influence of 1 wt-% (versus monomer) of the crude wood fibers on the free radical polymerization of styrene by varying the concentration of AIBN initiator. We compared the final styrene conversion after 6 h of polymerization performed at 90 °C in the presence or in the absence of the crude wood fibers (see Fig. 1). From the results of Fig. 1, it is possible to conclude that a concentration of *ca.* 5×10^{-3} M is sufficiently high to overcome the inhibiting effect of the lignin contained in the 1 wt-% of crude wood fibers. The macromolecular features of the PS chains obtained by radical polymerization of styrene with or without crude wood fibers in the medium are reported in Table 1. The slight decrease of the number-average molar mass with the increase of the dispersity reveals the occurrence of few irreversible transfer reactions with the ligno-cellulosic fibers.

3.2. Immobilization of chain transfer agent onto wood fibers (Fiber-g-CTA)

To enable grafting of the xanthate group acting as chain transfer agent for the MADIX process, the available surface hydroxyl groups of the wood fiber were first esterified by reaction with 2-bromopropionyl bromide as described in the experimental part. Infrared spectroscopy analysis of the modified fibers, carefully cleaned by solvent extractions, revealed the success of the grafting by the appearance of a peak at 1744 cm^{-1} corresponding to the ester group vibration (see Fig. 2).

The elemental analysis (see Table SI-1 in Supplementary data) of the Fiber-*g*-Br confirmed the presence of 0.8% of Br. The low bromine amount correlated to the low absorbance of the ester band in FTIR is in accordance with the low specific area ($\sim$0.1 m^2 g^{-1}) of the wood fibers exhibiting anisotropic shape of approximately 20–40 μm width and 2–3 mm long (see Fig. SI-1) associated with the hydrogen bonding between hydroxyl groups decreasing their reactivity. Investigation of various experimental conditions by increasing time, temperature and BrPBr concentration did not improve the yield of esterification. The xanthate group was introduced onto the wood fibers by a nucleophilic substitution between the Fiber-*g*-Br with potassium ethyl xanthate as displayed in Scheme 1. The elemental analysis of the Fiber-*g*-CTA showed the introduction of sulfur atoms (0.4%) with the concomitant decrease

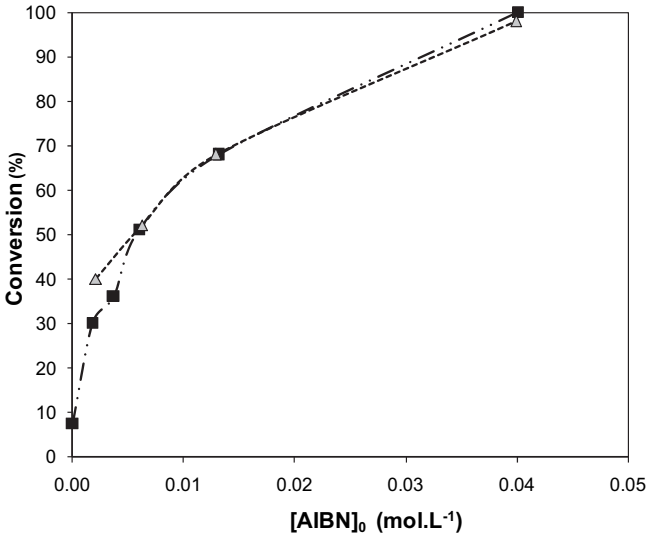

Fig. 1. Monomer conversion as a function of initial AIBN concentration for styrene free radical polymerization carried out in bulk at 90 °C for 6 h either in the presence (squares) or in the absence (triangles) of crude wood fibers (1 wt-% of fibers versus S).

Table 1
Stable free radical polymerization of styrene: effect of the presence of crude wood fibers.[a]

Wt-% Fiber	$M_{n,SEC}$ g mol^{-1}	M_w/M_n
0	47 780	4.4
1	34 445	4.9

[a] The polymerization was carried out at 90 °C in bulk ([St]$_0$ = 8.7 mol L^{-1}) with [AIBN]$_0$ = 4.0 × 10^{-2} mol L^{-1}.

of bromine atom content (<0.2%, see Table SI-1 in Supplementary data). These results were confirmed by the X-ray photoelectron spectroscopy (XPS) analysis of both Fiber-*g*-Br and Fiber-*g*-CTA. Indeed, the presence of a Br3d peak corresponding to the binding energy (70.6 eV–71.6 eV) of bromine [53] atoms is present in the XPS spectrum of Fiber-*g*-Br as displayed in Fig. 3A. The Br3d peak disappeared after the substitution step with *O*-ethyl xanthic acid potassium salt (Fig. 3B, XPS of Fiber-*g*-CTA) whereas a S2p core level doublet characteristic of sulfur atoms bonded to carbon (163.8 eV–165.0 eV) was observed in the XPS spectrum of Fiber-*g*-CTA (Fig. 3D) [54]. On the high energy side of the same spectrum (Fig. 3D and 168.6 eV–169.8 eV) [55], a small doublet (~7 atomic % of the whole sulfur content) already found in the *O*-ethyl xanthic acid potassium reagent is even observed. This component has been attributed to sulfate pollution traces of the commercial *O*-ethyl xanthic acid potassium. One of the important issues in XPS analysis of polymers is sample degradation. It is indeed well known that some polymers can be degraded by X-ray exposure [53]. In fact this degradation comes from the secondary electrons emitted during the X-ray exposure. In most of the cases this degradation is slow enough not to change the composition of the sample during the analysis but undergoes only by the reduction of the oxidation state of some elements [53]. In the present study, as generally observed for halogen element analysis, a bromine reduction effect occurs during the XPS electronic process leading to the rise up of a new doublet (marked with an asterisk in Fig. 3A) associated with high negative bromine (68.3 eV–69.3 eV).

3.3. Surface-initiated MADIX/RAFT polymerization from the modified wood fibers

3.3.1. Homopolymerization of VAc, BA or St from Fiber-g-CTA

Grafting of poly(vinyl acetate) (PVAc), poly(*n*-butyl acrylate) (P*n*BA) and polystyrene (PS) homopolymers was performed by immersing the xanthate-modified wood fibers into a mixture containing the monomer, the initiator (AIBN) and the free chain transfer agent (*O*-Ethyl S-(1-ethoxycarbonylethyl) xanthate) (see Scheme 1). Free CTA was added to enhance the control of the polymerization of both grafted and free polymer chains [44]. In addition, the presence of free chains enabled us to monitor the macromolecular features of the growing chains which can be considered similar to the grafted chains as described in the published studies devoted to surface-initiated controlled radical polymerization from inorganic substrates

Table 2
Surface-initiated MADIX polymerization of vinyl acetate, styrene, *n*-butyl acrylate and 4-vinylbenzyl chloride from modified wood fibers.

Entry	Initial Fiber	Monomer	Time h	Conv. %	[M]$_0$ mol L^{-1}	[CTA]$_0$ mol L^{-1}	[AIBN]$_0$ mol L^{-1}	Free polymer chains				Final fiber
								M_n theo [a] g mol^{-1}	M_n SEC [b] g mol^{-1}	M_w/M_n	F [c]	
1	Fiber-*g*-CTA	VAc [d]	15.5	82	10.8	2.2 × 10^{-2}	6.0 × 10^{-3}	32 920	32 500	1.82	1.01	Fiber-*g*-PVAc
2	Fiber-*g*-CTA	VAc [d]	16	86	10.8	5.8 × 10^{-2}	6.1 × 10^{-3}	13 680	16 150	1.76	0.85	Fiber-*g*-PVAc
3	Fiber-*g*-CTA	St [e]	24	63	8.7	2.5 × 10^{-2}	6.1 × 10^{-3}	20 130	33 700	1.85	0.60	Fiber-*g*-PS
4	Fiber-*g*-CTA	St [e]	24	60	8.7	4.7 × 10^{-2}	5.6 × 10^{-3}	11 030	25 000	1.64	0.44	Fiber-*g*-PS
5	Fiber-*g*-CTA	St [e]	23.3	66	8.7	2.3 × 10^{-1}	9.8 × 10^{-3}	2720	6000	1.90	0.45	Fiber-*g*-PS
6	Fiber-*g*-CTA	*n*BA [f]	7.5	95	3.5	6.1 × 10^{-2}	3.6 × 10^{-3}	7070	8000	1.94	0.88	Fiber-*g*-P*n*BA
7	Fiber-*g*-CTA	*n*BA [f]	7.0	95	3.5	1.8 × 10^{-2}	3.5 × 10^{-3}	22 770	20 600	2.10	1.10	Fiber-*g*-P*n*BA
8	Fiber-*g*-PS [g]	VBC [e]	46	27	7.0	2.3 × 10^{-2}	3.9 × 10^{-3}	11 590	28 550	2.18	/	Fiber-*g*-(PS-*b*-PVBC)
9	Fiber-*g*-CTA	VBC + St[e,h]	19	69	3.5 + 4.3	3.4 × 10^{-2}	6.5 × 10^{-3}	19 880	33 200	1.92	0.60	Fiber-*g*-(PS-*stat*-PVBC)

[a] Theoretical M_n calculated as follows: $M_n(\text{theo}) = M_{CTA} + [M_0]/[CTA]_0 + f_x[AIBN]_0 \times 1 - e^{-k_d t} \times \text{conversion} \times M_{monomer}$, with k_d the AIBN initiator dissociation rate constant ($k_{d,\ AIBN} = 5.5 \times 10^{-4}\ s^{-1}$ at 90 °C in styrene, $k_d = 9.4 \times 10^{-6}\ s^{-1}$ at 60 °C in ethyl acetate and $k_d = 3.6 \times 10^{-5}\ s^{-1}$ at 70 °C in ethyl acetate according to reference [77]) and *f* the initiator efficiency factor which could be considered as 0.6 for AIBN in bulk polymerization due to the cage effect.[78] [CTA]$_0$ corresponds to the initial concentration of free CTA, the number of moles of grafted CTA being negligible.

[b] M_n SEC corresponds to the experimental M_n measured by SEC of the free PS, PVAc, P*n*BA and PS-*stat*-PVBC polymers. For the synthesis of Fiber-*g*-(PS-*b*-PVBC), M_n SEC corresponds to the free PVBC chains.

[c] Efficiency of the free CTA: $F = M_n$ theo/M_n SEC = $[CTA]_{exp}/[CTA]_0$.

[d] Polymerization carried out at 60 °C.

[e] Polymerization carried out at 90 °C.

[f] Polymerization carried out at 70 °C in the presence of toluene.

[g] Fiber-*g*-PS from expt 4.

[h] The initial molar fraction of 4-vinylbenzyl chloride and styrene is 45:55 of VBC:S and the final composition of the copolymer is 51:49.

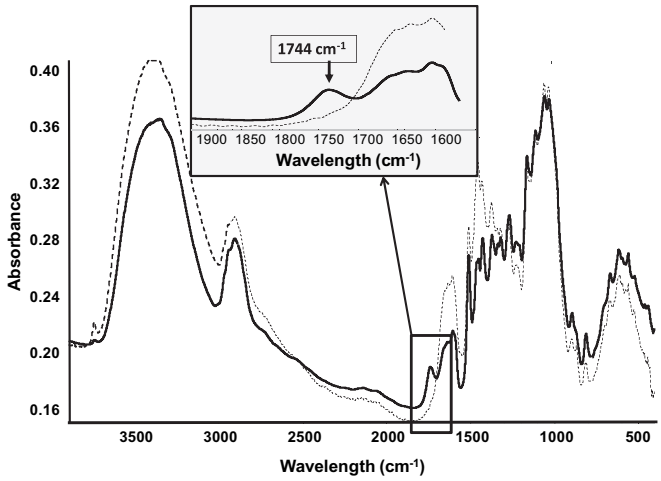

Fig. 2. FTIR spectra of the crude wood fibers (thin dashed line) and of the fibers modified by esterification (thick plain line, Fiber-*g*-Br, see Scheme 1).

[14,56–61]. Fukuda et al. [44] showed that the M_n of the graft (cleaved) polymer was very close to that of the free polymer, particularly if the RAFT-mediated graft polymerization of styrene initiated on silica particles was carried out in the presence of added free RAFT agent. The initial experimental conditions and the polymerization results of each experiment are gathered in Table 2. The number-average molar masses (M_n) of the free PVAc and P*n*BA chains match the theoretical molar masses for conversion above 80%. The higher value of the experimental M_n of the free PS chains compared to the theoretical ones at 60% of conversion is in accordance with a low chain transfer constant (C_{tr}) [62]. The chain transfer constant of the selected xanthate was determined by Adamy et al. [35] for styrene polymerization using both the Mayo and chain length distribution methods ($C_{tr} \sim 0.7$). As predicted by simulation and confirmed by experimental data [35], the low C_{tr} value of the xanthate chain transfer agent induces a broad molar mass distribution ($1.8 < Đ < 2.0$, see Table 2). Though the irreversible side reactions to lignin derivatives, which were described above for styrene conventional radical polymerization, might slightly affect the dispersity, the impact of the unmodified fibers was less pronounced for MADIX polymerization of styrene as shown by the results of Table SI-2 (Supplementary data). In spite of the low value of C_{tr}, MADIX is an efficient process with respect to tuning the final molar mass of the free chains. Hence the length of the grafted chains can be adjusted according to needs simply by varying the initial CTA concentration (see expts 1, 2, 3–5 and 6, 7, in Table 2, for comparison). SEM imaging of polystyrene grafted wood fibers exhibited a smoother surface in comparison with the initial crude wood fibers, as depicted in Fig. 4.

We studied the surface of the polymer grafted fibers by XPS analysis and the wettability of the modified wood fibers by contact angle (CA) measurements to confirm the chemical grafting of the polymer. It is important to note that all the polymer grafted fibers were carefully cleaned by soxhlet extraction to remove any ungrafted free polymer chains before further analysis (see details in the experimental part). As usually reported [63], the C1s spectrum of a polymer pattern can be precisely mathematically treated into the various chemical environments of carbon atoms (C–H, C–C, C–O, O–C=O…). In this study, the comparison of the XPS carbon signal of respectively the crude fiber, Fiber-*g*-PS and Fiber-*g*-(PS-*b*-PVBC) clearly revealed a global increase of the aliphatic carbon signal intensity (C_a, C1s binding energy (BE) = 285.0 eV) with a real decrease of the initial hydroxy-carbon signal (C_h, C1s binding energy (BE) = 286.5 eV) characteristic of the cellulosic units (see Fig. 5). This observation supports a homogeneous grafting of the polymer chains along the wood fiber with a final consequent I_a/I_h (aliphatic carbon/hydroxy-carbon) ratio up to 6.5 in the case of Fiber-*g*-(PS-*b*-PVBC).

To corroborate the efficient grafting of PVAc chains, a close-up XPS survey of the C1s core level region showed a clear evidence of the O–C=O group signal enhancement in the PVAc grafted wood fiber compared to the initial Fiber-*g*-CTA. This attests of an extension

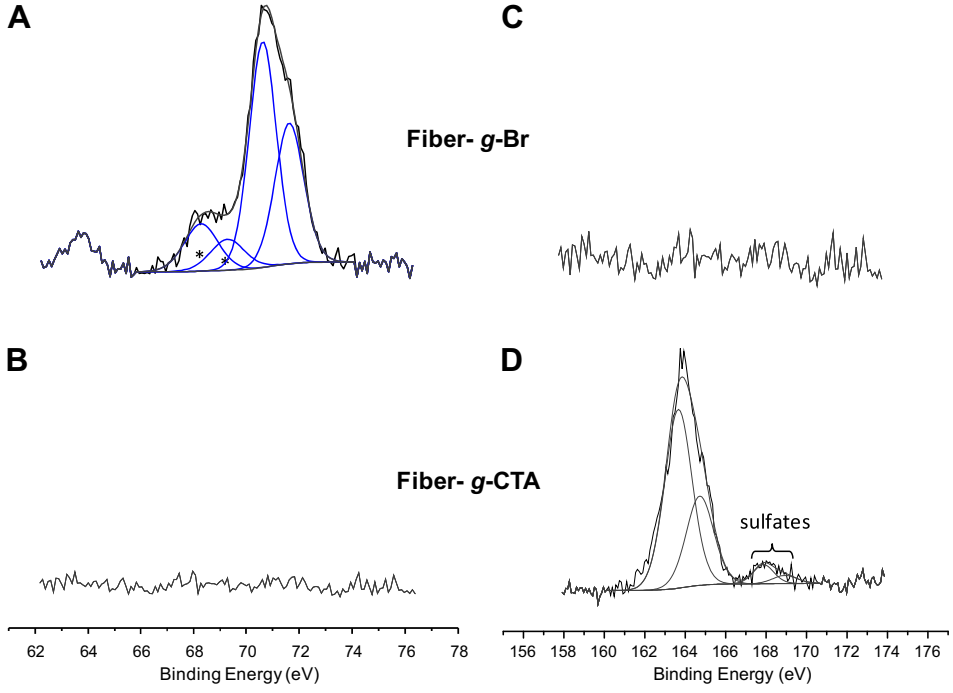

Fig. 3. X-ray photoelectron spectroscopy spectra of Br3d core level for (A) Fiber-*g*-Br, (B) Fiber-*g*-CTA and of S2p core level for (C) Fiber-*g*-Br, (D) Fiber-*g*-CTA.

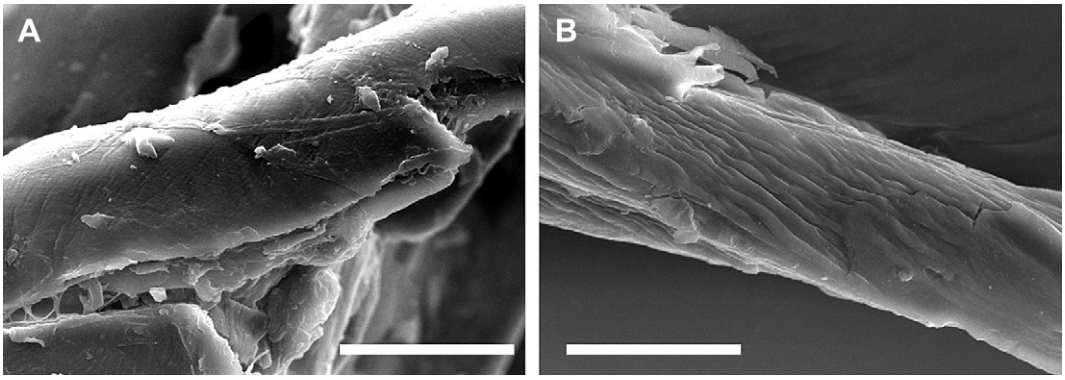

Fig. 4. SEM images of the crude pine wood fibers (A) and of the PS grafted wood fibers (expt 4 in Table 2) (B). The scale bar is 20 μm.

of the initial Fiber-*g*-CTA with a higher content of ester functions at the surface of the fibers (see Fig. SI-2 in Supplementary data).

Fig. 6 gathers the contact angle (CA) measurements of the wood fibers grafted with either the intermediate reactants (bromine and xanthate groups), or the hydrophobic polymer chains (PS and PS-PVBC) or the quaternized copolymers. The surface of the Fiber-*g*-PS pellet exhibited a constant CA of *ca.* 95° over a period of 20 min whereas the precursors Fiber-*g*-Br and Fiber-*g*-CTA quickly exhibited an hydrophilic character after few seconds. The CA of the crude wood fibers was not measurable as the water droplet was instantaneously adsorbed. The hydrophobicity of the Fiber-*g*-PS surface highlights the successful grafting of polystyrene chains via the MADIX process involving the grafted CTA.

We explored the effect of the Fiber-*g*-PS content on the wettability of wood fiber pellets. As illustrated in Fig. 7A, when the pellet was made from a mixture of crude fibers and Fiber-*g*-PS, 100 wt-% of Fiber-*g*-PS was required to provide the hydrophobic character. Such behavior is an indirect proof of the coverage homogeneity of all the wood fibers. On the other hand, pressing a Fiber-*g*-PS thin layer corresponding to 9 wt-% of the overall mass of the composite pellet conferred hydrophobic property on the wood surface (CA > 90°, Fig. 7B). Such behavior confirms the effective coverage of the fiber by a small amount of grafted polystyrene. This later point might present an interest for processing of laminated wood materials with non-leaching hydrophobicity.

In parallel, aging experiments were performed in order to assess the stability of the covalent link existing between the PS chains and the wood fibers. For that purpose, the Fiber-*g*-PS were subjected to temperature under humid atmosphere (see experimental part) for three months and subsequently cleaned by solvent extraction to remove any cleaved PS chains. No free PS chains were recovered by precipitation of the supernatant. Moreover, the remaining high value of the contact angle (90°, see Fig. SI-3 in Supplementary data) measured onto the Fiber-*g*-PS pellet confirms the stability of the long term stability of the grafted hydrophobic coating.

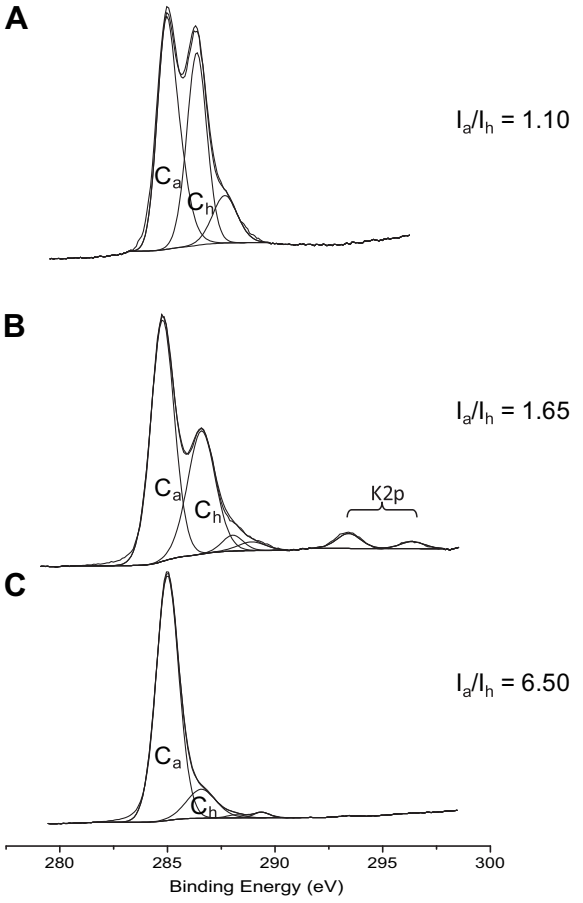

Fig. 5. X-ray photoelectron spectroscopy C1s spectra of the crude Fiber (A), Fiber-*g*-PS (B) and Fiber-*g*-(PS-*b*-PVBC) (C). The intensity ratios I_a/I_h (aliphatic carbon/hydroxyl-carbon) and the aliphatic carbon (C_a) and hydroxy-carbon (C_h) components are displayed.

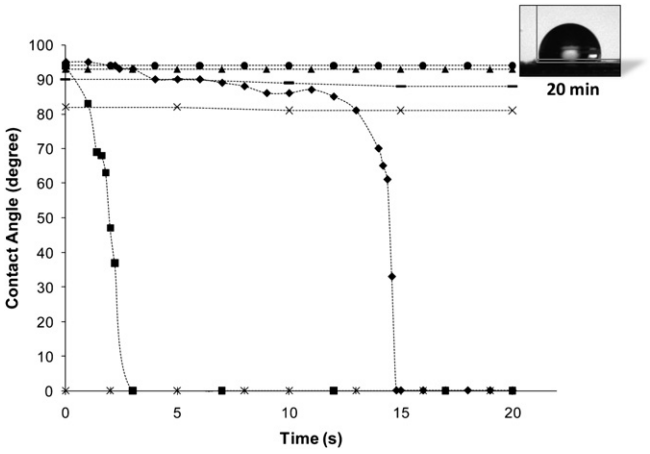

Fig. 6. Contact angle measurements of the grafted wood fibers as a function of time (in seconds): Fiber-*g*-Br (◆); Fiber-*g*-CTA (■); Fiber-*g*-PS (●); Fiber-*g*-(PS-*b*-PVBC) (▲); Fiber-*g*-(PS-*b*-PVBTEAC) (*); Fiber-*g*-(PS-*stat*-PVBC) (−); Fiber-*g*-(PS-*stat*-PVBDMDAC) (×). Additional image of the water drop deposited onto Fiber-*g*-PS pellet after 20 min.

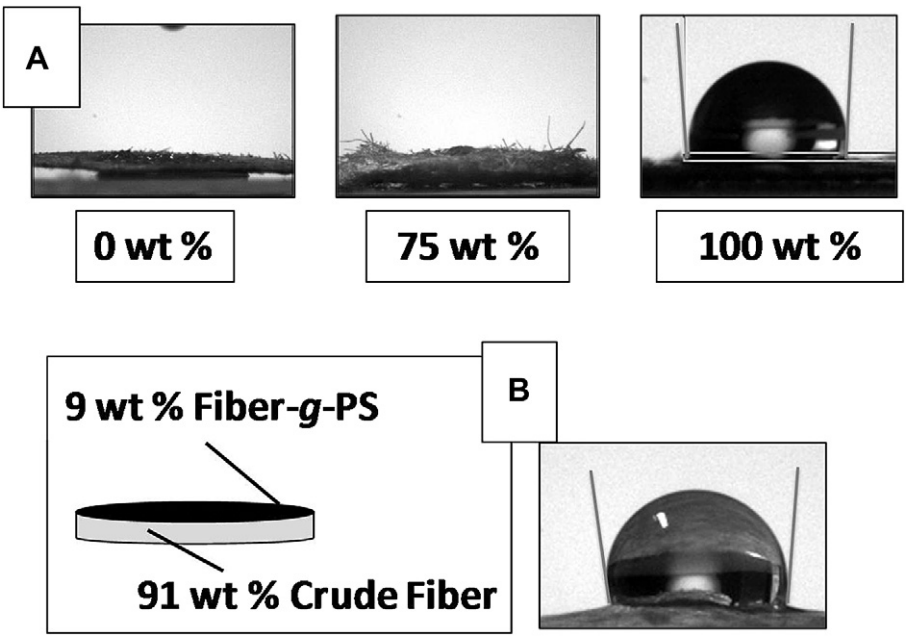

Fig. 7. Pictures of water droplet deposited onto either (A) a mixture of crude wood fibers and PS grafted wood fibers (wt-% of Fiber-*g*-PS is shown) or (B) a double layer of Fiber-*g*-PS (9 wt-%) and crude wood fibers. CA > 90° for pellet with 100 wt-% of Fiber-*g*-PS and for (B) sample.

3.3.2. Block copolymer grafting via chain extension of Fiber-g-PS with VBC and quaternization with triethylamine (Scheme 1, route A)

The Fiber-*g*-PS were chain extended with vinylbenzyl chloride (VBC) monomer in order to graft polystyrene-*block*-poly(vinylbenzyl chloride) (PS-*b*-PVBC) diblock copolymers from the fibers. The polymerization of VBC was performed in the presence of *O*-Ethyl S-(1-ethoxycarbonylethyl) xanthate as free CTA, AIBN as initiator and 1 wt-% of Fiber-*g*-PS as macromolecular CTA. Consequently, the recovered free polymer chains corresponded to PVBC which were analyzed by SEC. As observed for styrene polymerization, the experimental M_n of free PVBC was above the expected M_n with dispersity close to 2.0 (see expt 8 in Table 2). The grafting of the PVBC second block via surface-initiated MADIX polymerization from Fiber-*g*-PS was first estimated by elemental analysis of the modified fibers after the washing procedure. The presence of chlorine atoms (see Table SI-1 in Supplementary data) suggests the successful introduction of VBC units. The XPS analysis of the Fiber-*g*-(PS-*b*-PVBC) confirmed the introduction of VBC units by the presence of the chlorine atom signals (Cl2p BE = 200.3 eV–202.0 eV) associated with R–Cl groups (Fig. 8A) [54]. Note the characteristic doublet is accompanied with a less intense one (BE = 198.3 eV–200.0 eV) to take into account the asymmetry on the low energy side of the peak. Several attempts achieved over long periods, i.e. up to 1 h of analysis, brought up to light the reduction of chlorine under the X-ray beam, as previously reported in the literature [64]. Such behavior is highlighted by the appearance of a corresponding doublet marked with an asterisk in Fig. 8A which increases with experiment time. For the Fiber-*g*-(PS-*b*-PVBC), no trace of nitrogen is observed with a void N1s signal (Fig. 8C).

To assess the ability of the PS macromolecular CTA to re-initiate the VBC polymerization, free PS chains were extended with VBC in the absence of wood fibers. The overlay of the SEC chromatograms (see Fig. SI-4 in Supplementary data) showed the occurrence of chain extension with an incomplete efficiency in agreement with the low C_{tr} (<0.9) value determined for styrene polymerization with *O*-Ethyl S-(1-ethoxycarbonylethyl) xanthate. [34,35] In an attempt to achieve a better control of the diblock synthesis, poly(*n*-butyl acrylate) was used as a first block as the C_{tr} value of *O*-ethyl xanthates is slightly above 1 for acrylate polymerization [65]. A controlled experiment consisting in chain extension of the P*n*BA synthesized by MADIX (expt 6 in Table 2) with *n*BA monomer was first performed to control the chain end functionality of P*n*BA-CTA. The SEC analysis of the chain extension (see Fig. SI-5 in Supplementary data) showed a clear shift of the SEC chromatogram supporting the living character of the P*n*BA-CTA chains. Nevertheless, the overlay of the P*n*BA and P*n*BA-*b*-PVBC chromatograms indicated an incomplete chain extension of the P*n*BA macromolecular chain transfer agent by vinylbenzyl chloride MADIX polymerization (see Fig. SI-6 in Supplementary data). Despite the incomplete re-initiation of VBC polymerization from PS macromolecular chain transfer agent, the introduction of the second block into the modified fibers is able to drive the final properties. The contact angle of the water droplet deposited onto the surface of the fiber-*g*-(PS-*b*-PVBC) was 95° as both S and VBC units are hydrophobic whereas the complete loss of the surface hydrophobicity after quaternization of the grafted VBC units with triethylamine was evidenced in Fig. 6. Indeed, the CA of fiber-*g*-(PS-*b*-PVBTEAC) surface of 0° is characteristic of the hydrophilic cationic copolymer second block (Fig. 6). The comparison of N1s XPS spectra of fiber-*g*-(PS-*b*-PVBC) and fiber-*g*-(PS-*b*-PVBTEAC) confirmed the occurrence of the VBC quaternization by the presence of the peak corresponding to nitrogen binding energy (402.5 eV) in the fiber-*g*-(PS-*b*-PVBTEAC) spectrum (Fig. 8D). In the literature [54,66] previous studies performed on some nitrogen-containing polymers clearly indicate that this special binding energy corresponds to the nitrogen atoms in a N^+ ammonium form. Beside to the component of the N^+, another peak (marked with an asterisk in Fig. 8D) emerges in the XPS spectrum, which is explained by a reduction phenomenon under beam exposure as commonly observed for positive nitrogen atoms [67]. In the case of the Fiber-*g*-(PS-*b*-PVBTEAC), the ammonium entities co-exist with chlorine negative counter-ions (Cl^-) as displayed by the shift of the Cl2p doublet (Fig. 8B) toward lower binding energy (1.6 eV) in comparison with the initial R–Cl signal of the Fiber-*g*-(PS-*b*-PVBC) (Fig. 8A).

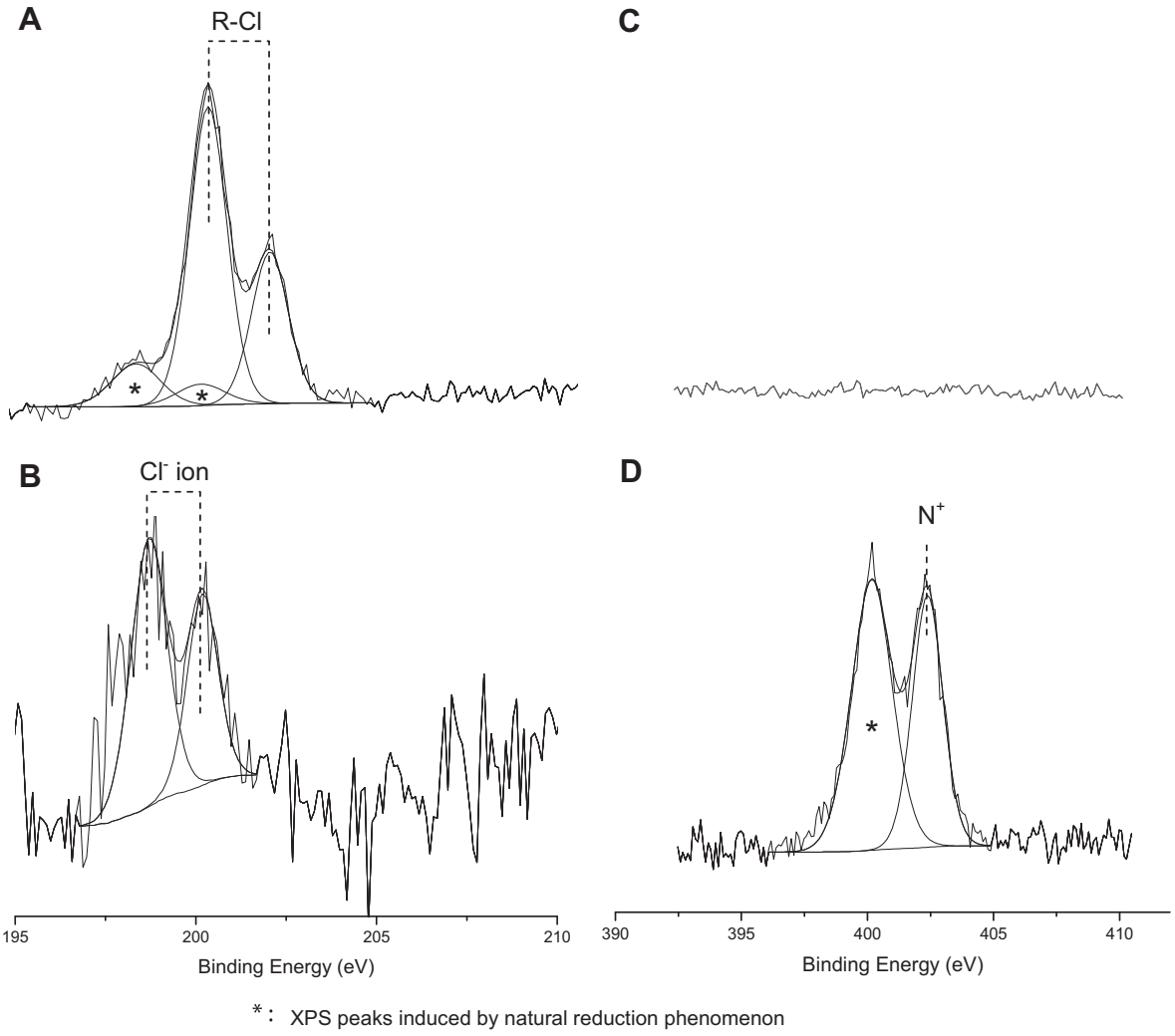

Fig. 8. X-ray photoelectron spectroscopy: Cl2p spectra of (A) Fiber-*g*-(PS-*b*-PVBC) and (B) Fiber-*g*-(PS-*b*-PVBTEAC), N1s spectra of (C) Fiber-*g*-(PS-*b*-PVBC) and (D) Fiber-*g*-(PS-*b*-PVBTEAC).

3.3.3. *Statistical copolymerization of S and VBC from modified fibers for quaternization with long alkyl chain (Scheme 1, route B)*

As described above, the wood fiber surface modification through a covalent grafting of a first PS hydrophobic block and a second hydrophilic block containing quaternary ammonium functions was achieved via the successive surface-initiated MADIX polymerization of S and VBC followed by a quaternization step. In spite of the combination of two interesting properties in the grafted chains, the final wood materials are hydrophilic and the thin inner PS layer might be insufficient to protect wood fibers from external humid exposure. To overcome this problem, we aimed to graft PS-*stat*-PVBC statistical copolymers via SI-MADIX polymerization from the fiber-*g*-CTA allowing a subsequent quaternization of VBC units with long alkyl chain amines as previously described by Chassenieux et al. [68,69] (see Scheme 1).

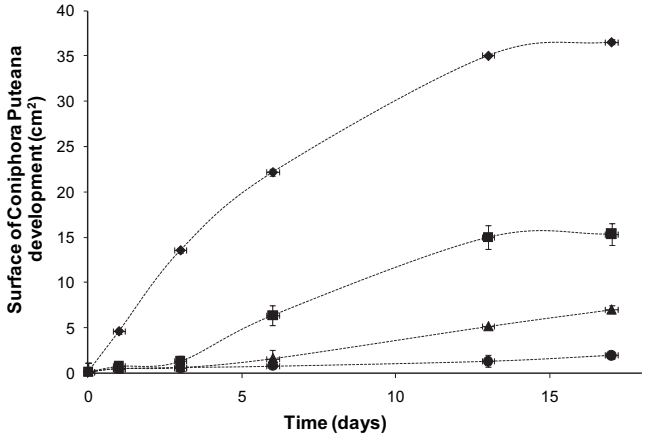

Fig. 9. Influence of the PVBTEAC weight fraction on the *Coniophora Puteana* growth: evolution of the surface area versus fungal exposure duration for various concentrations of PVBTEAC present in the culture medium. Weight percent of PVBTEAC versus medium culture weight: 0 wt-% (◆), 0.5 wt-% (■), 1 wt-% (▲), 2 wt-% (●).

The grafting of the precursor PS-*stat*-PVBC statistical copolymer was carried out in a similar manner as for the homopolymer grafting. The Fiber-*g*-CTA were mixed with the initiator, the *O*-Ethyl S-(1-ethoxycarbonylethyl) xanthate and the monomer mixture composed of 45 mol-% of VBC and 55 mol-% of S. The free polymer chains of the statistical copolymer exhibited a final composition of 51:49 mol-% of VBC:S, in accordance with the reactivity ratios ($r_{VBC} = 0.95$ and $r_S = 0.62$ [69]), with M_n of 30 000 g mol^{-1} and dispersity of *ca.* 2.0 (see expt 9 in Table 2). The elemental analysis of the recovered Fiber-*g*-(PS-*stat*-PVBC) showed the presence of chlorine atoms which was supported by the XPS analysis of the grafted fibers as depicted in Fig. SI-7. From the chlorine atom content obtained by elemental analysis (~1 wt-%), the amount of grafted copolymer was estimated at ~8 wt-% of the wood-based

material. Such low quantity of grafted polymer proved to be efficient enough to enhance the hydrophobicity of the wood fiber surface as shown by CA measurements (Fig. 6).

The Fiber-*g*-(PS-*stat*-PVBC) were derivatized with dimethyldocecylamine to introduce quaternary ammonium functions while keeping a certain hydrophobicity through the incorporation of the long alky chains. Indeed, the contact angle of the quaternized fibers (Fiber-*g*-(PS-*stat*-PVBDMDAC), see Fig. 6) was only slightly reduced to 80° compared to the CA of the initial Fiber-*g*-(PS-*stat*-PVBC) observed at 95°. We should note that the absolute values of the contact angles might be disturbed by the roughness of the wood fiber pellets but the noticeable difference between CA of Fiber-*g*-(PS-*stat*-PVBDMDAC) (80°) and CA of Fiber-*g*-(PS-*b*-PVBTEAC) (0°, see Fig. 6) reveals the interest of a quaternization with long alkyl chains. The success of the quaternization step was shown by XPS analysis of both Fiber-*g*-(PS-*stat*-PVBC) and Fiber-*g*-(PS-*stat*-PVBDMDAC). As depicted in Fig. SI-7, the chlorine peak is less defined after quaternization together with the obvious appearance of nitrogen atoms signal (see Scheme 1). The quaternization step being associated with an increase of the organic content at the fiber surface, the signal of chlorine becomes noisy as this element is minority represented among the whole atomic population within the chain (its atomic concentration decreases from 0.48 atomic % to 0.05 atomic %). A similar low atomic percentage ($\sim$ 0.06 atomic %) was recorded for the nitrogen content of Fiber-*g*-(PS-*stat*-PVBDMDAC) assuming a perfect N^+/Cl^- electrical balance. As observed for the Fiber-*g*-(PS-*b*-PVBTEAC), a probable reduction of the ammonium function occurred during the XPS experiment (Fig. SI-7). To confirm that point, an X-ray beam degradation experiment was run over 2 h onto the free PS-*stat*-PVBDMDAC polymer. The reduction phenomenon of nitrogen N^+ peak (BE = 401.6 eV) was observed with the progressive appearance of a new component (reduced nitrogen, BE = 398.9 eV) as displayed in Fig. SI-8 (Supplementary data). In parallel, the proton NMR spectra of both the initial free PS-*stat*-PVBC copolymer and the corresponding quaternized PS-*stat*-PVBDMDAC copolymer, the latter of which was recovered by precipitation, were recorded (depicted in Fig. SI-9, Supplementary data). The overlay of these spectra showed the complete quaternization of the initial copolymer together with the absence of residual tertiary amine. Despite this observation, the XPS spectrum of the PS-*stat*-PVBDMDAC copolymer still displays both signals of quaternized amine group and tertiary amine characteristic of the ammonium reduction (Fig. SI-8 in Supplementary data).

In conclusion, the proposed strategy allowed the covalent grafting of polymer chains made of several monomer units containing both hydrophobic moieties (styrene and alkyl chain) and quaternary ammonium groups.

3.4. Influence of the quaternized PVBTEAC homopolymer on the fungi expansion

The introduction of quaternary ammonium groups during the process of polymerization is a promising approach in the development of permanent non-leaching antibacterial materials. [1,27,70], The anti-microbial activity of polymer such as polysulfobetaines [71], secondary and tertiary poly(diallylammonium) salts [72] or of polymerizable 11-(dimethylamino)undecyl acrylate [73] has been recently studied against fungi. To the best of our knowledge, the influence of poly(vinylbenzyltriethylammonium chloride) (PVBTEAC) on fungi expansion has never been studied elsewhere. *C. puteana* causes an extensive decay of wood in buildings. It is a typical decomposer of cellulose and hemicellusose, leaving lignin essentially undigested or, in some cases, demethylated, oxidized, or slightly depolymerized. Hydroxyl radicals attack the hemicellulose enveloping cellulose microfibrils and thus initiate the brown-rot wood decay. [74,75] Subsequent action of fungal cellulases, which diffuse through the pores, leads to a rapid decrease in wood strength due to losses of cellulose and hemicellusose, turning wood into a brown lignin powder in the final stages.

The growing of the *Coniophora Puteana* was assessed by examining its surface expanding in the malt agar–agar culture medium with different PVBTEAC concentrations. The surface area was followed versus time (in days) as reported in Fig. 9. We observed a decrease of the growing rate with an increase of the cationic PVBTEAC polymer content up to 2 wt-% versus the overall medium culture weight. The chosen cationic homopolymer, present as a block in the copolymer chains grafted from the wood fiber, is able to affect the fungi development. This importance of decrease is similar with result obtained on *C. puteana* growth inhibition tests using efficient known biocides [76]. A comprehensive study of the fungicidal activity of all the materials described in the present study (free polymer and grafted wood fibers) is still underway and will be the purpose of a future publication.

4. Conclusions

Pinus Maritimus natural wood fibers were successfully modified by surface-initiated MADIX polymerization of vinyl acetate, *n*-butyl acrylate and styrene through the covalent grafting of a xanthate chain transfer agent. The molar mass of the free polymer chains can be tuned by the initial chain transfer agent concentration, which is known to impact the length of the grafted chains. The low amount of grafted polymer can enhance the hydrophobicity of the wood fibers to provide a non-leaching preservative to the wood-based biohybrid material. The polymer-fiber attachment proved to be stable after aging experiment under humidity and temperature conditions. Block and statistical copolymers of styrene and vinylbenzyl chloride were synthesized in order to introduce quaternary ammonium functions through the quaternization of VBC by either triethylamine or dimethyldodecylamine. The covalent grafting of the polymer chains was confirmed by X-ray Photoelectron Spectroscopy analysis of the modified wood fibers carefully cleaned by a washing procedure to remove any ungrafted species. The presence of the chlorine atom of PVBC and the appearance of signals characteristic of nitrogen atom (ammonium form) binding energy after quaternization of the PS-PVBC copolymer was shown by XPS analysis of the polymer grafted wood fibers. Finally, the effect on limiting fungi expansion was studied. In conclusion, the proposed strategy enabled us to tune the surface properties of raw wood fibers coming from renewable resources by incorporating a slight amount of a well-defined polymer thin layer through a controlled radical polymerization method.

Acknowledgments

V. Pellerin, G. Clisson, A. Khoukh and E. Péré are respectively thanked for their help in SEM, SEC, NMR and FTIR. Conseil Général des Landes is acknowledged for funding of D. Tastet thesis and BEMA (Bois Ecoconception Matériaux Aquitaine) for financial support. P. Palos, G. Labat, S. Grelier, P. Grandinot and A. Allal are thanked for discussions. The authors are grateful to FINSA Mediland for providing wood fibers.

Appendix. Supplementary data

Supplementary data related to this article can be found online at doi:10.1016/j.polymer.2010.12.046.

References

[1] Lee SB, Koepsel RR, Morley SW, Matyjaszewski K, Sun YJ, Russell AJ. Biomacromolecules 2004;5:877–82.
[2] Lindqvist J, Nystrom D, Ostmark E, Antoni P, Carlmark A, Johansson M, et al. Biomacromolecules 2008;9(8):2139–45.
[3] Bledzki AK, Gassan J. Progress in Polymer Science 1999;24:221–74.
[4] Radhakrishnan B, Ranjan R, Brittain WJ. Soft Matter 2006;2(5):386–96.
[5] Husseman M, Malmstrom E, McNamara M, Mate M, Mecerreyes D, Benoit DG, et al. Macromolecules 1999;32(5):1424–31.
[6] Kruk M, Dufour B, Celer EB, Kowalewski T, Jaroniec M, Matyjaszewski K. The Journal of Physical Chemistry B 2005;109(19):9216–25.
[7] Pasetto P, Blas H, Audouin F, Boissiere C, Sanchez C, Save M, et al. Macromolecules 2009;42(16):5983–95.
[8] Matrab T, Chehimi MM, Perruchot C, Adenier A, Guillez A, Save M, et al. Langmuir 2005;21(10):4686–94.
[9] Kaiser A, Dutz S, Schmidt AM. Journal of Polymer Science Part A-Polymer Chemistry 2009;47(24):7012–20.
[10] Albuerne J, Boschetti-de-Fierro A, Abetz V. Journal of Polymer Science Part B-Polymer Physics 2010;48(10):1035–46.
[11] Datsyuk V, Guerret-Piecourt C, Dagreou S, Billon L, Dupin JC, Flahaut E, et al. Carbon 2005;43(4):873–6.
[12] Huang JY, Murata H, Koepsel RR, Russell AJ, Matyjaszewski K. Biomacromolecules 2007;8(5):1396–9.
[13] Yoshikawa C, Goto A, Tsujii Y, Fukuda T, Yamamoto K, Kishida A. Macromolecules 2005;38(11):4604–10.
[14] Tsujii Y, Ohno K, Yamamoto S, Goto A, Fukuda T. Advances in Polymer Science 2006;197:1–45.
[15] Advincula RC, Brittain WJ, Caster KC, Rühe J. In: Advincula RC, Brittain WJ, Caster KC, Rühe J, editors. Polymer brushes. Weinheim, Germany: Wiley-VCH; 2004.
[16] Haddleton DM, Ohno K. Biomacromolecules 2000;1(2):152–6.
[17] Daneault C, Glaied O, Dube M, Chabot B. Journal of Colloid and Interface Science 2009;333(1):145–51.
[18] Zampano G, Bertoldo M, Bronco S. Carbohydrate Polymers 2009;75(1):22–31.
[19] Hansson S, Ostmark E, Carlmark A, Malmström E. ACS Applied Materials & Interfaces 2009;1(11):2651–9.
[20] Kadla JF, Ifuku S. Biomacromolecules 2008;9(11):3308–13.
[21] Coskun M, Mür M, Scedil T. Polymer International 2005;54(2):342–7.
[22] Carlmark A, Malmstrom E. Biomacromolecules 2003;4(6):1740–5.
[23] Carlmark A, Malmström E. Journal of the American Chemical Society 2002;124(6):900–1.
[24] Perrier S, Takolpuckdee P, Westwood J, Lewis DM. Macromolecules 2004;37(8):2709–17.
[25] Roy D, Guthrie JT, Perrier S. Macromolecules 2005;38(25):10363–72.
[26] Perrier S, Roy D, Guthrie JT. Australian Journal of Chemistry 2006;59(10):737–41.
[27] Roy D, Knapp JS, Guthrie JT, Perrier S. Biomacromolecules 2008;9(1):91–9.
[28] Roy D, Guthrie JT, Perrier S. Soft Matter 2008;4(1):145–55.
[29] Barsbay M, Güven O, Davis TP, Barner-Kowollik C, Barner L. Polymer 2009;50(4):973–82.
[30] Roy D, Semsarilar M, Guthrie JT, Perrier S. Chemical Society Reviews 2009;38(7):2046–64.
[31] Tizzotti M, Charlot A, Fleury E, Stenzel MH, Bernard J. Macromolecular Rapid Communications 2010;31:1751–72.
[32] Charmot D, Corpart P, Adam H, Zard SZ, Biadatti T, Bouhadir G. Macromolecular Symposia 2000;150:23.
[33] Corpart P, Charmot D, Biadatti T, Zard S, Michelet D. In: Rhodia Chimie, editor. vol. WO 9858974; 1998.
[34] Destarac M, Brochon C, Catala JM, Wilczewska A, Zard SZ. Macromolecular Chemistry and Physics 2002;203(16):2281–9.
[35] Adamy M, van Herk AM, Destarac M, Monteiro MJ. Macromolecules 2003;36(7):2293–301.
[36] Destarac M, Bzducha W, Taton D, Gauthier-Gillaizeau I, Zard SZ. Macromolecular Rapid Communications 2002;23(17):1049–54.
[37] Bernard J, Favier A, Davis TP, Barner-Kowollik C, Stenzel MH. Polymer 2006;47(4):1073–80.
[38] Bernard J, Favier A, Zhang L, Nilasaroya A, Davis TP, Barner-Kowollik C, et al. Macromolecules 2005;38(13):5475–84.
[39] Favier A, Barner-Kowollik C, Davis TP, Stenzel MH. Macromolecular Chemistry and Physics 2004;205(7):925–36.
[40] Stenzel MH, Cummins L, Roberts GE, Davis TP, Vana P, Barner-Kowollik C. Macromolecular Chemistry and Physics 2003;204(9):1160–8.
[41] Theis A, Davis TP, Stenzel MH, Barner-Kowollik C. Polymer 2006;47(4):999–1010.
[42] Fleet R, McLeary JB, Grumel V, Weber WG, Matahwa H, Sanderson RD. European Polymer Journal 2008;44(9):2899–911.
[43] Chong YK, Krstina J, Le TPT, Moad G, Postma A, Rizzardo E, et al. Macromolecules 2003;36(7):2256–72.
[44] Tsujii Y, Ejaz M, Sato K, Goto A, Fukuda T. Macromolecules 2001;34(26):8872–8.
[45] Lakrout H, Creton C, Ahn DC, Shull KR. Macromolecules 2001;34(21):7448–58.
[46] Keskin H, Atar M, Izciler M. Construction and Building Materials 2009;23(2):634–43.
[47] Save M, Manguian M, Chassenieux C, Charleux B. Macromolecules 2005;38:280–9.
[48] Strazielle C, Benoit H, Vogl O. European Polymer Journal 1978;14(5):331–4.
[49] Canè F, Capaccioli T. European Polymer Journal 1978;14(3):185–8.
[50] Beuermann S, Paquet DA, McMinn JH, Hutchinson RA. Macromolecules 1996;29:4206–15.
[51] Le Digabel F, Avérous L. Carbohydrate Polymers 2006;66(4):537–45.
[52] Cunha CD, Deffieux A, Fontanille M. Journal of Applied Polymer Science 1992;44(7):1205–12.
[53] Paynter RW. Surface and Interface Analysis 2002;33(1):14–22.
[54] Beamson G, Briggs D, editors. High resolution XPS of organic polymers. NYC, USA: John Wiley & Sons; 1992.
[55] Wagner CD, Riggs WM, Davis LE, Moulder JF. In: Muilenberg GE, editor. Handbook of X-ray photoelectron spectroscopy; 1979. Eden Prairie, Minnesota.
[56] Parvole J, Laruelle G, Khoukh A, Billon L. Macromolecular Chemistry and Physics 2005;206:372–82.
[57] Bartholome C, Beyou E, Bourgeat-Lami E, Chaumont P, Zydowicz N. Polymer 2005;46:8502–10.
[58] Bartholome C, Beyou E, Bourgeat-Lami E, Chaumont P, Lefebvre F, Zydowicz N. Macromolecules; 2005:1099–106.
[59] Inoubli R, Dagreou S, Delville MH, Lapp A, Peyrelasse J, Billon L. Soft Matter 2007;3(8):1014–24.
[60] Deleuze C, Delville MH, Pellerin V, Derail C, Billon L. Macromolecules 2009;42:5303–9.
[61] Audouin F, Blas H, Pasetto P, Beaunier P, Boissiere C, Sanchez C, et al. Macromolecular Rapid Communications 2008;29(11):914–21.
[62] Muller AHE, Zhuang R, Yan D, Litvinenko G. Macromolecules 1995;28(12):4326–33.
[63] Stark NM, Matuana LM. Polymer Degradation and Stability 2007;92(10):1883–90.
[64] Dupin J-C, Martinez H, Guimon C, Dumitriu E, Fechete I. Applied Clay Science 2004;27(1–2):95–106.
[65] Chapon P, Mignaud C, Lizarraga G, Destarac M. Macromolecular Rapid Communications 2003;24(1):87–91.
[66] Rodrigues PC, Muraro M, Garcia CM, Souza GP, Abbate M, Schreiner WH, et al. European Polymer Journal 2001;37(11):2217–23.
[67] Wells SK, Giergiel J, Land TA, Lindquist JM, Hemminger JC. Surface Science 1991;257(1–3):129–45.
[68] Chassenieux C, Fundin J, Ducouret G, Iliopoulos I. Journal of Molecular Structure 2000;554(1):99–108.
[69] Manguian M, Save M, Chassenieux C, Charleux B. Colloid & Polymer Science 2005;284(2):142–50.
[70] Kawabata N, Inoue T, Tomita H. Epidemiology and Infection 1992;108(01):123–34.
[71] Garg G, Chauhan GS, Gupta R, Ahn JH. Journal of Colloid and Interface Science 2010;344(1):90–6.
[72] Timofeeva LM, Kleshcheva NA, Moroz AF, Didenko LV. Biomacromolecules 2009;10(11):2976–86.
[73] Caillier L, de Givenchy ET, Levy R, Vandenberghe Y, Géribaldi S, Guittard F. European Journal of Medicinal Chemistry 2009;44(8):3201–8.
[74] Green F, Highley TL. International Biodeterioration & Biodegradation 1997;39(2–3):113–24.
[75] Hyde SM, Wood PM. Microbiology 1997;143:259–66.
[76] Temiz A, Alfredsen G, Eikenes M, Terzev N. Bioresource Technology 2008;99:2102–6.
[77] Brandrup J, Immergut EH, Grulke EA, Abe A, Bloch DR, editors. Polymer handbook; 1999.
[78] Kulkarni MG, Mashelkar RA, Doraiswamy LK. Journal of Polymer Science: Polymer Letters Edition 1979;17(11):713–7.

Polymer 52 (2011) 617–621

Contents lists available at ScienceDirect

Polymer

journal homepage: www.elsevier.com/locate/polymer

Alkylation of polyethyleneimine for homogeneous ligands in ATRP

Artun Zorvaryan, Sebnem Inceoglu, Metin H. Acar*

Istanbul Technical University, Chemistry Department, Maslak 34469, Istanbul, Turkey

ARTICLE INFO

Article history:
Received 14 August 2010
Received in revised form
16 December 2010
Accepted 18 December 2010
Available online 24 December 2010

Keywords:
Atom transfer radical polymerization (ATRP)
Homogeneous polymerization
Polyethyleneimine ligand

ABSTRACT

Ethylated and butylated polyethyleneimine ligands were synthesized and employed in copper catalyzed atom transfer radical polymerization of styrene and methyl methacrylate with suitable initiators in order to obtain homogeneous polymerizations, resulting in well defined polymers with low polydispersities. Linear curves drawn from kinetics and conversion–molecular weight plots indicate that all the polymerizations were successfully controlled. In ATRP reactions of S and MMA, the apparent rate of polymerization, k_p^{app}, exhibits a plateau at [Ligand]/[CuBr] $\geq$ 0.5 ratio for both ligands. The apparent rate constant also decreases by increasing the alkyl chain length of the alkylated polyethyleneimine ligand. Ethylated and butylated polyethyleneimine ligands in ATRP of S and MMA were found to be faster than the existing ATRP ligands.

1. Introduction

Atom transfer radical polymerization (ATRP) [1–9] is one of the most useful controlled/radical polymerization methods in scientific area containing multi-components system; each component, which are initiator, metal catalyst, ligand, monomer and solvent, plays an important role in the system. Since the development of ATRP, a wide variety of these components have been investigated to improve the polymerization process. To achieve the minimum requirements such as fast initiation and reversible deactivation, which depends on the redox process, the choice of the ligand has a significant impact. The design of transition metal catalyst complex system allows not only control over the topologies, composition, molecular weight and molecular weight distribution of the polymers but also determines the homogeneity or heterogeneity of the polymerization media. In the literature, relationships between the structure and the effect of alkyl chain length of nitrogen based ligands have been extensively studied [10–44]. To summarize, only aliphatic-branched and aromatic long alkyl chain containing ligands have shown homogeneous polymerization, while most of other systems show heterogeneous polymerization.

The structure of the catalyst complex which depends on the complexing ligand, solvent and temperature has been reviewed extensively [45]. Ligand geometry also plays an important role during the polymerization reaction since cyclizations can occur during the polymerization [46].

The use of multidentate linear amines, N,N,N′,N″,N″-pentamethyldiethylene triamine (PMDETA) and N,N,N′,N″,N‴,N‴-hexamethyltriethylenetetramine (HMTETA) as ligands, results in faster polymerization of styrene (S) and methyl acrylate (MA) compared to catalysts prepared with dinonylbipyridine (dNbpy) in homogeneous polymerization condition. A 1:1 ratio of copper(I) salt to those ligands is often sufficient to achieve maximum rates and optimum control over polymerization [14] even under heterogeneous condition. The reports indicate that the best ratio of ligand to transition metal for any specific polymerization may depend on both the monomer and the catalyst [47].

N-alkylated linear or branched polyethyleneimines used as catalyst (charge transfer or phase transfer) and surfactants have been synthesized with a variety of short or long alkyl chain such as $-CH_3$ [48], $-C_3H_7$ [49], $-C_{10}H_{21}$ [50], $-C_{12}H_{25}$ [48,50–55], $-C_{13}H_{27}$ [56], $-C_{14}H_{29}$ [37,51,52], $-C_{16}H_{33}$ [51,52,56,57], $-C_{18}H_{37}$ [51,52], $-C_{20}H_{41}$ [52], $-C_{22}H_{45}$ [51,54].

In our previous studies, we have examined a series of alkylated linear amine ligands (ALALs) which provide fast polymerization under homogeneous conditions compared to other available and most widely used ATRP ligands. We have shown that even changing the methyl group of PMDETA to ethyl causes homogeneity and an increased reaction rate in the polymerization system [28,41,42]. In recent years, several other articles demonstrating homogeneous polymerization condition have been published on other types of ligand design such as pentasubstituted diethylenetriamine ligand [32], hexasubstituded triethylenetetramine ligand [43], hexasubstituded TREN-based amine ligands [31,34] and multisubstituted hyperbranched polyethyleneimine ligand [44].

* Corresponding author. Tel./fax: +90 212 285 3230.
E-mail address: macar@itu.edu.tr (M.H. Acar).

0032-3861/$ – see front matter © 2010 Elsevier Ltd. All rights reserved.
doi:10.1016/j.polymer.2010.12.041

Herein, we report the synthesis of ethylated (EPEI) and butylated (BPEI) linear polyethyleneimine (PEI) as new ATRP ligands and their efficiency in the copper-mediated ATRP of styrene (S) and methyl methacrylate (MMA) to demonstrate 10 dentate alkylated linear amines whether useful as homogenous ligand and to enlarge the ligands library in ATRP. Ligand/catalyst ratio and comparison of the chain length of the alkyl groups were undertaken to optimize the amount of the ligands and its characteristics in homogeneous ATRP process. Additionally, the comparison of new multidentated ATRP ligands (EPEI and BPEI) with the widely used ligands such as PMDETA, DiNBpy and Me_6Tren was carried out.

2. Experimental

2.1. Materials

Linear polyethyleneimine ($M_w = 423\ g\ mol^{-1}$; EIMS m/z 375.5 (M^+)), bromobutane (99%), copper(I) bromide (CuBr, 99.99%), and potassium carbonate (99+%), N,N,N′,N″,N″-pentamethylenediethylenetriamine (PMDETA, 98+%) were purchased from the Aldrich Chemical Co.; methyl methacrylate (MMA, 99%), styrene (S, 99%), iodoethane (98%), ethyl-2-bromoisobutyrate (EBIB, 98%, used for MMA), ethyl-2-bromopropionate (EBP, 99%, used for S) were purchased from Across Organics Co.; anhydrous sodium sulphate (99%) was purchased from J.T. Baker Co. Ethylated and butylated polyethyleneimine, EPEI and BPEI, respectively, were synthesized according to literature procedure [28,41,42]. All other reagents were of analytical grade and used as received.

2.2. Synthesis

2.2.1. Synthesis of ethylated polyethyleneimine (EPEI)

Iodoethane (96.5 mL, 1.1 mol) was placed into 1 L round-bottom flask with 300 mL ethanol. While the solution was stirred at room temperature, 35 mL of polyethyleneimine (0.0885 mol) and 245 g (1.77 mol) of potassium carbonate were added to the solution and the mixture was refluxed for 3 days. After addition of a second amount of potassium carbonate (245 g, 1.77 mol), the reaction mixture was refluxed for 3 more days. Subsequently, the mixture was filtered and ethanol was evaporated in rotavap. Product was extracted by distilled water and ethyl acetate in separatory funnel. After separation, organic phase was dried over anhydrous Na_2SO_4, filtered off and ethyl acetate was evaporated in rotavap. Then the viscous product was obtained after being dried in a vacuum oven (conversion: 19%). EIMS m/z 771 (M^+); M_{EPEI} (calculated) = 770 g mol^{-1}, ^{1}H NMR ($CDCl_3$): δ 2.6–2.3 ppm (5H, s), 1.0–0.9 ppm (3H, s).

2.2.2. Synthesis of butylated polyethyleneimine (BPEI)

Bromobutane (63 ml, 0.56 mol) was placed into 1 L round-bottom flask with 300 mL ethanol. While the solution was stirred at room temperature, 18 mL of polyethyleneimine (0.045 mol) and 122.3 g (0.89 mol) of potassium carbonate were added to the solution. Same procedure was performed as EPEI, to achieve the synthesis and purification process of BPEI. Viscous product was obtained (conversion: 69.5%). M_{BPEI} (calculated) = 1306 g mol^{-1}, ^{1}H NMR ($CDCl_3$): δ 2.6–2.0 ppm (5H, m), 1.6–1.1 ppm (4H, m), 1.1–0.7 ppm (3H, s).

2.2.3. Polymerization of S and MMA using EPEI and BPEI

A typical ATRP procedure was performed as follows. Catalyst, CuBr (74.6 mg, 5.2×10^{-4} mol for S and 53.8 mg, 3.75×10^{-4} mol for MMA) was placed in a 48 ml of custom-made Schlenk flask, which was sealed with a Teflon stopper and contained a side arm with a Teflon valve. Then the flask was deoxygenated by vacuum-thaw-nitrogen cycles three times. 12 ml of S (0.104 mol) or 8 ml of MMA (0.075 mol), solvent (6 ml of toluene for S and 8 ml of anisole for MMA) and EPEI or BPEI as ligand at different ratios were added to the flask, respectively. Finally, suitable initiator 0.068 ml of EBP (5.2×10^{-4} mol, for S) or 0.055 ml of EBIB (3.75×10^{-4} mol, for MMA) was added. Then the flask was immediately placed in a thermostatically controlled oil bath at 400 rpm stirring rate (110 °C for S, 80 °C for MMA). All liquid components were pre-bubbled by nitrogen and added into the flask under nitrogen atmosphere. An aliquot was taken periodically via a syringe under nitrogen atmosphere to follow the kinetics of the polymerization process. The aliquot either precipitated in methanol, filtered and dried in order to have gravimetric measurements or after dilution in THF or dichloromethane, methanol was added as internal standard in order to have gas chromatography (GC) measurements.

2.3. Characterization

The ^{1}H NMR spectra were recorded on a Bruker spectrometer (250 MHz) in $CDCl_3$ solution using tetramethylsilane (TMS) as internal standard for the characterization of ligands. Mass spectra were recorded at an ionizing voltage of 70 eV. Elemental analysis was carried out by Thermo Finnegan (Flash 1112 series).

Molecular weight (M_n) and polydispersity index (M_w/M_n) of the polymers were determined by a gel permeation chromatography (GPC) instrument. An Agilent Model 1100 consisting of a pump, a refractive index detector and four Waters Styragel columns as HR 5E, HR 4E, HR 3, HR 2, and THF was used as eluent at a flow rate of 0.3 ml/min at 30 °C. Molecular weights were calibrated using polystyrene or poly(methyl methacrylate) standards.

Monomer conversion was determined by gravimetrically and/or ATI Unicam 610 Series Gas Chromatography equipped with an FID detector using a J&W Scientific 15 m DB WAX Widebore. Injector and detector temperatures were kept constant at 280 and 285 °C, respectively. Initial column temperature is 40 °C, finally reaching up to 200 °C with a heating rate of 40 °C/min.

3. Results and discussions

3.1. Synthesis of ethylated and butylated polyethyleneimine (EPEI, BPEI)

EPEI and BPEI were synthesized according to Scheme 1, using the procedure reported in our earlier work [28,41,42]. During the

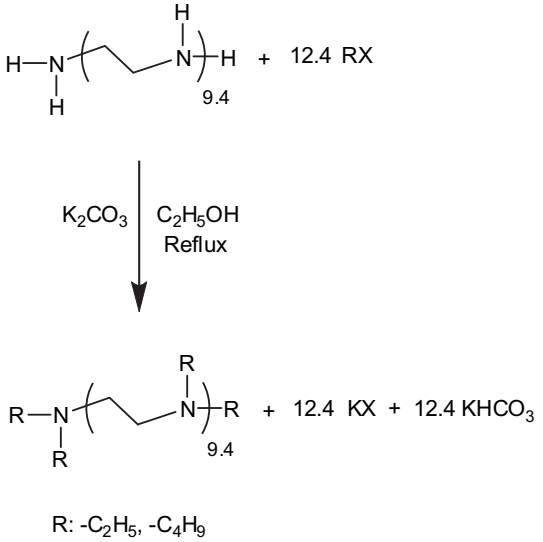

Scheme 1. General route for the synthesis of EPEI and BPEI.

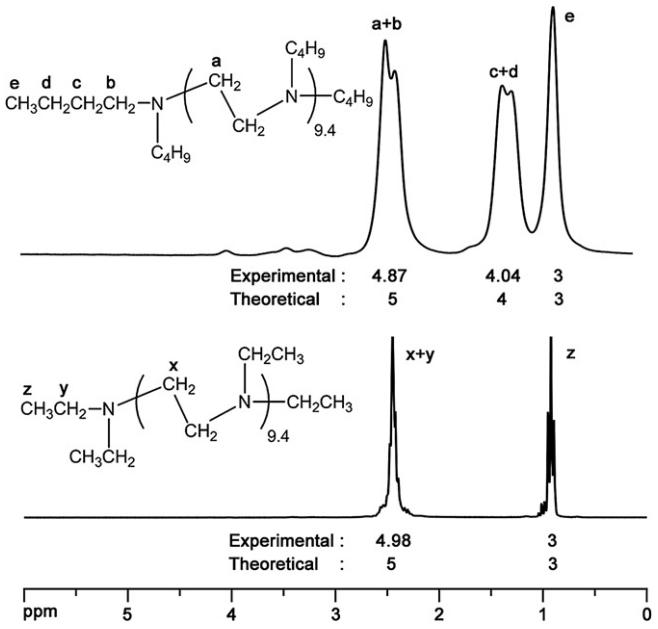

Fig. 1. ^{1}H NMR Spectrum of EPEI and BPEI in $CDCl_3$.

extraction, solubility tendency of EPEI towards water resulted in low conversion of purified product; even for BPEI purification stage same behavior was observed. However, the longer alkyl chains of BPEI were provided less solubility in water comparing EPEI.

Structures and purity of the ligand were assigned by ^{1}H NMR spectra given below in Fig. 1. As shown in Fig. 1, EPEI and BPEI have two and three different types of hydrogen atoms, respectively. Hydrogen atoms attached to the adjacent carbon atom of the nitrogen are represented as "a and x" and "b and y", the end carbon atom of alkyl substituent is represented as "z" for EPEI and "e" for BPEI and the other type of the hydrogen atoms for BPEI are attached to the carbon atoms between them are represented as "c" and "d". The ratio of integral values of those hydrogen atoms was found close to the theoretical ratios (5/3, x + y/z for EPEI; 5/4/3, a + b/c + d/e for BPEI). As can be seen from ^{1}H NMR spectra, same integral values with the theoretical ones for corresponding protons show that pure EPEI ligand was obtained. Observed small peaks at 3–4 ppm regions for BPEI ligand can be concluded that 2.6% quaternization occurred.

The elemental analysis results of PEI, EPEI and BPEI are tabulated in Table 1. The calculated and experimental values for carbon, hydrogen and nitrogen elements are very close in each case. Gas chromatographic analysis didn't reveal any trace of alkyl halide residue in the product. The obtained ligands were characterized by elemental analyses, NMR and GC–MS measurements and had good agreements with theoretical results. This result can be concluded that the high/complete alkylations were achieved in both cases.

Table 1
Elemental analysis results of the PEI, EPEI and BPEI.

Elemental Analysis	PEI		EPEI		BPEI	
	Calc.	Found	Calc.	Found	Calc.	Found
C %	53.52	53.65	68.03	68.20	73.51	72.95
H %	34.53	34.45	18.92	18.96	13.03	13.58
N %	11.95	11.90	13.05	12.84	13.46	13.46

3.2. Polymerization of S and MMA using EPEI and BPEI

Both ligands, EPEI and BPEI form soluble copper halide complexes in organic solvents including S and MMA. After investigation of conditions the following ratio was applied in the ATRP of S and MMA; $[Monomer]_o/[Initiator]_o/[Catalyst]_o/[Ligand]_o = 200/1/1/x$. During the polymerization, the reaction mixture becomes homogeneous and dark brown for S and light green for MMA in the presence of each ligand. To quantify the effect of ligand amount, a series of kinetic studies were carried out under the same ATRP experimental conditions with increasing amount of ligand introduced into the system. The results of polymerizations are shown in Table 2. All of the obtained polymers showed unimodal molecular weight distributions and polydispersities in the range of 1.07–1.65 (during the kinetic studies), 1.07–1.25 (at the end of the polymerization).

A representative semi-logarithmic kinetic plots (Fig. 2a) of ATRP of MMA using BPEI; and S using EPEI and BPEI as ligand which is entirely homogeneous during the polymerization shows a linear dependence of $\ln([M]_o/[M])$ versus time. Linear relationships were obtained in all cases. These indicate that the polymerization reactions are first order with respect to the monomer concentration in the polymerization and demonstrated that the growing radical concentration remains constant during the polymerization. Complex formation of the catalyst with ethylated and butylated polyethyleneimine ligand was suitable to carry out the ATRP process in homogeneous media.

Fig. 2b shows molecular weight and polydispersity index versus conversion plot of S polymerization using BPEI, it is given as a representative example for a chosen ligand ratio ([Ligand]/[CuBr]=1). The linearity of molecular weight versus conversion plot and decreasing PDI with conversion also demonstrated the controlled radical polymerization behavior. Molecular weights of the polymers were

Table 2
Kinetic results of ATRP of S and MMA using various ligands.[a]

Monomer	Ligand	[Ligand]/[CuBr]	k_p^{app} (10^{-4} s^{-1})
		x	
S	EPEI	0.15	1.17
S	EPEI	0.30	1.33
S	EPEI	0.45	1.48
S	EPEI	0.60	1.42
S	EPEI	0.75	1.43
S	EPEI	1.00	1.60
S	EPEI	1.25	1.62
S	BPEI	0.15	0.30
S	BPEI	0.30	0.47
S	BPEI	0.45	0.63
S	BPEI	0.60	0.63
S	BPEI	0.75	0.60
S	BPEI	1.00	0.65
S	BPEI	1.25	0.70
S[b]	PMDETA	1.00	0.78
S[b]	Me_6TREN	1.00	0.78
S[b]	DiNBpy	1.00	0.12
MMA	BPEI	0.15	1.18
MMA	BPEI	0.30	1.50
MMA	BPEI	0.45	1.80
MMA	BPEI	0.60	1.90
MMA	BPEI	0.75	1.80
MMA	BPEI	1.00	1.98
MMA	PMDETA	1.00	1.22
MMA[c]	Me_6TREN	1.00	1.27
MMA[c]	DiNBpy	1.00	0.42

[a] $[S]_o/[EBP]_o/[CuBr]_o/[Ligand]_o = [MMA]_o/[EBIB]_o/[CuBr]_o/[Ligand]_o = 200/1/1/x$. $[S]_o = 5.6$ mol L^{-1} in toluene at 110 °C. $[MMA]_o = 4.6$ mol L^{-1} in anisole at 80 °C. Conversions were calculated by gravimetric measurement for S/EPEI and GC for S/BPEI and MMA/BPEI.

[b] $[S]_o = 7.91$ mol L^{-1} in anisole at 110 °C [42].

[c] $[MMA]_o = 6.09$ mol L^{-1} in anisole at 80 °C [42].

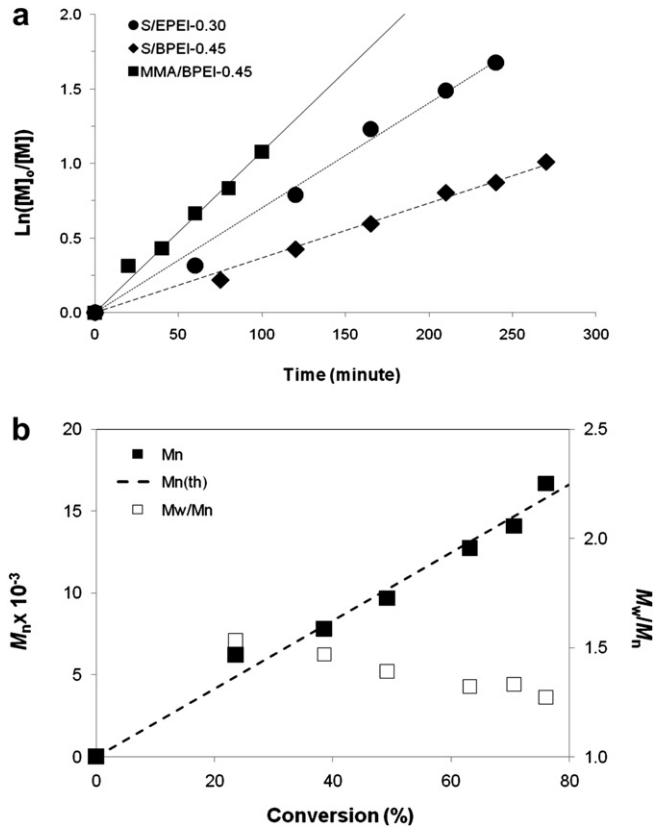

Fig. 2. a) Kinetic plots for ATRP of S and MMA. [S]: 5.6 mol L^{-1} in toluene at 110 °C. $[S]_o/[EBP]_o/[CuBr]_o/[EPEI]_o = 200/1/1/0.30$, $[S]_o/[EBP]_o/[CuBr]_o/[BPEI]_o = 200/1/1/0.45$, $[MMA]_o = 4.6$ mol L^{-1} in anisole at 80 °C, $[MMA]_o/[EBIB]_o/[CuBr]_o/[BPEI]_o = 200/1/1/0.45$. b) Molecular weight versus conversion plot for ATRP of S using BPEI at 110 °C. $[S]_o$: 5.60 mol L^{-1} in toluene. $[S]_o/[EBrP]_o/[CuBr]_o/[BPEI]_o = 200/1/1/1$.

identical with the theoretical ones, indicating that the initiator efficiency is unity.

Fig. 3 shows the apparent rate of polymerization (k_p^{app}) of MMA using BPEI and S using EPEI and BPEI as a function of [Ligand]/[CuBr] ratio. In ATRP reactions of MMA and S the rate of polymerization achieves a plateau value around [Ligand]/[CuBr] = 0.5 ratio for both ligands, means that each ligand is complexing with 2 equiv of CuBr where the maximum rate of polymerization is observed. The apparent rate constant, k_p^{app} decreases by increasing the alkyl chain length of the alkylated polyethyleneimine ligand which can be seen for S polymerization in Table 2.

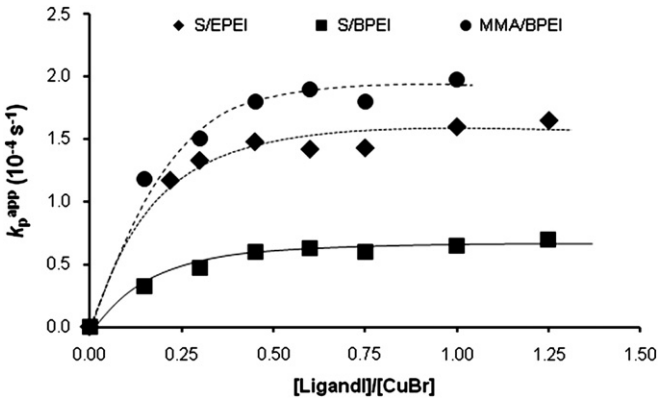

Fig. 3. [Ligand]/[CuBr] ratio versus k_p^{app} plot for ATRP of S and MMA.

In order to compare the effect of alkylated polyethyleneimine ligands with PMDETA as well-known ATRP ligand, an ATRP of MMA was carried out under the same condition (Table 2). ATRP of S using EPEI ligand is faster than other ATRP ligands, even butylated polyethyleneimine ligand containing longer alkyl chain, BPEI, leads to a faster MMA polymerization than PMDETA in same reaction condition. As can be seen from Table 2, EPEI for S and BPEI for MMA in ATRP were faster than the other well-known ligands such as Me_6-Tren and DiNBpy using the same ligand/catalyst ratio, even at lower monomer concentrations.

4. Conclusion

Two types of alkylated polyethyleneimine ligands were synthesized under simple reaction conditions. ATRP of S and MMA using both ligands exhibited homogeneous polymerization in a controlled fashion and relatively fast polymerization reactions compared to other ATRP ligands. All polymerization rates show first order kinetics with respect to monomer concentration and linear increase of molecular weight–conversion plots close to or overlapping with theoretical one. The rate of polymerizations shows a plateau value when the ligand-to-catalyst ratio is 0.5 or over, i.e. both ethylated and butylated polyethyleneimine ligands form a complex with two catalyst molecules. Polymerizations rate were faster for EPEI than BPEI due to the mobility provided by short alkyl chains. Moreover, both ligands provide faster ATRP in homogenously than the commonly used ATRP ligands.

Acknowledgement

The financial support from Research Foundation of Istanbul Technical University is gratefully acknowledged.

References

[1] Wang JS, Matyjaszewski K. Macromolecules 1995;28(23):7901–10.
[2] Wang JS, Matyjaszewski K. Journal of the American Chemical Society 1995;117(20):5614–5.
[3] Kato M, Kamigaito M, Sawamoto M, Higashimura T. Macromolecules 1995;28(5):1721–3.
[4] Percec V, Barboiu B. Macromolecules 1995;28(23):7970–2.
[5] Matyjaszewski K, editor. Controlled radical polymerization. ACS Symposium Series 685. Washington, D.C.: ACS; 1998.
[6] Matyjaszewski K, editor. Controlled/living radical polymerization. Progress in ATRP, NMP, and RAFT. ACS Symposium Series 768. Washington, D.C.: ACS; 2000.
[7] Kamigaito M, Ando T, Sawamoto M. Chemical Reviews 2001;101(12):3689–745.
[8] Matyjaszewski K, Xia JH. Chemical Reviews 2001;101(9):2921–90.
[9] Matyjaszewski K, Xia J. Fundamentals of atom transfer radical polymerization. In: Matyjaszewski K, Davis TP, editors. Handbook of radical polymerization. New York: John Wiley and Sons, Inc.; 2002. p. 602.
[10] Patten TE, Xia JH, Abernathy T, Matyjaszewski K. Science 1996;272(5263):866–8.
[11] Percec V, Barboiu B, Neumann A, Ronda JC, Zhao M. Macromolecules 1996;29(10):3665–8.
[12] Haddleton DM, Clark AJ, Crossman MC, Duncalf DJ, Heming AM, Morsley SR, et al. Chemical Communications 1997;(13):1173–4.
[13] Matyjaszewski K, Patten TE, Xia JH. Journal of the American Chemical Society 1997;119(4):674–80.
[14] Xia JH, Matyjaszewski K. Macromolecules 1997;30(25):7697–700.
[15] Xia JH, Gaynor SG, Matyjaszewski K. Macromolecules 1998;31(17):5958–9.
[16] Haddleton DM, Crossman MC, Dana BH, Duncalf DJ, Heming AM, Kukulj D, et al. Macromolecules 1999;32(7):2110–9.
[17] Kickelbick G, Matyjaszewski K. Macromolecular Rapid Communications 1999;20(6):341–6.
[18] Qui J, Shipp D, Gaynor SG, Matyjaszewski K. Polymer Preprints 1999;40(2):418.
[19] Schubert US, Hochwimmer G, Spindler CE, Nuyken O. Macromolecular Rapid Communications 1999;20(6):351–5.
[20] Schubert US, Spindler CE, Eschbaumer C, Nuyken O. Polymer Preprints 1999;40(2):416.
[21] Xia JH, Matyjaszewski K. Macromolecules 1999;32(8):2434–7.
[22] Queffelec J, Gaynor SG, Matyjaszewski K. Macromolecules 2000;33(23):8629–39.
[23] Shen YQ, Zhu SP, Zeng FQ, Pelton RH. Macromolecular Chemistry and Physics 2000;201(11):1169–75.

[24] Matyjaszewski K, Gobelt B, Paik HJ, Horwitz CP. Macromolecules 2001;34(3):430–40.
[25] Shen YQ, Zhu SP. Macromolecules 2001;34(25):8603–9.
[26] Shen YQ, Zhu SP, Pelton R. Macromolecules 2001;34(10):3182–5.
[27] Gibson VC, O'Reilly RK, Reed W, Wass DF, White AJP, Williams DJ. Chemical Communications 2002;(17):1850–1.
[28] Acar MH, Bicak N. Journal of Polymer Science Part A-Polymer Chemistry 2003;41(11):1677–80.
[29] Inoue Y, Matyjaszewski K. Macromolecules 2003;36(20):7432–8.
[30] Iovu M, Maithufi N, Mapolie S. Macromolecular Symposia 2003;193:209–26.
[31] Barre G, Taton D, Lastcoueres D, Vincent JM. Journal of the American Chemical Society 2004;126(25):7764–5.
[32] Chu J, Chen J, Zhang KD. Journal of Polymer Science Part A-Polymer Chemistry 2004;42(8):1963–9.
[33] Ding SJ, Shen YQ, Radosz M. Journal of Polymer Science Part A-Polymer Chemistry 2004;42(14):3553–62.
[34] Gromada J, Spanswick J, Matyjaszewski K. Macromolecular Chemistry and Physics 2004;205(5):551–66.
[35] Inceoglu S, Olugebefola SC, Acar MH, Mayes AM. Designed Monomers and Polymers 2004;7(1–2):181–9.
[36] Inoue Y, Matyjaszewski K. Macromolecules 2004;37(11):4014–21.
[37] Gainanova GA, Zhil'tsova EP, Kudryavtseva LA, Lukashenko SS, Timosheva AP, Burilov AR, et al. Russian Journal of General Chemistry 2006;76(11):1788–94.
[38] Monge S, Darcos V, Haddleton DM. Journal of Polymer Science Part A-Polymer Chemistry 2004;42(24):6299–308.
[39] Nguyen JV, Jones CW. Journal of Polymer Science Part A-Polymer Chemistry 2004;42(6):1384–99.
[40] O'Reilly RK, Gibson VC, White AJP, Williams DJ. Macromolecules 2004;23(17):2921–8.
[41] Acar MH, Becer CR, Ondur HA, Inceoglu S. Polymer Preprints 2005;46(2):433–4.
[42] Acar MH, Becer CR, Ondur HA, Inceoglu S. Alkylated linear amine ligands for homogeneous atom transfer radical polymerization. In: Matyjaszewski K, editor. Controlled/living radical polymerization: from synthesis to materials. ACS Symposium Series 994. Washington, D.C.: ACS; 2005. p. 97–110.
[43] Becer CR, Hoogenboom R, Fournier D, Schubert US. Macromolecular Rapid Communications 2007;28(10):1161–6.
[44] Shen Z, Chen Y, Frey H, Stiriba SE. Macromolecules 2006;39(6):2092–9.
[45] Pintauer T, Matyjaszewski K. Coordination Chemistry Reviews 2005;249(11–12):1155–84.
[46] Clark AJ, Filik RP, Thomas GH. Tetrahedron Letters 1999;40(26):4885–8.
[47] Xia J, Zhang X, Matyjaszewski K. In: Matyjaszewski K, editor. Controlled/living radical polymerization. Progress in ATRP, NMP, and RAFT. ACS Symposium Series 768. Washington, D.C.: ACS; 2000. p. 207.
[48] Haimov A, Cohen H, Neumann R. Journal of the American Chemical Society 2004;126(38):11762–3.
[49] Johnson TW, Klotz IM. Macromolecules 1974;7(2):149–53.
[50] Budzynski DM, Myatt EA, Benight AS. Journal of Macromolecular Science-Pure and Applied Chemistry 1993;A30:117–25.
[51] Noding G, Heitz W. Macromolecular Chemistry and Physics 1998;199(8):1637–44.
[52] Shi HF, Zhao Y, Zhang XQ, Jiang SC, Wang DJ, Han CC, et al. Macromolecules 2004;37(26):9933–40.
[53] Vasylyev MV, Maayan G, Hovav Y, Haimov A, Neumann R. Organic Letters 2006;8(24):5445–8.
[54] Haldar J, An DQ, de Cienfuegos LA, Chen JZ, Klibanov AM. Proceedings of the National Academy of Sciences of the United States of America 2006;103(47):17667–71.
[55] Liu L, Brreslow R. Journal of the American Chemical Society 2002;124(18):4978–9.
[56] Pshezhetskii VS, Nikolaev GM, Lukjanova AP. European Polymer Journal 1977;13(5):423–9.
[57] Wang W, Qu XZ, Gray AI, Tetley L, Uchegbu IF. Macromolecules 2004;37(24):9114–22.

Polymer 52 (2011) 622–628

Contents lists available at ScienceDirect

Polymer

journal homepage: www.elsevier.com/locate/polymer

Poly (acrylonitrile – *co* -1-vinylimidazole): A new melt processable carbon fiber precursor

Wenjin Deng [a], Alexander Lobovsky [b], Scott T. Iacono [a,2], Tianyu Wu [d], Neetu Tomar [a], Stephen M. Budy [a,3], Timothy Long [d], Wesley P. Hoffman [c], Dennis W. Smith Jr. [a,*,1]

[a] Department of Chemistry, Clemson University, Clemson, SC 29634, USA
[b] Advanced Fiber Engineering, LLC, 8 Floral Ct, Westfield, NJ 07090, USA
[c] AFMC AFRL/RZSM, US Air Force Research Lab, Edwards AFB, CA 93524, USA
[d] Department of Chemistry, Macromolecules and Interfaces Institute, Virginia Tech, Blacksburg, VA 24061, USA

ARTICLE INFO

Article history:
Received 16 September 2010
Received in revised form
25 November 2010
Accepted 27 November 2010
Available online 4 December 2010

Keywords:
Carbon fiber precursor
Thermal cross-linking
Melt processable

ABSTRACT

Acrylonitrile/1-vinylimidazole (AN/VIM) copolymers containing various mol% of VIM were synthesized by free radical solution polymerization. The copolymers were characterized by Attenuated Total Reflectance-Fourier Transform Infrared (ATR-FTIR) spectroscopy, ^{1}H NMR spectroscopy, gel permeation chromatography (GPC) and differential scanning calorimetry (DSC). Char yields of the copolymers were 40–48% as determined by thermogravimetric analysis (TGA) while gel fractions were found to be 90–99% depending upon the composition, temperature and time. The complex viscosity of the precursor copolymers was measured as a function of composition and temperature. 82/18 mol% of AN/VIM copolymer based carbon fiber precursor was successfully processed by solvent-free melt spinning at 192 °C and the melt-spun fiber was characterized by DSC, ATR-IR, and X-ray Diffraction (XRD).

1. Introduction

Carbon fiber polymer composites have attracted worldwide interest in sporting goods and aerospace industries due to their excellent specific strength, stiffness and lightweight [1–3]. Thus the synthesis [4–6], structural characterization [7–19], and cyclization studies [19] of PAN based precursors have received a great deal of attention in recent years. PAN based carbon fibers are usually produced by the following steps: 1) Spinning of precursors; 2) oxidative stabilization and carbonization of fiber precursors. Solution spinning of the precursors is carried out at different drawing rates while stabilization typically occurs around 200–300 °C in air, which leads to the formation of a ladder polymer necessary to obtain a high quality carbon fiber. The step of forming ladder polymers is very important, as it influences the physical properties and the microstructure of the resultant carbon fibers. Subsequently, carbonization is carried out at temperature of 1000–1400 °C in an inert atmosphere which removes nearly all of the non-carbon elements. The resulting carbon fibers are used to produce the reinforced polymer composites which are known to give high strength, high modulus, light weight and high heat resistance [3].

In general, commercial PAN precursors degrade before they melt therefore, the precursor fibers are commonly solution-spun (20–30 wt% solution) from polar solvents [20]. However, the solution-spinning process requires solvent recovery and higher processing costs which restricts their applications. There is a need to prepare cost effective carbon fibers to expand their applications including automotive industries. The replacement of solution spinning by a melt -spinning process is one of the major approaches which can help in producing cost effective carbon fiber precursors. In recent years, researchers have explored the possibilities to synthesize melt processable carbon fiber precursors [20,21]. Melt processable PAN copolymers in combination with other comonomers such as methyl acrylate [22], methacrylic acid [12], and itaconic acid [23] are commercialized but their thermal stabilization is still a challenge. Recently McGrath et al., has reported the melt processable carbon fiber precursors based on terpolymers of acrylonitrile, methyl acrylate and acryloyl benzophenone (ABP) [22].

* Corresponding author. Tel.: +1 864 207 0661.
E-mail address: dwsmith@utdallas.edu (D.W. Smith).
[1] Present address: The University of Texas at Dallas, 800 W Campbell Rd. BE26, Richardson, TX 75080-3021, USA.
[2] Present address: Department of Chemistry, United States Air Force Academy, USAF Academy, CO 80840, USA.
[3] Present address: Department of Chemistry & Biochemistry. University of Arizona, Tucson, AZ 85721, USA.

0032-3861/$ – see front matter © 2010 Elsevier Ltd. All rights reserved.
doi:10.1016/j.polymer.2010.11.054

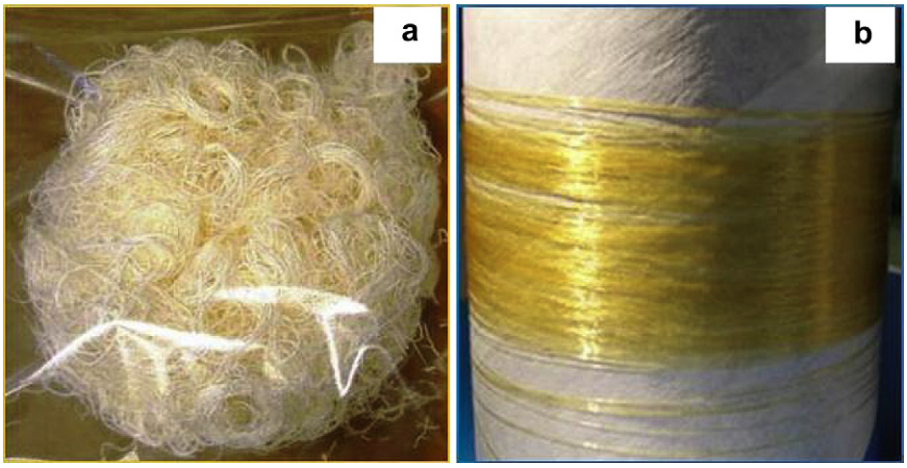

Fig. 1. Photograph of (a) 82/18 AN/VIM copolymer; (b) melt-spun fiber of 82/18 AN/VIM.

These precursors can be stabilized by UV light, which sometimes is not sufficient enough for cross-linking (~65% gel fraction) [22,24] and again add cost specialized technique.

The objective of our study is to synthesize melt-processable carbon fiber precursors which have the capability of thermal stabilization in air which would make them cost effective and widen their applications. AN/VIM copolymers [25,26] have been reported by several researchers, but to the best of our knowledge none of AN/VIM copolymer compositions has been reported for carbon fiber applications. VIM comonomer can disrupt PAN crystallinity to make it melt-processable, while the unsaturated pendant imidazole groups enable the precursor to be thermally cross-linkable. Also, VIM will help in balancing the atomic ratio of nitrogen to carbon (N/C) which is related to microstructure of these precursors and further affects the structure and mechanical properties of carbon fibers [27–29]. The gel fraction, char yield and rheological properties of these copolymers were studied. Here, based on rheological studies and optimum char yield, 82/18 AN/VIM composition was chosen for melt spinning and has been discussed in detail. Thermal and structural characterization of successful melt-spun fiber was also studied.

2. Experimental

2.1. Materials

2,2′-Azobis(2-methylpropionitrile) (AIBN), 1-vinylimidazole (VIM), acrylonitrile(AN), N,N-dimethylformamide (DMF), dimethyl sulfoxide (DMSO) and 1-Dodecanethiol were purchased from the Aldrich Chemical Co. All reagents were used as received.

2.2. Synthesis of carbon fiber precursor

The solution polymerization of AN and VIM by varying feed ratio was carried out in a 250 mL flask fitted with a thermocouple probe, condenser, addition funnel and nitrogen inlet. The flask was charged with 60 mL DMF and purged with nitrogen for 30 min.

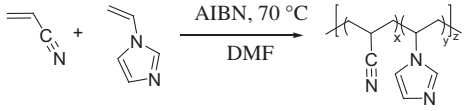

Scheme 1. Free radical copolymerization of AN with VIM.

Then the monomers, AIBN and chain transfer agent, 1-dodecanethiol were added drop wise into the flask over a period of 2–5 h. The polymerization reactions were carried out at 70 °C with continuous stirring. The copolymer was precipitated in de-ionized water, filtered and washed with methanol and hexane to remove residual monomers and then dried in vacuum oven for two days till constant weight was obtained (Fig. 1a).

2.3. Characterization of copolymer precursors and melt-spun fiber

^{1}H NMR spectrum was obtained with JEOL ECX-300 spectrometer using DMSO-d_6 as solvent. Size exclusion chromatography (SEC) was used to determine the molecular weights of polymers in *N,N*-dimethyformamide (DMF) at 50 °C at 1 mL/min flow rate on a Waters SEC instrument equipped with two Waters Styragel HR5E (DMF) columns, a Waters 717 plus autosampler, a Waters 2414 differential refractive index detector and a Wyatt Technologies miniDAWN multiangle laser light scattering (MALLS) detector. Malvern Zetasizer Nano was used for dynamic light scattering of polymer solution (1 mg/mL, 25 °C) and three test cycles were carried out. An Ostwald Viscometer was used to measure the intrinsic viscosity ([η]) of copolymer in (0.01 g/mL polymer in DMSO at 25 °C) by using following equation [30]:

$$[\eta] = \left(\sqrt{2}/c\right)\left(\eta_{sp} - \ln\eta_{rel}\right)^{0.5}$$

where [η] is intrinsic viscosity, c = concentration of polymer solution (g/dL); η_{sp} = specific viscosity; η_{rel} = relative viscosity.

Attenuated total reflectance-Fourier transform infrared (ATR-FTIR) analysis of copolymers was performed on a Thermo-Nicolet

Table 1
Feed and copolymer compositions of AN/VIM copolymers by starve-fed addition*.

In feed (mol%)		In copolymer [a] (mol%)	
VIM	AN	VIM	AN
0	100	0	100
10	90	14	86
12	88	16	84
18	82	22	78
21	79	27	73
25	75	37	63

*Solution polymerization of AN and VIM in DMF initiated by AIBN at 70 °C for 16 h.
[a] Determined by ^{1}H NMR.

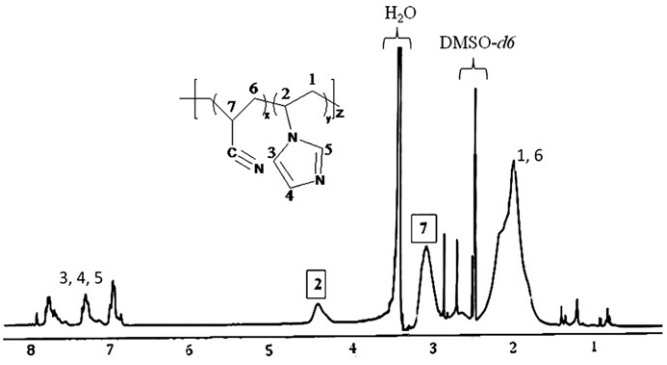

Fig. 2. ^{1}H NMR of 82/18 AN/VIM copolymer.

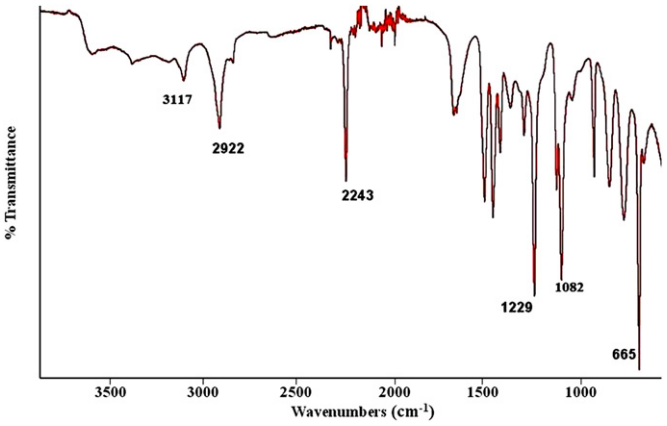

Fig. 3. ATR-FTIR spectrum of 82/18 AN/VIM copolymer.

Magna 550 FTIR spectrophotometer with a high endurance diamond ATR attachment. The thermal stability and char yield of all the copolymers were performed by using Mettler-Toledo 851 thermogravimetric analyzer at controlled conditions of temperature and time conditions to simulate the similar conditions as those used in conversion of precursors into carbon fibers [20].

Differential scanning calorimetry (DSC) was performed on a TA Q1000 instrument in nitrogen at a heating rate of 10 °C min^{-1}. The glass transition temperature (T_g) was obtained from a second heating cycle using TA Universal Analysis 2000 software suite.

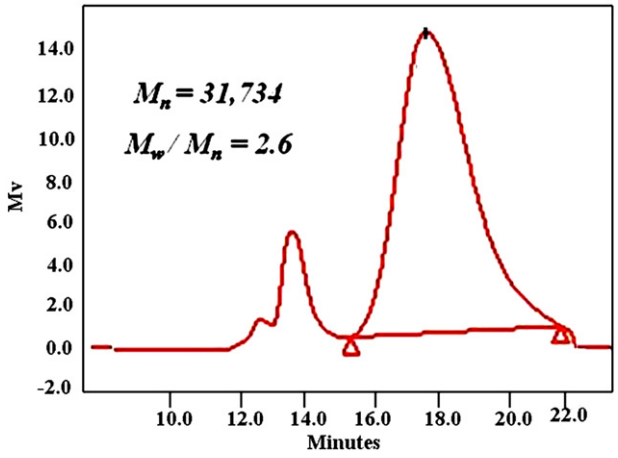

Fig. 4. Gel permeation chromatogram of 82/18 AN/VIM copolymer in DMF.

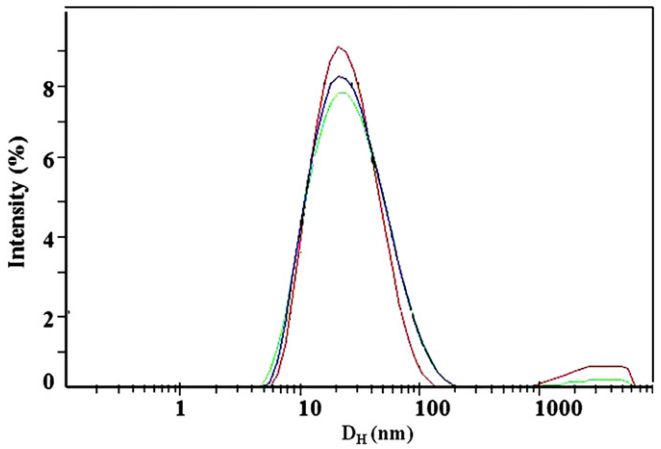

Fig. 5. Particle size of 82/18 AN/VIM copolymer in DMF solution by DLS.

The Scintag XDS 2000 X-ray diffractometer was used for X-ray diffraction analysis of melt-spun fiber. The count time is 1.300 s, step scan rate is 0.02 °/min and the range is 5.00–70.00°. Dynamic oscillatory shear properties of the copolymers were determined by well calibrated TA instruments ARES LS/M LS001-270i (Rheometric Scientific) in N_2 atmosphere. Frequency sweep ranging between 0.1 and 100 rad/s was performed by using cone-plate at 0.1% strain and 200 °C. Strain sweep was conducted at 10 rad/s and 200 °C in order to determine the linear viscoelastic region of these copolymers. Dynamic time sweeps were carried out at 0.1% strain and angular frequency of 1 rad/s at 205 °C and 210 °C for 25 min. Dynamic temperature sweeps of 88/12 and 82/18 AN/VIM copolymers were studied at 2 °C/min from 160 to 220 °C at 0.1 rad/s and 0.1% strain.

2.4. Melt-spinning of AN/VIM copolymer precursor

Fiber spinning was performed at Advanced Fiber Engineering, LLC, Westfield, NJ. 82/18 AN/VIM copolymer precursor ($[\eta] = 0.59$ dL/g) was ground into coarse granules in a grinder and these copolymer granules were vacuum dried at 65 °C for 3 h. An Instron 3211 capillary rheometer (capillary diameter, $D = 0.030$ inches) was used to draw the fibers. In a typical trial, ~9 g of copolymer was loaded in preheated rheometer at 180 °C under nitrogen atmosphere and left there to heat up for 10 min, after that drawing temperature was raised to 192 °C. Melt-spun fiber (Fig. 1b) was collected by winding on 3 inches diameter bobbin rotating at 84 rpm.

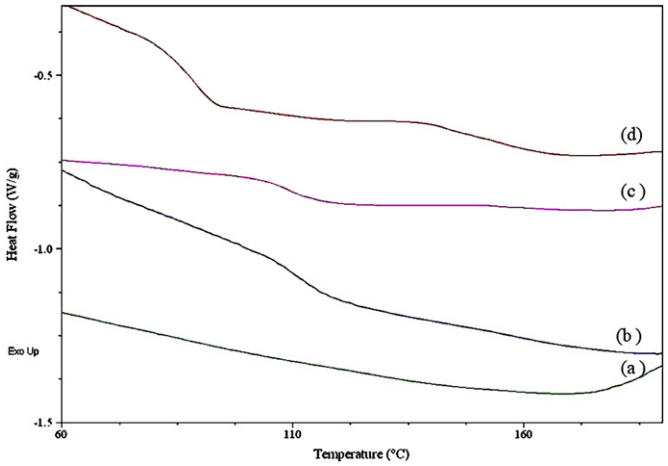

Fig. 6. DSC thermograms of (a) AN homopolymer; (b) 87/13 AN/VIM; (c) 84/16 AN/VIM; and (d) 81/19 AN/VIM copolymers.

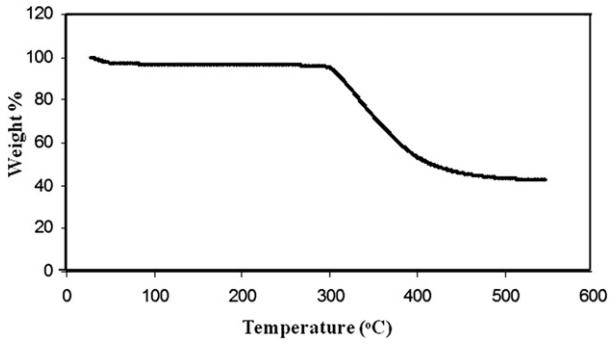

Fig. 7. TGA curve of 82/18 AN/VIM copolymer in N_2.

Table 2
Char yields of various AN/VIM copolymers.

AN/VIM copolymer (feed mol%)	Char yield[a] wt (%)
90/10	47
88/12	48
82/18	47
79/21	40
75/25	40

[a] Determined by TGA.

2.5. Char yield and gel fraction testing

Char yields of the copolymers were obtained by heating at 10 °C/min from ambient temperature to 220 °C in air followed by isothermal at 220 °C for 3 h with increase in temperature from 220 to 550 °C in N_2 and again isothermal at 550 °C for 3 h in N_2 [20]. In order to calculate the gel fraction, the copolymers were first stabilized by heating at 210 °C for 2 h or 250 °C for 5 h respectively in an oven in air and then immersed in DMF solvent for 3 days. The gels were filtered, washed with methanol, and dried in vacuum for 7 days till constant weight.

3. Results and discussion

3.1. Composition of the copolymer precursor

The schematic representation for the synthesis of AN with VIM is shown in Scheme 1. Addition of monomers was carried out by two different methods: "one pot" method and "starve-fed addition" method. In the "one pot" method, VIM content of the copolymer measured by ^{1}H NMR was almost twice the feed molar ratio. The higher composition of VIM in "one pot" copolymers can be very well understood based on the reactivity ratios of these two monomers as $r_{1\ AN} = 0.24$ and $r_{2\ VIM} = 0.12$ [25]. It was observed that this polar donor–acceptor (AN-VIM) pair intended to form alternating copolymer [25,31,32]. In order to better control the composition drifts, we have used "starve-fed addition" method to synthesize AN/VIM copolymers. The copolymer composition determined by ^{1}H NMR (Table 1), shows the feed molar ratio of copolymer was reasonably represented in the copolymer structure prepared by "starve-fed addition" method. In this study we have used feed molar ratio to describe the results unless otherwise NMR measured composition ratio is stated.

A typical ^{1}H NMR spectrum of 82/18 AN/VIM copolymer is shown in Fig. 2. ^{1}H NMR signals at δ 2.0 represent the backbone CH_2 from VIM and AN linkages. Signals at δ 3.1 indicate backbone CH units from AN enchainment, while signals at δ 4.4 represent backbone CH of VIM and signals ranging δ 7.8–6.8 describe the unsaturated CH groups in VIM. Fig. 3 depicts the ATR-FTIR spectrum of 82/18 AN/VIM copolymer. Backbone CH_2 stretching for the AN unit occurs at 2922 cm^{-1} and CN stretching signals are clearly visible at 2243 cm^{-1}. For the VIM unit, C–H ring stretching was observed at 3117 cm^{-1}, backbone CH_2 stretching at 2922 cm^{-1}, C–N ring stretching at 1229 cm^{-1}, C–H ring in-phase bending at 1082 cm^{-1} and C–N = ring stretching at 665 cm^{-1}.

3.2. GPC and DLS of AN/VIM copolymer precursor

Relative molecular weights of AN/VIM copolymers to polystyrene standards were determined using size exclusion chromatography in DMF. A bimodal distribution was observed for all copolymer compositions. The bimodal distribution curve of 88/12 AN/VIM copolymer ($\overline{M}_n$ = 31,734 g/mol, $\overline{M}_w$ = 82,508 g/mol, PDI = 2.6) is shown in Fig. 4. For the current study, the molecular weight is reported for the larger fraction, which corresponds to the bigger peak occurring around 18 min elution time, since the smaller fraction (corresponding to the smaller peak occurring around 14 min elution time) exceeds the calibration range (maximum 3,390,000 g/mol). Particle size and distribution curves (three repeated tests) of the copolymer solution were observed in the DLS (Fig. 5). This bimodal distribution in GPC could possibly be due to chain transfer of copolymer [33] or due to attack on the other polymerization site of the pendant imidazole group [34] which may lead to branching.

3.3. Glass transition temperatures of AN/VIM copolymer precursor

Fig. 6 shows the DSC curves of polyacrylonitrile and AN/VIM copolymers from 60 to 200 °C. No T_g signal was observed in the case

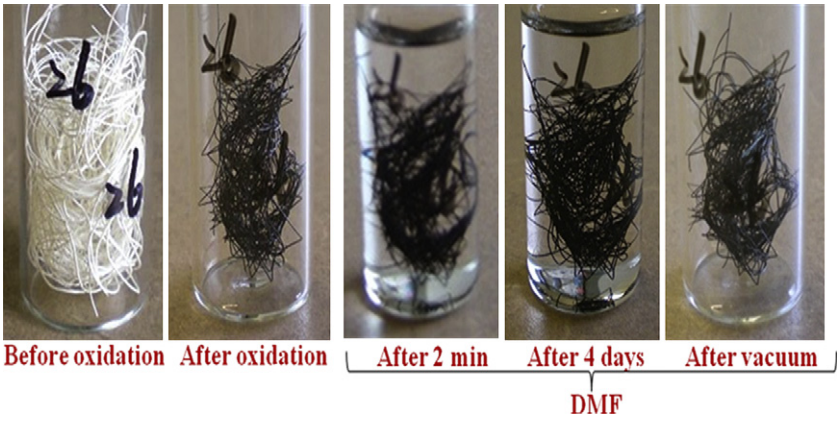

Fig. 8. Photographs of copolymers before and after oxidation during gel fraction experiment (oxidized copolymer retained its shape in DMF even after 7 days.).

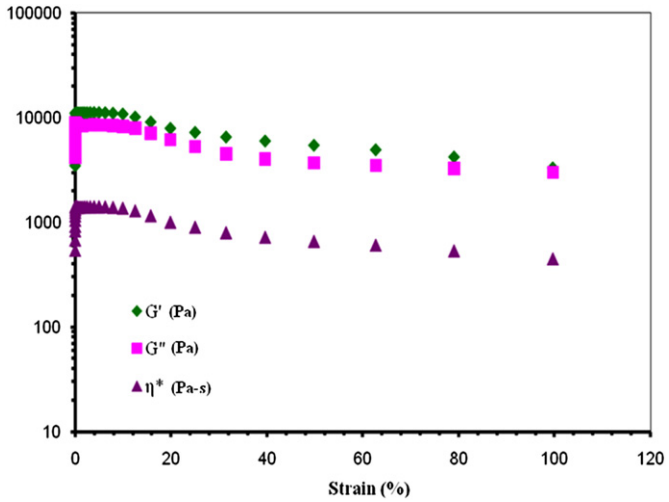

Fig. 9. Dynamic strain sweep of 82/18 AN/VIM copolymer (200 °C, 10 rad/s).

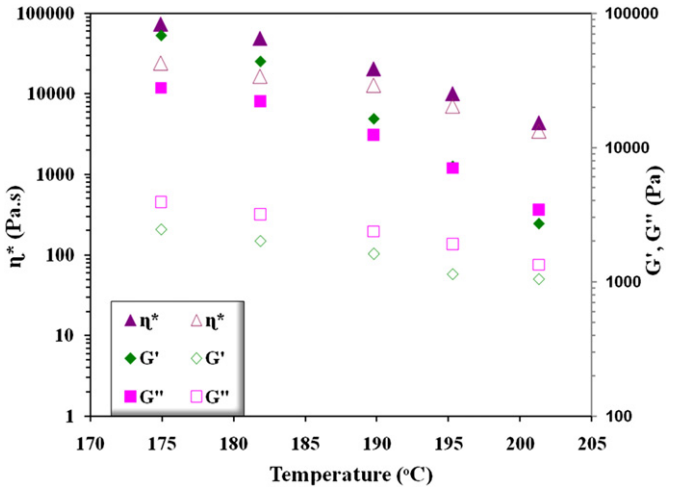

Fig. 11. Dynamic temperature sweep of 82/18 AN/VIM copolymer (open symbol) and 88/12 AN/VIM copolymer (closed symbol) at 0.1 rad/s, 0.1% strain.

of acrylonitrile homopolymer [35] but copolymers exhibited T_g values *i.e.* T_g of 87/13 AN/VIM copolymer at 117 °C; T_g of 84/16 AN/VIM copolymer at 106 °C. For 81/19 AN/VIM copolymer, two T_g were exhibited, T_{g1} at 93 °C and T_{g2} at 160 °C. Other researchers have also observed these two transitions and were attributed to the onset of backbone chain mobility and intermolecular bonding associated with the nitrile groups [36–38]. The decrease in transition temperatures with the increase of VIM molar ratio can be attributed to the disrupted long-range order of the acrylonitrile structure by the introduction of the comonomer with bulky side substituent hence resulting in reduction in dipole–dipole interactions. However, no clear melting peak was observed by DSC curve for the copolymers, which is consistent with the other reports [39]. For the polymers with high acrylonitrile content, a first-order phase transition (melting) is typically not observed due to the inter-chain interactions between polar nitrile substituents as reported by Hutchinson [40].

3.4. Decomposition temperature and char yield of AN/VIM polymer

TGA studies were performed to determine the initial decomposition temperature and char yield of the copolymers. The initial decomposition temperature for the copolymers was 300–310 °C. A representative TGA curve of 82/18 AN/VIM copolymer is shown in Fig. 7. All the copolymers showed rapid weight loss when the temperature is higher than approximately 310 °C.

Char yields of various AN/VIM copolymers (Table 2) were obtained by TGA under the similar conditions as was reported by McGrath et al. [20]. The average char yields of AN/VIM copolymers were found to be in the range of 40–48% depending upon the composition of copolymers. The copolymers with 10–18% VIM have the char yields of 47–48%, which are comparable with that of commercial PAN fibers *i.e.* 50% [41]. This led us to conclude that VIM concentration 10–18 mol% can be effectively used for carbon fiber precursors.

3.5. Gel fraction of AN/VIM copolymer precursors

Cross-linking ability of AN/VIM copolymer precursors was determined by using their gel fraction after heating at 210 °C/2 h or 250 °C/5 h in air. The color of the copolymers changed from white to brown and then black during stabilization as expected. The stabilized black copolymers were insoluble in DMF, showing good cross-linking ability (Fig. 8). The average gel fraction of 88/12 AN/VIM copolymer was about 99% while average gel fractions of 82/18 AN/VIM copolymers was ~90% at 210 °C for 2 h in the air. However, at higher temperature and longer time (250 °C for 5 h), the gel fraction of 82/18 AN/VIM copolymer increased to 99%. The requirement of higher temperature with increasing VIM concentration to get high

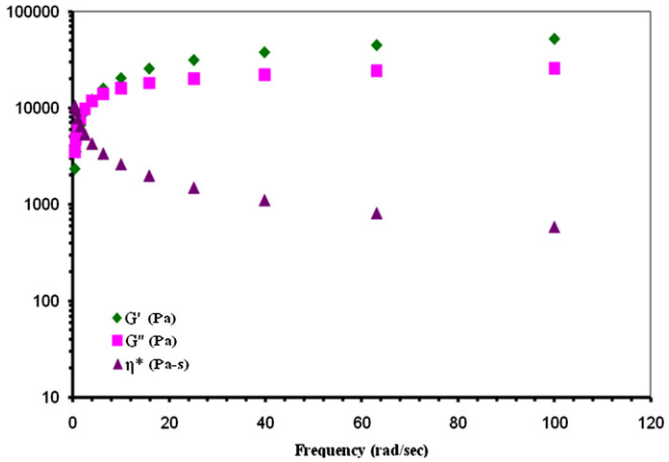

Fig. 10. Dynamic frequency sweep of 82/18 AN/VIM copolymer (200 °C, 0.1% strain).

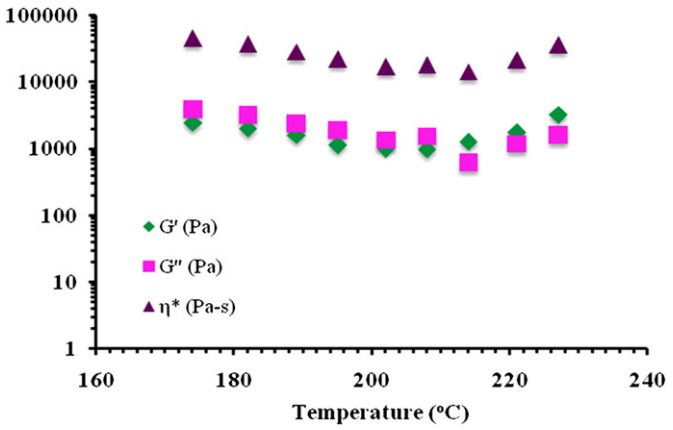

Fig. 12. Dynamic temperature sweep of 82/18 AN/VIM copolymer (0.1 rad/s, 0.1% strain).

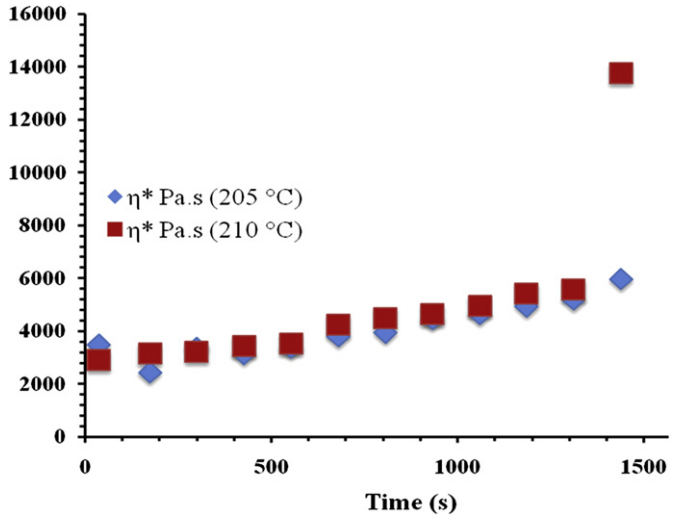

Fig. 13. Dynamic time sweep viscosity of 82/18 AN/VIM copolymer CF33 at 0.1% strain, 1 rad/s, at 205 °C and 210 °C.

gel fraction may be due to presence of comonomers with bulky side groups which introduces a slower step in the stabilization [39]. These results are consistent with the rheological data (discussed in Section 3.6).

The gel fractions of these thermally stabilized copolymers are better than the gel fraction (~65%) of melt-spun carbon fiber precursor which are stabilized by UV light [42]. Both gel fraction and char yield results support that AN/VIM copolymers can be thermally cross-linked in air, which makes it a promising carbon fiber precursor.

3.6. Rheology study of AN/VIM copolymer precursors

The melt processability of the various copolymers was assessed by rheological measurements as melt processing windows depend upon the copolymer composition. To ensure that dynamic oscillatory measurements were made in the linear viscoelastic region for the polymers, strain sweeps were performed at 200 °C, which is well below the cross-linking and degradation temperature of these copolymers. The storage modulus (G'), loss modulus (G'') and complex viscosity (η^*) was found to be constant up to a strain of 10% for the various AN/VIM copolymer compositions. The strain sweep curve of 82/18 copolymer is shown in Fig. 9, where the

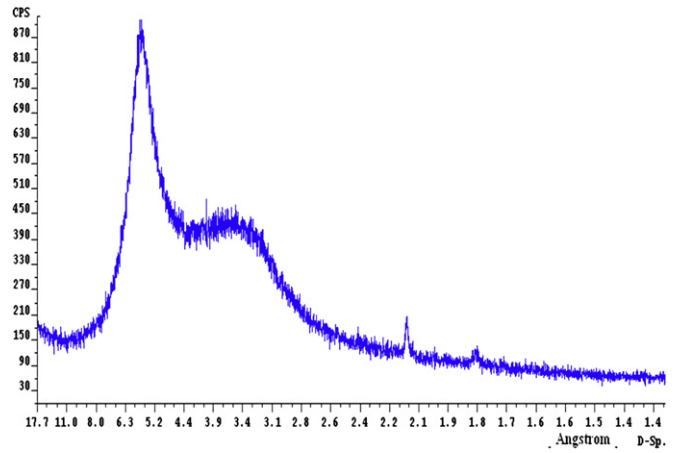

Fig. 14. 1D X-ray spectrum of melt-spun fiber of 82/18 AN/VIM (Count time: 1.300 s; Step scan rate: 0.02 °/min; Range: 5.00–70.00 (°)).

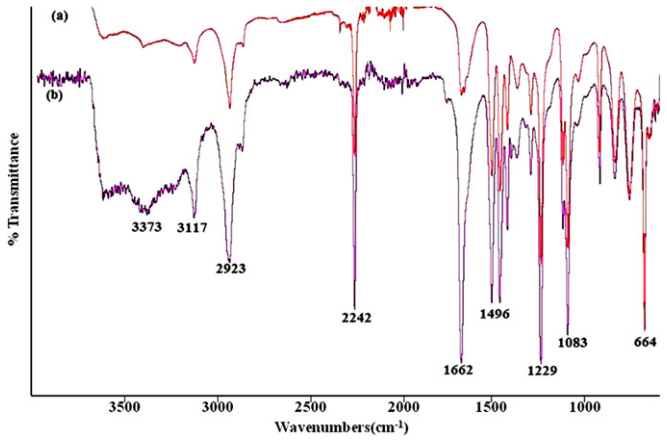

Fig. 15. ATR-FTIR spectrum of (a) 82/18 AN/VIM copolymer before melt processing, (b) melt-spun fiber of 82/18 AN/VIM.

viscosity kept constant at the low strain range. A strain of 0.1% was chosen for further dynamic viscosity testing in this study. Fig. 10 shows the frequency-dependent viscoelastic property of 82/18 AN/VIM copolymer. The viscosity of AN/VIM copolymer decreased sharply when the frequency increased.

The dynamic temperature sweep of AN/VIM copolymer was determined at 0.1% strain and 0.1 rad/s frequency in N_2 atmosphere. A significant dependence of the dynamic viscosity on the copolymer composition was observed. The homopolymer of acrylonitrile was too viscous to measure the viscosity at these testing conditions, while AN/VIM copolymers showed much lower viscosities. Viscosities of 88/12 and 82/18 AN/VIM copolymer are presented in the Fig. 11. The viscosity of 82/18 AN/VIM copolymer was lower by ~45% as compared to that of 88/12 AN/VIM copolymer. Viscosities of AN/VIM copolymer with higher VIM contents were also examined, yet no appreciable change in viscosity was observed with increase in VIM content. The 82/18 AN/VIM copolymer registered the lowest value of viscosity and good char yield of 47%, therefore, this composition was selected for further studies.

Fig. 12 is the dynamic temperature sweep of 82/18 AN/VIM copolymer (0.1 rad/s, 0.1% strain), which shows one critical temperature exists for the copolymer, above which, the η^*, G' and G'' all increased instead of continuing to decrease with temperature rise due to the reactions between active pendant groups. The viscosity of the copolymer precursor is required to be stable at the melt-spinning temperature for a certain time for fiber drawing. Dynamic time sweep was

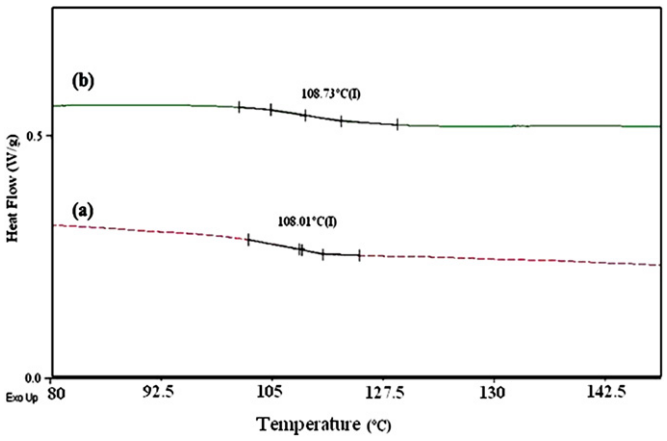

Fig. 16. DSC thermograms of (a) 82/18 AN/VIM copolymer before melt processing; (b) melt-spun fiber of 82/18 AN/VIM.

used to determine the viscosity stability of the 82/18 AN/VIM copolymer. At 205 °C, the viscosity was relatively steady for 25 min, while at 210 °C the viscosity increased sharply after 20 min (Fig. 13). The high jump in viscosity observed is likely due to intermolecular cross-linking. In order to ensure a stable copolymer viscosity for 25 min, the melt-spinning temperature should be lower than 210 °C.

3.7. Characterization of the melt-spun fiber

Successful melt-spun fiber of 82/18 AN/VIM copolymer drawn at 192 °C is shown in Fig. 1b and characterized by ATR-IR, DSC and X-ray diffraction.

The X-ray diffraction spectrum of melt-spun fiber of 82/18 AN/VIM copolymer, Fig. 14 was used to determine the preferred orientation of carbon layers and degree of crystallinity. A sharp reflection peak at 5.8 Å was observed (Fig. 14) which is comparable to that reported by Bashir [43]. The degree of crystallinity was about 35%. The ATR-IR spectrum is shown in Fig. 15 where N–H stretching at 3373 cm^{-1}, C–H ring stretching at 3117 cm^{-1}, backbone C–H stretching at 2923 cm^{-1}, C≡N stretching at 2242 cm^{-1}, C=C stretching at 1662 cm^{-1}, C=N ring stretch at 1496 cm^{-1}, and imidazole ring vibrations at 1229, 1083, 664 cm^{-1} are observed in the copolymer as well as its melt-spun fiber. This indicates that no significant cross-linking was observed even after processing at 192 °C.The T_g of 82/18 AN/VIM copolymer as well as its melt-spun fiber (Fig. 16) was around 108 °C, which is in good agreement with above mentioned result.

4. Conclusions

AN/VIM copolymers with various molar ratio of VIM were successfully prepared and characterized. DSC results show that T_g decreases with the increasing VIM content, which suggests that the VIM helped to disrupt interchain interactions of AN unites. The VIM content also greatly reduced the melt viscosity thus improving processability of the precursor. Successful melt spinning of the 82/18 AN/VIM copolymer precursor was carried out at 192 °C and the resulting melt-spun fiber was characterized by XRD, DSC and ATR-IR. High gel fraction and char yield of the copolymer shows its thermal cross-linking ability.

Acknowledgements

The authors thank the U.S. Air Force Research Laboratory, U.S. Department of Energy and the Robert A. Welch Foundation for financial support. We also thank Dr. G. Harrison, J. Conrad and E. Vasquez (Clemson University) for providing dynamic viscosity testing facilities.

References

[1] Edie DD. Carbon 1998;36:345.
[2] Bahl OP, Donnet JB, Wang TK, Rebouillat S, Peng JCM, editors. Carbon fibers. 3rd ed. New York: Marcel Dekker; 1998. p. 1–84 [Chapter 1].
[3] Cantwell WJ, Morton J. Compos 1991;22:347.
[4] Soulis S, Simitzis J. Polym Int 2005;54:1474.
[5] Bashir Z. J Macromol Sci: Phys B 2001;40:41.
[6] Boguslavsky L, Baruch S, Margel S. J Colloid Interface Sci 2005;71:289.
[7] Godshall D, Rangarajan P, Baird DG, Wilkes GL, Bhanu VA, McGrath JE. Polymer 2003;44:4221.
[8] Gupta AK, Paliwal DK, Bajaj P. J Appl Polym Sci 1996;59:1819.
[9] Bhanu VA, Rangarajan P, Wiles K, Bortner M, Sankarpandian M, Godshall D, et al. Polymer 2002;43:4841.
[10] Gupta AK, Paliwal DK, Bajaj P. J Appl Polym Sci 1998;70:2703.
[11] Dalton S, Healton F, Budd PM. Polymer 1999;40:5531.
[12] Bajaj P, Sreekumar TV, Sen K. Polymer 2001;42:1707.
[13] Bashir Z, Rastogi S. J Macromol Sci: B, Phys 2005;44:55.
[14] Beltz LA, Gustatson RR. Carbon 1996;34:561.
[15] Wangxi Z, Jie L, Gang W. Carbon 2003;41:2805.
[16] Devasia R, Nair CPR, Sivadasan P, Katherine BK, Ninan KN. J Appl Polym Sci 2003;88:915.
[17] Hu XP, Hsien YL. Polymer 1997;38:1491.
[18] Devasia R, Nair CPR, Sadhana R, Babu NS, Ninan KN. J Appl Polym Sci 2006;100:3055.
[19] Jiang H, Wu C, Zhang A, Yang P. Compos Sci Technol 1987;29:33.
[20] Rangarajan P, Yang J, Bhanu VA, Godshall D, McGrath J, Wilkes G, et al. J Appl Polym Sci 2002;85:69–83.
[21] Rangarajan P, Bhanu VA, Godshall D, Wilkes GL, McGrath JE, Baird DG. Polymer 2002;43:2699–709.
[22] Naskar AK, Walker RA, Proulx S, Edie DD, Ogale AA. Carbon 2005;43:1065–72.
[23] Bajaj P, Roopanwal AK. J Macromol Sci Rev Macromol Chem Phys 1997;C37:97.
[24] Mukundan T, Bhanu VA, Wiles KB, Johnson H, Bortner M, Baird DG, et al. Polymer 2006;47:4163–71.
[25] Pekel N, Rzaev ZMO, Guven O. Macromol Chem Phys 2004;205:1088.
[26] Kalyanova NF, Barash AN, Zverev MP. J Fibre Chem 1997;29.
[27] Ishida H, Frederick P. J Appl Polym Sci 1986;32:5021.
[28] Deng W, Lobovsky A, Iacono ST, Hoffman WP, Smith Jr DW. Polym Prepr (Am Chem Soc Div Polym Chem) 2009;50:237.
[29] Gugion M, Oberlin A. Compos Sci Technol 1986;27:1.
[30] Sperling LH. Introduction to physical polymer science. 4th ed. Wiley, John & Sons; 2005. p. 110.
[31] Brabdrup J, Immergut EH. Polymer Handbook. 3rd ed., vol. II. New York: Wiley; 1989. p. 271.
[32] Brabdrup J, Immergut EH. Polymer Handbook. 3rd ed., vol. II. New York: Wiley; 1989. p. 184.
[33] Garcia-Rubio LH, Hamielec AE. J Appl Polym Sci 1979;23:1397.
[34] Bamford CH, Schofield E. Polymer 1981;22:1227;
Masaki M, Ozawa K, Kokufutta E. Colloid Polym Sci 2009;287:1369.
[35] Hutchinson SR. Thermoplastic Polyacrylonitrile 2005; 22: 1227.
[36] Bashir Z. Indian J Fibre Textile Res 1999;1:24.
[37] Andrews RD, Kimmel RM. J Polym Sci 1965;B 13:167.
[38] Henrici-Olive G, Olive S. Adv Polym Sci 1979;32:123.
[39] Bajaj P, Padmanaban M. Eur Polym J 1984;20:513.
[40] Hutchinson SR. Thermoplastic Polyacrylonitrile 2005; 22: 61.
[41] Gupta AK, Paliwal DK, Bajaj P. J Macromol Sci Rev Macromol Chem Phys 1991;C31:1.
[42] Rangarajan PB, Godshall D, Wilkes GL, McGrath JE, Baird DG. Polymer 2002;43:2699.
[43] Bashir Z. Carbon 1991;29:1081.

Polymer 52 (2011) 629–634

Contents lists available at ScienceDirect

Polymer

journal homepage: www.elsevier.com/locate/polymer

Effect of a combination of hexamethylphosphoramide and alkyl alcohol on the stereospecificity of radical polymerization of *N*-isopropylacrylamide

Tomohiro Hirano*, Akihiro Morikami, Yasuhiro Fujioka, Koichi Ute

Department of Chemical Science and Technology, Institute of Technology and Science, The University of Tokushima, 2-1 Minamijosanjima, Tokushima 770-8506, Japan

ARTICLE INFO

Article history:
Received 25 October 2010
Received in revised form
13 December 2010
Accepted 15 December 2010
Available online 22 December 2010

Keywords:
Hydrogen bonding
N-Isopropylacrylamide
Stereospecific radical polymerization

ABSTRACT

Radical polymerization of *N*-isopropylacrylamide (NIPAAm) was investigated at low temperatures in the presence of both hexamethylphosphoramide (HMPA) and alkyl alcohols. Although HMPA and alkyl alcohols separately induced syndiotactic specificity in NIPAAm polymerization in toluene at low temperatures, a combination of HMPA and less bulky alkyl alcohols, such as methanol and ethanol, was found to induce isotactic specificity at −80 °C. NMR analysis of mixtures of NIPAAm, ethanol and HMPA suggested the formation of a 1:1:1 complex through O−H•••O=C and N−H•••O=P hydrogen bonding. It is believed that the steric effect of HMPA enhanced by cooperative hydrogen bonding was responsible for the combined effect of HMPA and alkyl alcohols in inducing isotactic specificity.

1. Introduction

We have reported stereospecific radical polymerization of *N*-isopropylacrylamide (NIPAAm) via complex formation of NIPAAm with additives through hydrogen bonding interactions [1–5]. For example, addition of phosphoric acid derivatives such as hexamethylphosphoramide (HMPA) [1] and tri-*n*-butyl phosphate (TBP) [2] to radical polymerization of NIPAAm in toluene at low temperatures induced syndiotactic specificity. Polymer with 70% *racemo* (*r*) dyad content was obtained by adding a 2-fold amount of HMPA relative to monomer in NIPAAm polymerization in toluene at −60 °C. However, further decrease of the temperature to −80 °C reduced the syndiotactic specificity.

Alkyl alcohols were also shown to induce syndiotactic specificity in NIPAAm polymerization in toluene at low temperatures [3]. The induced syndiotactic specificity depended on both the bulkiness of the added alcohol and the polymerization temperature. For instance, polymer with 71% *r* dyad content was obtained by polymerizing NIPAAm in toluene at −60 °C in the presence of a 4-fold amount of 3-methyl-3-pentanol (3Me3PenOH), whereas 63% *r* dyad content was obtained by addition of methanol (MeOH) under the same conditions.

Poly(NIPAAm) has been extensively studied as a temperature-sensitive polymer material [6–8]. Recent developments in stereospecific polymerization have revealed that the stereoregularity of poly(NIPAAm) significantly affects the phase transition behavior [3,5,9–11]. Although our method is promising for facile preparation of syndiotactic poly(NIPAAm)s, further improvement of stereospecificity in NIPAAm polymerization is desired, because poly(NIPAAm) with higher syndiotacticity can be obtained by anionic polymerization of methoxymethyl-protected NIPAAm monomer [10].

Thus, radical polymerization of NIPAAm in the presence of both HMPA and alkyl alcohols was investigated, because further improvement in the syndiotactic specificity was expected by combining two kinds of syndiotactic specificity inducers. However, contrary to our expectations an increase in isotactic specificity was observed. We report herein the results of polymerization of NIPAAm in the presence of both HMPA and alkyl alcohols, and propose a mechanism based on the structure of the hydrogen bonding-assisted complex formed by NIPAAm and the additives.

2. Experimental

2.1. Materials

NIPAAm (Tokyo Chemical Industry Co., Japan) was recrystallized from hexane-toluene mixture. Toluene was purified by washing with sulfuric acid, water and 5% aqueous NaOH, followed by fractional distillation. MeOH, ethanol (EtOH), acetonitrile, dichloromethane (Kanto Chemical Co., Japan), isopropyl alcohol (*i*PrOH), *tert*-butyl alcohol (*t*BuOH; Tokyo Chemical Industry Co., Japan), 3Me3PenOH, tri-*n*-butylborane (*n*-Bu_3B), purchased as a 1.0 M tetrahydrofuran (THF) solution, and HMPA (Aldrich Chemical Co., Japan) were used without further purification.

* Corresponding author. Tel.: +81 88 656 7403; fax: +81 88 656 7404.
E-mail address: hirano@chem.tokushima-u.ac.jp (T. Hirano).

0032-3861/$ – see front matter © 2010 Elsevier Ltd. All rights reserved.
doi:10.1016/j.polymer.2010.12.035

Table 1
Radical polymerization of NIPAAm in methanol for 24 h at low temperatures in the absence or presence of HMPA.

Run	$[HMPA]_0$ mol l^{-1}	Temp. °C	Yield %	Tacticity(%)[a]		M_n[b] × 10^{-4}	M_w/M_n[b]
				m	*r*		
1	0.0	0	67	45	55	3.31	1.9
2	0.0	−20	56	43	57	4.17	1.7
3	0.0	−40	54	43	57	5.02	1.7
4	0.0	−60	76	44	56	6.34	1.4
5	0.0	−80	75	46	54	7.64	1.7
6	2.0	0	32	46	54	2.30	1.4
7	2.0	−20	58	45	55	2.68	1.4
8	2.0	−40	78	50	50	3.31	1.5
9	2.0	−60	96	49	51	3.97	1.9
10[c]	2.0	−80	85	52	48	7.43	1.8

$[NIPAAm]_0 = 1.0$ mol l^{-1}, $[n\text{-}Bu_3B]_0 = 0.10$ mol l^{-1}.
[a] Determined by ^1H NMR signals due to methylene group.
[b] Determined by SEC (polystyrene standards).
[c] Monomer, polymer or both precipitated during the polymerization reaction.

2.2. Polymerization

A typical polymerization procedure was as follows. NIPAAm (0.628 g, 5.5 mmol), HMPA (1.97 g, 11 mmol), and EtOH (0.506 g, 11 mmol) were diluted with toluene to a total volume of 5 ml, of which 4 ml was transferred to a glass ampoule and cooled to −80 °C. Polymerization was initiated by adding an aliquot of *n*-Bu_3B solution (0.21 ml, 1.0 mol l^{-1}) to the solution. The reaction was terminated after 24 h by adding 2,6-di-*t*-butyl-4-methylphenol in THF (0.5 ml, 1.0 mol l^{-1}) at the polymerization temperature. The polymerization mixture was poured into diethyl ether (150 ml), and the precipitated polymer was collected by filtration or centrifugation, and dried *in vacuo*. The polymer yield was determined gravimetrically.

2.3. Measurements

^1H and ^{13}C NMR spectra were obtained using an EX-400 spectrometer or an ECX-400 spectrometer (JEOL Ltd., Japan) operated at 400 MHz for ^1H and 100 MHz for ^{13}C. The dyad tacticity of the polymers was determined from the ^1H NMR signals of the methylene groups in the main chain, in deuterated dimethyl sulfoxide (DMSO-d_6) at 150 °C. The triad tacticity of the polymers was determined from the ^{13}C NMR signals of the methine groups in the main chain, in a mixed solvent (DMSO-d_6:D_2O:$H(CF_2)_4CH_2OH$ = 75:10:15 wt%) at 100 °C [5]. ^1H and ^{13}C NMR spectra of the mixture of NIPAAm, HMPA and/or EtOH were obtained in toluene-d_8 at −80 °C. The molecular weights and molecular weight distributions of the polymers were determined by size exclusion chromatography (SEC), using polystyrene samples as molecular weight standards. SEC was performed with an HLC 8220 chromatograph (Tosoh Co., Japan) equipped with TSK gel columns (SuperHM-M (6.5 mm ID × 150 mm) and SuperHM-H (6.5 mm ID × 150 mm), Tosoh Co., Japan). Dimethylformamide containing LiBr (10 mmol l^{-1}) was used as eluent at 40 °C with flow rate 0.35 ml min^{-1}. The initial polymer concentration was 1.0 mg ml^{-1}.

3. Results and discussion

3.1. Radical polymerization of NIPAAm in MeOH at low temperatures in the presence or absence of HMPA

Radical polymerization of NIPAAm was carried out in MeOH at low temperatures for 24 h in the presence or absence of HMPA (Table 1).

Table 2
Radical polymerization of NIPAAm in toluene at low temperatures for 24 h in the presence of HMPA and alcohol.

Run	Added alcohol	$[Alcohol]_0$ mol l^{-1}	$[HMPA]_0$ mol l^{-1}	Temp. °C	Yield %	Tacticity(%)[a]		M_n[b] × 10^{-4}	M_w/M_n[b]
						m	*r*		
1	MeOH	1.0	2.0	0	74	40	60	2.13	1.6
2	MeOH	1.0	2.0	−20	72	39	61	2.27	1.5
3	MeOH	1.0	2.0	−40	>99	39	61	2.26	2.5
4	MeOH	1.0	2.0	−60	98	42	58	1.86	2.2
5	MeOH	1.0	2.0	−80	64	53	47	0.87	1.7
6	MeOH	2.0	2.0	−80	76	55	45	1.69	1.5
7[c]	None	0.0	0.0	−80	78	46	54	3.85	2.7
8	None	0.0	2.0	−80	51	40	60	1.20	1.9
9	EtOH	0.5	2.0	−80	74	48	52	1.48	1.5
10	EtOH	1.0	2.0	−80	62	53	47	0.84	1.6
11	EtOH	2.0	0.0	−80	94	37	63	4.47	2.0
12	EtOH	2.0	0.5	−80	98	45	55	5.53	3.0
13	EtOH	2.0	1.0	−80	95	50	50	4.50	2.5
14	EtOH	2.0	2.0	−80	48	54	46	1.05	1.5
15	*i*PrOH	1.0	2.0	−80	45	47	53	2.12	1.7
16[c]	*i*PrOH	2.0	2.0	−80	60	48	52	2.57	2.0
17	*t*BuOH	1.0	2.0	−80	39	40	60	1.13	1.4
18[c]	*t*BuOH	2.0	2.0	−80	82	41	59	4.01	2.4
19[c]	3Me3PenOH	1.0	2.0	−80	39	43	57	1.20	1.4
20[c]	3Me3PenOH	2.0	2.0	−80	54	42	58	2.04	2.4

$[NIPAAm]_0 = 1.0$ mol l^{-1}, $[n\text{-}Bu_3B]_0 = 0.10$ mol l^{-1}, $[HMPA]_0 = 2.0$ mol l^{-1}.
[a] Determined by ^1H NMR signals due to methylene group.
[b] Determined by SEC (polystyrene standards).
[c] Monomer, polymer or both precipitated during the polymerization reaction.

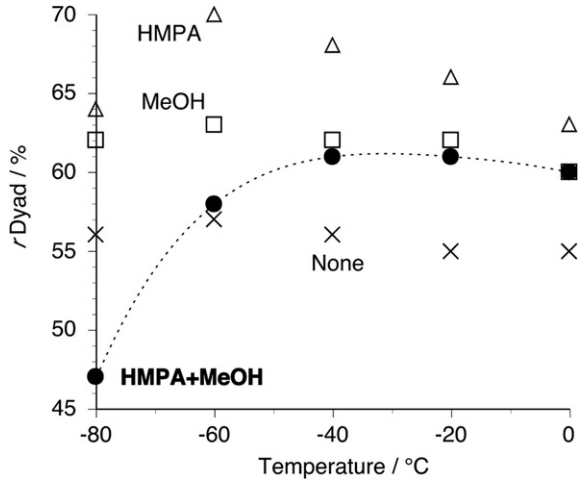

Fig. 1. Relationship between the polymerization temperature and *r* dyad content of poly(NIPAAm) prepared in toluene at low temperatures in the presence or absence of MeOH and/or HMPA.

The *r* dyad contents of the polymers obtained in MeOH as solvent (Table 1, runs 1–5) were comparable with those obtained in toluene, although the *r* dyad content of the polymers obtained increased slightly with the use of MeOH as an additive in the NIPAAm polymerization in toluene [3]. It is suggested that decreasing the polarity of the polymerization system by dilution with toluene is important for the alcohol-mediated syndiotactic-specific radical polymerization of NIPAAm, because complex formation of NIPAAm monomer with alkyl alcohols, which is responsible for the induction of syndiotactic specificity, is efficiently promoted [12].

The effect of HMPA on stereospecificity in NIPAAm polymerization in MeOH was examined (Table 1, runs 6–10). Regardless of the temperature, the *r* dyad contents of the polymers obtained were lower than those of the polymers prepared without HMPA. HMPA induced syndiotactic specificity in NIPAAm polymerization, even when polar molecules such as acetone and acetonitrile were used as solvents [12]. Thus, combining HMPA and alkyl alcohol brought about an unexpected effect on the stereospecificity of NIPAAm polymerization.

3.2. Effect of a combination of HMPA and alkyl alcohol on stereospecificity in the radical polymerization of NIPAAm

To examine the effect of a combination of HMPA and alkyl alcohol on the stereospecificity, polymerization of NIPAAm (1.0 mol l^{-1}) was carried out in toluene at low temperatures in the presence of both HMPA (2.0 mol l^{-1}) and MeOH (1.0 mol l^{-1}) (Table 2, runs 1–5). Fig. 1 shows the relationship between the polymerization temperature and the *r* dyad content of the polymers obtained. The *r* dyad contents of the polymers prepared in toluene in the presence or absence of HMPA [1] or MeOH [3] are also plotted in the Figure.

The *r* dyad contents of the polymers obtained at temperatures above −40 °C increased slightly compared with those of the polymers obtained in the absence of the syndiotactic specificity inducers, and were comparable with the *r* dyad contents of the polymers obtained in the presence of MeOH alone. However, further decrease of the temperature drastically decreased the *r* dyad content, and polymer rich in *m* dyad was obtained at −80 °C. This means that the stereospecificity changed from syndiotactic to isotactic by reducing the polymerization temperature. A similar tendency was observed in the radical polymerization of NIPAAm in the presence of esters of phosphoric acid, such as TBP [2].

The effect of the structure of the added alcohol was investigated at −80 °C in the presence of HMPA (Table 2, runs 5–8, 10, 14–20). Compared with the polymer obtained in the presence of HMPA alone (Table 2, run 8), addition of a less bulky alcohol such as MeOH or EtOH significantly increased the *m* dyad content of the polymers obtained (Table 2, runs 5–6, 10, and 14), whereas bulky alcohols such as *t*BuOH and 3Me3PenOH scarcely affected the stereoregularity (Table 2, runs 17–20). These results suggest that the combined effect is achieved only when less bulky alcohol was present together with HMPA at −80 °C [13].

To examine the effect of the amounts of alkyl alcohol and HMPA on the stereospecificity, radical polymerization of NIPAAm (1.0 mol l^{-1}) was carried out in toluene at −80 °C at several ratios of EtOH and HMPA (Table 2, runs 7–14). When the concentration of HMPA was kept at 2.0 mol l^{-1}, the *m* dyad content of the polymers obtained increased gradually with increase in $[EtOH]_0$ (Table 2, runs 8–10 and 14). Similarly, when the concentration of EtOH was kept at 2.0 mol l^{-1}, the *m* dyad content of the polymers obtained increased gradually with increase in $[HMPA]_0$ (Table 2, runs 11–14). In both cases, however, addition of alcohol or HMPA in excess was less effective, suggesting that equimolar amounts of both alcohol and

Table 3
Radical polymerization of NIPAAm at low temperatures for 24 h in the presence of HMPA and alcohol.

Run	Solvent	Added alcohol	$[Alcohol]_0$ mol l^{-1}	$[HMPA]_0$ mol l^{-1}	Temp.°C	Yield%	Tacticity (%)[a]		M_n[b] × 10^{-4}	M_w/M_n[b]
							m	*r*		
1	CH_3CN	None	0.0	0.0	−40	>99	57	43	2.09	1.6
2	CH_3CN	None	0.0	2.0	−40	89	50	50	0.80	1.6
3	CH_3CN	MeOH	2.0	0.0	−40	40	49	51	1.32	1.5
4	CH_3CN	MeOH	2.0	2.0	−40	88	58	42	1.11	1.9
5	CH_3CN	EtOH	2.0	0.0	−40	62	48	52	1.46	1.6
6	CH_3CN	EtOH	2.0	2.0	−40	89	55	45	1.30	1.7
7[c]	$CH_3CN + CH_2Cl_2$	None	0.0	0.0	−80	52	56	44	1.01	1.7
8[c]	$CH_3CN + CH_2Cl_2$	None	0.0	2.0	−80	85	60	40	2.64	1.5
9[c]	$CH_3CN + CH_2Cl_2$	MeOH	2.0	0.0	−80	64	47	53	2.08	2.1
10[c]	$CH_3CN + CH_2Cl_2$	MeOH	2.0	0.5	−80	61	52	48	3.49	2.5
11[c]	$CH_3CN + CH_2Cl_2$	MeOH	2.0	1.0	−80	94	61	39	2.26	1.8
12[c]	$CH_3CN + CH_2Cl_2$	MeOH	2.0	2.0	−80	64	67	33	4.11	1.3
13[c]	$CH_3CN + CH_2Cl_2$	EtOH	2.0	0.0	−80	91	42	58	4.01	2.1
14[c]	$CH_3CN + CH_2Cl_2$	EtOH	2.0	2.0	−80	>99	67	33	1.24	1.1

$[NIPAAm]_0 = 1.0$ mol l^{-1}, $[n\text{-}Bu_3B]_0 = 0.10$ mol l^{-1}.
[a] Determined by ^1H NMR signals due to methylene group.
[b] Determined by SEC (polystyrene standards).
[c] Monomer, polymer or both precipitated during the polymerization reaction.

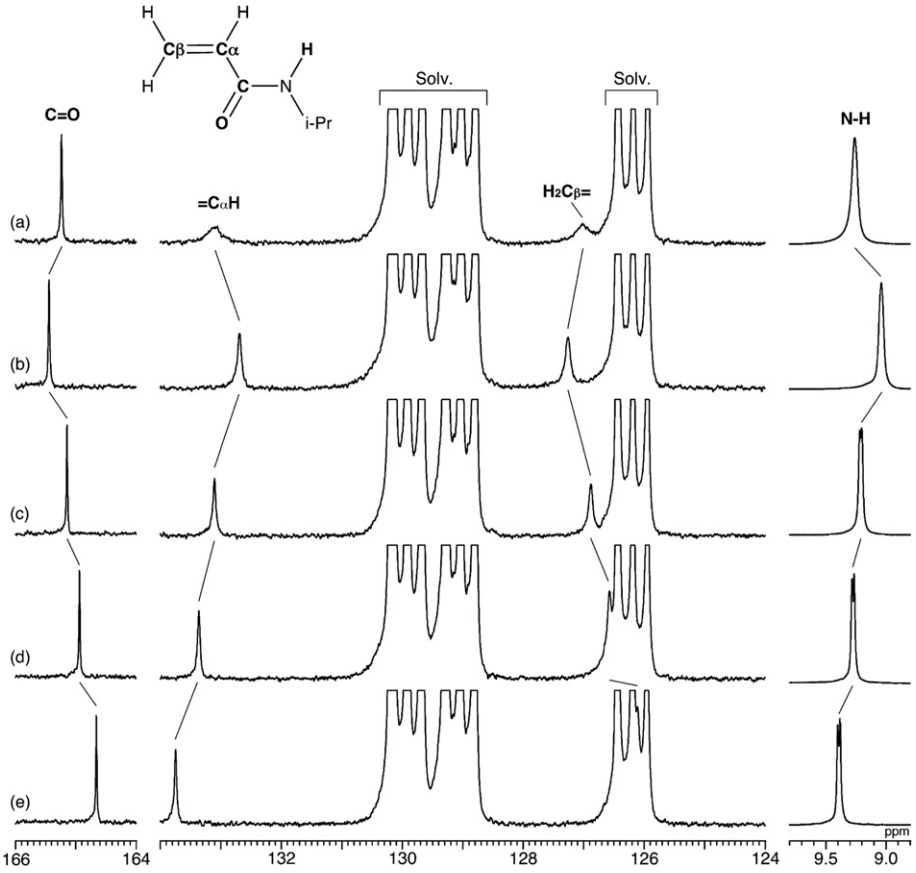

Fig. 2. Expanded ^{1}H and ^{13}C NMR spectra of NIPAAm ($[NIPAAm]_0 = 0.2$ mol l^{-1}) in toluene-d_8 at −80 °C in the presence or absence of EtOH and/or HMPA. (a) $[EtOH]_0 = [HMPA]_0 = 0$ mol l^{-1}; (b) $[EtOH]_0 = 0.4$ mol l^{-1}; (c) $[EtOH]_0 = 0.4$ mol l^{-1}, $[HMPA]_0 = 0.1$ mol l^{-1}; (d) $[EtOH]_0 = 0.4$ mol l^{-1}, $[HMPA]_0 = 0.2$ mol l^{-1}; (e) $[EtOH]_0 = 0.4$ mol l^{-1}, $[HMPA]_0 = 0.4$ mol l^{-1}.

HMPA relative to NIPAAm were necessary to significantly induce isotactic specificity.

3.3. Solvent effect of the isotactic specificity induced by a combination of HMPA and alkyl alcohol

Use of CH_3CN as solvent increased the isotactic specificity of radical polymerization of NIPAAm at low temperatures [12]. To examine the solvent effect polymerization was carried out in CH_3CN at −40 °C in the presence of both HMPA and less bulky alcohols such as MeOH and EtOH (Table 3, runs 1–6). The combined effect of HMPA and alkyl alcohol was observed, but the *m* dyad contents of the polymers were comparable with that of poly(NIPAAm) obtained in the absence of both HMPA and alkyl alcohol.

CH_3CN was mixed with CH_2Cl_2 in 1:1 (vol:vol) proportion to carry out polymerization at −80 °C [4]. Although the polymerizations proceeded heterogeneously, induced isotactic specificity was successfully enhanced [14], resulting in the formation of polymer with 67% *m* dyad content at relatively high yield.

3.4. Mechanistic considerations for the isotactic specificity induced by a combination of HMPA and alkyl alcohol

NMR analysis was carried out in toluene-d_8 at −80 °C to examine the structure of the complex formed by NIPAAm and the additives (Fig. 2). On adding a 2-fold amount of EtOH to NIPAAm, the carbonyl carbon (C = O) and β-methylene carbon ($H_2C =$) signals exhibited downfield shifts, whereas the α-methine carbon (= CH) and amide proton (N–H) signals showed upfield shifts (Fig. 2a–b), suggesting that NIPAAm formed a 1:2 complex with ethanol through hydrogen bonding interaction as shown below [3].

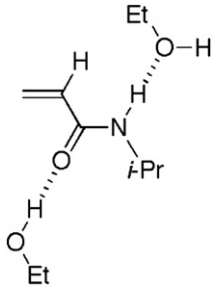

Those signals, however, shifted in the reverse direction when HMPA in half the amount of NIPAAm was added to the NIPAAm-EtOH mixture (Fig. 2c). This tendency was enhanced with increase in the amount of HMPA (Fig. 2d–e). Addition of both HMPA and EtOH improved solubility of NIPAAm in toluene. As reported previously [1], HMPA formed 1:1 complex with NIPAAm through an N–H•••O=P hydrogen bonding, regardless of the temperature. Alcohol was suggested to form 1:2 complex with NIPAAm through a cooperative hydrogen bonding O–H•••O=C–N–H•••O [3]. In addition, fluorinated alcohol formed 1:1 complex with NIPAAm through an O–H•••O=C hydrogen bonding [5]. The NMR signals for a 1:2:2 mixture of NIPAAm:EtOH:HMPA (Fig. 2e) were sharper than

those for NIPAAm alone (Fig. 2a), indicating that NIPAAm form hydrogen bonding interaction with HMPA and/or EtOH. The circumstantial evidence suggested that NIPAAm formed a 1:1:1 complex with EtOH and HMPA through cooperative hydrogen bonding interactions [15–17] as shown below.

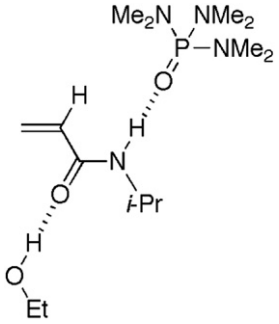

As reported previously [2], polymer rich in *m* dyad was obtained by radical polymerization of NIPAAm in toluene at −80 °C in the presence of TBP, whereas polymer rich in *r* dyad was obtained under the same conditions except for increased temperature. The structure of the complex was assumed to be responsible for the change in stereospecificity, because NIPAAm formed a 1:1 complex at 0 °C and a 1:2 complex at −80 °C. In other words, larger steric hindrance by doubly coordinated TBPs changed the stereospecificity in NIPAAm polymerization (Scheme 1). A similar effect was observed in radical polymerization of methacrylates, where bulky monomers such as triphenylmethyl [18,19] and 1-phenyldibenzosuberyl [20] methacrylates gave isotactic polymers, and less bulky monomers such as methyl methacrylate gave syndiotactic polymers.

The cooperative hydrogen bonding interaction in the 1:1:1 complex should strengthen each of the hydrogen bonding interactions, i.e. O–H•••O=C and N–H•••O=P. The strengthened N–H•••O=P hydrogen bond should enhance the steric hindrance of the coordinated HMPA compared with that in the 1:1 NIPAAm-HMPA complex. As a result of the enhanced steric hindrance of HMPA, isotactic specificity was significantly induced by a mechanism similar to that for polymerization of the methacrylates (Scheme 2).

Table 4 summarizes the triad tacticities and the probabilities of *r*-addition to *m*-ended radical ($P_{m/r}$) and *m*-addition to *r*-ended radical ($P_{r/m}$) in first-order Markovian statistics for the polymers prepared in toluene at −80 °C in the presence or absence of EtOH and/or HMPA. Stereoregulation obeyed Bernoullian statistics in the absence of syndiotactic specificity inducers, because the sum of the probabilities ($P_{m/r} + P_{r/m}$) was close to unity. Addition of HMPA not only influenced the stereospecificity of polymerization but also caused a deviation from the Bernoullian model, probably because the stereoselectivity of the propagating reaction in the HMPA-mediated syndiotactic-specific polymerization gradually varied with conversion [21].

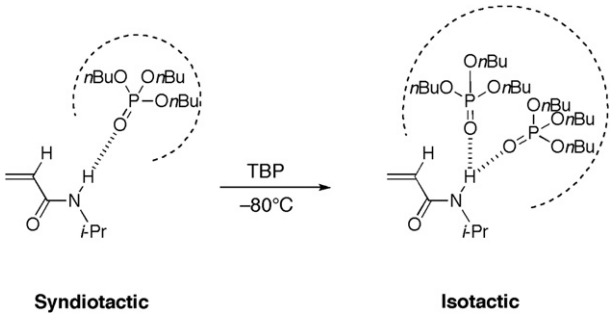

Scheme 1. Change of the stereospecificity in NIPAAm polymerization from syndiotactic to isotactic because of the steric effect of TBP enhanced by formation of a 1:2 complex.

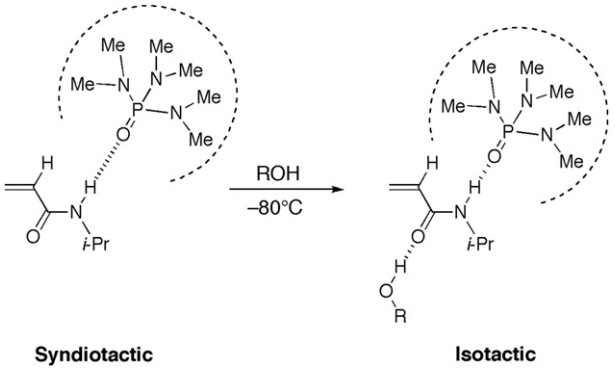

Scheme 2. Change of the stereospecificity in NIPAAm polymerization from syndiotactic to isotactic because of the steric effect of HMPA enhanced by formation of cooperative hydrogen bonding in the 1:1:1 complex.

Table 4
Triad tacticities and the probabilities of *r*-addition to *m*-ended radical ($P_{m/r}$), and *m*-addition to *r*-ended radical ($P_{r/m}$) in first-order Markovian statistics for the polymers prepared in toluene at −80 °C in the presence or absence of EtOH and/or HMPA.

$[EtOH]_0$ mol l^{-1}	$[HMPA]_0$ mol l^{-1}	Triad tacticity (%)			$P_{m/r}$	$P_{r/m}$	$P_{m/r} + P_{r/m}$
		mm	*mr*	*rr*			
0.0	0.0	22	47	31	0.52	0.43	0.95
0.0	2.0	22	35	43	0.44	0.29	0.73
2.0	0.0	12	51	37	0.68	0.41	1.09
2.0	0.5	20	50	30	0.56	0.45	1.01
2.0	1.0	27	45	28	0.45	0.45	0.90
2.0	2.0	36	34	30	0.32	0.36	0.68

On the other hand, addition of EtOH obeyed the Bernoullian model, although the stereospecificity of polymerization was slightly affected. The addition of HMPA to the polymerization system in the presence of EtOH also caused a deviation from the Bernoullian model, suggesting that the stereoselectivity of the propagating reaction varied with conversion even when HMPA was present together with EtOH. It should be noted that addition of HMPA drastically reduced the *r*-selectivity by *m*-ended radical, whereas the stereoselectivity by *r*-ended radical was only slightly affected. A similar tendency was observed in radical polymerization of methacrylates in toluene at 60 °C; changing the monomer from diphenylmethyl methacrylate to triphenylmethyl methacrylate afforded syndiotactic and isotactic polymers, respectively [18,22]. Consequently, the induced isotactic specificity was expected to arise predominantly from the increasing *m*-selectivity by *m*-ended radical due to the steric effect, enhanced by the cooperative hydrogen bonding interaction.

4. Conclusions

The combined effect of HMPA and alkyl alcohols on stereospecificity in NIPAAm polymerization was investigated. A combination of HMPA and less bulky alkyl alcohol induced isotactic specificity in the polymerization at −80 °C, although both additives induced syndiotactic specificity when used separately. NMR

analysis of the mixtures of NIPAAm and the additives suggested the formation of a 1:1:1 complex, assuming that isotactic specificity was induced by the steric effect of HMPA enhanced by a cooperative hydrogen bonding effect.

We concluded previously [21] that incorporation of monomer and/or the propagating chain-end free from complexation with HMPA was the reason that the syndiotactic specificity induced by HMPA decreased by lowering the temperature to −80 °C, because complex formation between NIPAAm and HMPA through N–H•••O=P hydrogen bonding reduced the monomer reactivity due to the cross-conjugated structure of NIPAAm. The findings described in the present paper, however, suggest that the steric effect of HMPA enhanced by strengthened N–H•••O=P hydrogen bonding interaction with decrease in the temperature to −80 °C is an alternative reason for the reduction of the syndiotactic specificity induced by HMPA.

Acknowledgments

This work was supported in part by a Grant-in-Aid for Young Scientists (B) (18750102) from the Ministry of Education, Culture, Sports, Science and Technology.

References

[1] Hirano T, Miki H, Seno M, Sato T. Polymer 2005;46(11):3693–9.
[2] Hirano T, Ishii S, Kitajima H, Seno M, Sato T. J Polym Sci Part A Polym Chem 2005;43(1):50–62.
[3] Hirano T, Okumura Y, Kitajima H, Seno M, Sato T. J Polym Sci Part A Polym Chem 2006;44(15):4450–60.
[4] Hirano T, Ishizu H, Yamaoka R, Ute K, Sato T. Polymer 2009;50(15):3522–7.
[5] Hirano T, Kamikubo T, Okumura Y, Bando Y, Yamaoka R, Mori T, et al. J Polym Sci Part A Polym Chem 2009;47(10):2539–50.
[6] Heskins M, Guillet JE. J Macromol Sci A Chem 1968;2(8):1441–55.
[7] Schild HG. Prog Polym Sci 1992;17(2):163–249.
[8] Rzaev ZMO, Dinçer S, Pişkin E. Prog Polym Sci 2007;32(5):534–95.
[9] Ray B, Okamoto Y, Kamigaito M, Sawamoto M, Seno K, Kanaoka S, et al. Polym J 2005;37(3):234–7.
[10] Ito M, Ishizone TJ. Polym Sci Part A Polym Chem 2006;44(16):4832–45.
[11] Katsumoto Y, Kubosaki N. Macromolecules 2008;41(15):5955–6.
[12] Hirano T, Kamikubo T, Fujioka Y, Sato T. Eur Polym J 2008;44(4):1053–9.
[13] Bulky alcohols such as 3Me3PenOH showed enhanced steric effect to improve syndiotactic specificity, when only alcohol was added into radical polymerization of NIPAAm in toluene at low temperatures [3]. In the polymerization system in this paper, however, combining alcohol and HMPA induced isotactic specificity, instead of syndiotactic specificity. Thus, it was suggested that dependence of bulkiness of the added alcohol on stereospecificity depended on the induced stereospecificity.
[14] Addition of HMPA increased *m* dyad content of the polymer obtained in the mixed solvent (CH_3CN + CH_2Cl_2) at −80 °C, probably because the solvent formed cooperative hydrogen bonding C–H•••O=C–N–H•••O=P with NIPAAm. In fact, HMPA induced syndiotactic specificity of NIPAAm polymerization in CH_3CN or CH_2Cl_2 decreased even at −40 °C or −60 °C [12].
[15] Etter MC, Urbanczyk-Lipkowska Z, Zia-Ebrahimi M, Panunto TW. J Am Chem Soc 1990;112(23):8415–26.
[16] Guo H, Karplus M. J Phys Chem 1994;98(29):7104–5.
[17] Gung BW, Zhu Z. Tetrahedron Lett 1996;37(13):2189–92.
[18] Yuki H, Hatada K, Niinomi T, Kikuchi Y. Polym J 1970;1(1):36–45.
[19] Nakano T, Matsuda A, Okamoto Y. Polym J 1996;28(6):556–8.
[20] Nakano T, Mori M, Okamoto Y. Macromolecules 1993;26(4):867–8.
[21] Hirano T, Miki H, Seno M, Sato T. Polymer 2005;46(15):5501–5.
[22] Diphenylmethyl methacrylate: $P_{m/r} = 0.91$ and $P_{r/m} = 0.27$, triphenylmethyl methacrylate: $P_{m/r} = 0.15$ and $P_{r/m} = 0.44$. The values were calculated from the triad tacticities in the literature [18].

Polymer 52 (2011) 635–645

Contents lists available at ScienceDirect

Polymer

journal homepage: www.elsevier.com/locate/polymer

RAFT polymerization of diacrylate derivatives having different spacers in dilute conditions

Hideharu Mori [a,b,*], Masahiro Tsukamoto [a]

[a] Department of Polymer Science and Engineering, Graduate School of Science and Engineering, Yamagata University, 4-3-16, Jonan, Yonezawa, 992-8510, Japan
[b] Department of Organic Device Engineering, Graduate School of Science and Engineering, Yamagata University, 4-3-16, Jonan, Yonezawa, 992-8510, Japan

ARTICLE INFO

Article history:
Received 30 September 2010
Received in revised form
12 December 2010
Accepted 15 December 2010
Available online 22 December 2010

Keywords:
RAFT polymerization
Divinyl monomer
Branched polymer

ABSTRACT

Reversible addition-fragmentation chain transfer (RAFT) polymerization of four divinyl monomers, 1,4-butanediol diacrylate (BDDA) and three poly(ethylene glycol) diacrylates (PEGDAs), were investigated under dilute conditions ([M] = 0.2–0.05 mol/L). RAFT polymerization of BDDA using a dithiocarbamate-type chain transfer agent (CTA) afforded soluble polymers, whereas a cross-linked product was obtained by conventional radical polymerization. The monomer concentration, the nature of the CTA, and the CTA/initiator ratio were found to affect the polymerization behavior and structure of the resulting polymers, which is attributed to the relative propensities for intermolecular propagating/cross-linking reactions and intramolecular cyclization. RAFT polymerizations of three PEGDAs (PEG258DA, average M_n = 258; PEG575DA, average M_n = 575; PEG700DA, average M_n = 700) having different lengths of PEG spacers (n = 3, 10, 13, respectively) were also conducted under dilute conditions. Water-soluble polymers were synthesized by one-step RAFT polymerization of PEGDAs having longer spacers (n = 10 and 13), whereas RAFT polymerization of PEGDA (n = 3) afforded polymers soluble in organic solvents. The product obtained by RAFT polymerization of PEGDA (n = 10) showed a characteristic thermoresponsive property, lower critical solution temperature (LCST), in aqueous solution.

1. Introduction

Recently, considerable attention has been paid to the synthesis of branched polymers using radical copolymerization of commercial monovinyl monomer and divinyl monomers. A facile and cost-effective approach to synthesizing branched vinyl polymers has been described, in which a chain transfer agent (CTA) (typically thiol) is added to a conventional radical copolymerization of a monovinyl monomer and a divinyl comonomer [1–3]. In the presence of the CTA, the molecular weight of the primary chains is limited and gelation can be suppressed, resulting in the formation of soluble polymers having branched structures. There is also increasing interest in the employment of controlled radical copolymerization techniques for the synthesis of branched polymers and gels with more homogeneous structures. For example, several studies have reported the synthesis of branched polymers [4–8] and gels [9–13] by atom transfer radical copolymerization of conventional vinyl monomers with divinyl cross-linkers. Reversible addition-fragmentation chain transfer (RAFT) copolymerization has also been employed for the synthesis of branched polymers [8,14–18] and homogeneous polymer networks [13,19] via one-step copolymerization. The controlled radical copolymerization of a vinyl monomer with a divinyl monomer is a facile approach to obtain functional branched polymers because different types of functional groups can be incorporated into a polymer, depending on the chemical nature of the monovinyl and divinyl monomers. In addition, the chain architecture can be modified by a suitable choice of the ratio of the monovinyl/divinyl monomers in the feed. Various branched polymers have been obtained by controlled radical copolymerization of divinyl monomers and functional comonomers, such as acrylamide [18,20], 2-aminoethyl acrylate [14], 2-hydroxypropyl (meth)acrylate [5,16], and acrylic acid [20].

In conventional radical polymerization, the addition of even small amounts of a bifunctional monomer (cross-linker) leads to the production of a cross-linked network. The gelation observed is dependent on the concentration of monomers present. The system undergoes macrogelation in the case of concentrated solutions or microgelation under conditions of high dilution. For example, it was reported that bulk copolymerization of methyl methacrylate with small amounts of ethylene glycol dimethacrylate led to cyclization

* Corresponding author. Department of Polymer Science and Engineering, Graduate School of Science and Engineering, Yamagata University, 4-3-16, Jonan, Yonezawa, 992-8510, Japan. Tel.: +81 238 26 3765; fax: +81 238 26 3092.
E-mail address: h.mori@yz.yamagata-u.ac.jp (H. Mori).

0032-3861/$ – see front matter © 2010 Elsevier Ltd. All rights reserved.
doi:10.1016/j.polymer.2010.12.032

of approximately 3–4% of the pendant vinyl group, and the fraction of the cyclization rapidly increased with dilution [21]. Atom transfer radical copolymerization of methyl acrylate with ethylene glycol diacrylate led to macroscopic gelation when conducted at a higher monomer concentration, whereas a soluble, branched copolymer was obtained at a lower monomer concentration [12]. Modeling of branching and gelation in RAFT copolymerization of monovinyl/divinyl systems indicated that the gel point was significantly postponed by increasing the RAFT agent concentration [22]. It was also suggested that gel point is postponed by the presence of the intermolecular cyclization, and its effect becomes significant in a dilute polymerization system. Recently, the importance of the critical overlap concentration when exploring the relative propensities for intermolecular branching and intramolecular cyclization was demonstrated in a model system, in which branched polymers were obtained by quaternization of near-monodisperse poly[(2-dimethylamino)ethyl methacrylate] using bis(2-iodoethoxy) ethane [23]. They concluded that the intermolecular branching is preferable at polymer concentrations higher than the critical overlap concentration (around 10% w/v for their model system), whereas intramolecular cyclization is much more likely below that concentration. Hence, it is reasonable to consider that the monomer concentration is one of the important factors for obtaining branched polymers by controlled radical copolymerization of a monovinyl monomer and a divinyl comonomer.

Compared to the branched polymers obtained by controlled radical copolymerization of monovinyl/divinyl systems, less attention has been paid to the homopolymerization of divinyl monomer via controlled radical polymerization [24–27]. Homopolymerization of ethylene glycol dimethacrylate using atom transfer radical polymerization was studied in bulk at 70 °C, in which gelation occurred at relatively low monomer conversions (<10%) [24]. Reaction kinetics and gelation behavior in atom transfer radical polymerization, RAFT polymerization, and conventional radical polymerization of oligo(ethylene glycol) dimethacrylate were also investigated in bulk [27]. RAFT polymerization of oligo(ethylene glycol) dimethacrylate with longer spacers was reported to produce more homogeneous networks with a lower cross-linking density than conventional radical polymerization. Atom transfer radical polymerization [28,29] and RAFT polymerization [30] of asymmetrical divinyl monomers have been reported, and branching, cyclization, and cross-linking proceeded, depending on the structure of the asymmetrical divinyl monomers, the polymerization system, and reaction conditions. RAFT polymerization of allyl methacrylate led to a polymer with five- and six-membered rings, whereas the formation of branching rather than intramolecular cycles proceeded in the case of the polymerization of an asymmetrical divinyl monomer having a longer spacer [30].

Cyclopolymerization of bifunctional monomers has attracted additional research interest. In order to produce cyclopolymers without gelation, the cyclopolymerization should proceed through sequential intramolecular cyclization and intermolecular propagation, which generally produce thermodynamically stable five- or six-membered rings as the repeating units along the backbone. Recently, much attention has been paid to controlled radical cyclopolymerization of bifunctional monomers. For example, RAFT polymerizations of diallyldimethylammonium chloride [31] and *tert*-butyl α-(hydroxymethyl)acrylate ether dimer [32] under suitable conditions proceeded in controlled fashion to produce well-defined cyclopolymers with five- and six-membered rings, respectively. Controlled cyclopolymerizations through quantitative large-ring formation were achieved by RAFT polymerization of bisacrylamide [33] and bismethacrylate [34] derivatives with a specific conformation favorable to ring-closing. In these systems, efficient ring-closing intramolecular cyclization should occur predominantly compared to intermolecular reactions leading to a cross-linked product, by means of constrained conformation.

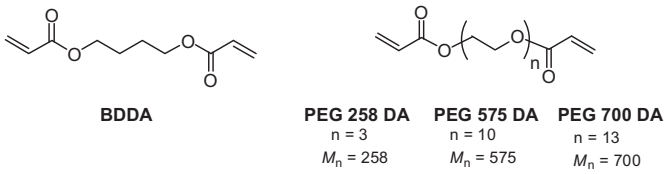

Scheme 1. Structures of the divinyl monomers used in this study.

RAFT polymerization of four diacrylates, 1,4-butanediol diacrylate (BDDA) and three poly(ethylene glycol) diacrylates (PEGDA)s (PEG258DA, average M_n = 258; PEG575DA, average M_n = 575; EG700DA average M_n = 700) having different lengths of PEG spacers (n = 3, 10, 13, respectively, as shown in Scheme 1) in dilute solution is now reported. Initially, we investigated the RAFT polymerization of BDDA using three different CTAs, as shown in Scheme 2, in order to find the optimum conditions for obtaining soluble polymers having a relatively high molecular weight with sufficient yield. Molecular weight, polydispersity, solution properties, and structures of the resulting polymers were evaluated by gel permeation chromatography (GPC)/viscosity, GPC/right-angle laser light scattering (RALLS), and ^{1}H NMR measurements. The relative propensities for intermolecular propagating/cross-linking reactions and intramolecular cyclization were assessed using these data coupled with kinetic information. We then describe the RAFT polymerization of PEGDAs having different lengths of PEG spacers (n = 3, 10, 13) and the synthesis of water-soluble hyperbranched polymers. Finally, the thermally induced phase separation behaviors of the poly(PEG575DA) obtained under different conditions in aqueous solution are reported.

2. Experimental

2.1. Materials

2,2′-Azobis(isobutyronitrile) (AIBN, Kanto Chemical, 97%) was purified by recrystallization from methanol. 1,4-butanediol diacrylate (BDDA, Aldrich, 90%) was washed with aqueous NaOH solution (10%), dried with $CaCl_2$, and then distilled at reduced pressure. Poly(ethylene glycol) diacrylates (PEG258DA, average M_n = 258; PEG575DA, average M_n = 575; PEG700DA, average M_n = 700) were purchased from Aldrich, and passed through an alumina column to remove the polymerization inhibitor. 1,4-Dioxane (Kanto Chemical, 99%) was distilled from sodium wire. Note that distilled dioxane was stored under nitrogen atmosphere in the dark, which was carefully employed for the polymerization because of the possible effect of peroxide impurities in the solvent [35]. The synthesis of benzyl 1-pyrrolecarbodithioate (CTA 1) was conducted according to the procedure reported previously [36,37]. *O*-Ethyl-*S*-(1-methoxycarbonyl) ethyldithiocarbonate (CTA 2) [38,39] and *O*-ethyl-*S*-(1-phenylethyl) dithiocarbonate (CTA 3) [40–42] were synthesized by the reaction of potassium ethyl xanthogenate with corresponding bromide (methyl 2-bromopropionate for CTA 2, and 1-bromoethyl benzene for CTA 3) according to a procedure previously reported.

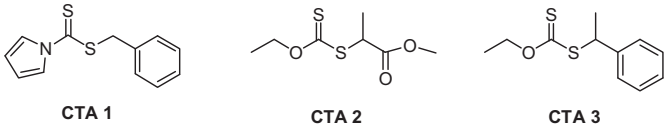

Scheme 2. Structures of the chain transfer agents (CTAs) used in this study.

2.2. General polymerization procedure

All polymerizations were carried out with AIBN as an initiator in a degassed sealed tube. A representative example is as follows: BDDA (0.10 g, 0.50 mmol), CTA 1 (2.87 mg, 0.0123 mmol), AIBN (0.4 mg, 0.0025 mmol), and anhydrous 1,4-dioxane (5.0 mL) were placed in a dry glass ampule equipped with a magnetic stirring bar, and then the solution was degassed by three freeze-evacuate-thaw cycles. After the ampoule was flame-sealed under reduced pressure, the solution was stirred at 60 °C for 24 h. The crude polymer was purified by reprecipitation into a large excess of methanol, and the resulting product was dried under vacuum at room temperature to yield poly(BDDA) as a pale yellow solid (yield = 57%, 0.057 g). The polymer had M_n = 8100 and M_w/M_n = 1.44 according to GPC using polystyrene standards. The resulting polymer was soluble in THF, 1,4-dioxane, chloroform, ethyl acetate, and *N*,*N*-dimethylformamide, and insoluble in *n*-hexane, diethylether, methanol, and water. ^{1}H NMR ($CDCl_3$): δ 1.0–2.0 (broad m, 8H, CH_2–CH, –C(=O)–O–CH_2–CH_2–), δ 2.1–2.7 (broad m, 2H, CH_2–CH), δ 3.5–5.0 (broad m, 4H, –C(=O) –O–CH_2–CH_2–).

2.3. Measurements

^{1}H NMR (400 MHz) and ^{13}C NMR (100 MHz) spectra were recorded with a JEOL JNM-ECX400. Elemental analysis was carried out on a Perkin–Elmer 2400II CHNS/O analyzer.

Number-average molecular weight (M_n) and molecular weight distribution (M_w/M_n) were estimated by GPC using a system consisting of a Tosoh DP-8020 pump and a Viscotek TDA model-301 triple detector array (refractive index (RI), viscosity, and right-angle laser light scattering detector (RALLS) detector; wavelength = 670 nm). The column set was as follows: a guard column [TSK-guard column H_{XL}-H, 4.0 cm] and four consecutive columns [Tosoh TSK-GELs (exclusion limited molecular weight): GMH_{XL} (4×10^8), $G4000H_{XL}$ (4×10^5), $G3000H_{XL}$ (6×10^4), $G2500H_{XL}$ (2×10^4), 30 cm each] eluted with THF at a flow rate of 1.0 mL/min. Polystyrene standards were employed for calibration. GPC/RALLS was also performed to determine the absolute molecular weights of poly(BDDA). The excess RI increment, dn/dc = 0.119 for poly(BDDA), was measured in THF at 25 °C using a DRM1021 differential refractometer operating at 633 nm.

The UV–vis spectra were recorded using a JASCO V-630BIO UV–vis spectrophotometer. The phase separation temperatures of the aqueous solutions of the polymers (2.0 mg/mL) were measured by monitoring the transmittance of a 500 nm light beam through a quartz sample cell. The transmittance was recorded on a JASCO V-630BIO UV–vis spectrophotometer equipped with a temperature controller system (JASCO EHC-716 and EHC-717). The polymer solutions were filtered using Millipore Teflon filters with a pore size of 0.2 μm before the measurement. The temperature was increased at a rate of 1.0 °C/min in heating scans between 10 and 70 °C.

3. Results and discussion

3.1. RAFT polymerization of 1,4-butanediol diacrylate (BDDA)

Initially, RAFT polymerization of a divinyl monomer, 1,4-butanediol diacrylate (BDDA), was investigated using an AIBN initiator with three different chain transfer agents (CTAs). The dithiocarbamate-type CTA 1, in which a nitrogen lone pair is part of an aromatic ring system, is efficient as a mediating agent for RAFT polymerizations of conventional conjugated monomers, such as methyl acrylate [43], styrene [36,43], and *N*-isopropylacrylamide [44]. In contrast, dithiocarbonates (xanthates) are known to be useful for controlling the radical polymerization of nonconjugated *O*-vinyl and *N*-vinyl monomers, such as vinyl acetate [45–47], *N*-vinylpyrrolidone [47–51], *N*-vinylcarbazole [42,52,53], *N*-vinylindole [54], and *N*-vinylphthalimide [39]. CTA 2 has also been used for the polymerization of acrylic acid and acrylamide [55]. Initially, we examined the influences of CTA and polymerization conditions in terms of the polymer yield, molecular weight, and the polydispersity of the resulting poly(BDDA)s.

In this system, rapid equilibrium between the active propagating radicals and the dormant polymeric thiocarbonylthio compounds provides equal probability for all chains to grow and the suppression of radical–radical termination. The propagating radicals can react with free divinyl monomer and the pendant vinyl groups tethered to the polymer backbone. The former can be regarded as conventional intermolecular propagation, and the latter can be divided into two categories; intermolecular and intramolecular reactions. The intermolecular reactions between the propagating radicals and the pendant vinyl groups generate branched polymers with an apparent increase in molecular weight. This means that a significant increase in molecular weight during the polymerization of a divinyl monomer suggests preferable intermolecular reactions compared to the intramolecular reactions. Finally, insoluble cross-linked products are formed as polymer networks when the number of reacted pendant vinyl groups per primary chain reaches a critical value [9,12]. In contrast, the intramolecular reactions between the propagating radicals and the pendant vinyl groups consume the pendant vinyl groups to afford cyclic products but have no significant influence on the molecular weight. In general, sequential intramolecular cyclization and intermolecular propagation led to the generation of cyclopolymers having ring structures as the repeating units along the backbone. In other words, the competition between intermolecular propagating/cross-linking reactions and intramolecular cyclization is a crucial factor for the formation of cyclopolymer, branched polymer, or cross-linked product. Various factors, such as monomer concentration, structures of CTAs and divinyl monomers, and polymerization conditions, may affect the competition between intermolecular and intramolecular reactions.

The polymerization of BDDA was carried out using AIBN as an initiator at $[M]_0/[CTA]_0/[AIBN]_0$ = 200/5/1 in 1,4-dioxane at 60 °C for 24 h under different monomer concentrations. The results are summarized in Table 1. When the polymerization of BDDA was carried out using the dithiocarbamate-type CTA (CTA 1) under dilute conditions ([M] = 0.2 mol/L), the characteristic pale yellow solution remained without any significant change in viscosity during the polymerization. The soluble polymer was obtained as a pale yellow powder after the precipitation into methanol and the polymer yield was 68%. As expected, the difference in the monomer concentration led to the different polymerization behavior and polymeric architecture. Indeed, the RAFT polymerization of BDDA at low monomer concentrations ([M] $\leq$ 0.2 mol/L) afforded a soluble product, suggesting that the cyclizations are efficient enough to prevent cross-linking. In contrast, gelation was observed at a higher monomer concentration ([M] = 0.3 mol/L). These results are consistent with general tendencies, in which the copolymerization of difunctional monomers under dilute conditions enhances the intramolecular cyclization reaction, delaying or even preventing the occurrence of gelation [12,19].

Fig. 1a demonstrates the GPC traces of poly(BDDA)s obtained with CTA 1 at different monomer concentrations. At low concentration ([M] = 0.05 mol/L), the GPC trace of the resulting polymer shows a symmetrical peak with a relatively narrow molecular weight distribution (M_w/M_n < 1.3). This result suggests that the dithiocarbamate-type CTA 1 leads to a degree of control, since the polydispersities significantly less than 1.5 cannot be achieved via a conventional radical polymerization process. The increase in the

Table 1
Effects of Chain Transfer Agent (CTA) and Monomer Concentration on RAFT Polymerization of 1,4-Butanediol Diacrylate (BDDA) with 2,2′-Azobis(isobutyronitrile) (AIBN) in dioxane at 60 °C for 24 h.[a]

Run	CTA	[M] mol/L	Yield[b] (%)	M_n (M_w/M_n)			Vinyl content (%)	α[f]
				GPC-RI[c]	GPC-RALLS[d]	GPC-Visco [e]		
1	CTA 1	0.3	–[g]	–	–	–	–	–
2	CTA 1	0.2	68	13,000 (2.45)	23,000 (3.81)	30,000 (3.54)	6.6	0.26
3	CTA 1	0.1	56	8100 (1.44)	12,000 (1.78)	16,000 (1.73)	2.6	0.25
4	CTA 1	0.05	33	7500 (1.21)	11,000 (1.23)	9200 (1.21)	1.6	0.36
5	CTA 2	0.2	77	29,000 (6.15)	28,000 (7.91)	91,000 (16.0)	0.3	0.26
6	CTA 2	0.1	78	13,000 (1.89)	20,000 (2.61)	30,000 (3.05)	0.5	0.19
7	CTA 3	0.2	64	20,000 (3.37)	18,000 (7.85)	47,000 (6.18)	0.6	0.27

[a] [BDDA]/[CTA]/[AIBN] = 200/5/1.
[b] MeOH-insoluble part.
[c] Number-average molecular weight (M_n) and molecular weight distribution (M_w/M_n) were measured by gel permeation chromatography (GPC) using polystyrene standards in THF.
[d] GPC/RALLS measurement in THF, dn/dc = 0.119 (mL/g).
[e] GPC/Viscosity measurement in THF.
[f] Mark-Houwink exponent α.
[g] Formation of cross-linked polymer.

monomer concentration led to an increase in the polymer yield with increasing molecular weight. As shown in Fig. 1a, the appearance of broad elution peaks in the higher molecular weight region is detected at a higher monomer concentration ([M] = 0.2 mol/L). The determination of the molecular weight of branched polymers is complicated by the fact that the hydrodynamic volume for a given molecular weight differs significantly from that of a linear sample. Therefore, the use of a linear calibration curve in GPC leads to erroneous results. This problem can be overcome by the use of mass-sensitive online detectors, such as a light scattering detector or a viscosity detector using the universal calibration principle. In this study, characterization of the poly(BDDA)s obtained by RAFT polymerization of the divinyl monomer under dilute conditions was conducted by GPC, GPC/viscosity, and GPC/RALLS. For poly(BDDA)s obtained with CTA 1 at [M] = 0.1–0.2 mol/L, the number-average molecular weights determined by GPC/viscosity and GPC/RALLS are apparently higher than those obtained from GPC using polystyrene standards as shown in Table 1. In particular, the molecular weights determined by GPC/viscosity differ much more from those obtained by conventional GPC (RI detector) than the molecular weights obtained by GPC/RALLS. As can be seen in Fig. 1a–c, broad peaks with significant tailing peaks in low molecular weight areas are detected in conventional GPC (RI detector) and GPC/viscosity traces of poly(BDDA)s obtained with CTA 1 at [M] = 0.1–0.2 mol/L. In contrast, the GPC traces from the light scattering detector showed preponderant responses at low elution time (i.e., a high molecular weight fraction). Here it is necessary to take into account the influence of the RI increment, dn/dc, because the different structures, branched and cyclic structures, may affect the value of dn/dc, leading to a deviation in the absolute molecular weights. Relationships between dilute solution viscosity and molecular weight have been determined for many branched systems, and the Mark–Houwink constant typically varies between 0.5 and 0.2, depending on the degree of branching. In contrast, the exponent is typically in the region of 0.6–0.8 for linear homopolymers in a good solvent with a random coil conformation. The Mark–Houwink exponents of poly(BDDA)s obtained with CTA 1 at [M] = 0.1–0.2 mol/L are significantly low (α = 0.25–0.26), suggesting the branched structures. In order to develop a useful method for preparing branched polymers effectively, it is necessary to find a condition in which a higher monomer concentration can be used. Unfortunately, our attempts in this direction were unsuccessful. Nevertheless, it was demonstrated that soluble branched polymers could reasonably be obtained by RAFT polymerization of a diacrylate in dilute conditions.

An NMR technique was used to determine the concentration of vinyl groups in the side chains and the chain-end structure. The ^{1}H NMR spectrum of the poly(BDDA) obtained with CTA 1 at [M] = 0.1 mol/L is presented in Fig. 2. The characteristic peaks at 0.5–3.0 ppm (–CH_2–CH_2CH_2–CH_2– and –CH_2CH– in the main chain) and 3.4–5.0 ppm (–O–CH_2–) are clearly seen; these peaks are attributed to poly(BDDA). In this system, branching arises via the reaction of one vinyl group in BDDA to produce polymer chains containing pendant C=C bonds in the initial step, followed by the reactions of these pendant groups with other growing polymer chains. The pendant vinyl groups can also be consumed by the intramolecular reactions with the propagating radicals to produce cyclic structures. The ^{1}H NMR spectrum shows clear evidence for unreacted pendant acrylate groups with the vinylic H atom resonances at 5.6–6.6 ppm. The content of the unreacted vinyl group can be calculated by comparison of the area of the peak at 3.4–5.0 ppm corresponding to the 4 protons in the sum of the fully reacted (branching and ring-closing) BDDA and the pendant unreacted BDDA residues to the peak at 5.6–5.9 ppm (peak “h”) corresponding to one proton of the vinyl group using the equation:

$$\frac{1x}{4x + 4(1-x)} = \frac{\text{Integral at } 5.6 - 5.9 \text{ ppm}}{\text{Integral at } 3.4 - 5.0 \text{ ppm}} \quad (1)$$

where x is the fraction of the unreacted vinyl group and 1-x is the fraction of the fully reacted (branching and ring-closing) BDDA residue in the resulting poly(BDDA)s. As can be seen in Table 1, the content of the unreacted vinyl group was 2.6% at [M] = 0.1 mol/L. In other words, about 97% of the pendant C=C bonds formed in the initial step are reacted with growing polymer chains to produce branched or cyclic architecture. A higher monomer concentration ([M] = 0.2 mol/L) leads to the formation of a poly(BDDA) having a higher content of the unreacted vinyl group with a higher molecular weight and a broad molecular weight distribution. The presence of the unreacted pendant structure in the poly(BDDA) was also confirmed by ^{13}C NMR measurement, in which the vinylic resonance was clearly visible at 120–140 ppm (see Figure S1 in Supporting Information).

The CTA-derived initiator may produce the polymer with CTA fragments at the polymer chain ends (α-chain end with the benzyl group and ω-chain end with the dithiocarbamate group in the case of CTA 1). As shown in Fig. 2, aromatic peaks are clearly visible at 6.0–8.0 ppm, which correspond to the benzyl and pyrrole fragments at the chain ends of the polymer. This is an indication that the polymer chain end is mainly capped with the fragments of CTA

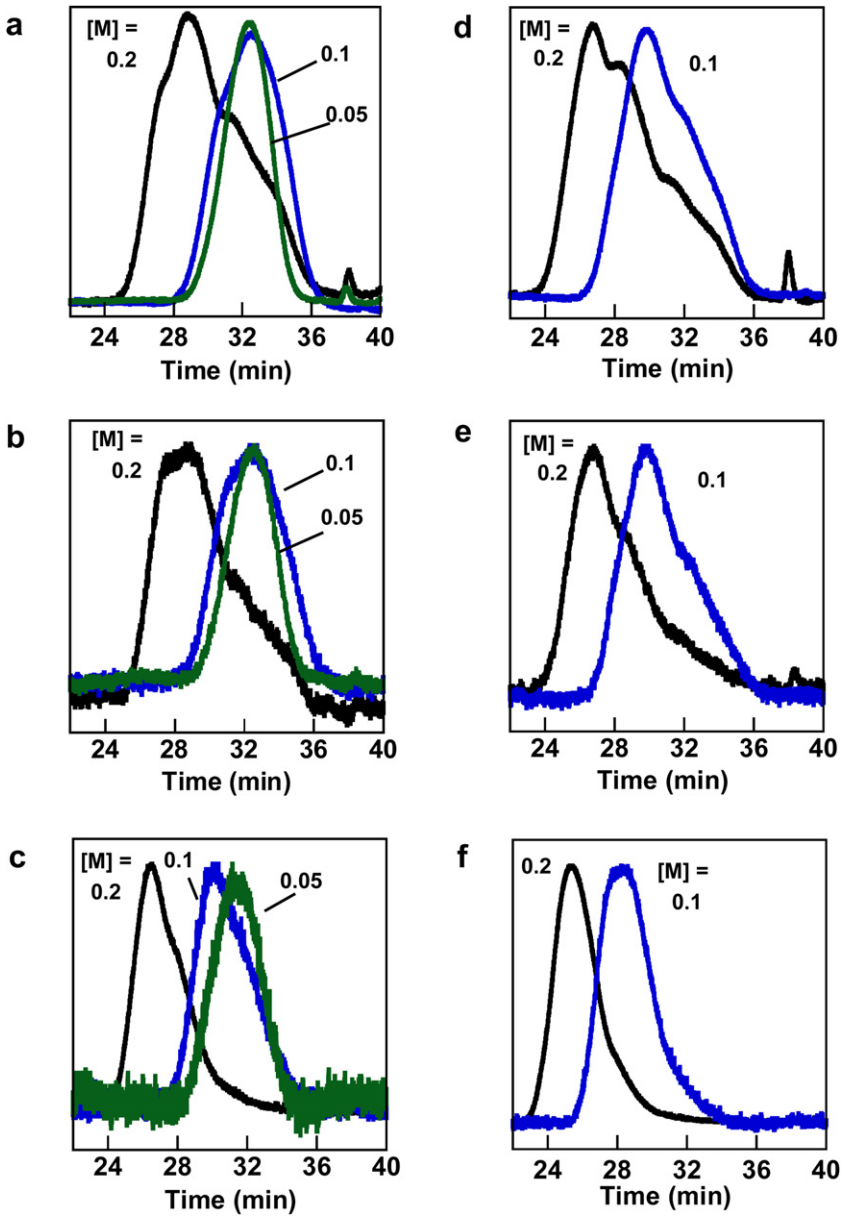

Fig. 1. GPC traces of poly(BDDA)s prepared by RAFT polymerizations with CTA 1 (a–c) and CTA 2 (d–f) at $[BDDA]_0/[CTA]_0/[AIBN]_0 = 200/5/1$ under different monomer concentrations (mol/L) by RI detector (a, d), viscosity detector (b, e), and light scattering (RALLS) detector (c, f). See Table 1 for detailed polymerization conditions.

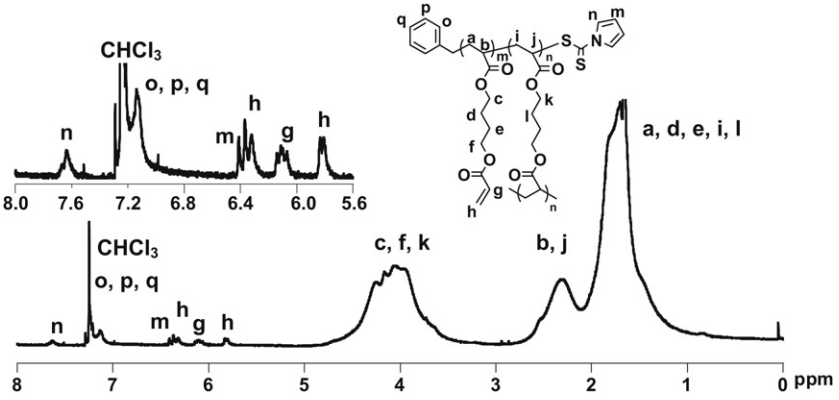

Fig. 2. ^1H NMR spectrum ($CDCl_3$) of the poly(BDDA) prepared by RAFT polymerization with CTA 1 at $[BDDA]_0/[CTA]_0/[AIBN]_0 = 200/5/1$ at [M] = 0.1 mol/L.

Table 2
Effect of Difunctional Monomer/Chain Transfer Agent/Initiator on RAFT Polymerization of 1,4-Butanediol Diacrylate (BDDA) Using 2,2′-Azobis(isobutyronitrile) (AIBN) and Benzyl 1-Pyrrolecarbodithioate (CTA 1) in 1,4-dioxane at 60 °C for 24 h.[a]

Run	[BDDA]/[CTA]/[AIBN]	Yield[b] (%)	M_n (M_w/M_n)			Content (%)[f]		α[g]
			GPC-RI[c]	GPC-RALLS[d]	GPC-Visco[e]	vinyl	CTA	
1	200/5/1	56	8100 (1.44)	12,000 (1.78)	16,000 (1.73)	2.6	1.4	0.25
2	200/10/1	61	6500 (1.42)	11,000 (1.74)	13,000 (1.55)	4.0	2.0	0.27
3	200/20/1	47	5100 (1.30)	6800 (1.69)	7600 (1.41)	5.9	3.0	0.24

[a] [M] = 0.1 mol/L.
[b] MeOH-insoluble part.
[c] Number-average molecular weight (M_n) and molecular weight distribution (M_w/M_n) were measured by gel permeation chromatography (GPC) using polystyrene standards in THF with RI detector.
[d] Measured by GPC in THF with RALLS detector.
[e] Measured by GPC in THF with viscosity detector.
[f] Determined by ^{1}H NMR spectroscopy ($CDCl_3$).
[g] Mark-Houwink exponent α.

as expected according to the general mechanism of the RAFT process. The content of the end group, calculated by comparison of the area of the peak at 7.4–7.8 ppm (peak "n") corresponding to the two protons of the end group (pyrrole Z-group) to the peak at 3.4–5.0 ppm corresponding to the 4 protons of the BDDA residue, is 1.4% Since the peak of the pyrrole Z-group was employed for the calculation, the content of the end group is independent of the structure of the R-group. Note that RAFT polymerization using the dithiocarbamate-type CTA 1 occasionally produced the polymer possessing the expected transfer agent end groups together with the initiator-derived polymer [44].

The polymerization of BDDA using the xanthate-type CTA 2 at [M] = 0.2 mol/L produced the soluble poly(BDDA) having a higher molecular weight and a broader molecular weight distribution ($M_{n,\text{GPC-RI}} = 29{,}000$, $M_w/M_n = 6.15$). The apparent molecular weight determined by a conventional GPC is much lower than the value determined by GPC/viscosity using the universal calibration ($M_{n,\text{GPC-VISCO}} = 91000$), indicating a lower hydrodynamic volume of the poly(BDDA) obtained with CTA 2. The polymer yield and molecular weights decreased with decreasing monomer concentration, which was the same tendency observed in the polymerization with the dithiocarbamate-type CTA 1. The residual vinyl content of the polymer obtained at a lower concentration is slightly higher than that produced at a higher concentration, which goes against the trend observed in the products with CTA 1. This may be because the competition between intermolecular propagating/cross-linking reactions and intramolecular cyclization is affected by the monomer concentration as well as the nature of the CTA. As can be seen in Fig. 1d, bimodal and multimodal peaks are detected in SEC traces of poly(BDDA)s prepared with CTA 2. In particular, the remarkable peaks in the higher molecular weight region are seen at higher monomer concentration. In the case of the polymerization with the xanthate-type CTA 3, the molecular weight and polydispersity of poly(BDDA) were lower than those with the xanthate-type CTA 2. In contrast, no significant difference in the polymer yield, the vinyl content, and the Mark–Houwink constant, was observed between the poly(BDDA)s obtained with CTA 2 and CTA 3. In both cases, the contents of the unreacted vinyl group in the resulting poly(BDDA)s were less than 1%, quantities apparently lower than those for the polymers obtained with the dithiocarbamate-type CTA 1.

3.2. Effect of CTA/initiator ratio

The CTA/initiator ratio plays a role in determining the overall success of a RAFT polymerization with respect to control over the molecular weight and molecular weight distribution with a sufficiently fast polymerization rate [56,57]. In order to evaluate the effect of the CTA/initiator ratio, the polymerization of BDDA was conducted with the dithiocarbamate-type CTA 1 at different $[CTA]_0$:$[AIBN]_0$ ratios between 5 and 20, keeping the monomer-to-initiator ratio at a constant value of $[BDDA]_0/[AIBN]_0 = 200/1$. Under these conditions, the concentrations of BDDA and AIBN were constant, and the CTA concentration was substantially different. As can be seen in Table 2, a higher $[CTA]_0$:$[AIBN]_0$ ratio led to the formation of poly(BDDA)s with lower molecular weights and a higher content of the unreacted vinyl group. In contrast, the $[CTA]_0/[AIBN]_0$ ratio had no significant effect on the polymer yield and Mark–Houwink constant. In all cases, the molecular weights determined by GPC/viscosity ($M_{n,\text{GPC-VISCO}} = 16{,}000$–$7600$) were

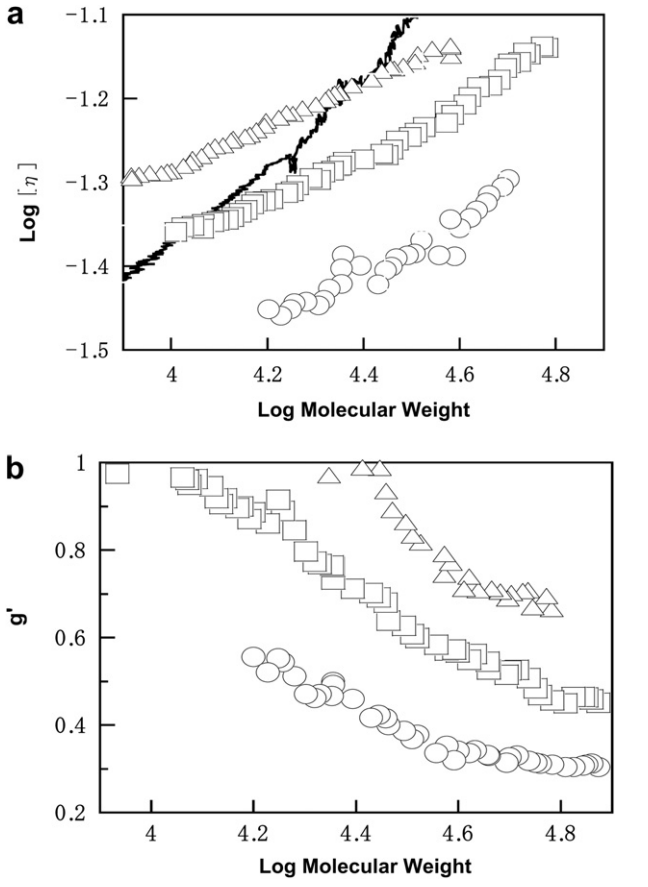

Fig. 3. (a) Mark–Houwink plots and (b) contraction factors, $g' = [\eta]_{branched}/[\eta]_{linear}$, for the polymers obtained by RAFT polymerization of BDDA with the dithiocarbamate-type CTA 1 at different CTA-to-initiator ratios: $[CTA]_0/[AIBN]_0 = 5$ (○), 10 (□), 20 (△), keeping the monomer-to-initiator ratio at a constant value of $[BDDA]_0/[AIBN]_0 = 200/1$. See Table 2 for detailed polymerization conditions. The intrinsic viscosity of a linear poly(ethyl acrylate) (–) is given for comparison.

slightly higher than the corresponding apparent molecular weights, indicating a lower hydrodynamic volume of the resulting polymers. As expected, the content of the end group increases with increasing CTA/initiator ratio (Table 2).

The corresponding Mark–Houwink plots, log [η] versus log M, and contraction factors, $g' = [\eta]_{branched}/[\eta]_{linear}$, as a function of log M are presented in Fig. 3. A plot of a linear poly(ethyl acrylate) is shown as a comparison. The viscosities of the poly(BDDA)s obtained at $[CTA]_0/[AIBN]_0 = 5–10$ are apparently less than that of the linear one. In particular, the intrinsic viscosity of the poly (BDDA) obtained at $[BDDA]_0/[CTA]_0/[AIBN]_0 = 200/5/1$ is less than 50% of that of the linear one. The contraction factors for all the branched polymers decrease with increasing molecular weights, as shown in Fig. 3b, which indicates a compact structure in solution. There is only a slight difference in the slopes of the plots of contracted volume versus log molecular weight for the poly(BDDA)s obtained at different conditions, but the values at each molecular weight decrease obviously with decreasing CTA-to-initiator ratio. These results indicate that the apparent discrepancy between molecular weights determined from GPC/viscosity compared to conventional GPC arises from a systematic decrease in the contraction factor, g′, resulting from a more compact architecture with an increased number of branches at lower CTA-to-initiator ratios. In contrast, higher CTA-to-initiator ratio may lead to preferable intramolecular cyclization, resulting in the formation of more cyclopolymers having ring structures.

3.3. Kinetic study

The kinetics investigation of the RAFT polymerization of BDDA was conducted using two different CTAs at $[BDDA]_0/[CTA]_0/[AIBN]_0 = 200/5/1$ in dry 1,4-dioxane under dilute conditions ([M] = 0.1 mol/L) at 60 °C. Fig. 4a and d show the variations in the monomer conversion and $\ln([M]_0/[M]_t)$ versus polymerization time for the polymerization with CTA 1 and CTA 2. Note that the dithiocarbamate-type CTA 1 is suitable for controlling the radical polymerization of conventional monovinyl acrylate via the RAFT process [43], whereas the dithiocarbonate-type CTA 2 is less

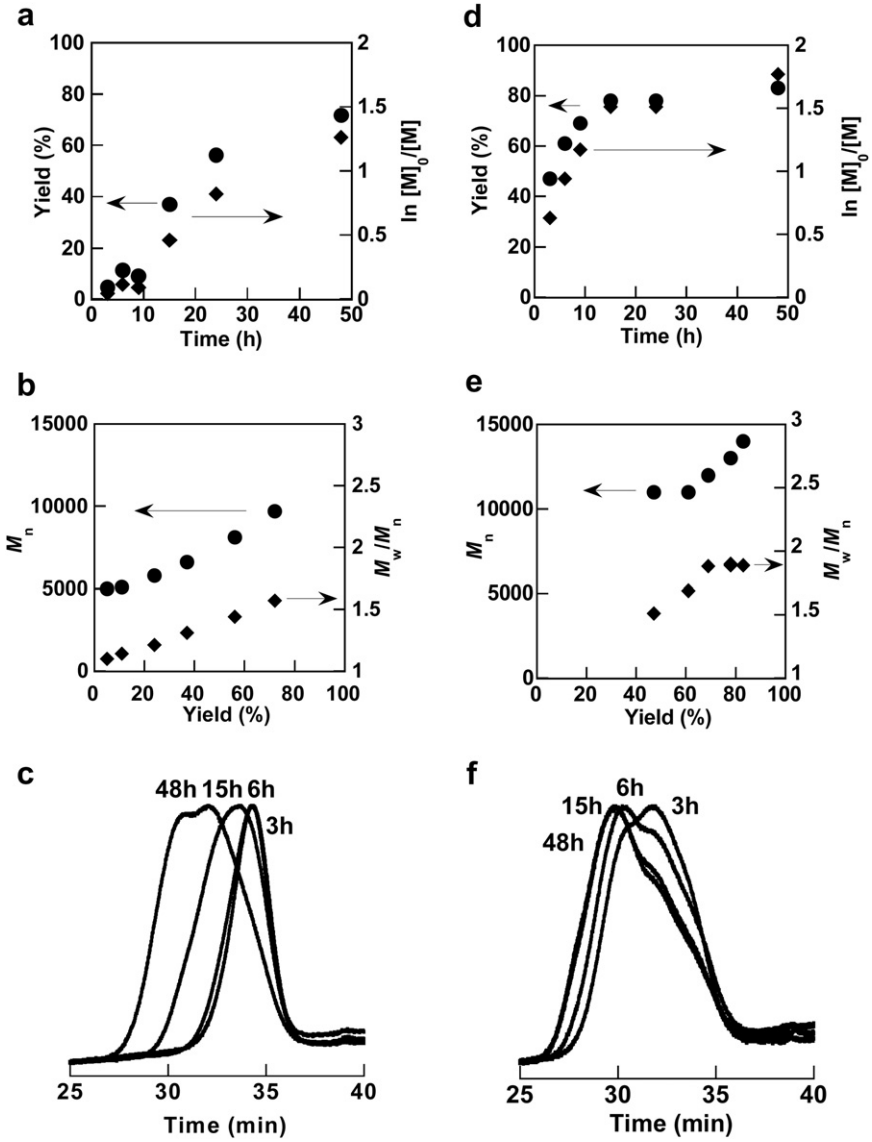

Fig. 4. (a,d) Time-conversion (circles) and first-order kinetic (squares) plots for the polymerization of 1,4-butanediol diacrylate (BDDA) with 2,2′-azobis(isobutyronitrile) (AIBN) in the presence of (a–c) benzyl 1-pyrrolecarbodithioate (CTA 1) and (d–f) *O*-ethyl-*S*-(1-methoxycarbonyl) ethyldithiocarbonate (CTA 2) in 1,4-dioxane at 60 °C. Monomer concentration = 0.1 mol/L. [BDDA]/[CTA]/[AIBN] = 200/5/1. (b,e) Number-average molecular weight (circles) and polydispersity (squares) as a function of polymer yield. (c,f) Evolution of GPC traces of the products with polymerization time.

Table 3
RAFT Polymerization of 1,4-Butanediol Diacrylate (BDDA) Using 2,2′-Azobis(isobutyronitrile) (AIBN) and Benzyl 1-pyrrolecarbodithioate (CTA 1) in 1,4-dioxane at 60 °C.[a]

Run	Time (h)	Yield[b] (%)	M_n (M_w/M_n)			Content (%)[f]		α[g]
			GPC-RI[c]	GPC-RALLS[d]	GPC-Visco[e]	Vinyl	CTA	
1	3	5	5000 (1.10)	–	11,000 (1.09)	–	–	0.43
2	6	11	5100 (1.14)	6600 (1.16)	9000 (1.16)	–	–	0.33
3	9	24	5800 (1.21)	8000 (1.26)	12,000 (1.26)	7.4	2.2	0.31
4	15	37	6600 (1.31)	8500 (1.61)	13,000 (1.49)	5.8	1.7	0.23
5	24	56	8100 (1.44)	12,000 (1.78)	16,000 (1.73)	2.6	1.4	0.25
6	48	72	9700 (1.57)	15,000 (1.99)	20,000 (2.00)	1.6	0.56	0.26

[a] [BDDA]/[CTA 1]/[AIBN] = 200/5/1, [M] = 0.1 mol/L.
[b] MeOH-insoluble part.
[c] Number-average molecular weight (M_n) and molecular weight distribution (M_w/M_n) were measured by gel permeation chromatography (GPC) using polystyrene standards in THF with RI detector.
[d] Measured by GPC in THF with RALLS detector.
[e] Measured by GPC in THF with viscosity detector.
[f] Determined by ^{1}H NMR spectroscopy ($CDCl_3$).
[g] Mark-Houwink exponent α.

effective with acrylate. When the reaction was conducted with CTA 1, the polymer yield increased with the polymerization time and a relatively high conversion (72%) was reached after 48 h. An almost linear first-order kinetic plot is seen up to about 60% conversion (Fig. 4a). As shown in Fig. 4b, the number-average molecular weight increased with polymer yield, and a positive intercept of the M_n vs polymer yield is observed clearly. For the RAFT polymerization of a conventional monovinyl monomer, such positive intercept is reported to occur when the rate of polymerization is greater than the rate of addition to CTA [58]. In our system, the linear M_n vs polymer yield relationship passing through the origin could be obtained only if the cyclopolymerization proceeds predominantly in a controlled fashion. Hence, the positive intercept may originate from simultaneous intermolecular reactions and intramolecular cyclization. A progressive increase in polydispersity indices (M_w/M_n) with the polymer yield is also seen. The GPC traces (RI) of poly(BDDA)s obtained at different reaction times are shown in Fig. 4c. At the initial stage of the polymerization (3–6 h), the resulting polymers show symmetrical GPC peaks with a relatively narrow molecular weight distribution ($M_w/M_n < 1.2$). No significant difference was detected in the GPC traces between the RI detector, viscosity, and light scattering (RALLS) responses (See Figure S2 in Supporting Information). These results suggest that the intramolecular cyclization rather than the intermolecular reaction proceeds predominantly during the early stages of the polymerization under dilute conditions with CTA 1. As shown in Table 3, the contents of the pendant vinyl group and the end group decrease with polymerization time. Additionally, a slight decrease in the Mark–Houwink constant is detected at longer polymerization times. Hence, it is reasonable to conclude that the pendant double bonds are consumed preferentially by the intramolecular cyclization due to their locally high concentration in the vicinity of propagating radicals under dilute conditions. In contrast, the appearance of broad elution peaks in the higher molecular weight region is seen with increasing polymerization time (Fig. 4c), suggesting the formation of branched poly(BDDA)s with relatively high molecular weights and a broad molecular weight distribution at the last stage of the polymerization.

When the reaction was conducted with CTA 2, the polymer yield increased rapidly with polymerization time and reached a plateau at approximately 80% yield after 15 h. The polymerization rate was apparently faster for the polymerization with the xanthate-type CTA 2 than for the dithiocarbamate-type CTA 1. This behavior is consistent with the general tendencies of RAFT polymerization, in which the transfer constants decrease in the series where Z is alkyl ≈ alkylthio ≈ pyrrole >> alkoxy [36,56]. In other words, slow addition-fragmentation equilibrium during the polymerization with the xanthate-type CTA 2 led to rapid polymerization.

As shown in Fig. 4e, the number-average molecular weight and polydispersity increase with polymer yield. Nevertheless, the products obtained with CTA 2 had higher molecular weighs and broader molecular weight distributions compared to those obtained with CTA 1. The contents of the pendant vinyl groups of the products obtained with CTA 2 were also lower than those with CTA 1 as shown in Tables 3 and 4. Since the xanthate-type CTA 2 is a less effective mediating agent for RAFT polymerizations of acrylate derivatives, it is assumed that the probability of selective cyclization was relatively low and the formation of branching

Table 4
RAFT Polymerization of 1,4-Butanediol Diacrylate (BDDA) Using 2,2′-Azobis(isobutyronitrile) (AIBN) and *o*-Ethyl-S-(1-methoxy carbonyl) ethyl dithiocarbonate (CTA 2) in 1,4-dioxane at 60 °C.[a]

Run	Time (h)	Yield[b] (%)	M_n(M_w/M_n)			Vinyl Content (%)[f]	α[g]
			GPC-RI[c]	GPC-RALLS[d]	GPC-Visco[e]		
1	3	47	11,000 (1.51)	13,000 (1.77)	26,000 (1.89)	5.2	0.24
3	6	61	11,000 (1.69)	14,000 (2.31)	25,000 (2.31)	2.1	0.24
5	9	69	12,000 (1.88)	17,000 (2.52)	25,000 (2.75)	1.3	0.23
7	15	78	13,000 (1.90)	17,000 (2.67)	29,000 (2.99)	0.90	0.20
8	24	78	13,000 (1.89)	20,000 (2.61)	30,000 (3.05)	0.50	0.19
9	48	83	14,000 (1.89)	18,000 (2.82)	32,000 (2.79)	0	0.24

[a] [BDDA]/[CTA 2]/[AIBN] = 200/5/1, [M] = 0.1 mol/L.
[b] MeOH – insoluble part.
[c] Number-average molecular weight (M_n) and molecular weight distribution (M_w/M_n) were measured by gel permeation chromatography (GPC) using polystyrene standards in THF with RI detector.
[d] Measured by GPC in THF with RALLS detector.
[e] Measured by GPC in THF with viscosity detector.
[f] Determined by ^{1}H NMR spectroscopy ($CDCl_3$).
[g] Mark-Houwink exponent α.

rather than intramolecular cycles proceeded in the case of the polymerization with CTA 2. These results are consistent with the general tendency that a higher transfer constant may afford better overall control of the polymerization, due to a decrease in the number of radicals available for unfavorable side reactions, but result in a longer polymerization time.

3.4. RAFT polymerization of poly(ethylene glycol) diacrylates (PEGDAs)

We investigated the RAFT polymerization of poly(ethylene glycol) diacrylates (PEGDAs) having different lengths of PEG spacers (n = 3, 10, 13) in dilute conditions. In this system, the pendant double bonds tethered to the polymer backbone were substantially more mobile than that of the poly(BDDA) in dilute conditions because of the existence of flexible and long PEG spacers. In general, the structure and length of the spacers between two vinyl groups play a critical role in determining the formation of branched polymers, cross-linked products, or cyclopolymers by polymerization of divinyl monomers. For example, the study of RAFT copolymerization of 2-hydroxypropyl acrylate and diacrylates having different structures demonstrated that the bulkier and less flexible divinyl monomer, bisphenol A ethoxylated diacrylate, was less likely to undergo cyclization than shorter and more flexible ethyleneglycol diacrylate [16]. RAFT polymerization of oligo (ethylene glycol) dimethacrylate with shorter spacers in bulk was also reported to yield more heterogeneous networks because higher local concentrations of pendant double bonds in the vicinity of propagating radicals facilitated intramolecular reactions to afford more cyclic structures [27]. Similarly, suppression of the gel point with increasing length of the ethylene glycol spacers was observed in the photopolymerization of ethylene glycol di(meth)acrylates [59]. In contrast, it was demonstrated that the structure and length of the spacers between two acrylate groups had no significant effect on the intramolecular cyclization of pendant vinyl groups and the gel points during atom transfer radical copolymerization of methyl acrylate and diacrylates [12].

In this study, the polymerizations of PEGDAs having different spacer lengths were conducted at $[PEGDA]_0/[CTA]_0/[AIBN]_0 = 200/5/1$ in 1,4-dioxane at 60 °C for 24 h under dilute conditions ([M] = 0.1 and 0.2 mol/L). The resulting polymers were evaluated by conventional GPC, GPC/viscosity, and ^{1}H NMR measurements, and the results are summarized in Table 5. When the polymerization of PEG258DA was conducted at $[PEG258DA]_0$ = 0.2 mol/L, the polymerization proceeded homogeneously with the dithiocarbamate-type CTA 1. The resulting polymer was soluble in many organic solvents such as THF, chloroform, ethyl acetate, and toluene, even if the polymer yield was more than 60%. The presence of the unreacted pendant structure was clearly confirmed by ^{1}H and ^{13}C NMR measurements (see Figures S3 and S4, Supporting Information). The dithioester chain end structure was also detected by a ^{1}H NMR spectrum of the resulting product. In contrast, cross-linked products were obtained by RAFT polymerization of PEG258DA with the xanthate-type CTA 2 and conventional radical polymerization without CTA under the same conditions (see Table S1, Supporting Information). The polymerization at a lower monomer concentration ([M] = 0.1 mol/L) led to a slight decrease in the polymer yield with decreasing molecular weight and the Mark–Houwink exponent. The content of the unreacted vinyl group also decreased with decreasing monomer concentration. These tendencies are consistent with those observed in RAFT polymerization of BDDA, suggesting no significant difference between BDDA and PEG258DA in relative propensities for intermolecular propagating/cross-linking reactions and intramolecular cyclization in dilute conditions.

The polymerization of PEG575DA at [M] = 0.2 mol/L using the dithiocarbamate-type CTA 1 afforded a soluble polymer, while an insoluble product was obtained by the polymerization with CTA 2. The polymerization at a lower monomer concentration ([M] = 0.1 mol/L) led to a slight decrease in the polymer yield with decreasing molecular weight. In this case, a decrease in the monomer concentration led to an increase in the contents of the unreacted pendant group and dithioester-end group (see Figure S5, Supporting Information) with an increasing Mark–Houwink exponent. Additionally, poly(PEG575DA) obtained with CTA 1 at [M] = 0.1 mol/L had relatively low polydispersity, which may be due to the preferable ring-closing reactions. The polymerization of PEG700DA at [M] = 0.2 mol/L using the dithiocarbamate-type CTA 1 afforded an insoluble polymer, whereas the polymerization at a lower monomer concentration ([M] = 0.1 mol/L) led to the formation of a soluble polymer having a relatively low molecular weight and high content of the unreacted vinyl group (see Figure S6, Supporting Information). These results suggest the significant influence of the spacer length between the vinyl moieties of the diacrylates on the polymerization rate and relative propensities for intermolecular propagating/cross-linking reactions and intramolecular cyclization.

3.5. Thermoresponsive properties

The polymers obtained from PEG575DA and PEG700DA were soluble in polar solvents involving water and methanol in addition to many organic solvents, such as THF, chloroform, ethyl acetate,

Table 5
RAFT Polymerization of Poly(ethylene glycol) Diacrylate (PEGDA) Using 2,2′-Azobis(isobutyronitrile) (AIBN) and Benzyl 1-Pyrrolecarbodithioate (CTA 1) in 1,4-dioxane at 60 °C for 24 h.[a]

Run	Diacrylate[b]	[M] mol/L	Yield[c] (%)	M_n (M_w/M_n)		Content (%)[f]		α[g]
				GPC-RI[d]	GPC-Visco[e]	vinyl	CTA	
1	PEG258DA	0.2	62	11,000 (1.35)	21,000 (1.30)	0.50	3.0	0.30
2	PEG258DA	0.1	40	9700 (1.15)	18,000 (1.43)	0	0.80	0.05
3	PEG575DA	0.2	63	8400 (1.34)	16,000 (1.86)	2.0	2.6	0.04
4	PEG575DA	0.1	54	8900 (1.18)	13,000 (1.18)	7.2	3.2	0.39
5	PEG700DA	0.2	—[h]	—	—	—	—	—
6	PEG700DA	0.1	45	3700 (1.37)	3800 (2.11)	10	2.0	0.05

[a] [PEGDA]/[CTA 1]/[AIBN] = 200/5/1.
[b] See Scheme 1.
[c] Diethyl ether-insoluble part.
[d] Number-average molecular weight (M_n) and molecular weight distribution (M_w/M_n) were measured by gel permeation chromatography (GPC) using polystyrene standards in THF with RI detector.
[e] Measured by GPC in THF with viscosity detector.
[f] Determined by ^{1}H NMR spectroscopy ($CDCl_3$).
[g] Mark-Houwink exponent α.
[h] Formation of cross-linked polymer.

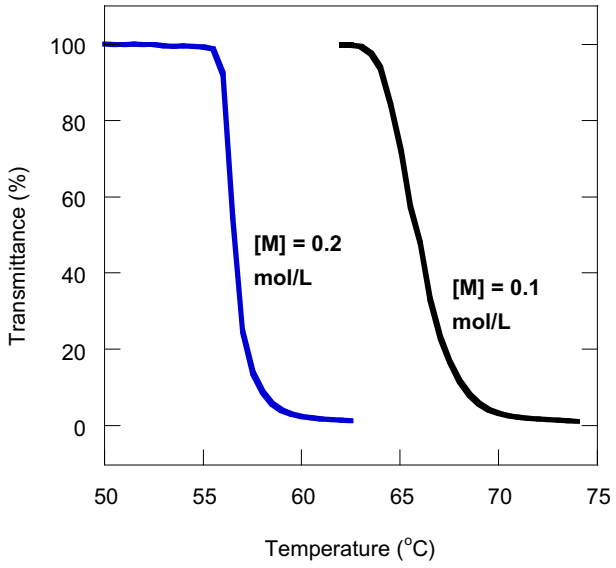

Fig. 5. Temperature dependence of the transmittance at 500 nm in aqueous solutions (polymer conc. = 2.0 mg/mL) of poly(PEG575DA)s obtained with the dithiocarbamate-type CTA 1 at $[M]_0/[CTA]_0/[AIBN]_0 = 200/5/1$ under different monomer concentrations.

and toluene. Among them, the product obtained by RAFT polymerization of PEG575DA ($n = 10$) showed a characteristic thermoresponsive property, lower critical solution temperature (LCST), in aqueous solution. The thermally induced phase separation behavior in water was monitored by UV (500 nm), in which the heating rate was fixed at 1.0 °C/min. We initially evaluated the thermoresponsive properties of poly(PEG575DA)s obtained with the dithiocarbamate-type CTA 1 at $[M]_0/[CTA]_0/[AIBN]_0 = 200/5/1$ under different monomer concentrations. As can be seen in Fig. 5, the poly(PEG575DA) prepared at [M] = 0.2 mol/L was soluble in water at low temperature, which undergo a clear phase transition upon heating. The transmittance decreased gradually within the 56–58 °C range, indicating a relatively sharp phase separation. The phase transition temperature varied from around 57 °C at [M] = 0.2 mol/L to 66 °C at [M] = 0.1 mol/L, which may be attributed to the higher content of the cyclopolymers and/or the higher degree of branching of the poly(PEG575DA)s obtained at low monomer concentrations. This is an indication that different polymer architectures obtained by RAFT polymerization at different monomer concentrations affect the phase separation temperature. In contrast, no thermoresponsive property (LCST) was observed in an aqueous solution of poly(PEG700DA), which was soluble in water, independent of the solution temperature. These results also demonstrate that the poly(PEG575DA)s show a characteristic temperature-responsive property, in which the transition temperature can be manipulated in the range of 57–66 °C by selecting polymerization conditions.

4. Conclusion

This study reports the RAFT polymerization of diacrylate derivatives having different spacers under dilute conditions ([M] = 0.2–0.05 M). The effects of the monomer concentration, the nature of the CTA, and the CTA/initiator ratio were investigated in terms of the polymerization behavior, mechanisms, and structures of the resulting polymers. The cross-linking reaction of BDDA was effectively suppressed with decreasing monomer concentration in the presence of the dithiocarbamate-type CTA 1, which was mainly due to preferable intramolecular cyclization compared to intermolecular propagating/cross-linking reactions. Kinetic study of the RAFT polymerization of BDDA with CTA 1 suggested that the intramolecular cyclization rather than intermolecular reaction proceeds predominantly during the early stages of the polymerization under dilute conditions with CTA 1, whereas branched poly(BDDA)s with a relatively high molecular weight and a broad molecular weight distribution are formed at the last stage of the polymerization. RAFT polymerization of PEGDAs having different lengths of PEG spacers ($n = 3, 10, 13$) indicated that the structure and length of the diacrylate spacers have a significant influence on the polymerization rate and relative propensities for intermolecular propagating/cross-linking reactions and intramolecular cyclization. Water-soluble polymers and thermoresponsive polymers were obtained by RAFT polymerizations of PEG700DA and PEG575DA having longer PEG spacers ($n = 13$ and 10), respectively.

Acknowledgments

The authors acknowledge Prof. Takeshi Endo (Molecular Engineering Institute, Kinki University) for useful discussion.

Appendix. Supporting information

Supplementary data related to this article can be found online at doi:10.1016/j.polymer.2010.12.032.

References

[1] O'Brien N, McKee A, Sherrington DC, Slark AT, Titterton A. Polymer Communication 2000;41:6027–31.
[2] Isaure F, Cormack PAG, Sherrington DC. Macromolecules 2004;37:2096–105.
[3] Isaure F, Cormack PAG, Sherrington DC. Journal of Materials Chemistry 2003;13:2701–10.
[4] Isaure F, Cormack PAG, Graham S, Sherrington DC, Armes SP, Bütün V. Chemical Communications (Cambridge, United Kingdom); 2004:1138–9.
[5] Li Y, Armes SP. Macromolecules 2005;38:8155–62.
[6] Bannister I, Billingham NC, Armes SP, Rannard SP, Findlay P. Macromolecules 2006;39:7483–92.
[7] Wang AR, Zhu S. Journal of Polymer Science Part A: Polymer Chemistry 2005;43:5710–4.
[8] Rosselgong J, Armes SP, Barton WRS, Price D. Macromolecules 2010; 43:2145–56.
[9] Gao H, Min K, Matyjaszewski K. Macromolecules 2007;40:7763–70.
[10] Gao H, Min K, Matyjaszewski K. Macromolecules 2009;42:8039–43.
[11] Camp WV, Gao H, Du Prez FE, Matyjaszewski K. Journal of Polymer Science Part A: Polymer Chemistry 2010;48:2016–23.
[12] Gao H, Li W, Matyjaszewski K. Macromolecules 2008;41:2335–40.
[13] Yua Q, Xua S, Zhanga H, Dinga Y, Zhu S. Polymer 2009;50:3488–94.
[14] Li Y, Armes SP. Macromolecules 2009;42:939–45.
[15] Liu BL, Kazlauciunas A, Guthrie JT, Perrier S. Macromolecules 2005;38:2131–6.
[16] Vo C-D, Rosselgong J, Armes SP, Billingham NC. Macromolecules 2007; 40:7119–25.
[17] Rosselgong J, Armes SP, Barton W, Price D. Macromolecules 2009; 42:5919–24.
[18] Wang W-J, Wang D, Li B-G, Zhu S. Macromolecules 2010;43:4062–9.
[19] Norisuye T, Morinaga T, Tran-Cong-Miyata Q, Goto A, Fukuda T, Shibayama M. Polymer 2005;46:1982–94.
[20] Taton D, Baussard J-F, Dupayage L, Poly J, Gnanou Y, Ponsinet V, et al. Chemical Communications; 2006:1953–5.
[21] Landin DT, Macosko CW. Macromolecules 1988;21:846–51.
[22] Wang R, Luo Y, Li B-G, Zhu S. Macromolecules 2009;42:85–94.
[23] Li Y, Ryan AJ, Armes SP. Macromolecules 2008;41:5577–81.
[24] Yu Q, Zeng F, Zhu S. Macromolecules 2001;34:1612–8.
[25] Yu Q, Zhang J, Cheng M, Zhu S. Macromolecular Chemistry and Physics 2006;207:287–94.
[26] Yu Q, Zhou M, Ding Y, Jiang B, Zhu S. Polymer 2007;48:7058–64.
[27] Yu Q, Zhu Y, Ding Y, Zhu S. Macromolecular Chemistry and Physics 2008; 209:551–6.
[28] París R, Fuente JLdl. Journal of Polymer Science Part A: Polymer Chemistry 2005;43:2395–406.
[29] Nagelsdiek R, Mennicken M, Maier B, Keul H, Höcker H. Macromolecules 2004;37:8923–32.
[30] Lin Y, Liu X, Li X, Zhan J, Li Y. Journal of Polymer Science Part A: Polymer Chemistry 2007;45:26–40.
[31] Assem Y, Chaffey-Millar H, Barner-Kowollik C, Wegner G, Agarwal S. Macromolecules 2007;40:3907–13.
[32] Erkoc S, Acar AE. Macromolecules 2008;41:9019–24.

[33] Nagai A, Ochiai B, Endo T. Macromolecules 2005;38:2547–9.
[34] Ochiai B, Ootani Y, Endo T. Journal of American Chemical Society 2008; 38:10832–3.
[35] Vana P, Albertin L, Barner L, Davis TP, Barner-Kowollik C. Journal of Polymer Science Part A: Polymer Chemistry 2002;40:4032–7.
[36] Chiefari J, Mayadunne RTA, Moad CL, Moad G, Rizzardo E, Postma A, et al. Macromolecules 2003;36:2273–83.
[37] Mori H, Nakano S, Endo T. Macromolecules 2005;38:8192–201.
[38] Destarac M, Brochon C, Catala JM, Wilczewska A, Zard SZ. Macromolecular Chemistry and Physics 2002;203:2281–9.
[39] Maki Y, Mori H, Endo T. Macromolecular Chemistry and Physics 2007; 208:2589–99.
[40] Ladaviere C, Dörr N, Claverie JP. Macromolecules 2001;34:5370–2.
[41] Gaillard N, Guyot A, Claverie J. Journal of Polymer Science Part A: Polymer Chemistry 2003;41:684–98.
[42] Mori H, Ookuma H, Nakano S, Endo T. Macromolecular Chemistry and Physics 2006;207:1005–17.
[43] Mayadunne RTA, Rizzardo E, Chiefari J, Chong YK, Moad G, Thang SH. Macromolecules 1999;32:6977–80.
[44] Schilli C, Lanzendörfer MG, Müller AHE. Macromolecules 2002;35:6819–27.
[45] Coote ML, Radom L. Macromolecules 2004;37:590–6.
[46] Stenzel MH, Cummins L, Roberts GE, Davis TR, Vana P, Barner-Kowollik C. Macromolecular Chemistry and Physics 2003;204:1160–8.
[47] Nguyen TLU, Eagles K, Davis TP, Barner-Kowollik C, Stenzel MH. Journal of Polymer Science Part A: Polymer Chemistry 2006;44:4372–83.
[48] Wan DC, Satoh K, Kamigaito M, Okamoto Y. Macromolecules 2005; 38:10397–405.
[49] Pound G, McLeary JB, McKenzie JM, Lange RFM, Klumperman B. Macromolecules 2006;39:7796–7.
[50] Pound G, Aguesse F, McLeary JB, Lange RFM, Klumperman B. Macromolecules 2007;40:8861–71.
[51] Pound G, Eksteen Z, Pfukwa R, Mckenzie JM, Lange RFM, Klumperman B. Journal of Polymer Science Part A: Polymer Chemistry 2008;46:6575–93.
[52] Mori H, Ookuma H, Endo T. Macromolecular Symposia 2007;249-250:406–11.
[53] Mori H, Ookuma H, Endo T. Macromolecules 2008;41:6925–34.
[54] Maki Y, Mori H, Endo T. Macromolecules 2007;40:6119–30.
[55] Taton D, Wilczewska A-Z, Destarac M. Macromolecular Rapid Communications 2001;22:1497–503.
[56] Moad G, Chiefari J, Chong YK, Krstina J, Mayadunne RTA, Postma A, et al. Polymer International 2000;49:993–1001.
[57] Favier A, Charreyre M- T. Macromolecular Rapid Communications 2006;27: 653–92.
[58] Vana P, Davis TP, Barner-Kowollik C. Macromolecular Theory and Simulations 2002;11:823–35.
[59] Cook WD. Journal of Polymer Science Part A: Polymer Chemistry 1993;31: 1053–67.

Polymer 52 (2011) 646–651

Contents lists available at ScienceDirect

Polymer

journal homepage: www.elsevier.com/locate/polymer

Cis and *trans* radicals generated in helical poly(propargyl acetate)s prepared using a [Rh(norbornadiene)Cl]$_2$ catalyst

Yoshiaki Yoshida [a], Yasuteru Mawatari [a], Chigusa Seki [a], Toshifumi Hiraoki [b], Haruo Matsuyama [a,**], Masayoshi Tabata [a,*]

[a] Department of Applied Chemistry, Graduate School of Engineering, Muroran Institute of Technology, 27-1 Mizumoto-cho, Muroran, Hokkaido 050-8585, Japan
[b] Department of Applied Physics, Graduate School of Engineering, Hokkaido University, Sapporo, Hokkaido 060-8628, Japan

ARTICLE INFO

Article history:
Received 12 October 2010
Received in revised form
8 December 2010
Accepted 10 December 2010
Available online 21 December 2010

Keywords:
Poly(propargyl acetate)
Rh catalyst
Electron spin resonance

ABSTRACT

The poly(propargyl acetate) (**A**) having a helical *cis–transoid* structure was stereospecifically prepared using the Rh complex catalyst, [Rh(norbornadiene)Cl]$_2$, in MeOH or NEt_3 solvent at 0 and 40 °C in moderate yield. Electron spin resonance (ESR) analysis of the polymer revealed the formation of the *cis* (**B**) and *trans* (**C**) radicals which were produced through the thermal rotational scission of the helical *cis* C=C bonds in the main-chain during the polymerization. The spatial and geometrical structure was successfully deduced using the two analogues' polymers in which either methyl or methylene group is deuterated, by the aide of computer simulation of the observed ESR spectra together with the calculation of spin density of the two radicals.

1. Introduction

Substituted polyacetylenes (SPs) have been considered as the typical conjugated polymers, which have interesting properties, e.g., pressure induced *cis*-to-*trans* isomerization [1], helix and columnar formations [2], molecular recognition ability [3–7], and non-linear optical (NLO) [8,9] and anti-ferromagnetic (AFM) properties due to the *cis* and/or *trans* radical spins generated in the polymers [10,11]. The AFM properties are potentially important for a new type of time memory materials similar to human's neuron system [12]. The AFM property of the polymers was increased at the lower temperature, e.g., 58–114 K and in the prolonged time when the polymer was kept without magnetic field at a low temperature and finally the magnetization was saturated [13]. It was reported that poly(propargyl ester)s (PPE)s has humidity sensitive properties among the conjugated polymers which can be prepared by using Mo, W, Pd transition metal catalysts [14]. Recently, the polymerization of propargyl ester (PE) by using the so-called Zwitter ionic Rh catalyst in tetrahydrofuran, THF, was reported by Masuda and Noyori [15]. This catalyst is inactive in MeOH because of its deactivation in alcoholic solvent. In the present report using a monodentate Rh catalyst: [Rh(nbd)Cl]$_2$/NEt_3, (nbd = norbornadiene), we describe the polymerization of PE in MeOH. Radical species involved in the resultant *cis–transoid* poly(propargyl acetate)s (PPA)s were analyzed by Electron spin resonance (ESR) method and a spatial geometrical structure of the *cis* and *trans* radicals could be successfully determined. Both radicals (**B** and **C**) were produced through rotational scission of the *cis* C=C bonds of the *cis–transoid* polymer (**A**) by thermally induced *cis*-to-*trans* isomerization during the polymerization and/or on standing the polymer solution at room temperature [1d] by the so-called pressure induced *cis*-to-*trans* isomerization [1a–c] (see Scheme 1).

It is noteworthy that PPE was prepared as another promising candidate of the anti-ferromagnetic polymer, i.e., "Polymer Timer" which is expected to show a large increment of magnetization even when the PPE was cooled down to more than 114 K without magnetic field as mentioned above.

2. Experimental section

2.1. Measurements

Number and weight average molecular weights (M_n and M_w) of polymers were measured using JASCO GPC 900-1 equipped with two Shodex K-806L columns and RI detector. Chloroform was used as an eluent at 40 °C and poly(styrene) standards (M_n = 800–1,090,000) were employed for calibration. ^{1}H NMR and ^{13}C NMR spectra were

* Corresponding author. Tel./fax: +81 143 46 5963.
** Corresponding author. Tel.: +81 143 46 5752.
E-mail addresses: matsuyama@mmm.muroran-it.ac.jp (H. Matsuyama), tabata@mmm.muroran-it.ac.jp (M. Tabata).

0032-3861/$ – see front matter © 2011 Elsevier Ltd. All rights reserved.
doi:10.1016/j.polymer.2010.12.023

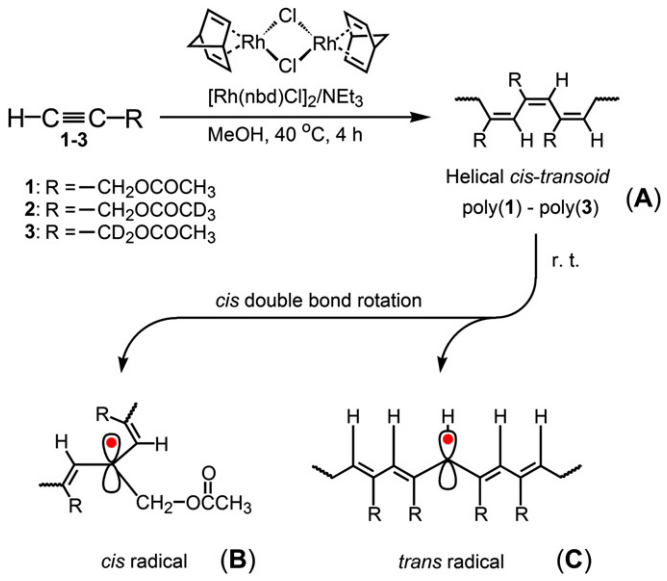

Scheme 1. Polymerization of monomers **1**–**3** and thermal *cis*-to-*trans* isomerization.

measured on a JEOL JNM-EX270 and Bruker DSX-300 using chloroform-*d* as a solvent at room temperature. ESR spectra were recorded on a JEOL FE3XG (9.44 GHz) with 100 kHz field modulation at room temperature. A signal due to Mn^{2+} bedded in MgO was used for calibration of the magnetic field. In order to observe detailed information for the hyperfine coupling constant of the ESR spectra the second derivative spectra were measured at room temperature using lower microwave power. The energetically optimal conformation of PPA together with its spin density in order to explain the ESR spectral data was deduced by using semi-empirical quantum chemical calculation AM1 method [16]. Computer simulation of the observed ESR spectra was performed using our own program [17].

2.2. Materials

2.2.1. Synthesis of propargyl acetate (*1*)

To a stirring mixture of 15.1 g (0.27 mol) of propargyl alcohol (TCI), 30.4 g (0.38 mol) of pyridine (KANTO) and 3.3 g (0.03 mol) of 4-(*N*,*N*-dimethylamino)pyridine (Aldrich) in 288 mL of dichloromethane (DCM), a solution of 25 g (0.32 mol) of acetyl chloride (KANTO) in 32 mL of DCM was added dropwise at 0–5 °C. After stirring for 24 h at room temperature, the resulting mixture was washed with a 5% HCl solution and distilled water. The organic layer was dried over anhydrous sodium sulfate, and the solvent was removed by distillation under nitrogen. The crude product was purified by distillation (44 °C/42 mmHg) to give a colorless liquid (20.7 g, 66%). ^{1}H NMR ($CDCl_3$, TMS): $\delta = 2.11$ (s, 3H, $-CH_3$,), 2.49 (s, 1H, H—C≡C), 4.68 (s, 2H, HC≡C—CH_2—). ^{13}C NMR ($CDCl_3$, TMS): $\delta = 20.52$, 51.74, 74.70, 77.48, 169.70.

2.2.2. Synthesis of propargyl trideuterio acetate (*2*)

A mixture of 100 mL of benzene, 6.0 g (0.09 mol) of tetradeuteroacetic acid (TCI), 8.4 g (0.15 mol) of propargyl alcohol, and 1.7 g (0.01 mol) of *p*-toluenesulfonic acid (Wako) was refluxed for 6 h with Dean–Stark apparatus. The resulting mixture was washed with a 5% sodium hydrogen carbonate solution and distilled water. After the organic layer was dried over anhydrous sodium sulfate, the solvent was removed by distillation under nitrogen. The crude product was purified by distillation (59 °C/102 mmHg) to give a colorless liquid (3.1 g, 34%). ^{1}H NMR ($CDCl_3$, TMS): $\delta = 2.49$ (s, 1H, H—C≡C), 4.68 (s, 2H, HC≡C—CH_2—). ^{13}C NMR ($CDCl_3$, TMS): $\delta = 20.21$, 51.76, 74.71, 77.48, 169.78.

2.2.3. Synthesis of α,α-dideuterio-propargyl alcohol (*3′*)

To a stirred suspension of 5 g (0.12 mol) of lithium aluminum deuteride (LAD) (Taiyo Nippon Sanso) in 540 mL of dry ether, a mixture of 20.6 g (0.21 mol) of ethyl propiolate (TCI) in 160 mL of dry ether was added slowly dropwise. The reaction mixture was stirred for 1.5 h at −78 °C and then quenched carefully with 10 mL of distilled water, 5 mL of a 15% NaOH solution and 10 mL of distilled water. After stirring for 12 h, the mixture was passed through a short alumina column, and the solvent was distilled off. The crude product was purified by distillation under nitrogen, and the fraction between 60 and 108 °C was collected to give the α,α-deuterio-propargyl alcohol (**3′**) as a colorless liquid (4.5 g, 38%), which was used without further purification in the next step.

2.2.4. Synthesis of α,α-dideuterio-propargyl acetate (*3*)

To a stirred mixture of 68 mL of dry ether, 4.5 g (0.08 mol) of the crude α,α-dideuterio-propargyl alcohol (**3′**), 8.8 g (0.09 mol) of pyridine, and 0.95 g (8 mmol) of 4-(*N*,*N*-dimethylamino)pyridine, a mixture of 7.3 g (0.09 mol) of acetyl chloride in 9.3 mL of ether was added dropwise at 0–5 °C. After stirring for 12 h at room temperature, the resulting mixture was washed with 5% HCl solution and distilled water. The organic layer was dried over anhydrous sodium sulfate, and the solvent was distillated off under nitrogen. The crude product was purified by distillation (58 °C/96 mmHg) to give a colorless liquid (2.3 g, 28%). ^{1}H NMR ($CDCl_3$, TMS): $\delta = 2.11$ (s, 3H, $-CH_3$), 2.47 (s, 3H, H—C≡C). ^{13}C NMR ($CDCl_3$, TMS): 20.49, 51.28, 74.66, 77.47, 169.75 (Scheme 2).

2.3. Polymerization

PPAs were obtained by the polymerization of propargyl acetate (PA) initiated with a monodentate Rh catalyst, $[Rh(nbd)Cl]_2/NEt_3$, as shown in Scheme 1. In a typical procedure, 0.1×10^{-3} mol of PA and the calculated amount of the catalyst (0.1×10^{-3} mol) were dissolved in MeOH or NEt_3 solvent using a specially designed U-shaped ampoule [1], and the polymerization was carried out for 4 h at given temperatures in the solvent with constant shaking. The resulting solution was poured into excess amount of MeOH to precipitate a polymer. The resulting polymer was washed with MeOH and dried under dynamic vacuum, *ca.* 10^{-2} torr for 12 h at RT. The yield of the polymer was determined by gravimetry (Table 1).

*Poly(propargyl acetate): poly(**1**).* ^{1}H NMR ($CDCl_3$, TMS): $\delta = 2.05$ (s, 3H, $-CH_3$), 4.61 (s, 1H, HC═C—CH_2—,), 6.28 (s, 1H, HC═C—). ^{13}C

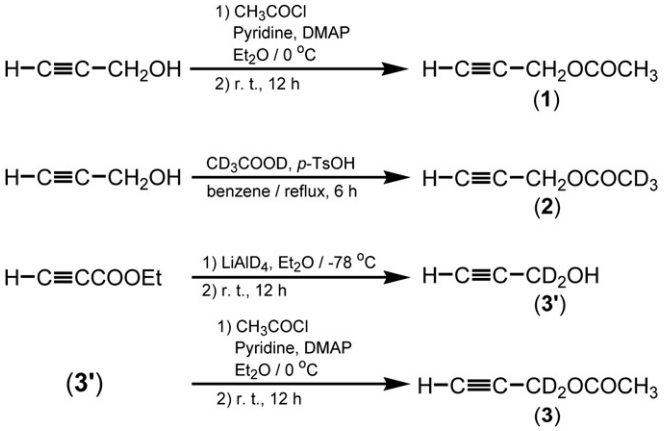

Scheme 2. Synthesis of propargyl acetates (**1**), (**2**), and (**3**).

Table 1
Polymerization of PAs using the $[Rh(nbd)Cl]_2$ catalyst.[a]

Run	Monomer	Solvent	Cocat.[b] ([cocat.]/[cat.])	Temp. (°C)	Yield[c] (%)	M_n[d] ($/10^4$)	M_w/M_n[d]	*cis*[e] (%)
1	1	MeOH	–	40	Trace	–	–	–
2	1	NEt_3	–	0	43	0.7	1.9	73
3	1	NEt_3	–	40	43	0.6	1.9	70
4	1	MeOH	100	0	79	0.5	1.8	70
5	1	MeOH	100	40	57	0.5	2.0	77
6	2	MeOH	100	40	44	0.7	1.8	85
7	3	MeOH	100	40	37	0.8	1.9	82

[a] $[M]_0 = 0.1$ mol/L, $[M]_0/[Cat.] = 100$.
[b] NEt_3 was used as cocatalyst.
[c] Insoluble fraction in methanol.
[d] $CHCl_3$ soluble part and estimated by GPC(PSt, $CHCl_3$).
[e] $CHCl_3$ soluble part and determined by ^1H NMR($CDCl_3$).

NMR ($CDCl_3$, TMS): $\delta = 20.6, 66.6, 128.3, 134.4, 170.5$. *Poly(propargyl deuterio-acetate)s: poly(**2**).* ^1H NMR ($CDCl_3$, TMS): $\delta = 4.61$ (s, 1H, HC═C–CH_2–), 6.28 (s, 1H, HC═C–). ^{13}C NMR ($CDCl_3$, TMS): $\delta = 20.6$, 66.6, 128.3, 134.4, 170.5. Anal. Calcd for $C_5H_3D_3O_2$: C, 59.39; H(D), 8.97. Found: C, 57.79; H(D), 8.69. *Poly(α,α-dideuterio-propargyl acetate): poly(**3**).* ^1H NMR ($CDCl_3$, TMS): $\delta = 2.05$ (s, 3H, $-CH_3$), 6.28 (s, 1H, HC═C–). ^{13}C NMR ($CDCl_3$, TMS): $\delta = 20.6$, 66.6, 128.3, 134.4, 170.5. Anal. Calcd for $C_5H_4D_2O_2$: C, 59.99; H(D), 8.05. Found: C, 58.72; H(D), 7.80. The elemental analysis for the deuteron was calculated by using the ^1H NMR spectral data of the two deuterated polymers.

3. Results and discussion

3.1. Polymerization

Poly(propargyl acetate)s (PPA)s were obtained by polymerization of monomers **1**, **2**, and **3** using the monodentate Rh catalyst: $[Rh(nbd)Cl]_2/NEt_3$ in MeOH or NEt_3 as the polymerization solvent. The yield with number and weight average molecular weights (M_n and M_w) and its distributions (M_w/M_n), and *cis* % are listed in Table 1. In the case of poly(**1**), Poly(**2**), and poly(**3**), *cis* content was carefully estimated by comparison of integrated ratio of vinyl proton and methyl or methylene protons observed in the ^1H NMR spectra.

Previously, we have reported that an organic solvent such as MeOH, THF, and NEt_3 with lone pair electrons acts as a good polymerization cocatalyst because the solvent stabilizes the Rh catalyst as the propagation species which was dissociated to a monodentate Rh catalyst from the bidentate Rh complex catalyst [1,18,19]. However, we found that the highest yield was observed when the polymerization of monomer **1** was performed under the conditions of NEt_3 as the cocatalyst in MeOH at 0 °C (Table 1, run 4). It is noteworthy that aliphatic acetylene ester monomers, e.g., alkylpropiorates unlike this PA monomer did not polymerize in NEt_3 [20]. Poly(**1**) (Table 1, run 5) prepared in MeOH at 40 °C, poly(**2**) and poly(**3**) (Table 1, runs 6 and 7) deuterated at either methyl or methylene moieties, respectively, were used in order to unequivocally determine the spatial geometrical structure of the *cis* and *trans* radicals stabilized in the resulting polymer using the ESR method at room temperature as mentioned below.

3.2. Polymer structure

The structure of the polymers was elucidated by ^1H NMR and ^{13}C NMR spectroscopies. The ^1H NMR spectra of poly(**1**), poly(**2**), and poly(**3**) are shown in Fig. 1. The ethynyl proton signal, H–C≡, observed at 2.53 ppm in their monomers (**1**, **2**, and **3**) disappeared completely and the new olefinic protons for polyene main-chain, which suggest a *cis–transoid* structure of the main-chain, were

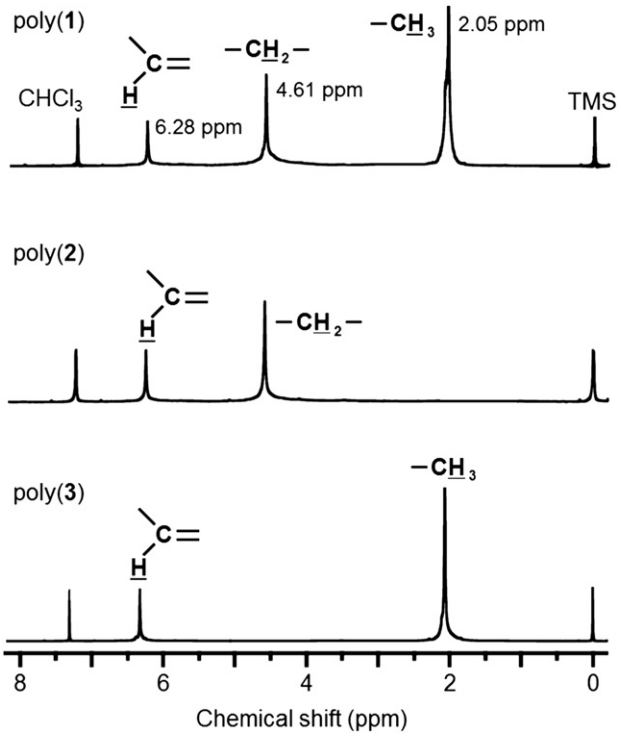

Fig. 1. ^1H NMR spectra of poly(**1**), poly(**2**), and poly(**3**) (300 MHz, $CDCl_3$) prepared with runs 5, 6, and 7 in Table 1.

observed at 6.28 ppm. The spectra of the deuterated polymers, poly(**2**) and poly(**3**), also supported their structures as shown in Fig. 1. The *cis* % of the polymers in Table 1 were determined according to the method of the literature [1].

3.3. ESR spectra

Previously, we reported that the ESR spectra of the radicals of aromatic polyacetylenes were observed before and after compression of the polymers, and the *cis* and *trans* radicals are produced through the *cis*-to-*trans* isomerization *via* the rotational scission of the helical *cis* C═C bond [1a,b,c,d], as shown in Scheme 1. ESR parameters of poly(**1**), poly(**2**), and poly(**3**) are summarized in Table 2. In addition, the *g* value of the observed radicals was used to deduce the geometrical structures, i.e., *cis* form or *trans* form, when one heteroatom such as N, S, and I is involved within the side-chain of the polyacetylene molecules [1e,21–23]. Such a heteroatom has a relatively large spin orbit coupling constant, ζ compared with that of the hydrocarbon atoms [22–24]. We have also revealed that these heteroatom can shift the *g* value to a lower magnetic field, especially in the *cis* form, although such a shift is extremely small for *trans* form, because of spatial decoupling of the magnetic interaction due to the unpaired electron between the side-chain and the planar *trans* main-chain. This indicates that the side-chain and the planar *trans* π-conjugation plane are nearly perpendicular to each other where such strong magnetic interaction is decoupled between the heteroatom in the side-chain and the unpaired electrons in the main-chain.

3.4. Spectral simulation of poly(*1*)

We examined whether two ESR signals corresponding to the *cis* and *trans* radicals were also observable in case of the freshly prepared poly(**1**) at room temperature. Consequently, we observed a fairly strong ESR spectrum as shown in Fig. 2a, although the

Table 2
ESR parameters of PPAs.[a]

Polymer	Radical	*g* value	$a^{H\alpha}$ (G)	$a^{H\beta1,2}$ (G)	$a^{H\beta3,4}$ (G)	$a^{H\gamma}$ (G)	ΔH_{msl}[b] (G)	Spins/*g* (/10^{16})	Unit/spin (/10^5)
poly(**1**)[c]	*cis*	2.0044	–	6.0	19.0	–	4.5	1.91	3.21
	trans	2.0027	16.0	–	–	4.0	6.0		
poly(**2**)[d]	*cis*	2.0044	–	6.0	19.0	–	4.5	2.75	2.16
	trans	2.0027	16.0	–	–	4.0	6.0		
poly(**3**)[e]	*cis*	2.0044	–	6.0	2.9	–	4.5	2.45	2.45
	trans	2.0027	16.0	–	–	4.0	6.0		

[a] Observed at room temperature.
[b] ΔH_{msl} = line width.
[c] Prepared by using the polymerization conditions of run 5 in Table 1.
[d] Prepared by using the polymerization conditions of run 6 in Table 1.
[e] Prepared by using the polymerization conditions of run 7 in Table 1.

pressure was not imposed to the polymer. To the best of our knowledge such ESR spectrum has never been reported up to date. Therefore, in order to spectroscopically determine whether the two paramagnetic chemical species, i.e., *cis* and *trans* radicals, are generated in poly(**1**), the so-called microwave power saturation effect was also examined at 1 mW and 0.001 mW, respectively [1d,21]. It was clear that the spectral line shape and its intensity was changed with decreasing microwave power (see Fig. 2b), by which fairly small hyperfine coupling (hfc) pattern compared with that of Fig. 2a were detected. The newly observed coupling pattern may reflect the existence of the two types of radicals involved in the polymer, poly(**1**). Therefore, in order to obtain more detailed hfc data for each radical the second derivative ESR spectrum was also measured at a fairly lower microwave power, i.e., 0.001 mW, as shown in Fig. 2c.

As a working hypothesis the ESR spectrum of Fig. 2c is considered to be superimposed with a triple–triplet and a doublet line spectra due to the *cis* and *trans* radicals, respectively, as shown in Fig. 2e with the stick diagram. Such a preliminary assignment may be supported by our previous experimental facts, i.e., the *cis* and *trans* radicals generated in the substituted polyacetylene polymers are observed as the sum of the so-called odd and even line ESR spectra, respectively [1e,5,21].

3.5. Spectral simulation of poly(**2**)

The poly(**2**) deuterated at the methyl moiety, $-CD_3$, in the side-chain gave the completely same ESR spectra as shown in the Fig. 2a–c. This result strongly indicates that the three protons of the methyl group of the side-chain are never magnetically interacted with the two chemical species, i.e., the *cis* and/or *trans* radicals which are detectable by the ESR technique.

3.6. Spectral simulation of poly(**3**)

Another deuterated polymer, poly(**3**), was also examined whether the spectral change is induced at room temperature. The second derivative ESR spectra of poly(**3**) were also measured at different microwave power of 1 mW and 0.001 mW, respectively, at room temperature. It is clear that notably large spectral changes took place as shown in Figs. 2c and 3b. These spectral change undoubtedly proves that the large triplet line of poly(**1**) (see Fig. 2e) comes from not the two vinyl protons of the main-chain but the methylene protons in the side-chain of poly(**3**) (see Schemes 1 and 3). Therefore, according to the stick diagram (see Figs. 2e and 3d) the spectra were successfully simulated assuming that the *cis* radical (**B**) has such the triple–triplet spectrum with the hfc: $a^{H\beta3} = a^{H\beta4} = 19.0$ G due to the two methylene protons, and $a^{H\beta1} = a^{H\beta2} = 6.0$ G due to two main-chain vinyl protons, line width, $\Delta H_{msl} = 4.5$ G and $g = 2.0044 \pm 0.0005$, and the *trans* radical (**C**) shows a doublet spectrum with a $a^{H\alpha} = 16.0$ G due to the one main-chain H_α proton, and $a^{H\gamma1} = a^{H\gamma2} = 4.0$ G and line width, $\Delta H_{msl} = 6.0$ G and $g = 2.0027 \pm 0.0005$ as shown in Fig. 2e. Thus, the simulated spectrum, Fig. 2d well agreed with that of the observed one, Fig. 2c each other.

The ESR spectrum of poly(**3**) was also simulated by considering the so-called gyromagnetic ratio of the proton and deuteron, $\gamma^H/\gamma^D = 6.5$ [22], as shown in Fig. 3b and c. Thus, this experiment strongly proves that the observed spectra are undoubtedly superimposed with those of the *cis* and *trans* radicals (**B** and **C**). This also suggests that the highest spin density of the resulting *cis* radical (**B**) localizes at not only main-chain protons, $H_{\beta1}$ and $H_{\beta2}$, but also the two methylene protons; $H_{\beta3}$ and $H_{\beta4}$, in the side-chain of poly(**1**) in Fig. 4a, and this result is similar to poly(*p*-halogenated phenylacetylene)s [24] and poly(*p*-sulfoxide phenylacetylene) [21].

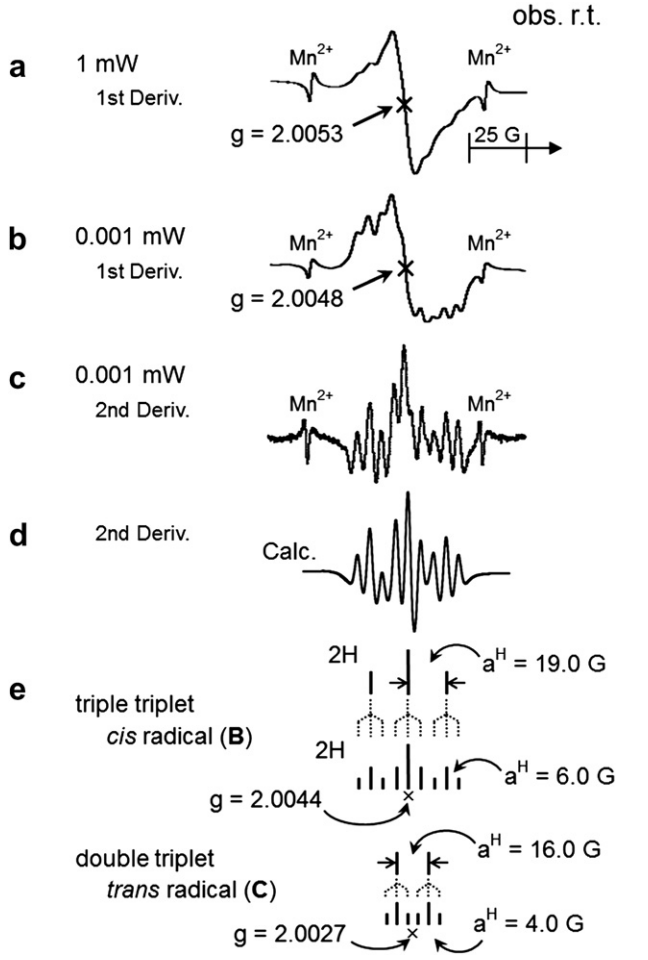

Fig. 2. ESR spectra of poly(**1**) (a) observed at 1 mW, (b) observed at 0.001 mW, (c) second derivative ESR spectrum observed at 0.001 mW, (d) simulated spectrum, and (e) stick diagram.

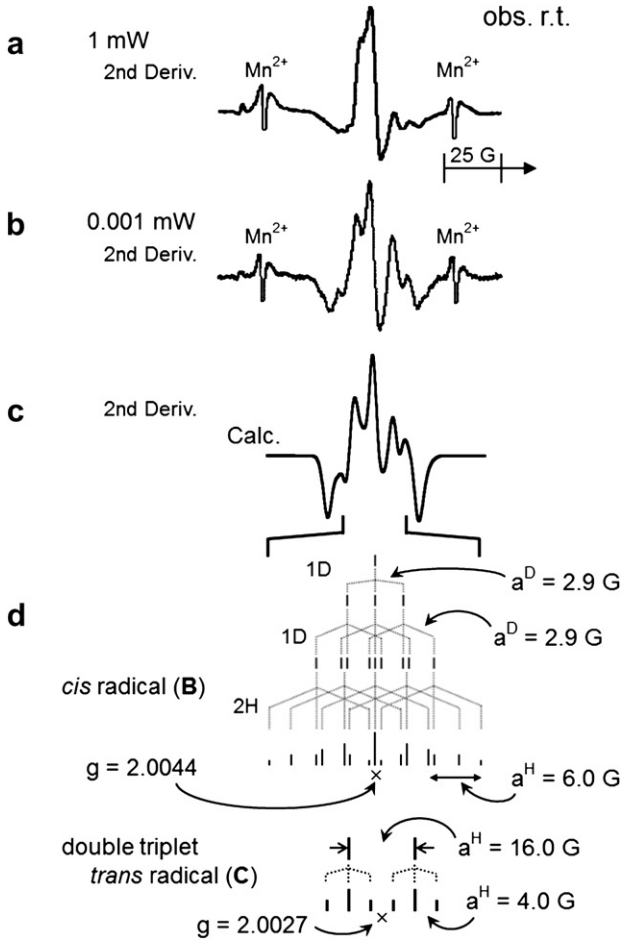

Fig. 3. Second derivative ESR spectra of poly(**3**) (a) observed at 1 mW, (b) observed at 0.001 mW, (c) simulated spectrum, and (d) stick diagram.

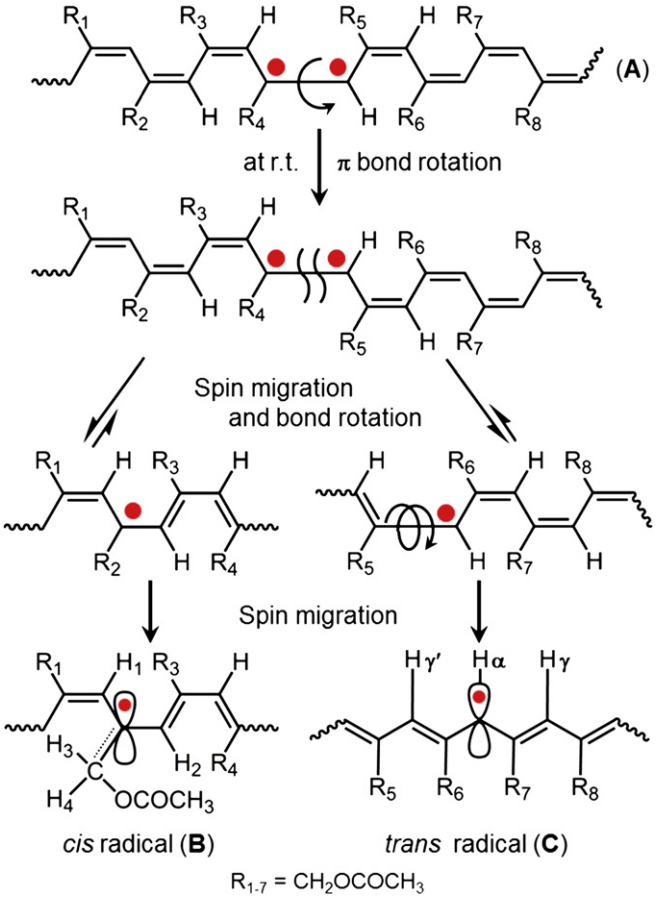

Scheme 3. Possible thermal-induced *cis*-to-*trans* isomerization through rotation hemolysis of the *cis* double bond.

On the other hand, the doublet line spectrum as shown in Fig. 2e was reasonably calculated by assuming that only one H_α proton can magnetically couple with the unpaired electron as the *trans* radical as shown in Fig. 4b. In other words, neither the main-chain $H_{\gamma 1}$ and $H_{\gamma 2}$ protons nor the side-chain CH_2 protons magnetically couples with an unpaired electron of the *trans* radical because the 2p orbital of unpaired electron and the side-chain plane are spatially perpendicular each other, as shown in Fig. 4b. Thus the *trans* radical was also proven to show ESR spectrum with the simple double triplet line unlike the previous case of the *trans* radicals which were generated by the so-called pressure induced *cis*-to-*trans* isomerization where the *trans* radical hold a fairy planar conjugation structure, i.e., a fairly narrow Lorentzian single line spectrum was observed and suggested π-conjugation such as the so-called soliton reflecting fast motional narrowing of the unpaired electron [2b,19,26].

3.7. Semi-empirical quantum chemical calculation

Conformational analysis using the AM1 program [19] was performed assuming a model compound of poly(**1**) to determine the most energetically stable conformation of their isomers and distribution of the unpaired electrons produced by the rotational scission of the pristine *cis* C═C bond during not only the polymerization but also on standing the polymer solution at room temperature (see Scheme 3). In order to calculate the most energetically stable structure by using the AM1 calculation a model structure which comprises 20 monomer sequences with an unpaired electrons for the *cis* radical was adopted. After that the further simplified *cis* radical model as depicted in Fig. 4a was used to calculate the spin density of the *cis* radical. The AM1 calculation showed that in the *cis* radical the C_α, $C_{\beta 1}$, $C_{\beta 2}$, and $C_{\beta 3}$ takes a planar plane with a sp^2 configuration and an angle, θ_1 and $\theta_2 = 75°$, θ_3 and $\theta_4 = 30°$, respectively. The calculation revealed that the spin density appeared at not only ether oxygen, −O−, but also until the carbonyl oxygen, C═O to some extent. This means that the spin density due to unpaired electron generated through the rotational scission of the helical *cis* C═C double bonds in the main-chain can migrate to the methylene moiety and the O−C═O moiety in the side-chain (see Scheme 3). Therefore, according to the AM1 calculation the observed large *g* value, i.e., 2.0044 ± 0.0005, due to the *cis* radical is reasonably explained by the migration of the spin density to the O−C═O moiety because of its fairly large spin orbit coupling constant, i.e., ζ value as mentioned above and the large ζ value make the *g* value shift to a lower magnetic field as observed in Figs. 2 and 3. Thus we can successfully explain the reason why the *g* value of the *cis* radical is fairly large, 2.0044 ± 0.0005 compared to 2.0027 ± 0.0005 of the *trans* radical. The very large spin density can be delocalized even on the ether oxygen and carbonyl oxygen atoms which have also a large orbit coupling constant $\zeta = 151$ [22], although the spin orbit coupling constant responsible for the −O−C═O group has been unknown up to date.

The doublet line of ESR as shown in Figs. 2e and 3d may also be reasonably attributed to that of the *trans* radical stabilized in the conjugated main-chain, because the resulting *trans* sequences have a fairly twisted configuration which can localize the spin density as the π-radical, i.e., a planer plane made by the C_α, $C_{\beta'}$, and C_β allows the magnetic coupling between the unpaired electron and H_α to

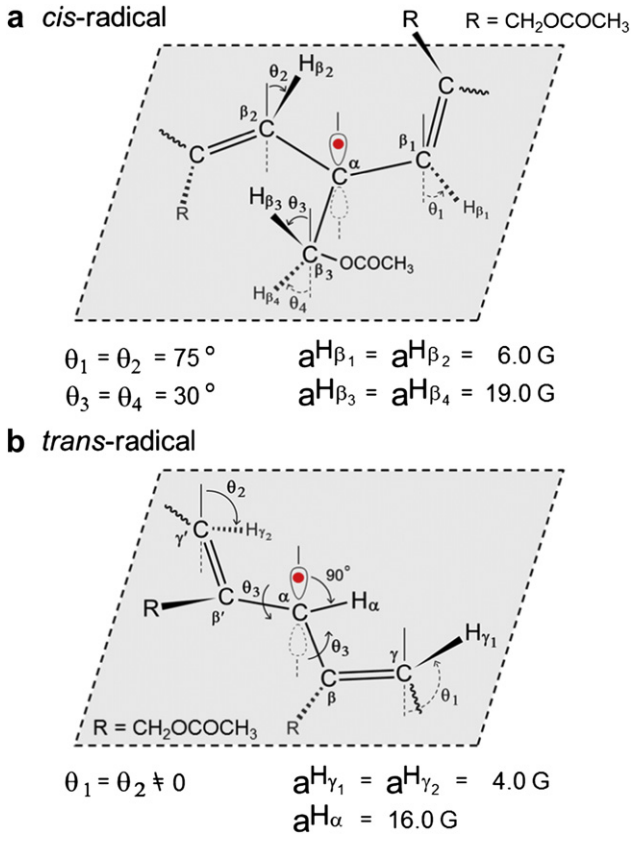

Fig. 4. Proposed radical structures for poly(**1**) (a) *cis* radical and (b) *trans* radical.

give such a doublet spectra (see Figs. 2d, e, 3c, d, and 4b), though a mobile unpaired electron similar to the so-called soliton of the substituted polyacetylenes has been shown to stabilize in the seven main-chain protons and to give a singlet line spectrum [1d,25,26]. Thus, the AM1 calculation consistently explains our experimental results without problem.

The aromatic polyacetylenes having a small amount of the spin density at the oxygen atom of the side-chain moiety may show an interesting magnetic behavior like the so-called spin glass as a novel time memory material [13] and become also magnetic materials for a useful radical cell [27].

4. Conclusion

The stereospecific polymerization of propargyl acetate and two propargyl acetates' analogues deuterated at the either methyl or methylene moiety was successfully performed using a Rh catalyst, $[Rh(nbd)Cl]_2$, MeOH and NEt_3 solvents at 0 and 40 °C and the corresponding *cis–transoid* polymers was obtained selectively in moderate yields. The polymerization even at the temperature induced the *cis*-to-*trans* isomerization, which was observed by the measurement of the ESR spectra. The ESR spectrum is considered to be composed of the *cis* radical whose spin density migrate to not only the main-chain but also the side-chain, i.e., $-CH_2-$ and $-O-C=O$ moiety giving the large *g* value, $g = 2.0044 \pm 0.0005$. On the other hand, the spin density of the *trans* radical is localized in the only main-chain which affords a smaller *g* value compared to that of the *cis* radical, which is a typical hydrocarbon radical.

References

[1] (a) Tabata M, Takamura K, Yokota Y, Nozaki T, Miyasaka H, Kodaira K. Macromolecules 1994;27:6234–6;
(b) Tabata M, Tanaka Y, Sadahiro Y, Sone T, Yokota K, Miura I. Macromolecules 1997;30:5200–4;
(c) Huang K, Tabata M, Mawatari Y, Miyasaka A, Sato E, Sadahiro Y, et al. J Macromol Sci Pure Appl Chem 2005;43:2836–50;
(d) D'Amato R, Sone T, Tabata M, Sadahiro Y, Russo MV, Furlani A. Macromolecules 1998;31:8660–5;
(e) Huang K, Mawatari Y, Tabata M, Sone T, Miyasaka A, Sadahiro Y. Macromol Chem Phys 2004;205:762–70.

[2] (a) Tabata M, Sone T, Sadahiro Y, Yokota K, Nozaki Y. J Polym Sci Part A Polym Chem 1998;36:217–23;
(b) Mawatari Y, Tabata M, Sone K, Ito Y, Sadahiro. Macromolecules 2001;34:3776–82.

[3] (a) Aoki T, Shinohara K, Oikawa E. Chem Lett 1993;22:2009–12;
(b) Teraguchi M, Suzuki J, Kaneko T, Aoki T, Masuda T. Macromolecules 2003;36:9694–7.

[4] (a) Suzuki Y, Tabei J, Shiotsuki M, Inai Y, Sanda F, Masuda T. Macromolecules 2008;41:1086–93;
(b) Tabata M, Sone T, Sadahiro Y. Macromol Chem Phys 1999;200:265–82;
(c) Nakako H, Nomura R, Tabata M. Macromolecules 1999;32:2861–4.

[5] (a) Yashima E, Maeda Y, Okamoto Y. J Am Chem Soc 1998;120:8895–6;
(b) Yashima E, Matsushima T, Okamoto Y. J Am Chem Soc 1997;119:6345–59;
(c) Nonokawa R, Yashima E. J Am Chem Soc 2003;125:1278–83.

[6] Liu JH, Yan JJ, Chen EQ, Lam JWY, Dong YP, Liang DH, et al. Polymer 2008;49:3366–70.

[7] Dening TJ, Novak BM. J Am Chem Soc 1992;114:7926–7.

[8] (a) Neher D, Wolf A, Bubeck C, Wegner G. Chem Phys Lett 1989;163:116–22;
(b) Bredas JL, Adant C, Tacks P, Persoons A, Pierce M. Chem Rev 1994;94:243–78;
(c) Falconieri M, D'Amato R, Russo MV, Furlani A. Nonlinear Opt 2001;27:439–42.

[9] (a) Tabata M, Sone T, Yokota K, Wada T, Sasabe H. Nonlinear Opt 1999;22:341–4;
(b) Wada T, Wang L, Okawa H, Masuda T, Tabata M, Wan M, et al. Mol Cryst Liq Cryst 1997;294:245–50.

[10] (a) Korshak YV, Medvedeva TV, Ovchinnikov AA, Spector V. Nature 1987;326:370–2;
(b) Tyutyulkov N, Müllen K, Baumgarten M, Ivanova A, Tadjer A. Synth Met 2003;139:99–107.

[11] (a) Tabata M, Takamura H, Yokota K, Nozaki Y, Hoshina T, Minakawa H, et al. Macromolecules 1994;27:6234–6;
(b) Tabata M, Nozaki Y, Yang W, Yokota K, Tazuke Y. Proc Jpn Acad 1995;71:219–24.

[12] (a) Fisher KH, Herz JA. In: Spin glass. Cambridge University Press; 1991. p. 30;
(b) Pregjean JJ, Souletie J. J Phys 1980;41:1335–52;
(c) Floch L, Hammann F, Ocio J, Vincent M. Euro Phys Lett 1992;18:647–52;
(d) Xenikos DG, Multer H, Jouan C, Suilpice A, Tholence JL. Solid State Commun 1997;102:681–5.

[13] (a) Tabata M, Watanabe Y, Muto S. Macromol Chem Phys 2004;205:1174–8;
(b) Watanabe Y, Muto S, Tabata M. Jpn J Appl Phys Part 2 Lett 2004;43:300–2.

[14] (a) Masuda T, Higashimura T. Adv Polym Sci 1986;81:121–65;
(b) Masuda T, Tachimori H. J Macromol Sci Pure Appl Chem 1994;A31:1675–90;
(c) Yang MJ, Sun HM, Ling MF. Acta Polym Sin 2000;2:161;
(d) Sun HM, Yang MJ, Ling MF. Chin Chem Lett 2000;11:1097–110;
(e) Yan MJ, Li Y. Sens Actuators B 2002;86:155–9;
(f) Zhan XW, Yang MJ, Sun HM. Macromol Rapid Commun 2001;22:530–4;
(g) Kunzler J, Percec V. J Polym Sci Polym Chem Ed 1990;28:1221–36.

[15] (a) Nomura R, Tabei J, Masuda T. J Am Chem Soc 2001;123:8430–1;
(b) Gao GZ, Sanda F, Masuda T. Macromolecules 2003;36:3932–7;
(c) Zhang W, Tabei J, Shiotsuki M, Masuda T. Polym Bull 2006;57:463–72;
(d) Kishimoto Y, Itou M, Miyatake T, Ikariya T, Noyori R. Macromolecules 1995;28:6662–6.

[16] AM1 calculations were carried out with Spartan'04 Windows ver. 1.03 (Wavefunction, Inc.).

[17] Lefebvre R, Maruani J. J Chem Phys 1965;42:1480–96. The original program for the computer simulation was modified to superpose two spectra having different *g* values.

[18] (a) Tabata M, Yang W, Yokota K. Polym J 1990;22:1105–7;
(b) Yang W, Tabata M, Yokota K. Polym J 1991;23:1135–8;
(c) Tabata M, Yang W, Yokota K. J Polym Sci Part A Polym Chem 1994;32:1113–20;
(d) Lindgren M, Lee HS, Yang W, Tabata M, Yokota K. Polymer 1991;32:1532–4.

[19] Sone T, Amato R, Mawatari Y, Tabata M, Furlanl A, Russo MV. J Polym Sci Part A Polym Chem 2004;42:2365–76.

[20] McCulloch AW, McInnes AG. Can J Chem 1974;52:3569–76.

[21] Huang K, Mawatari Y, Miyasaka A, Sadahiro Y, Tabata M, Kashiwaya Y. Polymer 2007;48:6366–73.

[22] Pshezhetskii SY, Kotov AG, Milincuk VA, Rozinskii VI, Tupikov VI. ESR of free radicals in radiation chemistry. New York: Wiley; 1972.

[23] Tabata M, Lund A. Chem Phys 1983;75:379–88.

[24] Miyasaka A, Sone T, Mawatari Y, Setayesh S, Mullen K, Tabata M. Macromol Chem Phys 2006;207:1938–44.

[25] (a) Harada T, Tasumi M, Shirakawa H, Ikeda S. Chem Lett; 1978:1411–4;
(b) Shirakawa H, Ito T, Ikeda S. Macromol Chem 1978;179:1565–73.

[26] Weinberger BR, Ehrenfreund E, Pron A, Heeger AJ, Mac Diarmid AG. J Chem Phys 1980;72:4749–55.

[27] Hustedt EJ, Thoman H, Robinson BH. J Chem Phys 1990;92:978–95.

Polymer 52 (2011) 652–657

Contents lists available at ScienceDirect

Polymer

journal homepage: www.elsevier.com/locate/polymer

Synthesis of ultra-thin polypyrrole nanosheets for chemical sensor applications

Sang Soo Jeon [a], Hyeun Hwan An [b], Chong Seung Yoon [b,*], Seung Soon Im [a,*]

[a] Department of Fiber and Polymer Engineering, Hanyang University, Seoul 133-791, Republic of Korea
[b] Division of Materials Science and Engineering, Hanyang University, Seoul 133-791, Republic of Korea

ARTICLE INFO

Article history:
Received 21 October 2010
Received in revised form
4 December 2010
Accepted 12 December 2010
Available online 21 December 2010

Keywords:
Chemical sensor
Nanosheet
Polypyrrole

ABSTRACT

Ultra-thin polypyrrole nanosheets (UPNSs) are fabricated by organic crystal surface-induced polymerization (OCSP) of pyrrole in an aqueous suspension containing hydrated crystals of sodium decylsulfonate ($C_{10}SO_3Na$) below the Krafft temperature using $FeCl_3$ as an oxidant. The hydrated $C_{10}SO_3Na$ crystals are used as templates through electrostatic binding of the cationic polypyrrole (PPy) chains oxidized by Fe(III) ions on the anionic $C_{10}SO_3Na$ crystal surface. The resulting UPNSs have a single layer thickness of ~21 nm, widths between 2 and 6 μm, and lengths greater than 10 μm. The UPNSs are composed of a single continuous PPy domain. Moreover, the UPNSs exhibit higher conductivity (30.6 Scm^{-1}) and longer conjugation lengths than the PPy nanoparticles (2.4 Scm^{-1}) prepared using emulsion polymerization. We systematically investigate the UPNSs as gas sensors for detecting and quantifying toxic gases such as HCl and NH_3. The UPNSs exhibit much higher gas sensitivity and faster response times compared with the PPy nanoparticles.

1. Introduction

Conducting polymers are generally infusible and insoluble in most common solvents [1]. Thus, to improve their dispersibility and processibility, they are often fabricated in nanoparticulate/fibrous forms [2,3]. Due to the high surface/volume ratio and the quantum size effects, these low-dimensional conducting polymers have unique physical and chemical properties compared with their bulk counterparts [4]. Nanostructured conducting polymers have been widely studied for potential use in sensors, electronics, and optical devices [1,2,5–9]. Although progress has been made to advance the synthesis and applications of conducting polymers, large-scale fabrication of nanostructured conducting polymers with controlled morphologies and sizes has not been fully achieved.

In addition to hard template methods [9–11], fabrication of nanoscale conducting polymer structures by micelle aggregation of surfactants as nanoreactors has shown promise for preparing shape- and size-controlled conducting polymer nanoparticles [12,13], nanofibers [14], and nanotubes [15]. The critical micelle concentration (CMC), defined as the concentration of the surfactant, and the Krafft point, i.e., the temperature above which thermodynamically stable micelles are formed, are the two primary surfactant characteristics necessary to form stable micelle aggregates [16]. Fig. 1 shows a schematic phase diagram of a surfactant and water. As the concentration of the surfactant increases above the CMC and Krafft point, the micelles will change from spherical to cylindrical and finally to a lamellar phase to reduce the surface area of the hydrophilic surfactant head groups. On the other hand, below the Krafft point, the surfactants do not form micelles, but produce hydrated crystals.

Most previous studies have used the interior of the micelle as a soft template, and the final morphology and size of the conducting polymers were dictated by the polymerization temperature, surfactant or monomer concentration, and type of continuous phase (water or oil). However, recently, a route for fabricating spiral nanostructured conducting polymers using hydrated surfactant crystals of sodium dodecylsulfonate and cetyltrimethylammonium bromide as a template below the Krafft point was reported [17,18]. The growth of this unusual morphology arose from the spiral dislocation structures on the hydrated crystal surface and was induced by ammonium persulfate (APS). Moreover, we reported an organic crystal surface-induced polymerization (OCSP) method capable of producing polypyrrole (PPy) microstructures with an improved structural order and high electrical conductivity (~400 Scm^{-1}) using organic crystals of a series of sulfobenzoic acid salts as the soluble template [19,20]. This method relies on a shape-copying process based on electrostatic interactions between anionic organic crystal surfaces and cationic PPy chains.

* Corresponding authors. Tel.: +82 2 2220 0495; fax: +82 2 2297 5859.
E-mail addresses: csyoon@hanyang.ac.kr (C.S. Yoon), imss007@hanyang.ac.kr (S.S. Im).

0032-3861/$ – see front matter © 2010 Elsevier Ltd. All rights reserved.
doi:10.1016/j.polymer.2010.12.021

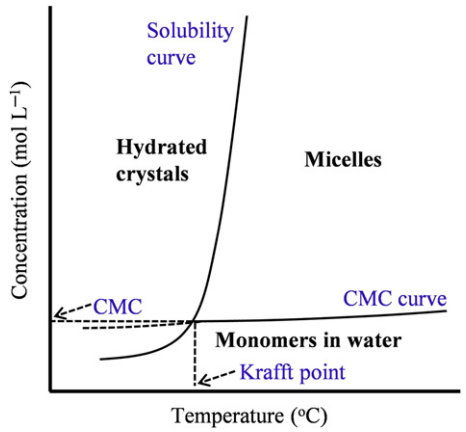

Fig. 1. A schematic phase diagram of the surfactant and water.

Here, we describe a facile approach to produce ultra-thin polypyrrole nanosheets (UPNSs) using an OCSP method in an aqueous suspension containing hydrated surfactant crystals of sodium decylsulfonate ($C_{10}SO_3Na$) below the Krafft point. Our study is unique because the hydrated $C_{10}SO_3Na$ crystals were used as templates for the fabrication of UPNSs with a thickness of ~21 nm by OCSP, and the UPNS were synthesized on a large scale in a facile manner. In addition, as with other conducting polymers, PPy can be used as a chemical sensor for detecting various chemical species including acids and bases via doping–dedoping mechanism [6–9]. Especially, nanostructured conducting polymer chemical sensors provide more improved sensitivity and faster response compared to their bulk counterparts due to the porous structure and large surface area of nanostructures [6–9]. Therefore, we also demonstrated that the UPNSs were capable of detecting and quantifying toxic gases such as hydrochloric acid (HCl) and ammonia (NH_3).

2. Experimental

2.1. Materials

Pyrrole was purified by distillation under reduced pressure and stored at 2 °C prior to use. Iron(III) chloride ($FeCl_3$) and ammonium persulfate (APS) were used as oxidants with no further purification. Sodium decylsulfonate ($C_{10}SO_3Na$) was used as received.

2.2. Synthesis

In a typical synthesis, $C_{10}SO_3Na$ (2.44 g, 10 mmol) were dissolved in distilled water (100 mL) at 30 °C, and the solution was cooled to 0 °C. White hydrated $C_{10}SO_3Na$ crystals appeared quickly in the transparent solution. Pyrrole (1.01 g, 15 mmol) was added to the solution and stirred for 30 min. A pre-cooled $FeCl_3$ solution (30 mmol dissolved in 20 mL of distilled water) was added dropwise (15 mL/h) to the above mixture, and the white mixture gradually turned black. After 3 h, the PPy precipitates were filtered and washed, and dried in a vacuum oven at 60 °C for 24 h. To compare the properties of the UPNSs with those of PPy nanoparticles, PPy nanoparticles were synthesized by emulsion polymerization using APS (3.42 g, 15 mmol) as an oxidant at 30 °C, and all other conditions were kept the same.

2.3. Characterization

The conductivity (298 K) of a pressed pellet of the dried samples was measured using the four-probe method. The morphologies of the resulting PPys were observed using scanning electron microscopy (SEM, JEOL JSM6340) and transmission electron microscopy (TEM, JEOL 2010). To measure the thickness of the ultra-thin PPy layer, a cross-section of the PPy fabricated by OCSP was prepared by embedding the PPy sample in an epoxy and grinding it until it was flat. The morphology of the hydrated $C_{10}SO_3Na$ crystals was observed using optical microscopy (OM, Olympus BX-51). X-ray diffraction (XRD, Rigaku D/MAX-2500) using Cu Kα radiation and atomic force microscopy (AFM, PSIA XE-100) were used to analyze the structures and surface morphologies of the hydrated $C_{10}SO_3Na$ crystals and the resulting PPys. FT-IR spectra of the PPys were recorded on a PerkinElmer Spectrum 100 FT-IR spectrometer. As shown schematically in Fig. 7a, interdigitated gold electrodes with 25 pairs of fingers (dimensions: 14-μm spacing, 5-mm length, 50-nm thickness) were patterned on a silicon oxide substrate by photolithography. An ethanol-based solution (0.1 mL) containing 10 wt% of PPy sample was dropped onto the gold electrode. After vacuum drying for 5 h, the electrode was placed in a 500-mL round flask with an air inlet/outlet valve. The vacuum of the round flask was maintained at approximately 1 Torr throughout the gas sensing process. HCl or NH_3 (20–100 ppm) was quickly injected into the flask, and the electrical resistances were measured in real-time with a digital multimeter (Keithley 2000) connected to a computer. Fully dedoped PPys and those doped with NaOH and HCl solutions were used to measure changes in the electrical resistance prior to HCl and NH_3 gas exposure.

3. Results and discussion

Fig. 2 shows the morphological characteristics of UPNSs fabricated by OCSP using hydrated $C_{10}SO_3Na$ crystals as a template. The SEM image in Fig. 2a shows multiple layers of UPNSs that covered the entire surface of the glass substrate, whereas a single sheet of UPNS is shown in Fig. 2b and c. The SEM and TEM images verify that the single UPNS was rectangular shaped with a width of ~2–6 μm and a length greater than 10 μm. Fig. 2d shows a magnified TEM image of the partially punctured region marked in Fig. 2c, which shows that the single UPNS was actually composed of two layers of UPNSs that were loosely held together. The cross-sectional TEM image in Fig. 2e produced by microtome shows that the thickness of a single layer of UPNS was ~20 nm. The surface of the UPNS layer (Fig. 2f) had a smooth texture, as indicated by the uniform grain contrast of the TEM image. The smooth texture of the UPNS suggests that the nanosheet consisted of a single continuous domain of PPy with no particle boundaries. An AFM scan and the corresponding depth profile (Fig. 2g and h) confirmed that the UPNS surface was quite flat, with occasional wrinkles of ~6 μm, and the combined thickness of the top and bottom PPy layers was ~42 nm, which agreed with the value obtained from the cross-sectional TEM image in Fig. 2f. The morphology of the delineated UPNSs from TEM and AFM showed a single UPNS composed of two layers of PPy, possibly due to the collapse of a hollow structure. Additionally, the flat surface texture indicates that the UPNS was likely a single continuous domain, unlike other PPy structures that typically contain interconnected spherical or ellipsoidal PPy nanoparticles [17–20].

As reported in our previous studies [19,20], the molecular structure of organic crystals, as well as the presence of anionic groups on crystal surfaces, were crucial for the formation of shape-copied PPy micro/nanostructures by OCSP based on electrostatic interactions [9,21,22]. The OM image (Fig. 3a) of hydrated $C_{10}SO_3Na$ crystals prior to the polymerization of pyrrole shows that their shapes and dimensions were similar to those of the OCSP-synthesized UPNSs (Fig. 2). The inset shows that the XRD patterns of hydrated $C_{10}SO_3Na$ crystals prior to polymerization and those that

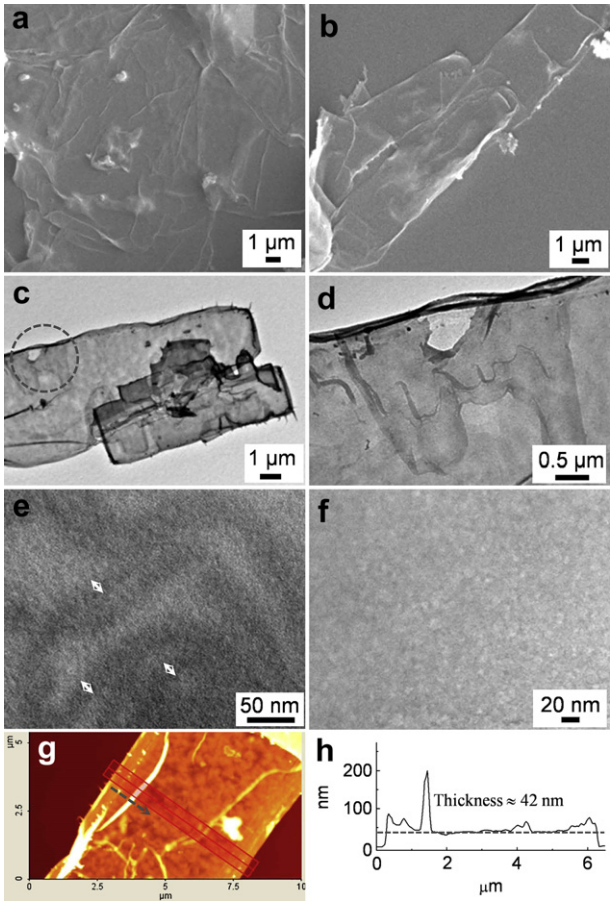

Fig. 2. (a,b) SEM and (c, d, e, f) TEM images of UPNS. (d) A magnified image of the circle in (c). (e) Microtomed cross-section of UPNSs. (f) A magnified image of the UPNS surface. (g) AFM image of UPNS. (h) Depth analysis of the rectangular box shown in (g). The arrow in (g) indicates the scan direction of the depth analysis.

precipitated in pure water or in the presence of $FeCl_3$ (data not shown) were identical. The OM and XRD results indicate that pyrrole and $FeCl_3$ had no effect on the crystallization of the $C_{10}SO_3Na$ molecules, and the hydrated $C_{10}SO_3Na$ crystals, once formed, were very stable. In addition, the diffraction peaks at $2\theta = 4.05, 8.00, 12.00, 15.95$, and 24.05° corresponded to d-spacing ratios of $1:^1/2:1/3:1/4:1/5$ and crystalline planes of (001), (002), (003), (004), and (005) for $C_{10}SO_3Na$. The XRD data suggests that the hydrated $C_{10}SO_3Na$ crystal had a lamellar structure formed by consecutive head-to-head stacking of the bimolecular layer (thickness ~2.23 nm). An AFM image of a $C_{10}SO_3Na$ crystal and its depth profile are shown in Fig. 3b and c. The width and average thickness of the crystal were approximately 14 μm and 178 nm, respectively. However, because the PPy structure fabricated by OCSP copied the shape of the original organic crystal, as previously demonstrated [19,20], there was a large discrepancy between the thicknesses of the hydrated $C_{10}SO_3Na$ crystal (~178 nm) and the UPNS (~21 nm). The discrepancy can be easily explained by assuming that a hollow structure produced during the OCSP process collapsed.

A schematic depiction of the procedure for the synthesis of UPNSs by OCSP is presented in Fig. 4a. Ionic hydrocarbon surfactants, including $C_{10}SO_3Na$, can exist in three different states (solution, micelles, and hydrated crystals) depending on the temperature and concentration of the aqueous system [16]. Although the $C_{10}SO_3Na$ molecules formed stable micelles above their CMC (3.5×10^{-2} mol L^{-1}) and Krafft point (23 °C), hydrated crystals were produced above the CMC and below the Krafft point [23,24]. When the temperature of the micelle solution dropped to 0 °C, below its Krafft point, hydrated $C_{10}SO_3Na$ crystals were produced (Fig. 4, a1). The magnified illustration in Fig. 4, a1 shows the possible lamellar structure formed by $C_{10}SO_3Na$ molecules. Because the surface of the crystals was composed of anionic sulfonate head groups of the $C_{10}SO_3Na$ molecules, upon initiation of the pyrrole polymerization using $FeCl_3$ as an oxidant, the positively-charged PPy chains grew on both the top and bottom surfaces of the anionic crystal via electrostatic interactions (Fig. 4, a2). PPy formed in this manner is thought to be dominated by homogeneous nucleation of pyrrole on the negatively charged crystal surface, resulting in a smooth and continuous domain with no particle boundaries, as shown in Fig. 2. Finally, the two-layered UPNS that polymerized on the top and bottom surfaces of the crystals remained as the hydrated $C_{10}SO_3Na$ crystals dissolved with complete washing and filtering (Fig. 4, a3). On the other hand, the final morphology of PPy could be altered by simply increasing the polymerization temperature and by adding APS instead of $FeCl_3$ as the oxidant. Fig. 4b shows the general scheme for the emulsion polymerization used to produce PPy nanoparticles. When the polymerization temperature was elevated from 0 °C (below the Krafft point) to 30 °C (above the Krafft point), the hydrated $C_{10}SO_3Na$ crystals dissolved and formed a stable micelle suspension (Fig. 4, b1). Pyrroles were then added, and the hydrophobic pyrroles penetrated into the hydrophobic inner space of the micelles (Fig. 4, b2). Subsequently, APS was used to polymerize the pyrroles inside the individual micelles (Fig. 4, b3). Finally, spherical PPy nanoparticles were obtained by washing and filtering (Fig. 4, b4).

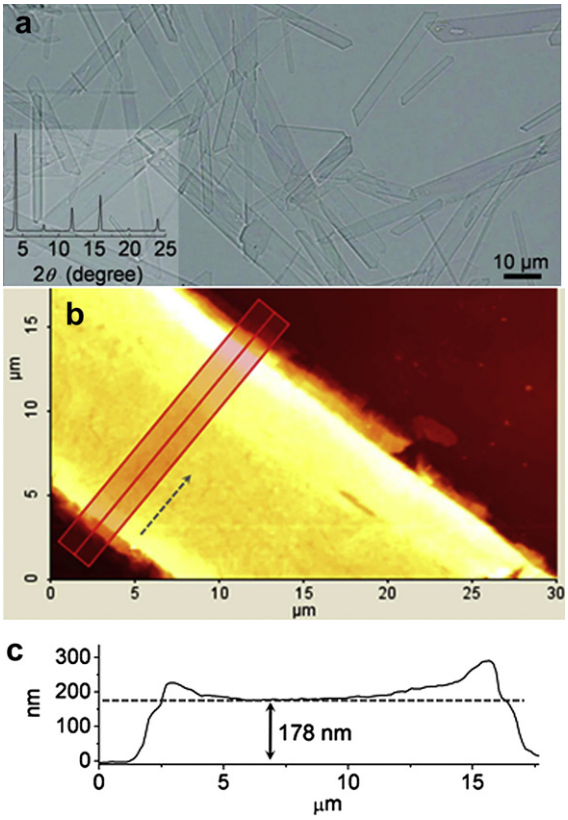

Fig. 3. Typical (a) OM and (b) AFM images of hydrated $C_{10}SO_3Na$ crystals prior to polymerization. The inset in (a) shows the XRD pattern of hydrated $C_{10}SO_3Na$ crystals precipitated in our polymerization medium at 0 °C before adding the $FeCl_3$ solution. (c) Depth analysis of the rectangular box shown in (b). The arrow in (b) indicates the scan direction of the depth analysis.

The choice of oxidant was an important factor to fabricate well-defined UPNSs. When APS was added dropwise instead of $FeCl_3$, bulky PPys were produced (Fig. 5a). Additionally, no UPNSs were observed when $FeCl_3$ was added in one step instead of dropwise (data not shown). Dropwise addition of $FeCl_3$ formed well-defined UPNSs because its lower oxidation/reduction potential (ORP) (0.77 V) compared with APS (2.01 V) [25] led to a slow polymerization rate. Because the positively-charged PPy chains, initiated by dropwise addition of $FeCl_3$ with vigorous stirring, had sufficient time for physical bonding to the negatively charged surface ($-SO_3^-$) of the hydrated $C_{10}SO_3Na$ crystals through electrostatic interactions, PPys were primarily synthesized on the crystal surface. On the other hand, APS, with a relatively higher ORP, induced a faster polymerization reaction. Thus, monomers were polymerized randomly without adsorbing on the crystal surface, similar to the bulk state. Therefore, APS was a more suitable oxidant than $FeCl_3$ for producing PPy nanoparticles by emulsion polymerization using $C_{10}SO_3Na$ as a surfactant. Fig. 5b shows the SEM and TEM images of the spherical PPy nanoparticles with diameters of about 30–50 nm produced by emulsion polymerization above the Krafft point.

FT-IR spectroscopy of the PPy samples suggests that the UPNSs fabricated by OCSP had characteristic peaks nearly identical to those of PPy nanoparticles synthesized by emulsion polymerization (Fig. 6a). The absorption bands at ~1584 and 1489 cm^{-1} (anti-symmetric and symmetric stretching modes in the pyrrole ring), 1328 and 1054 cm^{-1} (N–H and C–H deformation vibrations), and 1225 and 933 cm^{-1} (stretching vibrations in the doped PPy) were observed in both PPy samples [26–28]. However, the PPy nanoparticle spectrum shows a weak peak at 1712 cm^{-1}, which corresponds to the carbonyl group, suggesting that a large number of carbonyl defects were incorporated into the PPy chains due to over-oxidation at the elevated polymerization temperature [29]. These structural defects can reduce the structural order and the packing density of the PPy chains that were predominantly crystallized by π-stacking between inter-pyrrole rings [30]. Thus, various constrained structures of PPy chains caused shifts in the positions of absorption bands from 1400 to 1700 cm^{-1} (Fig. 6b). The peaks at 1584 and 1489 cm^{-1}, ascribed to stretching vibrations of pyrrole rings, were red-shifted by ~28 cm^{-1} in the UPNSs. This may have been due to a decrease in the force constant caused by restricted vibrational motion in the UPNSs with a higher packing density or structural order, which is consistent with previous results [31]. In addition, it was reported that these bands were affected by changes in the extent of delocalization in the PPy chains [26,27]. Especially, the changes can be easily estimated by taking the ratio of the integrated absorption intensity of the 1560 cm^{-1} band to the 1470 cm^{-1} band. Martin et al. have noted that longer conjugation length critically led to a higher conductivity and experimentally, the effective conjugation length was inversely proportional to the

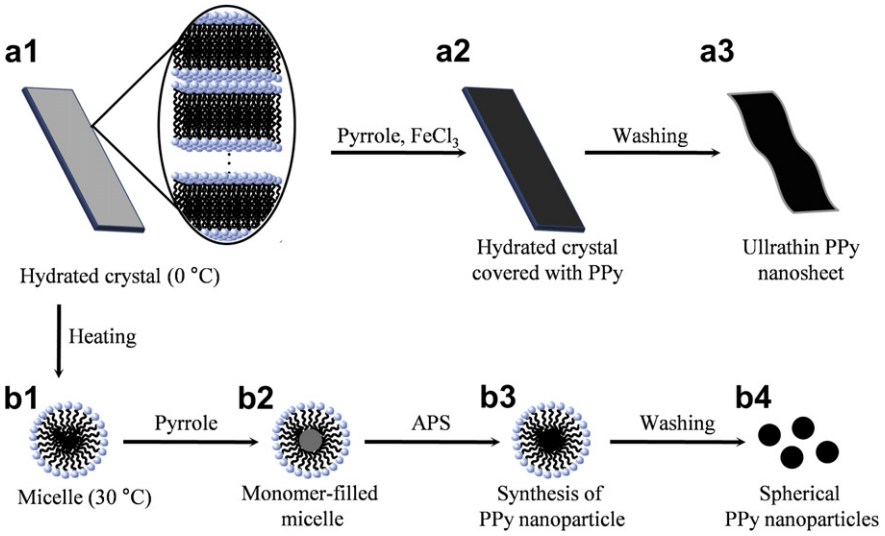

Fig. 4. Schematic illustration of the synthesis procedure for UPNSs and PPy nanoparticles via two different pathways using $C_{10}SO_3Na$ molecules: (a) OCSP process, and (b) emulsion polymerization.

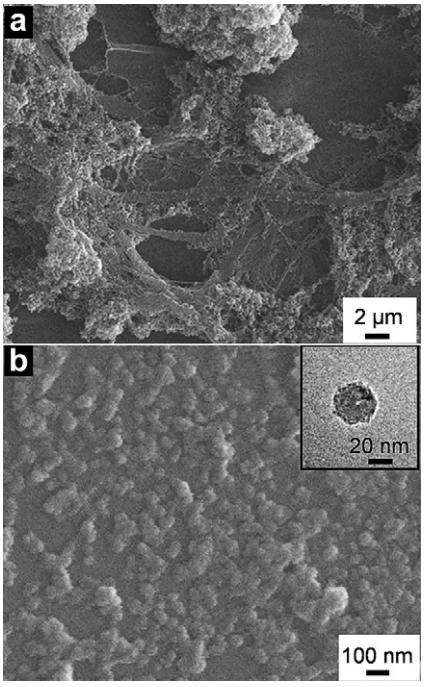

Fig. 5. SEM images of PPy samples prepared under different synthetic conditions. (a) OCSP process at 0 °C using APS as an oxidant. (b) Emulsion polymerization at 30 °C using APS as an oxidant. The inset shows the magnified TEM image of a PPy nanoparticle.

ratio of the peak areas at 1560 and 1470 cm^{-1} (A_{1560}/A_{1470}) [32]. The calculated A_{1560}/A_{1470} values were 3.43 and 7.78 in the UPNSs and PPy nanoparticles, respectively. The peak ratio, along with the fact that the electrical conductivity of the UPNSs (30.6 Scm^{-1}) was significantly higher than that of the PPy nanoparticles (2.4 Scm^{-1}), indicates that the UPNSs fabricated by OCSP had longer effective conjugation lengths than the PPy nanoparticles prepared by emulsion polymerization. However, compared to our previous results [19,20], the UPNSs prepared by OCSP exhibited the lower conductivity of 30.6 Scm^{-1}, which may be due to the absence of aromatic groups in $C_{10}SO_3Na$ molecule. It is known that PPys can form strong pi-stacks with the assistance of aromatic and planar dopants, such as aromatic sulfonates crystallized by pi-stacking, and therefore exhibit the enhanced conductivity [33].

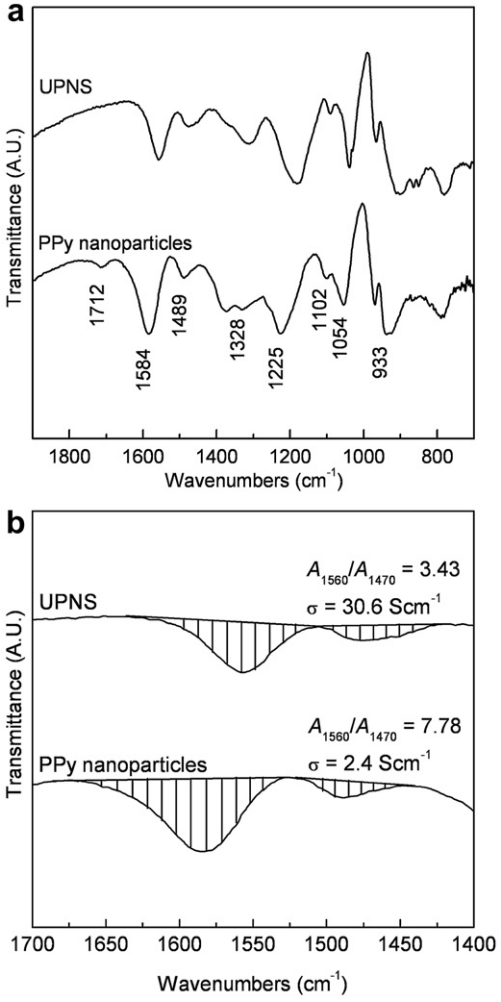

Fig. 6. FT-IR study of PPy samples: (a) Transmission FT-IR spectra and (b) A_{1560}/A_{1470}. The 1560- and 1470-cm^{-1} bands are highlighted in the spectra.

Conducting polymer nanostructures with higher surface areas and porosity are useful for chemical sensor applications [9,34,35]. Thus, we investigated the capability of UPNSs as chemical sensors for gaseous HCl and NH_3, and we compared the results with those

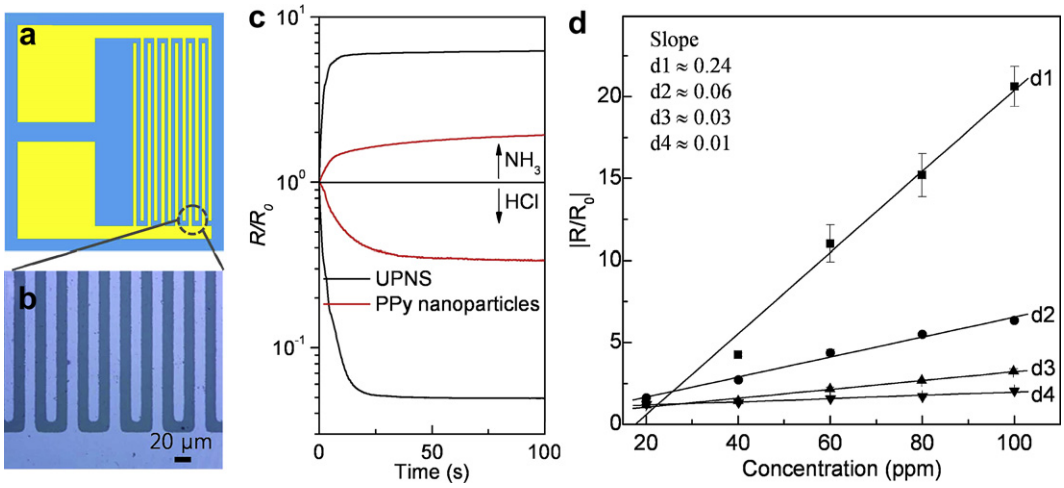

Fig. 7. (a) Schematic illustration of an interdigitated gold electrode substrate. (b) OM image of the interdigitated gold electrode substrate. (c) Response of PPy nanoparticles and UPNSs upon exposure to 100 ppm HCl and NH_3 vapor. Dedoped and doped PPy samples were used to detect HCl and NH_3, respectively. (d) Response sensitivity (absolute value) of UPNSs (d1 and d2) and PPy nanoparticles (d3 and d4) as a function of gas concentration: (d1 and d3) HCl and (d2 and d4) NH_3.

of PPy nanoparticles prepared by emulsion polymerization. Fig. 7a and b show a schematic illustration of an interdigitated gold electrode substrate and OM image of the electrode, respectively. Chemical sensors were fabricated by dropping a 10 wt% PPy dispersion onto the electrodes. The real-time R/R_0 upon exposure to HCl and NH_3 (100 ppm) are shown in Fig. 7c. R/R_0 is the resistance (R) normalized to the initial resistance (R_0) prior to gas exposure. For both HCl and NH_3, the response amplitudes of the UPNSs were much higher than those of the PPy nanoparticles. Moreover, the response time evaluated from the onset point of the R/R_0 signal was also much faster for the UPNSs (13 s in HCl and 5.4 s in NH_3) than for the PPy nanoparticles (17 s in HCl and 10 s in NH_3). To further evaluate the sensor sensitivity of UPNSs, the response amplitudes of the two PPy samples were measured as a function of vapor concentration from 20 to 100 ppm. Although the sensitivities, expressed in terms of the slope of the linear-fitted resistance ratio (absolute value), was as high as 0.24 (Fig. 7, d1) and 0.06 (Fig. 7, d2) in UPNSs with increasing HCl and NH_3 concentrations, PPy nanoparticles had lower response sensitivities of 0.03 (Fig. 7, d3) and 0.01 (Fig. 7, d4). Both PPy samples were more sensitive to HCl vapor than to NH_3 vapor, which agrees with previous studies [34–36]. The enhanced performance of the UPNSs as chemical sensors is comparable to sensors made from the PPy nanofibers [37,38]. However, in contrast to previous studies [9,34,35], the relatively low surface area of the UPNSs in the present study did not appear to degrade the enhanced sensitivity or delay the response time because the Brunauer–Emmett–Teller (BET) surface area of the UPNSs ($\approx$43.6 $m^2\ g^{-1}$) was much smaller than that of the PPy nanoparticles ($\approx$61.6 $m^2\ g^{-1}$). Based on the morphology of the UPNSs, the dimensions of the UPNSs ($\sim$21 nm thick, 2–6 μm wide, and tens of μm long) provided useful insight into the enhanced sensor performance. Although a single UPNS allowed gap-free contact between two interdigitated electrode fingers, several hundred PPy nanoparticles with diameters of 30–50 nm were required to form a conduction path between two electrode fingers. Although the increased surface area enabled increased adsorption of analyte vapors on the PPy nanoparticles, numerous particle boundaries of the PPy nanoparticles increased the resistance between electrodes by hampering the charge transport. On the other hand, the ultra-thin single PPy structure with no phase boundaries allowed the analyte vapors to readily diffuse into the UPNS and also facilitated charge transport between electrode fingers with no interparticle contact resistance, giving enhanced and fast responses.

4. Conclusion

Hydrated $C_{10}SO_3Na$ surfactant crystals with rectangular-shaped nanosheets were formed by decreasing the temperature of the micellar solution below the Krafft point. The hydrated $C_{10}SO_3Na$ crystals were used as a template for the fabrication of UPNSs by OCSP based on the electrostatic interaction between the negatively charged template surface and the cationic PPy chains oxidized by Fe (III) ions. This simple approach demonstrated that two-layered UPNSs (single layer thickness of $\sim$21 nm) were fabricated by localized polymerization on the top and bottom surfaces of the hydrated $C_{10}SO_3Na$ crystals. The fabricated UPNSs had a smooth surface composed of a single PPy structure with no PPy aggregates. The resulting UPNSs displayed enhanced electrical conductivity and longer effective conjugation lengths compared with the PPy nanoparticles. Moreover, although the surface area of the UPNSs was smaller than that of the PPy nanoparticles, the ultra-thin single structure led to enhanced sensitivity and faster response times for HCl and NH_3 vapor analysis. This ultra-thin conducting PPy should have useful applications in chemical sensors and electronic devices.

Acknowledgements

This work was supported by Basic Science Research Program through the National Research Foundation of Korea (NRF) grant funded from the Ministry of Education, Science and Technology (MEST) of Korea for the Center for Next Generation Dye-sensitized Solar Cells (No. 2010-0001842) and research fund of Hanyang Universitiy (HYU-2010-T).

References

[1] Gangopadhyay R, De A. Chem Mater 2000;12:608.
[2] Jang J. Adv Polym Sci 2006;199:189.
[3] Wallace GG, Moulten SE, Misoska VJ, Kane-Maguire LAP, Innis PC. Mater Forum 2002;26:29.
[4] Roduner E. Chem Soc Rev 2006;35:583.
[5] MacDiarmid AG. Synth Met 1997;84:27.
[6] Li D, Huang J, Kaner RB. Acc Chem Res 2009;42:135.
[7] Yoon H, Jang J. Adv Funct Mater 2009;19:1.
[8] Rajesh Ahuja T, Kumar D. Sens Actuator B Chem 2009;136:275.
[9] Tran HD, Li D, Kaner RB. Adv Mater 2009;21:1487.
[10] Martin CR. Chem Mater 1996;8:1739.
[11] Wu CG, Bein T. Science 1994;264:1757.
[12] Kim BJ, Oh SG, Han MG, Im SS. Langmuir 2000;16:5841.
[13] Jang J, Yoon H. Small 2005;1:1195.
[14] Han MG, Foulger SH. Small 2006;2:1164.
[15] Jang J, Yoon H. Chem Commun; 2003:720.
[16] Morrison ID, Ross S. Colloidal dispersions. New York: Wiley; 2002 [chapter 13].
[17] Wang Y, Chen W, Zhou D, Xue G. Macromol Chem Phys 2009;210:936.
[18] Wang Y, Yu C, Li Z, Zhou D, Chen W, Xue G. Colloid Polym Sci 2009;287:1325.
[19] Jeon SS, Park JK, Yoon CS, Im SS. Langmuir 2009;25:11420.
[20] Jeon SS, Yoon CS, Im SS. Polymer 2010;51:5400.
[21] Yao L, Shao L, Peng Z, Zhang L, Fei C, Lv F, et al. Liq Cryst 2007;34:761.
[22] He Y, Yuan J, Shi G. J Mater Chem 2005;15:859.
[23] Tartar HV, Wright KA. J Am Chem Soc 1939;61:539.
[24] Akune T, Abe M, Murata Y, Maki T, Moroi Y, Furuya H, et al. J Colloid Interface Sci 1996;181:136.
[25] Zhang L, Wan M, Wei Y. Macromol Rapid Commun 2006;27:366.
[26] Tian B, Zerbi G. J Chem Phys 1989;92:3886.
[27] Tian B, Zerbi G. J Chem Phys 1989;92:3892.
[28] Omastová M, Trchová M, Kovářová J, Stejskal J. Synth Met 2003;138:447.
[29] Liang W, Lei J, Martin CR. Synth Met 1992;52:227.
[30] Warren MR, Madden JD. Synth Met 2006;156:724.
[31] Geetha S, Trivedi DC. J Mater Sci 2005;16:329.
[32] Menon VP, Lei J, Martin CR. Chem Mater 1996;8:2382.
[33] Wynne KJ, Street GB. Macromolecules 1985;18:2361.
[34] Huang J, Virji S, Weiller BH, Kaner RB. J Am Chem Soc 2003;125:314.
[35] Virji S, Huang J, Kaner RB, Weiller BH. Nano Lett 2004;4:491.
[36] Jang J, Bae J. Sens Actuators B 2007;122:7.
[37] Tran HD, Shin K, Hong WG, D'arcy JM, Kojima RW, Weiller BH, et al. Macromol Rapid Commun 2007;28:2289.
[38] Chartuprayoon N, Hangarter CM, Rheem Y, Jung H, Myung NV. J Phys Chem C 2010;114:11103.

Polymer 52 (2011) 658–666

Contents lists available at ScienceDirect

Polymer

journal homepage: www.elsevier.com/locate/polymer

Amphiphilic chitosan graft copolymer via combination of ROP, ATRP and click chemistry: Synthesis, self-assembly, thermosensitivity, fluorescence, and controlled drug release

Weizhong Yuan [a,b,*], Xiaofei Li [a], Shuying Gu [a,b], Amin Cao [c], Jie Ren [a,b]

[a] Institute of Nano and Bio-polymeric Materials, School of Materials Science and Engineering, Tongji University, Shanghai 20092, People's Republic of China
[b] Key Laboratory of Advanced Civil Materials, Ministry of Education, Shanghai 200092, People's Republic of China
[c] Laboratory for Polymer Materials, Shanghai Institute of Organic Chemistry, Chinese Academy of Sciences, Shanghai 200032, People's Republic of China

ARTICLE INFO

Article history:
Received 12 October 2010
Received in revised form
17 November 2010
Accepted 21 December 2010
Available online 30 December 2010

Keywords:
Chitosan graft copolymers
Click chemistry
Self-assembly

ABSTRACT

Novel amphiphilic chitosan-*g*-poly(ϵ-caprolactone)-(*g*-poly(2-(2-methoxyethoxy)ethyl methacrylate)-*co*-oligo(ethylene glycol) methacrylate) (CS-*g*-PCL(-*g*-P(MEO_2MA-*co*-OEGMA))) copolymers with double side chains of PCL and P(MEO_2MA-*co*-OEGMA) were synthesized via combination of ring-opening polymerization (ROP), atom transfer radical polymerization (ATRP) and click chemistry. The molar ratio of PCL and P(MEO_2MA-*co*-OEGMA) was varied through variation of the feed ratio and the coupling efficiency of click chemistry is comparatively high. The graft copolymers can assemble into spherical micelles. The micelles show thermosensitive properties and the lower critical solution temperatures (LCSTs) were influenced by CS chains and the ratio of PCL and P(MEO_2MA-*co*-OEGMA) side chains. Moreover, the micelles can reversibly swell and shrink in response to the change of temperatures. Furthermore, the micelles present obvious fluorescence and the fluorescent intensity can be adjusted by altering the temperatures. The investigation of doxorubicin release from the micelles indicated that the release rate of the drug could be effectively controlled by altering the temperatures.

1. Introduction

Chitosan (CS) is a typical natural polyaminosaccharide with good biocompatibility, biodegradability, nontoxicity, and bioactivity [1–3]. Therefore, it has wide applications in biomedical field. The graft modification has been explored as a convenient method to overcome the insolubility of CS in common solvents and develop multifunctional CS copolymers [4–10]. A series of novel functional CS graft copolymers were synthesized by ring-opening polymerization (ROP) and atom transfer radical polymerization (ATRP) with grafting-from or grafting-onto approaches [11–16]. However, CS copolymers prepared with these approaches present some defects, such as low graft efficiency, complex preparing process, and synthetic difficulties of complex structure.

Click chemistry termed by Sharpless and coworkers has been introduced into the synthesis of novel polymeric materials [17–19]. Among these, the Cu(I)-catalyzed version of the Husigen 1,3-cycloaddition of azides and alkynes has been recently receiving attention as a facile, highly efficient, and stereoselective reaction coupled with excellent functional group compatibility [20–28]. These important features allow for the tailor-made synthesis of polymers with well-defined and complex chain structures and unique properties [22,29–45]. Matyjaszewski and Gao reported the synthesis of poly(2-hydroxyethyl methacrylate)-*graft*-poly(ethylene oxide) (PHEMA-*g*-PEO) molecular brush by grafting-onto method via combination of ATRP and click chemistry [46]. Emrick et al. reported the preparation of aliphatic polyesters with poly(ethylene glycol) and oligopeptide side chains via click chemistry [47]. Liu et al. reported the synthesis of well-defined amphiphilic copolymer brushes possessing alternating poly(methyl methacrylate) and poly(*N*-isopropylacrylamide) via combination of ATRP and click chemistry [48]. Wang et al. prepared amphiphilic centipede-like brush copolymers with poly(ε-caprolactone) (PCL) and poly(ethyl ethylene phosphate) side segments via combination of ROP and click chemistry by one-pot syntheses strategy. The polymer brush can self-assemble into stable aggregates [49]. Huang et al. reported the preparation of the amphiphilic graft copolymer with miktoarm star-shaped side chain by click chemistry [50]. To graft copolymers, the side chains with

* Corresponding author. Institute of Nano and Bio-polymeric Materials, School of Materials Science and Engineering, Tongji University, Shanghai 20092, People's Republic of China. Tel./fax: +86 21 65989238.
E-mail address: yuanwz@tongji.edu.cn (W. Yuan).

0032-3861/$ – see front matter © 2010 Elsevier Ltd. All rights reserved.
doi:10.1016/j.polymer.2010.12.052

well-defined and complex structure can be designed and prepared beforehand, and then these side chains were linked into the backbone to form expected copolymers by grafting-onto method via click chemistry. Up to now, only a few CS graft copolymers have been synthesized via click chemistry [51–54].

Thermosensitive polymers have attracted considerable interest for several biomedical applications such as smart bioactive surfaces, selective bioseparation, affinity control, or drug delivery. Among these polymers, the random copolymers of 2-(2-methoxyethoxy)ethyl methacrylate (MEO_2MA) and oligo(ethylene glycol) methacrylate (OEGMA) (P(MEO_2MA-*co*-OEGMA)) are more attractive for their wide and tunable lower critical solution temperature (LCST) between 26 °C and 90 °C depending on OEGMA content in water, which means that they can undertake a reversible change of swelling and collapse in water at temperature close to physiological ones [55–57]. Moreover, these poly(ethylene glycol)-based copolymers are expected to be hydrophilic, nontoxic, biocompatible, and non-immunogenic [57]. On the other hand, PCL has been extensively used for drug delivery system and biodegradable sutures because of its biodegradability, biocompatibility, and good drug permeability [58–60].

Pyrene compounds and pyrene-containing polymers are attracting interest due to their excellent fluorescence and long-lived excited state, and therefore have been used as the fluorescent probe, labeling chromophore, fluorescence-detecting materials, optoelectronic devices, and drug delivery vesicles [61–64].

In this work, amphiphilic CS graft copolymers with double side chains of PCL and P(MEO_2MA-*co*-OEGMA) were easily synthesized via combination of ROP, ATRP and click chemistry (Scheme 1). The ratio of PCL and P(MEO_2MA-*co*-OEGMA) was varied to alter the hydrophilic/hydrophobic balance. Self-assembly behavior and thermosensitive properties of CS graft copolymers in water were investigated. The terminal pyrene group of PCL endowed the CS copolymer with fluorescence and the fluorescent intensity was characterized. Finally, the controlled drug release behavior of CS graft copolymer micelles at buffer solution was investigated at different temperatures.

2. Experimental

2.1. Materials

CS (viscosity = 200 CP, degree of deacetylation = 80%) and 1-pyrenemethanol were purchased from Aldrich and dried *in vacuo* at 60 °C for 24 h before use. CL (Acros Organic, USA) was distilled under reduced pressure after being treated with CaH_2. Phthalic anhydride (PA), *N*,*N*′*N*′,*N*″,*N*″-pentamethyldiethylenetriamine (PMDETA, Acros Organic, USA), 1-(3-dimethylaminopropyl)-3-ethylcarbodiimide hydrochloride (EDC·HCl), hydroxybenzotriazole (HOBt), sodium azide (NaN_3, Alfa Aesar), succinic anhydride (Fluka, USA), propargyl alcohol (Alfa Aesar), 1-pyrenemethanol (Aldrich, USA), 2-bromoisobutyryl bromide (Aldrich, USA) and ethyl 2-bromoisobutyrate (Aldrich, USA) were used as received. MEO_2MA and OEGMA (M_n = 475) were purchased from Aldrich and passed through a column of activated basic alumina to remove inhibitors. Tin 2-ethylhexanoate ($SnO(ct)_2$, Aldrich, USA) was distilled under reduced pressure. CuCl, CuBr, and 2,2′-bipyridine (bpy) were recrystallized, dried under vacuum. Methylene chloride, chloroform, triethylamine, tetrahydrofuran (THF), *n*-hexane, and *N*,*N*-dimethylformamide (DMF) were dried over CaH_2.

2.2. Characterization

ATR FT-IR spectra of the samples were recorded on an AVATAR 360 ESP FT-IR spectrometer equipped with a single reflection ATR system. ^{1}H NMR spectra were obtained from a Bruker DMX 500 NMR spectrometer with $CDCl_3$ or DMSO-d_6 as the solvent. The chemical shifts were relative to tetramethylsilane. The molecular weight and molecular weight distribution were measured on a Viscotek TDA 302 gel permeation chromatography equipped with two columns (GMHHR-H, M Mixed Bed). THF was used as eluent at a flow rate of 1 mL/min at 30 °C. The morphology of copolymer micelles was observed with a JEOL JEM-2010 TEM at an accelerating voltage of 120 kV. The micelles solutions were prepared at room temperature or heated up to 42 °C rapidly. Then, a small drop from

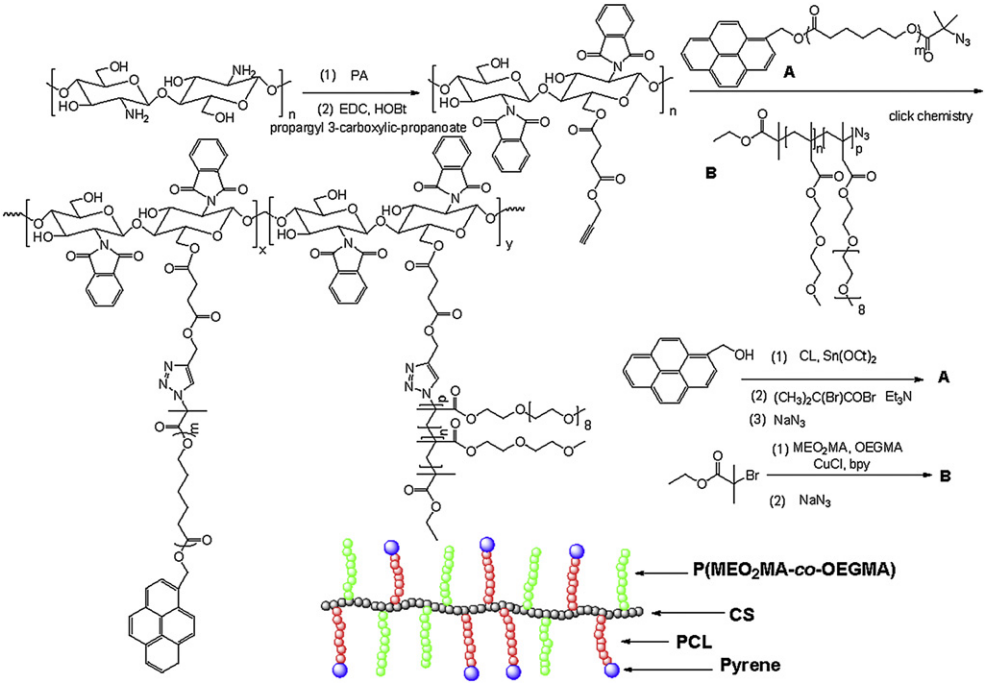

Scheme 1. Synthesis of CS-*g*-PCL(-*g*-P(MEO_2MA-*co*-OEGMA)) copolymer via combination of ROP, ATRP and click chemistry.

the aqueous copolymers solution was deposited onto carbon-coated copper TEM grid at room temperature. The excess of copolymer solution was wiped off with a filter paper, and the grid was dried under ambient atmosphere for 12 h. The transmittances of CS graft copolymers micelles aqueous solutions at various temperatures were measured at a wavelength of 500 nm on a UV–vis spectrophotometer. The LCST values of the copolymer micelles solutions were defined as the temperature producing a 50% decrease in transmittance. The hydrodynamic diameters (D_h) of the copolymers micelles were determined using a dynamic light scattering spectrophotometer (DLS). The fluorescence emission measurements were carried out using a fluorescence spectrophotometer (Perkin–Elmer). The copolymer micelles aqueous solutions (1 mg/mL) were poured into quartz cuvette. The emission spectra were recorded with an excitation wavelength at 320 nm.

2.3. Synthesis of alkynyl CS

CS was heated with excess phthalic anhydride (PA) (PA/GlcN unit = 3/1 mol/mol) in anhydrous DMF to give phthaloyl CS according to previously reported procedure [12]. Then, the dried phthaloyl CS (2 g, 7.04 mmol of GlcN units), propargyl 3-carboxylic-propanoate (prepared according to the literature [65], 6.614 g, 42.4 mmol), EDC·HCl (8.128 g, 42.4 mmol), and HOBt (3.175 g, 23.5 mmol) were dissolved in 150 mL of anhydrous DMF, and the reaction was performed at room temperature for 24 h under argon atmosphere. Then, the solution was poured into excess deionized water. After filtration, the obtained solid product was dissolved with DMF and precipitated with deionized water. The processes were repeated for three times. The purified solid product was dried in vacuum at 40 °C.

^{1}H NMR (DMSO-d_6, δ, ppm): 7.50–7.89 (aromatic protons), 4.70 (COOCH_2C≡CH), 2.74 (OOCCH_2CH_2COO), 2.55 (COOCH$_2$C≡CH), 2.56–5.43 (protons of CS chain).

2.4. Synthesis of pyrene–PCL–N_3

Pyrene–PCL–N_3 was synthesized by three steps. Firstly, pyrene–PCL–OH was synthesized by ROP of CL with 1-pyrenemethanol as initiator. A typical procedure was as follows. CL (15 g, 131.4 mmol), 1-pyrenemethanol (1.017 g, 4.38 mmol), and Sn(Oct)$_2$ (53 mg, 131.4 μmmol) were added into a fire-dried polymerization tube quickly. The tube was then connected to a Schlenk line, where exhausting-refilling processes were repeated for three times. The tube was put into an oil bath at 115 °C under argon atmosphere with stirring and cooled to room temperature after polymerization for 24 h the resulting product was dissolved in chloroform and precipitated twice in methanol. The purified polymer was dried in vacuum at room temperature. Secondly, the dried pyrene–PCL–OH (10 g, 3.125 mmol) was dissolved in anhydrous methylene chloride (100 mL) under stirring. To this solution was added triethylamine (1.265 g, 12.5 mmol) under argon atmosphere at room temperature. The mixture was stirred and cooled to 0 °C with ice bath. 2-Bromoisobutyryl bromide (2.874 g, 12.5 mmol) in anhydrous methylene chloride (30 mL) was added dropwise to the mixture within 40 min. The reaction mixture was stirred for 40 h at room temperature before it was washed with saturated $NaHCO_3$ aqueous solution and deionized water. The powder of pyrene–PCL–Br was obtained by filtration and dried in vacuum. Finally, pyrene–PCL–Br (6 g, 1.79 mmol), NaN_3 (4.655 g, 71.6 mmol), and DMF (150 mL) were added into a 250-mL round-bottom flask equipment with a magnetic stirrer, and the reaction was carried out at 45 °C for 48 h. After removing most of the solvents at reduced pressure, the remaining portion was diluted with methylene chloride and passed through a neutral alumina column to remove residual sodium salts, and then precipitated into an excess of cold *n*-hexane. The obtained product was then dried in vacuum.

Pyrene–PCL–OH: $M_{n,NMR}$ = 3200, $M_{n,GPC}$ = 3100, M_w/M_n = 1.21. ^{1}H NMR ($CDCl_3$, δ, ppm): 8.04–8.30 (protons of pyrene groups), 5.84 (CH_2OOC), 4.06 (OOCCH$_2$CH$_2$CH$_2$CH$_2$CH_2O), 3.64 (OOCCH$_2$CH$_2$CH$_2$CH$_2$CH$_2$CH_2OH), 2.30 (OOCCH_2CH$_2$CH$_2$CH$_2$CH$_2$O), 1.66 (OOCCH$_2$CH_2CH$_2$CH_2CH$_2$CH$_2$O), 1.39 (OOCCH$_2$CH$_2$CH_2CH$_2$CH$_2$O).

Pyrene–PCL–Br: $M_{n,NMR}$ = 3350, $M_{n,GPC}$ = 3200, M_w/M_n = 1.20. ^{1}H NMR ($CDCl_3$, δ, ppm): 8.02–8.30 (protons of pyrene groups), 5.84 (CH_2OOC), 4.06 (OOCCH$_2$CH$_2$CH$_2$CH$_2$CH_2O), 2.30 (OOCCH_2CH$_2$CH$_2$CH$_2$CH$_2$O), 1.92 (OOC(CH_3)$_2$Br), 1.66 (OOCCH$_2$CH_2CH$_2$CH_2CH$_2$CH$_2$O), 1.38 (OOCCH$_2$CH$_2$CH_2CH$_2$CH$_2$O).

Pyrene–PCL–N_3: $M_{n,NMR}$ = 3300, $M_{n,GPC}$ = 3200, M_w/M_n = 1.22. ^{1}H NMR ($CDCl_3$, δ, ppm): 8.02–8.30 (protons of pyrene groups), 5.84 (CH_2OOC), 4.06 (OOCCH$_2$CH$_2$CH$_2$CH$_2$CH_2O), 2.30 (OOCCH_2CH$_2$CH$_2$CH$_2$CH$_2$O), 1.66 (OOCCH$_2$CH_2CH$_2$CH_2CH$_2$CH$_2$O), 1.46 (OOC(CH_3)$_2$N$_3$), 1.38 (OOCCH$_2$CH$_2$CH_2CH$_2$CH$_2$O).

2.5. Synthesis of P(MEO$_2$MA-co-OEGMA)–N_3

P(MEO$_2$MA-*co*-OEGMA)–N_3 was prepared by two steps. Firstly, a dried Schlenk flask with a magnetic stirrer was charged with CuCl (115 mg, 1.155 mmol), bpy (361 mg, 2.31 mmol), ethyl 2-bromoisobutyrate (0.225 g, 1.155 mmol), MEO$_2$MA (10 g, 53.13 mmol), OEGMA (2.1945 g, 4.62 mmol), and ethanol (10 mL). The flask was degassed with three freeze-evacuate-thaw cycles. Then, the polymerization was performed at 60 °C for 3 h. After being cooled to room temperature, the reaction flask was open to air, and the crude product was diluted with ethanol and passed through a neutral alumina column to remove the copper catalysts. Then the filtered solution was purified by dialysis (molecular weight cut-off: 3000 Da) against water to remove unreacted MEO$_2$MA and OEGMA. Water was removed by azeotropic distillation with ethanol and the purified P(MEO$_2$MA-*co*-OEGMA)–Br was obtained. Secondly, P(MEO$_2$MA-*co*-OEGMA)–Br (5 g, 0.877 mmol), NaN_3 (2.282 g, 35.1 mmol), and DMF (60 mL) were added into a 100-mL round-bottom flask equipped with a magnetic stirrer, and the reaction was carried out at 45 °C for 48 h. After removing most of the solvents at reduced pressure, the remaining portion was diluted with THF and passed through a neutral alumina column to remove residual sodium salts, and then precipitated into an excess of cold *n*-hexane. The obtained product was then dried in vacuum.

P(MEO$_2$MA-*co*-OEGMA)–Br: $M_{n,GPC}$ = 5800, M_w/M_n = 1.26. ^{1}H NMR ($CDCl_3$, δ, ppm): 4.01–4.20 (COOCH_2CH$_2$O), 3.48–3.80 (OCH_2CH_2O), 3.34–3.45 (OCH$_2$CH$_2$OCH_3), 1.69–2.09 (CH_2C(CH$_3$)), 0.74–1.16 (CH$_2$C(CH_3)).

P(MEO$_2$MA-*co*-OEGMA)–N_3: $M_{n,GPC}$ = 5700, M_w/M_n = 1.28. ATR FT-IR (cm^{-1}): 3023, 2882 (ν_{C-H}), 2120 ($\nu_{azide\ group}$), 1724 ($\nu_{C=O}$).

2.6. Synthesis of amphiphilic CS graft copolymer with double side chains of PCL and P(MEO$_2$MA-co-OEGMA) (CS-g-PCL(-g-P(MEO$_2$MA-co-OEGMA))

Amphiphilic CS graft copolymers were prepared via click chemistry. A typical procedure was as follows. Alkynyl CS (94 mg, containing 0.1 mmol of alkynyl groups), pyrene–PCL–N_3 (0.99 g, 0.3 mmol), and P(MEO$_2$MA-*co*-OEGMA)–N_3 (0.57 g, 0.1 mmol) were dissolved in DMF (50 mL). Then CuBr (57 mg, 0.4 mmol) and PMDETA (84 μL, 0.4 mmol) were added into the above solution. After degassed via three freeze-evacuate-thaw cycles, the reaction was carried out at 65 °C for 48 h. The resulting copolymer was obtained by dialysis against THF to remove unreacted pyrene–PCL–N_3 and P(MEO$_2$MA-

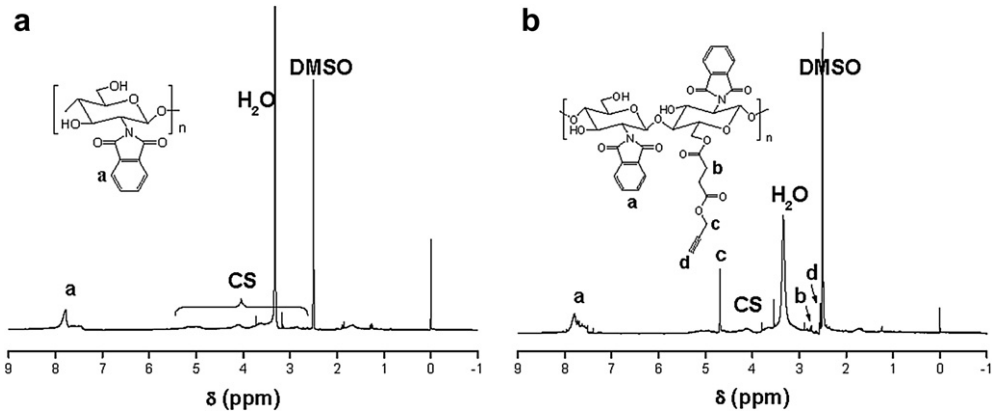

Fig. 1. ^{1}H NMR spectrum of alkynyl CS.

co-OEGMA)–N_3. The resulting product was obtained by precipitated from *n*-hexane.

^{1}H NMR (DMSO-d_6, δ, ppm): 8.10–8.36 (protons of pyrene groups), 7.95 (proton in 1,2,3-triazole group), 7.74–7.88 (aromatic protons), 5.83 (CH_2OOC), 5.08 ($COOCH_2C(N)=C(N)$), 3.88–4.21 ($OOCCH_2CH_2CH_2CH_2CH_2O$ and $COOCH_2CH_2O$), 3.42–3.75 (OCH_2-CH_2O), 3.10–3.35 ($OCH_2CH_2OCH_3$), 2.26 ($OOCCH_2CH_2CH_2CH_2CH_2O$), 1.61–2.04 ($CH_2C(CH_3)$), 1.53 ($OOCCH_2CH_2CH_2CH_2CH_2O$), 1.29 ($OOCCH_2CH_2CH_2CH_2CH_2O$), 0.60–1.07 ($CH_2C(CH_3)$).

2.7. Preparation of self-assembled micelles of CS graft copolymers

Samples for transmittance, TEM, DLS, and fluorescence were prepared as follows. CS graft copolymer (50 mg) was dissolved in DMF (10 mL) and subsequently dialyzed against distilled water for 72 h (molecular weight cut-off: 14000 Da). During the dialysis process, CS graft copolymers self-assembled into micelles with CS and PCL core and P(MEO_2MA-*co*-OEGMA) corona. For different measurements, the micelles solutions can be diluted to different concentrations by distilled water and equilibrated at 25 °C for 48 h. The micelles solutions had a concentration of 2 mg/mL for transmittance measurement and 1 mg/mL for TEM, DLS, and fluorescence measurements.

2.8. Controlled drug release behavior of CS-g-PCL(-g-P(MEO_2MA-co-OEGMA)) micelles

Doxorubicin hydrochloride (2 mg) was stirred with triethylamine (1 mL) in DMF (3 mL) overnight to obtain the doxorubicin. Then CS-*g*-PCL(-*g*-P(MEO_2MA-*co*-OEGMA)) copolymer (Sample 2,

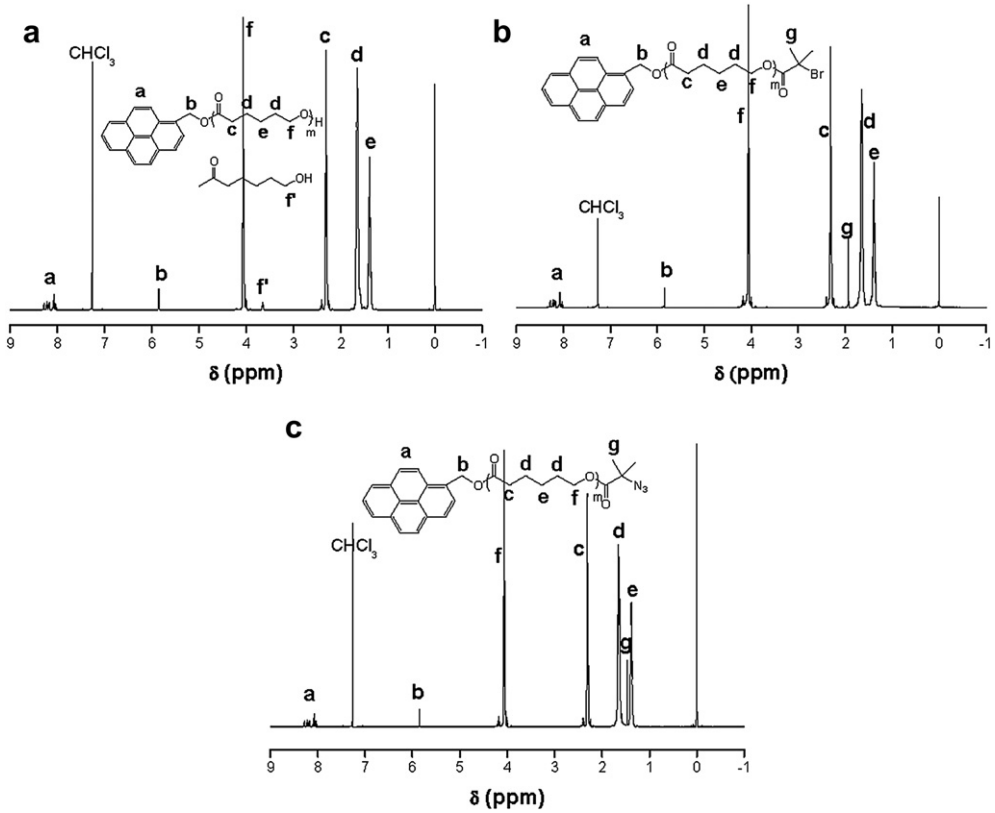

Fig. 2. ^{1}H NMR spectra of (a) pyrne–PCL–OH, (b) pyrene–PCL–Br, and (c) pyrene–PCL–N_3.

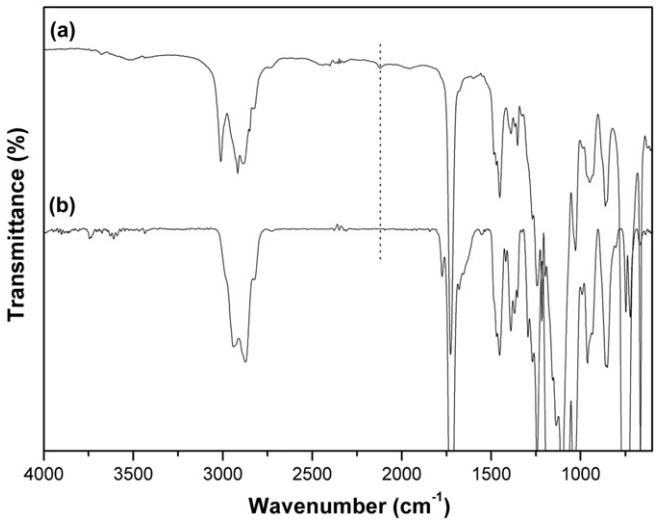

Fig. 3. ATR FT-IR spectra of (a) P(MEO_2MA-*co*-OEGMA)–N_3 and (b) CS-*g*-PCL(-*g*-P(MEO_2MA-*co*-OEGMA)).

40 mg) was dissolved in the solution. The solution was put into a dialysis membrane (molecular weight cut-off: 14000 Da) and dialyzed against distilled water (1000 mL) at 25 °C for 24 h. The UV absorbance of the dialysis solution was used to determine the amount of unloaded doxorubicin, which was used further to calculate the encapsulation efficiency (EE%). The total amount of doxorubicin fed initially in PBS solution was 2 mg. The EE% is defined as:

$$\mathrm{EE\%} = \frac{(\text{total amount of Dox}) - (\text{unloaded amount of Dox})}{\text{total amount of Dox}} \times 100\%$$

The EE% was found to be 52%.

For investigation of the drug release, the resulting drug-loaded micelles were added into 7 mL of PBS solution. These suspensions were transferred into dialysis membrane (molecular weight cut-off: 14000 Da), which were then immersed into 10 mL of PBS 7.4 solution at 25 °C and 43 °C, respectively. At predetermined time intervals, 10 mL of each dialysis medium was removed for measurement and the same amount of fresh PBS solution was added. The concentration of drug was determined by UV–vis spectroscopy at 497 nm. The amount of drug released from copolymer micelles was determined by measuring the difference in concentration of the PBS solution before and after incubating with the drug-loaded micelles. Each sample was measured for three times and the data were given as the average values based on three independent measurements.

3. Results and discussion

3.1. Preparation of CS-g-PCL(-g-P(MEO_2MA-co-OEGMA))

Amphiphilic CS graft copolymers with double side chains of PCL and P(MEO_2MA-*co*-OEGMA) prepared via combination of ROP, ATRP and click chemistry. In order to adjust the hydrophilic/hydrophobic balance of CS graft copolymers, the feed ratio of PCL and P(MEO_2MA-*co*-OEGMA) was varied (mol%/mol%: 0/100, 25/75, 50/50, and 75/25).

CS can be easily converted to phthaloyl CS by the phthaloylation of amino groups of CS and the ^{1}H NMR spectrum of phthaloyl CS was shown in Fig. 1a. Introduction of phthaloyl groups can reduce the inter- or intra-molecular hydrogen bonds, which results in the solubility of CS in organic solvents such as DMSO and DMF. Thus, this will facilitate the hydroxyl groups of CS to react with propargyl 3-carboxylic-propanoate by the EDC reaction under homogeneous conditions. The chemical structure of alkynyl CS was confirmed by ^{1}H NMR spectrum (Fig. 1b). The signal at 7.50–7.89 ppm (a) should be attributed to protons of phthaloyl groups. The signals at 2.72 ppm (b), 4.70 ppm (c), and 2.55 ppm (d) can be ascribed to methylene protons next to carbonyl, methylene protons and alkynyl protons of the terminal propargyl group, respectively. The content of alkynyl groups of CS calculated from the integral ratio of peaks c to peak a is 0.36 (36 alkynyl groups per 100 GlcN units).

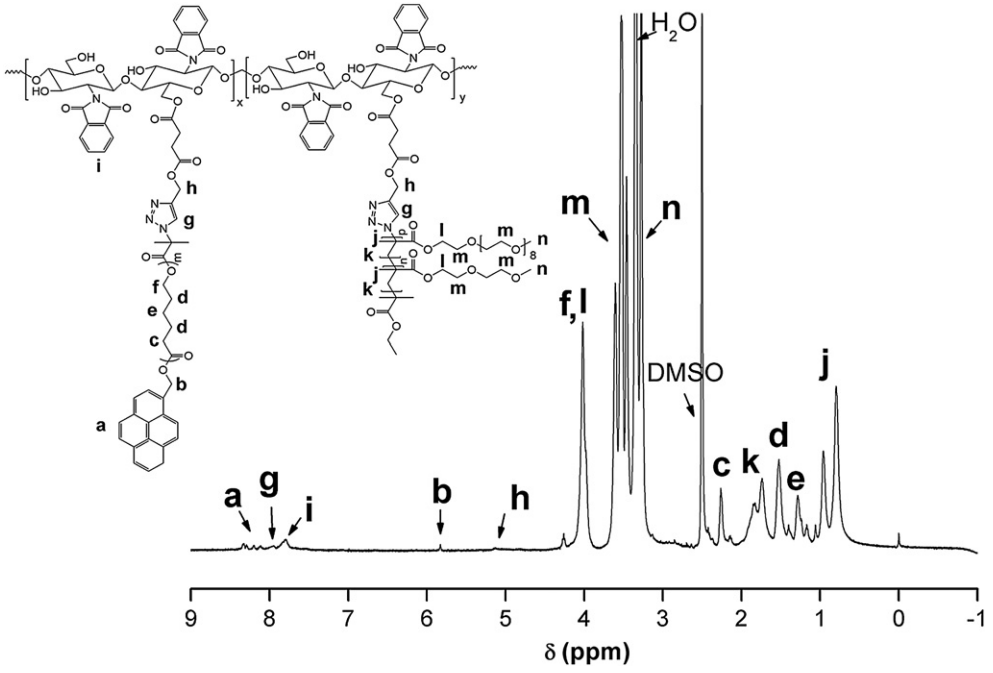

Fig. 4. ^{1}H NMR spectrum of CS-*g*-PCL(-*g*-P(MEO_2MA-*co*-OEGMA)) (sample 4).

Pyrene–PCL–N_3 was prepared by three steps. Pyrene–PCL–OH was synthesized by ROP of CL with 1-pyrenemethanol used as initiator. ^{1}H NMR spectrum of pyrene–PCL–OH is shown in Fig. 2a. The major resonance signals (c–f) are attributed to PCL chains. The signals at 8.04–8.30 ppm (a) and 5.84 ppm (b) should be ascribed to protons of pyrene groups and methylene next to pyrene groups. The signal at 3.64 ppm (f′) can be attributed to the methylene protons next to terminal hydroxyl groups of pyrene–PCL–OH. The molecular weight of pyrene–PCL–OH determined with ^{1}H NMR can be calculated by the integral ratio of peaks f to peak f′. Pyrene–PCL–Br was obtained by the reaction of pyrene–PCL–OH with excess 2-bromoisobutyryl bromide. ^{1}H NMR is shown in Fig. 2b. The signal at 3.64 ppm disappeared completely, while novel signal corresponding to the methyl protons next to the terminal bromine at 1.92 ppm (g) appeared. Pyrene–PCL–N_3 was obtained by the reaction of pyrene–PCL–Br with NaN_3. The nucleophilic substitution reaction of the terminal bromine groups with excess NaN_3 in DMF was very rapid. The chemical structure of pyrene-PCL–N_3 was confirmed by ^{1}H NMR spectrum (Fig. 2c). The signal at 1.92 ppm disappeared completely, and the signal at 1.46 ppm (g) appeared, which confirmed all the terminal bromine groups have been transformed to azide groups.

P(MEO_2MA-*co*-OEGMA)–N_3 was prepared by two steps. P(MEO_2MA-*co*-OEGMA)–Br was synthesized by ATRP of MEO_2MA and OEGMA with ethyl 2-bromoisobutyrate used as initiator. The feed molar ratio of MEO_2MA and OEGMA is 92%:8% (mol%:mol%), because the LCST value of linear P(MEO_2MA-*co*-OEGMA) is about 37 °C (close to physiological temperature) when the content of OEGMA in copolymer is 8% [55]. The chemical structure of was confirmed by ^{1}H NMR spectrum (see Supplementary material, Fig. S1). The corresponding protons signals of P(MEO_2MA-*co*-OEGMA) can be detected. The virtual molar ratio of MEO_2MA and OEGMA units in P(MEO_2MA-*co*-OEGMA)–Br calculated from the integral ratio of peaks c to peak d is 92.5%:7.5% (mol%/mol%). P(MEO_2MA-*co*-OEGMA)–N_3 was obtained by the reaction of P(MEO_2MA-*co*-OEGMA)–Br with NaN_3. In this study, an excess of NaN_3 was used to ensure the complete transformation of terminal bromine groups to azide groups. The azide groups in P(MEO_2MA-*co*-OEGMA)–N_3 cannot be characterized with ^{1}H NMR spectrum, therefore, ATR FT-IR spectrum was used to confirm the presence of azide groups. As shown in Fig. 3a peak at 2120 cm^{-1} can be observed. It is the characteristic peak of azide absorbance peak in P(MEO_2MA-*co*-OEGMA)–N_3.

The synthesis of amphiphilic CS graft copolymers with double side chains, CS-*g*-PCL(-*g*-P(MEO_2MA-*co*-OEGMA)), were accomplished via the click reaction between pyrene–PCL–N_3, P(MEO_2MA-*co*-OEGMA)–N_3 and alkynyl CS. After click reaction, the absorbance peak of azide group disappeared (as shown in Fig. 3b). A typical ^{1}H NMR spectrum is shown in Fig. 4. The characteristic signals of CS, PCL and P(MEO_2MA-*co*-OEGMA) were observed clearly. In comparison with that of alkynyl CS, the signals at 4.70 ppm and 2.55 ppm disappeared and a new peak at 5.08 ppm (h) that was assigned to methylene protons next to 1,2,3-triazole groups can be observed. Moreover, a new peak at 7.95 ppm (g) should be attributed to methine proton in 1,2,3-triazole groups. The actual ratio of PCL and P(MEO_2MA-*co*-OEGMA) can be calculated by the integral ratio of methylene protons (c) in PCL and methylene protons (k) in P(MEO_2MA-*co*-OEGMA). The coupling efficiency of click chemistry can be calculated by the integral ratio of the protons of phthaloyl groups (i) and peak c or peak k, and the results were listed in Table 1. As shown in Table 1, the actual ratio of PCL side chains is lower than the feed ratio, which should be ascribed to the presence of large pyrene groups hindering the click reaction of pyrene–PCL–N_3 and alkynyl CS. The coupling efficiency of copolymers is above 80%, indicating the high efficiency of click chemistry.

Table 1
Synthesis of CS-*g*-PCL(-*g*-P(MEO_2MA-*co*-OEGMA)) copolymers via click chemistry.

Sample	PCL/P(MEO_2MA-*co*-OEGMA) (mol%/mol%)		Coupling efficiency[a] (%)
	Feed ratio	Actual ratio[a]	
1	0/100	0/100	85.7
2	25/75	8/82	84.3
3	50/50	22/78	81.9
4	75/25	38/62	81.6

[a] The actual ratio and coupling efficiency of click chemistry were determined by ^{1}H NMR spectroscopy.

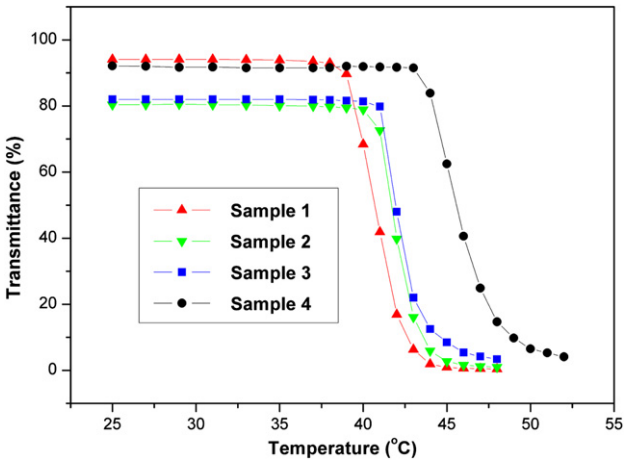

Fig. 5. Transmittance curves of CS-*g*-P(MEO_2MA-*co*-OEGMA) (Sample 1) and CS-*g*-PCL(-*g*-P(MEO_2MA-*co*-OEGMA)) (sample 2–4) micelles solutions (concentration: 2 mg/mL).

3.2. *Self-assembly behavior and thermosensitive properties of CS-g-PCL(-g-P(MEO_2MA-co-OEGMA))*

As an amphiphilic graft copolymer, CS-*g*-PCL(-*g*-P(MEO_2MA-*co*-OEGMA)) can self-assemble into micelles. The hydrophilic P(MEO_2MA-*co*-OEGMA) side chains are mainly in the corona of the micelles, whereas the hydrophobic backbones of CS and PCL side chains are mainly in the core of the micelles. Fig. 5 shows the transmittance curves of CS-*g*-P(MEO_2MA-*co*-OEGMA) (sample 1)

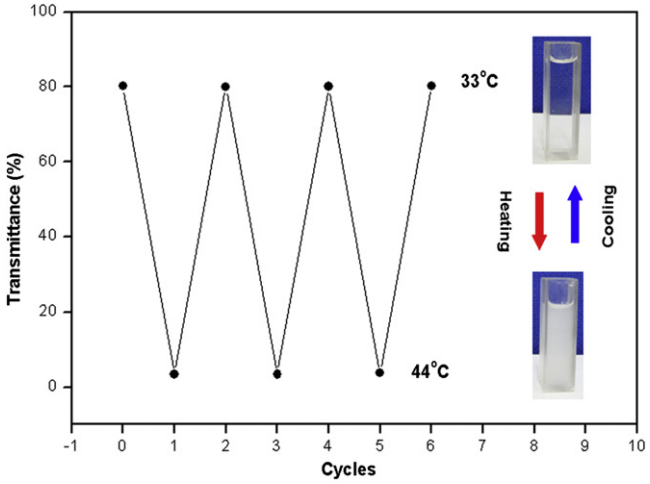

Fig. 6. Plots of transmittance as a function of temperature for CS-*g*-P(MEO_2MA-*co*-OEGMA) copolymer micelle solution (sample 2) (concentration: 2 mg/mL).

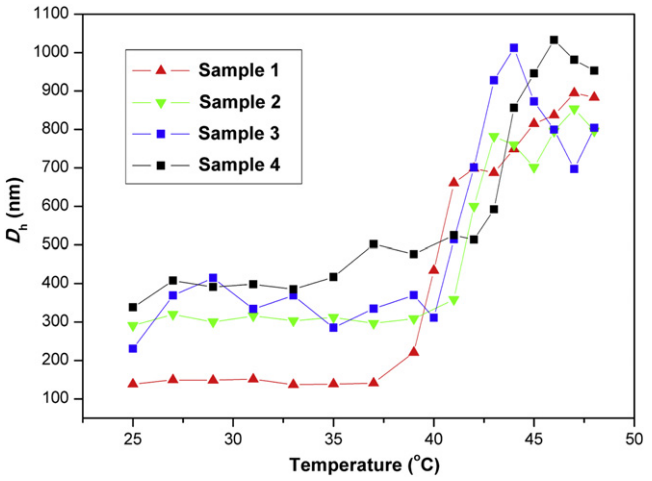

Fig. 7. Temperature dependence of hydrodynamic diameters (D_h) for CS-*g*-P(MEO_2MA-*co*-OEGMA) copolymers micelles (sample 1) and CS-*g*-PCL(-*g*-P(MEO_2MA-*co*-OEGMA)) (sample 2–4) micelles solutions (concentration: 1 mg/mL).

and CS-*g*-PCL(-*g*-P(MEO_2MA-*co*-OEGMA)) (sample 2–4) micelles solutions. It can be seen that the transmittance curves show sharp transition during heating process. The LSCT of sample 1 is 40.7 °C and higher than that of corresponding pure P(MEO_2MA-*co*-OEGMA), which indicates that CS backbones probably influence the phase transition. Moreover, the LCST values of sample 2, sample 3, and sample 4 are 41.9 °C, 42.3 °C, and 45.8 °C respectively. Obviously, the presence of PCL side chains can enhance the temperatures of the phase transition and the LSCT values increase with the increase of PCL content in graft copolymers. As shown in Fig. 6, reversible transformation of transparency and turbidity occurred in CS-*g*-PCL (-*g*-P(MEO_2MA-*co*-OEGMA)) (sample 2) micelles solution during the reversible cooling and heating cycles. Obviously, the phase transition of the micelles is reversible, indicated that the CS copolymer micelles solution can undertake a reversible change of swelling and collapse. Fig. 7 shows the plots of the hydrodynamic diameters (D_h) of sample 1–4 in water as a function of temperature. In the lower temperature ranges, the D_h values are relatively small and change slightly. For example, the D_h of sample 1 is about 138 nm at 25 °C. The D_h values of sample 2–4 are larger than that of sample 1, because the presence of PCL segments in copolymers increases the hydrophobicity of copolymer, which will result in the formation of micelles with larger sizes. In contrast, the values increase drastically in the higher temperature ranges. At low temperatures, P(MEO_2MA-*co*-OEGMA) side chains of CS-*g*-P(MEO_2MA-*co*-OEGMA) (sample 1) or CS-*g*-PCL (-*g*-P(MEO_2MA-*co*-OEGMA)) (sample 2–4) copolymers exist in random coil conformation owing to the hydrogen-bonding interaction between P(MEO_2MA-*co*-OEGMA) chains and the water molecules. When the temperature increases above the LCST, polymers chains shrink into a globular structure because the hydrogen bonds between ether oxygen of P(MEO_2MA-*co*-OEGMA) and water are broken, and P(MEO_2MA-*co*-OEGMA) chains collapse and become hydrophobic. Namely, at elevated temperatures, P(MEO_2MA-*co*-OEGMA) segments within micelles are getting insoluble, and this

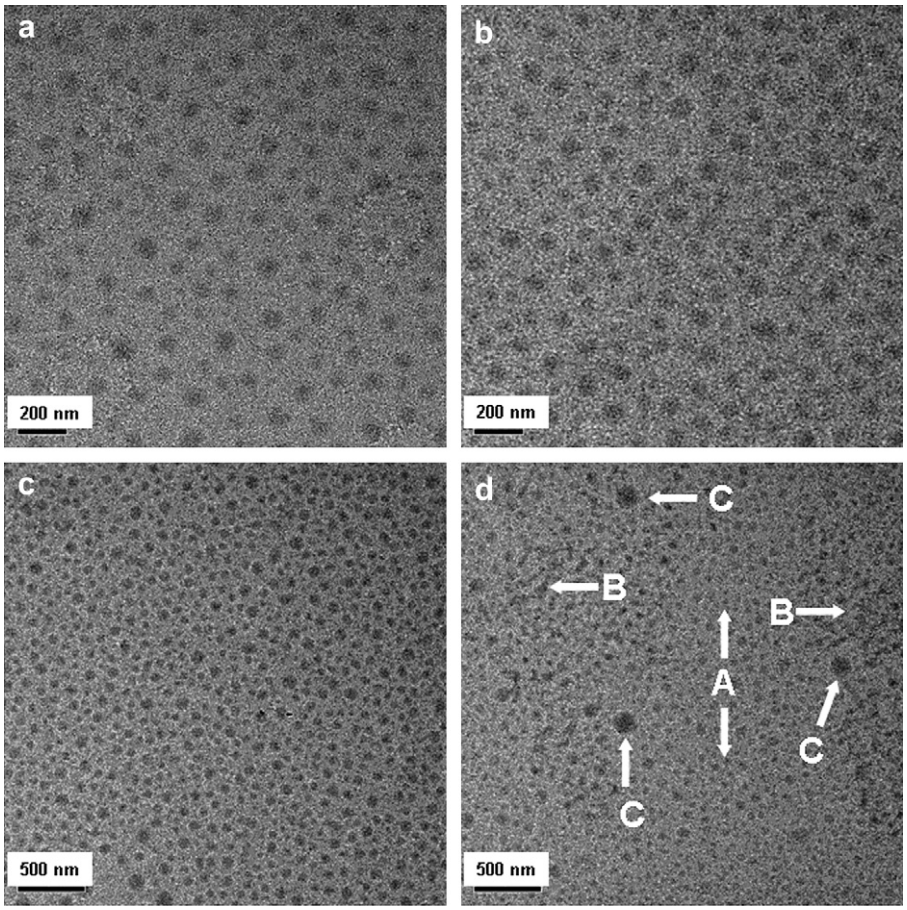

Fig. 8. TEM images of (a) CS-*g*-P(MEO_2MA-*co*-OEGMA) micelles (sample 1) and (b–c) CS-*g*-PCL(-*g*-P(MEO_2MA-*co*-OEGMA)) micelles (sample 2) at 25 °C, and (d) micelles of sample 2 at 42 °C (concentration: 1 mg/mL).

breaks the hydrophilic/hydrophobic balances of originally formed micelles at lower temperatures. Therefore, the intermolecular hydrophobic attractions are thermodynamically favored and micelles aggregate occur, which results in the increase of the D_h and visible turbidity. TEM images of micelles of CS graft copolymers were shown in Fig. 8. The actual morphologies of these micelles can be observed. As shown in Fig. 8a and b, the diameter of spherical nanoparticles of sample 2 (about 90 nm) is slightly larger than that of sample 1 (about 75 nm) at 25 °C, which is in accordance to the trend of results of DLS. It is noteworthy that the size of the micelles determined by DLS is large than that observed by TEM, which is attributed to the micelles dehydration caused by solvent evaporation and therefore the collapse and shrinkage of micelles in TEM experiment. Compared to the micelles of sample 2 (Fig. 8c) at 25 °C, the micelles shows different morphology at 42 °C (Fig. 8d). In A zone, the size of micelles is obviously smaller than that in Fig. 8c, which should be attributed to the collapse of corona of micelles at higher temperature. However, the shrunk micelles tend to aggregate into larger nanoparticles. B zone shows the process of aggregation of micelles clearly. Then, spherical nanoparticles with larger sizes formed as shown in C.

3.3. Fluorescence of the micelles of CS-g-PCL(-g-P(MEO$_2$MA-co-OEGMA))

In order to investigate the effect of structural variation of the micelles on their fluorescence properties, the fluorescence of micelles was measured at under and above the LCST of micelles aqueous solution. The maximum-excitation wavelength of pyrene was 320 nm according to the measurement of UV–vis spectroscopy. Fig. 9 shows the fluorescence spectra of CS-*g*-PCL(-*g*-P(MEO$_2$MA-*co*-OEGMA)) (Sample 4) micelles aqueous solution measured at 25 °C and 46 °C. Two strong emissions appeared at 382 and 400 nm. However, the fluorescent intensity decreased to some extent with the increase of temperature from 25 °C to 46 °C. Namely, the fluorescence of copolymer micelles can be detected above or under the LCST of micelles solution and the fluorescent intensity can be adjusted by altering the temperatures of micelles solutions. On the other hand, the transmission behavior of micelles can be detected by the alteration of fluorescent intensity. Above the LSCT, micelles solutions turn turbidity, and the scattering effect of turbidity of micelles solution decreased the fluorescent intensity. Moreover, above the LCST, P(MEO$_2$MA-*co*-OEGMA) chains present

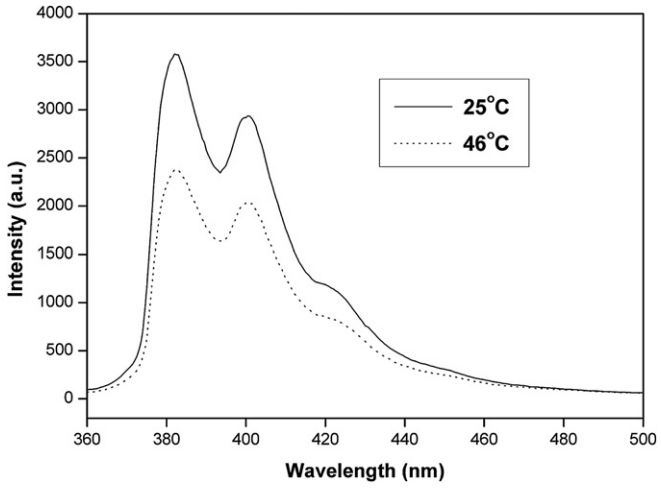

Fig. 9. Fluorescence spectra of CS-*g*-PCL(-*g*-P(MEO$_2$MA-*co*-OEGMA)) micelles (sample 4) at 25 °C and 46 °C, respectively (concentration: 1 mg/mL).

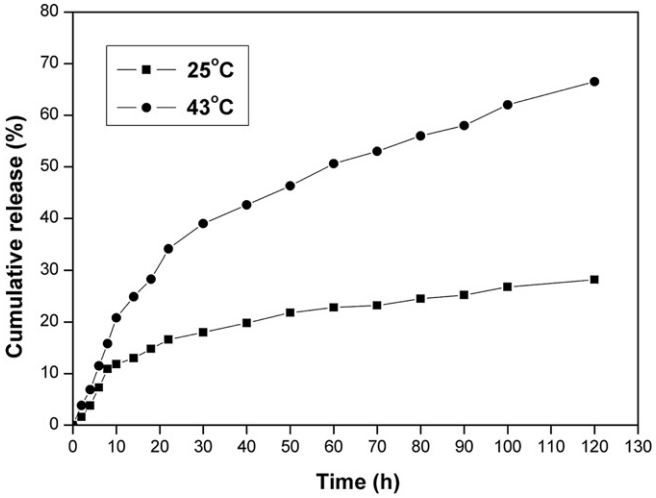

Fig. 10. Drug release of CS-*g*-PCL(-*g*-P(MEO$_2$MA-*co*-OEGMA)) micelles (sample 2) in PBS at 25 °C and 43 °C, respectively.

shrinking conformation and the terminal pyrene groups on PCL tend to aggregation. The aggregation of pyrene groups and the heating process of solution lead to the high local concentration of pyrene and enhance the collision probability between pyrene molecules and pyrene may form dimmer, which leads to the decrease of fluorescent intensity.

3.4. Controlled drug release behavior of CS-g-PCL(-g-P(MEO$_2$MA-co-OEGMA)) micelles

Considering the thermosensitivity of CS graft copolymer micelles, the micelles could be expected to become an intelligent carrier in controlled drug release system. Doxorubicin is a kind of hydrophobic antitumor agent and used as a model drug to investigate the controlled properties of the micelles. The drug release from thermosensitive micelles was investigated in PBS pH 7.4 and the data were shown in Fig. 10. The drug release profile from micelles shows greater changes with the temperature alterations around the LCST. Under the LCST (25 °C), the highly hydrated P(MEO$_2$MA-*co*-OEGMA) segments can stabilize the hydrophobic/hydrophilic core-shell structure of micelles, allowing small amount of drug diffused out. Therefore, the drug release rate is slow and about 72% drug still remains in the core of the micelles after 120 h. However, when the temperature increased above the LCST (43 °C), the drug release is accelerated due to the temperature-induced structural changes of the micelles. The P(MEO$_2$MA-*co*-OEGMA) shell becomes hydrophobic and the micellar core-shell structure is deformed. As a result, the hydrophobic drug incorporated in core diffused out quickly and about 67% drug is released from the micelles. The investigation of model drug doxorubicin release from CS copolymer micelles indicated that the release rate of the drug could be effectively controlled by altering the temperatures.

4. Conclusions

Amphiphilic CS-*g*-PCL(-*g*-P(MEO$_2$MA-*co*-OEGMA)) copolymers with double side chains of PCL and P(MEO$_2$MA-*co*-OEGMA) were successfully prepared via combination of ROP, ATRP and click chemistry. The coupling efficiency of click chemistry is comparatively high and the graft ratio of PCL and P(MEO$_2$MA-*co*-OEGMA) can be adjusted via alteration of the feed ratio of pyrene–PCL–N_3 and P(MEO$_2$MA-*co*-OEGMA)–N_3 due to the unique properties of click chemistry. CS graft copolymers can assemble into micelles in

water. The self-assembly behavior and thermosensitive properties of CS graft copolymers micelles were investigated by TEM, DLS, and transmittance. Investigations show that the LCST values of CS graft copolymers micelles solutions were effected by the CS chains and ratio of PCL and P(MEO_2MA-*co*-OEGMA) segments. Furthermore, the micelles can reversibly swell and shrink in response to the change of temperatures. Fluorescent intensity of the micelles can be adjusted by altering the temperatures of micelles solutions. The investigation of model drug doxorubicin release from the micelles indicated that the release rate of the drug could be effectively controlled by altering the temperatures.

Acknowledgments

The authors gratefully acknowledge the financial support of the National Natural Science Foundation of China (no. 20804029).

Supplementary material

Supplementary material associated with this article can be found in online version at doi:10.1016/j.polymer.2010.12.052.

References

[1] Lee KY, Mooney D. J Chem Rev 2001;101(7):1869–80.
[2] Ravi Kumar MNV, Muzzarelli RAA, Muzzarelli C, Sashiwa H, Domb A. J Chem Rev 2004;104(12):6017–84.
[3] Rana D, Matsuura T. Chem Rev 2010;110(4):2448–71.
[4] Jenkins DW, Hudson SM. Chem Rev 2001;101(11):3245–74.
[5] Marie E, Landfester K, Antonietti M. Biomacromolecules 2002;3(3):475–81.
[6] Qian F, Cui FY, Ding JY, Tang C, Yin CH. Biomacromolecules 2006;7(10):2722–7.
[7] Recillas M, Silva LL, Peniche C, Goycoolea FM, Rinaudo M, Argüelles-Monal WM. Biomacromolecules 2009;10(6):1633–41.
[8] Millotti G, Samberger C, Fröhlich E, Bernkop-Schnürch A. Biomacromolecules 2009;10(11):3023–7.
[9] Li N, Bai RB, Liu CK. Langmuir 2005;21(25):11780–7.
[10] Chang KL, Higuchi Y, Kawakami S, Yamashita F, Hashida M. Bioconjug Chem 2010;21(6):1087–95.
[11] Feng H, Dong CM. Biomacromolecules 2006;7(11):3069–75.
[12] Feng H, Dong CM. Carbohydr Polym 2007;70:258–64.
[13] Feng H, Dong CM. J Polym Sci Part A Polym Chem 2006;44(18):5353–61.
[14] Liu L, Chen LX, Fang YE. Macromol Rapid Commun 2006;27:1988–94.
[15] Yu HJ, Chen XS, Lu TC, Sun J, Tian HY, Hu J, et al. Biomacromolecules 2007;8(5):1425–35.
[16] Munro NH, Hanton LR, Moratti SC, Robinson BH. Carbohydr Polym 2009;77(3):496–505.
[17] Rostovtsev VV, Green LG, Fokin VV, Sharpless KB. Angew Chem Int Ed 2002;41:2596–9.
[18] Kolb HC, Finn MG, Sharpless KB. Angew Chem Int Ed 2001;40:2004–21.
[19] Wu P, Feldman AK, Nugent AK, Hawker CJ, Scheel A, Voit B, et al. Angew Chem Int Ed 2004;43:3928–32.
[20] Malkoch M, Schleicher K, Drockenmuller E, Hawker CJ, Russell TP, Wu P, et al. Macromolecules 2005;38(9):3663–78.
[21] Wang Q, Chan TR, Hilgraf R, Fokin VV, Sharpless KB, Finn MG. J Am Chem Soc 2003;125(11):3192–3.
[22] Helms B, Mynar JL, Hawker CJ, Frechet JMJ. J Am Chem Soc 2004;126(46):15020–1.
[23] Sumerlin BS, Tsarevsky NV, Louche G, Lee RY, Matyjaszewski K. Macromolecules 2005;38(18):7540–5.
[24] Lee LV, Mitchell ML, Huang SJ, Fokin VV, Sharpless KB, Wong CH. J Am Chem Soc 2003;125(32):9588–9.
[25] Manetsch R, Krasinski A, Radic Z, Raushel J, Taylor P, Sharpless KB, et al. J Am Chem Soc 2004;126(40):12809–18.
[26] Krasinski A, Radic Z, Manetsch R, Raushel J, Taylor P, Sharpless KB, et al. J Am Chem Soc 2005;127(18):6686–92.
[27] Lin PC, Ueng SH, Yu SH, Jan MD, Adak AK, Yu CC, et al. Org Lett 2007;9(11):2131–4.
[28] Zhang Y, Luo SZ, Tang YJ, Yu L, Hou KY, Cheng JP, et al. Anal Chem 2006;78(7):2001–8.
[29] Vora A, Singh K, Webster DC. Polymer 2009;50(13):2768–74.
[30] Riva R, Lussis P, Lenoir S, Jérôme C, Jérôme R, Lecomte P. Polymer 2008;49(8):2023–8.
[31] Hua C, Peng SM, Dong CM. Macromolecules 2008;41(18):6686–95.
[32] Hua C, Dong CM, Wei Y. Biomacromolecules 2009;10(5):1140–8.
[33] Riva R, Schmeits S, Jérôme C, Jérôme R, Lecomte P. Macromolecules 2007;40(4):796–803.
[34] Zhu J, Zhu XL, Kang ET, Neoh KG. Polymer 2007;48(24):6992–9.
[35] Urbani CN, Bell CA, Lonsdale D, Whittaker MR, Monteiro MJ. Macromolecules 2008;41(1):76–86.
[36] Urbani CN, Bell CA, Lonsdale DE, Whittaker MR, Monteiro MJ. Macromolecules 2007;40(19):7056–9.
[37] Lonsdale DE, Bell CA, Monteiro MJ. Macromolecules 2010;43(7):3331–9.
[38] Urbani CN, Bell CA, Whittaker MR, Monteiro MJ. Macromolecules 2008;41(4):1057–60.
[39] Zhang JY, Zhou YM, Zhu ZY, Ge ZS, Liu SY. Macromolecules 2008;41(4):1444–54.
[40] Xue XQ, Zhu J, Zhang ZB, Cheng ZP, Tu YF, Zhu XL. Polymer 2010;51(14):3083–90.
[41] Xu J, Ye J, Liu SY. Macromolecules 2007;40(25):9103–10.
[42] Yang LP, Dong XH, Pan CY. J Polym Sci Part A Polym Chem 2008;46(23):7757–72.
[43] Chemykh A, Agag T, Ishida H. Polymer 2009;50(2):382–90.
[44] Durmaz H, Dag A, Hizal A, Hizal G, Tunca U. J Polym Sci Part A Polym Chem 2008;46(21):7091–100.
[45] Li CH, Ge ZS, Liu HW, Liu SY. J Polym Sci Part A Polym Chem 2009;47(16):4001–13.
[46] Gao HF, Matyjaszewski K. J Am Chem Soc 2007;129(20):6633–9.
[47] Parrish B, Breitenkamp RB, Emrick T. J Am Chem Soc 2005;127(20):7404–10.
[48] Yin J, Ge ZS, Liu H, Liu SY. J Polym Sci Part A Polym Chem 2009;47(10):2608–19.
[49] Yuan YY, Du Q, Wang YC, Wang J. Macromolecules 2010;43(4):1739–46.
[50] Luo XL, Wang GW, Pang XC, Huang JL. Macromolecules 2008;41(7):2315–7.
[51] Lallana E, Fernandez-Megia E, Riguera R. J Am Chem Soc 2009;131(16):5748–50.
[52] Bao HQ, Li L, Gan LH, Ping Y, Li J, Ravi P. Macromolecules 2010;43(13):5679–87.
[53] Bao HQ, Li L, Leong WC, Gan LH. J Phys Chem B 2010;114(32):10666–73.
[54] Yuan WZ, Zhao ZD, Gu SY, Ren J. J Polym Sci Part A Polym Chem 2010;48(15):3476–86.
[55] Lutz JF, Akdemir Ö, Hoth A. J Am Chem Soc 2006;128(40):13046–7.
[56] Jonas AM, Glinel K, Nysten B, Huck WTS. Macromolecules 2007;40(13):4403–5.
[57] Badi N, Lutz JF. J Control Release 2009;140(3):224–9.
[58] Uhrich KE, Cannizzaro SM, Langer RS, Shakesheff KM. Chem Rev 1999;99(11):3181–98.
[59] Yuan WZ, Yuan JY, Zhang FB, Xie XM. Biomacromolecules 2007;8(4):1101–8.
[60] Yuan WZ, Yuan JY, Zhang FB, Xie XM, Pan CY. Macromolecules 2007;40(25):9094–102.
[61] Pokhrel MR, Bossmann SH. J Phys Chem B 2000;104(10):2215–23.
[62] Schatz C, Smith EG, Armes SP, Wanless EJ. Langmuir 2008;24(15):8325–31.
[63] Nishikawa K, Yekta A, Pham HH, Winnik MA. Langmuir 1998;14(25):7119–29.
[64] Oh HJ, Kim JH, Kim EY. Macromolecules 2008;41(19):7160–5.
[65] Shi GY, Yang LP, Pan CY. J Polym Sci Part A Polym Chem 2008;46(19):6496–508.

Polymer 52 (2011) 667–675

Contents lists available at ScienceDirect

Polymer

journal homepage: www.elsevier.com/locate/polymer

Preparation of isotactic polypropylene/polystyrene blends by diffusion and subsequent polymerization of styrene in isotactic polypropylene pellets

Xue-Rong Yao, Jian Yu*, Zhao-Xia Guo

Key Laboratory of Advanced Materials (MOE), Department of Chemical Engineering, Tsinghua University, Beijing 100084, PR China

ARTICLE INFO

Article history:
Received 25 June 2010
Received in revised form
17 December 2010
Accepted 22 December 2010
Available online 30 December 2010

Keywords:
Pellets
Diffusion
Blend

ABSTRACT

Isotactic polypropylene (iPP) pellets were used to prepare isotactic polypropylene/polystyrene (iPP/PS) blends by diffusion and subsequent polymerization of styrene in water medium, with initiator benzoyl peroxide (BPO) added after diffusion of styrene. Two methods, differencing in whether the excess monomer was removed after diffusion, were used and parameters influencing PS contents were investigated. Diffusion kinetic study showed that the diffusion coefficient at 90 °C is 2.8 times that at 80 °C due to the α relaxation of iPP segments. Investigation on the distribution state of styrene in the mixture before diffusion revealed that most styrene adsorbed on the surface of iPP pellets, and thus the diffusion behavior of styrene into iPP pellets in water medium is similar to that in bulk styrene. Phase morphology of a typical iPP/PS blend showed an average particle size of about 90 nm in the inner part of the iPP pellets. The diametrical distributions of PS showed that styrene can diffuse up to the center of the pellets at 90 °C. It is important to note that the depth of styrene is limited when the initiator BPO is added along with styrene, providing a good explanation for the previously reported ineffective solid-state modification of melt-extruded iPP pellets.

1. Introduction

Nanoblends, in which the dispersed-phase domains exhibit length scales of 100 nm or less, is of growing interest due to the potential for enhanced properties [1–5]. For most polymer blends processed under typical extrusion conditions, it is hard to achieve nanoblends as the ultimate particle size results from the competition between thermomechanics and thermodynamics [2]. In contrast, *in situ* polymerization of one monomer inside a polymer matrix has been demonstrated to be a feasible and promising method to produce nanoblends [1,3–5]. For example, Picchioni et al. [4,5] prepared isotactic polypropylene/polystyrene (iPP/PS) nanoblends with a particle size of 10–50 nm via diffusion and *in situ* polymerization of styrene in porous iPP powders. This method of making polymer alloys was first recognized by Montecatini/Himont/Montell, who developed the 'Hivalloy' and 'Catalloy' reactor alloy processes, in the beginning of the 1990s [6–9]. One of the important bases of the processes is the porous morphology of iPP powders, which have a multigrain-structure and are directly from the polymerization reactor. It is commonly accepted that the transport of the components (the monomer and the initiator) to the place of reaction consists of diffusion in porous regions of the iPP-grain (macroparticle), mass transfer to the surface of the microparticles, and subsequent absorption and diffusion into the amorphous phase [6].

In contrast to multigrain native iPP powders, iPP pellets, which are more commonly used in the plastic production, were reported to be ineffective in solid-state modification because the rate of mass transfer to the reaction place was too small [6] and the depth of penetration was limited [10]. However, iPP films or HDPE plaques were reported to be successful in the solid-state modification [11–14]. Kryszewski et al. [11–13] immersed iPP films in styrene (containing a photoinitiator) at 45 or 65 °C for diffusion and subsequent polymerization of styrene. Kung et al. [14] used supercritical CO_2 as a solvent to aid the infusion of styrene and a radical initiator into HDPE plaques. Both papers [11,14] reported much higher amounts of PS incorporation than that of the equilibrium uptake of styrene due to continuous diffusion of styrene into the substrate during polymerization. And meanwhile, styrene was demonstrated to permeate throughout the spherulitic structure of the substrates. These successful examples encourage us to investigate diffusion and subsequent polymerization of styrene in iPP pellets in order to obtain iPP/PS nano-alloys, which are expected to be directly used in plastic production. This paper gives a full account of our investigation. The parameters influencing the amount of PS incorporation and the diffusion kinetics are discussed

* Corresponding author. Tel.: +86 010 62797966; fax: +86 010 62770304.
E-mail address: yujian03@mail.tsinghua.edu.cn (J. Yu).

0032-3861/$ – see front matter © 2010 Elsevier Ltd. All rights reserved.
doi:10.1016/j.polymer.2010.12.050

in detail. The distribution state of styrene in the mixture before diffusion is investigated in order to understand the procedure. The phase morphology of the obtained iPP/PS blends is observed by field emission scanning electron microscopy (FESEM) after permanganic etching of the amorphous region of iPP. The diametrical distribution of PS in an iPP pellet is determined by microscopic Fourier transform infrared spectroscopy (Micro FTIR).

2. Experimental

2.1. Materials

The matrix polymer used in this work was commercial grade iPP, S1003 with a melt flow index of 3.2 g/10 min, a density of 0.905 g/cm^3, a pellet diameter of approximately 4.5 mm, a crystallinity of 40% (determined by DSC), and purchased from Yanshan Petroleum and Chemical, China. Polyvinyl alcohol (PVA) was provided by Beijing Organic Chemical Plant, with a degree of polymerization of 1750 ± 50 and a degree of alcoholysis of 88%. Chloroform was analytical grade and used as received. Benzoyl peroxide (BPO) was purified by recrystallization from chloroform/methanol. Styrene was distilled under reduced pressure.

2.2. Preparation of iPP/PS blends

To a 250 ml flask equipped with a condenser and a mechanical stirrer were added 20 g of iPP, 52.5 ml of pure water and 7.5 ml of 0.8 wt.% aqueous polyvinyl alcohol as a suspending agent. The mixture was heated with a water bath while stirring and then maintained at the required diffusion temperature (T_d) (30–90 °C). Afterward, 6 g of styrene (unless the amount of styrene is the variable), that is 30% to the weight of iPP, was added to the flask and diffusion proceeded for different diffusion time (t_d). Subsequently the diffusion systems were treated using two different methods. In Method 1, the mixture was heated up to 90 °C, then added 5% initiator BPO (to the weight of styrene, unless the amount of BPO is the variable) dissolved in 2 ml of chloroform, and maintained at 90 °C for 3 h (unless t_p is the variable) to complete polymerization. In Method 2, the pellets in the original flask were separated by vacuum filtration and transferred into a new flask with 60 ml of pure water preheated to 90 °C. Then, initiator dissolved in chloroform was added and polymerization at 90 °C proceeded for 3 h (unless t_p is the variable) under stirring. For both methods, the pellets were separated from the suspension after polymerization, washed and dried to a constant weight. In latter discussion, different preparation conditions are denominated with a 3-number system 'A0B', where 'A0' is the diffusion temperature and 'B' is the method. For example, '601' means the diffusion temperature (T_d) is 60 °C and the polymerization is carried out by Method 1, and similarly '902' means the diffusion process occurs at 90 °C and the polymerization is carried out by Method 2.

2.3. Measurement of PS content

PS in the final iPP/PS blends consists of the surface PS and the inner PS. The total, inner and surface PS contents were defined as follows:

$$\text{Total PS content}(\%) = \frac{m_{\text{totalPS}}}{m_{\text{iPP}}} \times 100\% = \frac{m_{\text{innerPS}} + m_{\text{surfacePS}}}{m_{\text{iPP}}} \times 100\%$$

$$\text{Inner PS content}(\%) = \frac{m_{\text{innerPS}}}{m_{\text{iPP}}} \times 100\%$$

$$\text{Surface PS content}(\%) = \frac{m_{\text{surfacePS}}}{m_{\text{iPP}}} \times 100\% = \text{total PS content}(\%) - \text{inner PS content}(\%)$$

where $m_{innerPS}$ is the mass of the inner PS in the iPP/PS blends; $m_{surfacePS}$ is the mass of the PS on the surface of iPP pellets; m_{iPP} is the initial mass of the iPP before impregnating.

The inner PS content was calculated as follows:

$$\text{Inner PS content}(\%) = \left(\frac{m_2}{m_1} \times \frac{m_4}{m_3} - 1\right) \times 100\%$$

where m_1 was the total mass of the original iPP, and m_2 was the total mass of the iPP/PS blends after diffusion and polymerization of styrene. To determine the inner PS content, iPP/PS blends with a mass of m_3 ($m_3 < m_1$) was stirred in chloroform at room temperature for 20 min to remove the surface PS and dried to a constant weight m_4.

2.4. Dynamic mechanical analysis (DMA)

Dynamic mechanical analysis (DMA) was performed with a TA instrument dynamical analyzer (model 2980) at a fixed frequency of 1 Hz from −100 °C to 150 °C with a heating rate of 2.5 °C/min. For DMA tests, iPP pellets were hot pressed into films of 0.075 mm thickness, and a rectangle of about 10 mm width and 40 mm length was cut from the film for characterization.

2.5. Microscopic Fourier transform infrared spectroscopy (Micro FTIR)

Samples with a thickness of 15 μm were cut by a microtome (YD-1508R, Zhejiang Jinhua Yidi Medical Equipment Factory) and Micro FTIR was performed with Thermo-Nicolet 6700 FTIR and Nicolet Continuum FTIR Microscope, with a microsampling area of 100 × 100 μm^2. Infrared spectra were recorded along the diameter of the pellets. A_1/A_2 defined as the ratio of the peak areas of the absorptions at 758 cm^{-1} and 1167 cm^{-1}, characteristics of the PS and iPP respectively, reflecting the content of PS in the sample.

2.6. Field emission scanning electron microscopy (FESEM)

The morphology of the samples was visualized by JSM-7401 field emission scanning electron microscope (FESEM) at an accelerating voltage of 1 kV. Cross sections of the pellets for FESEM were obtained by cutting the pellets using the same microtome mentioned above and then etched for 1 h with stirring in a mixture of water (5 g), sulfuric acid (6 g, 95%), orthophosphoric acid (9 g, 85%) and potassium permanganate (0.08 g) to remove the amorphous fraction of iPP for a better observation of the PS particles. Next, each sample was washed ultrasonically in water for 5 min and then in acetone for another 5 min.

3. Results and discussion

3.1. Blend synthesis

It was reported that the industrial solid-state modification processes carried out directly in the monomer without any other reaction medium often yielded very inhomogeneous products and the reactor had to be shut down due to serious caking, while

processes carried out in water steam yielded homogeneous products without any caking in the reactor [15]. Therefore, in this work water was used as the diffusion and polymerization medium in order to prevent the occurrence of caking, and PVA was used as a suspending agent. First in this work, comparative experiments were carried out on two different ways of the initiator addition, one is adding the initiator BPO along with the monomer before the diffusion process, and the other is adding BPO after diffusion of styrene. The first way is commonly used in both industrial processes and academic research [4,6]. In both cases, diffusion of styrene was carried out at 60 °C for a certain time, followed by polymerization at 90 °C for 3 h. Both Method 1 and 2 described in the experimental section were used. The amounts of styrene and iPP were fixed at 6 g and 20 g, respectively. As shown in Fig. 1, the inner PS content is lower when BPO was added along with styrene than that of the other case where BPO was added after diffusion of styrene, no matter which method was used. One possible explanation may be the occurrence of partial initiation of BPO during diffusion process, resulting in polymerization of styrene which inhibits diffusion of styrene into the inner parts of the iPP pellets. Therefore, in later investigation BPO was always added after diffusion of styrene for a certain time at a specific diffusion temperature, as described in the experimental section.

Next, the effects of the amounts of styrene and BPO, polymerization time (t_p), and diffusion temperature and time (T_d and t_d) on the total and the inner PS contents were investigated. Thus, diffusion of 6 g of styrene (unless the amount of styrene is the variable) was carried out at 90 °C for 1 h (unless T_d and t_d are the variables), followed by polymerization of styrene at 90 °C for 3 h (unless t_p is the variable) using both Method 1 and 2 with the addition of 5% BPO to the weight of styrene (unless the amount of BPO is the variable). The amount of iPP was always fixed to 20 g. Fig. 2 shows the total and the inner PS contents as a function of the amount of styrene. With Method 1, the total PS content increases almost linearly with the increase in the amount of styrene, approaching to the theoretical values as indicated by the solid line in Fig. 2, while the inner PS content increases initially and then levels off when the amount of styrene reaches 30% to the weight of iPP, i.e. 6 g. This indicates that the extra amount of styrene polymerizes outside the iPP pellets, being the reason for caking at a high styrene addition (such as 10 g, 50% to the weight of the iPP). With Method 2, both the total and the inner PS contents increase initially and then levels off

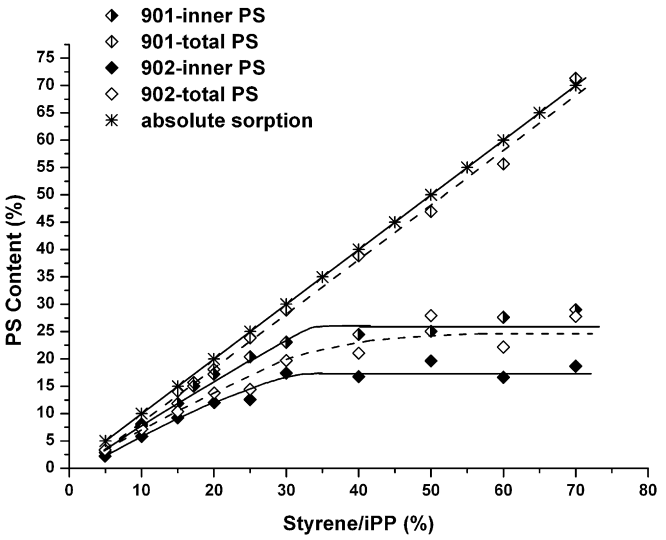

Fig. 2. Total and inner PS contents as a function of styrene/iPP.

at 30% styrene (6 g). This is because that most of the excess styrene which is not incorporated into the iPP pellets has already been removed by filtration before polymerization. And the total PS content is always slightly higher than the inner PS content, due to the small amount of PS coated on the surface of the iPP pellets.

Fig. 3 shows the effect of the amount of BPO on the total and the inner PS contents. With both Method 1 and 2, the total and the inner PS contents increase rapidly with the increase in the amount of BPO up to 1% (to the weight of styrene), and then do not change significantly with further increase in the amount of BPO. As shown in Fig. 4, the change of t_p from 1 h to 5 h does not bring obvious change in the total and the inner PS contents with both Method 1 and 2.

The effects of T_d and t_d on the inner PS content are shown in Fig. 5. It can be seen that the time to reach equilibrium is reduced and the equilibrium value is increased when T_d increases independently of which Method (1 or 2) was used. As will be shown in the next section, when T_d increases, the segmental mobility of iPP chains increases, leading to an increase in diffusion coefficient, therefore the time to reach the equilibrium decreases. The increase

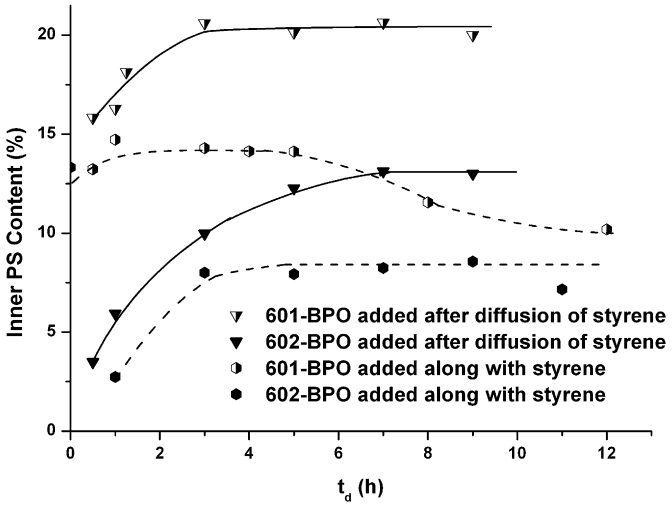

Fig. 1. Comparative experiments on two different ways of the initiator addition. '601' and '602' denote experiments carried out at $T_d = 60$ °C by Method 1 and 2 respectively.

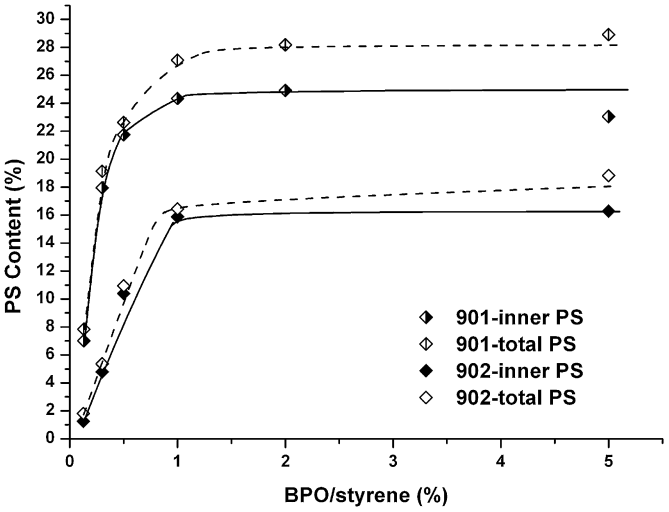

Fig. 3. Total and inner PS contents as a function of BPO/styrene.

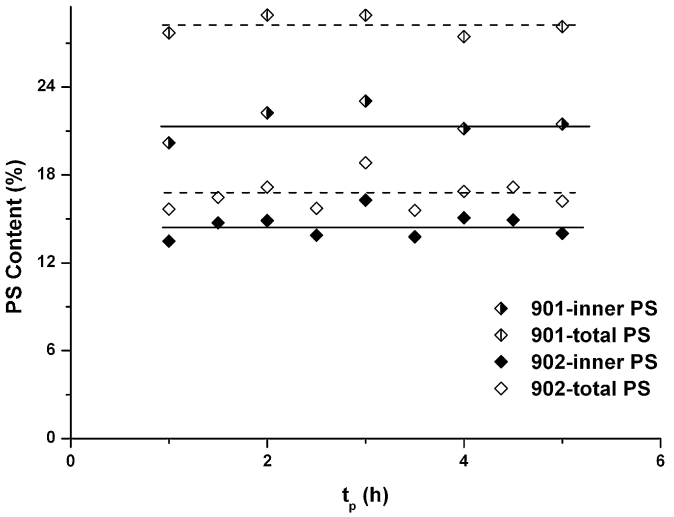

Fig. 4. Total and inner PS contents as a function of t_p.

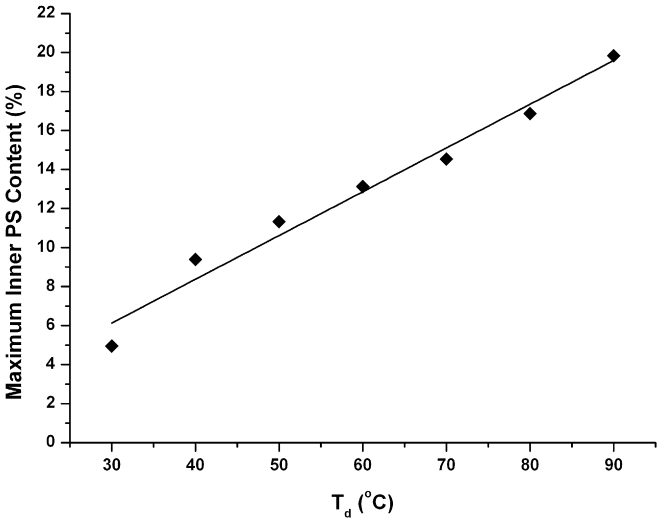

Fig. 6. Maximum inner PS content as a function of T_d.

in the segmental mobility also increases the fractional free volume inside the iPP pellets, which leads to more adsorption of the monomer according to Peterlin [16], and as a result, the equilibrium value of the inner PS content increases (Fig. 6).

As shown in Figs. 2–5, the equilibrium values of the inner PS content obtained in Method 1 are always higher than in Method 2 (for example, 23% to iPP for 901 while 18% for 902), indicating some diffusion of styrene into iPP pellets during polymerization in Method 1 where extra styrene was not removed before the addition of the initiator BPO. This is in agreement with the literature reports [11–14] where different substrate and different polymerization technology were used. However, the amount of styrene penetrating into iPP during polymerization (for example, 28% of that of the diffusion stage for 901 with $t_d = 1$ h) is considerably different from the results in the literature [11,14], where the PS incorporation was several times of the equilibrium styrene uptake, presumably due to the differences in substrate and polymerization technique. A possible reason for the diffusion of styrene into the iPP pellets during polymerization may be the new free volume created in the matrix during polymerization, as the density of styrene is drastically lower than that of PS [12]. However, this is certainly not the only reason, because the amount of styrene diffused into the iPP pellets during polymerization is higher than the predicted value calculated from the density change. The preferred diffusion of styrene inside the already polymerized PS areas, as pointed by Trznadel et al. [11], may also be an important reason for the diffusion of styrene into the iPP pellets during polymerization in Method 1.

3.2. Diffusion kinetics

The diffusion ability of styrene into iPP pellets was evaluated in terms of the inner PS content after diffusion and subsequent polymerization of styrene using Method 2 where the non-adsorbed styrene was removed before polymerization. The data in Fig. 5 for Method 2 were used, and the adsorption curves at different t_d with the abscissa scaled in $t_d^{1/2}$ are shown in Fig. 7. By comparison with the typical plots of diffusion [17,18], it is recognized that the diffusion behaviors above 60 °C have characteristics of Fickian diffusion processes.

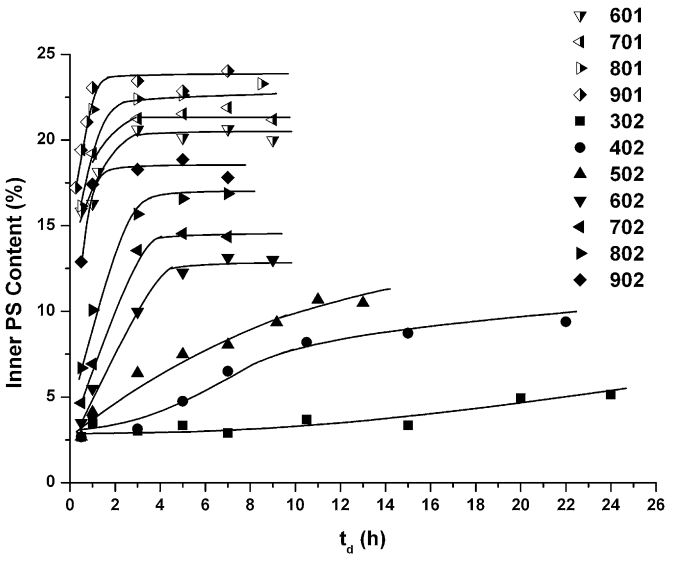

Fig. 5. Inner PS content as a function of t_d at different T_d.

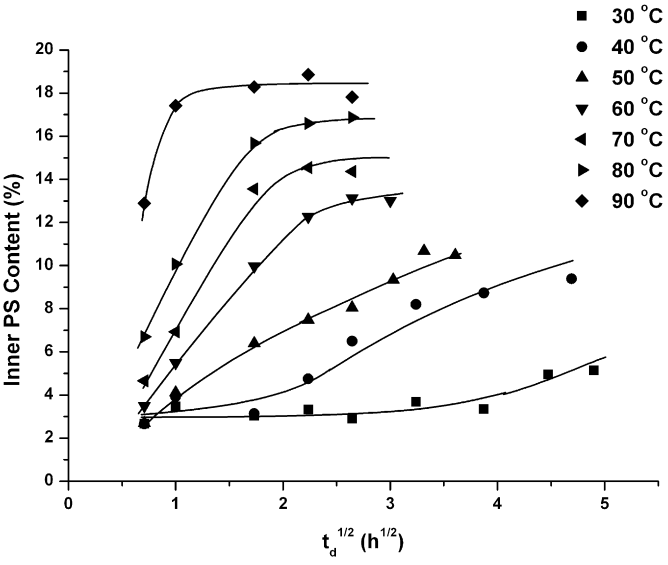

Fig. 7. Inner PS content as a function of $t_d^{1/2}$ at different T_d.

The diffusion coefficient determines the rate to reach the equilibrium conditions [6]. The average diffusion coefficients D above 60 °C can be calculated using the model of Fickian diffusion from a well-stirred solution of limited volume [17] supposing the iPP pellet as a uniform sphere with a radius of a. In the model it is supposed that the sphere occupies the space r < a, while the volume of the bath of solution (excluding the space occupied by the sphere) is V. The concentration of the solute in the solution is always uniform and is initially C_0. The sphere is initially free from solute. The total amount of solute M_t in the sphere after time t is expressed as a fraction of the corresponding quantity after infinite time by the relation

$$\frac{M_t}{M_\infty} = 1 - \sum_{n=1}^{\infty} \frac{6\alpha(\alpha+1)\exp(-Dq_n^2 t/a^2)}{9 + 9\alpha + q_n^2\alpha^2},$$

where the q_ns are the non-zero roots of

$$\tan q_n = \frac{3q_n}{3 + \alpha q_n^2},$$

the parameter α is expressed in terms of the final fractional uptake of solute by the sphere by the relation

$$\frac{M_\infty}{VC_0} = \frac{1}{1+\alpha}.$$

Using this model, the diffusion coefficient divided by the square of sphere radius D/a^2 can be calculated with the experimental data series of M_t/M_∞ vs. t and then results of D at different T_d were obtained with an average radius (a) of 2.25 mm, as listed in Table 1. The natural logarithms of D plotted vs. $1/T_d$ are shown in Fig. 8.

The curve doesn't show a simple linear relationship. An abrupt increase in ln$D$ was observed when T_d increases from 80 to 90 °C. Therefore, the dependence of the diffusion coefficients on temperature cannot be simply described by the following Arrhenius formula

$$\ln D = \ln D_0 - \frac{Q}{RT}.$$

For a better understanding of the phenomenon from the view of segmental mobility, dynamic mechanical analysis (DMA) of the original iPP was performed. Fig. 9 shows the temperature dependencies of the storage modulus (E') and the loss factor (tan δ). The sample exhibits three maxima on the tan δ curve which are contributed to the following relaxation: γ (around −50 °C), β (around 10 °C) and α (above 35 °C with maximum at around 88 °C). The γ process is usually assigned to the local mode relaxation in the amorphous phase, and the β process is related to the glass transition, while the α relaxation is related to the crystalline phase and occurs in the regions where interlamellar shear is the predominant form of mechanical deformation [19]. Because of the α relaxation, the segmental mobility of the amorphous part of iPP increases significantly at 90 °C. Therefore, it is understandable that the diffusion coefficient is much higher at 90 °C, 2.8 times of that at 80 °C.

Table 1
D/a^2 results at different T_d with a = 2.25 mm.

T_d (°C)	D/a^2 (s^{-1})	D (m^2/s)
60	1.17×10^{-5}	5.93×10^{-11}
70	1.36×10^{-5}	6.90×10^{-11}
80	1.34×10^{-5}	6.78×10^{-11}
90	3.82×10^{-5}	1.93×10^{-10}

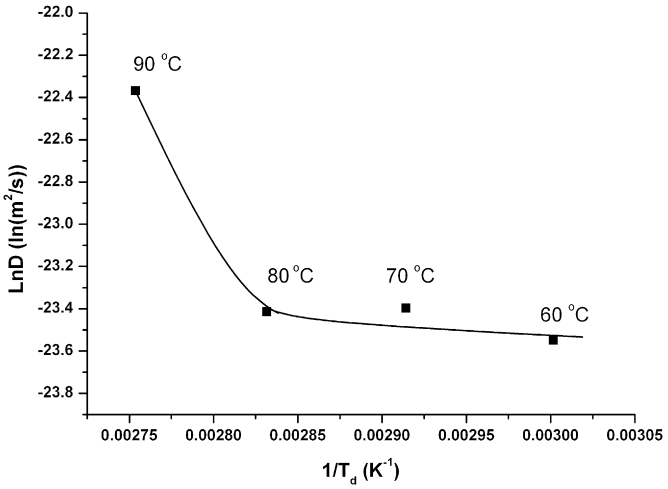

Fig. 8. Results of lnD vs. $1/T_d$.

3.3. Distribution state of styrene in the mixture before diffusion

In order to understand the success of the current recipe in the solid-state modification of iPP pellets and the roles of water and PVA, the distribution state of styrene in the mixture before diffusion was investigated. Thus, styrene and PVA were sequentially added to the mixture of iPP/water at room temperature. The amount of each component is the same as in recipe '901'. For better observation, a petri dish was used as the container and a small amount of green oleodye (phthalocyanine green) was mixed into the styrene to color it. Photos were taken after stopping the stirring. As shown in Fig. 10a and b, the iPP pellets are not wetted by water due to their hydrophobicity. When styrene is added, it goes to the surface of the iPP pellets as indicated by the contour around iPP pellets (Fig. 10c and d), because the surface tensions of styrene and iPP are similar (27.4 [20] and 29.4 mN/m [21], respectively), while that of water is much higher (71.2 mN/m [20]). And the iPP pellets gather together to reduce the contact area between styrene and water. When PVA is added (Fig. 10e and f), most of the styrene is still surrounding the iPP pellets and some isolated styrene droplets (as indicated by the green spots in the water) stabilized by PVA coexist. Bubbles can be seen by neat eyes along the contour of the aggregates of iPP pellets and among the iPP pellets due to the presence of

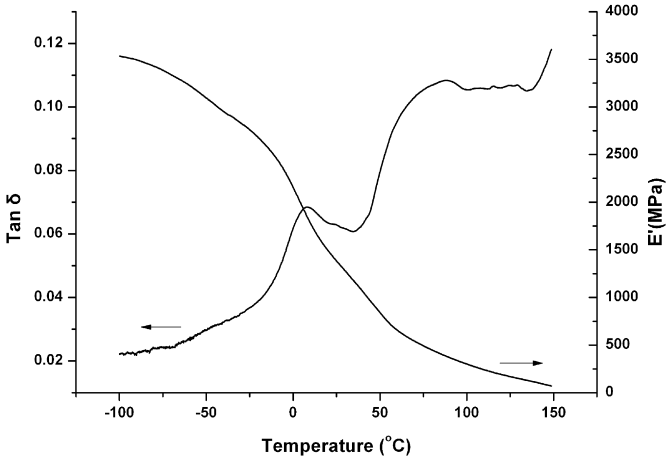

Fig. 9. E′ and tan δ of the original iPP as a function of temperature.

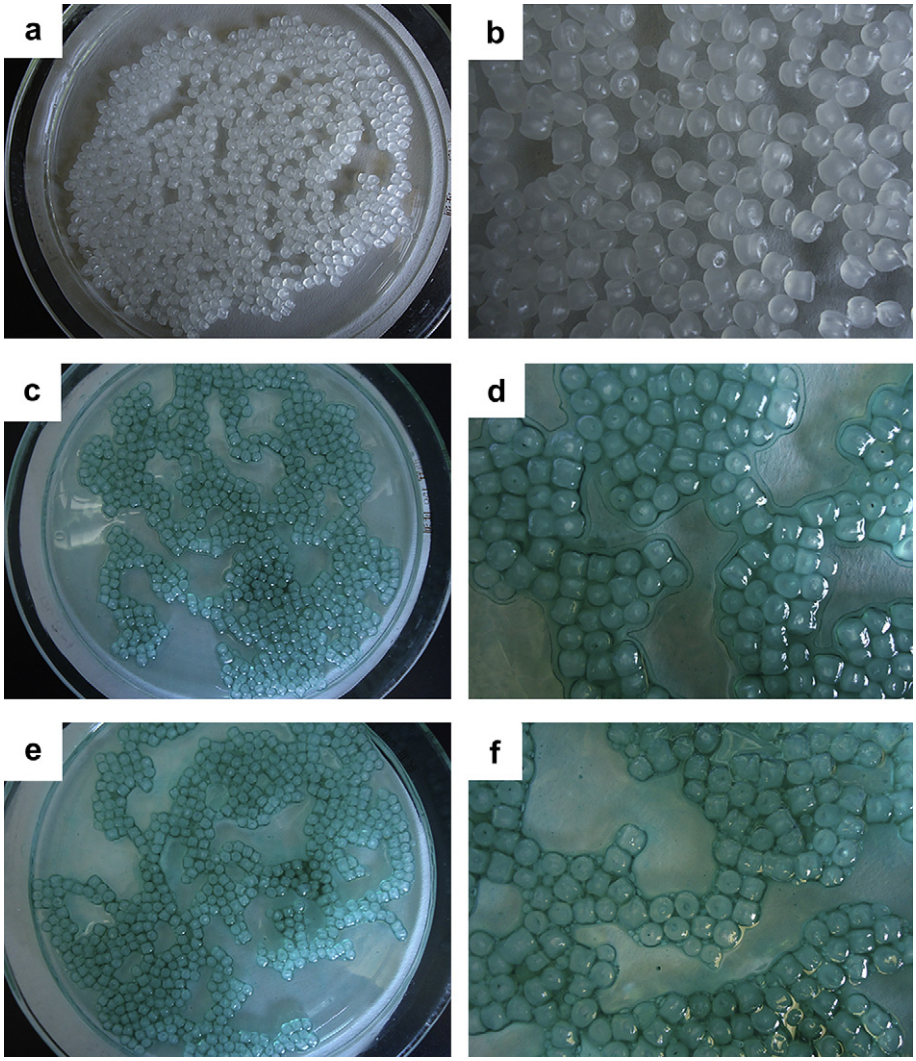

Fig. 10. Photos of the mixtures: (a & b) H_2O + PP; (c & d) H_2O + PP + Styrene (with dye); (e & f) H_2O + PP + Styrene (with dye) + PVA.

PVA. This is understandable because PVA is apt to stay between styrene and water to reduce the interfacial tension.

The above observation confirms that most of the styrene is adsorbed on the surface of iPP pellets before diffusing into the iPP pellets when water is used as the dispersing medium, no matter PVA is present or not. Comparative diffusion experiments in bulk styrene and in water medium without PVA were then carried out and similar amounts of styrene adsorption (14% and 13%, respectively) were obtained as compared to that of recipe '902' (15%), revealing that the presence of water and PVA has little effect on diffusion of styrene. Therefore, it can be concluded that the diffusion behavior of styrene into iPP pellets in water medium is similar to that in bulk styrene. The diffusion coefficients in Section 3.2 should be actual diffusion coefficients. The role of water in the current recipe (typically '901') is to facilitate heat transfer, because in the current styrene/iPP proportion the volume of styrene is too small to fully immerse the iPP pellets if the diffusion is carried out in bulk styrene, and this will be a problem for heat transfer during mass production. The use of PVA can make the procedure more feasible by avoiding caking during polymerization.

The distribution state of styrene in the typical diffusion system '901' before diffusion is shown in Fig. 11. Most of the styrene is adsorbed on the surface of the iPP pellets and a small amount of the styrene exists in the form of droplets in water. This is evidenced by surface morphology of the product. As shown in Fig. 12, the surface of the original iPP is rough, while that of the product is smooth. And the surface of the product is back to rough after removal of the PS by chloroform, revealing that the iPP pellets are covered with

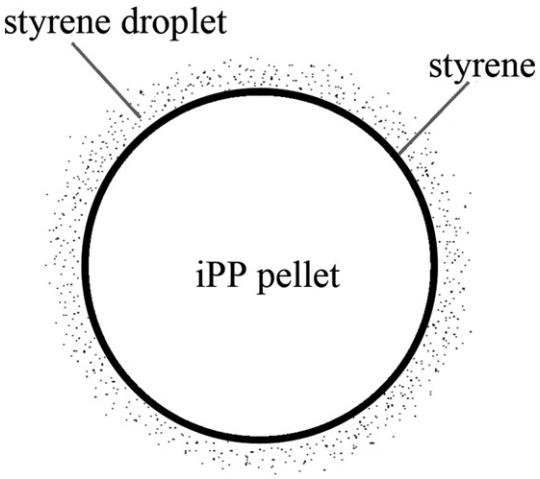

Fig. 11. Distribution state of styrene before diffusion.

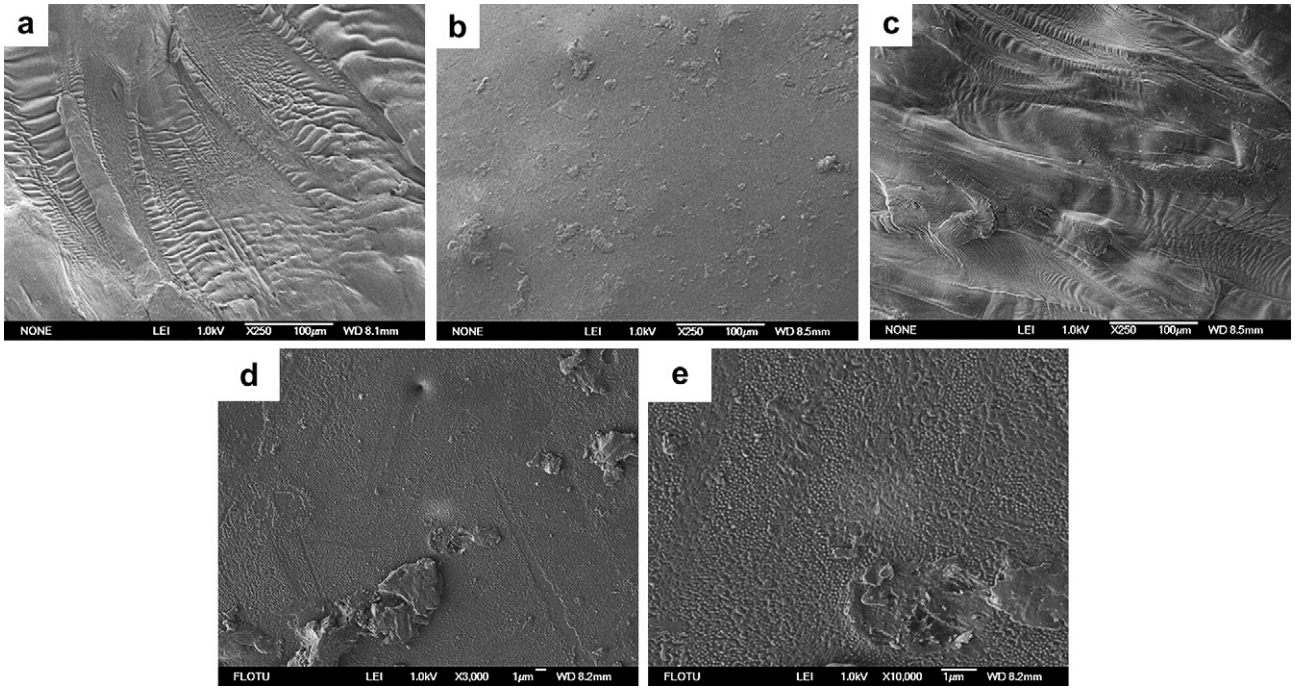

Fig. 12. FESEM micrographs: (a) surface of the original iPP pellets, ×250; (b, d and e): surface of the product by typical '901' process, ×250, ×3000, ×10000, respectively; (c) surface of the product by typical '901' process after removal of the surface PS by chloroform, ×250.

a layer of PS. At high magnifications (Fig. 12d and e), small PS particles (about 80 nm) and irregularly-shaped bigger blocks of PS (maybe resulted from aggregation of PS particles) were observed on top of PS layer. This in combination with the fact that PS is found in the filtrate after isolation of the product indicates existence of styrene droplets before diffusion and polymerization.

The isolated product contains 29% PS (to iPP by weight), corresponding to 97% of the styrene feeding. After deduction of the amounts of the small PS particles (~0.2% of the styrene feeding) and the bigger blocks of PS (~2% of the styrene feeding) on top of the PS layer, styrene adsorbed on iPP pellets before diffusion is estimated to be about 95% of the feeding, corresponding to

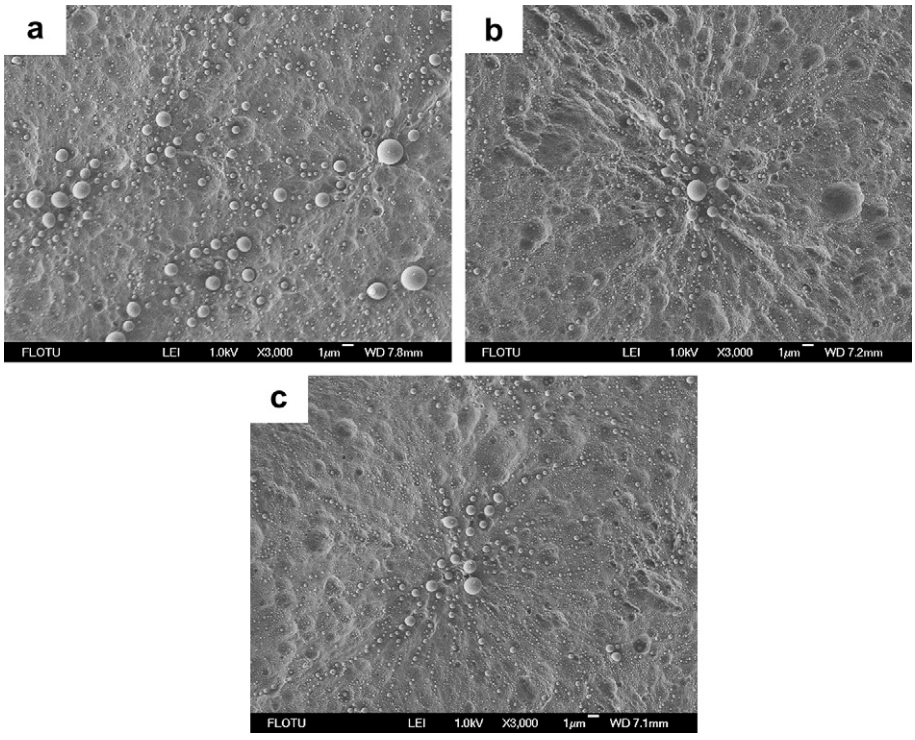

Fig. 13. FESEM images of the cross section of a typical iPP/PS blend (sample 901): (a) near the surface; (b) at mid-depth from the surface to the centre; and (c) in the centre.

a thickness of approximately 0.1 mm, basically in agreement with Fig. 10f. The styrene droplets in water before diffusion account about 5% of the feeding accordingly.

3.4. Phase morphology

Fig. 13 shows FESEM images of the cross section of a typical iPP/PS blend (sample 901, PS/iPP = 23%, with preparation conditions of styrene/iPP = 6 g/20 g, t_d = 1 h, BPO/styrene = 5%) from the surface to the centre of a pellet after etching the amorphous portion of iPP. It is obvious that PS particles are distributed in the amorphous areas of the matrix or regions with lower perfection such as the core of the spherulites and regions between lamellae. The PS particles in the core of the spherulites (micron size) are much bigger than those along the radius of the spherulites, i.e. between lamellae (tens of nanometers), implying a certain lack of crystallinity in the core of the spherulites [14]. The particle size distribution is obviously different at the area close to the surface of the pellets as compared to those at the mid-depth (from the surface to the centre) and the center. The latter two places have practically similar particle size distribution. More big PS particles of micron level size were found close to the surface of the pellet (Fig. 13a), while only a few big PS particles at the core of spherulites were observed in the rest area of the pellet (Fig. 13b and c). This phenomenon is related to the original crystalline morphology of iPP pellets formed in the production process. When iPP pellets were melt-extruded, the cooling rate of the pellets at the surface was higher than in the centre, resulting in formation of smaller and less perfect spherulites near the surface [22], therefore more free volume for adsorption of styrene and bigger particle size. The average particle size in Fig. 13b and c is about 90 nm due to the confinement of the amorphous phase of rather regular spherulites away from the surface.

3.5. Distribution of PS determined by Micro FTIR

The distribution of the formed PS in iPP pellets was investigated by Micro FTIR. The spectra of the cross sections of single pellets were recorded along the diameter from one end to the other. The ratio of the peak intensities at 758 and 1167 cm^{-1}, A_1/A_2, was taken as a measure for the PS/iPP composition ratio. The resulting profiles for samples prepared by different methods with t_d = 1 h at different T_d as a function of the distance from one end of the diameter are shown in Fig. 14. The shape of the curves is similar, with a nearly homogeneous distribution of PS inside the pellet and an increase of

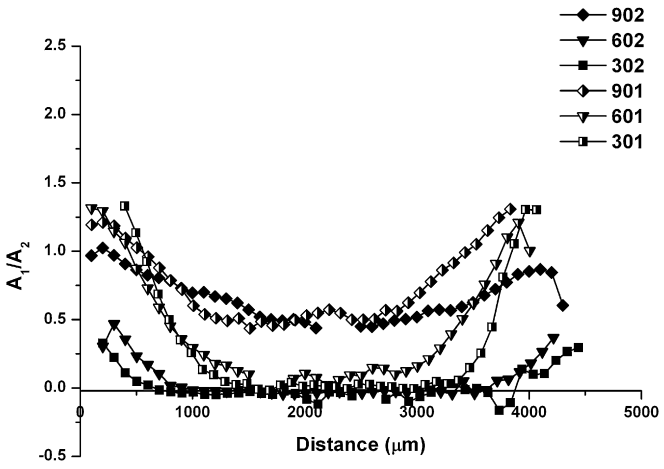

Fig. 14. Micro FTIR profiles of iPP/PS pellets.

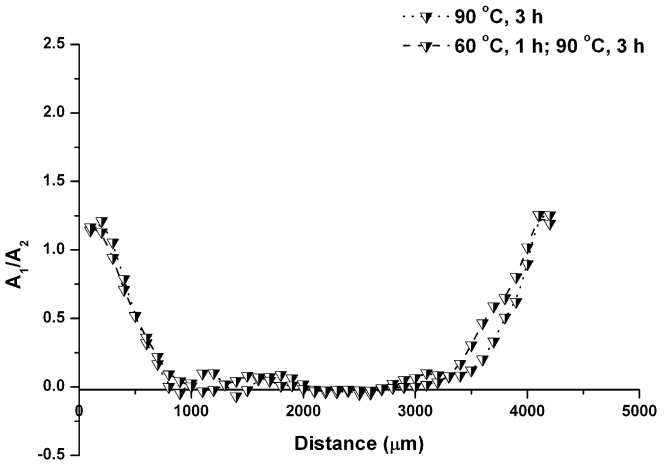

Fig. 15. Micro FTIR profiles of iPP/PS pellets prepared with BPO added along with styrene.

PS on approaching the pellet edge. Styrene can penetrate into the center of the pellet at 90 °C, while the depth of penetration is limited when T_d lowers to 60 and 30 °C. Denicola et al. [10] reported a limit of 0.5 mm for the depth of penetration when melt-extruded iPP pellets were soaked in a mixture of styrene and initiator at 100 °C and 130 °C. The difference between the current case and the literature results could be related to the different ways of the initiator addition although different polymerization techniques were used. As discussed earlier in the section of blend synthesis, addition of the initiator along with the monomer in the diffusion stage results in polymerization of the monomer, which inhibits diffusion of styrene into the inner parts of the iPP pellets. To verify this point, in this work BPO was added along with styrene, followed by diffusion and polymerization for 3 h at 90 °C, the depth of penetration was found to be around 1 mm (Fig. 15). Alternatively, the reaction mixture was allowed to stir at 60 °C for 1 h before increasing to 90 °C, again the depth of penetration was limited to 1 mm (Fig. 15).

4. Conclusion

iPP pellets are effective as the matrix for preparation of iPP/PS blends comprising up to 23% inner PS content by diffusion and subsequent polymerization of styrene in water medium with polyvinyl alcohol (PVA) as a suspending agent. The way of the initiator addition was found to have significant impact on inner PS content and the depth of penetration. Addition of BPO after diffusion of styrene is better than simultaneous addition with styrene. In the former the inner PS content is higher, and styrene can diffuse into the center of iPP pellets at 90 °C, while in the latter the depth of penetration is limited.

Both the methods investigated in this work, differencing in the presence (Method 1) and absence (Method 2) of the excess styrene in the polymerization stage, can be used for the blend preparation. Method 1 gives more PS incorporation than Method 2 because of the continuous diffusion of styrene into iPP during polymerization. Method 2 is particularly useful in diffusion kinetic study. The diffusion behavior above 60 °C has characteristics of Fickian diffusion. The average diffusion coefficients above 60 °C calculated using a typical model of Fickian diffusion show a big increase at 90 °C, being 2.8 times of that at 80 °C. This was attributed to the α relaxation of iPP segments.

In the initial mixture before diffusion, most styrene is adsorbed on the surface of iPP pellets while styrene droplets coexist. The

diffusion of styrene into iPP pellets in the current procedure is similar to that in bulk styrene.

FESEM observation of a typical iPP/PS blend shows that PS particles are distributed in the amorphous areas of the matrix or regions with lower perfection such as the core of the spherulites and regions between lamellae. The average particle size in the regions of mid-depth to the center of the pellets is about 90 nm, while that near the surface is bigger due to existence of smaller and less perfect spherulites formed near the surface in the production stage of iPP pellets.

PS distribution investigated by Micro FTIR shows that the diffusion temperature is very important in view of the depth of penetration. Styrene can penetrate into the center of the pellet at 90 °C, while the depth of penetration is limited when the diffusion temperature lowers to 60 and 30 °C. At 90 °C, the distribution of PS is almost homogeneous inside the pellet and the PS content increases on approaching the pellet edge.

References

[1] Tao Y, Kim J, Torkelson JM. Polymer 2006;47:6773–81.
[2] Hu GH, Cartier H. Macromolecules 1999;32:4713–8.
[3] Shimizu H, Li Y, Kaito A, Sano H. Macromolecules 2005;38:7880–3.
[4] Picchioni F, Goossens JGP, Duin MV, Magusin P. J Appl Polym Sci 2003;89:3279–91.
[5] Picchioni F, Goossens JGP, Duin MV. J Appl Polym Sci 2005;97:575–83.
[6] Ratzsch M, Arnold M, Borsig E, Bucka H, Reichelt N. Prog Polym Sci 2002;27:1195–282.
[7] Simonazzi T, Cecchin G, Mazzullo S. Prog Polym Sci 1991;16:303–29.
[8] Galli P, Haylock JC. Prog Polym Sci 1991;16:443–62.
[9] Galli P. Prog Polym Sci 1994;19:959–74.
[10] DeNicola AJ, Fava RA. Polym Mater Sci Eng 1997;76:162–3.
[11] Trznadel M, Milczarek P, Kryszewski M. J Appl Polym Sci 1991;43:1125–31.
[12] Pluta M, Milczarek P, Wlochowicz A, Kryszewski M. Acta Polymerica 1991;42:485–92.
[13] Pluta M, Milczarek P, Wlochowicz A, Kryszewski M. Acta Polymerica 1991;42:306–14.
[14] Kung E, Lesser AJ, McCarthy TJ. Macromolecules 1998;31:4160–9.
[15] US 5585435.
[16] Peterlin A. J Macromol Sci Phys 1975;B11:57–87.
[17] Crank J. The mathematics of diffusion. 2nd ed. New York: Oxford University Press; 1975.
[18] Rebenfeld L, Makarewicz PJ, Weigmann HD, Wilkes GL. J Macromol Sci-Rev Macromol Chem Phys 1976;C15(2):279–393.
[19] Pluta M, Morawiec J, Kryszewski M, Kowalewski T. J Thermal Anal 1996;46:1061–79.
[20] Zaitsev SY, Generalova AN, Marchenkoa SB, Makievski AV, Krägeld J, Miller R. Colloids Surf A 2004;239:145–9.
[21] Souheng W. Polymer interface and adhesion. New York: Dekker; 1982.
[22] Aboulfaraj M, Ulrich B, Dahoun A, Sell CG. Polymer 1993;34:4817–25.

Polymer 52 (2011) 676–682

Contents lists available at ScienceDirect

Polymer

journal homepage: www.elsevier.com/locate/polymer

Thermo- and pH-responsive HPC-*g*-AA/AA hydrogels for controlled drug delivery applications

Zhe Zhang [a], Li Chen [a,*], Changwen Zhao [b], Yunyan Bai [a], Mingxiao Deng [a], Hongling Shan [a], Xiuli Zhuang [b], Xuesi Chen [b,*], Xiabin Jing [b]

[a] Department of Chemistry, Northeast Normal University, Changchun 130022, PR China
[b] Key Laboratory of Polymer Ecomaterials, Changchun Institute of Applied Chemistry, Changchun 130022, PR China

ARTICLE INFO

Article history:
Received 9 April 2010
Received in revised form
12 November 2010
Accepted 22 December 2010
Available online 30 December 2010

Keywords:
Acrylic acid
Hydroxypropylcellulose
Smart hydrogels

ABSTRACT

This paper describes smart hydrogels composed of pH-sensitive poly(acrylic acid) (PAA) and biodegradable temperature-sensitive hydroxypropylcellulose-*g*-acrylic acid (HPC-*g*-AA) for controlled drug delivery applications. In a pH-responsive manner, the hydrogels with the higher HPC-*g*-AA content resulted in the lower equilibrium swelling. Although temperature had little influence on the swelling of the hydrogels, optical transmittance of the hydrogels was changed as a function of temperature, which reflecting that the HPC parts of hydrogel became hydrophobic at temperature above the lower critical solution temperature (LCST). Scanning electron microscopic analysis revealed that the pore size and the morphology of the hydrogels could be controlled by changing the composition of AA and the crosslinking density. Using BSA as a model drug, *in vitro* drug release experiment was carried out in artificial gastric juice (pH = 1.2) for the first 2 h and then in artificial intestinal liquid (pH = 6.8) for the subsequent 6 h. The release profiles indicated that both HPC-*g*-AA and AA contents played important roles in the drug release behaviors. The temperature- and pH-responsive HPC-*g*-AA/AA hydrogels might be exploited for wide applications in controlled drug delivery.

1. Introduction

Hydrogels are three-dimensional, cross-linked networks of water-soluble polymers. Intelligent hydrogels that respond to environmental physical and chemical stimuli, such as pH, temperature, light, magnetic field, electric field, and chemical substances, have attracted much attention in recent years [1–9]. "Smart" materials that can alter their phase or other properties when recognizing special stimuli are advised to be of great potential in biomedical and pharmaceutical field such as drug release [10–12]. Among the above-mentioned stimuli, pH and temperature are the most common physical and chemical ones used in biotechnological and biomedical applications, so temperature- and pH-sensitive hydrogels have been extensively investigated [13–20]. However, most of the synthetic temperature- and pH-sensitive polymers are not biodegradable, which becomes a serious limitation in some applications [21]. Therefore, more and more attentions have been concentrated on the development of biodegradable temperature- and pH-sensitive hydrogels based on natural macromolecules [22–24].

Polymers comprised of pendent carboxylic groups, such as poly (acrylic acid) (PAA), are typical acidic pH-responsive polymers [25]. Hydrogels that contain carboxylic groups show pH-sensitive swelling–deswelling behaviors and are widely used in controlled drug release [18–20].

One of the most popular temperature-sensitive polymers for biorelated applications is poly(*N*-isopropylacrylamide) (PNIPAAm). PNIPAAm is a typical temperature-sensitive polymer with a volume phase transition around the lower critical solution temperature (LCST, about 32 °C) in aqueous solution. However, the poor biocompatibility of PNIPAAm and other acrylamide related polymers may be a limitation to be used widely [26]. Therefore, many efforts have been made to replace PNIPAAm with biocompatible temperature-sensitive materials [27].

Hydroxypropylcellulose (HPC) is a biodegradable, biocompatible and derivative of natural macromolecules, which exhibits a well-defined lower critical solution temperature in aqueous solution at about 41 °C and a remarkable hydration-dehydration change in aqueous solution in response to relatively changes at temperature around the LCST. Below the LCST, the HPC chains hydrate to form an expanded structure due to its hydrophilicity. Conversely, above the LCST, the HPC chains dehydrate to form a shrunken structure because of the hydrophilic-to-hydrophobic

* Corresponding authors.
E-mail addresses: chenl686@nenu.edu.cn (L. Chen), xschen@ciac.jl.cn (X. Chen).

0032-3861/$ – see front matter © 2010 Elsevier Ltd. All rights reserved.
doi:10.1016/j.polymer.2010.12.048

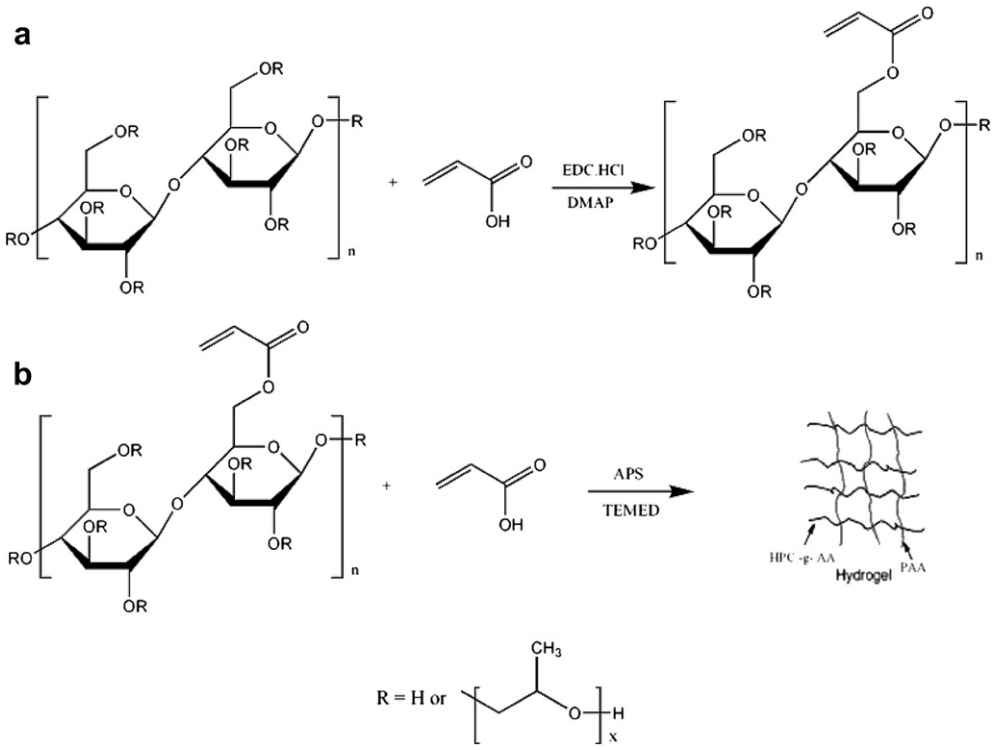

Scheme 1. Synthetic route of HPC-*g*-AA (a) and hydrogels (b).

transition. This property is due to the reversible formation and cleavage of the hydrogen bonds between the HPC and surrounding water molecules with changing temperature. The LCST can be appropriately elevated or reduced by copolymerizing HPC with a more hydrophilic monomer or a more hydrophobic monomer. According to its unique hydrophilic/hydrophobic change, thermo-responsive HPC-based hydrogels have been prepared for controlled delivery of hydrophilic drugs [28–30]. The loading of hydrophilic drugs can be carried out in aqueous condition at low temperatures, which reduces the risk of denaturation of protein drugs in a hostile environment. Moreover, the release rate can be modulated by changing the hydrophilicity to hydrophobicity of the HPC induced by temperature increasing. The advantage of the HPC over many other synthetic thermally responsive macromolecules is that the HPC is one of the cellulose ethers which has been approved by the United States Food and Drug Administration for the use in food, drug, and cosmetics [31]. HPC-*g*-AA particles with semi-interpenetrating polymer network (IPN) structure have been synthesized to show good temperature-sensitive and potential for drug release application [32]. However, the main problem of this semi-interpenetrating polymer network is that it is not stable.

From the viewpoint of applications, it is necessary to explore biocompatible and biodegradable hydrogels for biomedical usage without losing their intelligent properties, such as pH- and thermo-sensitivity. In this paper, a series of hybrid hydrogels composed of hydroxypropylcellulose (HPC)-*g*-acrylic acid (HPC-*g*-AA) and PAA were synthesized and the as-prepared materials exhibited temperature and pH response capabilities. Because of the ester bond conjugated between the HPC chains and PAA chains, the hydrogels show biodegradability under enzyme. The influences of pH and temperature on the swelling behaviors of the hydrogels were also investigated. In addition, the LCST of the hydrogels increased with the pH value increasing due to the PAA exhibiting more hydrophilicity at the higher pH value, so the hydrogels exhibited an especial pH-dependent temperature-sensitivity. Based on these pH-dependent swelling behaviors and pH-dependent temperature-sensitivity, intelligent oral drug release system could be achieved.

2. Experimental section

2.1. Materials

HPC (M_w = 100,000) was purchased from Acros Organics. Acrylic acid was obtained from Shanghai Chemical Reagent Co. (China) and used after distillation under reduced pressure. Trichloromethane was dried over CaH_2, and distilled before use. 4-Dimethylaminopyridine (DMAP 98% Fluka) and 1-ethyl-3-(3-dimethyllaminopropyl) carbodiimide hydrochloride (EDC·HCl, Shanghai GL Biochem, China) were used as received. Ammonium persulfate (APS) and *N*, *N*, *N*′, *N*′-tetramethylethylenediamine (TEMED) were obtained from Shanghai Chemical Reagent Co. (China) and used directly.

The artificial gastric juice and artificial intestinal liquid were prepared as follows. 7 mL of hydrochloric acid (37 wt%) and 2.0 g sodium chloride dissolved in 1000 mL of deionized water to prepare artificial gastric juice. 6.8 g potassium dihydrogen phosphate was dissolved in 500 mL of deionized water, and then the pH value was adjusted to 6.8 and the solution was diluted to 1000 mL to get artificial intestinal liquid.

2.2. Synthesis of HPC-g-acrylic acid

Typically, 1.0 g HPC and 0.09 mL of AA (10 mol% with respect to hydroxyl group of HPC) were dissolved in 30 mL of trichloromethane. After dissolution, EDC·HCl (0.27 g, 1.4 mmol) and DMAP (0.04 g, 0.14 mmol) were added as the coupling agent and catalyst, respectively. The mixture was mixed thoroughly and then quickly poured into a glass mold. The reaction was allowed to proceed at room temperature for 24 h. The product was collected by

Table 1
Feed compositions of the hydrogels.

Samples	Feed compositions					
	HPC-*g*-AA/mg	AA/mg	APS/mg	TEMED/μL	H_2O/mL	AA%
Gel 1	20	380	20	20	4	95
Gel 2	60	340	20	20	4	85
Gel 3	100	300	20	20	4	75
Gel 4	200	200	20	20	4	50
Gel 5	300	100	20	20	4	25
Gel 6	380	20	20	20	4	5
Gel 7	392	8	20	20	4	2

precipitation in 10-fold ethyl ether. Then, the product was redissolved in trichloromethane and precipitated at least twice in ethyl ether. After vacuum drying for 24 h, HPC-*g*-AA was obtained in 70% yield.

2.3. Synthesis of the hydrogels

The method of preparing the pH- and temperature-responsive hydrogel is shown in Scheme 1. Typically, 400 mg mixture of HPC-*g*-AA and AA at given HPC-*g*-AA/AA weight ratio (as shown in Table 1) were dissolved in 4 mL of deionized water. After dissolution, the radical polymerization was carried out at 25 °C for 12 h, using APS (5.0 wt% based on HPC-*g*-AA and AA) as an initiator and TEMED as an accelerator. The compositions of the monomers and other reactants were listed in Table 1. After gelation, the hydrogel samples were transferred into a 200 mL beaker and immersed into deionized water, and the deionized water was refreshed six times in the first day and then four times a day for the following 6 days to remove the impurities.

2.4. Characterization

Proton nuclear magnetic resonance (^{1}H NMR) spectra were recorded by a Bruker 300 MHz spectrometer. FT-IR spectra were recorded on a Bruker Vertex 70 Fourier Transform Infrared spectrometer using the KBr disk method.

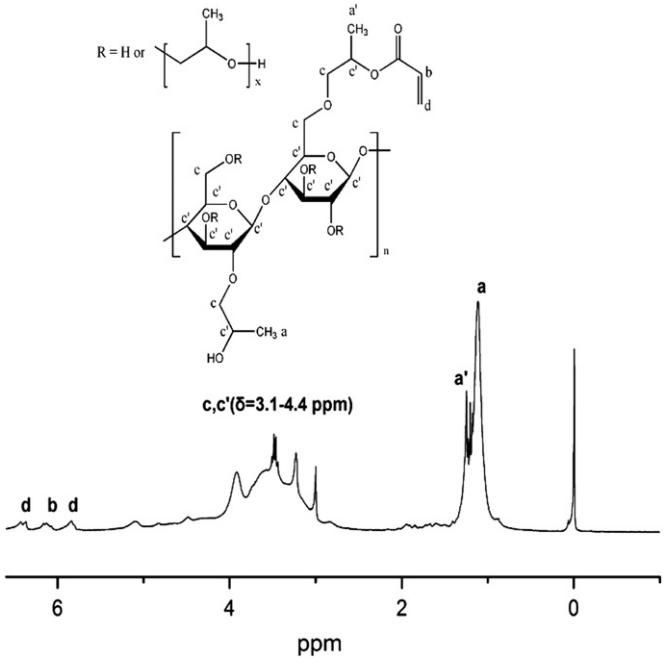

Fig. 1. ^{1}H NMR spectrum of HPC-*g*-AA.

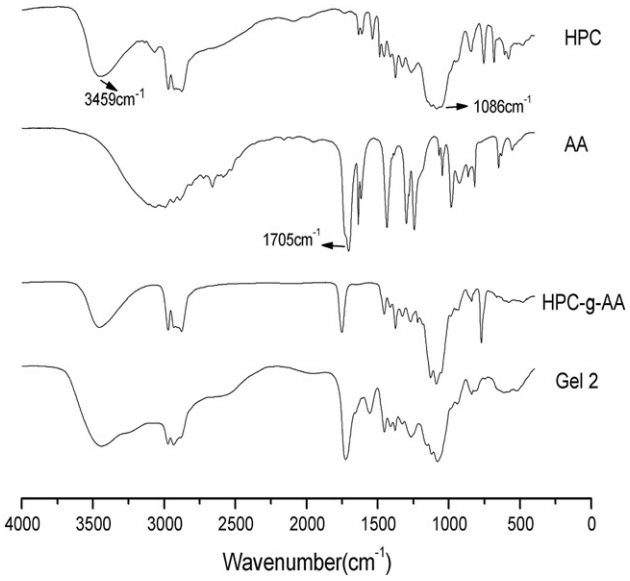

Fig. 2. FT-IR spectra of HPC, AA, HPC-*g*-AA, and Gel 2.

The morphologies of the hydrogels were investigated by environmental scanning electron microscopy (ESEM) on an XL 30 ESEM FEG Scanning Electron Microscope (Micrion FEI PHILIPS). The hydrogel samples were swollen in water for 48 h to reach equilibrium, and then quickly put into liquid nitrogen for 10 min and transferred into a freeze-dryer for 72 h. The samples were then loaded on the surface of a copper SEM specimen holder and sputter coated with gold before observation.

Phase transition measurements were carried out on a UV/vis spectrometer (Shimadzu UV-2401PC) equipped with a temperature controller (Shimadzu S-1700) with a hydrogel slab mounted in a glass cuvette. The heating rate was 0.5 °C/min over the temperature range of 25–60 °C.

2.5. Swelling of the hydrogels

To measure the swelling ratio of the hydrogels, the dried weighed quantity hydrogels were immersed into various solutions with certain pH and temperature for 2 days. The buffer solution was replaced frequently throughout the swelling process to insure the complete equilibration at the desired pH. The swelling ratio (gram per gram) SR of the hydrogels was calculated accurately according to the following equation:

$$SR = (W_t - W_0)/W_0 \quad (1)$$

where W_t and W_0 are the weights of the swollen gels and dried samples, respectively. All the experiments were carried out in triplicate, and the average values were reported.

2.6. In vitro enzymatic degradation of the hydrogels

The biodegradation of hydrogels was carried out in a small vial containing a small piece of dry hydrogel in 50 mL of PB solution (pH 7.4) with lipase (1 mg/mL). The mixture was then incubated at 37 °C with constant shaking (100 rpm). At different time intervals, the samples were taken out, rinsed thoroughly with deionized water and then lyophilized to calculate the dry weights of the hydrogels. The solution was replaced twice a day in order to maintain the

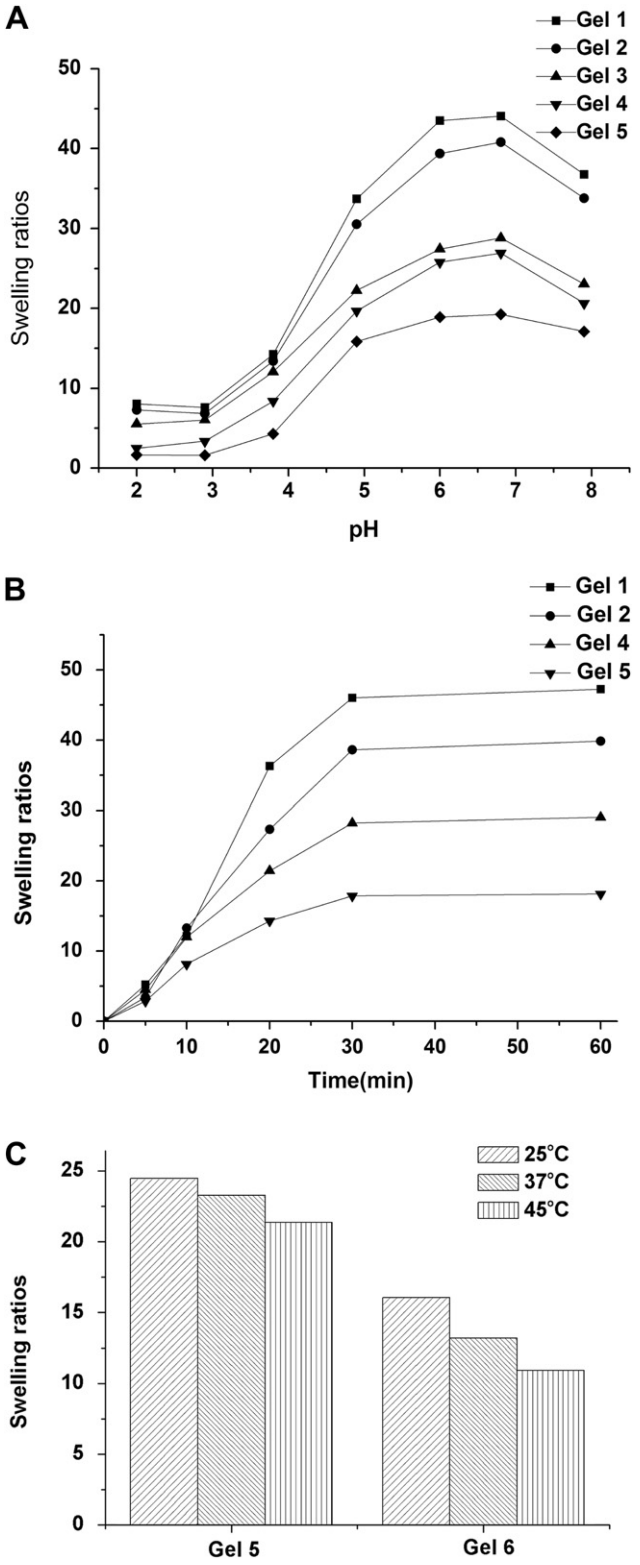

Fig. 3. Equilibrium swelling ratios of the hydrogels at different pH value (A), swelling kinetics of the hydrogels at 37 °C and pH 7.4 (B), and equilibrium swelling ratios of Gel 5 and Gel 6 at different temperature (C).

enzymatic activity. The percentage of remaining weight W_l (%) was calculated based on the following equation:

$$W_l(\%) = W_d/W_0 \times 100 \quad (2)$$

where W_0 is the original weight of the dried gel sample before immersion, and W_d is the weight of the dried sample after degradation at predetermined days.

2.7. Drug release studies

A hydrophilic model drug, bovine serum albumin, was loaded into the hydrogels by a swelling-diffusion method. The drug solution (5 mg/mL) was prepared in a 0.01 M phosphated buffer at pH 7.4. Then a dried and weighted cylindrical hydrogel was placed in 20 mL drug solution and allowed to swell for 1 day at 37 °C. After swelling equilibrium, the hydrogels were taken out and rinsed thoroughly with artificial gastric juice (pH = 1.2). The left drug solution and the artificial gastric juice used to rinse the drug-loaded hydrogel were collected together and further diluted to 50 mL in a volumetric flask. Then the amount of bovine serum albumin left in the loading medium was determined by a UV/vis spectrophotometer (Shimadzu UV-2401PC) at a wavelength of 280 nm.

To study the release behavior of drug from the hydrogels, the drug-loaded hydrogels were immersed into 15 mL of artificial gastric juice (pH = 1.2) for 2 h and then in artificial intestinal liquid (pH = 6.8) for another 6 h. The samples were incubated at 37 °C with constant shaking (100 rpm). At selected time intervals, 0.5 mL medium was withdrawn and replaced with 0.5 mL fresh solvent. The amount of released bovine serum albumin was quantified by the UV/vis spectrophotometer. All the release experiments were carried out in duplicate, and the averaged results were obtained.

3. Results and discussion

3.1. Synthesis and characterization

The HPC-*g*-AA was prepared by esterification between HPC and AA in the presence of EDC·HCl and DMAP as the coupling agent and catalyst, respectively, as depicted in Scheme 1(a). The hydroxyl groups of HPC reacted with AA to form HPC-*g*-AA with active double bond. To determine whether the double bond originated from acrylic acid bonded to HPC (Scheme 1), ^{1}H NMR measurement was carried out. As shown in Fig. 1a, the proton resonance absorption peaks of the double bond from AA appear at 6.44, 5.83, and 6.10 ppm, which confirm the coupling of the acryloyl group. The degree of substitution of HPC with AA is calculated by the following equation:

$$\text{AA graft efficiency}(\text{mol}\%) = \{I_b/[I_{c,c'} - (I_a + I_{a'})]\} * 7/3 * 100 \quad (3)$$

where I_b, $I_{c,c'}$, I_a and $I_{a'}$ are the integral values of the peaks at 6.10 ppm, 3.1–4.3 ppm, 1.2 ppm and 1.4 ppm, respectively. The degree of HPC modification with AA is 11 mol%.

The hydrogels were prepared by free radical polymerization using APS as an initiator according to the procedures described in Scheme 1(b). This free radical polymerization not only occurred in water but also successfully proceeded in DMSO.

The FT-IR spectra of HPC, AA, HPC-*g*-AA and Gel 2 are shown in Fig. 2. Comparison of the IR spectrum of HPC-*g*-AA and Gel 2 with that of HPC shows that new absorption appears at 1750 cm^{-1} (ν_{CO}), which can be assigned to the carbonyl group to confirm the formation of the acryloyl groups. The characteristic absorption of carbonyl group from the AA and hydroxyl from HPC at about 3459 cm^{-1} (ν_{OH}) of hydrogels were also observed in the IR spectrum of Gel 2. These results clearly confirmed that the biodegradable pH- and temperature-sensitive hydrogels were prepared.

3.2. Swelling behaviors

The swelling behaviors of hydrogels were measured at various pH values (I = 0.5 M) as shown in Fig. 3. The hydrogels exhibited

a lower swelling ratio in the acidic medium and the corresponding swelling ratios increased with an increasing pH value, while in the alkali medium the corresponding swelling ratios decreased with the pH value increasing due to the poor solubility of HPC in the alkali medium. For instance at pH 2.0, the swelling ratios of Gel 1 to Gel 5 were 8.0, 7.3, 5.5, 2.5, and 1.6, respectively. At pH 6.8, the swelling ratios increase to 44.0, 40.8, 28.8, 26.9 and 19.2, respectively. However, in the alkaline medium (pH 7.9), the swelling ratios were 36.8, 33.8, 23.0, 20.7 and 17.1, respectively, which were lower than those at pH 6.8. This is because that the hydrogen bonding interactions between the free carboxylic acid groups of the hydrogel networks were strong in the acid medium and the hydrogel network became tight and compact which resulted in lower swelling ratios. However, in the neutral medium, the hydrogen bonds could be broken and electrostatic repulsion among PAA segments could repel chain moieties in the network leading to higher swelling ratios. This finding is also in agreement with previous studies [18–20].

As shown in Fig. 3A, the influence of pH value on the swelling ratios was most remarkable for Gel 1. It was also found that although the swelling ratios of each hydrogel were different at different pH values, the swelling ratio of which became lower with the increase in HPC-*g*-AA amount at a specific pH value. The reason was that PAA chains exhibited better hydrophilcity compared with HPC-*g*-AA chains, so the hydrogels containing more PAA chains showed higher swelling ratios. Fig. 3B indicates the swelling rate of hydrogels at pH 6.8. It was found that all the hydrogels exhibited a fast swelling and reached equilibrium within 30 min. The temperature-responsive swelling ratios of the hydrogels were also measured. The results are shown in Fig. 3C. It could be seen that the hydrogels had a higher swelling ratio at the lower temperature, and the corresponding swelling ratios decreased with the temperature increasing. The swelling ratios of Gel 6 decreased obviously because of its high content of temperature-sensitive HPC-*g*-AA segments.

3.3. Phase transition studies

The phase transition behaviors of the hydrogels were characterized by monitoring the turbidity of the hydrogels as the temperature changed. Because the hydrophilicity of PAA could be tuned by pH variation, the phase transition behaviors were expected to show pH-dependence based on the tunable hydrophilicity of the PAA component. As shown in Fig. 4, both Gel 4 and Gel 6 showed a lower transmittance at a lower pH value, while the LCST of Gel 4 and Gel 6 increased with the pH increasing due to the better hydrophilicity of PAA at the higher pH value. Furthermore, as shown in Fig. 5, the transmittance percentage of the hydrogels decreased as the weight percentage of PAA increased, while the phase transition would become sharper if the content of temperature-sensitive HPC-*g*-AA segments increased. These phenomena should be attributed to the hydrophilicity of the PAA segments at pH 7.0. In this case, the higher content of PAA led to a more hydrophilic hydrogel, resulting in a less change in transmittance during phase transition.

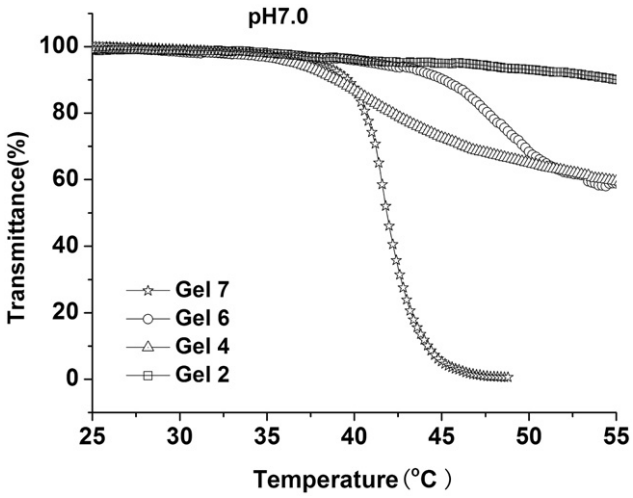

Fig. 5. Effect of temperature on the phase transition behavior of the hydrogels at pH 7.0.

3.4. In vitro enzymatic biodegradability of hydrogels

The hydrogels were immersed into 50 mL of PB solution (pH 7.4) with lipase (1 mg/mL) at 37 °C to investigate the degradation behavior (Fig. 6). In our experiments all the hydrogels showed various extents of weight loss. It was founded that the lower content of HPC-*g*-AA in the hydrogels resulted in the more rapid degradation rate. Gel 1 lost 43% of its weight in 50 mL of PB solution (pH 7.4) with lipase (1 mg/mL) after 10 days, while corresponding weight loss of Gel 4 and Gel 6 were only 17% and 10%, respectively. The degradation rate decreased with the order of Gel 1 > Gel 4 > Gel 6. Because of the ester bond conjugated between the HPC chains and PAA chains, the hydrogels containing less HPC-*g*-AA exhibited higher degradation rate.

3.5. Hydrogels morphology

To examine the surface and interior structures of the hydrogels in swollen state, ESEM measurement was performed. As shown in

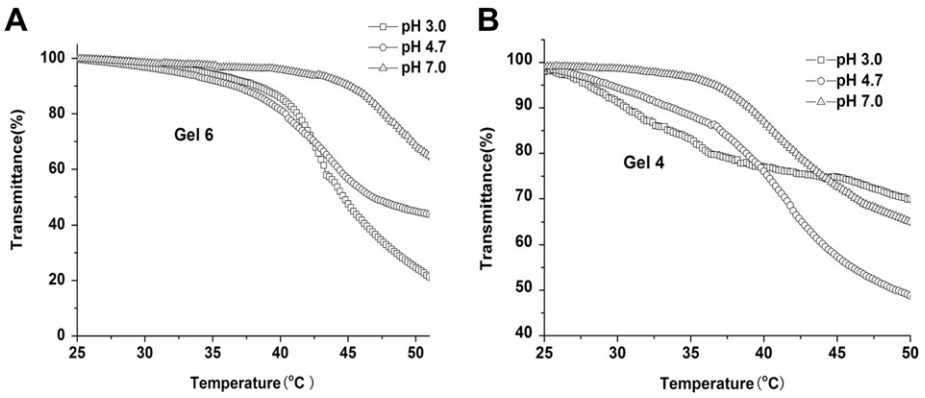

Fig. 4. Effect of temperature on the phase transition behavior of Gel 6 (A) and Gel 4 (B) at different pH value.

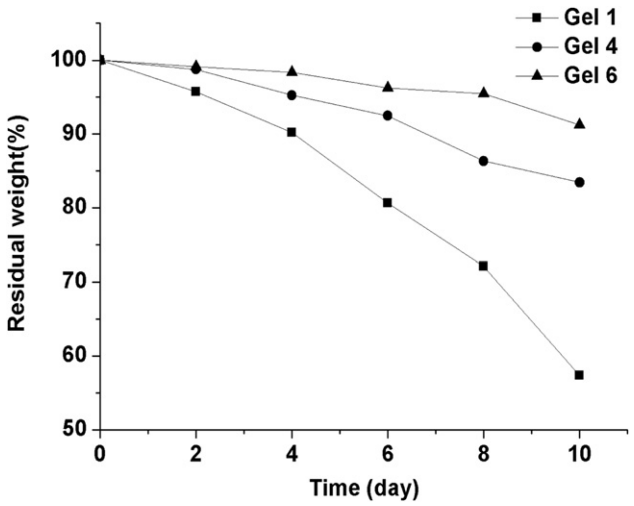

Fig. 6. Degradation of the hydrogels in 50 mL of PB solution (pH 7.4) with lipase (1 mg/mL) at 37 °C.

Fig. 7, the SEM images of freeze-dried HPC-*g*-AA/AA hydrogels exhibited a highly macroporous sponge like structure and the pore size of the hydrogels containing more HPC-*g*-AA was bigger than those containing less HPC-*g*-AA. The pore sizes of hydrogels had a close relationship with the crosslinking level and the materials composed of the hydrogels. So the pore sizes and structures were depended on the content of HPC-g-AA. It was found that the pore sizes decreased in the order of Gel 4 > Gel 5 > Gel 2 > Gel 1. The reason is that: the crosslinking level increased as the content of HPC-*g*-AA increased, but HPC-*g*-AA has a large molecular weight and a rigid backbone, thus the Gel 4 with more HPC-*g*-AA contents has bigger pore sizes and more irregular structure than others. As the crosslinking level further increased, the pore size of Gel 5 was smaller than Gel 4. Compared with PAA chain, HPC with ring structure of saccharides shows more rigidity. It is worth mentioning that during the free radical copolymerization less $CH_2{=}CH_2-$ groups of HPC-*g*-AA react with PAA because of the steric effect, so the hydrogels containing more HPC-*g*-AA exhibit lower crosslinking level and larger pore size.

3.6. *In vitro* release of BSA

In vitro BSA release profiles of hydrogels in artificial gastric juice (pH = 1.2) for the first 2 h and then in artificial intestinal liquid (pH = 6.8) for the subsequent 6 h were investigated at 37 °C, and the results were shown in Fig. 8. It was found that there was a burst release at the initial stage. The relatively rapid release at the initial stage was attributed to the release of drug located at the hydrogels surface. When the hydrogel was placed into the buffer solution, the drug at the hydrogels surface could be dissolved immediately, leading to the burst release. The initial burst release of BSA from other drug carriers was also reported previously [33–35]. The cumulative release amount from the hydrogels was lower in the artificial gastric juice after the initial burst releases at the first 2 h, while in artificial intestinal liquid the rate of release became rapid especially in the first half hour due to the higher swelling ratio in artificial intestinal liquid. After the burst releases, the hydrogels served as diffusion barriers and the drugs were mainly released by the diffusion mechanism. The release rate in artificial gastric juice decreased in the order of Gel 5 > Gel 4 > Gel 3 > Gel 2, which was consistent with the change in the content of pH-sensitive PAA within the hydrogels. Higher PAA content resulted in lower swelling ratios and less BSA released from the hydrogel. In contrast, the release rate in artificial intestinal liquid decreased in the order of Gel 4 > Gel 2 > Gel 3 > Gel 5, which due to both the pore size and the swelling ratios. For example, for Gel 4 about 80% BSA released after 8 h, whereas the corresponding cumulative release amount for Gel 2, Gel 3 and Gel 5 were 78%, 74%, and 63%, respectively.

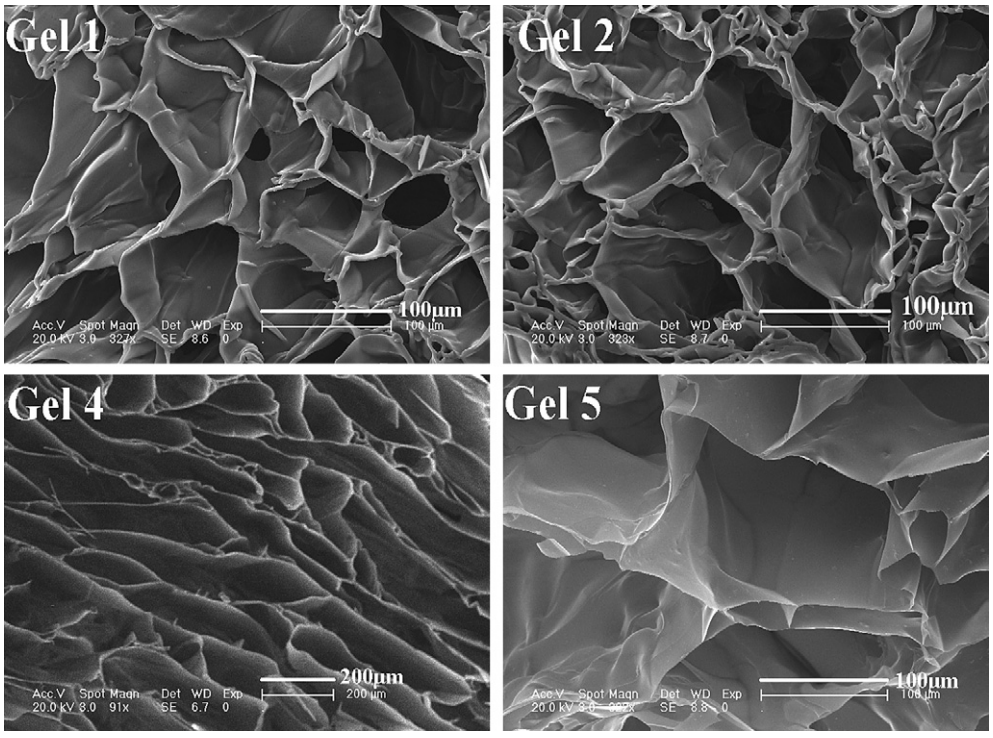

Fig. 7. SEM micrographs of the hydrogels.

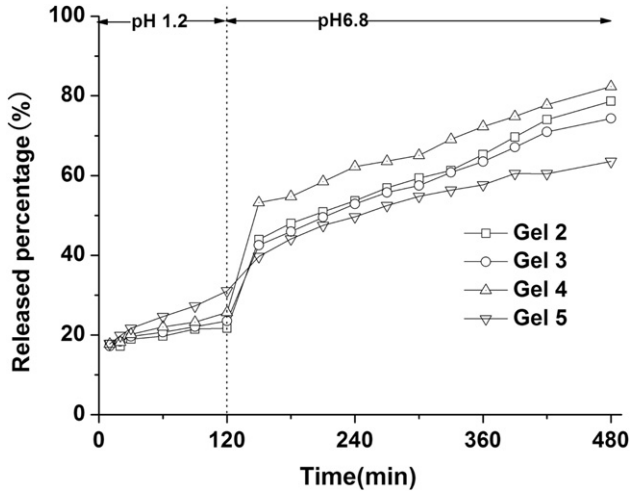

Fig. 8. Cumulative release of BSA from the hydrogels as a function of time at 37 °C.

Therefore, it can be concluded that the HPC-*g*-AA and PAA segments have cooperative effect on the drug release rate.

4. Conclusion

A series of pH- and temperature-sensitive hydrogels were synthesized by the radical copolymerization between HPC-*g*-AA and PAA using APS as the initiator. The hydrogels exhibited pH sensitivity and a higher swelling ratio was observed at a higher pH value in the solution. Although there was no remarkable difference between the equilibrium swelling ratios at different temperature, the temperature exhibited great influence on the optical transmittance of hydrogels, which determined that the HPC-*g*-AA moieties of hydrogels exhibited a hydrophobic property at temperature above its LCST. ESEM observations revealed that all the hydrogels had similar highly macroporous sponge like structures and a higher HPC-*g*-AA weight percentage resulted in a larger pore size. The hydrogels showed biodegradability and the degradation rate could be controlled by changing the composition ratio. The *in vitro* release data of BSA from the hydrogels demonstrated that the drug release rate at pH 1.2 was slower than that at pH 6.8 due to the protonation of the PAA part at an acidic condition. The results showed the possibility of using this pH- and temperature-sensitive hydrogel as an intelligent drug delivery carrier.

Acknowledgement

This project is financially supported by the National Natural Science Foundation for Young Scholar of China (50903012) and the Jilin Provincial Research Foundation for Young Scholar (20090143).

References

[1] Chaterji S, Kwon IK, Park K. Prog Polym Sci 2007;32:1083–122.
[2] Peppas NA. Int J Pharm 2004;277:11–7.
[3] Ulijn RV, Bibi N, Jayawarna V, Thornton PD, Todd SJ, Mart RJ, et al. Mater Today 2007;10:40–8.
[4] Lee KY, Yuk SH. Prog Polym Sci 2007;32:669–97.
[5] Peppas NA, Hilt JZ, Khademhosseini A, Langer R. Adv Mater 2006;18:1345–60.
[6] Kim SJ, Kim MS, Kim SI, Spinks GM, Kim BC, Wallace GG. Chem Mater 2006;18:5805–9.
[7] Sangeetha NM, Maitra U. Chem Soc Rev 2005;34:821–36.
[8] Luo Y, Shoichet MS. Nat Mater 2004;3:249–53.
[9] Von Recum HA, Kim SW, Kikuchi A, Okuhara M, Sakurai Y, Okano T. J Biomed Mater Res 1998;40:631–9.
[10] Hoare TR, Kohane DS. Polymer 2008;49:1993–2007.
[11] Soussan E, Cassel S, Blanzat M, Rico-Lattes I. Angew Chem Int Ed 2009;48:274–88.
[12] He CL, Kim SW, Lee DS. J Control. Release 2008;127:189–207.
[13] Namkung S, Chu CC. J Biomater Sci Polym Ed 2007;18:901–24.
[14] Xiang YQ, Zhang Y, Chen DJ. Polym Int 2006;55:1407–12.
[15] Zhao Y, Kang J, Tan TW. Polymer 2006;47:7702–10.
[16] Katime I, Quintana JR, Valderruten NE, Cesteros LC. Macromol Chem Phys 2006;207:2121–7.
[17] Shim WS, Yoo JS, Bae YH, Lee DS. Biomacromolecules 2005;6(6):2930–4.
[18] Zhang XZ, Wu DQ, Chu CC. Biomaterials 2004;25:4719–30.
[19] Zhang C, Zhao K, Hu T, Cui X, Brown N, Boland T. J Controlled Release 2008;131:128–36.
[20] Liu F, Urban MW. Macromolecules 2008;41:6531–9.
[21] Schild HG. Prog Polym Sci 1992;17:163–249.
[22] Jiang HL, Zhu KJ. J Appl Polym Sci 2006;99:2320–9.
[23] Casadei MA, Pitarresi G, Calabrese R, Paolicelli P, Giammona G. Biomacromolecules 2008;9:43–9.
[24] Gyenes T, Torma V, Gyarmati B, Zrinyi M. Acta Biomater 2008;4:733–44.
[25] Myung D, Koh WU, Ko JM, Hu Y, Carrasco M, Noolandi J, et al. Polymer 2007;48:5376–87.
[26] Lau AC, Wu C. Macromolecules 1999;32:581–4.
[27] Alzari V, Monticelli O, Nuvoli D, Keeny JM, Mariani A. Biomacromolecules 2009;10:2672–7.
[28] Cai T, Hu ZB. Macromolecules 2003;36:6559–64.
[29] Gao J, Haidar G, Lu XH, Hu ZB. Macromolecules 2001;34:2242–7.
[30] Lu XH, Hu ZB, Gao J. Macromolecules 2000;33:8698–702.
[31] Lu XH, Hu ZB, Schwartz J. Macromolecules 2002;35:9164–8.
[32] Chen Y, Ding D, Mao ZQ, He YF, Hu Y, Wu Y, et al. Biomacromolecules 2008;9:2609–14.
[33] Patil NS, Dordick JS, Rethwisch DG. Biomaterials 1996;17:2343–450.
[34] Chiba M, Hanes J, Langer R. Biomaterials 1997;18:893–901.
[35] Zhang YL, Chu CC. J Mater Sci Mater Med 2002;13:773–81.

Polymer 52 (2011) 683–693

Contents lists available at ScienceDirect

Polymer

journal homepage: www.elsevier.com/locate/polymer

Synthesis of non-collapsed hollow polymeric nanoparticles with shell thickness on the order of polymer gyration radius

Ye Changhuai, Luo Yingwu*, Liu Xuesong

The State Key Laboratory of Chemical Engineering, Department of Chemical and Biological Engineering, Zhejiang University, Hangzhou 310027, PR China

ARTICLE INFO

Article history:
Received 27 October 2010
Received in revised form
10 December 2010
Accepted 14 December 2010
Available online 21 December 2010

Keywords:
Hollow nanoparticles
Living radical polymerization
Miniemulsion polymerization

ABSTRACT

The hollow polymeric nanoparticles of poly(styrene-co-divinylbenzene) of ultra-thin shell were synthesized by the interfacial RAFT miniemulsion polymerization with various particle sizes, void fractions and crosslinking degrees. With the void fraction increased, the hollow nanoparticles were more likely to collapse once dried. This collapse could be suppressed by simply increasing the level of crosslinker. The fraction of the collapsed hollow particles decreased nearly linearly with the increasing level of crosslinker. The non-collapsed hollow nanoparticles with a void fraction about 60% and shell thickness of 11.5 nm were fabricated with the crosslinker (divinylbenzene) of 0.67 mass fraction based on monomers. The resulted polymeric shell of the hollow nanoparticles was mesoporous, which had high surface area 514 m^2/g, extremely large pore volume 2.74 ml/g and a most probable pore diameter of 9 nm. The structures of the hollow nanoparticles were mechanically stable not only in the solvent but also under harsh conditions like high temperature (200 °C) and strong shear. Additionally, the hollow nanoparticles were able to be fully re-dispersed in the solvent. The average hollow particle diameter was tuned from 70 nm to 199 nm by decreasing the level of the amphiphilic RAFT agent. The shell thickness was tuned from 10.6 nm to 19.3 nm by changing the core/shell ratios.

1. Introduction

In the past decade, considerable efforts have been devoted to obtain well-defined hollow micro/nano-particles [1–5]. The unique core/shell nanostructures offer many new opportunities in a large variety of application fields. On one hand, the properties like dielectric constant, refractive index [6], density, thermal conductivity could be largely tuned by the void of the hollow particles, leading to many emerging functional materials like anti-reflective coatings [7], opaque polymers [8] and super thermal insulation materials [9]. On the other hand, the hollow nanoparticles could be used as nano-containers and nanoreactors, which catalyzes many new applications. Applications of hollow nanoparticles in lithium batteries [10], catalyst [7] and sensors [11], and biomedical applications [12] are emerging.

The synthesis of polymeric hollow micro/nano-particles has been extensively investigated, which was mainly driven by the possible applications in drug delivery [13,14]. Many novel techniques such as block copolymer self-assembly in the selective solvent [15,16], layer-by-layer assembly of polyelectrolyte on the performed particle template [17], living radical polymerization initiating from the performed particle template [18], self-assembling of phase-separated polymer (SaPSeP) method [19–21] and interfacial confined (mini)emulsion polymerization [22,23], were proposed to synthesize the polymeric nanocapsules. The hollow particles were then obtained by the removal of the core materials. Layer-by-layer assembly method showed fine control over particle size and shell thickness in the nano-scale. However, these synthesis methods involving many repeated procedures are too tedious and time-costing. SaPSeP was used to synthesize the micrometer size hollow particles and the core-shell structures were found to be sensitive to the system parameters. Block copolymer self-assembly were often carried out in a very dilute solution. Interfacial confined miniemulsion polymerization presents a versatile route to prepare core/shell polymer structures, which is simple, highly efficient, green and scalable up.

It is critically important for the hollow nanoparticles to prevent from the collapse during post-treatment in the applications of the nanoparticles as the block units of bulk materials. Unfortunately, the hollow nanoparticles would collapse irreversibly once dried. So far, the as-prepared hollow polymer nanoparticles, especially with a relative large void fraction, are only stable while kept in solution. Co et al. [22] utilized interfacial free-radical alternating copolymerization to prepare liquid-core nanocapsules. The nanocapsules

* Corresponding author.
E-mail address: yingwu.luo@zju.edu.cn (L. Yingwu).

0032-3861/$ – see front matter © 2010 Elsevier Ltd. All rights reserved.
doi:10.1016/j.polymer.2010.12.030

had an average diameter of 218 nm and the shell thickness was about 10 nm. The TEM images showed the capsules were collapsed and flat. Matyjaszewski et al. [4] reported hollow polymeric nanocapsules with a crosslinked shell were prepared through an interfacially confined copolymerization via an activator generated by electron transfer atom transfer radical polymerization in a miniemulsion system. The collapse of hollow nanocapsules was also observed during the isolation procedures and subsequent drying. In Wooley's work [15], the micelle shell of diblock copolymer was post-crosslinked. The subsequent degradation of the core block led to the formation of covalent-stabilized nanocapsules. Such a crosslinked structure cannot be degraded by solvent. However, after deposition on substrates, the hollow nanoparticles collapsed into highly flattened objects. Hawker et al. [24] also used the post-crosslinking strategy to synthesize the crosslinked nanocapsules. The polymer brush growing from the surface of silica nanoparticles via living radical polymerization was successively crosslinked. The hollow crosslinked nanoparticles were obtained by the removal of silica nanoparticles. It was found that the individuality of nanoparticles could remain stable against solvent dissolution and under thermal heating. However, the hollow nanostructures were collapsed when the core template was removed. Walt et al. [1] reported surface-initiated controlled/living radical polymerization to prepare hollow polymer microspheres by chemical etching. The well-defined hollow spheres without collapse were obtained but the particles were a few micrometers in diameter and several hundred nanometers in shell thickness. McDonald et al. [25] introduced a two-stage method of emulsion polymerization to produce voided particles by encapsulation of a nonsolvent. The obtained particles with 230 nm in diameter and 33% void fraction were not collapsed. In such a process, when the void fraction was increased up to 50%, the particle diameter increased up to 1 μm.

The reasons for the collapse of hollow polymer nanoparticles are not clearly known yet. For micrometer size hollow polymer particles, the buckling could occur due to the decreased tensile modulus of the low-crosslinked polymer shell in the presence of some solvent [26]. For the hollow polymeric nanoparticles of 100 nm in diameter, the shell thickness, which is determined by the particle size and void fraction, is often on the order of 10 nm. It is expected that the mechanical properties of polymeric structures would be size-dependent with dimensions from 10 to 100 nm since the gyration radius of polymeric molecules are on the order of 5–10-nm. Unfortunately, much less is known about the properties of amorphous polymeric nanoscopic structures. Simulations on polystyrene have revealed that the Young's modulus of polystyrene exhibits a pronounced decrease below 50 nm. Furthermore, the calculations indicated the existence of mechanical inhomogeneities on the scale of a few nanometers [27,28]. On the other hand, with the particle size decreased to 100 nm order of magnitude, the capillary forces become significant during drying [29,30]. The poor mechanical properties of polymeric nano-thin shell together with the strong capillary force present a great challenge for fabricating the hollow polymeric nanoparticles, which are non-collapsed during drying and other post-applications. To our best knowledge, there is no report on the synthesis of non-collapsed hollow polymeric nanoparticles with shell thickness on the order of 10 nm. Generally speaking, crosslinking can increase the mechanical properties of polymer materials. However, post-crosslinking of the hollow nanocapsules failed to obtain the non-collapsed hollow nanoparticles [15,24]. In this paper, the hollow polymeric nanoparticles with the crosslinked polymer shell will be fabricated with the interfacial RAFT miniemulsion polymerization, which was previously invented by our group [23]. The mechanism of the interfacial RAFT miniemulsion polymerization [23] allows us to synthesize the hollow nanoparticles with tunable void fractions, particle sizes, and crosslinking degrees. Particularly, the crosslinking degree can be increased up to an unprecedentedly high level. The influence of these structural parameters on the collapse of the hollow polymer nanoparticles will be investigated, aiming at the synthesis of the non-collapsed hollow polymer particles.

2. Experimental section

2.1. Material

Methacrylic acid (MAA, CP) and styrene (St, CP) were dried via activated molecular sieve and distilled under reduced pressure. Methyl methacrylate (MMA, CP) was washed with 10% NaOH aqueous solution and then distilled under reduced pressure. Divinylbenzene (DVB, 80%) was washed with 10% NaOH aqueous solution and then dried via activated molecular sieve. Azobis-(isobutyronitrile) (AIBN) was purified by re-crystallization in ethanol. 4-cyano-4-(dodecylsulfanylthiocarbonyl) sulfanylpentanoic acid (CDPA) was prepared according to literature [31]. 4,4′-Azobis(4-cyanopentanoic acid) (V-501, 98%), dioxane (AR), Paraffin (Tm = 25 °C), sodium hydroxide (NaOH, AR), sodium nitrite (AR) and sodium lauryl sulphate (SDS, 85%) were used as received.

2.2. Synthesis of hollow nanoparticles

The amphiphilic RAFT agent (amphi-RAFT) was synthesized by RAFT solution copolymerization of MMA and MAA mediated by CDPA. 2.00 g CDPA, 0.22 g V501, 7.67 g MAA and 5.98 g MMA were dissolved in 31.73 g dioxane, then the solution was transferred into a three-necked round flask to polymerization at 80 °C for 8 h. The monomer conversion was almost 100%. The theoretical Mn was 3154 g/mol. The Mn and polydispersity index (PDI) of the obtained amphi-RAFT were measured to be 2780 g/mol and 1.22, respectively from gel permeation chromatograph (GPC). Considering the measurement errors, GPC results suggested that the RAFT polymerization should be well controlled. So, the obtained amphi-RAFT had the structure as designed, which is shown in Scheme 1.

Miniemulsions were prepared according to the previous report [32]. 0.6 g amphi-RAFT, 0.12 g NaOH together with 0.1 g $NaNO_2$ were dissolved in 80 g deionized water. The pH value of the aqueous solution was then adjusted to 6.4 by diluted vitriol aqueous solution. The oil phase, a total amount of 20 g containing St, DVB (crosslinker), paraffin (core material) and 0.1 g AIBN, was mixed with the aqueous solution. The mixture was pre-emulsified by magnetic stirring for 30 min. After that, the coarse emulsion was subjected to ultrasonication (JOY-II, 600W) for 10 min to form miniemulsion. In order to enhance the stability of miniemulsion, an additional 0.1 g SDS was post added to the miniemulsion. The final miniemulsion was transferred to a 250 mL four-neck round flask in nitrogen atmosphere. The polymerization was started by elevating temperature to 70 °C and lasted for 6.5–8 h. After polymerization, the product latex of nanoparticles was demulsified by HCl solution and re-dispersed in THF for over 12 h. Thus, the core material (paraffin) was dissolved completely in THF and the nanoparticles without paraffin were precipitated from their THF solution by n-hexane. The hollow nanoparticles were obtained after removing n-hexane by drying at 75 °C oven for over 3 h.

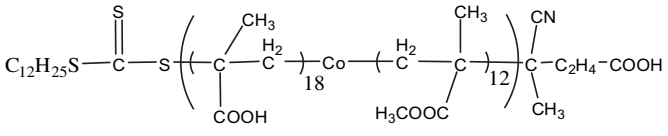

Scheme 1. The structure of the amphi-RAFT.

2.3. GPC analysis

Number-average molecular weight (Mn) and PDI (Mw/Mn) were measured by gel permeation chromatography with Waters styragel columns HR 4, 3, and 1. Tetrahydrofuran (THF) was used as the eluent. A flow rate was 1 mL/min. Molar masses were calculated by using the calibration curve based on polystyrene standards (molar mass range, 100–710000 g/mol for columns HR 4, 3, and 1).

2.4. Monomer conversion

Monomer conversion was measured by gravimetry.

2.5. pH value measurement

The pH values of the amphi-RAFT aqueous solution were determined by a pH meter (LEICI PHS-2C) equipped with the electrode E-201-C.

2.6. TEM observations

The morphologies of hollow nanoparticles were visualized by transmission electron microscopy (JEOL JEMACRO-1230) at the operating voltage of 80 kv.

2.7. SEM observations

The morphologies of hollow nanoparticles were observed with scanning electron microscope (Hitach S4800 and ULTRA 55) at the operating voltage of 5 kv.

2.8. BET

Nitrogen adsorption and desorption isotherms were performed at −196 °C by Autosorb-1-C (Quantachrome Company) and the degassing temperature was 150 °C.

2.9. DLS

The particle size of re-dispersed hollow nanoparticles was measured by dynamic light scattering with a Malvern ZETASIZER 3000.

3. Results and discussion

The formation of nanoparticles in the process of RAFT interfacial miniemulsion polymerization.

In a typical miniemulsion, the oil droplets of 30–500 nm in diameter are dispersed in water in concentration of about 10^{17}/L water. In the well-controlled miniemulsion polymerization, the oil droplets of monomer act as the nanoreactors in which polymerization takes place, resulting in polymeric nanoparticles with sizes close to the original droplets [33,34]. When the oil droplets are designed to be a mixture of monomer with an inner liquid oil, the polymerization could trigger phase separation, leading to the formation of core/shell structures with a polymeric shell encasing the liquid oil in the cases where the interfacial tensions of each phase are suitable [35]. However, a highly crosslinked polymer shell is difficult to be fabricated by the conventional miniemulsion polymerization, where the polymerization occurs homogenously within the oil droplets, since the formed crosslinked polymer is not able to move to oil/water interface [36]. Recently, the amphi-RAFT was used to construct an interfacial confined living miniemulsion polymerization [23,32], where the radical polymerization was confined at the interface of the droplets/water. The process is particularly suitable for fabricating the polymer core/shell structures since the polymeric nano-shell is in-situ formed by the living growth of the polymer chains during the polymerization.

In the Exp.1 (refer to Table 1), the hollow nanoparticles sampled at different monomer conversions were observed by TEM and SEM (Fig. 1). The monomer conversion reached 89% at 390 min. As seen in Fig. 1, the core/shell structures were clearly seen from low conversion and the shell of the hollow particles gradually thickened with the increase of monomer conversion. However, when the conversion was low, like 33%, the shell of the hollow particles was very thin, just a few nanometers, and the crosslinking density might also be relatively low. As a result, all of the hollow nanoparticles were collapsed and aggregated together to form honeycomb structures, as seen in Fig. 1 (right). With the polymerization going on, the thickness of the polymer shell increased and the collapse became gradually less severe. As a matter of fact, at 89% conversion, where the thickness of the polymer shell was about 17 nm, almost all of the hollow nanoparticles remained sphere shape without collapse. During the whole course of the polymerization, the average particle diameter by volume remained roughly constant at about 108 nm.

3.1. Effect of crosslinking degree of the polymer shell on the collapse of the hollow nanoparticles

To investigate the effect of crosslinking degree of the polymer shell, the fraction of DVB (crosslinker) among monomers was changed from 0.12 to 0.48 (Exp.2–Exp.5 and Exp.7). The morphologies of the resulted hollow particles were observed by TEM and

Table 1
The recipe for miniemulsion polymerization.

Exp.	shell/core[a]	Crosslinker fraction[b]	St g	RAFT g	DVB g	Paraffin g	Conversion %	Calculated void fraction
1	3:1	0.40	7.50	0.6	7.50	5.00	89	0.34
2	2:1	0.12	11.33	0.6	2.00	6.67	99	0.41
3	2:1	0.24	9.33	0.6	4.00	6.67	97	0.41
4	2:1	0.32	8.00	0.6	5.33	6.67	92	0.42
5	2:1	0.48	5.33	0.6	8.00	6.67	94	0.42
6	4:1	0.40	8.00	0.6	8.00	4.00	95	0.26
7	2:1	0.40	6.66	0.6	6.66	6.67	90	0.43
8	1:1	0.40	5.00	0.6	5.00	10.00	94	0.59
9	3:1	0.40	7.50	1.2	7.50	5.00	80	0.36
10	3:1	0.40	7.50	0.2	7.50	5.00	87	0.34
11	1:1	0.67	1.70	0.6	8.30	10.00	94	0.59

[a] The shell/core is mass ratio of shell to core.
[b] The crosslinker fraction is based on mass fraction among monomer.

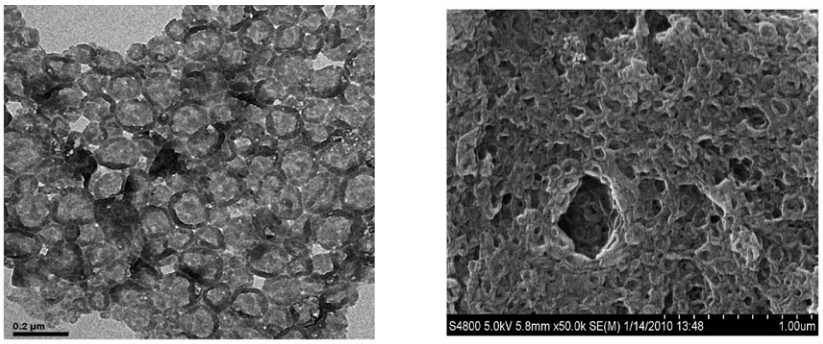

A 33%

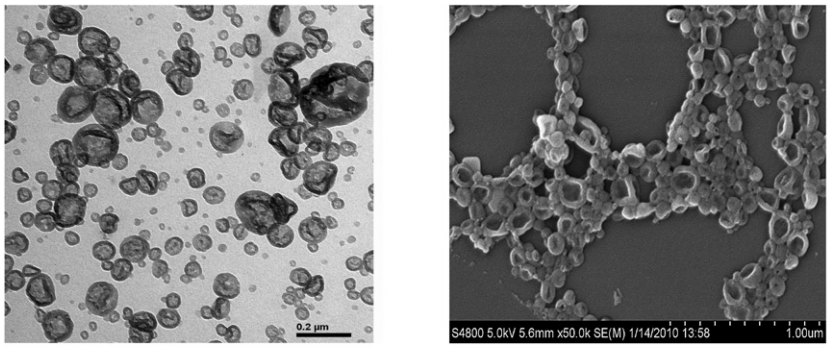

B 52%

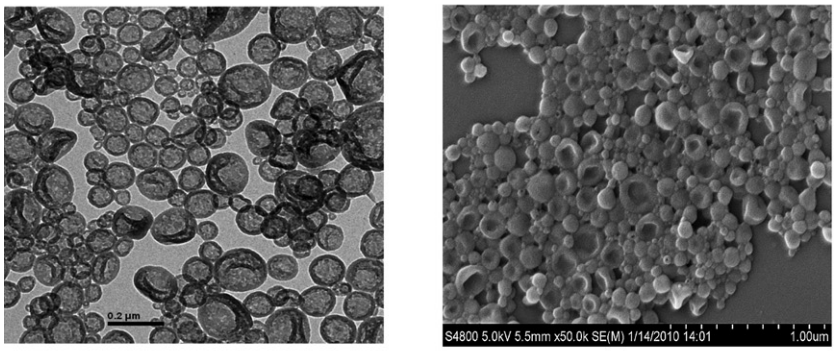

C 67%

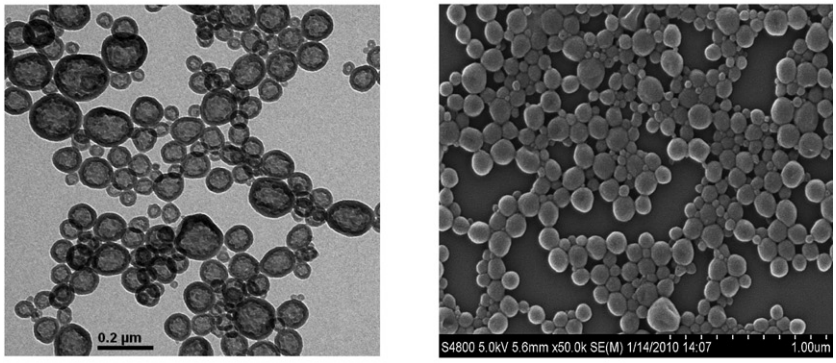

D 89%

Fig. 1. TEM images (left) and SEM images (right) of hollow nanoparticles at various conversions. The mass fraction of DVB was 0.40 and the amount of amphi-RAFT was 0.6g with the shell/core = 3:1.

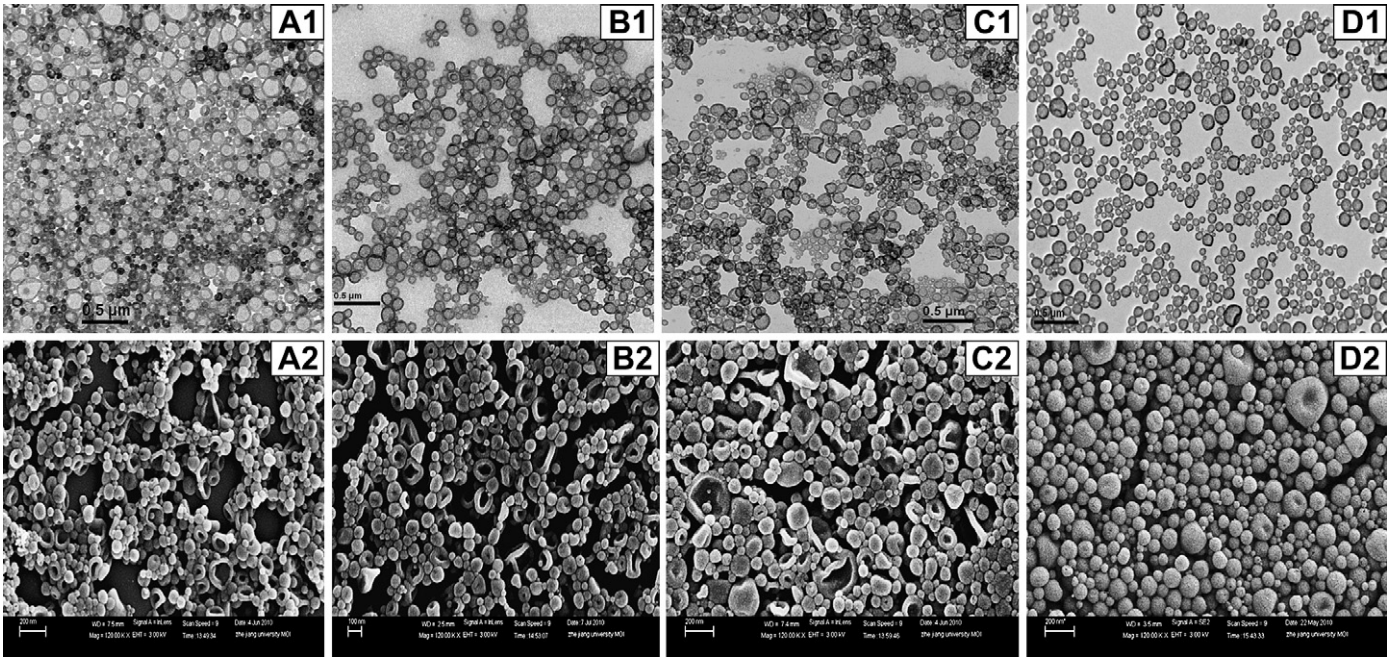

Fig. 2. TEM (top) and SEM (bottom) images for hollow nanoparticles with different mass fractions of crosslinker, (A1, A2): 0.12, (B1, B2): 0.24, (C1, C2): 0.32 and (D1, D2): 0.48. The amount of amphi-RAFT was 0.6 g with shell/core = 2:1.

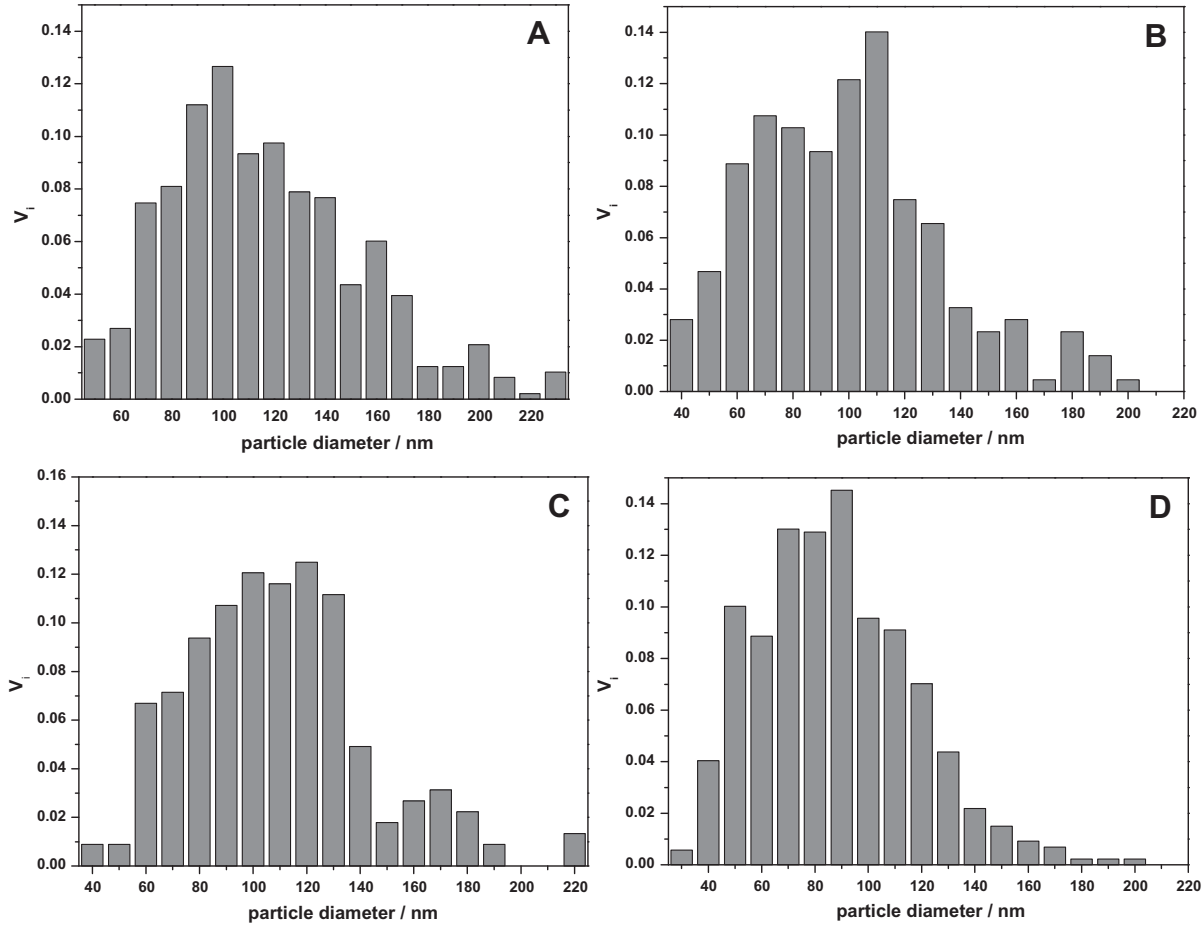

Fig. 3. Size distributions by number of hollow nanoparticles with different mass fraction of crosslinker, A: 0.12, B: 0.24, C: 0.32, D: 0.48, statistically counted from TEM images. The amount of amphi-RAFT was 0.6 g with shell/core = 2:1.

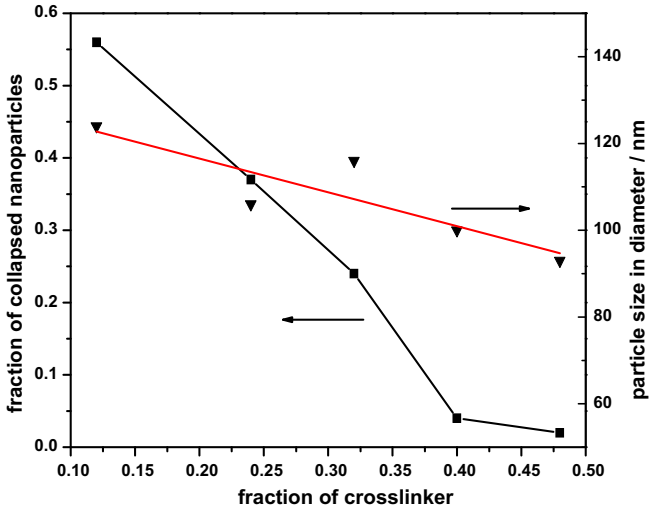

Fig. 4. The effect of mass fraction of crosslinker on the particle size by volume and the fraction of collapsed hollow nanoparticles. The amount of amphi-RAFT was 0.6 g with shell/core = 2:1.

SEM. The typical images are shown in Fig. 2. As shown in Fig. 2, the core/shell structures are clearly seen in all cases. Fig. 3 shows size distributions by number of hollow nanoparticles with different mass fraction of crosslinker statistically counted from TEM images. The average particle sizes by volume decreased from 124 nm at DVB = 0.12–93 nm at DVB = 0.48. The fraction of the collapsed nanoparticles, which was obtained by statistically counting the particles with obvious buckling among over 500 particles from SEM images, decreased quickly from 0.56 at DVB = 0.12 to 0.04 at DVB = 0.40 and then leveled off, as seen in Fig. 4. It is suggested that increasing the crosslinking degree of the polymer shell offer an effective approach against the collapsing forces due to the increase in the stiffness of the polymer shell.

3.2. Effect of void fraction on the collapse of the hollow nanoparticles

It is easy to tune the void fraction of the hollow nanoparticles by changing the ratio of monomer to paraffin (core materials). In Exp.6–Exp.8 and Exp.1, the ratio was changed from 4/1 to 1/1 while the other conditions remained the same. Accordingly, the theoretical void fraction would be tuned from 0.26 to 0.59. From the TEM images shown in Fig. 5, almost all of the particles showed core/shell structures. Fig. 6 shows size distributions by number of hollow nanoparticles with various void fractions statistically counted from TEM images. The volume average particle size of the hollow nanopartciles for each case was quite constant at about 110 nm in diameter while the thickness of shell decreased roughly linearly from 19.3 nm to 10.6 nm as the theoretical void fraction increased from 0.26 to 0.59, as seen in Fig. 7. From the B group images in Fig. 5, it is evident that the increased void fraction would increase the fraction of the collapsed particles. The statistic data are presented in Fig. 7. In the case of 0.26 void fraction, few particles were collapsed. When the void fraction increases to 0.59, a quarter of hollow nanoparticles were collapsed. According to the thin shell theory [37,38], the critical pressure, P_c, for the onset of bucking is given by Eq. (1).

$$P_c = \frac{2Eh^2}{\sqrt{3(1-\nu^2)}R^2} \tag{1}$$

where E and ν are Young's modulus and Poisson ratio of polymeric shell, h and R are the thickness of shell and radius of hollow particles, respectively. P_c decreases with decrease of h/R, which is reciprocal proportion to the void fraction.

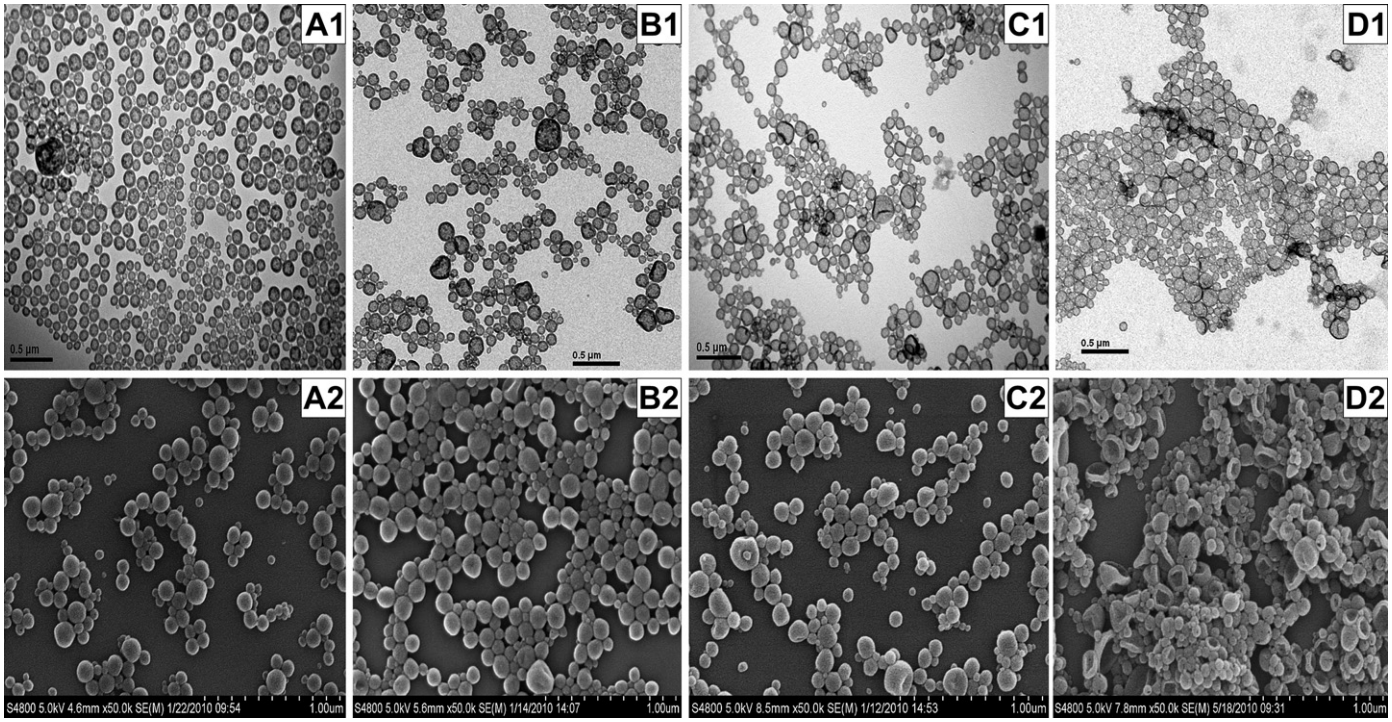

Fig. 5. TEM and SEM images for hollow nanoparticles at various void fractions (A1, A2): 0.26, (B1, B2): 0.34, (C1, C2): 0.43, (D1, D2): 0.59. The mass fraction of DVB was 0.40 and the amount of RAFT was 0.6 g.

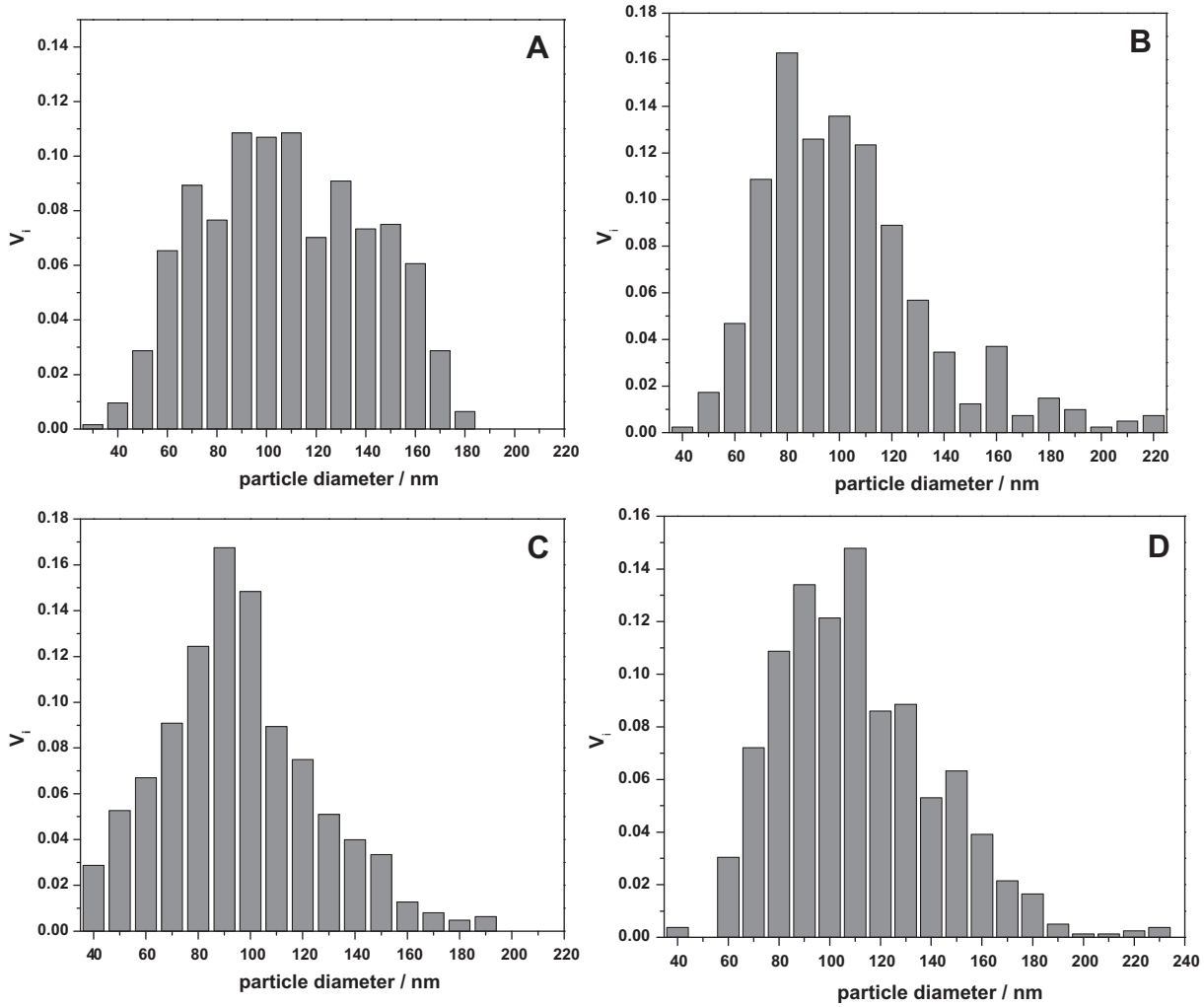

Fig. 6. Size distributions by number of hollow nanoparticles at various void fractions, A: 0.26, B: 0.34, C: 0.43, D: 0.59, counted statistically by TEM images. The mass fraction of DVB was 0.40 and the amount of RAFT was 0.6 g.

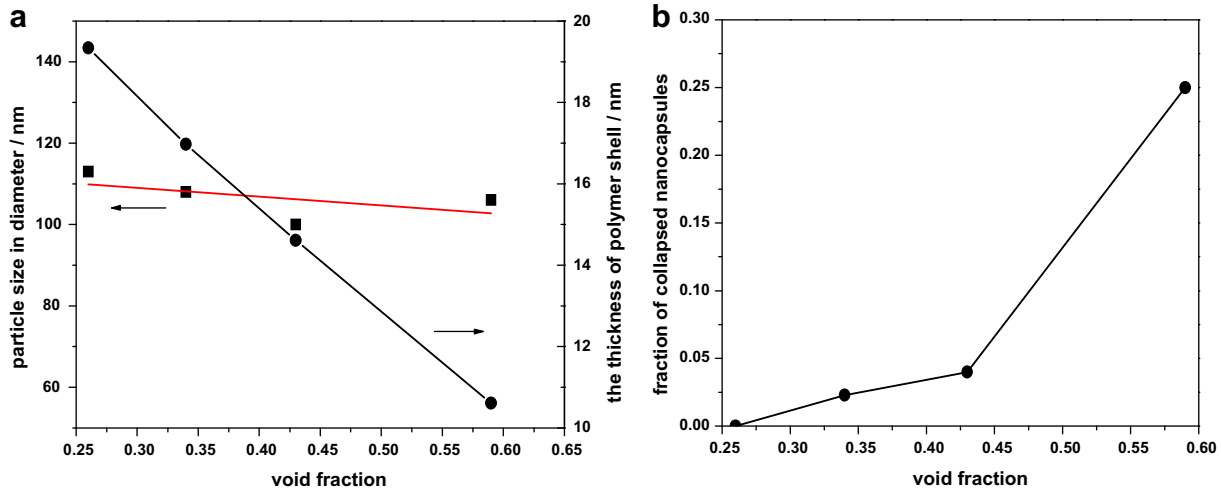

Fig. 7. The effect of void fractions on (a) particle size and shell thickness, (b) the fraction of collapsed hollow nanoparticles. The mass fraction of DVB was 0.40 and the amount of RAFT was 0.6 g.

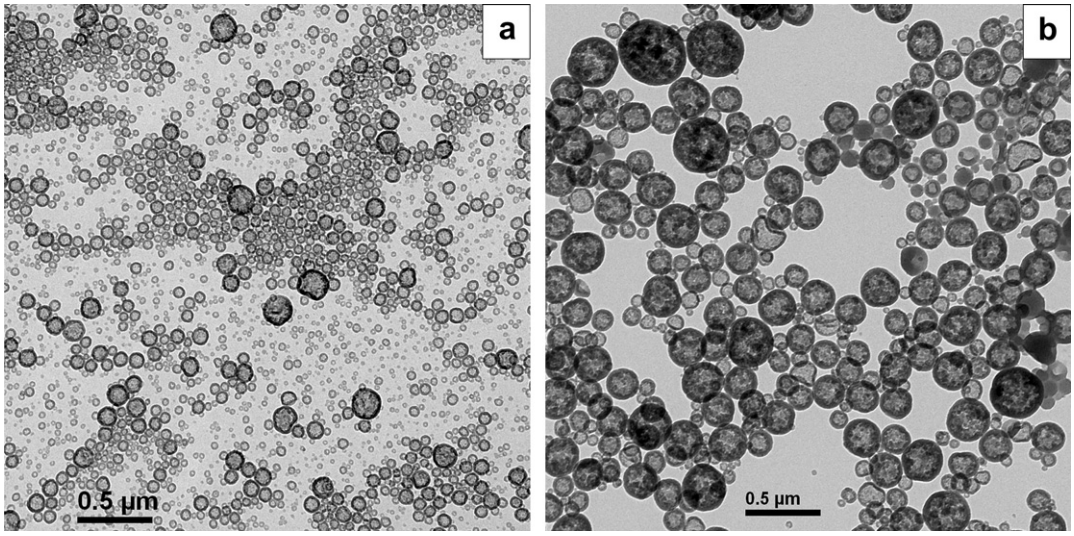

Fig. 8. The comparison of TEM images for hollow nanoparticles used (a) 1.2 g and (b) 0.2 g amphi-RAFT as surfactant. The mass fraction of DVB was 0.40 with shell/core = 3:1.

For the SEM images, it was seen that those bigger nanoparticles were more likely to collapse than their smaller counterparts in the same sample. To explain this, we should turn to the mechanism of miniemulsion polymerization. In miniemulsion polymerization, the particles are directly converted from the monomer droplets. In most cases, the droplet size distribution of the original miniemulsion is quite broad. On the other hand, the polymerization rate within smaller particles is higher than those bigger ones due to the so-called compartmentalization effect, leading to the migration of monomer from the larger particles to the smaller ones [39]. As a result, the larger particles would have a relative lower ratio of shell to core since the core material (paraffin) can not transport across water due to the extremely low water solubility.

3.3. Tuning the size of nanoparticles

The particle size depends on the level of surfactant used in the miniemulsion polymerization. The size of hollow nanoparticles can be easily tuned by simply adjusting the level of the amphiphilic RAFT agent. Compared to Exp.1, the amount of the amphi-RAFT was increased by a factor 2 in Exp.9 and decreased by a factor 3 in Exp.10. Accordingly, the volume average size of hollow nanoparticles changed to 70 nm in Exp.9 and 199 nm in Exp.10. The size distributions by number of hollow nanoparticles statistically counted from TEM images are shown in Fig. 9. The core/shell structures were well-defined with few particle collapsed in both cases, as seen in Fig. 8.

3.4. Synthesis of high void fraction non-collapsed hollow nanoparticles and the microstructures of the shell

According to the above results, we synthesized the hollow nanoparticles with high void fraction in Exp.11. The void fraction was set to 0.59 and the DVB fraction was as high as 0.67 as listed in Table 1. The TEM and SEM images from Fig. 10 show that almost all of the hollow nanoparticles were not collapsed. The average particle size by volume was about 103 nm. The shell thickness derived from TEM images was 11.5 nm, which was a little higher than the theoretical value 8.3 nm. The deviation might stem from the significant volume of mesopores existed in polymer shell, as discussed later.

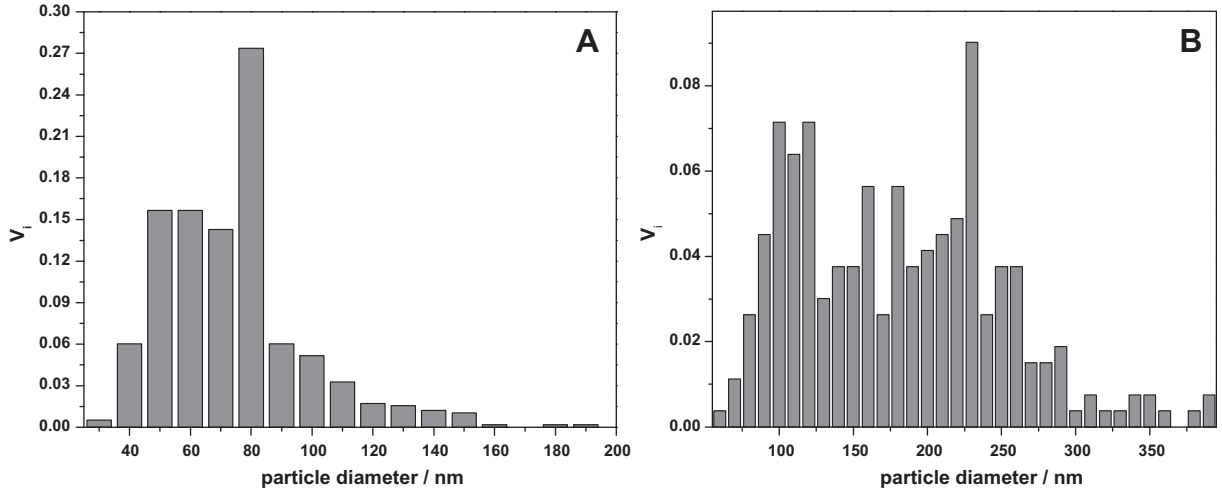

Fig. 9. Size distributions by number of hollow nanoparticles used (a) 1.2 g and (b) 0.2 g amphi-RAFT as surfactant. The mass fraction of DVB was 0.40 with shell/core = 3:1.

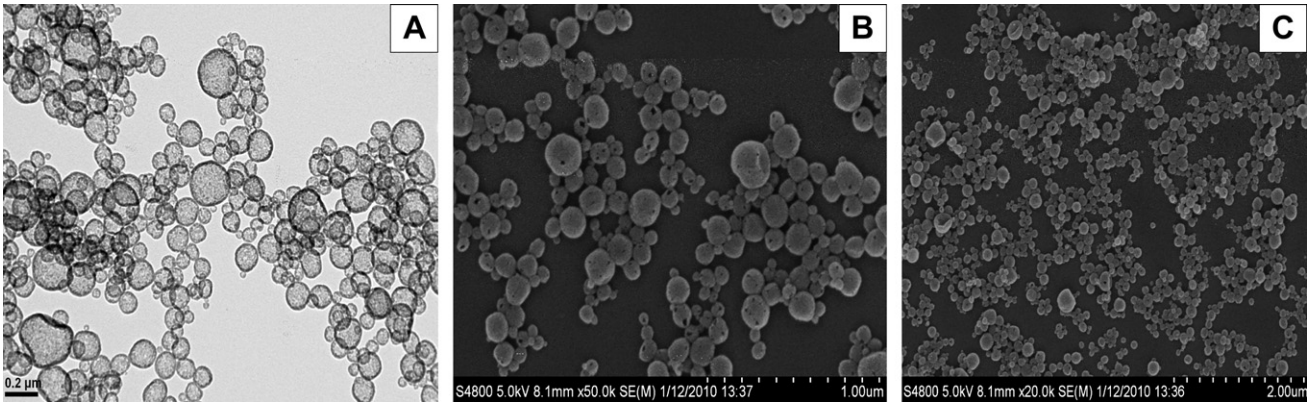

Fig. 10. (A) TEM images for hollow nanoparticles; SEM images for hollow nanoparticles at (B) 80000X (C) 20000X. The mass fraction of DVB was 0.67 and the amount of amphi-RAFT was 0.6 g with shell/core = 1:1.

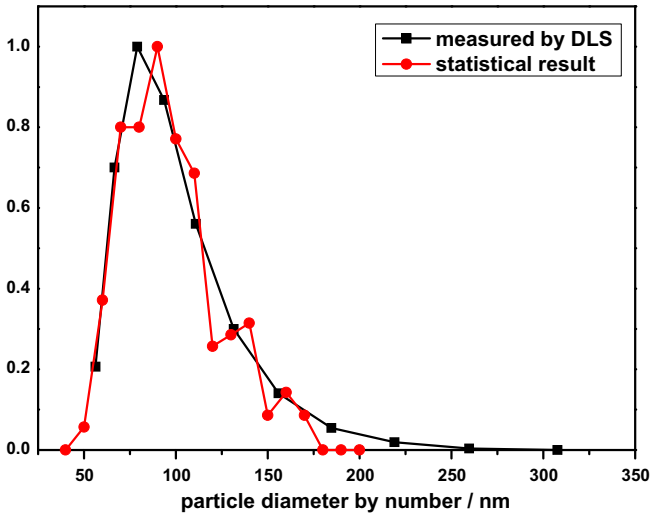

Fig. 11. The comparison of the particle size distributions between re-dispersed hollow nanoparticles by DLS and statistical result. The mass fraction of DVB was 0.67 and the amount of amphi-RAFT was 0.6 g with shell/core = 1:1.

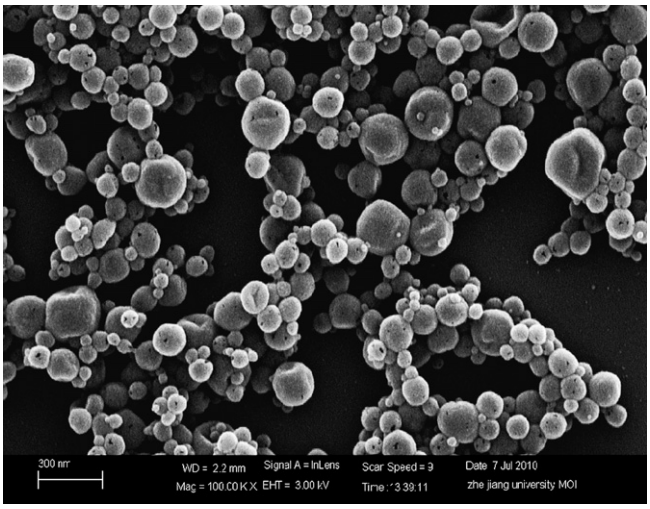

Fig. 12. SEM images for hollow nanoparticles after the thermal treatment at 200 °C for 2 h. The mass fraction of DVB was 0.67 and the amount of amphi-RAFT was 0.6 g with shell/core = 1:1.

3.5. Structural stability against solvent and re-dispersion in solvent

The highly crosslinked polymer shell not only enhanced the mechanical property of the hollow nanoparticles but also improved the structure stability in solvents. As described in the experimental section, the hollow nanoparticles were prepared by dispersing the nanocapsules of paraffin into THF to extract the paraffin. As evident in TEM images of the collected hollow nanoparticles in Fig. 10, no debris of the degraded particles was found, indicating the polymer shell was actually a covalently-bonded network. Furthermore, we studied on the re-dispersion property by re-dispersing the dried hollow nanoparticles in THF. After the magnetic stirring for 12 h in THF, the dispersion was then subjected to ultrasonication by an ultrasonic cleaner to improve the dispersion degree. It was found that the dried hollow nanoparticles were completely dispersed in THF to form a light blue dispersion, which was stable for a few days. The result of DLS measurement indicates the hollow nanoparticles should be fully re-dispersed in the solvent with a number average diameter of 93.3 nm, in excellent agreement with statistical results from the TEM images. As seen in the Fig. 11, the normalized particle size distribution from DLS is in good agreement with the statistical one from TEM observations.

3.6. Thermal and shear stability for hollow nanoparticles

The sample of Exp.11 was remained at 200 °C for 2 h. Interestingly, the morphology of hollow nanoparticles was hardly changed under such high temperature as seen from Fig. 12.

To study on the shear stability, the dispersion of the hollow nanoparticles in THF was subjected to ultrasonication (JOY-II, 600W) for 10 min. The SEM images as shown in Fig. 13 indicate the morphology of the hollow particles remained as good as the original. It is clear that the hollow nanoparticles were mechanically robust to resist the strong shear from the ultrasonication.

3.7. Mesopores in the polymer shell

The nitrogen adsorption and desorption isotherms data for the hollow nanoparticles of Exp.11 is presented in Fig. 14. DFT model was used to calculate the pore size distribution, giving a most probable pore diameter of about 9 nm, surface area 514 m^2/g and total pore volume 2.74 ml/g. Because of the deviation between model and actual pore type, the distribution of pore size is just a reference. The detail mechanism for the formation of the mesopores is not clear yet. Likely, they were formed by the paraffin left in the highly crosslinked polymer shell.

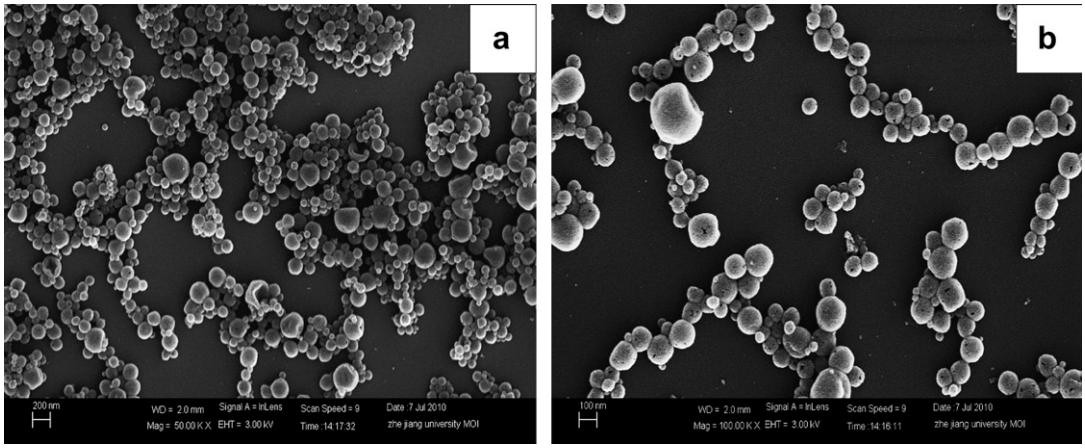

Fig. 13. SEM images for hollow nanoparticles after ultrasonic treatment (a) 50000X, (b) 120000X. The mass fraction of DVB was 0.67 and the amount of amphi-RAFT was 0.6 g with shell/core = 1:1.

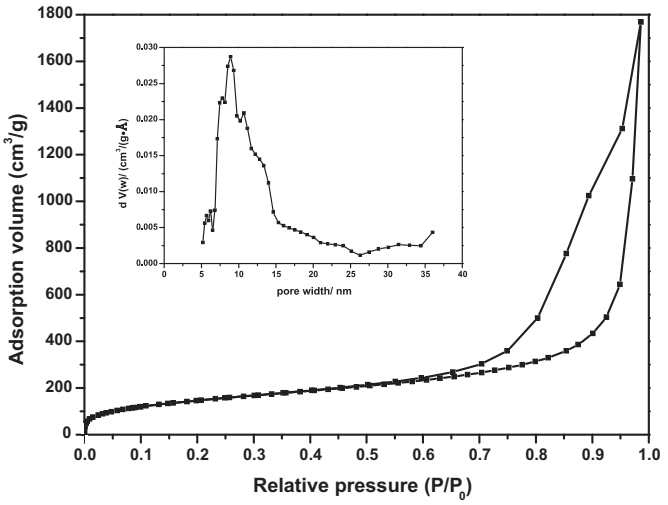

Fig. 14. Nitrogen adsorption–desorption isotherm and corresponding pore size distribution of hollow nanoparticles with shell/core = 1:1. The mass fraction of DVB was 0.67 and the amount of amphi-RAFT was 0.6 g.

4. Conclusion

The non-collapsed hollow polymeric nanoparticles were synthesized by the interfacial RAFT miniemulsion polymerization. The volume average particle diameter was tuned from 70 nm to 199 nm by decreasing the level of the amphiphilic RAFT agent. The shell thickness was tuned between 10.6 nm and 19.3 nm by changing the core/shell ratios. With the void fraction increasing, the hollow nanoparticles are more likely to collapse. This collapse could be suppressed by simply increasing the amount of crosslinker. The fraction of the collapsed hollow particles decreased nearly linearly with the increasing level of crosslinker. The hollow nanoparticles with a void fraction about 0.6 and shell thickness of 11.5 nm could be fabricated without collapse with about 0.67 mass fraction of DVB. In such a case, the polymer shell of the hollow nanoparticles is mesoporous, which has high surface area 514 m^2/g, extremely large pore volume 2.74 ml/g and a most probable pore diameter of 9 nm. The structures of the hollow nanoparticles are very stable not only in the solvent but also under harsh conditions like high temperature (200 °C) and strong shear. The hollow nanoparticles are also able to fully re-dispersed in the solvent.

The non-collapsed hollow polymeric nanoparticles, which were not able to be fabricated previously, would hold great application promising in many fields like functional coatings, catalyst, sensors and ultrason contrast agent, considering that many physical constants like refractive index, density, dielectric constant, heat conductivity can be largely tuned and the polymeric shell can be easily functionalization by re-activating the polymerization and the mesoporous properties of the polymeric shell.

Acknowledgements

The authors would like to thank the National Science Foundation of China (NSFC) for Award #20474057, #20836007 as well as for New Century Excellent Talent in University, Research Fund for the Doctoral Program of Higher Education of China.

References

[1] Mandal TK, Fleming MS, Walt DR. Chem Mater 2000;12:3481–7.
[2] Shi XY, Shen MW, Mohwald H. Prog Polym Sci 2004;29:987–1019.
[3] Lou XW, Archer LA, Yang ZC. Adv Mater 2008;20:3987–4019.
[4] Li WW, Matyjaszewski K, Albrecht K, Krystyna M. Macromolecules 2009;42:8228–33.
[5] Jang J, Ha H. Chem Mater 2003;15:2109–11.
[6] Guillemot F, Brunet-Bruneau A, Bourgeat-Lami E, Gacoin T, Barthel E, Boilot J-P. Chem Mater 2010;22:2822–8.
[7] Kim SW, Kim M, Lee WY, Hyeon T. J Am Chem Soc 2002;124:7642–3.
[8] McDonald CJ, Devon MJ. Adv Colloid Interfac 2002;99:181–213.
[9] Yoldas BE, Annen MJ, Bostaph J. Chem Mater 2000;12:2475–84.
[10] Lou XW, Wang Y, Yuan C, Lee JY, Archer LA. Adv Mater 2006;18:2325–9.
[11] Martinez CJ, Hockey B, Montgomery CB, Semancik S. Langmuir 2005;21:7937–44.
[12] Mailander V, Landfester K. Biomacromolecules 2009;10:2379–400.
[13] Liu KH, Chen SY, Liu DM, Liu TY. Macromolecules 2008;41:6511–6.
[14] Bae KH, Lee YH, Park TG. Biomacromolecules 2007;8:650–6.
[15] Thurmond KB, Kowalewski T, Wooley KL. J Am Chem Soc 1997;119:6656–65.
[16] Liu S, Weaver JVM, Tang YQ, Billingham NC, Armes SP, Tribe K. Macromolecules 2002;35:6121–31.
[17] Caruso F, Caruso RA, Mohwald H. Science 1998;282:1111–4.
[18] Wendland MS, Zimmerman SC. J Am Chem Soc 1999;121:1389–90.
[19] Okada M, Matoba T, Okubo M. Colloid Polym Sci 2004;282:193–7.
[20] Kobayashi H, Miyanada E, Okubo M. Langmuir 2007;23:8703–8.
[21] Zetterlund Per B, Saka Y, Okubo M. Macromol Chem Phys 2009;210:140–9.
[22] Scott C, Wu D, Ho CC, Co CC. J Am Chem Soc 2005;127:4160–1.
[23] Luo YW, Gu HY. Macromol Rapid Commun 2006;27:21–5.
[24] Blomberg S, Ostberg S, Harth E, Bosman AW, Van Horn B, Hawker CJ. J Polym Sci Part A Polym Chem 2002;40:1309–20.
[25] McDonald CJ, Bouck KJ, Chaput AB. Macromolecules 2000;33:1593–605.
[26] Okubo M, Minami H, Morikawa K. Colloid Polym Sci 2003;281:214–9.
[27] de Pablo JJ, Nealey PF. Eighth Annual Symposium on Frontiers of Engineering. Washington D.C: The National Academies Press; 2003.
[28] Stafford CM, Vogt BD, Harrison C, Julthongpiput D, Huang R. Macromolecules 2006;39:5095–9.

[29] Visschers M, Laven J, Linde RVD. Prog Org Coat 1997;31:311.
[30] Bohme TR, de Pablo JJ. J Chem Phys 2002;116:9939–51.
[31] Moad G, Chong YK, Postma A, Rizzardo E, Thang SH. Polymer 2005;46:8458–68.
[32] Lu FJ, Luo YW, Li BG. Ind Eng Chem Res 2010;49:2206–12.
[33] Van Zyl AJP, Bosch RFP, McLeary JB, Sanderson RD, Klumperman B. Polymer 2005;46:3607–15.
[34] Landfester K. Angew Chem Int Ed 2009;48:4488–507.
[35] Antonietti M, Landfester K. Prog Polym Sci 2002;27:689–757.
[36] Luo YW, Zhou XD. J Polym Sci Part A Polym Chem 2004;42:2145–54.
[37] Fery A, Weinkamer R. Polymer 2007;48:7221–35.
[38] Gao C, Donath E, Moya S, Dudnik V, Möhwald H. Eur Phys J E 2001;5:21–7.
[39] Luo YW, Gu HY. Polymer 2007;48:2362–72.

Polymer 52 (2011) 694–699

Contents lists available at ScienceDirect

Polymer

journal homepage: www.elsevier.com/locate/polymer

Dodecyl methacrylate as a crosslinker in the preparation of tough polyacrylamide hydrogels

Suzan Abdurrahmanoglu [a], Miray Cilingir [b], Oguz Okay [b,*]

[a] Marmara University, Department of Chemistry, 34722 Istanbul, Turkey
[b] Istanbul Technical University, Department of Chemistry, 34469 Istanbul, Turkey

ARTICLE INFO

Article history:
Received 7 October 2010
Received in revised form
16 December 2010
Accepted 17 December 2010
Available online 24 December 2010

Keywords:
Hydrogels
Toughness
Elasticity

ABSTRACT

Copolymerization of acrylamide with dodecyl methacrylate (C12) solubilized in aqueous micelles of sodium dodecyl sulfate produces tough hydrogels exhibiting moduli of elasticity around 1 kPa. Swelling and gel fraction measurements show that the hydrophobic associations acting as temporary crosslinks are too strong to be destroyed in water during the expansion of the gel network. An order of magnitude larger value of loss factor tan δ of the hydrogels formed using the hydrophobe C12 as compared to the conventional hydrogels indicates the dynamic nature of their crosslink zones. The hydrogels are more homogeneous than the corresponding gels prepared by a chemical crosslinker, as determined by the static light scattering measurements. Mechanical tests indicate that, in addition to the dodecyl domains, permanent crosslinks are also needed to obtain hydrogels that are mechanically stable up to 250% elongation ratios.

1. Introduction

Although synthetic hydrogels resemble natural biological soft materials, their mechanical properties greatly differ from those of biological gels [1]. For example, conventional hydrogels formed by free-radical crosslinking copolymerization are normally very brittle when handled in the swollen state, which limits their technological applications. This feature originates from the very low resistance of chemical hydrogels to crack propagation due to the lack of an efficient energy dissipation mechanism in the gel network [2–4]. To obtain a hydrogel with a high degree of toughness, one has to increase the overall viscoelastic dissipation along the gel sample by introducing dissipative mechanisms at the molecular level. A number of techniques for toughening of gels have been proposed including the double network gels [5–7], topological gels [8], nanocomposite hydrogels [9], and cryogels [10]. Hydrogels with improved mechanical properties were also prepared using gamma-ray induced polymerization of micellar solutions containing a surfmer and *N*-isopropylacrylamide (NIPAAm) [11]. The blocks of polymerized surfmer form micellar aggregates acting as physical crosslinks while slightly crosslinked blocks of poly(NIPAAm) connect the individual micelles.

We have recently shown that hydrophobically modified chemically crosslinked polyacrylamide (PAAm) hydrogels prepared by micellar polymerization technique exhibit a high degree of toughness, i.e., a very large extensibility at break [12]. Incorporation of hydrophobes with an alkyl chain length $x > 4$ into hydrophilic PAAm network chains results in an increase in the viscous modulus of hydrogels due to the formation of associations inside the gel network. However, in addition to the hydrophobic comonomer with alkyl chain lengths between 4 and 8 carbons, a chemical crosslinker was also used in the gel preparation to prevent the solubility of the resulting hydrogels [12]. Here, we used dodecyl methacrylate (C12) as the hydrophobic comonomer in the micellar copolymerization of acrylamide in the absence of a crosslinker. As will be seen below, the presence of a small amount of C12 in the comonomer feed leads to the formation of hydrogels with a gel fraction above 0.80. This highlights a new route for the preparation of high-toughness hydrogels without using a chemical crosslinker.

2. Experimental section

2.1. Materials

Acrylamide (AAm, Merck), dodecyl methacrylate (C12, Fluka), *N*,*N*′-methylenebis(acrylamide) (BAAm, Merck), sodium dodecyl sulfate (SDS, Sigma), ammonium persulfate (APS, Fluka), and *N*,*N*,*N*′,*N*′-tetramethylethylenediamine (TEMED, Fluka) were used as received. The hydrogels were prepared by free-radical micellar copolymerization of AAm and the hydrophobic comonomer C12 in aqueous SDS solutions at 25 °C. For comparison, polymerization

* Corresponding author. Tel.: +90 212 2853156; fax: +90 212 2856386.
E-mail address: okayo@itu.edu.tr (O. Okay).

0032-3861/$ – see front matter © 2010 Elsevier Ltd. All rights reserved.
doi:10.1016/j.polymer.2010.12.044

reactions were also carried out in the presence of the chemical crosslinker BAAm. The concentration of SDS in the reaction solution was 7 w/v % which is much above its critical micelle concentration (0.25 w/v %) [13]. The initial concentration of the total monomer was set to 5 w/v % throughout the experiments while the hydrophobe content in the comonomer mixture was varied between 0 and 10 mol %. APS (3.5 mM) and TEMED (0.25 mL/100 mL reaction solution) were used as the redox initiator system. Polymerization reactions were carried out in plastic syringes of 4 and 10 mm internal diameters as well as between the parallel plates of the rheometer (Gemini 150 Rheometer system, Bohlin Instruments) equipped with a Peltier device for temperature control. The synthetic procedure was similar to that given in our previous publication [12] (see Supplementary data for details).

2.2. Characterization

The hydrogels formed within the rheometer were subjected to frequency-sweep tests at a deformation amplitude $\gamma_o = 0.01$ over the frequency (ω) range 10^{-2} to 10^{1} rad/s both in up and down directions. They were also subjected to stress–relaxation experiments at 25 °C. An abrupt shear deformation of controlled strain amplitude γ_o was applied to the gel samples and the resulting stress $\sigma(t, \gamma_o)$ was monitored as a function of time. The time t after application of step deformation represents a time scale that describes the motion of the PAAm strands in the network and is equivalent to the inverse of the frequency ω in an oscillatory test [14]. Here, we report the relaxation modulus $G(t, \gamma_o)$ as functions of the relaxation time t and strain amplitude γ_o. The experiments were conducted with increasing strain amplitudes γ_o from 0.01 to 10. For each gel, stress–relaxation experiments at various γ_o were conducted starting from a value of the relaxation modulus deviating less than 10% from the modulus measured at $\gamma_o = 0.01$.

Cylindrical hydrogel samples prepared within the syringes were subjected to tensile mechanical tests as well as to swelling measurements, as described before [12]. During the swelling period of the hydrogels, the concentration of SDS extracted from the gel phase was estimated using the methylene blue (MB) method [15]. The optical absorbance of the chloroform phase was measured at 650 nm with a T80 UV–vis spectrophotometer. The conversion of monomers to the crosslinked polymer (mass of crosslinked polymer/initial mass of the monomer) was calculated from the masses of dry, extracted polymer network and from the comonomer feed.

The light scattering measurements were carried out at 24 °C using a commercial multi-angle light scattering DAWN EOS (Wyatt Technologies Corporation) equipped with a vertically polarized 30 mW Gallium–arsenide laser operating at $\lambda = 690$ nm and 18 simultaneously detected scattering angles. The light scattering system was calibrated against a toluene standard. The scattered light intensities from gels were recorded from 42.8° to 142.5°, which correspond to the scattering vector q range 8.8×10^{-4}–2.3×10^{-3} Å, where $q = (4\pi n/\lambda)\sin(\theta/2)$, θ the scattering angle, λ the wavelength of the incident light in vacuum, n the refractive index of the medium. The gels subjected to the measurements were prepared in the light scattering cuvettes. The reaction solutions were filtered through membrane filters (pore size = 0.2 μm) directly into the cuvettes. For calculation of excess scattering from gels, all the micellar polymerizations were repeated under the same experimental conditions except that the hydrophobe C12 was not used. Excess scattering intensities from gels $R_{ex}(q)$ were calculated as $R_{ex}(q) = R_{gel}(q) - R_{sol}(q)$, where $R_{gel}(q)$ and $R_{sol}(q)$ are the Rayleigh ratios for gel and polymer solution, respectively.

3. Results and discussion

3.1. Hydrophobic associations instead of permanent crosslinks

We first monitored the micellar polymerization of acrylamide (AAm) with and without the hydrophobe C12 by real-time rheological measurements. Fig. 1A and B show the elastic modulus G' and the loss factor tan δ during the micellar polymerization of AAm alone and with 1 mol % C12. For comparison, G' and tan δ during the micellar polymerization of AAm in the presence of 1 mol % chemical crosslinker BAAm are also shown in the figures. In the absence of the hydrophobe (open symbols), AAm polymerization leads to the formation of a polymer solution with an elastic modulus of a few Pascal's and a loss factor larger than unity. Addition of 1 mol % C12 into the comonomer feed drastically changes the reaction profile (filled circles); the elastic modulus G' rapidly increases with the onset of the reactions and, a viscoelastic gel with G' in the order of 10^3 Pa and with a loss factor around 0.1 was obtained. This indicates

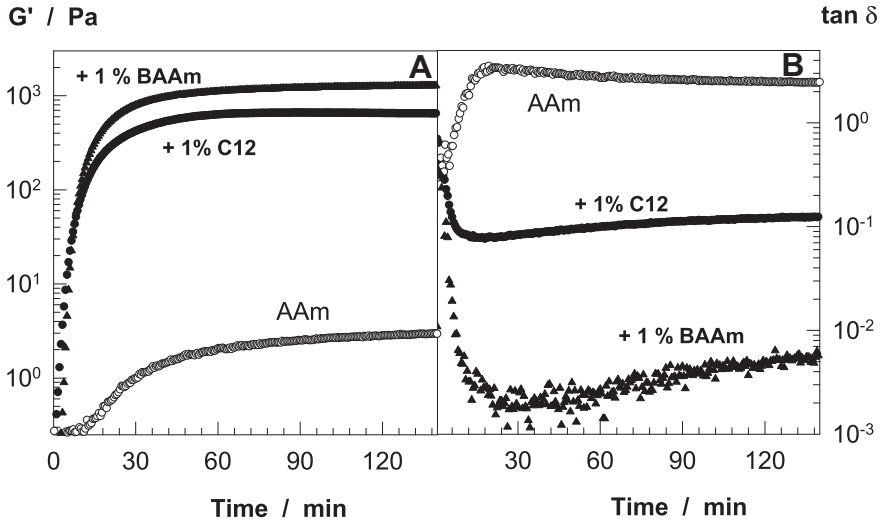

Fig. 1. Elastic modulus G' (A) and the loss factor tan δ (B) during the micellar polymerization of AAm alone (open symbols), with 1 mol % C12 (filled circles), and 1 mol % BAAm (filled triangles). $\omega = 6.28$ rad/s. $\gamma_o = 0.01$.

formation of hydrophobic associations in the solution acting as crosslink zones between the polymer chains. Fig. 1 also shows that the effect of the chemical crosslinker BAAm is similar to that of the hydrophobe C12, except that tan δ obtained using BAAm is about one order of magnitude smaller than that obtained using C12. For the present system containing hydrophobic associations, tan δ may be considered as the ratio of crosslinks being broken down and reconstituted during dynamic strains to those remaining intact and unchanged. An order of magnitude larger value of tan δ of hydrogels formed by hydrophobic associations thus indicates dynamic nature of their crosslink zones.

Fig. 2A shows the mechanical spectra of solutions of PAAm with 0, 1 and 5 mol % C12 prepared under the same experimental conditions. PAAm solution prepared in the absence of C12 exhibits a liquid-like response typical for a semi-dilute polymer solution, i.e., G'' exceeds G' at low frequency while there is a crossover between G' and G'' at a high frequency. Incorporation of 1 mol % dodecyl groups into the PAAm backbone shifts the crossover frequency from 10^2 to 10^{-2} rad/s indicating formation of strong and long lived associations between the blocks of dodecyl groups in the semi-dilute solution. Recent light scattering results of Ivanova et al indeed show formation of strong associations in solutions of PAAm's with 2–5 mol % C12 [16]. Moreover, increasing C12 content from 1 to 5 mol % increases both G' and G'' and the crossover frequency shifts outside of the experimental window. The solid curve in Fig. 2A shows G' versus frequency plot of the chemically crosslinked gel with 1 mol % BAAm; G' of the chemical gel is independent of frequency while G'' remains on a low level less than three orders of magnitude smaller than G' (not shown in the figure). Comparison of the results obtained using C12 and BAAm indicates that the gels behave similar at short experimental time scales while deviations appear at frequencies below 0.8 rad/s corresponding to time scales longer than 1.2 s.

Swelling tests showed that the gels were insoluble in water if C12 concentration in the comonomer feed was 3 mol % or above. As seen in Fig. 2B where the relative swelling ratio m_{rel} (swollen gel mass/mass of gel after preparation) is plotted against the swelling time of the hydrogels, m_{rel} rapidly increases and, after attaining a maximum, it decreases again until it reaches a limiting value after about 17d. It was found that, during the initial swelling period, namely up to 100 h of swelling time, SDS exists in the external solution whose concentration rapidly decreases below the detection limit (0.20 mg/L) after 200 h. Thus, large swelling ratios at short times and the appearance of maxima in the swelling curves are due to the osmotic pressure of the counterions of SDS, converting the gels into polyelectrolyte ones. However, as the swelling time is increased, SDS moves from the gel to the solution phase so that the swelling ratio decreases again until attaining an equilibrium value at long times. Equilibrium swelling ratio measurements showed that m_{rel} is equal to 0.6 ± 0.1 for C12 contents between 4 and 8% while gel fraction was above 0.80. The results indicate that the hydrophobic associations are too strong to be destroyed in water during the expansion of the gel network and hydrogels could be obtained without a chemical crosslinker.

A characteristic feature of the conventional gels prepared by a chemical crosslinker is the inhomogeneous distribution of the crosslink density, known as the spatial gel inhomogeneity [17,18]. Since the incorporation of mobile crosslink zones into the gel network may reduce the spatial gel inhomogeneity [19,20], the microstructure of the hydrogels formed by the hydrophobe C12 was investigated by static light scattering technique. Fig. 3A shows the excess scattering $R_{ex}(q)$ for gels prepared with 3–5 mol % C12 plotted as a function of the scattering vector q. For comparison, Fig. 3B shows $R_{ex}(q)$ vs. q plots reported for chemically crosslinked PAAm hydrogels of comparable moduli of elasticity prepared at three different BAAm concentrations [21,22]. The chemical gels were prepared at the same monomer concentration as the present gels. We see that, both covalently and non-covalently crosslinked hydrogels exhibit excess scattering $R_{ex}(q)$ in the range of 10^{-4} cm^{-1}. The scattering curves of chemical gels are rather flat, while those of physical gels show a considerable q-dependence, indicating the presence of correlations on a much larger length scale than observed in the former gels. Further, for the chemical gels, increasing BAAm content increases both the elastic modulus and the excess scattering. This is expected due to the fact that the spatial fluctuations of polymer concentration are amplified with increasing crosslink density [17,18]. In contrast, however, although the excess scattering increases with increasing C12 content from 3 to 5% and the gels became opaque above 5% C12, the elastic modulus does not change much. This means that the presence of 3 mol % C12 suffices to obtain a hydrogel with an elastic modulus between 1 and 2 kPa, while additional amounts of C12 enhance the

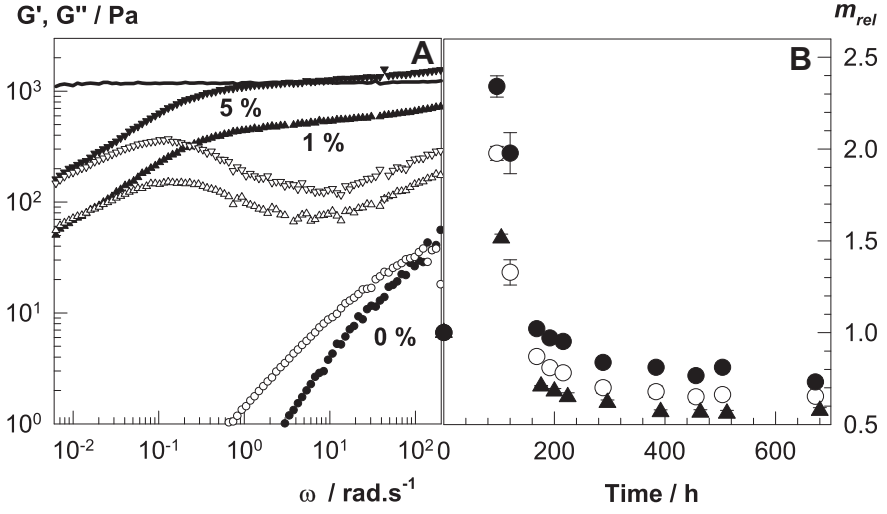

Fig. 2. (A): G' (filled symbols) and G'' (open symbols) of PAAm solutions with 0 (circles), 1 (triangles up) and 5 mol % C12 (triangles down) shown as a function of the frequency ω. For comparison, G' versus ω plot of PAAm gel formed using 1 mol % BAAm is also shown by the solid curve. $\gamma_o = 0.01$. (B): Relative weight swelling ratio m_{rel} of hydrogels shown as a function of the swelling time. C12 = 4 (○), 6 (●), and 7 mol % (▲).

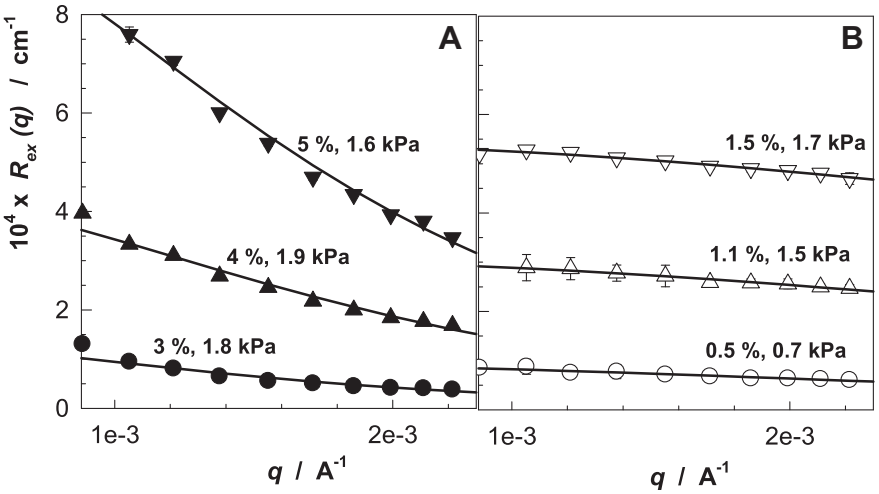

Fig. 3. Excess scattering intensities $R_{ex}(q)$ shown as a function of the scattering vector q for PAAm gels formed by the hydrophobe C12 (A) and the crosslinker BAAm (B). The gels are at the state just after their preparation. C12 = 3 (●), 4 (▲), and 5 mol % (▼). BAAm = 0.54 (○), 1.1 (△), and 1.5 mol % (▽). The elastic moduli of gels are indicated. The data of the chemical PAAm gels were taken from Refs. [21,22]. The solid curves are calculation results using eq.(1).

gel inhomogeneities. As a consequence, $R_{ex}(q)$ of gels formed at 3% C12 is much smaller than that of the chemical gels of the same crosslink density.

To interpret the excess scattering data of gels, Debye–Bueche (DB) equation was used [23–25]:

$$R_{ex}(q) = \frac{4\pi K\xi^3\langle\eta^2\rangle}{\left(1+q^2\xi^2\right)^2} \quad (1)$$

where K being the optical constant, $K = \pi^2 n^2 \lambda^{-4}$, ξ is the correlation length of the scatterers, and $\langle\eta^2\rangle$ is the mean square fluctuation of the refractive index. According to eq. (1), the slope and the intercept of $R_{ex}(q)^{-1/2}$ vs. q^2 plot (DB plot) give ξ and $\langle\eta^2\rangle$ of a gel sample (see Fig. S1 and related text for details). Calculations showed that the correlation length ξ of the scatterers is 38 ± 3 nm for gels made by C12, which is about two-fold larger than that calculated for the chemical gels (17 ± 5 nm). This larger value of ξ can be attributed to the larger size of the clusters formed due to the hydrophobic associations. The mean square fluctuations $\langle\eta^2\rangle$ of the refractive index is $(1.1 \pm 0.9) \times 10^{-7}$, while for the chemical gels, they are one order of magnitude larger, $\langle\eta^2\rangle = (22.2 \pm 2) \times 10^{-6}$. With the refractive index increment of PAAm in water at 21 °C, $dn/dc = 0.163$ mL/g [26], this converts to static concentration fluctuations $\sqrt{\langle\delta c^2\rangle} = 2.0 \times 10^{-3}$ and 9.1×10^{-3} for gels made by C12 and BAAm, respectively. Thus, since the mean polymer concentration in both gels is 5%, the average relative static concentration fluctuations on a length scale of a few tens of nm reduces from 18 to 4% by replacing the chemical crosslinks with mobile crosslink zones. This means that the dynamic nature of the crosslinks in the present hydrogels reduces the spatial gel inhomogeneities, as also observed before in topological gels [19,20].

3.2. Hydrophobic associations together with permanent crosslinks

In this section, the chemical crosslinker BAAm was included into the micellar copolymerization system of AAm and C12 to obtain both permanent and temporary crosslink zones in the hydrogels. As expected, the elastic modulus G′ increased and the plateau became broader as the crosslinker ratio X (molar ratio of BAAm to the monomers AAm + C12) is increased, i.e., as the number of permanent crosslinks is increased (Fig. S2). Fig. 4A and B show the effect of the amount of the hydrophobe in the comonomer feed on the mechanical spectra of PAAm gels formed at a crosslinker ratio $X = 1/80$. Addition of the hydrophobe increases G' at high frequencies indicating that the hydrophobic associations inside the gel network are detected as permanent crosslinks at short experimental time scales. The larger the amount of the hydrophobe in the comonomer feed, the larger G' at high frequencies. Further, the maximum in viscous modulus G'' shifts to slightly lower frequencies and its magnitude increases with increasing C12% due to the increase in the amount of the dissipated energy. Calculations indicate that, as the amount of C12 is increased from 0.5 to 5 mol %, the number of hydrophobes in each hydrophobic block also increases from 1 to 8 (see Supplementary data). As a consequence, more energy is dissipated because increasing hydrophobe length minimizes the exposure of the hydrophobic moieties to the aqueous environment.

To elucidate dynamics of the crosslink points in hydrophobically modified hydrogels further, stress-relaxation experiments were conducted. Fig. 4C shows typical relaxation profiles of hydrogels without and with 5% C12, where the relaxation modulus $G(t,\gamma_o)$ is shown as a function of time scale t for various strain amplitudes γ_o. $G(t,\gamma_o)$ of the hydrogel containing hydrophobic blocks decreases with increasing time and approaches to that of the conventional hydrogel at long times, in accord with the short frequency range of the mechanical spectra (Fig. 4A). Another result is that the modulus of hydrophobically modified hydrogel increases at a given time scale (strain hardening) while the conventional gel does not show this behavior. In Fig. 4D, the relaxation moduli G_t at a given time scale t are plotted as a function of the strain amplitude γ_o for the hydrogel with 5% C12. Hydrogel is in the linear regime for strain γ_o below 80%, while they exhibit strain hardening for γ_o between 80 and 150%, before softening at higher strains. The shorter the time scale, the larger the degree of strain hardening, the larger the yield strain γ_c, i.e., the strain at which the modulus starts decreasing. Since strain hardening behavior only appears after hydrophobic modification, the results suggest that applied strain contributes the organization degree of the dodecyl blocks inside the gel network so that the modulus increases.

3.3. Mechanical properties

Fig. 5A and B represent tensile stress–strain data of the hydrogels prepared at various levels of C12 with and without the chemical

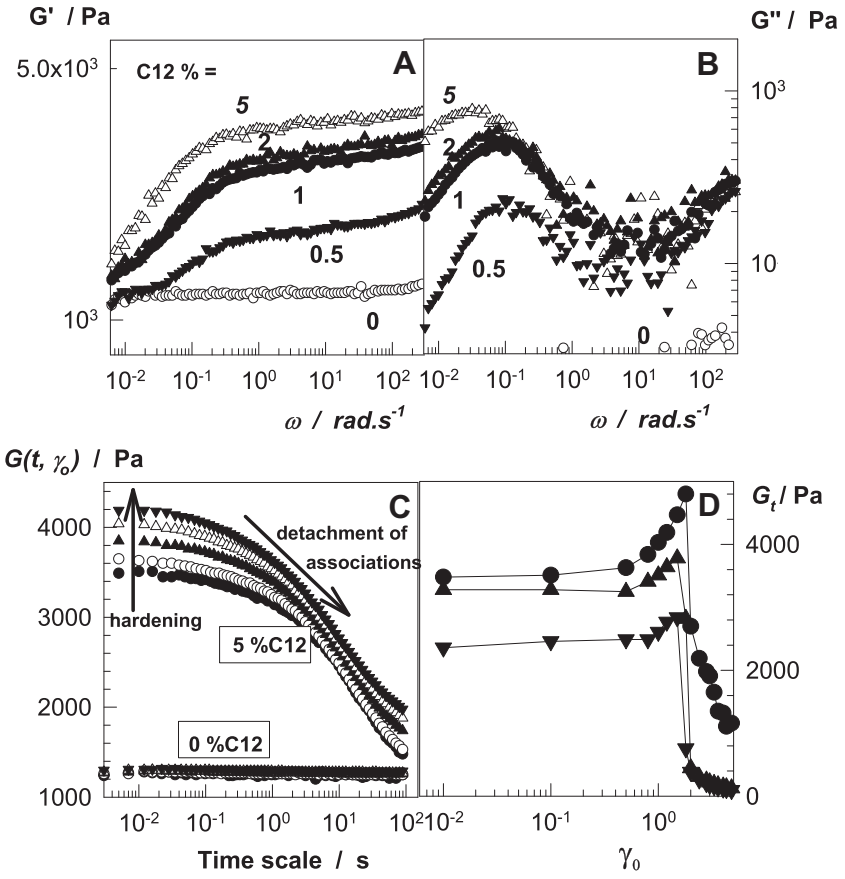

Fig. 4. (A, B): G' (A) and G'' (B) of PAAm hydrogels containing dodecyl groups shown as a function of the frequency ω measured after 2 h of reaction time. $\gamma_o = 0.01$. $X = 1/80$. SDS = 7%. C12 = 0 (○), 0.5 (▼), 1 (●), 2 (▲), and 5 mol % (△). (C): The relaxation modulus $G(t, \gamma_o)$ of PAAm hydrogels with 0 and 5 mol % C12 as a function of time scale t for various strain amplitudes γ_o. $X = 1/80$. $\gamma_o = 0.10$ (●), 0.50 (○), 0.80 (▲), 1.00 (△), and 1.20 (▼). Figure D was derived from C for hydrogels with 5% C12 and shows the relaxation modulus G_t at given time scale t as a function of γ_o. $t = 0.01$ (●), 1 (▲), and 10 s (▼).

crosslinker BAAm, respectively. C12 contents are indicated in the figures. In the absence of C12 (not shown in the figures), PAAm solutions formed under the experimental conditions flowed under gravity, while PAAm gels prepared using BAAm always broke before obtaining precise mechanical data. Addition of C12 into the comonomer feed leads to the formation of gels withstanding very large extension ratios. In the absence of the chemical crosslinker BAAm, the gels start flowing above 450% elongation ratios (Fig. 5A), while the presence of both permanent and temporary crosslinks produces both tough and elastic hydrogels (Fig. 5B). The hydrogels with 10 mol % C12 exhibit more than 250% elongation ratio at break and ultimate tensile strength of about 80 kPa. The results demonstrate that both permanent and temporary crosslinks are required to obtain tough and elastic hydrogels.

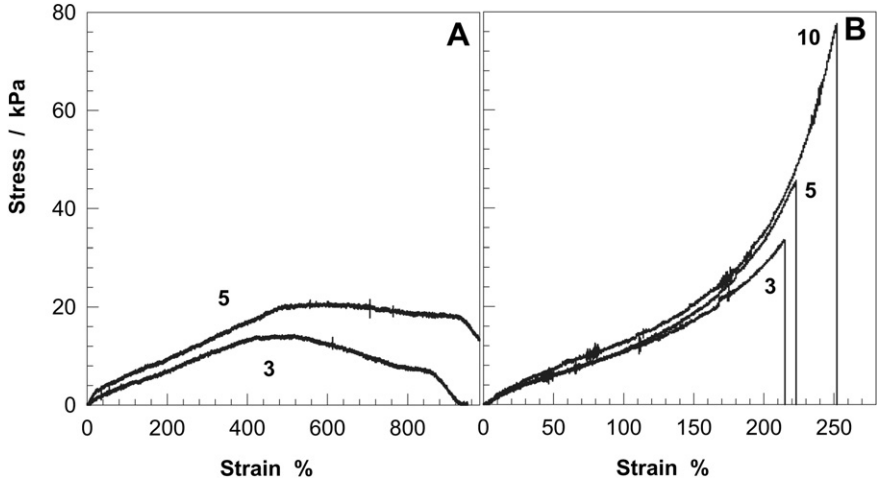

Fig. 5. Stress–strain curves of hydrophobically modified PAAm hydrogels with various C12 mol % indicated. $X = 0$ (A) and 1/80 (B).

4. Conclusions

Incorporation of dodecyl blocks into the hydrophilic PAAm chains leads to the formation of strong and long lived intermolecular hydrophobic associations. The three-dimensional network structure formed due to the dodecyl domains preserves its integrity in the presence of excess water, indicating that the approach presented here allows preparation of tough hydrogels without the use of a chemical crosslinker. Compared to the chemical gels, the mobility of the crosslink zones in the present hydrogels reduces the degree of spatial gel inhomogeneity. Mechanical tests also show that, in addition to the dodecyl domains, permanent crosslinks are also needed to obtain hydrogels that are mechanically stable up to 250% elongation ratios. The hydrogels exhibit strain hardening behavior due to the organization of dodecyl blocks under the applied strain.

Acknowledgements

Work was supported by the Scientific and Technical Research Council of Turkey (TUBITAK), TBAG–109T646. O.O. thanks Turkish Academy of Sciences (TUBA) for the partial support.

Appendix. Supplementary data

Supplementary data related to this article can be found online at doi:10.1016/j.polymer.2010.12.044.

References

[1] Storm C, Pastore JJ, MacKintosh FC, Lubensky TC, Janmey PA. Nature 2005;435:191.
[2] Ahagon A, Gent AN. J Polym Sci Polym Phys Ed 1975;13:1903.
[3] Brown HR. Macromolecules 2007;40:3815.
[4] Johnson JA, Turro NJ, Koberstein JT, Mark JE. Prog Polym Sci 2010;35:332.
[5] Gong JP, Katsuyama Y, Kurokawa T, Osada Y. Adv Mater 2003;15:1155.
[6] Tanaka Y, Gong JP, Osada Y. Prog Polym Sci 2005;30:1.
[7] Tang QT, Sun X, Li Q, Wu J, Lin J. Colloids Surf A 2009;346:91.
[8] Okumura Y, Ito K. Adv Mater 2001;13:485.
[9] Haraguchi K, Takehisa T. Adv Mater 2002;14:1120.
[10] Ceylan D, Okay O. Macromolecules 2007;40:8742.
[11] Friedrich T, Tieke B, Meyer M, Pyckhout-Hintzen W, Pipich V. J Phys Chem B 2010;114:5666.
[12] Abdurrahmanoglu S, Can V, Okay O. Polymer 2009;50:5449.
[13] Turro NJ, Yekta A. J Am Chem Soc 1978;100:5951.
[14] Orakdogen N, Erman B, Okay O. Macromolecules 2010;43:1530.
[15] ISO 7875-1, Water quality. Determination of surfactants. Part 1: determination of anionic surfactants by measurement of the methylene blue index (MBAS); 1996. USO/TC 147.
[16] Ivanova EM, Blagodatskikh IV, Vasileva OV, Barabanova AI, Khokhlov AR. Polym Sci Ser A 2008;50:9.
[17] Shibayama M. Macromol Chem Phys 1998;199:1.
[18] Bastide J, Candau SJ, Cohen Addad JP. In: Physical properties of polymeric gels. Wiley; 1996. p. 143.
[19] Karino T, Okumura Y, Ito K, Shibayama M. Macromolecules 2004;37:6177.
[20] Karino T, Shibayama M, Ito K. Physica B 2006;385-386:692.
[21] Kizilay M, Okay O. Polymer 2003;44:5239.
[22] Orakdogen N, Okay O. Polym Bull 2006;57:631.
[23] Debye PJ. J Chem Phys 1959;31:680.
[24] Bueche FJ. Colloid Interface 1970;33:61.
[25] Debye P, Bueche AM. J Appl Phys 1949;20:518.
[26] Orakdogen N, Okay O. J Appl Polym Sci 2007;103:3228.

Polymer 52 (2011) 700–707

Contents lists available at ScienceDirect

Polymer

journal homepage: www.elsevier.com/locate/polymer

Physicochemical driving forces behind exfoliation process of a synthetic montmorillonite in PDMS polymers

Cyril Vaulot, Pascal Ziegler, Bassel Haidar*

Institut de Science des Matériaux de Mulhouse, IS2M-CNRS LRC 7228, UHA, 15 rue Jean Starcky, BP 2488, 68057 Mulhouse, France

ARTICLE INFO

Article history:
Received 19 March 2010
Received in revised form
23 July 2010
Accepted 15 December 2010
Available online 22 December 2010

Keywords:
Clay exfoliation
Flow calorimetry
Surface energy

ABSTRACT

The conditions under which exfoliation of organo-montmorillonite in Poly(dimethylsiloxane) elastomers may occur were investigated via a three approaches: determination of the inter-platelet distance (as measured by WAXS), the surface energy evaluation (via inverse gas chromatography) of the polymer matrix and the clays, and measurement of heat of interaction (using a flow microcalorimeter in heptane) between polymers and the clay. The exfoliation efficiency is estimated by performing dynamic mechanical measurements. The results indicate that compatibilization and geometrical considerations are not sufficient requirements to transform clay particles into platelets. It evidences the determinant role of specific interactions between the reactive polymer end-groups and the filler surface. Polymer conformation on the clay surface and heat of adsorption associating "dispersive or London" forces and hydrogen bonding of respectively trimethyl- and hydroxyl-terminated polymer are evaluated.

1. Introduction

The present development of engineering polymers seeks the reinforcement of the polymer matrix, improving strength, stiffness, thermal stability, barrier properties, toughness and optical properties without complicating too much the processing step. In conventional composites, including macroscopically separated phases, the property enhancement is achieved using a 30–40 weight percent of filler. Without this, a rubbery matrix for instance, is almost useless. During the last two decades, an alternative way was prospected, developing new polymer–clay nanocomposites. Indeed, improvements are already observed, even with a small weight percents of fillers [1]. Moreover, all polymer–clay systems are not necessarily true nanocomposites. If polymers are unable to intercalate between the clay platelets, conventional microcomposites are formed. Nanocomposites are considered exclusively in cases where the mineral is integrated at the nanoscale: *intercalated* when the periodic multilayer structure of the clay is preserved after the intercalation of polymer inside the galleries. The distance between individual layers is simply increased in comparison to the initial value. The nanocomposites are called *exfoliated* (delaminated) nanocomposites when the clay particles are disintegrated into discrete 1 nm thick platelets, randomly distributed in the polymer. Particles of layered silicates in a pristine state can only be easily dispersed in hydrophilic polymers. Therefore, a "compatibilization" procedure of the silicate has to be applied before the manufacturing of the nanocomposite in a hydrophobic matrix. Generally, the alkali metal ions (such as Na+) located inside the interlayer spaces are exchanged with amphiphilic alkyl ammonium salts. Such a procedure renders the hydrophilic clay organophilic and thus simplifies the clay dispersion, and increases, at the same time, the inter-platelet distance facilitating the polymer penetrations. Only then, melt intercalation, solution blending and in-situ polymerization processes can be foreseen as the three main ways for the manufacturing of polymer–clay nanocomposites [2–6].

Melt intercalation is the most relevant approach for rubber blend applications since it requires the same tools used to achieve conventional filled rubbers. Physico-chemical properties of both polymer and clay are among the most important driving forces controlling, in this case, an exfoliation mechanism. In this work, we shall try to establish a relation between the surface characteristics of the two constituents, their affinity toward each other and the accomplishment of the exfoliation process. Therefore, three parameters, considered to play a major role in the exfoliation process, are investigated: the inter-platelet distance measured by X-ray diffraction (XRD), the surface energies of polymers and clays determined by inverse gas chromatography (IGC) and the heat of adsorption of polymer molecules on clays surfaces estimated by flow micro-calorimetry (FMC).

* Corresponding author. Tel.: +33 3 89 60 88 06; fax: +33 3 89 60 87 99.
E-mail address: bassel.haidar@uha.fr (B. Haidar).

0032-3861/$ – see front matter © 2010 Elsevier Ltd. All rights reserved.
doi:10.1016/j.polymer.2010.12.034

2. Materials

2.1. Polymers

Two different series of Poly(dimethylsiloxane) elastomers (PDMS) were purchased from GELEST-ABCR: silanol-terminated and trimethylsiloxy-terminated elastomers. The molecular weights (MW), the concentrations (c*) of polymer solutions and the radius of gyration (R_g) of the polymers are displayed in Table 1.

2.2. Clay synthesis

A synthetic layered silicate, montmorillonite Nax(Al(2 − x)Mgx)$Si_4O_{10}(OH)_2$, x = 0.3, was prepared in our laboratory using a hydrothermal method in a fluoride media [9]. According to the elemental analysis, its unit cell formula is: $Na_{0.26}Si_{4.06}Al_{1.70}Mg_{0.20}O_{10}(OH_{1.85}F_{0.15})$.The negative charge of such a silicate layer is compensated by Na+ ions located in the interlayer galleries and the total Cation Exchange Capacity (CEC) of the clay was determined by elemental analyses [10] and methylene bleu titration [11] and found to be approximately 71 m eq/100 g. The fine structure of the synthesized montmorillonite was confirmed by wide angle XRD as reported elsewhere [9] and shown in Fig. 1.

The organophilic treatments were made by dispersing pristine clay in an aqueous solution (at 60 °C) of Octadecyltrimethyl ammonium bromide (ODTMABr, $C_{21}H_{46}NBr$, MW = 392.52 g/mol), purchased from Fluka. The suspension was left under stirring during 24 h before centrifugation and extraction of the excess reactant using distilled water. The amount of ODTMABr was varied during treatment in the 1–3.5 CEC range and the amounts of ODTMABr retained in the organoclay were determined by elemental (bromine and carbon) and thermogravimetric analysis. Elemental analyses were performed at the "Service Central d'Analyse de Solaize" CNRS using silver nitrate titration for bromine and a combustion technique for Carbon.

2.3. XRD

The characterization of the different clays was performed on crushed and sieved powders. Only the 100–400 μm fraction was considered. The same fraction was used for other investigations throughout this paper. The wideangle X-ray diffraction, WAXS, measurements were carried out at 25 °C in reflection with an X'PERT diffractometer from Philips using the Cu Kα radiation (λ = 1.54 nm).

2.4. IGC [12]

The Inverse gas chromatography apparatus is a FISONS' chromatograph GC 8000. Injectors, columns oven and ionization flame detector (FID) are computer controlled, data integrations are made using AZUR software. Helium is used as vector gas at a flow rate of about 15 cm^3/min. The columns are made of stainless steel of 2 mm interior diameter and a length of 200 mm. Powders were prepared as mentioned in the XRD section. The homogeneity of the stationary phase has been assured by vibration in order to reduce the space died between the grains. Columns were stabilized by heat treatment above the highest measurement temperature under a helium flow for 12 h. Measurements were made in the 120–160 °C temperature range. A series of n alcanes (C1–C16) was used as probes. The dispersive or London component, γ_S^D, of the surface energy, was estimated according to the Dorris and Gray equation [13]:

$$\gamma_S^D = \frac{(\Delta G_a(CH_2))^2}{4 \cdot N^2 \cdot a_{CH_2}{}^2 \cdot \gamma_{CH_2}{}^2} \quad (1)$$

The free energy ΔG°_a (C_nH_{2n+2}) is based on the experimentally determined slope of the equation

$$\Delta G^\circ_a(C_nH_{2n+2}) = -RT \cdot \ln(V_n) + C(T) \quad (2)$$

where V_n is the net retention volume, R, T and C are the gas constant, the temperature (K) and a constant depending of the reference state respectively. $\Delta G_a(CH_2)$ is the free energy increment by of methylene group. The theoretical base of the IGC and the experimental procedure are detailed elsewhere [13]

2.5. Surface area

The powder surface areas were estimated from low temperature nitrogen adsorption isotherms and application of the BET equation [14]. Adsorption isotherms were determined using a Micromeretics ASAP 2020 apparatus.

2.6. FMC

Adsorption enthalpies were determined at 20 °C in heptane (Spectrosol, 99.9%, chromatography grade), a good solvent for PDMS, using liquid flow micro-calorimetry (FMC, Microscal with a Perkin–Elmer Totalchrom Workstation integrator). It was verified that heptane does not dissolve the ODTMABr used in the clay modification, and therefore, does not harm the organoclay structure during the FMC measurements. The effluent flow rate was maintained constant at 3.3 ml/h. The amount of powder required to fill up the measurement cell depends on the powder density: for pristine clay this amount was around 110 mg. FMC measurements

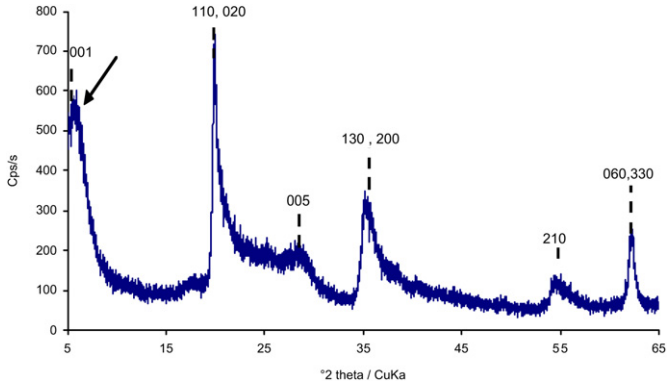

Fig. 1. XRD pattern of pristine MMT at the wide angles. Arrow points to the d_{001} reflexes corresponding to an inter-platelet distance of about 1.3 nm (interlayers spacing from 0.3 nm).

Table 1
MW, heptane concentrations (c*) and gyration values (R_g) of polymers [7,8].

Silanol-terminated PDMS				Trimethylsiloxy-terminated PDMS			
Specimen	MW g/mol	c*[a] g/l	R_g[b] nm	Specimen	MW g/mol	c* g/l	R_g nm
OH-800	780	483	1.0	CH_3-4000	4000	131	2.4
OH-5100	5150	107	2.7	CH_3-9430	9430	66	3.7
OH-18000	18400	39	5.2	CH_3-29000	29000	27	6.5
OH-23000	23500	32	5.9	CH_3-49000	49000	18	8.5
OH-44000	44400	19	8.1	CH_3-91700	91700	11	11.6
OH-47000	47200	18	8.3	CH_3-139000	139000	8	14.3
OH-49000	49000	18	8.5	CH_3-420000	420000	3	24.8
OH-77000	77000	12	10.6				
OH-139000	139000	8	14.3				

[a] c* estimated according to the results of Lapp et al.: c* #k $MW^{-4/5}$.
[b] R_g estimated according to the Flory's equation: $R_g^2 = n \cdot b^2/6$ with n, the number of monomer units and b, the statistical length of the polymer segments (b = 0.561 nm).

were performed in the pulse mode. Infinitesimal amounts of polymer solutions, compared to the specimen surface, were injected through a 20 μL loop. The polymer concentration was fixed at 10 g/l. This choice implies that different molecular weights are in different regimes of dilution relative to c* as mentioned in Table 1 (the concentration defining the border between the dilute and semi-dilute regions, c*, is representative of the concentration at which polymer chain entanglement is first observed). However, it has been verified that the dilution, that occurs when the polymer solution passes through the measurement cell, is high enough to bring the concentration of even the highest molecular weight down to below its c*.

The FMC is built in such a way that if any thermal exchange occurs, when the solute comes into contact with the powder, a peak (positive or negative for endo- or exo-thermal event respectively) is registered. The calibration is made by comparing the area of the detected FMC signal to a known heat impulse generated via a resistive heating element inside the measurement cell. The unadsorbed fraction of the solute is detected by a downstream detector, a refractometer (refractoMonitor IV, LDC analytical). One should keep in mind that the FMC-measured net heat change, Q, may not be a pure enthalpy of the only polymer segments adsorption, ΔH_{ads}, but rather a sum of different elements gathering contributions of several other thermal events [15]. The most important would be (i) the displacement of solvent molecule from the solid surface by the solute segment but also (ii) the heat of mixing (dilution) between the solute polymer segments and the carrier solvent when the solution goes through the powder dregs and (iii) the possibility of forming a multilayer adsorption of polymer segments accumulated on the same portion of the solid surface. Nevertheless, all these contributions may be considered, to a first approximation, as constant for a given solute/solid couple and experimental conditions. Therefore Q may be anticipated as, to some extent an overestimated, value of ΔH_{ads}.

In general, small molecules (oligomers up to a few hundreds of mol/g) are adsorbed on a solid surface in a reversible way as shown by the exothermic adsorption and endothermic desorption peaks in Fig. 2 (a-left). The injected solute recovers almost completely in the downstream detector (a-right). When macromolecules are adsorbed in an irreversible way (as attested by a singular positive peak, b-left in Fig. 2), only a portion of the injected solute leaves the measurement cell to the refractometer (Fig. 2, b-right).

2.7. Polymer–clay mixing process

Polymer-solid mixtures were obtained by mixing clay and dry polymer (being more or less viscous liquid depending on the MW) in a glass vial. The mixtures were first manually pre-mixed before being sonicated. Sonication conditions were fixed in this study for all experiments (15 min using a CENCO instrument with a microtip, 88 W, at room temperature) although it was reported that the type of mixing may influence the exfoliation process [16–19].

The different mixtures were prepared, taking into account the original pristine silicate content and expressed according to the polymer in phr (per hundred grams of rubber). So, according to the kind of clay, a sample called "X phr" contains for 100 g of polymer:

- X g of pristine clay
- 1234·X g of organoclay 1 CEC
- 1528·X g of organoclay 2 CEC
- 1878·X g of organoclay 3,5 CEC

Different factors were calculated on the base of the actual organic content as determined experimentally.

2.8. Dynamic mechanical properties

Dynamic mechanical properties were studied on filled and unfilled polymers on a Metravib VA 4000 viscoanalyser. A sample was introduced in a cylindrical measurement cell having a 10 mm inner diameter and sheared by a piston of 6 mm diameter. The shearing frequency was fixed at 10 Hz with 10 μm amplitude. In a typical test, a specimen was first cooled from room temperature to −150 °C at −10 °C/min. Then, measurements were made in the −150–150 °C temperature range at a ramp rate of 5 °C/min.

3. Results

3.1. Inter-platelet distance

Fig. 3 shows X-Ray diffractograms of the pristine and organoclays with various organic contents. We observe by following the d_{001} reflexes a clear increase of the interlayers spacing from 0.3 nm for pristine clay to 1 nm for the 1 CEC treated clay and 3.2 nm for

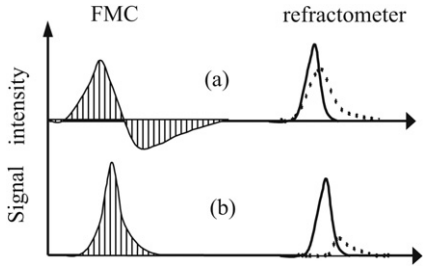

Fig. 2. Example of FMC data for (a) a low molecular mass PDMS (MW < 400 g/mol) and (b) a high molecular mass PDMS (MW > 2000 g/mol). The data, shown on the left side, are thermal data directly related to the temperature of the FMC cell and those, on the right side, are the differential refractometer signal. The dashed line shows the signal corresponding to the adsorption response when the clay is in the cell. The bold lines concern the reference data corresponding to zero adsorption (simulated by using an empty cell).

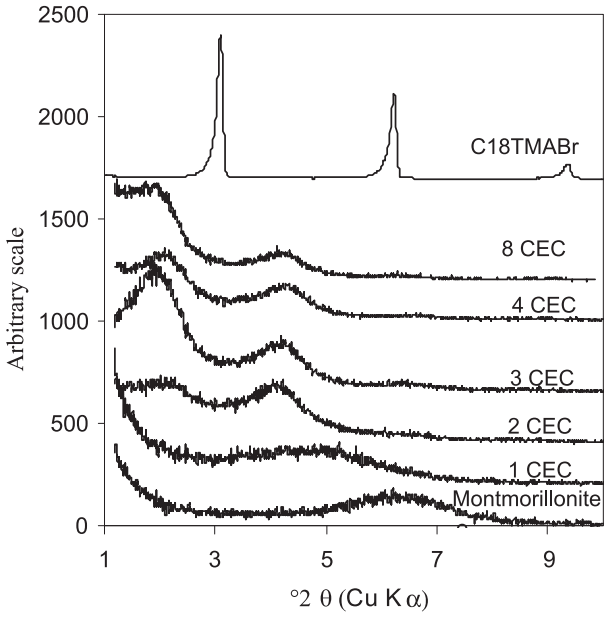

Fig. 3. WAXS curves of the modified clay samples (1, 2 and 3.5 CEC) after water extraction. The diffractograms of pristine MMT and pure ODTMABr are shown as references. The loose peak shown for the pristine MMT corresponds to the sharp peak indicated by an arrow in Fig. 1.

Table 2
Clays specimens organic content, obtained by C and Br elemental analyses, and interlayer distances measured by XRD.

Treatment (in eq. CEC)	C % ±1	Br % ± 0.1	d_{001}[a] distance (nm) ±0.1
Pristine (0 CEC)	~0	~0	1.3
1CEC	16	~0	2.0
2CEC	25	3.8	4.2
3.5 CEC	32	6.9	4.2

[a] Interlayer distance = interlayer spacing + platelet thickness (~1 nm).

both the 2 and the 3.5 CEC organoclays. Interlayer distance levels off at 3.2 nm while organic content continues to increase as shown in Table 2. ODTMABr adsorption beyond the exchange capacity limit (1 CEC) was thoroughly discussed in the literature and mainly attributed to physical interactions between free surfactant molecules and ionically exchanged ones [20–22]. With the exception of the d_{001} peak the diffractograms of the modified MMT's remains identical to the pristine one showed in Fig. 1.

The organization and structuring, of the different fractions of the organic phase, results in a more complex X-Ray diffractogram as shown in Fig. 3 for both 2 and 3.5 CEC clays and was also discussed in the literature [23]. It is noteworthy to compare, on Fig. 4, the distance between platelets of different clays to the dimension of the polymer molecules which are supposed to intercalate clay galleries.

It appears that inter-platelets spacing, of the most heavily modified clays (i.e.2 and 3.5 CEC), is in the R_g range of about a 17000 g/mol macromolecule. It decreases to match the size of ~2500 and few hundreds g/mol MW's for 1CEC and pristine clays respectively. Thus, there are normally no geometrical obstruction preventing molecules with R_g smaller than the clay spacing to penetrate the clays galleries, i.e. relatively large molecules (up to 17000 g/mol) into the most organically modified clays, 2500 g/mol into 1CEC clays and small oligomers (<400 g/mol) into the pristine clay. This view supposes that organic molecules come close to the solid in a random-coils conformation neglecting the possibility for a more defolded conformation under which the macromolecule would be able to intercalate the clay by capillary, reptation or creeping mechanisms. Such possibilities would further favor the intercalation process, at least from this somewhat over simplistic geometrical view.

3.2. Surface energies

There are different types of cohesive forces in a material depending on the types of interactions existing between their molecules and that can be globally classified as dispersive and polar interactions. Surface free energy of a solid, γ_S, (defined as half of the energy necessary to cleave a unit plane into two parallel planes) can be expressed as the sum of several components

$$\gamma_s = \gamma_p + \gamma_d \tag{3}$$

γ_p and γ_d refer to polar and dispersive contributions respectively. The effect of dispersive or London forces is universal. Thus, this component of the surface free energy is particularly important. Let us focuses our attention, in this section, on the dispersive component of the surface energy as it can be routinely measured by IGC. (The polar contribution to the PDMS–clay interactions were examined using flow micro-calorimetry and is described in the next section).

When only dispersive forces are responsible for the interaction between two materials (like a macromolecule, M, and a clay, C), the energy of adhesion, W_d, between those two materials would correspond to the geometric mean value of their γ_d [24].

$$W_d = 2(\gamma_{dM} \cdot \gamma_{dC})^{1/2} \tag{4}$$

In such polymer–clay systems, we may consider that, when two adjacent clay platelets are cleaved, two polymer "units" are also cleaved. Here, "unit" of polymer refers to whatever polymer is needed to cover the newly created clay surfaces. Therefore, the total change in adhesive energy, ΔW, in the exfoliation process may be expressed as:

$$\begin{aligned} \Delta W &= 2(\gamma_{dM}\cdot\gamma_{dM})^{1/2} + 2(\gamma_{dC}\cdot\gamma_{dC})^{1/2} - 4(\gamma_{dM}\cdot\gamma_{dC})^{1/2} \\ \Delta W &= [2(\gamma_{dM})^{1/2} - 2(\gamma_{dC})^{1/2}]^2 \end{aligned} \tag{5}$$

Thus, when $\Delta W = 0$, the attractive potential between clay platelets would be compensated by those created between polymer and platelet. This suggests that the origin of the exfoliation hindrance is the difference in surface energies between clay and polymer. From the thermodynamic point of view, the exfoliation of clay in a polymer matrix is possible only when the energy characteristics of both components are identical. The greater the difference in their surface energies and the more difficult is the exfoliation process; unless the adhesive energies between polymer and platelet surface due to polar interactions are so high that they are able to offset the effect of the difference in surface energies and cohesive energies of clay and polymer themselves as we will see in a next section. In fact several interesting analyses were made to simulate the extent on interactions between layered silicate sheets before and after organic modifications with a variety of chain lengths, CEC values and alkyl ammonium head group functionalities. Heinz et al. [25,26] demonstrated that in pristine clays the electrostatic contribution to the cleavage energy is predominant compared to the dispersive contribution. This electrostatic contribution virtually vanishes if organic interlayer is over 0.8 nm thick (in our case this would correspond to any organo-treatment above 1CEC), the cleavage energy is then reduced to its only dispersive component and exfoliation would become supposedly more feasible.

Fig. 5 shows, as expected [27], a significant decrease of the dispersive component of free surface energy measured at high temperatures from more than 150 mJ/m^2 to less than 50 mJ/m^2 levels upon 1CEC organic treatment of pristine clay and a steady decrease with temperature from 120 to 160 °C for both clays. In order to estimate the values of γ_S^D at room temperature for the clay and to compare it to those of the polymers, the clay linear relationship γ_S^D – temperature was extrapolated to room temperature as shown in Fig. 5.

The estimated dispersive component of the surface energy (Fig. 6) decreases sharply with increasing organic treatments and

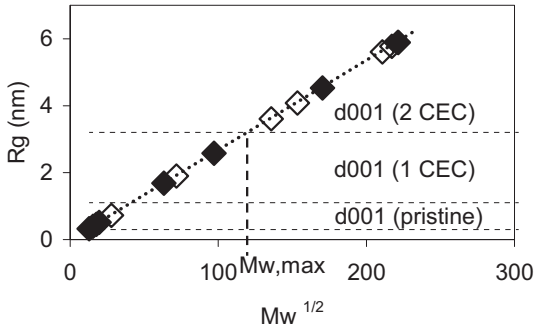

Fig. 4. R_g of PDMS molecules as a function of the square root of MW. Horizontal lines mark the sizes of the inter-platelets spacing. Open and full diamonds relate to OH and CH_3 terminated polymers respectively.

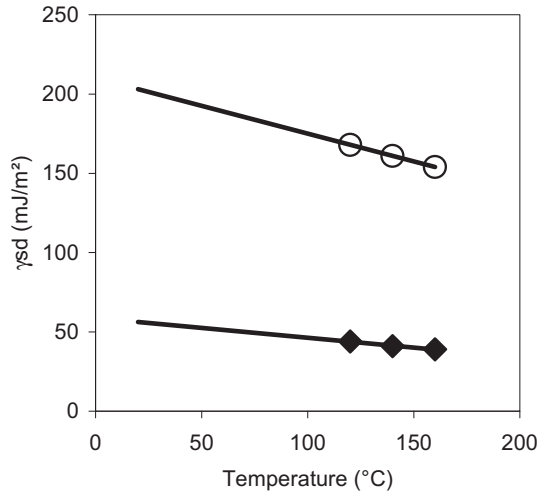

Fig. 5. Dispersive Surface energy components, γ_S^D of pristine (open symbols) and 1 CEC (bold symbols) clays as a function of temperature

tends to reach an asymptotic value slightly off the polymer γ_S^D value given in the literature (~21 mJ/m^2) [28]. On the basis of the above discussion, the difference in surface energies between clay and polymer is minimized upon organic treatments. Therefore and from a thermodynamic viewpoint, the exfoliation in a polymer matrix should be possible if the clay is previously modified by an organic treatment.

3.3. Affinity and heat of adsorption

To illustrate our FMC observations, the results and the way it can be treated, we shall examine firstly the case of the pristine clays modified with the two series of polymers (Fig. 7).

The net heats of adsorption of the two silanol- and trimethylsiloxy-terminated PDMS series show different behaviors when the polymer MW is increased. The heat of adsorption of the polymers terminated by trimethylsiloxy groups is virtually independent of the molecular weight while the heat of adsorption of silanol-terminated molecules decreases sharply with increasing MW and stabilizes at a threshold level comparable to the one observed for trimethylsiloxy-terminated series. The influence of the polarity of the polymer end-groups on the heat of adsorption becomes undetectable when the molecular weight of the polymer grows to about 15000 g/mol or above.

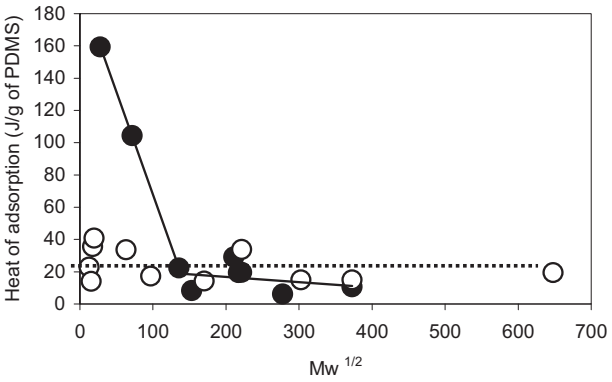

Fig. 7. Heat of adsorption, as measured by FMC for silanol- (bold symbols) and trimethylsiloxy-terminated (open symbols) PDMS, on pristine clay as a function of MW (square root is used for clarity and lines have been drawn through the data points to aid the visualization of the trend).

Another aspect of the adsorption mechanism of polymers on pristine clay is reflected by following the adsorbed fraction of the solute in each injection pulse as a function of the MW in Fig. 8. Despite the fact that the amount of injected molecule in each pulse is relatively low compared to the available surface, as it has been mentioned in the experimental section, the adsorption is not total, i.e. the amount of adsorbed polymer terminated by trimethylsiloxy groups is rather low (~30% of the injection) and practically independent of the molecular weigh while it decreases with increasing MW for the silanol-terminated series from a high fraction (~90%) level to stabilize at the same (30%) level as the trimethylsiloxy-terminated one. One should emphasize here that the adsorption, as measured by FMC, is a dynamic process dependent not only on the flow rate and the adsorbent/solute nature, size… but also on the manner the powder is packed inside the measurement cell and

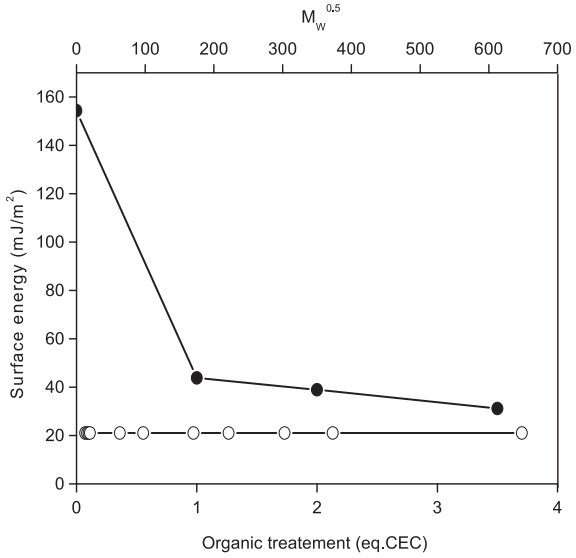

Fig. 6. γ_S^D at 20 °C dependence on organic treatment (eq. CEC) (bold symbol) and its independence on MW (open symbol). A line has been drawn through the data points to aid the visualization of the trend.

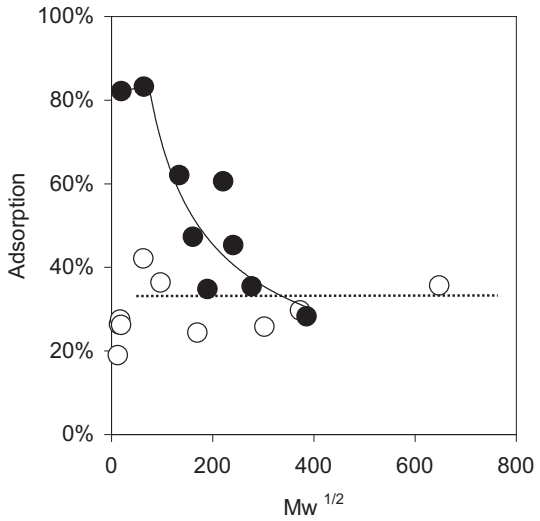

Fig. 8. Fraction of adsorbed molecules on each pulse as measured by downstream detector for silanol- (bold symbols) and trimethylsiloxy-terminated (open symbols) PDMS on pristine clay as a function of MW (square root is used for clarity and lines have been drawn through the data points to aid visualization of the trend).

the pass-way taken by the molecules throughout the cell. This packing may differ from one measurement to another (in practice we renew the packing for each molecular weight) which may explain the scatter of the data in Fig. 8. Therefore, the normalization of the heat of adsorption by the actual amount of adsorbed molecules is required. If the net heat of adsorption is "*Q*", in joule, and the actual amount of adsorped molecule is "*m*", in moles, then $Q/m = Q_{mol}$ is the molar heat of adsorption. Fig. 9 gathers the evolutions of the Q_{mol} of the treated and untreated clays with both silanol- and trimethylsiloxy-terminated polymers.

The molar heat of adsorption of the trimethylsiloxy-terminated polymers on pristine clay shows persistent dependency on the molecular weight that fits quite well a power law such as:

$$Q \approx MW^{x} \tag{6}$$

where *x* is a constant. In this case, the scaling exponent, *x*, was found to be equal to 0.8. Such value is relatively high compared to 0.5 which would have been the value of *x* for a random coil conformation of the polymer chain and that would have raised a linear (unshown) relationship instead of the curve in Fig. 9. This value for *x* suggests that the polymer chains adopt a rather plane conformation which means that the macromolecule is to some extent defolded. The extrapolation of the $Q_{mol} = f(MW)$ relationship (Fig. 9) down on the MW coordinate axis to the molecular weight of one monomer unite, $-O-Si(CH_3)_2-$, leads to a fairly precise estimation of the contact heat of adsorption of one segment unit (polymer–surface) of 17.5 kJ/mol. This value outranks typical physical bonds, but remains acceptable for strong physical interactions [29]. In any case, from the estimated heat of adsorption of one segment unite, combined to the actual Q_{mol} of each polymer, we can easily determine M_{seg}, the average molecular weight of a segment between two successive adsorbing points. M_{seg} was found somewhat constant and rather small, in the 400 g/mol range, corresponding to only 5 monomer units in average.

Surprisingly, the same power law used to express the results of the trimethylsiloxy-terminated series on pristine clay fits reasonably well the results of silanol-terminated polymers on the same pristine clay as seen in Fig. 9. The relative dispersion of the results, in this case, restrains our attempt to detect any particularity in the behavior of the two smallest hydroxyl-terminated molecular weights. The particularity concerning the behavior of these two MW's which is shown on the Figs. 6 and 7 is largely attenuated upon normalization by the amount of adsorbed molecules. The two series may reasonably be classified under the same type of a general behavior with the same value of *x* as long as the clay is unmodified.

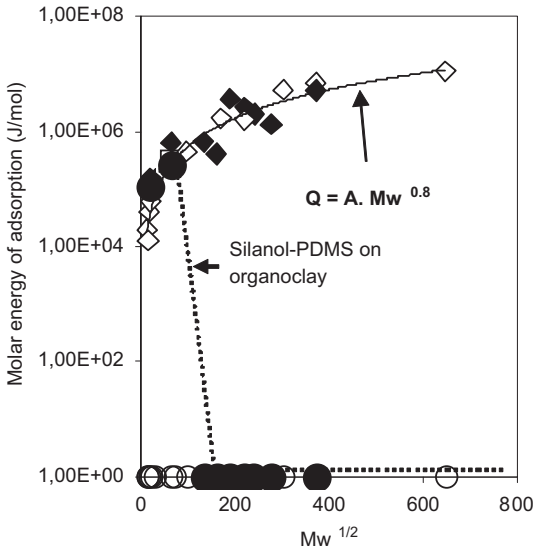

Fig. 9. Molar heat of adsorption of silanol- (bold symbols) and trimethylsiloxy-terminated (open symbols) PDMS on pristine (diamond) and modified (circle) clays as a function of the square root of MW. The curves represent the best fit of experimental results.

Organically modified clays, regardless of their degree of modification, exhibit a completely different feature depending on the polymer end-groups. While the trimethylsiloxy-terminated polymers, independently of their MW, fail to have any thermally detectable exchange with modified clays as shown in Fig. 9, silanol-terminated ones start by exchanging an appreciable amount of heat, a plateau of Q_{mol} may be averaged at around 86 kJ/mol, for the two lowest molecular weights <5000 g/mol. Then, Q_{mol} decreases sharply to reach its zero level for higher MW's, reflecting the decline of the end group's contribution. Since the trimethylsiloxy-terminated polymers do not exchange any heat with organo-modified clays, we may assume that the backbone of the silanol-terminated PDMS does not participate either in the heat exchanged with organoclays. Consequently, Q_{mol} of silanol-terminated PDMS may be exclusively attributed to the effect of its end groups and the heat of adsorption of one silanol group Q_{molOH}, is simply the half of the molecular heat of adsorption, which is equal to 43 kJ/mol of adsorbed hydroxyl group and may be ranked on the high side of hydrogen bounds [30].

4. Discussion

The interest of clay exfoliation in polymer matrixes is to develop many individual foils that, thanks to their huge number, high form factors and high surface area, are able to modify substantially the polymer phase behavior and thus to transform the macroscopic properties of the composite. The high number of a platelets, the high form factor per volume unite bring the percolation ratio of the solid phase to a very low solid content. The high surface area insures an intimate polymer–surface contact for a large number of macromolecules which, especially for a rubbery matrix, is a source of chains immobilization and ultimately of reinforcement. Clay exfoliations up to a complete "delamination" (after Gardolinski's definition "*Delamination*" denotes "*the process of separation of the individual layers of the exfoliated particles*") [31] in polymer matrixes are usually evidenced by the vanishing of the clay d_{001} peak from its XR diffractogram. However, the low solid content in nanocomposite makes extremely difficult the detection of any clay XR signal, even of the non-exfoliated clay. TEM investigation may also be used to observe single, intercalated and pristine platelets. But for rubbery materials and especially high mobile ones, like PDMS, the matrix should be crosslinked, which may affect the exfoliation process. Moreover, it is also tricky to slice such crosslinked low T_g polymer (−120 °C) into thin sections by microtomy. Rheological properties measurements sound to be the most convenient and statistically representative approach to evaluate the real effect of the solid on polymer behavior: this mean to estimate clay's dispersion and degrees of exfoliation. A clay content of 3% was selected as sufficiently low to discriminate between exfoliated and un-exfoliated clays, since the effect of such content of pristine clay is reported to be marginal. Results are presented in Fig. 10 in terms of G'/G'_0 where G' is the shear modulus of the composite and G'_0 is the same modulus of the corresponding unfilled polymer.

From all the examined composites, just a few show remarkable effects on their modulus upon the addition of 3% of clay. In fact, we observe in Fig. 10 that untreated clay shows no mechanical improvement at this low clay content and only low MW of silanol-terminated polymers on all modified clays exhibit an appreciable

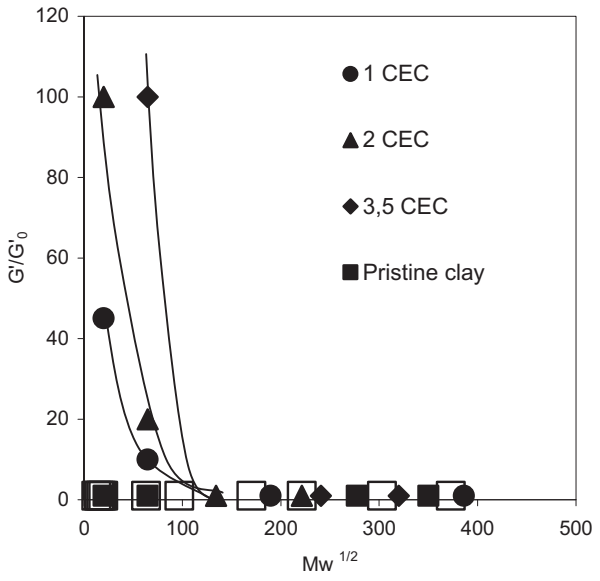

Fig. 10. G'/G'_0 for silanol- (bold symbols) and trimethylsiloxy-terminated (open symbols) PDMS on different clays as a function of MW (square root is used for clarity and lines were drawn through the data points to aid the visualization of the trend).

extent of mechanical improvement. It is also remarkable the extent of mechanical improvement increases with increasing the degree of organic treatment from 1 to 2 and then to 3.5 CEC.

It is tempting at this point to link the improvement of mechanical properties of the composites to some extent of a likely exfoliation of its clay particles. The fairly good matching of the results presented in the Figs. 9 and 10 suggests that systems in which the polymer chains are able to exchange polar interactions with clay surface platelets are precisely those who present some kind of exfoliation. Adsorption, per say, does not appear to be a good indicator of the exfoliation, since trimethylsiloxy-terminated PDMS exchange heat with pristine clay without showing any rheological improvement, adsorption in this case presumable takes place at the external surface of the clay particles. However, if polar interactions are an essential requirement, it is not sufficient to achieve exfoliation. For example, low molecular weight silanol-terminated polymers do exchange an appreciable amount of heat with the pristine clay surface (Fig. 7) but do not show any reinforcement effect and thus any reflect of a significant exfoliation of unmodified clay particles. Surface energy modification obeys the physicochemical criterium (discussed in surface energy section here above) in a similar way at all treatment ratios, from 1 to 3.5 CEC (there is no substantial change of γ_S^D) and thus should have the same effect on allowing the polymer chain to come close enough to the solid surface. Still, the improvement of mechanical properties is so dependent of the extent of organic treatment (Fig. 10). In addition, there is virtually no further increase of the inter-platelet spacing (Table 2) when the organic treatment goes from 2 to 3.5 CEC, therefore, geometrical criterium does not explain furthermore this dependency, the swelling of the clay, as such, by increasing the inter-platelet spacing upon organic treatment does not seem to play a key role in the exfoliation process, since the size of several tested macromolecules are well below the distance between platelet but remain inactive in the exfoliation process as long as other criteria are not met. Similarly, the reduction of cleavage energy mentioned before [25,26] is not supposed to progress beyond its level at 1CEC and cannot be responsible of the CEC-behavior dependency shown in Fig. 9. The limit of the role that may be plaid by the reduction of cleavage energy is in agreement with Brose et al. predictions [32] since they mentioned that even though the attractive interaction between platelet of modified clay is considerably lower than between the pristine clay, the exfoliation process requires shear stresses which remain higher than what mixing tools may offer; these authors propose a peeling process that through which compatible polymer chain intercalate into clay galleries and achieve exfoliation. Our results stress the role of polar groups (OH-end groups) in the exfoliation process. One should keep in mind that clay galleries hold a good number of active polar groups (hydroxyl) which may remain accessible even after organic modifications. Such internal groups are capable to attract the polymer OH-end groups and drag the whole macromolecule behind it as long as the MW of the polymer is not too high.

5. Conclusion

In this paper, we do identify the driving forces governing the polymer penetration process into the interlayer media of the clays. It appears that polymer–clay compatibilization and geometrical considerations are not sufficient requirements to reduce clay particles into discrete individual platelets. In fact, neither reducing the dispersive surface energy of the hydrophilic clay by an organic treatment to match the surface energy of the polymer nor expanding the clay inter-platelet distance to a level larger than the radius of gyration of the polymer nor even, the reduction of cleavage energy are enough conditions to achieve exfoliation. The key-factor of this process is the establishment of specific interactions between the polymer (in our case, end-groups) and the platelets internal polar groups. The macromolecule has to be attracted into the inter-platelet space by sufficiently strong and specific interactions in order to overcome the remaining cohesive interactions holding together organoclay layers and produce exfoliation. Such interactions do not operate if the clay is hydrophilic (the polymer cannot sufficiently approach the solid). In the case where they are due to polar end-groups, such interaction ceases to be attractively efficient when the MW becomes too large. The calorimetric technique is an adequate approach for the detection of dispersive and polar polymer–filler interactions and for the determination of the polymer conformations on the solid surface.

References

[1] Alexandre M, Dubois Ph. Materials Science and Engineering Reports A 1994;281:1.
[2] Weimer MW, Chen H, Giannelis EP, Sogah DY. Journal of the American Chemical Society 1999;121:1615.
[3] Kiersnowski A, Dabrowski A, Budde H, Kressler J, Piglowski J. European Polymer Journal 2004;40:2591.
[4] Xie W, Hwu JM, Yiang GJ, Buthelezi TM, Pan WP. Polymer Engineering and Science 2003;43:214.
[5] Tsen CR, Wu JY, Lee HY, Chang FC. Polymer 2001;42:10063.
[6] Noh MW, Lee DC. Polymer Bulletin 1999;42:619.
[7] Lapp A, Picot C, Strazielle C. Journal of Physical Letters 1985;46:1031.
[8] Flory PJ. Statistical mechanics of chain molecules. New York, USA: Interscience; 1969. p 174.
[9] Rheinoldt M, Miehe-Brendle J, Delmotte L, Thuillier MH, Le Dred R, Cortes R, et al. European Journal of Inorganic Chemistry 2001;11:2831.
[10] Lagaly G. Clay Minerals 1981;16:1.
[11] Kahr G, Madsen FT. Applied Clay Science 1995;9:327.
[12] Brendle E, Papirer E. In: Nardin M, Papirer E, editors. Powders and fibers: interfacial science and applications. Surfactant science series, vol. 137. New-York, USA: CRC Press; 2007. p. 47.
[13] Dorris MG, Gray DG. Journal of Colloid and Interface Science 1979;77:353.
[14] Brunauer S, Emmett PH, Teller E. Journal of the American Chemical Society 1938;60:309.
[15] Pettersson A, Rosenholm JB. Langmuir 2002;18:8447.
[16] Ginzburg VV, Balazs AC. Macromolecules 1999;32:5681.
[17] Dennis HR, Hunter DL, Chang D, Kim S, White JL, Cho JW, et al. Polymer 2001;42:9513.
[18] Burnside SD, Giannelis EP. Chemistry of Materials 1995;7:1597.
[19] Schmidt DF, Clement F, Giannelis EP. Advanced Functional Materials 2006;16:417.

[20] Grim RE, Allaway WH, Cuthbert FL. Journal of the American Ceramic Society 1947;30:137.
[21] Jordan JW. Mineral Magazine and Journal of the Mineralogical Society 1949;28:598.
[22] Cowan CT, White D. Transactions of the Faraday Society 1958;691:54.
[23] Vaulot C. PhD thesis, Mulhouse: Université de Haute-Alsace; 2008.
[24] Fowkes FM. Journal of Physical Chemistry 1962;66:382.
[25] Heinz H, Vaia RA, Farmer BL. Journal of Chemical Physics 2006;124:224713.
[26] Fu YT, Heinz H. Chemistry of Materials 2010;22:1595.
[27] Kădăr F, Szăzdi L, Fekete E, Pukănszky B. Langmuir 2006;22:7848.
[28] Barrere M, Ganachaud F, Bendejacq D, Dourges MA, Maitre C, Hemery P. Polymer 2001;42:7239.
[29] Piguet C, Ouali N, Koeller S. Les interactions Moléculaires, Lecture of general Chemistry. Université de Genève; 2007.
[30] Emsley J. Chemical Society Review 1980;T9:91T.
[31] Gardolinski JEFC. PhD Thesis, Kiel: Christian-Albrechts University; 2005
Lagaly G, Gardolinski JEFC. Clay Minerals 2005;40:547–56.
[32] Borse NK, Kamal MR. Polymer Engineering and Science 2009;49:641.

Polymer 52 (2011) 708–717

Contents lists available at ScienceDirect

Polymer

journal homepage: www.elsevier.com/locate/polymer

Effect of surface nucleation on isothermal crystallization kinetics: Theory, simulation and experiment

Yury Yuryev, Paula Wood-Adams*

Concordia University, Center for Applied Research on Polymers and Composites (CREPEC), Department of Mechanical and Industrial Engineering, 1455 de Maisonneuve Blvd West, EV004.251, Montreal, Quebec, Canada H3G 1M8

ARTICLE INFO

Article history:
Received 12 September 2010
Received in revised form
16 December 2010
Accepted 18 December 2010
Available online 24 December 2010

Keywords:
Surface nucleation
Crystallization kinetics
Isothermal crystallization

ABSTRACT

Surface nucleation of poly(L/D-lactide) at the interface with aluminum was studied by performing isothermal DSC analysis of amorphous samples of varying thickness between 100 °C and 130 °C. To ensure complete wetting of the aluminum surface, a hot melt laminating process was used to prepare the samples. Theoretical aspects of surface crystallization kinetics were explored and the resulting model was compared with the results of Monte-Carlo simulations. Three stages of surface crystallization were identified depending on the growth geometry: (1) impingement-free growth, (2) increasingly laterally-constrained transverse growth, and (3) interstitial growth. By fitting the Monte-Carlo simulation to the experimental half-times of crystallization the surface nucleation concentration and the bulk nucleation rate was estimated at 4 different temperatures. It was found that both surface nucleation concentration and the bulk nucleation concentration decrease with increasing crystallization temperature.

1. Introduction

Surface induced nucleation and the subsequent formation of transcrystallinity is a phenomenon occurring in many practical instances of polymer crystallization. The presence of virtually any foreign surface in intimate contact with a crystallizing polymer causes surface nucleation [1]. This phenomenon has been observed for wide range of polymer-surface pairs; in particular, intense surface nucleation has been observed in polymers in contact with other polymers [2–34] and glass fibers [5,6], carbon [7–9] and aluminum [10–13]. The nucleating ability of the later is often attributed to alumina which is always present in the form of a thin layer on an aluminum surface [14]. In some cases of surface induced nucleation, the nuclei concentration is very high and almost immediately upon the onset of crystallization, the growing crystallites coalesce in the lateral direction leading to the formation of a so-called transcrystallinity region propagating normal to the foreign surface as a unified front. Transcrystallinity is often observed during processing on tool contact, in reinforced polymers around inclusions and even in immiscible polymer blends along phase boundaries.

In order to evaluate the substrate activity, Chatterjee [14] followed by Ishida and Bussi [15] related the nucleation ability of the surface to the interfacial free energy difference, $\Delta\sigma$:

$$\Delta\sigma = \gamma_{cs} + \gamma_{cm} + \gamma_{ms} \tag{1}$$

where γ_{cs}, γ_{cm}, γ_{ms} are the crystal-substrate, crystal-melt and melt-substrate interfacial free energies respectively. A lower value of $\Delta\sigma$ indicates a more favorable nucleation condition. Therefore, when considering the nucleating ability of a foreign surface, one should compare $\Delta\sigma$ to $\Delta\sigma'$, which is interfacial free energy difference for homogeneously nucleated crystal-melt interface. A higher $\Delta\sigma'/\Delta\sigma$ ratio indicates a higher tendency for surface nucleation.

According to nucleation theory, an overall nucleation rate, $I(T)$, at temperature, T, is determined by the critical excess free energy due to the creation of a nucleus, ΔG^*:

$$\Delta G^* = \frac{16\sigma\sigma_e\Delta\sigma\left(T_m^0\right)^2}{\Delta T^2\Delta H_f^2} \tag{2}$$

where σ and σ_e are the crystal surface energy and fold energy respectively, ΔT is the degree of supercooling, T_m^0 is equilibrium melting temperature, ΔH_f is crystal heat of fusion. Here we are considering surface nucleation and we have therefore incorporated $\Delta\sigma$ in Eq. (2). In the case of homogeneous nucleation $\Delta\sigma'$ would be incorporated instead.

* Corresponding author. Tel.: +1 514 848 2424x3138; fax: +1 514 848 3175.
E-mail addresses: i_iourie@encs.concordia.ca (Y. Yuryev), Paula.Wood-Adams@concordia.ca (P. Wood-Adams).

0032-3861/$ – see front matter © 2010 Elsevier Ltd. All rights reserved.
doi:10.1016/j.polymer.2010.12.043

Since the formation of transcrystallinity requires a high surface nucleation rate, whether or not it is observed depends on a number of *parameters* other than the nature of the interface alone. Therefore transcrystallinity, while very common, is not the only pattern of surface induced crystallization development. Considering the significant dependence of ΔG^* on the degree of supercooling (Eq. (2)), it can be assumed that even for those surface-polymer pairs exhibiting strong transcrystallinity under some conditions, there will be always a temperature range of rather limited surface nucleation concentration. Additionally, surface nucleation cannot be considered as a standalone process as it will normally be accompanied by bulk nucleation which must also be considered if one tries to understand the overall crystallization kinetics. The relative effect of surface and bulk nucleation on the overall crystallization kinetics is determined by the $\Delta\sigma$ to $\Delta\sigma'$ ratio, the crystallization temperature and the interfacial area to volume ratio. As the degree of supercooling decreases, surface nucleation will also decrease and the pattern of crystalline formation will transform from transcrystallinity to the growth of relatively sparse surface induced crystallites. Simultaneously, the relative contributions of surface and bulk crystallization to the overall kinetics will change.

A related issue is the induction time of nucleation which can significantly affect observed crystallization kinetics. It is commonly accepted that induction time t_i is an inverse function of nucleation rate but a recent study indicates a more complex and indirect relation between these two parameters [16]. It can be expected that crystallization kinetics of a polymer–substrate system will be affected by both a changing nucleation concentration and a changing induction time.

One reason that surface nucleation is a topic of importance is that it may inadvertently enter into experimental studies using instrumental techniques such as differential scanning calorimetry (DSC) which involve samples of 0.3–30 mg of polymer. Such small samples have high surface to volume ratios, leading to situations were surface nucleation can significantly affect the overall crystallization pattern [17] and can in fact mask the bulk crystallization processes which may be the primary focus of the experiment. The results of DSC studies can therefore be significantly different from the crystallization behavour of the bulk material and demonstrate pronounced thickness dependence [12]. Surface nucleation could also be a serious issue during polymer crystallization studies using new DSC techniques where extremely small samples, sometimes less than 0.1 mg are used [18]. The obvious solution is to increase the thickness of the sample reducing the relative impact of surface nucleation but unfortunately increasing temperature non-uniformity across the sample thickness. This temperature non-uniformity is caused by the crystallization heat [19,20] and the low thermal conductivity of the polymer [21] for which the instrument cannot compensate quickly enough. Such temperature disturbances, of course, also affect the crystallization kinetics [22].

A number of studies have been dedicated to revealing the influence of sample thickness on shape and magnitude of DSC traces [10,12,23]. Many of these studies neglect the possibility of surface nucleation, which can lead to erroneous conclusions. The deficiency of this approach is clearly seen in the extensive study of Hargis and Grady [23] who looked at the crystallization of polyethylene samples of varying thickness via DSC. The authors attribute the observed thickness-dependant crystallization kinetics solely to the heat transfer issue. However, the DSC samples were encased in aluminum pans and there are numerous observations of transcrystallinity initiated at the polyethylene–aluminum interface [14]. Polyethylene crystallizes very quickly, making the exact determination of kinetics data from DSC results problematic and the separation of surface nucleation and heat transfer effects nearly impossible. Additionally, the thickness dependency of the crystallinity rate as a function of time curves in reference [23] can be substantially explained by surface induced nucleation as we will show in this work. Altogether significant doubt remains as to the interpretation of such data.

Hence it is necessary to create experimental conditions when surface nucleation can be unmistakably detected and its effect on crystallization kinetics can be correctly measured. The simplest way to separate crystallization heat, apparatus thermal stabilization effects and crystallization kinetics itself is to choose a polymer crystallizing at a significantly slower rate than polyethylene or polypropylene which are usually used in these experiments and whose crystallization times are comparable to many DSC apparatus thermal stabilization times [19,24]. In this work, we chose to study poly(L/D-lactide) for this reason. This and other considerations for our choice of polymer will be addressed in detail.

The few existing studies of the dependence of surface nucleation concentration on temperature are focused on reinforced polymer systems. While transcrystallinity is very common in reinforced systems and can be easily observed, the complex shape of reinforcement-polymer interface and difficulties in correct determination of interfacial area make these systems extremely difficult for quantitative studies. This necessitates the studies of relatively simple systems having uniform shape and predictable interface area, e.g. flat discs or plates. Billon et al. [25] presented the studies of transcrystallization in flat, disk-like, polyamide samples in contact with an aluminum surface during non-isothermal crystallization. These authors also performed a theoretical analysis of crystallization kinetics of systems having different thickness in the presence of surface nucleation. They also proposed a technique for determining surface nucleation concentration from crystallization kinetics [13]. This technique is based on a modified Kolmogoroff–Avrami–Evans theory that accounts for surface nucleation and requires the availability of heterogeneous bulk nucleation concentration and growth rate data. This model also simplifies surface crystallization kinetics to the case of pure transcrystalline growth making it increasingly inaccurate as the thickness of the specimen decreases.

Little is written in the literature about the effect of surface crystallization on overall crystallization kinetics. While epitaxial growth is characterized by a significantly lower Avrami exponent than that of 3-dimensional growth, it should be noted that this applies only for a completely formed growth front. Before such a front is formed, the kinetics of surface crystallization maintains its three-dimensional nature but with a planar arrangement of nuclei. This leads to crystallization kinetics that follows the Avrami equation with an exponent that is lower than that for bulk nucleation but higher than that for pure 1-dimensional growth. Therefore it is possible that surface nucleation is the cause of lower than expected Avrami exponents obtained in many DSC studies especially for slower crystallizing polymers such as polylactide.

The kinetics of crystallization in the presence of surface nucleation depends on many factors: growth rate, induction time, surface nucleation concentration, bulk nucleation rate, sample thickness, the slope of the growth rate vs. temperature curve in the vicinity of crystallization temperature and the heat transfer parameters of the DSC apparatus and the polymer. Many researchers tend to use thin samples to accommodate heat transfer and thermal inertia issues. While decreasing the sample thickness reduces these problems, the possible presence of surface nucleation could significantly affect experimental results especially for very thin samples. This makes us believe that the proper evaluation of the relative importance of these factors on crystallization kinetics would be an important input for understanding and interpretation of experimental data. Here we attempt to do just that. While most studies of surface crystallization are dedicated to fiber or particle

reinforced systems, we have chosen to study the simpler planar polymer–substrate interface. This allows us to generalize the theoretical aspects and provides a convenient experimental variable, sample thickness, for control over the relative importance of surface and bulk nucleation at each temperature. In this way we can observe separately the effect of each of these phenomena on the overall kinetics allowing us to validate our theoretical and numerical results.

2. Experimental methods

This research was intended to reveal the effects of surface induced nucleation on the crystallization kinetics of poly(L/D-lactide) specimens having different thicknesses. This polymer was chosen over PE or PP which are commonly used for fundamental crystallization studies for several reasons. The crystallization rate of poly(L/D-lactide) is moderate and approximately 10–40 times slower than that of fast crystallizing polymers such as HDPE and PP. This extended crystallization time allows us to dramatically decrease the impact of the initial temperature transient (when cooling to the crystallization temperature) on the results. This also allows for a decreased crystallization heat flow rate, leading to a more uniform temperature field across the sample. Additionally, poly(L/D-lactide) has a lower crystallization heat as compared to HDPE or PP (~39 J/g as compared to. ~156 J/g and ~105 J/g [26] respectively) also contributing to a lower heat flow during crystallization. Poly(L/D-lactide) also has rather broad crystallization temperature range as compared to fast crystallizing polymers ~ 70 °C as compared to ~15 °C for HDPE. As well as providing more room for experiments, this means that the magnitude of the derivative of crystallization rate with respect to temperature for poly(L/D-lactide) is significantly lower than for fast crystallizing polymers making it less sensitive to temperature non-uniformity. On the other hand, polymers that undergo extremely slow crystallization (such as polystyrene) challenge the DSC sensitivity limits. Finally, poly(L/D-lactide) has a rather low bulk nucleation rate allowing us to unambiguously detect surface induced crystallization. For these reasons as well as its current practical significance and its above room temperature glass transition, poly(L/D-lactide) is a particularly good model material for these studies.

The poly(L/D-lactide) sample used here was supplied by Biomer (Germany). It is a commercially available poly(L/D-lactide) copolymer containing 2% of D-lactide (L 9000). It was found via gel permeation chromatography measurements that this polymer has a number average molecular weight of 50,000 and a polydispersity index of 2.0. The glass transition of this polymer is 59.1 °C and its melting point is 171.2 °C (5 °C/min heating/cooling). The thermal transitions and spherulitic growth rates of this polymer have previously been described [27].

The presence of oxygen and humidity leads to noticeable degradation of poly(L/D-lactide) even at temperatures below its melting point and sample preparation is therefore extremely important. The pellets were thoroughly dried at 80 °C in a vacuum oven for 24 h immediately prior to pressing into disks of 1.25 mm thickness at 185 °C in a Carver hydraulic press. This drying procedure reduced the adsorbed water content in the polymer from 0.26 wt% to 0.03 wt% significantly suppressing the influence of hydrolysis during the experiments. Samples with controlled thickness were prepared by further pressing the disks between the hot plates of a rotational rheometer (MCR 500 model of Anton Paar) at 180 °C under a nitrogen atmosphere (oxygen content of less than 2.5 ppm). The precise control of the plate alignment afforded by the rheometer allowed us to produce samples of controlled thickness with ±0.002 mm tolerance. The use of liquefied nitrogen as source of the protective medium also assures the absence of humidity in the nitrogen.

The choice of the substrate material was based on the numerous observations of surface nucleation on contact with aluminum. Also, aluminum is commonly used to encase polymer samples for thermal analysis, thus the study of its nucleating abilities has a practical importance. During the preliminary experiments using DSC aluminum pans as the substrate, it was found that while the crystallization kinetics showed a clear thickness dependency, the experimental results had significant variation. This large variation was caused by non-uniform contact between the sample and aluminum pan leading to variation of interfacial area from experiment to experiment. The cold pressing of sealed DSC pans does not provide for a complete wetting the aluminum surface during subsequent melting, making the spatial distribution of surface nucleation sites unpredictable. In order to reduce this uncertainty, the samples were melt laminated between layers of thin aluminum foil (12 μm thickness) ensuring reliable contact between polymer and the substrate over a defined area. The laminated sample was then hermetically pressure-sealed in a DSC pan to ensure good thermal contact between surfaces and to retain the shape and dimensions of the sample during the premelting stage. The foil thickness was 8 times less than that of the pan providing a negligibly small thermal resistance. The differential scanning calorimetry (DSC) measurements were performed using a ThermalAnalyst Q10 system calibrated using an indium standard. The DSC data sampling rate was 2 acquisitions per second which ensured highly precise crystallization curves. The surface area of the samples ranged from 16.4 to 25.2 mm^2 and the polymer weight was in the range of 1.4–22.6 mg depending on the thickness which ranged from 58 μm to 1.2 mm. The temperature protocol was designed to ensure conditions as close as possible to isothermal crystallization (Fig. 1). The baseline references were individually determined for each experimental temperature. In this regard, an empty sample pan was used to measure the thermal response of the DSC apparatus when subjected to rapid cooling before reaching the crystallization temperature. This method produces baseline curves which are specific to each combination of high temperature soak (interval 2 in Fig. 1), rapid cooling rate (interval 3) and crystallization temperature (interval 4). The overall melting heat obtained in interval 6 of the temperature protocol for each particular

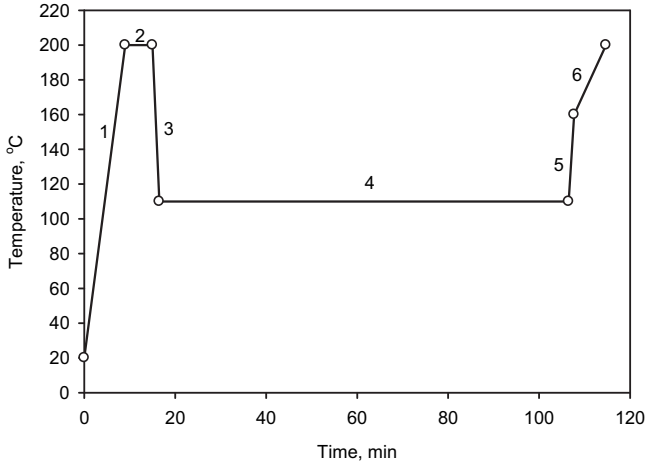

Fig. 1. Temperature protocol for DSC experiments. The sample was first heated to 200 °C (30 °C above the melting point) at 20 °C/min (1) then held at 200 °C for 5 min to erase the thermal history (2). Next, the sample was rapidly cooled at 50 °C/min (3) to the isothermal crystallization temperature (4) and held for a predetermined time. Next, the sample was rapidly heated at 50 °C/min to 150 °C to avoid secondary crystallization (5) and finally heated to 200 °C at 5 °C/min (6).

experiment was used for the determination of the baseline offset and to ensure that the dwell time in interval 4 was sufficient for the crystallization process to complete (Fig. 2).

The DSC data were converted into crystallinity as a function of time curves as follows. The ultimate heat of crystallization ΔH_∞ is the area between heat flow from the sample and the shifted baseline curve:

$$\Delta H_\infty = \int_0^{t=\infty} \left(\frac{\partial Q}{\partial \tau}\right) \mathrm{d}\tau \tag{3}$$

where Q is the heat flow of crystallization. Then the heat evolved until time t is:

$$\Delta H_t = \int_0^{t} \left(\frac{\partial Q}{\partial \tau}\right) \mathrm{d}\tau \tag{4}$$

and the fraction of transformed material is found from the following:

$$\alpha(t) = \frac{\Delta H_t}{\Delta H_\infty} \tag{5}$$

Note that the fraction transformed material here is not the same as the true fraction crystallinity which would be evaluated using the heat of fusion of poly(L/D-lactide).

3. Numerical methods

A Monte-Carlo simulation has been employed to study the combined and individual effects of surface and bulk nucleation on overall crystallization kinetics. This simulation is a useful tool for a broad parametric study which is experimentally impossible but is required for the validation of our theoretical analysis presented in the following section. Additionally, since the simulation does not include heat transfer effects, the divergence of experimental data and the simulation results under certain conditions can be used to evaluate the relative importance of surface nucleation and thermal effects.

The Monte-Carlo simulation presented here was intended to mimic heterogeneous surface crystallization occurring simultaneously with bulk crystallization. The simulated volume represents a rectangular plate of thickness d. The numerical simulation program used in this study was a modified version of a previously described simulation of homogeneous crystallization [28]. The homogeneous crystallization algorithm was adapted for mixed-type crystallization in the presence of surface nucleation. The major components of the algorithm were left intact, however the need to track a significant number of crystallizing entities required a simplification of the algorithm as a trade-off between precision and computation time. In particular, the determination of the crystallinity of the bordering elements was performed by a simple randomized switch following Raabe [29,30] instead of the more accurate approach that we have previously described [28].

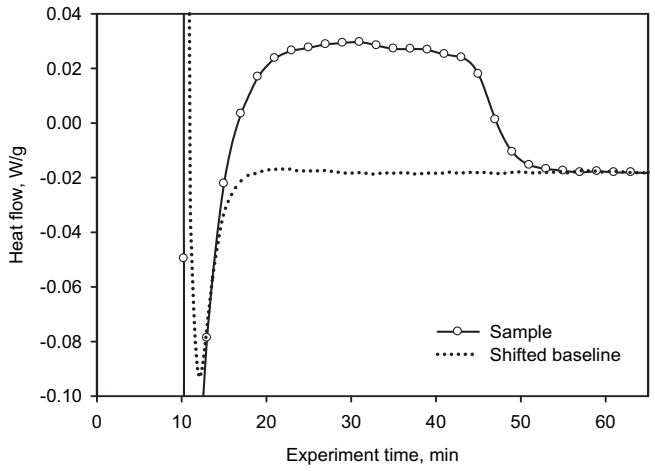

Fig. 2. An example of shifted baseline and crystallization heat curve (a 77 μm sample at 130 °C is shown). The sharp endotherm at about 10 min, present in the baseline and in the experimental data, is due to the thermal response of the apparatus.

The bulk nuclei were randomly seeded during the crystallization process in the manner previously described [28] based upon the bulk nucleation frequency, N, throughout a predetermined three-dimensional space. The algorithm assumed equal probability of nucleation throughout all untransformed material and that nucleation could occur only in the untransformed phase. The surface nucleation centers were seeded independently on both opposing surfaces with a density corresponding to the surface nucleation concentration N_s.

For a typical simulation the total number of crystallizing entities can exceed 10^5 making the tracking of a realistic sample volume time-consuming. Thus only a fraction of a DSC sample with a lateral dimension in the range of 500–1500 μm was simulated and the crystallization kinetics of that fraction was considered to be representative of the overall kinetics. Thus, the simulated space can be represented as a right rectangular cuboid with dimensions $a_x = a_y >> a_z$. The x and y dimension size was chosen individually for each simulation such that further expansion of these dimensions did not result in noticeable changes in crystallization behavour for a particular set of simulation parameters.

Right rectangular cuboid elements were used to evaluate the volume fraction crystallinity. (Note that the nucleation process is not affected by the element shape or size as the nuclei are placed randomly at any x, y, z coordinate within the untransformed simulation volume). The number of elements, m, for each simulation was in the range of 8×10^6 to 6.4×10^7 and was chosen to balance computational time and accuracy.

The probability of the formation of a crystallization site (nuclei) was considered to be equal throughout the volume of untransformed matter (bulk nucleation) and surfaces (surface nucleation). The nucleation rate N [s^{-1} m^{-3}] and concentration N_s [m^{-2}] were set to be constant in each particular simulation. The growth rate G also considered to be constant and equal in all three dimensions ($G_x = G_y = G_z$) and diffusion-independent. This is applicable for most isothermal crystallization cases and justified in many studies [31]. The ratio of densities of crystalline and amorphous phases ρ_c/ρ_l was accepted to be equal to 1 to avoid polymer-specific simulation bias. In practice, the density ratio for poly(L/D-lactide) can reach $\rho_c/\rho_l = 1.034$ for the fully transformed phase and does not have a significant impact on this particular simulation. It should be noted that degree of crystallinity we are referring in this study is the degree of phase transformation and not true crystallinity *per se*. Therefore, the crystallization parameters (N, N_s, G) and the sample thickness, d, are inputs to the simulation and the crystallinity as a function of time, α (t), is the output. The half-time of crystallization was determined as the moment of time when $\alpha = 0.5$.

The Avrami exponent n was calculated as the slope from the linear regression of as $\ln t$ vs. $\ln(-\ln(1-\alpha))$. It is well known that due to impingement phenomena an Avrami plot can deviate from linearity at higher degree of transformation. To maintain the uniformity of approach, the Avrami fit was performed within the data range of $\alpha = 0.001$–0.3. The lower limit was chosen in order to take into account the limited resolution of the simulation. The

upper limit of crystallinity of $\alpha = 0.3$ used for the Avrami exponent evaluation was chosen in compliance with recommendations of Lorenzo et al. [32].

4. Kinetics of surface crystallization: theory and simulation

We begin by considering the case when only surface induced nucleation occurs in an infinite plate with thickness d. When the surface nucleation concentration is very high, $N_s = \infty$, crystallinity builds up in the form of a uniform layer of transformed phase of thickness Gt and the crystal–amorphous interface can be represented by a plane. Considering two-sided crystallization, the fraction of transformed phase for this case can be expressed as:

$$\alpha_{N_s=\infty} = \frac{2Gt}{d} \tag{6}$$

In many cases the surface nucleation concentration is limited, which causes significant deviation from Eq. (6). Three stages of pure surface induced crystallization can be identified when $N_s \neq \infty$ (Fig. 3) corresponding to the growth geometry. In the first stage, the surface induced crystallites are growing without any impingement. This stage ends when impingement occurs at the surface. In stage 2 the crystallites are growing without confinement in the transverse direction but with increasing confinement in the lateral direction. Stage 2 ends when impingement occurs in the transverse direction. In the final stage growth occurs only in the small interstices. We refer to these three stages as: (1) impingement-free growth, (2) increasingly laterally-constrained transverse growth, and (3) interstitial growth.

The first stage of surface crystallization represents a particular case of heterogeneous bulk crystallization where the nuclei are distributed randomly on a plane and can be well described by Avrami–Evans equation:

$$\alpha_I = 1 - \exp(-kt^n) \tag{7}$$

where k is a crystallization constant and n is the Avrami exponent.

In order to illustrate this, we performed a series of Monte-Carlo simulations with varying surface nucleation concentration in which the bulk nucleation rate was set to 0 (Fig. 4). We then fit Eq. (7) to the initial portions of the $\alpha(t)$ results from each simulation. The fitting parameters are given in Table 1 and the quality of fit is illustrated in Fig. 4. We note that the Avrami exponent decreases as N_s increases due to an increasing number of lateral impingements. The kinetics approach pure transcrystalline growth as N_s increases and pure heterogeneous bulk crystallization kinetics as N_s decreases.

The initial stage of surface induced crystallization ends with complete lateral confinement of individual crystallites at the surface and the second stage of crystallization begins where primarily transverse growth occurs (Fig. 3). This leads to significant changes in crystallization kinetics. While for $N_s = \infty$, crystallinity increases linearly with time, for $N_s < \infty$, $\alpha(t)$ becomes a nonlinear function. The nonlinearity is caused by an increasing of radius of curvature of the growth front of each crystallizing entity. To accommodate an increasing radius of curvature, the confinement interface propagates with velocity v_c higher than the growth rate G:

$$v_c = \frac{G^2 t}{\sqrt{G^2 t^2 - \frac{1}{\pi f N_s}}} > G \tag{8}$$

where f is an equivalency coefficient which accounts for the fact that the confinement interface is polyhedral rather than circular. The concept and geometry of the confinement interface is shown in Fig. 5.

In order to derive an analytical expression for the evolution of crystallinity during the second stage of crystallization, it is necessary to use a simplified model of the shape of a typical crystallite. Due to the random placement of nuclei on the surface, the shape of a particular confined entity can be complex. In our model, we consider the equivalent crystallite to be a vertical cylinder capped with a segment of a sphere. The radius of curvature of the cap is Gt, the height of the cap is h, the height of the cylinder is $(Gt-h)$ and the diameter of the cylinder is given by the equivalent diameter, c_e.

The average surface area occupied by single crystallizing entity is:

$$A_c = \frac{1}{N_s} \tag{9}$$

Then the equivalent diameter c_e can be expressed as:

$$c_e = \sqrt{\frac{4}{\pi f N_s}} = 2\sqrt{h(2Gt - h)} \tag{10}$$

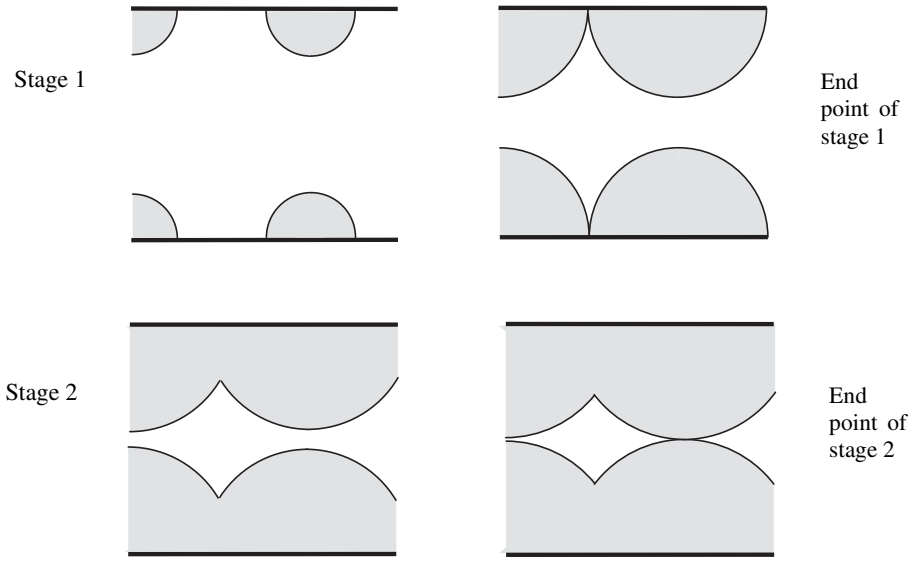

Fig. 3. Illustration of the first 2 stages of surface induced crystallization.

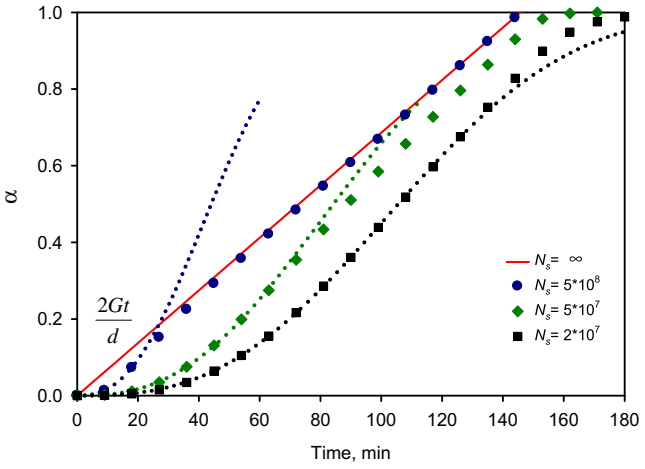

Fig. 4. Kinetics of surface crystallization for different surface nucleation concentration. Data points are the simulation results for $d = 500$ μm and $G = 1.715$ μm/min. Doted lines are fits of simulated crystallization data for the first stage of crystallization using Eq. (7).

and the volume of the equivalent crystallite, V_e, is:

$$V_e = \pi h\left[\frac{c_e^2}{8}+\frac{h^2}{6}\right] + \frac{\pi}{4}(Gt-h)c_e^2 \tag{11}$$

By combining Eqs. (10) and (11) we find:

$$V_e(t) = \frac{1}{fN_s}\sqrt{G^2t^2-\frac{1}{\pi fN_s}} + \left[Gt-\sqrt{G^2t^2-\frac{1}{\pi fN_s}}\right]\left[\frac{1}{2fN_s} + \frac{\pi}{6}\left[Gt-\sqrt{G^2t^2-\frac{1}{\pi fN_s}}\right]^2\right] \tag{12}$$

and

$$\alpha_{II} = \frac{2fV_e(t)N_s}{d} \tag{13}$$

We make use of our Monte-Carlo simulation to evaluate the analytical model and determine the best value for our equivalency coefficient, $f = 0.48$ (Fig. 6). It should be noted that Eq. (12) provides real values for the crystallite volume only for the second stage of crystallization. The onset of the second stage is:

$$t_{II} = \frac{1}{G\sqrt{\pi fN_s}} \tag{14}$$

The final stage of crystallization begins when mutual impingement of the two crystallizing fronts occurs. At this moment, the transverse growth stops and the remaining untransformed phase in the small interstices is converted via an increase of radius of curvature of the equivalent spherical segment.

Table 1
The effect of surface nucleation concentration on the Avrami parameters for the initial stage of surface induced crystallization.

N_s, m^{-2}	k	n	R^2_{adj}
2×10^7	2.699×10^{-11}	2.738	0.999963
5×10^7	2.177×10^{-10}	2.566	0.999717
1×10^8	5.441×10^{-10}	2.514	0.999588
5×10^8	2.576×10^{-9}	2.465	0.999423

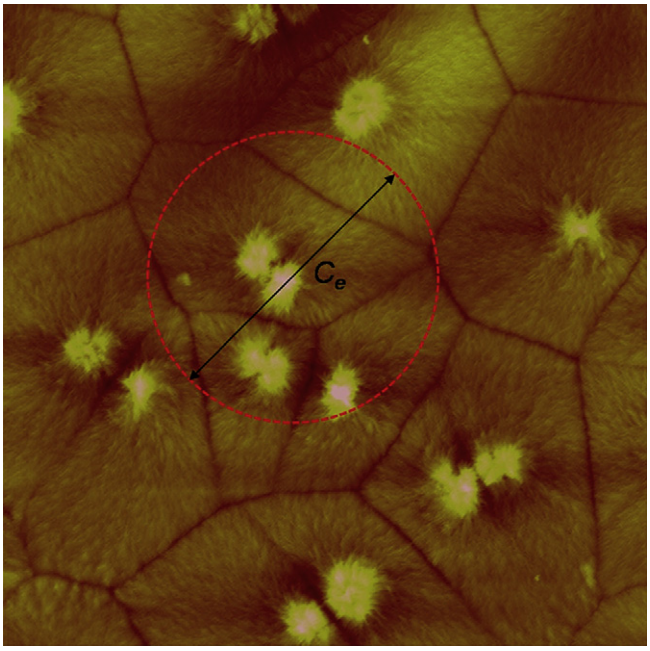

Fig. 5. An illustration of the concept of equivalent spherical segment. Image is a 100 μm by 100 μm AFM height image of a poly(L/D-lactide) film, surface crystallized at 120 °C on a glass surface and having local nucleation density of 1.3×10^9 m^{-2}. The dashed circle represents an equivalent diameter c_e corresponding to this nucleation concentration. The confinement interfaces show up as the dark lines bordering the crystallites.

It is also interesting to look at the crystallization rate curves, $d\alpha/dt$, as these curves have a characteristic shape in the case of surface induced crystallization. Using the Monte-Carlo simulation we have generated bulk crystallization curve to compare with our simulation results for pure surface induced crystallization and mixed crystallization when both types of crystallization are present (Fig. 7). As it can be seen, not the only shape of the curve but also the half-times of crystallization are significantly affected by spatial restrictions in the case of surface crystallization. Also, the three stages of growth are clearly visible in the case of pure surface crystallization which exhibits a characteristic flattened, broad peak.

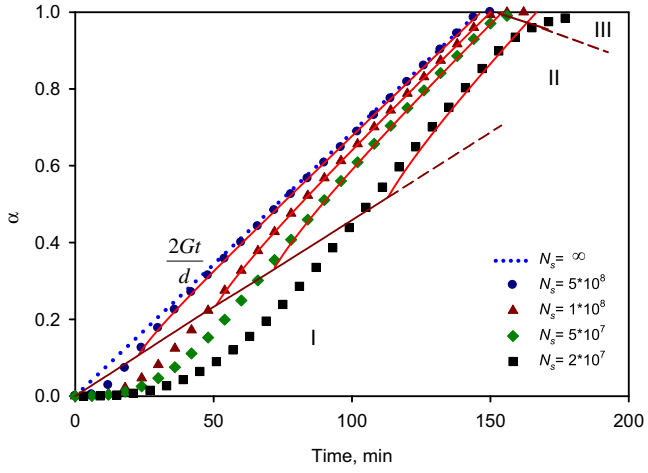

Fig. 6. The simulated crystallization kinetics (symbols) and corresponding analytical functions Eqs. 12 and 13 (solid lines). The three crystallization stages are denoted in roman numerals. Data for $d = 500$ μm and $G = 1.715$ μm/min are shown. The best fit value of f is 0.48.

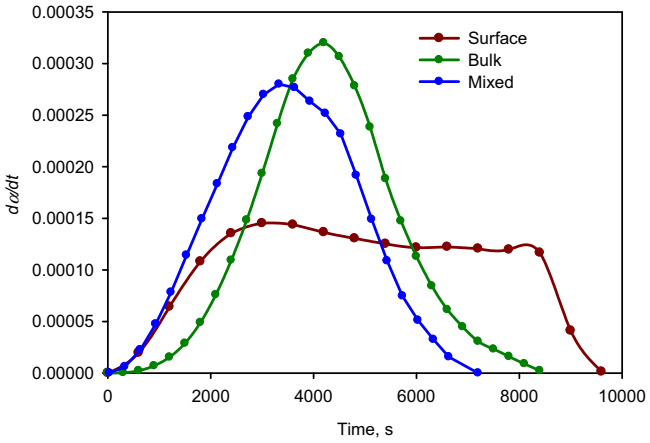

Fig. 7. Simulated crystallization rate curves showing 3 different types of crystallization: pure surface nucleation ($N_s = 10^8$ m^{-2}, $\tau_{½} = 4874$ s), pure bulk nucleation ($N = 10^8$ s^{-1} m^{-3}, $\tau_{½} = 4242$ s), and mixed nucleation ($N_s = 10^8$ m^{-2} and $N = 10^8$ s^{-1} m^{-3}, $\tau_{½} = 3533$ s). Data are the simulation results for $d = 500$ μm and $G = 1.715$ μm/min.

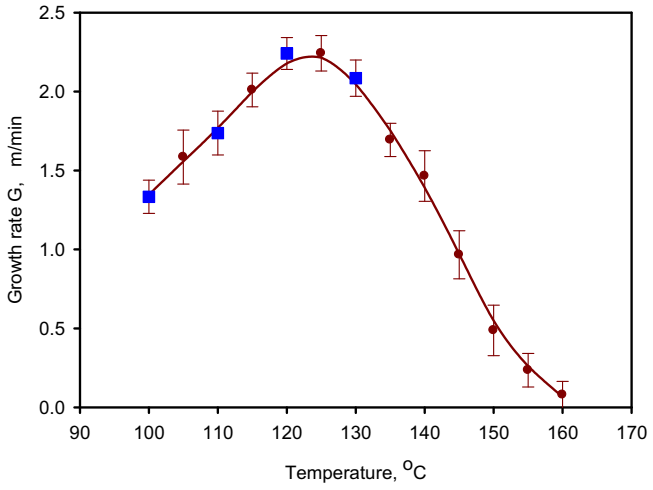

Fig. 9. The experimental spherulitic growth rate of the poly(L/D-lactide) used in thist study. Data are taken from Yuryev et al. [27]. The square symbols highlight the experimental conditions of this study.

Note that the mixed crystallization curve can be more or less distorted from the classical bulk crystallization shape depending on the two nucleation constants, the growth rate and the sample thickness.

5. Results and discussion

5.1. Experimental results

We begin by considering the experimentally determined half-times of crystallization which were extracted from the DSC traces as shown in Fig. 2 and Eq. (3) through (5). The results for laminated aluminum–polylactide–alumunium samples of varying thicknesses are summarized in Fig. 8 showing a pronounced thickness dependence. In particular, the half-times of crystallization are much smaller for the very thin samples as compared to the thick samples, due, likely, to the increased impact of surface nucleation. The effect of specimen thickness on half-time decreases as specimen thickness increases and ultimately, the half-time essentially plateaus for specimens thicker than 500 μm. This is consistent with surface nucleation, the impact of which is expected to diminish as

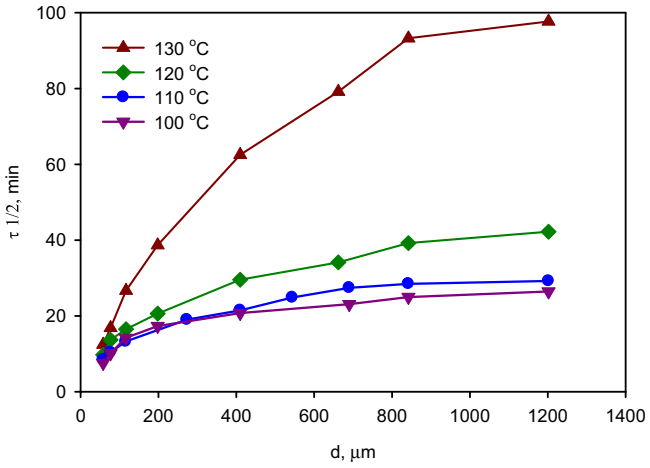

Fig. 8. Experimental half-times of crystallization of poly(L-lactide) sandwiched between aluminum surfaces.

the ratio of contact area to volume decreases. It should be noted that we also expect the half-time of bulk crystallization to be affected by specimen thickness due to spatial constraints imposed by crystallizing volume dimensions [28] diminishing the effect of the bulk crystallization on the overall kinetics. However, for the nucleation and growth rates observed in our experiments the spatial constraint effect is very small. The surface crystallization kinetics, on the other hand, is dramatically affected by the specimen thickness as given by Eq. (13).

The other important aspect to these data is the temperature dependence. Although the experimental window was limited to 100 °C–130 °C, we can still make some interesting inferences from the results. Firstly we see that $\tau_{½}$ is rather insensitive to temperature for thin samples indicating that it is primarily determined by the concentration of surface nuclei, which is expected to be athermal, and is less influenced by the growth rate, which is temperature dependant. It is important to note that for the thinnest samples, there is a small $\tau_{½}$ temperature dependency that is not consistent with the temperature dependency of the growth rate (Fig. 9) indicating that the surface nuclei concentration is somewhat affected by temperature. For the thicker samples, we see a much stronger and highly nonlinear influence of temperature on $\tau_{½}$. This is because the crystallization kinetics of the thicker samples is affected by both the bulk nucleation rate and the growth rate (Fig. 8) which are temperature dependant. It can be seen that most dramatic changes in half-time of crystallization happens at temperatures above 120 °C. The spherulitic growth rate is particularly important in this specific example because while both the surface and bulk nucleation concentration decrease with temperature at these conditions, the growth rate of poly(L/D-lactide) is noticeably higher at 120 °C as compared to 110 °C. At 130 °C the nucleation concentration is the lowest and the growth rate is also lower than that at 120 °C which causes a dramatic increase in $\tau_{½}$. It can be noticed that there is little difference between 100 °C and 110 °C curves. At the lower temperatures, the effect of the increasing bulk and surface nucleation concentrations is offset by the steadily decreasing growth rate resulting in only a minor half-time decrease.

While no explanation is needed as to nature of the effect of growth rate on the half-time of crystallization, it is very important to establish its magnitude. The growth rate, along with other parameters, is a component of the constant k in the Evans–Avrami

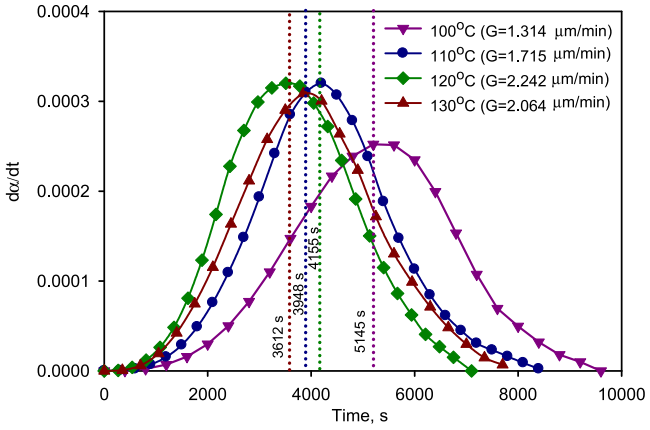

Fig. 10. The simulation of bulk crystallization kinetics of the system having $N = 1 \times 10^8$ s^{-1} m^{-3} with different growth rates. The dashed lines represent the half-time $\tau_{1/2}$ of crystallization.

Equation (Eq. (7)). The exact functional form of this dependency can be expressed directly only for some simple cases and for this reason the Monte-Carlo simulation is an obvious tool to study the effect of this factor on crystallization kinetics. The results of these simulations are shown in Fig. 10 where bulk crystallization rates of hypothetical systems having the same nucleation rate but different growth rates (equal to our experimental rates for poly(L/D-lactide)) are shown. We can see that even relatively small variations of growth rate significantly affect the crystallization kinetics.

Next we consider the kinetics in more detail by examining the experimental crystallization rate curves (Fig. 11). As expected [33], there is a distinctive induction time required for bulk nucleation to start and this induction time rapidly increases with temperature. This effect is most visible in Fig. 11d (130 °C) for the thickest sample. In this case, as surface nucleation has essentially no effect on the overall crystallinity, we can see a clear zero rate of crystallization in the first 500 s. The induction time of bulk nucleation is also visible in Fig. 11c (120 °C) for the 77 and 116 μm thick samples where we see a skewing of the top of the peak at induction. The ultimate enthalpy of crystallization gradually increased with the increasing isothermal crystallization temperature (Table 2). This observation was in accordance with a previous study of isothermal poly(L/D-lactide) crystallization [34].

The shape of the crystallization rate curves undergoes an evolution depending on the relative importance of surface and bulk nucleation, which is affected by both specimen thickness and temperature. For thicker samples, at all temperatures, the shape of the curve is symmetric as is typical of bulk crystallization. The same is true for thin samples at low temperatures. For thin samples, as the temperature increases, the shape of the curve transforms, showing a shoulder at short times, and under some conditions becoming the flattened peak characteristic of surface induced crystallization (Fig. 7). From this we can infer that while both surface and bulk nucleation concentration decrease as temperature

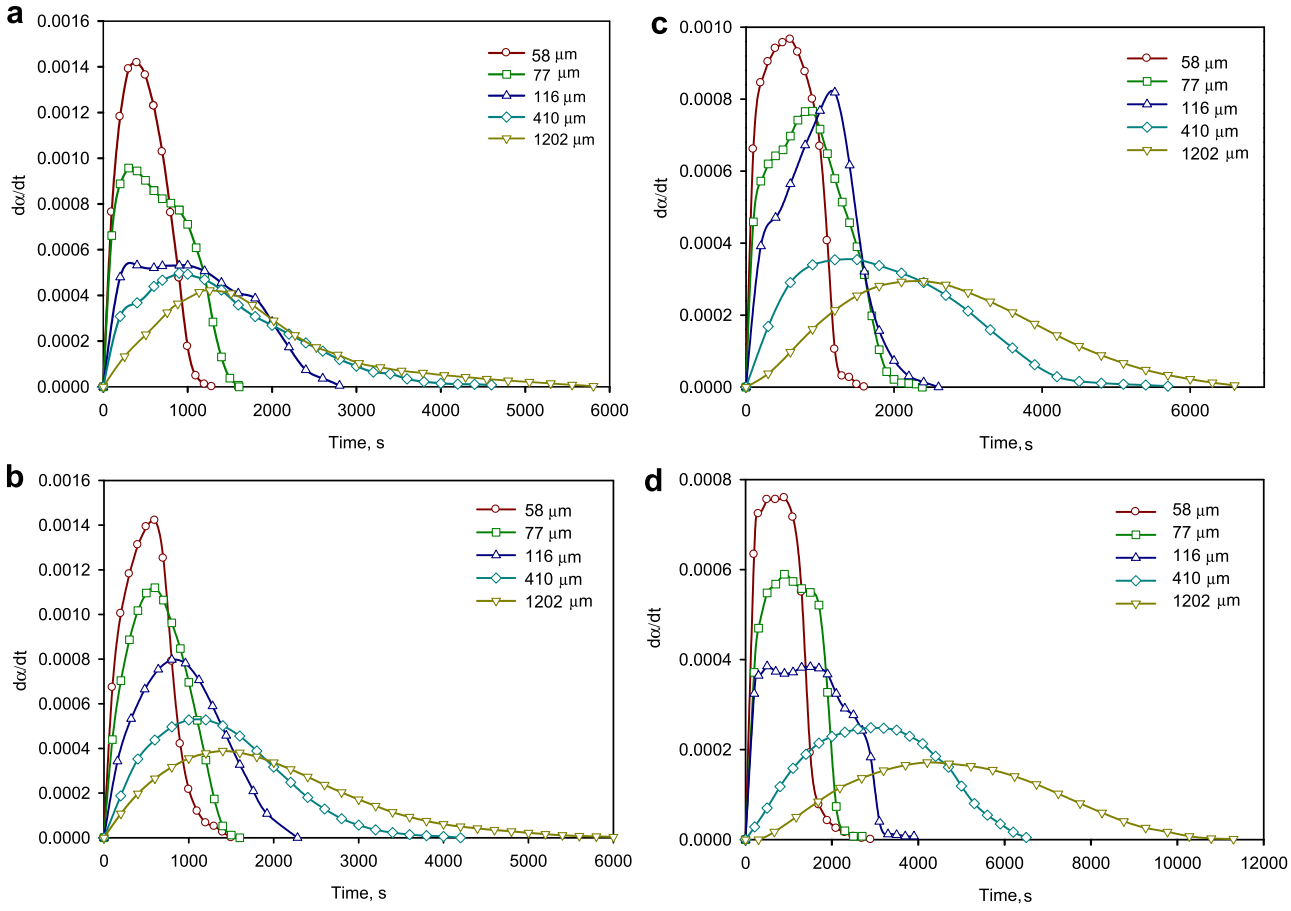

Fig. 11. The experimental crystallization kinetics data of the poly(L/D-lactide) samples of different thickness in contact with aluminum surface at a) 100 °C b) 110 °C; c) 120 °C; d) 130 °C. These curves were calculated from the DSC traces as explained in the Experimental methods section. Points have been thinned by a factor of 3000–24000 to allow for clear viewing of the behavour.

Table 2
The surface crystallization of poly(L/D-lactide) simulation results at different temperatures.

T, °C	N_s, m^{-2}	N, m^{-3} s^{-1}	$\tau_{1/2}(2D)$, min	$\tau_{1/2}(d=\infty)$, min	G, μm/min[a]	ΔH_∞, J/g[a]
100	2.49×10^{10}	3.11×10^{10}	1.89	26.76	1.314	38.21 ± 0.77
110	9.27×10^{9}	4.87×10^{9}	2.11	29.37	1.715	38.83 ± 0.53
120	2.05×10^{9}	4.17×10^{8}	2.76	41.48	2.242	40.32 ± 0.49
130	3.23×10^{8}	2.24×10^{7}	3.77	92.91	2.064	42.02 ± 0.68

[a] Experimental data.

increases, the bulk nucleation concentration decreases much more steeply.

5.2. Monte-Carlo simulation of crystallization kinetics of the samples of different thickness

Next we attempt to combine the experimental results with Monte-Carlo simulations in order extract nucleation density and rate from the results as well as to comment on the effect of heat transfer issues. To do this, we selected values of N_s and N that gave the best fits to the experimental $\tau_{½}$ data for the 4 thinnest samples at each temperature (Fig. 12 and Table 2). As expected, we found that while N_s decreases as temperature increases, it is much less sensitive to temperature than N (Table 2). This is consistent with the evolution of the experimental rate curves in Fig. 11 to a surface crystallization characteristic shape at higher temperatures. Accepting the idea that both types of nucleation are governed by a free energy difference ($\Delta\sigma$ or $\Delta\sigma'$) and all other parameters in Eq. (2) are the same, it can be concluded that the free energy difference function is the reason for the different temperature sensitivities of N and N_s. In fact, it can be shown with Eq. (2) that in all cases where surface nucleation is favorable (i.e. $\Delta\sigma' > \Delta\sigma$) we expect N to be more temperature sensitive than N_s.

The Monte-Carlo results exhibit the expected increase of $\tau_{1/2}$ with increasing thickness that gradually slows down reaching the limit of $\tau_{1/2}(d=\infty)$. Since the influence of surface nucleation decreases as the thickness increases, this limit was determined from the simulation as the half-time of crystallization at N_s=0 (dashed lines in Fig. 12). At d=0 the simulated system transforms to a two-dimensional case having surface nucleation concentration of N_{surf}=2N_s. The half-time of crystallization for this case $\tau_{1/2}(2D)$ is the time when half of the area is covered by crystallizing entities.

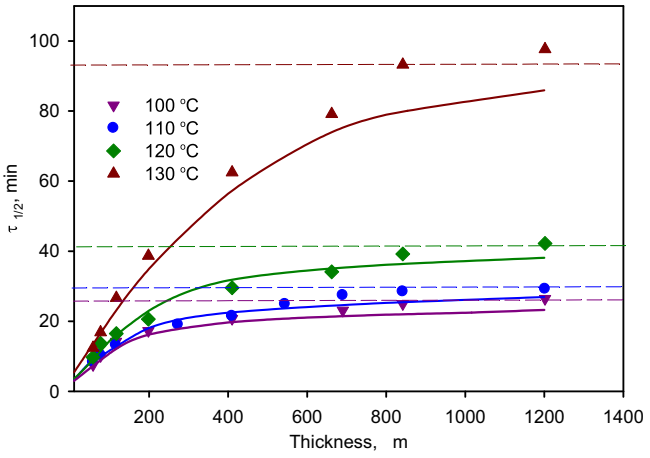

Fig. 12. The experimental data (symbols) and Monte-Carlo simulation results (solid lines). The dashed lines represent corresponding $\tau_{1/2}(d=\infty)$ lines.

As explained previously, there are factors other than growth rate, geometry, nucleation pattern and concentration that contribute to the crystallization behavour of polymers and are not included in our Monte-Carlo simulation. It appears that induction time and mixed nucleation are the most influential amongst them. While there is very little delay for onset of heterogeneous surface crystallization of poly(L/D-lactide), the bulk crystallization is characterized by an induction time. We have shown previously with a different experimental study, that for the poly(L/D-lactide) under investigation the induction time dramatically increases with the crystallization temperature from 2100 s at 140 °C to 35100 s at 155 °C [35]. For temperatures less than 140 °C we expect shorter but still significant induction times. We recall that the onset of bulk crystallization is clearly visible in several of the experimental crystallization rate curves (Fig. 11).

In this study we attempted to eliminate effects of thermal inertia and crystallization heat on isothermal crystallization kinetics by choosing a specific model polymer having moderate crystallization rate. We expect a temperature gradient due to crystallization heat to be approximately $\frac{\Delta T}{d} \propto \Delta H \frac{d\alpha}{dt}$. As explained in the Experimental methods section, the RHS of this proportionality for polyethylene is up to 160 times that of polylactide. Therefore, while temperature gradients are significant in such isothermal crystallization studies with PE they are much less so for polylactide. Nevertheless, we cannot completely neglect their impact and we expect that temperature disturbances are part of the reason for the increasing deviation of the experimental kinetics from the simulated kinetics with increasing sample thickness as temperature increases (Fig. 12). There are number of other reasons for the difference between simulation and experiment. First, the simulations presented in this study are based homogeneous nucleation in the bulk while in reality a significant portion is expected to be athermal nucleation. A thermal bulk nucleation is characterized by a lower Avrami exponent and our simulation would tend to overestimate the crystallization rate at final stages of crystallization for thick samples. Another possible contributing factor is nuclei clasterization. While the nucleation distribution in the simulation is perfectly random, in real studies nucleation centers often tend to aggregate into rather extended areas of elevated nucleation concentrations leaving significant areas free from crystallite growth. This contributes to both overall increase of observed crystallization time and asymmetry of crystallization curve. Our previous studies of thin film polylactide crystallization [27] showed that the nuclei clasterization is also typical for surface nucleation but it has less effect on overall crystallization kinetics due to lower dimensionality of surface crystallization.

6. Conclusions

In this study we revealed the crystallization kinetics of poly(L/D-lactide) in the presence of surface nucleation caused by intimate contact with aluminum surface. It was found that surface crystallization dramatically affects the crystallization kinetics of poly(L/D-lactide) changing both crystallization rate and the very shape of the crystallization curve. Because of the specific spatial arrangement of surface nuclei, crystallization kinetics in the presence of surface crystallization demonstrated a distinctive dependence on sample thickness. It was found that the half-time of crystallization can change up to an order of magnitude depending on sample thickness. For certain conditions, the crystallization rate curve exhibited a distinctive shape typical of surface nucleation. Theoretical aspects of surface nucleation were considered and three distinctive stages of surface crystallization were identified. Governing equations for the first two stages were suggested. These equations were verified using a Monte-Carlo simulation of pure

surface crystallization. The experimental conditions were also simulated with the Monte-Carlo framework allowing the estimation of surface nucleation concentrations and bulk nucleation rates, revealing their temperature dependence. It was found that both nucleation parameters decrease with increasing temperature while that of bulk nucleation is much more temperature sensitive in a highly nonlinear manner.

Acknowledgments

This work was supported by Auto 21; an NSERC funded Centre of Excellence.

References

[1] Fitchmun DR, Newman S. J Polym Sci Part A-2: Polym Phys 1970;8:1545–64.
[2] Grozdanov A, Bogoeva-Gaceva G. Compos Interfaces 1998;5(2):179–89.
[3] Wang C, Liu CR. Polymer 1999;40(2):289–98.
[4] Feldman A, Gonzalez MF, Marom G. Macromol Mater Eng 2003;288(11):861–6.
[5] Wagner HD, Lustiger A, Marzinsky CN, Mueller RR. Compos Sci Technol 1993; 48(1–4):181–4.
[6] Moon CK. J Appl Polym Sci 1994;54(1):73–82.
[7] Wood JR, Wagner HD, Marom G. J Mater Sci Lett 1995;14(22):1613–5.
[8] Zhang ZY, Zeng HM. J Appl Polym Sci 1993;48(11):1987–95.
[9] Zhang S, Minus ML, Zhu L, Wong C-P, Kumar S. Polymer 2008;49:1356–64.
[10] Billon N, Henaff V, Pelous E, Haudin JM. J Appl Polym Sci 2002;86:725–33.
[11] Billon N, Henaff V, Haudin JM. J Appl Polym Sci 2002;86:734–42.
[12] Gadzinowska K, Piorkowska E. Polymer 2003;48:790–9. 11–12.
[13] Billon N, Haudin JM. Colloid Polym Sci 1993;271:343–56.
[14] Chatterjee AM, Price FP, Newman S. J Polym Sci 1975;13:2369.
[15] Ishida H, Bussi P. Macromolecules 1991;24:3569–77.
[16] Fokin VM, Yuritsyn NS, Zanotto ED, Schmelzer JWP, Cabral AA. J Non Cryst Solids 2008;354(32):3785–92.
[17] Billon N, Esceleine JM, Haudin JM. Colloid Polym Sci 1989;267:668.
[18] Vanden Poel G, Mathot VBF. Thermochim Acta 2007;461:107–21.
[19] Piorkowska E, Galeski A. Polymer 1992;33:3985.
[20] Martins JA, Cruz Pinto JJC. J Appl Polym Sci 2004;91:125–31.
[21] Janeschitz-Kriegl H, Wippel H, Paulik C, Eder G. Colloid Polym Sci 1993;271: 1107–15.
[22] Wu CH, Eder G, Janeschitz-Kriegl H. Colloid Polym Sci 1993;271:1116–28.
[23] Hargis MJ, Grady BP. Thermochimica Acta 2006;443:147–58.
[24] Hernandez-Sanchez F, del Castillo LF, Vera-Graziano R. J App Polym Sci 2004;92:970–8.
[25] Billon N, Magnet C, Haudin JM, Lefebvre D. Colloid Polym Sci 1994;272: 633–54.
[26] Li JX, Cheung WL, Demin J. Polymer 1999;40:1219–22.
[27] Yuryev Y, Wood-Adams P, Heuzey M-C, Dubois C, Brisson J. Polymer 2008;49 (9):2306–20.
[28] Yuryev Y, Wood-Adams P. Macromol Theory Simul 2010;19(5):278–87.
[29] Raabe D. Acta Mater 2004;52:2653.
[30] Raabe D, Godara A. Model Simul Mater Sci Eng 2005;13:733.
[31] Mandelkern L. Crystallization of polymers. 2nd ed. Cambridge: Cambridge University Press; 2004.
[32] Lorenzo AT, Arnal M-L, Albuerne J, Muller AJ. Polym Test 2007;26:222–31.
[33] Kenny JM, Maffezzoli A, Nicolais L. Thermochim Acta 1993;227:83–95.
[34] Sarasua JR, Lopez Arraiza A, Balerdi P, Maiza I. J. Mater Sci 2005;40:1855–62.
[35] Yuryev Y, Wood-Adams P. J Polym Sci B Polym Phys 2010;48(7):812–22.

Polymer 52 (2011) 718–731

Contents lists available at ScienceDirect

Polymer

journal homepage: www.elsevier.com/locate/polymer

3D porous polymeric conductive material prepared using LbL deposition

Sepehr Ravati, Basil D. Favis*

CREPEC, Department of Chemical Engineering, École Polytechnique de Montréal, Montréal, Québec H3C3A7, Canada

ARTICLE INFO

Article history:
Received 31 August 2010
Received in revised form
26 November 2010
Accepted 1 December 2010
Available online 9 December 2010

Keywords:
Conductive
Layer-by-layer
Porous polymeric substrate

ABSTRACT

In this work a 3D porous polymeric conducting material is derived from a multi-percolated polymer blend system. The work has focused on the preparation of low surface area porous substrates from polymer blends followed by the deposition of polyaniline conductive polymer (PANI) on the internal porous surface using a layer-by-layer (LbL) technique. The approach reported here allows for the percolation threshold concentration of polyaniline conductive polymer (PANI) to be reduced to values of no more than 0.19%. Furthermore, depending on the amount of PANI deposited, the conductivity of the porous substrate can be controlled from 10^{-15} S cm^{-1} to 10^{-3} S cm^{-1}.

Ternary and quaternary multi-percolated systems comprised of high-density polyethylene (HDPE), polystyrene (PS), poly(methyl methacrylate) (PMMA) and poly(vinylidene fluoride) (PVDF) are prepared by melt mixing and subsequently annealed in order to obtain large interconnected phases. Selective extraction of PS, PMMA and PVDF result in a fully interconnected porous HDPE substrate of ultra-low surface area and highly uniform sized channels. This provides an ideal substrate for subsequent polyaniline (PANI) addition. Using a layer-by-layer (LbL) approach, alternating poly(styrene sulfonate) (PSS)/PANI layers are deposited on the internal surface of the 3-dimensional porous polymer substrate. The PANI and sodium poly(styrene sulfonate) (PSS) both adopt an inter-diffused network conformation on the surface. The sequential deposition of PSS and PANI has been studied in detail and the mass deposition profile demonstrates oscillatory behavior following a zigzag-type pattern. The presence of salt in the deposition solution results in a more uniform deposition and more thickly deposited PSS/PANI layers. The conductivity of these samples was measured and the conductivity can be controlled from 10^{-15} S cm^{-1} to 10^{-5} S cm^{-1} depending on the number of deposited layers. In the case of a porous sample which can be crushed, applying a load to the substrate can be used as an additional control parameter. In that sample a high load results in higher conductivity with values as high as 10^{-3} S cm^{-1} obtained. The work described above has focused on very low surface area porous substrates in order to generate a conductive device with the lowest possible concentration values of polyaniline, but high surface area substrates can also be readily prepared using this approach.

1. Introduction

One of the main contributions in polymer physics over the last 20 years has been the development of electronic devices consisting of conducting polymers [1–7]. This work has led to: the thin film deposition and microstructuring of conducting materials [1]; materials for energy technologies [2]; electroluminescent and electrochromic devices [3]; membranes and ion exchangers [4]; corrosion protection [5]; sensors [6] and artificial muscles [7]. Electron conductive polymers, which are the result of extended π-conjugation along the polymer backbone, fall into the class of conductive materials exhibiting semi-conducting behavior. The discovery of polymer light emitting diodes [8], in particular, has brought considerable attention to the efficacy and lifetime of semi-conducting polymer-based electronic devices. The magnitude of the electrical resistivity, or conductivity, determines the application field of the device and these polymeric optoelectronic devices can be classified in a number of different categories including: antistatic applications with a range of 10^{-14}–10^{-9} S cm^{-1}; electrostatic dissipation applications with a range of 10^{-9}–10^{-5} S cm^{-1}; and semi-conducting applications with a range of 10^{-6}–10^{0} S cm^{-1} [9]. By controlling the range of the conductivity, the development of devices such as polymeric photovoltaic devices [10], polymer-based lasers [11], and transistors [12] has received considerable attention recently.

Some of the principal approaches used in the preparation of polymeric conductive devices are the fabrication of ultrathin films by various strategies such as the Langmuir–Blodgett (LB) technique [13] and the self-assembled monolayer (SAM) method [14]. As well,

* Corresponding author. Tel.: +1 (514)3404711x4527; fax: +1 (514)3404159.
E-mail address: basil.favis@polymtl.ca (B.D. Favis).

0032-3861/$ – see front matter © 2010 Elsevier Ltd. All rights reserved.
doi:10.1016/j.polymer.2010.12.005

layer-by-layer (LbL) assembly allows for a high degree of control of material properties and architecture at the nanometer scale [15,16]. In less than 20 years since the introduction of the LbL technique [17], the electrochemical study of LbL films has grown from theory to functional devices, but, in most cases, thin films of conductive polymer are applied on 2D surfaces. One of the main requirements in this field is to further expand the range and potential of 3D conductive polymeric devices.

In an A/B heterophasic polymer blend, a low concentration of phase A forms droplets in a matrix of phase B. As the concentration is gradually increased the percolation point is reached and the continuity of phase A also increases. Near the phase inversion region a co-continuous morphology is observed [18]. A co-continuous morphology is defined as a state where each phase is completely continuous throughout the material. The co-continuous phase structure consists of two fully interconnected phases which mutually interpenetrate each other [19]. The percolation threshold is defined as the formation of long-range connectivity in random systems. Solid droplets typically demonstrate a percolation threshold at values of 0.16 by assuming that the occupation of a site or bond is completely random. A topic of significant interest in heterophasic polymer blends has been to examine the various factors which results in significant reductions in the percolation threshold concentration [20,21]. One of the most interesting approaches towards low percolation thresholds is the development of double percolated structures [22,23]. Zhang et al. [24] reported on a thermodynamically driven double percolated morphology in an HDPE/PS/PMMA blend which was essentially a fully continuous system, PS, encapsulating an already continuous system, PMMA. This type of structure allowed the percolation threshold for the encapsulating polymer to be reduced to well below 3%. This work demonstrated the potential of layering one phase onto another continuous structure as a powerful technique to reducing percolation thresholds.

In a ternary liquid system complete wetting can be described when one phase tends to spontaneously spread on the second phase in the matrix of third phase. For this purpose, Torza and Mason [25] and then Hobbs et al. [26] employed modified Harkins spreading coefficients (λ_{ij}) which is a simple and useful mathematical expression and thermodynamic explanation to predict wetting characteristic (phase morphology) of ternary systems.

$$\lambda_{ij} = \gamma_{jk} - \gamma_{ik} - \gamma_{ij} \quad (1)$$

λ_{ij} is defined as the spreading coefficient giving the tendency of component (i) to encapsulate or spread onto component (j) in the matrix of component (k). It can also physically be defined as the transition between the non-wet and wet states. γ_{ij}, γ_{ik} and γ_{jk} are the interfacial tensions of the different polymer pairs. A positive value for the spreading coefficient, such as λ_{ij}, determines that phase (i) spreads over phase (j) while negative values for all possible spreading coefficients indicates separately dispersed phases in a continuous matrix.

In co-continuous polymer blends, the solvent extraction of one phase is a route towards porous materials with a fully interconnected porosity. A number of studies have shown that the phase size of co-continuous structures can be closely controlled from about 100 nm to hundreds of microns. The interfacial tension and an annealing step are critical parameters in this regard. One of the most important ways to coarsen, or increase, the phase size of a co-continuous network is melt annealing [27]. It has been shown that the annealing of a PS/PE system could increase the phase size from 0.9 to 72 μm [28]. Yuan et al. [27] observed a linear time dependence for the coarsening of immiscible co-continuous blends and proposed a capillary pressure effect as the driving force of the coarsening process during static annealing. In the static coarsening of co-continuous polymers, some very low level flow does occur since the systems are fully interconnected throughout the material. This is why the static coarsening of co-continuous systems is much more significant than that for dispersed phase systems. Clearly, highly controlled co-continuous morphologies can be converted into highly controlled porous materials through the selective extraction of one of the phases.

The layer-by-layer deposition technique to produce a polyelectrolyte multilayer on the surface of a flat substrate was proposed by Decher et al. [29]. In the LbL approach, the adsorption process involves consecutive and alternate deposition of positively and negatively charged polyelectrolytes driven by electrostatic forces followed by a rinsing step with water. A number of factors can influence mass deposition by LbL such as: ionic strength [30], pH of solution [31], molecular weight of polyelectrolyte [32], concentration of polyelectrolytes [33], and charge density [34]. Repetitive deposition steps provide a precise control over the total thickness of the layers in the range from a few angstroms up to a few micrometers. The thickness increment after each deposition is referred to as a growth rate which is dictated by polyelectrolyte geometry, surface charges, and solution parameters [35]. Some of the most widely used polyelectrolytes are sodium poly(styrene sulfonate), poly (diallyldimethyl-ammonium) chloride, poly(ethyleneimine), poly (allylamine), poly(vinyl sulfate), and poly(acrylic acid). Recent advances in LBL techniques, in the non-conductive area, have demonstrated the possibility of templating multilayers onto 3D scale substrates. Caruso et al. [36] deposited LBL films onto a colloidal core. Subsequent removal of the core resulted in a thin-film shell. Roy et al. [37] deposited LBL films onto a fully interconnected porous PLLA surface and the subsequent removal of PLLA resulted in a 3D object comprised of a vast nanosheath network of high surface area and the highest void volume ever reported for a polymeric substrate.

Rubner et al. [38,39] were the first to apply the LbL technique in the field of electronically conductive polymers to construct poly (styrene sulfonate) (PSS)/polyaniline (PANI) bilayers onto thin films in order to prepare a conductive device. Important advances have been made in this area by employing various conjugated polymers such as polyaniline and polypyrrole [40–42]. Ferreira et al. [43] found that the solubility of PANI in an organic media such as dimethylacetamide (DMA) is much higher than that in water. A solution of doped polyaniline generally makes it more difficult to achieve the spontaneous adsorption of polyaniline chains onto a variety hydrophilic and hydrophobic surfaces [38]. The presence of salt in the solutions has a subtle effect. Generally, it screens the monomer–monomer repulsive interactions, leading to enhancement of adsorption [44]. Salt can play different roles in polyelectrolyte multilayer (PEM) formation and function, such as controlling the thickness increment of polyelectrolytes, the permeability [45], and the stability [46] of the multilayer. Most of the work published so far has revealed an increase in conductivity with an increase in the number of adsorbed PSS/PANI bilayers by measurement of electrical conductivity of LbL films deposited on a flat surface [47,48]. In most cases conductivity measured by four-point probe increases continuously with addition of layers until a saturation plateau is reached around the 13th bilayer or 25th layer.

Several other methods of preparation of conductive polymers have also been reported [49–51]. The most well-known method is melt blending in which, through the control of morphology and confining the pathways of the conductive materials in a multiphase system, a high conductivity with low percolation threshold can be achieved [20,52]. In this case, percolation thresholds of 3wt% carbon black [20] and 20wt% PANI [52] for melt-blended samples were obtained. A variation on the blend theme for generating anisotropically conductive material is to use block copolymers in

a self-assembled process. This method provides well-defined geometries with nanometer-size domains [53]. These mesophase textures of block copolymer can result in the in-situ polymerization of the conductive phase within one of the microphases of a block copolymer. For example, employing a conductive polymer as the in-situ phase resulted in a conductive nanocomposite with conductivies of 10^{-3} and 10^{-1} S cm^{-1} at 5wt% and 11 wt% polypyrrole, respectively [54]. The preparation of electrically conductive foams is another possible method to decrease the percolation threshold. In this case, the conductive polymer is formed within the dense polymer phase of the foam [55]. Fu et al. [56] were able to decrease the percolation threshold of conductive polymer to 5wt% by in-situ vapor phase copolymerization of pyrrole and N-methylpyrrole within a polyurethane foams. The conductivity of the composite foam was controlled from 10^{-1} to 10^{-7} S cm^{-1} via changing the density of the foam, conductive polymer concentration, and copolymer composition.

The principal objective of this work is to prepare a novel 3D porous polymeric conductive device, prepared via the LbL deposition of a conductive polyelectrolyte onto a 3D substrate of fully interconnected porosity generated from a co-continuous polymer blend. The work will involve the preparation of the blends and control of the phase size. Annealing of the co-continuous structure, followed by extraction of the porogen phases will be examined with a view to generating an ultra-low surface area, yet fully interconnected, porous material. Layer-by-layer adsorption of PSS/PANI onto the internal surface of the porous device will be carried out and details such as the growth rate and rate of adsorption and desorption of the polyelectrolytes will be examined. Finally the conductivity will be measured in order to examine the potential of the developed devices.

2. Experimental methods

2.1. Materials

Commercial homopolymers were used in this study to prepare the conductive substrate. Poly(methyl methacrylate) powder of $M_w = 12{,}000$ was obtained from Aldrich. High-density polyethylene, HDPE with a molecular weight of $M_w = 79{,}000$ was obtained from Petromont and polystyrene, PS with $M_w = 290{,}000$ was purchased from Dow Chemical. Polyvinylidene fluoride was obtained from Arkema. The polyelectrolytes used were polyaniline with $M_w = 20{,}000$ supplied by Aldrich as a polycation and poly (sodium 4-styrenesulfonate), $M_w = 70{,}000$ purchased from Sigma–Aldrich as polyanion. Densities in the melt states were determined via a fully automated PVT (pressure–volume–temperature) equipment supplied by Thermoelectron. Volume variation at controlled temperatures and pressures were determined. Some of the characteristic properties of the homopolymers are reported in Table 1.

Epofix resin containing 80–100% of Bisphenol-A-diglycidylether with a viscosity of 50 cP at 20 °C and Epofix hardener containing triethylenetetramine supplied by Struers company were employed to fill the pores of the template after LbL deposition. Sodium chloride 99.5% was purchased from Fluka. Ultrapure water with a resistivity of 18.2 MΩ cm was used in all experiments and was obtained from a Milli-Q plus system Millipore Biocel. For filtration of the PANI solution, glass fiber filters were purchased from Millipore with a diameter size of 47 mm.

2.2. Rheological analysis

A constant stress rheometer (SR 5000, Rheometric Scientific) equipped with a 25 mm parallel disk geometry was utilized to measure the linear viscoelastic properties of homopolymers containing 0.2% antioxidant. Measurements were carried out using a parallel-plate geometry with a gap of about 1.2 mm. The experiments were carried out under a nitrogen atmosphere at a temperature of 190 °C over a frequency range from 0.005 to 79.5 rad s^{-1}. The disc-shaped samples in the rheology tests were compression moulded at 190 °C. In order to determine the linear viscoelastic region, a stress sweep test was performed. The Carreau–Yasuda model [58] was employed to determine the zero shear viscosity of PVDF.

Table 1
Characteristic properties of homopolymers.

Material	Mw × 10^{-3} (g/mol)	Melt index (g/10 min)	$\eta^* \times 10^{-3}$ at 25 s^{-1} at 190 °C (Pa s)	Density (g/cm^3) at 20 °C	Density (g/cm^3) at 200 °C
Poly(methyl methacrylate)	12	–	0.04[a]	1.19	1
Polystyrene	290	–	1.5	1.04	0.97
High-density polyethylene	79	8.1	0.72	0.98	0.85
Polyvinyl difluoride	–	1.5	1.4[b]	1.77	1.6
Polyaniline	20	–	–	–	–
Poly(sodium 4-styrenesulfonate)	70	–	–	1.158	–

[a] Reported by Reignier and Favis [57].
[b] Zero shear viscosity of PVDF is 902,000 Pa s at 190 °C as calculated by the Carreau–Yasuda model [58].

2.3. Substrate preparation

Multi-component blends were prepared via melt blending under a flow of dry nitrogen in a 30 mL Plasti-Corder internal mixer (Brabender) operating at 200 °C and 50 rpm. The maximum shear rate at this speed is close to 25 s^{-1}. The real temperature achieved by the end of mixing experiment was approximately 185 °C. After converting the mass to volume (densities presented in Table 1), the mixing chamber was filled to 70% of its total volume. All the blends in this study were mixed for 8 min which is more than sufficient to allow the torque to achieve a constant value. Irganox antioxidant, supplied by CIBA, was added to the mixture at a level of 0.2 wt% to reduce the thermal oxidation of the components. After mixing, the samples were immediately cut from the mass and quenched in a cold water bath to freeze-in the morphology. All concentrations have been reported based on the component volume fraction shown in Table 2.

2.4. Annealing test

For the annealing experiments a compression molding press was employed. Small pieces of samples were cut from the blend and then sandwiched between two metal plates in a disc-shaped mould. The temperature of both upper and lower plates was set at 200 °C. The annealing was carried out under nitrogen in five steps. As a first step, both heating plates of the compression press were brought into contact with the sample pieces without imposing any

Table 2
Composition of polymer components in ternary and quaternary blends.

Samples	HDPE (%)	PS (%)	PMMA (%)	PVDF (%)
A	33	33	0	33
B	33	0	33	33
C	40	30	10	20
D	40	10	40	10

pressure for 5 min, in order to minimize any deformation or flow of the sample. After heating and melting the samples, pressure was applied for 15 min. After annealing, the samples were cooled by placing the samples in a large cold press for 3 min.

2.5. Solvent extraction

Solvent extraction was used to extract various components and generate porosity in the substrate. Selective solvent extraction also allows for the determination of the % continuity of the different components in the blend system using Eq. (2). The volume of the components before and after extraction is measured by weighing the sample and converting the weight to volume. As a primary advantage, solvent extraction is an absolute measurement of continuity.

$$\%\mathrm{Co}-\mathrm{continuity}=\frac{\sum_n V_{\mathrm{initial}}-\sum_n V_{\mathrm{final}}}{\sum_n V_{\mathrm{initial}}} \quad (2)$$

A homogenous blend is assumed when carrying out the selective solvent extraction of the PMMA, PS, and PVDF phases in dimethylformamide (DMF). Volume loss measurements were carried out for one week at room temperature and were used to calculate the extent of continuity of the PMMA, PS, and PVDF phases altogether. V_{initial} and V_{final} are the volume of one component or several components present in the sample before and after extraction calculated by weighing the sample and converting it to the volume. The % continuity represents the fraction of a phase that is continuous.

2.6. Layer-by-layer deposition

The solid substrate was alternatively immersed for 25 min in PSS and PANI solutions with intermediate water rinsing. An aqueous PSS solution of 10 mg/mL buffered to a pH of 2.5 was used as the negative polyelectrolyte solution. The PANI solution was prepared using a procedure by Cheung et al. [38]. A water bath with a pH adjusted to 2.5 was used to remove excess PSS and PANI on the surface of substrate after each dipping. The process was periodically interrupted and samples were dried first under a gentle flow air and then by putting samples in the vacuum oven for 30 min prior to weighing.

2.7. Filling the porous sample with a resin

A two-component epoxy (Epofix) was used to impregnate the pores of the porous substrates. Epofix resin and Epofix hardener were mixed and stirred carefully for at least 2 min by maintaining a mixing ratio of 15 to 2 parts by volume. The mixture was carefully poured into the mould. To eliminate air bubbling during the hardening, the Epovac vacuum impregnation unit was operated for 24 h. After evacuating the specimen chamber, the impregnating fluid is then introduced into the chamber under atmospheric pressure by means of a disposable plastic tube.

2.8. Characterization and phase morphology

2.8.1. Microtomy and scanning electron microscopy

Samples were cut and microtomed using a Leica-Jung RM 2065 equipped with a glass knife and a cryochamber type (LN 21). Other samples were fractured under liquid nitrogen known as cryo-fracture method. After chemical extraction with dimethylformamide to remove all components except HDPE, a JEOL JSM 840 scanning electron microscope was employed to observe the morphology of the samples. Photomicrographs were taken at a range of 5–12 keV after coating the surface of the sample with a gold/palladium alloy by plasma deposition.

2.8.2. Focused ion beam and atomic force microscopy

Cryomicrotoming of the specimens using a glass knife was carried out in order to obtain a perfectly flat surface for subsequent morphology observation. The samples were coated with a gold–palladium alloy. The surface of the samples was then treated and etched using a Hitachi focused ion beam FIB-2000A operated at 30 keV gallium beam. Further details of the FIB preparation are given in Virgilio et al. [59].

Finally, the topography of the sample surface was analyzed by tapping mode AFM using a Dimension 3100 scanning probe microscope equipped with a Nanoscope IIIa control module.

2.9. Conductivity measurements

DC electrical measurements were performed through the vertical thickness of the substrate at ambient temperature using a Keithley electrometer model 6517 working at a voltage range of 0–1000 V and ammeter range of 0–20 mA. In-house software was used to convert the data to conductance. In order to standardize the pressure for all samples, a 5 lb and 10 lb load was applied on the sample holders. Cylindrical specimens with a thickness of 1 mm and a radius of 1.25 cm were compression moulded and then electrical tests were performed under dry air. In this work a soft graphite sheet is placed between the sample surface and sensors in order to reduce contact resistance and to create sufficient contact for current to flow between the surface of the porous material and sensors. Note also that all the conductivity measurements in this work were carried out at the same load value (5 lb) except for two isolated points.

3. Results and discussion

3.1. Multiple-percolated morphology with large continuous domain phases

Since one of the principal objectives of this work is to determine the lowest possible percolation threshold for PANI in a 3D porous polymer conducting device, it was necessary to first prepare a polymer blend structure with large fully interconnected phases. Subsequent extraction of selected phases within that blend would thus allow for the preparation of a very low surface area, fully interconnected, porous polymer substrate (Fig. 1). As will be shown below, the most effective route towards this is via the preparation of a multi-percolated, multi-component polymer blend.

Recently [24,60], it has been shown that a ternary co-continuous (double percolated) morphology could be developed in which hierarchically ordered phases of HDPE/PS/PMMA were generated with all phases fully continuous. It was shown that this phenomenon was governed by the Harkins equation and is a thermodynamically driven process. A positive spreading coefficient of PS over PMMA ($\lambda_{\mathrm{PS/PMMA}}$) results in the PS phase locating at the intersection of the HDPE and PMMA phases [57,61]. Fig. 2a illustrates this case where in a 40/20/40 HDPE/PS/PMMA blend, PMMA phase is encapsulated by PS phase in the matrix of HDPE. By controlling the concentration of the phases, a region is determined in which all phases are fully continuous. A 40/10/50 HDPE/PS/PMMA ternary blend is another example of this region where the composition of PS was controlled to generate a PS shell down to a few hundred nm between two continuous HDPE and PMMA structures (Fig. 2b). Subsequently, the PS and PMMA phases can be extracted, yielding

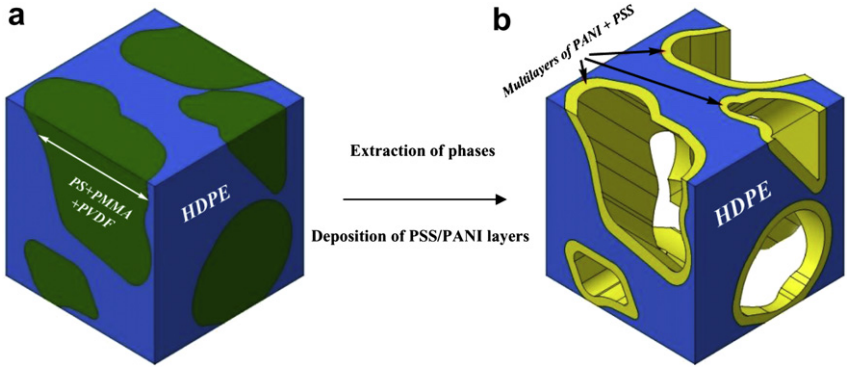

Fig. 1. 3D schematic showing the approach used to prepare the porous polymeric conducting device via LbL deposition. (a) Solid multi-percolated structure comprised of HDPE, PS, PMMA and PVDF after melt blending and annealing; and (b) porous polymeric conducting device after extraction of PS, PMMA and PVDF, followed by LbL deposition of PSS and PANI.

a fully interconnected porous HDPE substrate of about 60% void volume. This method can be employed to prepare substrates with higher void volume. For instance, in the 40/10/50 HDPE/PS/PMMA ternary blends if one could obtain a selective solvent for HDPE, the combined removal of HDPE and PMMA would yield a highly porous PS substrate of about 90% void volume.

Fig. 3 illustrates a comparison between binary co-continuous structures (single percolated) and a ternary one (double percolated) and shows that continuous phases can be generated at lower concentrations of each phase in the latter case due to the lower percolation threshold of those phases.

In Fig. 3a, it is shown that a double percolated HDPE/PMMA/PVDF blend, after PMMA and PVDF extraction, can result in a porous substrate of 33% HDPE which demonstrates a homogeneous, perfectly interconnected structure while a binary blend of 33% HDPE and 67% PVDF yields an imperfect continuous structure of HDPE (Fig. 3b). Extraction experiments indicate that 98% of the PMMA and PVDF were extracted in the ternary blend proving their high levels of continuity. In the case of the 33%HDPE/67%PVDF binary blend, extraction of PVDF resulted in a value of 108% of material indicating a significant quantity of HDPE present as dispersed entities within the PVDF. The fully continuous binary 50% HDPE/50% PVDF blend is also shown for comparison (Fig. 3c). Clearly, a double percolated morphology is a route towards fully continuous phases at low phase concentrations. The subsequent extraction of PMMA and PVDF leaves behind a fully interconnected porous HDPE substrate of low surface area. In this work, as HDPE substrates were exposed to polyelectrolyte solutions, extra-large pores also facilitated the penetration of the solution inward to the interconnected porous area.

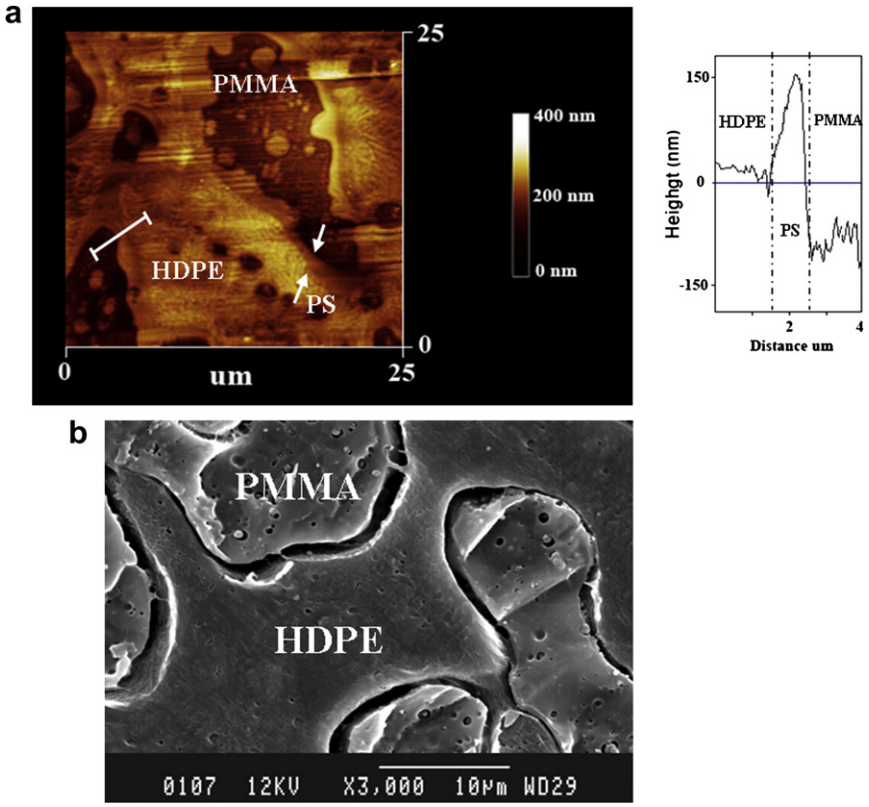

Fig. 2. (a) FIB-AFM topographic surface image of 40/20/40 HDPE/PS/PMMA. The topographical height vs. distance is shown to the right. The white line in the image indicates the trace line used in the height vs. distance analysis, and (b) scanning electron micrograph of 40/10/50 HDPE/PS/PMMA after extraction of the PS phase by cyclohexane.

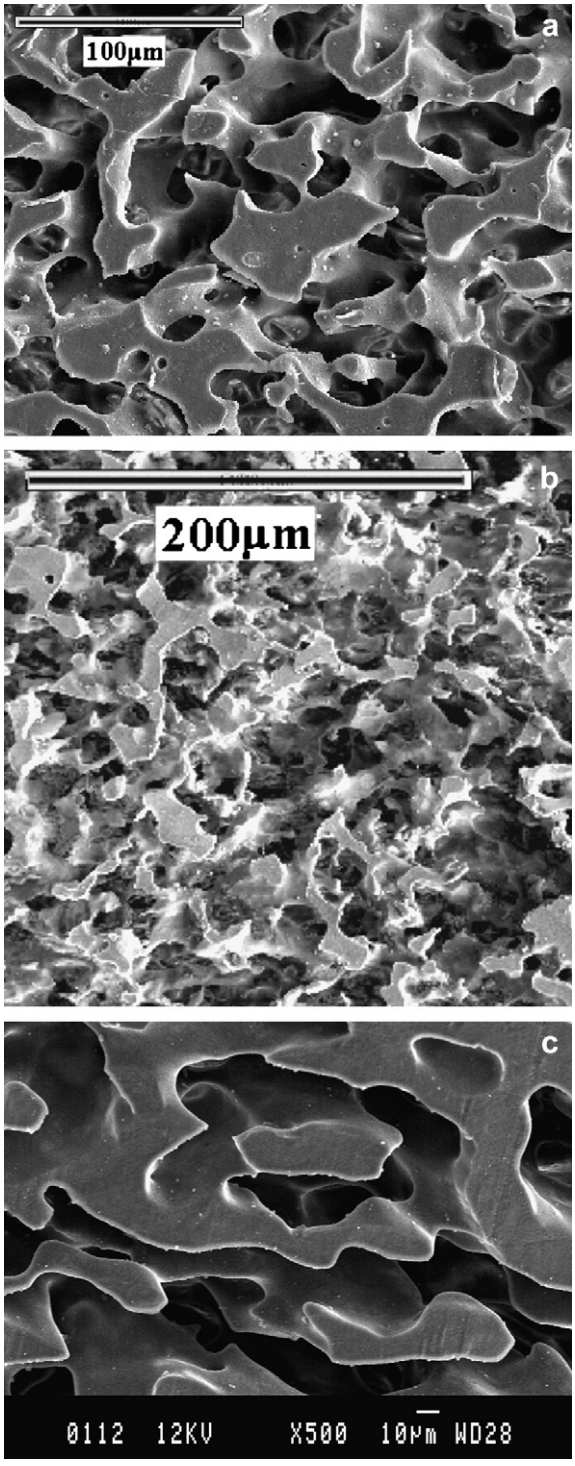

Fig. 3. Scanning electron micrographs of binary and ternary samples after extraction of all phases (except polyethylene) by DMF for (a) 33/33/33 HDPE/PMMA/PVDF, (b) 33/67 HDPE/PVDF, and (c) 50/50 HDPE/PVDF.

The addition of a fourth component to form a quaternary blend with a triple-percolated morphology between adjacent phases is also possible providing that the spreading coefficients of the fourth phase and the engulfed phases satisfy Harkins equations. A more detailed study of the generation of such structures is presented in a separate paper [62]. A triple-percolated morphology is particularly interesting in the present work since it provides a route towards the generation of porous channels of highly uniform size distribution. Fig. 4 demonstrates such a structure in which PMMA situates at the interface of PS and PVDF in an HDPE matrix. Thus this triple-percolated morphology follows the order HDPE/PS/PMMA/PVDF (Fig. 4a and b). Fig. 4a and b represents quaternary blends with the PMMA phase extracted, yielding PS layers engulfed in an HDPE matrix while the PVDF phase remains at the core encapsulated by extracted PMMA. The removal of the PS phase separates HDPE/PS/PMMA/PVDF into two parts: the HDPE matrix and PMMA/PVDF core (Fig. 4c). These figures unambiguously show that the PS and PMMA phases are situated between HDPE and PVDF, and a hierarchical structure of four different phases is spontaneously self-assembled. After the removal of all other phases, the final HDPE porous substrate exhibits a continuous structure with large pore sizes and macro-channels of highly uniform distribution. The uniformity of the double percolated morphology represented in Fig. 3a and that of the triple-percolated one shown in Fig. 4d are compared morphologically. The reason for the more uniform structure in the triple-percolated system is that the phases are distributed between three interfaces as opposed to be distributed between two interfaces in the double percolated system. Thus, the triple-percolated structure system appears to form phases which, after extraction, result in a substrate with a more uniform pore size distribution.

Four samples based on the ternary and quaternary systems of HDPE, PS, PMMA and PVDF will be the principal substrates used in subsequent experiments reported in this paper. These blends are shown in Table 2 and are designated as samples A – 33%HDPE/33%PS/33%PVDF; B – 33%HDPE/33%PMMA/33%PVDF; C – 40%HDPE/30%PS/10%PMMA/20%PVDF; and D – 40%HDPE/10%PS/40%PMMA/10%PVDF. It is possible to generate porous substrates of an even higher void volume (lower concentration of HDPE), however, the mechanical strength of those materials is quite low. Since the study of the effect of load on the conductivity of the sample is also one of the objectives of this work, the above concentrations were selected. These blends effectively allows for the preparation of an ultra-low surface area, fully interconnected porous substrate of high void volume.

3.1.1. *Annealing the samples in order to increase pore size*

It has been shown in the previous work that annealing co-continuous polymer blends is an excellent route towards significantly increasing the phase size and further lowering phase surface area. During this process of static annealing, thin parts of the continuous network merge into larger parts via capillary driving forces [27].

Double percolated HDPE/PS/PVDF and HDPE/PMMA/PVDF blends and triple-percolated HDPE/PS/PMMA/PVDF were subjected to quiescent annealing for 15 min in a compression molding press at very low contact pressures. This operation results in a substantial increase in the average phase size. Fig. 5 shows the morphology of the blends after annealing and subsequent extraction of all phases except for HDPE. The phase size increase is dramatic and is shown for sample B to increase from approximately 40 µm to 500 µm as exhibited morphologically in Fig. 5b and f. The phase increase before and after annealing for the other samples A, C, and D is also substantial and ranges from 5 to 15 times (Fig. 5). The results indicate that the coalescence of a multi-percolated system occurs much faster than coalescence in a binary blend. Yuan et al. [27] reported that, in the best case scenario, a binary blend requires approximately 40 min to coarsen from several microns to a phase size of about 160 microns. Consequently, the required annealing time to achieve 400–500 microns is estimated at about 2 h of annealing. It is proposed that geometrical restrictions in a multi-percolated system enormously accelerate coalescence effects while still maintaining full continuity of all components.

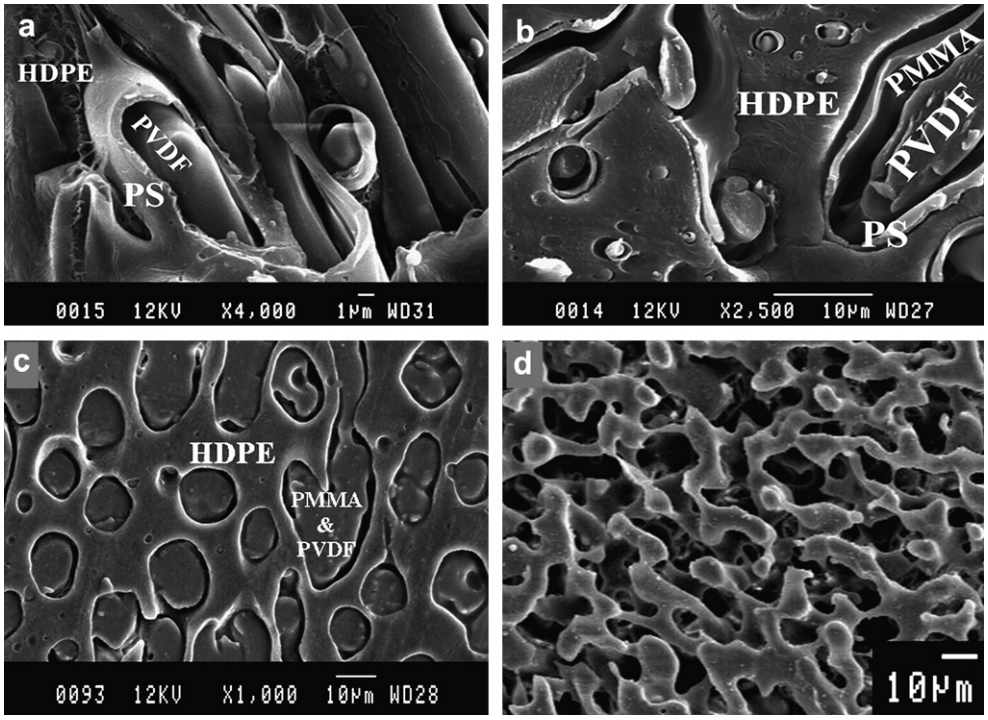

Fig. 4. Scanning electron micrographs of quaternary polymer blends for various compositions compounded via melt blending (a) 50/16/16/16 HDPE/PS/PMMA/PVDF after extraction of PMMA by acetic acid, (b) 50/20/10/20 HDPE/PS/PMMA/PVDF after extraction of PMMA by acetic acid, (c) 50/20/10/20 HDPE/PS/PMMA/PVDF after extraction of PS by cyclohexane, and (d) 40/10/40/10 HDPE/PS/PMMA/PVDF after extraction of all phases except HDPE by DMF.

3.1.2. Continuity and surface areas of substrates

Table 3 shows gravimetric data obtained after solvent extraction and demonstrates that in all cases the various phases within the HDPE are fully continuous. The continuity of all extracted phases for both annealed and unannealed samples is higher than 96%. Hence, the 33% volume fraction of HDPE in samples A and B and 40% in samples C and D results in a 67% and 60% void volume, respectively, after the extraction of all other phases. As well, the effect of annealing on reducing the surface area of the porous substrate is extremely evident as it was below the range which could be measured quantitatively by BET (Table 4).

Since the ultra-low surface area values are beyond the range of the BET equipment, the surface area of sample A (morphology shown in Fig. 5e) was estimated arithmetically. A porous disc-shape sample with a diameter of 2.5 cm and a length of 1 mm is assumed to be composed of numerous parallel cylinders from top to bottom with a diameter of 175 μm and a length of 1 mm. The diameter of cylinders is obtained from average diameter of HDPE cylindrical rods exhibited in Fig. 5e. Estimating the number of cylinders and the surface area per cylinder as 6818 and 0.00375 m^2/g, respectively, corresponds to a surface area of the porous device of approximately 0.01 m^2/g.

Hence, the work to this point has achieved fully interconnected porous substrates (samples A, B, C, and D) of ultra-low surface area (large pores) and a highly uniform pore size. All these samples will be used as substrates for the layer-by-layer deposition of polyaniline in

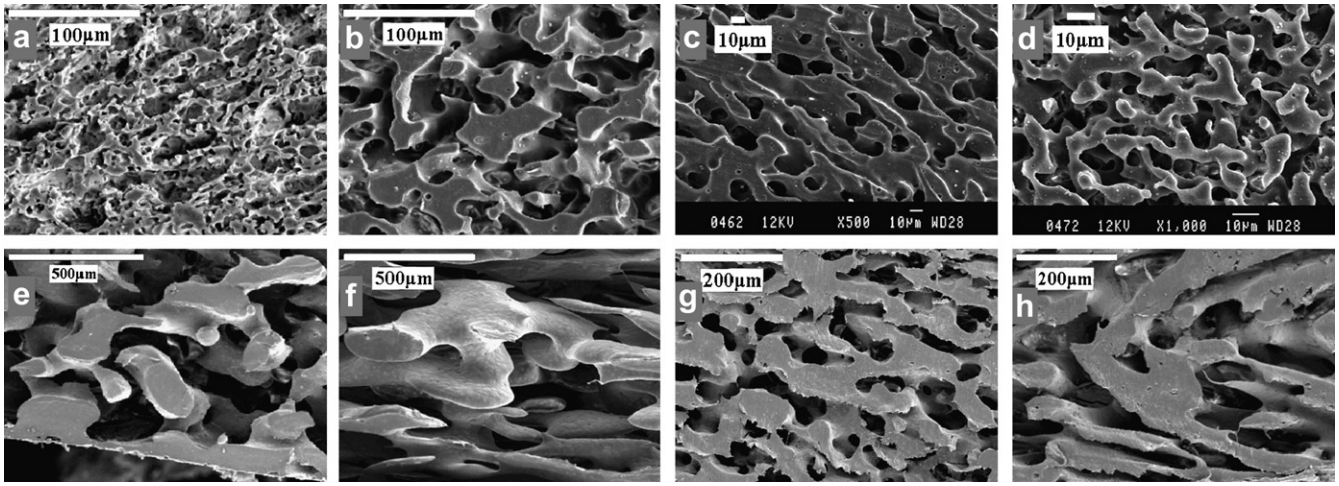

Fig. 5. Scanning electron microscope images of the morphologies of the porous structures showing the influence of annealing. The top row is without annealing, and the bottom row is after annealing. All components have been extracted except HDPE. (a, e) Sample (A); (b, f) sample (B); (c, g) sample (C); and (d, h) sample (D).

Table 3
Continuity of the porous morphology with and without annealing (PS, PMMA and PVDF extracted).

Sample	Continuity of (PS + PMMA + PVDF) no annealing (%)	Continuity of (PS + PMMA + PVDF) with annealing (%)
A	96.6	98.3
B	98	100
C	98.3	99.3
D	96	97.4

the subsequent parts of this work. Table 5 compares the surface area of porous sample A to the surface area of other co-continuous systems and demonstrates that, to our knowledge, this is the lowest surface area, fully interconnected porous polymer material ever presented in the literature. Table 5 also demonstrates the potential of preparing conductive devices from higher surface area co-continuous systems and underlines the versatility of the approach.

3.2. Layer-by-layer deposition of PSS/PANI

A layer-by-layer deposition technique was used to deposit PSS and PANI alternately on the internal surface of the prepared porous substrate (Fig. 6a and b). A PSS polyelectrolyte soluble in water was selected to be deposited first due to its ability to adsorb strongly on hydrophobic surfaces such as HDPE [65]. In a subsequent step, a semi-flexible PANI layer is deposited on a PSS layer as a result of a balance between electrostatic repulsion of charged monomers. Up to 38 PSS and PANI layers were deposited. In order to visually examine the multilayer assembly on the surface of the HDPE substrate, the void volumes or empty macro-channels were refilled with epoxy resin.

Microstructural information collected by SEM (Fig. 6c) and AFM (Fig. 6d) depicts a relatively thick polyelectrolyte multilayer as wide as 5.5 μm for 38 layers of PSS and PANI on the surface of the filled sample (B). Picart et al. [66] also reported a very thick multilayer film of 1 μm for 16 layers. They proposed that this thickness increase can be attributed to a diffusion of polyelectrolyte inwards and outwards in the multilayer during the LbL process. They also reported an exponential growth of layer thickness similar to the mechanism of mass growth in this work.

3.2.1. Mass deposition dynamics of PSS/PANI

Although the structural information for the construction of ultra-thin multilayers is extremely difficult to obtain, gravimetric measurements can interpret the molecular topology of the films that play the most important role in the formation of multilayers. Fig. 7 shows the quantification of mass deposition of each layer as measured by gravimetric techniques for various substrates in both the absence and presence of salt. It shows an unusual oscillating behavior of thickness growth. After dipping the substrate in the PSS solution, the deposition mass increases, followed by a decrease in deposition mass in a PANI solution due to the partial removal of a previously adsorbed layer. Some previous works [34,67,68] have also reported on the oscillating behavior of PSS polyelectrolytes due to the partial removal of previously adsorbed layers in subsequent operations. Schoeler et al. [34] related the extent of removed material to the critical charge density of the polyelectrolyte. Charge density for a polyelectrolyte is defined as the fraction of monomers in the polymer which are charged. If this fraction is much smaller than 1, the polyelectrolyte is weakly charged. Normally, weak polyelectrolytes tend to demonstrate an oscillating deposition. Dubas et al. [67] concluded that the drawing out of water molecules unassociated with specific ion pairs due to increasing external osmotic pressure is the main reason for the decrease in thickness at low salt concentrations. Tjipto et al. [68] related the oscillating behavior of a multilayer formed of poly(4-styrenesulfonic acid-co-maleic acid) and PDADMAC to the heterogeneity and roughness of the samples. Later in this paper it will be shown that all of these explanations are likely responsible for the oscillating deposition observed in this work. The addition of 1 molar salt to a PSS polyelectrolyte solution magnifies the extent of the oscillation behavior (Fig. 7a–d) and this will also be discussed in more detail in the next section.

A relationship between macropore sizes and mass deposition of layers is found. The approximate average macropore sizes for samples A, B, C and D after annealing are 300 μm, 500 μm, 100 μm, and 150 μm, respectively (see Fig. 5). Fig. 7 represents the maximum mass deposition for each sample: sample A attains 1.6% after deposition of 31 PSS/PANI layers and 0.82% after deposition of 32 layers. Sample (B) attains 2% and 1.16% after deposition of 31 and 32 layers. Samples C attains about 0.8% for 31 layers and 0.45% for 32 layers. Sample D attains about 1.2% and 0.9% after deposition of 31 and 32 layers. These results confirm that larger pore sizes facilitate the penetration of solution and thicker layers constructs.

3.2.2. Diffuse network structure of PSS/PANI

Lavalle et al. [69], using molecular labeling, observed a diffusion of a portion of polyelectrolytes in and out of the film in a nonlinear manner leading to exponential growth. This was observed when one of the polyelectrolytes used was weak as in the current work with PANI. Schlenoff et al. [46,70] have reported that the surface charge, propagated and inverted by sequential adsorption steps, is overneutralized (overcompensated) at each step. In that work, the multilayer/solution interface, the charge of the last-added polymer compensates the previous one by a factor φ. The opposite polymer charges are in exact stoichiometric ratio for $\varphi = 1$ yielding a steady-state thickness increment vs. layer number. The overcompensation

Table 4
Surface area measurements of porous polymer substrates by BET.

Sample	Surface area measured by BET (m^2/g) no annealing	Surface area measured by BET (m^2/g) with annealing
A	1.28	<0.01
B	0.70	<0.01
C	0.88	<0.01
D	0.74	<0.01

Table 5
Comparison of surface areas reported in previous studies and in the current work (last two rows).

Porous samples prepared by melt blending from this laboratory	Reported specific surface area measured by BET (m^2/g)
50/50 PLLA/PCL after LbL deposition of PSS/PDADMAC and extraction of both phases [37]	140
50/50 PLLA/PCL after 2 h annealing and after LbL deposition of PSS/PDADMAC and extraction of both phases [37]	63
40/60 HDPE/SEB (styrene–ethylene–butylene diblock copolymer) [63]	16
50/50 HDPE/SEB (styrene–ethylene–butylene diblock copolymer) [63]	13.15
50/50 HDPE/SEBS (styrene–ethylene–butylene–styrene triblock copolymer) [64]	8.2
40/60 HDPE/PS after extraction of PS [64]	0.82
33/33/33 HDPE/PMMA/PVDF after extraction of PMMA and PVDF	0.7
33/33/33 HDPE/PMMA/PVDF after 15 min annealing and extraction of PMMA and PVDF	≤0.01

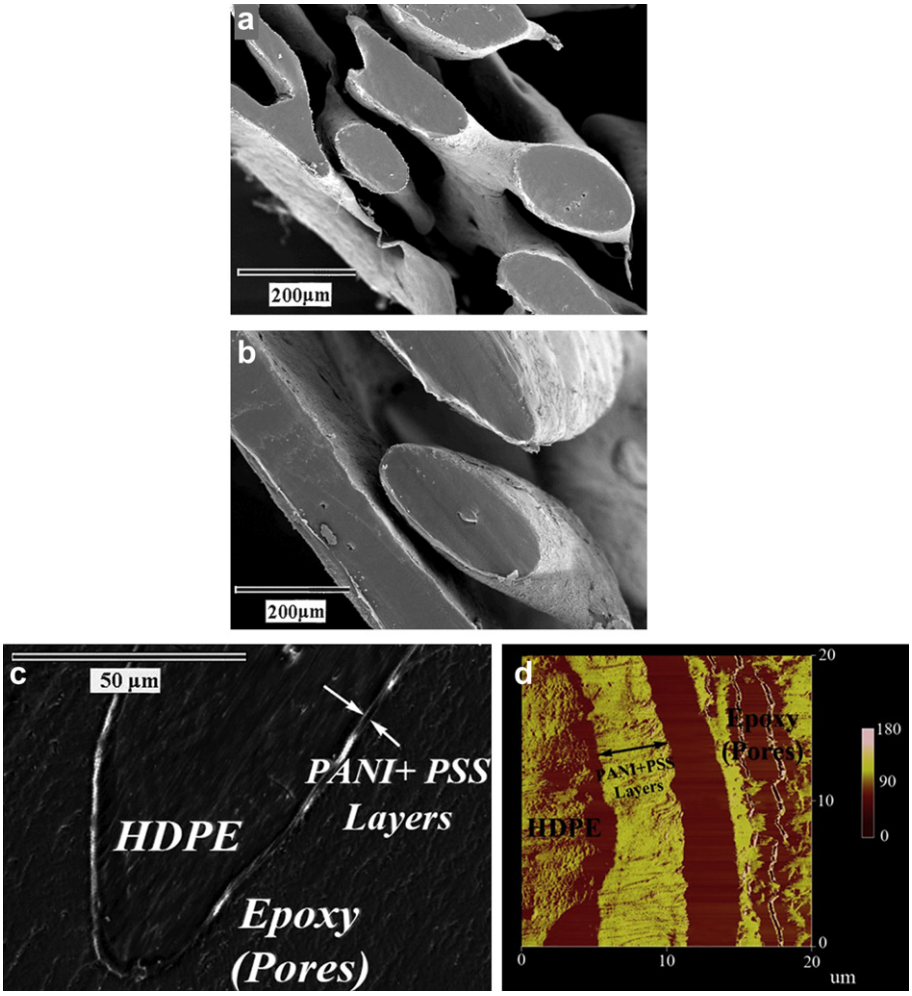

Fig. 6. (a, b) Scanning electron micrographs of the morphology of sample (B) after extraction of PMMA, PVDF and deposition of 38 PSS/PANI layers; (c, d) SEM and FIB-AFM of sample (B) after extraction of PMMA, PVDF and deposition of 38 PSS/PANI layers. Pores are filled with epoxy resin.

factor, phi, can be defined for multilayers when the charge factor has a value higher than 1. Overcompensation leads to excess charge density from the last-added polyelectrolyte, but only at the surface is φ "unrestricted" by bulk effects. At increasing length, l, from the interface into the multilayer, the level of overcompensation decreases in an exponential fashion demonstrating an over-compensation gradient [70].

The diffusion of a portion of polyelectrolytes in and out of the film in a nonlinear manner leading to exponential growth was proposed as a model for overcompensation [69]. In this mechanism, the first population was constituted of chains directly interacting with the surface of the multilayer, which are responsible for linearly growing films. The second population was constituted of free chains that diffuse into the multilayer over its whole surface and are responsible for exponential growth. In this study, when a substrate is brought into contact with a charged PSS solution, many free PSS chains paired with hydrated counter-ions in the solution diffuse throughout the film in the x, y, and z directions due to electrostatic interactions. Following this, the desorption or detachment of some layers is expected in an oppositely charged PANI solution when mobile chains diffuse out. As soon as they reach the surface, an additional reaction occurs between them and the oppositely charged chains available in the solution and an extra layer is formed. In this fashion, a diffuse network structure throughout the deposited thickness is observed in contrast to the formation of discrete polyelectrolyte layers in classic layer-by-layer deposition where strong polyelectrolytes are used.

Based on the above discussion, a schematic representation of film growth has been made to show the progressive formation of multilayers (Fig. 8). This schematic contrasts with the classic formation of well-separated hierarchical alternating multilayers observed in most work using the LbL approach. In the current work, the oscillating deposition indicates that PSS and PANI polyelectrolytes diffuse into the previously deposited layers. Like chains make contact with other like chains and consequently, an inter-diffused network of PANI and PSS is generated. In a following section, it will be shown that an increase in the conductivity is observed as a function of the number of PSS and PANI layers and it further confirms the formation of a continuous network of PANI inter-diffused with PSS. The degree of interconnection of this network becomes more pronounced as the number of deposited layers increases. As well, an increase in the number of deposited layers results in a rougher surface, leading to a further diffusion of free chains.

3.2.3. *The effect of salt on the mass deposition growth of PSS/PANI*

Salt is generally added in procedures involving LbL deposition. In the absence of salt, charged PSS and PANI in the solution adopt a more expanded rigid, rod-like configuration due to coulomb repulsion [71]. The role of salt is to gradually screen the

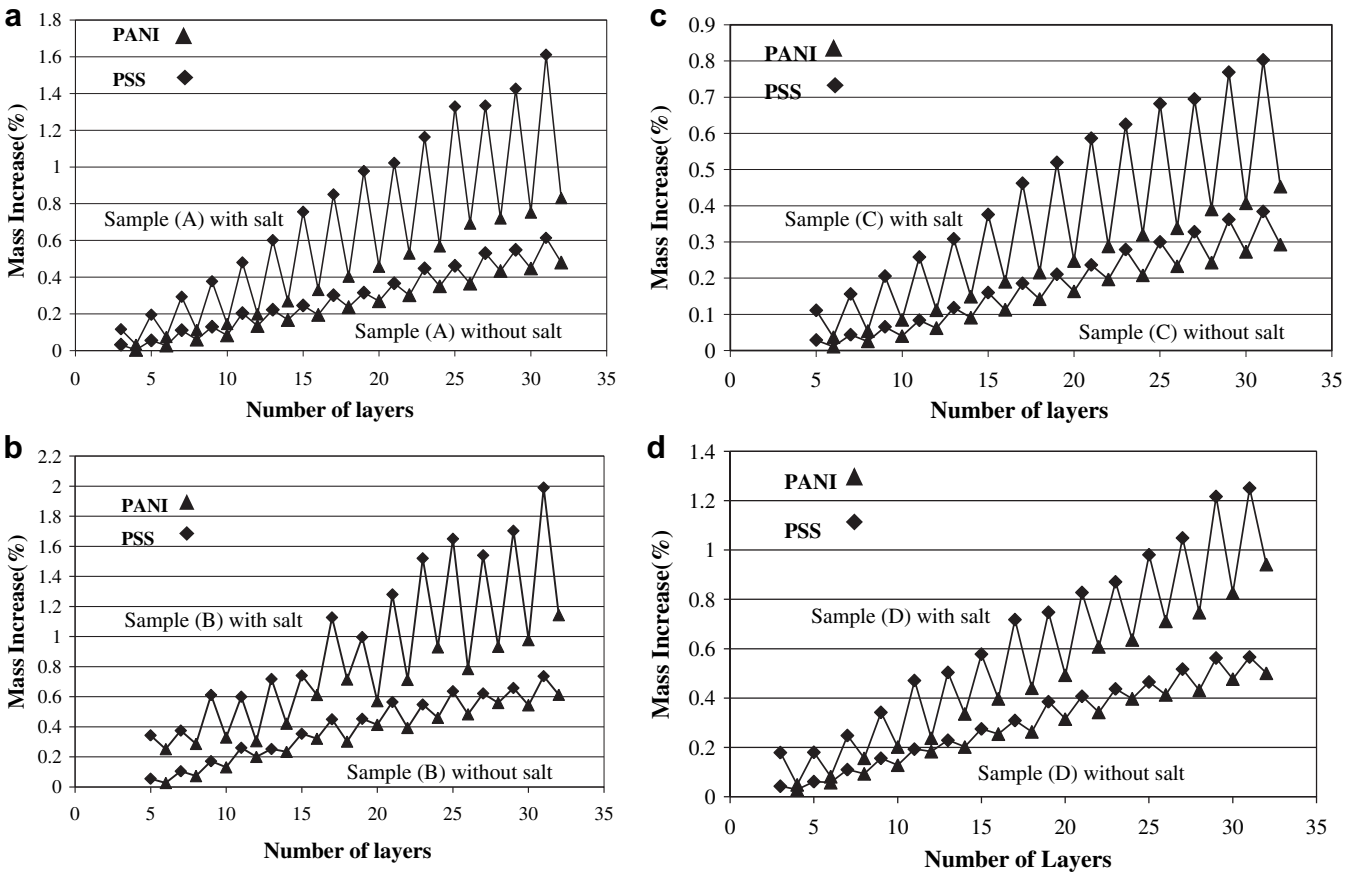

Fig. 7. Mass increase (%) indicating cumulative deposited mass as a function of number of deposited PSS and PANI layers for solutions containing salt and without salt. (a) Sample (A); (b) sample (B); (c) sample(C); and (d) sample (D).

monomer–monomer repulsive interactions between PSS charges with counter-ions and also bring them close together. It is interesting to note in Fig. 7 that the addition of salt significantly increases the oscillation behavior of the mass growth dynamics.

This oscillation behavior can be explained as follows: the number of PSS molecules that diffuse throughout the multilayer and the total concentration of these free chains depend on the electrostatic interaction forces that arise from total overcompensation. Two important parameters influencing the extent of overcompensation are the concentration of added salt and the number of layers. Thus, extra overcompensation is caused by the presence of NaCl in the PSS solution [72]. As well, the displacement of hydrated small salt counter-ions and charged polymer segments results in highly swollen polymers as attached water molecules are brought in [67]. Jaber et al. [73] showed that salt counter-ions can thermodynamically control up to 40% of the mass deposition of the multilayer construction due to this additional water content. Swelling and overcompensation occur simultaneously during the construction of the multilayer in the presence of salt [46], which is involved in the dramatic mass increase of the multilayer.

In a subsequent dipping step in the PANI solution, the electrostatic interaction between the diffused hydrated PSS with PANI chains inside the solution play a major role in the diffusion of free PSS chains out of the multilayer. At this step, in the presence of salt, a significant decrease in mass deposition is detected which is proportional to the mass increase in the previous step (PSS adsorption) as compared to a slight decrease in mass in solutions without salt. Consequently, the amount of thickness growth highly depends on the amount of salt that affects the electrostatic interactions and increases the driving force for diffusion in and out of the multilayer.

Mass deposition growth for the PSS/PANI system in cases where salt is both present and absent, is not linear since a progressive increase of each polyelectrolyte after its deposition is detected (Fig. 9). As the number of layers increases, the extent of free chains going inward and outward increases exponentially due to increase in the amount of overcompensation (Fig. 9). In other words, at each adsorption step, more PSS is adsorbed than that removed in the previous step, leading to nonlinear layer growth. The rates of increase and decrease of PSS and PANI at each step corresponding to diffusion in and out of the multilayer are almost double for solutions containing salt (Fig. 9).

3.3. Conductivity measurement of the conductive porous polymer device

The electrical conductivities of sample A – 33%HDPE/33%PS/33% PVDF and sample B – 33%HDPE/33%PMMA/33%PVDF were evaluated

Fig. 8. Schematic of exponential growth of PSS/PANI multilayer thickness on the internal surface of the substrate.

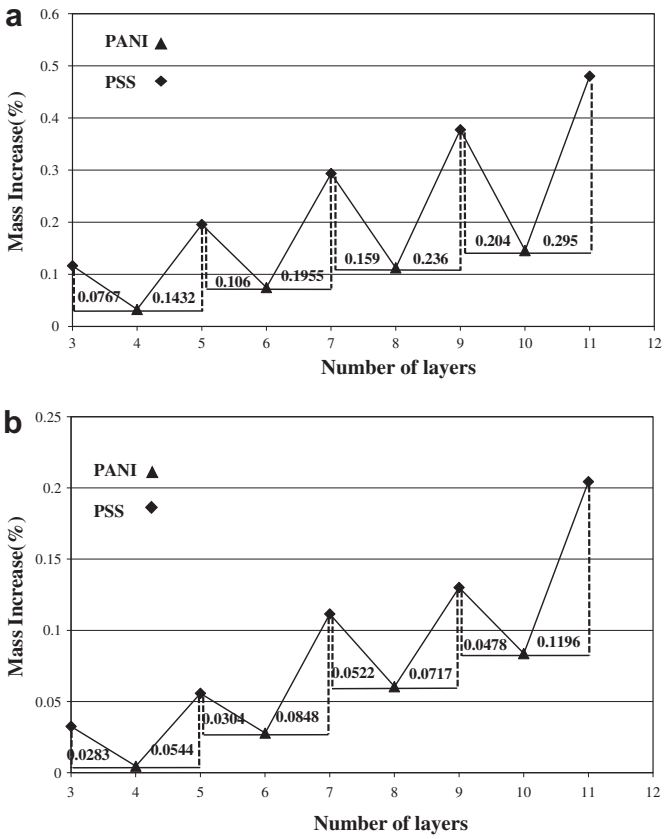

Fig. 9. Mass increase (%) indicating cumulative deposited mass as a function of number of deposited PSS and PANI layers for sample (A). (a) Solution containing salt, and (b) solution without salt.

as a function of the number of deposited PSS and PANI layers. The electrical conductivity of these samples increases by several orders of magnitude as a function of the number of deposited PSS/PANI layers until a saturation plateau is reached at approximately 32 layers (Fig. 10).

The first layers of conductive polymer deposited onto the internal walls of the porous sample do not produce a completely interconnected network due to the hydrophobic nature of the substrate (HDPE). It appears that the first few layers of conductive polymer are required to completely transform the hydrophobic surface. Hence, in such systems, the percolation threshold cannot be accurately reported due to an incomplete adherence of the first layers to the surface. However, it can be said that the percolation threshold of PANI in this porous device is achieved at a deposition level of no more than 8 layers. The deposition of 8 layers corresponds to 0.19 wt.% PANI for sample A and 0.28 wt.% for sample B. The conductivity saturation plateau is achieved at 32 layers which corresponds to 0.76% PANI for sample A and 1.1% for sample B. This dependence of conductivity on deposited layers confirms the hypothesis that deposited PSS and PANI form a network type construction as opposed to the formation of discrete PSS and PANI layers. In fact, this network formation allows for the fine tuning of conductivity over several orders of magnitude. Clearly, the deposition of only a few layers results in an incomplete network with disconnections in many parts and demonstrates a limited passage of electricity and thus yields a low conductivity value. By increasing the number of layers to 8 and 16, higher conductivity values are obtained and the conductivity is in the 10^{-9}–10^{-8} S cm^{-1} range. As more PANI chains are added they diffuse into the network resulting in a significant increase in network branches. The addition of further layers results in a plateau value for conductivity at approximately 10^{-6} S cm^{-1} for sample A and 10^{-5} S cm^{-1} for sample B. Beyond 32 layers, the further addition of PANI has no effect on the conductivity of the device. The conductivity of sample C and D after the deposition of 38 PSS/PANI layers was measured showing the values of 10^{-9} S cm^{-1} and 3×10^{-7} S cm^{-1}, respectively. The difference in the conductivity values can be dependent on several factors such as pore sizes and pore distribution; however, the most important one is the internal surface area of the substrate.

The addition of salt during the LbL process has little influence on the conductivity of the sample as shown in Fig. 10. Braga et al. [47] and Paloheimo et al. [48] reported that the electrical resistance of PANI/PSS layers with solutions of different polymer concentrations decreases as more layers are adsorbed until a saturation plateau is reached, between the 26th and 30th layer. This closely corresponds with the results observed in this work. It is very likely that the formation of a diffuse network structure in the current study is critical in obtaining high conductivity values. Discrete molecular layers added in a classic LbL protocol using strong polyelectrolytes would have likely resulted in a lower percolation threshold value, but also would not be capable of achieving the high conductivities observed at saturation as seen in this study.

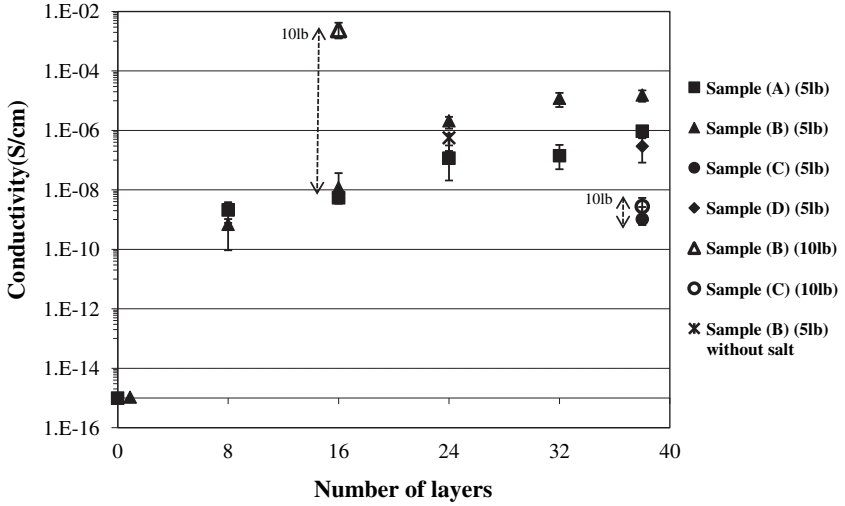

Fig. 10. Conductivity as a function of the number of deposited layers for various samples at a 5 lb load. The effect of a 10 lb load is shown for samples B and C as indicated by the arrows. Note that the only significant effect of the increased load on conductivity is when the sample is physically crushed for sample B.

In this work the conductance of the porous samples was converted to conductivity based on the general following equation:

$$\sigma = \frac{Gl}{A} \tag{3}$$

where G is conductance, A is cross-sectional area, l is length, and σ represents conductivity. As void domains and HDPE have conductivity values of zero and 10^{-15} S cm^{-1}, respectively, a sample including substrates, multilayers and void volumes can be considered as a whole conductive device with certain conductivity. In other words, a sample can be considered as an ultra-porous PANI network. In porous materials, pore geometry (including the pore size and distribution) plays a major role in the conductivity of the material [74], as well as the perfection of the contact between the conductive material and the nature of the material filling the pores [75]. It should be noted that in this work a soft graphite sheet is placed between the sample surface and sensors in order to reduce contact resistance. Note also that all the conductivity measurements in this work were carried out at the same load value (5 lb) except for two isolated points in Fig. 10 which were carried out at a higher load (10 lb). Finally, for materials of low conductivity and high resistance, as in the present work (10^{-15} S cm^{-1} to 10^{-5} S cm^{-1}), the effect of contact resistance is normally considered to be quite low. Combining all of this together, the measured conductance values should be quite precise. A number of theoretical and experimental models have been developed for applying porous-structure parameters, such as volume and pore concentration to calculate conductivity [76,77]. The detailed calculations for the estimation of conductivity using this approach for this type of porous device is described in more detail elsewhere [78].

3.4. Conductivity of the conductive porous polymer device under loads

The conductive porous polymer device developed in this study can be made to be sensitive to applied compression providing that the void volume percentage and the applied load is sufficiently high. The compression of sample B of 67 void % under a 10 lb load pushes and forces the rods and walls of the substrate to move inward. On the other hand, no deformation in sample C, which has a 60% void volume, is observed. In that latter case the mechanical strength of the walls of the device is sufficient to resist deformation resulting from the 10 lb applied load. In the case of physically crushed sample B, further contact between the walls of the sample after compression results in an increase in the conductivity from 10^{-8} S cm^{-1} up to 0.002 S cm^{-1} as shown in Fig. 10. Morphological analysis of sample B shows no change in the porous structure upon application of a 5 lb load which was the load used for virtually all conductivity testing in this study. Also, the comparison of a 5 lb load and a 10 lb load for sample C, prepared at 38 layers and shown in Fig. 10, has very little effect on the conductivity thus showing little effect of contact resistance. Note that the significant effect of a 10 lb load for sample B in Fig. 10 was due to the special case of physical crushing of the sample. This allows for another control parameter to achieve a wide range of conductivity in these conductive porous devices. It also opens up the potential to develop these devices as load bearing sensors.

4. Conclusions

This paper reports on the preparation of a novel 3D porous polymeric conducting device derived from multi-percolated polymer blend systems. The work has focused on the preparation of ultra-low surface area porous substrates followed by the deposition of polyaniline conductive polymer (PANI) on the internal porous surface using a layer-by-layer technique. In this way, the percolation threshold of PANI in this porous conductive device can be reduced to a value of no more than 0.19%. Furthermore, depending on the amount of PANI deposited, the electrical conductivity of the porous substrate can be controlled over several orders of magnitude from 10^{-15} S cm^{-1} to 10^{-3} S cm^{-1}.

Ternary and quaternary multi-percolated (hierarchically ordered) systems composed of high-density polyethylene (HDPE), polystyrene (PS), poly(methyl methacrylate) (PMMA) and poly (vinylidene fluoride) (PVDF) are melt-mixed and subsequently annealed in order to obtain large interconnected phases. Subsequent extraction of PS, PMMA and PVDF within that blend allows for the preparation of a fully interconnected porous HDPE substrate of ultra-low surface area and highly uniform sized channels. This provides an ideal substrate for subsequent polyaniline (PANI) addition. Using a layer-by-layer (LbL) approach, alternating poly (styrene sulfonate) (PSS)/PANI layers are deposited on the internal surface of the three-dimensional porous polymer substrate. The PANI and sodium poly(styrene sulfonate) (PSS) both adopt an interdiffused network conformation on the surface. The sequential mass deposition of PSS and PANI multilayers has been studied in detail and an oscillating behavior is observed, due primarily to the diffusion of PSS chains both in and out of the multilayer structure. Salt in the deposition solution highly affects the polyelectrolyte construction by allowing for a more uniform deposition and more thickly deposited PSS/PANI layers. The mass deposition growth for the PSS/PANI system in all cases is not linear. Conductivity measurements show that the conductivity of these samples increases from 10^{-15} S cm^{-1} to 10^{-5} S cm^{-1} as the number of deposited PANI layers increases until a saturation plateau is reached at approximately 32 layers. The conductive porous polymer device developed in this study can be made to be sensitive to applied compression providing that the void volume percentage and the applied load is sufficiently high. In one case it is shown that a higher 10 lb load was able to physically crush the sample and results in higher conductivity values with values as high as 10^{-3} S cm^{-1} obtained. Although this approach has been demonstrated here for an ultra-low surface area porous substrate, high surface area substrates can also be readily prepared.

Acknowledgements

The authors express appreciation to the Natural Sciences and Engineering Research Council of Canada for supporting this work. They also thank F. Normandin from the Institut des matériaux industriels for his assistance with the conductivity measurements of the samples.

References

[1] Heywang G, Jonas F. Poly(alkylenedioxythiophene)s – new, very stable conducting polymers. Adv Mater 1992;4:116–8.
[2] Roman LS, Andersson MR, Yohannes T, Inganás O. Photodiode performance and nanostructure of polythiophene/C60 blends. Adv Mater 1997;9:1164–8.
[3] Kraft A, Grimsdale Andrew C, Holmes Andrew B. Elektrolumineszierende konjugierte Polymere – Polymere erstrahlen in neuem Licht. Angewandte Chemie 1998;110:416–43.
[4] Schmidt VM, Tegtmeyer D, Heitbaum J. Transport of protons and water through polyaniline membranes studied with on-line mass spectrometry. J Electroanal Chem 1995;385:149–55.
[5] Wessling B. Passivation of metals by coating with polyaniline: corrosion potential shift and morphological changes. Adv Mater 1994;6:226–8.
[6] Contractor AQ, Sureshkumar TN, Narayanan R, Sukeerthi S, Lal R, Srinivasa RS. Conducting polymer-based biosensors. Electrochim Acta 1994;39:1321–4.
[7] Kaneto K, Kaneko M, Min Y, MacDiarmid AG. "Artificial muscle": electromechanical actuators using polyaniline films. Synth Met 1995;71:2211–2.
[8] Burroughes JH, Bradley DDC, Brown AR, Marks RN, Mackay K, Friend RH, et al. Light-emitting diodes based on conjugated polymers. Nature 1990;347:539–41.

[9] Margolis JM. Conductive polymers and plastics. New York: Chapman and Hall; 1989.
[10] Halls JJM, Walsh CA, Greenham NC, Marseglia EA, Friend RH, Moratti SC, et al. Efficient photodiodes from interpenetrating polymer networks. Nature 1995; 376:498–500.
[11] Tessler N, Denton GJ, Friend RH. Lasing from conjugated-polymer microcavities. Nature 1996;382:695–7.
[12] Garnier F, Hajlaoui R, Yassar A, Srivastava P. All-polymer field-effect transistor realized by printing techniques. Science 1994;265:1684–6.
[13] Zasadzinski JA, Viswanathan R, Madsen L, Garnaes J, Schwartz DK. Langmuir–Blodgett films. Science 1994;263:1726–33.
[14] Maoz R, Frydman E, Cohen SR, Sagiv J. Constructive nanolithography: site-defined silver self-assembly on nanoelectrochemically patterned monolayer templates. Adv Mater 2000;12:424–9.
[15] Love JC, Estroff LA, Kriebel JK, Nuzzo RG, Whitesides GM. Self-assembled monolayers of thiolates on metals as a form of nanotechnology. Chem Rev 2005;105:1103–70.
[16] Hammond PT. Form and function in multilayer assembly: new applications at the nanoscale. Adv Mater 2004;16:1271–93.
[17] Decher G, Hong JD, Schmitt J. Buildup of ultrathin multilayer films by a self-assembly process: III. Consecutively alternating adsorption of anionic and cationic polyelectrolytes on charged surfaces. Thin Solid Films 1992;210–211:831–5.
[18] Paul DR, Barlow JW. Polymer blends, vol. 18; 1980. pp. 109–168.
[19] Bourry D, Favis BD. Cocontinuity and phase inversion in HDPE/PS blends: influence of interfacial modification and elasticity. J Polym Sci Part B: Polym Phys 1998;36:1889–99.
[20] Gubbels F, Jerome R, Teyssie P, Vanlathem E, Deltour R, Calderone A, et al. Selective localization of carbon black in immiscible polymer blends: a useful tool to design electrical conductive composites. Macromolecules 1994;27:1972–4.
[21] Wang Y, Rubner MF. Electrically conductive semiinterpenetrating polymer networks of poly(3-octylthiophene). Macromolecules 2002;25:3284–90.
[22] Sumita M, Sakata K, Hayakawa Y, Asai S, Miyasaka K, Tanemura M. Double percolation effect on the electrical conductivity of conductive particles filled polymer blends. Colloid Polym Sci 1992;270:134–9.
[23] Levon K, Margolina A, Patashinsky AZ. Multiple percolation in conducting polymer blends. Macromolecules 2002;26:4061–3.
[24] Zhang J, Ravati S, Virgilio N, Favis BD. Ultralow percolation thresholds in ternary cocontinuous polymer blends. Macromolecules 2007;40:8817–20.
[25] Torza S, Mason SG. Three-phase interactions in shear and electrical fields. J Colloid Interface Sci 1970;33:67–83.
[26] Hobbs SY, Dekkers MEJ, Watkins VH. Effect of interfacial forces on polymer blend morphologies. Polymer 1988;29:1598–602.
[27] Yuan Z, Favis BD. Coarsening of immiscible co-continuous blends during quiescent annealing. AIChE J 2005;51:271–80.
[28] Sarazin P, Favis BD. Morphology control in co-continuous poly(L-lactide)/polystyrene blends: a route towards highly structured and interconnected porosity in poly(L-lactide) materials. Biomacromolecules 2003; 4:1669–79.
[29] Decher G, Hong JD. Buildup of ultrathin multilayer films by a self-assembly process, 1. Consecutive adsorption of anionic and cationic bipolar amphiphiles on charged surfaces. In: European conference on organized organic thin films; 1991, p. 321.
[30] Clark SL, Montague MF, Hammond PT. Ionic effects of sodium chloride on the templated deposition of polyelectrolytes using layer-by-layer ionic assembly. Macromolecules 1997;30:7237–44.
[31] Shiratori SS, Rubner MF. pH-dependent thickness behavior of sequentially adsorbed layers of weak polyelectrolytes. Macromolecules 2000; 33:4213–9.
[32] Sui Z, Salloum D, Schlenoff JB. Effect of molecular weight on the construction of polyelectrolyte multilayers: stripping versus sticking. Langmuir 2003;19: 2491–5.
[33] Ferreira M, Rubner MF. Molecular-level processing of conjugated polymers. 1. Layer-by-layer manipulation of conjugated polyions. Macromolecules 1995; 28:7107–14.
[34] Schoeler B, Kumaraswamy G, Caruso F. Investigation of the influence of polyelectrolyte charge density on the growth of multilayer thin films prepared by the layer-by-layer technique. Macromolecules 2002;35:889–97.
[35] Decher G. Fuzzy nanoassemblies: toward layered polymeric multicomposites. Science 1997;277:1232–7.
[36] Caruso F, Caruso RA, Mohwald H. Nanoengineering of inorganic and hybrid hollow spheres by colloidal templating. Science 1998;282:1111–4.
[37] Roy X, Sarazin P, Favis BD. Ultraporous nanosheath materials by layer-by-layer deposition onto co-continuous polymer-blend templates. Adv Mater 2006;18:1015–9.
[38] Cheung JH, Stockton WB, Rubner MF. Molecular-level processing of conjugated polymers. 3. Layer-by-layer manipulation of polyaniline via electrostatic interactions. Macromolecules 1997;30:2712–6.
[39] Fou AC, Rubner MF. Molecular-level processing of conjugated polymers. 2. Layer-by-layer manipulation of in-situ polymerized p-type doped conducting polymers. Macromolecules 2002;28:7115–20.
[40] Kim HS, Sohn BH, Lee W, Lee JK, Choi SJ, Kwon SJ. Multifunctional layer-by-layer self-assembly of conducting polymers and magnetic nanoparticles. Thin Solid Films 2002;419:173–7.
[41] Liang Z, Cabarcos OM, Allara DL, Wang Q. Hydrogen-bonding-directed layer-by-layer assembly of conjugated polymers. Adv Mater 2004;16:823–7.
[42] Ram MK, Salerno M, Adami M, Faraci P, Nicolini C. Physical properties of polyaniline films: assembled by the layer-by-layer technique. Langmuir 1999;15:1252–9.
[43] Ferreira M, Cheung JH, Rubner MF. Molecular self-assembly of conjugated polyions: A new process for fabricating multilayer thin film heterostructures. Thin Solid Films 1994;244:806–9.
[44] Dautzenberg H, Jaeger W, Kotz J, Phillip B, Seidel C, Stscherbina D. Polyelectrolytes – formation, characterization, application. Munich, Germany: Carl Hanser Verlag; 1994.
[45] Harris JJ, Bruening ML. Electrochemical and in situ ellipsometric investigation of the permeability and stability of layered polyelectrolyte films. Langmuir 2000;16:2006–13.
[46] Dubas ST, Schlenoff JB. Polyelectrolyte multilayers containing a weak polyacid: construction and deconstruction. Macromolecules 2001;34:3736–40.
[47] Braga GS, Paterno LG, Lima JPH, Fonseca FJ, de Andrade AM. Influence of the deposition parameters on the morphology and electrical conductivity of PANI/PSS self-assembled films. Mater Sci Eng C 2008;28:555–62.
[48] Paloheimo J, Laakso K, Isotalo H, Stubb H. Conductivity, thermoelectric power and field-effect mobility in self-assembled films of polyanilines and oligoanilines. Synth Met 1995;68:249–57.
[49] Mantovani GL, MacDiarmid AG, Mattoso LHC. Secondary doping in elastomeric polyaniline blends. Synth Met 1997;84:73–4.
[50] Yoon CO, Reghu M, Moses D, Cao Y, Heeger AJ. Transports in blends of conducting polymers. Synth Met 1995;69:255–8.
[51] Yoon CO, Reghu M, Moses D, Heeger AJ, Cao Y. Electrical transport in conductive blends of polyaniline in poly(methyl methacrylate). Synth Met 1994;63:47–52.
[52] Narkis M, Haba Y, Segal E, Zilberman M, Titelman GI, Siegmann A. Structured electrically conductive polyaniline/polymer blends. In: Fifth international symposium on polymers for advanced technologies, 31 August–5 September 1999. 8–12 ed. UK: Wiley; 2000. p. 665–73.
[53] Bates FS, Fredrickson GH. Block copolymer thermodynamics: theory and experiment. Annu Rev Phys Chem 1990;41:525–57.
[54] de Jesus MC, Weiss RA, Hahn SF. Synthesis of conductive nanocomposites by selective in situ polymerization of pyrrole within the lamellar microdomains of a block copolymer. Macromolecules 1998;31:2230–5.
[55] Fu Y, Palo DR, Erkey C, Weiss RA. Synthesis of conductive polypyrrole/polyurethane foams via a supercritical fluid process. Macromolecules 1997;30: 7611–3.
[56] Fu Y, Weiss RA, Gan PP, Bessette MD. Conductive elastomeric foams prepared by in situ vapor phase polymerization of pyrrole and copolymerization of pyrrole and *N*-methylpyrrole. Polym Eng Sci 1998;38:857–62.
[57] Reignier J, Favis BD. Control of the subinclusion microstructure in HDPE/PS/PMMA ternary blends. Macromolecules 2000;33:6998–7008.
[58] Yasuda K, Armstrong R, Cohen R. Shear flow properties of concentrated solutions of linear and star branched polystyrenes. Rheol Acta 1981;20: 163–78.
[59] Virgilio N, Favis BD, Pepin M-F, Desjardins P, L'Esperance G. High contrast imaging of interphases in ternary polymer blends using focused ion beam preparation and atomic force microscopy. Macromolecules 2005;38:2368–75.
[60] Ravati S, Favis BD. Morphological states for a ternary polymer blend demonstrating complete wetting. Polymer 2010;51:4547–61.
[61] Guo HF, Packirisamy S, Gvozdic NV, Meier DJ. Prediction and manipulation of the phase morphologies of multiphase polymer blends: 1. Ternary systems. Polymer 1997;38:785–94.
[62] Ravati S, Favis BD. Low percolation threshold conductive device derived from a five-component polymer blend. Polymer 2010;51:3669–84.
[63] Li J, Ma PL, Favis BD. The role of the blend interface type on morphology in cocontinuous polymer blends. Macromolecules 2002;35:2005–16.
[64] Li J, Favis BD. Characterizing co-continuous high density polyethylene/polystyrene blends. Polymer 2001;42:5047–53.
[65] Klitzing RV, Espert A, Asnacios A, Hellweg T, Colin A, Langevin D. Forces in foam films containing polyelectrolyte and surfactant. Colloids Surf A: Physicochem Eng Aspects 1999;149:131–40.
[66] Picart C, Lavalle P, Hubert P, Cuisinier FJG, Decher G, Schaaf P, et al. Buildup mechanism for poly(L-lysine)/hyaluronic acid films onto a solid surface. Langmuir 2001;17:7414–24.
[67] Dubas ST, Schlenoff JB. Swelling and smoothing of polyelectrolyte multilayers by salt. Langmuir 2001;17:7725–7.
[68] Tjipto E, Quinn JF, Caruso F. Layer-by-layer assembly of weak-strong copolymer polyelectrolytes: a route to morphological control of thin films. J Polym Sci Part A: Polym Chem 2007;45:4341–51.
[69] Lavalle P, Gergely C, Cuisinier FJG, Decher G, Schaaf P, Voegel JC, et al. Comparison of the structure of polyelectrolyte multilayer films exhibiting a linear and an exponential growth regime: an in situ atomic force microscopy study. Macromolecules 2002;35:4458–65.
[70] Schlenoff JB, Dubas ST. Mechanism of polyelectrolyte multilayer growth: charge overcompensation and distribution. Macromolecules 2001;34:592–8.
[71] Ha BY, Thirumalai D. Electrostatic persistence length of a polyelectrolyte chain. Macromolecules 1995;28:577–81.
[72] Klitzing R, Moehwald H. Proton concentration profile in ultrathin polyelectrolyte films. Langmuir 1995;11:3554–9.

[73] Jaber JA, Schlenoff JB. Counterfoils and water in polyelectrolyte multilayers: a tale of two polycations. Langmuir 2007;23:896–901.
[74] Solonin SM, Chernyshev LI. Effects of sintering conditions on the physicomechanical properties of porous tungsten. Soviet Powder Metall Met Ceram [Poroshkovaya Metallurgiya] 1975;14:806–8.
[75] Montes JM, Cuevas FG, Rodriguez JA, Herrera EJ. Electrical conductivity of sintered powder compacts. Powder Metall 2005;48:343–4.
[76] Lifshitz EM, Landau LD, Pitaevskii LP. Electrodynamics of continuous media, vol. 8; 1984.
[77] Skorokhov VV. The rheological principles of sintering theory. Kiev: Nauka; 1972.
[78] Ravati S, Ph.D thesis, Novel conductive polymer blends, Department of Chemical Engineering, École Polytechnique de Montréal, Montreal, Québec, Canada, 2010.

Polymer 52 (2011) 732–738

Contents lists available at ScienceDirect

Polymer

journal homepage: www.elsevier.com/locate/polymer

Experimental study of swelling and shrinking kinetics of spherical poly (*N*,*N*-diethylacrylamide) gel with continuous phase transition

Hideo Tajima*, Yuta Yoshida, Kazuaki Yamagiwa

Graduate School of Science and Technology, Niigata University, 2-8050 Ikarashi, Nishi-ku, Niigata 950-2181, Japan

ARTICLE INFO

Article history:
Received 10 August 2010
Received in revised form
3 December 2010
Accepted 14 December 2010
Available online 21 December 2010

Keywords:
Hydrogel
Kinetics
Swelling

ABSTRACT

The kinetics of swelling and shrinking of spherical particles of poly(*N*,*N*-diethylacrylamide) (DEAA) gel, prepared with static mixing technology, was investigated experimentally. The shrinking process was separated into late shrinking and initial shrinking by the skin layer effect. When the final temperature of temperature swing experiments was above the lower critical solution temperature (LCST) of polyDEAA, the apparent increase in the response rate constant (k_v) and the polymer diffusion constant (D) were due to reduction of the friction coefficient between polymer chains and water, arising from decrease in the water viscosity. When the final temperature was below the LCST, the main factor determining k_v and D was the change in the network structure of DEAA particles caused by the final temperature. The initial temperature affected the values of k_v and apparent diffusion constant D_{app} only in initial shrinking, in which the decrease in D with increase in the initial temperature came mainly from the spatial limitation.

1. Introduction

Temperature-sensitive hydrogels such as poly(*N*-isopropylacrylamide) (NIPA) and poly(*N*,*N*-diethylacrylamide) (DEAA) have been widely used for many applications because of their large, reversible changes in volume and other properties in response to small changes of temperature. Their applications include recycle adsorbents [1–7], chromatography [8–10], dehydrating agents [11], flow control actuators [12,13], sensor and lens materials [14,15], and biomedical [16–23] and tissue technology materials [24–28]. Adsorption of metal ions by hydrogels has attracted increasing attention over the past several years [3,4,29].

In applications of hydrogels as adsorbents, the important gel characteristics are not only the target material adsorption equilibrium but also the kinetics of adsorption and the volume change. Hydrogel kinetics depends on the hydrogel particle radius [30] and shape [31]. In addition, it is known that for NIPA gel, which shows a discontinuous phase transition, the swelling and shrinking rates change, depending on the initial and final temperatures in the temperature swing process [32]. The temperature swing over the lower critical solution temperature (LCST) of hydrogel is a very important factor for the adsorption function of a hydrogel because the response rate becomes infinitely slow in some cases. However, most adsorption studies for temperature-sensitive gels have been based on equilibrium adsorption, and limited information is available on the kinetics of volume change and adsorption. Although there have been many studies using polyDEAA (which has a continuous phase transition) for hydrogel application such as adsorbents, there have been few quantitative investigations of the kinetics of hydrogels with continuous phase transitions unlike polyNIPA. Swelling behavior of polyDEAA may not be the same as polyNIPA. For implementation of such temperature-sensitive hydrogels, it is crucial to know the dominant factors for the volume change rate of the hydrogels. When the temperature response rate is known, differences of not only equilibrium properties but also temperature response rate may be used for DEAA hydrogel application technologies.

The aim of this study was to elucidate the dominant factors for the response rate of polyDEAA gel. The swelling and shrinking rate of spherical polyDEAA gel particles is analyzed on the basis of the Tanaka–Fillmore theory [30] though many diffusion equations have been proposed. Although they have been commonly used in swelling and shrinking studies, non-spherical gels (cylinder, cube, sheet and so on) complicate the swelling and shrinking behavior and analysis because of the anisotropic volume change [31]. In the present study, spherical polyDEAA particles with radii of less than 1 mm were prepared by the method developed in our previous work [33] and used to measure the temperature response rate, since spherical gel particles have isotropic volume change. The results obtained in this study for the kinetics of a hydrogel with

* Corresponding author. Tel.: +81 25 262 7277; fax: +81 25 262 6781.
E-mail address: h_tajima@eng.niigata-u.ac.jp (H. Tajima).

0032-3861/$ – see front matter © 2010 Elsevier Ltd. All rights reserved.
doi:10.1016/j.polymer.2010.12.029

continuous phase transition will provide further information for implementing hydrogel applications such as adsorption and as biomedical materials.

2. Experimental

2.1. Spherical hydrogel particle preparation

PolyDEAA hydrogels were made from the temperature-sensitive monomer *N*,*N*-diethylacrylamide (DEAA; kindly supplied by Kojin Co. Ltd, Japan) and the photo-crosslinkable pre-polymer ENT3400 (40 wt.% aqueous solution; kindly provided by Kansai Paint Co. Ltd, Japan), which was used to enhance the strength of the gels. ENT3400 has a polyethylene glycol chain with degree of polymerization $n = 70$, and is thus hydrophilic [2]. The photo-initiator was 2-hydroxy-2-methyl-propiophenone (Aldrich Chemical Co. Ltd, UK). Hexadecane from Wako Chemical Co. Ltd, Japan, was used as the continuous phase: DEAA and ENT3400 were found in preliminary experiments to have low solubility in hexadecane. All reagents were used without further purification.

Spherical hydrogel particles were prepared from a liquid–liquid dispersion using static mixing technology, and photo-crosslinked by UV irradiation. The preparation method for polyDEAA particles has been reported in detail previously Ref. [33]. In brief, a pre-gel solution (DEAA-ENT3400 mixture with photo-initiator) was fed together with hexadecane to a Kenics static mixer by a peristaltic pump. The dispersed pre-gel drops were immediately irradiated with six UV lamps (wavelength 365 nm, power 2.65 mW cm^{-2}) in a downstream UV irradiation unit made from a Pyrex glass tube. After passing through the UV irradiation unit, the fluid containing polyDEAA particles was returned to the reaction mixture flask. The mixing-irradiation cycle was repeated for 2.5 min to ensure complete gelation of the drops of pre-gel solution. The resulting hydrogel particles were recovered by decantation of the continuous phase after the hydrogel preparation operation was stopped. A sample particle for swelling and shrinking measurements was selected from the particles after swelling in water at 293 K.

2.2. Hydrogel swelling and shrinking measurement

Because the lower critical solution temperature (LCST) of polyDEAA is about 306 K [34], the initial and final temperatures for swelling and shrinking were selected in the range 335.5–277 K to include the LCST for absorbent operation. The apparatus consisted of the measuring cell, two thermostated water tanks for initial and final temperature setting, a video microscope (Olympus PV-10, Japan), and a PC for video capture. The measuring cell was specially designed for observation of gel swelling and shrinking. The temperatures of the water tanks were controlled to within ±0.1 K.

The measuring cell packed with a polyDEAA particle and deionized water was kept at the initial temperature in a water tank. The equilibrium radius of the particle, attained after at least 2 h at the initial temperature, was defined as the initial radius. The measuring cell was quickly transferred to the second water tank set at the final temperature. The measuring cell experienced a sudden increase in temperature, and this time was defined as zero elapsed time. The time course of volume change of the polyDEAA particle was observed with the video microscope and recorded as a digital movie. Photographic images of the sample particle were taken from the digital movie, and the digitalized images analyzed with a Macintosh PC employing the image analysis program Image J-1.39u developed by the U.S. National Institutes of Health (available on the Internet at http://rsb.info.nih.gov/nih-image/). The Heywood diameter was used to evaluate the radius of the polyDEAA particle. The final radius of the particle was defined as the equilibrium radius at the final temperature. The swelling and shrinking experiments described above were carried out at least twice under the same conditions. The circularity of the selected sample particle at 293 K (different between maximum and minimum radius) was 12.4 μm. It was confirmed that the circularity of the sample hydrogel particle was in the range of 11.5–17.4 μm in all experimental runs.

To determine the swelling ratio of the polyDEAA particle, the equilibrium radius, 0.551 mm at 293 K, was measured in deionized water at temperatures in the temperature range from 277 K to 328 K. The swelling ratio, *S*, based on the equilibrium radius of the particle in water and normalized by the maximum change in the radius in the experimental temperature range, was calculated from the equation

$$S = \frac{a_T - a_{328}}{a_{277} - a_{328}}, \tag{1}$$

where a_T, a_{277} and a_{328} are the equilibrium radii of the polyDEAA gel particle at temperatures *T*, 277 K and 328 K, respectively.

2.3. Calculation of response rate constant and polymer diffusion constant

For hydrogel volume change analysis, several diffusion processes have been proposed base on Fickian [35] and non-Fickian diffusion (Tanaka–Fillmore [30–32] and Berens–Hofenberg [36,37]). In this study, the equation based on Tanaka–Fillmore theory was applied to analyze polyDEAA radius change for simplification and comparison to other data. The spherical hydrogel particle radius, *a*, during the swelling process is given by the following equation according to the Tanaka–Fillmore theory [30], where a_e, a_0 and $a(t)$ are the hydrogel radii at equilibrium, initially and at time *t*, and τ is the relaxation time:

$$\frac{a_e - a(t)}{a_e - a_0} = \frac{6}{\pi^2}\sum_{n=1}^{\infty}\frac{1}{n^2}\exp\left(-\frac{n^2 t}{\tau}\right) \tag{2}$$

The equation formula is similar to just the mathematical solution of the Fickian diffusion process for spheres. In this study $1/\tau$ is defined as the response rate constant k_v. When $\tau < t$, that is $t/\tau > 1$, Eq. (2) can be written in the simplified form

$$\frac{a_e - a(t)}{a_e - a_0} = \frac{6}{\pi^2}\exp(-k_v t) \tag{3}$$

In addition, the response rate constant is expressed by

$$k_v = \frac{1}{\tau} = \frac{\pi^2 D}{a_e^2} \tag{4}$$

where *D* is the polymer chain diffusion constant [30]. According to Eq. (3) the hydrogel radius *a* varies exponentially with time when $t/\tau > 1$. Fig. 1 shows typical experimental swelling data and the theoretical curve by Eqs. (2) and (3). Although the experimental temperature range included the LCST of polyDEAA, the data corresponded well to the theoretical curve by Eq. (2). All run in swelling process was well corresponding to the theoretical curve. The curve become almost linear for $t/\tau > 0.25$, and τ can be determined directly from the slope of the line based on Eq. (3) in this study as well as literature data [30,38] but non-linear behavior in the initial stage. Most of the k_v values could be evaluated from the slope of the line based on Eq. (3), and the polymer chain diffusion constant could be obtained from the k_v value according to Eq. (4). Note that temperature of the measuring cell and sample DEAA gel particle changes in initial swelling and shrinking processes. The measuring cell temperature responded rapidly to the sudden

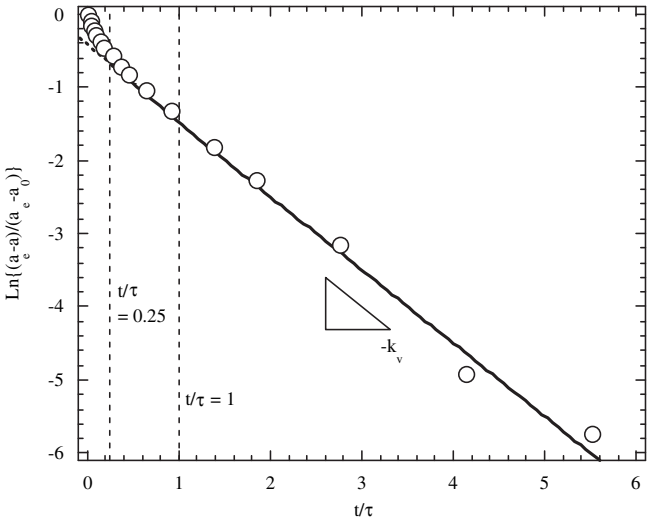

Fig. 1. Typical kinetics line of experimental data based on Tanaka–Fillmore theory. Conditions: a_0 = 0.285 mm at initial temperature 328 K, a_e = 0.562 mm at final temperature 293 K (swelling process). Open circle: experimental data, solid line: theory data by Eq. (2), dotted line: theory data by Eq. (3).

temperature change, whereas the radius of the polyDEAA particle changed much more slowly. For example, when radius of DEAA sample changes from 0.345 mm to 0.551 mm (swelling process with changing from 313 K to 293 K), non-linear behavior in the initial stage was finished at $t/\tau = 0.10$. In all experimental run, it was confirmed that non-linear behavior was within $t/\tau < 0.25$.

In the hydrogel shrinking process, especially when the temperature range includes the LCST, a skin layer forms on the hydrogel surface in initial stage of the process. It is known that hydrogel shrinking does not conform to the Tanaka–Fillmore theory because the dense skin layer initially and quickly formed on the particle surface inhibits hydrogel shrinking [32]. According to the literature [30], about 80% of the hydrogel volume change is completed at $t/\tau = 0.25$, and therefore it seems possible that the k_v value based on Eq. (3) includes mainly relaxation process of hydrogel after formed skin layer. For that reason the initial shrinking rate was also calculated to investigate skin layer formation and its effect on the shrinking process. As discussed in more detail below, however, because the kinetic line of overall shrinking process showed linearity with $t/\tau > 0.25$, it was determined that Eq. (3) was applicable to determine apparent diffusion constant D_{app} in shrinking process and the overall shrinking process was divided into two steps at $t/\tau = 0.25$. In the overall shrinking process, the volume change in the interval $0 < t/\tau < 0.25$ was defined as the initial shrinking, and that corresponding to $t/\tau > 0.25$ as the late shrinking. Eq. (3) can be applied only to the late shrinking step. The response rate constant in the initial shrinking step was calculated by fitting the experimental data to Eq. (2). Although the initial shrinking step was affected by the initial temperature change and skin formation, the diffusion constant obtained in the initial shrinking step was defined as apparent diffusion constant D_{app}.

3. Results and discussion

3.1. Visual observation of DEAA particle volume change

Spherical polyDEAA particles with equilibrium radius 0.25–0.81 mm at 293 K were prepared by static mixing technology. Fig. 2 shows typical observation results of the volume change of a polyDEAA particle (with equilibrium radius 0.551 mm at 293 K) in a temperature range that included the LCST of polyDEAA [34]. The volume of the particle changed with time, in both swelling and shrinking processes. The particle maintained spherical shape during the volume change, hence the Heywood diameter was applicable for evaluating the radius of the particle as a function of time and at equilibrium. The bubble generation reported previously for poly-NIPA [32,39,40] was not observed during shrinking of polyDEAA with final temperature above the LCST. It was thus confirmed that spherical polyDEAA particles were prepared without occluded air and were directly observable in spherical form.

The final radius of the polyDEAA particle was defined as the equilibrium radius, a_e, at a final temperature between 278 and 328 K. From the final radius the swelling ratio of the polyDEAA particles was calculated to confirm their thermo-sensitivity. Fig. 3 summarizes the normalized swelling ratio, S, of a polyDEAA particle at different temperatures. The S value continuously decreased with increasing temperature, and the radius of the gel particle in the vicinity of the LCST decreased by 80% compared with the radius at 278 K. The polyDEAA particle possessed to a large extent the thermo-sensitive properties of DEAA. It was judged from the results that polyDEAA particles exhibiting a continuous phase transition had been prepared.

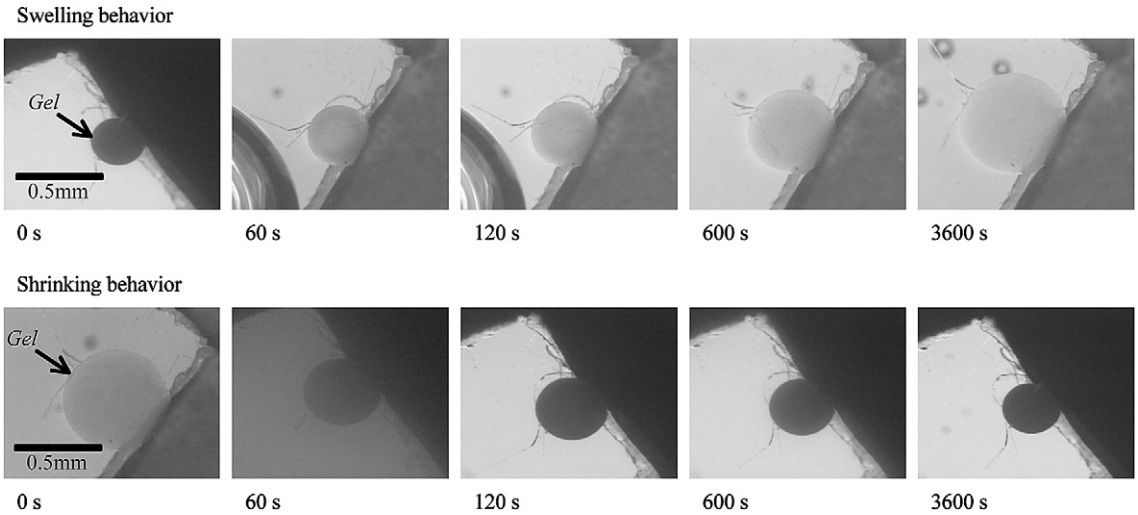

Fig. 2. Typical observations of polyDEAA particle volume change between temperatures including the LCST. Conditions: initial temperature 328 K and final temperature 278 K for swelling; initial temperature 278 K and final temperature 328 K for shrinking.

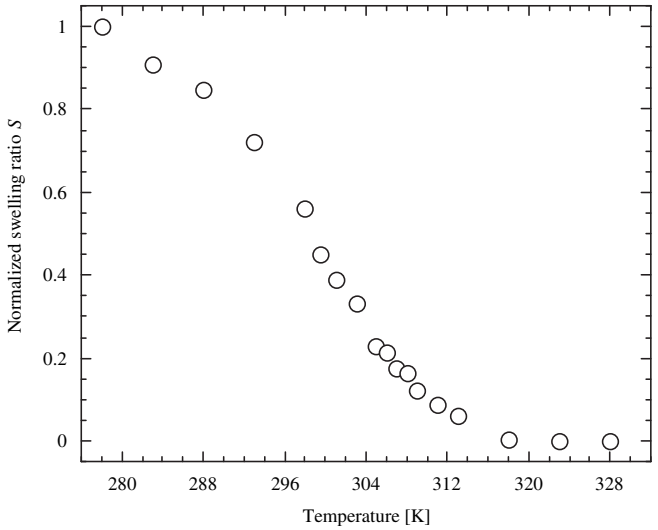

Fig. 3. Normalized equilibrium swelling ratio of polyDEAA particle in the temperature range 278–328 K.

3.2. Relationship between particle radius and response rate constant

The response rate constants of spherical polyDEAA particles with equilibrium radius 0.25–0.81 mm 293K were measured according to Eq. (3). The temperature swing was fixed at 313–293 K for swelling, and from 293 K to 313 K for shrinking. Fig. 4 shows the correlation of k_v with the equilibrium radius of a particle. The k_v values decreased as the inverse square of a_e, in accordance with Eq. (4). The polymer chain diffusion constant was evaluated from Eq. (4) as 6.59×10^{-11} m^2 s^{-1} in swelling and 5.01×10^{-11} m^2 s^{-1} in late shrinking. The D or D_{app} value obtained for the polyDEAA particles was of the same order of magnitude as for spherical polyacrylamide [30] and cylindrical polyNIPA [38] gels in water. Dense skin layer formation would be expected to reduce the value of D_{app} in the late shrinking step, as discussed in more detail below. It can be concluded, therefore, that the diffusion equation based on Tanaka–Fillmore theory is applicable for the response rate constant of polyDEAA gel.

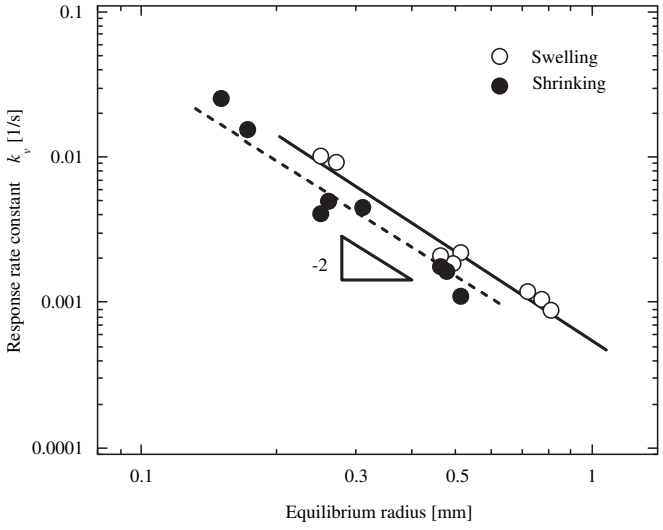

Fig. 4. Correlation of response rate constant of polyDEAA particle with equilibrium radius. Conditions: initial temperature 313 K and final temperature 293 K for swelling; initial temperature 293 K and final temperature 313 K for shrinking.

3.3. Effect of final temperature

It is known for polyNIPA gel (with discontinuous phase transition) that the swelling and shrinking rates depend on the initial and final temperature in the temperature swing process [32], but for polyDEAA with continuous phase transition there is little such information. Thus the effect of final temperature on the swelling and shrinking behavior of polyDEAA particles was investigated.

When the initial temperature was fixed at 328 K for swelling and 278 K for shrinking and the final temperature was varied, the k_v value depended on the final temperature. Fig. 5 shows the effect of the final temperature on the k_v value for a polyDEAA particle with equilibrium radius 0.551 mm at 293 K. When the final temperature was lower than the LCST of polyDEAA the k_v values for both swelling and late shrinking increased gradually with increasing final temperature. This result arises from the decrease in equilibrium radius of the particle with increase in final temperature. Fig. 6 shows that the kinetic line of the data at temperatures below than 306 K corresponded approximately to the theoretical line (solid line) for both swelling and shrinking. When the final temperature was higher than 306 K, so that the temperature swing spanned the LCST of polyDEAA, the k_v value for shrinking decreased with increase in the final temperature (Fig. 5) though the k_v value for swelling increased. In Fig. 6b, the kinetic line of the data for shrinking at final temperatures above 306 K (closed symbols) clearly deviates from the theoretical line. It has been reported that the shrinking behavior of polyNIPA hydrogel did not correspond to theory because a skin layer formed on the hydrogel surface [32]. These results indicate, therefore, that the late shrinking step at $t/\tau > 0.25$ is greatly influenced by the phase transition and the dense skin layer formation, which are not taken into account in the Tanaka–Fillmore theory.

To eliminate the effect of skin layer formation on the response rate constant, k_v in the initial shrinking regime was obtained by fitting the experimental data to the theoretical equation, Eq. (2), especially in the range $0 < t/\tau < 0.25$. Fig. 7 shows k_v for initial shrinking at various final temperatures. Both the initial shrinking rate constant and the swelling rate constant increased with increase in the final temperature. The initial shrinking rate for $0 < t/\tau < 0.25$, is, therefore, regarded as the uninfluenced intrinsic shrinking rate of the polyDEAA gel particle. For polyDEAA gel when the final temperature was near to the LCST, the critical slowing down of the transition that was reported for polyNIPA gel [32] was not observed.

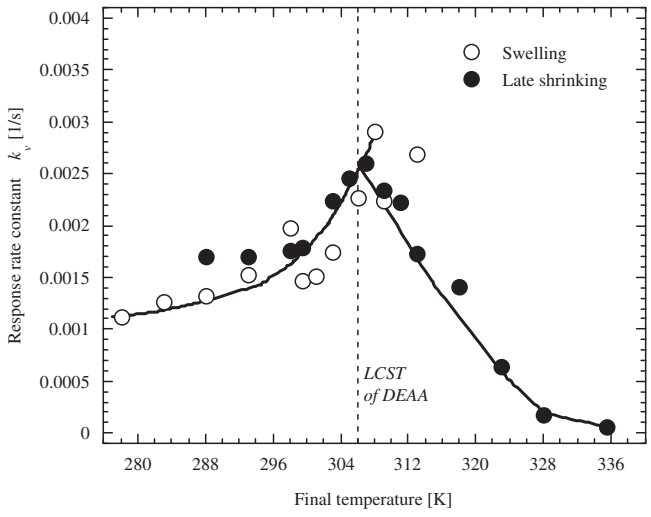

Fig. 5. Dependence of response rate constant for swelling and late shrinking on final temperature.

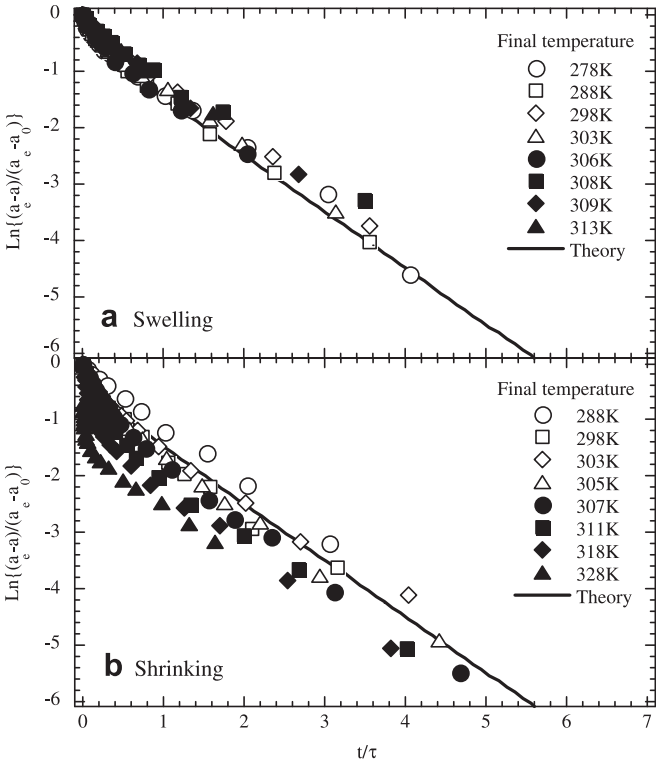

Fig. 6. Kinetics line for polyDEAA gel volume change. (a) Swelling, (b) shrinking process.

According to Eq. (4), k_v is affected not only by the equilibrium radius, which decreases with increasing final temperature, but also by the polymer chain diffusion constant. D was calculated from the experimental k_v value and Eq. (4) to eliminate the effect of the equilibrium radius on k_v. In Fig. 8a the calculated D values are shown as a function of the final temperature. When the final temperature was below about 300 K, the D value seemed to gradually decrease with increase in the final temperature. On the other hand, for final temperatures higher than 300 K, D increased with increase in the final temperature. The polymer chain diffusion constant is expressed by the following equation [41,42]

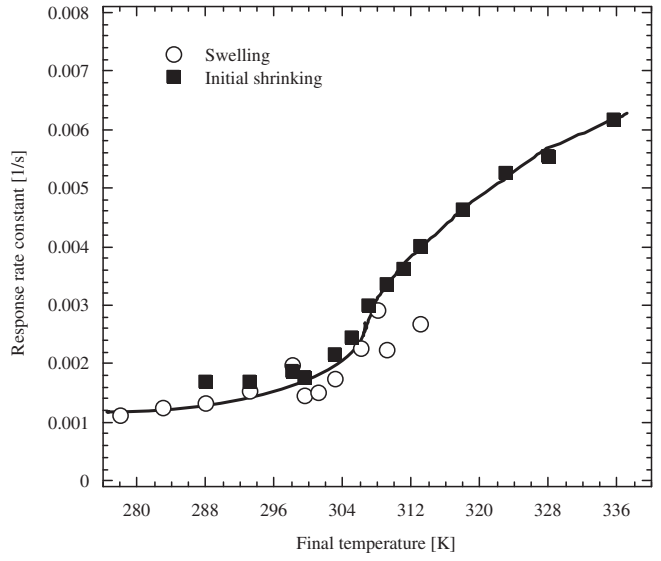

Fig. 7. Dependence of response rate constant for swelling and initial shrinking on final temperature.

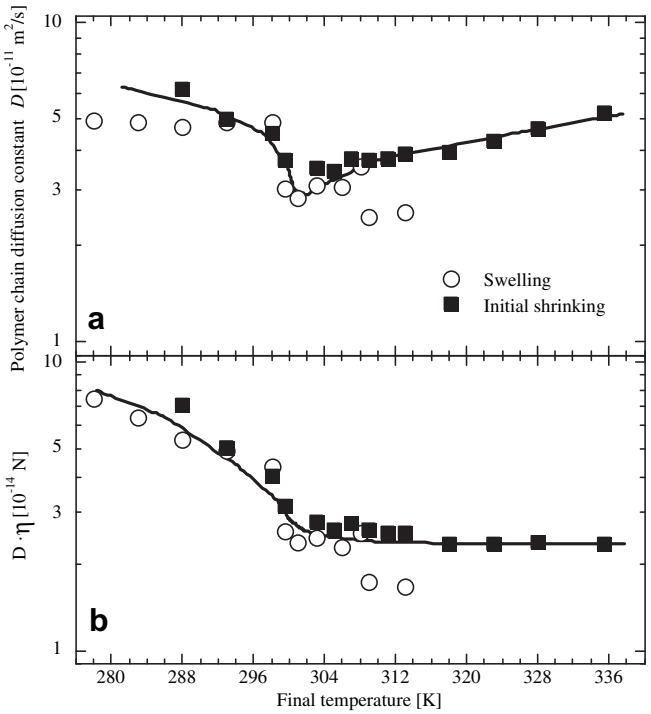

Fig. 8. Dependence of polymer chain diffusion constant on final temperature. (a) Diffusion constant, (b) normalized diffusion constant with water viscosity.

$$D = \frac{K + \frac{4}{3}\mu}{f} \cong \frac{K}{f} \tag{5}$$

where K is the osmotic bulk modulus, μ is the shear modulus, and f is the friction coefficient between the polymer network and the solvent. In many cases, the shear modulus of a hydrogel sphere with isotropic volume change is negligible because the shear modulus is smaller than the osmotic bulk modulus. In addition, the friction coefficient is proportional to the solvent viscosity, η, and inversely proportional to the square of the average mesh size of the network, ξ

$$f \propto \frac{\eta}{\xi^2} \tag{6}$$

and f normalized with η, that is f/η, is almost constant with temperature [41,42]. Because the solvent viscosity depends on temperature, the effect of water viscosity on the D value at the final temperature may be considerable. In this study, the D value was normalized with the viscosity of water η at the final temperature, because the friction coefficient f between prepared DEAA gel and water could not be obtained. Fig. 8b shows the final temperature dependence of D normalized with η, that is $D\eta$, which has units of Newton (N). Fig. 8b shows that the normalized D value decreased gradually with increasing final temperature, and became almost constant for final temperatures above 306 K. It can be concluded from these data that at temperatures above the LCST the apparent increase in k_v and D for polyDEAA particles can be attributed mainly to reduction of the friction coefficient between polymer chain and water arising from the decrease in water viscosity. The pore size of the gel particle, ξ, is stable in that temperature region because of the small volume change of polyDEAA gel. Below the LCST, the normalized D value as well as the equilibrium swelling ratio decreased with increase in the final temperature as shown in Fig. 3. The main factor is the polymer network structure of the polyDEAA particle changing with the final temperature. According to Eqs. (5) and (6), the friction coefficient increases with decrease in the

average mesh size of the network by shrinking of polyDEAA at high final temperatures, thus the polymer chain diffusion constant decreases as shown in Fig. 8b.

3.4. Effect of initial temperature

The final temperature was fixed at 278 K for swelling and 328 K for shrinking, and the initial temperature was varied. Because the final temperature was fixed, the equilibrium radius, a_e, of the polyDEAA particle and the water viscosity were constant. Fig. 9 shows the polymer chain diffusion constant calculated from k_v for various initial temperatures. The D values for both swelling and late shrinking (the data are scattered because of the small volume changes) were almost constant, but the D value for swelling was an order of magnitude higher than for late shrinking. The D values for swelling and late shrinking were independent of the initial temperature. Because the area around a polyDEAA gel particle is free space in the swelling process, polymer chain diffusion is undisturbed. The response rate in swelling is independent of the starting polymer network structure of the gel, and is significantly determined by the final temperature. On the other hand, the late shrinking process is greatly influenced by skin layer formation because the final temperature is above the LCST. In other words, the apparent starting polymer network in late shrinking has already shrunk, and thus the effect of the initial temperature is apparently not observed.

In the initial shrinking step the D_{app} value at the initial temperature 278 K, at which the polymer network structure of the polyDEAA particle is most expanded in the experimental range of initial temperatures, was almost same as for swelling. However, the D_{app} value for initial shrinking decreased with increase in the initial temperature, and almost reached the D value for late shrinking in the temperature range 308–312 K. This temperature is above the LCST of polyDEAA, and consequently the starting polymer network has already shrunk. Polymer chain diffusion is spatially and dramatically limited because the starting polymer network is already closely arranged at higher temperature. For an initial temperature below the LCST, the spatial limitation for polymer network diffusion is smaller than that in the late shrinking process, but larger than in the swelling process. The decrease in the D_{app} value for initial shrinking comes mainly from the spatial limitation.

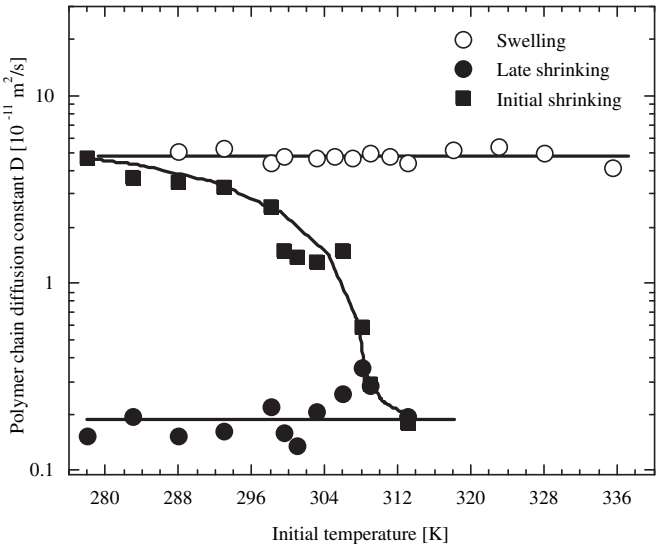

Fig. 9. Dependence of polymer chain diffusion constant on initial temperature.

4. Conclusion

The swelling and shrinking kinetics of polyDEAA gel with continuous volume phase transition were experimentally investigated with spherical gel particles, prepared using static mixing technology. Swelling and shrinking kinetics were analyzed based on Tanaka–Fillmore theory, and the polymer chain diffusion constant was easily evaluated from the equilibrium radius and the measured response rate constant. The shrinking step was separated into late shrinking including skin layer formation, and the initial shrinking process that eliminated the skin layer effect. When the final temperature was above the LCST of polyDEAA, the apparent increase in the k_v and D values was attributed mainly to reduction of the friction coefficient between polymer chain and water as a result of the decrease in the viscosity of water. When the final temperature was below the LCST, the main factor determining the k_v and D values is the change in the network structure of the polyDEAA particle due to the final temperature. The initial temperature affected the k_v and D values only in the initial shrinking process. The decrease in the D value for initial shrinking with increase in the initial temperature arises mainly from the spatial limitation. The results obtained in this study for the kinetics of polyDEAA will provide further information for implementing hydrogel applications such as adsorption materials.

Acknowledgments

The authors gratefully acknowledge Kansai Paint Co. Ltd., Japan for kindly providing the photo-crosslinkable pre-polymer ENT3400, and Kojin Co. Ltd., Japan for kindly supplying the temperature-sensitive monomer DEAA.

References

[1] Yamagiwa K, Komi T, Kumakura A, Yokoyama S, Yoshida M, Ohkawa A. Photo-crosslinked copolymer gel as an adsorbent for temperature-swing adsorption process. J Chem Eng Jpn 2004;37:1274–8.
[2] Yamagiwa K, Komi T, Yoshida M, Ohkawa A, Iida T. Temperature-swing adsorption of nonionic surfactant with photo-crosslinked polymeric gel. J Chem Eng Jpn 2001;34:1171–6.
[3] Tokuyama H, Yanagawa K, Sakohara S. Temperature swing adsorption of heavy metals on novel phosphate-type adsorbents using thermosensitive gels and/or polymers. Sep Purif Technol 2006;50:8–14.
[4] Tokuyama H, Kanehara A. Temperature swing adsorption of gold(III) ions on poly(N-isopropylacrylamide) gel. React Funct Polym 2007;67:136–43.
[5] Takeshita K, Matsumura T, Nakao Y. Separation of americium(III) and europium(III) by thermal-swing extraction using thermosensitive polymer gel. Prog Nucl Energy 2008;50:466–9.
[6] Panayiotou M, Freitag R. Synthesis and characterization of stimuli-responsive poly-(*N*,*N*′-diethylacrylamide) hydrogels. Polymer 2005;46:615–21.
[7] Huber DL, Manginell RP, Samara MA, Kim B, Bunker BC. Programmed adsorption and release of proteins in a microfluidic device. Science 2003;301:352–4.
[8] Hradil J, Mackova H, Horak D. Polarity and temperature-dependent properties of poly(*N*-isopropylacrylamide) and poly(*N*,*N*-diethylacryl-amide) hydrogels studied by liquid chromatography. Macromol Symp 2009;281:142–9.
[9] Kikuchi A, Okano T. Intelligent thermoresponsive polymeric stationary phases for aqueous chromatography of biological compounds. Prog Polym Sci 2002;27:1165–93.
[10] Kanazawa H, Kashiwase Y, Yamamoto K, Matsushima Y. Temperature-responsive liquid chromatography 2. Effects of hydrophobic groups in *N*-isopropylacrylamide copolymer-modified silica. Anal Chem 1997;69:823–30.
[11] Sakohara S, Ochiai E, Kusaka T. Dewatering of activated sludge by thermosensitive polymers. Sep Purif Technol 2007;56:296–302.
[12] Beebe DJ, Moore JS, Bauer JM, Yu Q, Liu RH, Devadoss C, et al. Functional hydrogel structures for autonomous flow control inside microfluidic channels. Nature 2000;404:588–90.
[13] Harmon ME, Tang M, Frank CW. A microfluidic actuator based on thermoresponsive hydrogels. Polymer 2003;44:4547–56.
[14] Suzuki H, Kumagai A. New type of glucose sensor based on enzymatic conversion of gel volume into liquid column length. Biomacromolecules 2004;5:486–91.

[15] Dong L, Agarwal AK, Beebe DJ, Jiang H. Adaptive liquid microlenses activated by stimuli responsive hydrogels. Nature 2006;442:551–4.
[16] Klouda L, Mikos AG. Thermoresponsive hydrogels in biomedical applications. Eur J Pharm Biopharm 2008;68:34–45.
[17] Fundueanu G, Constantin M, Ascenzi P. Poly(N-isopropylacrylamide-co-acrylamide) cross-linked thermoresponsive microspheres obtained from preformed polymers: influence of the physico-chemical characteristics of drugs on their release profiles. Acta Biomaterialia 2009;5:363–73.
[18] Panayiotou M, Pohner C, Vandevyver C, Wandrey C, Hilbring F, Freitag R. Synthesis and characterization of thermo-responsive poly(N,N′-diethylacrylamide) microgels. React Funct Polym 2007;67:807–19.
[19] Huang X, Lowe TL. Biodegradable thermoresponsive hydrogels for aqueous encapsulation and controlled release of hydrophilic model drugs. Biomacromolecules 2005;6:2131–9.
[20] Ito T, Yamaguchi T. Controlled release of model drugs through a molecular recognition ion gating membrane in response to a specific ion signal. Langmuir 2006;22:3945–9.
[21] Morita R, Honda R, Takahashi Y. Development of oral controlled release preparations, a PVA swelling controlled release system (SCRS). II. In vitro and in vivo evaluation. J Controlled Release 2000;68:115–20.
[22] Kost J, Langer R. Responsive polymeric delivery systems. Adv Drug Deliv Rev 2001;46:125–48.
[23] Sershen S, West J. Implantable, polymeric systems for modulated drug delivery. Adv Drug Deliv Rev 2002;54:1225–35.
[24] Pasparakis G, Cockayne A, Alexander C. Control of bacterial aggregation by thermoresponsive glycopolymers. J Am Chem Soc 2007;129:11014–5.
[25] Moran MT, Carroll WM, Selezneva I, Gorelov A, Rochev Y. Cell growth and detachment from protein-coated PNIPAAm-based copolymers. J Biomed Mater Res A 2007;81:870–6.
[26] Stile RA, Burghardt WR, Healy KE. Synthesis and characterization of injectable poly(N-isopropylacrylamide)-based hydrogels that support tissue formation in vitro. Macromolecules 1999;32:7370–9.
[27] Ito Y. Surface micropatterning to regulate cell functions. Biomaterials 1999;20:2333–42.
[28] von Recum H, Okano T, Kim SW. Growth factor release from thermally reversible tissue culture substrates. J Controlled Release 1998;55:121–30.
[29] Tokuyama H, Kanazawa R, Sakohara S. Equilibrium and kinetics for temperature swing adsorption of a target metal on molecular imprinted thermosensitive gel adsorbents. Sep Purif Technol 2005;44:152–9.
[30] Tanaka T, Fillmore J. Kinetics of swelling of gels. J Chem Phys 1979;70:1214–8.
[31] Li Y, Tanaka T. Kinetics of swelling and shrinking of gels. J Chem Phys 1990;92:1365–71.
[32] Matsuo SE, Tanaka T. Kinetics of discontinuous volume-phase transition of gels. J Chem Phys 1988;89:1695–703.
[33] Tajima H, Yoshida Y, Abiko S, Yamagiwa K. Size adjustment of spherical temperature-sensitive hydrogel beads by liquid–liquid dispersion using a Kenics static mixer. Chem Eng J 2010;156:479–86.
[34] Idziak I, Avoce D, Lessaed D, Grabel D, Zhu XX. Thermosensitivity of aqueous solutions of poly(N,N-diethylacrylamide). Macromolecules 1999;32:1260–3.
[35] Park GS. Radioactive studies of diffusion in polymer systems Part 3. Trans Faraday Soc 1961;57:2314–22.
[36] Berens AR, Hopfenberg HB. Diffusion and relaxation in glassy polymer powders: 2. Separation of diffusion and relaxation parameters. Polymer 1978;19:489–96.
[37] Rosa F, Bordado J, Casquilho M. Kinetics of water absorbency in AA/AMPS copolymers: applications of a diffusion-relaxation model. Polymer 2002;43:63–70.
[38] Takahashi K, Takigawa T, Masuda T. Swelling and deswelling kinetics of poly(N-isopropylacrylamide) gels. J Chem Phys 2004;120:2972–9.
[39] Shibayama M, Nagai K. Shrinking kinetics of poly-(N-isopropylacrylamide) gels T-jumped across their volume phase transition temperatures. Macromolecules 1999;32:7461–8.
[40] Okajima T, Harada I, Nishio K, Hirotsu S. Kinetics of volume phase transition in poly(N-isopropylacrylamide) gels. J Chem Phys 2002;116:9068–77.
[41] Tokita M, Tanaka T. Friction coefficient of polymer networks of gels. J Chem Phys 1991;95:4613–9.
[42] Tokita M, Tanaka T. Reversible decrease of gel-solvent friction. Science 1991;253:1121–3.

Polymer 52 (2011) 739–745

Contents lists available at ScienceDirect

Polymer

journal homepage: www.elsevier.com/locate/polymer

Formation and relaxation of the elastic strain generated by photocuring in polymer blends monitored by Mach–Zehnder interferometry

D.-T. Van-Pham, K. Sorioka, T. Norisuye, Q. Tran-Cong-Miyata*

Department of Macromolecular Science and Engineering, Graduate School of Science and Technology, Kyoto Institute of Technology, Matsugasaki, Sakyo-ku, Kyoto 606-8585, Japan

ARTICLE INFO

Article history:
Received 16 August 2010
Received in revised form
3 December 2010
Accepted 14 December 2010
Available online 21 December 2010

Keywords:
Photo-cross-link
Elastic deformation
Mach-Zehnder interferometry

ABSTRACT

The deformation associated with the photocuring reaction of an anthracene-labeled polystyrene (PSA) in a miscible blend with poly(vinyl methyl ether) (PVME) was *in situ* monitored at ambient temperature by using Mach–Zehnder interferometry (MZI).The curing kinetics of a PSA/PVME (30/70) blend was followed by observing the decrease in the absorption of the anthracene moieties upon irradiation using UV–visible spectroscopy. It was found that both the kinetics of the curing and deformation processes can be well described by the modified Kohlrausch–Williams–Watts (KWW) empirical function. The experimental results reveal a strong correlation between the photocuring and deformation processes of the blend. From the dynamic mechanical measurements performed for samples with different irradiation times, it was also found that the deformation process of the blend observed by MZI is controlled by the on-going cross-link-induced glassification process of the mixtures. These experimental results suggest that MZI is a useful technique to monitor *in situ* the local deformation and relaxation processes in photoreactive polymers.

1. Introduction

Deformation induced by chemical reactions, particularly curing, in polymeric systems is significant and important not only for practical applications, but also for fundamental understanding of extremely slow relaxation processes associated with polymer glassification. An example for the former case is control of the long-term stability and the precision of materials produced by laser-processing at microscopic length scales [1,2]. The latter strongly depends on the gap between the reaction temperature and the glass transition temperature (T_g) of the material under processing [3,4].

So far, several methods have been utilized to quantify the deformation or the elastic strain of polymeric materials in the presence of an external field. From the macroscopic viewpoint, conventional methods of mechanical testing can be used to characterize the deformation [5]. However, these methods are only efficient for samples with large sizes and are not suitable for *in situ* detection of microscopic responses of a sample subjected to an external field such as electric field or UV irradiation. Deformation under varying external conditions such as temporal [6] or spatial modulations [7,8] of UV irradiation intensity cannot be easily monitored by these conventional methods, particularly for deformation at the nanometer scales. Ellipsometry would be a powerful technique which could provide a useful tool to measure the thickness of the sample in the nanometer scales via the detection of amplitude and phase changes using polarized light [9]. In principle, the elastic strain or deformation of polymer films can be also monitored via measurements of the change in thickness by using the prism-coupler method [10] or neutron reflectivity experiments [11] taking advantages of the reflection phenomena of electromagnetic waves. Though the precise information can be obtained with these techniques, it requires sophisticated instruments and specifically designed samples such as deuterated or partially deuterated polymers for gaining contrast between different components. On the other hand, for crystalline materials, the deformation of crystal lattices can be exactly measured by using wide-angle X-ray scattering (WAXS) [12,13]. However, the method is limited to crystalline materials and therefore cannot sufficiently provide useful information on amorphous polymer materials.

From the viewpoint of micro-processing using light, it is desired to develop a method which is easily accessible and could help monitoring quickly the response of a polymer sample under UV irradiation by *in situ* measurements. To characterize the effects of reaction-induced deformation on the resulting morphology of phase-separating polymer blends, we have developed a Mach–Zehnder interferometer (MZI) system to measure *in situ* the deformation of polymers under UV irradiation [14]. The method was applied to measure *in situ* the deformation of a poly(ethyl acrylate) (PEA) bearing anthracene as a photo-cross-linker in the bulk state. It was found that during the

* Corresponding author. Tel./fax: +(81) 075 724 7862.
E-mail address: qui@kit.ac.jp (Q. Tran-Cong-Miyata).

0032-3861/$ – see front matter © 2010 Elsevier Ltd. All rights reserved.
doi:10.1016/j.polymer.2010.12.028

aging process, the time-dependent elastic strain generated in a photo-cross-linked PEA under various UV light intensities can be described as a universal function of reduced elapse time, a dimensionless parameter defined as the product between the elapse time and the aging rate [15]. The deformation of the mixtures of poly(vinyl methyl ether) and a polystyrene derivative was also measured and analyzed as a function of cross-link density [14]. In these experiments, it was found that for high cross-link density, the blend shrinks upon irradiation, whereas it partially recovers from the shrinkage upon irradiation with a low UV intensity. These results suggest that the glass transition process associated with the photo-cross-link would play a key role in the local deformation of the sample.

In order to elucidate the relation between the glass transition of the photo-cross-linked blend and the deformation observed by MZI, we have carried out systematic experiments using MZI combined with UV–vis spectroscopy and dynamic mechanical measurements. The experimental results are discussed in relation to the distance between the experimental temperatures and the glass transition temperature of the sample. Finally, the behavior of the strain relaxation observed for homopolymers and polymer blends will be discussed in terms of the inhomogeneity arising from the effects of blending.

2. Experimental

2.1. Sample preparation

In this study, a photoreactive blend of anthracene-labeled polystyrene (PSA) and poly(vinyl methyl ether) (PVME) was used as sample. These polymers were prepared by the method reported previously [16]. Briefly, PSA ($M_w = 1.9 \times 10^5$; $M_w/M_n = 1.9$) was synthesized by copolymerization of styrene and chloromethylstyrene (Tokyo Kaisei Inc.). The copolymer obtained by this way was labeled with anthracene by reacting with potassium salt of anthracene carboxylic acid (Aldrich Chemicals, recrystallized twice in ethanol) in anhydrous dimethylformamide (Aldrich Chemicals). The average label content of the resulting PSA is 52 anthracenes/chain (2.8 mol% in equivalent) as determined by UV–vis spectrometry (UV-1600, Shimadzu Inc., Japan). Poly (vinyl methyl ether) PVME, ($M_w = 1.9 \times 10^5$; $M_w/M_n = 1.9$) was purchased from Scientific Polymer Products Inc. and purified using toluene as good solvent and *n*-heptane as poor solvent. PSA/PVME (30/70) film with 25 μm thickness was prepared by solvent-casting method. The slow drying process was used to prevent bubbles and/or crack formation. To eliminate the residual stress which might develop during the sample preparation, the PSA/PVME blends were heated to 80 °C for 2 h and slowly quenched to room temperature prior to measurements. The chemical structures of poly (styrene-*stat*-chloromethylstyrene), anthracene-labeled polystyrene (PSA) and poly (vinyl methyl ether) (PVME) are respectively shown in Fig. 1.

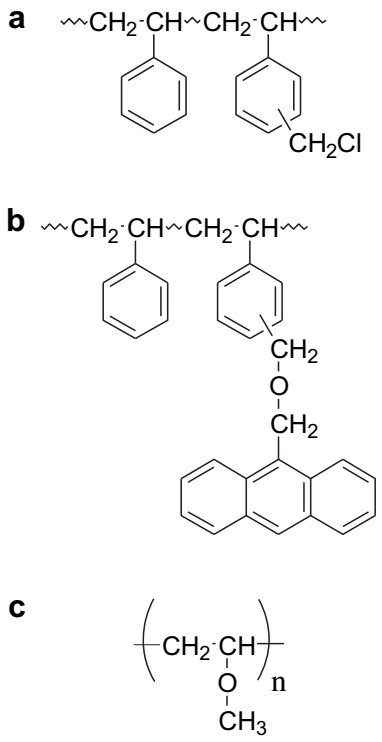

Fig. 1. Chemical structure of: (a), poly(styrene-*stat*-chloromethylstyrene) (PS); (b), anthracene-labeled polystyrene (PSA); (c), poly(vinyl methyl ether) (PVME).

2.2. Photodimerization kinetics of anthracene in PSA/PVME (30/70) mixtures

The photodimerization kinetics of anthracene moieties labeled on PSA chains was monitored by following the change in the absorbance of anthracene at 365 nm using a UV–vis spectrophotometer (Model UV-1600, Shimadzu Inc., Japan). A high-pressure He–Xe lamp (350 W, Moritex, Japan) equipped with an optical fiber was used for this irradiation process. The cross-link kinetics of the PSA component was examined by monitoring the time-evolution process of the normalized absorbance $OD_N(t_{irr})$ defined as:

$$OD_N(t_{irr}) = \frac{OD(t_{irr})}{OD(0)} \quad (1)$$

Here, $OD(0)$ is the initial absorbance of the sample observed at 365 nm and $OD(t_{irr})$ is the absorbance obtained after t_{irr} min. of irradiation. The progress of the cross-link reaction was obtained by analyzing the decay of the anthracene absorbance with irradiation time. Alternatively, the time evolution of the cross-link density $\gamma(t_{irr})$ was also calculated by using the following equation:

$$\gamma(t_{irr}) = \frac{\delta}{2}\cdot\frac{(OD(0) - OD(t_{irr}))}{OD(0)} \quad (2)$$

Here γ is the number of junctions between the two anthracene moieties labeled on the PSA, and δ is the average number of anthracenes labeled per PSA chain. The time-evolution of the normalized absorbance $OD_N(t_{irr})$ and the cross-link density $\gamma(t_{irr})$ was examined under various irradiation intensities. The experimental results on the reaction kinetics will be discussed later in correlation with the emerging strain *in situ* monitored by using Mach–Zehnder interferometry.

2.3. Observation of the strain formation by using Mach–Zehnder interferometry

In this study, a Mach–Zehnder interferometer (MZI) equipped with a He–Ne laser (10 mW, 632.8 nm, Uniphase Inc.) as a light source was employed to examine *in situ* the effects of photo-cross-link reaction on the deformation of the blend in the nanometer scales. The details of the instrument and the data analysis were described elsewhere [14,15]. In brief, the interference fringes of the sample were recorded after different intervals of irradiation time. Subsequently, the optical path length difference (OPLD) was calculated using the phase difference available from the fringe

patterns obtained before and after irradiation as described in detail elsewhere [14]. The time-evolution of the optical path length difference $OPLD(t_{irr})$ is defined as:

$$OPLD(t_{irr}) = [OPL(0) - OPL(t_{irr})] \quad (3)$$

where $OPL(0)$ and $OPL(t_{irr})$ are respectively the optical path lengths observed before and after an irradiation time t_{irr}.

The OPLD is related to the changes in both the refractive index and the thickness of the sample by the following equation:

$$OPLD(t_{irr}) = (n_s - n_0)\Delta d + d_0\Delta n_s + \Delta n_s \Delta d \quad (4)$$

where d_0, n_0 and n_s are respectively the initial thickness of the sample, the refractive indices of the air and sample before irradiation. Δd and Δn_s are respectively the changes in the sample thickness and refractive index.

Since the cross-term $(\Delta n_s \Delta d)$ is negligible, the optical path length difference $OPLD(t_{irr})$ can be approximately expressed as:

$$OPLD(t_{irr}) \cong (n_s - n_0)\Delta d + d_0\Delta n_s \quad (5)$$

In this work, the change in refractive index Δn associated with UV irradiation was measured by using a Prism Coupler (Metricon, Model 2100). Together with the OPLD calculated from Mach–Zehnder interferometry data, and Δn from the prism coupling experiments, the deformation Δn was obtained by Eq. (5). Under our experimental conditions, since the changes in the refractive index of the blend resulting from the photodimerization of anthracene are negligible for these PSA/PVME blends, the time-dependence of the deformation was finally calculated from:

$$\epsilon(t_{irr}) = \frac{\Delta d(t_{irr})}{d_0} = \frac{OPLD(t_{irr})}{(n_s - 1)d_0} \quad (6)$$

Here, the change in the sample thickness $\Delta d(t_{irr})$ is defined using $d(t_{irr})$, the sample thickness obtained after t_{irr} (min) of irradiation time:

$$\Delta d(t_{irr}) = [d(t_{irr}) - d_0] \quad (7)$$

$\epsilon(t_{irr})$ is the irradiation-time dependence of the deformation, n_s and d_0 are respectively the initial refractive index and the initial thickness of the sample.

2.4. Measurements of glass transition temperature (T_g) by dynamic mechanical analysis (DMA)

The glass transition temperature of a PSA/PVME (30/70) blend was measured by using a dynamic mechanical analyzer (DMA 2980, TA Instruments, Inc) with a heating rate of 2.0 °C/min under the frequency 1.0 Hz. The amplitude was set at ±5 μm. The mechanical loss tan δ was measured for this PSA/PVME (30/70) blend under different irradiation conditions. The glass transition temperature T_g was determined from the peak position of tan δ by using the non-linear least-squares regression program Universal Analysis 2000 installed on the instrument.

3. Results and discussion

3.1. Effects of irradiation intensity on the reaction kinetics

The effects of irradiation intensity on the reaction kinetics were examined under 9 different intensities ranging from 0.1 to 7.0 mW/cm^2 (I = 0.1, 0.5, 1.0, 2.0, 3.0, 4.0, 5.0, 6.0 and 7.0 mW/cm^2) for a PSA/PVME (30/70) blend. It was found that when the irradiation intensity changes, both the time-evolution of the normalized absorbance $OD_N(t_{irr})$ and the cross-link density $\gamma(t_{irr})$ follow the modified Kohlraush–Williams–Watts stretched exponential equation as shown respectively in Eqs. (8) and (9).

$$OD_N(t_{irr}) = (1 - B)\exp\left[-(k_c t_{irr})^{\alpha}\right] + B \quad (8)$$

$$\gamma(t_{irr}) = D\left[1 - \exp(-k_c t_{irr})^{\alpha}\right] \quad (9)$$

In these equations, k_c is the rate constant of the cross-link reaction. B and D are respectively the limiting reaction yield and the limiting cross-link density as $t_{irr} \to \infty$.

The data obtained for the cross-link reaction kinetics are shown in Fig. 2 for the irradiation intensity ranging from 0.1 to 7.0 mW/cm^2. By analyzing these kinetic data using Eqs. (8) and (9), it was found that as the irradiation intensity increases, the mean cross-link rate k_c increases, whereas the limiting cross-link density D which was taken as the limiting value obtained at long irradiation time in Fig. 2b, increases to some extent and eventually approaches a constant value at intensity higher than 5.0 mW/cm^2 as shown in Fig. 3. On the other hand, the inhomogeneity index α which expresses the degree of inhomogeneity kinetics associated with the cross-link reaction, lies in the range $0.9 \geq \alpha \geq 0.5$.

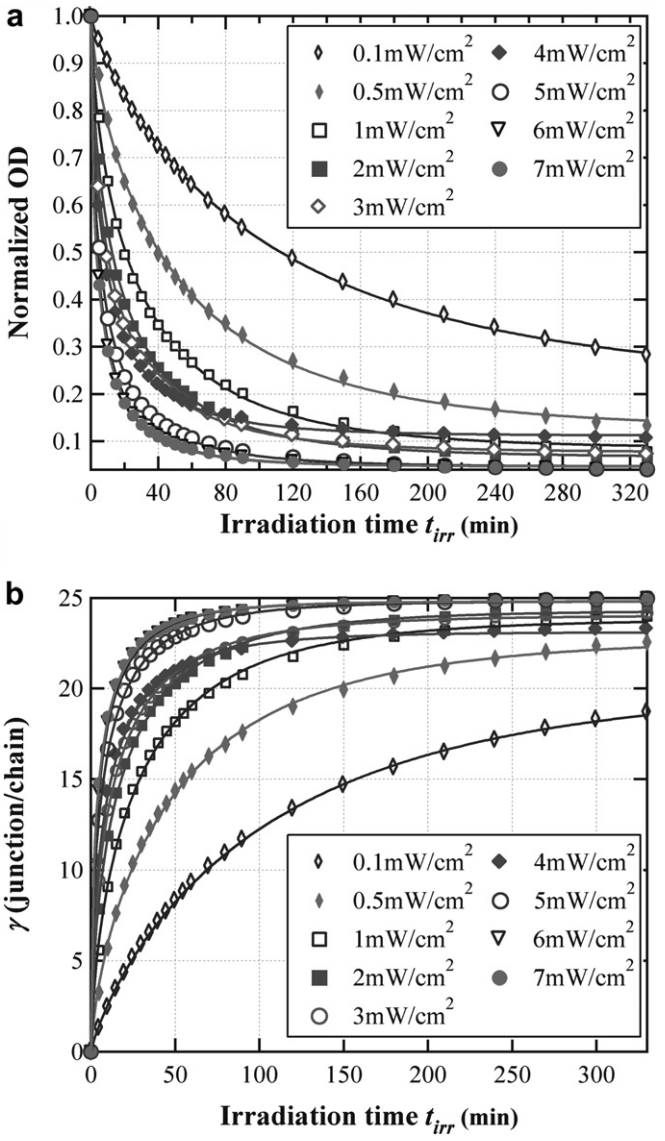

Fig. 2. Reaction kinetics observed for a PSA/PVME (30/70) under different irradiation intensities: (a), normalized absorbance OD; (b) cross-link density γ.

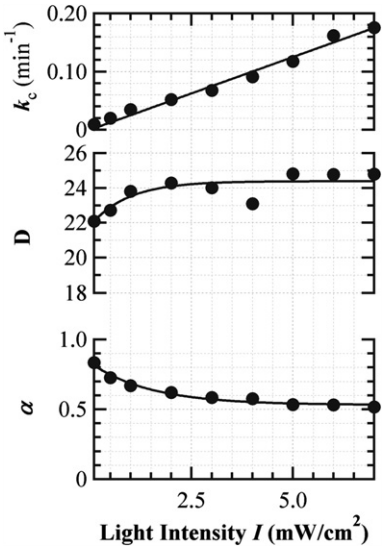

Fig. 3. Reaction kinetics parameters obtained for a PSA/PVME (30/70) blend under various irradiation intensities.

For low intensity, the cross-link reaction slightly deviates from the exponential function of irradiation time with the exponent $\alpha \approx 0.9$, whereas α decreases as the irradiation intensity increases, revealing an inhomogeneous growth associated with an increase in intensity. The effects of UV irradiation intensity on the deformation kinetics can be also seen later in the irradiation-induced strain observed at different light intensity. In general, chemical reactions in the bulk state of *homopolymer* do not proceed uniformly, i.e. indescribable by the mean-field kinetics, due to the local inhomogeneity of polymer (distribution of segmental free volumes) [17]. Since 1980's, this inhomogeneity has been analyzed using the Kohlrausch–Williams–Watts (KWW) stretched exponential kinetics in conjunction with glassification within the context of percolation transition [18]. For diffusion-controlled reactions in the bulk state of *homopolymers*, the KWW kinetics was used to analyze the experimental data [4]. For polymer *binary mixtures*, besides this segmental free volume distribution, additional inhomogeneity comes into play from the thermodynamic interactions between two polymers. This additional inhomogeneity might be expressed by the so-called square gradient theory [19]. Therefore, the inhomogeneity of reaction kinetics in polymer mixtures originated from the non-uniformity in both mobility and composition, whereas the inhomogeneity in homopolymer takes root from the non-uniform mobility. It should be noted that unlike the photodimerization of anthracene in homopolymer [15] where the dynamic inhomogeneity arises solely from the distribution of polymer segmental free volumes, additional inhomogeneity from the composition fluctuations would arise from thermodynamic interactions between the two components in the blend. Due to this additional interaction, the inhomogeneity associated with the glassification in polymer mixtures would be much greater compared to homopolymer systems.

The increase in inhomogeneity of the cross-link reaction upon increasing the light intensity can be attributed to greater rate of glassification of the blend under higher light intensity. Since the photodimerization of anthracene, a diffusion-controlled reaction, strongly depends on the environment viscosity [20], anthracene moieties far from each other in the reacting blend still can encounter and react until polymer segmental motions are frozen by glassification. Thus, the faster glassification generated by higher intensity would prevent the reaction between anthracene moieties which are far from each other during their excited lifetime, leading to an increase in inhomogeneity kinetics.

3.2. Effects of irradiation intensity on the deformation in situ observed by using a Mach–Zehnder interferometer

As described above, the strain associated with the irradiation process can be calculated from Eq. (6). The intensity dependence of the deformation ϵ observed with five different light intensities 1.0, 2.0, 3.0, 4.0 and 5.0 mW/cm^2 is illustrated in Fig. 4 for a PSA/PVME (30/70) blend at 21.5 °C over different irradiation time intervals. The negative value of ϵ indicates the systematical decrease in the optical path length with light intensity, and therefore in the thickness of the sample upon irradiation. It was found that similar to the cross-link kinetics, the dependence of the shrinkage of the blend on irradiation time can be fitted to the modified Kohlrausch–Williams–Watts (KWW) given in Eq. (10):

$$\epsilon(t_{\mathrm{irr}}) = E\left[1 - \exp(-k_d\, t_{\mathrm{irr}})^{\beta}\right] \tag{10}$$

where $\epsilon(t_{\mathrm{irr}})$ is the time-evolution of the elastic strain, E is the baseline expressing the limiting deformation; k_d is the deformation rate and β is the inhomogeneity index for the relaxation process of the elastic strain.

The kinetic parameters obtained for the deformation process, i.e. the average deformation rate k_d, the limiting deformation E, the equilibrium elastic strain and the inhomogeneity index β exhibit the dependence on the irradiation intensity similar to the case of cross-link. Namely, the average rate of deformation k_d increases with the light intensity, whereas the limiting deformation E and the inhomogeneity index β decrease with increasing the irradiation intensity and eventually seem to approach a constant value under high irradiation intensity as depicted in Fig. 5. It is worth noting that, as reported previously, for the case of homopolymer such as poly(ethyl acrylate) (PEA), the deformation kinetics observed by Mach–Zehnder interferometry during the photo-cross-linking process was well described by a single exponential function of irradiation time [15]. By combining the results obtained for homopolymers with the deformation kinetics observed for polymer blends shown in Fig. 4, these interferometric data suggest that the inhomogeneous kinetics of the deformation process in a binary mixture might reflect the inhomogeneity arising from the composition fluctuations in miscible binary mixtures. In other words, thermodynamic interactions between the two polymer components might contribute

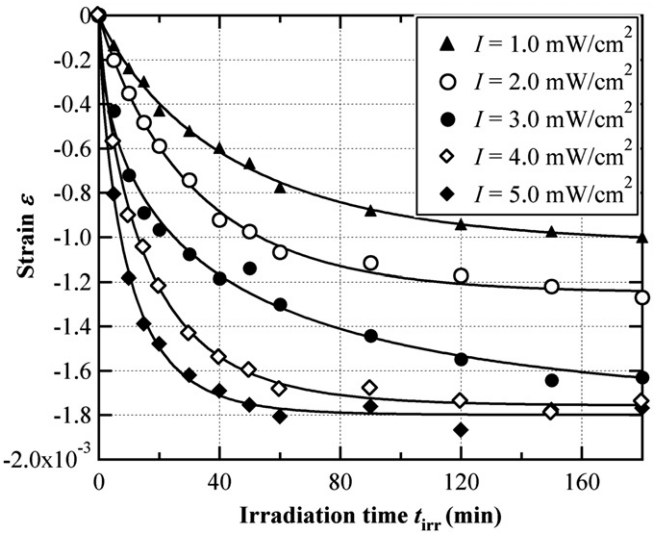

Fig. 4. Deformation kinetics observed at 21.5 °C for a PSA/PVME (30/70) blend under various irradiation intensities.

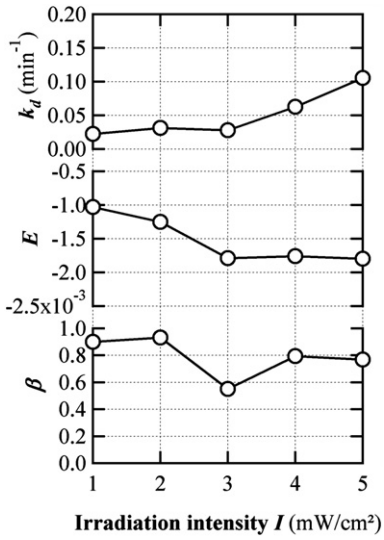

Fig. 5. Parameters of the deformation process observed for a PSA/PVME mixture under different irradiation intensities.

to the deviation of the deformation kinetics from the simple exponential relaxation. In general, compared to the characteristic length scales required for the photodimerization of anthracene, the length scales involving in the deformation kinetics of the blend might be larger, leading to different kinetics.

In order to verify the causality between the cross-link reaction and the deformation process in the photo-cross-linked PSA/PVME (30/70) blends, the mean rate of deformation k_d obtained by Mach–Zehnder interferometry is plotted versus the mean cross-link rate k_c measured by UV–vis spectroscopy in Fig. 6. A strong relationship was clearly observed within the range of the irradiation intensity, suggesting the causal relation between the cross-link process and the deformation kinetics observed *in situ* by Mach–Zehnder interferometer. To further investigate the correlation between the cross-link and the deformation processes of the PSA/PVME blend, the strain $\epsilon(t_{irr})$ defined in Eq. (6) was plotted versus the cross-link density $\gamma(t_{irr})$ in Fig. 7. Within the range of the UV intensity used in this work, a general tendency was observed for the cross-linked polymer: the elastic deformation ϵ increases with increasing γ, i.e. γ becomes more negative upon increasing γ. This general tendency can be more clearly seen in the reduced plot shown in Fig. 8 where the normalized strain defined as $\epsilon_r = (\epsilon/\epsilon_{max})$ was

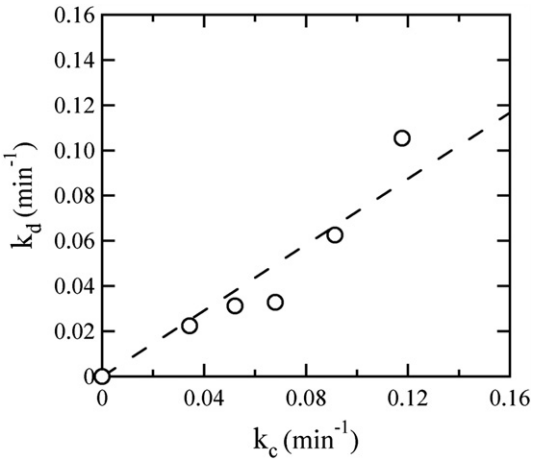

Fig. 6. Correlation between the rates of the cross-link reaction and the deformation process observed for a PSA/PVME (30/70) mixture at 21.5 °C.

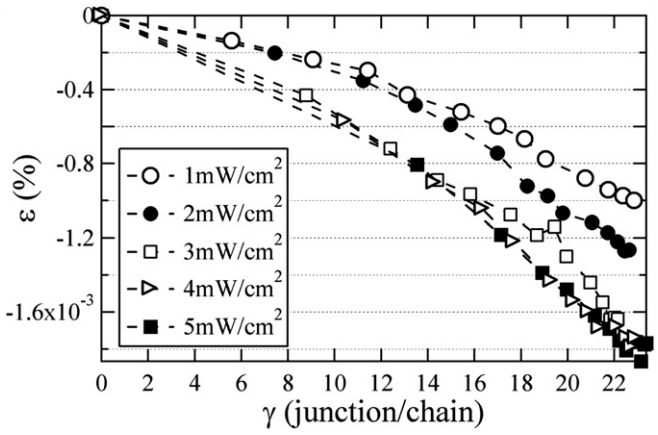

Fig. 7. Dependence of the elastic deformation on the cross-link density observed under various irradiation intensities for a PSA/PVME (30/70) mixture at 21.5 °C.

plotted versus the normalized cross-link density $\gamma_r = (\gamma/\gamma_{max})$ Here, γ_{max} and ϵ_{max} are taken respectively as the maximum magnitudes of cross-linked density and the elastic strain shown respectively in Figs. 2 and 4. These results suggest the existence of a general relation between the equilibrium deformation induced by irradiation and the cross-link density as observed respectively with Mach–Zehnder interferometer and UV–Vis photospectrometer.

3.3. Effects of the glass transition temperature on the deformation of polymer blends

Fig. 9 show two distinctly different behavior of the cross-link-induced strain observed during the course of irradiation for a PSA/PVME (30/70) blend photo-cross-linked respectively at 21.5 °C, i.e. $(T_g + 5°C)$ and at 25 °C, i.e. $(T_g + 8.5°C)$. Here, T_g indicates the glass transition temperature of the blend before irradiation. For the first 30 min of irradiation, the shrinkage revealed by an increase in the elastic strain ϵ was observed under both irradiation conditions. Furthermore, the rate of deformation is slightly larger for a PSA/PVME (30/70) blend irradiated at higher temperature. It was found that the blend cross-linked at 21.5 °C continuously shrinks during 180 min of irradiation, whereas the PSA/PVME (30/70) blend photo-cross-linked at a higher temperature (25.0 °C) exhibits a larger shrinkage in the first 30 min of irradiation and subsequently swells

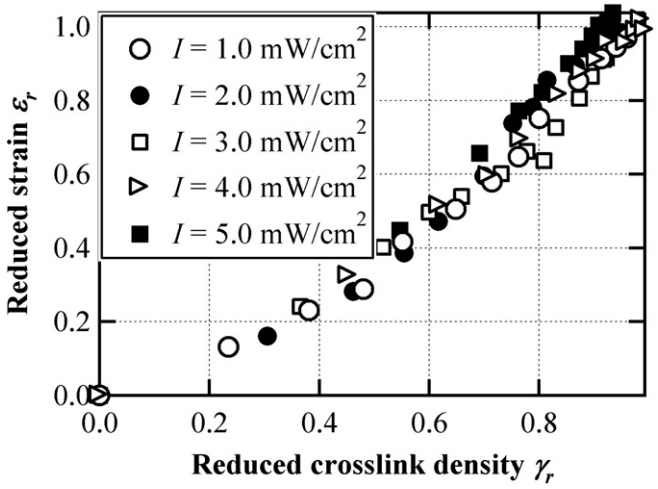

Fig. 8. Correlation between reduced strain ϵ_r ($\epsilon_r = \epsilon/\epsilon_{max}$) and reduced cross-link density γr ($\gamma_r = \gamma/\gamma_{max}$)obtained for a PSA/PVME (30/70) blend under different irradiation intensities.

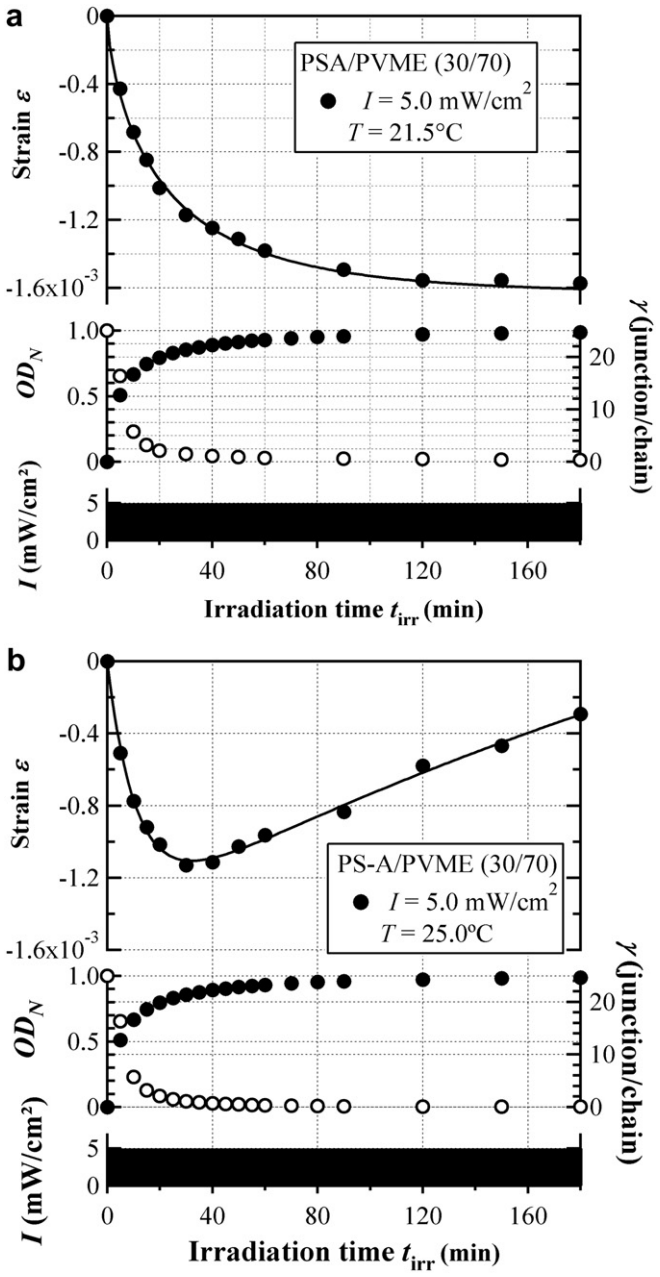

Fig. 9. Deformation observed for a PSA/PVME (30/70) blend at different temperatures: (a) 21.5 °C; (b) 25 °C. For comparison, the corresponding normalized optical density (○) and the corresponding cross-link density (●) were indicated in the same figures. The irradiation intensity I is 5.0 mW/cm^2.

back as revealed by a decrease in the elastic strain ϵ with irradiation time as shown in Fig. 9-b. For reference, the variation of the normalized absorbance of anthracene $OD_N(t_{irr})$ and the cross-link density $\gamma(t_{irr})$ of the blends monitored under these two irradiation conditions is depicted in the same figures.

In order to understand this deformation behavior, the glass transition temperature T_g of the blends irradiated in 30, 40 and 180 min was measured by dynamic mechanical analysis and are compared with the sample without irradiation. The irradiation time-dependence of the tan δ obtained at 1 Hz is shown in Fig. 10. From these results, it was found that as irradiation time increases, the peak of tan δ shifts to the high temperature side, revealing the increase in T_g of the blend with irradiation time. It should be noted that the data obtained for $t_{irr} = 40$ min were not shown in the figure because the difference with those obtained after $t_{irr} = 30$ min is not significant under the experimental conditions. The variation of the blend T_gs with irradiation time is illustrated in Fig. 11. On the other hand, the glass transition temperature T_g of the cross-linked blend determined from the peak of tan δ in DMA experiments was almost the same for the blends cross-linked at 21.5 °C and 25 °C, indicating that the effects of experimental temperature on T_g of the blends are not significant in this range of temperature. As expected, for shorter irradiation times 30 and 40 min, T_g are respectively 20.7 °C and 22.3 °C. Both T_gs obtained under these irradiation conditions are located below the experiment temperature of Fig. 9-b, i.e. 25 °C, whereas the experiment temperature of Fig. 9-a is sandwiched by these two T_gs. These data support the conclusion that the strain of the blend under irradiation is determined by the competition between the shrinking and swelling kinetics, resembling the kinetics of consecutive chemical reactions [21]. Actually, the irradiation-time dependence of the elastic strain shown in Fig. 9-b can be fitted to the difference between two exponential functions of irradiation time:

$$\epsilon(t_{irr}) = A_s \exp(-k_s t_{irr}) - A_r \exp(-k_r t_{irr}) + A_b \qquad (11)$$

where A_s and A_r are respectively the fraction of the shrinking and recovery processes. k_s, k_r are respectively the rate of the shrinking and recovery processes. A_b is the baseline, expressing the limiting strain as $t_{irr} \to \infty$. These kinetic parameters are given in the caption of Fig. 9.

Finally, the glass transition temperature T_g of this PSA/PVME(30/70) blend increases from 16.5 °C, before cross-link, to 26.3 °C after 180 min of irradiation with the UV intensity 5.0 mW/cm^2. The limiting value of the average cross-link density is $\gamma \approx 24$ junctions/chain calculated from the UV absorbance of the anthracene moieties. On the other hand, the tan δ of these cross-linked blends obtained after 180 min of irradiation reveals a broad peak with a maximum at 26.3 °C and a shoulder around −5 °C. Since the cross-linked blends are transparent after the experiments and particularly the cloud point of the blend is located at 109 °C which is very far away from the irradiation temperature, the double broad peaks of the tan δ depicted in Fig. 10 do not come from phase separation, but would instead reflect the "dynamic" inhomogeneity of the mixture. This feature originates from the large difference in mobility between the two miscible components, PVME and PSA/

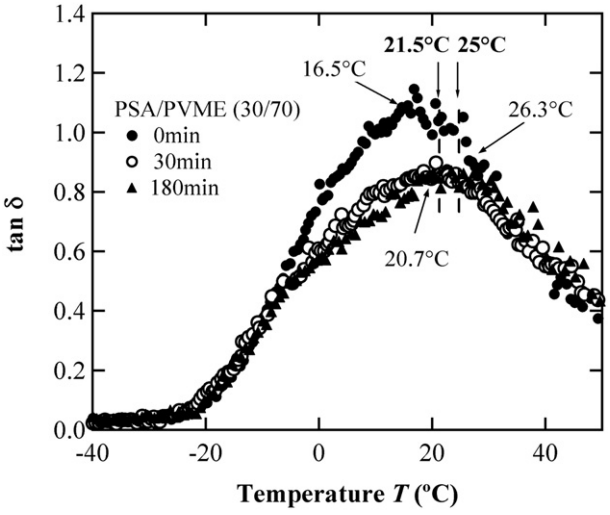

Fig. 10. The loss tan δ obtained by DMA at 1 Hz for a PSA/PVME (30/70) blend obtained before and after irradiation for 30 and 180 min with UV light (365 nm, 5.0 mW/cm^2). The corresponding T_gs are indicated in the figure. The experimental temperature was indicated by vertical arrow at the top.

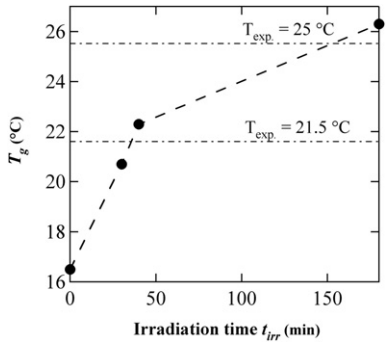

Fig. 11. Dependence of the glass transition temperature of a PSA/PVME (30/70) blend on irradiation time. The two irradiation temperatures are indicated by the dotted-dashed line.

cross-linked PSA. Such the behavior of tan δ was reported previously for binary miscible blends [22,23]. It is worth noting that the dynamic inhomogeneity phenomena have been observed in a number of miscible polymer mixtures and were extensively reviewed recently [24].

On the other hand, it is known that photodimerization of anthracene is controlled by viscosity of their environments [20]. Though the frequency range of segmental motions of the PSA component which could affect the cross-link reaction, is not clearly known [25], these dynamic mechanical data indicate that the experimental temperatures (21.5 and 25 °C) in the MZI experiments are located in between the glass transition temperatures of the blend *before* (16.5 °C) and *after* 180 min of irradiation (26.3 °C). In other words, as illustrated in Fig. 11, T_g of the blend is located below the experimental temperatures and the sample is in the rubber state before the irradiation cross-link process. During irradiation, T_g of the blend gradually increases and approaches the experimental temperature. As reported previously in recent experiments using MZI [14,15], depending upon the competitions between the cross-link reaction and the glassification, a reacting blend can exhibit three distinct behavior after irradiation is turned off: (1) swelling back when T_g of the cross-linked blend is still below the experimental temperature T_{exp}; (2) the blend continuously shrinks due to the physical aging process associated with the cross-link-induced glassification [15]; (3) for an intermediate cross-link density, the strain is apparently unchanged within the time scale of the observation. The experimental data illustrated in Fig. 9 reflect the kinetics of the deformation processes governed by the competition between the glassification and the elastic restoring processes of a sample under UV irradiation.

The experimental results described above demonstrate the capability of Mach–Zehnder interferometry not only in monitoring the glassification process of cross-linked polymers, but also in providing a tool to study the kinetics of glass transition and physical aging of polymers under photocuring. Furthermore, the information on the effects of polymer–polymer interactions (the Flory χ-parameter) on the shrinkage and the deformation kinetics would be important for materials processing using UV light in microlithography. These experiments are in progress and will be reported later.

4. Conclusions

By the combination of UV–vis spectroscopy and Mach–Zehnder interferometry (MZI), the kinetics of photo-cross-link and the subsequent deformation processes in an anthracene-labeled polystyrene/poly(vinyl methyl ether) (PSA/PVME) blend was *in situ* examined under various UV irradiation intensities The following results were obtained upon changing the UV light intensity.

1) The cross-link process can be well analyzed by using the modified Kohlrausch–Williams–Watts (KWW) kinetics, revealing the local inhomogeneity of the cross-link reaction in the mixture.
2) Deformation associated with the cross-link process *in situ* observed by MZI also exhibits the shrinkage which follows the modified Kohlrausch–Williams–Watts (KWW) function of irradiation time within the experimental time scales, suggesting the roles of composition fluctuations on the reaction kinetics in the polymer mixture. There exists a close correlation between the rate of cross-link and the rate of deformation. These results seem to reveal a general relation between the cross-link reaction and the resulting deformation.
3) The deformation kinetics is controlled by the glassification process of the sample, i.e. by the distance between the glass transition temperature T_g and the experimental temperature. This relative distance determines the swelling and shrinkage behavior of the cross-link blends.

Acknowledgement

The financial support from the Ministry of Education, Japan (MONKASHO) via the Scientific Research Type B (No. 20350107) and Research-on-Priority-Area Soft Matter Physics (No. 21015018) is greatly acknowledged. D.-T. V.-P. greatly appreciates the Scholarship from the Ministry of Education (MONKASHO), Japan to pursue the PhD program at Kyoto Institute of Technology, Japan.

References

[1] Haight R, Longo P, Wagner A. MRS Bulletin 2006;31:634–8. and other articles in this MRS Bulletin: Cahill DG, Yalisove SM. editors. Ultrafast lasers in materials Research, vol. 31.
[2] Cabrera M, Jezequel JY, Andre JC. Lasers in polymer science and technology: applications. Boca Raton. In: Fouassier JP, Rabek JF, editors. Florida: CRC Press, Inc; 1990. p. 73–95 [chapter 3].
[3] Tran-Cong-Miyata Q, Nakanishi H. Polymers, liquids and colloids in electric fields. In: Tsori Y, Steiner U, editors. New Jersey: World Scientific; 2009. p. 171–95 [chapter 6].
[4] Kataoka K, Harada A, Tamai T, Tran-Cong QJ. Polym Sci Polym Phys 1998;36:455–62.
[5] Nielsen LE, Landel RF. Mechanical properties of polymers and composites. 2nd ed. New York: Marcel Dekker Inc; 1994.
[6] Tran-Cong-Miyata Q, Nishigami S, Ito T, Komatsu S, Norisuye T. Nat Mater 2004;3:448–50.
[7] Tran-Cong-Miyata Q, Nishigami S, Yoshida S, Ito T, Ejiri K, Norisuye T. ACS Symposium Series. Nonlinear dynamics in polymeric systems, vol. 768. Washington DC: Am. Chem. Soc.; 2004. pp. 276–290 [chapter 22].
[8] Ishino S, Nakanishi H, Norisuye T, Awatsuji Y, Tran-Cong-Miyata Q. Macromol Rapid Commun 2006;27:758–62.
[9] Azzam RMA, Bashara NM. Ellipsometry and polarized light. North-Holland: Science; 1988.
[10] Tien PK. Appl Opt 1971;10:2395–413.
[11] Russell TP. Mater Sci Rep 1990;5:171–271.
[12] Poulsen HF, Wert JA, Neuefeind J, Honkimaki V, Daymond M. Nat Mater 2005;4:33–6.
[13] Robinson I, Harder R. Nat Mater 2009;8:291–8.
[14] Inoue K, Komatsu S, Trinh X-A, Norisuye T, Tran-Cong-Miyata QJ. Polym Sci Polym Phys 2005;43:2898–913.
[15] Van-Pham D-T, Sorioka K, Norisuye T, Tran-Cong-Miyata Q. Polym J 2009;41:260–5.
[16] Harada A, Tran-Cong Q. Macromolecules 1997;30:1643–50.
[17] Yu W-C, Sung CSP, Robertson RE. Macromolecules 1988;21:355–64.
[18] Cohen MH, Grest GS. Phys Rev B 1979;20:1077–98.
[19] Cahn JW, Hilliard JE. J Chem Phys 1958;28:258–67.
[20] Yoshizawa H, Ashikaga K, Yamamoto M, Tran-Cong Q. Polymer 1989;30:534–9.
[21] Atkins P, De Paula J. Physical chemistry. 8th ed. Oxford: Oxford University Press; 2006. pp. 811–18.
[22] Arbe A, Alegria A, Alberdi JM, Colmenero J, Hoffmann S, Willner L, et al. Macromolecules 1999;32:7572–81.
[23] Urakawa O, Fuse Y, Hori H, Tran-Cong Q, Yano O. Polymer 2001;42:765–73.
[24] Colmenero J, Arbe A. Soft Matter 2007;3:1474–85.
[25] Jarry JP, Monnerie L. Macromolecules 1979;12:927–32.

Polymer 52 (2011) 746–751

Contents lists available at ScienceDirect

Polymer

journal homepage: www.elsevier.com/locate/polymer

Macromolecular recognition by cyclodextrins. Interaction of cyclodextrins with poly(*N*-acryloyl-amino acids)

Wataru Oi [a], Akihito Hashidzume [a], Akira Harada [a,b,*]

[a] Department of Macromolecular Science, Graduate School of Science, Osaka University, 1-1 Machikaneyama-cho, Toyonaka, Osaka 560-0043, Japan
[b] Core Research for Evolutional Science and Technology (CREST), Japan Science and Technology Agency (JST), 5 Sanbancho, Chiyoda-ku, Tokyo 102-0075, Japan

ARTICLE INFO

Article history:
Received 24 September 2010
Received in revised form
4 December 2010
Accepted 14 December 2010
Available online 21 December 2010

Keywords:
Interaction
Cyclodextrins
Amino acids

ABSTRACT

The interactions of cyclodextrins (CDs) with poly(*N*-acryloyl-amino acids) (pAXaa) were investigated by ^{1}H NMR and two dimensional nuclear Overhauser effect spectroscopy (2D NOESY) to elucidate the effect of attachment of amino acid residues to the polymer chain. Using the ^{1}H NMR data measured at varying pAXaa concentrations, apparent association constants (*K*) were roughly estimated for the CDs/pAXaa systems. These apparent *K* values indicated that α-CD interacted with poly(*N*-acryloylphenylalanine) and with poly(*N*-acryloyltyrosine) and β-CD and γ-CD interacted with poly(*N*-acryloyltryptophan). Comparison of these apparent *K* values with those for the model compounds, i.e., amino acid sodium salts, revealed that the effect of attachment of amino acid residues to the polymer chain was stronger for a smaller amino acid residue.

1. Introduction

Living organisms maintain their living activities based on a number of chemical reactions, including syntheses of proteins, DNA, and ATP and digestion [1–3]. These biological chemical reactions proceed highly selectively in aqueous media under mild conditions (pH and temperature) and are thus environmentally benign and ideal. It may be important to understand and utilize the essences of chemical reactions in biological systems for realization of a sustainable society. Chemical reactions in biological systems start with the formation of well-defined supramolecular structures through the molecular recognition by biological macromolecules, such as proteins, nucleic acids, and polysaccharides. Thus, it is likely that macromolecular chains play crucial roles in the molecular recognition as well as the chemical reactions in biological systems. We have been thus working on the interaction of cyclodextrins (CDs) with water soluble polymers (WSPs) as model systems for biological macromolecular recognition [4–7].

Recent years have brought considerable interest in studying the interaction of CDs with WSPs from the viewpoint of environmentally benign applications based on aqueous systems. Most of the researches on the CD/WSP interaction have been focusing on control of solution properties of hydrophobically modified WSPs [8–28]. To the best of our knowledge, however, researches on the CD/WSP interaction have been scarce as model systems for biological molecular recognition apart from our researches. We reported several examples in which the selectivity of molecular recognition was enhanced or controlled by the steric effect of the polymer main chain [29,30], by multi-site interaction [31], and by competition with the interaction among side chains [32–34].

Recently, the solution properties of polymers of *N*-acryloyl-amino acids (pAXaa, Scheme 1) and their interaction with saccharides have been also investigated [35–37]. This is because pAXaa polymers, which carry an amino acid residue in each monomer unit, may have some relevancy to proteins although pAXaa polymers are acrylamide-based homopolymers, possess a carboxylic acid moiety per monomer unit, and have atactic structures unlike proteins. Since pAXaa polymers bear a variety of substituents, a series of pAXaa polymers allow ones to investigate the effect of the side chain on the macromolecular recognition. In this study, we have thus investigated the interaction of CDs with pAXaa mainly by NMR techniques to reveal the effect of attachment of amino acid residues to the polymer chain in macromolecular recognition.

2. Experimental

2.1. Materials

Cyclodextrins (α-CD, β-CD, and γ-CD) were purchased from Junsei Chemical and purified by recrystallization from water. Water

* Corresponding author. Department of Macromolecular Science, Graduate School of Science, Osaka University, 1-1 Machikaneyama-cho, Toyonaka, Osaka 560-0043, Japan. Tel./fax: +81 6850 5445.
E-mail address: harada@chem.sci.osaka-u.ac.jp (A. Harada).

0032-3861/$ – see front matter © 2010 Elsevier Ltd. All rights reserved.
doi:10.1016/j.polymer.2010.12.027

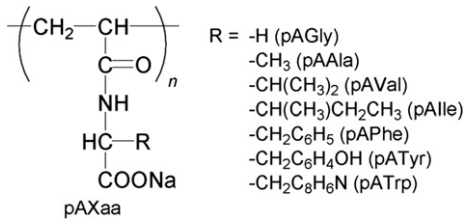

Scheme 1. Chemical structures of the polymers used in this study (pAXaa).

was purified with a Millipore Milli-Q system. The poly(*N*-acryloyl-amino acid) (pAXaa) samples were the same as those used in the previous studies [35–37]. Values of M_w and M_w/M_n for pAXaa were 1.5×10^4 to 9.7×10^4 and 1.3–2.8, respectively. All amino acids were purchased from Nacalai Tesque. Sodium salts of amino acids, used as model compounds in this study, were prepared by neutralization with an equimolar amount of NaOH and then recovered by freeze-drying.

2.2. Measurements

Sample solutions were prepared using D_2O. All the solutions were moderately basic (i.e., pD ~9). One dimensional ^{1}H NMR spectra were measured on a JEOL ECA 500 NMR spectrometer in D_2O at 30 °C. Two dimensional nuclear Overhauser effect spectroscopy (2D NOESY) data were recorded on a Varian UNITY INOVA plus 600 spectrometer at 30 °C. Mixing time before the acquisition of free induction decay was fixed at 150 or 200 ms to obtain a genuine NOE and to avoid the effect of spin diffusion.

3. Results

In the interaction of CDs with water soluble polymers, the conformation of polymer chains is sometimes critical because CD molecules are not accessible to the guest moieties if polymer chains take folded conformations through hydrophobic association of guest moieties [32,33]. Thus, it is important to describe the conformation of pAXaa polymers under the conditions used in the present study (i.e., in moderately basic media without added salt). A previous study demonstrated that pAVal and pAIle showed the same dependencies of hydrodynamic radius on the degree of polymerization as those for simple polyelectrolytes, e.g., poly(sodium 2-acrylamido-2-methyl-propane sulfonate) in 0.05 M NaCl at pH 10 [35]. More recently, the effect of the substituent effect on electrophoretic mobility of pAXaa polymers was investigated by capillary electrophoresis. It was demonstrated that the electrophoretic mobility was proportional to the cubic root of the hydrodynamic molar volume of the monomer unit, indicative of the free draining mechanism under the conditions for capillary electrophoresis (i.e., in 25 mM Borax at pH 9.3) [37]. On the basis of these reports, it is considered that the pAXaa polymers take similar expanded conformations independent on the amino acid residue under the present conditions.

The interactions of CDs with pAXaa polymers were investigated by ^{1}H NMR because the ^{1}H NMR technique does not require any chromophores. However, it was not possible to observe significant differences in broad ^{1}H NMR signals ascribed to the polymer-carrying amino acid residues in the absence and presence of CDs presumably because of weaker interaction and the limited solubility of CDs (especially for β-CD). Thus, ^{1}H NMR spectra were recorded at a constant CD concentration (1.0 mM) and varying concentrations of pAXaa. Fig. 1 shows partial ^{1}H NMR spectra for the C1 and C3 protons in CDs in the absence and presence of pAXaa (30 mM in the monomer unit). The spectrum in the presence of pAGly does not exhibit any shifts of the signals due to the C1 and C3 protons in α-CD, β-CD, or γ-CD (Fig. 1b), indicating that any CDs do not interact significantly with pAGly. In the case of pAAla, the spectrum for β-CD indicates only small shifts of the signals due to the C1 and C3 protons in the presence of the polymer whereas the spectra for α-CD and γ-CD do not (Fig. 1c). These spectra suggest that only β-CD interacts weakly with pAAla. The spectra for CDs in the presence of pAVal or pAIle show upfield shifted signals for the C1 and C3 protons (Fig. 1d and e), suggestive of the interaction of CDs with pAVal and with pAIle. The spectra in the presence of pAPhe, pATyr, and pATrp demonstrate larger upfield shifts of signals due to the C1 and C3 protons because of the effect of the ring current of aromatic amino acid residues in the polymer (Fig. 1f–h). Since pATrp possesses the largest aromatic rings (i.e., indolyl groups), it caused the largest upfield shifts among all the pAXaa polymers examined. These spectra are indicative of the considerable interaction of CDs with these three polymers bearing aromatic amino acid residues.

To compare the strengths of the interactions of CDs with pAXaa polymers, it is necessary to determine association constants (K). ^{1}H NMR for CDs were thus recorded at varying concentrations of pAXaa to estimate roughly apparent K values. Using these spectra, differences between the chemical shifts of the resonance bands due to the C1 and C3 protons were calculated to avoid an uncertainty in chemical shift values, and changes in the difference ($\Delta(\delta_{C1H} - \delta_{C3H})$) were plotted against the concentration of the monomer unit (c_m). Fig. 2 demonstrates a typical example of the CDs/pATrp systems. In the case of α-CD, $\Delta(\delta_{C1H} - \delta_{C3H})$ increases linearly with increasing c_m and the plots do not exhibit a tendency of saturation. In the cases of β-CD and γ-CD, on the other hand, $\Delta(\delta_{C1H} - \delta_{C3H})$ also increases with c_m and show a slight tendency of saturation. Given the formation of 1:1 inclusion complexes of CD and the monomer unit, apparent K values were estimated by fitting data in Fig. 2 using

$$\Delta(\delta_{C1H} - \delta_{C3H}) = aKc_m/(1 + Kc_m) \quad (1)$$

where a is a constant. The apparent K values estimated were $(2.3 \pm 0.6) \times 10^2$ and $(2.0 \pm 0.1) \times 10^1$ M^{-1} for β-CD and γ-CD, respectively, but it was not possible to estimate the apparent K value for α-CD, indicative of weak interaction.

Using the same manner, we attempted to estimate apparent K values for the CDs/pAXaa systems, in which significant shifts were observed in Fig. 1 (Table 1). In the cases of pAVal and pAIle, it was not possible to estimate apparent K values for any CDs because $\Delta(\delta_{C1H} - \delta_{C3H})$ values were very small or because no saturation tendency was observed (Figs. S1 and S2 in Supplementary data). In the cases of pAPhe and pATyr, apparent K values were estimated to be 8 ± 1 and $(1.9 \pm 0.7) \times 10^1$ M^{-1} for α-CD, respectively. However, it was unable to estimate apparent K values for β-CD and γ-CD because $\Delta(\delta_{C1H} - \delta_{C3H})$ values were very small or because no saturation tendency was observed (Figs. S3 and S4 in Supplementary data), although the shifts of the signals due to the C1 and C3 protons in CDs were significantly large. These observations indicate that only α-CD interacts significantly with pAPhe and with pATyr presumably because the sizes of β-CD and γ-CD cavities are slightly larger than those of the benzyl (pAPhe) and 4-hydroxybenzyl (pATyr) side chains. In the case of pATrp, apparent K values were estimated to be $(2.3 \pm 0.6) \times 10^2$ and $(2.0 \pm 0.1) \times 10^1$ M^{-1} for β-CD and γ-CD, respectively, but it was not possible to estimate the apparent K value for α-CD, as described above. This may be because the size of α-CD cavity is smaller than that of the 3-indolylmethyl side chain in pATrp.

The interactions of CDs with pAXaa polymers were confirmed by 2D NOESY NMR. Fig. 3 shows a typical example of 2D NOESY data for the CDs/pATrp systems. All the spectra show correlation signals

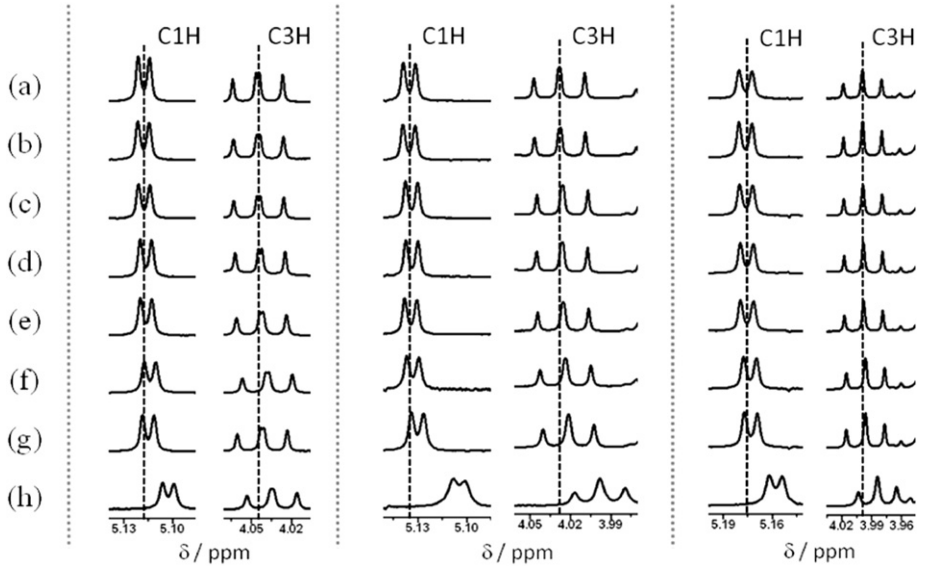

Fig. 1. ^{1}H NMR spectra for 1.0 mM α-CD (left), β-CD (center), and γ-CD (right) in the absence (a) and presence of pAXaa (30 mM in the monomer unit) in D_2O at 30 °C: pAGly (b), pAAla (c), pAVal (d), pAIle (e), pAPhe (f), pATyr (g), and pATrp (h).

between the signals ascribable to CD (3.7–4.0 ppm) and the signals ascribable to the indolyl group in pATrp (6.5–8.0 ppm), indicative of the interaction of CDs with Trp residues in pATrp. It is noteworthy that the correlation signals were clearly observed for the α-CD/pATrp system although it was not possible to estimate its apparent *K* value. These observations indicate that 2D NOESY NMR is a sensitive technique to investigate the interaction of CDs with water soluble polymers. As can be seen in Fig. S5 in Supplementary data, 2D NOESY data for the CDs/pAPhe systems also exhibited correlation signals ascribable to CD and the signals ascribable to the phenyl group in pAPhe (7.0–7.6 ppm). On the other hand, 2D NOESY data for the α-CD/pATyr and β-CD/pATyr systems indicated correlation signals between the signals ascribable to CD and the signals due to the 4-hydroxyphenyl groups (6.6–7.4 ppm), whereas the spectrum for the γ-CD/pATyr system did not exhibit significant correlation signals (Fig. S6 in Supplementary data). Furthermore, 2D NOESY data did not indicate significant correlation signals for the CDs/pAVal or CDs/pAIle systems (data not shown).

For the reference systems, the interactions of CDs with sodium salts of amino acids (Xaa), the corresponding pAXaa polymers of which indicated significant shifts of signals in ^{1}H NMR, were also investigated by ^{1}H NMR. Fig. 4 shows partial spectra for the signals of the C1 and C3 in CDs in the absence and presence of Xaa (30 mM). The spectra in the presence of Val and Ile exhibit slight upfield shifts of the signals due to the C1 and C3 protons for all the CDs examined, suggestive of the interaction of CDs with Val and with Ile. Similar to the cases of the corresponding polymers, the spectra in the presence of Phe, Tyr, and Trp demonstrate larger upfield shifts of the signals of the C1 and C3 protons, indicating that CDs interact considerably with these aromatic amino acids. To determine *K* values, ^{1}H NMR spectra were measured at a constant CD concentration (1.0 mM) and varying Xaa concentrations. Using these spectra, $\Delta(\delta_{C1H}-\delta_{C3H})$ values were also calculated and plotted against c_m, as can be seen in Fig. 5 (see also Figs. S7–S10 in Supplementary data). Values of *K* were determined by fitting data using Eq. (1), as listed in Table 2. These *K* values indicate that only β-CD interacts with Val and α-CD and β-CD interact with Ile. All the CDs examined interact significantly with aromatic amino acids, i.e., Phe, Tyr, and Trp.

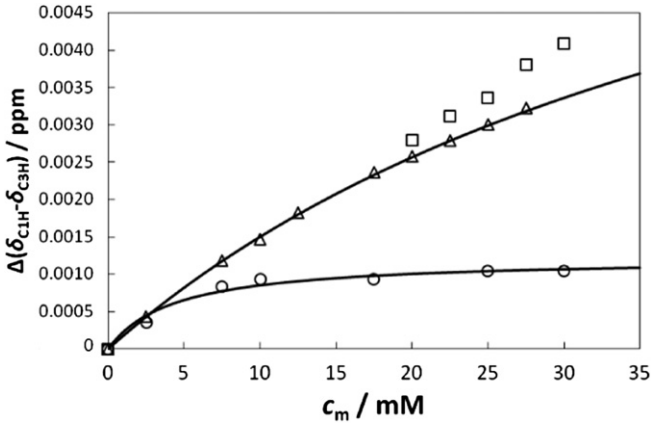

Fig. 2. $\Delta(\delta_{C1H}-\delta_{C3H})$ as a function of the concentration (c_m) of the monomer unit for the CDs/pATrp systems: α-CD (square), β-CD (circle), and γ-CD (triangle). The best fitted curves using Eq. (1) are also drawn.

4. Discussion

Here we compare the *K* values for the polymers with those for the model compounds to elucidate the effect of the attachment of amino acid residues onto the polymer chain, although it should be noted that the *K* values for the polymers are apparent ones because monomer units, i.e., binding sites, are extremely localized on the polymer chains in the interaction of CDs with the polymers. On the basis of *K* values in Tables 1 and 2, the amino acid residues can be

Table 1
Apparent association constants (*K*) for complex formation of CDs with pAXaa.

pAXaa	K/M^{-1}		
	α-CD	β-CD	γ-CD
pAVal	–[a]	–[a]	–[a]
pAIle	–[b]	–[b]	–[a]
pAPhe	8 ± 1	–[a]	–[a]
pATyr	$(1.9 \pm 0.7) \times 10^1$	–[b]	–[a]
pATrp	–[b]	$(2.3 \pm 0.6) \times 10^2$	$(2.0 \pm 0.1) \times 10^1$

[a] It was not possible to estimate the *K* value because of small shifts.
[b] It was not possible to estimate the *K* value because no saturation tendency was observed.

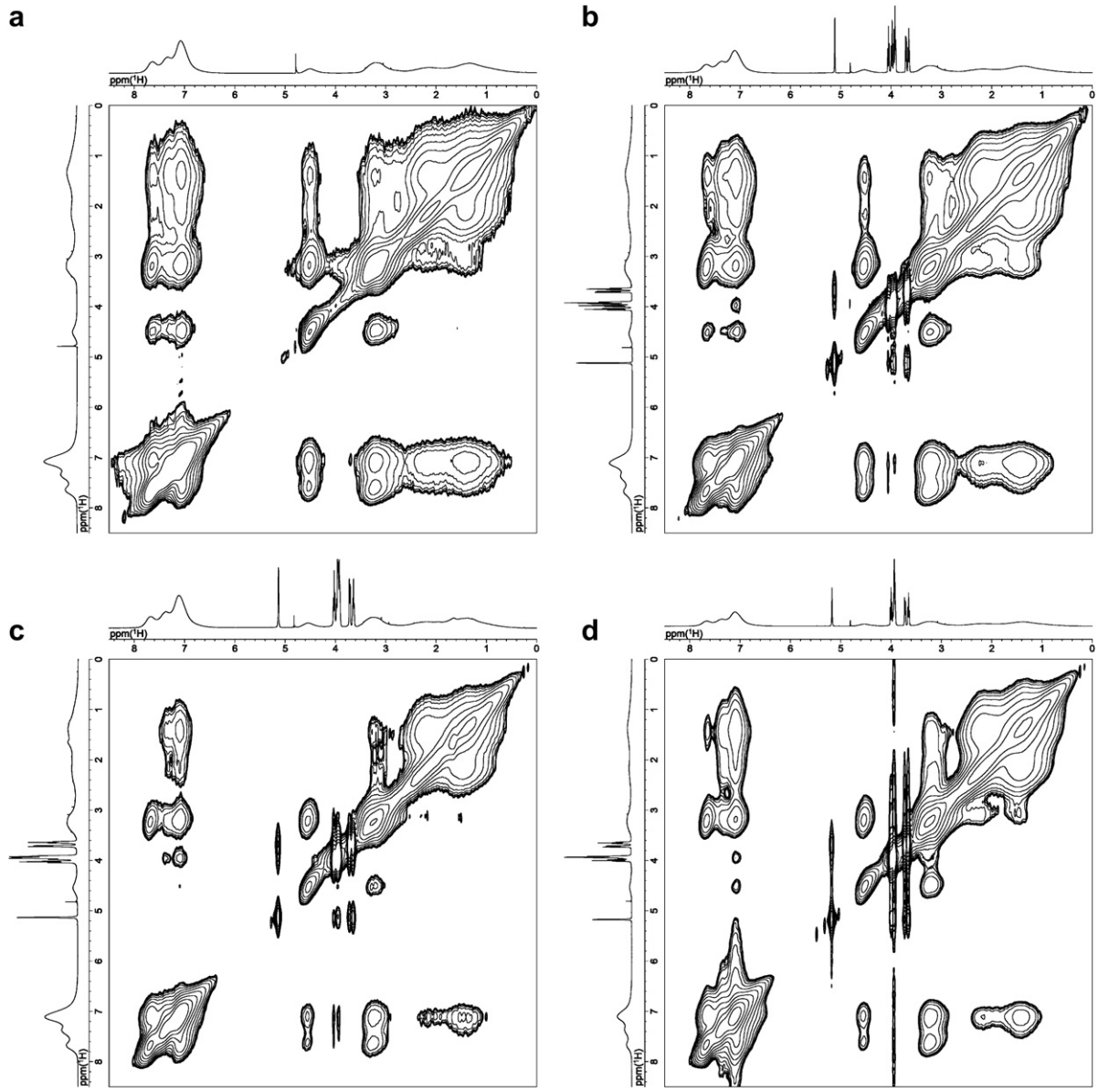

Fig. 3. 2D NOESY for pATrp (a), α-CD/pATrp (b), β-CD/pATrp (c), and γ-CD/pATrp (d), systems in D_2O at 30 °C.

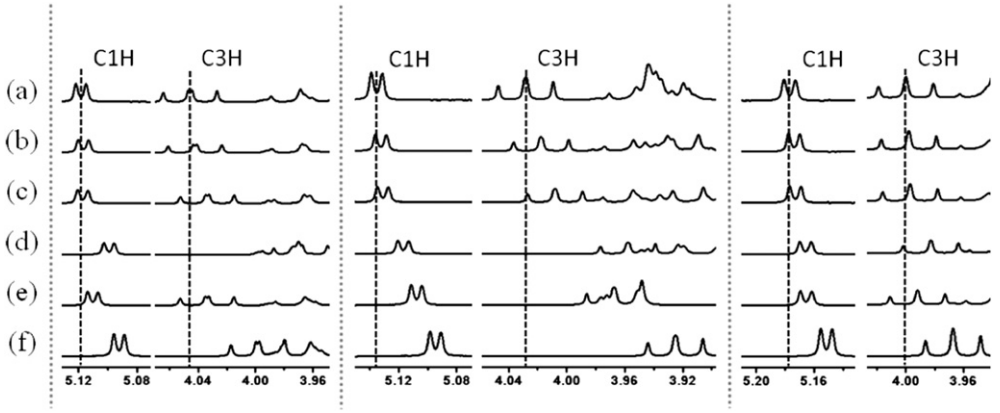

Fig. 4. ^{1}H NMR spectra for 1.0 mM α-CD (left), β-CD (center), and γ-CD (right) in the absence (a) and presence of Xaa (30 mM) in D_2O at 30 °C: Val (b), Ile (c), Phe (d), Tyr (e), and Trp (f).

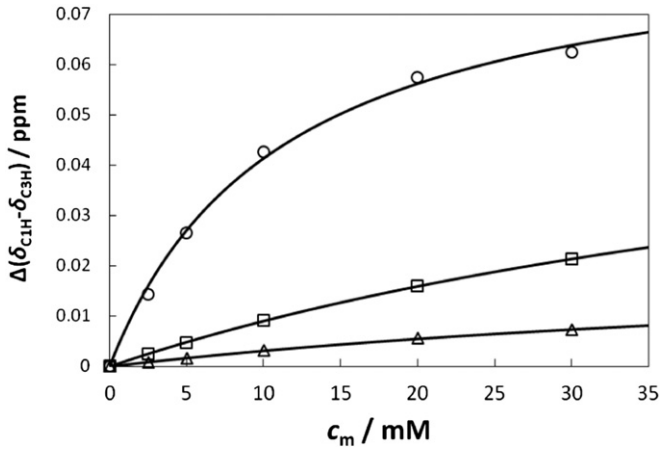

Fig. 5. $\Delta(\delta_{C1H} - \delta_{C3H})$ as a function of the concentration (c_m) of the model compound for the CDs/Trp systems: α-CD (square), β-CD (circle), and γ-CD (triangle). The best fitted curves using Eq. (1) are also drawn.

divided into three categories. Category I contains Val and Ile. The interactions of CDs with these amino acid residues could not be detected when they were bound to the polymer chain. Category II includes Phe and Tyr. When these residues were bound to the polymer chain, the interaction became significantly weaker compared to the interaction with the corresponding free amino acids, and showed a slightly enhanced selectivity for α-CD. Category III is Trp. When Trp was attached to the polymer chains the interaction did not changed so much and exhibited slightly increased selectivities for β-CD and γ-CD. It should be noted here that the molar volumes of amino acid residues of Categories I, II, and III are smaller (90.8–107.5 $cm^3\,mol^{-1}$), middle (121.2–123.1 $cm^3\,mol^{-1}$), and larger (143.9 $cm^3\,mol^{-1}$), respectively [38]. These observations indicate that when amino acid residues of a smaller molar volume are bound to the polymer chain, the interaction of CDs will become weaker compared to the interaction with the corresponding free amino acid.

When guest moieties are bound to the polymer chain, the effects of the polymer chains on the interaction of CDs with the guest moieties may include the effect of localized binding sites, the steric effect of the polymer main chain and neighboring side chains, and noncovalent bonds of CDs with neighboring side chains. The steric effect may hinder the interaction, whereas the effect of localized binding sites and the noncovalent bonds may assist the interaction. It is considered that the pAXaa polymers used in this study take almost the same conformation independent of the amino acid residue. Thus, the effect of localized binding sites and the steric effect of the polymer main chain may be virtually the same for all the pAXaa polymers and the steric effect of neighboring side chains may correspond to the molar volume of amino acid residues [37]. Since the interactions are reduced for most of all the systems examined in this study (other than the β-CD/pATrp and γ-CD/pATrp systems), the dominant effect of the polymer chain may be steric hindrance in the present CDs/pAXaa systems. The apparent K values for the β-CD/pATrp and γ-CD/pATrp systems are indicative of the effect of localized binding sites and noncovalent bonds between CD molecules and neighboring side chains.

Table 2
Association constants (K) for complex formation of CDs with Xaa.

Xaa	K/M^{-1}		
	α-CD	β-CD	γ-CD
Val	–[a]	7 ± 4	–[b]
Ile	$(2.60 \pm 0.08) \times 10^2$	9 ± 1	–[b]
Phe	$(1.9 \pm 0.2) \times 10^1$	$(8.8 \pm 0.4) \times 10^1$	3 ± 2
Tyr	$(5 \pm 2) \times 10^1$	$(1.40 \pm 0.05) \times 10^2$	$(2.8 \pm 0.8) \times 10^1$
Trp	$(1.5 \pm 0.1) \times 10^1$	$(8.9 \pm 0.9) \times 10^1$	$(1.6 \pm 0.3) \times 10^1$

[a] It was not possible to estimate the K value because no saturation tendency was observed.
[b] It was not possible to estimate the K value because of the formation of higher-order complexes.

Previously, we investigated the interaction of CDs with polyacrylamide-carrying alkyl groups by ^{1}H NMR and demonstrated the selectivities of CDs enhanced by the steric effect of the polymer main chain [29]. α-CD interacted with polymer-carrying *n*-butyl group ($K = 5.5 \times 10^1\ M^{-1}$) and did not with polymer-carrying *tert*-butyl group whereas β-CD interacted with polymer-carrying *tert*-butyl group ($K = 3.4 \times 10^2\ M^{-1}$) and did not with polymer-carrying *n*-butyl group. On the other hand, α-CD interacted with both the corresponding model compounds, i.e., *n*-butyl and *tert*-butyl alcohols, with K values of 2.0×10^1 and $6\ M^{-1}$, respectively. In the cases of polymer-carrying isooctyl and dodecyl groups, however, such an enhanced selectivity was not observed. These observations indicate that the steric effect of the polymer main chain is stronger for a smaller guest moiety bound to the polymer chain.

We also investigated the interaction of CDs with poly(*N*-methacryloyltryprophan) (pMTrp) and with poly(*N*-methacryloylphenylalanine) (pMPhe) and reported that CDs interacted with pMTrp but did not interact significantly with pMPhe [30]. Since Phe residue is smaller than Trp residue, Phe residue is dependent more strongly on the steric effect of the polymer main chain as well as neighboring side chains. It should be noted that the interaction of pMTrp with CDs exhibited broadening of ^{1}H NMR signals of CDs but did not indicate any shifts of CD signals, whereas the interaction of CDs with pATrp (and other pAXaa polymers) exhibited shifts of ^{1}H NMR signals of CDs but did not indicate significant broadening. These observations indicate that α-methyl groups have some significant effects, e.g., α-methyl groups may increase the syndiotacticity of the polymers obtained, may make the polymer chain more rigid, and may increase the hydrophobicity of microenvironment around guest moieties. At present we do not have any further evidences for what makes the differences in the interaction of CDs with pATrp and with pMTrp.

More recently, we have investigated the interaction of CDs with human and bovine serum albumins (HSA and BSA, respectively) by several characterization techniques, including steady state fluorescence, 2D NOESY NMR, and circular dichroism spectroscopy, to extend our study to the interaction of CDs with proteins [39]. The noteworthy is that α-CD and β-CD interacted with HSA but not with BSA although HSA and BSA show a high (ca. 76%) sequence homology. Characterization data indicated that α-CD and β-CD interacted with Phe and/or Tyr residues exposed on the surface of HSA. It is thus concluded that α-CD and β-CD discriminate subtle differences in neighboring amino acid residues around the Phe and Tyr residues. It is likely that the compactness of benzyl and 4-hydroxybenzyl groups is responsible for the strict discrimination by α-CD and β-CD.

Proteins (i.e., enzymes) catalyze a larger part of chemical reactions in biological systems. Proteins are made of ca. 20 types of amino acids of relatively small side chains [1–3]. A number of researches on molecular recognition using synthetic water soluble polymers indicate longer or bulky side chains are useful for strong interactions [8–28]. However, the smaller side chains, which are sensitive to their microenvironments, may be necessary for biological molecular recognition that requires responses to small variations of microenvironments.

5. Conclusion

The interactions of CDs with pAXaa were investigated by ^{1}H NMR and 2D NOESY to elucidate the effect of attachment of amino acid residues to the polymer chain. Using the ^{1}H NMR data measured at varying pAXaa concentrations, apparent association constants (K)

were roughly estimated. These apparent K values indicated that α-CD interacted with pAPhe ($K = 8 \pm 1\ M^{-1}$) and with pATyr {$K = (1.9 \pm 0.7) \times 10^1\ M^{-1}$} and β-CD and γ-CD interacted with pATrp {$K = (2.3 \pm 0.6) \times 10^2$ and $(2.0 \pm 0.1) \times 10^1\ M^{-1}$, respectively}. As reference systems, K values were also estimated for the CDs/Xaa systems by ^{1}H NMR. These K values indicate that only β-CD interacts with Val and α-CD and β-CD interact with Ile. All the CDs examined interact significantly with aromatic amino acids, i.e., Phe, Tyr, and Trp. Comparison of these K values for the CDs/pAXaa and CDs/Xaa systems indicated that when amino acid residues of a smaller molar volume are bound to the polymer chain, the interaction of CDs will become weaker compared to the interaction with the corresponding free amino acid.

Acknowledgements

The authors would like to express their acknowledgment to Mr. Seiji Adachi, Department of Chemistry, Graduate School of Science, Osaka University, for NOESY measurements. This research is supported in part by the CREST program of the JST.

Appendix. Supplementary data

Supplementary data associated with this article can be found in the online version, at doi:10.1016/j.polymer.2010.12.027.

References

[1] Voet D, Voet JG. Biochemistry. 3rd ed. New York: Wiley & Sons; 2004.
[2] Berg JM, Tymoczko JL, Stryer L. Biochemistry. 6th ed. New York: W.H. Freeman; 2007.
[3] Alberts B, Johnson A, Lewis J, Raff M, Roberts K, Walter P. Molecular biology of the cell. 5th ed. New York: Garland Publishing Inc.; 2008.
[4] Hashidzume A, Tomatsu I, Harada A. Polymer 2006;47:6011–27.
[5] Harada A, Hashidzume A, Takashima Y. Adv Polym Sci 2006;201:1–43.
[6] Harada A, Hashidzume A, Yamaguchi H, Takashima Y. Chem Rev (Washington, DC, US) 2009;109:5974–6023.
[7] Harada A, Hashidzume A. Aust J Chem 2010;63:599–610.
[8] Akiyoshi K, Sasaki Y, Kuroda K, Sunamoto J. Chem Lett 1998;27:93–4.
[9] Islam MF, Jenkins RD, Bassett DR, Lau W, Ou-Yang HD. Macromolecules 2000;33:2480–5.
[10] Ritter H, Sadowski O, Tepper E. Angew Chem Int Ed 2003;42:3171–3.
[11] Kretschmann O, Choi SW, Miyauchi M, Tomatsu I, Harada A, Ritter H. Angew Chem Int Ed 2006;45:4361–5.
[12] Kretschmann O, Steffens C, Ritter H. Angew Chem Int Ed 2007;46:2708–11.
[13] Koopmans C, Ritter H. J Am Chem Soc 2007;129:3502–3.
[14] Zheng P, Hu X, Zhao X, Li L, Tam KC, Gan LH. Macromol Rapid Commun 2004;25:678–82.
[15] Hu X, Zheng PJ, Zhao XY, Li L, Tam KC, Gan LH. Polymer 2004;45:6219–25.
[16] Zheng PJ, Wang C, Hu X, Tam KC, Li L. Macromolecules 2005;38:2859–64.
[17] Galant C, Kjøniksen A-L, Nguyen GTM, Knudsen KD, Nyström B. J Phys Chem B 2006;110:190–5.
[18] Beheshti N, Bu H, Zhu K, Kojniksen A-L, Knudsen KD, Pamies R, et al. J Phys Chem B 2006;110:6601–8.
[19] Guo X, Abdala AA, May BL, Lincoln SF, Khan SA, Prud'homme RK. Macromolecules 2005;38:3037–40.
[20] Guo X, Abdala AA, May BL, Lincoln SF, Khan SA, Prud'homme RK. Polymer 2006;47:2976–83.
[21] Li L, Guo X, Fu L, Prud'homme RK, Lincoln SF. Langmuir 2008;24:8290–6.
[22] Li L, Guo X, Wang J, Liu P, Prud'homme RK, May BL, et al. Macromolecules 2008;41:8677–81.
[23] Guo X, Wang J, Li L, Pham D-T, Clements P, Lincoln SF, et al. Macromol Rapid Commun 2010;31:300–4.
[24] Takashima Y, Nakayama T, Miyauchi M, Kawaguchi Y, Yamaguchi H, Harada A. Chem Lett 2004;33:890–1.
[25] Tomatsu I, Hashidzume A, Harada A. Macromol Rapid Commun 2005;26:825–9.
[26] Tomatsu I, Hashidzume A, Harada A. Macromolecules 2005;38:5223–7.
[27] Tomatsu I, Hashidzume A, Harada A. Macromol Rapid Commun 2006;27:238–41.
[28] Tomatsu I, Hashidzume A, Harada A. J Am Chem Soc 2006;128:2226–7.
[29] Harada A, Adachi H, Kawaguchi Y, Kamachi M. Macromolecules 1997;30:5181–2.
[30] Hashidzume A, Harada A. Polymer 2006;47:3448–54.
[31] Hashidzume A, Ito F, Tomatsu I, Harada A. Macromol Rapid Commun 2005;26:1151–4.
[32] Taura D, Hashidzume A, Harada A. Macromol Rapid Commun 2007;28:2306–10.
[33] Taura D, Hashidzume A, Okumura Y, Harada A. Macromolecules 2008;41:3640–5.
[34] Taura D, Taniguchi Y, Hashidzume A, Harada A. Macromol Rapid Commun 2009;30:1741–4.
[35] Kawata T, Hashidzume A, Sato T. Macromolecules 2007;40:1174–80.
[36] Hashidzume A, Tanaka A, Sato T. Polymer 2010;51:18–21.
[37] Hashidzume A, Kawata T, Tanaka A, Takabayashi Y, Sato T. J Chromatogr A 2010;1217:2990–2.
[38] Zamyatnin AA. Annu Rev Biophys Bioeng 1984;13:145–65.
[39] Oi W, Isobe M, Hashidzume A, Harada A. Macromol Rapid Commun, in press, doi:10.1002/marc.201000699.

Polymer 52 (2011) 752–759

Contents lists available at ScienceDirect

Polymer

journal homepage: www.elsevier.com/locate/polymer

Thermal and mechanical properties of microcellular thermoplastic SBS/PS/SBR blend: effect of crosslinking

Ruey-Sheng Shih [a,b], Shiao-Wei Kuo [c], Feng-Chih Chang [b,*]

[a] Microcell Composite Company, Tainan 717, Taiwan
[b] Institute of Applied Chemistry, National Chiao Tung University, Hsinchu 300, Taiwan
[c] Department of Materials and Optoelectronic Science, Center for Nanoscience and Nanotechnology, National Sun Yat-Sen University, Kaohsiung 804, Taiwan

ARTICLE INFO

Article history:
Received 29 June 2010
Received in revised form
30 November 2010
Accepted 14 December 2010
Available online 21 December 2010

Keywords:
SBS
SBR
Crosslinking

ABSTRACT

This study investigates the effect of peroxide crosslinking on the structure and mechanical properties for SBS/PS/SBR foams composed of polystyrene (PS), poly(styrene-*b*-butadiene) diblock copolymer (SBR-1502), and poly(styrene-*b*-butadiene-*b*-styrene) triblock copolymer (SBS). The cell size and its distribution of SBS/PS/SBR foams were investigated by SEM images, showing the smaller and denser of hollow cells for the SBS/PS/SBR foam containing the higher concentration of DCP (dicumyl peroxide). As expected, the density of the SBS/PS/SBR foams increases with increasing the content of DCP. The high density of polymeric foams exhibits the high mechanical properties such as hardness, shrinkage, tensile strength, tear strength, elongation at break, and compression set.

1. Introduction

Synthetic foams are composite materials prepared by filling a metal, polymer or ceramic matrix with hollow particles named microballoons or cells [1]. Foam polymers are two-phase gas–solid materials in which the solid polymer is continuous and gaseous cells are dispersed throughout the macromolecular support. They are important items in the economy because of technical, commercial and environmental issues; they represent an interesting dynamic in the twenty-first century society. These foams with hollow particles dispersed in the network matrix meet the need of practical commodities such as light weight, high toughness, excellent elasticity, and good resistance to thermal conductivity and acoustic reflection. With these unique properties, synthetic foams are widely applied in aircraft insulator, automotive parts, buildings fillers, packaging materials, electrical and household goods and so on. For example, refrigerator doors are filled with polyurethane (PU) foams to maintain the interior temperature for reduction in electricity consumption and sport shoes are assembled with poly(styrene-*b*-butadiene-*b*-styrene) (SBS) foams as shoe soles to cushion (shock absorption) in order to protect the heel from impact forces and enhance the athlete's performance [2]. Noticeably, polymer-supported foams account for a large number of application markets because of low-cost raw materials and easy processing of shape [3].

PU became important in the late 60s despite a complex fabrication process because they provided lower weight, greater comfort, and higher rebound resilience (elastic recovery). Thermoplastic rubbers (TPR) based on oil extended SBS were introduced in the 70s. They could be fabricated into shoe soles more easily than rubber with only minimal loss in performance. SBS is a synthetic rubber copolymer consisting of three segments of two polystyrene (PS) and one polybutadiene (PB). Due to the thermodynamic disfavor between two distinct compositions, the PS segments would self-assemble into separate microphases of PS aggregation in the PB matrix by distributing covalent bonds between PS and PB segments on the boundary of microdomains [4]. The confinement of two end groups of a PB chain on the surface of the PS hard domains can not only retard its deformation (a disentanglement process) under an external stress but also help to revert to its original size (an entanglement process) when the external stress is removed, showing the elasticity of an SBS rubber. This elastic property is very important for SBS foams because the growth of hollow gas cells in the SBS body can be restricted within a confined space (close cells) by the extended SBS networks when gas is released from the blowing agents. As well as physical additives such as CO_2, the blowing agents can be chemical additives such as azodicarbonamide (AC), decomposing to N_2, CO, and CO_2 at high temperatures (>120 °C). The latter is more expansive but has

* Corresponding author. Tel./fax: +886 3 5131512.
E-mail address: changfc@mail.nctu.edu.tw (F.-C. Chang).

0032-3861/$ – see front matter © 2010 Elsevier Ltd. All rights reserved.
doi:10.1016/j.polymer.2010.12.026

a brilliant performance on "a micellular closed foam" with the diameter of isolated cells smaller than 10 μm, probably due to the uniformly release of gas by controlling reaction temperatures [5]. Therefore, the addition of chemical blowing agents dominates the density of an SBS foam, playing an important role on the mechanical properties. However, the gas in close cells sometimes dissipates under frequent impact resulting in a so-called fatigue behavior, the progressive and localized structural damage that occurs when SBS foam is subjected to cycling loading due to the packing of polymer chains are not as dense as metals or glass, especially for those with low glass transition temperatures such as PB. This is the reason why a small number of crosslinking agents such as dicumyl peroxide (DCP) in this study are added to the SBS foams for the improvement of mechanical properties [6]. Prior to the blowing agent AC, the relatively labile DCP with the half-life temperature in dodecane at 117 °C for 10 h would decompose to two cumyloxyl radicals initiating the vinyl crosslinking reaction of PB domains [7].

In this study, we prepared six SBS foams with different densities by adjusting the compositions of AC and DCP, listed in Table 1. Instead of synthesizing new SBS copolymers with different compositions, the SBS copolymer containing 40 wt % PS was modified by blending with PS homopolymer and poly(styrene-*b*-butadiene) (SBR) diblock copolymer containing 23.5 wt % PS [8]. PS homopolymer was used to expand the size of PS domains and SBR copolymers can connect PS domains with these PB chains bearing a free end groups, making PB domains more flexible [9,10a,8a,8b]. Besides, the silicon dioxide (SiO_2) nanoparticles are also important trace additives for the heterogeneous growth of separated microballoons from these fine particles [11]. $CaCO_3$ is one of the inorganic additives that are widely used for plastics. We can make low priced and strong plastics by adding $CaCO_3$. Others such as pentaerythritol tertkis(3,5-di-*tert*-butyl-4-hydroxyhydrocinnamte) (PT) and white oil are used as antioxidant and processing oil. To give the homogeneous size distributions of gas cells from the inside out, the pressure loading between two hot plates, i.e., a compression mold coupled with a temperature control, is employed to control the expansion of gas cell [12]. The mechanical response of polymer foams depends on their architecture, and on the intrinsic properties of the materials in the cell wall [3b,3c]. Herein, the morphologies of microstructures such as the cell wall thickness, the size distribution and the shape of the cells are characterized by scanning electron microscopy (SEM). Thermal properties such as thermal stability can be measured by thermal gravity analyzer (TGA). In addition, dynamic mechanical properties such as elastic or loss modulus were characterized by dynamic mechanical analyzer (DMA) with a compression mode. Other properties are listed and discussed, including density, hardness, shrinkage, tensile strength, tear strength, elongation and compression set.

2. Experimental

2.1. Materials

Poly(styrene-*b*-butadiene-*b*-styrene) (SBS, KIBITON TPE PB-575, 33 wt % of oil content), polystyrene (PS, PS-336T), and poly(styrene-butadiene) copolymer (SBR-1502) are purchased from Chi Mei, En Chuan Chemical Industries, and TSRC Co., Ltd. in Taiwan, respectively. Pentaerythritol tetrakis(3,5-di-*tert*-butyl-4-hydroxyhydrocinnamate) (PT, 1010), silicon oxide (SiO_2, H-255 LD), white oil (WO, PW-150) are purchased from Sumitomo Chemical, PPG Industries, and Ever Light Ban Hon Co., Ltd., respectively. Azodicarbonamide (AC) and dicumyl peroxide (DCP) are purchased from Chemical Co., Ltd.

2.2. Preparation

The most significant mechanical property of an SBS foam is cushioning because the gas in the close cells can be compressed so as to absorb a shock from a transient impact and meanwhile, the extended SBS networks can get relaxed (Scheme 1) [13]. After the stress is released, the gas would dilated and then, be restricted within the extended SBS networks. The method of fabrication of SBS/PS/SBR foam samples involves five stages: (i) blending all compositions in a kneader and a two-roll mill at 120 °C according to the weight ratios listed in Table 1, (ii) making a sheet through a two-roll device, (iii) cutting it into pieces with a proper size, (iv) stacking a compression mold with a given quantity of them, (v) foaming under pressure of 120 kg/cm^2 at 160 °C for 20 min.

2.3. Characterization

A TA Instruments thermogravimetric analyzer, operated at a scan rate of 20 °C/min over temperatures ranging from 30 to 800 °C under a N_2 purge of 40 mL/min, was used to record TGA thermograms of samples on a Pt holder. Herein, sample is sandwiched between a flexed plate and a plate mounted on the drive shaft and compression stress is applied by the motor. The cylindrical compressive specimens were cut to diameter of 8.0 ± 0.05 mm and thickness of 2.5 ± 0.05 mm, and the rectangular tensile

Table 1
Compositions of SBS/PS/SBR polymer foam.

Samples	Compositions by phr[a]										
	Resins				Additives						
	SBS[b]	PS[c]	SBR-1502[d]	Total	PT[e]	SiO_2[f]	WO[g]	AC[h]	DCP[i]	$CaCO_3$	Total
I	86.4	8	5.6	100	0.3	1.3	3.2	4.66	0	36	45.46
II	86.4	8	5.6	100	0.3	1.3	3.2	4.66	0.1	36	45.56
III	86.4	8	5.6	100	0.3	1.3	3.2	4.66	0.12	36	45.58
IV	86.4	8	5.6	100	0.3	1.3	3.2	4.66	0.15	36	45.61
V	86.4	8	5.6	100	0.3	1.3	3.2	4.66	0.18	36	45.64
VI	86.4	8	5.6	100	0.3	1.3	3.2	4.66	0.2	36	45.66

[a] Parts per hundreds of resins (by weights).
[b] Poly(styrene-butadiene-styrene) triblock copolymer containing 40 wt % polystyrene block.
[c] Polystyrene.
[d] Poly(styrene-butadiene) diblock copolymer containing 23.5 wt % polystyrene block.
[e] Pentaerythritol tetrakis(3,5-di-*tert*-butyl-4-hydroxyhydrocinnamate).
[f] Silicon oxide.
[g] White oil.
[h] Azodicarbonamide.
[i] Dicumyl peroxide.

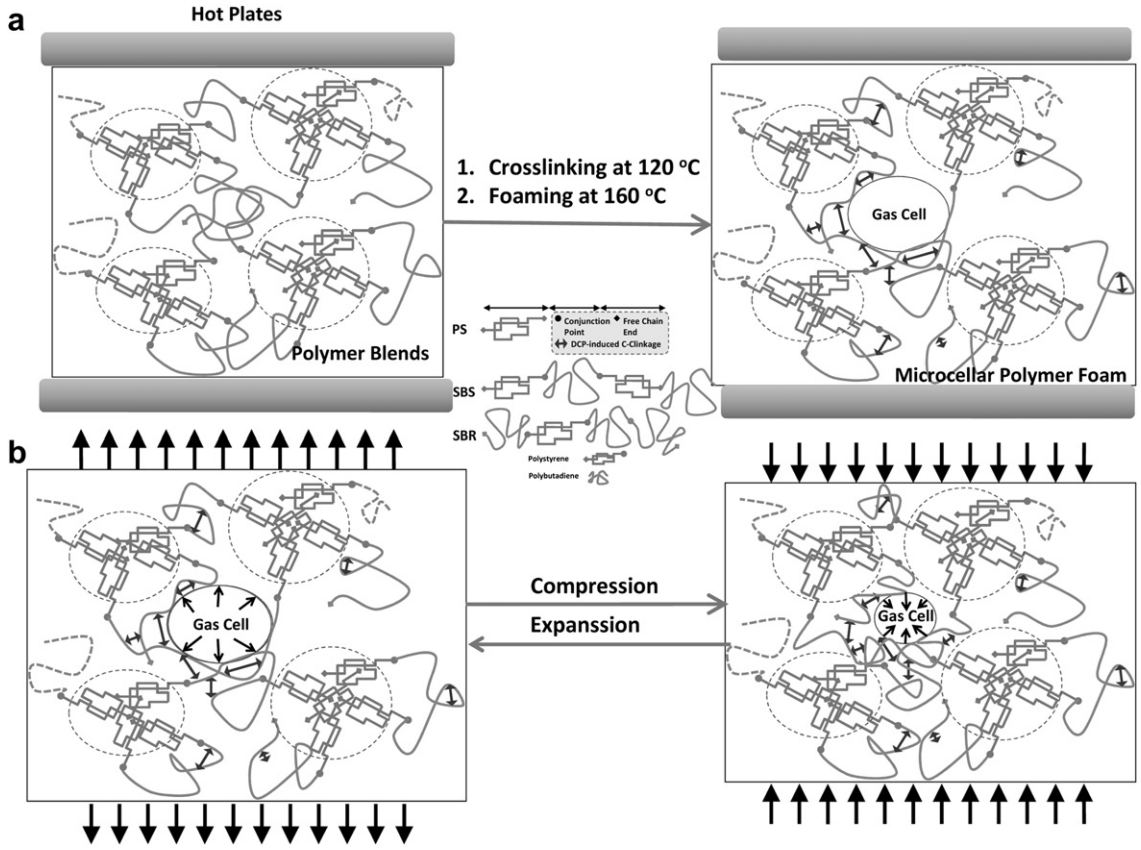

Scheme 1. (a) Compression molding and (b) elastic mechanism of SBS/PS/SBR polymer foam.

specimens were cut to length of 10.40 ± 0.05 mm, width of 7.12 ± 0.05 mm and thickness of 0.64 ± 0.05 mm. The PS/PB foams were fractured in liquid nitrogen and their surface and interface morphologies were examined using a Hitachi S-4800 FESEM. TEM images were taken for the samples with the butadiene segment stained with OsO_4, using a Hitachi H-7500 transmission electron microscope operated at an accelerating voltage of 100 kV. Ultrathin sections of the TEM samples (ca. 70 nm thickness) were prepared using a Leica Ultracut UCT microtome equipped with a diamond knife. Compression molding process is used to manufacture foam blocks of high thickness. This foaming process starts with the production of a solid sheet with the above mentioned components. A solid sheet is obtained from the previous mixture. In a first processing stage, the sheet is introduced into a mold which is closed under high-pressure (>200 bar). The mold is then heated at 160 °C in achieving suitable exotherm for further crosslinking reactions (decomposition of DCP). Simultaneously, the foaming reaction (decomposition of AC) also begins generating the gas for expansion. Finally, the samples were cut for morphological and mechanical testing. Mechanical properties for polymer foams were tested by following ASTM, including hardness, density, shrinkage, strength, elongation and compression set. Asker C hardness is measured with an Asker C durometer five times and averaged. The lower the Asker C number the softer or more compressive the foam. Compression set (CS) is measured by a modified ASTM D-395, Method B. The compression set test measures permanent set of the foam, the lower the permanent set the better the elastic recovery of the foam. Compression set was measured on three 1 in. × 1 in. × 0.5 in. foam pieces and averaged. The compression set was done at two different conditions. The first condition, which will be known at the 50 °C compression set, compressed the foam cubes by 50% for 6 h at 50 °C and then removed the compression, and the foam was allowed to recover for 30 min at room temperature. The final sample thickness was measured, and the permanent set was calculated using the following equation (1), where T_0 is the original sample thickness; T_f^{50} is the final sample thickness; and T_s is the spacer thickness. A foam sample is marked and measured for length and width. It is then put into an oven at 70 °C for 1 h at which time it is removed from the oven and allowed to cool (usually 1–4 h). Once cooled the length and width are measured, and the percentage shrinkage is calculated by the following equation (2), where T_0 is the original sample thickness and T_f^{70} is the final sample thickness.

$$CS(\%) = [(T_0 - T_f^{50})/(T_0 - T)] \times 100\% \quad (1)$$

$$Shrinkage(\%) = [(T_0 - T_f^{70})/T_0] \times 100\% \quad (2)$$

3. Results and discussion

3.1. Design of formula and process

The morphology of PS/PB microstructure after melt processing is shown in Fig. 1. As shown in Table 1, the resin with 44 wt % PS is composed of 86.4 wt % of SBS, 8.0 wt % of PS, and 5.6 wt % of SBR. After OsO_4 staining, the PB microdomains are dark, and the PS microdomains appear light. The morphological observation demonstrates that the star-block copolymer of TPE PB-575, the SBS film containing 40 wt % PS self-assembles to form worm-like PS separate phase in the PB continuous phase lacking long-range order in Fig. 1a. For the SBS/PS blends, the regularly swelling

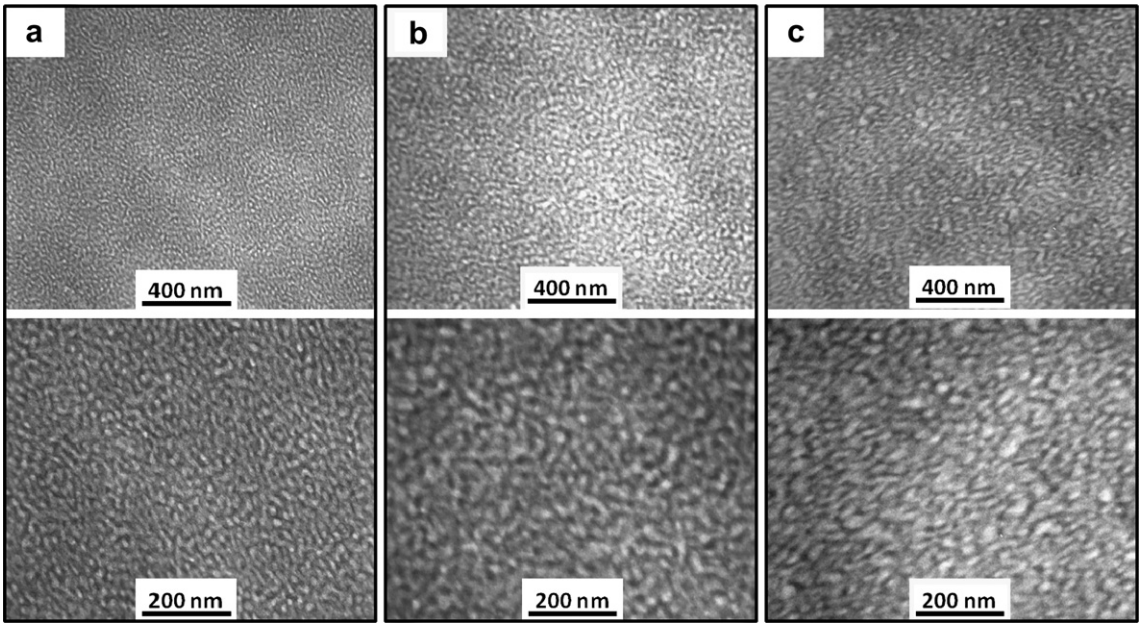

Fig. 1. TEM images of (a) SBS, (b) SBS-PS, and (c) SBS-PS-SBR films with the OsO_4-stained PB phase.

microdomains (the bright area) can be recognized. Therefore, we suggest that the major possibility to form completely dissolution of PS in SBS block copolymer. The morphological transformation can be observed from worm-like structure to network structure when SBS are blended with SBR as shown in Fig. 1c. The incorporation of SBR in the SBS-PS system may force the polystyrene segments, located originally in the interface between PB and PS block, to segregate to the polystyrene phase. It is reasonable to infer that the compatibilization is the results of entropic origin. The influence of the additives on the SBS star-block copolymer viscoelastic properties was investigated by preparing a series of additives/SBS blends. Fig. 2 plots E′ as function of temperature for the pure star-block copolymer and its blends. The result shows that there are significant reductions in E′ across the plateau region in a pure star-block copolymer (33 wt % oil content). Therefore, we suggest that oil acts as plasticizer above melting temperature. The storage modulus of the blends is much higher that of the pure star-block copolymer from −40 °C to 40 °C investigated. The mechanical properties change suggests that the miscibility between the blend is not good. The moduli of the modified systems improve 1-fold as compared to the neat systems to increased molecular entanglements. For pure SBS, two T_{gs} at −86 and 76 °C, are observed one can be assigned to the T_g of PB and the T_g of the PS, respectively. There is a little shift in the T_g of PB segment as the PS added. This means that the addition of PS leads to a significant change in the phase interaction of the SBS star-like copolymer. It is observed that calcium carbonate compounding provides enhanced stiffness to the SBS star copolymer. Moreover, the incorporation of SBR in the SBS-PS can transform morphological from worm-like structure to network structure. As observed, the network microstructure is available for bubble growth, this leads to larger cells and lower foam density [14].

The additions of PS and SBR in SBS could increase the size of PS domains and the strength of the boundary between PS and PB domains as shown in Scheme 1a. In addition to the blowing agent AC and the crosslinking agent DCP, the silicon dioxide (SiO_2) nanoparticles are also important trace additives for the heterogeneous growth of separated microballoons from these fine particles [11]. Others such as pentaerythritol tertkis(3,5-di-*tert*-butyl-4-hydroxyhydrocinnamte) (PT) and white oil are used as antioxidant, processing oil. DCP and AC are the common crosslinking and blowing agents of saturated or unsaturated polyolefins, respectively. DCP has a half-life of 10 h at 115 °C and 1 min at 171 °C [2b,15], and for chemically blown polyethylene, polyvinylchloride,

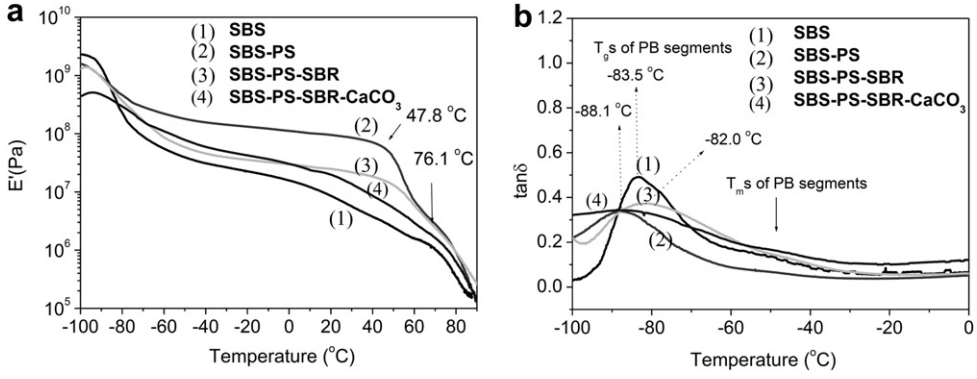

Fig. 2. Storage modulus responses and tan δ response from polymer blends at temperatures from −110 to 100 °C.

Table 2
Physical and mechanical properties.

Samples	Cell Size	Density[a]	Hardness[b]	Shrinkage[c]	Strength		Elongation[f]	CS[g]	VT[h]
					Tensile[d]	Tear[e]			
	(μm)	(g/cm^3)	(shore C)	(%)	(kg/cm^2)	(kg/cm)	(%)	(%)	(min)
I	28.5 ± 17.6	0.91	72	0	30.89	15.44	551	67	40
II	78.8 ± 30.5	0.14	15	4.0	7.0	2.6	350	88	9.2
III	65.1 ± 38.0	0.16	16	4.5	6.5	2.4	325	80	9.3
IV	57.0 ± 30.3	0.20	23	5.0	9.2	3.2	270	77	10.4
V	45.2 ± 23.2	0.21	26	5.0	10.2	3.8	233	73	10.2
VI	35.9 ± 20.8	0.24	32	7.5	10.0	3.7	198	65	11.1

[a] Tested by ASTM D792.
[b] Tested by ASTM D2240.
[c] Applied by ASTM D1204.
[d] Applied by ASTM D412-C.
[e] Applied by ASTM D624-C.
[f] Applied by ASTM D412.
[g] Compression Set is tested by ASTM D-395
[h] Vulcaization Time (t90).

or PS foams, the yellow-orange powders of AC is usually set to decompose at 195 °C because of the wide-range decomposition from 160 to 210 °C for the different particle size [16]. The different decomposition temperatures of DCP and AC allow the crosslinking reaction prior to the foaming process.

3.2. Microstructures

Values of the average cell size were determined as a representative parameter of the foam microstructure (Table 2). The final cell micrographs of the foams are shown in Fig. 1 under study. From this figure and the data of the cited tables, several interesting results can be inferred about the cellular structure of each type of materials. Foams produced from the decomposition of AC are isotropic, small and polyhedral-shaped (Fig. 3a). High magnificent micrographs (Fig. 3b) also show that partial cell walls with the thickness of about 10 μm can improve the mechanical strength of polymer scaffolds. This kind of structure is expected taking into account that no physical blowing agents are used in these materials and that foaming is carried out in an isotropic way, without any preferential direction of process or physical constraints. It is seen that sample I shows a very small numbers of cells which is nearly nonfoamed. With the increasing of DCP content 0.1–0.2 phr, it is observed that number of cells are increased and cells are created finer in size (Table 2). With the smaller average size of the cell of 35.9 ± 20.8 μm for Sample VI, the distribution of cells in the SBS/PS/

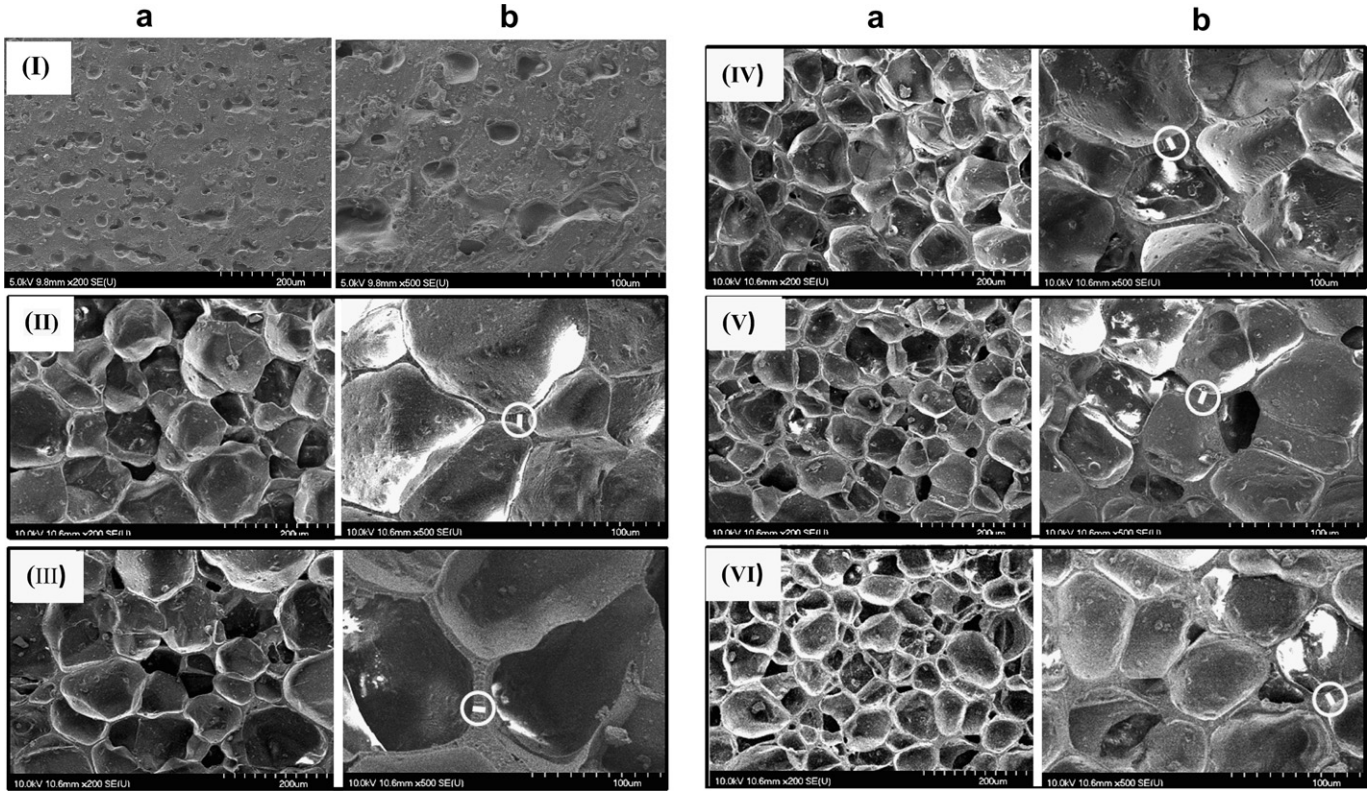

Fig. 3. SEM images of (a) surface regions and (b) internal regions at 200× and 500× magnification for samples I–VI. White spots are indicative of electron charge and white bars within a white cycle are 10 μm in length.

SBR foam would be denser, resulting in the higher density of 0.24 g/cm^3. As expected, in the presence of DCP, the partial ethylene group of PB chains could link together and form a chemical network. With increasing the content of crosslinking agent, the melting strength and the viscosity of SBS/PS/SBR blends at 160 °C would be strong enough to prevent from the diffusion and the combination of gas bubbles which is produced from the decomposition of AC. The blowing agent AC and the crosslinker of DCP were adjusted to get the same degree of foam density. Due to the foaming route a homogeneous cellular structure along foam block thickness has been observed by the SEM image on the surface and in the interior of SBS/PS/SBR foams (Fig. 3a and b). It is clearly observed that DCP agent plays a positive role with the refinement (cell size, shape and distribution) of microcellular structure compared to without crosslinker. The foam structural variability is likely to affect its mechanical properties. In the following discussion, we can observe the different properties with the effect of crosslinking agent.

The physical and mechanical properties of samples I–VI are listed in Table 2 [17]. No DCP composition shows higher values compared to crosslinking samples. With the crosslinking agent DCP from 0.1 to 0.2 phr, the density of SBS/PS/SBR foams would increase from 0.14 to 0.24 g/cm^3 due to the low expansion of the slightly crosslinked PB. Polymer crystallinity and degree of crosslinking have a significant effect on hardness of microcellular foams. For a material at a given degree of crosslinking, foam density also has a significant effect on hardness; the lower the density the softer the foam (see the hardness and the density of Samples I–VI in Table 2). However, there is usually a tradeoff between the positive attributes of lower foam density (softer, more comfortable foam at lower weight) and the positive attributes of compression set (rebound resilience, split tear, and heat shrinkage). A common approach used to optimize the combination of desirable features is to use a separate sock liner or insole close to the foot and a midsole underneath. The insole at low foam density (0.1–0.2 g/cm^3) provides maximum softness, while the midsole at higher foam density (0.18–0.35 g/cm^3) provides the high resilience, low compression set, high split tear, and low shrinkage. Table 2 shows that the cell density increased as the DCP increased, as expected. As a consequence, a higher cell population density is developed in the SBS/PS/SBR crosslinking foam.

The tensile strength of microcelluar foams without crosslinking is directly proportional to the foam density, which is simply controlled by the concentration of the blowing agent. Herein, with be involved in the crosslinking, the strength of microcellular SBS/PS/SBR foams increases more with the increase of the content of DCP. This is because the chemical linkages between PB chains would improve the resistance to the deformation (the displacement between chains) under the external force. While applying a load, the elongation of polymer rubbers is based on the extension

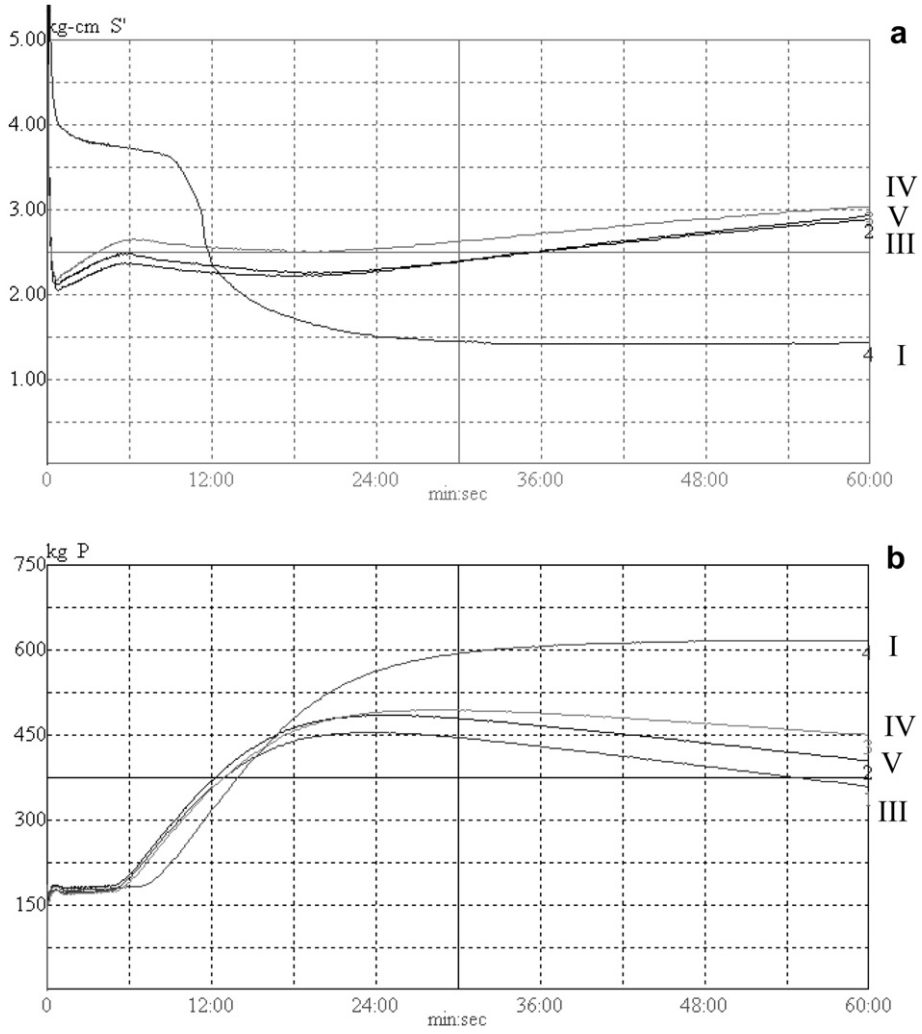

Fig. 4. Rheographs and blowing curves of SBS/PS/SBR blend at 160 °C.

of soft chains. With similar reasons to the tensile strength, the tensile elongation at break reduced with increasing the concentration of DCP because each crosslinking point would be a gel position which divides PB chains into smaller segments. High split tear relates to durability of the foam; that is, strength over the long term as well as the short term. As in the case of compression set, high split tear typically requires high foam density, and high degree of crosslinking (see the density and the tear strength of Samples I–VI in Table 2).

The compression set test measures permanent set of the foam, the lower the permanent set the better the elastic recovery of the foam. Low compression set is desirable to maintain cushioning for long term use, which in turn relates to durability with respect to comfort and rebound resilience. Low 50 °C compression set usually requires high foam density, and high degree of crosslinking, cf. the density and crosslinking effect on Samples II–VI in Table 2; however, high foam density negatively impacts the highly desirable trait of low weight, and high polymer crystallinity gives harder foams with low rebound resilience. Table 2 summarizes the t90 values, the period time to reach 90% maximum torque, of the crosslinked SBS/PS/SBR blends [18]. It can be seen from Table 2 that the incorporation of DCP has increased the value of VT. From theory [19], it is known that the torque difference showed shear dynamic modulus which indirectly related to the crosslink density of the compounds. Hence, it can be concluded that the increase of VT has contributed to the better crosslinking while adding more DCP. A typical MDR rheograph for the SBS/PS/SBR blend system is shown in Fig. 4. In both cases, S′ increases and foam pressure increases as the curing of the rubber progress. At a very short time (generally less than 2 min), however, there occurs a decrease in S′. This is due to the initial heat softening of the rubber compound. Therefore, the relationship between the vulcanization rate and blowing agent decomposition can be improved by the addition of crosslinking agent of DCP.

3.3. Thermal properties

The TGA curve of pristine SBS, SBR, and PS at a heating rate of 20 °C/min indicates the single stage of SBS starts decomposing around 400 °C and ends at about 500 °C [20]. However, the TGA curves of Samples I–VI (see Fig. 5 and Table 3) show three-step decompositions with these observations: the average onset points at 200, 417.0, 667.6 °C and the average weight loss of 23.3, 48.7 and 11.3 wt % for Stages A, B, and C, respectively. The first thermal decomposition temperature (150–340 °C) comes from the boiling of oil results in the loss of 23.3 wt % (~86.4 × 33 wt %). After decomposition of the oil, the blends containing SBS, SBR, and PS is stable up 500 °C, which is identical to the decomposition temperature of the above mentioned literatures. When the temperature reached 500 °C, the decomposition of $CaCO_3$ started and till 740 °C the mass weight constant. Here, the $CaCO_3$ was decomposed to CaO and CO_2. Therefore, Samples I–VI show the average residue yield of 15.0 wt % at 750 °C.

Table 3
Results of TGA thermograms.

Samples	Stage A		Stage B		Stage C		Residue
	OP[a] (°C)	WL[b] (wt %)	OP (°C)	WL (wt %)	OP (°C)	WL (wt %)	at 750 °C (wt %)
I	194.4	25.4	423.8	49.3	644.0	10.5	15.3
II	187.7	24.2	421.9	49.3	666.8	11.0	15.1
III	197.2	23.0	417.1	46.6	664.9	13.0	15.0
IV	197.2	23.7	411.3	48.7	669.8	10.7	15.0
V	197.4	23.2	416.9	50.1	666.2	11.5	14.8
VI	196.3	23.6	414.1	49.1	670.5	11.3	14.8
Average	195.0	23.8	417.5	48.8	663.7	11.3	15.0

[a] Onset point.
[b] Weight loss.

The T_g of the SBS/PS/SBR foam is especially important, depending on its usage, as in normal applications like a cushion it needs to be in its rubbery state to provide the desired characteristics. The DSC thermograms are not suitable for the investigation of T_g for microcellular polymers due to many insulating cavities in the matrix. For evaluation of thermal endurance in foamed plastics, temperature and time dependence of compression dynamic modulus of SBS/PS/SBR foams was investigated by dynamic viscoelastic measurements. Fig. 6 shows the tan δ (E″/E′) response from the Samples II to VI. The rheological behavior in terms of storage modulus, tan δ of the sample I is similar to neat systems. The intensity and position of the glass transition were dependent on the DCP content in these blends. In view of Samples II–VI, the T_g position shifts from −71.1 to −58 °C (the T_g of −86.7 °C for bulk SBS), showing the restriction of PB molecular motion by increasing DCP crosslinking agent. The transition at −15.4 °C might be the melting transition of short-ranging PB chains, which is confined within crosslinking points [21]. The tan δ peak temperature was 87 °C for Samples II–VI, which were in accord with the results obtained by Masson et al., who reported that the tan δ peak temperature of hard PS ranged from 55 to 90 °C depending on PS content [22]. The wide temperature range of the rubbery state from −50 °C to 60 °C implies that the crosslinking SBS/PS/SBR

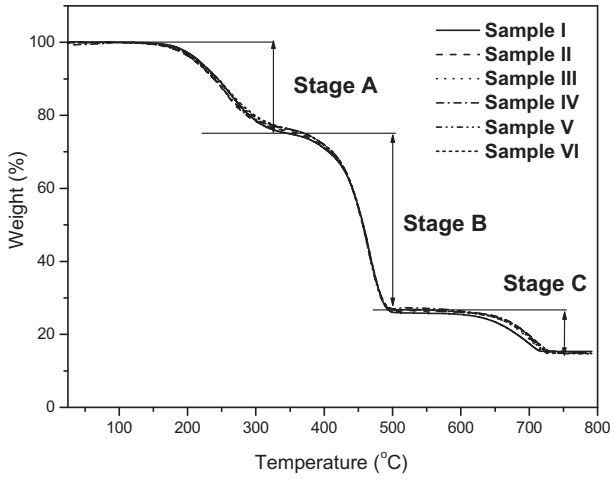

Fig. 5. TGA thermograms of samples I to V.

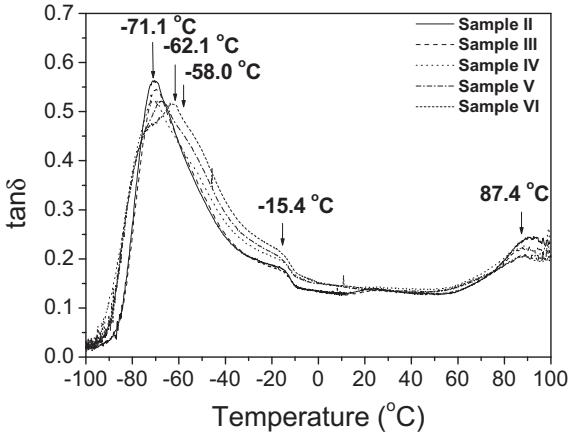

Fig. 6. Tan δ reponse from Samples II to VI at temperatures from −110 to 100 °C.

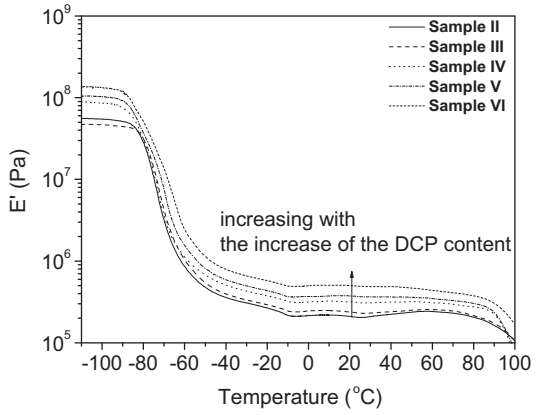

Fig. 7. Storage modulus responses from Samples I to VI at temperatures from −110 to 100 °C.

foams has a great quantity of world-wide cushioning applications from the polar region to the equatorial area.

Fig. 7 shows the storage modulus response from the Samples II to VI. At the fixed concentration of AC, the initial storage modulus at 20 °C increase with increasing the content of DCP. At crosslinker concentrations of 0.18 and 0.2 phr, constant values of 4 and 3.7×10^5 Pa, respectively. This increasing is due to the more crosslinking SBS/PS/SBR cell wall exhibits the stronger elastic properties to recovery its initial dimension after removing the external load. Thus, when the crosslinking condition is appropriate, the crosslinked SBS/SBR samples behave as a normal crosslinked rubber, as expected, even when the PS microdomains no longer act as physical crosslinks. Thus similar results to Fig. 6, the glass transitions of crosslinking soft PB domains and hard PS domains can be observed at around −70 °C and 90 °C. These phenomena indicate that the more content of DCP not only lead to higher storage modulus but also sustain the mechanical response at higher frequency.

4. Conclusions

The concentration of peroxide crosslinker, dicumyl peroxide (DCP), has a great effect on the size distribution of hollow cells and the results of mechanical properties. The SEM images of cross-section of PS/PB foams show the smaller and denser of cell distribution for Sample VI with the 0.2 phr of DCP in comparison with Samples I–V with the same content of blowing agent, azodicarbonamide (AC). With the increase of the DCP concentration, the density, the hardness, shrinkage, tensile strength, tear strength, and vulcaization time increase due to the slightly crosslinking of soft PB domains. The confinement of PB chain motion within crosslinking points retards the elongation at break and reduces the compression set. In addition, the results of dynamical mechanical analyses show the shift of glass transition temperature from −71.1 to −62.1 °C and the increase of initial storage modulus and storage modulus at 20 °C for the increase of the DCP concentration. Moreover, the more content of DCP not only lead to higher storage modulus but also sustain the mechanical response at higher frequency.

References

[1] Gibson LJ, Ashby MF. Celluar solids: structure and properties. 2nd ed. Oxford: Pergamon Press; 1988.
[2] (a) Saint-Michel F, Chazeau L, Cavaille JY, Chabert E. Compos Sci Technol 2006;66:2700;
(b) Dubois R, Karande S, Wright DP, Martinez FJ. Cell Plast 2002;38:149;
(c) Herrington R, Hock K, editors. Flexible polyurethane foams. 2nd ed. Midland: Dow Chemical Co.; 1997.
[3] (a) Hilyard NC, Cunningham A. Low density cellular plastics: physical basis of behavior. London: Chapman and Hall; 1994;
(b) Rodriguez-Perez MA. Adv Polym Sci 2005;184:97;
(c) Klempner D, Frish KC. Handbook of polymeric foams and foam technology. New York: Oxford University Press; 1991.
[4] (a) Holden G. Undertanding thermoplastic elastomers. Munich: Carl Hanser Verlag; 2000. pp. 15–35;
(b) Bates FS, Fredrickson GH. Annu Rev Phys Chem 1990;41:525;
(c) Leibler L. Macromolecules 1980;13:1602;
(d) Honeker CC, Thomas EL. Chem Mater 1996;8:1702;
(e) Pakula T, Saijo K, Kawai H, Hashimoto T. Macromolecules 1985;18:1294;
(f) Harada T, Bates FS, Lodge TP. Macromolecules 2003;36:5440.
[5] Colton JS. The nucleation of microcellular thermoplastic foam. Massachusetts: MIT; 1985.
[6] Jacob S. US Patent 7,319,121 B2; 2008.
[7] Gul RME. Eur Polym J 1999;35:2001.
[8] (a) Chaudhary BI, Barry RP, Tusim MH. J Cell Plat 2000;36:397;
(b) Chaudhary BI, Barry RP. J Cell Plat 1999;35:531.
[9] Jouenne S, Gonzaćlez-Lećon JA, Ruzette AV, Lodećfier P, Leibler L. Macromolecules 2008;41:9823.
[10] (a) Ruckdaschel H, Altstadt V, Muller AHE. Cell Polym 2007;26:367.
[11] (a) Cha SW, Yoon JD, Uto N. Cell Polym 2004;23:229;
(b) Ramesh NS, Lee ST. Cell Polym 2005;24:269;
(c) Caprioli G, Bernasconi R, Hamilton A, Liefferinge MV, Barettini S, Cappella A. J Cell Plast 1999;35:27;
(d) Park CB, Cheung LK, Song SW. Cell Polym 1998;17:221.
[12] (a) Martínez-Díez JA, Rodríguez-Pérez MA, De Saja JA. J Cell Plat 2001;37:21;
(b) Sims GLA, Khunniteekool C. Cell Polym 1996;15:1;
(c) Khunniteekool C. Cell Polym 1996;15:14.
[13] Tonkel RF, Gross AL. US Patent 4,894,933; 1990.
[14] McKay KW, Gros WA, Diehl CF. J Appl Polym Sci 1995;56:947.
[15] (a) Sims GLA, Sipaut CS. Cell Polym 2001;20:255;
(b) Sipaut CS, Sims GLA, Ariff ZM. Cell Polym 2008;27:11;
(c) Sipaut CS, Sims GLA, Mohamad Ibrahim MN. Cell Polym 2008;27:67;
(d) Rodríguez-Pérez MA, Almanza O, Ruiz-Herrero JL, de Saja JA. Cell Polym 2008;27:179;
(e) Mahapatron A, Mills NJ, Sims GLA. Cell Polym 1998;17:252;
(f) Sombatsompop N. Cell Polym 1998;17:63.
[16] (a) Zhou Q, Weiping G, Wu J, Wang J, Zhen HY, Wu Q. J Cell Plast 2000;36:126;
(b) Jaafar HAS, Sims GLA. Cell Polym 1993;12:303;
(c) Sims GLA, Sirithongtaworn W. Cell Polym 1997;16:271;
(d) Zhou Q, Cong CB. J Cell Plast 2005;41:225;
(e) Pop-Iliev R, Park CB, Fenton RG. J Cell Plast 2005;41:519.
[17] (a) Bureau MN, Gendron R. J Cell Plast 2003;39:353;
(b) Bureau MN, Champagne MF, Gendron R. J Cell Plast 2005;41:73.
[18] Ismail H, Chia HH. Eur Polym J 1998;34:1857.
[19] Ismail H, Freakley PK, Sutherland I, Sheng E. Eur Polym J 1995;31:1109.
[20] (a) Lu L, Yu H, Wang S, Zhang Y. J Appl Polym Sci 2009;112:524;
(b) Kwon E, Castaldi MJ. Environ Sci Technol 2009;43:5996;
(c) Bourbigot S, Gilman JW, Wilkie CA. Polym Deg Stab 2004;84:483.
[21] Brozek J, Budin J, Roda J. Therm Anal Calorim 2007;89:211.
[22] Masson JF, Bundalo-Perc S, Delgado A. J Polym Sci Part A Polym Phys 2005;43:276.

Polymer 52 (2011) 760–768

Contents lists available at ScienceDirect

Polymer

journal homepage: www.elsevier.com/locate/polymer

Nano-phase structures and mechanical properties of epoxy/acryl triblock copolymer alloys

Hajime Kishi [a,*], Yumi Kunimitsu [a], Jin Imade [a], Shinya Oshita [b], Yoshihiro Morishita [b], Mitsunori Asada [b]

[a] Graduate School of Engineering, University of Hyogo, 2167, Shosha, Himeji, Hyogo 671-2201, Japan
[b] Kuraray Co. Ltd., 1-1-3, Otemachi, Chiyoda-ku, Tokyo 100-8115, Japan

ARTICLE INFO

Article history:
Received 22 June 2010
Received in revised form
27 November 2010
Accepted 14 December 2010
Available online 22 December 2010

Keywords:
Epoxy
Block copolymer
Phase structure

ABSTRACT

Phase structures and mechanical properties of epoxy/acryl triblock copolymer alloys using several curing agents were studied. PMMA-*b*-PnBA-*b*-PMMA triblock copolymers synthesized by living anionic polymerization were applied as the toughening modifiers for the epoxy resins. An aromatic amine, an acid anhydride and an anionic polymerization catalyst as curing agents resulted in macro-phase separation in the epoxy/triblock copolymer blends during the cure process. However, a phenol novolac as the curing agent created nano-phase structures in the epoxy blends. The size of the spherical phases or cylindrical phases was about 40 nm in diameter, and the main component in the nano-phases was the PnBA of the triblock copolymer. The fracture toughness of the epoxy/triblock copolymer alloys with the nano-cylindrical phases reached 2530 J/m^2. The fracture toughness was more than twenty fold relative to the unmodified epoxy resin, and was equivalent to the toughness of polycarbonates.

1. Introduction

Epoxy resins are one of thermosetting polymers widely used as structural materials and adhesives in many industries, such as aerospace industries, automotive industries and electronics industries, for their good mechanical properties, high heat resistance and solvent resistance. Their distinguishing properties originate from their crosslinked chemical structure. However, the low fracture toughness relative to other engineering thermoplastic polymers originates also from the crosslinked structure restricting the molecular motion. They, therefore, need to be toughened to enable more applications.

It is well known that relatively low crosslinked epoxy resins can be toughened by the incorporation of elastomer phases, but more highly crosslinked epoxy resins are difficult to toughen in this way [1–6]. Also, the incorporation of elastomer tends to decrease both the modulus of elasticity and the heat resistance of the modified epoxy resins. Therefore, highly crosslinked epoxy polymer alloys modified with engineering thermoplastic resins, such as poly ether sulphones and poly ether imides, have been researched to achieve both high toughness and heat resistance [7–11]. The improvement in toughness depended on the phase-separated morphology of the cured polymer alloys. The phase separation occurred due to the change of free energy in the mixture elevated by the increase in the molecular weight during the curing process of the epoxy resins [12,13]. The sizes of the phase structures in the epoxy blends were in the order of sub-micrometers or micrometers [1–13].

Recently, block copolymers have attracted attention as modifiers for toughening of epoxy resins [14–29,33,34]. It is well known that the block copolymers themselves have nano-phase structures [30–32]. When the self-assembly ability of the block copolymers is activated in the epoxy blends, the phase separation of the polymer alloys is controlled in the order of nanometers. Bates et al. firstly created the nanostructured epoxy blends with amphiphilic block copolymers [14,15]. They synthesized poly(ethylene oxide)-*b*-poly (ethyl ethylene) (PEO-PEE) and poly(ethylene oxide)-*b*-poly (ethylene propylene) (PEO-PEP) diblock copolymers as modifiers for diglycidyl ether of bisphenol-A (DGEBA) type epoxy resins, and found the blends showed the phase structures in the nanometer scale. After the findings, various block copolymers such as poly (ethylene oxide)-*b*-poly(propylene oxide) (PEO-PPO) diblock copolymers, poly(ethylene oxide)-*b*-poly(butylene oxide) (PEO-PBO) diblock copolymers, and poly(ethylene oxide)-*b*-poly(propylene oxide)-*b*-poly(ethylene oxide) (PEO-PPO-PEO) triblock copolymers were synthesized as modifiers for epoxy resins to give nano-phase structures [16–21]. In concrete, spherical micelles, worm-like micelles, and vesicles were observed in the epoxy blends by altering the composition of the block copolymers.

* Corresponding author. Tel./fax: +81 79 267 4843.
E-mail address: kishi@eng.u-hyogo.ac.jp (H. Kishi).

0032-3861/$ – see front matter © 2010 Elsevier Ltd. All rights reserved.
doi:10.1016/j.polymer.2010.12.025

Ritzenthaler et al. studied epoxy/ABC triblock copolymer blends [22,23]. Interesting 'raspberry-like' morphology (spheres-on-spheres) in nano scale was observed in the polystyrene-*b*-polybutadiene-*b*-poly (methyl methacrylate) triblock polymer (PS–PB-PMMA)/DGEBA blends cured with MCDEA 4,4′- methylene-bis-(3-chloro 2,6-diethyl-aniline). Moreover, the triblock copolymer with increased PB content made 'onion-like' multilayered morphology in the DGEBA cured with MCDEA. On the other hand, the PS–PB-PMMA/DGEBA blends cured with 4, 4′-diamino diphenyl sulphone (DDS) instead of the MCDEA showed flocculated macro-phase separation. In their previous study on miscibility of epoxy/PMMA blends, Ritzenthaler et al clarified the PMMA is miscible in the DGEBA cured with MCDEA, but segregates in the DGEBA cured with DDS [24].

Meanwhile, Maiez-Tribut et al. indicated that random copolymers of methyl methacrylate (MMA) and N, N-dimethylacrylamide (DMA) can be used as a miscible block for the DGEBA cured with DDS [25]. As the results, they succeeded to make the nanostructure in DGEBA-DDS networks using the block copolymers with poly (*n*-butyl acrylate) as the immiscible block and the random copolymer P(MMA-*co*-DMA) as the miscible block. It was found that the P(MMA-*co*-DMA) block was effective to make nanostructure in DGEBA-polyetheramine system also [26].

Rebizant et al. synthesized SBMG tetrablock copolymer [polystyrene-*b*-polybutadiene-*b*-poly (methyl methacrylate)-*b*-poly (glycidyl methacrylate)] [27] and SBMA triblock copolymer [polystyrene-*b*-polybutadiene-*b*-poly[(methyl methacrylate)-*stat*-(methacrylic acid)] [28] as modifiers for DGEBA. They compared the reactive block copolymers with the nonreactive ones, and clarified the functional groups limit the macro-phase separation in the DDS-cured DGEBA and give the controlled morphology in nano scale.

Serrano et al. prepared nanostructured epoxy blends with polystyrene-*b*-polybutadiene (PS–PB) diblock copolymers [29]. The DGEBA/PS–PB diblock copolymer blends cured with MCDEA showed worm-like micelles or hexagonally-packed cylindrical micelles. The phase morphologies depended on the content of the block copolymers and the degree of epoxidation in the polybutadiene block, and the main component in the cylindrical micelles was glassy polystyrene. The G_{IC} of the blends with the hexagonally-packed cylinders was about 500 J/m^2, which was double the corresponding unmodified epoxy resin.

In terms of the toughening effect, a DGEBA/PEO-PBO diblock copolymer blends showed the branched cylindrical micelles, and the fracture toughness (the critical strain energy release rate; G_{IC}) of the blends reached 1560 J/m^2 [21].

Though the studies using various block copolymers as toughening modifiers for epoxy resins were reported as mentioned above, it is worth to research the effect of the curing agents on the phase structure of the epoxy/block copolymer blends from the wide range of the epoxy-curing systems. The modifiers for epoxy resins used in this study were two types of poly (methyl methacrylate) -*b*- poly (n-butyl acrylate) -*b*- poly (methyl methacrylate) (PMMA-*b*-PnBA-*b*-PMMA) triblock copolymers. The composition and the distribution of molecular weight of the block copolymers were controlled by living anionic polymerization. The PnBA as the middle segment of the triblock copolymers has elastomeric properties, and would be expected to work as the toughening agents in the epoxy blends. The first objective of the present work is to clarify the dominant factors that control the size of phase structures in the order of nanometers, using the PMMA-*b*-PnBA-*b*-PMMA triblock copolymers while altering the curing agents. Specifically, the next four kinds of curing agents were systematically selected from several epoxy-curing systems: aromatic amines, acid anhydrides, phenol novolacs, and anionic polymerization catalysts. Moreover, the relation between the mechanical properties, such as the fracture toughness and the modulus of elasticity, and the phase structures of the epoxy blends will be discussed.

2. Experimental procedure

2.1. Materials

The epoxy resin used in this study was diglycidyl ethers of bisphenol-A (DGEBA), JER828 (epoxy equivalent weight: 189 g/eq., provided by Japan Epoxy Resin). 4, 4′-diamino diphenyl sulphone (DDS, active amino-hydrogen equivalent weight: 62 g/eq.), phenol novolac (PN, hydroxyl group equivalent weight: 105 g/eq.), methyl nadic anhydride (MNA, acid anhydride equivalent weight: 178 g/eq.), and 2, 4, 6–tris (dimethyl amino methyl) phenol (DMP) as a catalyst for anionic polymerization of epoxy resin were compared as curing agents. In the cases of DDS, PN and MNA, the stoichiometric amount of the curing agents was added to the epoxy resin. Here, 2 phr of DMP was co-used as a catalyst with the MNA. Meanwhile, 0.5 phr of tri phenyl phosphine (TPP) was used as a catalyst with the PN.

Two types of PMMA-*b*-PnBA-*b*-PMMA triblock copolymers synthesized by living anionic polymerization (produced by Kuraray Co. Ltd.) were applied as the toughening modifiers for the epoxy resins. The two block copolymers (BCPs) had almost the same composition (the content of PnBA was 67–69 wt % in the copolymers). However, the molecular weight of the copolymers was different. One block copolymer (BCP1) was 60,000 on weight-average molecular weight, and the other block copolymer (BCP2) was 149,000. The characterization of the BCPs is shown in Table 1 in detail. The chemical structures of these materials are shown in Fig. 1.

2.2. Preparation of cured resins

Epoxy/BCP systems were cured by the following procedure. First, the BCP was mixed with the epoxy resin at room temperature. The resin mixture was heated while being stirred in an oil bath at 200 °C for 30 min to dissolve the triblock copolymer in the epoxy resin. After the mixture was cooled to lower than 100 °C, while being stirred the curing agent was added to the resin mixture and degassed. Then, the resin was cast into a pre-treated mold with a release agent. The curing condition using each curing agent was summarized in Table 2. After this procedure, the oven was switched off and the cured resins were allowed to cool slowly to room temperature.

2.3. Microscopy observation

2.3.1. Scanning electron Microscopy (SEM)

The fractured surfaces of the cured resins were observed by a scanning electron microscope (SEM: KEYENCE VE-9800, Japan). The samples were mounted on brass stubs and coated with a thin layer of gold using an ion sputter coater (JEOL JFC- 1100E, Japan).

2.3.2. Transmission electron Microscopy (TEM)

Thin sections were cryo-microtomed at −80 °C from the cured resins. The setting thickness was 40–50 nm. The microtomed thin

Table 1
Weight-average molecular weight (Mw), PnBA content and polydispersity of PMMA-PnBA-PMMA triblock copolymers (BCPs).

	Weight-average molecular weight (Mw)	PnBA content (wt%)	Polydispersity (Mw/Mn)
BCP1	60,000	67.5	1.25
BCP2	149,000	68.8	1.41

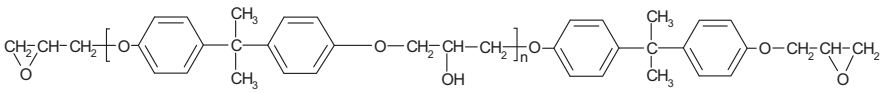

Diglycidyl ethers of bisphenol-A (DGEBA)

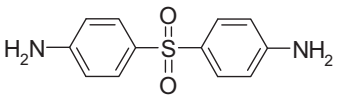

4, 4'-diamino diphenyl sulphone (DDS)

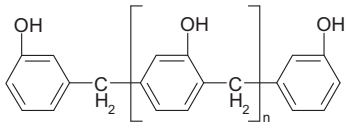

Phenol novolac (PN)

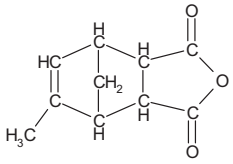

Methyl nadic anhydride (MNA)

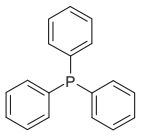

tri-phenyl phosphine (TPP)

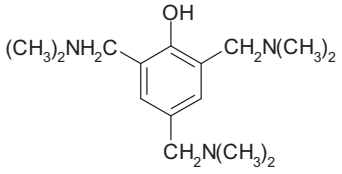

2, 4, 6-tris (dimethyl amino methyl) phenol (DMP)

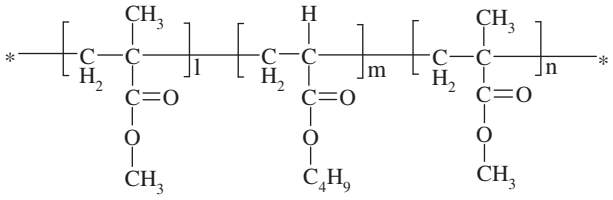

PMMA-PnBA-PMMA triblock copolymer (BCP)

Fig. 1. Chemical structure of epoxy resin, curing agents, and block copolymer.

sections of the cured resins were stained by vapor of RuO_4 and observed by a transmission electron microscope (TEM: HITACHI H-800NA, Japan) with 100 kV as the acceleration voltage.

2.3.3. Scanning probe Microscopy (SPM)

Phase images of the cured resins were obtained by scanning probe microscope (SPM: E-sweep, Seiko Instruments, Inc., Japan) in dynamic force mode. A silicon cantilever (SI-DF-20, Seiko Instruments, Inc., Japan) with an integrated tip was used for the observation. The cantilever has a dimension of 225 × 33 × 5 μm and a resonance frequency of around 130 kHz. The nominal tip radius is less than 10 nm. The contrast in phase images is affected by the viscoelastic properties of the sample surface. The harder, less viscous area is shown in darker color in this system.

Table 2
Types of curing systems and the curing conditions.

Type of curing system	Curing agent	Amount [phr]	Catalyst	Amount [phr]	Curing conditions
Amine	DDS	32.9	–	–	150 °C/3 h + 200 °C/2 h
Phenol	PN	55.6	TPP	0.5	120 °C/2 h + 150 °C/2 h
Acid anhydride	MNA	94.2	DMP	2.0	90 °C/2 h + 170 °C/2 h
Anionic polymerization	–	–	DMP	2.0	100 °C/4 h + 150 °C/2 h

2.4. Evaluation for viscoelasticity of the cured resins

The temperature dependencies of the viscoelastic properties (storage modulus: E′ and loss tangent: tanδ) of the cured resins were evaluated by dynamic mechanical analysis in tensile mode (DMA: DMS6100, Seiko Instruments, Inc., Japan). The dynamic frequency was 1 Hz and the amplitude was 10 μm. The specimens had a length of 40 mm (span: 20 mm), a width of 10 mm, and a thickness of 2 mm. The samples were tested over a temperature range between −100 °C and 250 °C in the heating rate of 2 °C/minute.

2.5. Evaluation for miscibility of polymers with epoxy resins

In order to assess the miscibility of the PMMA segment or the PnBA segment of the BCP in the epoxy resin/curing agent, the next model tests were conducted. Namely, homo PMMA (Mw = 600,000) or homo PnBA (Mw = 99,000) was added into DGEBA, and the mixture was stirred at 200 °C for 30 min. After cooling the solution to lower than 100 °C, each curing agent was added to the resin mixture with stirring and degassed. The resin mixtures were cured by the same conditions written in the Section 2.2, and the transparency of the cured resins were observed.

2.6. Fracture toughness assessment

Fracture toughness of the cured resins was measured by the single edge notched three-point bending (SEN-3PB) method according to ASTM D 5045. The dimensions of the specimens were 55 mm long (L) × 12 mm wide (W) × 6 mm thickness (B). The span for the bending test was 48 mm (S). The cracks were introduced by first cutting a notch using a low speed diamond saw, then hammering in a razor blade that had been immersed in liquid nitrogen. The initial crack length (a) was within the range of 6.1 ± 0.5 mm to satisfy the geometric requirement. The initial crack length (a) was measured precisely in each fractured specimen using an optical microscope for the calculation of the critical stress intensity factor (K_{IC}). The three-point bending tests were performed with a testing rate of 10 mm/min. at 23 °C using a testing machine (Intesco 210B). The K_{IC} was calculated using the following Eq. (1), where P is the value of force at fracture.

$$K_{IC} = \frac{PSf(a/W)}{BW^{3/2}} \quad (1)$$

Then, the critical strain energy release rate (G_{IC}) was calculated from the K_{IC}, modulus of elasticity (E) and Poisson's ratio ($\nu = 0.35$) of the specimen by using the Eq. (2).

$$G_{IC} = \frac{K_{IC}^2(1-\nu^2)}{E} \quad (2)$$

3. Results and discussion

3.1. Phase structures of cured epoxy/PMMA-PnBA-PMMA triblock copolymers

Fig. 2 shows overviews of the cured blend resins of epoxy/BCP2 (Mw = 149,000). Four curing agents, namely DDS (aromatic amine), MNA (acid anhydride), PN (phenol novolac), and DMP (a catalyst for anionic polymerization) were compared. The content of the BCP2 in the resins was 20 wt%. Only the PN-cured resin was transparent, and others were opaque. This suggested a difference in the sizes of the internal phase structures.

Figs. 3 and 4 show SEM photographs of the fractured surfaces of the epoxy/BCP2 blends that were fractured after cooling in liquid N_2.

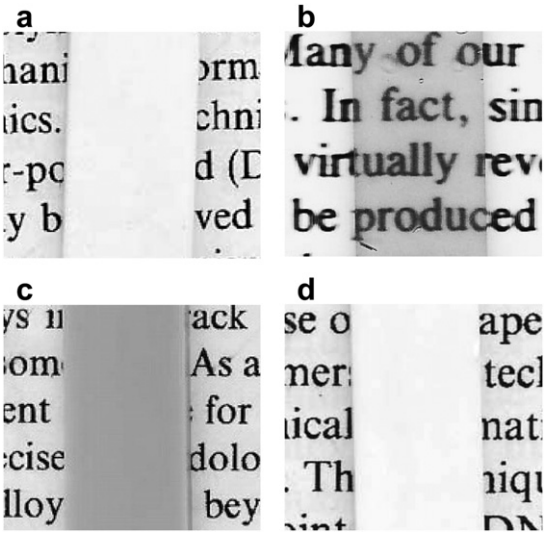

Fig. 2. Overviews of the cured blend resins of epoxy/PMMA-PnBA-PMMA triblock copolymer (BCP2: 20 wt %).

The morphology corresponds to the internal phase-separated structures of the blend resins. The DDS-cured, the MNA-cured and the DMP-cured blends showed rough fractured surfaces (Fig. 3). The dispersed phases were observed in the order of micrometer-sizes (Fig. 4). Meanwhile, the PN-cured blend showed relatively smooth surfaces in the low magnified observation (Fig. 3b). In the higher magnified observation, however, a lot of nano-cavities were regularly found in the PN-cured blends (Fig. 4b). The cavities with nanometer sizes are the cross sections and the partially lateral sections of the nano-cylindrical phases. The sizes of the cylinders were about 40 nm in diameter. Namely, only the PN-cured epoxy/BCP2 blend resin had the nano-phase structures among the four types of curing systems, though all cured resins were modified by the same BCP2. The situation on the macro-phase separation was same in case using BCP1 (Mw = 60,000) as the BCP2.

Fig. 5 shows the temperature dependencies of the viscoelastic properties (Dynamic Mechanical Analyses: DMA) of the four kinds of epoxy/BCP2 blends, which suggests phase components in the blends. Three epoxy/BCP2 blends using DDS, MNA and DMP indicated two or three glass transition temperatures (Tg) with the change of the storage modulus (E′) and the peaks of loss tangent (tanδ).The first Tg was around −50 °C corresponding to the Tg of PnBA segments of the BCP2. Specifically, considerable drops of E′ were commonly seen at this temperature in these three blend resins. The second Tg and the third Tg depended on the curing agents. In the DDS-cured epoxy, the second small Tg was at 120 °C and the third Tg was at 210 °C. The second Tg would be the Tg of PMMAs of the BCP2 with some epoxy components, and the third Tg corresponds to the epoxy networks. In the MNA-cured epoxy, the second Tg was at 110 °C derived from PMMAs, and the third Tg (160 °C) corresponds to the epoxy networks. In the DMP-cured epoxy, the second Tg was at 110 °C derived from both PMMAs and epoxy networks. In contrast to these three blends, the PN-cured epoxy/BCP2 blend displayed one sharp Tg at 120 °C, mainly corresponding to epoxy networks including PMMAs. The rather high Tg of the PMMA block would originate in the syndiotactic configuration synthesized by living anionic polymerization. The Tg of the pure PN-cured DGEBA and the Tg of the PMMA block of the pure BCP2 was close as shown in Fig. 5b. Therefore, it was difficult to discuss the miscibility of the PMMA and the epoxy from this result only. It is noteworthy that the drop of E′ around −50 °C was not clear in the PN-cured blend, which is different from other curing systems.

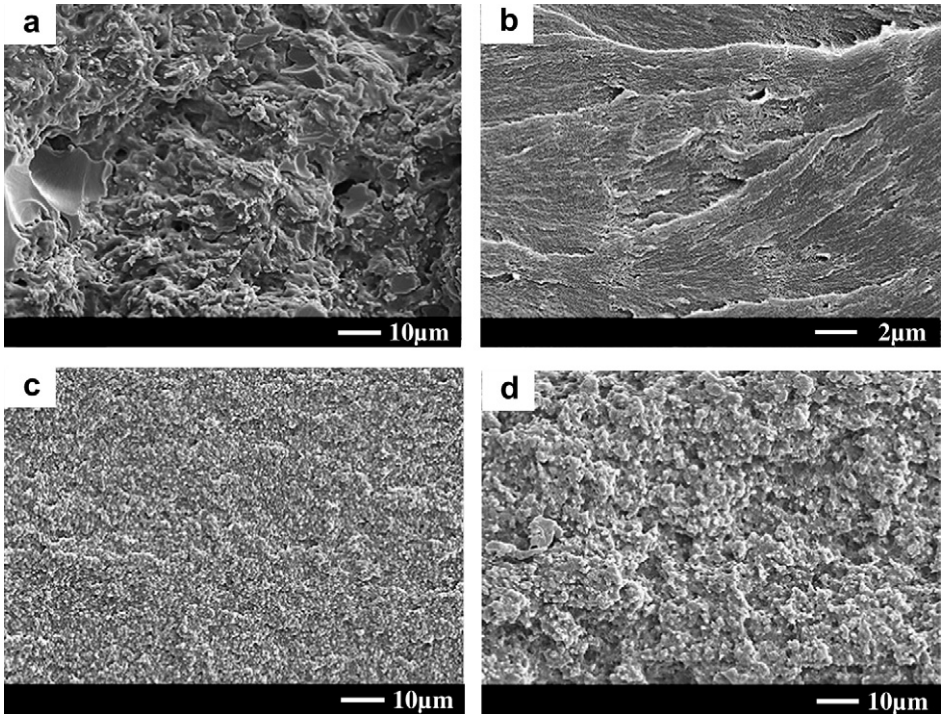

Fig. 3. SEM photographs of fracture surfaces of DGEBA/BCP2 (20 wt %) blend resins: (a) cured with DDS; (b) cured with PN; (c) cured with MNA; (d) cured with DMP. Note that the magnification of (b) is five times the others.

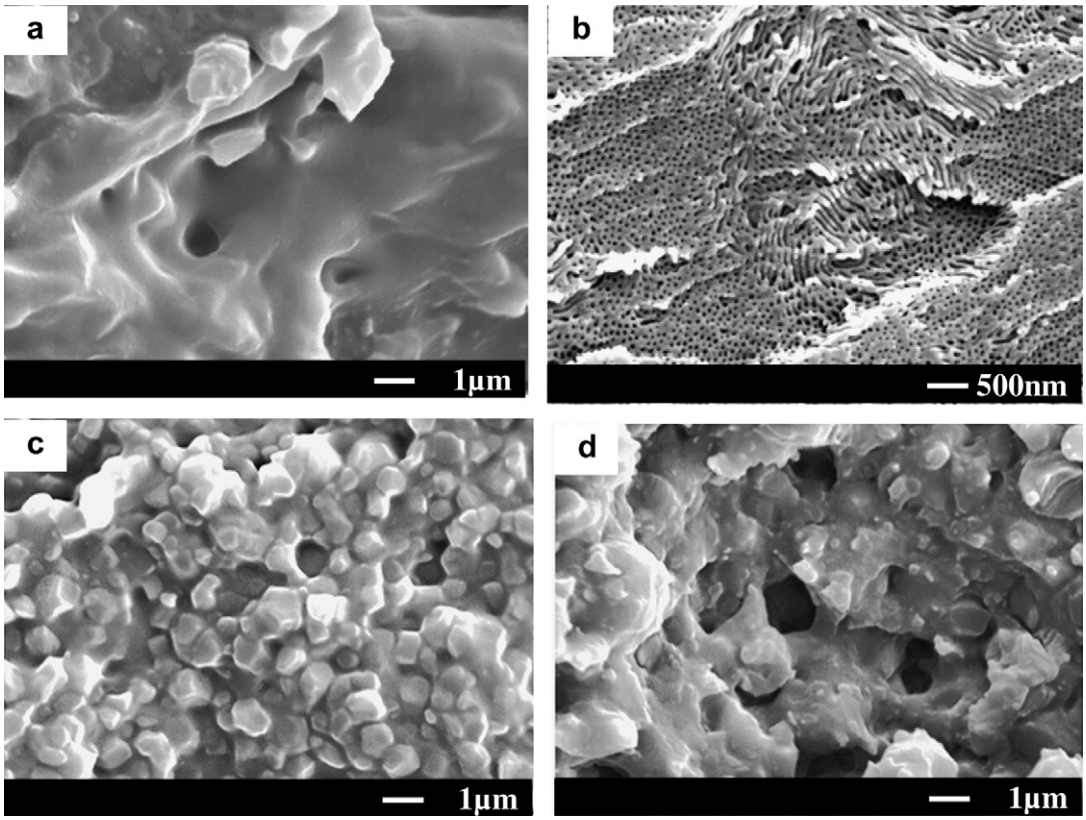

Fig. 4. SEM (high magnified) photographs of fracture surfaces of DGEBA/BCP2 (20 wt %) blend resins: (a) cured with DDS; (b) cured with PN; (c) cured with MNA; (d) cured with DMP. Note that the magnification of (b) is twice the others.

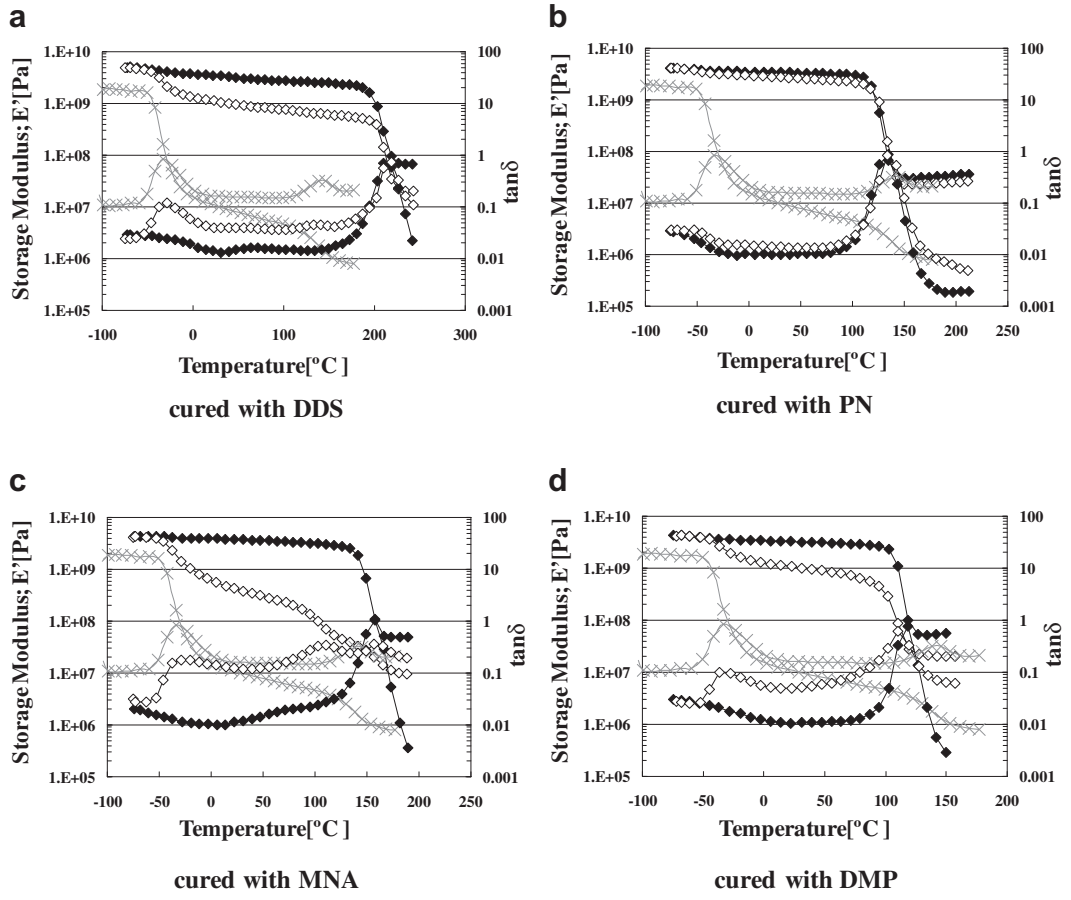

Fig. 5. Temperature dependencies of the viscoelastic properties (DMA) of resins: (a) cured with DDS; (b) cured with PN; (c) cured with MNA; (d) cured with DMP, ◆: pure DGEBA, ◇: DGEBA/BCP2 (20 wt %) blend, ×: pure BCP2.

SPM analyses were also conducted to examine the component of the nano-cylinders in the PN-cured epoxy/BCP2 blend. The phase images of the cured resin are shown in Fig. 6. The contrast in the phase images is affected by the viscoelastic properties of the component, and softer phases are expressed more brightly in the analyses. The nano-cylinders are brighter than the matrix part at room temperature (Fig. 6), that means the inside components of the cylinders are softer than the matrix. Therefore, the main component in the nano-cylinders was considered as the PnBA segments of the BCP2 that were elastomeric at room temperature. It is estimated that the other segments of the BCP2, ie. PMMAs, were incorporated into the epoxy-rich matrix.

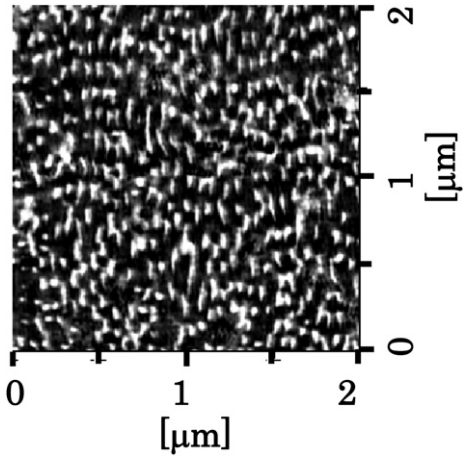

Fig. 6. Phase images by SPM of the PN-cured DGEBA/BCP2 (20 wt %) blend resins, measured at 25 °C.

From the fractured surfaces (Fig. 4) and the viscoelastic properties (Fig. 5), it was clarified that the macro-phase separation occurred in the three epoxy/BCP2 blends cured with DDS, MNA or DMP, where the micrometer-size domains were estimated as epoxy-rich phase dispersed in the BCP-rich matrix. Meanwhile, in the PN-cured epoxy/BCP2 blend, the elastomer (PnBA) -rich nano-cylinders were dispersed in the epoxy-rich glassy matrix (Figs. 4 and 6). As a result, the E′ of the PN-cured blend was clearly higher than other three blends at room temperature (Fig. 5).

Next, the dependence of the molecular weight of the BCPs on the phase structures of the PN-cured epoxy/BCP blends was examined precisely by TEM, as shown in Figs. 7 and 8. Two types of the BCPs (BCP1: Mw = 60,000 and BCP2: Mw = 149,000) were compared in the epoxy blends. The 10 wt% blend of the BCP1 had nano-cylindrical micelles randomly in any direction, as shown in the Fig. 7a. The 20 wt % blend of the BCP1 also gave the random nano-cylindrical micelles (Fig. 7b), though the periodical distance of the nano-micelles was narrower than in the case of 10 wt%. The continuity of the nano-cylindrical micelles of the 20 wt% blend of the BCP1 was higher than that of the 10 wt% blend. This probably caused the relatively low modulus of elasticity of the 20 wt% blend of the BCP1 (Table 3). Meanwhile, the epoxy blends with the BCP2 are shown in Fig. 8. The 10 wt % BCP2/epoxy blend displayed the spherical nano-micelles

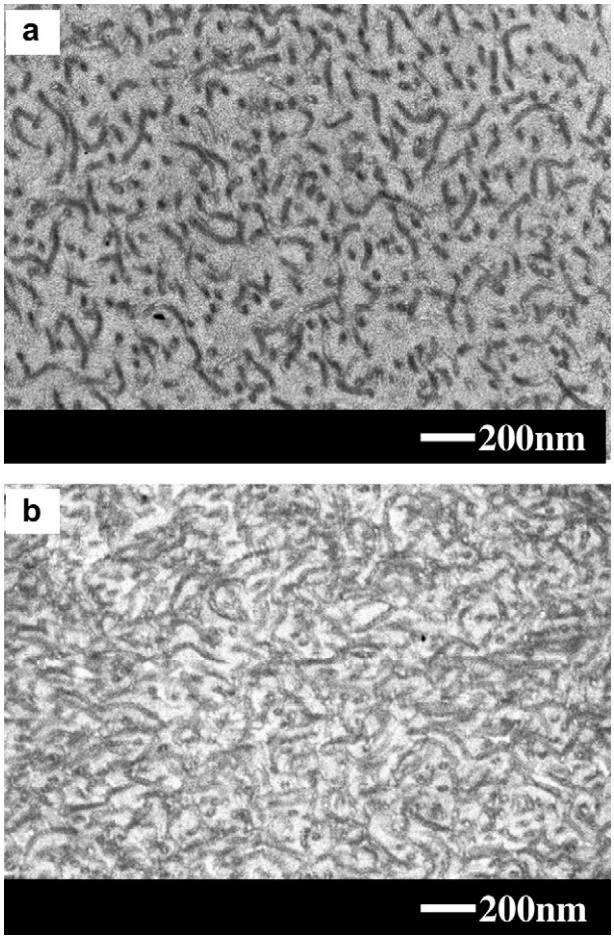

Fig. 7. TEM images of PN-cured DGEBA/BCP1 alloys. Content of the BCP1: (a) 10 wt %, (b) 20 wt %.

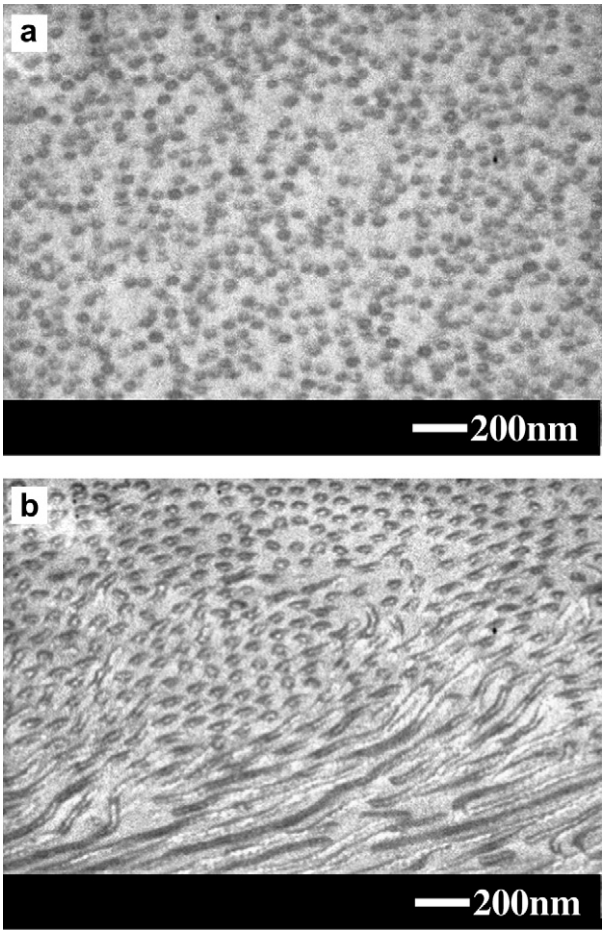

Fig. 8. TEM images of PN-cured DGEBA/BCP2 alloys. Content of the BCP2: (a) 10 wt %, (b) 20 wt %.

(Fig. 8a). In contrast, the 20 wt% BCP2/epoxy blend had the packed nano-cylinders dispersed in the epoxy-rich matrix. Both cross sections and lateral views of the nano-cylinders are seen in Fig. 8b. The inner component of these nano-micelles was estimated as PnBA segments of the BCP.

3.2. Key factor to achieve nano-phase structures in cured blends of epoxy/PMMA-PnBA-PMMA triblock copolymers

In order to assess the miscibility of the PMMA segment in the epoxy resins, the next model tests were conducted while changing the curing agents. Homo PMMA was dissolved in the uncured epoxy resin, and the mixtures were cured with the respective curing agents. Then, the transparency of the cured resins was examined, as shown in Fig. 9. It was found that only the PN-cured epoxy/PMMA blend was transparent, and the other three resins cured by DDS, MNA or DMP were opaque. This means that the PMMA segment was miscible with the PN-cured epoxy resin, but the PMMA segment was immiscible with the DDS-cured, MNA-cured and DMP-cured epoxy resins.

These model experiments indicate that the miscibility between the PMMA segments of the BCP and epoxy/curing agents was a key factor for the nano-phase structures in the cured blends. Namely, the PMMA segments are miscible with the PN-cured epoxy and would prevent the macro-aggregation of the PnBA segments that are immiscible with the PN-cured epoxy. Fig. 10 shows the concept to create the nano-phase structures in the epoxy/BCP blends. When one of the segments (ex.: PMMA in this study) of the BCPs is miscible with the epoxy even in the curing process and the other segments (ex.: PnBA in this study) are immiscible with the epoxy, the self-assembly ability of the BCPs works effectively in the blends. Therefore, the phase sizes of the polymer blends can be controlled in the order of nanometers.

3.3. Fracture toughness of cured epoxy/PMMA-PnBA-PMMA triblock copolymers

Table 3 shows the mechanical properties of the PN-cured epoxy/BCP blends in relation to the concentration (wt %) of the BCPs. The G_{IC} value of the unmodified epoxy resin cured by PN was 116 J/m^2. It was found that the fracture toughness of the epoxy/BCP blends with the nano-cylindrical phases increased dramatically. Namely, the G_{IC} of the 10 wt % BCP2 (Mw = 149,000)/epoxy blend was 1170 J/m^2. The G_{IC} of the 20 wt % BCP2/epoxy blend reached 2200 J/m^2. Moreover, the BCP1 with Mw = 60,000 gave higher G_{IC} (10 wt%: 2320 J/m^2,

Table 3
Critical strain energy release rate; G_{IC}, fracture toughness; K_{IC}, and modulus of elasticity; E of PN-cured epoxy/BCP blends.

No. of BCP	wt % of BCP in cured epoxy	G_{IC} (J/m^2)	K_{IC} (MPa m$^{1/2}$)	E (GPa)
–	0	116	0.64	3.10
BCP1	10	2320	2.49	2.35
BCP1	20	2530	2.37	1.95
BCP2	10	1170	1.87	2.63
BCP2	20	2200	2.51	2.52

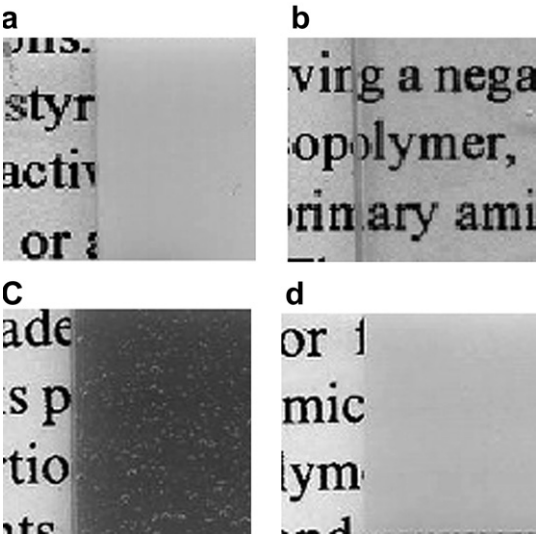

Fig. 9. Overviews of the cured blend resins of epoxy/homo PMMA (20 wt %): (a) cured with DDS; (b) cured with PN; (c) cured with MNA; (d) cured with DMP.

20 wt%: 2530 J/m^2) to the epoxy blends. The G_{IC} of the 20 wt% BCP1/epoxy blend was more than twenty fold relative to the unmodified epoxy resin, and that is equivalent to the toughness of polycarbonates [19]. Fig. 11 shows the fracture surfaces of the epoxy/BCP1 blends observed by SEM. Many cavities in several tens-nanometer sizes were observed on the fractured surfaces. From the SEM photographs in Fig. 11 and the TEM-photographs in Fig. 7, it was recognized that the nano-cavities on the fractured surfaces were derived from the PnBA nano-cylindrical micelles in the epoxy blends. Also, localized yielding of the epoxy-rich matrix around the nano-cavities was observed in Fig. 11.

Yee and co-workers [2–6] have elucidated the toughening mechanisms of the rubber-modified epoxies that have dispersed elastomer phases in micrometer-size. According to these authors, the role of the elastomer phases is to relieve the constraint in front of the crack tip by the cavitation [3–5]. This mechanism alters the stress field from triaxial tensile stress to shear stress in front of the crack tip, which promotes the formation of shear bands in the matrix resin [3–6]. Moreover, Sue et al. have clarified that nano-spheres of BCP with an average diameter of 15 nm were cavitated in the crack tip region of the specimens of DGEBA/PEP-PEO diblock copolymer blends [32]. They mentioned that the cavitation of the BCP phases and the shear banding of epoxy matrix would be the major mechanisms responsible for the significant toughening [32,33].

In this study, the PnBA nano-micelles have elastomeric properties, which would be suitable to produce cavitation under the triaxial tensile stress in front of the crack tip. In fact, many nano-

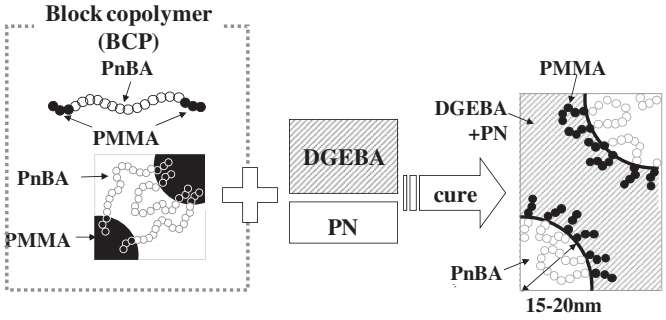

Fig. 10. Schematic illustration of the creation of the nano-phase structures in the epoxy/BCP blends: PMMA segments of the BCPs are miscible with DGEBA/PN, and PnBA segments are immiscible with the DGEBA/PN.

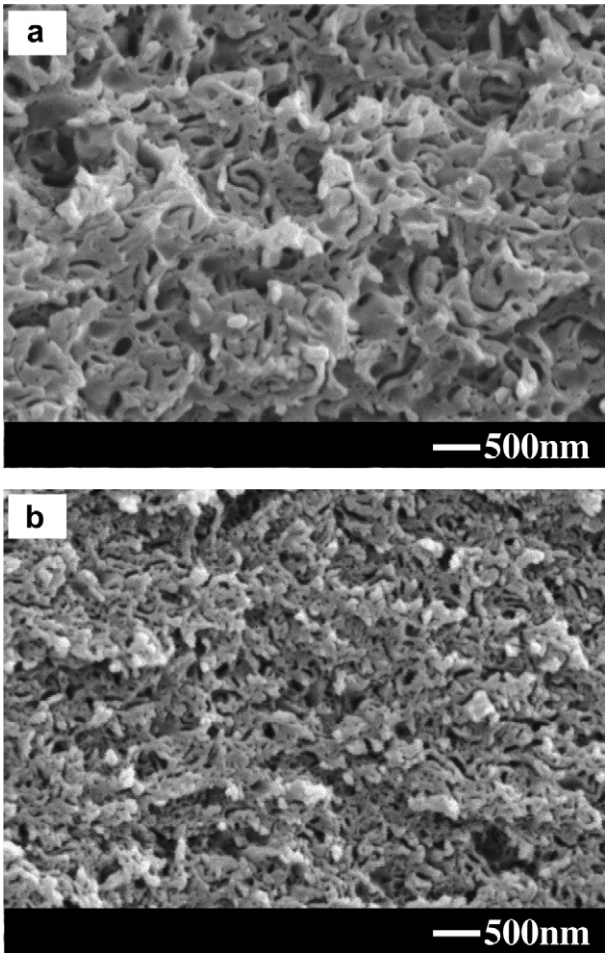

Fig. 11. SEM photographs of fracture surfaces of PN-cured DGEBA/BCP1 alloys. Content of the BCP1: (a) 10 wt %, (b) 20 wt %.

cavities were observed in the PN-cured epoxy/BCP1 blends on the fractured surfaces, irrespective of the amount of the BCP1 (Fig. 11). The change in the stress state by the cavitation of the nano-elastomer phases is considered to be a trigger for the formation of shear deformation of the epoxy-rich matrix. The large amount of plastic shear deformation of the epoxy-rich matrix could be responsible for the absorption of the given strain energy. The detail of the toughening mechanisms, for example on the morphology dependence, will be discussed in future studies.

4. Conclusions

(1) PMMA-*b*-PnBA-*b*-PMMA triblock copolymers synthesized by living anionic polymerization were studied as the toughening modifiers for epoxy resins. The sizes of the phase structures of the epoxy/triblock copolymer blends relied on the curing agents. Namely, aromatic amine (DDS), acid anhydride (MNA) and anionic polymerization catalyst (DMP) gave macro-phase separation in the blends during the curing process. However, a phenol novolac (PN) as the curing agent achieved nano-phase structures in the epoxy blends. The sizes of the spherical phases or cylindrical phases were about 40 nm in diameter, and the main component in the nano-phases was the PnBA of the triblock copolymers.

(2) The miscibility between the PMMA segments of the triblock copolymers and epoxy/curing agents was a key factor in creating the nano-phase structures in the blends.

(3) The epoxy blend including the triblock copolymer had several nano-phases, such as the nano-cylindrical micelles, the spherical micelles, and the aligned cylinders dispersed in epoxy-rich matrix. The morphologies depended on the content and the molecular weight of the PMMA-*b*-PnBA-*b*-PMMA triblock copolymers.

(4) The fracture toughness (the critical strain energy release rate; G_{IC}) of the epoxy/triblock copolymer alloys with the nano-cylindrical phases reached 2530 J/m^2. The fracture toughness was more than twenty fold relative to the unmodified epoxy resin.

References

[1] Kinloch AJ, Shaw SJ, Tod DA, Hunston DL. Polymer 1983;24:1341.
[2] Yee AF, Pearson RE. J Mater Sci 1986;21:2462.
[3] Pearson RE, Yee AF. J Mater Sci 1986;21:2475.
[4] Pearson RE, Yee AF. J Mater Sci 1989;24:2571.
[5] Yee AF, Li D, Li X. J Mater Sci 1993;28:6392.
[6] Kishi H, Shi Y-B, Huang J, Yee AF. J Mater Sci 1998;33:3479.
[7] Bucknall CB, Partridge IK. Polymer 1987;24:639.
[8] Raghava RS. J Polym Sci Part B Polym Phys 1987;25:1017.
[9] Bucknall CB, Gilbert AH. Polymer 1989;30:213.
[10] Cecere JA, Senger JS, McGrath JE, Steiner PA, Wong RS, Sacheva Y. Int SAMPE Symp 1987;32:1276.
[11] Kishi H, Odagiri N. In: Cantor B, Assender H, Grant P, editors. Series in materials science and engineering – aerospace materials. Institute of Physics Publishing; 2001. p. 187 [Chapter 14].
[12] Yamanaka K, Inoue T. Polymer 1989;30:662.
[13] Yamanaka K, Takagi Y, Inoue T. Polymer 1989;60:1839.
[14] Hillmyer MA, Lipic PM, Hajduk DA, Almdal K, Bates FS. J Am Chem Soc 1997;119:2749.
[15] Lipic PM, Bates FS, Hillymer MA. J Am Chem Soc 1998;120:8963.
[16] Mijovic J, Shen M, Sy JW, Mondragon I. Macromolecules 2000;33:5235.
[17] Dean JM, Lipic PM, Grubbs RB, Cook RF, Bates FS. J Polym Sci Part B Polym Phys 2001;39:2996.
[18] Guo Q, Thomann R, Gronski W. Macromolecules 2002;35:3133.
[19] Dean JM, Verghese NE, Pham HQ, Bates FS. Macromolecules 2003;36:9267.
[20] Dean JM, Grubbs RB, Saad W, Cook RF, Bates FS. J Polym Sci Part B Polym Phys 2003;41:2444.
[21] Wu J, Thio YS, Bates FS. J Polym Sci Part B Polym Phys 2005;43:1950.
[22] Ritzenthaler S, Court F, David L, Girard-Reydet E, Leibler L, Pascault JP. Macromolecules 2002;35(16):6245.
[23] Ritzenthaler S, Court F, Girard-Reydet E, Leibler L, Pascault JP. Macromolecules 2003;36(1):118.
[24] Ritzenthaler S, Girard-Reydet E, Pascault JP. Polymer 2000;41:6375.
[25] Maiez-Tribut S, Pascault JP, Soulé ER, Borrajo J, Williams RJJ. Macromolecules 2007;40(4):1268.
[26] Gerard P, Boupat NP, Fine T, Gervat L, Pascault JP. Macromol Symp 2007;256:55.
[27] Rebizant V, Abetz V, Tournihac F, Court F, Leibler L. Macromolecules 2003;36(26):9889.
[28] Rebizant V, Venet A-S, Tournihac F, Tournihac F, Girard-Reydet E, Navarro C, et al. Macromolecules 2004;37(21):8017.
[29] Serrano E, Tercjak A, Ocando C, Larranaga M, Parellada MD, Corona-Galvan S, et al. Macromol Chem Phys 2007;208:2281.
[30] Inoue T, Soen T, Hashimoto T, Kawai H. J Polym Sci 1969;A-2(7):1283.
[31] Matsuo M, Sagae S, Asai H. Polymer 1969;10:79.
[32] Matsen MW, Bates FS. Macromolecules 1996;29:1092.
[33] Liu J, Sue H-J, Thompson ZJ, Bates FS, Dettloff M, Jacob G, et al. Macromolecules 2008;41:7616.
[34] Thompson ZJ, Hillymer MA, Liu J, Sue H-J, Dettloff M, Bates FS. Macromolecules 2009;42:2333.

Polymer 52 (2011) 769–777

Contents lists available at ScienceDirect

Polymer

journal homepage: www.elsevier.com/locate/polymer

Reconsideration of the results of the two dimensional correlation infrared spectroscopic study on water diffusion process in poly(ε-caprolactone) matrix

Mengyin Wang, Peiyi Wu*

The Key Laboratory of Molecular Engineering of Polymers(Ministry of Education) and Department of Macromolecular Science and Laboratory of Advanced Materials, Fudan University, Shanghai 200433, People's Republic of China

ARTICLE INFO

Article history:
Received 29 March 2010
Received in revised form
20 December 2010
Accepted 22 December 2010
Available online 30 December 2010

Keywords:
Simulation
2D correlation spectra
Asynchronous spectrum

ABSTRACT

Two dimensional correlation spectroscopy (2DCOS) is a powerful technique which can enhance spectral resolution and probe a certain sequential order of spectral variations under external perturbation. However, in asynchronous 2D contour maps which provide richer valuable information than synchronous ones, some effects other than real asynchronicity (called spectral effects), such as position shift, band width change and band overlapping, may generate interfering cross peaks. In this paper, we performed a simulation in the region of OH stretching vibration of water to evaluate the contributions of spectral effects on a highly overlapped band and study the dynamic changes of water during diffusion process in poly(ε-caprolactone) (PCL) matrix. From the comparison between experimental and simulated asynchronous 2D correlation spectra, the detailed information on water diffusion process in PCL film can be extracted. It is demonstrated that artificial asynchronous cross peaks in the region of 3670–3570 cm^{-1} are induced by band overlapping and the bound and free water in PCL matrix change simultaneously.

1. Introduction

Generalized two dimensional correlation spectroscopy (2DCOS), introduced by Noda [1] in 1986, is a technique where the spectral intensity is defined as a function of two independent spectral variables. By spreading the original data over the second dimension, the spectral resolution is enhanced, and the features not readily observable in the conventional spectra are emphasized. Moreover, it can probe the specific sequential order of the spectral intensity variations under some certain external perturbations [2]. Owing to these advantages, 2DCOS is an attractive tool to investigate complex or highly overlapped bands.

2DCOS provides a pair of synchronous and asynchronous correlation spectra, which represent the overall similarity of the spectral intensity variations and the differences in dynamic behavior, respectively. The feature of asynchronous spectrum is very useful for resolution enhancement and sequential order determination [3]. However, compared with the synchronous ones, the asynchronous intensities are much easier to be effected by the spectral perturbations, like noise [4]. It has been found that other effects than real asynchronicity (spectral effects, hereafter), such as position shift, width change and band overlapping [5,6], can generate visible asynchronous cross peaks which may mislead the interpretation. Moreover, these spectral effects probably present some meaningful physical changes. For example, a shift of OH stretching band may indicate a change in the hydrogen bond strength. To determine the effect species, simulation approach has been successfully used [7–10]. Simulated spectra can be generated based on the experimental spectra under different hypotheses of spectral effects and provided for 2D correlation analysis. Comparisons between the experimental and simulated 2D correlation spectra can detect the most reasonable hypothesis. The aim of this study is to evaluate the contribution of spectral effects on 2D correlation spectra in a very highly overlapped spectral region. As a typical example, the dynamic changes of OH stretching band during the water diffusion process in PCL matrix have been analyzed.

The diffusion of small molecules through polymer matrix reflects many important properties of polymer materials and is closely related to their applications in different fields, such as packaging, drug delivery, membrane filtration and structural engineering [11–13]. Poly(ε-caprolactone) (PCL) is an attractive biomaterial with hydrophilic carbonyl group, which absorbs water easily. It has been found that the absorbed water on the polymer surface has a crucial influence to the subsequent events [14], which means the existence of water may affect the biocompatibility of the polymer. Therefore, the study on water diffusion in PCL has significant meaning for a better understanding to its biological applications.

During past several decades, various experimental methods have been utilized for diffusion investigations, such as gravimetric

* Corresponding author. Tel.: +86 21 55069652; fax: +86 21 65640293.
E-mail address: Peiyiwu@fudan.edu.cn (P. Wu).

0032-3861/$ – see front matter © 2010 Elsevier Ltd. All rights reserved.
doi:10.1016/j.polymer.2010.12.051

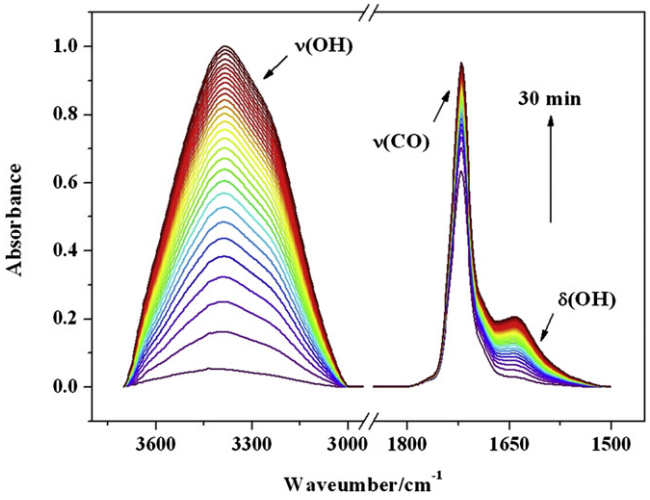

Fig. 1. Time-resolved ATR-FTIR spectra measured during water diffusion in PCL in the range of 3700–3000 and 1800–1500 cm^{-1}.

method [15], Raman spectroscopy [16–18] and even molecular dynamics simulation [19]. For the infrared-active research objects, the utilization of attenuated total reflection Fourier transform infrared (ATR-FTIR) spectroscopy makes good effort [20–23]. However, even by ATR-FTIR, a sensitive tool for hydrogen bonds, the observation of water molecules which have numerous interaction configurations corresponding to the environment remains difficult. Compared to deconvolution of rotational profile of vibrational band, which can increase the accuracy of the analysis [24–26], 2DCOS not only differentiates the highly overlapped bands, but also determines the dynamic changes of water during the diffusion process. According to these advantages, 2DCOS is very suitable for the study on water diffusion through polymer materials.

In this paper, we performed a simulation on a highly overlapped model band in the spectral region of OH stretching vibration to study the dynamic changes of water during diffusion process in PCL matrix. The simulated spectra were constructed from original spectra collected by ATR-FTIR, combined with different hypotheses of spectral effects. In order to extract more detailed information on diffusion process, the experimental spectra were collected with a longer investigated time range and a shorter time interval of measurement than our former studies [22,23]. By the combination method of 2DCOS and simulation, we got an insight into the different states of water molecules in PCL matrix and make a clear understanding of the dynamic diffusion process.

2. Experimental methods

2.1. Materials and samples preparation

Polymer film was prepared by solution casting from the solvent tetrahydrofuran (THF). PCL (CAPA 680, Solvay Co. in Britain, crystallinity 67%, M_W80000) was dissolved in THF at about 80 °C for 1 h to form a homogeneous solution with a concentration of 2%(m/v). After been stirred for 12 h at room temperature, the solution was casted onto a 75 × 25 mm microscope slide. The slide was immediately kept in the vacuum oven at room temperature for about 12 h to remove residual solvent completely. At last, the 75 × 25 mm film with the thickness of 16 μm was peeled off for ATR-FTIR measurement.

2.2. ATR diffusion experiments

The time-resolved ATR-FTIR measurements were carried out at room temperature using a Nicolet Nexus Smart ARK FTIR spectrometer equipped with a DTGS detector and a ZnSe IRE ATR crystal. The PCL film was sandwiched between a ZnSe IRE ATR crystal and a piece of filter paper, and then mounted on the ATR cell. Distilled water was injected into the filter paper; meanwhile, data collection was started by a macro program. Water penetrated through the film toward the ATR crystal. Considering the penetration depth of the light (≈0.5 μm) was much smaller than the thickness of the film (16 μm), the spectra collected by ATR-FTIR were mainly dominated by the water molecules diffusing through the film, rather than the ones absorbed by PCL. The spectra were collected at a resolution of 4 cm^{-1} by accumulating 16 scans. The time interval between two adjacent spectra was about 1 min. The measured spectral range was 4000–650 cm^{-1}, however, for 2D correlation analysis, only the OH stretching band (3700–3000 cm^{-1}) and OH bending band (1675–1600 cm^{-1}) were used.

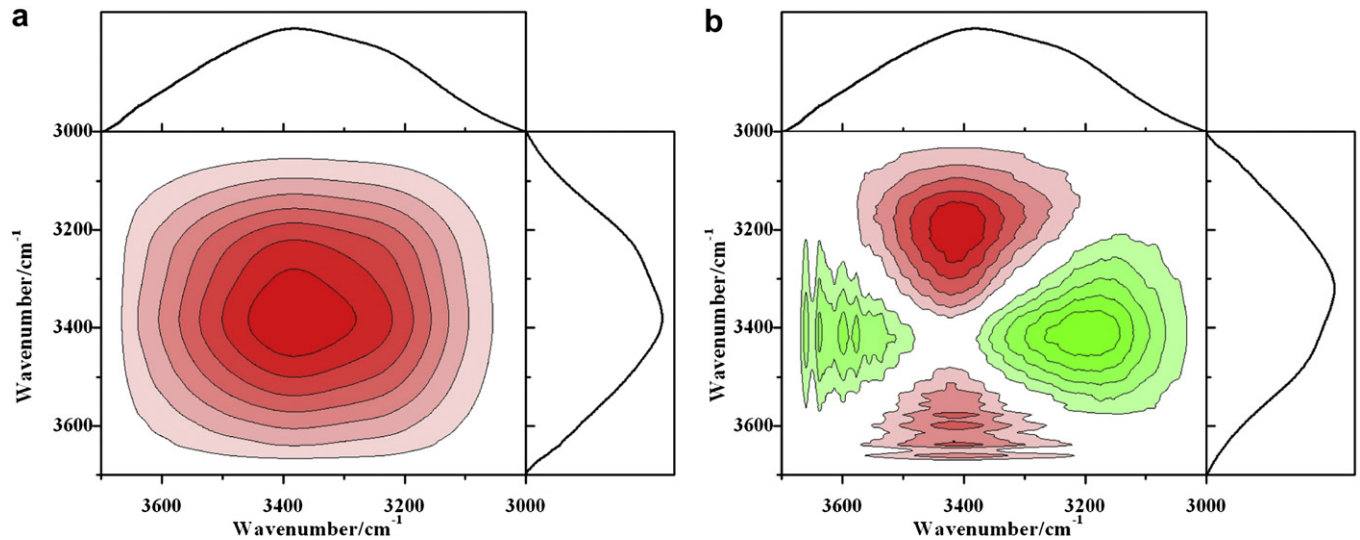

Fig. 2. (a) Synchronous and (b) asynchronous 2DCOS in 3700–3000 cm^{-1} region calculated from the time-resolved ATR-FTIR spectra of water diffusion in PCL film, with ● for positive peaks and ● for negative ones.

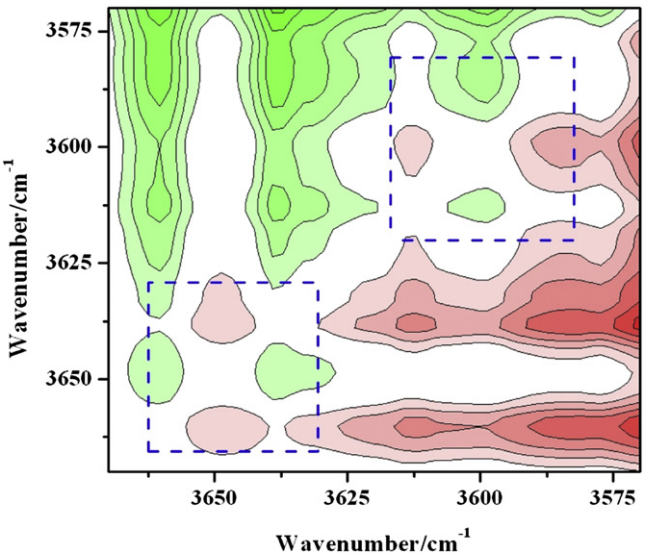

Fig. 3. Asynchronous 2DIR correlation spectra in the 3670–3570 cm^{-1} region calculated from the time-resolved ATR-FTIR spectra of water diffusion in PCL film.

2.3. 2D correlation analysis

Thirty spectra measured at intervals of 1 min were selected for the generalized 2D correlation analysis using the 2D software named 2D Shige (developed by Shigeaki Morita, Kwansei Gakuin University, Nishinomiya, Japan). The average spectrum was used as the reference spectrum. In resultant contour map, 2D correlation spectrum is shown in the center, and the time-averaged 1D spectrum is shown at right side and top. The red and green patterns represent positive and negative correlation intensities, respectively. According to the rules of Noda [3]: (1) a positive synchronous cross peak $\Psi(\nu_1, \nu_2)$ means spectral intensities at ν_1, ν_2 change in the same direction, while a negative one represents the opposite direction; (2)If $\Psi(\nu_1, \nu_2) > 0$, a positive asynchronous cross peak $\Phi(\nu_1, \nu_2)$ means ν_1 changes before ν_2 and a negative one shows ν_2 changes before ν_1. This rule is reversed if $\Psi(\nu_1, \nu_2) < 0$.

2.4. Simulation method

A series of simulated datasets are used for 2DCOS analysis in this study. All the simulated spectra are performed in 3700–3000 cm^{-1}, the wavenumber range of OH stretching vibration of water. Every spectrum is composed of some subbands, whose number and positions were determined from the experimental asynchronous contour plots, the band intensities and bandwidths were left to vary. The shape of all the subbands is Gaussian curves, and the function of the overall simulated spectrum can be expressed as

$$F(x) = \sum_{j=1}^{6} \varepsilon_j L c_j \exp\left[-\frac{(x - x_{0j})^2}{w_j} \cdot 4 \ln 2\right] \quad (1)$$

where ε_j is the absorptivity of the component j and set as 1; L is path length and set as 1; c_j is the concentration of the component j; x_{0j} is the peak position and w_j is the half width (HW) of the jth band. The simulation of c_j follows in an exponential increasing way based on the experiment one dimensional spectra and the resultant PCMW2D spectra, which will be described detailedly later.

The degree of band separation, δ_{ij}, is defined as [27]:

$$\delta = (x_{0j} - x_{0i})\left(\frac{1}{w_i} + \frac{1}{w_j}\right) \quad (2)$$

3. Results and discussion

3.1. ATR-FTIR spectra during diffusion process

Time-resolved ATR-FTIR spectra for the water diffusion in PCL film are shown in Fig. 1. Two bands are present in the range of 3700–3000 cm^{-1} and 1675–1575 cm^{-1} [22], representing the stretching and bending vibration of OH group in water respectively. The characteristic band around 1720 cm^{-1} is assigned to C=O stretching vibration of carbonyl group in PCL [28]. All these signals gradually increased with the diffusion time. More detailed analysis of the interaction between water and PCL is performed through 2DCOS and spectral simulation in the following. Compared to the OH bending vibration (δ(OH)) of water, the intensity of OH stretching vibration (ν(OH)) is stronger and varies more significantly, more appropriate as the main research object in next study.

3.2. Study of the ν(OH) band

Thirty spectra at equal time interval in the range of 3700–3000 cm^{-1} were firstly selected for 2D correlation analysis, and the results are shown in Fig. 2. There is only one positive autopeak

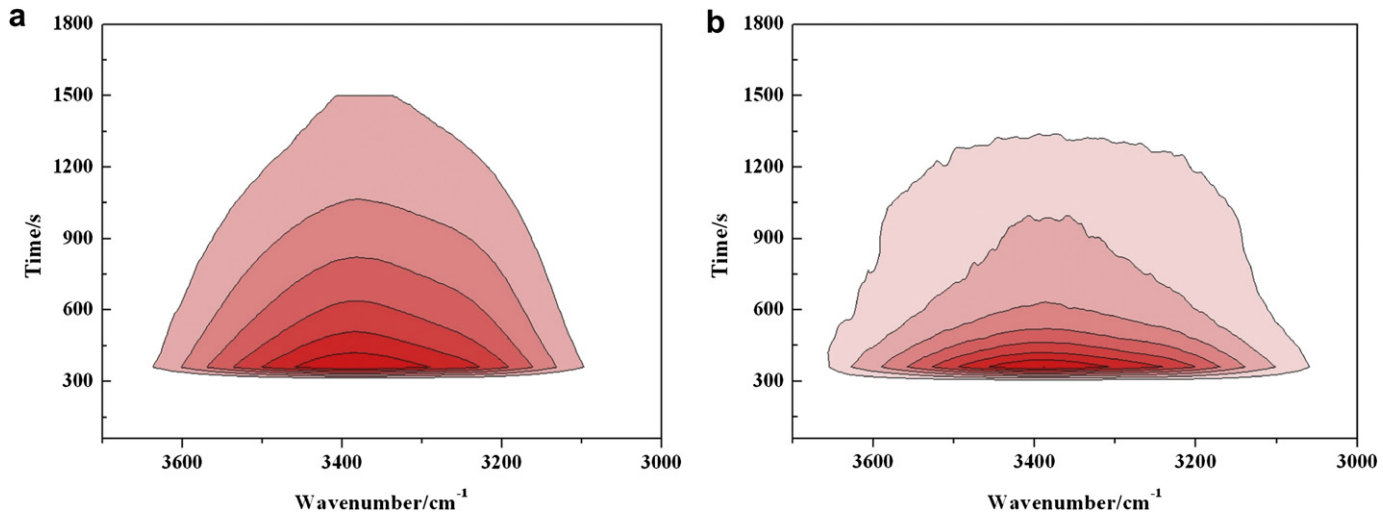

Fig. 4. (a) Synchronous and (b) asynchronous PCMW2D correlation spectra in 3700–3000 cm^{-1} region calculated from the time-resolved ATR-FTIR spectra of water diffusion in PCL.

Table 1
Summary of band position and spectral changes in simulated dataset.

	Peak Position/cm^{-1}	y_0	A	k	Interval of changes
Band I	3185	0.08	0.4	0.08	0–20
Band II	3410	0.1	0.7	0.1	0–20
Band III	3577	0.005	0.01	0.1	5–20
Band IV	3600	0.005	0.01	0.1	5–20
Band V	3637	0.005	0.01	0.1	5–20
Band VI	3660	0.005	0.01	0.1	5–20

located at 3385 cm^{-1} in synchronous correlation spectra (Fig. 2a); however more information can be derived from the corresponding asynchronous correlation spectra (Fig. 2b). From Fig. 2b, there are five cross peaks in the upper left side of the main diagonal line: (3410, 3185 cm^{-1}), (3660, 3410 cm^{-1}), (3637, 3410 cm^{-1}), (3600, 3410 cm^{-1}) and (3557, 3410 cm^{-1}). It indicates that the broad OH stretching band is split into six separate bands located at 3185, 3410, 3577, 3600, 3637 and 3660 cm^{-1}, respectively, which overlap in the 1D ATR-FTIR spectra.

In pure liquid water, 3185 cm^{-1} and 3410 cm^{-1} are assigned to fully hydrogen-bonded water molecules [21], where 3185 cm^{-1} is symmetric OH stretching (ν_s(OH)) band of tetrahedrally coordinated water with strong hydrogen bonding (Type I water, hereafter), and 3410 cm^{-1} is antisymmetric OH stretching (ν_{as}(OH)) band of bulk water that is not fully coordinated (Type II water, hereafter). Two additional bands at 3577 and 3637 cm^{-1} are contributed from ν_s(OH) and ν_{as}(OH) vibrations of bound water (Type III water, hereafter) [22] which has one hydroxyl group participating in hydrogen bonding to other water molecules, whereas the other hydrogen-bonded with the carbonyl groups in PCL. The last two bands 3600, 3660 cm^{-1} may come from the ν_s(OH) and ν_{as}(OH) vibrations of water without or with very weak hydrogen bonding, named by free water (Type IV water, hereafter) [20].

Except for enhancing spectral resolution, 2DCOS also provides useful information on sequential orders of the different water types. According to the rules by Noda [2], the sequence of the spectral changes of these bands mentioned above is as following: 3410 → 3185 → 3577, 3600, 3637, 3660 cm^{-1}. In this system, aggregated water molecules will first diffuse into PCL gradually, and Type I water diffuses more slowly than Type II water because it is larger in size with stronger hydrogen bonds. With time increasing, more and more water molecules are confined in the PCL network and the motion of water molecules is more restricted than before. Parts of them interact with C=O group of PCL to form new hydrogen bonds, as well as to induce the formation of free water along with the breaking of old ones.

The absorption intensities of bulk water are very strong, so the information on the relationship between Type III and Type IV water may be ignored easily. For further investigation, 2D correlation spectra in the range of 3670–3570 cm^{-1} were highlighted. All the synchronous cross peaks are positive and only the asynchronous contour map is shown in Fig. 3. It is interesting that the correlation intensities are very weak, even close to zero, between the ν(OH) bands of bound and free water, whereas, some new cross peaks are

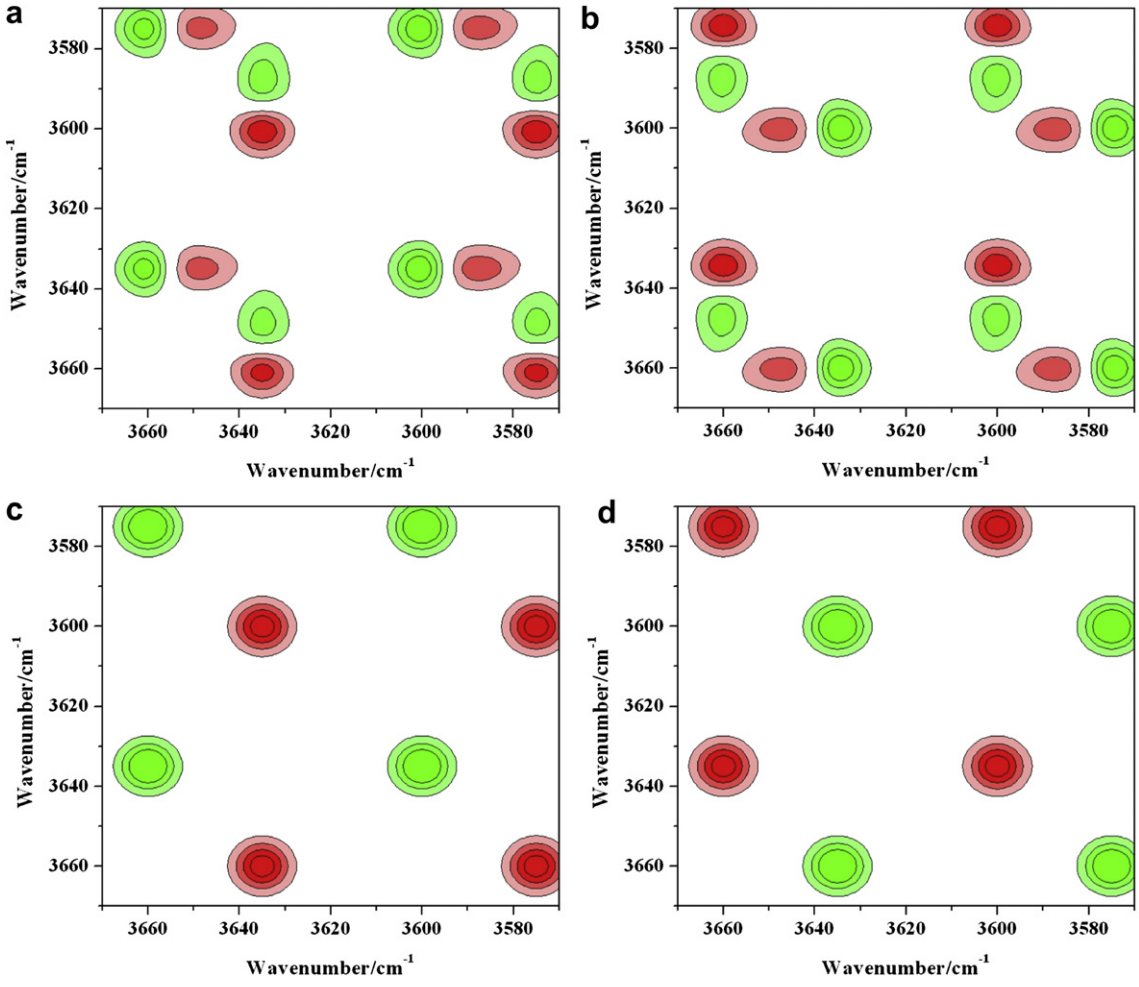

Fig. 5. Asynchronous 2DIR correlation spectra in 3670–3570 cm^{-1} region calculated from (a) Case I, (b) Case II, (c) Case III, (d) Case IV simulated dataset with P of 30%.

significant and emphasized in the dashed line frame, such as the positive cross peak at (3660, 3648 cm^{-1}) and the positive cross peak at (3648, 3637 cm^{-1}) in upper left side of main diagonal line. According to the Noda's rules [3], the ν(OH) vibrations of bound water and free water may change simultaneously and these artifacts were probably caused by certain spectral effects. 3648 cm^{-1} is located between ν_{as}(OH) of bound water (3637 cm^{-1}) and ν_{as}(OH) of free water (3660 cm^{-1}). It may be generated from a certain conversion between the two bands: band position shifts from one component to another or absorption intensity transforms from one to another. The ν(OH) bands are in a highly overlapped spectral region. Bands overlapping can also generate interfering cross peaks in 2DCOS maps [29]. In order to determine which spectral effect caused these artifacts, simulated spectra generated from the experimental spectra and the resultant 2D correlation spectra are used for 2D correlation analysis.

In this study, the concentration variation modes of different components were determined by perturbation-correlation moving-window two dimensional (PCMW2D) correlation spectroscopy, which is an extension of generalized 2DCOS. This new method provides a pair of synchronous and asynchronous 2D correlation spectra which are similar to the perturbation derivative and negative perturbation second derivative of original 1D spectra, respectively [30]. The resultant spectra pair can be used to monitor the spectral variation along the perturbation direction, and are always performed on a plane between a spectral variable (e.g., wavenumber) axis and a perturbation variable (e.g., time) axis. The PCMW2D correlation spectra in the region of 3700–3000 cm^{-1} are shown in Fig. 4. Both synchronous and asynchronous correlation intensities are positive. According to the rules summarized by Morita [30], the intensities of ν(OH) bands changed in a convex increment. So the concentration of the component j, c_j, follows the path defined as:

$$c_j(t) = y_{0j} + A\left(1 - e^{-k_j t}\right) \tag{3}$$

where t is the time variable, from 0 to 20; y_{0j} is the initial concentration, A is the correlation coefficient and k_j is the rate constant.

The simulated spectra are composed of six bands, Band I–Band VI, located at 3185, 3410, 3577, 3600, 3637, 3660 cm^{-1}. As shown in Fig. 1, the initial spectrum in ν(OH) region was asymmetrical, consisting of Type I and Type II water at least. Type I and Type II water dispersed in PCL film at the same time, but Type II varied before Type I, so $k_2 > k_1$. Type III and Type IV water were formed from bulk water later, assuming their rate constants are as same as k_2 with time delay. The value of y_0, A and k is determined by the peak fitting result of the overall ν(OH) profile, using the curve fitting routine provided in the Origin software. All the parameters are listed in Table 1.

As mentioned above, there are two possibilities about the cause of these artifacts: the conversion between bound water and free water, or the band overlapping. In condition without regard to overlap, the

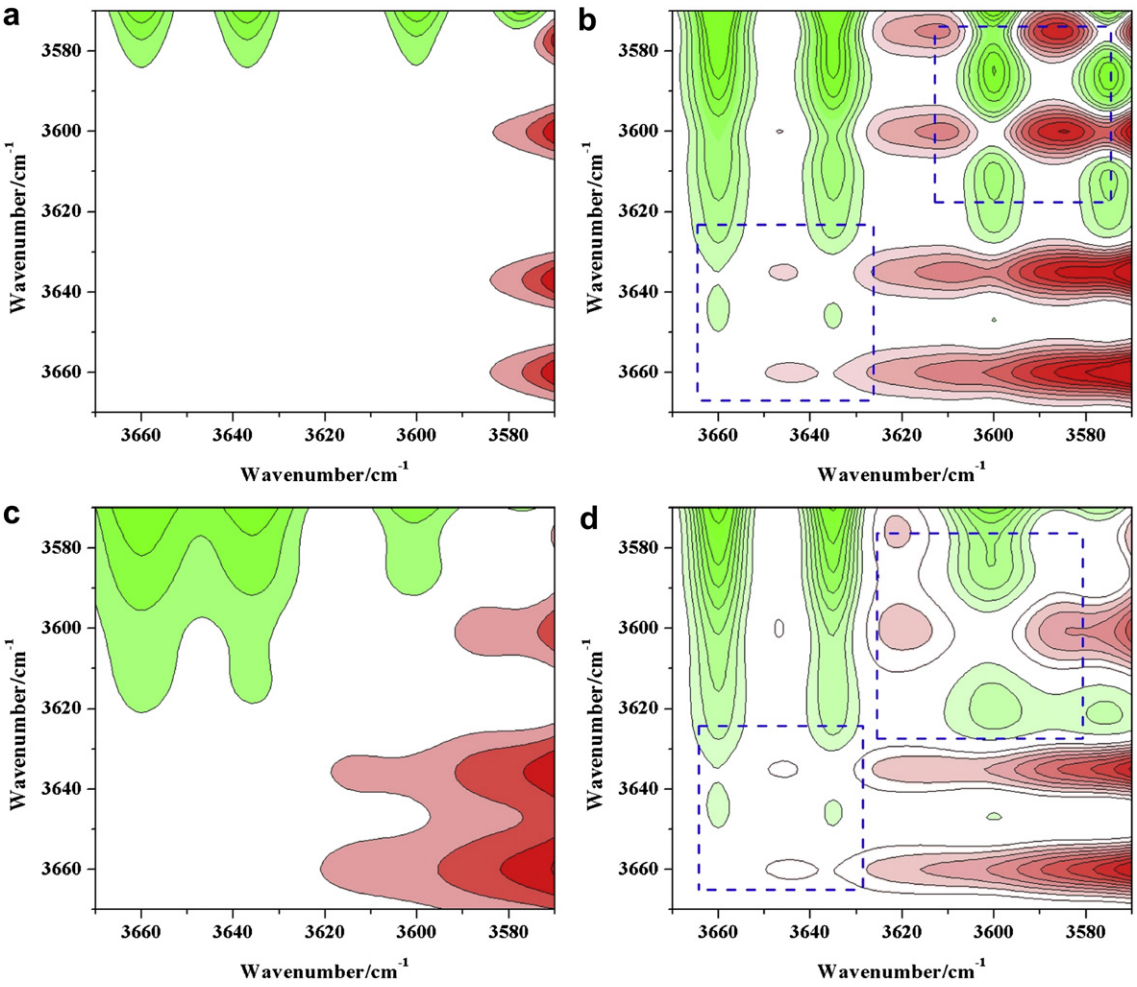

Fig. 6. Asynchronous 2DIR correlation spectra in 3670–3570 cm^{-1} region calculated from (a) Case V, (b) Case VI, (c) Case VII, (d) Case VIII simulated dataset with P of 30%.

effects of conversion were considered first. For OH stretching bands, the band width of water with weaker hydrogen bonds is narrower [20]. The half widths of Band I, II are set as 100 cm^{-1}, and the other fours are 10 cm^{-1} (denoted by: 100–100–10–10–10–10). During diffusion, parts of one water type may transform to the other with a conversion rate denoted as *P*, which induces band shift or intensity transition. Based on 2DCOS and PCMW2D spectra, the intensities of Band III–VI all increased with time, so *P* should follow the way: $c_j(t) < c_j(t+1)\cdot P, P < 56.5\%$. In our study, the value of *P* used for next simulation is 15%, 30% and 45%, respectively. There are four cases of the conversion:

- Case I: Bands of Type III water partly shift to Type IV, in another word, Band III shifts to Band IV and Band V shifts to Band VI, denoted by III → IV;
- Case II: Bands of Type IV water partly shift to Type III, in another word, Band IV shifts to Band III and Band VI shifts to Band V, denoted by IV → III;
- Case III: Bands of Type III water partly transform to Type IV, in another word, absorption intensities transform from Band III to Band IV and from Band V to Band VI, denoted by III↓IV↑;
- Case IV: Bands of Type IV water partly transform to Type III, in another word, absorption intensities transform from Band IV to Band III and from Band VI to Band V, denoted by III↑IV↓.

It should be noted that only the asynchronous 2D maps will be discussed later because all the synchronous contour maps are similar. The 2D correlation spectra calculated from the simulated spectra, in the region of 3570–3000 cm^{-1} and 3570–3000 cm^{-1} vs 3670–3570 cm^{-1}, are similar to the experimental ones and follow the same sequential orders. However, the 2D maps in the 3670–3570 cm^{-1} region are different, especially the asynchronous ones shown in Fig. 5. Fig. 5a and b indicates that band shift with intensity increasing can induce asynchronous cross peaks at (3660, 3648 cm^{-1}), (3648, 3637 cm^{-1}), (3600, 3588 cm^{-1}), (3588, 3577 cm^{-1}), where 3648 and 3588 cm^{-1} are both in the middle of the initial and terminal position of shift (3660/3637 and 3600/3577 cm^{-1}, respectively). If the shift is from low to high wavenumber, the sequential order is:

- 3648 → 3637 → 3660 cm^{-1}
- 3588 → 3577 → 3600 cm^{-1}

If the shift is from high to low wavenumber, the sequential order is:

- 3648 → 3660 → 3637 cm^{-1}
- 3588 → 3600 → 3577 cm^{-1}

As is demonstrated, shift of separated bands with intensity increasing can generate apparent artifacts in asynchronous 2D maps, located in the middle of the initial and terminal position, and the sequential order is:

- Artificial band → initial band → terminal band.

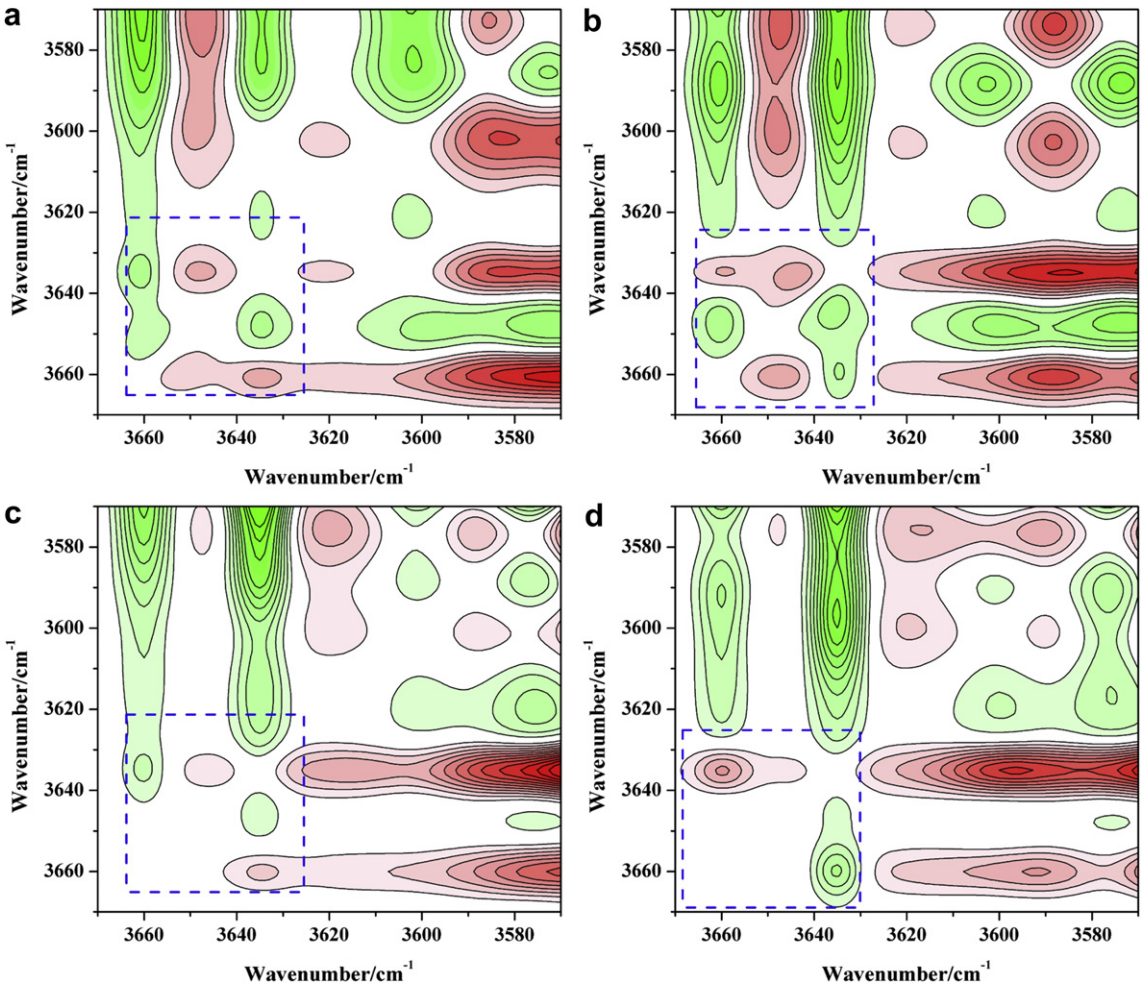

Fig. 7. Asynchronous 2DIR correlation spectra in 3670–3570 cm^{-1} region calculated from (a) Case IX, (b) Case X, (c) Case XI and (d) Case XII simulated dataset with *P* of 30%.

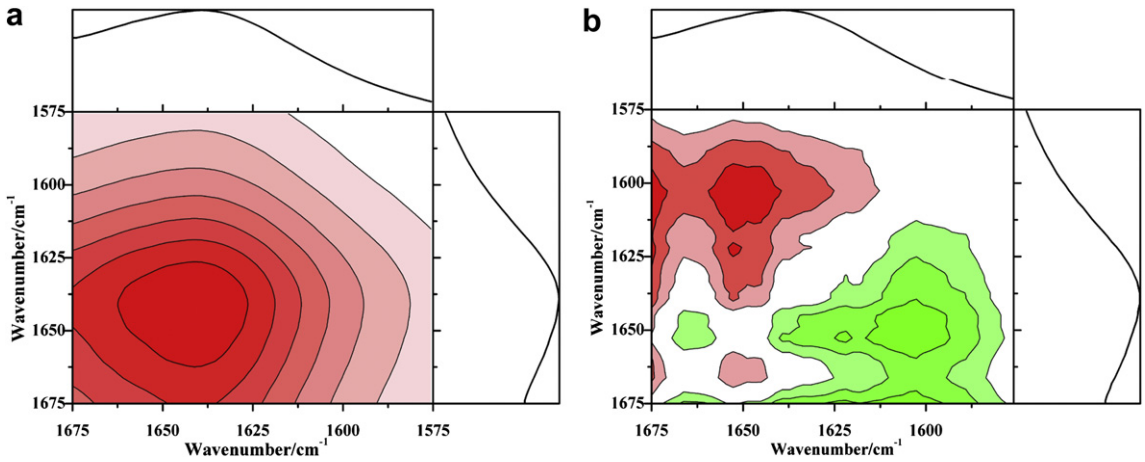

Fig. 8. (a) Synchronous and (b) asynchronous 2DCOS in 1675–1575 cm^{-1} region calculated from the time-resolved ATR-FTIR spectra of water diffusion in PCL film.

As shown in Fig. 5(c) and (d), intensity transition from one to another with intensity increasing can induce apparent correlation peaks between the two bands without artifacts. If the transition is from low to high wavenumber, the sequential order is:

- 3637 → 3660 cm^{-1}
- 3577 → 3600 cm^{-1}

If the transition is from high to low, the sequential order is:

- 3660 → 3637 cm^{-1}
- 3600 → 3577 cm^{-1}

It's demonstrated that intensity transition from two separated bands (A↓B↑) with intensity increasing would not induce any artifacts in asynchronous 2D maps and the sequential order is A → B. The 2D maps generated from simulated spectra with *P* as 15%, 45% are similar to the ones as 30% shown in Fig. 5. Obviously, the asynchronous spectra calculated from case I–IV are all different from the experimental one. In these maps, there are apparent asynchronous cross peaks between the ν(OH) bands of Type III and Type IV water, while the experimental correlation asynchronous intensities are close to zero. So the apparent artificial features in asynchronous 2D maps are more probably due to peak overlapping.

In order to determine the effect of overlap to 2DCOS, four simulated datasets with different half widths are designed. The half widths of six bands are set to:

- (Case V) 100–100–10–10–10–10 cm^{-1}
- (Case VI) 200–200–10–10–10–10 cm^{-1}
- (Case VII) 200–200–20–20–20–20 cm^{-1}
- (Case VIII) 200–200–20–20–10–10 cm^{-1}

The other parameters are same to the ones listed in Table 1 without considering the intensity conversion. Presented in Fig. 6 are the asynchronous 2D contour maps of the simulated spectra, where the ones in Fig. 6b and d are very similar to the experimental one, especially the Case VIII. According to Eq.(2), δ_{56} of Case V, Case VI and Case VIII are same of 4.6, however, there are apparent artifacts located at 3648 cm^{-1} only in Fig. 6b and d. So the artifacts may be induced by overlap between Band II and Band V, VI, because the last two are embedded within Band II if its half width is large enough, such as 200 cm^{-1}. From the comparison between Fig. 6b and Fig. 6c, it's shown that if the width of Band II is fixed at 200 cm^{-1}, the effect of overlapping would decrease with the increase of w_3–w_6, namely δ_{34} and δ_{56}. Among the different simulated datasets, the asynchronous 2D contour map of Case VIII, as shown in Fig. 6d, is the most similar to the experimental results. In Case VIII, Band III–VI are all embedded within the broad Band II and the value of δ_{34} is smaller than that of δ_{56}, so the interference of broad Band II on Band V and VI is greater and the artificial peaks between Band V and VI are more apparent. The simulation result indicates that band overlapping is the main cause of these artificial peaks.

If the conversion between bound water and free water existed in a highly overlapped spectral region, which kind of 2D correlation

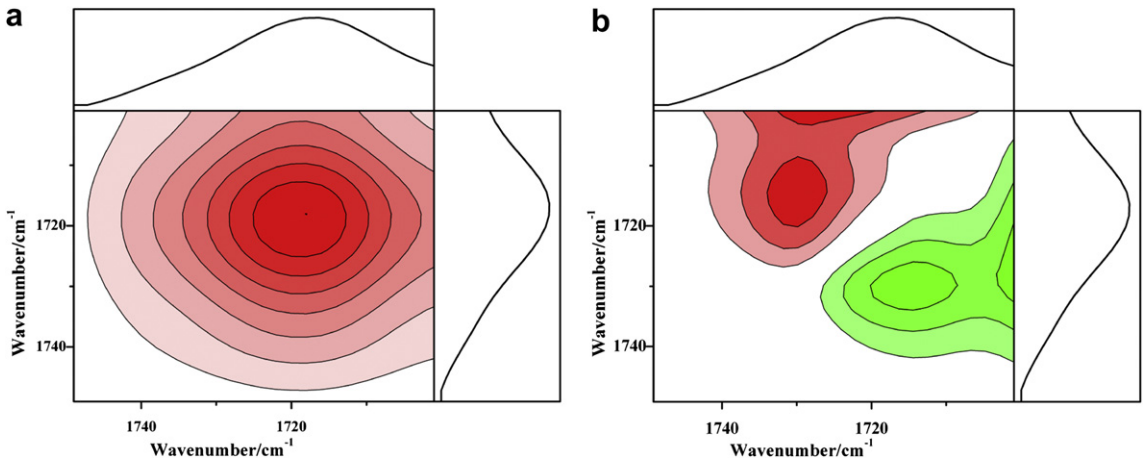

Fig. 9. (a) Synchronous and (b) asynchronous 2DCOS in 1750–1700 cm^{-1} region calculated from the time-resolved ATR-FTIR spectra of water diffusion in PCL film.

spectra would be performed? In order to solve this problem, a series of simulated spectra, Case VIIII–XII, are designed with the same conversion conditions as Case I–IV and the same spectral parameters as Case VIII. The results calculated from different value of *P*, 15%, 30% and 45%, are very similar, so only the asynchronous 2D correlation spectra with *P* of 30% are performed in Fig. 7 and the patterns highlighted in dashed line frame will be studied. As shown in Fig. 7a and b, there are artifacts at (3660, 3648 cm^{-1}), (3648, 3637 cm^{-1}) caused by highly overlapped bands shift and cross peaks at (3660, 3637 cm^{-1}). The sequential orders agree well with the rules mentioned above:

- Artificial band → initial band → terminal band.

As presented in Fig. 7c and d, with the absorption intensity transition from one to another, the interference of overlap on asynchronous peaks is weaker, while the correlation peaks at (3660, 3637 cm^{-1}) are well-marked. The sequential order in Case XI is 3637 → 3660 cm^{-1}, and in Case XII is reversed, both following the rules summarized before. The conversion between two bands at 3637 and 3660 cm^{-1} in a highly overlapped spectral region can induce asynchronous correlation peak at (3660, 3637 cm^{-1}), while in experimental 2D map, the value of Ψ(3660, 3637 cm^{-1}) is very small, even close to zero. So there may be no conversion between Type III and Type IV water. Bound water and free water are generated simultaneously with the formation of the new hydrogen bonds with PCL and the breaking of the old ones of bulk water.

3.3. Study of the δ(OH) band

Compared to the ν(OH) absorption band, the δ(OH) band at 1675–1575 cm^{-1} varies not very significantly. However, much

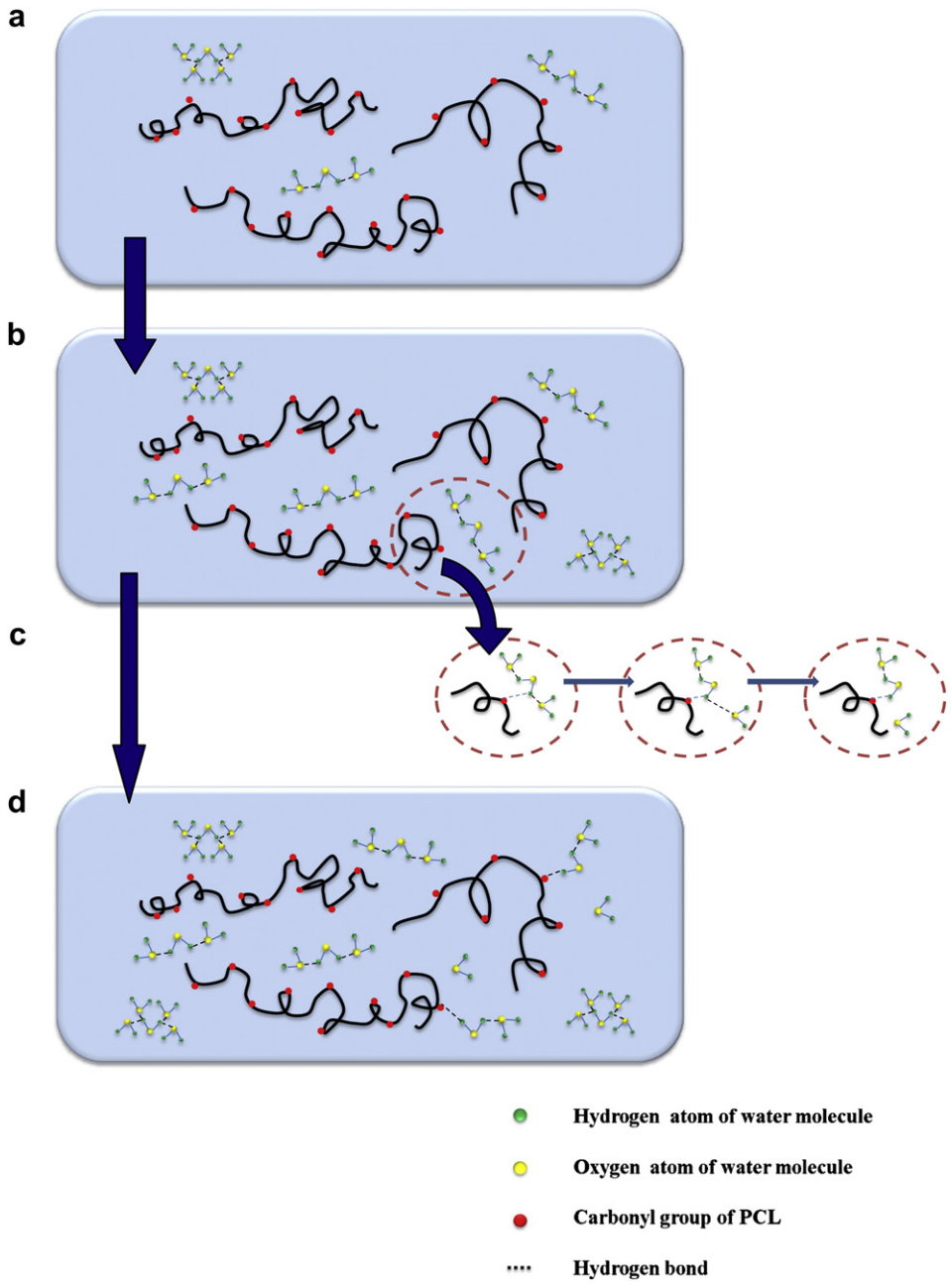

Scheme 1. Schematic diagram of water diffusion process in PCL at the interface contacted with ATR crystal.

useful information can be derived from this spectral region with the help of 2DCOS. There is only one auto peak at 1642 cm^{-1} in synchronous 2DCOS (Fig. 8a), while the asynchronous contour map (Fig. 8b) is information-rich. There is one positive cross peak at (1666, 1652 cm^{-1}) and two negative cross peaks at (1652, 1621 cm^{-1}), (1652, 1604 cm^{-1}) in the upper left of main diagonal line in Fig. 8b. It demonstrates that the δ(OH) band is composed of four bands with the position at 1666, 1652, 1621 and 1604 cm^{-1}, assigned to four different states of water molecules, respectively. As is well-known, when the strength of hydrogen bonds increases, the δ(OH) band of water will shift to a higher wavenumber [31]. Thus, 1666 cm^{-1} can be attributed to bulk water with strong hydrogen bonds, Type I water; 1652 is assigned to bulk water with moderate hydrogen bonds, Type II water; the band at 1621 cm^{-1} reveals Type III water, hydrogen-bonded with PCL and the last one, 1604 cm^{-1}, indicates Type IV water, the free water. The sequential order from 2DCOS is 1652 → 1666 → 1621, 1604 cm^{-1}, namely Type II → Type I → Type III, IV, as same as the result generated from ν(OH) band. Because the overlapping of δ(OH) bands is not very high, there are no visible artificial asynchronous cross peaks in the region of 1625–1600 cm^{-1}, the δ(OH) vibrations of Type III and Type IV water.

3.4. Study of the ν(C=O) band

As shown in Fig. 1, the intensity of the sharp band around 1720 cm^{-1} increased gradually with time, indicating that the hydrophilic group C=O associated with water during the diffusion process. The 2D correlation spectra shown in Fig. 9 provide us an insight into the diffusion process. The positive synchronous and asynchronous peaks at (1729, 1718 cm^{-1}) demonstrate the intensity of 1729 cm^{-1} changes prior to 1718 cm^{-1}. The ν(C=O) at a higher wavenumber presents a lower crystallinity degree [32], so the band at 1729 cm^{-1} may be assigned to an imperfect crystalline phase, while the other one is due to a well-ordered crystalline phase. It is proposed that little molecules do not diffuse through the crystalline phase in a semi-crystalline polymer [33]. Consequently, water molecules may diffuse into an imperfect crystalline region (1729 cm^{-1}) firstly, and then into a more ordered crystalline phase (1718 cm^{-1}). During the diffusion process, water molecules penetrate more easily though a loose amorphous region than a pack crystalline phase.

4. Conclusion

In this work, simulation has been used to study the spectral effects in the highly overlapped ν(OH) variation region of water during diffusion into PCL. The diffusion process was investigated by time-resolved ATR-FTIR combined with generalized 2DCOS. We figured out that there were at least four water types and the sequence of their intensity changes is: bulk water with moderate hydrogen bonds (Type II water) → bulk water with strong hydrogen bonds (Type I water) → bound water (Type III water), free water (Type IV water).

The simulation results indicated that the main cause of these asynchronous artifacts in the middle of ν_s(OH) bands or ν_{as}(OH) bands of bound and free water was band overlapping and there was no obvious conversion between bond and free water along with the water diffusion, that is to say, the spectral intensities of Type III and Type IV water in stretching model changed simultaneously.

The diffusion mechanism of water in PCL matrix is described in Scheme 1. From 2D correlation analysis and spectral simulation, the following conclusion can be drawn:

- Water molecules at first dispersed into PCL matrix and formed hydrogen bonds with carbonyl groups of PCL.
- Type II water with weaker hydrogen bonding diffused faster than Type I water.
- With the formation of new hydrogen bonds between water molecules and PCL, the hydrogen bonds of bulk water were broken. So the bound water and free water were generated simultaneously.
- Water preferred penetrating through the amorphous regions to diffusing into the crystalline phase of the PCL.

Acknowledgments

We gratefully acknowledge the financial support from National Science Foundation of China (NSFC) (20934002, 51073043), the National Basic Research Program of China (No. 2009CB930000). Valuable experimental data supported by Peng Yun is gratefully acknowledged.

References

[1] Noda I. Bull Am Phys Soc 1986;31(3):520–52.
[2] Noda I, Dowrey AE, Marcott C, Story GM, Ozaki Y. Appl Spectrosc 2000;54 (7):236A–48A.
[3] Noda I. Appl Spectrosc 1993;47(9):1329–36.
[4] Czarnecki MA. Appl Spectrosc 2003;57(8):991–5.
[5] Czarnecki MA. Appl Spectrosc 1998;52(12):1583–90.
[6] Czarnecki MA. Appl Spectrosc 2000;54(7):986–93.
[7] Arrondo JLR, Iloro I, Aguirre J, Goni FM. Spectr-Int J 2004;18(1):49–58.
[8] Iloro I, Pastrana-Rios B. J Mol Struct 2006;799(1–3):153–7.
[9] Pastrana-Rios B. J Mol Struct 2006;799(1–3):163–7.
[10] Shashilov VA, Lednev IK. J Am Chem Soc 2008;130(1):309–17.
[11] Ouattara B, Simard RE, Piette G, Begin A, Holley RA. J Food Sci 2000;65 (5):768–73.
[12] Bell CL, Peppas NA. Biomaterials 1996;17(12):1203–18.
[13] Wang YG, Combe C, Clark MM. J Membr Sci 2001;183(1):49–60.
[14] Tanaka M, Mochizuki A, Ishii N, Motomura T, Hatakeyama T. Biomacromolecules 2002;3(1):36–41.
[15] Rodriguez O, Fornasiero F, Arce A, Radke CJ, Prausnitz JM. Polymer 2003;44 (20):6323–33.
[16] Wolfs I, Desseyn HO. Spectrochim Acta A 1996;52(11):1521–8.
[17] Balabin RM. Phys Chem Chem Phys 2010;12(23):5980–2.
[18] Balabin RM. J Phys Chem Lett 2010;1(1):20–3.
[19] Mozaffari F, Eslami H, Moghadasi J. Polymer 2010;51(1):300–7.
[20] Sammon C, Mura C, Yarwood J, Everall N, Swart R, Hodge D. J Phys Chem B 1998;102(18):3402–11.
[21] Xiaohua Y, John P. J Polym Sci Part B Polym Phys 2002;40(10):980–91.
[22] Peng Y, Wu PY, Siesler HW. Biomacromolecules 2003;4(4):1041–4.
[23] Peng Y, Wu PY, Yang YL. J Chem Phys 2003;119(15):8075–9.
[24] Western CM. PGOPHER, A Program for simulating Rotational Structure. University of Bristol. http://pgopher.chm.bris.ac.uk.
[25] Balabin RM. J Phys Chem A 2009;113(6):1012–9.
[26] Balabin RM. J Phys Chem A 2009;113(17):4910–8.
[27] Fleissner G, Hage W, Hallbrucker A, Mayer E. Appl Spectrosc 1996;50(10): 1235–45.
[28] Wang J, Cheung MK, Mi Y. Polymer 2002;43(4):1357–64.
[29] Yu Z, Wang Y, Liu J. Appl Spectrosc 2005;59(3):388–91.
[30] Morita S, Shinzawa H, Noda I, Ozaki Y. Appl Spectrosc 2006;60(4):398–406.
[31] Kusanagi H, Yukawa S. Polymer 1994;35(26):5637–40.
[32] Unger M, Morita S, Sato H, Ozaki Y, Siesler HW. Appl Spectrosc 2009;63 (9):1034–40.
[33] Schlotter NE, Furlan PY. Polymer 1992;33(16):3323–42.

Polymer 52 (2011) 778–785

Contents lists available at ScienceDirect

Polymer

journal homepage: www.elsevier.com/locate/polymer

Polymer nanoparticle-based porous antireflective coating on flexible plastic substrate

Hao Jiang, Weizhou Zhao, Chaolong Li, Yuechuan Wang*

State Key Lab of Polymeric Materials Engineering, College of Polymer Science and Engineering, Sichuan University, Chengdu 610065, People's Republic of China

ARTICLE INFO

Article history:
Received 2 July 2010
Received in revised form
6 December 2010
Accepted 16 December 2010
Available online 23 December 2010

Keywords:
Antireflective
Polymer nanoparticles
Nanoporous film

ABSTRACT

Increased using of plastic optical elements has generated a need for applying antireflection coatings onto plastic substrates. In this paper we reported a facile method to preparing porous thin films on plastic substrates by spin-casting poly (methyl methacrylate) (PMMA)/polystyrene (PS) mixed latices, followed by selectively removing PS particles. The refractive index of the porous coating is directly related to its porosity which could be controlled by varying mixing fraction of the sacrificial PS particles. The obtained porous thin films exhibited excellent anti-reflective (AR) performance over visible range with minimum reflection of 0.02%. The powerful control on refractive index and the versatility of this method makes it practicable to prepare antireflective coating on various plastic substrates with optimal performance.

1. Introduction

Porous materials possess unique surface, structural, and bulk properties that are desired for important uses in various fields including separation, catalysis, sensor, optics, and photovoltaic. One promising use of porous material in optics is serving as single antireflective (AR) layer to increase light transmission and to avoid the formation of "ghost images" on optical substrates.

Various techniques have been explored to prepare porous materials for AR purpose. Many of them involve a subtractive step in which sacrificial material contained in a pre-deposited solid matrix is either burned out [1,2] or etched out by chemicals [3–8] to yield porous structure. Others utilize layer-by-layer deposition of polyelectrolytes [9] and block copolymer micelles [10]. Particularly, this sequential deposition process could produce uniform porous coating over large-area on highly textured surface with precise control over thickness and porosity. Constructing porous film using nanoparticles as building blocks is more efficient and provides means to manipulate porous structure. Various studies have shown that nanoparticle AR coatings can be built up by electrostatic deposition [11–17], convective assembly [18–20], and spin-casting [21,22]. Among these techniques, electrostatic deposition has been demonstrated to be powerful in fabricating porous structure and AR property control, although multi-cycle deposition steps are needed. With the above mentioned methods, porous films with low refractive indices (typically about 1.22) and film thickness in the range 80–150 nm (about a quarter of the visible light wavelength) are now able to be prepared and show excellent AR performance in the visible range.

Although there have been so many techniques developed for preparation of porous AR coating, however, few of them are applicable to plastic substrates. Plastics, such as poly(methyl methacrylate) (PMMA), poly(ethylene terephthalate) (PET) and polycarbonate (PC), due to their suitability for mass-production, light weight, low cost and toughness, have already displaced glass materials in many optical devices, e.g. flexible display, light emitting diode and organic photovoltaic devices. Extensive using of plastic materials for fabrication of optical components makes AR coating for plastics highly desirable to fulfill their optical function. On the other hand, the physical properties of plastics are constrained mainly by their chemical structures, which seriously limit their stability to heat, organic solvents, oxidation, and ionizing radiation. Most of plastics will melt or decompose when heated to a few hundred degrees Celsius. As a consequence, the subtractive techniques involving high temperature burning or chemical solvent etching are unsuitable for plastic substrates. Aqueous-based layer-by-layer assembly process is harmless to plastics and has been used to deposit nanoporous AR coating on plastic substrate [9,23]. One of the drawbacks associated with this technique is the repeated deposition of polyelectrolyte with rinsing and drying that makes the process complicated and time-consuming. Also, the plastic substrates need to be first treated with plasma or corona to

* Corresponding author. Fax: +86 2885405243.
E-mail address: wangyc@scu.edu.cn (Y. Wang).

0032-3861/$ – see front matter © 2010 Elsevier Ltd. All rights reserved.
doi:10.1016/j.polymer.2010.12.036

enhance the surface hydrophilicity. As to other techniques [19–21] used for glass substrates, their practical applicability to plastic substrate is still in question.

Instead of single-layer porous AR coating, multi-layer inorganic AR coating could be used. Assisted by plasma ion [24–27], coating temperature during vacuum deposition process could be greatly reduced so that multi-layer inorganic AR coatings can be deposited on plastic substrate. However, the significant difference in thermal expansion coefficient between the inorganic coating and plastic substrate will cause delamination and crack defects when surrounding temperature changes greatly. Also, it is still an open question that exposing plastics to high-energy radiation may or may not degrade polymers and change their refractive index. As a solution to this problem, "moth-eye structure" can be fabricated by directly etching polymeric substrate [28,29] or by UV or hot embossing from mother board [30–33]. Except the energy-consuming drawback, these procedures are difficulty to scale up. From the standpoint of practical applicability, efficient and scalable method suitable to prepare AR coatings on plastic substrates coupled with minimal substrate pretreatment is still lacking. Therefore, it is still a challenge to build AR coating on plastic substrates.

We have reported fast and facile preparation of single-layer nanoparticle AR coating on glass substrate by spin-casting PMMA latex particles with average size of 111 nm [22]. Optical transmittance of both sides coated glass slide was improved from 91% to 99.5%. The whole process will not do any damage to plastic substrate, and the deposited polymer nanoparticles are compatible with plastic substrate. So our method is applicable and most suitable for AR coating on plastic substrates. However, AR performance of nanoparticle coating is related with the packing structure and the size of nanoparticles used [20,21]. To locate reflectance minima in the visible range, particle coating thickness should be in the range of 80–150 nm. If using small nanoparticles (e.g. 40 nm), multi-layer stacking structure is needed, which leads to poor AR performance resulted from dense packing of nanoparticles; if large nanoparticles (e.g. 120 nm) were used, monolayer packing structure is required. In the latter case, variation of particle packing density will alter both the effective n and thickness, making it difficult to tune both of them to the desired value at the same time. Moreover, red shift of reflectance minima needs larger nanoparticles, which increases the risk of light scattering and impair AR performance.

To overcome this limitation associated with nanoparticle AR coating, in this work we prepared single-layer porous AR coating by spin-casting PMMA/PS binary polymer latex particles on PMMA substrate. The PMMA nanoparticles were used to form porous skeleton structure, while the PS particles were used as porogen to control the porosity. By this way, the porosity, therefore the refractive indices, of the resulted porous coating can be tailored to the optimal value required to realize zero reflection for PMMA substrate. Moreover, since both the coating and substrate are composed of the same polymeric material, coating defects, such as delamination and crack, are no longer existed. Experimental details, structure and optical properties of the porous AR coating are presented in the following sections.

2. Experimental section

2.1. Materials

Methyl methacrylate (MMA), styrene (St), potassium persulfate, sodium dodecyl sulfate (SDS) and cyclohexane were purchased from Shanghai Chemical Company China. MMA and St were purified by passing through activated basic alumina (Shanghai Chemical Company, China) prior to use. PMMA sheets were purchased from Leshan Fscreen Optical Material Co. Ltd., Sichuan, China.

65 nm PMMA and 44 nm PS latex nanoparticles were prepared by macroemulsion polymerizations. The typical procedure was as follows: 50 g of purified monomer, 2.4 g of SDS and 200 g of deioned water were added to a 500 mL three-necked flask equipped with a condenser and a thermometer. A coarse dispersion was formed by mechanical stirring for 30 min at room temperature. Immediately afterward, 0.1 g of potassium persulfate dissolved in 5 g of distilled water was added and the emulsion polymerization was carried out at 75 °C under nitrogen protection for 5 h. PMMA was crosslinked by 5 wt.% (relative to MMA) ethylene glycol dimethacrylate (EGDMA). The resulting latices were filtered with a sintered glass funnel and diluted to the required concentrations with deioned water.

21 nm average-sized PMMA nanoparticles were prepared by differential microemulsion polymerization [34,35]. 2.8 g of SDS and 150 g of deioned H_2O were added to a 500 mL three-necked flask equipped with a condenser and a thermometer. The flask was heated to 80 °C in silicone oil bath while deaerated with nitrogen. 0.2 g of KPS and 0.2 g of $NaHCO_3$ were dissolved in 3 g of H_2O and then introduced into flask followed by dropwisely adding 6 g of MMA in 20 min. 20 min after the adding of 6 g MMA, a mixture composed of 28 g of MMA 2 g of EGDMA and 0.68 g of pentanol was added in the same way in 2 h. The polymerization lasted for 3 h after completing monomer addition. Obtained PMMA latex was filtrated with a sintered glass funnel. Solid content of PMMA latex was 18.3% after filtration.

2.2. Methods

Spin-casting was carried out with a KW-4A spin coater (purchased from the Institute of Microelectronics, Chinese Academy of Sciences, Beijing) using aluminum chuck in a dust-free clean room. The total weight and concentration of polymer latices were fixed at 10 g and 10 wt.%, respectively. PMMA/PS binary latices with different mixing ratios were prepared as follows: First calculated amount of deioned water and 0.3 g SDS were added to PMMA latex placed in a 50 mL beaker, and stirred to form homogeneous mixture. PS latex was then added dropwisely, and kept stirring for a further 30 min to sufficiently mix the two latices. PMMA slices, 30 × 30 × 1 mm in size, were ultrasonic cleaned in ethanol for 10 min, then rinsed with deioned water and dried under clean nitrogen flow. The latex mixture was applied to the PMMA slides through a syringe mounted with a 0.45 μm filter head. As coated PMMA slides were sequentially immersed in 50 °C deioned water and 70 °C cyclohexane for 2 min to remove post-added SDS and PS particles, respectively. In the heating step, coated samples were heated at 100 °C for 30 min. To prevent PMMA substrate suffer from serious deformation, samples were held by wooden clamps and vertically hanged in the oven. Cleaning test was carried out with a 100 W ultrasonic cleaner (KQ2200E, Kunshan ultrasonic instrument Corporation). The tested samples were immersed in deioned water bath and horizontally fixed at 5 cm above the container bottom with the coated side facing down.

2.3. Characterization

Nanoparticle diameters were measured with a Brookhaven BI-200SM light scattering system at an angle of 90° (Brookhaven Instruments Corporation). Reflection spectra were recorded with a UV–Vis double beam spectrophotometer (model Specord 50, Analytik Jena AG) and with the 7° reflection attachment. To eliminate the backside reflection of the substrate, the other side of

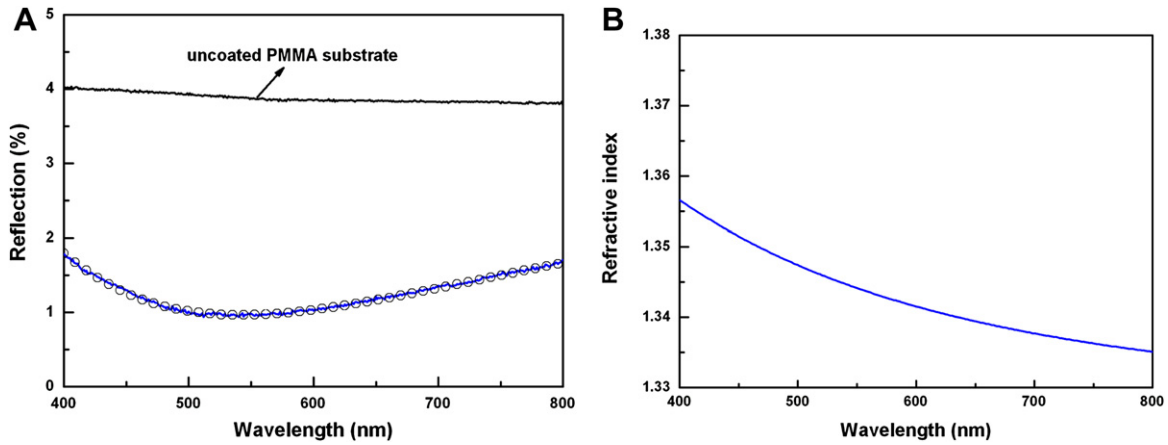

Fig. 1. A. Reflection spectra of PMMA slice spin-coated with 65 nm average-sized PMMA nanoparticles at 3000 rpm. Open symbols represent the calculated reflection of thin film with refractive index of 1.347 and a thickness of 101 nm; B. Cauchy type dispersion curve of 65 nm average-sized PMMA nanoparticle coating measured by spectroscopic ellipsometer.

PMMA slice was abraded with sand paper and then painted in black. Five samples were prepared under the same conditions. For each sample, reflectance was measured three times at three different places. The surface and cross section of the top morphology of the PMMA-particle coatings were characterized using AFM (Model Nanoscope IIIa Dimension 3100 system) and by SEM (XL30 ESEM FEG (FEI Company, US)). Thickness and refractive indices were measured using a M-2000V ellipsometer (J. A. Woollam Co., Inc.). Measurements were done over 200–1000 nm at 65°, 70° and 75° angle of incidence, respectively.

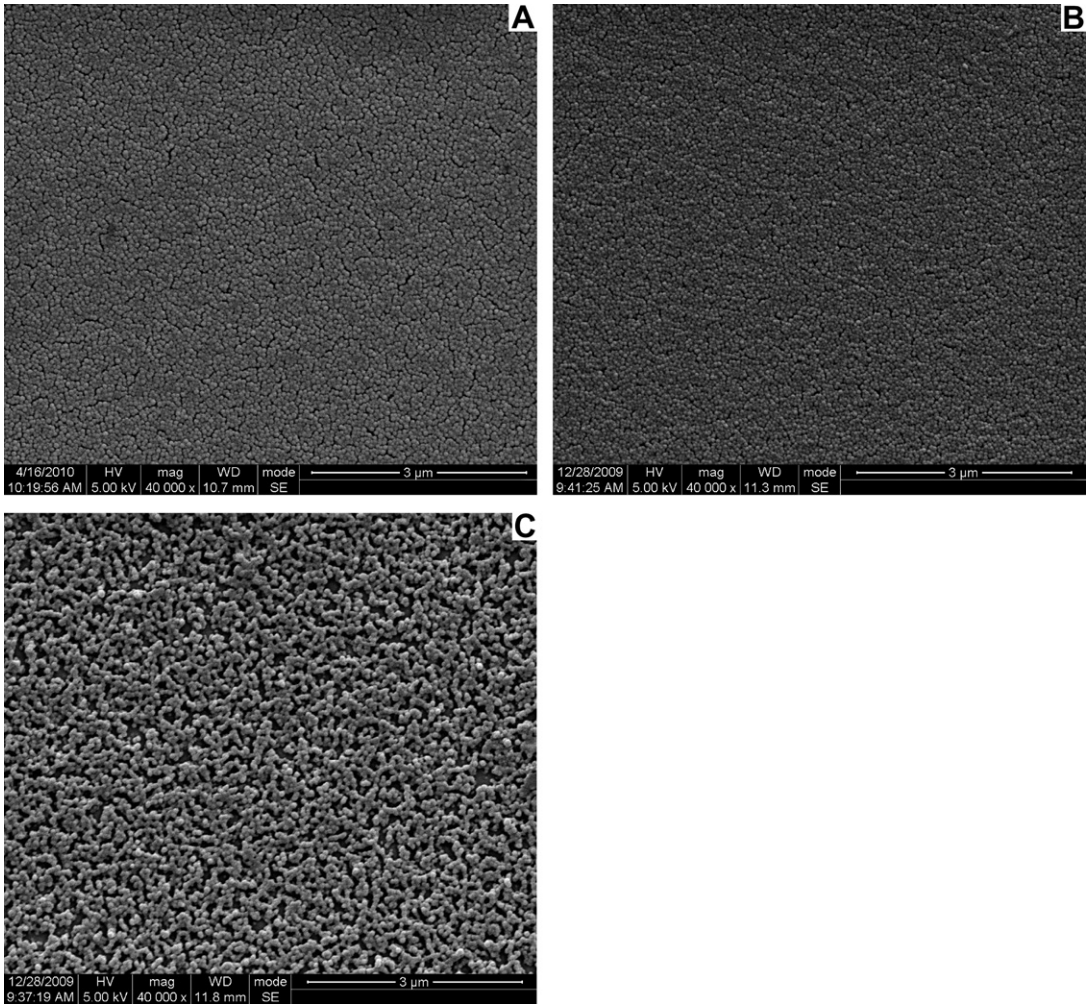

Fig. 2. Top-down SEM images of: A. all-PMMA nanoparticle coating; B. as coated PMMA/PS binary nanoparticle coating; C. after soaking in 70 °C cyclohexane for 2 min. PS loading fraction was 40 wt.% and spin speed was 3000 rpm.

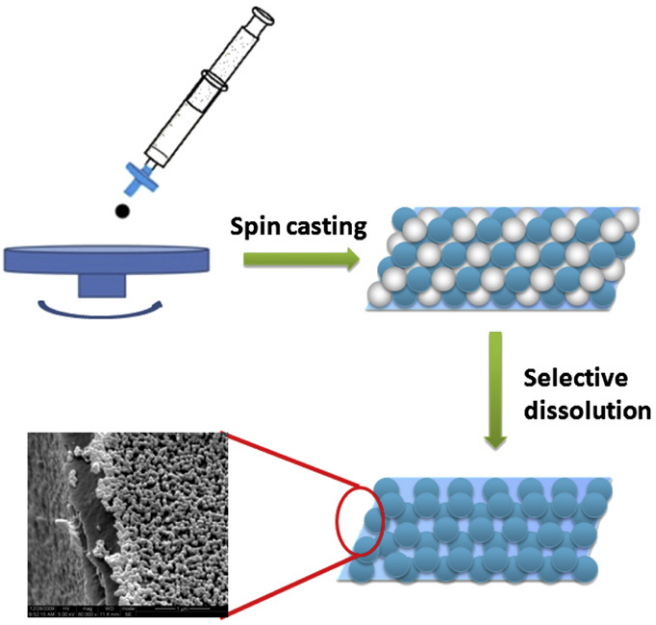

Scheme 1. Schematic illustration showing the preparation of porous coatings on PMMA substrates by spin-casting PS/PMMA binary latices and selective removal of PS particles. The top-down scanning electron microscopic (SEM) picture shows the porous surfaces at the edge of a fractured PMMA slide coated with PMMA nanoparticles.

3. Results and discussion

3.1. AR performance comparison of all PMMA and PMMA/PS binary nanoparticle coating

The optical property of all PMMA nanoparticles coating was first investigated. In order to promote wettability of PMMA latex on hydrophobic PMMA substrate surface, 0.3 wt.% SDS was post-added. After spin coating process, the both sides coated PMMA slides were immediately immersed in 50 °C deioned water for 2 min to remove post-added SDS, and then dried in clean hot nitrogen flow. Spin coating was performed at room temperature (~20 °C), which was much lower than the glass transition temperature (Tg) of the PMMA latex particles. Therefore, PMMA nanoparticles were not completely coalesced and large quantity of inter-particle pores preserved during coating process, which contributed to the AR property of nanoparticle coating. Fig. 1A shows the single-side reflection of PMMA slice spin-coated with 65 nm average-sized PMMA nanoparticles at 3000 rpm. For comparison, reflection of uncoated PMMA substrate is also showed. The minimum reflection is ~1% around 542 nm. Open symbols in Fig. 1A represent reflection of thin film with refractive index of 1.347 and a thickness of 101 nm calculated from Fresnel coefficient of reflection [36]. Spectroscopic ellipsometer characterization of the same nanoparticle coating shows that the film thickness is 101.56 ± 0.13 nm and dispersion curve is as shown in Fig. 1B. These physical constants measured on ellipsometer are consistent with parameters used in calculation, indicating that refractive index and physical thickness of the nanoparticle coating can be validly estimated by fitting experimental reflectance spectrum using Fresnel coefficient of reflection.

As shown in Fig. 1A, AR performance of all PMMA nanoparticle coating is suboptimal. This is ascribed to its relatively high refractive index, which is further related to the low porosity of densely packed PMMA particles (see Fig. 2A). For PMMA substrate (n_D^{22} 1.4913), the optimal refractive index for single-layer AR coating is $\sqrt{1.4913}$, namely 1.22, which corresponds to a porosity of 60% according to volume-averaged equation

$$n_{eff}^2 = n_p^2\left(1 - f_{pore}\right) + f_{pore} \quad (1)$$

in which n_{eff}, n_p and f_{pore} denote refractive index of porous coating, nanoparticle and pore volume fraction, respectively. While porosity of PMMA nanoparticle coating as showed in Fig. 2A is 33%, much lower than the optimal value. It is difficult to increase pore volume as long as the nanoparticles are multi-layer stacked as proved elsewhere [20,21]. Other strategy has to be sought to achieve better AR performance.

To improve AR performance of multi-layer PMMA nanoparticle coatings, 44 nm average-sized PS latex particles were homogeneously mixed with 65 nm PMMA particles and codeposited by spin-casting, followed by selective removal of PS particles in 70 °C cyclohexane for 2 min. The whole procedure is schematically illustrated in Scheme 1.

Fig. 2B gives the top-down image of PMMA/PS binary nanoparticles coating with a PS loading of 40% by weight. As can be seen from the picture, the overall structure is similar to all-PMMA particle coating: random dense packing structure with very short range ordering. Its reflection spectrum is shown in Fig. 3A in red solid line. Theoretically estimated thickness and effective refractive index n_{eff} are 136 nm and 1.355, respectively. This relative high n_{eff}

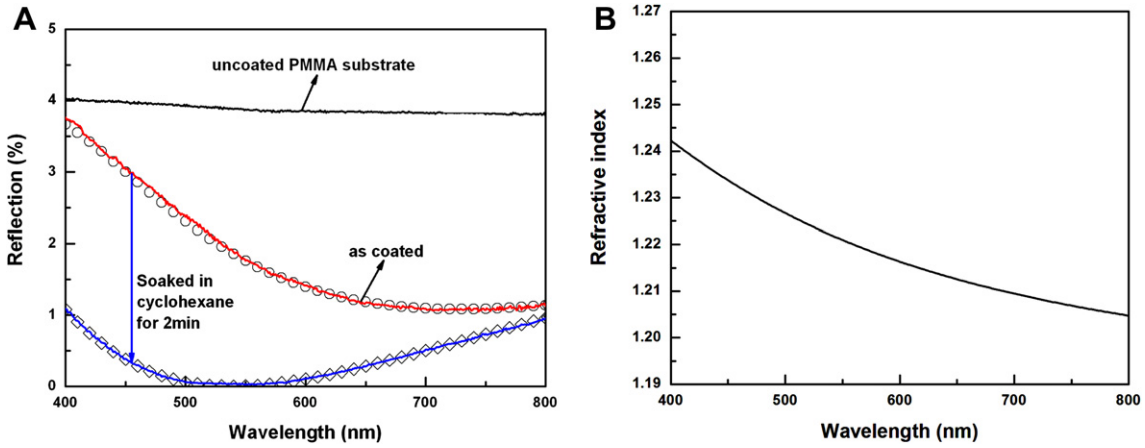

Fig. 3. A. Comparison of single-side reflections before and after removing PS particles. PS loading fraction is 40 wt.% and spin speed is 3000 rpm. Theoretical calculation results are shown in open symbols; B. Cauchy type dispersion curve of the developed porous coating measured by spectroscopic ellipsometer.

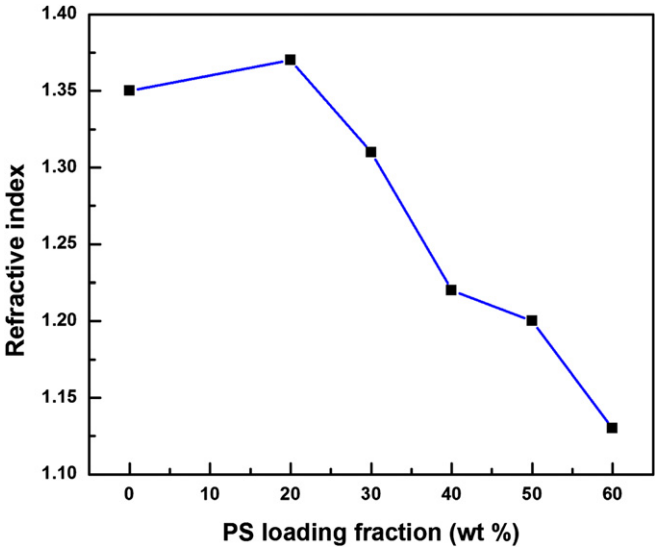

Fig. 4. Variation of refractive index as a function of PS loading without thermal-treating. These data were obtained by theoretically approximating the experimental reflection spectra.

is obviously due to the incorporation of PS particles. After removing PS particles, abundant pores are generated and uniformly distributed over large-area without cracks as shown in Fig. 2C. Accordingly, reflection (blue solid line in Fig. 3A) is dramatically reduced with detected minimum reflection of 0.02% around 543 nm. Theoretically fitting results indicate that thickness and n_{eff} of the resulted porous coating are 111 nm and 1.220, respectively. Ellipsometer characterization is also performed on such porous coating. The measured thickness is 112.35 ± 0.02 nm and resulted Cauchy type dispersion curve is shown in Fig. 3B with average value of 1.2201 over 400–800 nm. Again, theoretically estimated results consist well with the measured ones. It is noteworthy that removal of PS particles results in a thickness decrease, from 136 nm to 111 nm. This might be caused by thermal deformation of nanoparticle while soaking in 70 °C cyclohexane.

These data presented above prove the validity of our strategy to increase porosity as well as to improve AR performance. Moreover, the AR property can be tailored to meet different requirements by adjusting the n_{eff} and thickness of the porous nanoparticle coating as will be presented bellow.

3.2. Tuning AR property of PMMA/PS binary nanoparticle coating

For AR coatings, the ability to adjust AR property through tuning n_{eff} and coating thickness is highly desirable. In the case of porous polymer nanoparticle coating prepared by our method, both can be easily realized.

3.2.1. Tuning n_{eff}

Because the n_{eff} of the porous coating is a function of its porosity, tuning n_{eff} can be implemented by adjusting its porosity. In our case, the total porosity f_{pore} is composed of two portions: the one that originally existed in the nanoparticle coating f_1 and the one released by removal of PS particles f_2. Variation of both f_1 and f_2 will change n_{eff}.

The porosity f_1 is depend on the nanoparticle size distribution [20]. Since PMMA and PS nanoparticles used in this work have different sizes, change in PS particle content will alter the porosity portion f_1. Therefore, variation of PS loading fraction will not only vary porosity f_2 but also change f_1, thus to precisely adjust n_{eff}, experimental dependence of n_{eff} on PS loading fraction is needed. A group of porous coatings were prepared from 65 nm PMMA/44 nm PS binary latices with different PS loading fractions and the theoretically estimated n_{eff} of the resulted porous coating are plotted against PS loading as shown in Fig. 4. As PS loading fraction increases from 0 wt.% to 60 wt.%, n_{eff} almost linearly decreases from 1.347 to 1.130 except to the point with 20 wt.% PS loading. For the irregular case of 20 wt.% PS loading, number of PS particle is much fewer than that of PMMA particle. As a result, PS particle will be closely surrounded by PMMA particles making it difficult for cyclohexane to touch PS particles and dissolve them. Also, PS possesses higher refractive index than PMMA, so the n_{eff} slightly increased. This empirical dependence of the n_{eff} on the PS loading fraction allows a precisely control over the n_{eff} to satisfy various optimal AR requirements on different substrates. For the PMMA substrate used in this work, the optimal n_{eff} is 1.22, which corresponds to 40 wt.% PS loading in Fig. 4. Porous coating resulted from binary latex with 40 wt.% PS loading exhibits nearly zero reflection at 543 nm as shown in Fig. 3A.

Except tuning n_{eff} by varying PS loading fraction, the n_{eff} can also be adjusted by changing the nanoparticle size. Smaller nanoparticles will pack more efficiently and might suffer stronger capillary force than bigger ones during deposition process, both of which would diminish the porosity portion f_1. To demonstrate this point, in lieu of 65 nm PMMA nanoparticles, 21 nm average-sized

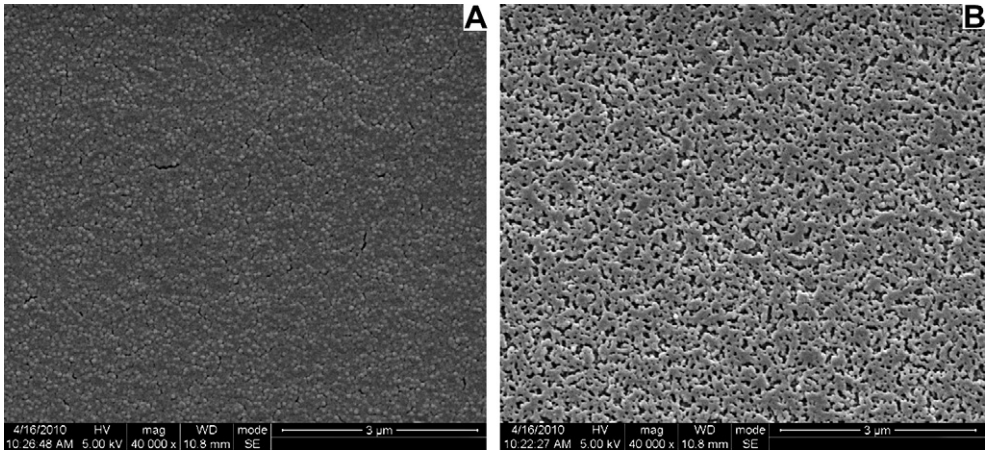

Fig. 5. Top-down SEM images of: A. as coated 21 nm PMMA/44 nm PS binary nanoparticle coating; B. after soaking in 70 °C cyclohexane for 2 min. PS loading fraction was 40 wt.% and spin speed was 3500 rpm.

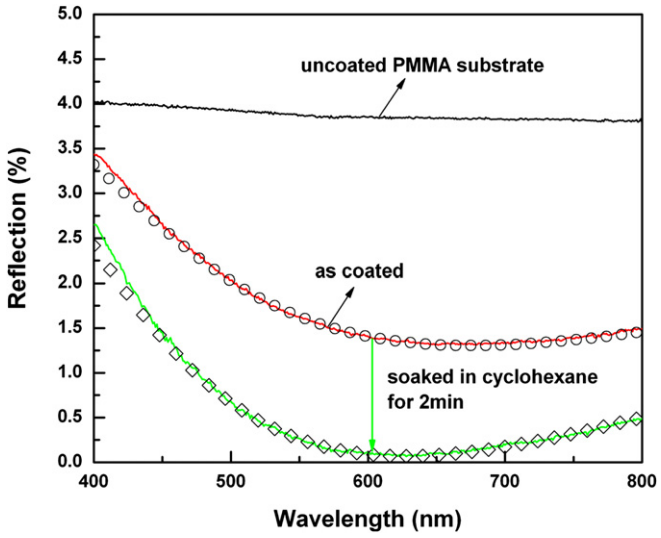

Fig. 6. Comparison of single-side reflections before and after removing 44 nm PS particles.

ones were mixed with 44 nm PS particles. The top-down SEM image of PMMA-21nm/PS-44nm binary nanoparticle coating with PS loading of 40 wt.% before and after soaking in cyclohexane are shown in Fig. 5 and the corresponding reflection spectra are given in Fig. 6. The PMMA-21/PS-44 particle coating presents different top morphologies compared to PMMA-65/PS-44 one. As coated, 21 nm PMMA particles fuse together to form a continuous matrix with PS particles embedded therein as shown in Fig. 5A. Correspondingly, the reflection (sold red line in Fig. 6) and estimated n_{eff} (1.379) are higher than that of PMMA-65/PS-44 coating with the same PS loading. Consequently, after dissolving PS particles, n_{eff} is reduced to 1.253 instead of 1.22.

3.2.2. *Thickness adjusting*

Apart from tuning refractive indices, coating thickness can also be easily adjusted in multiple ways: (1). changing spin speeds; (2). altering concentration of polymer latices; (3). preparing different nanoparticle size; (4). layer-by-layer spin-casting nanoparticles of different size. Since minimum reflection wavelength λ_{min} is linearly dependent on the coating thickness, $\lambda_{min} = 4n_{eff}d\cos\varphi$, where d is the coating thickness and φ is refractive angle, a variation in thickness adjusts the location of λ_{min} as shown in Fig. 7A. By changing latex concentration and spin speed, coating thickness is varied between 163 and 87 nm, accordingly λ_{min} is shifted between 785 and 430 nm, across the whole visible range. When plotting the λ_{min} as a function of coating thickness in Fig. 7B, the measured data are in good agreement with the solid line based on $\lambda_{min} = 4n_{eff}d\cos\varphi$. Consequently, simple but precise control of both refractive index and coating thickness allows us to prepare AR coating on different substrates with desired performance.

4. Improving the mechanical and adhesion strength of porous PMMA coating through thermal-treatment

In consideration of practical using, mechanical and adhesion strength of the polymer particle coatings should be enhanced. To attain these aims, we utilized the plasticity property of polymers. Specifically a pre-heating step was performed at 100 °C for 30 min before removal of PS particles. This thermal-treatment is intended to cause fusion between adjacent nanoparticles and between PMMA nanoparticles and PMMA substrate, leading to necking areas increase to strengthen the coating system. However, interparticle fusion will decrease the total porosity due to the diminishing of the porosity portion f_1. In the case of 40 wt.% PS loading, the refractive index can only be reduced to 1.250 if the particle coating was pre-heated at 100 °C for 30 min. Therefore, to achieve the optimal refractive index value 1.22, more PS particles have to be mixed.

As before, the experimental dependence of refractive indices on PS mixing fraction after introducing thermal-treatment step was studied first and the results were given in Fig. 8. It can be seen from Fig. 8, with the PS loading fraction increases from 30 wt.% to 80 wt.%, n_{eff} continuously decreases from 1.324 to 1.070 and the PS loading corresponding to the optimal n_{eff} of 1.22 increases to 50 wt.%. Surface morphology and reflection spectra variation of PMMA/PS nanoparticle coating (mixed at weight ratio of 1:1) corresponding to each step are showed in Fig. 9 and Fig. 10A, respectively. As coated, surface topography of the binary coating is the same as before (Fig. 9A). Theoretically approximated thickness and n_{eff} are 144 nm and 1.370, respectively. During thermal-treatment, nanoparticles are deformed and particle boundaries become vague as shown in Fig. 9B. Accordingly, the thickness shrinks to 120 nm and n_{eff} increases to 1.460 (blue solid line in Fig. 10A) and large number of pores is generated by soaking in

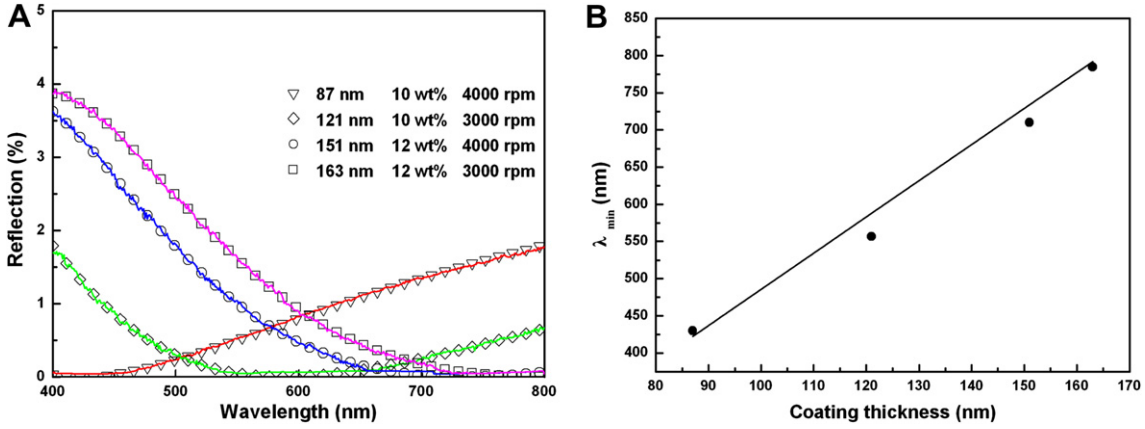

Fig. 7. A. Influence of minimum reflection wavelength with coating thickness. Open symbols represent theoretically calculated spectra. PS loading fraction is 50 wt.%; B. Dependence of minimum reflection wavelength on coating thickness. Solid cycle represents measure data and solid line is calculated according to $\lambda_{min} = 4ndcos\varphi$, where d is the coating thickness and φ is refractive angle.

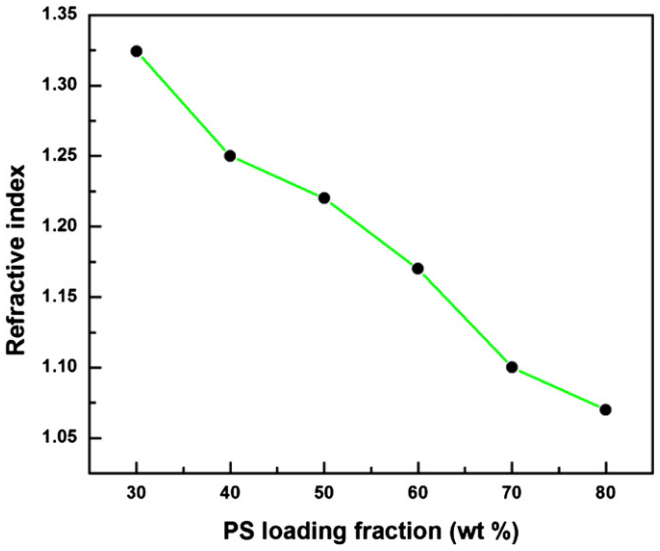

Fig. 8. Variation of refractive index as a function of PS loading with thermal-treatment. The refractive index data were obtained by theoretically approximating experimental reflection spectra.

cyclohexane (Fig. 9C). Unlike unheated binary nanoparticle coating, thickness is almost unchanged (121 nm) after removal of PS particles, while refractive index is remarkably reduced to 1.223. Ellipsometer characterization shows that the porous coating thickness is 119.68 ± 0.23 nm and dispersive curve is as shown in Fig. 10B, both of which are matched well with approximated parameters.

To examine the improvement of the mechanical and adhesion strength of porous coating through thermal-treatment, a cleaning testment was performed with a 100 W ultrasonic cleaner. To the unheated porous coatings prepared with 50 wt.% PS loading, 2 min ultrasonic clean in deioned water will wash the nanoparticles away and PMMA substrate surface is showed up. The thermal-treated porous coatings prepared with the same PS loading were firstly exposed to outdoor environment for a week, and then subjected to ultrasonic clean test. The variations of reflective spectra toward ultrasonic clean were recorded and showed in Fig. 11. The reflection spectrum as prepared is showed in solid blue line in Fig. 11, and the reflection is increased due to dust contamination after outdoor exposing experiment. Then by ultrasonic cleaning the samples in water for 1 min, the AR performance is recovered. Prolonging cleaning time to 10 min does not change the reflection spectra. Further increasing ultrasonic time will wash off the porous coating around the edges of PMMA substrate. Compared to unheated porous coatings, the mechanical and adhesion strength of the heated ones are certainly improved through thermal-treatment. Although this improvement is not very good here, there is still room for the mechanical and adhesion strength of porous coating to be further enhanced by increasing the cross-link degree of the PMMA nanoparticles and by optimizing the thermal-treatment conditions, such as prolonging heating time, changing heating medium, etc.

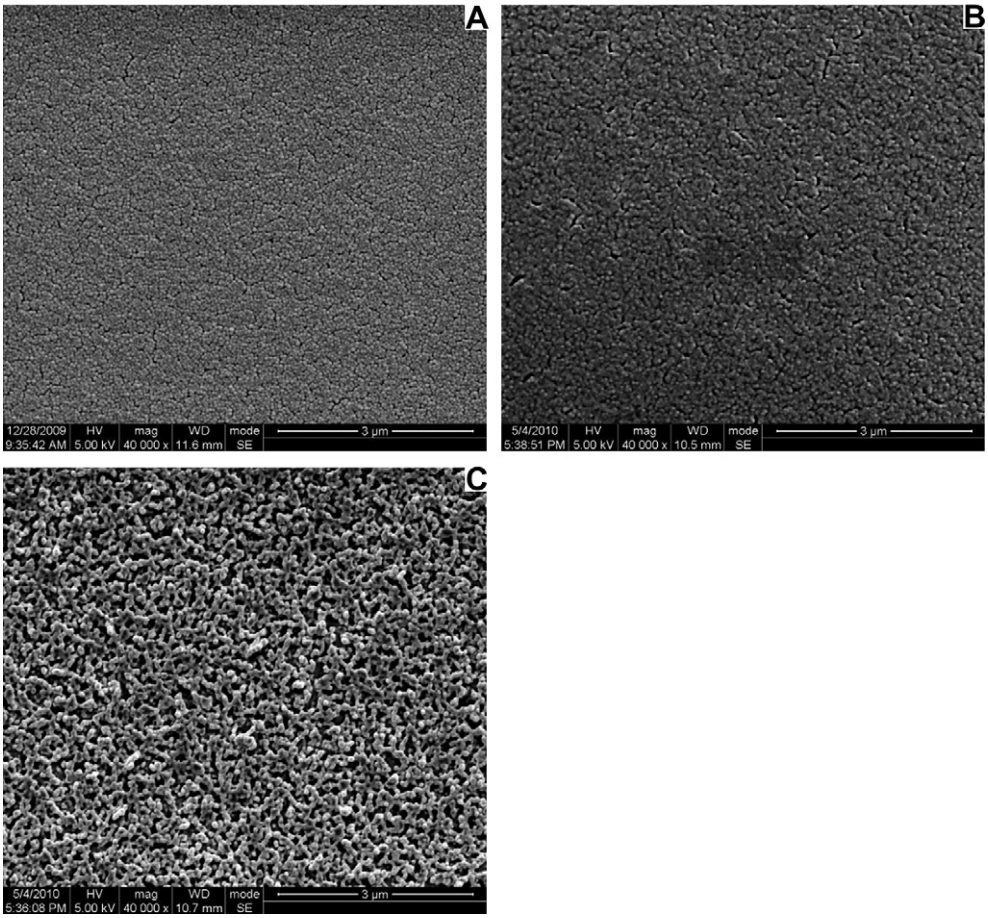

Fig. 9. Top-down SEM images of: A. as coated; B. after heated at 100 °C for 30 min; C. after soaking in 70 °C cyclohexane for 2 min. PS loading fraction was 50 wt.% and spin speed was 3000 rpm.

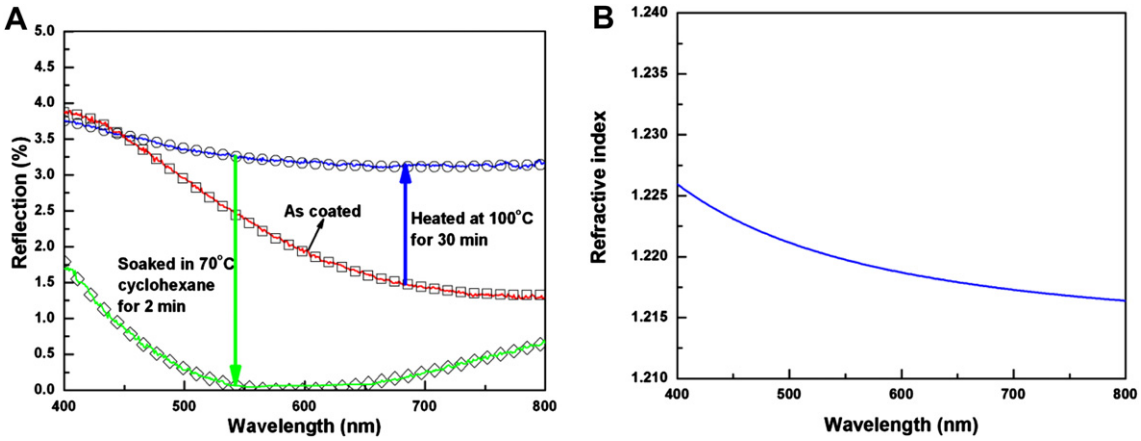

Fig. 10. A. Variation of single-side reflections of PMMA slide coated with binary latices containing 50 wt.% of PS and by spin speed at 3000 rpm. Theoretical calculation results are shown in open symbols; B. Cauchy type dispersion curve of the developed porous coating measured by spectroscopic ellipsometer.

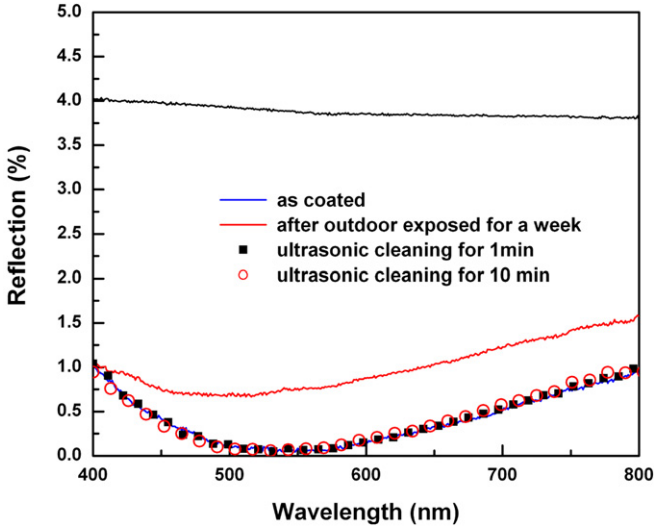

Fig. 11. Variation of single-side reflection spectra of thermal-treated porous coating (50 wt.% PS loading) on PMMA slice toward the ultrasonic clean in water.

5. Conclusion

In conclusion, a facile method to prepare porous antireflective coating on PMMA substrate by spin-casting PMMA/PS binary latexes followed by selective removal of PS particles is established in this work. The obtained porous coating exhibited excellent AR performance with minimum reflectance of ~0.02% in the visible range. The effective refractive index n_{eff} of the porous AR coating can be continuously adjusted in the range of 1.347–1.130 and 1.324–1.070 for the unheated and heated porous coating respectively. Also the coating thickness can be adjusted by changing latex concentration and the spin speed to shift the minimum reflection wavelength across the whole visible range. Consequently, AR performance of the porous AR coating prepared can be tailored to meet various requirements. Thermal-treatmented at 100 °C for 30 min, the resulted porous PMMA coating is stable to ultrasonic clean in water for 10 min. In principle, there is no limitation in the selection and combination of the nanoparticle materials. Such polymer nanoparticle-based porous coating can be fabricated on various plastic substrates with desired AR properties. Moreover this method is potentially scalable to a large-area process.

Acknowledgments

This work is financially supported by Nature Science Foundation of China, project No. 20974067.

References

[1] Kim S, Cho J, Char K. Langmuir 2007;23:6737.
[2] Biswas K, Gangopadhyay S, Kim HC, Miller RD. Thin Solid Films 2006; 514:350.
[3] Walheim S, Schaffer E, Mlynek J, Steiner U. Science 1999;283:520.
[4] Li X, Gao J, Xue LJ, Han Y. Adv Funct Mater 2010;20:259.
[5] Kuo CY, Chen YY, Lu SY. ACS Appl Mater Interfaces 2009;1:72.
[6] Joo W, Park MS, Kim JK. Langmuir 2006;22:7960.
[7] Xu T, Kim HC, DeRouchey J, Seney C, Levesque C, Martin P, et al. Polymer 2001;42:9091.
[8] Joo W, Kim HJ, Kim JK. Langmuir 2010;26:5110.
[9] Hiller J, Mendelsohn JD, Rubner MF. Nat Mater 2002;1:59.
[10] Cho J, Hong J, Char K, Caruso F. J Am Chem Soc 2006;128:9935.
[11] Gemici Z, Schwachulla PI, Williamson EH, Rubner MF, Cohen RE. Nano Lett 2009;9:1064.
[12] Li Y, Liu F, Sun J. Chem Commun 2009;19:2730.
[13] Wu ZZ, Walish J, Nolte A, Zhai L, Cohen RE, Rubner MF. Adv Mater 2006;18:2699.
[14] Lee D, Rubner MF, Cohen RE. Nano Lett 2006;6:2305.
[15] Zhang XT, Sato O, Taguchi M, Einaga Y, Murakami T, Fujishima A. Chem Mater 2005;17:696.
[16] Koo HY, Yi DK, Yoo SJ, Kim DY. Adv Mater 2004;16:274.
[17] Hattori H. Adv Mater 2001;13:51.
[18] Zhang XT, Fujishima A, Jin M, Emeline AV, Murakami T. J Phys Chem B 2006;110:25142.
[19] Zhao Y, Wang JS, Mao GZ. Opt Lett 2005;30:1885.
[20] Prevo BG, Hwang Y, Velev OD. Chem Mater 2005;17:3642.
[21] Ha JW, Park IJ, Lee SB. Macromolecules 2008;41:8800.
[22] Jiang H, Yu K, Wang YC. Opt Lett 2007;32:575.
[23] Gemici Z, Shimomura H, Cohen RE, Rubner MF. Langmuir 2008;24:2168.
[24] Schulz U, Schallenberg UB, Kaiser N. Appl Opt 2002;41:3107.
[25] Lee HR, Kim DJ, Lee KH. Surf Coat Technol 2001;142:468.
[26] Allen J, Tregunna A. J Phys D Appl Phys 1988;21:92.
[27] Laux S, Kaiser N, Niederwald H, Mertin M, Ehlers H, Ristau D. Adv Opt Interfer Coat 1999;3738:76.
[28] Schulz U, Munzert P, Leitel R, Wendling I, Kaiser N, Tunnermann A. Opt Express 2007;15:13108.
[29] Kaless A, Schulz U, Munzert P, Kaiser N. Surf Coat Technol 2005;200:58.
[30] Wang J, Xu P, Li XL, Shen J, Wu GM, Zhou B. J Sol-Gel Sci Technol 2002;23:73.
[31] David C, Haberling P, Schnieper M, Sochtig J, Aschokke C. Microelectron Eng 2002;61-2:435.
[32] Funamoto A, Lee S, Kawabata Y, Ohira M, Uchida D, Aoyama S, et al. Sci Techno Adv Mater 2007;8:208.
[33] Gombert A, Glaubitt W, Rose K, Dreibholz J, Blasi B, Heinzel A, et al. Sol Energy 2000;68:357.
[34] He GW, Pan Q. Macromol Rapid Commun 2004;25:1545.
[35] Kong XF, Wu Q, Hu WC, Wang Z. J Polym Sci Part A Polym Chem 2008;46:4522–8.
[36] Knittl Z. Optics of thin films. New York: John Wiley & Sons, Ltd.; 1976.

Polymer 52 (2011) 786–792

Contents lists available at ScienceDirect

Polymer

journal homepage: www.elsevier.com/locate/polymer

Electrorheological properties of thermo-oxidative polypyrrole nanofibers

Xiang Xia, Jianbo Yin*, Pengfei Qiang, Xiaopeng Zhao**

Smart Materials Laboratory, Department of Applied Physics, Northwestern Polytechnical University, Xi'an 710129, P. R. China

ARTICLE INFO

Article history:
Received 1 September 2010
Received in revised form
20 November 2010
Accepted 13 December 2010
Available online 21 December 2010

Keywords:
Polypyrrole
Nanofibers
Electrorheology

ABSTRACT

Using a chemical oxidative polymerization, polypyrrole (PPy) nanofibers were synthesized. After further thermo-oxidative treatment in air, the conductivity of PPy nanofibers was adjusted to a suitable level for use as a non-conventional nanofiber-based electrorheological (ER) suspension. Under electric fields, rheological properties of thermo-oxidative PPy nanofiber suspension were characterized. It showed that the nanofiber suspension possessed notable ER effect and low current density. Especially, the yield stress and shear modulus of nanofiber suspension were stronger than that of conventional granular suspension at the same volume fraction though the off-field viscosity of former was lower than that of latter. The ER effect and current density of thermo-oxidative PPy nanofiber suspension depended on the thermo-oxidative time and the nanofibers obtained after treatment for 3–5 h at 240 °C exhibited the optimal ER performances. It also showed that the thermo-oxidative PPy nanofiber suspension could maintain good ER properties within a wide operating temperature range of 25–115 °C.

1. Introduction

As an inherent conducting polymer, polypyrrole (PPy) has attracted much attention due to its excellent characteristics including high electrical conductivity, redox property, facile synthesis, and good environmental stability. PPy has found use in many fields such as biosensors, gas sensors, microactuators, antielectrostatic coatings, solid electrolytic capacitor, displays, polymeric batteries, electronic devices, and so on [1–7]. As an important electrically active polymer, PPy is also frequently employed in electrorheological (ER) fluids [8]. ER fluids are smart suspensions consisting of polarizable particles dispersed in a non-conducting liquid. On the application of an external electric field, ER fluids exhibit drastic and reversible changes in rheological properties (viscosity, shear stress, and shear modulus) due to the formation of particle chains or columns along the electric field [9]. In particular, the rheological properties can be accurately controlled by tuning electric field strengths. This rapid and reversible electrically controlled mechanical response makes ER fluids to have potential applications in mechanical, biomedical, and robotic fields [10–13]. Although the performances of ER fluids are similar to those of magnetorheological (MR) fluids under an applied magnetic field [14], most available ER fluids exhibit a far inferior mechanical property under an applied electric field. To satisfy the practical applications, current researches have focused on the synthesis of anhydrous ER materials with versatile performance including high yield stress, low current density, low particle settling, wide operating temperature range, etc., [15–18].

As important anhydrous ER systems, conducting polymers such as polyaniline (PANI), PPy, polythiophene (PTh), and their composites have been widely investigated due to their low density, tunable conductivity, high polarizability, environmental stability, and good ER efficiency [19–39]. Among these materials, PPy is one of the most promising candidates for its excellent environmental stability [8]. To satisfy ER fluid applications, however, the conductivity of PPy needs to reduce to a suitable level. The common approach to reduce conductivity is to immerse PPy particles in alkali solution. However, different from other polymer conductors such as PANI, the realization of significant decrease of conductivity of PPy by alkali dedoping is more difficult and consequently the electrical current through PPy-based ER fluids is often large and the power consumption is high. By controlling oxidant amount, Kim et al. have controlled the conductivity of PPy in a certain range and investigated the dependence of ER effect on oxidant amount [30]. Furthermore, Kim et al. also reported a way to restrict high conduction by the formation of double coated PPy particles [31]. Recently, it was reported that another interesting way to decrease conductivity was to intercalate PPy into clays or mesoporous materials [28,32,35–38]. However, the amount of intercalated PPy by this way was too small.

On the other hand, the morphology of ER particles is also important to ER performances [40–44]. In particular, it is interesting that compared with the suspensions of spherical particles the suspensions containing fiber-like particles were found to show enhanced ER and even improved dispersion stability recently [45–53]. And this enhanced effect had also been observed in MR systems [54–57]. In

* Corresponding author. Tel.: +86 29 8843 1662; fax: +86 29 8849 1000.
** Corresponding author.
E-mail addresses: jbyin@nwpu.edu.cn (J. Yin), xpzhao@nwpu.edu.cn (X. Zhao).

0032-3861/$ – see front matter © 2010 Elsevier Ltd. All rights reserved.
doi:10.1016/j.polymer.2010.12.018

the recent report, we confirmed that compared with conventional granular ER fluids, the ER fluids based on elongated nanofibers (such as titanate nanotubes [45], PANI nanofibers [48,49], and carbonaceous nanotubes [52]) exhibited better suspension stability and ER effect because the elongated morphology might have larger induced dipole moments and interparticle interactions. Using titanate nanotubes as hard templates, Li and coworkers further investigated the ER properties of titanate/conducting polymer composites [50,58].

In this study, considering the advantages of PPy as ER materials and to attempt to extend the understanding about particle morphology effect on ER properties, we developed a kind of thermo-oxidative PPy nanofibers by a modified chemical oxidative polymerization and a thermo-oxidative post-treatment in air and investigated their ER properties when dispersed in silicone oil. The merits of thermo-oxidative PPy nanofibers include not only elongated morphology but also tunable conductivity achieved by simple heating treatment in air, which were confirmed to be able to induce notable ER effect and low current density. In particular, when compared to the conventional granular thermo-oxidative PPy suspension, the thermo-oxidative PPy nanofiber suspension showed higher yield stress and shear modulus under electric fields, further indicating the potential of the thermo-oxidative PPy nanofibers as active ER materials. We here present the preparation and structure of the thermo-oxidative PPy nanofibers and the ER properties as a function of the electric field strength, thermo-oxidative time, and operating temperature.

2. Experimental

2.1. Synthesis of PPy nanofibers and thermo-oxidative treatment

All chemicals were of analytical grade and other reagents (ammonium persulfate (APS) and β-naphthalene sulfuric acid (β-NSA)) were used as received except for pyrrole monomer which was distilled under reduced pressure before using. The PPy nanofibers were synthesized according to the procedure descried in Ref. [59] with modification by our laboratory. Firstly, 6 g of NSA and 0.5 ml of pyrrole monomer were dissolved in 20 ml of deionized water with stirring in ice bath. Secondly, 2.85 g of APS was dissolved in 5 ml of deionized water, and then was added drop wise into the above solution containing pyrrole and NSA under stirring. After reaction for 12 h, a black PPy nanofiber suspension was formed. Finally, the PPy nanofibers were collected by filter with water- and ethanol-washing and then were dried at 80 °C in vacuum. To make a comparison, the granular PPy was also synthesized with the same reagents according the conventional method [59].

The conductivity of as-synthesized PPy nanofibers and granular PPy was too high to use in ER fluids. Commonly, a dedoping process in aqueous solution of ammonia was used to decrease the conductivity. However, the decreasing level of conductivity of PPy by this way was limited and thus often resulted in high current density and low dielectric breakdown strength. Different from the conventional way, we here employed a thermo-oxidative treatment at 240 °C in air to reduce the conductivity of PPy. Here, the set thermo-oxidative temperature of 240 °C was deduced according to the TGA result and relative Ref. [60]. It is noted that the PPy nanofibers degraded rapidly when the temperature was higher than 250 °C and as a result it was difficult to control the conductivity of PPy to a suitable level for ER fluid application. When the PPy was treated at temperature lower than 220 °C, however, it was very time-consuming to reduce the conductivity of PPy to a suitable level. Therefore, the moderate temperature of 240 °C was chosen for the thermo-oxidative treatment of PPy nanofibers in the present experiment. By adjusting the heating time, we could well control the conductivity of PPy to a suitable level for ER fluid application. At the same time, this method could also ensure the anhydrous characteristic of nanofibers. In addition, it should point out that the conductivity of as-synthesized PPy nanofibers was much higher than that of as-synthesized granular PPy. This is resulted from higher NSA dosage for the synthesis of PPy nanofibers. For a rational ER comparison, we here controlled the conductivity of both PPy nanofibers and granular PPy to the same level by adjusting the heating time (5 h for PPy nanofibers and 3 h for granular PPy).

2.2. Preparation of ER suspensions

The ER suspensions were prepared by rapidly infusing silicone oil (dielectric constant of 2.7 ~ 2.9, viscosity of 50 mPa·s, density of 0.96 g/cm^3 at 25 °C) into the bottle of thermo-oxidative PPy at 240 °C. After stirring and ultrasonic treatment, we obtained uniform suspensions, in which most of nanofibers were independently dispersed in medium oil according to optical microscopes. The volume fraction of particles in suspensions was defined by the ratio of particle volume to total suspension volume. The density of thermo-oxidative PPy was measured by a pycnometer [52]. To decrease the effect of porosity on density, the pycnometer was placed in an ultrasonic cleaning bath and connected to a vacuum pump. After sonication under reduced pressure for 10 min, the density was measured.

2.3. Characterization

The particle morphology was observed by scanning electron microscopy (SEM, JSM-6700). The chemical groups were determined by Fourier Infrared spectra (FT-IR, JASCO FT/IR-470 Plus Fourier Infrared spectrometer) in the range 400–4000 cm^{-1} at 4 cm^{-1} resolution. The dc conductivities (σ_{dc}) of PPy nanofibers were measured by a two-point method using a digital conductance meter (DDC-11) on pressed pellets. The ER properties were characterized by a stress-controlled electrorheometer (Thermo Haake RS600) with parallel plate system (PP ER35, the gap between plates was 1.0 mm), WYZ-010 DC high-voltage generator (0–10 kV, 0–2 mA), oil bath system (−25 to 125 °C, Phoenix), and PC computer. The steady flow curves of shear stress–shear rate were measured by the controlled shear rate (CSR) mode within the shear rate range of 0.1–1000 s^{-1}. The yield stress was approximately obtained at the low shear rate regions. In dynamic test, the amplitude sweep test of modulus as a function of stress at a constant frequency (0.5 Hz) was initially attempted to find a linear viscoelastic region, and then the dynamic viscoelastic properties were measured as function of frequency at the stress in the linear regions. The same stress was chosen for all ER fluids in order to make a reasonable comparison. To ensure data consistency, all the measurements were repeated three times and electric field was applied for 1 min prior to applying shearing or sweeping. The current through ER suspensions were recorded by an amperometer connected with electrorheometer.

3. Results and discussion

Fig. 1 shows SEM images of the as-synthesized PPy and thermo-oxidative PPy. The as-synthesized PPy by the conventional methods is typically granular sample with spherical morphology (see Fig. 1 (a)). The diameter of granular PPy is about 100–200 nm. However, when the NSA concentration is increased and the reaction is taken place in ice bath, most of PPy show nanofiber morphology with diameter of 100–200 nm and length of 1–2 μm (see Fig. 1(c)). The formation of PPy nanofibers may be induced by the template effect of self-assemble NSA micelles [59]. After further thermo-oxidative treatment at 240 °C in air, the morphology of PPy nanofibers and granular PPy is well preserved as shown in Fig. 1(b) and (d).

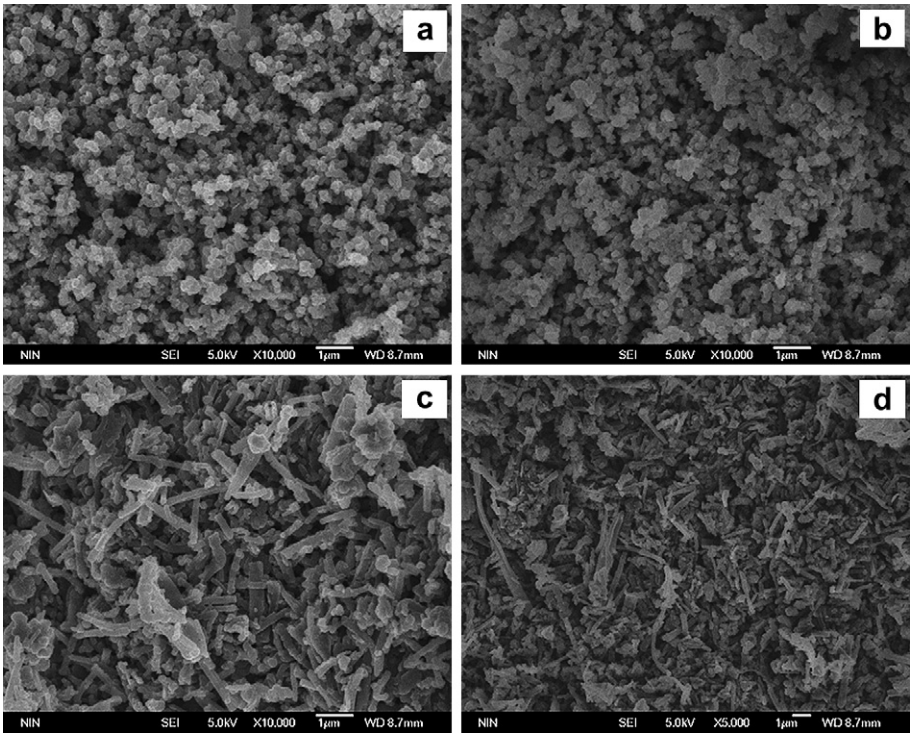

Fig. 1. SEM images of PPy: (a) as-synthesized granular PPy; (b) thermo-oxidative granular PPy; (c) as-synthesized PPy nanofibers; and (d) thermo-oxidative PPy nanofibers.

Fig. 2 shows the change of IR spectra of PPy nanofibers before and after thermo-oxidative treatment. It is seen that the as-synthesized PPy nanofibers show the typical absorption bands of conductive PPy at 1550 cm^{-1} (the C═C stretching vibration in the ring of pyrrole), and 1474 cm^{-1} (the C–N stretching vibration in the ring), 1310 cm^{-1} (the C–H or C–N in-plane deformation), 1186 cm^{-1} (the breathing vibration of the pyrrole ring, which overlaps with the SO_3 stretching vibration), 1092 cm^{-1} (in-plane deformation vibration of N^+H_2 which is formed on the PPy chains by protonation), 1044 cm^{-1} (the C–H and N–H in-plane deformation vibration), 965 cm^{-1} (the C–C out of plane ring deformation vibration), 916 cm^{-1} (C–H out of plane deformation vibration of the ring), 792 cm^{-1} (C–H out of plane ring deformation), 676 cm^{-1} (C–C out of plane ring deformation or C–H rocking), and 620 cm^{-1} (N–H out of plane vibration) [61]. The broad absorption band at the wave number higher than 2000 cm^{-1} is a typical conducting form of PPy due to free-charge absorption. After thermo-oxidative treatment at 240 °C, there is a significant decrease in the electronic transition band absorption at higher than 2000 cm^{-1} and a blue shift of the peak at 1550 cm^{-1}–1582 cm^{-1}. It is attributed to the loss of conductively conjugated species in PPy [62]. Furthermore, the disappearance of the bands at 1474, 1310, and 916 cm^{-1} and the formation of hydroxyl band at 3000–3400 cm^{-1} as well as the intensity enhancement of the carbonyl band at 1720 cm^{-1} also indicate a thermo-oxidative degradation of conjugated PPy [61]. As the thermo-oxidative time increases, the intensity of IR peaks reduces and some of the peaks (such as the peaks at 965, 820, 754, 560 cm^{-1}) further disappear, indicating that the conjugated PPy further degrades and starts to transform towards amorphous carbon. Meanwhile, the conductivity of PPy nanofibers continuously declines with the thermo-oxidative time ($\sigma_{dc} = 3.7 \times 10^{-8}$ S/cm after 3 h treatment, 1.3×10^{-8} S/cm after 4 h, 6.5×10^{-9} S/cm after 5 h, 2.0×10^{-9} S/cm after 6 h, and 5.1×10^{-10} S/cm after 10 h), which can also be reflected by the leaking current density as shown in Fig. 6(c). In addition, the change of IR spectra of granular PPy before and after thermo-oxidative treatment is similar to that of PPy nanofibers (see Fig. 3).

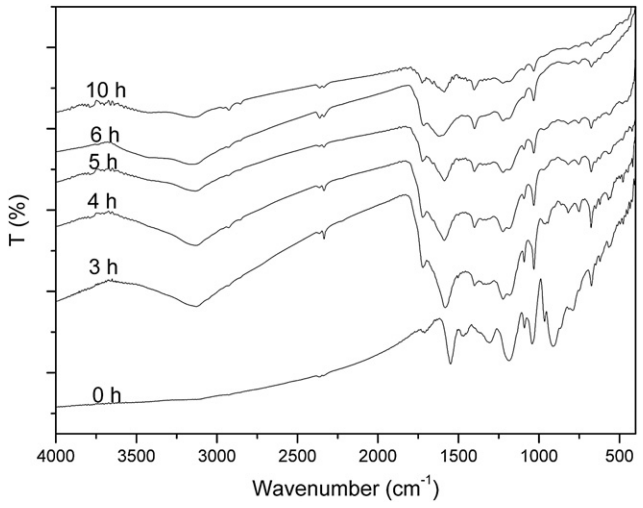

Fig. 2. FT-IR spectra of PPy nanofibers as a function of thermo-oxidative time at 240 °C in air.

Under dc electric fields, the flow curves of shear stress as a function of shear rate for the thermo-oxidative PPy nanofiber suspension and granular PPy suspension are present in Fig. 4(a) and (b), respectively. In the absence of electric fields, both suspensions show a slight departure from the Newtonian fluid behavior at low shear strain rate region (<100 s^{-1}) but the Newtonian fluid behavior at high shear rate (>100 s^{-1}). The no-field viscosity (0.26 Pa·s, calculated at high shear rate region) of PPy nanofiber suspension is slightly lower than that (0.29 Pa·s) of granular PPy suspension. When an electric field is applied, both suspensions exhibit a clear increase in shear stress and behave like a Bingham fluid with a notable yield stress. This is attributed to the fact that the particles polarize and

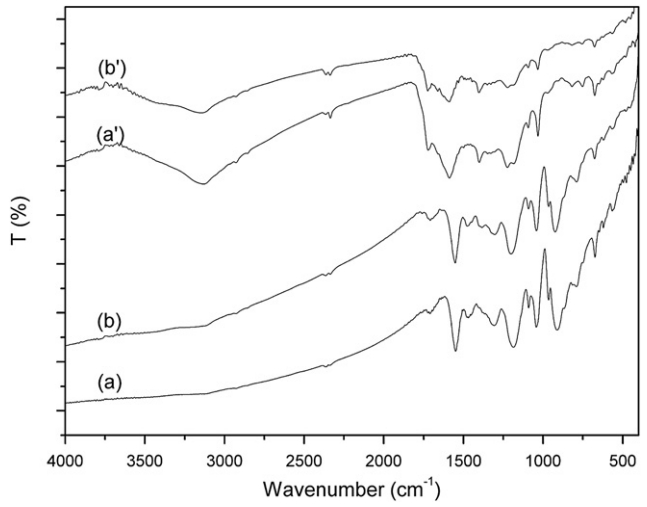

Fig. 3. FT-IR spectra of PPy: (a) as-synthesized PPy nanofibers; (b) as-synthesized granular PPy; (a′) thermo-oxidative PPy nanofibers; and (b′) thermo-oxidative granular PPy.

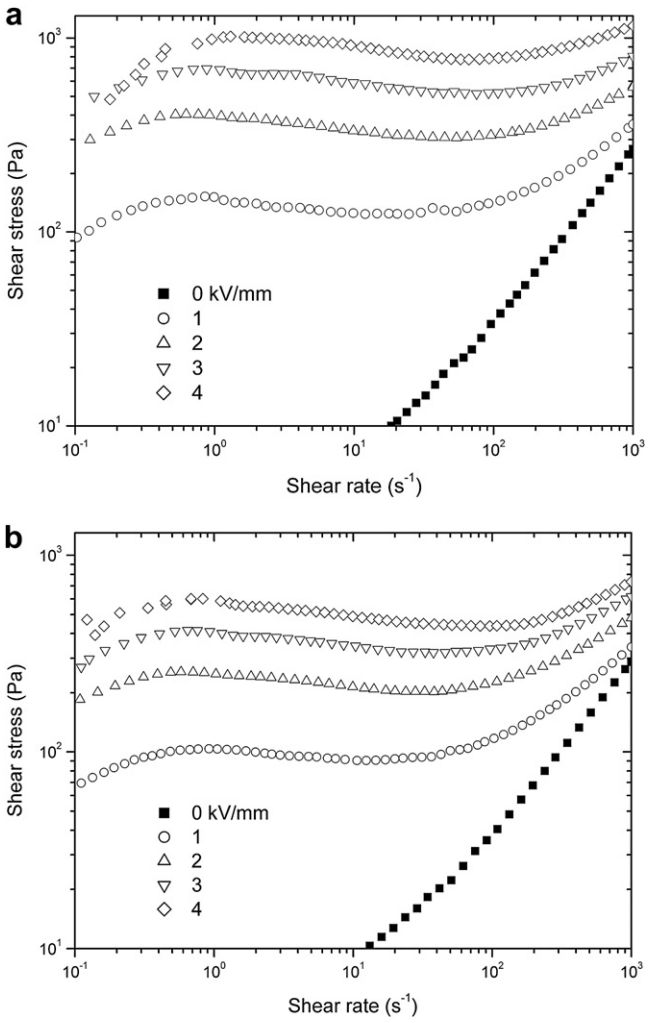

Fig. 4. Shear stress as a function of shear rate for the thermo-oxidative PPy suspensions under different dc electric fields: (a) nanofiber; and (b) granular (10 vol.%, $T = 25\ ^{\circ}C$).

attract each other to form chains or columns along the direction of the field to prevent the flow of suspensions [10]. Although the no-field viscosity of PPy nanofiber suspension is slightly lower than that of the granular PPy suspension, it is interesting to note that the electric field-induced shear stress and ER efficiency (defined by $(\tau_E - \tau_0)/\tau_0$ or $(\eta_E - \eta_0)/\eta_0$, where τ_E and η_E are shear stress and shear viscosity under an electric field and τ_0 and η_0 are the shear stress and shear viscosity without electric field, respectively) of former are much higher than those of latter at the same electric field strength. For example, the shear stress is 785 Pa (100 s^{-1})/1157 Pa (1000 s^{-1}) at 4 kV/mm for PPy nanofiber suspension, which are much higher than 438 Pa (100 s^{-1})/735 Pa (1000 s^{-1}) for the granular PPy suspension. Meanwhile, the ER efficiency of PPy nanofiber suspension is about 21.7 (100 s^{-1})/3.4 (1000 s^{-1}) at 4 kV/mm, which are about twice as high as 10.8 (100 s^{-1})/1.5 (1000 s^{-1}) of the granular PPy suspension.

Fig. 5 shows the dependence of yield stress and current density on electric field strength for thermo-oxidative PPy suspensions. It can be found that the yield stress of thermo-oxidative PPy nanofiber suspension is much higher than that of granular suspension under the same electric field though the current density of former is slightly higher than that of latter. The analogical results have also been observed recently in ER fluids including commercial carbon nanotubes [46], PANI nanofibers [48,49], and carbonaceous nanotubes [52]. Furthermore, several groups have also found analogical enhanced MR effect in magnetic nanofiber suspensions when compared with conventional magnetic sphere suspensions [54–57]. It has been reported that the applied electric field tended to induce larger dipole moments in elongated particles compared to spherical particles at the same volume and thus lead to larger interparticle interaction [41]. At the same time, the viscous drag force and interparticle friction in a fibrous suspension might be also enhanced due to the formation of complex ER structures under electric fields [52,63]. Therefore, the enhanced dipole moments and viscous drag force or interparticle friction may be responsible for the higher yield stress of thermo-oxidative PPy nanofiber suspension compared to the granular suspension. Furthermore, by the power–law relation, $\tau_y \propto E^{\alpha}$, the relationship of yield stresses and electric fields can be fitted as shown in Fig. 5. The exponent α is 1.33 ± 0.02 for thermo-oxidative PPy nanofiber suspension and 1.25 ± 0.03 for granular suspension, respectively. The α values departing from 2, which is predicted with the classic polarization model [64], can be attributed to several factors, such as particle concentration, shape,

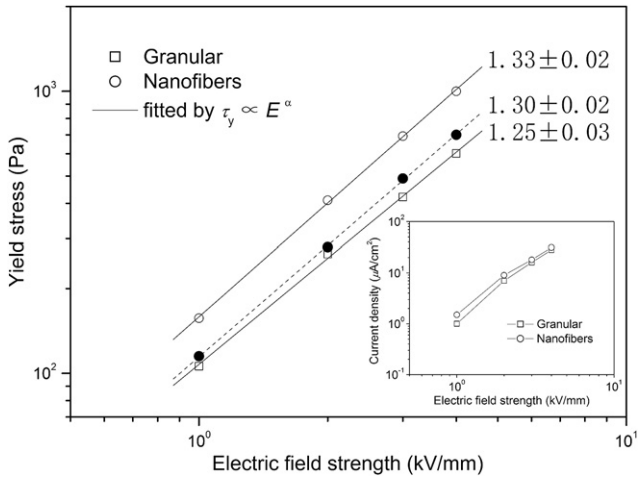

Fig. 5. Yield stress and current density (inset) as a function of electric field strength for thermo-oxidative PPy suspensions ($T = 25\ ^{\circ}C$, 10 vol.%). The solid circle symbol represents the yield stress of suspension of PPy nanofibers with lower aspect ratio.

multi-disperse, and nonlinear conductivity of oil, etc., [26,47,48,65]. However, the α of thermo-oxidative PPy nanofiber suspension is larger than α of granular suspension, which is different from the result obtained from the ER fluids based on PANI nanofibers [48,49]. The reason for this remains unknown and needs to be further investigated in future. To give a primary understanding about the influence of elongated shape or aspect ratio on ER effect, we specially synthesized the PPy nanofiber sample with lower aspect ratio of 3–5 according to the SEM (not shown here) by decreasing the ratio of β-NSA (4 g) to PPy (0.5 mL). The thermo-oxide time for this PPy sample was set as 4 h at 240 °C in air in order to make its conductivity ($\sigma_{dc} = 4.6 \times 10^{-9}$ S/cm) be close to that of the longer PPy nanofibers ($\sigma_{dc} = 6.5 \times 10^{-9}$ S/cm) and granular PPy ($\sigma_{dc} = 5.8 \times 10^{-9}$ S/cm). It is noted that the yield stress is decreased when using the PPy nanofibers with lower aspect ratio as the dispersal phase of suspension (see solid circle point symbol in Fig. 5). Thus, we consider that the elongated shape may be responsible for the enhanced yield stress. Due to the presence of mechanical stirring in the present reaction, however, it's difficult to synthesize longer PPy nanofibers.

On the other hand, the solidified ER fluids under electric fields often show a linear viscoelastic behavior when subjected to a small stress or a small strain. Fig. 6(a) and (b) show the storage modulus (G') and loss modulus (G'') as functions of shear frequency for thermo-oxidative PPy nanofiber and granular PPy suspensions, respectively. It is found that G' and G'' increase with increasing electric field strength, and the suspensions become more elastic and stiffer at higher electric field, which is revealed by the fact that G' is larger than G'' in the linear viscoelastic range. At the same electric field, however, G' of the thermo-oxidative PPy nanofiber suspension is higher than that of granular suspension. It indicates that compared to the granular suspension the thermo-oxidative PPy nanofiber suspension has higher rigidity, which also confirms its higher ER effect.

It is found that the ER effect of thermo-oxidative PPy depends on the thermo-oxidative time. Fig. 7 shows the yield stress and current density of suspensions of thermo-oxidative PPy obtained with different heating time. When the heating time is smaller than 3 h, the conductivity of resulted PPy nanofibers is too high to finish ER test due to the occurrence of electrical short. After thermo-oxidative treatment for 3 h, the current density of suspension is decreased to 110 μA/cm^2 at 3 kV/mm, which is in an acceptable range by many ER devices [16]. When the heating time is for 4 h ~ 5 h, the yield stress only exhibits a very slight decrease but the current density continuously declines (see Fig. 7(b)). This may be derived from the fact that the conductivities of these thermo-oxidative PPy nanofibers ($\sigma_{dc} = 1.3 \times 10^{-8}$ S/cm after 4 h and 6.5×10^{-9} S/cm after 5 h) are still in a moderate range for good ER effect [65]. When the heating time is longer than 5 h, however, the yield stress of thermo-oxidative PPy nanofiber suspension shows

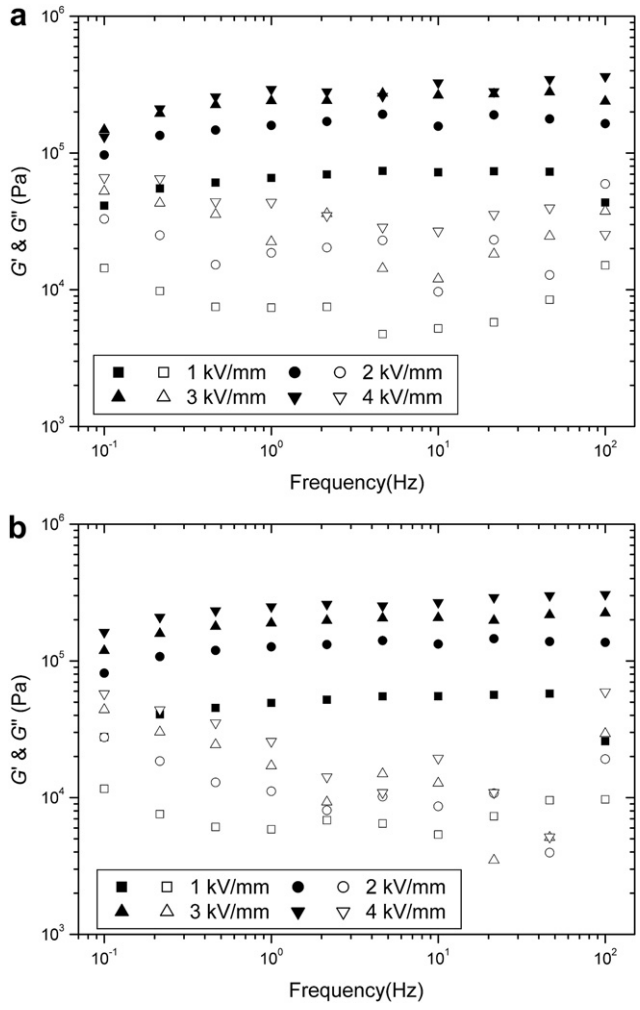

Fig. 6. Storage modulus (G', solid symbol) and loss modulus (G'', open symbol) as a function of shear frequency for thermo-oxidative PPy suspensions: (a) nanofiber; and (b) granular (10 vol.%, $T = 25$ °C).

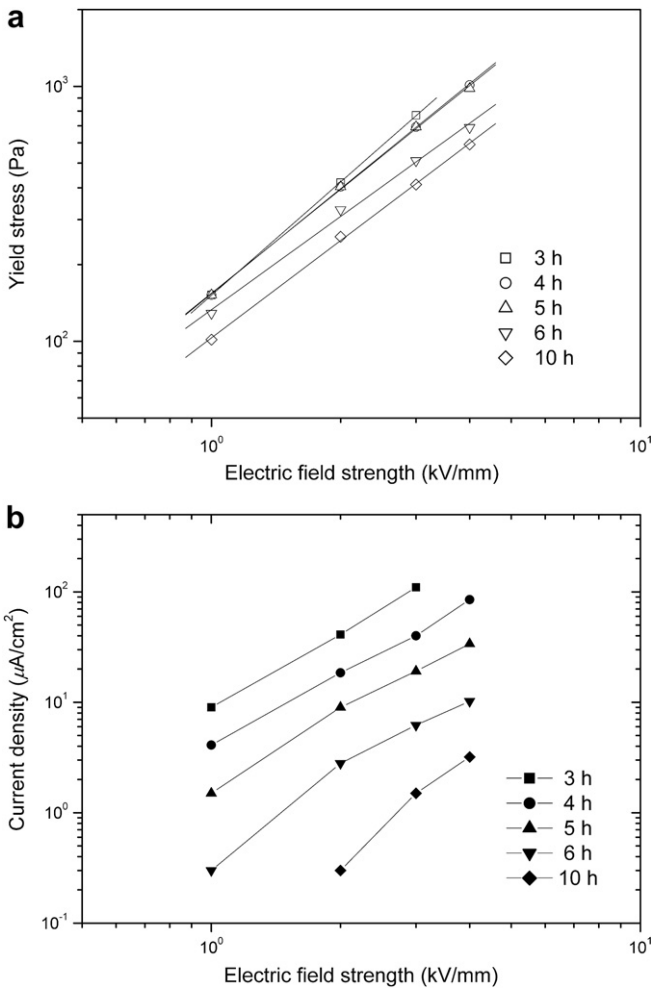

Fig. 7. Yield stress (a) and current density (b) of suspensions of thermo-oxidative PPy nanofibers obtained after different heating times ($T = 25$ °C, 10 vol.%).

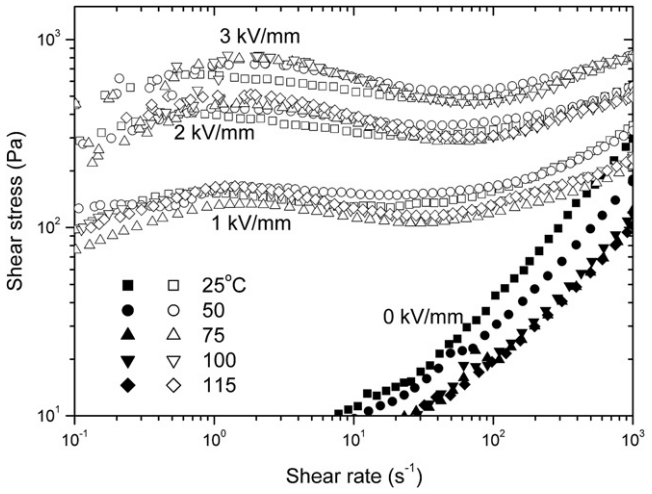

Fig. 8. Flow curves of shear stress vs. shear rate for thermo-oxidative PPy nanofiber suspension at different operating temperatures (10 vol.%).

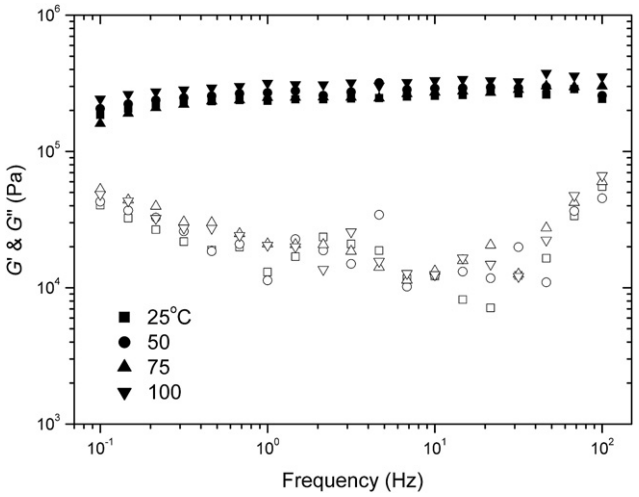

Fig. 10. Storage modulus (G', solid symbol) and loss modulus (G'', open symbol) at 3 kV/mm as a function of frequency for thermo-oxidative PPy nanofiber suspension at different operating temperatures (10 vol.%).

a significant decrease. This can be attributed to the fact that long-term thermo-oxidative treatment has deeply degraded the conjugated structure of PPy and thus largely decreased the conductivity mismatch of PPy particles with host oil. In addition, it should point out that compared to some other PPy ER fluids [30,36,58] the present thermo-oxidative PPy nanofiber suspension exhibit lower current density and higher dielectric breakdown strength (>5 kV/mm).

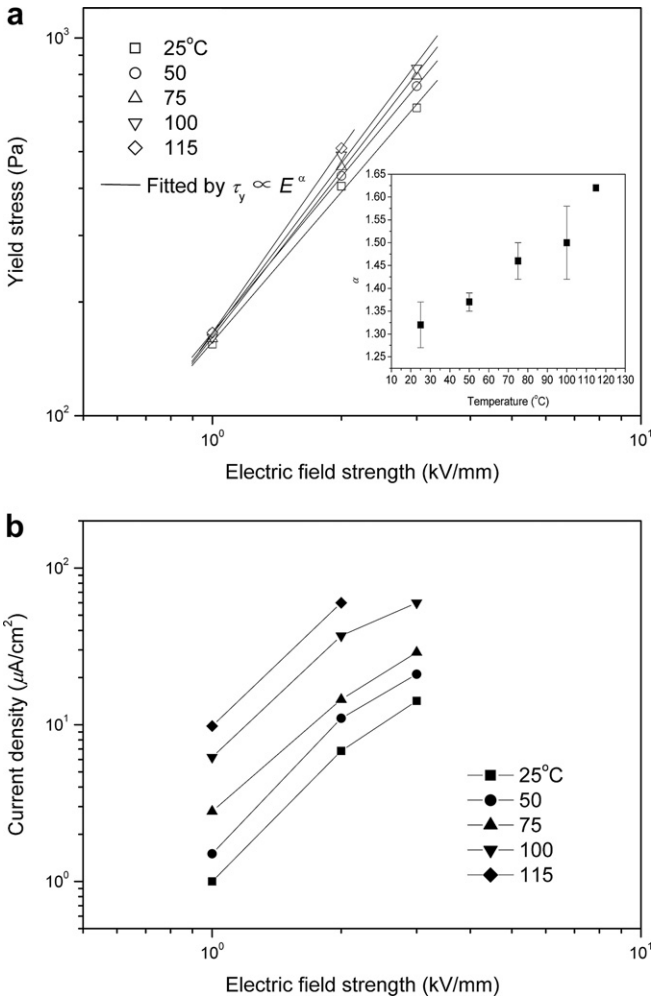

Fig. 9. Yield stress (a) and current density (b) as a function of electric field strength for thermo-oxidative PPy nanofiber suspension at different operating temperatures (10 vol.%).

Finally, the effect of operating temperatures on the ER property of thermo-oxidative PPy nanofiber suspension is investigated as shown in Fig. 8. It is found that the yield stress and ER efficiency under electric fields increase with operating temperatures though the no-field viscosity decreases. Meanwhile, the rheological curves of shear stress vs. shear rate also maintain a stable level in the wide shear rate region even at high temperatures. These indicate that the thermo-oxidative PPy nanofiber suspension possesses good temperature stability. In the practical application, ER fluids with good ER effect over a wide operating temperature range are especially needed. In the water-activated ER system, temperature elevation often causes the evaporation of adsorbed water and consequently the ER effect decreases [15]. The good temperature stability of the present thermo-oxidative PPy nanofiber suspension indicates that its ER effect mainly arises from the intrinsic bulk properties rather than extrinsic factors such as water activator. That is, increasing temperature tends to increase the conductivity of thermo-oxidative PPy nanofibers and then enhance the polarization force so as to overcome the Brownian force intensified by increased temperature. Furthermore, we also used the power–law relation $\tau_y \propto E^{\alpha}$ to fit the correlation of yield stresses and electric fields at different operating temperatures as shown in Fig. 9(a). It is seen that the exponent α value increases with increased operating temperatures. This may be because the increasing temperature has decreased medium viscosity and enhanced the conductivity mismatch between nanofibers and host oil and thus improved the polarization response of particles [65]. However, the upper limit (<115 °C at 3 kV/mm, see Fig. 9(b)) of temperature dependence of present thermo-oxidative PPy nanofiber ER system is influenced by the current overload of electrorheometer. In addition, the effect of operating temperature on dynamic viscoelastic property is shown in Fig. 10. Although G'' shows less change, G' tends to increase with temperature elevation. This also confirms that the thermo-oxidative PPy nanofiber suspension possesses good temperature effect.

4. Conclusions

We prepared a thermo-oxidative PPy nanofiber based ER suspension by a chemical oxidative polymerization and further

thermo-oxidative treatment at 240 °C in air and investigated its ER properties by comparing with the corresponding thermo-oxidative granular PPy suspension. The measurements involving steady shear viscosity and dynamic viscoelastic properties showed that the suspension of thermo-oxidative PPy nanofibers possessed higher ER effect compared with the corresponding suspension of thermo-oxidative granular PPy at the same volume fraction. Furthermore, the ER effect and current density of thermo-oxidative PPy nanofiber suspensions depended on the thermo-oxidative time and the nanofibers obtained after heating for 3–5 h at 240 °C exhibited the optimal ER performance. The temperature effect test showed that the thermo-oxidative PPy nanofiber suspension could maintain good ER effect in a broad operating temperature range of 25–115 °C.

Acknowledgements

This work is supported by National Natural Science Foundation of China(No. 50602036; 50936002), and NPU Foundation for Fundamental Research (No. JC201051).

References

[1] Zhang XY, Manohar SK. J Am Chem Soc 2005;127:14156.
[2] Ikegame M, Tajima K, Aida T. Angew Chem Int Ed 2003;42:2154.
[3] Lee ES, Park JH, Wallace GG, Bae YH. Polym Int 2004;53:400.
[4] Kemp NT, Flanagan GU, Kaiser AB, Trodahl HJ, Chapman B, Partridge AC, et al. Synth Met 1999;101:434.
[5] Fonner JM, Schmidt CE, Ren PY. Polymer 2010;51:4985.
[6] Cruz GJ, Olayo MG, López OG, Gomez LM, Morales J, Olayo R. Polymer 2010; 51:4314.
[7] Redondo MI, García MV, de la Blanca ES, Pablos M, Carrillo I, González-Tejera MJ, et al. Polymer 2010;51:1728.
[8] Kim DH, Kim YD. J Ind Eng Chem 2007;13:879.
[9] Hasley TC. Science 1992;258:761.
[10] Couter SP, Weiss KD, Carlson JD. J Intell Mater Syst Struct 1993;4:248.
[11] Böse H, Berkemeier J, Trendler A. In: Proceedings of the ACTUATOR 2000 Conference, 19–21 June 2000 Germany.
[12] Hao T. Adv Mater 2001;13:1847.
[13] Zhao XP, Yin JB, Tang H. In: Reece PL, editor. Smart materials and structures: new research. Nova Science Publishing; 2006. p. 1–66.
[14] Fang FF, Choi HJ, Seo Y. ACS Appl Mater Interfaces 2010;2:54.
[15] Block H, Kelly JP. J Phys D Appl Phys 1988;21:1661.
[16] Weiss KD, Carlson JD, Coulter JP. J Intell Mater Syst Struct 1993;4:13.
[17] Zhao XP, Yin JB. J Ind Eng Chem 2006;12:184.
[18] Choi HJ, Jhon MS. Soft Matter 2009;5:1562.
[19] Block H, Kelly JP, Qin A. Langmuir 1990;6:6.
[20] Gow C, Zukoski CF. J Colloid Interface Sci 1990;136:175.
[21] Teare GC, Ratcliffe NM. J Mater Chem 1996;6:301.
[22] Goodwin JW, Markham GM, Vincent B. J Phys Chem B 1997;101:1961.
[23] Choi HJ, Kim TW, Cho MS, Kim SG, Jhon MS. Eur Polym J 1997;33:699.
[24] Quadrat O, Stejskal J, Kratochvíl P, Klason C, McQueen D, Kubát J, et al. Synth Met 1998;97:37.
[25] Wu SZ, Zeng F, Shen JR. Polymer J 1998;30:451.
[26] Kim JW, Kim SG, Choi HJ, Jhon MS. Macromol Rapid Commun 1999;20:450.
[27] Gozdalik A, Wycislik H, Plocharski J. Synth Met 2000;109:147.
[28] Kim SG, Kim JW, Choi HJ, Suh MS, Shin MJ, Jhon MS. Colloid Polym Sci 2000; 278:894.
[29] Lu J, Zhao XP. J Mater Chem 2002;12:2603.
[30] Kim YD, Song IC. J Mater Sci 2002;37:5051.
[31] Kim YD, Park DH. Colloid Polym Sci 2002;280:828.
[32] Kim JW, Liu F, Choi HJ, Hong SH, Joo J. Polymer 2003;44:289.
[33] Yoon DJ, Kim YD. J Colloid Interface Sci 2006;303:573.
[34] Kim YD, Kim JH. Synth Met 2008;158:479.
[35] Cheng Q, Pavlinek V, Lengalova A, Li C, Belza T, Saha P. Micropor Mesopor Mater 2006;94:193.
[36] Wei C, Zhu YH, Jin Y, Yang XL, Li CZ. Mater Res Bull 2008;43:3263.
[37] Park DP, Lim ST, Lim JY, Choi HJ, Choi SB. J Appl Polym Sci 2009;112:1365.
[38] Fang FF, Choi HJ, Ahn WS. Micropor Mesopor Mater 2010;130:338.
[39] Hong JY, Kwon E, Jang J. Soft Matter 2009;5:951.
[40] Asano K, Suto H, Yatsuzuka K. J Electrost 1997;40–41:573.
[41] Kanu RC, Shaw MT. J Rheol 1998;42:657.
[42] Otsubo Y. Colloids Surf A Physicochem Eng Asp 1999;153(1–3):459.
[43] Lengalova A, Pavlinek V, Saha P, Quadrat O, Stejskal J. Colloids Surf A Physicochem Eng Asp 2003;227:1.
[44] Yin JB, Zhao XP, Xiang LQ, Xia X, Zhang ZS. Soft Matter 2009;5:4687.
[45] Yin JB, Zhao XP. Nanotechnology 2006;17:192.
[46] Lin C, Shan JW. Phys Fluid 2007;19:121702.
[47] Tsuda K, Takeda Y, Ogura H, Otsubo Y. Colloids Surf A Physicochem Eng Asp 2007;299:262.
[48] Yin JB, Zhao XP, Xia X, Xiang LQ, Qiao YP. Polymer 2008;49:4413.
[49] Yin JB, Xia X, Xiang LQ, Qiao YP, Zhao XP. Smart Mater Struct 2009;18:095007.
[50] Cheng Q, Pavlinek V, He Y, Li C, Saha P. Colloid Polym Sci 2009;287:435.
[51] Liu YD, Fang FF, Choi HJ. Mater Lett 2010;64:154.
[52] Yin JB, Xia X, Xiang LQ, Zhao XP. Carbon 2010;48:2958.
[53] Yin JB, Xia X, Xiang LQ, Zhao XP. J Mater Chem 2010;20:7096.
[54] López- López MT, Vertelov G, Bossis G, Kuzhir P, Durán JDG. J Mater Chem 2007;17:3839.
[55] Bell1 RC, Karli JO, Vavreck AN, Zimmerman DT, Ngatu GT, Wereley NM. Smart Mater Struct 2008;17:015028.
[56] de Vicente J, Segovia-Gutiérrez JP, Andablo-Reyes E, Vereda F, Hidalgo-Álvarez RJ. Chem Phys 2009;131:194902.
[57] Gomez-Ramirez A, López- López MT, Durán JDG, Gonzalez-Caballero F. Soft Matter 2009;5:3888.
[58] Luo MF, He Y, Cheng QL, Li CZ. J Macromol Sci Part B Phys 2010;49:419.
[59] Yang YS, Liu J, Wan MX. Nanotechnology 2002;13:771.
[60] Thieblemont JC, Brun A, Marty J, Planche MF. Polymer 1995;36:1605.
[61] Omastova M, Trchova M, Kovarova J, Stejskal J. Synth Met 2003;138:447.
[62] Mathys GI, Truong VT. Synth Met 1997;89:103.
[63] López- López MT, Kuzhir P, Bossis G. J Rheol 2009;53:115.
[64] Klingenberg DJ, Zukoski CF. J Chem Phys 1991;94:6160.
[65] Kim SG, Lim JY, Sung JH, Choi HJ, Seo Y. Polymer 2007;48:6622.

Polymer 52 (2011) 793–803

Contents lists available at ScienceDirect

Polymer

journal homepage: www.elsevier.com/locate/polymer

"Reservoir" and "barrier" effects of ABC block copolymer micelle in hydroxyapatite mineralization control

Jia Yao, Huan Wu, Yuelei Ruan, Jun Guan, Annan Wang, Haoran Li*

Department of Chemistry, Zhejiang University, Hangzhou 310027, People's Republic of China

ARTICLE INFO

Article history:
Received 23 July 2010
Received in revised form
25 November 2010
Accepted 13 December 2010
Available online 21 December 2010

Keywords:
PEG–PAA–PCL
Amphiphilic block copolymer
Mineralization

ABSTRACT

An amphiphilic triblock poly (ethylene glycol)–block-poly (acrylate acid)–block-poly (ϵ-caprolactone) (PEG–PAA–PCL) copolymer was synthesized by sequential anionic polymerization. By comparing with diblock copolymer poly (acrylic acid)–block-poly (ϵ-caprolactone) (PAA–PCL), the triblock copolymer (PEG–PAA–PCL) micelle has core–shell–corona structure, which possesses better dispersion, could be a good candidate as structure template for the controlled mineralization of hydroxyapatite (HA). The interactions between inorganic ions and polymers were studied by using Ca^{2+} ion selective electrode and zeta potential, which indicated the "reservoir" effect of micelles and the "barrier" effect of PEG segments during mineralization process. Ca^{2+} ions can penetrate through the corona and interact with PAA segments. When PO_4^{3-} ions were added, Ca^{2+} ions diffuse out, and react with PO_4^{3-} ions to form the new apatite layer. Thus the supersaturation could be well tuned by the triblock copolymer micelles, and the nucleation and crystal growth in nano scale could be controlled by appropriate usage of this template system.

1. Introduction

Hydroxyapatite, $Ca_{10}(PO_4)_6(OH)_2$ (denoted as HA), a form of bioceramic material [1], is present in bone, teeth, and tendons to give these organs stability, hardness, and function [2]. Owing to its bioactive property, HA is widely used in medicine and dentistry as a material for metallic implant coatings, or for bone cavity fillings [3–5]. Controlled mineralization of HA is a hot topic in chemistry, materials, biology and nanotechnology [6–12].

HA hollow nanostructures are considered to be advantageous because of their large specific surface area and high capacity for loading drug, protein or DNA molecules. Several methods have been developed to prepare HA hollow nanostructures, for example, polyelectrolyte-mediated mineralization [13,14], ultrasonic-assisted route [15], etc. Bio-inorganic microcapsules from templating protein [16] and porous nanocomposites of PEG–PLA/calcium phosphate were reported for medicinal application [17].

In recent years, the strategy of using organic templates to control the nucleation, growth, and alignment of inorganic particles has been extensively applied to the biomimetic morphogenesis of inorganic materials with complex forms [18–25]. In the recent work, surfactants [26] and block copolymers [27–29] were used as templates to tune the morphology of HA materials, including hollow spherical morphology. In this way, the template plays an important role in the nucleation and growth of HA crystals and determines their size, morphology, and orientation in the composite material.

With the development of synthesis techniques, many functional block copolymers were designed for different applications [30–33]. However, when AB-type or ABA-type block copolymers perform as templates, their micelles will adsorb inorganic materials, then the shells become unstable, always resulting in secondary or higher-level aggregates [34], which lead to limited control in mineralization. Fortunately, the ordered self-assemblies, formed by ABC-type triblock copolymers, have more independent parameters on their phase behavior [35,36], and can be promising soft templates for regulating nano-sized inorganic materials [37]. Thus, in the present paper, an amphiphilic triblock copolymer poly (ethylene glycol)–block-poly (acrylate acid)–block-poly (ϵ-caprolactone) (PEG–PAA–PCL) was designed to act as a template to control HA mineralization. The core–shell–corona (c–s–c) structure of its aggregate [38], which is formed by the hydrophobic PCL segments (core), PAA segments with functional groups (shell) and the water-soluble PEG segments (corona), respectively, facilitates good micelle dispersion, and is hoped to perform good control on HA nano spheres mineralization.

Usually, mineralization control relies on thermodynamic or kinetic mechanisms, and in most cases, the nucleation is the key step in building up a complex structure [39]. The supersaturation is a major driving force for nucleation in solutions, thus the nucleation and growth kinetics could be tuned by adjusting solution supersaturation [40,41]. However, due to the lack of enough

* Corresponding author. Fax: +86 571 87951895.
E-mail address: lihr@zju.edu.cn (H. Li).

0032-3861/$ – see front matter © 2010 Elsevier Ltd. All rights reserved.
doi:10.1016/j.polymer.2010.12.017

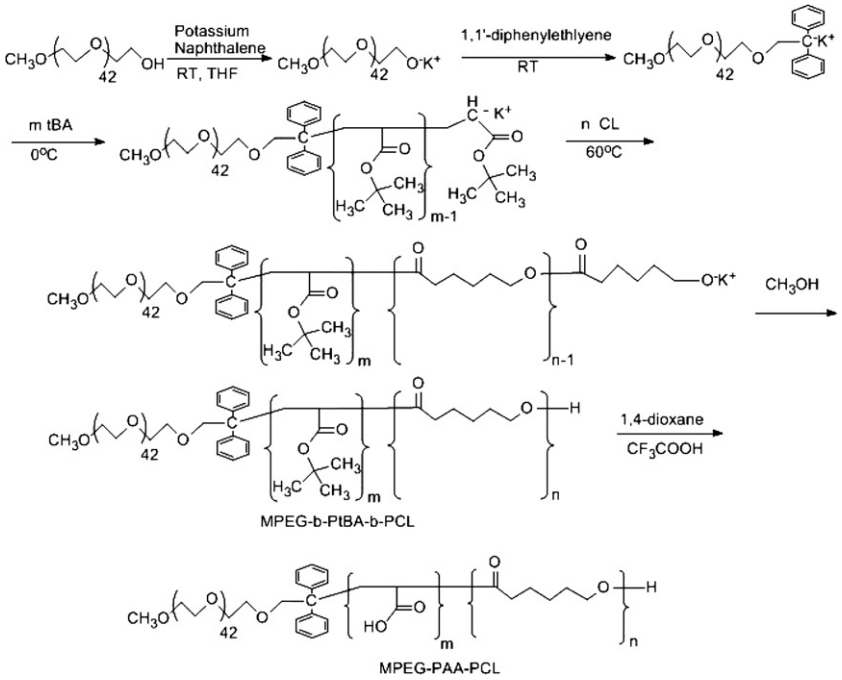

Scheme 1. Synthesis of PEG–PAA–PCL.

information such as ion distribution in the nucleation process, the mechanism of the morphology control is still not very clear from the viewpoint of supersaturation. Recently, the stable prenucleation calcium carbonate clusters were studied by measuring free Ca^{2+} concentration [42], which provided important information to mineralization control.

As an extension for the study on synthesis of hollow spherical HA [28], we present a detailed investigation on the templating effect of PEG–PAA–PCL for controlled mineralization of HA. The free Ca^{2+} concentration, zeta potential and pH value were pursued and the solution supersaturation was monitored to analyze the effect of polymer on HA formation, and we found the amphiphilic triblock copolymer PEG–PAA–PCL with a c–s–c micelle structure played a role differing from the diblock copolymer PAA–PCL. "Reservoir" and "barrier" effects of this ABC block copolymer micelle in mineralization control were proposed. We hope this study will not only provide a new understanding of the mineralization mechanism of HA, but also a way for the development of biocompatible materials by utilizing novel designed polymers. Such HA nano spheres are interesting and might be useful as novel drug delivery carriers, ceramics precursors, reinforcing fillers, or biomedical implants.

2. Experimental section

2.1. Materials

The monohydroxy capped poly (ethylene oxide) (MePEG-OH, Mn = 1900) was obtained from Aldrich Chemicals. Trace amounts of water were removed from MePEG-OH by vacuum applied to the molten polymer at 55 °C for 1 h.

Tert-butyl acrylate (tBA) obtained from Aldrich Chemicals was passed through a column of activated alumina to remove the stabilizing agents, dried over calcium hydride for 48 h at room temperature, then vacuum distilled and stored under a nitrogen atmosphere at −20 °C. The required amount of the distilled tBA was taken into a flask to which was added drop by drop 25 %wt $AlEt_3$ solution in hexane until a persistent yellow green color was observed. tBA was redistilled under reduced pressure, just prior to polymerization experiment [43].

ϵ-Caprolactone (ϵ-CL, from Aldrich Chemicals, 99%) obtained from Aldrich Chemicals was dried over calcium hydride for 48 h at room temperature, and distilled under reduced pressure just before use.

Potassium di (trimethylsilicon) amide ($[(CH_3)_3Si]_2N^-K^+$) in toluene (0.5 M) was purchased from AlfaAesar.

Tetrahydrofuran (THF) purchased from Sinopharm Chemical Reagent Co., Ltd was dried by refluxing over potassium, and distilled just before use.

Potassium naphthalene (0.5 M) was prepared by our lab: dissolving naphthalene in THF and refluxing this solution over potassium until the compound becomes dark blue, the ratio of potassium and naphthalene is 1:1.

$CaCl_2$, K_3PO_4, CF_3COOH, 1,1′-diphenylethylene, 1,4-dioxane, and petroleum ether (bp. 60–90 °C) were purchased from Sinopharm Chemical Reagent Co., Ltd and used without further purification. All solvents were of analytical grade and were used as received, unless stated specially.

Table 1
Basic parameters of the precursor (PEG–PtBA–PCL) of the two triblock copolymers and the precursor (PtBA–PCL) of the diblock copolymers with different block lengths.

Polymer	Monomer (mmol)			Percentage of hydrolysis	Mn			PDI (GPC)
	PEG	tBA	CL		Theory	NMR	GPC	
PEG_{43}–$PtBA_{21}$–PCL_{35}	1	31.25	45.25	90	9744	8578	9234	1.37
PEG_{43}–$PtBA_{40}$–PCL_{47}	1	60.50	60.55	91	16,420	12,378	12,745	1.31
$PtBA_{32}$–PCL_{47}	0	60.50	60.55	88	14,692	9626	10,592	1.33

Table 2
Mineralization of HA at pH 9 (Ca:P = 1.67:1).

Sample	Template (3×10^{-4} g/mL, 50 mL)	Quantity of COO^- (mol)	Total quantity of Ca^{2+} and introduction method in a period (0.01 M $CaCl_2$)	Total quantity of PO_4^{3-} and introduction method in a period (0.01 M K_3PO_4)
1	Blank	0	1.5×10^{-5} mol, 50 μL × 30	0.9×10^{-5} mol, 50 μL × 16
2	Copolymer 1	3.0×10^{-5}	1.5×10^{-5} mol, 50 μL × 30	0.9×10^{-5} mol, 50 μL × 16
3	Copolymer 2	4.2×10^{-5}	1.5×10^{-5} mol, 1500 μL × 1	0.9×10^{-5} mol, 900 μL × 1
4	Copolymer 2	4.2×10^{-5}	1.5×10^{-5} mol, 50 μL × 30	0.9×10^{-5} mol, 50 μL × 16
5	Copolymer 3	4.0×10^{-5}	1.5×10^{-5} mol, 50 μL × 30	0.9×10^{-5} mol, 50 μL × 16

Mineralization of HA was performed for 3 periods.

2.2. Characterization methods

2.2.1. Nuclear magnetic resonance spectroscopy

The ^1H NMR spectroscopy of polymers were measured in $CDCl_3$ (>99.8%, SDS, Peypin, France) on a Bruker ARX 500 NMR spectrometer.

2.2.2. Gel permeation chromatography

The molecular weights and molecular weight distributions of polymers were determined with a gel permeation chromatography, using HPLC-grade THF as mobile phase at a flow rate of 1 mL/min and a GMH-HR M (Viscotek, Houston, TX) column. The molecular weights of the polymers were calibrated against polystyrene (Polymer Laboratories, Shropshire, UK). The injected volumes were 0.1 mL and the polymer concentrations were 3 g/L.

2.2.3. Dynamic light scattering

Dynamic light scattering measurements were performed with a Brookhaven Instruments Corp. 90 Plus/BI-MAS analyzer and a 150 W argon laser at a wavelength of 658 nm. The scattering angle used for the measurements was 90°. For each sample, three to five repeated measurements were taken. The concentration of the filtered polymer solutions (using 450 nm filter) investigated by light scattering is 0.3–0.5 g/L. From dynamic light scattering, the hydrodynamic radii (Rh) of micelles were obtained.

2.2.4. Transmission electron microscopy

For each sample of TEM, a drop of copolymer solution was placed onto a copper grid (200 mesh) precoated with carbon film followed by immediate frozen by liquid nitrogen. The sample then was dried by lyophilization. Measurements were conducted using a JEM-1230 transmission electron microscope operated at an accelerating voltage of 110 kV.

2.2.5. Scanning electron microscopy

SEM was carried out with a Sirion FEG-SEM (FEI, USA). Samples were prepared by evaporating a drop of the sample solutions on a glass plate, and gold was coated on the sample surface with 80 s sputtering time, 2 mbar pressure, and 18 mA current.

2.2.6. X-ray powder diffraction

X-ray powder diffraction was performed with a Rigaku RAXIS-RAPID powder X-ray diffractometer in Bragg-Brentano geometry, using Cu Kα radiation. The diffraction pattern was collected in the 2θ range 5–80°.

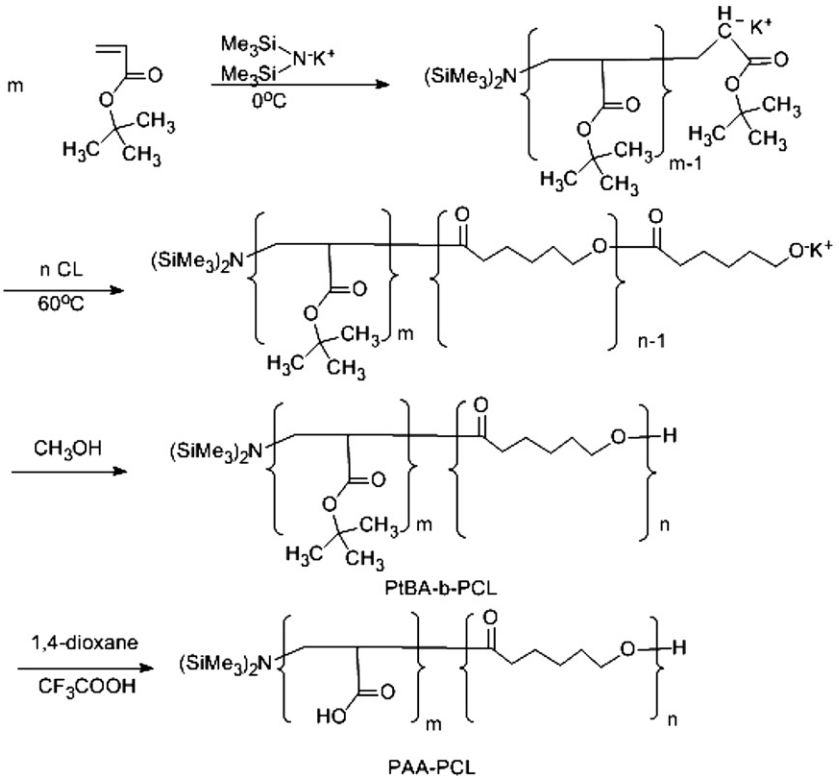

Scheme 2. Synthesis of PAA–PCL.

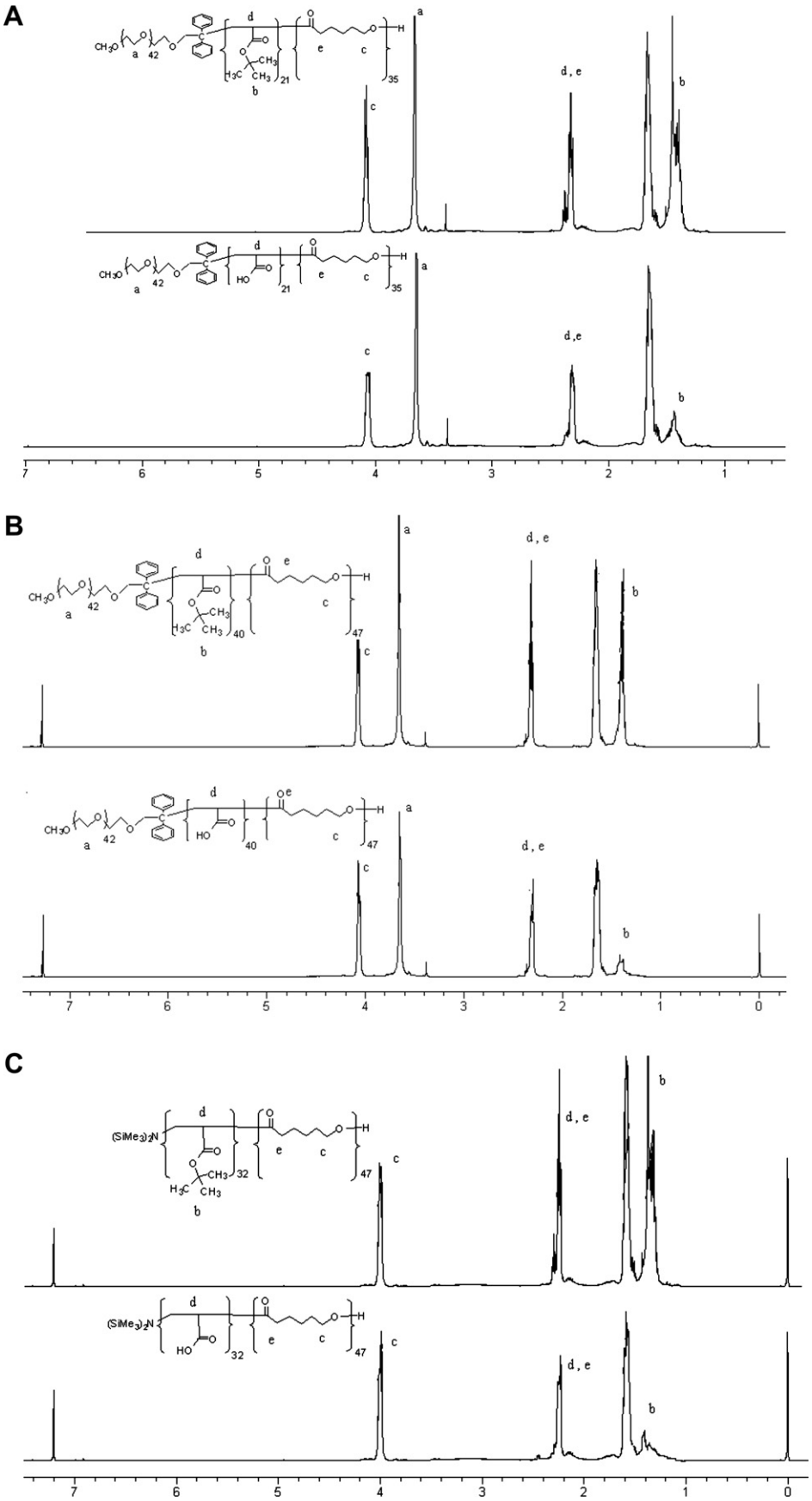

Fig. 1. A: ^{1}H NMR spectrum PEG_{43}–$PtBA_{21}$–PCL_{35} before and after hydrolysis. B: ^{1}H NMR spectrum PEG_{43}–$PtBA_{40}$–PCL_{47} before and after hydrolysis. C: ^{1}H NMR spectrum $PtBA_{32}$–PCL_{47} before and after hydrolysis.

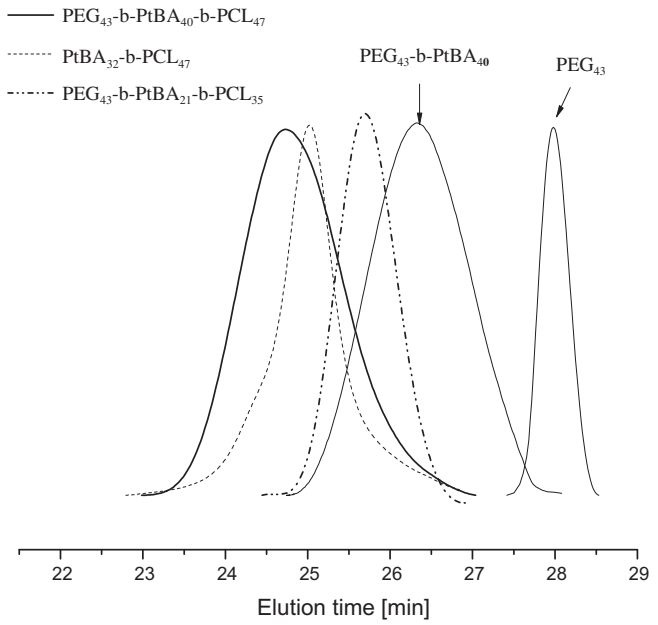

Fig. 2. GPC curves of block copolymers, where PEG_{43} and PEG_{43}–$PtBA_{40}$ curves are compared to illustrate the propagation of the block copolymers.

2.2.7. Potentiometric titration

The interactions between polymer and Ca^{2+} were investigated using the electromotive force technique coupled with a Ca^{2+} ion selective electrode (Ca^{2+} ISE) and a reference Hg/Hg_2Cl_2 electrode. The titration experiments were conducted using the Radiometer TIM 840. Titration of $CaCl_2$ solution into deionized water was measured to calibrate the electrode, the Nernst equation is emf = Alog $C_{Ca^{2+}}$ + B, which was used to calculate the mobile Ca^{2+} ion concentration from the emf value, was calibrated during every measurement.

2.2.8. Infrared spectroscopy (IR)

Infrared spectroscopy was recorded using a Nicolet FT-IR/Nexus 470.

2.2.9. Zeta potential

Zeta potential measurements were carried out with Zetasizer (Malvern ZEN3600). All samples were passed through a membrane filter (450 nm pore size) before detection. The polymer concentration was fixed at 0.3 g/L for zeta potential measurement.

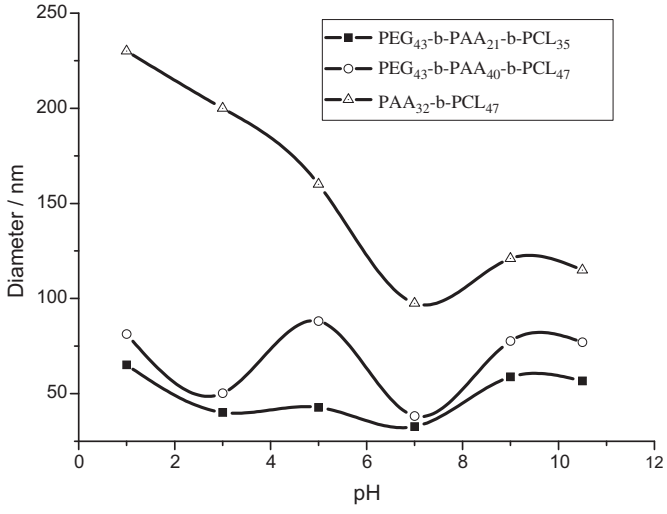

Fig. 3. Diameters of micelles at different pH while at 25 °C.

Table 3
Supersaturation of HA nucleation and growth.

Sample	Template	σ		
		Period 1	Period 2	Period 3
1	Blank	4.78×10^{20}	3.33×10^{19}	3.12×10^{19}
2	Copolymer 1	7.91×10^{17}	8.04×10^{17}	8.21×10^{17}
3	Copolymer 2	8.90×10^{20}	1.37×10^{22}	4.19×10^{22}
4	Copolymer 2	9.72×10^{16}	9.84×10^{16}	9.12×10^{16}
5	Copolymer 3	1.01×10^{19}	9.73×10^{18}	9.70×10^{18}

Changes in supersaturation during the periodical addition of $CaCl_2$ and K_3PO_4 into solutions. Sample 1, 2, 4, 5: total $CaCl_2$ volume is 1500 μL (50 μL × 30), total K_3PO_4 volume is 900 μL (50 μL × 16); Sample 3: total $CaCl_2$ volume is 1500 μL (1500 μL × 1), total K_3PO_4 volume is 900 μL (900 μL × 1). Supersaturation was calculated by the equation $\sigma = \frac{[\alpha(Ca^{2+})]^5[\alpha(PO_4^{3-})]^3[\alpha(OH^-)]}{K_{sp}(HAp)}$, σ is defined as the supersaturation of a solution, being the source of a driving force for mineralization in solution [1]. Each of data was obtained when K_3PO_4 was added into solution for the first time after the addition of 1500 μL $CaCl_2$. Each σ value represents initial supersaturation of a solution in each period. K_{sp} is the solubility product, and α(i) is the activity of species i. Concentration c(i) is used in the equation to replace α(i). The experimental error of mobile Ca^{2+} concentration is within ±2%.

2.3. Synthesis of triblock polymer and diblock polymer

The triblock poly (ethylene glycol)–block-poly (acrylate acid)–block-poly (ϵ-caprolactone) (PEG–PAA–PCL) copolymer and the diblock copolymer poly (acrylic acid)–block-poly (ϵ-caprolactone) (PAA–PCL) were synthesized by sequential anionic polymerization. The detailed procedures of the synthesis are shown in the Supplementary Data.

2.4. Mineralization of hydroxyapatite in the presence of block copolymers

2.4.1. Preparation of polymer solution

The sample of triblock copolymer (0.075 g) was dissolved in 10 mL THF, and 20 mL deionized water was added into the solution in 4 h. Then the solution was transferred to a dialysis bag (molecular weight cut-off = 14 000) and dialyzed against distilled water for 1 day by changing water once per 3 h. The dialyzed solution was fixed to 250 mL as a stock solution. The self-assembly behavior of the solutions was studied by using DLS technique. The same operation was done on the diblock copolymer.

2.4.2. Mineralization of HA

A Series of $CaCl_2$ standard solution was prepared from 10^{-5} M to 10^{-1} M for calibrating the electrode. From the titration curves of pH and conductivity, we found that the carboxylic acid groups are mostly neutralized to carboxylate groups at >pH 7. To make sure the formation of HA, at ~pH 9, a known amount of stock polymer solution was applied to tune the mineralization of HA by titrating with $CaCl_2$ and K_3PO_4 (Table 2). The precipitation of $Ca_{10}(PO_4)_6(OH)_2$ was carried out in a glass vessel at room temperature. Each operation of addition of Ca^{2+} and PO_4^{3-} was performed every 5 min, and the whole addition of 1500 μL $CaCl_2$ and 900 μL K_3PO_4 was defined as one mineralization period. The precipitation of calcium by the addition of potassium phosphate was performed, 12 h after $CaCl_2$ (0.01 M) had been added into the sample 2, 3, 4 and 5, to insure the coupling of Ca^{2+} with COO^- groups of PAA segments. The stoichiometric amount of phosphate in water (0.01 M) was added to yield a Ca:P ratio of 1.67:1 under vigorous stirring. The pH value and emf were measured when $CaCl_2$ or K_3PO_4 was added into solution. The resultant mixture was aged for 16 h to induce the formation of apatite, and the sample was preserved for

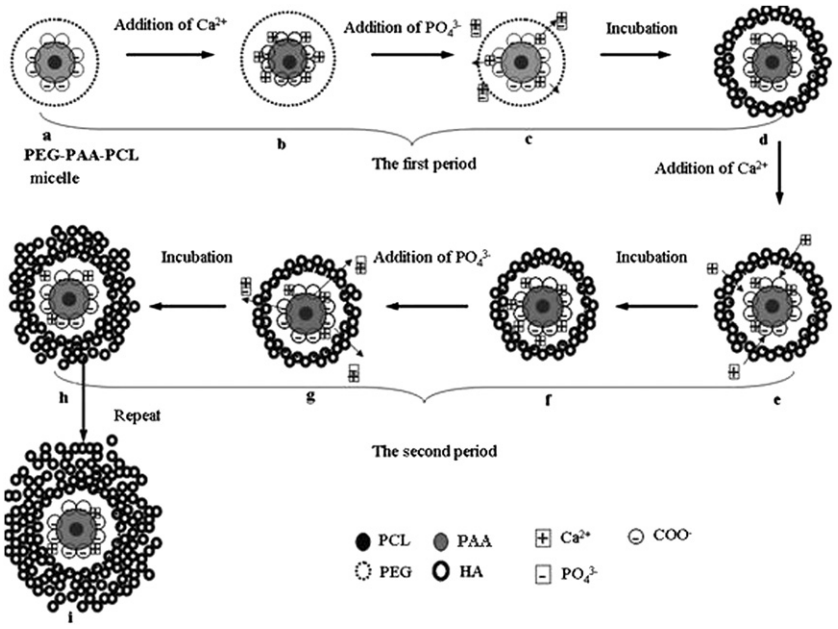

Scheme 3. Formation mechanism of HA.

zeta potential measurement. The above operation was repeated for 3 times. The obtained complex was washed, and then calcined in a muffle furnace in air at 650 °C for 1 h.

3. Results and discussion

3.1. Synthesis and characterization of polymers

The synthesis of PEG–PAA–PCL was carried out using sequential anionic polymerization with potassium naphthalene as initiator (Scheme 1). The potassium naphthalene was dropped into the PEG to become a potassium alcoholate macro-initiator. A few drops of 1, 1′-diphenylethlyene were added into the solution before the addition of tBA. This progress converts oxyanion into diphenylalkyl anion, providing a less sterically hindered, which initiated tBA with less unwanted competing reaction with ester functionality. After ϵ-CL was injected into the reactor, a relatively high temperature (60 °C) is applied comparing with normal polymerization, for the high temperature would be beneficial to the ring open polymerization (ROP). The final amphiphilic copolymer PEG–PAA–PCL was obtained by hydrolysis of PtBA into PAA using trifluoroacetic acid in 1,4-dioxane. The molecular weight of the precursor (PEG–PtBA–PCL) of the two triblock copolymers differing only in the relative block lengths, determined by ^{1}H NMR and GPC, are summarized in Table 1. The main difference among two triblock copolymers is the content of PAA block length, which changes from 21 (copolymer 1) to 40 (copolymer 2).

The synthesis of PAA–PCL was carried out using sequential anionic polymerization with potassium di (trimethylsilicon) amide ($[(CH_3)_3Si]_2N^-K^+$) as initiator (Scheme 2). The molecular weight of the precursor (PtBA–PCL) of the diblock copolymer determined by ^{1}H NMR and GPC is also summarized in Table 1.

Fig. 1 shows the ^{1}H NMR spectra of polymers PEG_{43}–$PtBA_{40}$–PCL_{47}, PEG_{43}–$PtBA_{21}$–PCL_{35}, and $PtBA_{32}$–PCL_{47} before and after hydrolysis. In Fig. 1A, the peak a is assigned to the methylene group of PEG, peak b to the methyl protons of tBA, and peaks d and e to the methine group of PtBA and PCL, respectively. Peak c is attributed to the methylene group next to the oxygen of PCL. Peaks b and c attributed to PtBA and PCL, respectively, appear with subsequent reaction demonstrating the successful copolymerization. After hydrolysis of the PtBA, the sharp peak b disappears, which indicates the removal of tert-butyl groups and the formation of an amphiphilic block polymer as expected. The percentages of

Table 4
Zeta potential of different templates (ξ/mv).

Template	pH = 9	Period 1		Period 2		Period 3	
		$1-Ca^{2+}$	$1-PO_4^{3-}$	$2-Ca^{2+}$	$2-PO_4^{3-}$	$3-Ca^{2+}$	$3-PO_4^{3-}$
Copolymer 1	−48.2	−14.6	−26.1	−12.4	−23.2	−9.3	−22.9
Copolymer 2	−51.2	−11.2	−24.5	−9.9	−22.7	−6.1	−20.2
Copolymer 3	−46.4	−18.7	−29.6	−16.7	−27.9	−14.8	−26.5

The experimental error of zeta potential is within ±0.5mv.

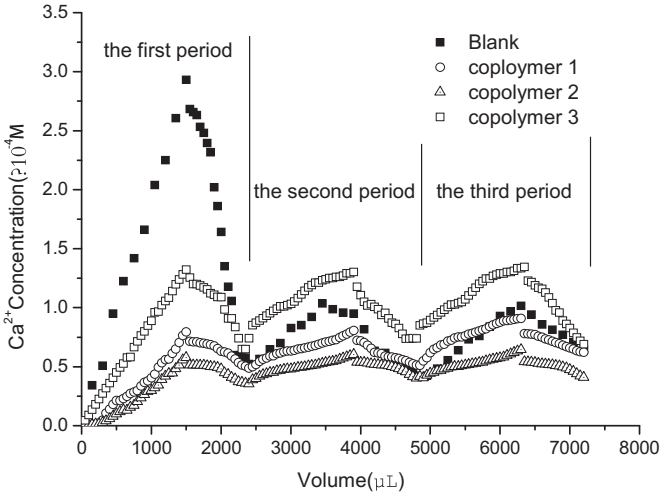

Fig. 4. Changes in Ca^{2+} ions concentration in three mineralization periods Ca^{2+} ions concentration versus whole additive volume (including $CaCl_2$ and K_3PO_4) for copolymer solutions and blank solution. $CaCl_2$ and K_3PO_4 were periodically added into copolymer solutions (50 μL/5 min, total $CaCl_2$ volume is 1500 μL, total K_3PO_4 volume is 900 μL, corresponding to Table 2, Sample 1, 2, 4, 5).

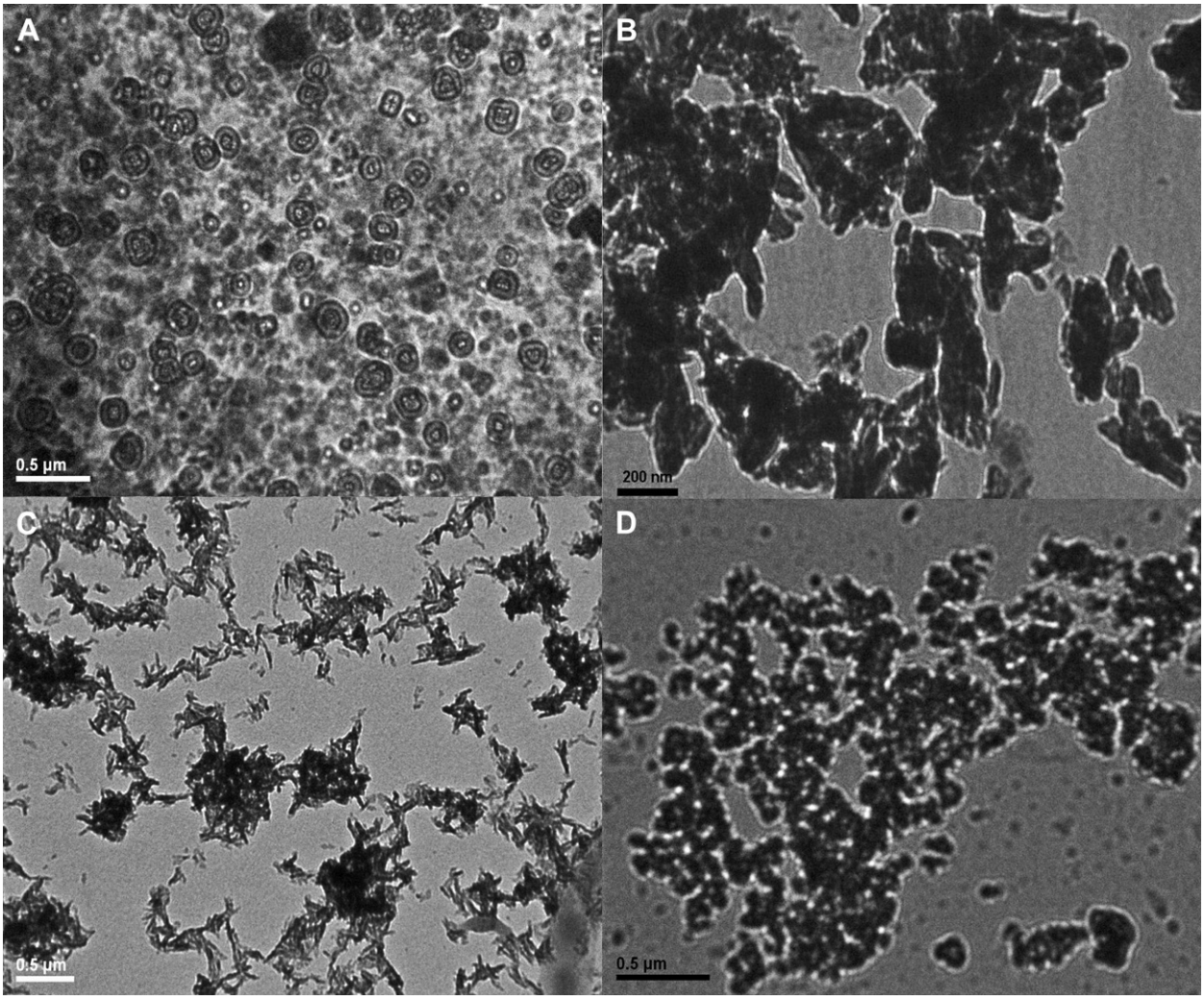

Fig. 5. TEM image of micrographs of HA crystallite aggregates obtained from solution A: HA crystallite aggregates obtained from triblock copolymer solution (corresponding to Table 2, Sample 4); B: HA crystallite aggregates obtained from diblock copolymer solution (corresponding to Table 2, Sample 5); C: HA crystallite aggregates obtained from blank solution (corresponding to Table 2, Sample 1); D: HA crystallite aggregates obtained from triblock copolymer solution (corresponding to Table 2, Sample 3).

hydrolysis of the copolymers were determined by calculating the ratio of the integrated peak areas of the unhydrolyzed part to the original part of tert-butyl groups. The hydrolysis ratio of PtBA to PAA was above 90% according to the NMR results.

Fig. 2 shows the GPC curves of PEG_{43}–$PtBA_{40}$–PCL_{47}, PEG_{43}–$PtBA_{21}$–PCL_{35}, and $PtBA_{32}$–PCL_{47}, where PEG_{43} and PEG_{43}–$PtBA_{40}$ curves are compared to illustrate the propagation of the block copolymers. These polymers were characterized by GPC with linear polystyrene standards in THF. The *Mn* obtained by GPC and NMR are similar, but the polydispersity index (PDI) is not very low. It revealed that anionic polymerization of alkyl acrylate is rather complicated due to side reactions associated with ester functionality. The symmetric peak without a shoulder in the molecular-weight region indicates the copolymers can be considered to have uniform molecular weight.

3.2. Self-assembly behavior of amphiphilic block copolymer

The characteristics of copolymer 1 (PEG_{43}–PAA_{21}–PCL_{35}), copolymer 2 (PEG_{43}–PAA_{40}–PCL_{47}), and copolymer 3 (PAA_{32}–PCL_{47}) in an aqueous phase were investigated by DLS, which measured the hydrodynamic diameters of the micelles. Fig. 3 shows the changes of the micelle sizes at different pH. The morphology evolution is quite complicated for these block copolymers. At low pH (<1), the PAA segments are hydrophobic, which easily aggregate with themselves or PCL segments. When the environment becomes less acidic, the solubility of the PAA segments goes higher, hence the large aggregates begin to separate when pH changes from 1 to 3, and the radii decrease. The pKa of PAA is ~4.30; hence most of carboxylic acid groups of PAA segments deprotonate to carboxylate groups at pH 3–7. The balance between the electrostatic repulsion effect of shell structure and the effect of segregation makes a drift of radii at this pH range. In this work, the smallest micelle size occurs at ~pH 7 for all the three block copolymers. When pH > 9, the size of micelles shows no obvious change, suggesting the stable micelle structure at relatively high pH condition.

The micelle size of copolymer 2 is larger than that of copolymer 1, and variety of the micelle size of copolymer 2 is more intense than that of copolymer 1 possibly due to longer PAA segments. Comparing with those of copolymers 1 and 2, at low pH (<7), the particle size of copolymer 3 is much larger. This phenomenon indicated that the hydrophilic PEG segments in triblock copolymer are in favor of keeping the micelle as small aggregate.

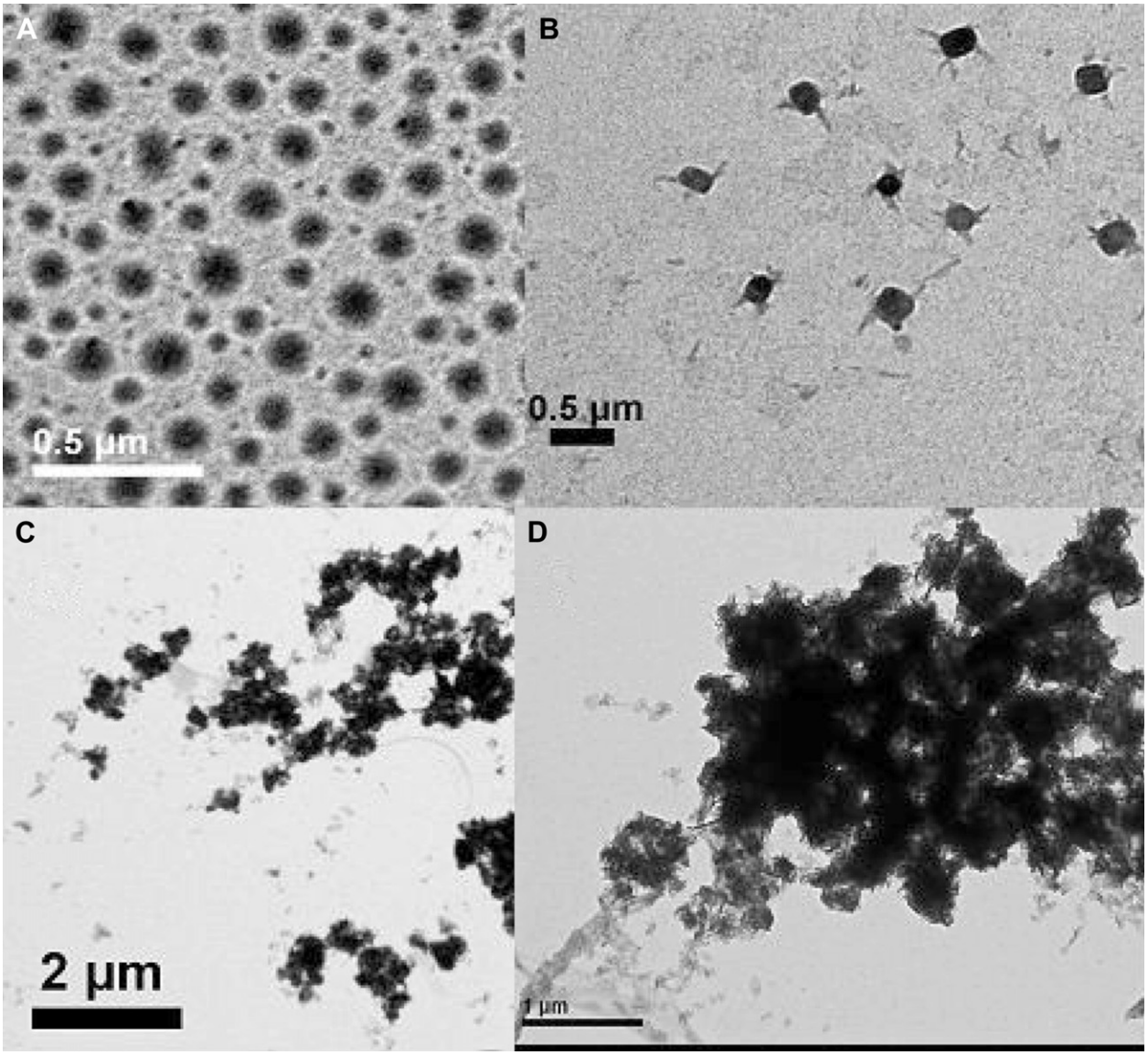

Fig. 6. TEM image of micrographs of HA crystallite aggregates obtained from triblock copolymer solution in different mineralization period A, B, C and D represent the 1st, 4th, 5th and 7th mineralization period respectively.

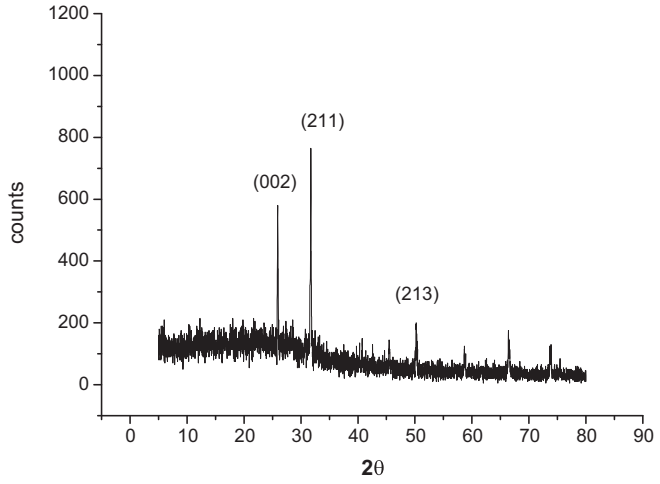

Fig. 7. XRD spectra of HA obtained from the solution of triblock copolymer 2.

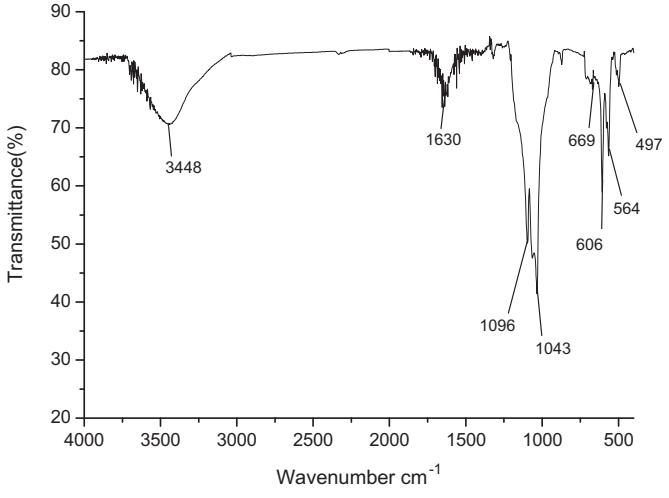

Fig. 8. FT-IR spectra of HA obtained from the solution of triblock copolymer 2.

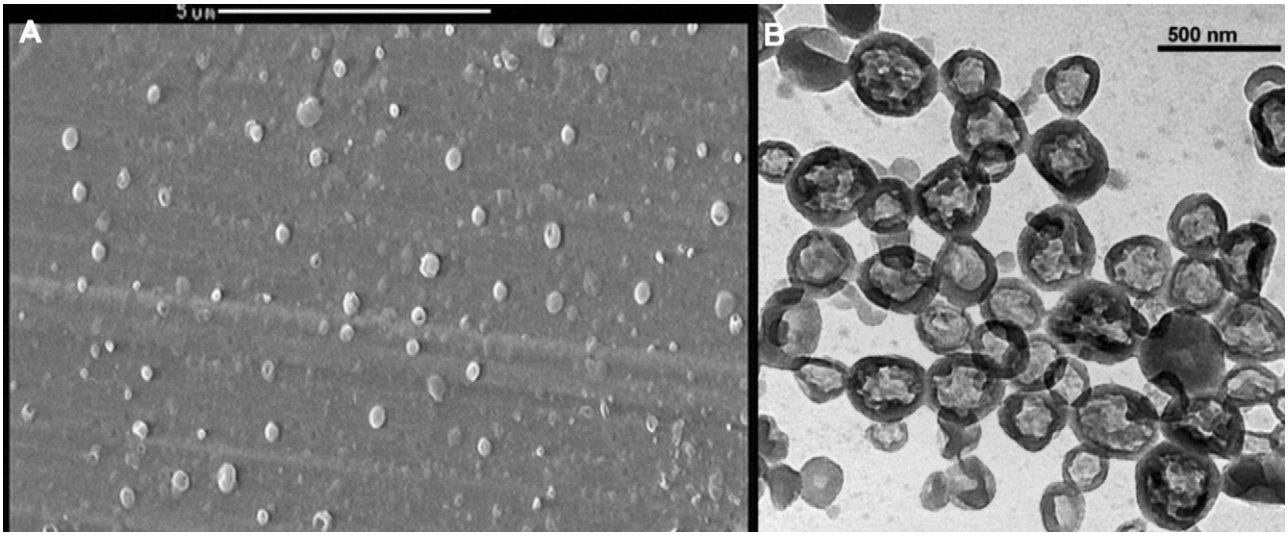

Fig. 9. micrographs of HA nano sphere after calcination A: SEM image; B: TEM image.

At pH 9, the triblock copolymer spontaneously forms the star-like micelle consisting of a dense PCL core, a stretched PAA shell and a PEG corona, and is hoped to be suitable for tuning mineralization of HA.

3.3. HA mineralization tuned by block copolymers

In nature, nucleation plays an important role as the first step of mineralization in building up a complex structure. However, the nucleation process is hard to study since the nuclei are usually unstable because of their high surface energy and grow soon after their formation. There are only a few studies on this key process up to now [39,41]. As we know, the supersaturation of a solution is the source of a driving force for mineralization. Jiang et al. [40] found that the adsorbed ChS (Chondroitin 4-sulfate) leads to a stronger interaction and a better structural match between the substrate and HA at low supersaturation, whereas it leads to structural mismatch between the substrate and HA at high supersaturation. To understand the mechanism of mineralization, we examined the effect of copolymers on the nucleation and growth of HA from the viewpoints of supersaturation and Ca^{2+} ion distribution.

3.3.1. Supersaturation control

Several processes were designed to study mineralization of HA, which is shown in Table 2. For all of these block copolymer systems, COOH groups were ionized to COO^- groups (pH > 7). When Ca^{2+} ions were introduced into polymer solutions, the PAA segments were neutralized by this kind of alkali earth metal ion. The reaction of calcium with phosphate was performed after 12 h incubation of Ca^{2+} onto micelles, to form apatite layers. During mineralization, zeta potential, emf, and pH value were measured. The pH value varied in the range of 8.5–9.5 for the whole process. Supersaturation data of the solutions were calculated based on the concentration of mobile Ca^{2+} ions by the emf measurement.

Supersaturation value maintaining at a low level is benefit to HA controlled mineralization, to avoid the so-called supersaturation-driven interfacial structure mismatch [40]. Compared with the blank solution (sample 1 in Table 3), the supersaturation [1] values of copolymer solutions (sample 2, 4, and 5 in Table 3) during the first mineralization period shifted to smaller, which suggests that the block copolymers may be able to control HA mineralization via tuning the supersaturation.

In addition, supersaturation of sample 4 presents the lower value than that of sample 3, in which the $CaCl_2$ and K_3PO_4 were added into solution at one time. These data indicate that adding $CaCl_2$ and K_3PO_4 time after time tends to better control the HA mineralization.

3.3.2. Calcium reservoir

The possible mechanism of block copolymer tuned mineralization of HA is proposed and demonstrated in Scheme 3. Initially, the zeta potential was highly negative at pH 9 (Scheme 3a), whereas the negative value rapidly decreased as the Ca^{2+} was added (Table 4, Scheme 3b). The Ca^{2+} ions passed through the corona to react with PAA segments, thus there was lower concentration of mobile Ca^{2+} ions in the solution. Stoichiometric Ca^{2+} ions did not couple with COO^- groups completely; hence the micelles still possess negative charge. When PO_4^{3-} ions were added, the Ca^{2+} ions that are bounded to the micelles can be released from PAA segments to react with PO_4^{3-} and OH^- ions to form apatite layers around the micelles (Scheme 3c and d). As a result, the zeta potential returned to highly negative and mobile Ca^{2+} ions concentration decreased. Afterwards, periodical additions of $CaCl_2$ and K_3PO_4 into the solutions caused the fluctuation of zeta potential and mobile Ca^{2+} ions concentration (Scheme 3e–i). Obviously, the block copolymer micelles served as “calcium reservoirs” in the mineralization process.

For the second and third periods of “blank” sample, we can find the concentration of mobile Ca^{2+} did not change obviously as the first period, which means after the first run, the HA crystallites have already formed, thus the latter mineralization will be affected by the HA crystallites.

3.3.3. Barrier on a reservoir

The data of zeta potential (Table 4) show the fluctuation in the mineralization process, and the concentration of mobile Ca^{2+} ions also fluctuated (Fig. 4). The trends of the fluctuations are consistent with the mechanism demonstrated in Scheme 3.

In Table 4, an interesting phenomenon in the HA mineralization was found. The difference ($\Delta\xi$) between zeta potential values ξ (pH = 9) and ξ (1−Ca^{2+}) of copolymer can represent the quantity of immobilization of Ca^{2+} ions. There were similar quantity of COO^- in copolymer 2 and 3, however, $\Delta\xi_{Copolymer3}$ (27.7 mV) was much less than $\Delta\xi_{Copolymer2}$ (40.0 mV), which indicated the PAA segment was

not the only factor in adsorption of Ca^{2+} ions. PEG segments should play a role in stabilizing Ca^{2+} ions due to the weak interaction, and we give the name as "barrier effect" of PEG segments, which is a supplement to the "reservoir effect" of the micelle.

The "barrier effect" of PEG segments means that: as PO_4^{3-} ions were added, Ca^{2+} ions penetrated out through the PEG corona to react with PO_4^{3-} and OH^- ions in bulk, and formed the apatite around the corona (Scheme 3c and d); Ca^{2+} ions released from corona structure slowly, which provide a relatively mild nucleation condition with low supersaturation (Table 3); in the next periods, Ca^{2+} ions penetrate in/out through interstice of the formed apatite layer and PEG corona as ion-transferred channel, to tune the mineralization. This tunable mechanism is similar to the function of the "barrier" on a "reservoir".

3.3.4. Morphology

Nucleation of HA tuned by copolymers via low supersaturation will facilitate the formation of well aligned HA assembly. The typical TEM micrographs in Fig. 5A and C for copolymers 2 solution and blank solution show that the aggregates of copolymers 2 form spherical particles, however, the needlelike morphology forms in the blank solution, which confirms the role of copolymer in the crystallization behavior of HA.

As shown in Fig. 5A, there are two dark loops in each spherical particle. The inner loop possessed an average diameter between 50 and 80 nm consistent with average diameter of copolymer micelles (Fig. 3). However, the rigorous control of the inner space of the HA particle is still a challenge, due to the complicated process in the mineralization, including ion condensation, crystallization, polymer swell or shrink, etc. After three times mineralization periods, as shown in Fig. 5A, the external loop possesses an average diameter about 300 nm consisting of apatite layer. The shell thickness of nano sphere is obviously thicker than that in the earlier work [28], indicating an effective method for fabrication of controlled structure. HA crystallites are also formed around the diblock copolymer micelles, but parts of Ca^{2+} and PO_4^{3-} ions tend to diffuse in the bulk. Hence, there is more proportion of prism morphology in the TEM images (Fig. 5B).

The TEM image of HA crystallite aggregates in Fig. 5D was obtained from copolymer 2 solution with directly adding the whole quantity of inorganic ions, where there are many prism forms outside the copolymer micelles. This result indicates that the method of adding Ca^{2+} and PO_4^{3-} ions time after time tends to form spherical particles and is better for crystalline control of HA due to lower supersaturation.

Further investigation on mineralization is shown in Fig. 6, possibly indicating limited "barrier effect" of PEG segments. Fig. 6A is the picture of the aggregates after the first mineralization period, where the HA layer is still unstable that cannot be observed by TEM. After the 3rd mineralization period (Fig. 5A), we can find there are spherical particles with two dark loops. However, there is needlelike morphology forming around HA spheres (Fig. 6B) in the 4th mineralization. With more quantity of Ca^{2+} and PO_4^{3-} ions added, HA spheres are fully coated with needlelike prisms and fabricate larger aggregates from the 5th to 7th mineralization period (Fig. 6C and D). The above phenomenon embarrassing the further growth of shell thickness, will be studied in the future.

After calcination in a muffle furnace, we got HA nano sphere. FT-IR and XRD results are summarized in Figs. 7 and 8, respectively. The IR peaks at 1096, 1043, 606, 669 cm^{-1} correspond to characteristic PO_4^{3-} infrared vibration. The peaks at 3448, 1630 cm^{-1} correspond to characteristic O–H infrared vibration. The XRD peaks at $2\theta = 25.9^\circ$, 31.8°, $50.2^\circ$are assigned to (002), (211) and (213) planes of the diffraction of hydroxyapatite. Under the control of triblock copolymer, spherical particles of 300 nm in size are observed in the center of the SEM image (Fig. 9A). There are also some parts of spherical particles possessing larger diameter. Aggregation of particles during calcination process may contribute to this phenomenon. The TEM image (Fig. 9B) clearly illustrates the hollow space in the HA particles, and the wall is rather thick and consistent with the image of Fig. 5A, which indicates the calcination did not seriously change the HA morphology. These results provide strong evidence that triblock copolymer PEG–PAA–PCL has a good influence on the morphology control for producing porous HA materials.

4. Conclusion

Nano-sized HA-polymer hybrid spheres were obtained using a molecule that contains three structural motifs varying in function. The copolymer was employed as a dispersed template for the controlled mineralization of calcium phosphate from aqueous solution by different means. Triblock copolymer can keep the structural match domain at a much lower supersaturation level and facilitate the formation of well aligned HA assembly. Our study on triblock copolymer solution revealed interesting interactions between PEG–PAA–PCL and Ca^{2+} ions. The triblock copolymer plays a role of "reservoir", and PEG segments forming the corona structure is a "barrier" during mineralization process. We studied the formation mechanism of HA. The interstice within the apatite layer adhered to corona can be used as ion-transferred channel, through which Ca^{2+} ions release from copolymer micelles as Ca^{2+} ions source to form subsequent HA crystals. The shell thickness of nano sphere is obviously thicker than that in the earlier work, indicating an effective method for fabrication of controlled structure. These nano-sized hydroxyapatite spheres, growing from the surface of corona structure, may be useful as novel drug delivery carriers, ceramic precursors, reinforcing fillers, or biomedical implants.

Acknowledgement

This work was supported by the National Natural Science Foundation of China (No. 20873121), National Basic Research Program (No. 2009CB930104), the Scientific Research Foundation for the Returned Overseas Chinese Scholars, State Education Ministry (J20060126), and Scientific Research Fund of Zhejiang Provincial Education Department (Z200701142).

Appendix. Supplementary material

Supplementary data related to this article can be found online at doi:10.1016/j.polymer.2010.12.017.

References

[1] Dorozhkin SV, Epple M. Angew Chem Int Ed Engl 2002;41:3130–46.
[2] Mann S, Webb J, Williams RJP. Biomineralization: chemical and biological perspectives. New York: VCH Publishers; 1989.
[3] Currey J. Nature 2001;414:699.
[4] Thompson JB, Kindt JH, Drake B, Hansma HG, Morse DE, Hansma PK. Nature 2001;414:773–6.
[5] Yamashita Y, Uchida A, Yamakawa T, Shinto Y, Araki N, Kato K. Int Orthop 1998;22:247–51.
[6] Murphy WL, Mooney DJ. J Am Chem Soc 2002;124:1910–7.
[7] Tanahashi M, Yao T, Kokubo T, Minoda M, Miyamoto T, Nakamura T, et al. J Biomed Mater Res 1995;29:349–57.
[8] Zhang RY, Ma PX. Macromol Biosci 2004;4:100–11.
[9] Bajpai AK, Singh R. Polym Int 2007;56:557–68.
[10] Taguchi T, Muraoka Y, Matsuyama H, Kishida A, Akashi M. Biomaterials 2001;22:53–8.
[11] Stupp SI, Braun PV. Science 1997;277:1242–8.
[12] Kawashita M, Nakao M, Minoda M, Kim HM, Beppu T, Miyamoto T, et al. Biomaterials 2003;24:2477–84.

[13] Bigi A, Boanini E, Walsh D, Mann S. Angew Chem Int Ed Engl 2002;41:2163–6.
[14] Peytcheva A, Colfen H, Schnablegger H, Antonietti M. Colloid Polym Sci 2002;280:218–27.
[15] Cai YR, Pan HH, Xu XR, Hu QH, Li L, Tang RK. Mater Chem 2007;19:3081–3.
[16] Jutza G, Boker A. J Mater Chem 2010;20:4299–304.
[17] Tang QL, Zhu YJ, Duan YR, Wang Q, Wang KW, Cao SW, et al. Dalton Trans 2010;39:4435–9.
[18] Mann S. Angew Chem Int Ed Engl 2000;39:3393–406.
[19] Mann S, Ozin GA. Nature 1996;382:313–8.
[20] Kniep R, Busch S. Angew Chem Int Ed Engl 1996;35:2624–6.
[21] Yang H, Coombs N, Ozin GA. Nature 1997;386:692–5.
[22] Antonietti M, Grohn F, Hartmann J, Bronstein L. Angew Chem Int Ed Engl 1997;36:2080–3.
[23] Qi LM, Colfen H, Antonietti M. Angew Chem Int Ed Engl 2000;39:604.
[24] Schachschal S, Pich A, Adler HJ. Langmuir 2008;24:5129–34.
[25] Colfen H. Macromol Rapid Commun 2001;22:219–52.
[26] Yao J, Tjandra W, Chen YZ, Tam KC, Ma J, Soh B. J Mater Chem 2003;13:3053–7.
[27] Tjandra W, Yao J, Ravi P, Tam KC, Alamsjah A. Chem Mater 2005;17:4865–72.
[28] Tjandra W, Ravi P, Yao J, Tam KC. Nanotechnology 2006;17:5988–94.
[29] Hu YY, Yusufoglu Y, Kanapathipillai M, Yang CY, Wu YQ, Thiyagarajan P, et al. Soft Matter 2009;5:4311–20.
[30] Lee RS, Chen WH, Huang YT. Polymer 2010;51:5942–51.
[31] Hu ZG, Fan XS, Wang HJ, Wang JJ. Polymer 2009;50:4175–81.
[32] Wang L, Hu P, Tirelli N. Polymer 2009;50:2863–73.
[33] Wang DR, Liu JP, Ye G, Wang XG. Polymer 2009;50:418–27.
[34] Liu TB, Xie Y, Chu B. Langmuir 2000;16:9015–22.
[35] Stadler R, Auschra C, Beckmann J, Krappe U, Voigtmartin I, Leibler L. Macromolecules 1995;28:3080–97.
[36] Erukhimovich I, Abetz V, Stadler R. Macromolecules 1997;30:7435–43.
[37] Bates FS, Fredrickson GH. Phys Today 1999;52:32–8.
[38] Gohy JF, Willet N, Varshney S, Zhang JX, Jerome R. Angew Chem Int Ed Engl 2001;40:3214–6.
[39] Xu AW, Ma YR, Colfen H. J Mater Chem 2007;17:415–49.
[40] Jiang HD, Liu XY, Zhang G, Li Y. J Biol Chem 2005;280:42061–6.
[41] Anuar N, Daud WRW, Roberts KJ, Kamarudin SK, Tasirin SM. Cryst Growth Des 2009;9:2853–62.
[42] Gebauer D, Volkel A, Colfen H. Science 2008;322:1819–22.
[43] Baskaran D, Sivaram S. Macromolecules 1997;30:1550–5.

Polymer 52 (2011) 804–813

Contents lists available at ScienceDirect

Polymer

journal homepage: www.elsevier.com/locate/polymer

Photophysical and electroluminescent properties of a Series of Monochromatic red-emitting europium-complexed nonconjugated copolymers based on diphenylphosphine oxide modified polyvinylcarbazole

Hui Xu [a,*], Rui Zhu [b], Ping Zhao [c], Ling-Hai Xie [b], Wei Huang [b,*]

[a] Key Laboratory of Functional Inorganic Material Chemistry (Heilongjiang Univeristy), Ministry of Education & School of Chemistry and Materials, Heilongjiang University, 74 XueFu Road, Harbin 150080, PR China
[b] Institute of Advanced Materials (IAM), Jiangsu Key Laboratory of Organic Electronics and Flat-Panel Displays, NanjingUniversity of Posts and Telecommunications (NJUPT), 66 XinMoFan Road, Nanjing 210003, PR China
[c] Key Laboratory for Advanced Materials and Institute of Fine Chemicals, East China University of Science & Technology, Shanghai 200237, PR China

ARTICLE INFO

Article history:
Received 22 August 2010
Received in revised form
12 November 2010
Accepted 9 December 2010
Available online 17 December 2010

Keywords:
Eu-chelated copolymer
Intra-chain energy transfer
Electroluminescence

ABSTRACT

Two novel copolymers **P1** and **P2** were prepared by using the polymerizable aryl phosphine oxide based Eu(TTA)$_3$VBCzDPO (**EuM**) (**VBCzDPO** = 3,6-bis(diphenyl-phosphoryl)-9-(4- vinylbenzyl)-9H-carbazole) and vinylcarbazole as the monomers with the compositions of 1:99 and 1:33, respectively. It is showed that the stronger coordinate ability of bidentate APO ligands facilitates the stability of the complex monomer during polymerization, and their beetling coordinate sites and adjustable structure efficiently reduce the steric effect of bulky **EuM**. Both of photoluminescent (PL) spectra in solution and solid of the copolymers exhibited improved emission from Eu^{3+} ion. The high PL quantum yield (PL QY) in solid of 60% is realized. Further investigation indicates that for the intra-chain energy transfer **VBCzDPO** serves as the intermediate and bridge between PVK and Eu(TTA)$_3$, which ensures the high efficiency of whole intra-chain energy transfer. The pure-red emission from the devices of **P1** and **P2** was demonstrated.

1. Introduction

The luminescent polymers have been paid much attention since their applications in polymeric light-emitting diodes (PLEDs) [1] and sensors [2–6]. The electroluminescent (EL) polymers seem very attractive with an important advantage of solution-processability, which is believed to be most promising for low-cost and large-area display device fabrication [7]. However, as the fluorescent emitters and the mixtures with polydisperse molecules, EL polymers have the common disadvantages of low EL efficiency and poor color purity. Following the demonstration of small molecular electrophosphorescent dyes, the transition–metal complex segments were introduced into the main chains and side chains to construct the electrophosphorescent polymers [8–14]. The breakthrough of the EL efficiencies was realized. However, the full widths at half maximum (FWHM) of these polymers were still around 100 nm, which becomes a main constraint for their application in high color purity display devices [15]. It is well-known that the lanthanide complexes, such as Eu^{3+} and Tb^{3+} complexes, have the highest color purity, in which the europium(III) contained luminescent materials have been extensively studied as one kind of the most important red-emitting materials in organic light-emitting diodes (OLEDs) because of their interesting properties, such as the pure red monochromic characteristic emission with FWHM of 5–10 nm, high photoluminescent (PL) efficiency, chemical environmental stability and theoretically approaching 100% internal quantum efficiency [16–19]. In order to reduce the remarkable concentration quenching and triplet–triplet (*T*–*T*) annihilation in solid state, many bright and efficient electroluminescent devices based on small molecular Eu^{3+} complexes are achieved through the doping/blending approach [16–30], in which 4,4′-N,N′-dicarbazolebiphenyl (CBP) [31], 2-biphenyl-4-yl-5-(4-tert-butyl-phenyl)-1,3,4-oxadiazole (PBD) [32] and polyvinylcarbazole (PVK) [33] with high triplet excited energy levels are often used as the hosts. Nevertheless, the worse phase separation in the doping and blending systems is still a problem inducing the remarkable decreasing of EL performances [34,35].

As an alternative of doping/blending systems, the EL Eu-complexed polymers become attractive as the electrophosphorescent polymers with the much improved color purity. It is believed that through the covalent linkage with the polymeric host matrixes the Eu^{3+} complex moieties can be dispersed more uniformly in the hosts

* Corresponding authors.
E-mail addresses: hxu@hlju.edu.cn (H. Xu), wei-huang@njupt.edu.cn (W. Huang).

0032-3861/$ – see front matter © 2010 Elsevier Ltd. All rights reserved.
doi:10.1016/j.polymer.2010.12.016

[36–42]. And the more efficient energy transfer from the main chains to the Eu^{3+}-complexed moieties can be expected [43]. The polymerizable carboxylic acids [41,42,44], 2,2′-bipyridine (bpy) derivatives [45,46] and phenanthroline (phen) derivatives [47] are used as the ligands to form the nonconjugated and conjugated Eu-complexed polymers. Recently, the Eu^{3+}-containing polymers based on three β-diketone ligands and polymerizable neutral ligands, including phen and bpy derivatives, are focused on [43,45,46,48]. And several polymers realize the EL brightness more than 10 cd m^{-2} [42,44,48]. Nevertheless, these neutral ligands seem inferior in polymerization and often induced the uncontrolable proportion of europium-complexation in the copolymers. Therefore, the stable polymerizable Eu-chelated monomers are still imperative for efficient luminescent copolymers. Although it is believed that the intra-chain energy transfer is from the backbones to Eu^{3+}-chelate moieties through charge transfer (CT) [47], the exact intra-chain energy transfer process between backbones, linker ligands and Eu^{3+}-containing moieties is not yet clear, which is significant for the purposeful design of efficient PL and EL Eu-complexed polymers.

In this work, a polymerizable aryl phosphine oxide (APO) ligand 3,6-bis(diphenyl-phosphoryl)-9-(4-vinylbenzyl)-9H-carbazole (**VBCzDPO**) and the corresponding Eu^{3+} complex $Eu(TTA)_3$VBCzDPO (**EuM**) were designed and synthesized (Scheme 1). Two copolymers **P1** and **P2** were prepared by using the complex and vinylcarbazole as the monomers with the compositions of 1:99 and 1:33, respectively. The dramatic high PL efficiencies around 60% in film were realized. The remarkable solid emission amplification phenomenon was observed. The efficient intra-chain energy transfer between the PVK segments to the complex segments was firstly investigated by measuring the excited energy levels of the functional segments. The pure red emissions attributed to Eu^{3+} from the PLEDs were demonstrated.

2. Experimental

2.1. Materials and Instruments

All the reagents and solvents used for the synthesis were purchased from Aldrich, Acros and Fluka companies. Compounds used for EL device fabrication were purchased from Lumthec Corporation. All the reagents were used without further purification.

^{1}H NMR spectra were recorded using a Varian Mercury plus 400NB spectrometer relative to tetramethylsilane (TMS) as internal standard. Molecular masses were determined by an SHIMADZU laser desorption/ionization time-of-flight mass spectrometer (LDI-TOF-MASS) or an SHIMADZU GCMS-QP2010 plus equipped with DB-5 ms column. Elemental analyses were performed on a Vario EL III elemental analyzer. Gel permeation chromatography (GPC)

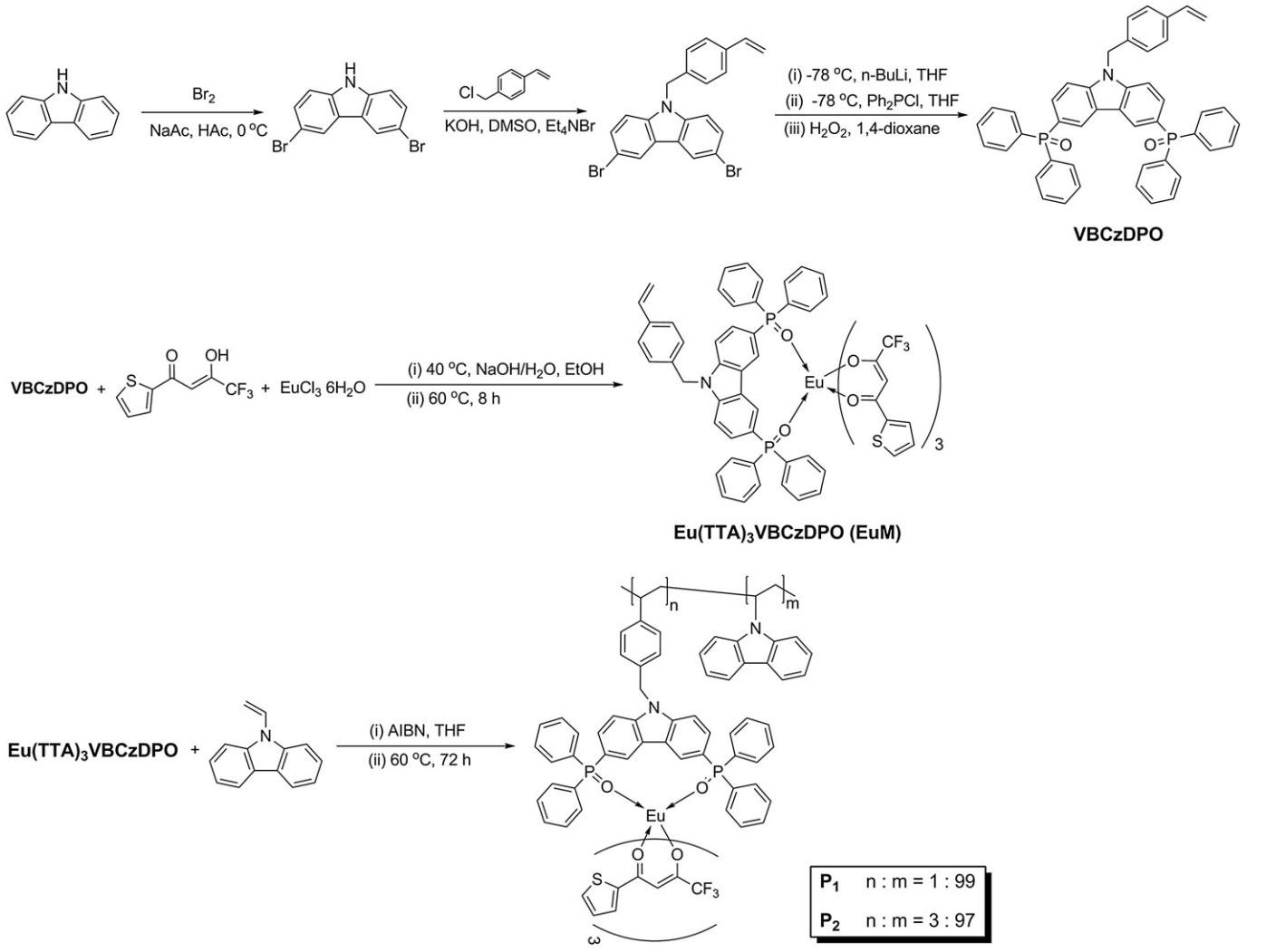

Scheme 1. Synthetic Routine of the Eu^{3+} Complexed Copolymers.

analysis was conducted with an HP1100 HPLC system equipped with 7911 GP-502 and GP NXC columns using polystyrenes as the standard and tetrahydrofuran (THF) as the eluant at a flow rate of 1.0 mL min^{-1} and 35 °C. Cyclic voltammetric (CV) studies were conducted using an Eco Chemie B. V. AUTOLAB potentiostat in a typical three-electrode cell with a platinum sheet working electrode, a platinum wire counter electrode, and a silver/silver nitrate (Ag/Ag^+) reference electrode. All electrochemical experiments were carried out under a nitrogen atmosphere at room temperature. Absorption and photoluminescence (PL) emission spectra of the target compounds were measured in dichloromethane using an SHIMADZU UV-3150 spectrophotometer and an SHIMADZU RF-5301PC spectrophotometer, respectively. Phosphorescence spectra and Time-Resolved spectra were measured in dichloromethane using an Edinburgh FLS 920 fluorescence spectrophotometer at 77 K cooling by liquid nitrogen.

2.2. Synthesis

2.2.1. 3,6-Dibromo-9-(4-vinylbenzyl)-9H-carbazole

3,6-Dibromocarbazole (3.25 g, 10 mmol) and tetraethylammonium bromide (210 mg, 1 mmol) were dissolved in DMSO (50 ml) and then KOH aqueous solution (2 M, 6 ml) was added slowly. The mixture was stirred at room temperature (R. T.) for half an hour. Then 4-vinylbenzyl chloride (1.3 ml, 1.84 g, 12 mmol) in DMSO (10 ml) was added in dropwise. The mixture was reacted overnight at R. T. in the dark, and then poured into water and extracted with dichloromethane. The organic layer was dried with anhydrous $MgSO_4$ and the solvent was removed in vacuo. The residue was purified by flash column chromatography using dichloromethane/petroleum ether as eluent to obtain 3,6-dibromo-9-(4- vinylbenzyl)-9H-carbazole (3.98 g) as white powder with yield of 90%. ^{1}H NMR ($CDCl_3$, 400 MHz): δ = 8.180 (s, 2H), 7.534 (d, J = 8.4 Hz, 2H), 7.311 (d, J = 8.4 Hz, 2H), 7.238 (d, J = 8.8 Hz, 2H), 7.029 (d, J = 8.0 Hz, 2H), 6.682 (q, J_1 = 10.8 Hz, J_2 = 17.6 Hz, 1H), 5.710 (d, J = 17.6 Hz, 1H), 5.454 (s, 2H), 5.234 ppm (d, J = 10.8 Hz, 1H); GC–MS: m/z (%): 441 (100) M^+; elemental analysis calcd (%) for $C_{21}H_{15}Br_2N$: C 57.17, H 3.43, N 3.17; found: C 57.22, H 3.41, N 3.43.

2.2.2. 3,6-bis(diphenylphosphoryl)-9-(4-vinylbenzyl)-9H-carbazole (*VBCzDPO*)

3,6-dibromo-9-(4-vinylbenzyl)-9H-carbazole (4.41 g, 10 mmol) was dissolved in absolute ether (50 ml) and then formed lithium salts by 1.6 M *n*-BuLi/hexane solution (7.5 ml, 12 mmol) at −78 °C for 1 h. Then diphenyl phosphine chloride (2.3 ml, 13 mmol) was added at −78 °C in drops. The mixture was reacted at −78 °C for 1 h and then at room temperature overnight. The phosphine crude product was obtained and purified by flash column chromatography using dichloromethane as eluent. Yield: 4.45 g of yellowish powder (65%). The phosphine (638 mg, 1 mmol) was subsequently dissolved in 1,4-dioxane (5 ml). And then the phosphine was oxidized by 30% hydrogen peroxide (0.11 ml, 1.1 mmol) for 4 h to form the ligand **VBCzDPO** quantitatively as white powder. ^{1}H NMR (400 MHz, $CDCl_3$): δ = 7.669–7.775 (m, 12H), 7.410–7.492 (m, 6H), 7.306–7.396 (m, 10H), 7.027 (d, J = 8.0 Hz, 2H), 6.690 (q, J_1 = 10.8 Hz, J_2 = 17.6 Hz, 1H), 5.714 (d, J = 17.6 Hz, 1H), 5.456 (s, 2H), 5.238 ppm (d, J = 10.8 Hz, 1H); LDI-TOF: m/z (%): 683 (100) M^+; FTIR (KBr pellet, cm^{-1}): 3076, 2918, 1630 (*C*]*C* stretching), 1482, 1438 (C–P stretching), 1314, 1264, 1177 (*P*]*O* stretching), 1129, 959, 755, 727, 692, 551, 525, 435; elemental analysis calcd (%) for $C_{45}H_{35}NO_2P_2$: C 79.05, H 5.16, N 2.05, O 4.68; found: C 79.39, H 5.07, N 2.36, O 4.80.

2.2.3. Preparation of the europium monomer Eu(TTA)$_3$VBCzDPO (*EuM*)

The complex was prepared according to the well established protocols [49]. 2-thenoyltrifluoroacetone (TTA) (672.7 mg, 3 mmol) was dissolved in ethanol (10 ml), NaOH (120 mg, 3 mmol) in water solution (2 M) was added to remove the H^+ in the TTA molecule, then $EuCl_3$ $6H_2O$ (370.1 mg, 1 mmol) in water solution was added dropwise and stirred at 40 °C for 30 min, and then **VBCzDPO** (683 mg, 1 mmol) in ethanol was added in drops and stirred at 40 °C for 8 h in dark to afford the complex as white precipitation. Purification can be accomplished by precipitation from concentrated ethanol and water solution with yield of 71%. ^{1}H NMR (400 MHz, $CDCl_3$): δ = 9.289–10.443 (m, 10H), 7.148–8.052 (m, 23H), 6.955 (s, 3H), 6.296–6.731 (m, 7H), 5.927–6.229 (br, 1H), 4.924–5.142 (br, 1H), 4.439–4.757 ppm (br, 2H); MALDI-TOF: m/z (%): 1499 (100) M^+; FTIR (KBr pellet, cm^{-1}): 3060, 2975, 1632 (*C*]*O* stretching), 1608 (*C*]*O* stretching), 1537 (*C*]*C* stretching in TTA), 1504, 1468, 1439 (C–P stretching), 1413, 1357, 1304, 1245, 1230, 1180 (P]O stretching), 1142, 1095, 1061, 934, 784, 726, 708, 694, 642, 580, 537, 520; elemental analysis calcd (%) for $C_{69}H_{47}EuF_9NO_8P_2S_3$: C 55.28, H 3.16, Eu 10.14, N 0.93, O 8.54, S 6.42; found: C 55.34, H 3.21, Eu 9.99, N 1.17, O 8.68, S 6.53.

2.2.4. Preparation of Gd(NO$_3$)$_3$VBCzDPO

For triplet energy level measurement Gadolinium complex comprising VBCzDPO without TTAs were also synthesized [50–52]. **VBCzDPO** (341 mg, 0.5 mmol) was dissolved in ethanol (15 ml). Gd $(NO_3)_3(H_2O)_6$ (226 mg, 0.5 mmol) in water (0.1 ml) was added dropwise under stirring and the solution was heated to 40 °C for 4 h. The Gadolinium complex was recrystallized from concentrated methanol-water mixed solvent. Elemental analysis calcd (%) for $C_{45}H_{35}GdN_4O_{11}P_2$: C 52.63, H 3.44, N 5.46, O 17.14; found: C 52.77, H 3.38, N 5.57, O 17.39.

2.2.5. Preparation of the europium chelating copolymers

A mixture of N-vinyl carbarzole (1.16 g, 6.0 mmol), Eu $(TTA)_3$VBCzDPO (89.36 mg, 0.060 mmol for **P1** and 300.99 mg, 0.20 mmol for **P2**) and AIBN initiator (10 mg, 0.5 mol% of the total monomers) was dissolved in dry tetrahydrofuran (THF) (5 mL) in a glass polymerization tube. The homogeneous solution was purged with argon for 5 min and sealed under a reduced argon atmosphere. The mixture was heated to 60 °C with continuous stirring for 72 h. The reaction mixture remained clear throughout the copolymerization process. The viscous mixture was diluted with THF (5 mL) and precipitated into methanol (100 mL) under vigorous stirring. The reprecipitation procedure was repeated for three times. The resulting solid material was collected by filtration. The copolymer was further purified by Soxhlet extraction with boiling acetone for 48 h, and finally dried in a vacuum oven at 50 °C for 24 h.

2.2.5.1. P1. with yield of 78% as white powder. ^{1}H NMR (300 MHz, $CDCl_3$): δ = 7.701, 7.195, 7.016, 6.917, 6.557, 6.407, 6.247, 4.911, 4.135, 3.462, 3.174, 2.568, 1.792, 1.561, 1.442, 1.277, 1.079, 0.898 ppm; ^{13}C NMR (300 MHz, $CDCl_3$): δ = 140.046, 137.861, 137.351, 137.410, 125.351, 125.050, 123.821, 122.189, 121.979, 120.249, 119.167, 118.894, 118.652, 110.356, 108.120, 107.986, 107.780, 107.496, 50.175, 49.314, 48.195, 36.126 ppm; FTIR (KBr pellet, cm^{-1}): 3047, 2929, 1882, 1624, 1597, 1538 (*C*]*C* stretching in TTA), 1483, 1452, 1332, 1223, 1157, 1124, 1026, 1003, 923, 840, 744, 720, 420; Elemental analysis calcd (%): C 84.74, H 5.51, N 6.79, S 0.47, O 0.62; found: C 85.59, H 5.42, N 6.93, S 0.59, O 0.78; Molecular weight: M_n = 9576, M_w = 17187, PDI = 1.79. The content of Eu^{3+} = 0.79 wt %. Polymer composition: n:m = 1:99, which is determined according to the results of elemental analysis and Eu^{3+} titration [46].

2.2.5.2. P2. with yield of 55% as white powder. ^{1}H NMR (300 MHz, $CDCl_3$): δ = 7.729, 7.175, 7.017, 6.940, 6.574, 6.445, 6.243, 5.001, 4.148, 3.505, 3.250, 2.566, 1.852, 1.566, 1.444, 1.274, 1.097, 0.923 ppm; ^{13}C NMR (300 MHz, $CDCl_3$): δ = 140.096, 137.917, 137.353, 137.411,

125.374, 124.998, 123.940, 122.210, 121.899, 120.214, 119.203, 118.891, 118.634, 110.352, 108.124, 107.989, 107.785, 107.490, 50.175, 49.314, 48.196, 36.126 ppm; FTIR (KBr pellet, cm^{-1}): 3048, 2930, 1882, 1625, 1598, 1538 (*C*]*C* stretching in TTA), 1483, 1452, 1333, 1223, 1157, 1124, 1026, 1003, 923, 840, 744, 720, 421; Elemental analysis calcd (%): C 80.90, H 5.20, N 6.03, S 1.24, O 1.65; found: C 81.79, H 5.05, N 6.37, S 1.36, O 1.81; Molecular weight: $M_n = 6510$, $M_w = 9200$, PDI = 1.79. The content of $Eu^{3+} = 2.05$ wt %. Polymer composition: n:m = 1:33, which is determined according to the results of elemental analysis and Eu^{3+} titration [46].

2.2.6. Fabrication and Testing of PLEDs

PLEDs were fabricated by spin coat with two configurations of ITO/PEDOT:PSS (40 nm)/Copolymer (80 nm)/Ba (4 nm)/Al (120 nm) and ITO/PEDOT: PSS (40 nm)/Copolymer:PBD (80 nm) (30%, 80 nm)/Ba (4 nm)/Al (120 nm), wherein PEDOT:PSS is poly(3,4-ethylenedioxythiophene):poly(styrene sulfonate) as the hole-injection/transporting layer, PBD is 2-biphenyl-4-yl-5-(4-tert-butyl-phenyl)- 1,3,4oxadiazole as the electron-transporting host, and ITO and Ba/Al were used as the anode and cathode, respectively [53]. PLED was fabricated on pre-patterned indium-tin oxide (ITO) with sheet resistance 10^{-20} Ω/□. The substrate was ultrasonic cleaned with acetone, detergent, deionized water, and 2-propanol. Oxygen plasma treatment was made for 4 min as the final step just before film coating. Onto the ITO glass was spin-coated a layer-of polyethylenedioxythiophene-polystyrene sulfonic acid (PEDOT:PSS) film with thickness of 40 nm from its aqueous dispersion. PEDOT:PSS film was dried at 80 °C for 3 h in the vacuum oven. The solution of the polymer was prepared under nitrogen atmosphere and spin-coated on to PEDOT:PSS layer. Typical thickness of the emitting layer was 80 nm. Then a thin layer of barium as an electron injection cathode and the subsequent 130 nm thick aluminum protection layers were thermally deposited by vacuum evaporation through a mask at a base pressure below 2×10^{-4} Pa. The cathode area defines the active area of the device. The typical active area of the devices in this study is 0.15 cm^2. The EL layer spin coating process and the device performance tests were carried out within a glove-box under nitrogen atmosphere. Current-voltage (I-V) characteristics were recorded with a Keithley 236 source meter. EL spectra were obtained by Oriel Instaspec IV CCD spectrograph. Luminance was measured by a PR 705 photometer (Photo Research). The external quantum efficiencies were determined by a Si photodiode with calibration in an integrating sphere (IS080, Labsphere).

3. Results and discussion

3.1. Design, synthesis and characteristics

Because β-diketone ligands can realize much more efficient energy transfer to Eu^{3+} ions than other kinds of anion ligands, such as benzoic acid derivatives, introduction of Eu^{3+} complexes into polymeric matrixes through the linkage of polymerizable chelate neutral ligands would have advantages in obtaining high luminescent efficiencies. The suitable polymerizable neutral ligands should have several characteristics, such as strong coordinate ability, structure adjustability, protuberant coordinate sites and inertia of modification. The bidentate APO ligands conform to these requirements, whose structures are formed through six C—P single bonds and two *P*]*O* double bonds. The coordinate O atom is separated from the bulky aryl groups by P atom. The rotatability and angle-variability of the C—P single bond can afford considerable structural adjustment. In addiction, it is known that O—Eu bond is much stronger than N—Eu bond. Thus, we believe that the APO ligands have the potential as the favorable neutral ligands for EL europium-complexed polymers.

The functional bidentate APO structure was designed as the hole-transporting carbazole bridged two electron-transporting and coordinate diphenylphosphine oxide (DPPO) moieties. The polymerizable 4-vinylbenzyl chloride was used to substitute the active hydrogen at 9-position of carbazole. The final polymeric main chain actually was designed as a macro ligand with the structure of DPPO modified PVK. The efficient intra-chain energy transfer from *N*-ethenylcarbazole segments to Eu-chelate moieties is expected. Using 4-vinylbenzyl as the linker of main chain and DPPO modified carbazole elongates the distance between them and consequently reduces the steric, which facilitates the polymerization and prevents the decomposition of the complex monomer.

The polymerizable APO ligand **VBCzDPO** was conveniently prepared from 3,6-dibromocarbazole through three steps of benzylation, phosphorization and oxidation, which is outlined in Scheme 1. The Eu^{3+} complex monomer $Eu(TTA)_3$VBCzDPO (**EuM**) was synthesized according to the well established procedure with moderate yields [49]. The formation of APO based Eu^{3+} complex was reasonably proved by FTIR spectrum of **EuM** (Fig. 1), in which not only the vibration absorptionsattributed to *C*]*O* (1631 cm^{-1}) and *C*]*C* (1537 cm^{-1}) in TTA, but also the characteristic absorption peaksoriginated from $\nu_{C\text{-}P}$ (1438 cm^{-1}) and $\nu_{P=O}$ (1177 cm^{-1}) in **VBCzDPO** are recognized. The europium-complexed copolymer **P1** and **P2** were prepared by the classic free radical copolymerization of **EuM** with *N*-vinylcarbazole (NVK), using AIBN as the initiator, in dry THF (Scheme 1). For the doping devices of the small molecular Eu^{3+} complexes, when the doping concentration increases from 1% to 2%, the maximum brightness and efficiency remarkably decrease for 50% [31]. Although because of the covalent bonding the self-aggregation of Eu^{3+} complex moieties in Eu-complexed polymers can be restrained, the inter-chain and intra-chain interaction may also induce the concentration quenching. Therefore, to investigate the influence of the composition of the copolymers on their EL performance, in the present work, the initial feed ratios of **EuM** to *N*-vinylcarbazole were 0.03:3.0 and 0.1:3.0. GPC analysis (polystyrene as the standard for calibration) showed that the number-average molecular weight (M_n) and weight-average molecular weight (M_w) of the polymers are 9576 and 17187 for **P1**, and 6510 and 9200 for **P2**, respectively. The polydispersity indexes (PDI) are 1.79. According to the results of elemental analysis, the compositions of the copolymers (n:m M ratio) were about 1:99 and 1:33. The feed ratio of **P1** is very close to its actual composition, which means that the reactivity of **EuM** to NVK is similar with the reactivity between NVKs. Furthermore, **P1** has the slightly higher M_n, M_w and PDI than those of the 4-vinylbenzoic acid based Eu-

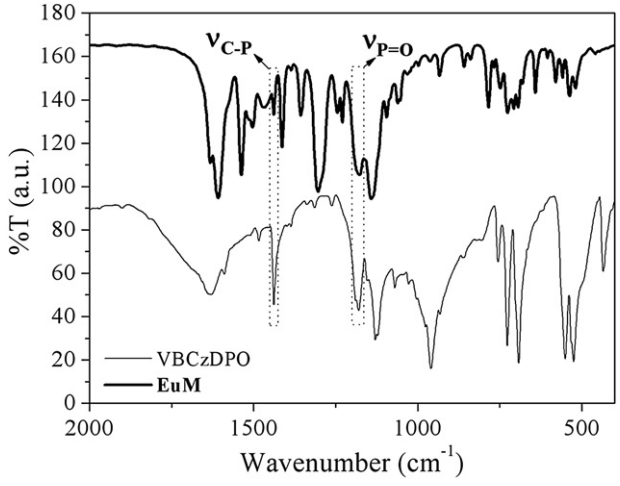

Fig. 1. FTIR spectra of VBCzDPO and EuM.

complexed polymer with similar composition ratio [44]. It proves that the strong coordinate ability of bidentate APO ligands facilitates the stability of the complex monomer during polymerization and their beetling coordinate sites and adjustable structure efficiently reduce the steric effect of bulky **EuM**. Thus, the efficient radical polymerization can occur between **EuM** and NVK. However, it is noticed that the molecular weight and yield of the copolymers remarkably decrease along with the increasing of **EuM**:NVK feed ratio. And the differences between the copolymer compositions and the feed ratios increase from **P1** to **P2**. The main reason might be that along with the increasing of **EuM** molar quantity, the possibility of collision between **EuM**s also increases. Although the bidentate APO ligand has the adjustable structure, the polymerization between bulky **EuM**s is much more difficult than that between **EuM** and NVK. Thus, these collisions might induce the chain termination or chain transfer, which reduce the molecular weight of **P2**. Nevertheless, M_n and M_w of **P2** are still larger than those of the phenanthroline derivative based Eu-complexed polymer with the same composition ratio [48]. The resulted copolymers are readily soluble in common organic solvents, such as THF, dichloromethane, chloroform and toluene, and can be easily cast into transparent and uniform thin films. The copolymers were characterized by ^{1}H NMR, ^{13}C NMR, FTIR and elemental analysis. In their ^{1}H NMR spectra, the proton peaks attributed to vinyl groups of NVK and **EuM** have completely disappeared and all the peaks grow rather broad, which suggest the successful polymerization.

The FTIR spectrum of **P1** was shown in Fig. 2, which is very similar with the FTIR spectrum of pure PVK. Two sharp and strongest absorption peaks at 720 and 744 cm^{-1} are attributed to the characteristic absorptions of the carbazole moieties. Because of the formation of polymer and the low contents of **EuM** in the polymers, the strong and wide-dispersed absorption peaks of PVK segments almost cover all of the characteristic absorption peaks of **EuM**, such as β-diketone absorption band at 1625 cm^{-1}, vibration absorption peak of C–P at 1438 cm^{-1} and *P*]*O* stretching vibration absorption around 1180 cm^{-1}. Nevertheless, fortunately, covalent attachment of Eu^{3+} complex unit to the polymer backbones is strongly supported by the *C*]*C* stretching vibrations of the coordinated TTA ligand around 1535 cm^{-1}, which is a strong absorption peak in the spectrum of **EuM** and a much weaker peak in that of **P1** [48].

3.2. Optical properties

The UV/Vis absorption spectra of **P1** and **P2** in dilute CH_2Cl_2 solution (1×10^{-5} mol L^{-1}) are almost same with that of PVK (Fig. 3 and Table 1). The peaks at 344, 331, 295 and 242 nm are associated with the absorption of carbazole moieties in PVK segments. Therefore, as the major component, PVK segments in **P1** and **P2** serve as the energy absorption "antenna". Nevertheless, the long-wavelength absorption (360–400 nm) mainly originated from the $\pi \rightarrow \pi^*$ transition of the ligands in Eu-chelated segments is recognized. Moreover, it is noticeable that the intensities of the absorption edges increase from PVK, **P1** to **P2**, gradually.

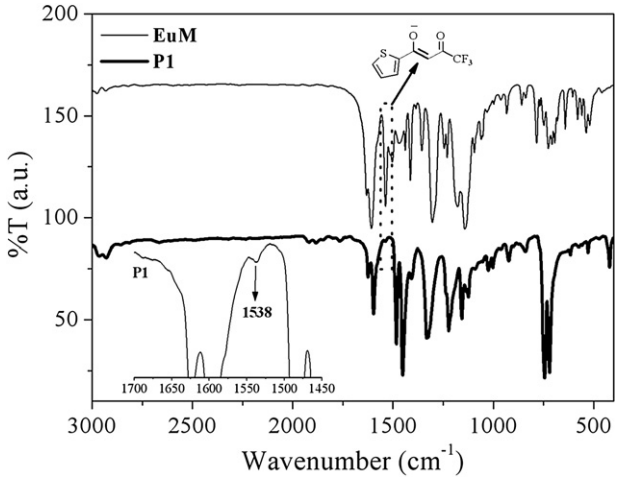

Fig. 2. FTIR spectra of EuM and P1.

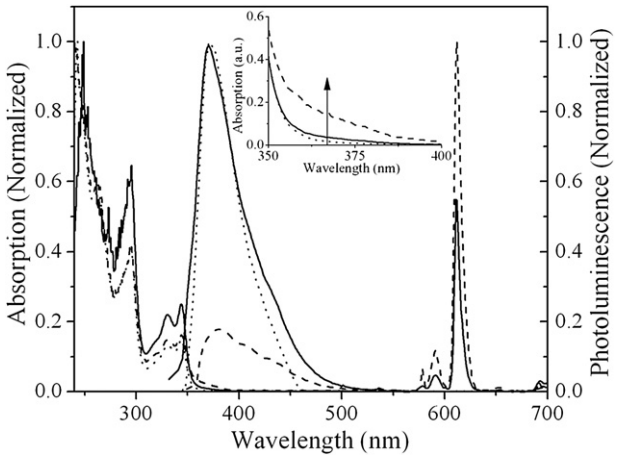

Fig. 3. UV/Vis and PL spectra of P1 (solid line), P2 (dash line) and PVK (dot line) in CH_2Cl_2.

In the PL spectra of **P1** and **P2** in dilute CH_2Cl_2 solution (1×10^{-5} mol L^{-1}) (Fig. 3), the wide emissions with the maximum at 370 nm correspond to deactivation of π^* states of their PVK segments, which consist of three components: the emissions of isolated carbazoles (350–360 nm) and excimers of partially overlapping carbazoles (370–380 nm) and fully overlapping carbazoles (400–420 nm). These emissions correspond to the heterotactic, isotactic and sydiotactic stereochemical sequences of the neighboring carbazole groups in the main chains [44]. The characteristic emissions of Eu^{3+} ion at 579, 593, 612, 653 and 692 nm originated from $^5D_0$-^7F_j ($j = 0$–4) transitions are recognized. The main peak is at 612 nm as the pure red emission. Significantly, in the previous work about 4-vinylbenzoic acid based Eu-complexed PVK copolymers (with Eu^{3+} complex monomer contents of 0.01 and 0.03) [42,44], the PL intensity ratios of Eu^{3+}-originated emission to PVK-originated emission are 0.13:1 and 0.38:1, respectively. Even for the polymerizable phenanthroline derivative based PVK copolymer (with Eu^{3+} complex monomer content of 0.03) [48], the ratio is about 1:1. In sharp contrast to these weak emissions from Eu-complexed segments, for **P1** and **P2**, the ratios remarkably increase to 0.55:1 and 5.5:1, respectively. Obviously, the compact and

Table 1
The optical properties of the compounds.

Compound	Absorption peak (nm)[a]	Emission peak (nm)[a]	PL Q.Y. (%)	Lifetime (μs)
VBCzDPO	343, 328, 293	369	–	–
EuM	343, 272	578, 591, 611, 652, 692	51.3 [b]/34.7[c]	397.08
P1	344, 331, 295, 242	372, 578, 591, 612, 652, 692	22.1 [b]/55.6[c]	187.57 (44.3%), 431.40 (55.7%)
P2	344, 331, 295. 242	380, 578, 591, 612, 652, 692	41.6 [b]/62.5[c]	182.94 (44.2%), 439.34 (55.8%)
PVK	344, 331, 295, 242	371	–	–

[a] in CH_2Cl_2, 1×10^{-5} mol L^{-1}.
[b] using $Ru(bpy)_3Cl_2$ as standard in CH_2Cl_2 solution.
[c] by an integrating sphere in film.

flexible structure of **EuM** remarkably improves the interaction with surrounding carbazole moieties. The main chains formed by NVK and **VBCzDPO** actually serve as the macro neutral ligands for the pendent $Eu(TTA)_3$ moieties, which is much different with the relatively separated systems in the former works. Therefore, **P1** and **P2** have remarkably improved intra-chain energy transfer.

The PL spectra of **P1** and **P2** in film (Fig. 4) only consist of the characteristic emissions from Eu^{3+} ion. The PVK-originated emission is nearly disappeared. Compared with their solution spectra the main emission peaks are at 615 nm. It is also noticed that the PL spectra in film of **P1** and **P2** are nearly the same. It means that in solid the energy transfer from the polymer main chain to the pendent Eu^{3+} complex segments is very efficient even at the complex content as low as 1%, which is remarkably superior to other reported Eu-complexed copolymers. Obviously, this improvement is induced by the efficient energy transfer. The relative PL quantum yield (PL QY) of Eu^{3+}-originated emissions of **EuM**, **P1** and **P2** were measured by using $Ru(bpy)_3Cl$ in deaerated water as the standard (Table 1). **EuM** has a considerably high PL QY of 51.3%. However, since the worse aggregation induced concentration quenching and *T*–*T* annihilation, its PL QY in film reduces to 34.7%. Contrarily, **P1** and **P2** have much lower relative PL QY in solution. Especially for **P1** its relative PL QY is only 22.1%, which is less than a half of that of **EuM**. The sufficient energy transfer from PVK segments to Eu^{3+} in solution should be the main factor reducing the relative PL QY of **P1** and **P2**. Inspiringly, the remarkable solid emission amplification was observed that in film PL QY of both **P1** and **P2** are remarkably improved to around 60%, which are more than 1.5 times of that of **EuM**. Obviously, the emission amplification in film is mainly induced by the highly improved intra-chain and inter-chain energy transfer from PVK segments to **EuM** segments. In addition, because of the separation of $Eu(TTA)_3$ by PVK segments, the concentration quenching and *T*–*T* annihilation are successfully restrained in **P1** and **P2**, which is one of the main reasons for their much higher PL QY in solid than **EuM** in solid and solution.

3.3. Intra-chain energy transfer in the copolymers

In order to understand the role of the each and every component of the copolymers in the intra-chain energy transfer process, their optical properties were measured. The europium-chelated polymers can be divided into three components: PVK segments, the coordinate site **VBCzDPO** and the red-emitting $Eu(TTA)_3$ cores. All of these moieties should be involved in the intra-chain energy transfer process.

Fig. 5 shows UV/vis and PL spectra of **VBCzDPO** in CH_2Cl_2, and phosphorescent spectrum of $Gd(NO_3)_3$VBCzDPO was measured to find out the first triplet excited energy level (T_1) of the ligand in the lanthanide complexes. It is showed that the absorption spectrum of **VBCzDPO** is very similar to that of PVK, in which the peaks at 343 and 328 nm are attributed to the carbazole moieties and the absorption of intramolecular charge transfer (ICT) excited state at the same wavelength range makes these peaks become obtuse. **VBCzDPO** has a sharp main emission peak at 369 nm with a shoulder peak at 354 nm. Its Gd^{3+} complex has a wide blue emission at 430 nm at 77 K as the phosphorescent emission. The PL emission of PVK is at 371 nm (Fig. 6). In order to determine its T_1 level, its phosphorescent spectrum in CH_2Cl_2 was measured at 77K. It is found that the phosphorescent spectrum of PVK consists of several peaks, in which the first peak at 388 nm can be attributed to the fluorescent emission of PVK from its first singlet excited state (S_1) with slight red shift of 16 nm at low-temperature, and the second peak at 430 nm should be the first emission peak of phosphorescence corresponding to the $0 \rightarrow 0$ transition of PVK. S_1 and T_1 of the ligands are estimated by referencing the absorbance edge and the phosphorescent peak emission wavelengths. For comparison, the singlet and triplet state energy levels are summarized in Table 2 and illustrated in Fig. 7.

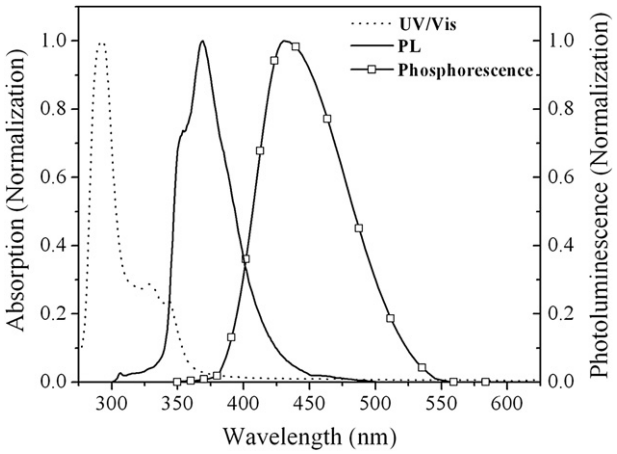

Fig. 5. UV and PL spectra of VBCzDPO and Phosphorescent spectrum of Gd $(NO_3)_3$VBCzDPO in CH_2Cl_2.

It is showed that S_1 and T_1 energy levels of PVK are higher than those of **VBCzDPO**, but the energy gaps (ΔE_S and ΔE_T) between the corresponding energy levels of PVK and **VBCzDPO** are very small as 0.08 eV. These closed energy levels make the reversible energy transfer from **VBCzDPO** to PVK possible. Even so, since PVK segments are the energy absorbing antenna as the major repeat

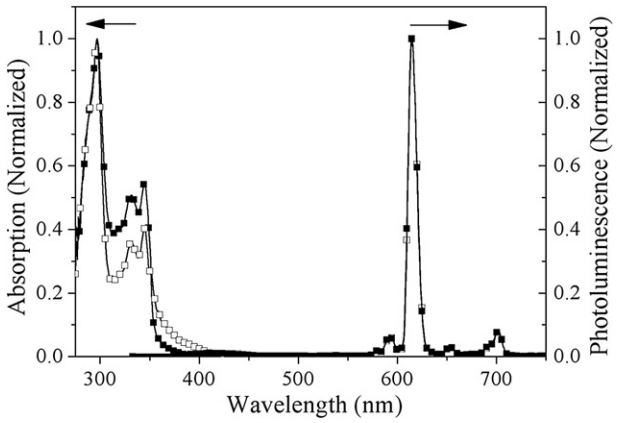

Fig. 4. PL spectra of P1 (closed square) and P2 (open square) in film.

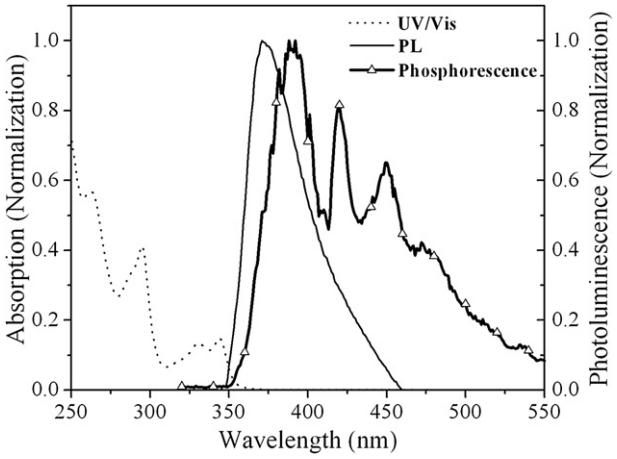

Fig. 6. UV, PL and Phosphorescent spectra of PVK in CH_2Cl_2.

Table 2
First excited energy levels of the components in P1 and P2.

Component	Absorption edge (nm)	Phosphorescence peak (nm)	S_1 level (eV)	T_1 level (eV)
PVK	353	419	3.51	2.96
VBCzDPO	361	430	3.43	2.88
TTA	397	527	3.12	2.35

units in the copolymers, the positive energy transfer from PVK segments to **VBCzDPO** should be dominate. Significantly, S_1 and T_1 energy levels of **VBCzDPO** successfully fit those of TTA with ΔE_S and ΔE_T of 0.31 and 0.53 eV, respectively, which meet the requirement of efficient intramolecular energy transfer. These efficient energy transfers from **VBCzDPO** to TTA, further to Eu^{3+}, also reduce the possibility of reverse energy transfer to PVK segements. According to the positions of excited energy levels of the components, the mechanism of intra-chain energy transfer process in **P1** and **P2** can be suggested: firstly, PVK segments are excited to their S_1 excited state by absorbing energy, then the energy either directly transfers to S_1 level of TTA or transfers to S_1 level of **VBCzDPO** then to that of TTA. Part of the S_1 energy of **VBCzDPO** can transfer to its T_1 level through intersystem crossing (ISC), and then transfer to T_1 level of TTA. The S_1 energy of TTA obtained from PVK and **VBCzDPO** also consequently transfers to its T_1 level. Thus, most of the energy absorbed by the copolymer matrix finally converges to T_1 level of TTA, and consequently transfers to $^5D_0$ of Eu^{3+}. It indicates that for the singlet and triplet intra-chain energy transfer **VBCzDPO** serves as the intermediate and bridge between PVK and $Eu(TTA)_3$. And if considering PVK and **VBCzDPO** as an integrated macro-neutral-ligand, TTA also has the indispensable effect as the intermediate and bridge for the energy transfer between the copolymer main chain and Eu^{3+}. In the whole process, according to the position of the energy levels and the energy gaps the most efficient steps should be the singlet and triplet energy transfers from **VBCzDPO** to TTA, which ensures the high efficiency of whole intra-chain energy transfer.

3.4. Thermal properties

The differential scanning calorimetry (DSC) analysis was performed to investigate the phase stability of the copolymers (Fig. 8). The glass-transition temperatures (T_g) of **P1** and **P2** are about 200 °C, which is equivalent with that of PVK homopolymer. Even so, **P1** and **P2** still exhibit the excellent phase stability compared with many other soluble light-emitting polymers.

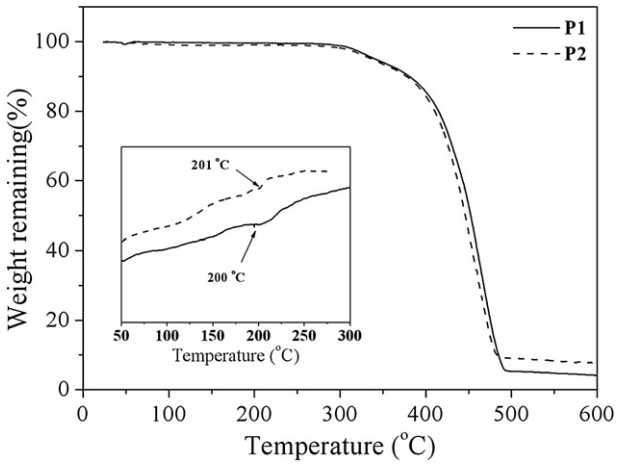

Fig. 8. DSC (inserted) and TGA curves of P1 (solid line) and P2 (dash line).

The thermal stability of **P1** and **P2** was investigated by thermogravimetric analysis (TGA). The temperatures of the thermal decomposition (T_d, 5%-weight-loss temperatures) of **P1** and **P2** are 337 and 341 °C, respectively, which are lower than that of PVK (439 °C). Obviously, since the coordinate bond is much weaker, the initial decomposition process mainly involves O-Eu bond rupture in **EuM** and decomposition of $Eu(TTA)_3$. Nevertheless, **P1** and **P2** still have good thermal stability with T_d more than 300 °C.

3.5. EL performances

In order to investigate the EL properties of **P1** and **P2**, two types of spin-coated devices were fabricated with different configurations as ITO/PEDOT:PSS (40 nm)/Copolymer (80 nm)/Ba (4 nm)/Al (120 nm) and ITO/PEDOT:PSS (40 nm)/Copolymer:PBD (80 nm) (30%, 80 nm)/Ba (4 nm)/Al (120 nm). Device **A** and **B** were based on **P1** and **P2** with the former configuration, respectively. And device **C** and **D** were based on **P1** and **P2** with the latter configuration, respectively.

EL spectra of all of the devices consist of the characteristic Eu^{3+} emissions with the main peak at 615 nm as pure red emission (Fig. 9). Different with EL spectra of the doping devices, in which the short-wavelength emissions from the hosts often became distinct along with the increasing of voltage [31], even at the highest voltage EL spectra of **A**-**D** are still very stable. This proves

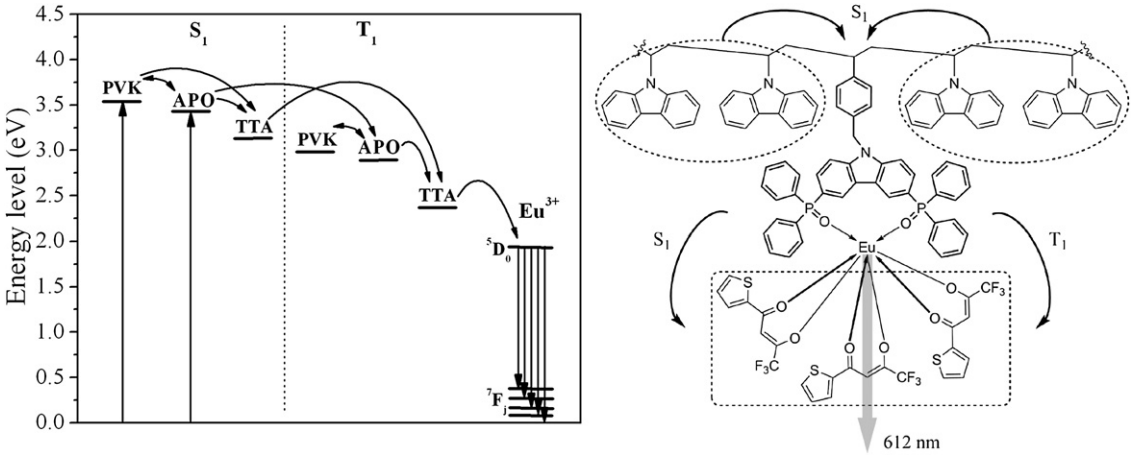

Fig. 7. Schematic energy level diagram and the energy transfer process: S_1, first excited singlet state; T_1, first excited triplet state; APO, VBCzDPO.

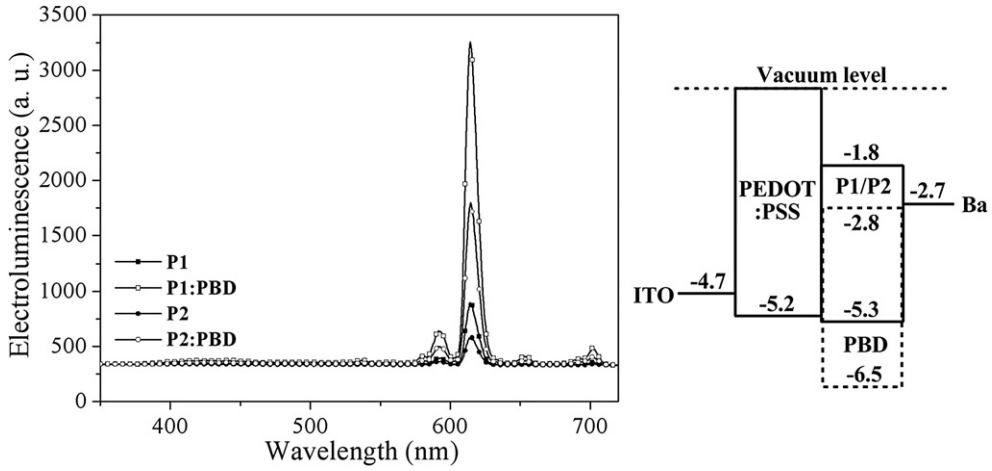

Fig. 9. EL spectra of the devices at their highest voltages and the schematic energy level diagram of the devices (The frontier energy levels of the copolymers are estimated according to electrochemical analysis (SI 2)).

the efficient energy transfer from PVK segments to $Eu(TTA)_3$ moieties.

The turn-on voltage of **A** is 16.0 V at 1 cd m^{-2}, and its maximum brightness of 11.2 cd m^{-2} was achieved at 21.0 V with the current density of 610.3 mA cm^{-2}. Device **B** had a turn-on voltage at 18.5 V. The maximum brightness of device **B** was 9.1 cd m^{-2} at 24.5 V with the current density of 305.9 mA cm^{-2} (Fig. 10). It is showed that the turn-on voltage of **A** is lower than that of **B**. At the same voltages, the current densities of **A** are much higher than those of **B**. Therefore, **P1** exhibits much stronger carrier injection and transport ability than **P2**. The main reason might be that since the majority of **P1** and **P2** is PVK segment the major carrier in **A** and **B** is hole. The hole-injection ability of **VBCzDPO** is much weaker than PVK segments, thus, the hole-injection and transporting ability of the main chain is weakened if increasing the content of **VBCzDPO**. Although the electron injection ability of **EuM** is much stronger than that of PVK segments, because of the wrapping and embedment of the pendent **EuM** moieties by PVK segment, the improvement of electron injection and transporting by increasing the content of **EuM** from 1% to 3% is limited. Therefore, the carrier-injection and transporting in **A** is superior to that in **B**. However, it is noticeable that the maximum brightness of **A** is similar with that of **B**. Furthermore, the Brightness-Current Density (B-*J*) curves of **A** and **B** show that at the same current densities, brightness of **B** is higher than that of **A** (Fig. 11). This is much different with the doping devices, in which the brightness remarkably decreased along with increasing of the doping concentration. According to EL spectra of **A** and **B**, the absence of the short-wavelength emission from PVK segments suggests the efficient exciton migration and Förster energy transfer in both **P1** and **P2**. If EL process of **A** and **B** mainly involves in these two channels, **A** should have similar brightness with **B** at the same current density. The brightness of **A** might be even higher than that of **B** because of the worse concentration quenching of **P2**. According to electrochemical analysis, LUMO energy levels of PVK segments and Eu-chelate segments are −1.84 and −3.2 eV, respectively (SI 2). Thus, the Eu-chelate repeat units introduce electron traps with a depth of as high as 1.36 eV, which makes the electron capture highly efficient. Thus, after electron trapped in Eu-chelate segments, the surrounding holes would be attracted by the Coulomb force to form CT excitons. Obviously, with the higher Eu-chelate content **P2** can form more excitons than **P1**, and finally realized the higher EL brightness. It implies that for **A** and **B**, the carrier trapping might be the main channel involved in their EL process.

It is showed that the difficulty of electron injection and transporting is the main reason for the low brightness of **A** and **B**. In order to improve the electron injection and preserve the advantage of the good hole injection, PBD was blended in the emitting layer

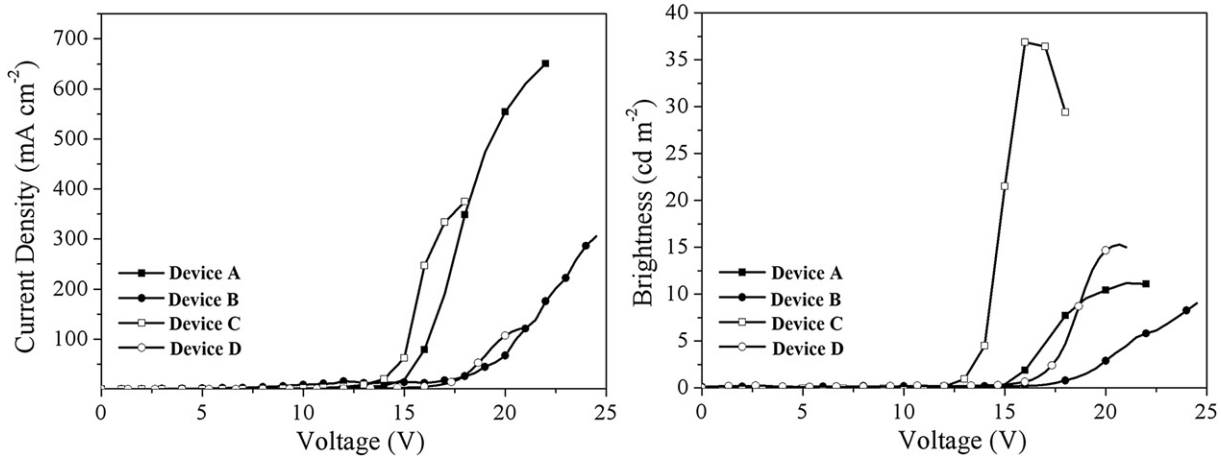

Fig. 10. Current density-Voltage (*J*–V) curves and Brightness-Voltage (B–V) curves of device A-D.

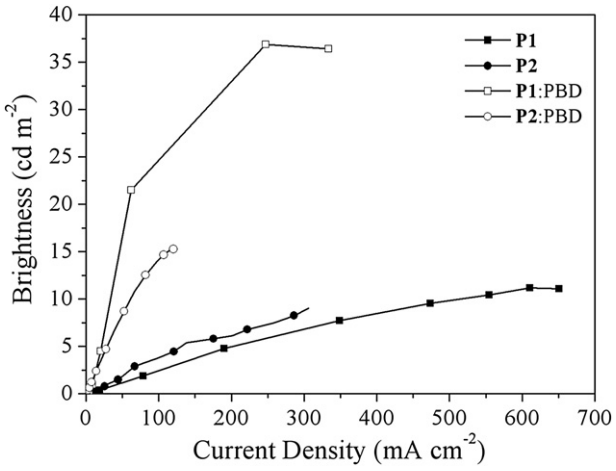

Fig. 11. Brightness-Current Density (B–*J*) curves of device A-D.

with concentration of 30% [32]. The LUMO level of PBD is −2.8 eV, which fits to the vacuum level of Ba as −2.7 eV (Fig. 9). It is showed that at the same voltages the current densities of **C** and **D** are higher than those of the corresponding **A** and **B**, respectively. The turn-on voltage of **C** is remarkably reduced to 13 V, and its maximum brightness of 36.9 cd m^{-2} was achieved at 16.0 V with the current density of 247.1 mA cm^{-2}. **D** had a turn-on voltage of 16.5 V. The maximum brightness of **D** was 14.7 cd m^{-2} at 20.0 V with the current density of 106.8 mA cm^{-2} (Fig. 10). Compared with **A** and **B**, the turn-on voltages of **C** and **D** were much lower because of their improved electron injection and transporting. The brightness of **C** and **D** was several times of those of **A** and **B**, respectively. It is interesting that at the same current densities the brightness of **C** is much higher than that of **D**, which is just contrary to the relationship between **A** and **B**. After blending, the electron can be easily injected in the emitting layers. The increasing of the concentration of electron greatly facilitates the formation of excitons. Although parts of the excitons were still formed by carrier-trapping, after the saturation of the traps, most of the excitons were formed at PVK segments, then, the energy transfers to Eu-chelate segments through exciton migration and Förster energy transfer. For these two channels, because of the high exciton concentration, the reduction of concentration quenching and *T*–*T* annihilation becomes dominate in brightness and efficiencies. Therefore, although **P2** still has the advantage in carrier capture, its higher content of **EuM** induces the worse concentration quenching and further decreases EL performance of **D**. Contrarily, after blending, compared with **A** the electron injection in **C** was remarkably improved, which not only solves the limited exciton concentration due to the low Eu^{3+} content, but also highlights the advantage of **P1** in restraining concentration quenching and *T*–*T* annihilation. The more remarkable improvement from **A** to **C** further suggests that for the blending **C** and **D** the main channels in EL process might be exciton migration and Förster energy transfer.

Therefore, it can be suggested that at lower exciton concentration the charge trapping should be the main channel for EL process, however, along with the increasing of exciton concentration, the exciton migration and Förster energy transfer become dominant. Even for **C** and **D** their major carrier is hole. Most of holes injected were not involved in the recombination, but directly reached cathode as loop current. As the two-layer devices, the current densities of **A** ~ **D** were much higher, which remarkably reduce the EL efficiencies. Nevertheless, the turn-on voltage of 13 V and maximum brightness of 36 cd m^{-2} of **C** is favorable compared to the blending devices based on similar emitting lay as PVK:PBD:Eu^{3+} complex [33], and is comparable with the three-layer device based on the similar Eu-complexed copolymer containing phenanthroline derivatives [48]. However, the EL performance of **P1** and **P2** was till inferior to those of small molecular phosphine oxide Eu^{3+} complexes, which may be attributed to the simple configuration of devices fabricated through spin coating, the possibility of reversible energy transfer between Eu-complexed moieties and PVK segments, and the different emission process of PL and EL. Through the device optimization, EL performance of **P1** and **P2** would be further improved.

4. Conclusion

Two copolymers **P1** and **P2** were prepared by using the polymerizable APO ligand based Eu^{3+} complex $Eu(TTA)_3$VBCzDPO (**EuM**) and vinylcarbazole as the monomers in the ratios of 1:99 and 1:33, respectively. Our investigations showed that the functionalized APO ligand and the corresponding Eu-chelate segments significantly improve the properties of the Eu-complexed nonconjugated copolymers. It is showed that the stronger coordinate ability of bidentate APO ligands facilitates the stability of the complex monomer during polymerization. Their beetling coordinate sites and adjustable structure efficiently reduce the steric effect of bulky **EuM**. Both of **P1** and **P2** exhibit the enhanced emission from Eu^{3+} ion and the high PL QY in solid of 60%, which implies the efficient intra- and inter-chain energy transfer in **P1** and **P2**. Further investigation of intra-chain energy transfer process indicates that in the singlet and triplet intra-chain energy transfer process **VBCzDPO** serves as the intermediate and bridge between PVK and $Eu(TTA)_3$. The suitable position of the energy levels and the energy gaps make the positive singlet and triplet energy transfers from **VBCzDPO** to TTA much more rapid and efficient than the possible reverse energy transfer from **VBCzDPO** to PVK segments, which ensures the high efficiency of whole intra-chain energy transfer. The pure-red emission from the devices of **P1** and **P2** was demonstrated. Favorable EL performance including a low turn-on voltage of 13 V and maximum brightness of 36 cd m^{-2} were realized. Our results demonstrate the potential application of polymerizable APO ligands in high performance EL europium-complexed polymers. The further purposeful chemical modification of APO ligands is ongoing in our laboratory. It has been showed that the suitable excited energy levels of APO ligands have strong effect on the intra-chain energy transfer and the charge trapping is one of the most important channels in EL process. Through introducing different functional groups, the excited energy levels and the frontier orbital levels of APO ligands can be conveniently tuned. The lower turn-on voltage, higher brightness and efficiency would be realized.

Acknowledgements

This project was financially supported by NSFC (50903028 and 20972043), Science and Technology Bureau of Heilongjiang Province (QC08C10), Education Bureau of Heilongjiang Province (10td03), Innovation Fund of KLFIMC, the Supporting Program of Innovation teams of HLJU (hdtd2010-08) and Heilongjiang University Funds for Distinguished Young Teachers.

Appendix Supplementary data

Supplementary data related to this article can be found online at doi:10.1016/j.polymer.2010.12.016.

References

[1] Burroughes JH, Bradley DDC, Brown AR, Marks RN, Mackay K, Friend RH, et al. Nature 1990;347:539–41.

[2] Stork M, Gaylord BS, Heeger AJ, Bazan GC. Adv Mater 2002;14:361–6.
[3] Gaylord BS, Heeger AJ, Bazan GC. J Am Chem Soc 2003;125:896–900.
[4] Thomas III SW, Joly GD, Swager TM. Chem Rev 2007;107:1339–86.
[5] Lo PK, Sleiman HF. Macromolecules 2008;41:5590–603.
[6] Abbel R, Schenning APHJ, Meijer EW. J Polym Sci A Polym Chem 2009;47:4215–33.
[7] Yang XH, Müller DC, Neher D, Meerholz K. Adv Mater 2006;18:948–54.
[8] Chen X, Liao JL, Liang Y, Ahmed MO, Tseng HE, Chen SA. J Am Chem Soc 2003;125:636–7.
[9] Sandee AJ, Williams CK, Evans NR, Davies JE, Boothby CE, Köhler A, et al. J Am Chem Soc 2004;126:7041–8.
[10] Liu SJ, Zhao Q, Chen R-F, Deng Y, Fan QL, Li FY, et al. Chem Eur J 2006;12:4351–61.
[11] Lee PI, Hsu SLC. J Polym Sci A Polym Chem 2007;45:1492–8.
[12] Zhuang WL, Zhang Y, Hou Q, Wang L, Cao Y. J Polym Sci A Polym Chem 2006;44:4174–86.
[13] Jiang JX, Jiang CY, Yang W, Zhen HY, Huang F, Cao Y. Macromolecules 2005;38:4072–80.
[14] Park MJ, Lee JH, Kwak JH, Jung IH, Park JH, Kong HY, et al. Macromolecules 2009;42:5551–7.
[15] Grimsdale AC, Chan KL, Martin RE, Jokisz PG, Holmes AB. Chem Rev 2009;109:897–1091. 5.
[16] Kido J, Okamoto Y. Chem Rev 2002;102:2357–68.
[17] Zhou D, Zhu X, Zhu J, Cheng Z. Polymer 2008;49:3048–53.
[18] Ling Q, Yang M, Wu Z, Zhang X, Wang L, Zhang W. Polymer 2001;42:4605–10.
[19] Bonzanini RE, Girotto M, Gonçalves MC, Radovanovic E, Muniz EC, Rubira AF. Polymer 2005;46:253–9.
[20] Bassett AP, Magennis SW, Glover PB, Lewis DJ, Spencer N, Parsons S, et al. Cola, LDPikramenou Z. J Am Chem Soc 2004;126:9413–24.
[21] Li SF, Zhong G, Zhu WH, Li FY, Pan JF, Huang W, et al. J Mater Chem 2005;15:3221–8.
[22] Wang JF, Wang R, Yang J, Zheng ZP, Carducci MD, Cayou T, et al. J Am Chem Soc 2001;123:6179–80.
[23] Xin H, Li FY, Guan M, Huang CH, Sun M, Wang KZ, et al. J Appl Phys 2003;94:4729–31.
[24] Sun PP, Duan JP, Lih JJ, Cheng CH. Adv Funct Mater 2003;13:683–91.
[25] Robinson MR, O'Reganc MB, Bazan GC. Chem Commun; 2000:1645–6.
[26] Zheng YX, Cardinali F, Armaroli N, Accorsi G. Eur J Inorg Chem 2008;12:2075–80.
[27] Yu JB, Zhou L, Zhang HJ, Zheng YX, Li HR, Deng RP, et al. Inorg Chem 2005;44:1611–8.
[28] Zhu XH, Wang LH, Ru J, Huang W, Fang JF, Ma DG. J Mater Chem 2004;14:2732–4.
[29] Raj DBA, Biju S, Reddy MLP. Dalton Trans; 2009:7519–28.
[30] Moudam O, Rowan BC, Alamiry M, Richardson P, Richards BS, Jones AC, et al. Chem Commun; 2009:6649–51.
[31] Adachi C, Baldo MA, Forrest SR. J Appl Phys 2008;87:8049–55.
[32] Kido J, Hayase H, Hongawa K, Nagai K, Okuyama K. Appl Phys Lett 1994;65: 2124–6.
[33] Li TX, Fukuyama H, Yamagata Y, Lan HL, Kido J. Polym Adv Technol 2004;15:302–5.
[34] Xu H, Yin K, Huang W. Chem Eur J 2007;13:10281–93.
[35] Sun M, Xin H, Wang KZ, Zhang YA, Jin LP, Huang CH. Chem Commun; 2003:702–3.
[36] Pei J, Liu LX, Yu LW, Lai YH, Niu YH, Cao Y. Macromolecules 2002;35:7274–80.
[37] Ling QD, Kang ET, Neoh KG, Huang W. Macromolecules 2003;36:6995–7003.
[38] Lenaerts P, Driesen K, Van Deun R, Binnemans K. Chem Mater 2005;17: 2148–54.
[39] Lenaerts P, Storms A, Mullens J, D'Haen J, Gorller-Walrand C, Binnemans K, et al. Chem Mater 2005;17:5194–201.
[40] Ling QD, Wang W, Song Y, Zhu CX, Chan DSH, Kang ET, et al. J Phys Chem B 2006;110:23995–4001.
[41] Balamurugan A, Reddy MLP, Jayakannan M. J Phys Chem B 2009;113: 14128–38.
[42] Yang MJ, Ling QD, Hiller M, Fun XZ, Liu X, Wang LH, et al. J Polym Sci Part A Polym Chem 2000;38:3405–11.
[43] Chen XY, Yang XP, Holliday B. J Am Chem Soc 2008;130:1546–7.
[44] Ling QD, Cai QJ, Kang ET, Neoh KG, Zhu FR, Huang W. J Mater Chem 2004;14:2741–8.
[45] Cheng YX, Zou XW, Zhu D, Zhu TS, Liu Y, Zhang SW, et al. J Polym Sci Part A Polym Chem 2007;45:650–60.
[46] Wen GA, Zhu XR, Wang LH, Feng JC, Zhu R, Wei W, et al. J Polym Sci Part A Polym Chem 2007;45:388–94.
[47] Zhang ZG, Yuan JB, Tang HJ, Tang H, Wang LN, Zhang KL. J Polym Sci Part A Polym Chem 2009;47:210–21.
[48] Wang LH, Wang W, Zhang WG, Kang ET, Huang W. Chem Mater 2000;12:2212–8.
[49] Melby LR, Rose NJ, Abranmson E, Caris JC. J Am Chem Soc 1964;86:5117–25.
[50] Xu H, Wang LH, Zhu XH, Yin K, Zhong GY, Hou XY, et al. J Phys Chem B 2006;110:3023–9.
[51] Xu H, Yin K, Wang LH, Huang W. Thin Solid Films 2008;516:8487–92.
[52] Xin H, Shi M, Gao XC, Huang YY, Gong ZL, Nie DB, et al. J Phys Chem B 2004;108:10796–800.
[53] Wei XQ, Peng JB, Cheng JB, Xie MG, Lu ZY, Li C, et al. Adv Funct Mater 2007;17:3319–25.

Polymer 52 (2011) 814–821

Contents lists available at ScienceDirect

Polymer

journal homepage: www.elsevier.com/locate/polymer

Spectroscopic and thermal analyses of α′ and α crystalline forms of poly(L-lactic acid)

Jeffrey P. Kalish [a], Kaoru Aou [a,1], Xiaozhen Yang [a,b], Shaw Ling Hsu [a,*]

[a] Department of Polymer Science and Engineering, Materials Research Science and Engineering Center, University of Massachusetts, Amherst, MA 01003, USA
[b] Institute of Chemistry, Chinese Academy of Sciences, Beijing 100080, China

ARTICLE INFO

Article history:
Received 2 November 2010
Received in revised form
13 December 2010
Accepted 18 December 2010
Available online 24 December 2010

Keywords:
Poly(l-lactic acid)
Polymorphic Phase
Crystallization

ABSTRACT

Poly(lactic acid) samples rich in α′ or α crystals have been characterized using spectroscopic and thermal methods. Cryogenic infrared and Raman spectroscopy were used to probe the differences in chain conformation and packing. Compared to the α crystal, the α′ crystal has weakened specific carbonyl and methyl interactions. Experimental spectroscopic analysis in conjunction with simulation studies have shown that the α′ crystal has uniform conformational disorder in the C_α–C torsion angle. This disorder in chain conformation and packing leads to different crystalline forms with different stabilities. The difference in thermal stability was quantified by measuring enthalpic change at melting for both crystalline forms. Significantly different values for the two crystalline forms were obtained ($\Delta H_m^o(\alpha') = 57 \pm 3\ J\ g^{-1}$ and $\Delta H_m^o(\alpha) = 96 \pm 3\ J\ g^{-1}$). The transformation from the less stable α′ to the more stable α phase has been characterized. This analysis provides an explanation to the double melting peaks usually found in PLLA samples.

1. Introduction

Poly(lactic acid) (PLA) has a number of attractive properties (biodegradability, biocompatibility, semicrystalline, synthesized from non-petroleum feedstock and others) and is being developed into both specialized and commodity applications [1,2]. A number of polymorphic crystalline structures, α′, α, β and γ, have been postulated for poly(L-lactic acid) (PLLA) homopolymers [3–6]. Each of these has distinctly different structural parameters. The α′ or α crystal is formed under most processing conditions depending on thermal history. The γ crystalline phase, with very different chain conformation and packing as compared to the α phase, has also been proposed [4]. The β phase is formed at elevated temperatures by deforming α crystals [5,6].

Our study focus on the α′ crystalline phase that has been proposed recently [7]. This new crystalline structure forms at temperatures below 120 °C, lower than that of the single crystal of the α form [7]. This new crystalline phase is different from the α phase with differences in both chain conformation and packing [8]. However similar chain conformation in the α′ and α structures with greater distortion for the α′ helix has been reported [9]. The α′ crystalline form has been described as quasi-hexagonal with perturbed rotational and longitudinal ordering, similar to the rotator phase of paraffinic crystals [10].

It is worthwhile to comment on the assertions in literature regarding the α′ and the β forms being the same structure [11,12]. The α′ crystals are formed at lower temperatures than the α phase. Whereas the β phase forms at elevated temperatures by deforming α crystals. Unless the β form can revert to the α form through thermal annealing, it must be concluded that the α′ and the β forms are two distinct structures differing from previous analyses [11,12]. It has also been shown that the α′ structure is a discrete phase, not the β phase [7].

In this study, we paid particular attention to the α′ crystalline phase and characterized the structural differences as compared to the more stable α phase. Although α phase is much more extensively studied as compared to the α′ phase, most commercial PLA products are processed with experimental conditions favoring the α′ form. Therefore, it is prudent to understand more thoroughly the similarities and differences between the two structures.

The α′ and α crystalline phases are remarkably similar as shown in Fig. 1 [13,14]. When projected perpendicular to the helical axis, the two crystalline phases, each with a column of radius 2.74 Å, show differences of only three percent in the *b*-axis and one

* Corresponding author. Tel.: +1 413 577 1411.
E-mail address: slhsu@polysci.umass.edu (S.L. Hsu).
[1] Present address: PU Global Product R&D, The Dow Chemical Company. Freeport, TX 77541, United States.

0032-3861/$ – see front matter © 2010 Elsevier Ltd. All rights reserved.
doi:10.1016/j.polymer.2010.12.042

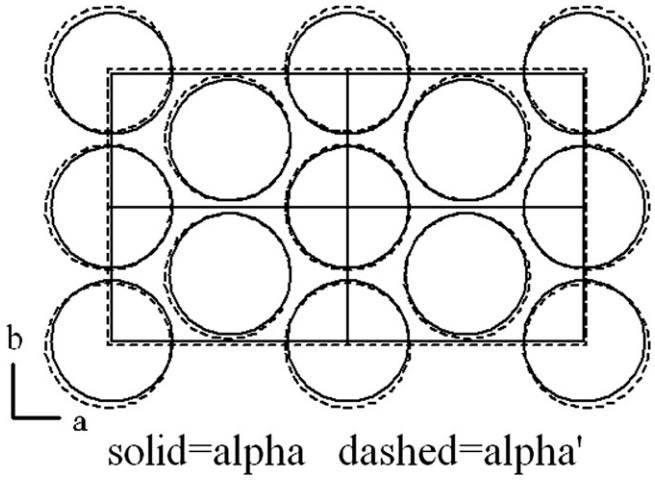

Fig. 1. Unit cells of the α and α′ structures from literature [9].

percent in the *a*-axis. In fact, very few characterization techniques are able to differentiate the two crystalline forms [7,8,14,15]. Double melting peaks assignable to the two crystalline phases have been observed in PLLA [11,12,16]. Many physical properties of PLA also exhibit a transition for crystallization temperatures above and below 120 °C. For example, spherulitic growth rate [12,16–18]; crystallinity [16,19,20]; double-to-single melting peak behavior [16,20]; lamellar thickness [21,22]; crystallization rate [12]; and X-ray diffraction pattern all exhibit differences for different crystallization temperatures, thus indicating the presence of different crystalline phases [10–12,23].

As shown in Fig. 1, crystalline features of the α and α′ phases are similar, thus difficult to differentiate. The melting events of many PLA crystals overlap making analysis difficult. Each of the polymorphic phases must be accounted in the data analysis. Even the equilibrium melting endotherms have not been obtained. Without it, it is difficult to explain the development of some most simplistic properties. In many cases, even the degree of crystallinity of processed samples is difficult to ascertain.

In this study, we have employed a combination of vibrational spectroscopy and thermal analysis to characterize the crystalline features of the two PLA crystalline phases. Spectroscopic features associated with chain packing, chain conformation, and specific interactions in PLLA crystalline forms have a significant impact in different thermal properties and relative structural stability. In our previous studies, vibrational spectroscopy has been used to characterize the PLA chain conformation [24]. Based on experimental studies in conjunction with simulation studies, it was concluded that the rotational isomeric states of the PLA chain. The *tg′t* structure (10/3 helix) is the dominant structure, accounts for ~80% of the chain conformation. The other three possible low energy forms, 2/1 (*tt′t*), 4/1 (*tg′g*) or 5/1 (*tt′g*) helix account for the rest (20%) of conformational distribution. This conclusion would suggest that PLA is relatively stiff polymer, which is consistent with the slow quiescent crystallization and the extremely fast crystallization kinetics when PLA is deformed [24–26]. In this study we have used similar techniques to characterize the chain conformation in both α and α′ crystalline forms.

In order to understand more fully the differences of the two crystalline forms, an analysis of chain packing is also necessary. As shown in Fig. 1, the diffraction data obtained so far have not provided the definitive differences in the atomic placement in the unit cell thus unable to provide detailed differences in the chain packing. Based on our simulation and experimental results, the difference between the fully crystalline structure (100% *tg′t*) and the fully disordered (80% tg′t and 20% other three chain conformations, *tt′t*, *tg′g*, *tt′g*) is only ~18 J/g. In addition, the difference in the melting temperature of a stereocomplex is far above the melting temperatures of either PLLA or PDLA crystals. Yet the densities of the three samples are virtually identical. These are characteristics typical of systems with strong secondary interactions, which can be characterized by vibrational spectroscopy. Therefore, it is important to identify the exact placement of the functional groups in the unit cell and their relative orientation. Only then would it be possible to understand the physical properties of the two PLA crystalline phases.

We have conducted such structural characterization studies in the past for the α crystal and the stereocomplex using group theoretical methods and/or cryogenic conditions [27]. In those cases, relevant inter-molecular interactions were identified [28]. However, the group theoretical approach is not feasible for the α′ crystal, owing to the fact that a sufficiently large spherulite sample cannot be obtained. In the current study, we have focused on the low frequency vibrations in both infrared absorption and Raman scattering. Those bands are sensitive to the differences in the magnitude and specificity of inter-molecular interactions. It is also known that the completely symmetric A modes have dipole changes parallel to the chain axis [29]. Instead we will focus on the E modes with transition dipoles perpendicular to the helical axis. These modes are expected to be sensitive to the large dipoles stabilizing the various PLA crystals.

When thermal data are analyzed, one can observe a conversion process of the α′-form into the α form upon annealing [16,20]. Analysis of the melting of α′ crystals is convoluted with the transformation into α crystals. By employing a thermal method developed previously [30,31], it is possible to obtain the equilibrium enthalpic change at melting for the two crystalline phases. The spectroscopic analyses carried out in this study provide a much stronger foundation to explain the calorimetric data obtained for the two PLA crystalline forms.

2. Experimental methods

2.1. Materials

Samples of poly(L-lactic acid), or PLLA, of 1.2% D-lactyl content were received from NatureWorks LLC and used for crystallization studies. Tetrahydrofuran (THF) which is a poor solvent for PLA α crystals but a good solvent for amorphous PLA, was used as received from Fisher Scientific, and was used in Soxhlet extraction of the α crystal.

2.2. Wide-angle X-ray diffraction

X'Pert PRO from PANalytical was used to acquire one-dimensional wide-angle X-ray diffraction patterns. The Cu-K_α line was used as the incident radiation ($\lambda = 1.542$ Å).

2.3. Dispersive Raman microspectroscopy

A Jobin-Yvon Horiba LabRam HR800 dispersive Raman spectrometer (HeNe gas laser, $\lambda = 632.8$ nm) was used to acquire the Raman spectra of semicrystalline PLA with a custom built cold stage. Liquid nitrogen was pumped through a thermally conductive (copper) sample stage. A thin glass cover slip covers the cell to prevent condensation on the sample. The top of the glass cover slip and sample stage were purged with dry air to prevent condensation on the glass. Spectral resolution was maintained at 4 cm^{-1} near the lasing line.

2.4. Fourier-transform infrared spectroscopy

Cryogenic transmission infrared spectra for PLA were measured at near-liquid nitrogen and room temperatures using a Bruker IFS-113v vacuum FT-IR spectrometer and a custom built cold cell [27,32]. Spectral resolution was maintained at 4 cm^{-1}. Owing to their wide frequency range of transparency and their resistance to substantial thermal shock such as quenching from the melt to room temperature, zinc selenide windows were used. PLA samples were solvent-cast, dried, then melt-quenched from 220 °C/min to room temperature, followed by cold-crystallization for one day. Far infrared spectra were acquired using a Perkin–Elmer Spectrum 400 spectrometer, 256 scans were coadded, and a spectral resolution of 4 cm^{-1} was maintained. A custom built cold cell was retrofitted with polyethylene windows for transmission in the far infrared region.

2.5. Differential scanning calorimetry

A TA Instruments DSC Model Q100 was used to measure the enthalpy of fusion of PLA samples. A heating rate of 20 °C min^{-1} was used for all scans, starting at 0 °C to obtain good baselines in both the glassy and rubbery temperature ranges. Hermetic aluminum pans were used as sample holders. The lids to the pans were pressed so that thermal contact with the sample was improved. Indium and water were used as a standard to calibrate the temperature at their onset melting points of 156.6 and 0.0 °C, respectively. The indium heat of fusion (28.6 J g^{-1}) was used to calibrate the calorimeter for the heat flow [33]. The change in heat capacity, or ΔC_p, at the glass transition for melt-quenched PLA (0.53 J g^{-1} K^{-1}) was also used as an internal calibration standard for heat flow.

2.6. PLA crystallization

For measurement of X-ray and Raman data, samples each weighing 30–50 mg were first melt-pressed at 230 °C for 1 min, followed by a rapid quench to room temperature by sandwiching between two large metal heat sinks. Subsequent isothermal crystallization was carried out using a calibrated Watlow PID controller with a T-type (copper-constantan) thermocouple. This experimental setup was calibrated to the melting (0.0 °C) and boiling (100.0 °C) points of de-ionized water. The stability of the temperature control was 0.1–0.2 °C.

3. Results and discussions

For structural analysis of the α′ and α crystals, two types of samples were prepared, one crystallized at 90.0 °C and another at 160.0 °C, which corresponds to predominantly α′ and α crystalline samples, respectively [8,10–12]. The presence of the triplet in the carbonyl stretching region (Fig. 2) confirms the presence of α crystals [27], as does the presence of many detailed X-ray diffractions (Fig. 3) [34]. X-ray diffraction spacings observed are consistent with previously reported data [13]. It is well understood that the differences in X-ray diffraction pattern correspond to difference in lateral spacing of the α′ and α crystal, with the α′ crystal having a slightly larger unit cell [13].

We have separated the spectroscopic analysis of the two types of samples, one rich in α′ crystals and the other rich in α crystals, into two thrusts, one dealing with chain conformation and the other part dealing with chain packing. The analyses are based on both experimental data presented here and simulations carried out in this study together with previous ones [24–26]. Various normal coordinate analyses have been carried out using model conformations

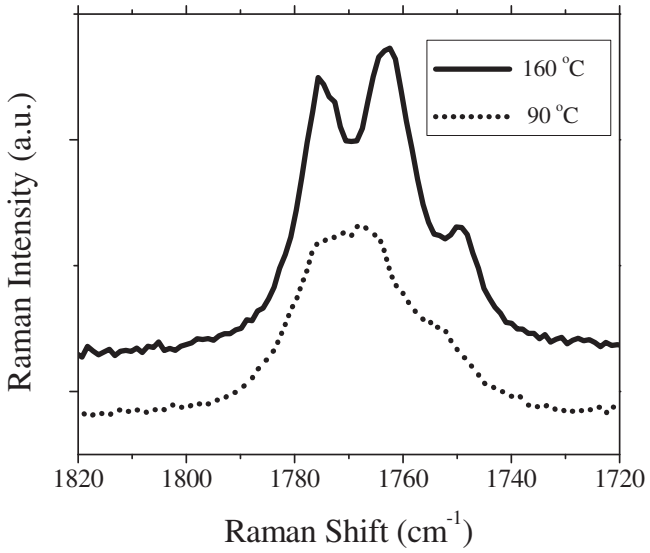

Fig. 2. Raman spectra of the carbonyl stretching region of PLA samples crystallized at 90.0 °C and 160.0 °C.

predicted [35]. The conformations of the 2/1, 3/1, 4/1 and 5/1 helices are formed by continuous sequences of *tt′t*, *tg′t*, *tg′g* and *tt′g* conformers respectively. In addition, we have carried out normal coordinate analyses for the chain conformation distribution of completely disordered PLA polymers [24,25]. The force field used is consistent with the structures employed and transferred directly from the ones developed for small molecules [26]. In order to simulate Raman spectra, we have employed the polarizability additivity model and used transferred bond polarizability elements with no adjustable parameters [26].

It is remarkable that the two crystalline forms have virtually identical infrared and Raman features. For example, the bands sensitive to conformational differences in the 400 and 1000–1200 cm^{-1} regions are almost identical for the two crystalline phases. The most significant differences are seen in the 200 cm^{-1} region, Fig. 4. The lowering in the frequency of the 200 cm^{-1} band is consistent with the fact that α′ phase has greater degree of disorder

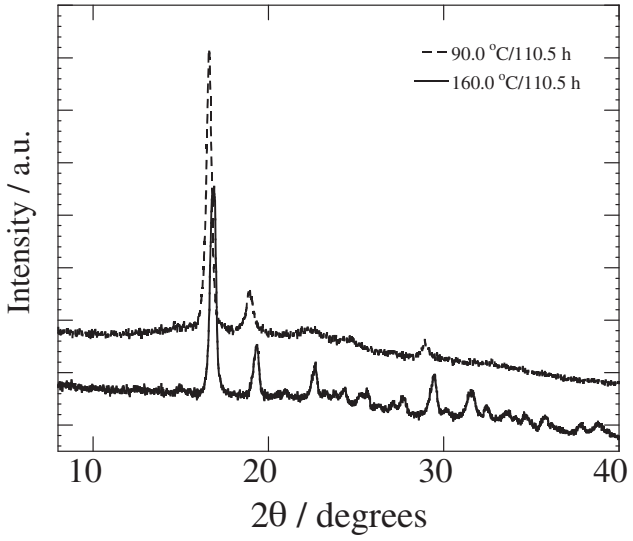

Fig. 3. Wide-angle X-ray diffraction profile of crystalline PLA crystallized at 90.0 °C and 160.0 °C.

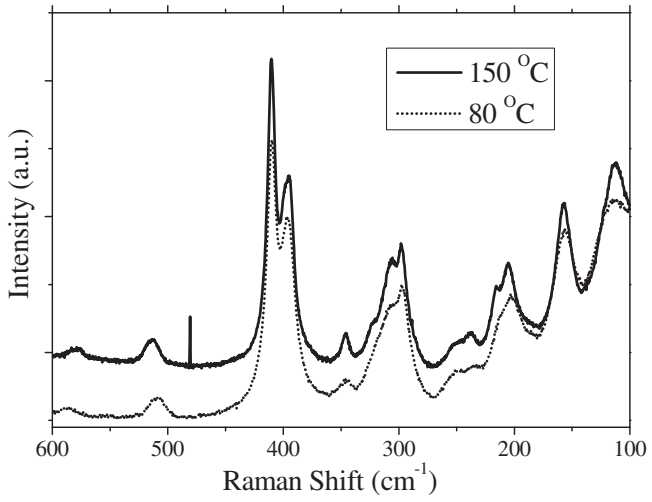

Fig. 4. Raman spectra in the 100–600 cm^{-1} region of PLA crystallized at 90.0 °C and 160.0 °C.

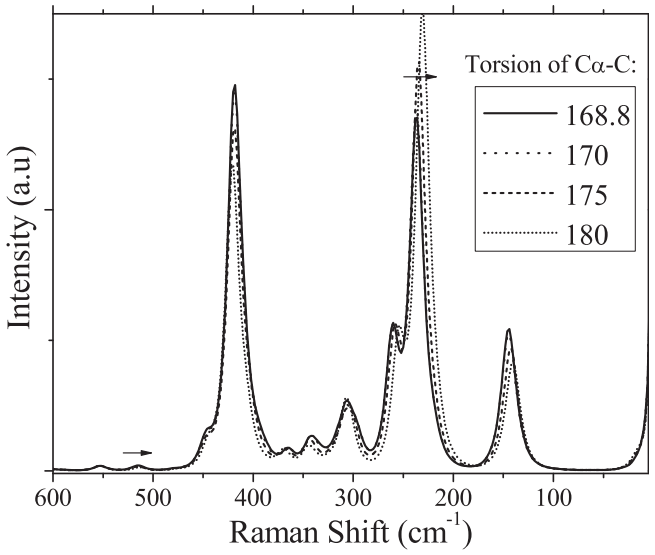

Fig. 6. Simulated spectra of distributed disorder in the C_α–C dihedral angle.

than the α phase. Two types of structural disorder have been considered. A slight localized defect is a possibility, but it is also possible to change the valence angles associated with each rotational isomeric state to simulate a distributed disorder. Our simulated Raman spectra of a *tg′t* chain with a couple of isolated *tt′g* or *tt′t* sequences perturbs the spectra sufficiently to cause a significant increase in the skeletal mode causing a degradation of spectroscopic features and the emergence of the 190 cm^{-1} band. Fig. 5 simulates two *tt′g* defects incorporated into an all *tg′t* chain. In contrast, when the C_α–C *trans* dihedral angle is changed from 168 to 180°, the bands in the 200 cm^{-1} region shift in position as observed. Fig. 6 shows the progression of the 200 cm^{-1} band as the C_α–C dihedral angle changes from 168.8 to 180°. Similar to the experimental data in Fig. 5, the α′ phase seems to be better represented by a larger torsion angle. Therefore, based on the combination of experimental and simulation data, one would then conclude that distortion of the chain conformation in the α′ structure is distributed throughout the chain and not a localized type.

Pertinent vibrational assignments are summarized in Table 1. Fig. 7 shows "far"-infrared spectra (200–700 cm^{-1}) for these two samples acquired at room temperature (20 °C) and near-liquid nitrogen temperature (−170 °C). The spectroscopic data obtained at low temperature are presented to show enhancement in intermolecular interaction due to the thermal contraction of the crystal, a technique that was employed for other PLA crystals in the past [27]. Similar to the Raman active vibrations, the difference between the α′ and α crystalline phases is insignificant. Generally speaking, Raman vibrations are more sensitive to changes in chain conformation. But a few infrared active bands also exhibit differences between the two crystalline samples, α′ and α. For example the peak position of the 510 cm^{-1} peak shift upwards by 5 cm^{-1} corresponding to a change from α′ structure to the α phase. This vibration at ~510 cm^{-1} is assigned to CCO skeletal bending underneath carbonyl, which is sensitive to chain conformation [35]. At low temperatures this peak does not shift in frequency, indicating that it is insensitive to packing changes. Thus the frequency shift observed must be due to slightly different chain conformation between the α′ and α phase. This skeletal bending vibration depends on two bonds, the ether bond (C–O) and the C_α–C bond. The ester bond is always assumed to be planar so disorder was incorporated into the C_α–C dihedral angle. The simulation of torsion disorder in Fig. 6 also predicts the direction of this frequency shift. Again, the α′ phase is better represented by incorporating disorder into the C_α–C dihedral angle.

A number of bands exhibit evidence of crystal field splitting in the α crystal but not in the α′ phase. Of particular interest is the splitting of the 398 cm^{-1} E mode (C=O in plane bending) and the appearance of the 315 cm^{-1} E mode in the α crystal. At low

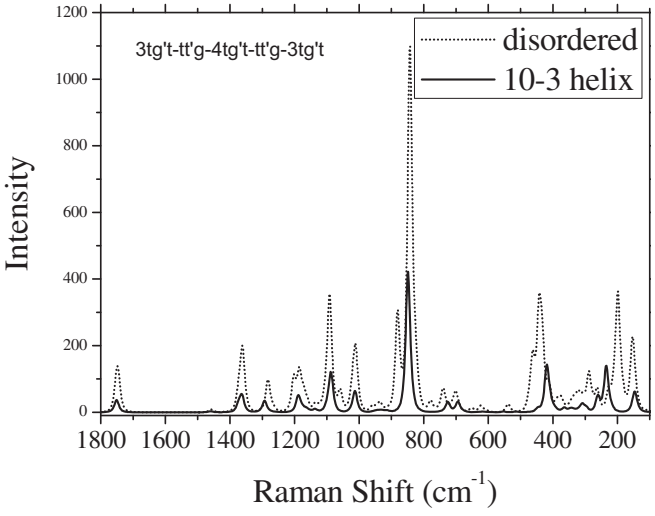

Fig. 5. Simulated spectra of two isolated *tt′g* defects in a *tg′t* chain.

Table 1
Assignments for specific vibrations analyzed [35].

Frequency (cm^{-1})	Mode	Assignment (PED)
315	E	CH_3 side chain bending (31)
398	E	C=O in plane bending (32)
510	E	CCO bending (34), O–C stretching in backbone (16)
756	E	C=O in plane bending (18), C–CH_3 stretching (11)
737	A	C=O out of plane bending (28), C–CH_3 stretching (23), CH_3 side chain bending (19)
710	A	C=O out of plane bending (41), C=O deformation (18)
685	E	C=O out of plane bending (61)
1030	A	CH_3 rocking (50), CH bending (27)

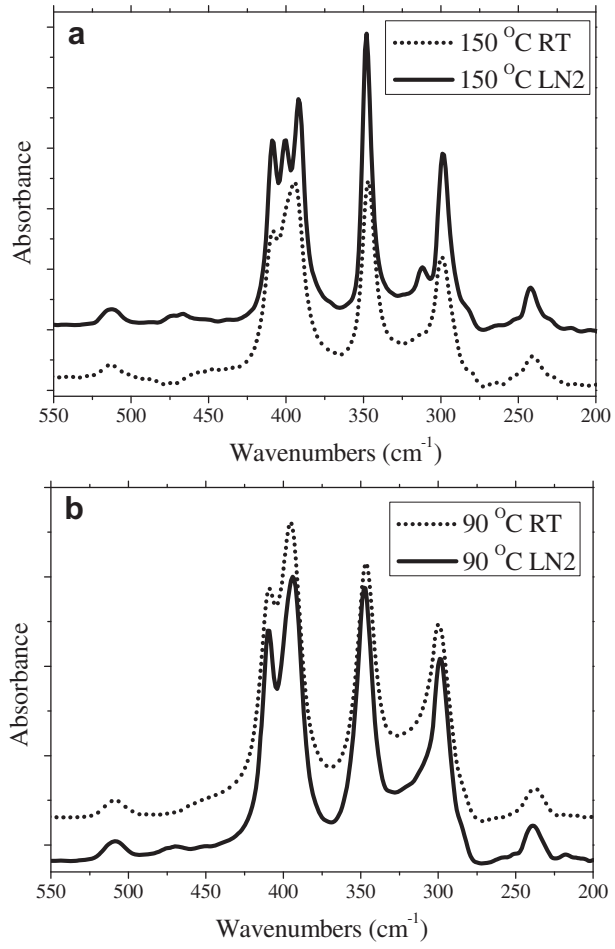

Fig. 7. Far infrared spectra in the 200–550 cm^{-1} region. "RT" refers to room temperature measurement and "LN2" to about −170 °C.

temperatures, E mode vibrations that reflect specific interactions show great enhancement. In the case of the α crystal, Fig. 7 shows significant crystal field splitting due to carbonyl and methyl interactions. These specific interactions are not present in the α′ phase. Vibrations in the far infrared region show slight differences in chain conformation, but significant differences in specific interactions involving carbonyl functional groups.

We focused on the crystallinity-sensitive 923 cm^{-1} peak [6,35–37]. Both samples have approximately the same crystallinity as judged from the 923 cm^{-1} peak intensity (Fig. 8) [6]. The multiple complex splitting in the 750–690 cm^{-1}, which is characteristic of the PLA 10/3 helix is only present in the α crystal [27]. This region is much less complex for the α′ sample. The sample crystallized at 71 °C should contain mostly α′ crystals [7]. We interpret that the inter-molecular order is much less well defined for the α′ crystal as compared to the α crystal. This is consistent with X-ray diffraction patterns reported for the α′ crystal form, when only three layer lines are observed [7,11], as opposed to the usual 10 layer lines for the 10/3 helix of the α crystal [34]. The 760–690 cm^{-1} region features suggests a helix different from the 10/3 helix in the α′ crystal. In the case of the α′ crystal, helical distortion could disturb specific interactions that exist in the α crystal.

The carbonyl stretching region, 1700–1800 cm^{-1}, supports the conclusion that the PLLA α′ crystal has weakened specific interactions as compared to the α crystal. A five-fold splitting was found in our previous study on the α crystal [27]. Such a splitting can also be seen in the 130 °C crystallized PLLA (Fig. 8). The 71 °C crystallized PLLA, which is mostly α′ crystals, shows a carbonyl band which has a single broad peak with a weakly resolved shoulder. For the PLLA α crystal, the carbonyl band splitting is due to interactions and coupling between carbonyl groups [38].

The CH stretching region of the Raman spectra, 2800–3100 cm^{-1}, are shown in Fig. 9. The multiple complex splitting exist only in samples predominantly consisting of α crystals. Typically the CH stretching region is insensitive to interactions and physical structure. However, Fermi resonance interactions have proven to be

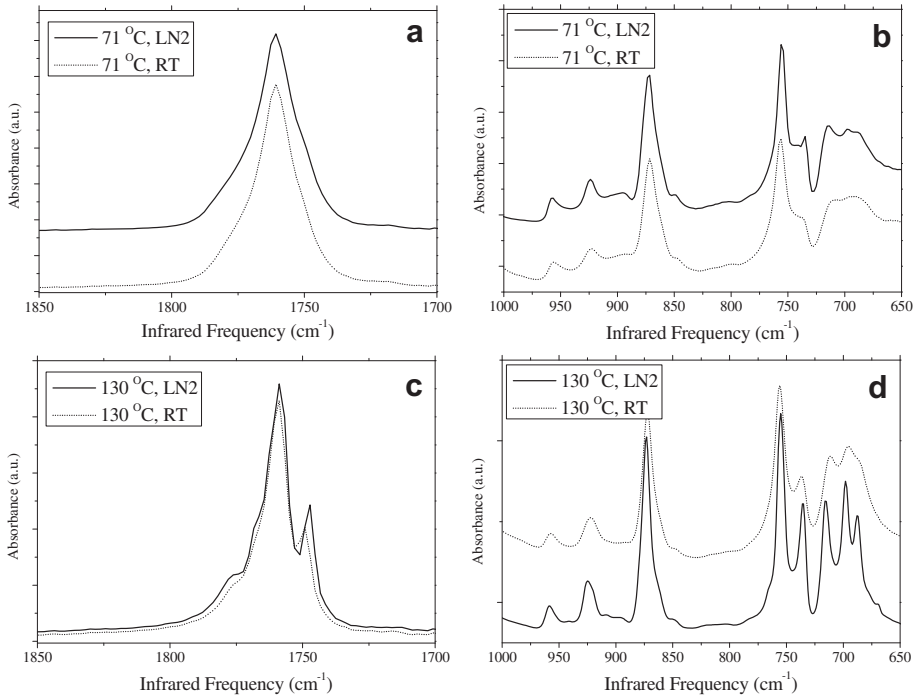

Fig. 8. Fourier-transform infrared spectra in the 650–1000 cm^{-1} and carbonyl region of PLA crystallized at (a and b) 71 °C for one day, and (c and d) 130 °C for one day. "RT" refers to room temperature measurement and "LN2" to about −170 °C.

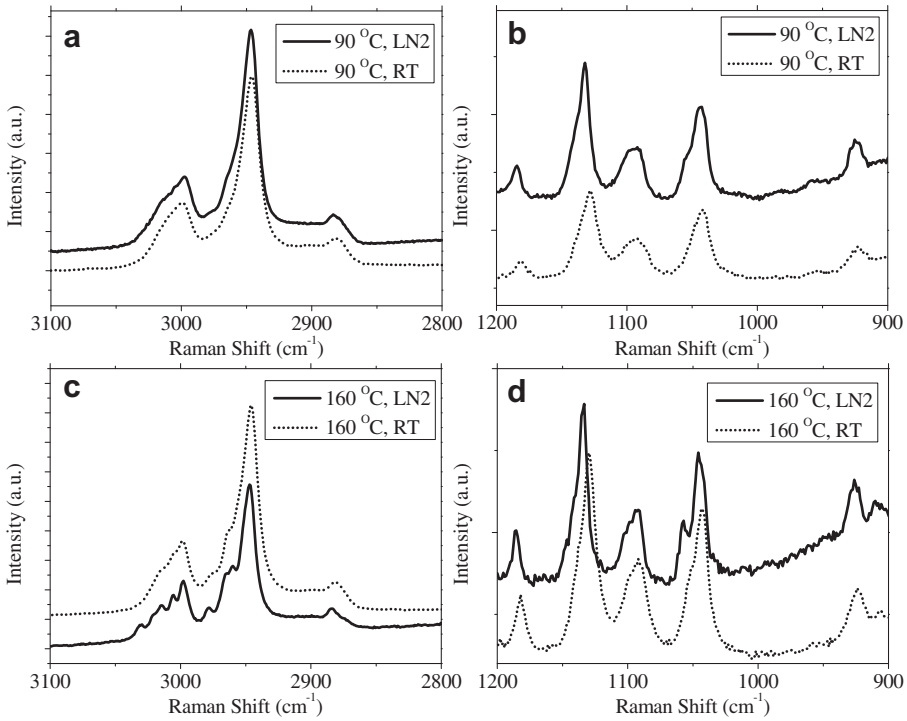

Fig. 9. Raman spectra in the CH stretching region and the 900–1200 cm^{-1} region of PLA crystallized at 90.0 °C and 160.0 °C "RT" refers to room temperature measurement and "LN2" to about −170 °C.

responsible for the unexpected features observed in this region [39]. The multiple components only exist for the methyl stretching. All of our observations summarized above indicate the presence of interactions involving methyl and carbonyl functional groups for the α crystal, which have been previously suggested [10]. The peak around 1030 cm^{-1}, assigned to methyl rocking and CH bending, exhibits crystal field splitting in the α crystal but not in the α′ phase. The vibrational spectra, infrared and Raman, of α′ rich samples are characteristic of a single chain approximation, suggesting chains of similar conformation exist but lack specific interactions [38]. Again, such splitting is not observed in the α′ phase, indicating the lack of specific interactions in this phase.

The ability of the solid-state transformation of the two crystal forms was evaluated. PLA crystals were grown at 90.0 °C and then annealed at 160.0 °C. A second experiment involved PLA crystals prepared at 160.0 °C then annealed at 90.0 °C. The X-ray diffraction patterns from the two sets of samples are shown in Fig. 10. As can be seen in the figure, both samples exhibit similar diffraction patterns, including higher angle peaks. It is clear that the 160.0 °C crystallized sample did not change after conditioning at lower temperature, whereas the 90.0 °C crystallized sample transformed to a predominantly α crystalline sample after annealing at 160.0 °C. These changes demonstrate that the α′ to α transformation is an irreversible process, with the α crystal being the more stable phase.

We aim to characterize the differences of the two structures, especially their relative stability. The difference in solubility of the

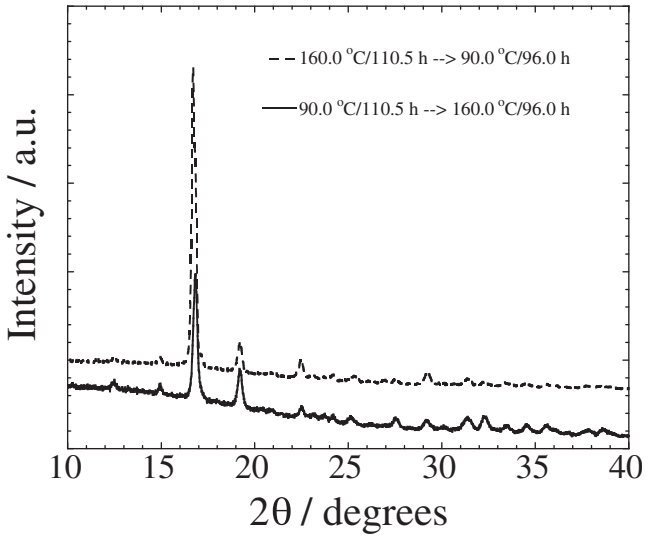

Fig. 10. Wide-angle X-ray diffraction profile of semicrystalline PLA annealed concurrently at two temperatures.

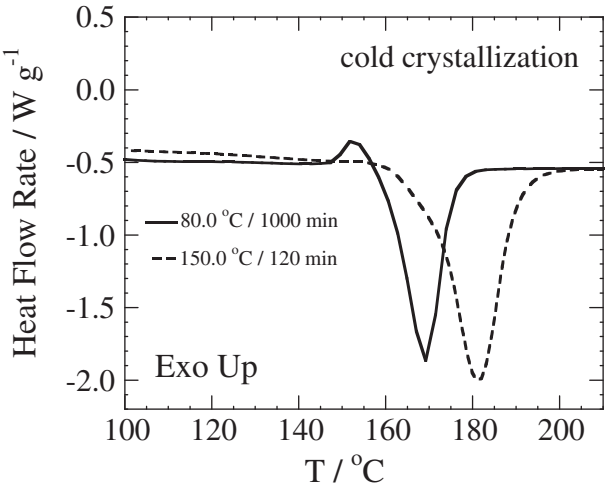

Fig. 11. DSC scans of PLA samples crystallized at 80.0 °C and 150.0 °C.

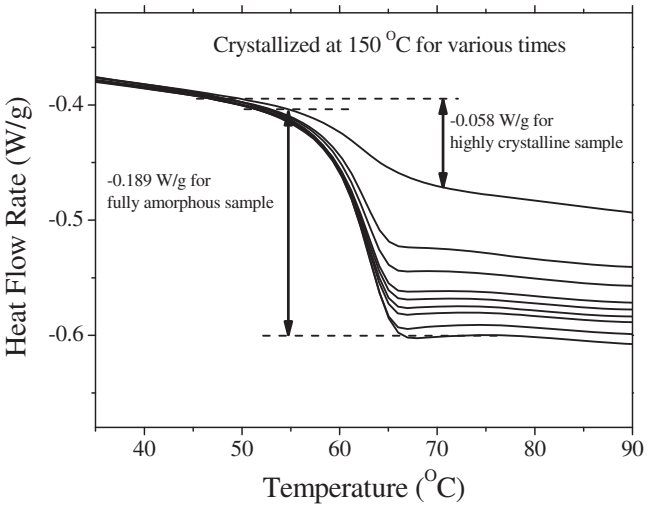

Fig. 12. An example of ΔC_p analysis for the calorimetric determination of ΔH_m for 100% crystal [30,31].

two crystal forms is quite interesting. We found that most of the samples crystallized at higher temperatures are insoluble in THF. In contrast, for α' crystals, the solubility is much higher. The slight disorder in chain conformation and changes in packing between the α' and α crystalline phases effect the solubility and should have a significant impact on the thermal properties of PLA. Therefore, it is important to establish the different enthalpic change, ΔH_m^0, for α' and α crystalline phases.

In order to evaluate the relative stability of the α and α' crystals, a calorimetric method developed by Pyda and Wunderlich was used [30,31]. It is important to note that the melting endotherm (and thus ΔH_m) of α' structure cannot be observed in isolation, as the structure transforms into α crystals during calorimetric measurements. In the net melting enthalpy calculated, the enthalpic change is $\Delta H_{m,\mathrm{net}}(\alpha') + \Delta H_{m,\mathrm{net}}(\alpha)$, where the variables refer to the net melting enthalpies of the α' and α crystals, respectively. The melting transitions for two samples, one rich in α' and the other in α crystals, is shown in Fig. 11. A small exotherm prior to major melting is seen in the α' sample, which is characteristic of this phase [13]. In the Pyda/Wunderlich method, the heat flow change at the glass transition is evaluated by extrapolating the glassy and liquid heat flow baselines toward the glass transition, as shown in Fig. 12. PLA crystal melting endotherm data and their extrapolation to 100% crystalline ΔH_m are presented in Fig. 13(a) and (b) for the lowest and highest crystallization condition tested, respectively. As seen in Fig. 13, the data shows a clearly linear relationship. From Fig. 13, we use $\Delta H_m^o(\alpha') = 57 \pm 3\ \mathrm{J\,g^{-1}}$ and $\Delta H_m^o(\alpha) = 96 \pm 3\ \mathrm{J\,g^{-1}}$ to be associated with fully crystalline α' and α phases, respectively.

When there is a mixture of two crystalline forms, the overall crystallinity is a sum of the respective crystallinity of the two forms. Crystallinity would therefore be calculated as:

$$X_C = \frac{\Delta H_m(\alpha')}{\Delta H_m^o(\alpha')} + \frac{\Delta H_m(\alpha)}{\Delta H_m^o(\alpha)} \quad (1)$$

where X_c denotes the degree of crystallinity, whereas $\Delta H_m(X)$ and $\Delta H_m(X)$ refer to the observed and 100% crystallinity melting enthalpies, respectively, of crystal form X. When PLA crystals exhibit double melting peaks in their DSC data, a relatively fast heating rate of 20 °C/min is always used to limit the occurrence of reorganization during thermal measurements. It is clear that the identification of the origins of melting peaks requires careful consideration of crystallization conditions and structures formed in the cases where double melting peaks are observed.

The observed difference in thermal properties and stability of different forms of PLA, α' and α, is substantial and needs to be explained in terms of their structural differences. Both α' and α crystals have the *tg′t* helical chain conformation. The α' phase was determined to contain distortion of the C_α–C dihedral angle. As mentioned above, the difference in stability of the two forms was determined quantitatively using DSC. The equilibrium melting enthalpy for the α' phase was about two-thirds the value of the α crystalline phase. Because of the uncertainties in the diffraction analyses, we have used a combination of experimental and simulation spectroscopic studies to examine the structural differences of the α' and α crystalline phases.

The infrared spectra also do not differ significantly for samples at different crystallization temperatures with the largest change being 5 $\mathrm{cm^{-1}}$ for the 510 $\mathrm{cm^{-1}}$ infrared active band (skeletal bend and stretch). However, a number of bands narrowed considerably. The multiple components of a number of bands are clearly resolved at low temperature. The principal differences between α' and α-rich samples are observed in vibrations involving carbonyl group and methyl group. The differences can be attributed to specific interactions involving these functional groups. These interactions are responsible for the much larger melting enthalpy of the α phase compared to the α' phase. The differences in structure are reflected in the changes in the unit cell dimensions. Our own diffraction data are consistent with published data. These differences in packing are related to the atomic placement of the C=O groups such that specific dipole interactions present in the α crystal are perturbed in the α' phase. Carbonyl and methyl interactions have been identified in the α crystal but are weakened or not present in the α' crystal [10]. We have used our normal coordinate analysis to identify these specific interactions.

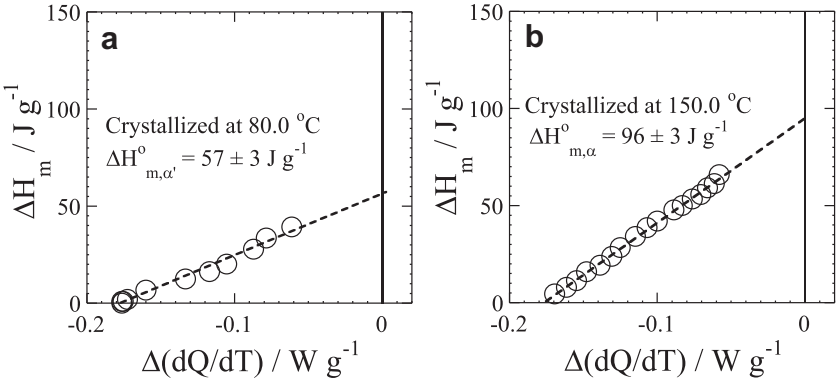

Fig. 13. (a) ΔH_m analysis of predominantly α' crystal sample prepared at 80.0 °C; (b) ΔH_m analysis of predominantly α crystal sample prepared at 150.0 °C.

Therefore, it is our conclusion that although the unit cell parameters differ by only a few percent difference between the α′ and α crystalline forms, interchain interactions seem to be most responsible for the difference in enthalpies observed. The dipole interactions in PLA α crystal are strong and specific. When the structure becomes disordered, these interactions become weaker. These dipole interactions greatly enhance the properties and stability of the α crystal phase. In PLLA, a slight disorder affects the thermal properties significantly.

4. Conclusions

Vibrational spectra of α′- and α-rich PLLA samples suggested that in the α′ crystal there is conformational disorder of the C_α–C dihedral angle. The spectra also indicated that the α′ crystal lacks specific carbonyl and methyl interactions and has looser packing than the α crystal. The effect of these structural differences and interactions between the two crystal forms was reflected in their relative thermal stability. Equilibrium melting enthalpies of the two crystal forms, α′ and α, were calculated by extrapolation of the glass transition to a 100% crystal ($\Delta H_m^o(\alpha') = 57 \pm 3\ J\ g^{-1}$ and $\Delta H_m^o(\alpha) = 96 \pm 3\ J\ g^{-1}$). The difference in the melting enthalpies reflects the overall trend in stability. Solubility differences in hot THF also support the conclusion that the α′ structure is less stable than the α phase. X-ray diffraction confirmed that the α′ to α solid-state conversion is irreversible. The coexistence of polymorphic phases has profound implications in the interpretation and analysis of data.

Acknowledgments

We thank the National Science Foundation Materials Research Science and Engineering Center (NSF-MRSEC) at the University of Massachusetts for facility support. We also thank Jed Randall of NatureWorks for providing the poly(lactic acid) sample.

References

[1] Auras R, Harte B, Selke S. Macromol Biosci 2004;4(9):835–64.
[2] Garlotta D. J Polym Environ 2001;9(2):63–84.
[3] Puiggali J, Ikada Y, Tsuji H, Cartier L, Okihara T, Lotz B. Polymer 2000;41(25):8921–30.
[4] Cartier L, Okihara T, Ikada Y, Tsuji H, Puiggali J, Lotz B. Polymer 2000;41(25):8909–19.
[5] Sawai D, Takahashi K, Imamura T, Nakamura K, Kanamoto T, Hyon SH. J Polym Sci B Polym Phys 2002;40(1):95–104.
[6] Sawai D, Takahashi K, Sasashige A, Kanamoto T, Hyon SH. Macromolecules 2003;36(10):3601–5.
[7] Zhang JM, Duan YX, Sato H, Tsuji H, Noda I, Yan S, et al. Macromolecules 2005;38(19):8012–21.
[8] Zhang JM, Tashiro K, Domb AJ, Tsuji HT. Macromol Symp 2006;242:274–8.
[9] Kawai T, Rahman N, Matsuba G, Nishida K, Kanaya T, Nakano M, et al. Macromolecules 2007;40(26):9463–9.
[10] Cho TY, Strobl G. Polymer 2006;47(4):1036–43.
[11] Ohtani Y, Okumura K, Kawaguchi A. J Macromol Sci B Phys 2003;42(3–4):875–88.
[12] Yasuniwa M, Tsubakihara S, Iura K, Ono Y, Dan Y, Takahashi K. Polymer 2006;47(21):7554–63.
[13] Zhang J, Tashiro K, Tsuji H, Domb AJ. Macromolecules 2008;41(4):1352–7.
[14] Pan PJ, Zhu B, Kai WH, Dong T, Inoue Y. Macromolecules 2008;41(12):4296–304.
[15] Zhang JM, Tsuji H, Noda I, Ozaki Y. Macromolecules 2004;37(17):6433–9.
[16] Di Lorenzo ML. J Appl Polym Sci 2006;100(4):3145–51.
[17] Di Lorenzo ML. Polymer 2001;42(23):9441–6.
[18] Di Lorenzo ML. Eur Polym J 2005;41(3):569–75.
[19] Iannace S, Nicolais L. J Appl Polym Sci 1997;64(5):911–9.
[20] Di Lorenzo ML. Macromol Symp 2006;234:176–83.
[21] Huang J, Lisowski MS, Runt J, Hall ES, Kean RT, Buehler N, et al. Macromolecules 1998;31(8):2593–9.
[22] Vasanthakumari R, Pennings AJ. Polymer 1983;24(2):175–8.
[23] Zhang JM, Tashiro K, Tsuji H, Domb AJ. Macromolecules 2007;40(4):1049–54.
[24] Yang X, Kang S, Yang Y, Aou K, Hsu SL. Polymer 2004;45(12):4241–8.
[25] Kang S, Zhang G, Aou K, Hsu SL, Stidham HD, Yang X. J Chem Phys 2003;118(7):3430–6.
[26] Yang X, Kang S, Hsu SL, Stidham HD, Smith PB, Leugers A. Macromolecules 2001;34(14):5037–41.
[27] Aou K, Hsu SL. Macromolecules 2006;39(9):3337–44.
[28] Aou K. Effect of molecular structure on the thermal stability of amorphous and semicrystalline poly(lactic acid). Polymer science and engineering. Amherst, MA: University of Massachusetts Amherst; 2007.
[29] Turrell G. Infrared and Raman spectra of crystals. New York: Academic Press; 1972.
[30] Pyda M, Boller A, Grebowicz J, Chuah H, Lebedev BV, Wunderlich B. J Polym Sci B Polym Phys 1998;36(14):2499–511.
[31] Pyda M, Bopp RC, Wunderlich B. J Chem Thermodyn 2004;36(9):731–42.
[32] Hsu SL, Reynolds N, Bohan SP, Strauss HL, Snyder RG. Macromolecules 1990;23(21):4565–75.
[33] Lide DR. CRC handbook of chemistry and physics. Boca Raton: CRC Press; 1999.
[34] Hoogsteen W, Postema AR, Pennings AJ, ten Brinke G, Zugenmaier P. Macromolecules 1990;23(2):634–42.
[35] Kang S, Hsu SL, Stidham HD, Smith PB, Leugers MA, Yang X. Macromolecules 2001;34(13):4542–8.
[36] Kister G, Cassanas G, Vert M, Pauvert B, Terol A. J Raman Spectrosc 1995;26(4):307–11.
[37] Krikorian V, Pochan DJ. Macromolecules 2005;38(15):6520–7.
[38] Meaurio E, de Arenaza IM, Lizundia E, Sarasua JR. Macromolecules 2009;42(15):5717–27.
[39] Snyder RG, Hsu SL, Krimm S. Spectrochim Acta A Mol Biomol Spectrosc 1978;34(4):395–406.

Polymer 52 (2011) 822–829

Contents lists available at ScienceDirect

Polymer

journal homepage: www.elsevier.com/locate/polymer

Effect of chain-length of *n*-alkane on solvent-induced crystallization and solvent exchange phenomenon in syndiotactic polystyrene

E. Bhoje Gowd [a,b,*], Kohji Tashiro [a,*]

[a] Department of Future Industry-oriented Basic Science and Materials, Graduate School of Engineering, Toyota Technological Institute, Tempaku, Nagoya 468-8511, Japan
[b] Department of Materials and Minerals, National Institute for Interdisciplinary Science and Technology, CSIR, Trivandrum-695019, India

ARTICLE INFO

Article history:
Received 19 July 2010
Received in revised form
21 October 2010
Accepted 7 November 2010
Available online 13 November 2010

Keywords:
Syndiotactic polystyrene
Crystallization
Solvent exchange phenomenon

ABSTRACT

The effect of molecular size and the vapor pressure of a series of *n*-alkanes as a solvent on solvent-induced crystallization of amorphous sPS and also the solvent exchange phenomenon in the δ form of syndiotactic polystyrene (sPS) were investigated by means of FT-IR spectroscopy and X-ray diffraction. The crystallization of amorphous sPS was found to be very much influenced by the molecular size and the vapor pressure of the *n*-alkanes used. At room temperature, *n*-alkanes with six and seven carbon atoms crystallize the sPS into the δ form, whereas the longer *n*-alkanes did not induce the crystallization of the amorphous sPS. By increasing the crystallization temperature to 50 °C, the vapor pressure of *n*-alkanes increases and as a result *n*-alkanes with eight to ten carbon atoms crystallize the amorphous sPS into the γ form unlike the cases of *n*-hexane and *n*-heptane. On further increasing the chain-length of *n*-alkanes to *n*-tridecane and *n*-hexadecane, no crystallization of amorphous sPS was observed even at 50 °C. By keeping the crystallization behavior in mind, we used these *n*-alkanes to exchange the existing solvent in the δ form of sPS/chloroform complex. *n*-Alkanes with six and seven carbon atoms easily replace the chloroform enclosed in the crystal lattice at room temperature and the d_{010} lattice spacing was found to increase according to the molecular size of the solvent used in the exchange process. *n*-Alkanes with eight to ten carbon atoms could also replace the chloroform enclosed in the crystal lattice at room temperature. But in this case the d_{010} lattice spacing was found to be similar or lower than that of the δ form of sPS/chloroform complex and a new reflection was observed $2\theta = 6.6^{\circ}$, indicating the formation of the ε form. On the other hand, longer *n*-alkanes (C13 and C16) did not intrude into the cavities of the δ form at room temperature. By increasing the solvent exchange temperature to 50 °C, the longer *n*-alkanes (C13 and C16) also replaced the existing chloroform in the δ form and structure transformed to the ε form. In this way, we found that the crystallization and solvent exchange process of sPS using *n*-alkanes is quite complicated and depends strongly on the chain-length of *n*-alkane molecule.

1. Introduction

Syndiotactic polystyrene (sPS) exhibits the various types of crystal modifications with the different molecular conformations as well as the different chain packing structures depending on the preparation conditions [1–47,49–57]. The application of external condition, e.g. temperature, solvent atmosphere etc., causes quite complicated phase transitions. The α and β forms with all-trans planar-zigzag (T_4) conformation are commonly obtained by thermal crystallization procedures [2–11]. The α form is obtained by cooling the melt rapidly, while the β form can be obtained by cooling the melt slowly [2–11]. They are further classified into the disordered forms (α′ and β′) and the ordered forms (α″ and β″) [2–11]. A mesophase of all-trans planar-zigzag conformation was also reported, which can be obtained by stretching the amorphous sample around the glass transition temperature [12].

SPS is also known to crystallize in many kinds of low molecular-mass guest molecules at room temperature [13–47,49–57]. Depending on the polymer–solvent interactions, sPS crystallizes mainly into three different crystalline forms known as δ, γ and ε

* Corresponding authors. Department of Future Industry-oriented Basic Science and Materials, Graduate School of Engineering, Toyota Technological Institute, Tempaku, Nagoya 468-8511, Japan.
E-mail addresses: bhojegowd@yahoo.com (E.B. Gowd), ktashiro@toyota-ti.ac.jp (K. Tashiro).

0032-3861/$ – see front matter © 2010 Elsevier Ltd. All rights reserved.
doi:10.1016/j.polymer.2010.11.015

forms with s(2/1)2 helical chains (generated by TTGG conformational sequences). The δ form is a molecular complex with solvent molecules in the crystal lattice, whereas the γ form is solvent-free. Recently, the δ form is further classified into *clathrates* and *intercalates* [39–41]. In *clathrates* the low molecular weight compounds are trapped as guest molecules into the cavities of the sPS and are characterized by a stiochiometric molar ratio (monomeric-unit: guest) of 4:1 [13–22]. On the other hand in *intercalates* the guest molecules are not isolated into cavities but contiguous inside the layers and intercalated with monolayers of enantiomorphous polymer helices with a stiochiometric molar ratio (monomeric-unit:guest) of 2:1 [39–41]. By extracting the guest molecules from the clathrates using suitable procedures, so-called empty δ (δ_e) form can be obtained [15–17,27]. The δ_e form also retains the helical structure similar to δ and γ forms but with the cavities which had been occupied by solvent molecules [15–17,27]. Recently reported ε form of sPS is characterized by channel-shaped cavities crossing the unit cells along the *c* direction [58–61]. The solvent exchange phenomenon in clathrates is another important area attracting many researchers to understand the polymer–solvent interactions [42–47]. Tashiro et al. [43] showed that the solvent exchange occurs smoothly between toluene, chloroform and benzene and the order of solvent exchange rate depends on polymer–solvent interactions as well as the size of the solvent molecules. Kaneko et al. [44–46] showed that incorporating the larger molecules into the cavity of the δ form by solvent exchange phenomenon has expanded the range of guest molecules for the sPS clathrates.

Though many authors studied the solvent-induced crystallization and solvent exchange phenomena using different pair of solvent molecules, a concrete conclusion is not yet drawn about the polymer–solvent interactions. For example, we may have such kind of questions that why the solvents like acetone and supercritical carbon dioxide, which are known to crystallize the amorphous sPS into the γ form at room temperature, can remove the existing solvent molecules in the δ form to yield the δ_e form. Why do not other volatile solvents like methylene chloride, chloroform give the δ_e form during solvent exchange process? Is it possible to get the δ_e form with other solvent molecules which can crystallize the amorphous sPS into the γ form at room temperature? What happens during the exchange phenomena of the solvent molecules, which can form the δ form at room temperature? In order to understand the above questions, we have chosen a series of *n*-alkanes as solvent molecules for sPS in this paper. By changing the length of the alkanes, the molecular size and the vapor pressure of the solvent can be changed. We will describe here the behavior of a series of *n*-alkanes starting from *n*-hexane to *n*-hexadecane as a solvent molecule for the investigation of the crystallization of amorphous sPS as well as the study of the solvent exchange phenomenon from the δ form of sPS/chloroform complex. As for the complex between sPS and *n*-alkanes, Uda et al. studied the solvent exchange phenomena using *n*-alkanes from *n*-hexane to *n*-decane on the basis of infrared spectra [44,45] and solid-state NMR/quasi-elastic neutron scattering data [46]. But they did not look into the X-ray patterns after solvent exchange to know the change in crystal lattice. Besides they did not investigate the crystallization phenomenon itself for this pair of sPS glass and *n*-alkanes.

In the present paper we have shown the details of the X-ray diffraction data and the infrared spectra for the phenomena of the solvent-induced crystallization of sPS in the presence of longer *n*-alkanes and the solvent exchange phenomenon between chloroform and *n*-alkanes using both the unoriented and uniaxially oriented samples. It should be emphasized here that we have utilized the uniaxially oriented samples as well as the unoriented samples since the overlapped X-ray reflections can be separated well for the detailed investigation of the structural changes. Most of the previously reported papers did not use such samples, making the discussion quite ambiguous.

2. Experimental section

2.1. Samples

sPS pellets ($M_w = 272\,000$, $M_w/M_n = 2.28$) were kindly supplied by Idemitsu Petrochemical Co., Ltd. The glassy samples were prepared by quenching the melt into ice water. The thickness of the unoriented films was about 30 μm for the infrared spectral measurements and 100 μm for the X-ray diffraction measurements. A small piece of rectangular shape was cut out of 100 μm thick amorphous strip and stretched by about five times the original length above the hot plate around the glass transition temperature (97 °C). These unoriented and uniaxially oriented samples were dipped in chloroform for 2 days at room temperature and *n*-alkanes for 4 days at room temperature and also at 50 °C. In another set of experiments the δ form of sPS/chloroform complex was dipped in series of alkanes ranging from *n*-hexane to *n*-decane at room temperature and in *n*-tridecane and *n*-hexadecane at 50 °C. The samples removed from solvents were kept at ambient temperature until they became perfectly dry. These samples were further analyzed by X-ray diffraction and infrared spectra and were found to be semicrystalline with a degree of crystallinity in the range 30–40%.

2.2. Measurements

The oriented samples were set on a goniometer head of the X-ray diffraction apparatus. The fiber diagrams were recorded using an imaging plate system DIP 1000 (MAC Science Co. Japan) with graphite-monochromatized Cu Kα line as an incident X-ray beam. In the case of unoriented samples, the X-ray diffraction system was a Rigaku/TTR-III X-ray diffractometer with Cu *K*α line as an incident X-ray beam. The X-ray diffraction profiles were measured in a reflection mode in the 2θ range of 10-30° at scanning rate of 5°/min. The infrared spectra were measured at a resolving power of 1 cm^{-1} with a Varian FTS 7000 series FT-IR spectrometer.

3. Results and discussion

3.1. Crystallization of amorphous sPS in n-alkanes

3.1.1. Unoriented samples

The amorphous films were dipped in a series of *n*-alkanes at room temperature for 4 days. Fig. 1(a) shows the infrared spectra of these samples in the frequency region 595–615 cm^{-1}. Tashiro and co-workers [20,21] showed that the 590–620 cm^{-1} infrared frequency region is sensitive to the chain packing mode and a pair of bands is known to distinguish the δ, empty δ (δ_e) and γ crystalline forms of sPS having the same helical chain conformation. In Fig. 1(a), the samples dipped in *n*-hexane and *n*-heptane showed a pair of bands whereas longer *n*-alkanes did not show any infrared bands in this region. From the position of the infrared bands, it is identified that the samples dipped in *n*-hexane (608.0 and 599.8 cm^{-1}) and *n*-heptane (609.0 and 599.5 cm^{-1}) are crystallized into the δ form, whereas the samples dipped in longer *n*-alkanes did not crystallize at room temperature. The crystallization behavior of these samples is further confirmed by powder X-ray diffraction patterns. Fig. 1(b) shows the powder X-ray diffraction patterns of *n*-alkanes dipped samples at room temperature. As shown by the arrows, the powder X-ray diffraction patterns of the *n*-hexane ($2\theta = 8.0, 10.3, 16.9, 20.5, 23.2, 28.0°$) and *n*-heptane ($2\theta = 7.9, 10.1, 16.6, 20.3, 23.0, 28.2°$)

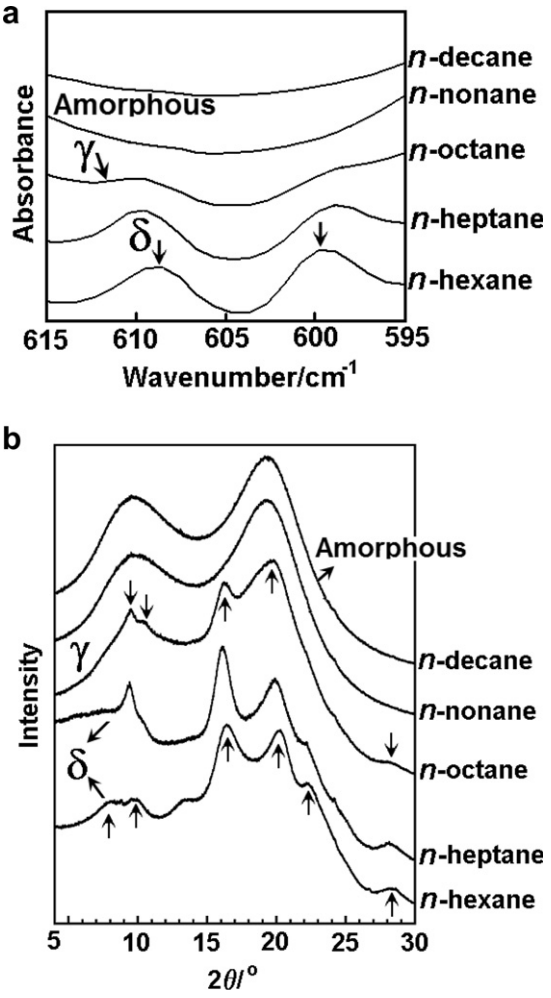

Fig. 1. (a) Infrared spectra in the frequency region of 595–615 cm^{-1} (b) Powder X-ray diffraction patterns measured at room temperature for various samples of the sPS/*n*-alkane crystallized at room temperature.

dipped samples showed the reflections characteristics of the δ form. The peak positions and intensities are different from those of the other sPS/solvent complexes. The d_{010} lattice spacing, which is the distance between the nearest neighboring polymer chains, increases with the change in chain-length of *n*-alkane from *n*-hexane (d_{010} = 10.9 Å) to *n*-heptane (d_{010} = 11.1 Å). The sample dipped in *n*-octane crystallized partially and the reflections are characteristics of the γ form. On the other hand, the samples dipped in longer alkanes did not show any reflection peaks, indicating that the amorphous sPS remains unaltered at room temperature. Guerra et al. [47] also showed that the *n*-alkanes longer than heptane could not form a complex with the sPS. Such a difference in crystallization behavior may be due to the difference in the diffusion behavior of longer *n*-alkanes into the amorphous sPS at room temperature, which depends mainly on the vapor pressure of *n*-alkanes. Table 1 gives the vapor pressure and molecular volume for various *n*-alkanes. As seen in Table 1, the vapor pressure decreases rapidly with an increase in chain-length of *n*-alkanes at room temperature [48]. As a result the diffusion of these longer alkanes into amorphous sPS is difficult at room temperature and no crystallization is observed at room temperature.

According to well-known Le Chatelier's principle [49], increasing the temperature of a system increases the amount of vapor present, and so the saturated vapor pressure increases. Based on this idea, we dipped amorphous sPS into the longer *n*-alkanes at slightly higher

Table 1
Molecular volume and vapor pressure data for various *n*-alkanes.

n-Alkanes	Vapor pressure kPa at 20 °C [48]	Molecular face volume (Å^3) estimated by molecular face thoery [51]
n-Hexane	17.0	119.3
n-Heptane	4.60	141.4
n-Octane	1.33	164.9
n-Nonane	0.42	188.1
n-Decane	0.17	209.4

temperature (50 °C) so that the vapor pressure of the longer *n*-alkanes increases and the molecules diffuse into the amorphous sPS. Fig. 2 (a) and (b) show, respectively, the X-ray diffraction patterns and the infrared spectra of the samples dipped in longer *n*-alkanes at 50 °C for 4 days. The characteristic peak positions of the powder X-ray diffraction patterns ($2\theta = 9.2, 10.3, 16.0, 20.0, 28.3°$) revealed that the samples are crystallized into the γ form in *n*-octane, *n*-nonane and *n*-decane at 50 °C, but not into the δ form like *n*-hexane and *n*-heptane. The corresponding infrared spectra show the bands at 610.0 and 598.5 cm^{-1}, which were assigned to the γ form. In this way it has been found that the longer alkanes (*n*-octane to *n*-decane) can

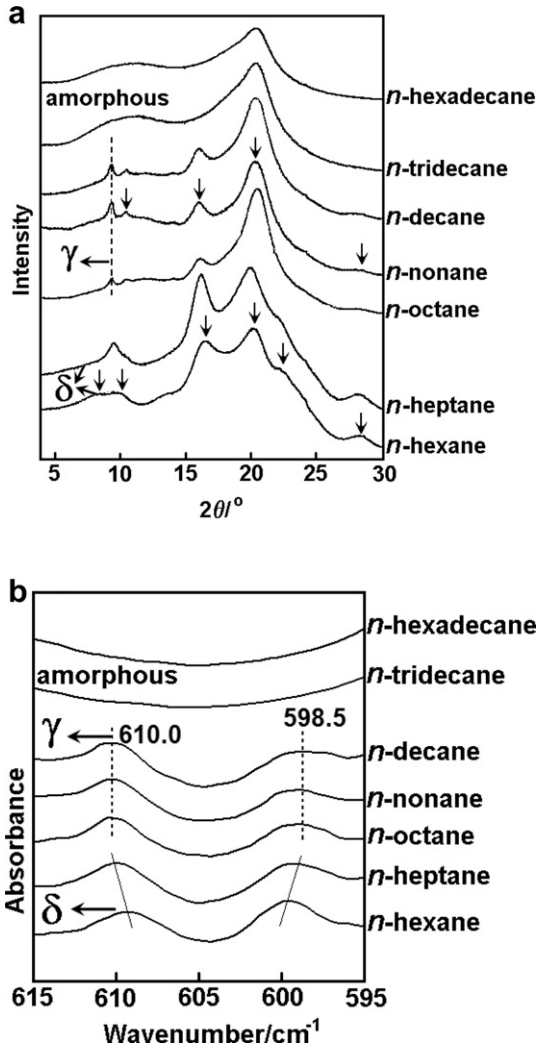

Fig. 2. (a) Powder X-ray diffraction patterns (b) Infrared spectra in the frequency region of 595–615 cm^{-1} measured at room temperature for the various samples of the sPS/*n*-alkane crystallized at 50 °C.

induce crystallization of amorphous sPS. The formation of the γ form in longer *n*-alkanes may be due to two different reasons as mentioned below. (i) Molecular size of *n*-alkanes above n-octane are too large (>165 Å^3) (Table 1) to be enclosed as guests into the cavities of the δ form [50], where the cavity volume of the nanoporous δ_e form is nearly 120–160 Å^3 (see Fig. 3 for schematic representation of the δ_e form with empty cavities) [40,51] and (ii) solubility of *n*-alkanes into the amorphous region of sPS is rather low and decreases rapidly with an increase in chain-length. On further increasing the chain-length of *n*-alkane to *n*-tridecane and *n*-hexadecane, the amorphous sPS did not crystallize even at 50 °C. This may be again due to the poor diffusion and low solubility of longer *n*-alkanes.

3.1.2. Uniaxailly oriented samples

We also utilized *uniaxially oriented* samples to understand the solvent-induced crystallization of sPS. As drawn samples, with a mesophase of all-trans planar-zigzag conformation easily recrystallized in to the δ form in presence of *n*-hexane and *n*-heptane. On the other hand, the *uniaxially oriented* samples dipped in longer *n*-alkanes above *n*-octane did not crystallize even at 50 °C. These results suggested that chain orientation in the amorphous phase also has a significant role on the diffusion behavior of *n*-alkanes and as a consequence on the crystallization behavior of sPS. It is also worth mentioning here that the other solvents like acetone or supercritical CO_2, which crystallize the unoriented glassy samples into the γ form at room temperature, did not induce any crystallization of the *uniaxially oriented* samples like longer *n*-alkanes. Preparing the γ form using uniaxially oriented samples at room temperature is still a challenging task. The fiber diagram of uniaxially oriented γ form obtained so far is only by heating the uniaxially oriented δ form above 100 °C [52–55]. These observations clearly suggest that longer *n*-alkanes (*n*-octane to *n*-decane) and other solvents like acetone, supercritical CO_2 have similar kind of interactions with amorphous sPS and both of these solvents only crystallize the unoriented sPS into the γ form but not the uniaxially oriented sample.

In this way, we observed that the chain-length of *n*-alkane has a remarkable influence on the diffusion behavior and as a consequence on the crystallization behavior of sPS. By keeping the crystallization behavior in mind, we used these *n*-alkanes for the better understanding of the solvent exchange phenomena in the sPS clathrates using both unoriented and uniaxially oriented samples.

3.2. Solvent exchange phenomena using n-alkanes

3.2.1. Unoriented samples

The solvent exchange process was performed by dipping the δ form of sPS/chloroform complex in a series of *n*-alkanes (*n*-hexane to *n*-hexadecane) for 4 days at room temperature. Fig. 4 shows the infrared spectra after the solvent exchange in the frequency region 1120–1240 cm^{-1} along with the δ form of sPS/chloroform complex, where the relatively isolated chloroform band is dominant at 1219 cm^{-1}. After the solvent exchange, the band at 2956 cm^{-1} due to *n*-alkanes appeared, while the band at 1219 cm^{-1} due to chloroform almost disappeared. Uda et al. [45] also reported such spectral changes using ATR-FTIR spectroscopy during the solvent exchange process. The bands characteristic of TTGG conformation were kept almost unchanged after the solvent exchange process. These spectral changes clearly suggested that the chloroform molecules are replaced by *n*-alkanes from *n*-hexane to *n*-decane at room temperature. In the preceding section, it has been found that the longer *n*-alkanes (*n*-octane to *n*-decane) did not diffuse into the amorphous sPS at room temperature. But during solvent exchange phenomena, these *n*-alkanes were found to diffuse through the sample and replace the existing chloroform in the crystalline lattice. Uda et al. [44,45] suggested that the diffusion of larger *n*-alkanes into the smaller cavities of the original δ form is due to the plasticizing effect caused by the residual solvent molecules in the amorphous region of the δ form. On further increasing the chain-length of *n*-alkanes (*n*-tridecane and *n*-hexadecane), we found that solvent exchange did not occur at room temperature. By increasing the solvent exchange temperature to 50 °C, these alkanes were also found to replace the chloroform. We have shown that *n*-tridecane and *n*-hexadecane, which are unable to diffuse into the amorphous phase, diffuse into the δ form during solvent exchange phenomenon at slightly higher temperature.

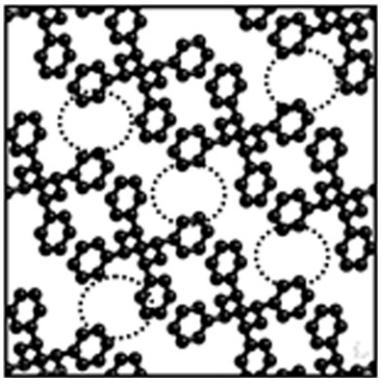

Fig. 3. Schematic representation of the crystal lattice of the nanoporous δ_e form.

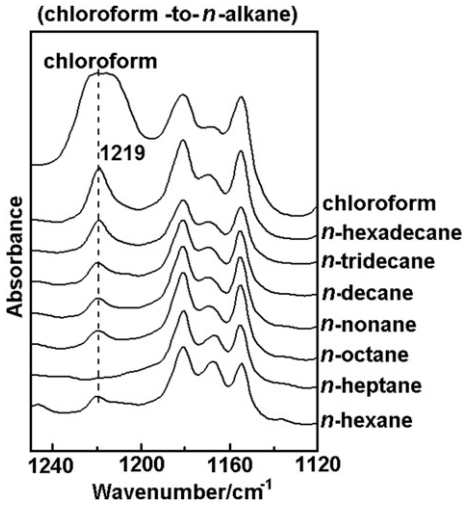

Fig. 4. Infrared spectra in the frequency region of 1120–1240 cm^{-1} for various sPS/*n*-alkane samples after the solvent exchange from chloroform to *n*-alkanes. The solvent exchange was performed at room temperature for the *n*-alkanes from 6 to 10 carbon atoms and at 50 °C for 13 and 16 carbon atoms. SPS/chloroform spectrum is also given at the top for the purpose of comparison.

The X-ray diffraction measurements were performed on various samples after the solvent exchange process to understand the change in crystal lattice. Fig. 5 shows the powder X-ray diffraction patterns of various samples after solvent exchange. The X-ray diffraction profiles of *n*-hexane and *n*-heptane exchanged samples are almost similar to the patterns shown in Fig. 2. On the other hand, the X-ray diffraction patterns of the samples with longer alkanes showed a new reflection at $2\theta = 6.6°$, which is different not only from the sPS/chloroform complex but also from the δ form of any other solvent complexes observed so far.

3.2.2. Uniaxially oriented samples

As the X-ray reflections of the unoriented samples are overlapping in a complicated manner, we utilized the *uniaxially oriented*

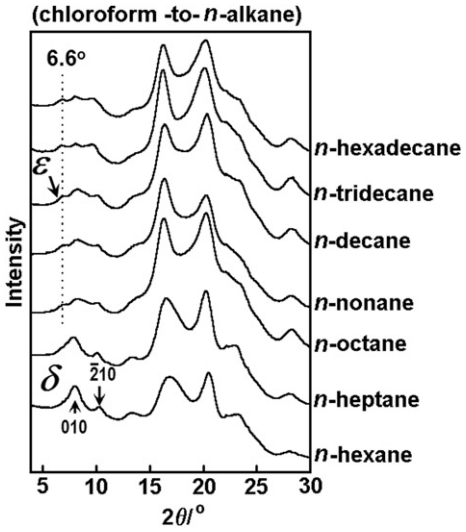

Fig. 5. Powder X-ray diffraction patterns for various sPS/*n*-alkane samples after the solvent exchange from chloroform to *n*-alkanes. The solvent exchange was performed at room temperature for the *n*-alkanes from 6 to 10 carbon atoms and at 50 °C for 13 and 16 carbon atoms. SPS/chloroform pattern is also given at the bottom for the purpose of comparison.

samples to avoid the overlap of reflections. In another set of experiments, the *uniaxially oriented* δ form of sPS/chloroform sample was used for the solvent exchange process with *n*-alkanes. It is worth highlighting here that only *n*-hexane and *n*-heptane replaced the chloroform at room temperature, the longer *n*-alkanes from *n*-octane to *n*-decane replaced the chloroform at 50 °C and *n*-tridecane and *n*-hexadecane did not replace the chloroform even at 50 °C in the case of *uniaxially oriented* samples. These results suggest that the chain orientation has a significant effect in controlling the diffusion behavior of *n*-alkanes in the amorphous phase.

Fig. 6 shows a series of X-ray fiber diagrams after solvent exchange. Almost all the fiber diagrams look alike other than the differences on the equatorial line. The change in the equatorial line profile evaluated from the fiber diagram is shown in Fig. 7. The equatorial patterns of the *n*-hexane and *n*-heptane containing samples are similar to that of chloroform sample with the slight variation in the peak positions and intensities. The d_{010} lattice spacing is estimated for all the samples after the solvent exchange and given in Fig. 8. The d_{010} lattice spacing of the *n*-hexane and *n*-heptane containing samples is increased compared with that of the sPS/chloroform complex. A slight increase in the d_{010} was also observed with the increase in chain-length of *n*-alkane from *n*-hexane to *n*-heptane, which may be due to the increase in the distance between the *ac* layers with respect to the molecular volume of solvent residing in the cavities of the crystalline lattice. Fig. 9(a) shows the schematic representation of a possible packing of *n*-hexane and *n*-heptane molecules within the cavities of the δ form. In this case, the distance between the *ac* layers increases only when the *n*-alkanes (*n*-hexane and *n*-heptane) oriented roughly perpendicular to the crystalline chain axis. Based on these results, we may say that *n*-hexane and *n*-heptane do not only replace the chloroform in the cavities of the crystalline lattice, but also expand the crystalline lattice. In the previous section, we have seen that these two solvents readily form the molecular complex with sPS. From these observations, we conclude here that the solvents which are capable of forming the complexes with sPS not only replace the old solvent during solvent exchange phenomenon, but also modify the crystalline lattice with respect to the new solvent and the crystal structure remains as the δ form.

On the other hand, the equatorial patterns of the *n*-octane, *n*-nonane and *n*-decane containing samples are not only different from the pattern of sPS/chloroform complex, but also from that of

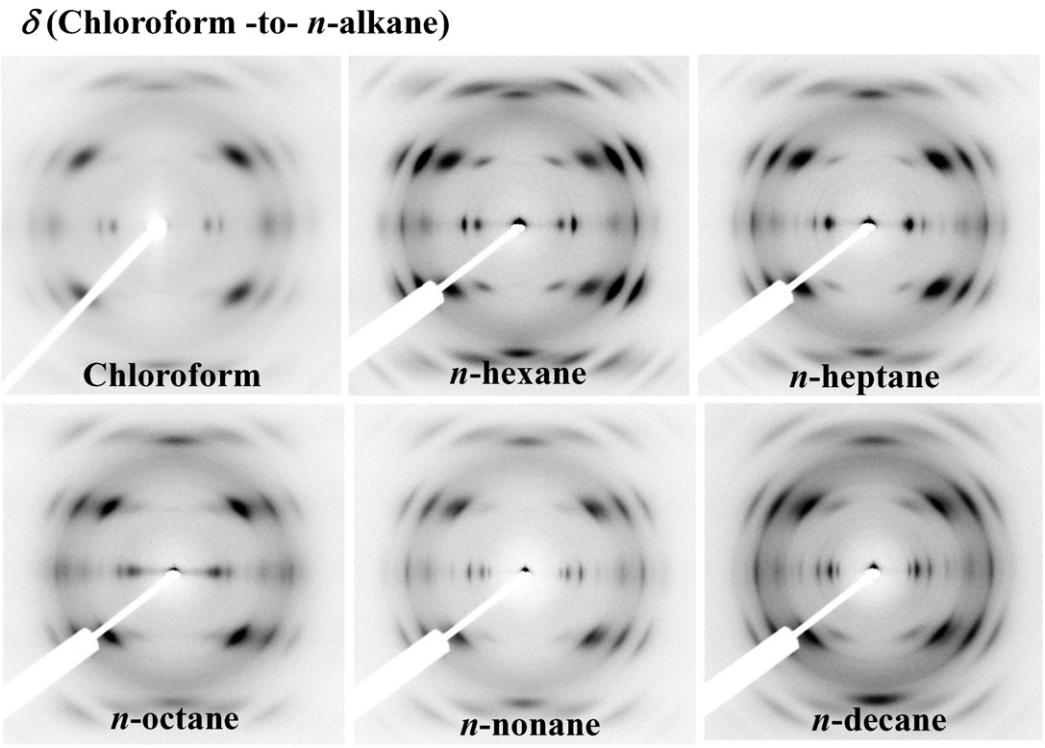

Fig. 6. X-ray fiber diagrams of the uniaxially oriented δ form samples containing *n*-alkanes (*n*-hexane to *n*-decane) after the solvent exchange from chloroform to *n*-alkanes. SPS/chloroform fiber diagram is also given for the purpose of comparison.

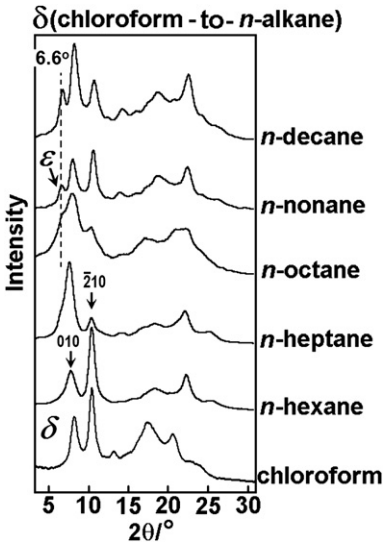

Fig. 7. X-ray diffraction profile on the equatorial line of the δ form derived from the Fig. 6.

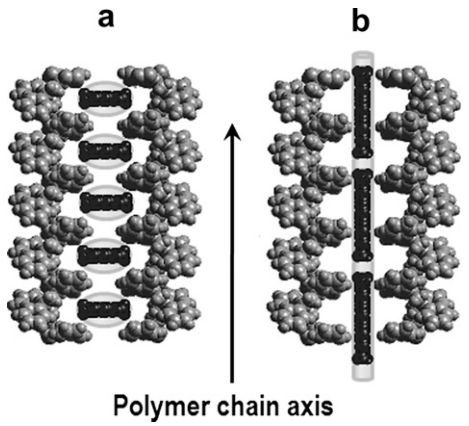

Fig. 9. Schematic illustration of possible packing arrangements of *n*-alkanes between one pair of polymer chains in sPS-*n*-alkane complex systems. (a) *n*-Alkanes with molecular volume < 160 Å^3 (*n*-hexane and *n*-heptane) (b) *n*-alkanes with molecular volume > 160 Å^3 (above *n*-octane).

n-hexane and *n*-heptane containing samples. A new reflection appeared at $2\theta = 6.6^\circ$ on the equatorial line for these samples. Before going into the details of this new reflection, the d_{010} lattice spacing of these complexes is compared. Based on the molecular size of *n*-alkanes, it is expected that the d_{010} lattice spacing should increase with the chain-length. But, as seen in Fig. 8, the d_{010} of these samples is almost the same or lower than that of the δ form of sPS/chloroform complex regardless of the molecular size and is smaller than that of *n*-hexane and *n*-heptane containing samples. Such a situation is possible only when the longer *n*-alkanes (*n*-octane to *n*-decane) reside in crystalline lattice with their main molecular axis parallel to the polymer chain axis with an all-*trans* conformation as shown schematically in Fig. 9(b). In the previous section, we found that these longer *n*-alkanes crystallize the amorphous sPS into the γ form, not into the δ form. By combining these two observations, we are speculating here that the solvents which are crystallizing the sPS into the γ form during solvent-induced crystallization, replace the old solvent during solvent exchange phenomenon and these solvents are too large to accommodate themselves within the small cavities of the original δ form. It is worth recalling here that the other solvents like acetone and supercritical CO_2, which are known to crystallize the amorphous sPS into the γ form, also replace the existing solvent during solvent exchange process from the δ form without disturbing cavities between the sPS chains [15–17,22,27]. Tashiro et al. [43] showed that after the solvent exchange these solvent molecules evaporated away from the sample at ambient atmosphere and the

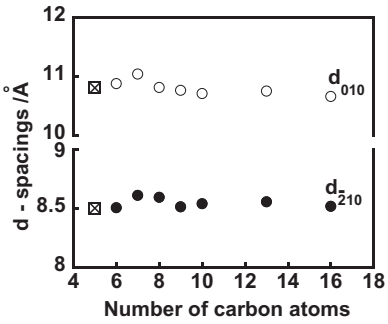

Fig. 8. Chain-length dependence of *n*-alkane on the d_{010} and $d_{\bar{2}10}$ lattice spacing of sPS/*n*-alkane complex after the solvent exchange phenomena. SPS/chloroform lattice spacings (⊠) are also given for the purpose of comparison.

δ form transformed to the so-called δ_e form. They also showed that the interaction between the sPS chains and acetone is much weaker as known from the lower solubility of sPS into acetone. Here we are speculating that the solvents from *n*-octane to *n*-decane also have a similar kind of interaction with sPS as that of acetone and supercritical CO_2. Since acetone and supercritical CO_2 are volatile solvents they evaporate away easily at ambient atmosphere and give the δ_e form. But solvents such as *n*-octane, *n*-nonane and *n*-decane have high boiling points and can not evaporate. Hence these solvents are trapped in between the ac layers of the crystal lattice without much interaction with sPS chains. Uda et al. [45] also showed that the packing of *n*-alkane molecules in the lattice became tight as the chain-length increased based on the frequency shift of methyl asymmetric stretching band of *n*-alkanes. We also used deuterated decane (*d*-decane) in the solvent exchange experiments. Fig. 10 gives the infrared spectra of *d*-decane, and the two complexes after solvent exchange with sPS/*d*-decane and sPS/*n*-decane. The amount of *d*-decane inside the sPS lattice is small in quantity and the infrared bands of *d*-decane are almost hidden by the strong bands of sPS. A careful comparison between the infrared spectra of *d*-decane and the *d*-decane inside the cavities of sPS, shows some frequency shift in the band positions, which may be due to several factors such as polymer–solvent interactions, molecular deformation and conformation change. In particular the spectra of *d*-decane trapped in between the *ac* layers of the crystalline lattice of sPS show a broadening of the CD_2 stretching bands along with the lower frequency shift. It is well known that the frequency and band width associated to the methylene stretching bands are sensitive to the conformational change and are also affected by interchain vibrational coupling and librotorsional motions [56]. It might be speculated here that the alkane chains trapped in between the *ac* layers of the crystalline lattice change the conformation from the disordered type to more ordered trans-like form (see Fig. 9(b)). This was pointed out also by Kaneko et al. [46] on the basis of solid-state NMR and quasi-elastic neutron scattering data. On the other hand, *n*-hexane and *n*-heptane are considered to remain in the extended state inside the crystalline lattice because these solvents could modify the crystalline lattice of sPS during solvent exchange process.

A new reflection appeared at $2\theta = 6.6^\circ$ on the equatorial line of longer *n*-alkanes is also helpful in understanding the solvent exchange behavior and the appearance of this reflection supports the above discussion. It is worth highlighting here that in our previous paper [55] we showed that the δ_e form of sPS/chloroform

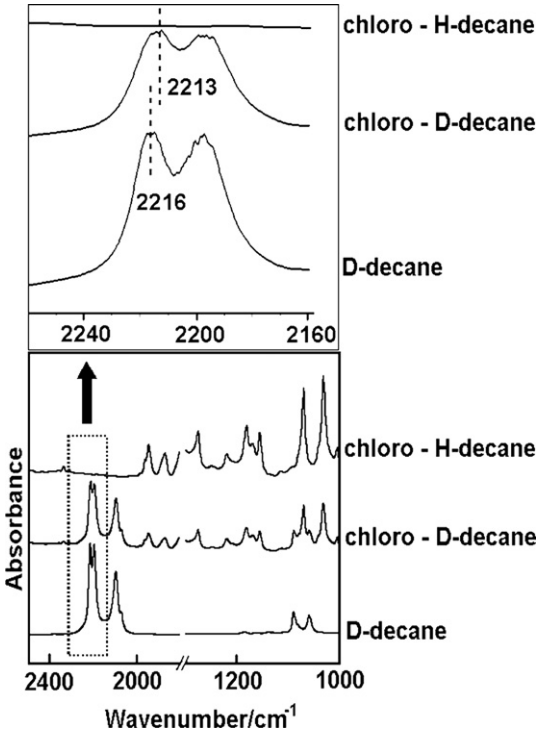

Fig. 10. Comparison of the infrared spectra of the solvent *d*-decane with sPS/*d*-decane and sPS/*n*-decane complexes after the solvent exchange from chloroform to *n*-alkanes. Expanded 2160–2260 cm^{-1} region is showed above.

complex gives a new reflection on the equatorial line at the same position $2\theta = 6.6^{\circ}$. Very recently, Rizzo et al. [60-63] also observed the X-ray pattern similar to the X-ray pattern reported for the δ_e form of sPS/chloroform complex by a different route and they called it as a new ε crystalline form. They obtained the nanoporous ε form by chloroform sorption in γ form samples and its subsequent desorption. This form presents 4 chains in the s(2/1)2 helical conformation packed in an orthorhombic unit cell according to the space group *Pbcn*. The ε form is characterized by channel-shaped cavities crossing the unit cells along the *c* direction. In our previous study, the ε form is obtained by exchanging the chloroform from sPS/chloroform complex with acetone [55]. In the present study, after exchanging the chloroform from sPS/chloroform complex with longer *n*-alkanes, the new reflection at $2\theta = 6.6^{\circ}$ appeared along with the $\bar{2}10$ reflection at $2\theta = 10.2^{\circ}$. It is important to emphasize here that, in both the cases, sPS/chloroform complex was used for the solvent exchange process with the solvents (acetone and longer *n*-alkanes), which crystallize the amorphous sPS into the γ form. It means that the longer *n*-alkanes and acetone behave similarly during the solvent exchange process. On the other hand, as seen in Figs. 5 and 7, *n*-hexane and *n*-heptane, which crystallize the amorphous sPS into the δ form, did not give this reflection after the solvent exchange process. These results also support that the solvent which causes the δ form during crystallization, remains as the δ form with the modified crystal lattice during solvent exchange process and the other solvents, which induce the γ form during solvent-induced crystallization, can obtain the ε form by replacing the existing solvent during exchange process. These results clearly suggested that after the solvent exchange the longer *n*-alkanes hosted in the channels of the ε form with their main molecular axis roughly parallel to the polymer chain axis with an all-*trans* conformation as shown in Fig. 9(b). It is already demonstrated such a possibility of accommodating the guest molecules being longer than the sPS repetition period in the ε form due to the presence of channels passing the unit cells from side to side along the *c* direction [60, 62, 63]. In this way *n*-alkanes are very helpful in understanding the polymer–solvent interactions based on the crystallization phenomenon and the solvent exchange process between any pair of solvents.

4. Conclusions

In the present paper we investigated the influence of molecular size and the vapor pressure of a series of *n*-alkanes as a solvent on solvent-induced crystallization of amorphous sPS and also the solvent exchange phenomenon in the δ form of sPS. *n*-Hexane and *n*-heptane crystallize the amorphous sPS into the δ form at room temperature, suggesting that these two solvents can diffuse into the sPS easily. When these two solvents are used for exchanging the chloroform in the δ form of sPS/chloroform complex, the crystalline lattice has expanded after the exchange process as confirmed by the d_{010} lattice spacing. On the other hand, the longer *n*-alkanes from *n*-octane to *n*-decane, could not crystallize the amorphous sPS at room temperature. By increasing the crystallization temperature to 50 °C, we found that unlike *n*-hexane and *n*-heptane these solvents induce the γ form. This may be due to the molecular size of n-alkanes, which are too large to be enclosed as guest molecules inside the δ form. But interestingly, in the solvent exchange process, these longer alkanes from *n*-octane to *n*-decane could replace the chloroform at room temperature. After the solvent exchange, the d_{010} lattice spacing of sPS/chloroform complex did not change much with respect to the molecular size of *n*-alkane above *n*-octane. In addition, a new crystalline reflection was observed at $2\theta = 6.6^{\circ}$ after the solvent exchange process and the new X-ray pattern observed is similar to the pattern reported for the ε form. On further increasing the chain-length of *n*-alkanes to *n*-tridecane and *n*-hexadecane, no solvent-induced crystallization was observed even at 50 °C. However, these solvents found to intrude into the crystalline lattice of the δ form of sPS/chloroform complex after the solvent exchange. In this way we found that solvent-induced crystallization and solvent exchange phenomenon are dependent on the molecular size and also the vapor pressure of the solvent molecules. In addition to these results, in the case of *uni-axially oriented* samples the chain orientation has a significant effect in controlling the diffusion behavior of *n*-alkanes in the amorphous phase.

Acknowledgements

This work was financially supported by MEXT "Collaboration with Local Communities" Project (2005–2009). The authors thank Idemitsu Petrochemicals Co. Ltd., Japan, for supplying the sPS sample. Authors also thank Dr. Kummetha Raghunatha Reddy for performing some of the experiments presented in this paper. One of the author, EBG thanks Department of Science and Technology (Government of India) for the award of a Ramanujan Fellowship.

References

[1] Kobayashi M, Nakaoki T, Ishihara N. Macromolecules 1989;22:4377.
[2] Guerra G, Vitagliano VM, De Rosa C, Petraccone V, Corradini P. Macromolecules 1990;23:1539.
[3] Vittoria V, Filho AR, De Candia F. J Macromol Sci Phys 1990;B29:411.
[4] Woo EM, Sun YS, Yang CP. Prog Polym Sci 2001;26:945.
[5] Cimmino S, di Pace E, Martuscelli E, Silvestre C. Polymer 1991;32:1080.
[6] De Rosa C, Rapacciuolo M, Guerra G, Petraccone V. Polymer 1992;33:1423.
[7] Woo EM, Sun YS, Lee ML. Polymer 1999;40:4425.
[8] De Rosa C. Macromolecules 1996;29:8460.
[9] De Rosa C, Guerra G, Petraccone V, Corradini P. Polym J 1991;23:1435.
[10] Cartier L, Okihara T, Lotz B. Macromolecules 1998;31:3303.
[11] Chatani Y, Shimane Y, Ijitsu T, Yukinari T. Polymer 1993;34:1625.

[12] Auriemma F, Petraccone V, Poggetto FD, De Rosa C, Guerra G, Manfredi C, et al. Macromolecules 1993;26:3772.
[13] Immirzi A, De Candia F, Iannelli P, Zambelli A, Vittoria V. Makromol Chem Rapid Commun 1988;9:761.
[14] Vittoria V, De Candia F, Iannelli P, Immirzi A. Makromol Chem Rapid Commun 1988;9:765.
[15] Manfredi C, De Rosa C, Guerra G, Rapacciuolo M, Auriemma F, Corradini P. Macromol Chem Phys 1995;196:2795.
[16] Reverchon E, Guerra G, Venditto V. J Appl Polym Sci 1999;74:2077.
[17] De Rosa C, Guerra G, Petraccone V, Pirozzi B. Macromolecules 1997;30:4147.
[18] Guadagno L, Baldi P, Vittoria V, Guerra G. Macromol Chem Phys 1998;199:2671.
[19] Gowd EB, Nair SS, Ramesh C. Macromolecules 2002;35:8509.
[20] Gowd EB, Nair SS, Ramesh C, Tashiro K. Macromolecules 2003;36:7388.
[21] Yoshioka A, Tashiro K. Macromolecules 2003;36:3001.
[22] Ma W, Yu J, He J. Macromolecules 2005;38:4755.
[23] De Candia F, Romano G, Russo R, Vittoria V. Colloid Polym Sci 1993;271:454.
[24] Vittoria V, Russo R, Candia FD. Polymer 1991;32:3371.
[25] Tashiro K, Ueno Y, Yoshioka A, Kobayashi M. Macromolecules 2001;34:310.
[26] Tashiro K, Yoshioka A. Macromolecules 2002;35:410.
[27] Ma W, Yu J, He J. Macromolecules 2004;37:6912.
[28] Rizzo P, Albunia AR, Guerra G. Polymer 2005;46:9549.
[29] Chatani Y, Shimane Y, Inagaki T, Ijitsu T, Yukinari T, Shikuma H. Polymer 1993;34:1620.
[30] Rastogi S, Goossens JGP, Lemstra PJ. Macromolecules 1998;31:2983.
[31] Reynolds NM, Hsu SL. Macromolecules 1990;23:3463.
[32] Kobayashi M, Nakaoki T, Ishihara N. Macromolecules 1990;23:78.
[33] Reynolds NM, Stidham HD, Hsu SL. Macromolecules 1991;24:3662.
[34] Kellar EJC, Galiotis C, Andrews EH. Macromolecules 1996;29:3515.
[35] Capitani D, De Rosa C, Ferrando A, Grassi A, Segre AL. Macromolecules 1992;25:3874.
[36] Gowd EB, Tashiro K. Macromolecules 2007;40:5366.
[37] Gomezls MA, Tonelli AE. Macromolecules 1990;23:3385.
[38] Tamai Y, Fukuda M. Macromol Rapid Commun 2002;23:891.
[39] Petraccone V, Tarallo O, Venditto V, Guerra G. Macromolecules 2005;38:6965.
[40] Tarallo O, Petraccone V, Venditto V, Guerra G. Polymer 2006;47:2402.
[41] De Girolamo Del Mauro A, Carotenuto M, Venditto V, Petraccone V, Scoponi M, Guerra G. Chem Mater 2007;19:6041.
[42] Chatani Y, Shimane Y, Inoue Y, Inagaki T, Ishioka T, Ijitsu T, et al. Polymer 1992;33:488.
[43] Yoshioka A, Tashiro K. Macromolecules 2003;36:3593.
[44] Uda Y, Kaneko F, Kawaguchi T. Polymer 2004;45:2221.
[45] Uda Y, Kaneko F, Kawaguchi T. Macromolecules 2005;38:3320.
[46] Kaneko F, Uda Y, Kawaguchi T, Ute K, Yamamuro O. Macromol Symp 2006;242:113.
[47] Guerra G, Milano G, Venditto V, Lofferedo F, Ruiz de Ballesteros O, Cavallo L, et al. Macromol Symp 1999;138:131.
[48] Vapor pressure data was picked from The International Program on Chemical Safety-INCHEM WebPages. International chemical safety card (ICSC) numbers: *n*-hexane: 0279, *n*-heptane: 0657, *n*-octane: 0933, *n*-nonane: 1245, and *n*-decane: 0428
[49] Atkins PW. Physical chemistry. 6th ed. Oxford: Oxford University Press; 1998.
[50] Gong L-D, Yang Z-Z. J Comput Chem 2010;31:2098.
[51] Milano G, Venditto V, Guerra G, Cavallo L, Ciambelli P, Sannino D. Chem Mater 2001;13:1506.
[52] Gowd EB, Shibayama N, Tashiro K. Macromol Symp 2006;241:257.
[53] Gowd EB, Shibayama N, Tashiro K. Macromolecules 2007;40:6291.
[54] Gowd EB, Shibayama N, Tashiro K. Macromolecules 2008;41:2541.
[55] Gowd EB, Shibayama N, Tashiro K. Macromolecules 2006;39:8412.
[56] Snyder RG, Strauss HL, Elliger CA. J Phys Chem 1982;86:5145.
[57] Gowd EB, Tashiro K. Macromolecules 2008;41:9814.
[58] Gowd EB, Tashiro K, Ramesh C. Prog Polym Sci 2009;34:280.
[59] Milano G, Guerra G. Prog Mater Sci 2009;54:68.
[60] Rizzo P, Daniel C, De Girolamo Del Mauro A, Guerra G. Chem Mater 2007;19:3864.
[61] Rizzo P, Daniello C, De Girolamo Del Mauro A, Guerra G. Macromolecules 2007;40:9470.
[62] Petraccone V, Ruiz de Ballesteros O, Tarallo O, Rizzo P, Guerra G. Chem Mater 2008;20:3663.
[63] Tarallo O, Schiavone MM, Petraccone V. Macromolecules 2010;43:1455.

Polymer 52 (2011) 830–836

Contents lists available at ScienceDirect

Polymer

journal homepage: www.elsevier.com/locate/polymer

Acetylation of plant cellulose fiber in supercritical carbon dioxide

Takashi Nishino [a,*], Masaru Kotera [a], Mari Suetsugu [a], Hiroki Murakami [a], Yoshimasa Urushihara [b]

[a] Department of Chemical Science and Engineering, Graduate School of Engineering, Kobe University, Rokko, Nada, Kobe 657-8501, Japan
[b] Hyogo Science and Technology Association, Kouto, Tatsuno 679-5165, Japan

ARTICLE INFO

Article history:
Received 1 July 2010
Received in revised form
9 November 2010
Accepted 18 November 2010
Available online 23 December 2010

Keywords:
Cellulose
Supercritical carbon dioxide
Acetylation

ABSTRACT

Natural cellulosic ramie fiber was acetylated using supercritical carbon dioxide (sc-CO_2) as a reaction medium. The structure and properties of the acetylated fibers were investigated using infrared spectroscopy, scanning electron microscopy, X-ray diffraction (including synchrotron microbeam X-ray diffraction), nano-Raman scattering, and a tensile test. The acetylation reaction proceeded without using an organic solvent, and it reached to the core part of the fiber within a short period while maintaining the fiber morphology. The crystallites of cellulose triacetate II and cellulose coexist in the fiber. The acetylated fiber with an average degree of substitution of 1.9 showed high modulus (34.5 GPa) and high strength (763 MPa), which are the highest values for cellulose diacetate so far reported to date.

1. Introduction

Cellulose is the most abundant natural linear homopolymer, and gathers much attention from environmental point of view. Besides having ecological benefits, cellulose plays a significant role in the structural support of plants, wood, and composites because of its high mechanical properties [1]. Together with a relatively high elastic modulus of 138 GPa for the crystalline regions in the direction parallel to the chain axis [2], inter/intra-hydrogen bonds stabilize the molecule itself, and connect it tightly to neighboring ones [3], which contribute to the high mechanical performance of cellulose. On the other hand, these strong hydrogen bonds prevent cellulose from melting, dissolving and being easily processed. To give cellulose thermal and/or easy wet processability, celluloses are often chemically modified through esterification [4]. Among many cellulose esters, cellulose acetate (CA) is the most popular, and is used as fiber, film, paint, filters, and dialyzers [5]. Two kinds of acetylation process, that is, a solution process and a vapor phase process have been proposed. Industrial acetylation has generally been performed using the solution process, in which acetic anhydride and a catalyst are added to cellulose dispersion in an organic solvent such as methylene chloride (homogeneous process) [6] or in diluents such as toluene (heterogeneous process) [7]. During the conversion of cellulose into cellulose acetate, the former system becomes homogeneous, which results in a high degree of substitution. The acetylation is an exothermic reaction, so large amounts of organic solvent, diluents, and cooling energy are needed in order to avoid depolymerization of the chains. However, this is undesirable from both economic and ecological viewpoints even when using sustainable cellulose as a starting material. On the contrary, cellulose was found to be easily acetylated by exposing the vapor phase in the presence of acetic anhydride vapor [8]. The vapor phase process was once commercialized with 20 tons produced per day in Japan; however, this was suspended in 1967.

In this study, we propose an alternative new process for the acetylation of plant cellulose fiber using supercritical carbon dioxide (sc-CO_2) as a reaction medium. The peculiar properties of supercritical conditions, such as low viscosity, high diffusion, easy separation, and no surface tension, have attracted a lot of interest and led to applications that include extraction [9], dyeing [10], foaming [11], and organic/polymer synthesis [12].

With relevance to cellulose, supercritical water is reported to be useful for hydrolysis and gasification [13,14]. Supercritical ammonia has been used for the crystal transformation from cellulose I to III_I [15,16], and supercritical methanol has been utilized for CA fiber formation [17]. Nanoporous cellulose aerogels were obtained by sc-CO_2 drying [18,19]. Recently, Yin et al. reported the application of sc-CO_2 for the synthesis of cellulose carbamate from cotton [20]. They employed severe sc-CO_2 conditions such as a 140 °C temperature and 18 MPa of pressure, for a total period of 9.5 h; however, the degree of substitution (DS) was limited to 1.3 per glucose unit. On the contrary, we reported here the preparation of cellulose acetate with a higher DS from natural plant fiber (ramie) using shorter and milder sc-CO_2 conditions. The structure and

* Corresponding author. Tel.: +81 78 803 6164; fax: +81 78 803 6198.
E-mail address: tnishino@kobe-u.ac.jp (T. Nishino).

0032-3861/$ – see front matter © 2010 Elsevier Ltd. All rights reserved.
doi:10.1016/j.polymer.2010.11.059

mechanical properties of CA fiber were investigated. In particular, the space distribution of acetyl groups in a chemically modified single fiber was analyzed using synchrotron microbeam X-ray diffraction and nano-Raman scattering.

2. Experimental section

2.1. Sample preparation

The plant cellulose fiber used in this study was refined ramie supplied by Toyobo Co.Ltd. Prior to acetylation, the fiber was pretreated by immersing it in glacial acetic acid containing 5% w/w of $ZnCl_2$ at 25 °C for 24 h [21]. The pretreated fibers were pressed between filter paper to remove the pretreatment solution, then they were fixed at both ends to a rectangular shaped metal frame (60 mm × 20 mm). The fibers were sealed in a high pressure reactor (inner volume: 138 ml) with acetic anhydride (5 ml), then subjected to 9.8 MPa of pressure with CO_2 at 70 °C. During the reaction, the fibers were kept separated from the liquid phase of acetic anhydride. After the designated time, the temperature and pressure were reduced to ambient levels. The fibers were rinsed with running water, then with distilled water to neutralize them. Finally, they were dried at room temperature and further dried in a vacuum at 60 °C for 12 h. For comparison, a vapor phase process was also carried out in the presence of acetic anhydride at 70 °C under reduced pressure of 2×10^{-3} Pa.

2.2. Measurements

Fourier transform infrared spectroscopy (FTIR) measurements were performed with an FTIR spectrophotometer (PerkinElmer Co., Ltd. Spectrum GX) with 10 scans at a resolution of 2 cm^{-1}. All the spectra were recorded in the transmission mode in the wavenumber range from 400 to 4000 cm^{-1} using the KBr method. After a base-line correction, the absorption A_{1740} of the carbonyl stretching band at 1740 cm^{-1} was quantified using the absorption A_{1050} of the ether stretching of the glucopyranose ring at 1050 cm^{-1} as an internal standard. The DS value was evaluated by the following equation (1):

$$DS = 0.77(A_{1740}/A_{1050})^2 + 1.39(A_{1740}/A_{1050}) \quad (1)$$

This equation was obtained from the preliminary experiments by drawing a calibration curve between A_{1740}/A_{1050} and the DS value from ^1H NMR using a mixture of ramie and commercial CA (Sigma-Aldrich Co.) (see Supporting Fig. S1).

Soxhlet extraction was performed using chloroform and acetone, successively. The residual weight was measured after 24 h extraction followed by drying. In this study, chloroform extracted and acetone extracted fractions were regarded as cellulose triacetate, and secondary acetate, respectively.

Nano-Raman scattering was recorded with a Nanofinder®30 (Tokyo Instruments, Inc). A cross section of the single fiber was irradiated by an Ar ion laser beam (Stabilite® 2017-AR (Spectra-physics Laser, Inc.)) with a wavelength of 514.5 nm. The laser power was 0.75 mW, and the irradiation time was 60 s. The space resolution was estimated to be 300 nm. The single fiber was embedded into polyethylene, and the cross section was prepared by cutting normal to the fiber axis with a cross section polisher (JEOL Ltd. SM-09010) using the Ar ion beam accelerated at 4 kV and 70 μA.

X-ray diffraction photographs were recorded on an imaging plate (IP) having a camera length of 37.5 mm. The bundle of the fibers was irradiated in the direction perpendicular to the fiber axis by Cu Kα radiation, generated with a Rigaku RINT-2000 at 40 kV, 20 mA. The equatorial diffraction profile was detected using an X-ray goniometer with a symmetric reflection geometry. The integral width of the reflection was corrected for the Cu Kα doublet and an instrumental broadening. The crystallite size D was estimated using Scherrer's equation (2) [22]:

$$D = \lambda/\beta\cos\theta \quad (2)$$

where $\lambda = 1.5418$Å, β; corrected integral width, and θ; Bragg angle.

Synchrotron X-ray microbeam experiments were performed at the Hyogo-ID BL24XU of SPring-8 [23,24]. The 15 keV X-ray microbeam (wavelength: 1.2398 Å) was obtained by passing the X-ray beam through a zone plate made of tantalum. The focused beam size at the sample position was evaluated to be 1.1 μm (vertical) × 1.8 μm (horizontal). The single fiber was irradiated by the X-ray microbeam, and the diffraction was detected by IP. The sample position was driven by a precise stepping motor with a spatial resolution of 62.5 nm, and the diffraction of the skin part of the single fiber was distinguished from that of the core part. The irradiated position on the sample was determined by monitoring the intensity of the Thomson scattering from the sample using a silicon drift detector (SDD; Rontec XFlash 2001). The X-ray exposure time was 300 s for each pattern, and the sample-to-detector distance was 88.1 mm.

The fiber morphology was observed using a scanning electron microscope (SEM) (JSM-5610LVS (JEOL)), at an accelerating voltage of 20 kV. Pt/Pd was deposited on the surface prior to the observation.

The stress–strain curve of the single fiber was measured using a tensile tester (Autograph AGS-1kND, Shimadzu) at 25 °C. The initial length of the specimen was 20 mm, and the extension rate

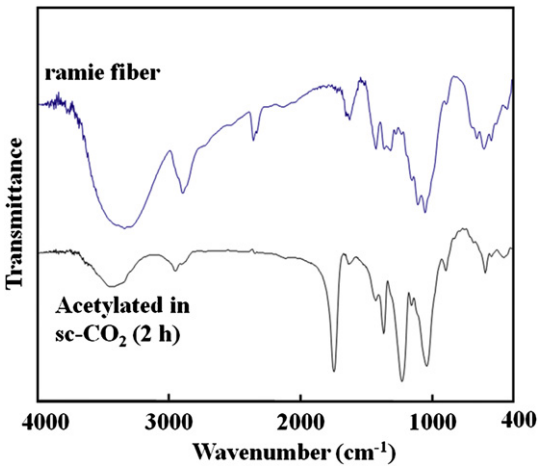

Fig. 1. FTIR spectra of ramie fiber before and after acetylation in sc-CO_2 at 70 °C, 9.8 MPa for 2 h.

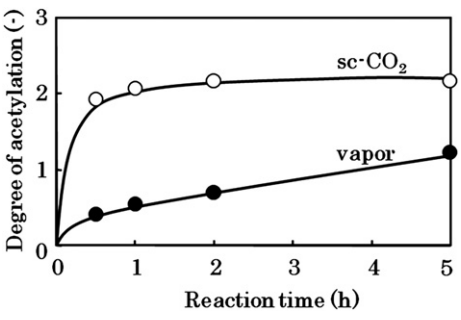

Fig. 2. Relationship between the reaction time and the degree of acetylation of ramie fiber acetylated in different media at 70 °C.

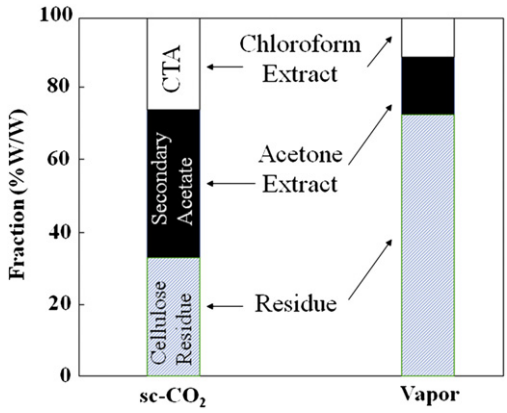

Fig. 3. Fractions of cellulose triacetate, secondary acetate and cellulose residue of ramie fiber acetylated for 2 h in different media.

was 2 mm/min. A cross-sectional area was evaluated using the density, the weight, and the length of the fiber. The average values and standard deviations of the Young's modulus Y and tensile strength σ_{max}, and the elongation ϵ_{max} at the break were evaluated for five tested specimens. For comparison, commercial CA (Daicel Chemical Ind. LTD.) film cast from dichloromethane was also tested. The film was crystallized as CTA II with the crystallinity of 36%.

3. Results and discussion

Fig. 1 shows the FTIR spectra of the ramie fiber before and after reaction for 2 h in sc-CO_2. The original ramie shows a typical IR spectrum of a natural cellulose I_β rich sample. The apparent cellulose I_β mass fraction f_β was 79%, which was evaluated using the following equation (3) [25]:

$$f_\beta = -2.55[A_{750}/(A_{750}+A_{710})] + 1.32 \quad (3)$$

After reaction, the absorption of the OH stretching bands, located at the region from 3200 to 3600 cm^{-1}, decreased, and a carbonyl stretching band appeared around 1740 cm^{-1}. These phenomena occurred because the hydroxyl groups were substituted by acetyl groups during the reaction. This confirmed that the acetylation progressed in sc-CO_2.

Fig. 2 shows the effect of reaction time on the DS value of ramie fibers in (open circles) sc-CO_2, and in (filled circles) the vapor phase. The DS value increased as the reaction time with the high rate, and it reached a plateau around 2.2 after acetylation in sc-CO_2 for more than 1 h. The high rate and high conversion of acetylation are due to high diffusivity of sc-CO_2 in the fiber. This is in contrast to the case of acetylation in the vapor phase, where the acetylation rate and the attained DS value were both lower.

Fig. 3 shows the weight fractions of CTA, secondary acetate, and the residual cellulose of the ramie fiber acetylated for 2 h in different media. By the Soxhlet extraction, we found that CTA, secondary acetate and cellulose coexisted in the acetylated fiber. The sum of CTA and secondary acetate fractions reached 66% w/w for the fibers acetylated in sc-CO_2 after 2 h. This corresponds to the averaged DS values of 1.6, which was lower than the DS values shown in Fig. 2. The results from the extraction are thought to underestimate the DS value for various reasons; one possibility is that the chloroform soluble fraction does not always reach the DS value of 3. Nevertheless, these indicate a wide distribution of the DS value within the fiber, and the fractions of CTA and secondary acetate in the fiber acetylated in sc-CO_2 were much larger than those in the vapor phase.

Fig. 4 shows the SEM images of the ramie fiber before and after acetylation for 2 h in sc-CO_2. The fiber surface of the ramie was smooth, and the average diameter was around 30 μm. These features remained unchanged even after acetylation for 2 h. From the X-ray fiber photograph in each corner, the ramie fiber showed high crystallinity and a high degree of crystallite orientation, which was also preserved after acetylation. These images reveal that the fiber shape and the crystallite orientation were maintained during acetylation in sc-CO_2. In addition to the reflections originated from cellulose I, several other diffraction spots could be observed after acetylation.

Fig. 5 shows the equatorial diffraction profiles of a bundle of ramie fibers, that consisted of ramie fibers acetylated in different media. As mentioned before, the original ramie fiber showed high crystallinity with a cellulose I_β rich profile. In addition, several diffraction peaks appeared around $2\theta = 9$, 10,13,17, and 19° for the fibers acetylated both in sc-CO_2 and vapor. These can be indexed with the crystalline peaks of CTA II modification [26]. It is well known that CTA II is produced by homogeneous acetylation in a solution, where cellulose acetate is first dissolved into the solvent, then resolidified and crystallized. However, in this study, acetylation was performed without adding solvent and while maintaining the gross morphology of the fiber as shown in Fig. 4. The residual acetic acid both after the pretreatment and that produced as a byproduct of the acetylation reaction may act as a swelling agent of the fiber with the help of sc-CO_2. Acetylation is said to take place together with erosion of the crystallites of the native cellulose [27,28]. This was revealed by the line broadening of the main diffraction peak for the 200 reflection of cellulose I_β [3]. The values in Fig. 5 show the D value for the 200 reflection ($2\theta = 22.4°$) of

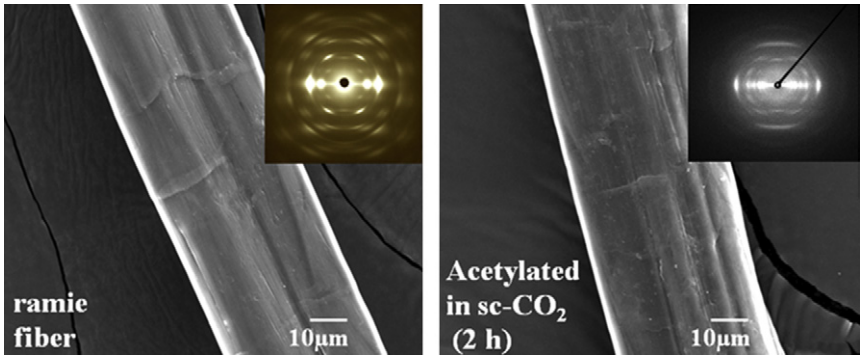

Fig. 4. Scanning electron micrographs of ramie fiber before and after acetylation in sc-CO_2 at 70 °C, 9.8 MPa for 2 h. The corner X-ray fiber photographs were taken by irradiating Cu Kα radiation to the fiber bundle in the direction perpendicular to the fiber axis.

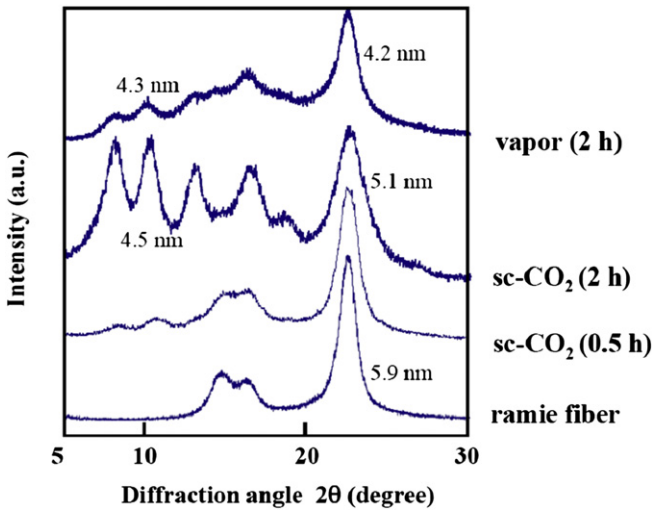

Fig. 5. Equatorial X-ray diffraction profiles of a bundle of ramie fibers, ramie fibers acetylated in vapor phase, and those acetylated in sc-CO_2. The numbers indicate the crystallite size D.

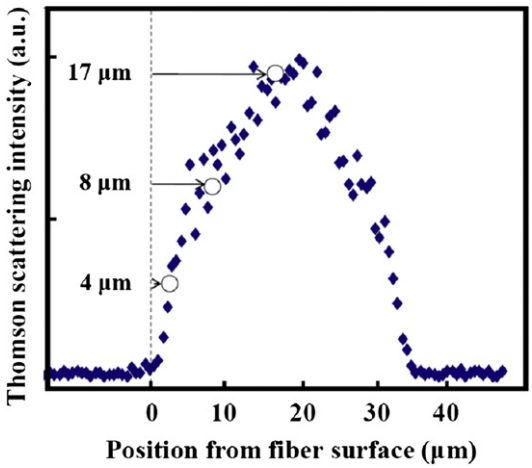

Fig. 6. Intensity profile of Thomson scattering across the fiber diameter of a ramie single fiber acetylated in sc-CO_2 at 70 °C, 9.8 MPa for 2 h.

cellulose I_β and the 110 reflection ($2\theta = 10.6°$) of CTA II. The D value of cellulose decreased by acetylation, which suggests the reaction mechanism described above is applicable in this study. Accordingly, it is thought that acetylation started within the amorphous region of cellulose fiber preferentially, then progressed toward the exterior to the center of the cellulose crystallites. During the reaction, acetylated chains were once partially swollen within the fiber and were then resolidified and crystallized as CTA II *in situ*. Using sc-CO_2, especially after a 2 h reaction, the crystallinity of CTA was found to be much higher than that acetylated in the vapor phase. Even after acetylated in vapor phase for 5 h, the crystallinity remained low. Again, swelling in sc-CO_2 stimulates chain mobility, which results in a high rate of crystallization even at low temperature (70 °C). Reaction process and the corresponding crystalline form of ramie fiber acetylated in sc-CO_2 are schematically shown in Scheme 1.

The results in Fig. 5 give the structural information averaged across the fiber because the experiments were carried out for the fiber bundle using the laboratory X-ray generator. In order to get the local structural data within a single fiber, the single fiber was irradiated by a synchrotron X-ray microbeam.

Fig. 6 shows the intensity profile of Thomson scattering across the fiber diameter of the ramie single fiber after acetylation in sc-CO_2 for 2 h, using a synchrotron radiation X-ray microbeam (SPring-8). When the X-ray beam impinges on a material, the X-rays are scattered by the electrons in the material, which is called Thomson scattering, and its intensity is proportional to the number of irradiated electrons [23]. Thus, the position on the single fiber irradiated by X-ray microbeam can be precisely determined by monitoring the intensity of the Thomson scattering [24]. By convoluting the intensity profile using a sample shape with a beam profile, the fiber diameter was determined to be 34 μm in this case. The microbeam X-ray diffraction was also performed at each irradiated position of the fiber.

Fig. 7 shows the synchrotron microbeam X-ray diffraction profiles of the fiber acetylated in sc-CO_2 for 2 h, together with that of the original ramie single fiber. The irradiated positions were 4, 8, and 17 μm from the fiber surface of the acetylated sample, respectively. Although the diffraction peaks are sharp compared with those in Fig. 5 due to the high beam directionality of the synchrotron source, the diffraction profiles of ramie fiber and acetylated ramie fiber were intrinsically the same as those in Fig. 5, respectively. In addition, the diffraction profiles were identical irrespective of the irradiated position. This suggests that the crystallinity of CTA was almost equivalent from the skin part to the core part of the fiber. Thus the 2 h reaction seems to be sufficient for the acetylation/crystallization of the whole fiber.

Fig. 8 shows a) the nano-Raman scattering, b) an optical photograph, and c) the distribution of the relative band intensity of the carbonyl stretching (1735 cm^{-1}) of the ramie single fiber after acetylation in sc-CO_2 for 2 h. The Raman scattering in Fig. 8a) gives a typical spectrum of cellulose acetate [29]. The band intensity of

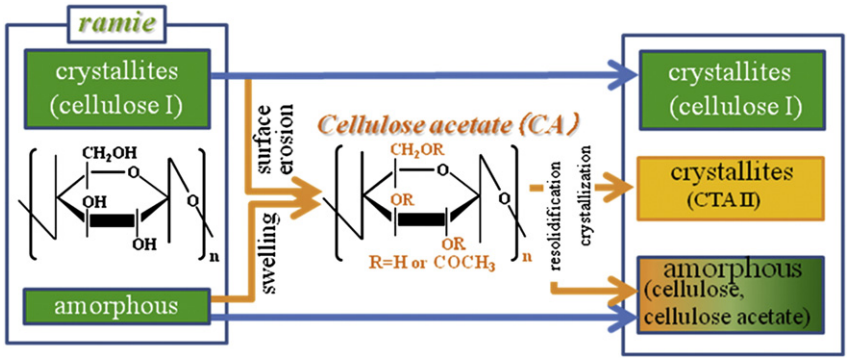

Scheme 1. Reaction process and the corresponding crystalline form of ramie fiber acetylated in sc-CO_2.

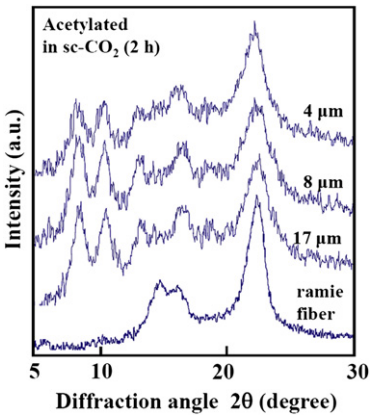

Fig. 7. Synchrotron microbeam X-ray diffraction profiles ($\lambda = 1.2398$ Å) of ramie single fiber before and after acetylation in sc-CO_2 at 70 °C, 9.8 MPa for 2 h.

the carbonyl stretching was normalized using the band intensity of the methylene bending (at 1378 cm^{-1}) along the broken line in Fig. 8b) on the cross section of the fiber. The relative band intensity in Fig. 8c) was almost constant along the cross section of the fiber. The lumen (hollow microtube inside the native plant fiber) could be observed, where no Raman scattering was detected. These results reveal that the acetyl groups were distributed almost uniformly from the skin part to the core part of the single fiber after acetylation in sc-CO_2 for 2 h.

Fig. 9 shows the synchrotron microbeam X-ray diffraction profiles of the ramie single fiber acetylated in sc-CO_2 for 0.5 h. Although the signal/noise ratio was not very high, the diffraction peak from CTA II was observed on the profile at 1 μm from the fiber surface, which overlaps with the cellulose reflections. In contrast, the diffraction peaks from CTA II were very weak on the profile at 3 μm and 10 μm, and their overall profiles were almost same as that

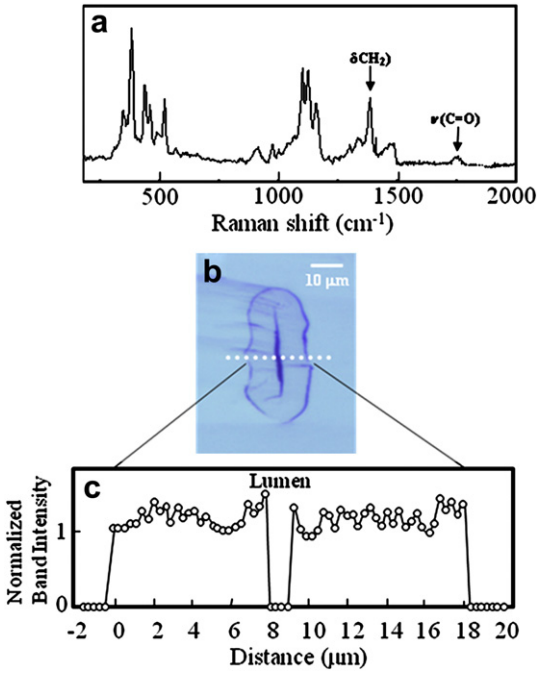

Fig. 8. a) Nano-Raman scattering, b) optical photograph, and c) the distribution of the relative band intensity of carbonyl stretching (1735 cm^{-1}) normalized with that of the methylene bending (at 1378 cm^{-1}), along the broken line in b) on a cross section of the ramie single fiber acetylated in sc-CO_2 at 70 °C, 9.8 MPa for 2 h.

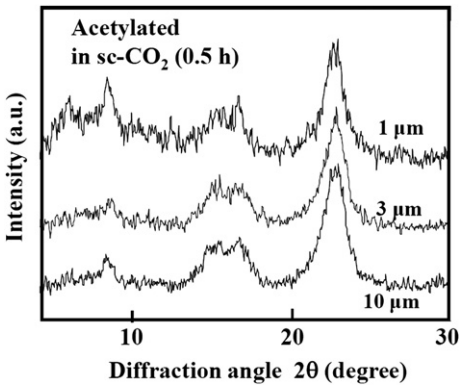

Fig. 9. Synchrotron microbeam X-ray diffraction profiles ($\lambda = 1.2398$ Å) of ramie single fiber acetylated in sc-CO_2 at 70 °C, 9.8 MPa for 0.5 h.

of cellulose. In addition, the main 200 reflection of cellulose remained sharp in all cases. These results suggest that the surface of the fiber was acetylated and partially crystallized as CTA II, but most of the core part was not acetylated during the short 0.5 h treatment time.

Fig. 10 shows a) the nano-Raman scatterings at positions of A and B indicated in b), b) an optical photograph, and c) the distribution of the relative band intensities of the carbonyl stretching along the broken line in Fig. 10b) on a cross section of the ramie single fiber after acetylation in sc-CO_2 for 0.5 h. The spectrum at the A position was basically identical to those in Fig. 8a). On the

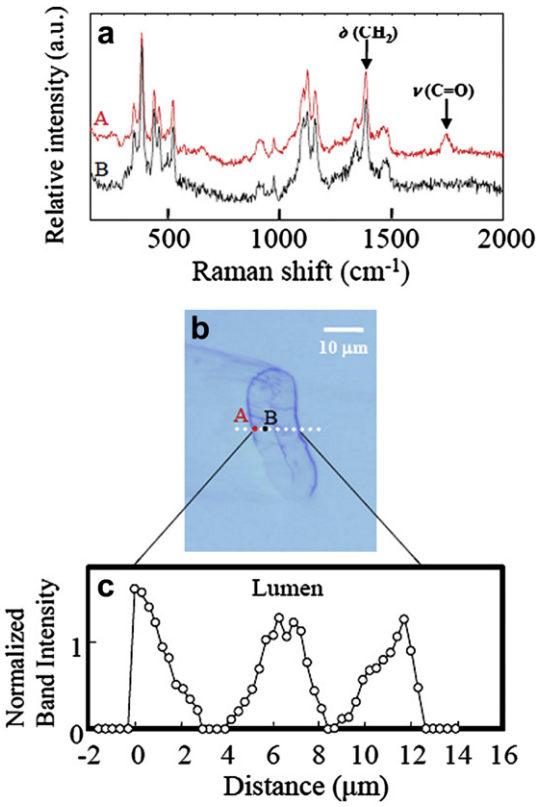

Fig. 10. a) Nano-Raman scatterings at the position of A and B in b), b) optical photograph, and c) distribution of relative band intensity of carbonyl stretching (1735 cm^{-1}) normalized with that of the methylene bending (at 1378 cm^{-1}), along the broken line in b) on a cross section of the ramie single fiber acetylated in sc-CO_2 at 70 °C, 9.8 MPa for 0.5 h.

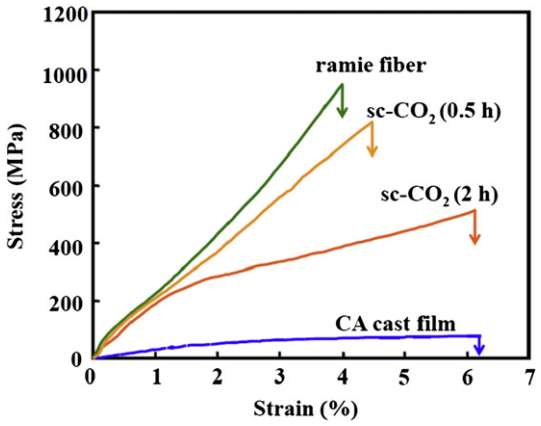

Fig. 11. Stress–strain curves of ramie single fiber, cellulose acetate film, and ramie single fiber acetylated in sc-CO_2 at 70 °C, 9.8 MPa for 0.5 h and 2 h.

contrary, the carbonyl band was not observed in the spectrum at the B position. The normalized band intensity in c) indicates the zigzag distribution of the carbonyl groups across the fiber. This reveals that the acetylation was started both from the exterior and the interior (lumen side) of the single fiber, and it proceeded into the fiber bulk. However, the reaction was not completed in the whole fiber within the reaction time of 0.5 h. These features correspond to the X-ray diffraction results described above. The acetylation from the interior shows that the reagents penetrated into the lumen. The results shown in Fig. 10 suggest that so-called functionally graded material can be produced with very simple procedure by the chemical reaction using sc-CO_2. Next, we describe the results of tensile tests that were conducted to investigate changes in the mechanical properties through acetylation.

Fig. 11 shows the stress–strain curves of single ramie fibers before and after acetylation in sc-CO_2 for 0.5 h and 2 h. The tensile strength σ_{max}, Young's modulus *Y*, and the elongation ϵ_{max} at the break are summarized in Table 1, together with their standard deviations. The degree of substitution is also indicated. The original ramie fiber had high elastic modulus and high tensile strength. This is because ramie is known to possess the highest mechanical properties among various plant fibers [30]. Compared with the original values, the *Y* and σ_{max} values were lower after acetylation. However, the *Y* values and the σ_{max} values for the acetylated fibers were much higher than those (*Y* value up to 5.4 GPa and σ_{max} value up to 173 MPa) of the conventional CTA film (as shown in Fig. 11 and Table 1) and CTA fibers [31]. The elastic modulus of the crystalline regions of CTA II in the direction parallel to the chain axis is 33.2 GPa, which is the maximum attainable modulus of CTA II [32]. The *Y* values in this study were lower than this crystal modulus, however, to the best of our knowledge, these are the highest macroscopic modulus reported to date for cellulose diacetate.

Table 1
Young's modulus *Y*, tensile strength σ_{max}, and the elongation ϵ_{max} at the break of a ramie single fiber, that acetylated in sc-CO_2 at 70 °C, 9.8 MPa for 0.5 h and 2 h, and cellulose acetate film together with standard deviations.

	Y(GPa)	σ_{max}(MPa)	ϵ_{max}(%)	DS
Ramie	38.0(7.4)	878(190)	3.9(0.9)	–
Acetylated ramie in sc-CO_2 0.5 h	34.5(5.6)	763(77)	4.3(1.0)	1.93
Acetylated ramie in sc-CO_2 2 h	23.6(2.2)	512(64)	6.1(1.3)	2.16
CA cast film	3.3(0.4)	87(16)	6.2(3.6)	2.86

These excellent mechanical properties attributed to the coexistence of the crystallites of CTA II and native cellulose. Accordingly, sc-CO_2 was found to be an effective medium for the chemical modification of cellulose with maintaining the fiber shape and high mechanical properties of the original cellulose.

4. Conclusions

Natural plant cellulose fiber was acetylated using sc-CO_2 as a reaction medium. Using microbeam X-ray diffraction and nano-Raman scattering, the acetylation reaction was found to proceed from both the exterior and interior (lumen side) of the single fiber, and to reach the core part of the fiber within 2 h. This high acetylation rate was due to the high diffusivity of sc-CO_2 in the fiber. The space distribution and the crystalline features of cellulose acetate were found to depend on the reaction time. The fiber shape was maintained even after acetylation, and the crystallites of cellulose and CTA II coexisted within the fiber. The acetylated (DS = 1.9) fiber showed high modulus (34.5 GPa) and high strength (763 MPa). These are thought to be the highest values for cellulose diacetate so far observed. sc-CO_2 was found to be an effective and environmentally friendly reaction medium for the acetylation of cellulose without using an organic solvent.

Acknowledgment

The authors would like to acknowledge the financial support by a Grant-on-Aid for Scientific Research from the Ministry of Education, Culture, Science, Sports and Technology, Japan (No. 20246100). Special Coordination Funds for Promoting Science and Technology, Creation of Innovation Centers for Advanced Interdisciplinary Research Areas (Innovative Bioproduction Kobe), MEXT, Japan are also acknowledged. The authors would like to thank Professor Y.Kagoshima, University of Hyogo, for his continued support in the microdiffraction experiments at BL24XU of SPring-8.

Appendix. Supplementary data

Supplementary data related to this article can be found online at doi:10.1016/j.polymer.2010.11.059.

References

[1] Bos HL, Van Den Oever MJA, Peters OCJJ. J Mater Sci 2002;37:1683–92.
[2] Nishino T, Takano K, Nakamae K. J Polym Sci Part B: Polym Phys 1995;33:1647–51.
[3] Nishiyama Y, Langan P, Chanzy H. J Am Chem Soc 2002;124:9074–82.
[4] Edgar KJ, Buchanan CM, Debenham JS, Rundquist PA, Seiler BD. Prog Polym Sci 2001;26:1605–88.
[5] Heinze T, Liebert T, Koschella A. Esterification of polysaccharides. Berlin, Heidelberg, New York: Springer; 2006.
[6] Zugenmaier P. Macromol Symp 2004;208:81–166.
[7] Sassi J-F, Chanzy H. Cellulose 1995;2:111–27.
[8] Sakurada I, Sakaguchi Y. Sen'i Gakkaishi 1957;13:67–8.
[9] Weijers C, de Rooij RD, Agarwal US, de Wit G, Lemstra PJ. J Appl Polym Sci 2006;101:4487–92.
[10] Liu Z-T, Zhang L, Liu Z, Gao Z, Dong W, Xiong H, et al. Ind Eng Chem Res 2006;45:8932–8.
[11] Jacobs LJM, Kemmere MF, Keurentjes JTF. Green Chem 2008;10:731–8.
[12] Lee H, Terry E, Zong M, Arrowsmith N, Perrier S, Thurecht KJ, et al. J Am Chem Soc 2008;130:12242–3.
[13] Sasaki S, Fang Z, Fukushima Y, Adschiri T, Arai K. Ind Eng Chem Res 2000;39:2883–90.
[14] Resende FLP, Neff ME, Savage PE. Energy Fuels 2007;21:3637–43.
[15] Nishiyama Y, Kuga S, Wada M, Okano T. Macromolecules 1997;30:6395–7.
[16] Wada M, Heux L, Isogai A, Nishiyama Y, Chanzy H, Sugiyama J. Macromolecules 2001;34:1237–43.
[17] Aniedobe NE, Thies MC. Macromolecules 1997;30:2792–4.
[18] Gavillon R, Budtova T. Biomacromolecules 2008;9:269–77.

[19] Cai J, Kimura S, Wada M, Kuga S. Biomacromolecules 2009;10:87–94.
[20] Yin C, Li J, Xu Q, Peng Q, Liu Y, Shen X. Carbohydr Polym 2007;67:147–54.
[21] Sakurada I, Sakaguchi Y, Yamaguchi T. Sen'i Gakkaishi 1957;13:72–3.
[22] Alexander LE. X-ray diffraction methods in polymer science. New York: John Wiley & Sons; 1969 [Chapter 7].
[23] Kagoshima Y, Takai K, Ibuki T, Yokoyama Y, Hashida T, Yokoyama K, et al. Nucl Instrum Methods A 2001;467–468:872–6.
[24] Kotera M, Nishino T, Taura T, Saito M, Nakai A, Koyama T, et al. Composite Interfaces 2007;14:63–72.
[25] Yamamoto H, Horii F, Hirai A. Cellulose 1996;3:229–42.
[26] Deus C, Friebolin H, Siefert E. Makromol Chem 1991;192:75–83.
[27] Roche E, Chanzy H, Boudeulle M, Marchesault RH, Sundararajan P. Macromolecules 1978;11:86–94.
[28] Glegg RE, Ingerick D, Parmerter RR, Salzer JST, Warburton RS. J Polym Sci , Part A2 1968;6:745–73.
[29] Adebajo MO, Frost RL, Kloprogge JT, Kokoot S. Spectrochim Acta Part A 2006;64:448–53.
[30] Nishino T, Matsuda I, Hirao K. Macromolecules 2004;37:7683–7.
[31] Handbook of fibers. 3rd ed. Tokyo, Maruzen: The society of fiber science and technology, Japan; 2004. p.920.
[32] Nishino T, Takano K, Nakamae K, Saitaka K, Itakura S, Azuma J, et al. J Polym Sci Part B: Polym Phys 1995;33:611–8.

Polymer 52 (2011) 837–843

Contents lists available at ScienceDirect

Polymer

journal homepage: www.elsevier.com/locate/polymer

Micro-flowers of poly(*p*-phenylene pyromelliteimide) crystals

Kanji Wakabayashi [a], Tetsuya Uchida [b], Shinichi Yamazaki [a], Kunio Kimura [a,*]

[a] Graduate School of Environmental Science, Okayama University, 3-1-1 Tsushima-naka, Kita-ku, Okayama 700-8530, Japan
[b] Graduate School of Natural Science and Technology, Okayama University, 3-1-1 Tsushima-naka, Kita-ku, Okayama 700-8530, Japan

ARTICLE INFO

Article history:
Received 20 September 2010
Received in revised form
28 November 2010
Accepted 12 December 2010
Available online 21 December 2010

Keywords:
Crystallization
Morphology
Polyimide

ABSTRACT

Morphology control of poly(*p*-phenylene pyromelliteimide) (PPPI) crystals was examined using reaction-induced crystallization of oligomers during solution polymerization of self-polymerizable *N*-(4′-aminophenyl)-3-carboxyl-4-alkoxycarbonylphthalimide. Micro-flowers of the PPPI needle-like crystals were formed in which the needle-like crystals grew radially from the center part as petals. The molecules aligned regularly along the long axis of the needle-like crystal. The structure of alkoxy group in the monomer and the monomer concentration influenced the size of the needle-like crystals, and their average length and width were changeable from 640 nm to 1.69 μm and from 110 nm to 210 nm, respectively. The average thickness was 20 nm. The obtained micro-flowers possessed high crystallinity and exhibited excellent thermal stability.

1. Introduction

Aromatic polyimides have been paid much attention as high performance polymers and they have been widely used [1–4]. Among them, poly(*p*-phenylene pyromelliteimide) (PPPI) is the most rigid polyimide, and therefore it is expectable to possess the highest performance [5,6]. Morphology of polymers with molecular orientation is of great importance to obtain essential properties, and the ideal morphology must be a one-dimensional structure such as a needle-like crystal and a fiber, especially for the usage as reinforcements. It is somewhat troublesome to control the morphology of PPPI with highly ordered molecular orientation by conventional techniques because of its intractability. In order to overcome the intractability, PPPI has been generally prepared by a two-step procedure *via* the synthesis of the corresponding soluble poly(amic acid) precursor, and the following imidization. However, the molecular orientation of poly(amic acid) precursor is difficult due to the structural irregularity caused by *meta* and *para* catenation of amide linkage, and the rapid crystallization during imidization prevents controlling the molecular orientation of PPPI [7,8]. Although various chemical modifications have been also attempted to improve its processability [7–11], these modifications usually decrease the essential properties predicted from the rigid molecular structure.

We studied the morphology control of PPPI using reaction-induced phase separation during isothermal polymerization of pyromellitic dianhydride (PMDA) and *p*-phenylene diamine (PPDA) [12,13]. Lozenge-shaped crystals, aggregates of plate crystals and microspheres of PPPI were obtained so far. The previous results reveal that the behavior of the phase separation is significantly influenced by the degree of imidization of oligomer leading to the drastic change in the morphology of PPPI [12]. The structural irregularity of precursor oligo(amic acid) caused by *meta* and *para* catenation of amide linkage lowers the freezing point of the precipitated oligomers resulting in the induction of the liquid–liquid phase separation to form the microsphere. Further, the structural irregularity damages the crystallizability of the oligomers to form the crystals having clear habit. Additionally, the chemical structure of the oligomer end-groups also affects the morphology of the crystals [14,15]. In order to prepare the crystals having clear habit such as needle-like crystals by the crystallization of oligomers, it is at least necessary to precipitate the fully cyclized oligoimides having regular structure.

On the basis of these results, self-polymerizable monomers **1a** and **1b**, which contained an imide linkage, were designed as shown in Scheme 1 and the morphology control of PPPI was performed using reaction-induced crystallization during the polymerization of them.

2. Experimental

2.1. Materials

Pyromellitic dianhydride (PMDA) was purchased from Aldrich Co. Ltd. and used as received. 4-Nitroaniline purchased from Tokyo Chemical Incorporation Co. Ltd. was used after recrystallization from acetone. Tetrahydrofuran (THF), *n*-hexane, methanol, ethanol and *N*-methyl-2-pyrolidone (NMP) were purchased from Nacalai Tesque Co. Ltd. THF and *n*-hexane were used after distillation over

* Corresponding author. Tel./fax: +81 86 251 8902.
E-mail address: polykim@cc.okayama-u.ac.jp (K. Kimura).

0032-3861/$ – see front matter © 2010 Elsevier Ltd. All rights reserved.
doi:10.1016/j.polymer.2010.12.022

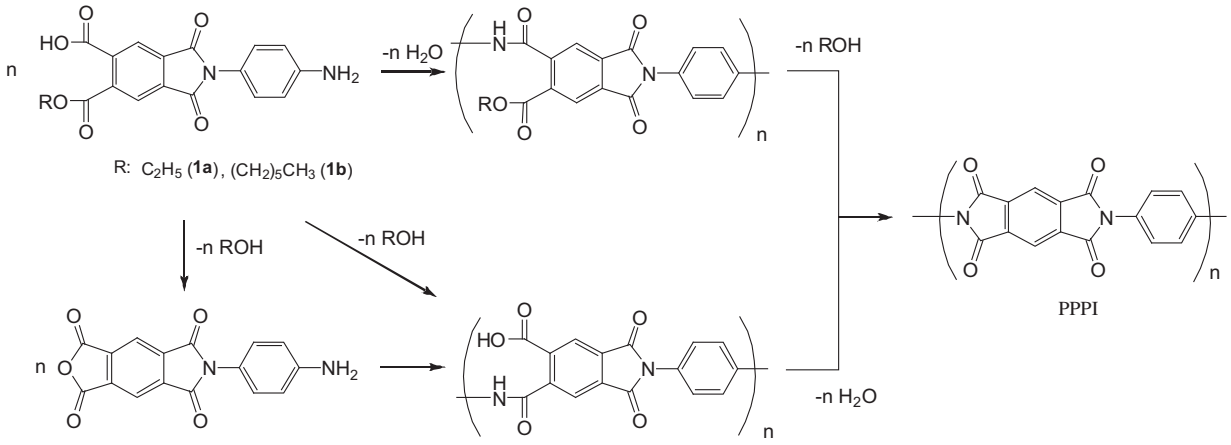

Scheme 1. Preparation of PPPI from self-condensation monomer; monomer **1** (R: $-C_2H_5$(**1a**), $-(CH_2)_5CH_3$)(**1b**)).

calcium hydride. Absolute methanol and ethanol were obtained by distillation over magnesium methoxide and magnesium ethoxide, respectively. NMP was used after dehydration over molecular sieves 4A. A mixture of isomers of dibenzyltoluene (DBT) was purchased from Matsumura Oil Co. Ltd. (Trade name: Barrel Therm 400, MW: 380, b.p.: 382 °C) and purified by distillation under reduced pressure (170–175 °C/0.2 mmHg).

2.2. Measurements

Morphology of the products was observed on a HITACHI S-3500N scanning electron microscope at 20 kV. Samples were dried, sputtered with platinum/palladium. Average shape parameters of the products were determined by taking the average of over 100 observation values. A selected-area electron diffraction (SAED) was taken by a JEOL 2000EX (Tokyo, Japan) transmission electron microscope (TEM) at 200 kV. ^{1}H NMR spectra were recorded on a JEOL AL300 SC-NMR at 300 MHz. Infrared (IR) spectra were recorded on a JASCO FT/IR-410 spectrometer. Wide angle X-ray scattering (WAXS) pattern was measured on a RIGAKU MiniFlex diffractometer with nickel-filtered CuKα radiation (35 kV, 20 mA). Matrix assisted laser desorption ionization time-of-flight mass spectrometry (MALDI-TOF MS) was performed on a Bruker Daltonics AutoFLEX MALDI-TOF MS system operating with a 337-nm N_2 laser. Spectra were obtained in the linear positive mode with an accelerating potential of 20 kV. Mass calibration was performed with angiotensin I (MW 1296.69) and insulin B (MW 3496.96) from a Sequazyme peptide mass standard kit. The samples were then prepared by the evaporation–grinding method and measured in 3-aminoquinoline as a matrix doped with potassium trifluoroacetate salt according to the reported procedure [13,16]. Thermogravimetric analysis was performed on a Perkin-Elmer TGA-7 with a scanning rate of 20 °C min^{-1} in N_2.

2.3. Monomer synthesis

2.3.1. Pyromellitic monoanhydride (PMMA) (*2*)

PMDA (43.6 g, 0.20 mol) and THF (400 mL) were placed into a three-necked round bottom flask equipped with a thermometer, a dropping funnel and a drying tube. THF solution (30 mL) contained water (5 mL, 0.28 mol) was added dropwise into the mixture at 20 °C over 48 h. After the addition, the solution was stirred for another 24 h. The solution was dried with sodium sulfate. 250 mL of THF was evaporated and absolute *n*-hexane was slowly added into the solution at 20 °C until precipitation occurred. The precipitates were removed by filtration and then filtrate was stood under −20 °C for 12 h. White needle crystals were collected by suction filtration and dried under vacuum at 40 °C for 12 h. The purity of PMMA **2** in the crystals was 96% estimated by ^{1}H NMR. Yield: 22 g (47%), m.p.: 273 °C. IR (KBr): 3100–2500, 1858, 1795, 1778, 1715, 1482, 1425, 1254, 1144, 1107, 1006, 890, 731, 683, ^{1}H NMR (300 MHz, acetone-d_6) δ(ppm): 8.38 (s, 2H).

2.3.2. 4,5-Dicarboxy N-(4′-nitrophenyl)phthalimide (CNPI) (*3*)

4-Nitroaniline (4.15 g, 0.03 mol) and NMP (50 mL) were placed into a three-necked flask equipped with a thermometer and a condenser. The solution was heated to 90 °C under N_2 atmosphere and then PMMA **2** (7.23 g, 0.03 mol) was added. The mixture was stirred for 30 min. The mixture was gradually colored to orange with time. Acetic anhydride (7 mL) and pyridine (0.5 ml) were added into the mixture at 100 °C and stirred for 3 h. After the filtration of the mixture, the filtrate was allowed to cool at 50 °C and then poured into 1 L of the water. The precipitates were collected by filtration and dried at 50 °C under vacuum for 12 h. Recrystallization from THF gave pale yellow crystals of CNPI **3** with yield of 52%. m.p.: 233 °C, IR (KBr, cm^{-1}): 3100–2500 (br), 1782, 1729, 1718, 1618, 1594, 1523, 1495, 1346, 1252, 1218, 1142, 1115, 1093, 1011, 928, 895, 845, 750, 695, ^{1}H NMR (300 MHz, acetone-d_6) δ(ppm): 8.46–8.43 (d, 2H, $J = 9.2$ Hz), 8.29 (s, 2H), 7.91–7.88 (d, 2H, $J = 9.2$ Hz). Anal. Calcd for $C_{16}H_8O_8N_2$ (356.24): C, 53.94; H, 2.26; N, 7.86. Found: C, 55.29; H, 3.54; N, 8.98.

2.3.3. CNPI anhydride (*4*)

CNPI **3** (3.5 g) and acetic anhydride (100 mL) were heated at 140 °C for 1 h in N_2 atmosphere. The reaction mixture was condensed by the distillation of acetic anhydride, and white solids were precipitated after cooling at 25 °C. The solids were collected by filtration and then recrystallized from acetic anhydride. CNPI anhydride **4** was obtained as white crystals with yield of 85%. m.p.: 272 °C. IR (KBr, cm^{-1}): 3109, 1866, 1778, 1726, 1596, 1525, 1516, 1459, 1375, 1348, 1299, 1206, 1120, 903, 839, 809, 746, 720, ^{1}H NMR (300 MHz, acetone-d_6) δ(ppm): 8.60 (s, 2H) 8.49–8.44 (m, 2H), 7.94–7.89 (m, 2H). Anal. Calcd for $C_{16}H_6O_7N_2$ (338.22): C, 56.78; H, 1.79; N, 8.28. Found: C, 60.81; H, 2.30; N, 6.28.

2.3.4. 4-Carboxy 5-ethoxycarbonyl N-(4′-nitrophenyl)phthalimide (CENPI) (*5a*)

CNPI anhydride **4** (3.0 g) and ethanol (100 mL) were refluxed for 6 h. Ethanol was evaporated to obtain yellow solids. Recrystallization from ethanol gave white needle crystal of CENPI **5a** with yield of 81%. m.p.: 217 °C. ^{1}H NMR (300 MHz, acetone-d_6) δ(ppm): 8.47–8.42 (m, 2H) 8.33 (d, 1H, $J = 0.5$ Hz), 8.22 (d, 1H, $J = 0.5$ Hz), 7.92–7.87 (m, 2H), 4.44–4.37 (q, 2H, $J = 7.2$ Hz), 1.39–1.35 (t, 3H, $J = 7.2$ Hz). IR (KBr, cm^{-1}): 3117, 3059, 2998, 3100–2500 (br), 1787,

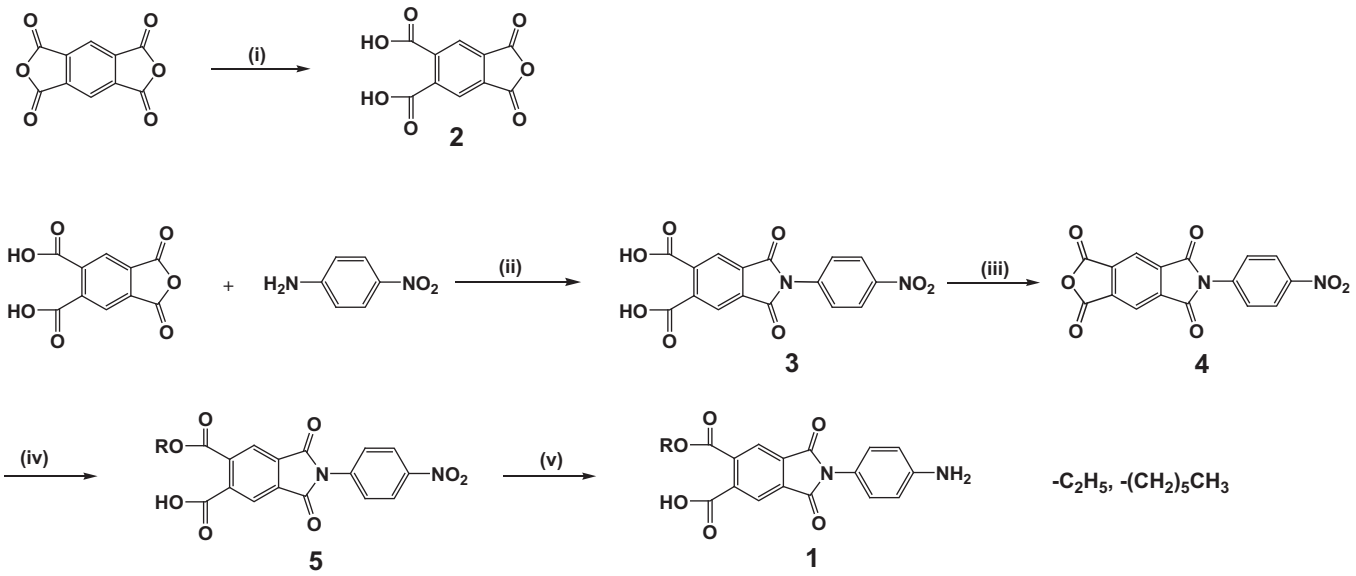

Scheme 2. Synthesis of monomer **1** (R: $-C_2H_5$(**1a**), $-(CH_2)_5CH_3$(**1b**)) (i) H_2O, THF; (ii) (1) NMP, 100 °C, (2) Acetic anhydride/pyridine; (iii) Acetic anhydride, reflux; (iv) Ethanol or 1-hexanol, reflux; (v) H_2, ethanol or methanol. 25 °C.

1730, 1697, 1594, 1520, 1494, 1448, 1385, 1343, 1289, 1266, 1221, 1138, 1104, 849, 720. Anal. Calcd for $C_{18}H_{12}O_8N_2$ (384.30): C, 56.22; H, 4.16; N, 7.29. Found: C, 56.14; H, 2.91; N, 7.16.

2.3.5. 4-Carboxy 5-hexyloxycarbonyl N-(4′-nitrophenyl) phthalimide (CHNPI) (**5b**)

CNPI anhydride **4** (4.5 g) and 1-hexanol (50 mL) were heated at 120 °C for 3 h. The mixture was allowed to cool at 25 °C. White leaf-like crystal was precipitated. Recrystallization from 1-hexanol gave white leaf-like crystals of CHNPI **5b** with yield of 3.6 g (62%). m.p.: 176 °C. ^{1}H NMR (300 MHz, DMSO-d_6) δ(ppm): 13.99 (s, 1H), 8.44–8.41 (d, 2H, $J = 9.0$ Hz), 8.23 (s, 1H), 8.19 (s, 1H), 7.81–7.79 (d, 2H, $J = 9.2$ Hz), 4.30–4.26 (t, 2H, $J = 6.6$ Hz), 1.74–1.65 (m, 2H), 1.39–1.29 (m, 6H), 0.89–0.84 (t, 3H, $J = 6.8$ Hz). IR (KBr, cm^{-1}): 3400–2400 (br), 2922, 2856, 1784, 1736, 1692, 1592, 1523, 1496, 1404, 1341, 1285, 1223, 1126, 1114, 1054, 858, 751, 720. Anal. Calcd for $C_{22}H_{20}O_8N_2$ (440.40): C, 60.00; H, 4.58; N, 6.36. Found: C, 59.09; H, 3.78; N, 7.46.

2.3.6. N-(4′-Aminophenyl)-3-carboxyl-4-ethoxycarbonylphthalimide (**1a**)

CENPI **5a** (1.5 g) and absolute ethanol (300 mL) were placed into a three-necked round bottom flask equipped with a thermometer and gas inlet and outlet tubes. 10% Pd/C (0.15 g) was added and the mixture was vigorously stirred under H_2 atmosphere at 25 °C for 6 h. Pd/C was removed by filtration with celite and the filtrate was evaporated at 25 °C. Recrystallization from the mixed solvent of methanol and water (v/v 5/1) gave pale yellow needle crystals of monomer **1a** with the yield of 39%. m.p.: 227–255 °C. ^{1}H NMR (300 MHz, DMSO-d_6) δ(ppm): 8.12 (s, 1H), 8.09 (s, 1H), 7.04–7.01 (d, 2H, $J = 8.4$ Hz), 6.65–6.62 (d, 2H, $J = 8.6$ Hz), 4.36–4.29 (q, 2H, $J = 7.0$ Hz), 1.33–1.28 (t, 3H, $J = 7.2$ Hz). IR (KBr): 3476, 3377, 2978, 2871, 2612, 2104, 1780, 1719, 1620, 1601, 1519, 1469, 1427, 1375, 1344, 1261, 1220, 1177, 1131, 738. Anal. Calcd for $C_{18}H_{14}O_6N_2$ (354.31): C, 61.00; H, 3.98; N, 7.91. Found: C, 60.10; H, 4.40; N, 6.31.

2.3.7. N-(4′-Aminophenyl)-3-carboxyl-4-hexyloxycarbonylphthalimide (**1b**)

Monomer **1b** was prepared from CENPI **5b** and methanol in the similar manner of monomer **1a**. Recrystallization from mixed solvent of methanol and water (v/v 5/1) below 50 °C afforded needle crystals of monomer **1b** with the yield of 44%. m.p.: 174 °C, ^{1}H NMR (300 MHz, DMSO-d_6) δ(ppm): 8.12 (s, 1H), 8.07 (s, 1H), 7.03–7.01 (d, 2H, $J = 8.6$ Hz), 6.65–6.62 (d, 2H, $J = 8.6$ Hz), 4.29–4.24 (t, 2H, $J = 6.4$ Hz), 1.73–1.64 (m, 2H, $J = 6.4$ Hz), 1.39–1.28 (m, 6H), 0.88–0.84 (t, 3H, $J = 6.4$ Hz). IR (KBr): 3483, 3388, 3051, 3002, 2932, 2605, 1780, 1727, 1719, 1621, 1602, 1580, 1518, 1469, 1428, 1372, 1264,

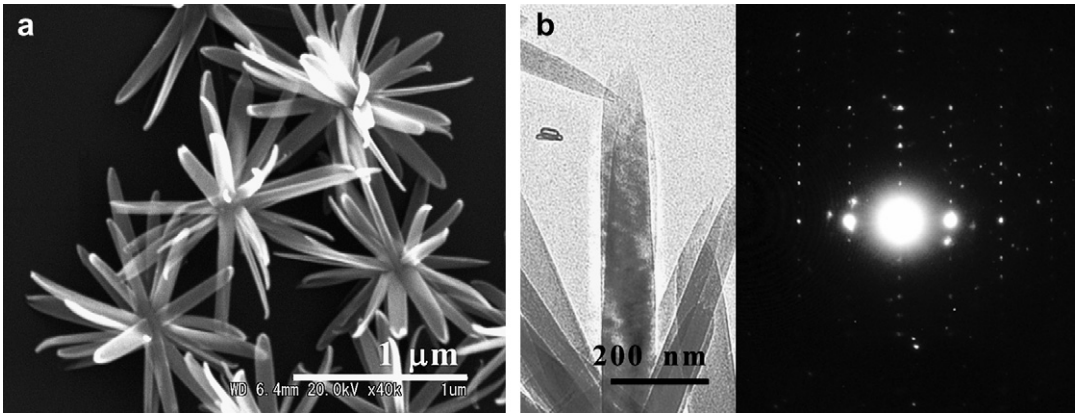

Fig. 1. (a) A SEM and (b) a TEM image with a selected-area electron diffraction pattern of the PPPI crystals prepared from monomer **1a** at a concentration of 0.25% (run no. 2).

1221, 1132, 1023, 1024, 784. Anal. Calcd for $C_{22}H_{22}O_6N_2$ (410.65): C, 64.82; H, 5.40; N, 6.82. Found: C, 64.28; H, 5.27; N, 6.73.

2.4. Polymer preparation

DBT (20 mL) was placed into a cylindrical flask equipped with gas inlet and outlet tubes, and heated up to 330 °C in N_2 atmosphere. Monomer **1a** (0.061 g, 0.17 mmol) was added into the solution at 330 °C under stirring. The stirring was stopped when monomer **1a** was entirely dissolved. The polymerization was carried out at 330 °C for 6 h with no stirring. Polymerization concentration, defined as (calculated polymer weight/solvent volume) X 100 in this study, was 0.25%. The solution became turbid immediately and the pale yellow crystals were formed with time. After 6 h, the crystals were collected by filtration at 330 °C to avoid the precipitation of oligomers during cooling. The collected crystals were washed with *n*-hexane and acetone several times, and then dried at 25 °C for 12 h. Oligomers dissolving in the solution at 330 °C were collected by pouring the filtrate into *n*-hexane. The precipitated oligomers were collected by filtration, washed with *n*-hexane and fried at 40 °C under vacuum for 12 h. Polymerizations of monomer **1b** were also carried out in a similar manner.

3. Results and discussion

Three polymerization routes are possibly thought as also depicted in Scheme 1, that is, *via* a direct amidation with elimination of water, *via* an amidation with elimination of alcohol, and *via* a formation of anhydride. The monomers were synthesized from the pyromellitic monoanhydride and *p*-nitroaniline as shown in Scheme 2. Polymerizations were carried out at 330 °C in a mixture of dibenzyltoluene isomers at a concentration of 0.15–0.5%. The solution was stirred until the monomers were entirely dissolved and then the polymerization was continued without stirring in N_2 atmosphere. The solution became turbid in the initial stage of the polymerization, and then the crystals grew with time. After 6 h, the crystals formed in the solution were collected by filtration. Table 1 presents results of the polymerizations.

Yields of the crystals were 67–82% and they increased with the concentration. Fine flowers comprised of needle-like crystals were formed under these conditions. The flower-like crystals obtained from monomer **1a** at a concentration of 0.25% were representatively shown in Fig. 1.

The needle-like crystals grew radially from the center part as petals. The average length, width and thickness of the needle-like crystals were 710, 110 and 20 nm, respectively. The width and the thickness did not change depending on the concentration, but the length slightly increased with the concentration. Chemical structure of the needle-like crystals was measured on FT-IR spectrometry.

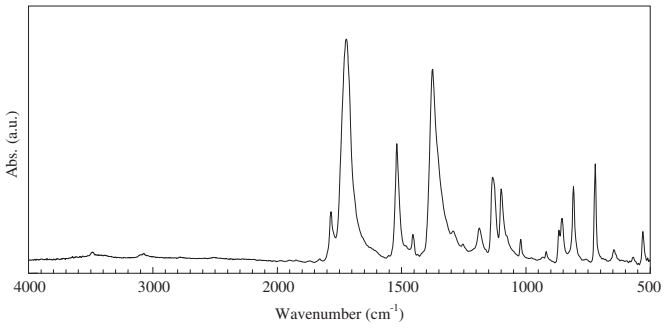

Fig. 2. IR absorption spectrum of PPPI crystals prepared from monomer **1a** at a concentration of 0.25% (run no. 2).

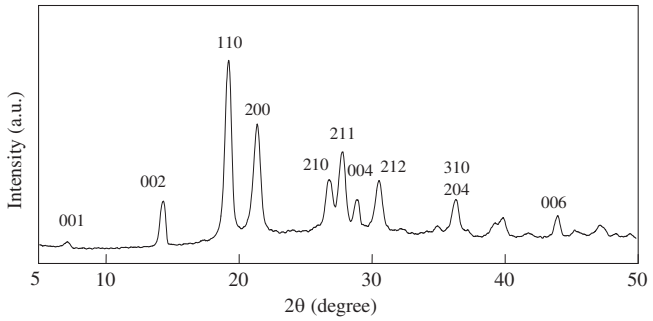

Fig. 3. WAXS intensity profile of PPPI crystals prepared from monomer **1a** at a concentration of 0.25% (run no. 2).

Fig. 2 is the spectrum of the needle-like crystals prepared at a concentration of 0.25% (run no. 2). Characteristic bands of C=O and C–N stretching of imide linkage clearly appeared at 1780, 1720 cm^{-1} and 1380 cm^{-1}, respectively. The bands of an amide linkage and a carboxylic acid were not observed at all. Furthermore, the bands of end-groups such as amino, an ethyl ester, a carboxyl and an anhydride group had disappeared. These results show that high molecular weight PPPI was prepared as a form of the needle-like crystal. In a WAXS intensity profile of the needle-like crystal, refraction peaks were very sharp and diffuse halo caused by an amorphous part could hardly be detected as shown in Fig. 3.

The needle-like crystals possessed quite high crystallinity. All peaks could be assigned by the orthorhombic unit cell of PPPI previously reported [5,17]. To examine the molecular alignment in the crystal, a selected-area electron diffraction was taken as shown in Fig. 1. A diffraction pattern was not a true fiber pattern of cylindrical symmetry and it was like a single crystal pattern. These diffractions could be also assigned according to the orthorhombic unit cell of PPPI and the *c* axis was identical with the direction of the long axis of the needle-like crystal. This result reveals that the PPPI molecules align regularly along the long axis of the crystal. This needle-like morphology with the molecular orientation is desirable to obtain the essential properties as aforesaid.

In order to clarify the structure of the precipitated oligomers, the oligomers recovered from the solution at the initial stage of the polymerization were analyzed by MALDI-TOF mass spectrometry. The spectrum and the peak assignments were shown in Fig. 4 and Table 2. A monomer and oligomers up to tetramers mainly composed

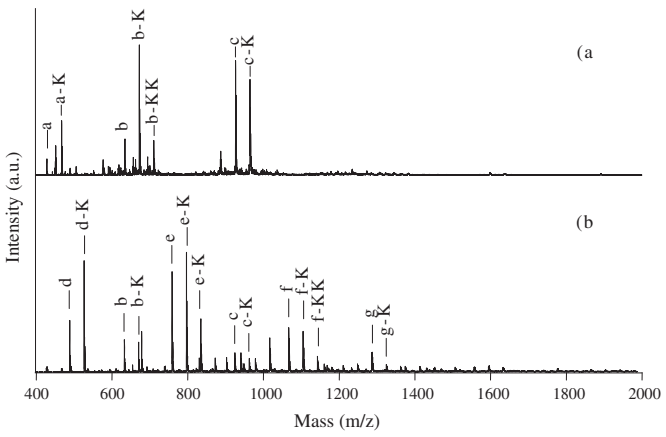

Fig. 4. MALDI-TOF mass spectra of oligomers recovered from solution after 10 min of polymerization of monomer **1a** at a concentration of 0.25%. (a) Dithranol and (b) 3-aminoquinoline were used as matrices. Peak code "a-K" means one potassium adduct of an oligomer assigned by peak code 'a' shown in Table 2.

Table 1
Preparation of PPPI crystals.[a]

Run no.	Polymerization conditions		Yield (%)	Average size of needle-like crystals		T_{10}[c] (°C)
	Monomer	Conc. (%)		Length[b] (nm)	Width (nm)	
1	**1a**	0.15	66.7	640	110	674
2		0.25	73.0	710	110	610
3		0.50	81.6	720	110	598
4	**1b**	0.1	86.0	660	120	653
5		0.25	87.6	810	130	677
6		1.0	94.9	1230	150	687
7		2.0	97.5	1690	210	656

[a] Polymerizations were carried out in a mixture of dibenzyltoluene isomers at 330 °C for 6 h.
[b] Length of needle-like crystals from center part.
[c] Temperatures of 10 wt% loss were measured on a TGA with a heating rate of 20 °C min^{-1}.

of imide linkages were detected. The oligoimides larger than pentamers might be precipitated to form the needle-like crystal and the polymerization proceeds in the crystals to increase molecular weight. In this self-polymerization, both the structural regularity of oligoimide end-groups and the stoichiometric balance between two reactive end-groups are strictly compensated comparing with the polymerization of PMDA and PPDA. The drawbacks for the preparation of the crystals caused by the structural irregularity of oligo (amic acid) were completely conquered. The needle-like crystals, so-called whiskers, of aromatic polymers had been prepared by the crystallization during the isothermal polymerization [18,19]. The spiral growth mechanism caused by the screw dislocation had been proposed as one of the possible mechanisms of the whiskers. Based on the robust similarity of the morphological feature with the molecular alignment, it is likely thought that the PPPI needle-like crystals may be formed according to the mechanism similar to the whisker. As aforesaid, the needle-like crystals grew radially from the center part as petals. The nuclei for needle-like crystals might aggregate, bringing about the flower-like morphology. The formation mechanism of the PPPI needle-like crystal has not been clarified so far, and further study is needed.

Hexyl ester monomer **1b** was polymerized instead of ethyl ester monomer **1a** to investigate the influence of oligomer end-groups on the morphology. Results were also summarized in Table 1. The polymerization of monomer **1b** also afforded the PPPI needle-like crystals at a concentration of 0.15–2.0% with the yield of 86–98% as shown in Fig. 5. The sizes of the crystals prepared at a concentration of 0.1% were averagely 660 nm in length, 120 nm in width and 20 nm in thickness. Higher concentration gave longer the needle-like crystals. The sizes of the crystals prepared at a concentration of 2.0% were averagely 1.69 μm in length and 210 nm in width. The thickness was 20 nm. From the MALDI-TOF mass spectroscopy, the needle-like crystals from monomer **1b** were formed by the crystallization of fully cyclized oligoimides. Based on this fact, the cyclized oligoimides are precipitated to form the crystals, and hence, the morphology of the crystals is not so susceptible to the chemical structure of monomers. The width of the needle-like crystals prepared from monomer **1b** is larger than that from monomer **1a** at the same concentration. The size of the crystals is generally determined by both the size of nucleus, which relates to the degree of super-saturation, and the

Table 2
Structural assignments of peaks detected in MALDI-TOF mass spectra.

Peak code[a]	Mass (m/z)		Structure	n
	Obs.	Calc.		
a	428.78	430.52	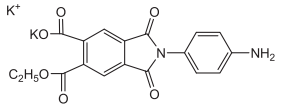	
b	634.75	636.58	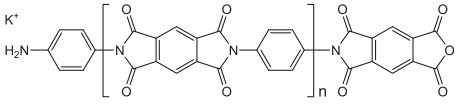	1
c	926.87	926.81		2
d	490.82	490.53	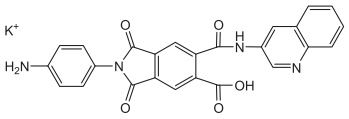	
e	761.06	761.68	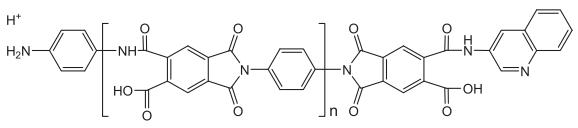	1
f	1069.1	1069.9		2
g	1289.9	1069.9	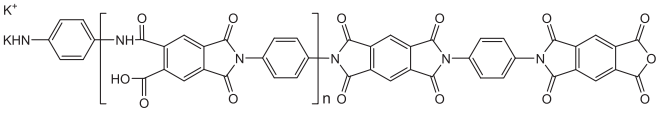	2

[a] Peak codes were shown in Fig. 4.

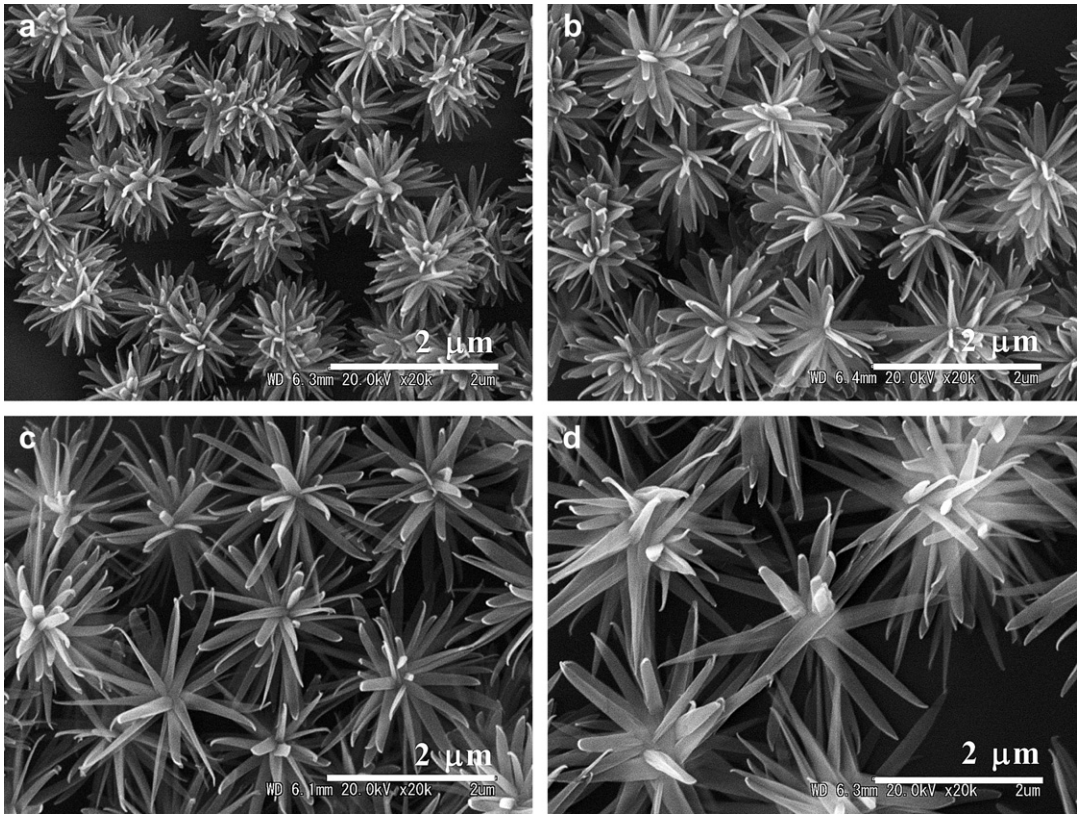

Fig. 5. SEM images of micro-flowers of needle-like PPPI crystals prepared from monomer **1b** at concentrations of (a) 0.1%, (b) 0.25%, (c) 1.0% and (d) 2.0%.

growth rate. It is well known that if the degree of super-saturation is low when the nucleation occurs, the nuclei having larger size are usually formed [19–21]. The larger size of the crystals prepared from monomer **1b** may be attributed to the lower degree of super-saturation of the oligomers prepared from monomer **1b** because of longer alkoxy end-group. The length of the needle-like crystals prepared from monomer **1b** is also larger. This is due to the higher yield of the crystals. The thicknesses of the crystals are almost 20 nm, being not influenced by the structure of monomer and the polymerization concentration. This seems to be attributed to the direction of the crystal growth, and further study is needed to clarify.

Thermal stability of the PPPI needle-like crystals prepared from monomers **1a** and **1b** was estimated on thermogravimetric analysis. Temperatures of 10 wt% loss in N_2 atmosphere were in the range of 598–687 °C as presented in Table 1 and these crystals exhibited excellent thermal stability.

4. Conclusion

Micro-flowers of the PPPI needle-like crystals were prepared by the polymerization of self-polymerizable monomers **1a**, in which the needle-like crystals grew radially from the center part as petals. The average length, width and thickness of the needle-like crystals were 710 nm, 110 nm and 20 nm, respectively. The molecules aligned regularly along the long axis of the needle-like crystal. The polymerization of monomer **1b** also afforded the micro-flowers of the PPPI needle-like crystals at a concentration of 0.15–2.0% with the yield of 86–98%. The sizes of the crystals prepared at a concentration of 0.1% were averagely 660 nm in length and 120 nm in width. Those prepared at a concentration of 2.0% were averagely 1.69 μm in length and 210 nm in width. The thickness was 20 nm. Higher concentration gave longer the needle-like crystals. The size of the flower-like crystals was controllable by the structure of a monomer and the monomer concentration. The micro-flowers possessed high crystallinity and exhibited excellent thermal stability.

Acknowledgment

This work was supported in part by a Grant-in-Aid (No. 21350127) for Scientific Research from the Ministry of Education, Science, and Culture, Japan.

References

[1] Sroog CE. J Polym Sci Macromol Rev 1976;11:161–208.
[2] Bessonov MI, Koton MM, Kudryavtsev VV, Laius LA. In: Polyimides: thermally stable polymers. New York: Consultants Bureau; 1987.
[3] Wilson F, Stenzenberger H, Hergenrother PM. In: Polyimides. New York: Blackie; 1990.
[4] Mittal KL. In: Polyimides, synthesis, characterization, and application. New York: Plenum Press; 1984.
[5] Tashiro K, Kobayashi M. Sen'i Gakkaishi 1987;43:78–91.
[6] Tashiro K. Prog Polym Sci 1993;18:377–435.
[7] Koton MM. Polym Sci USSR 1979;21:2756–67.
[8] Jinda T, Matsuda T. Sen'i Gakkaishi 1986;42:554–9. CAN 106:34436.
[9] Kaneda T, Katsura T, Nakagawa K, Makino H, Horio M. J Appl Polym Sci 1986;32:3133–49.
[10] Kaneda T, Katsura T, Nakagawa K, Makino H, Horio M. J Appl Polym Sci 1986;32:3151–76.
[11] Jinda T, Matsuda T, Sakamoto M. Sen'i Gakkaishi 1984;40:480–9. CAN 102:80106.
[12] Kimura K, Zhuang J, Wakabayashi K, Yamashita Y. Macromolecules 2003;36:6292–4.
[13] Wakabayashi K, Uchida T, Yamazaki S, Kimura K, Shimamura K. Macromolecules 2007;40:239–46.
[14] Kimura K, Nakajima D, Kobashi K, Kohama S, Uchida T, Yamashita Y. Polym J 2005;37:471–9.
[15] Kimura K, Kurihara Y, Ohmori H, Kohama S, Yamazaki S, Yamashita Y. Polymer 2007;48:3429–36.

[16] Gies AP, Nonidez WK, Anthamatten M, Cook RC, Mays JW. Rapid Commun Mass Spectrom 2002;16:1903–10.
[17] Baklagina YG, Milevskaya IS, Yefanova NV, Sidorovich AV, Zubkov VA. Vysokomol Soyed 1976;A18:1235–42. CAN85:78555.
[18] Yamashita Y, Endo S, Kimura K. Makromol Chem Rapid Commun 1988;9:687–91.
[19] Yamashita Y, Kimura K. In: Polymeric materials encyclopedia. Boca Raton: CRC Press; 1996. p. 8707–13.
[20] Sarker AK, Kimura K, Yokoyama F, Yamashita Y. High Perform Polym 2000;13:351–64.
[21] Kimura K, Sarker AK, Ohmori H, Yamashita Y. J Appl Polym Sci 2003;87:1129–36.

Polymer 52 (2011) 844–853

Contents lists available at ScienceDirect

Polymer

journal homepage: www.elsevier.com/locate/polymer

Existence of microdomain orientation in thermoplastic elastomer through a case study of SEBS electrospun fibers

Wonchalerm Rungswang [a], Masaya Kotaki [b], Takuma Shimojima [c], Go Kimura [c], Shinichi Sakurai [c,**], Suwabun Chirachanchai [a,*]

[a] The Petroleum and Petrochemical College, Chulalongkorn University, Soi Chula 12, Phyathai Road, Pathumwan, Bangkok 10330, Thailand
[b] Department of Advanced Fibro-science, Kyoto Institute of Technology, Matsugasaki, Sakyo-ku, Kyoto 606 8585, Japan
[c] Department of Macromolecular Science & Engineering, Graduate School of Science and Technology, Kyoto Institute of Technology, Matsugasaki, Sakyo-ku, Kyoto 606 8585, Japan

ARTICLE INFO

Article history:
Received 20 August 2010
Received in revised form
7 December 2010
Accepted 12 December 2010
Available online 21 December 2010

Keywords:
Thermoplastic elastomer
Electrospun fiber
Microdomain orientation

ABSTRACT

Although the microdomains of polymeric systems including the thermoplastic elastomers in the as-spun electrospun fiber were reported, the orientation of microdomains has not yet been well clarified. The present work shows an existence of microdomain orientation through a case study of a well-aligned electrospun fibers of polystyrene-block-poly(ethylene-co-1-butene)-block-polystyrene triblock copolymer (SEBS) obtained from an electrospinning unit equipped with a rotational disk fiber-collector. Two-dimensional small-angle X-ray scattering (2D-SAXS) patterns of the as-spun electrospining SEBS fibers show elliptical and four-point patterns suggesting an orientation of distorted and fragmented lamellar microdomains. The electrospun fibers obtained from a low rotational disk collector speed (31.5 m/min) exhibits a significant microdomain distortion whereas the fibers obtained from high take-up velocities (310 m/min, 620 m/min, and 1240 m/min) show higher fragmented-microdomain stretching. By annealing the electrospun fibers, the fibers develop an isotropic SAXS pattern with traces of the remained anisotropic orientation. Based on the above mentioned evidences in SEBS, the present work, for the first time, clarifies that the as-spun thermoplastic elastomers fibers show not just a simple microdomain as used to be observed by transmission electron microscope (TEM) but rather with orientation which can be confirmed by SAXS.

1. Introduction

For decades, the uses of thermoplastic elastomers (TPEs) have been increasing due to advantages of thermoplastic and elastomeric properties related to high strength and toughness. At present, the development of TPEs has reached a certain level where a variety of TPE copolymers are available [1,2]. Polystyrene-b-poly(ethylene-co-1-butene)-b-polystyrene triblock copolymer (SEBS) is one of the earliest developed TPEs and is used in daily-use tools, automotive parts, construction adhesives, and so on, because of their superior weathering resistance resulting from the hydrogenation of unsaturated chemical linkages [3–5]. The SEBS consists of a hard block (polystyrene block, or S block) and a soft block (poly(ethylene-co-butene) block, or EB block). This material is a typical block copolymer with self-aggregation of the internal structure. Since the solubility parameters of these two blocks are significantly different, microphase separation of the S microdomains in the EB matrix is generated, especially when the styrene content is less than 30%.

Up to present, various microphase-separated morphologies of polystyrene based block, mostly in films, have been reported, for example, spherical [6], cylindrical [7,8], and lamellar shape [9]. The morphology of microdomains are found to be depending on several factors, such as polystyrene weight fraction [10], solvent type [11,12], and temperature [13,14], etc. Several examples of TPEs in film form have been reported about microdomain distortion and its orientation including how microdomain induced specific mechanical properties [15,16].

Electrospinning is known as a technique for fabricating ultrafine fiber, ranging from nano- to micro-scale via electric force [17]. In the case of TPEs, electrospinning might be an effective way to utilize an intense stress in a confined geometry to control the microdomain orientation as seen in thermoplastic case. For example, Fong and Reneker reported a small and peculiar shape of phase-separated domain in the electrospun fibers of a polystyrene-b-polybutadiene-b-

* Corresponding author. Tel.: +66 2 218 4134; fax: +66 2 215 4459.
** Corresponding author. Tel.: +81 75 724 7864.
E-mail addresses: shin@kit.ac.jp (S. Sakurai), csuwabun@chula.ac.th (S. Chirachanchai).

0032-3861/$ – see front matter © 2010 Elsevier Ltd. All rights reserved.
doi:10.1016/j.polymer.2010.12.019

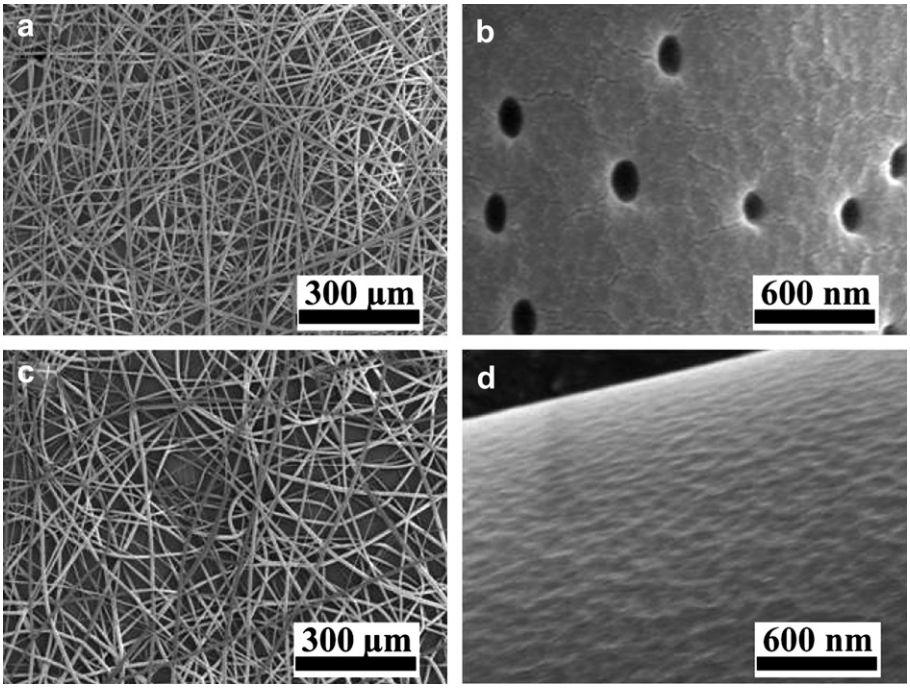

Fig. 1. SEM micrographs of SEBS electrospun microfibers obtained from an accelerating voltage of 20 kV: (a) and (b) under 30% RH; (c) and (d) under 23% RH.

polystyrene triblock copolymer (SBS) due to high evaporation rate of volatile solvents and at that time the polymer chain mobility was limited to end up with a segregation in a thermodynamically non-equilibrated microdomain structure [18]. Ma et al [19]. and Kalra et al., [20], showed the relevant results, especially a small and disordered structure of the microdomains, which were termed as the non-equilibrium state of microphase separation in electrospun TPEs, as evidenced from transmission electron microscope (TEM) images.

Up to present the lamellar microdomains and their orientation of the TPE films have been reported and it seems that the microdomains of the films are similar to those of the fibers. In the case of SEBS film, it was reported that the microdomain orientation of SEBS was due to shear force [21]. For fibers, although electrospinning is a technique that favors the chain alignment to give orientation of the microdomain morphology, to our best knowledge there is no report related to microdomain orientation in the as-spun fiber. Most dealt with the electrospun fibers with irregular microdomain which an annealing and stretching process further develops fiber orientation.

Surprisingly, when we prepared the SEBS fibers by using an electrospinning system equipped with a rotational disk collector which can control the speed of the fiber-collector followed by a careful morphology analysis based on SAXS patterns, we found anisotropic microdomain orientation existed in our SEBS. In other words, the results confirm that there is microdomain orientation in the TPEs fibers. The present work, thus, aims to show an existence of microdomain orientation in TPEs through a case study of electrospun SEBS which the factors involved in microdomain orientation in the fibers such as the control of fiber alignment via an electrospun system equipped with disk collector and the annealing process were also taken in our consideration.

2. Experimental section

2.1. Materials

SEBS triblock copolymer (specification: 32 wt % styrene content, Mw = 80 000 g/mol and Mn = 50 000 g/mol, and melt flow

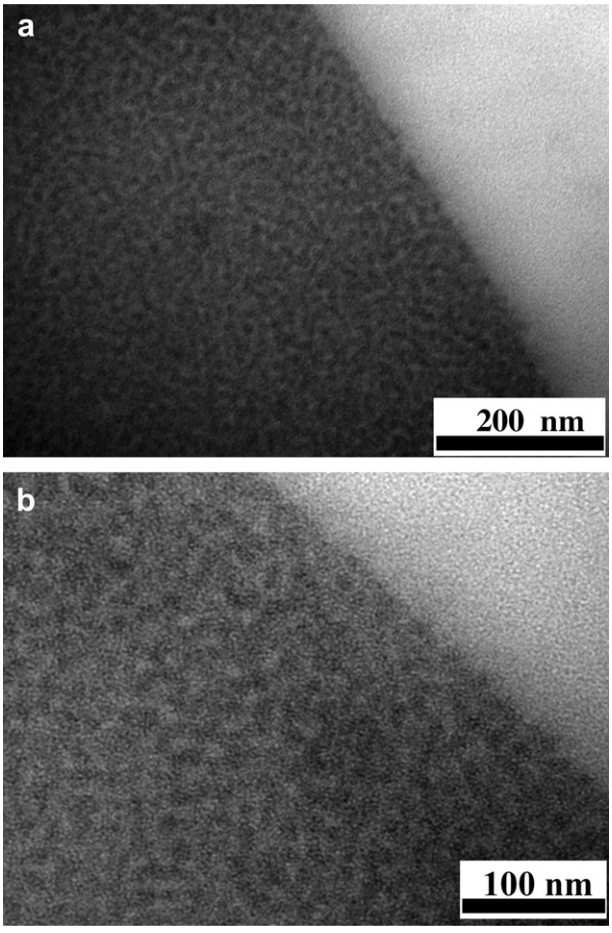

Fig. 2. Cross-sectional TEM micrographs of SEBS electrospun fibers collected at a 1240 m/min take-up velocity at: (a) 25 000 times and (b) 40 000 times for magnification. PS microdomains stained with ruthenium tetroxide were appearing dark.

index = 5 g/10°min (230 °C for 2.16 kg)) was a gift from Asahi Kasei Chemicals Cooperation, Japan. Chloroform and toluene were purchased from Nacalai Tesque, Inc., Japan. All chemicals were used without further purification.

2.2. Preparation of SEBS film

SEBS solutions (18% w/w) were prepared by dissolving SEBS in chloroform/toluene (80/20 wt/wt) mixed solvent. The homogeneous solution was cast on the teflon sheet, and dry it at room temperature for 7 days.

2.3. Preparation of SEBS electrospun fibers

SEBS solution (18% w/w) was prepared by dissolving SEBS in chloroform/toluene (80/20 wt/wt) mixed solvent. The homogeneous solution obtained was electrospun to fibers by using a Nanon Electrospinning Setup (MECC Co., Ltd., Japan) equipped with an originally

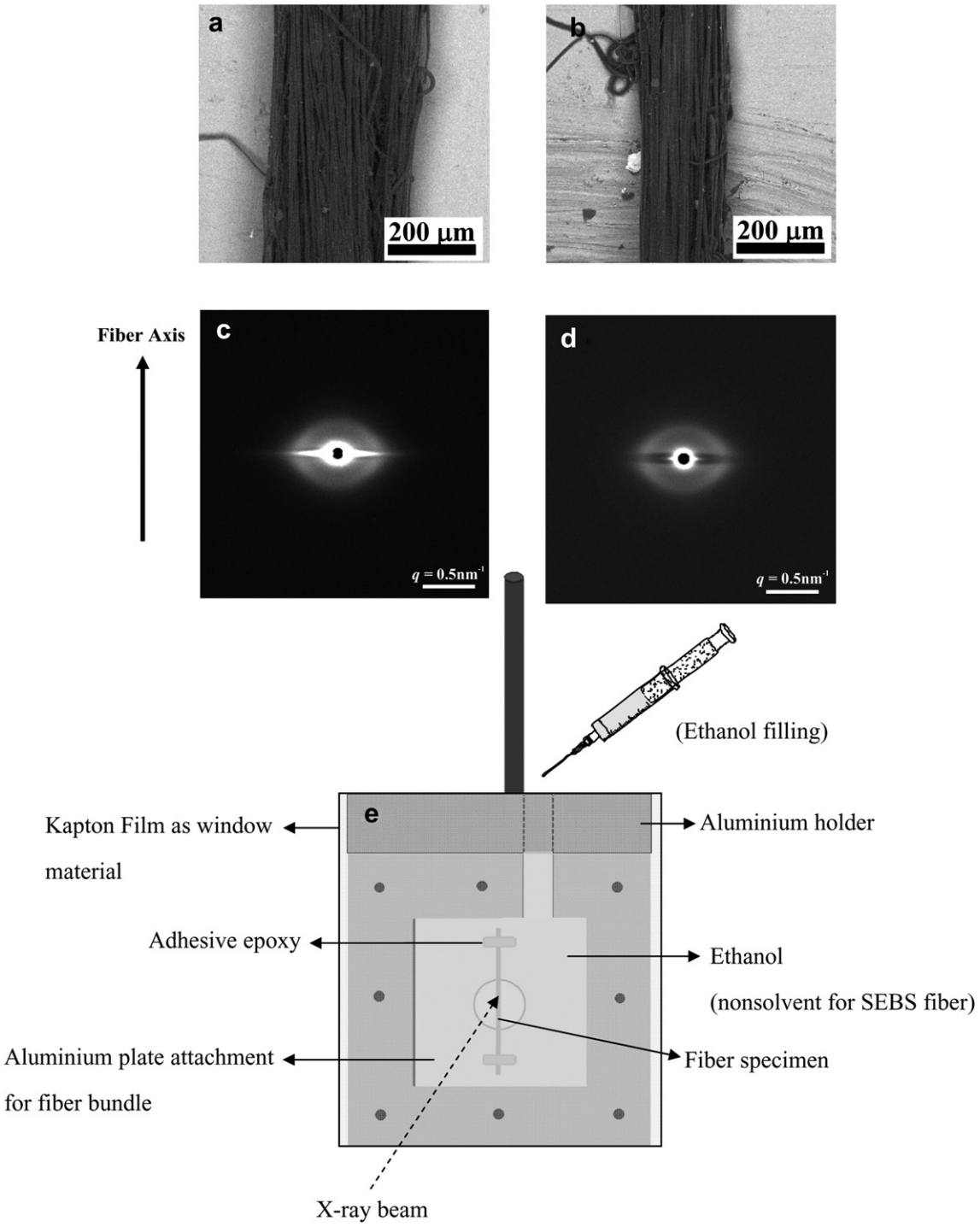

Fig. 3. TM micrographs of SEBS electrospun fibers collected at (a) 31.5 m/min, and (b) 1240 m/min; and 2D-SAXS patterns of SEBS electrospun fibers collected at 31.5 m/min for: (c) in an air chamber, and (d) in ethanol-filled chamber; and (e) illustration of ethanol-filled chamber.

designed rotational disk collector. The spinning conditions were: accelerated voltage, 20 kV; volumetric flow rate, 0.5 mL/h; and tip-to-collector distance, 15 cm. The fibers were collected onto an aluminium foil. The take-up velocity of the rotational disk collector was varied, i.e., 31.5 m/min, 310 m/min, 620 m/min and 1240 m/min. The relative humidity for spinning was in the range of 30–32%.

2.4. Characterization

The surface of the SEBS electrospun fibers was observed by a JEOL JSM-5200 scanning electron microscope, and the average fiber diameter was determined by ImageJ Software. The fiber alignment appearances were observed by a Hitachi-TM3000 Tabletop Microscope (TM) with accelerating voltage of 5 kV. TEM observation, the fibers were stained with ruthenium tetroxide vapor (RuO_4) and microtomed at room temperature before taking the images by a Hitachi TEM Zero H-7650 with accelerating voltage of 100 kV. 2D-SAXS measurements were carried out at the RIKEN structural biology beamline I (BL45XU) SPring-8, Hyogo, Japan. The 2D-SAXS patterns (300 mm × 300 mm area) were recorded using a RIGAKU R-AXIS IV++ equipped with an imaging plate detector. The X-ray wavelength, λ, was tuned at $\lambda = 0.10$ nm, and the q values defined by $q = (4\pi/\lambda) \sin(\theta/2)$ (θ: scattering angle) were calibrated by chicken tendon collagen having the spacing of 65.3 nm.

3. Results and discussion

In order to control the microdomain structures in the SEBS fibers, the fibers were prepared under a variation of fiber stretching force based on the adjustable take-up velocity (from 31.5 m/min to 1240 m/min). To simplify our work, the electrospinning parameters were preliminary studied to select the optimal conditions. The optimal fiber spinning condition was; SEBS solution (80:20/chloroform:

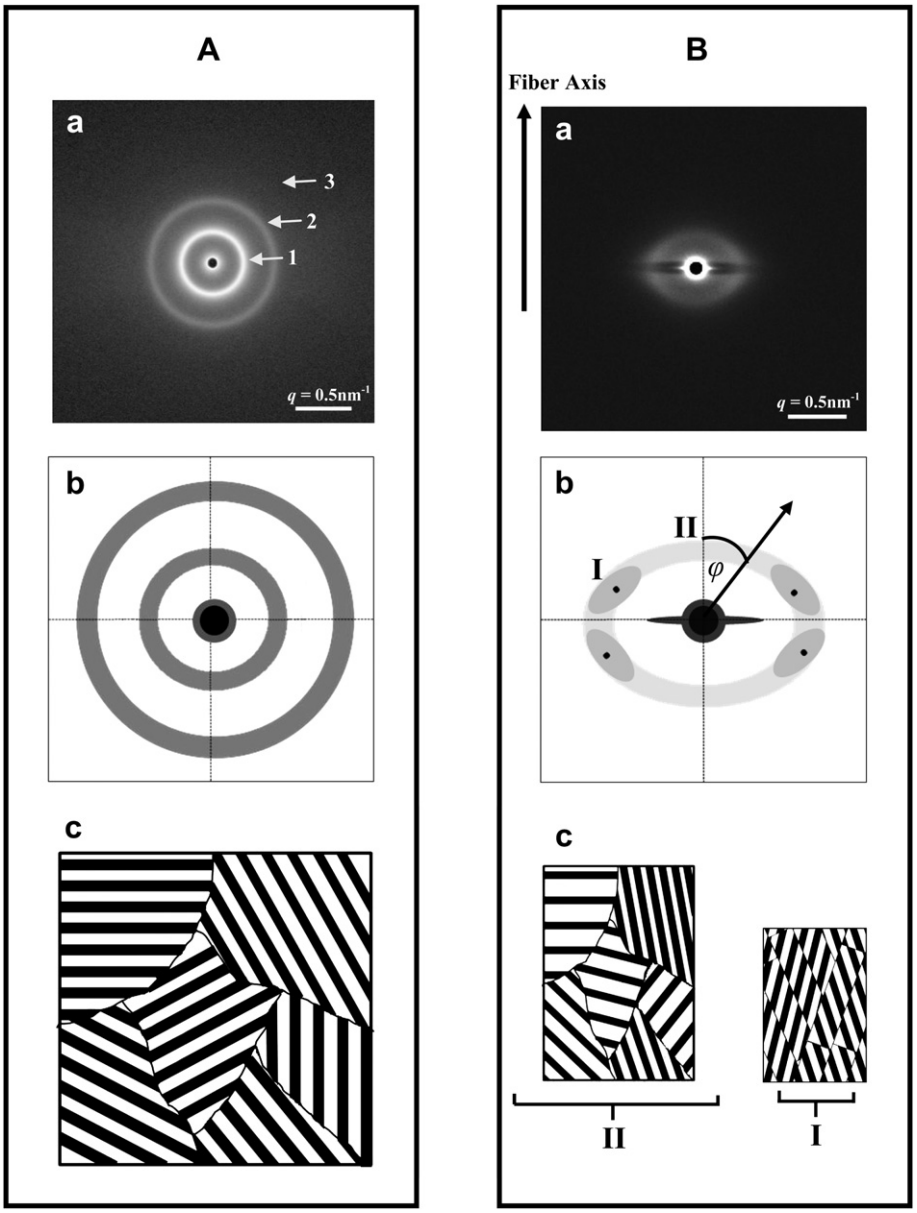

Fig. 4. (a) 2D-SAXS patterns in a logarithmic scale for the scattering intensity (b) schematic 2D-SAXS patterns, and (c) possible schematic models to represent (a) for SEBS film (A), and SEBS electrospun fibers collected at 31.5 m/min (B).

toluene) 18% w/w under an accelerated spinning voltage of 20 kV. The above mentioned condition gives beadless fibers with a 6.0 μm diameter (Fig. 1(a)). However, the fibers contain some pores with diameters of 150–240 nm (Fig. 1(b)) which could be eliminated after the relative humidity was adjusted to be 23% (Fig. 1(c, d)).

3.1. Microdomain morphology

Fong and Reneker reported confined microdomains in electrospun nanofiber. The report also showed an irregular shape of the microdomains under an elongational flow [18]. Kalra et al. pointed out that the irregular microdomains were inevitable as it was

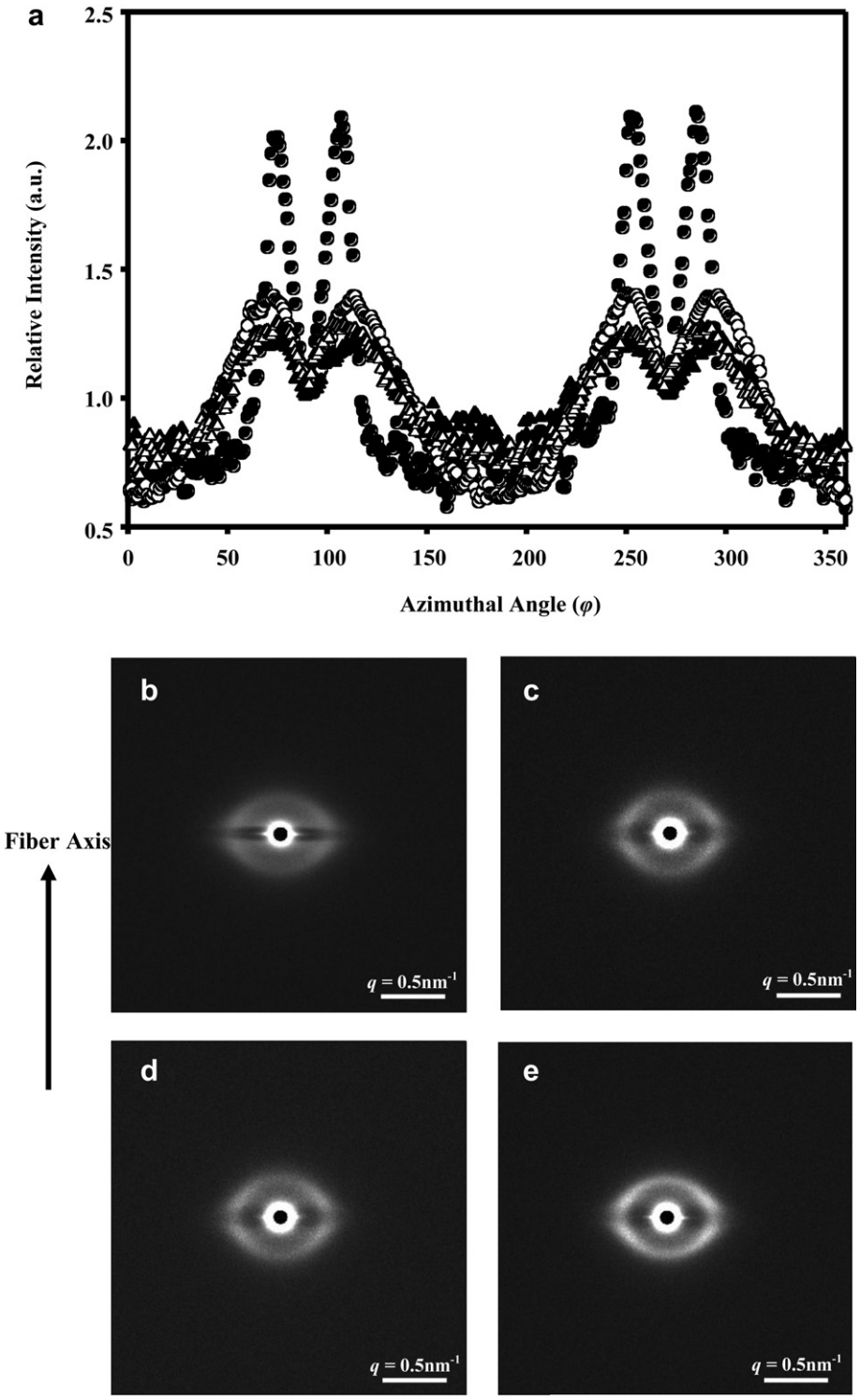

Fig. 5. 2D-SAXS patterns of the fibers collected at: (a) 31.5 m/min, (b) 310 m/min, (c) 620 m/min, (d) 1240 m/min; and (e) intensity distribution as a function of the azimuthal angle φ along the elliptic peak (azimuthal scan) of the SEBS electrospun fibers collected at 31.5 m/min (●), 310 m/min (○), 620 m/min (▲) and 1240 m/min (△).

Table 1
Peak positions, q_0 *and* q_{90}, and lamellar repeating period for φ[c] $= 0°$ and $\varphi = 90°$, respectively, obtained from 2D-SAXS patterns of SEBS electrospun collected at various take-up velocities compared with those of bulk film.

Sample	Peak positions (nm^{-1})[a]		*r* ratio (q_{90}/q_0)	Lamellar repeating period (nm)[b]	
	q_0 at azimuthal angle $\varphi = 0°$	q_{90} at azimuthal angle $\varphi = 90°$		Azimuthal angle $\varphi = 0°$	Azimuthal angle $\varphi = 90°$
Cast film	0.243	0.239	1.02	25.9	26.4
Electrospun at 31.5 m/min	0.286	0.355	1.24	21.9	17.7
Electrospun at 310.0 m/min	0.305	0.350	1.15	20.6	17.9
Electrospun at 620.0 m/min	0.298	0.349	1.17	21.1	18.0
Electrospun at 1240.0 m/min	0.290	0.341	1.17	21.6	18.4
Anneale[d] electrospun at 620.0 m/min	0.274	0.281	1.03	22.9	22.3
Annealed electrospun at 1240.0 m/min	0.274	0.284	1.02	22.9	22.1

[a] measured at the first-order scattering maximum.
[b] calculated by Bragg's equation.
[c] φ azimuthal angle with respect to fiber axis for the 2D-SAXS patterns.
[d] annealing at 170 °C for 3 h.

generated via a non-equilibrium state of fiber spinning. This point is different from the case of film where regular microdomains obtained from an equilibrium state [20]. Ma et al. demonstrated a long-range order of lamellar and spherical microdomain structures for triblock and diblock copolymers, respectively, by using a two-fluid coaxial electrospinning technique to maintain the shape of fiber during annealing [19]. Here, an attempt to identify the microdomains in the fibers was made by using a cross-sectional microtoming TEM. As shown in Fig. 2(a),(b), small and irregular microdomains are observed which appear to be similar to those in previous reports [18–20].

The microdomain structure was further investigated by using 2D-SAXS technique. In this step, the fibers were carefully aligned during the fibers deposited on the disk collector and the alignment was confirmed by TM micrographs (Fig. 3(a)) before carrying out 2D-SAXS measurement. It should be noted that the fibers alignment appearances obtained from the high take-up velocity (Fig. 3(a)) and the low one (Fig. 3(b)) are similar. Fig. 3(c) shows a 2D-SAXS pattern of SEBS with intense streaks ascribed to the total reflection of X-ray from the surface of fibers. Fig. 3(e) shows a sample chamber attachment in which a particular solvent was filled. As the electron density of ethanol is close to that of the SEBS

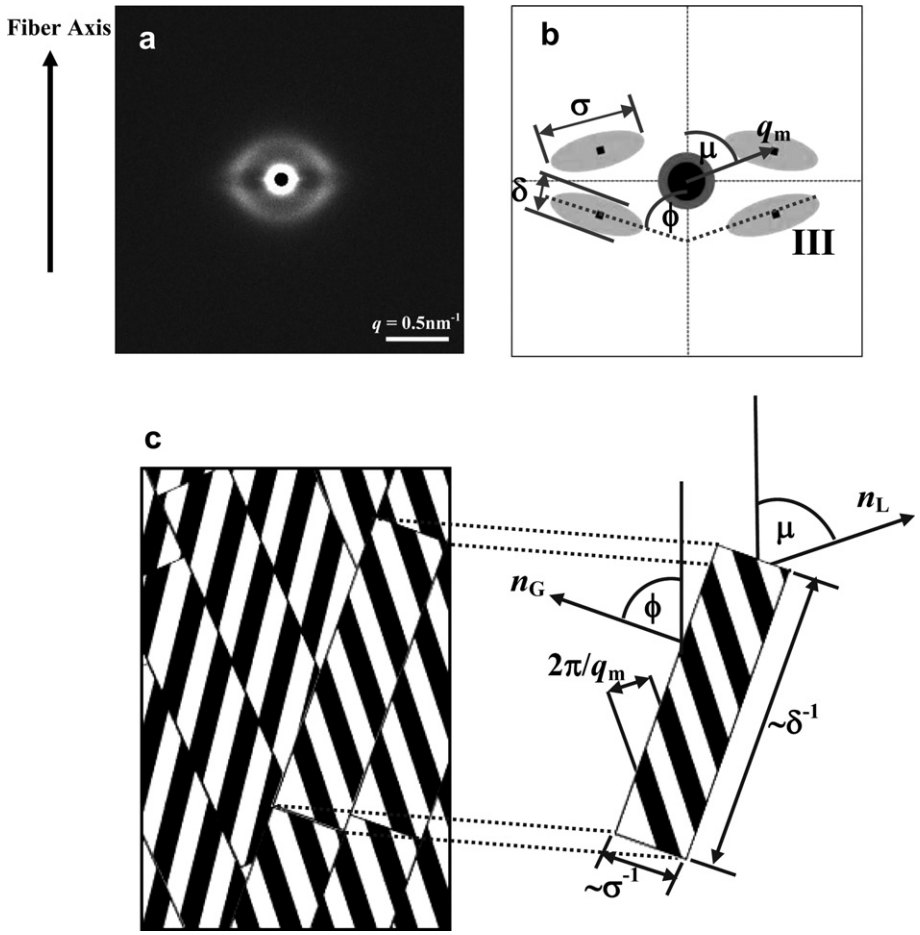

Fig. 6. 2D-SAXS patterns of the fibers collected at (a) 620 m/min, (b) schematic draw including structural parameter, and (c) possible lamellar-microdomain models including structural parameter.

fibers, the total reflection was almost eliminated. Fig. 3(d) shows a 2D-SAXS pattern after applying the contrast–matching method using an ethanol chamber (see more discussion in Fig. 4(B)(a)). This means that by using this ethanol chamber, we can observe microdomains in details without the disturbance of streaks.

3.2. Microdomain orientation

The electrospun fibers were handled with care to avoid spoiling the microdomains and were set in the ethanol-filled chamber for 2D-SAXS measurements. There might be some differences in orientation level based on the plural fibers containing in a bundle of fibers, however, it should be pointed out here that the results obtained represented the average characters of fiber alignment regarding to those plural fibers. In other words, it is presumed that all fibers in each bundle have more or less identical internal structure. Fig. 4(B)(a) shows a 2D-SAXS pattern revealing microdomains with orientation, which is dramatically different from that of the film. In other words, the result not only shows the microdomain formation as reported previously [18,19] but also for the first time, unveils the existence of short-range ordered microdomains and the microdomain orientation of thermoplastic elastomer in the as-spun electrospinning fiber. Fig. 4(B)(b) highlights two important aspects, i.e., (i) a relatively intense four-spot pattern (pattern I), and (ii) a weak elliptical peak (pattern II). The four-spot pattern suggests microdomain arrangement [22,23] whereas elliptical pattern implies microdomain distortion [25,26] as can be schematically drawn in Fig. 4(B)(c). The four-spot pattern, so-called herringbone structure, might come from the fracture of the glassy lamellar microdomains, and/or clusters of the tiny grains oriented obliquely to the stretch direction.

To clarify the four-spot pattern, an intensity distribution along the elliptical peak as a function of the azimuthal angle, φ, was traced (Fig. 5(a)). Here, φ is considered in clockwise starting from $\varphi^{\circ}=^{\circ}0$ at the meridional direction pointing upward (parallel to the fiber axis). The azimuthal scans for the fibers obtained show four-spot pattern where the peaks appear at about 65°, 115°, 245° and 295°. This implies important information, i.e., an existence of microdomain orientation. In fact, this type of four-spot pattern is exactly similar to those reported by Séguela and Prudhomme for the fractured lamellar microdomains of the stretched SBS triblock copolymer film resulting in microdomain orientation [24]. In other words, their results support us about the microdomain orientation in our SEBS electrospun fibers. It should also be noted that the fibers obtained from different rotational collector speeds show a similar four-spot pattern with the same peak positions. This confirms that the microdomain orientation exists in all cases of the fibers.

Fig. 4B(a) and (b) clearly show that the repeating period is maximum in the lamellar direction perpendicular to the fiber axis and it decreases with an increase in φ. This refers to the elliptical pattern (pattern II). Shin et al. and Mita et al. reported that the weak elliptical pattern indicated a distortion of the lamellar microdomains [25,26]. In addition, a dark streak (Fig. 4(B)(a)) is observed in the equatorial direction which is similar to those reported by Kume et al. [27] and Moses et al. [28]. Although microdomain orientation may occur in various directions, the dark streak in the direction perpendicular to the fiber axis indicates the lack of the microdomain oriented in the direction parallel to the fiber axis.

The microdomain orientation in electrospun fibers might be due to the stress field while the fibers were drawn. Therefore, we speculated that the microdomains might form in the first step when the polymer solution was solidified in the spin line. At that time an orientation, which depends on the stress field applied to the fibers, might generate. This can be seen from an elliptic SAXS pattern. As the stress was more intense, the lamellar microdomains

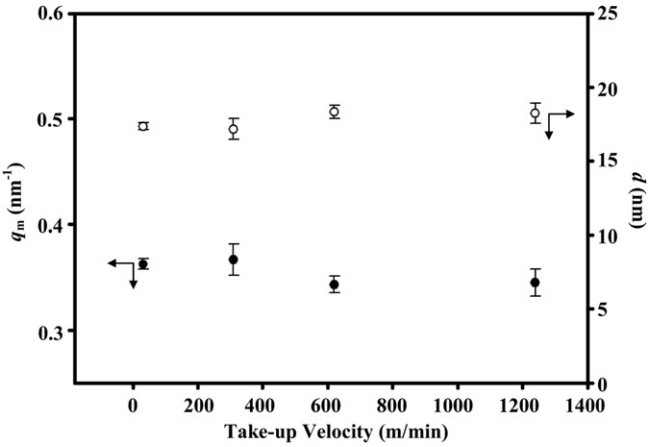

Fig. 7. Parameters q_m (the magnitude of q vector at the peak), and d (lamellar repeating periods) of the SEBS fibers collected at various take-up velocities.

were aligned parallel (or almost parallel) to the fiber axis, and, at a certain stress level, the microdomains were fractured resulting in the lack of parallel-lamellar microdomains. As a consequence, the fractured lamellar oriented obliquely to the fiber axis to give four-spot pattern in 2D-SAXS pattern.

It should be noted that in most cases, the plate collector is used to collect the electrospun fibers. As the fibers are randomly spread on the collector, there is no alignment. However, in our case, the fibers were carefully collected on a rotational disk collector with a controllable rotating speed. This initiates the fibers to align in the rotating direction and allowed us the morphological analysis in details, especially by using 2D-SAXS.

It comes to our question whether an increase in rotational speed relates to an increase in microdomain orientation or not. Therefore, the fibers were collected at various take-up velocities, i.e., 31.5 m/min, 310 m/min, 620 m/min and 1240 m/min, and the fiber diameter obtained were found to be 6.3 μm, 4.6 μm, 3.3 μm and 2.5 μm, respectively. Surprisingly, the fibers collected at the lowest rotational disk speed (31.5 m/min, Fig. 5(a)) shows the most intense peaks as compared to the fibers collected from other high rotational speeds (Fig. 5(b)–(d)).

It is clear that although the take-up velocities of the rotational disk collector were varied, the 2D-SAXS patterns of each fiber are similar. When the elliptical patterns were considered carefully, it was found that the SEBS electrospun fibers collected at the lowest take-up velocity (31.5 m/min) shows the most significant elliptical shape. From Fig. 5(b)–(e), the first-order scattering maxima at

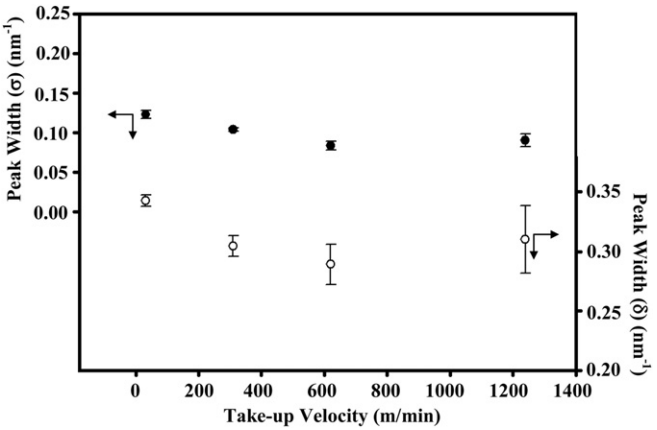

Fig. 8. Peak width σ, and δ of the SEBS fibers collected at various take-up velocities.

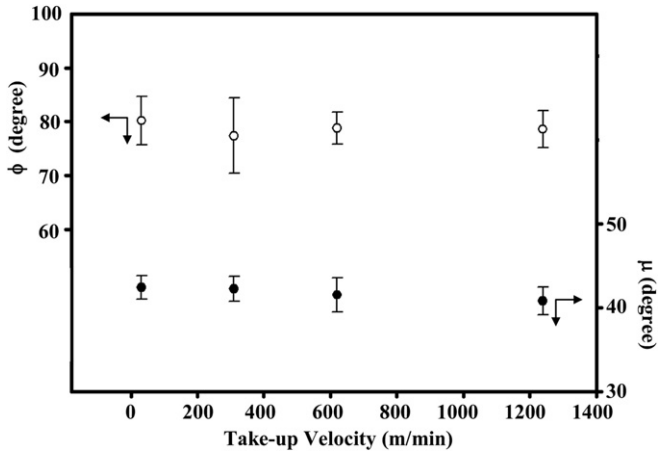

Fig. 9. Angle μ, and φ of the SEBS fibers collected at various take-up velocities.

$\varphi = 0^\circ$ and $\varphi = 90^\circ$ for q_0 and q_{90}, respectively, were measured and summarized in Table 1. The $r\,(=q_{90}/q_0)$ value quantifies the extent of distortion in the lamellar repeating distance. For the cast film, the r ratio is about one, indicating an isotropic lamellar. On the contrary, the r values for the electrospun fibers are in the range of 1.15–1.24 indicating anisotropic lamellae. Especially, the electrospun fibers collected at 31.5 m/min show the highest r value (1.24), confirming the most distorted lamellae. However, it should be noted that the r values of all samples are close, not that much shift from one (as small as 1.3 nm or even less than this).

Based on the herringbone structure, five structural parameters from 2D-SAXS pattern were further evaluated [22]. Fig. 6 shows schematic explanations for those parameters in both 2D-SAXS pattern (Fig. 6(b)) and lamellar-microdomain model (Fig. 6(c)). The magnitude of q vector, which can be calculated from the repeating lamellar period (d) as $d = 2\pi/q_m$, is q_m. The widths of the elliptical spots are assigned to the parameters σ and δ, as shown in Fig. 6(b). These parameters are inversely proportional to the size of a lamellar grain as shown in Fig. 6(c). The angle between the q vector and fiber axis is assigned to the parameter μ while an oblique angle of the elliptical spot with respect to the fiber axis is assigned to φ. For the lamellar-microdomain model, μ and φ are ascribed to the angle between the fiber axis and the vector normal to lamellar microdomains (n_L) and the one normal to the grain (n_G), respectively.

As shown in Fig. 7, the q_m value slightly decreases, or in other words, d increases, as the take-up velocity increases. The stretching of lamellar microdomains can also be confirmed from the decreases of σ and δ. Fig. 8 shows that when the take-up velocity increases, the grain size of the lamellae increases. This can be schematically illustrated in Fig. 10. It should be noted that the decrease in q_m, and the increases in σ and δ with the take-up velocity are not that significant and at the same time the parameters μ and φ are maintained at about 40° and 80°, respectively (Fig. 9). These quantitative analyses confirm the existence of orientation in microdomain, though it is slightly. This leads to the point how we can improve orientation of SEBS electrospun fibers which will be reported in our up-coming article.

Here, we propose two possible factors to control the microdomain distortion and orientation in the as-spun electrospinning fiber upon applying shear force from rotational-disk collector. The first one is the shearing factor which promotes the microdomain stretching and orientation. When the fibers were collected at high speed, the fibers were stretched as a consequence of the shear stress at the first

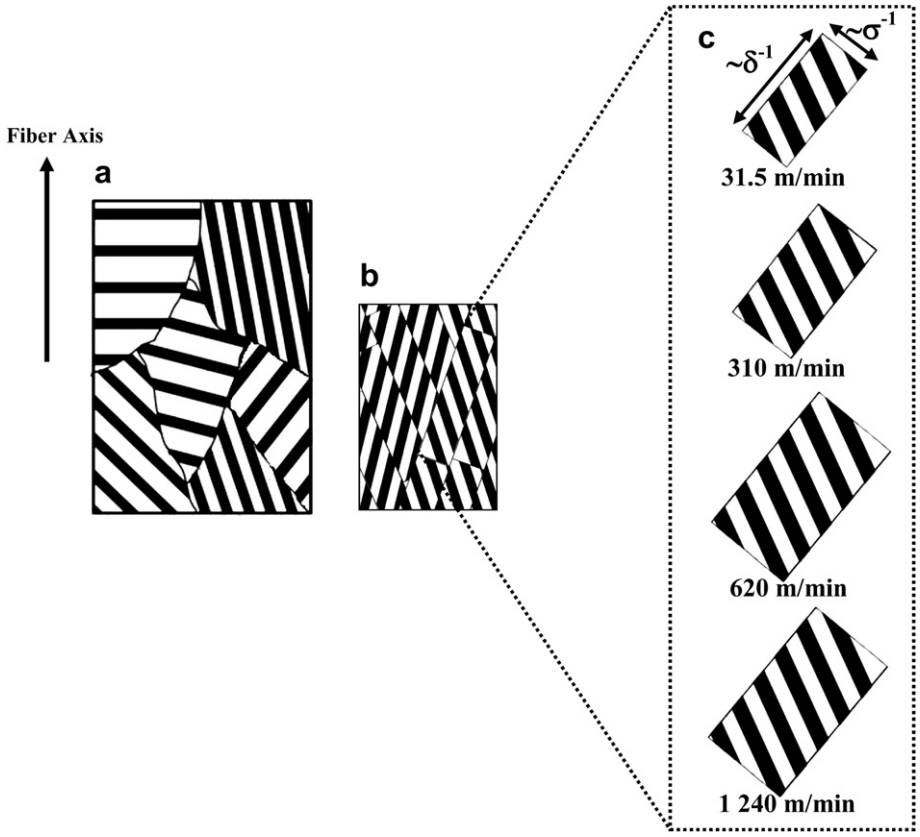

Fig. 10. Possible models of: (a) distorted-lamellar microdomains, (b) fragmented-lamellar microdomains in the SEBS fibers at various take-up velocities, (c) schematic grain size (δ^{-1} and σ^{-1}) regarding to take-up velocities.

contact between the collector and the spinning jet. This brought in the reduction of the fiber diameters, microdomain distortion and orientation. Therefore, we could observe the stretching of the herringbone structure only when the fibers were collected from the take-up velocity less than 620 m/min as summarized in Fig. 10. The second one is the solvent evaporation during spinning which causes vitrification of PS microdomains. The time for solvent evaporation of the fiber obtained via the high rotational collector speed is short as compared to the one via the low collector speed. In the case of the lowest take-up speed, 31.5 m/min, during the fibers were stretched on the rotational disk collector; the solvent evaporation might be completed. As a result, we can observe the most significant lamellar distortion from the fibers obtained from the lowest take-up speed (31.5 m/min).

To conclude the development of the lamellar microdomains in the as-spun fibers, the lamellar-microdomain model was schematically drawn in Fig. 10. Fig. 10(a) shows distorted lamellar microdomains to represent elliptic pattern, whereas Fig. 10(b) shows fragmented-lamellar microdomains, herringbone structure, to represent four-point pattern. Here, the take-up velocity induced significant differences in size of fragmented-lamellar grain. Fig. 10(c) is a schematic to emphasize how the grain size (δ^{-1} and σ^{-1}) is increased as the take-up velocity increased.

To examine the effect of thermal annealing, the 2D-SAXS patterns for the thermally annealed fiber samples were measured. In order to avoid the melt fracture of the fibers during thermal annealing, the fibers were coated with epoxy followed by annealing at 170 °C for 3 h. Fig. 11 reveals the lamellar microdomains retained after annealing. Sakurai et al. reported a microdomain orientation in crosslinked SBS film under uniaxial stretching at a temperature above its Tg (130 °C) as analyzed by SAXS pattern [16]. In our case, adhesive epoxy was used to fix the fiber dimension, so that some extent of the maintaining force against shrinkage would be anticipated. It should be noted that the electrospun fibers were annealed without any physical constraints such as clamping. Fig. 11(a) shows the 2D-SAXS pattern of the fibers obtained from the condition using the disk collector speed at 1240 m/min followed by thermal annealing. The annealing brings in the isotropic 2D-SAXS pattern with traces of a pair of distinct spots in the equatorial direction. This suggests an orientation of the microdomain lamellae parallel to the fiber axis which was once existed in the fiber. Thermal annealing also diminishes anisotropy in the lamellar repeating distance,

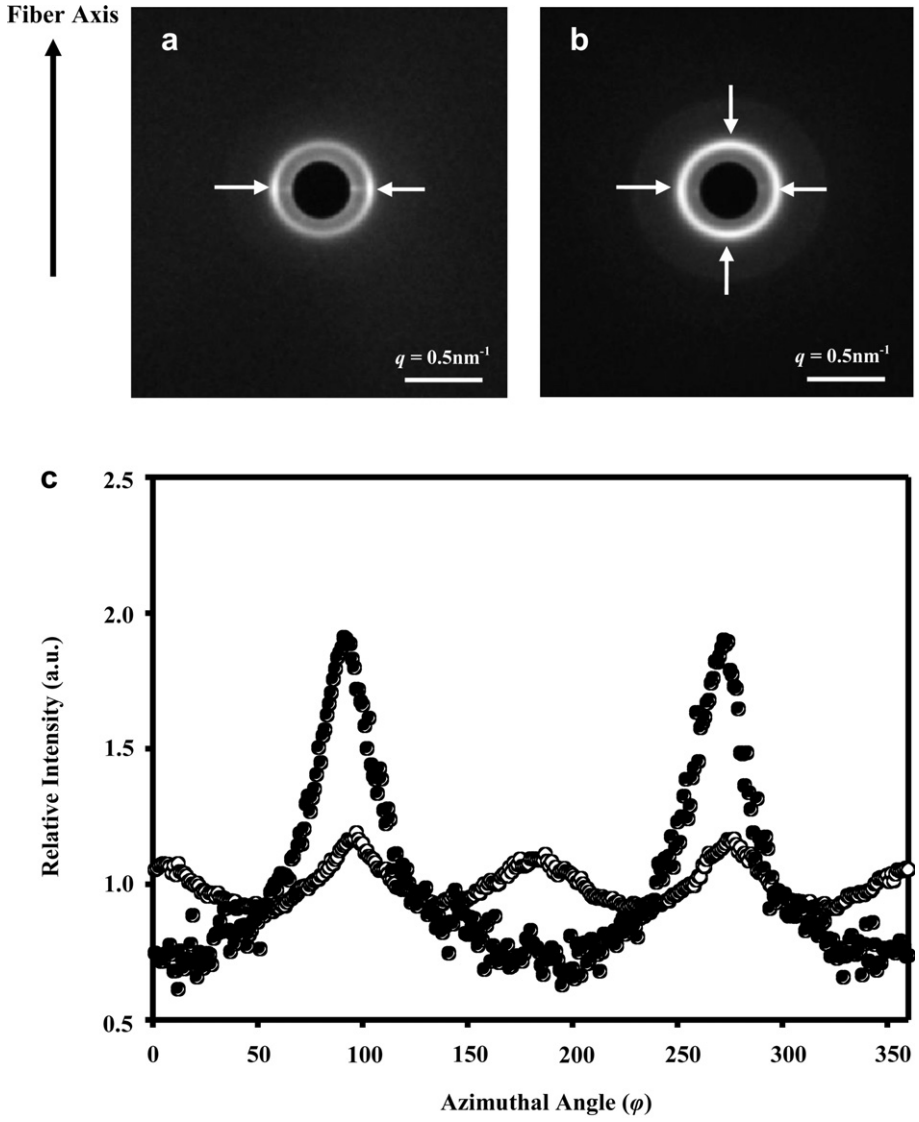

Fig. 11. 2D-SAXS patterns in a logarithmic scale of: (a) 1240 m/min, and (b) 620 m/min and; (c) azimuthal–scan profile for annealed SEBS electrospun fibers collected at 1240 m/min (●) and 620 m/min (○).

irrespective of the azimuthal angle. As shown in Table 1, the annealed electrospun fibers show the decreases of r values from 1.17 to 1.03, which is similar to that of the film. This implies the change of anisotropic to isotropic microdomains upon the thermal annealing. In the case of the fibers collected by a take-up velocity at 620 m/min (Fig. 11(b)), the microdomains are weakly oriented in two directions parallel and perpendicular to the fiber axis, respectively. This can be more clearly observed from the four peaks in the azimuthal profile in Fig. 11(c).

4. Conclusions

Up to the present, thermoplastic elastomers are known about isotropic morphological microdomain which can be clearly seen by TEM. The present work, for the first time, demonstrates an existence of microdomain orientation through a case study of electrospun SEBS. In order to study on this, the electrospinning system was equipped with a rotational disk collector to allow the fiber alignment and control the fiber shear rate whereas the 2D-SAXS sample chamber was filled with ethanol to observe microdomain without the disturbance of the streaks. The 2D-SAXS of the electrospun SEBS fibers qualitatively showed elliptical pattern implying microdomain distortion and four-spot pattern suggesting an arrangement and orientation of fragmented microdomains. The fibers collected at the lowest rotational disk speed (31.5 m/min) showed the most significant elliptical shape in SAXS pattern as compared to the fibers collected from other higher rotational speeds. The microdomain distortions of the fibers collected from all rotational disk speed were quantitatively analyzed based on the r values of the first-order scattering maxima at $\varphi = 0^\circ$ and $\varphi = 90^\circ$. The values of the electrospun fibers collected at 31.5 m/min showed the highest r value (1.24) and overall they were in the range of 1.15–1.24 indicating anisotropic lamellae. By simply annealing the electrospun fibers, the r values were reduced to about 1, suggesting the change of anisotropic to isotropic microdomains. We speculate that the microdomains might form as soon as the polymer solution was ejected from the needle and at that time the shearing promotes the microdomain stretching and orientation whereas the solvent evaporation causes verification. Therefore, the fibers obtained from the lowest rotational disk take-up velocity were stretched in a certain time for solvent evaporation completion resulting in the most significant lamellar distortion.

As the present work shows the microdomains of electrospun fibers with diameter at micrometer scale, there might be a question whether this microdomains are existed in fibers at nanometer scale or not. The fact that SEBS in chloroform/toluene has relatively low conductivity; this obstructed us to obtain the fibers in nanometer level to answer the above question. However, as the TEM images of our fibers and of those in previous reports are similar, we speculated that the microdomains should exist in those nanofibers. In addition, as the stretch based on electrostatic force is one of the key factors to control the fibers to be nanometer size, it is natural to expect to see the ordered-microdomain orientation. We believe that a good sample preparation with 2D-SAXS analyses of nanofibers should provide us exact information about the ordered-microdomain orientation.

Acknowledgments

S. C. and W. R. would like to express their gratitude to the Royal Golden Jubilee Program (the Thailand Research Fund (PHD/0058/2550)), and the Japan Student Services Organization (JASSO). The authors acknowledge Dr. Eiko Nakazawa and Akiko Fujisawa for microtoming, and the Hitachi High-Technologies Corporation, Japan, for TEM measurement. The gratitude is also to Asahi Kasei Chemicals Corporation, Japan for SEBS. The SAXS measurements were conducted at the SPring-8 under the approved number 2009A1153.

References

[1] Holden G, Kricheldorf HR, Quirk RP. Thermoplastic elastomers. 3rd ed. Hanser Verlag; 2004. p. 2–3.
[2] Spontak RJ, Patel NP. Curr Opin Colloid Interface Sci 2000;5:334–41.
[3] Bhowmick AK, Stephens HL. Handbook of elastomers. 2nd ed. CRC Press; 2000. p. 327–330.
[4] Brydson JA, Rapra Technology Limited. Thermoplastic elastomers: properties and applications. iSmithers Rapra Publishing; 1995. p. 3–7.
[5] Schweitzer PA. Corrosion resistance of elastomers. CRC Press; 1990. p. 69–71.
[6] Wang Y, Hong X, Liu B, Ma C, Zhang C. Macromolecules 2008;41:5799–808.
[7] Heck B, Arends P, Ganter M, Kressler J, StÜhn B. Macromolecules 1997;30:4559–66.
[8] Figueiredo P, Geppert S, Brandsch R, Bar G, Thomann R, Spontak RJ, et al. Macromolecules 2001;34:171–80.
[9] Ma M, Titievsky K, Thomas EL, Rutledge GC. Nano Lett 2009;9(4):1678–83.
[10] Mogi Y, Kotsuji H, Kaneko Y, Mori K, Matsushita Y, Noda I. Macromolecules 1992;25:5408–11.
[11] Kim J, Kim B, Jung B, Kang YS, Ha HY, Oh I, et al. Macromol Rapid Commun 2002;23:753–6.
[12] Liu Y, Li M, Bansil R, Steinhart M. Macromolecules 2007;40:9482–90.
[13] Sakurai S, Momii T, Taie K, Shibayama M, Nomura S. Macromolecules 1993;26:485–91.
[14] Sakurai S, Kawada H, Hashimoto T. Macromolecules 1993;26:5796–802.
[15] Honeker CC, Thomas EL. Chem Mater 1996;8:1702–14.
[16] Sakurai S, Aida S, Okamoto S, Ono T, Imaizumi K, Nomura S. Macromolecules 2001;34:3672–8.
[17] Ramakrishna S, Fujihara K, Teo WE, Teo TE, Ma Z. An Introduction to electrospinning and nanofibers. World Scientific Publishing Co. Pte. Ltd; 2005.
[18] Fong H, Reneker DH. J Polym Sci Part B Polym Phys 1999;37:3488–93.
[19] Ma M, Krikorian V, Yu JH, Thomas EL, Rutledge GC. Nano Lett 2006;6(12):2969–72.
[20] Kalra V, Kakad PA, Mendez S, Ivannikov T, Kamperman M, Joo YL. Macromolecules 2006;39:5453–7.
[21] Kobori Y, Kwon YK, Okamoto M, Kotaka T. Macromolecules 2003;36:1656–64.
[22] Polis DL, Winey KI. Macromolecules 1996;29:8180–7.
[23] Sakurai S, Aida S, Okamoto S, Sakurai K, Nomura S. Macromolecules 2003;36:1930–9.
[24] Séguela R, Prud'homme J. Macromolecules 1981;14:197–202.
[25] Shin G, Sakamoto N, Saijo K, Suehiro S, Ito K, Amemiya Y, et al. Macromolecules 2000;33:9002–14.
[26] Mita K, Tanaka H, Saijo K, Takenaka M, Hashimoto T. Polymer 2008;49:5146–57.
[27] Kume T, Hashimoto T. String phase in Semidilute polystyrene solutions under Steady shear flow. In: Flow-induced structure in polymers. American Chemical Society; 1995. p. 35–47.
[28] Moses E, Kume T, Hashimoto T. Phys Rev Lett 1994;72:2037–40.

Polymer 52 (2011) 854–865

Contents lists available at ScienceDirect

Polymer

journal homepage: www.elsevier.com/locate/polymer

Statistical properties for the self-condensing vinyl polymerization in presence of multifunctional core initiators

Zuo-Fei Zhao [a], Hai-Jun Wang [a,b,c,*], Xin-Wu Ba [a,c]

[a] College of Chemistry and Environment Science, Hebei University, Baoding 071002, PR China
[b] International Centre for Materials Physics, Chinese Academy of Sciences, Shenyang 110016, PR China
[c] Key Laboratory of Medicinal Chemistry and Molecular Diagnosis, Ministry of Education, Hebei University, Baoding 071002, PR China

ARTICLE INFO

Article history:
Received 25 October 2010
Received in revised form
21 December 2010
Accepted 23 December 2010
Available online 1 January 2011

Keywords:
Partition function
Free energy
Radius of gyration

ABSTRACT

The self-condensing vinyl polymerization system consisting of inimers and multifunctional core initiators is studied by the principle of statistical mechanics. From viewpoints of functional groups and polymers, two types of canonical partition functions are constructed and further are proved to be consistent with each other. In this way, the explicit expressions of equilibrium free energy and law of mass action concerning the polymerization are obtained, and then the equilibrium size distribution functions of hyperbranched polymers are given. With the help of the size distribution functions, the *k*-th mean square radii of gyration of hyperbranched polymers with and without a core are derived, respectively. In order to investigate the effect of core initiators on the statistical properties of the system, the number and functionality of core initiators have been explicitly taken into account, and the variations of relevant physical quantities against the conversion of vinyl groups under various conditions are presented. It is shown that the presence of core initiator results in a significant influence on average properties of the system, which can be explained from the competition between polymers with and those without a core initiator in their growth process.

1. Introduction

Since the starburst dendrimers were discovered in 1979 by Tomalia and coworkers [1], highly branched polymers have been pursued intensively by chemists for their special structural properties and potential utilizations [2–7]. Of which, dendritic polymers such as dendrimers and hyperbranched polymers have caused particular interests. As is well known, the physical and chemical properties of polymer materials are closely related to their structures. In comparison with the linear architectures, dendritic polymers exhibit structural properties of more branches and globularity [1–7]. These characteristic structures endow dendritic polymers with the properties of relatively low viscosity, high solubility, without entanglement and with numerous terminal groups, thereby attract an intense attention.

Compared with dendrimers, hyperbranched polymers have imperfect structures, but possess the feature of relatively simpler synthesis [2–7], and therefore can be industrialized more conveniently. So far, two main pathways of preparing hyperbranched polymers have been used. One is the polycondensation of AB_g type monomers ($g \geq 2$), where only the reactions between different groups of A and B can take place. This idea was initially proposed by Flory in 1952 [8], and turned into reality by Webster and Kim in 1990 [3]. Since then the synthesis of hyperbranched polymers has been strongly expanded [7–11]. The other is the self-condensing vinyl polymerization (SCVP) of AB^* type monomers proposed by Fréchet in 1995 [5], in which A denotes a vinyl group and B^* represents a functional group that can initiate group A into a propagating site A^*. The feature of this approach is that the vinyl group A can undergo self-polymerization, and hence this kind of synthetic route is called SCVP. In the light of this synthetic route, a series of experiments about different SCVP systems have been performed, which include the SCVP system of pure inimers [12], the binary copolymerization SCVP systems of inimers and multifunctional core initiators [13–15], inimers and monomers [16–20] as well as the ternary copolymerization SCVP system of inimers, monomers and multifunctional core initiators [21]. These experiments indicate that SCVP systems have a broad prospect not only in polymer science but also in industry and engineering.

With the development of relevant experiments, theoretical investigations about different SCVP systems have been made as well. In 1997, an SCVP system of pure inimers was investigated for the first time by Müller, Yan and Wulkow [22,23], where the word "inimer" was firstly used. In essence, an inimer refers to a monomer

* Corresponding author. Key Laboratory of Medicinal Chemistry and Molecular Diagnosis, Ministry of Education, Hebei University, Baoding 071002, PR China.
E-mail address: whj@mail.hbu.cn (H.-J. Wang).

0032-3861/$ – see front matter © 2010 Elsevier Ltd. All rights reserved.
doi:10.1016/j.polymer.2010.12.053

which can initiate other monomers, and it is often signed as AB^* [22–35]. Subsequently, many other SCVP systems have been extensively studied by some groups through various methods. For example, the binary copolymerization SCVP systems (inimers and multifunctional core initiators, inimers and monomers) were studied from different aspects by methods of kinetic differential equation [24,25], Monte Carlo simulation [30–32], generation functions [33,34] and matrix notation [36]. More recently, a ternary copolymerization SCVP system of inmers, monomers and multifunctional core initiators has been studied by Zhou and Yan through kinetic differential equations [26]. In these studies, much attention has been payed to the reaction mechanism and kinetics of SCVP, the size distribution function of polymers, the number-, weight-, z-average molecular weights, the polydispersity index, the degree of branching, and so forth [22–35]. Furthermore, some factors such as the presence of core initiators [27–34], the feed rate of monomers or core initiators [28,29,33] and the molar ratio of monomer to inimer [24,25,35] are incorporated to investigate their influences on the properties of the system. These theoretical works have not only offered a lot of valuable information to learn about various SCVP systems but also caused some new research interests.

This investigation is motivated by the fact that the addition of core initiators could affect the structure and properties of the hyperbranched polymers [13–15,26–28], and the main purpose of this paper is twofold. The former is devoted to the application of the principle of statistical mechanics to the SCVP system in presence of multifunctional core initiators, which not only associates the average physical quantities with external conditions, but also provides a way to study thermodynamic properties of the system. The latter is focused on the influences of multifunctional core initiators on average properties of the system, in which the mean square radius of gyration is of particular interest.

The present discussions are performed by the principle of statistical mechanics. Specifically, starting with two canonical partition functions constructed from viewpoints of polymers and functional groups, some average physical properties of the system are studied, which mainly include the equilibrium free energy, law of mass action, equilibrium size distribution functions and the mean square radii of gyration. To investigate the effect of core initiators on these average physical quantities, the number and functionality of core initiators have been explicitly taken into account since they are closely related to the structural property of hyperbranched polymers. The present results show that the two factors play an important role in the statistical properties of the system. To compare the present results with the previous, throughout the paper two classical assumptions of ideal polymerization used in previous studies have been adopted [22–29,35], i.e. (1). All the vinyl groups A are of equal reactivities and react independently one another, so do the active sites; (2). Intramolecular reactions are neglected in the polymerization such that all the molecules in the system grow in a tree-like manner.

The remainder of this paper is organized as follows. In Section 2, in terms of two canonical partitions constructed from viewpoints of polymers and functional groups, the equilibrium free energy, the law of mass action and the equilibrium size distribution functions are obtained. In Section 3, the mean square radii of gyration for hyperbranched polymers with and without a core initiator are carried out. In Section 4, as an application of the proposed method, the equation of state and isothermal compressibility of the system due to polymerization are given, and further the numbers of four types of structural units (monomers, terminal units, chain units and branched units) are calculated. To show the influence of core initiators on the above average properties, in Sections 3 and 4, the plots of related physical quantities against conversion of vinyl groups under various conditions are presented. In addition, some related problems and the limitations of the paper are discussed in this section. In Section 5, a summary of the paper is made.

2. Application of the method of statistical mechanics in SCVP system

In the SCVP system under study, all of the active sites B^*, no matter which is offered by multifunctional core initiators B_f^* or by inimers AB^*, can initiate the vinyl groups A of other molecules such that a new active site A^* is produced accompanying the generation of a new bond. Such an initiation process is in essence a vinyl group A of a molecule reacting with an active site (A^*or B^*) of another one, in which A^* and B^* can react with a vinyl group A with the rate constants k_a and k_b, respectively. To compare with some results obtained by previous works [26–28], in this work the rate constants k_a and k_b have been considered to be same, i.e., $k_a = k_b$. This means that A^* and B^* have the same possibilities to react with any of vinyl groups. Note that the consumption of an old active site (A^*or B^*) leads to a new active site A^*, therefore the number of active sites in the system keeps conservative.

Through successive reactions, monomers (inimers and core initiators) can be linked up to form hyperbranched polymers with various sizes and different configurations [5,22–35]. Because of the presence of multifunctional core initiators, two types of hyperbranched polymers can be produced: one with a core initiator B_f^* and the other without. To illustrate the difference between the two types of hyperbranched polymers more apparently, here two octamers with and without a core initiator B_f^* are shown in Fig. 1, where the core initiator is modeled as a B_4^*. For an octamer without a core, the number of active sites is equal to its degree of polymerization, while for an octamer with a core initiator B_f^*, the number of active sites is $(7 + f)$.

Consider there exist N inimers of AB^* and M core initiators of B_f^* in the initial system, then at a given time, without loss of generality one can suppose that there are Λ bonds generated in the system. Through these bonds, a number of hyperbranched polymers are formed, and as a result the physical and chemical properties of the system also change with the conversion of vinyl groups A. To identify the two types of hyperbranched polymers in the system, throughout the paper the physical quantities with a superscript of "c" always correspond to those of polymers with a core.

For a system consisting of a great number of species, the method of statistical mechanics is naturally a powerful tool to study its related physical and chemical properties. In doing so, the relationship between an average physical quantity and thermodynamic conditions can be obtained. For this purpose, it is necessary to construct a partition function of the system. The partition function of the present system can be constructed from two different viewpoints: one is associated with the number of ways of forming hyperbranched polymers, the other with the number of ways of bonding from functional groups. Furthermore, the two partition functions with different forms would be proved to be consistent with each other.

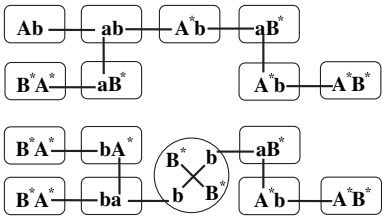

Fig. 1. The schematic of two types of octamers, where a core initiator is represented by a B_4^*, and two lowercase letters a and b represent the reacted active sites A^* and B^*, respectively.

2.1. The construction of partition function from the viewpoint of polymers

Through polymerization, hyperbranched polymers of various sizes and structures appear. Therefore one can study the system from the viewpoint of hyperbranched polymers with isomeric structures. Starting with this viewpoint, a canonical partition function of the system can be constructed as follows

$$Q_1(N,M,\Lambda) = C_1(N,M,\Lambda)[q(T)]^{\Lambda} \tag{1}$$

where $q(T)$ denotes the relative probability of generating a bond from an active site and a vinyl group A, which is related to the thermodynamical conditions of the system (Pressure P, Volume V and Temperature T). The exponent of $q(T)$ means that there are Λ bonds generated in the system. The factor $C_1(N,M,\Lambda)$ denotes the number of ways of forming all the possible hyperbranched polymers by N inimers of AB^* and M core initiators of B_f^* through Λ bonds, which is closely related to entropy change induced by the formation of polymers with linear or branched structures.

In accordance with the reaction dynamics, the physical quantity $q(T)$ associated with thermodynamical conditions and a bonding energy ε_b, can be written as

$$q(T) = \frac{\upsilon}{V}[\exp(-\beta\varepsilon_b) - 1] \tag{2}$$

where $\beta^{-1} \equiv k_B T$ with the Boltzmann constant k_B, and the bonding energy ε_b is mainly determined by the changes in electronic structures of reactants. The expression reflects the fact that to generate a new bond, two conditions must be satisfied simultaneously: one is that an active site and a vinyl group must close each other to a bonding volume υ, the other is the change in energy, ε_b, must also satisfy the bonding requirement. Clearly, if ε_b in eq. (2) is zero, it is impossible to form polymers because of $q(T) = 0$ in this case. For the SCVP system of interest, one can arrive at a relation $q(T) \cong (\upsilon/V)\exp(-\beta\varepsilon_b)$ due to a large and negative bonding energy.

The quantity $C_1(N,M,\Lambda)$ in eq. (1) is a combinational factor with the form as

$$C_1(N,M,\Lambda) = N!M! \prod_m \frac{(\omega_m^c)^{P_m^c}}{P_m^c!} \frac{(\omega_m)^{P_m}}{P_m!} \tag{3}$$

where P_m^c denotes the number of $(m+1)$-mers consisting of a core initiator and m inimers, and P_m denotes the number of m-mers without a core initiator, respectively. The factors of ω_m^c and ω_m represent the corresponding numbers of forming such polymers. According to the kinetic equations given by Zhou and Yan [26], there exist f possible ways when an inimer connects with the core initiator B_f^*. Meanwhile, recall that there are $(f+m)$ active sites in an $(m+1)$-mer with a core initiator, therefore the possible ways of forming the other $(m-1)$ bonds are $(f+m)^{m-1}$. Furthermore, consider the indistinguishableness of the m inimers, the combinatorial factor ω_m^c can be given by $\omega_m^c = (1/m!)f(f+m)^{m-1}$. For an m-mer without a core, the factor ω_m can be obtained as $\omega_m = (1/m!)m^{m-1}$, which is the same as that in the SCVP system of pure inimers [23], and the corresponding interpretation has been made in a previous work [37].

2.2. The construction of partition function from the viewpoint of functional groups

For the present system, the generation of a new bond corresponds to the consumption of a vinyl group A and an active site (A^*or B^*). Thus one can also start with the viewpoint of functional groups and bonds to investigate the statistical properties of the SCVP system. The canonical partition function associated with such a viewpoint, $Q_2(N,M,\Lambda)$, can be constructed by writing

$$Q_2(N,M,\Lambda) = C_2(N,M,\Lambda)[q(T)]^{\Lambda} \tag{4}$$

in which the physical interpretation of $q(T)$ and its exponent are the same as that in eq. (2), while the quantity $C_2(N,M,\Lambda)$ is a combinatorial factor which denotes the different ways of generating Λ bonds via N vinyl groups A, N active sites B^* from inimers and fM active sites B^* from core initiators, and one can express it as

$$C_2(N,M,\Lambda) = \frac{N!}{(N-\Lambda)!\Lambda!}(N+fM)^{\Lambda} \tag{5}$$

This expression can be interpreted as follows. On the one hand, the generation of Λ bonds requires Λ vinyl groups A out of N indistinguishable AB^* inimers, and there are $N!/(N-\Lambda)!\Lambda!$ ways to select. On the other hand, due to the conservation of active sites, there are $(N+fM)\Lambda$ ways for $(N+fM)$ active sites to participate Λ times reactions. Accordingly, the number of ways of generating Λ bonds can be given by eq. (5).

Thus far, two kinds of partition functions from different viewpoints have been obtained for the same system and over the same reference state in which there are no bonds generated. As an application of the two partition functions, the analytical expressions of equilibrium free energy, law of mass action and the equilibrium size distribution functions (ESDFs) for hyperbranched polymers with and without a core would be derived.

2.3. Free energy, law of mass action and equilibrium size distribution functions

Making use of partition functions in eqs. (1) and (4), the corresponding free energies of the system, $F_1(\Lambda)$ and $F_2(\Lambda)$, can be obtained as

$$F_1(\Lambda) = -\beta^{-1}[\Lambda \ln q(T) + \ln C_1(N,M,\Lambda)] \tag{6}$$

$$F_2(\Lambda) = -\beta^{-1}[\Lambda \ln q(T) + \ln C_2(N,M,\Lambda)] \tag{7}$$

Both of the first terms on the right hand side of the two equations are associated with the changes in bonding energy, and the second terms are associated with the changes in configuration entropy. Minimizing the free energy $F_2(\Lambda)$ with respect to Λ, the equilibrium free energy $F_{eq}(\lambda)$ and the corresponding equilibrium condition can be carried out

$$F_{eq}(\lambda) = \beta^{-1} N \ln\left(1 - \frac{\lambda}{N}\right) \tag{8}$$

$$\frac{\lambda}{(N+fM)(N-\lambda)} = \frac{\upsilon}{V}[\exp(-\beta\varepsilon_b) - 1] = q(T) \tag{9}$$

where λ is the value of Λ at the equilibrium state. The equilibrium free energy in eq. (8) is directly related to the numbers of bonds and inimers, and can be used for any value of λ. Eq. (9) is in essence the law of mass action for the present SCVP system, and where $q(T)$ is associated with the numbers of bonds (λ), active centers $(N+fM)$ and unreacted vinyl groups $(N-\lambda)$. Eqs. (8) and (9) give the relationships between the number of bonds and thermodynamical quantities, then they can be used to investigate physical and chemical properties of the system.

As an application of the free energy, we will derive the ESDFs for hyperbranched polymers with and without a core initiator. For this purpose, three restrictions satisfied by P_m and P_m^c should be noted, i.e.

$$\Lambda = \sum_{m=1}(m-1)P_m + \sum_{m=1} mP_m^c \tag{10}$$

$$M = \sum_{m=0} P_m^c, N = \sum_{m=0} m(P_m + P_m^c) \tag{11}$$

The restriction of eq. (10) comes from the assumption that all hyperbranched polymers grow in a treelike manner. Thus the total number of the bonds must be subject to the restriction of eq. (10) since there only exist $(m-1)$ bonds in an m-mer without a core, and m bonds in an $(m+1)$-mer with a core. As for the two restrictions in eq. (11), the former describes the fact that each of the hyperbranched polymers with a core possesses only one core, while the latter stems from the fact that the number of structural units in the system is conservative. These restrictions have been explicitly used in previous studies [27,28].

Obviously, in the equilibrium state $F_1(\Lambda = \lambda)$ and $F_2(\Lambda = \lambda)$ should possess the same minimum. Thus upon comparing eq. (6) with eq. (7), one may find that $C_1(N,M,\lambda) = C_2(N,M,\lambda)$. Differentiating both sides of this equation with respect to P_m^c and P_m, and considering the three restrictions in eqs. (10) and (11), the ESDFs of hyperbranched polymers, $\mathcal{P}_m^c$ and $\mathcal{P}_m$, can be given by

$$\begin{aligned}\mathcal{P}_m^c &= M\omega_m^c\left(\tfrac{x}{\gamma}\right)^m \exp\left[-(m+f)\tfrac{x}{\gamma}\right],\\ \mathcal{P}_m &= N\omega_m(1-x)\left(\tfrac{x}{\gamma}\right)^{m-1}\exp\left(-m\tfrac{x}{\gamma}\right)\end{aligned} \tag{12}$$

where $x = \lambda/N$ is defined as the conversion of vinyl groups A, and $\gamma = 1 + fr$ has been introduced with $r = M/N$ being the molar ratio of core initiator to inimer. The ESDF $\mathcal{P}_m^c$ denotes the number of $(m+1)$-mers with a core in the equilibrium state, and $\mathcal{P}_m$, the number of m-mers without a core. These results are identical with those obtained by Zhou and Yan [26]. (By solving the corresponding differential kinetic equations, they studied a ternary copolymerization SCVP system consisting of inimers, monomers and core initiators, which would reduce to the present system when monomers are excluded. Accordingly, one can substitute $\alpha = 1$ into eqs. (15) and (16) of Ref.(26) to check the corresponding results.)

Furthermore, with the aid of the physical quantity $q(T)$ in eq. (9), $\mathcal{P}_m^c$ and $\mathcal{P}_m$ can be rewritten as

$$\begin{aligned}\mathcal{P}_m^c &= \omega_m^c(\mathcal{P}_1)^m\mathcal{P}_0^c[q(T)]^m,\\ \mathcal{P}_m &= \omega_m(\mathcal{P}_1)^m[q(T)]^{m-1}\end{aligned} \tag{13}$$

in which $\mathcal{P}_1 = N(1-x)\exp(-x/\gamma)$ and $\mathcal{P}_0^c = M\exp(-fx/\gamma)$, denote the numbers of inimers AB^* and core initiators B_f^* in the equilibrium state, respectively. The expressions reflect the fact that an $(m+1)$-mer with a core needs m inimers and one core initiator react m times, while an m-mer without a core needs m inimers react $(m-1)$ times. These relationships agree well with the theory of reaction dynamics for polymerization [38].

Interestingly, the ESDFs of hyperbranched polymers and the equilibrium free energy can also be derived from the chemical equilibrium theory. Notice that when the SCVP system lies in the equilibrium state, the following equilibrium conditions should be satisfied

$$\mu_m^c \equiv \mu_0^c + \mu_m, \mu_m \equiv m\mu_1 \tag{14}$$

where $\mu_m^c = \partial F(\Lambda)/\partial P_m^c$ and $\mu_m = \partial F(\Lambda)/\partial P_m$ are the chemical potentials of an $(m+1)$-mer with a core and an m-mer without a core, respectively, and in which $F(\Lambda)$ may be either $F_1(\Lambda)$ or $F_2(\Lambda)$. Substituting the free energy $F_2(\Lambda)$ of eq. (7) into the two definitions and making use of the restrictions in eq. (10) yields

$$\begin{aligned}\mu_m^c &= \beta^{-1}\left\{m\ln\left[(1-x)\exp\left(-\frac{x}{\gamma}\right)\right] - f\frac{x}{\gamma}\right\},\ \mu_m\\ &= \beta^{-1}m\ln\left[(1-x)\exp\left(-\frac{x}{\gamma}\right)\right]\end{aligned} \tag{15}$$

Based on the chemical equilibrium theory, the equilibrium free energy $F_{eq}(\lambda)$ can be expressed as $F_{eq}(\lambda) = M\mu_0^c + N\mu_1 + \beta^{-1}\lambda$, and then in terms of eq. (15) the same form of $F_{eq}(\lambda)$ as that in eq. (8) can be found again. Alternatively, $F_1(\Lambda)$ in eq. (6) also can be used to evaluate the chemical potentials of μ_m^c and μ_m. Upon differentiating $F_1(\Lambda)$ with respect to P_m^c and P_m under three restrictions in eqs. (10) and (11), the chemical equilibrium potentials, μ_m^c and μ_m, can be expressed as functions of P_m^c and P_m, respectively. In so doing, by means of chemical equilibrium conditions given in eq. (14), the same expressions of ESDFs as those of eq. (12) can be derived once again.

The ESDFs in eq. (12) can be used to define the corresponding k-th ($k = 0, 1, 2,\ldots$) moments for hyperbranched polymers with and without a core as

$$M_k^c = \sum_m (m+1)^k\mathcal{P}_m^c, M_k = \sum_m m^k\mathcal{P}_m \tag{16}$$

In general, starting with such a definition, a recursion formula satisfied by the $(k+1)$-th moment and the k-th moment can be found. This means that if a starting point of polymer moments is selected, the higher moments can be easily derived. Accordingly, the number-, weight- and z-average molecular weights can be obtained in a straightforward manner, which are the basic parameters to characterize a polymerization system [39]. In this paper, the mass of a core initiator is assumed to be the same as that of an inimer, and has been arranged to be 1. In this way, instead of these average molecular weights, the explicit expressions of the number-, weight-, z-average degrees of polymerization and polydispersity index for two types of polymers and the whole system are obtained, respectively. For brevity, the detailed derivation of the k-th moments and these average degrees of polymerization has been given in Appendix A. These results agree well with those obtained in previous works [27,28]. Meanwhile, these results can degenerate to the SCVP system of pure inimers [23,37]. In particular, the k-th moments for polymers with and without a core would be used to calculate the corresponding mean square radii of gyration, as shown in the proceeding section.

Now, by the principle of statistical mechanics, two different methods have been used to obtain the ESDFs of the SCVP system in presence of multifunctional core initiators. These results indicate that the two canonical partitions constructed from two different viewpoints are consistent with each other. More importantly, by the equilibrium free energy and law of mass action, on the one hand several thermodynamic properties such as the equation of state and isothermal compressibility of the system can be studied, and on the other hand some average physical quantities as a function of conversion x, are now correlated with thermodynamic quantities of the system.

3. The k-th mean square radii of gyration

As is well known, the mean square radius of gyration (MSRG) plays a fundamental role in characterizing the dimension of branched polymers [39]. For hyperbranched polymers, the Kramers theorem can be used to evaluate the MSRG of m-mers [40]. The theorem associates the dimension of hyperbranched polymers with their purely structural properties. By the method, any m-mer can be divided into two moieties of an m_h-mer and an $(m-m_h)$-mer by cutting the h-th bond in the m-mer imaginarily [39,40]. Then one

can consider the contribution of bonds and average it over all possible ways of such cutting, the MSRG for m-mers $\langle R_m^2 \rangle$ can be written as the form Refs. [39,40]

$$\left\langle R_m^2 \right\rangle = \frac{b^2}{m}\langle m_h(m-m_h)\rangle \tag{17}$$

where b is the Kuhn bond length, and the quantity $\langle m_h(m-m_h)\rangle$ denotes the average of $m_h(m-m_h)$ over all the possible configurations of m-mers with isomeric structures. In this average, the number of structural units m_h ranges from 1 to $(m-1)$. In essence, this ensemble average for all m-mers is identical with the time average for a given m-mer over the fluctuations in its square radius of gyration due to Brownian motion. To calculate the MSRG, the Kramers theorem in eq. (17) can be generalized to several forms [39–42]. It has been shown that when the kinetic differential equation is known, the following relation is more convenient for the calculation of MSRG of m-mers [40–42]

$$\left\langle R_m^2 \right\rangle = \frac{b^2}{m^2}\sum_{m_h<m} m_h(m-m_h)D(m,m_h) \tag{18}$$

where $D(m,m_h)$ denotes the number of a type of bonds that split an m-mer into an m_h-mer and an $(m-m_h)$-mer.

In order to characterize a polymerization system by MSRG, one can average the MSRG over all polymers of various sizes. A customary treatment is to introduce the k-th MSRG of polymers with and without a core in such a way that

$$\begin{aligned}\langle R^2\rangle_k^c &= \sum_m (m+1)^k \left\langle R_m^2 \right\rangle^c \mathcal{P}_m^c (k=0,1,2,\ldots)\\ \langle R^2\rangle_k &= \sum_m m^k \left\langle R_m^2 \right\rangle \mathcal{P}_m (k=0,1,2,\ldots)\end{aligned} \tag{19}$$

In order to show the effect of core initiators on the dimension of hyperbranched polymers, two different kinds of polymers with and without a core will be discussed separately. For ease of presentation, the k-th mean square radii of gyration of polymers are also given directly and the corresponding derivations of MSRGs are detailed in Appendix B.

For hyperbranched polymers with a core, the first, second and third MSRGs are obtained as (for details, see eqs. (B7), (B8) and (B10) of Appendix B)

$$\langle R^2\rangle_1^c = fMb^2\gamma \exp\left[(1-f)\frac{x}{\gamma}\right]\frac{1}{x}\int_0^x B(y)dy \tag{20}$$

$$\langle R^2\rangle_2^c = \frac{fMb^2\gamma x}{(\gamma-x)^4}\left[\gamma^2+(f-1)(\gamma-x)x\right] \tag{21}$$

$$\langle R^2\rangle_3^c = \frac{fMb^2\gamma x}{(\gamma-x)^6}S_3^c(\gamma,x) \tag{22}$$

where functions $B(y)$ and $S_3^c(\gamma,x)$ have been defined by eqs. (B11) and (B9), respectively.

The corresponding first, second and third MSRGs of hyperbranched polymers without a core in the system are given by (for details, see eqs. (B18)–(B20) of Appendix B)

$$\langle R^2\rangle_1 = \frac{Nb^2\gamma}{2}\frac{x(1-x)}{(\gamma-x)^2} \tag{23}$$

$$\langle R^2\rangle_2 = \frac{Nb^2\gamma^3 x(1-x)}{(\gamma-x)^4} \tag{24}$$

$$\langle R^2\rangle_3 = \frac{2Nb^2\gamma^4 x(1-x)(\gamma+x)}{(\gamma-x)^6} \tag{25}$$

When the conversion x equals to 1, $\langle R^2\rangle_1$, $\langle R^2\rangle_2$ and $\langle R^2\rangle_3$ become zero because at the end of reactions ($x=1$), all the hyperbranched polymers without a core have linked with polymers with a core. This is consistent with the growth process of hyperbranched polymers in the present system. It can be also found that, as $\gamma=1$, these results degenerate to their corresponding forms in the SCVP system of pure inimers [37].

For a large m, by applying Stirling approximation to $\mathcal{P}_m^c$ and $\mathcal{P}_m$, and then consider the definition of the k-th MSRGs for polymers with and without a core, one can find that

$$\begin{aligned}\langle R^2\rangle_k^c &\propto \int_0^\infty (m+1)^{k-\frac{3}{2}}\left\langle R_m^2\right\rangle^c \exp\left[-\frac{m+1}{2}\left(1-\frac{x}{\gamma}\right)^2\right]dm,\\ \langle R^2\rangle_k &\propto \int_0^\infty m^{k-\frac{3}{2}}\left\langle R_m^2\right\rangle \exp\left[-\frac{m}{2}\left(1-\frac{x}{\gamma}\right)^2\right]dm\end{aligned} \tag{26}$$

In obtaining this, the summation over index m has been replaced by an integral form, and in each expression a factor containing N, γ and x has been neglected, for brevity. Combining the corresponding results in eqs. (20)–(25) and by means of inverse Laplace transformation, one can find that $\left\langle R_m^2\right\rangle^c \propto (m+1)^{1/2}$ and $\left\langle R_m^2\right\rangle \propto m^{1/2}$. This means that the scaling exponent of $\left\langle R_m^2\right\rangle^c$ and $\left\langle R_m^2\right\rangle$ with respect to the degree of polymerization is $\eta = 1/2$, which agrees well with the famous result proposed by Zimm and Stockmayer [43].

To show the effect of core initiators on the MSRGs, the plots of $\langle R^2\rangle_1^c$ and $\langle R^2\rangle_1$, $\langle R^2\rangle_2^c$ and $\langle R^2\rangle_2$ as well as $\langle R^2\rangle_3^c$ and $\langle R^2\rangle_3$ (in unit of Nb^2) against x for various f and r are presented in Figs. 2–7, in which the full symbols correspond to the MSRGs of polymers with a core and the empty ones to those without a core.

For the polymers with a core, the results in Figs. 2–7 indicate that the MSRGs have three common features:

(i) They increase monotonically as the conversion x increases, and vary rapidly at high conversion x. In the present system, hyperbranched polymers with and without a core grow independently at the initial stage. Therefore at a low conversion, these quantities increase smoothly for various f.

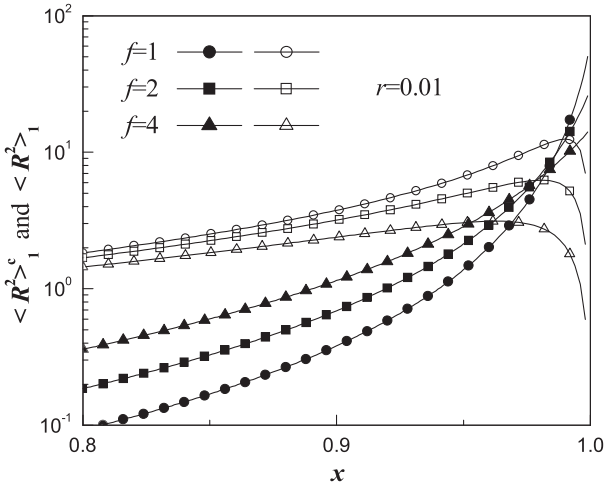

Fig. 2. The plots of $\langle R^2\rangle_1^c$ and $\langle R^2\rangle_1$ in unit of Nb^2 against x under the conditions of $r=0.01$ and $f=1$, 2 and 4. Full symbols: $\langle R^2\rangle_1^c$; empty symbols: $\langle R^2\rangle_1$. The same type symbols (full and empty): circles, $f=1$; squares, $f=2$; triangles, $f=4$.

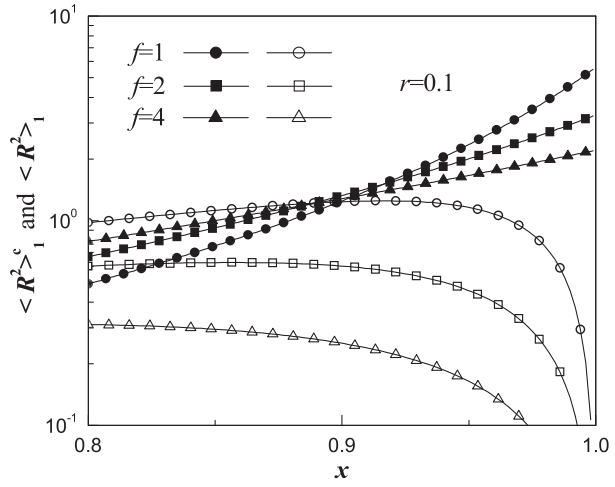

Fig. 3. The plots of $\langle R^2\rangle_1^c$ and $\langle R^2\rangle_1$ in unit of Nb^2 against x under the conditions of $r = 0.1$ and $f = 1$, 2 and 4. Full symbols: $\langle R^2\rangle_1^c$; Empty symbols: $\langle R^2\rangle_1$. The same type symbols (full and empty): circles, $f = 1$; squares, $f = 2$; triangles, $f = 4$.

Accompanying the proceeding of reactions, the reactions between polymers with and without a core could occur. This leads to a rapid increase of these quantities at high conversion.

(ii) They decrease monotonically as the molar ratio r increases. This kind of tendency can be found by comparing Fig. 2 with Fig. 3, Fig. 4 with Fig. 5 and Fig. 6 with Fig. 7, respectively. This is because for a given functionality f, a larger r would result in more active sites. According to the assumption we made, each of active sites has the same possibility of reacting with a vinyl group A, and thus in average, the larger the molar ratio r, the smaller the statistical weights in the related physical quantities. This kind of tendency becomes more obvious at high conversion x.

(iii) The dependence of these average physical quantities on the functionality f undergoes a transition. Namely, at the initial stage, they increase with the increase in functionality f, but after a conversion x, this tendency inverses. The reason can be qualitatively analyzed as follows. For a given r, a higher functionality f can offer more active sites which are favorable to the growth of polymers with a core. This leads to that, at a low conversion, the MSRGs for hyperbranched polymers with a core in the case of high functionality are larger than those in the case of low functionality. Seen from Fig. 10 in Appendix A, one can find that $\langle M\rangle_n^c$ of high functionality is always larger than that of low functionality, and the difference between them also has a maximum at a conversion, say x_0. This means that above the conversion x_0, the structural units connecting with the core initiator of low functionality are more than those connecting with the core of high functionality, and hence results in a large statistical weight in MSRGs. Consequently, this kind of transition takes place. In fact, when the conversion x approaches 1, the polymers without a core become less and less, and thus $\langle R^2\rangle_1^c$, $\langle R^2\rangle_2^c$ and $\langle R^2\rangle_3^c$ characterize in essence the mean dimension of the whole system.

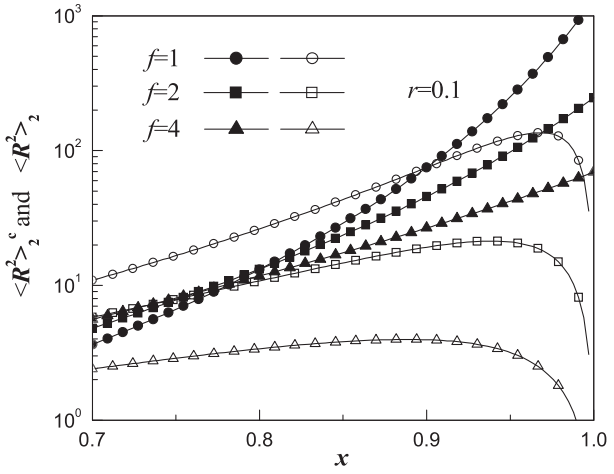

Fig. 5. The plots of $\langle R^2\rangle_2^c$ and $\langle R^2\rangle_2$ in unit of Nb^2 against x with the same conditions as those in Fig. 3.

For polymers without a core, the curves of MSRGs in Figs. 2–7 show that all of them decrease monotonically as either r or f increases, and each of them goes through a maximum. In a sense, these maximums indicate that in average, the largest dimension of polymers without a core appears only when the conversion is over a certain conversion determined by both f and r, below which one can think the growth of polymers with and without a core to be independent of each other, and above which the reactions among two types of polymers take place. This leads the radii of gyration for polymers without a core to a rapid decrease, and such a situation can also be reflected by the fact that the k-th mean square radii of gyration pass through their maximum and thereafter begin to

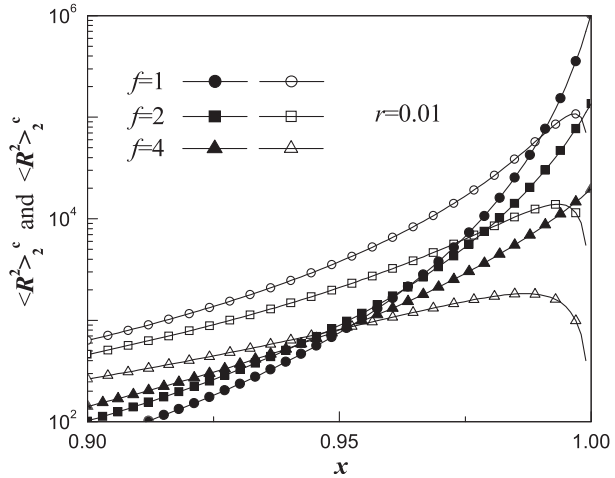

Fig. 4. The plots of $\langle R^2\rangle_2^c$ and $\langle R^2\rangle_2$ in unit of Nb^2 against x with the same conditions as those in Fig. 2.

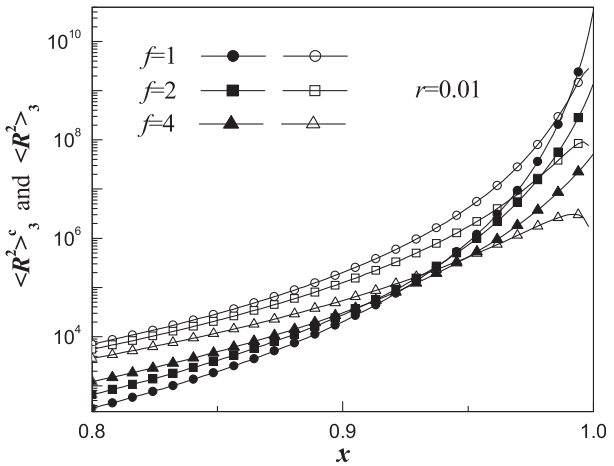

Fig. 6. The plots of $\langle R^2\rangle_3^c$ and $\langle R^2\rangle_3$ in unit of Nb^2 against x with the same conditions as those in Fig. 2.

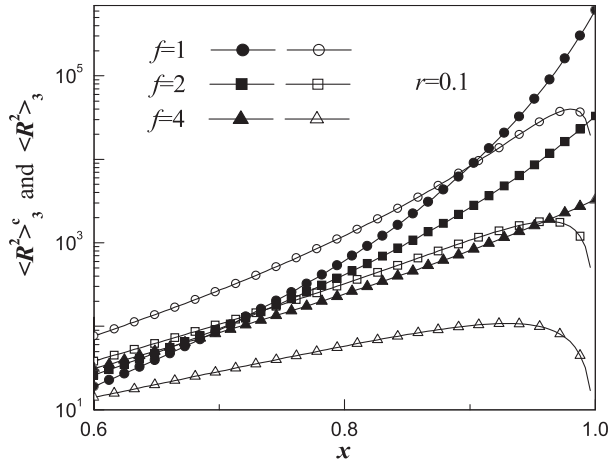

Fig. 7. The plots of $\langle R^2\rangle_3^c$ and $\langle R^2\rangle_3$ in unit of Nb^2 against x with the same conditions as those in Fig. 3.

decrease. Meanwhile, the conversion corresponding to the maximum is advanced when either the functionality f or the molar ratio r increases. This signifies that one can synthesize hyperbranched polymers with a desired average dimension by designing a proper functionality f and molar ratio r. Of course, at the same time one must consider its average molecular weights or degrees of polymerization for practical uses. This is just the main aim of adding core initiators in the system.

4. Several applications of the method of statistical mechanics and the related discussions

The method of statistical mechanics has been demonstrated to be efficient for the SCVP system of interest, and as a result a new way of deriving ESDFs of hyperbranched polymers is proposed. In the system, the number of molecules decreases one by one from its initial value $(N + M)$ with an increase in the number of bonds. In a sense, this can be considered as a kind of fluctuation in molecular number induced by the connectivity. Clearly, such a change also affects the statistical and thermodynamic properties of the system. In this section, as an application of the method of statistical mechanics, an oversimplified model (an ideal gas model) would be used to discuss the equation of state and the isothermal compressibility due to polymerization.

In terms of the equilibrium free energy in eq. (8) and the law of mass action in eq. (9), taking the ideal system as a reference state and making use of the relation $P = -(\partial F_{eq}(\lambda)/\partial V)|_T$, the equation of state can be given by

$$P = \beta^{-1}(n - \rho) \tag{27}$$

where $n = (N + M)/V$ and $\rho = \lambda/V$ are the number densities of structural units and bonds, respectively. This equation indicates that the pressure decreases with the increasing of bonds since the connectivity between molecules reduces their freedoms of thermal motion.

As is well known, the molecular number density fluctuation is closely related to the isothermal compressibility of the system, which reflects the spatial correlation between molecules induced by polymerization. Starting with the equation of state and considering the law of mass action in eq. (9), the isothermal compressibility χ_T can be obtained as follows

$$\chi_T = \frac{1}{n}\left(\frac{\partial n}{\partial P}\right)_T = \frac{\beta}{n}\langle\overline{M}\rangle_w \tag{28}$$

where the quantity $\langle\overline{M}\rangle_w$ has been given in eq. (A13). This means that the response of the molecular number density to a very small fluctuation of pressure increases with the increase in conversion x. In fact, the isothermal compressibility χ_T measures the static structure factor $S(\vec{q})$ in the long wavelength limit (the wave number $q \to 0$), namely

$$\frac{\chi_T}{\chi_T^{id}} = \lim_{q\to 0} S(\vec{q}) = \langle\overline{M}\rangle_w \tag{29}$$

where $\chi_T^{id} = \beta/n$ denotes the isothermal compressibility for the ideal reference state, and the vector $\vec{q}$ in $S(\vec{q})$ is the wave vector. This is evident since more and more molecules link with one another through bonds, and therefore the spatial correlation between molecules increases with the increase in conversion and can be characterized by a measurement of χ_T.

With the proceeding of polymerization, monomers could turn into terminal units, chain units and branched units. In other words, the structural units in the system can be classified as the following four types: (1) Monomer. This refers to a monomer that does not participate any reactions; (2) Terminal unit. This refers to a monomer that only one of its groups has reacted; (3) Chain unit. This refers to a monomer that only two of its groups participate the reactions; (4) Branched unit. This refers to a monomer that three or more of its groups have reacted.

Experimentally, the chemical shifts of branched units, chain units, and terminal units are distinct from one another, therefore the NMR technique can be used to characterize hyperbranched polymers such that some useful information on the structures of hyperbranched polymers can be obtained. Theoretically, the numbers of these distinct structural units can be calculated in a straightforward manner, and their variations as a function of conversion may be presented. In this section, to investigate the influence of core initiators on the structures of hyperbranched polymers, it is devoted to calculate the numbers of four types of structural units mentioned above.

In the present SCVP system, $\mathcal{P}_0^c(x) = M\exp(-fx/\gamma)$ and $\mathcal{P}_1(x) = N(1-x)\exp(-x/\gamma)$ denote the numbers of inimers and core initiators at conversion x, respectively. Thus the probability that any of active sites (A^* and B^*) does not react is $\exp(-x/\gamma)$, and the probability of finding it participating the reaction is $[1-\exp(-x/\gamma)]$. Letting $p = 1-\exp(-x/\gamma)$, the numbers of monomers, terminal units, chain units and branched units denoted respectively by $N_{m.}$, $N_{t.u.}$, $N_{c.u.}$ and $N_{b.u.}$ can be obtained as follows

$$\begin{aligned}
N_{m.} &= N(1-x)(1-p) + M(1-p)^f,\\
N_{t.u.} &= N\left[x(1-p)^2 + (1-x)p\right] + fMp(1-p)^{f-1},\\
N_{c.u.} &= 2Nxp(1-p) + M\frac{f(f-1)}{2}p^2(1-p)^{f-2},\\
N_{b.u.} &= Nxp^2 + M\sum_{i=3}^{f}\frac{f!}{i!(f-i)!}p^i(1-p)^{f-i}
\end{aligned} \tag{30}$$

From eq. (30), one can find that the sum of four types of structural units is $(N + M)$, and this result is identical with the above analysis. To show the variations in relative numbers of four types of structural units, the plots of $N_{m.}$, $N_{t.u.}$, $N_{c.u.}$ and $N_{b.u.}$ scaled in $(N + M)$ are presented in Fig. 8 for $f = 4$ under the cases of $r = 0.01$ and 0.1. The curves in Fig. 8 indicate that as conversion x increases, (i) the number of monomers decreases monotonically, (ii) the numbers of chain units and branched units increase monotonically, (iii) the number of terminal units increases at the initial stage and reaches a maximum, then decreases continually, and (iv) the larger the molar ratio, the less the number of branched units. These results coincide with the growth mechanism of polymers.

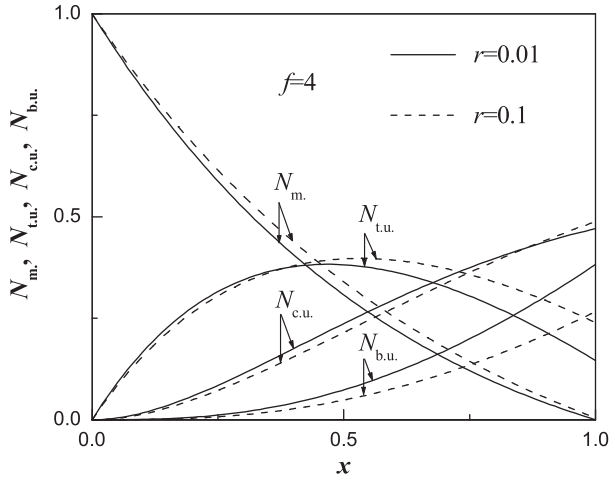

Fig. 8. The plots of $N_{m.}$, $N_{t.u.}$, $N_{c.u.}$ and $N_{b.u.}$ scaled in $(M + N)$ against x. The solid lines and dashed lines are presented for $f = 4$ under the cases of $r = 0.01$ and $r = 0.1$, respectively.

In the investigations on hyperbranched polymers, the degree of branching (DB) and the fraction of branched-points (FB) are usually used to characterize branched structures of polymers. In general, DB can be defined by DB $= (N_{b.u.} + N_{t.u.} - f)/(N + M - f)$ such that it is unity for perfect dendrimers and 0 for linear chain [44], while the FB is defined by FB $= N_{b.u.}/(N + M)$. Both of them are closely related to the number of branched units though their definitions are different from each other. Obviously, once the numbers of four types of structural units are given, DB and FB can be obtained. In this paper, FB is used to study the effect of core initiators on the branched property of polymers, and the curves of FB against the conversion x under various r and f are plotted in Fig. 9.

The curves in Fig. 9 indicate that FB increases monotonically with an increase in conversion x, but at a given conversion, it decreases monotonically as either the molar ratio r or the functionality f increases. This means that the presence of core initiators would lead the number of branched units to a decrease as compared with that in the SCVP system of pure inimers. In other words, a smaller molar ratio r and functionality f are more favorable to create branched units as many as possible.

Now we consider several limitations of the study. First, two types of active sites (A^* and B^*) are assumed to possess equal reactivities on reacting with a vinyl group. This deviates from the practical system

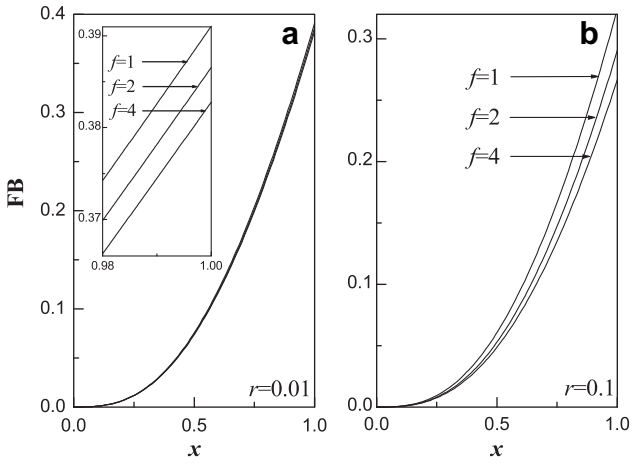

Fig. 9. The plots of FB against x under various f and r, the panels a and b correspond to the cases of $r = 0.01$ and 0.1, and in each panel the functionality f is taken to be 1, 2 and 4.

even for the same type of active sites. In addition, all the vinyl groups are also assumed to be of equal reactivity and react independently one another. In fact, the reactivity of a functional group can be influenced by many factors such as the steric effect and the substitute effect [44,45], whether it is an active site or a vinyl group. Therefore as a result, the structures and properties of hyperbranched polymers might be different from those in the case of equal reactivity, as noted in previous studies [23,25,31,34,46]. Second, the intramolecular reactions have been neglected as an approximation. In the present system, the cyclization cannot take place for a hyperbranched polymer with a core at all, thus such an approximation is actually aimed at the hyperbranched polymers without a core. Once the cyclization occurs in such a hyperbranched polymer, this polymer can no longer link with any other polymer with a core. Accordingly, some average physical quantities of the system would be affected. For example, cyclization can limit the molecular weight distributions and lower the polydispersity [44]. Third, in this paper a batch process (the core initiators and the inimers are mixed instantaneously) is considered. However, for practical uses, a semi-batch process of adding inimers slowly has attracted both theoretical and experimental interests [28,47]. Depending on the adding rate and ways (regularly or randomly), the system becomes time dependent and therefore a rigorous analytical treatment is not a trivial task. To our knowledge, such a non-stationary system requires the method of non-equilibrium statistical mechanics. Nevertheless, some methods such as Monte Carlo simulation can still serve as a powerful tool to perform the relevant investigations.

Experimentally, one is always intended to prepare the hyperbranched polymers with a desired characteristic property. For this purpose, it is necessary to anticipate some proper polymerization conditions when the reactants are chosen such as the stoichiometric relation between reactants, the functionality of monomers, catalysts and solution. As for the present system, once the reactants are fixed, the molar ratio r and the functionality f become main parameters to modify the structures and properties of hyperbranched polymers. On account of the relevant results, one can draw a conclusion that the effect of the core initiators on the average degrees of polymerization, polydispersity index and MSRG of the system is significant, and thus these results are helpful to an experimental design.

5. Summary

To summarize, two different viewpoints have been used to study the SCVP system in the presence of multifunctional core initiators based on the principle of statistical mechanics. The ESDFs for hyperbranched polymers with and without a core have been obtained. These results indicate that the two types of partition functions constructed from different viewpoints are consistent with each other. As an application, the k-th moments, the number-, weight-, z-average degrees of polymerization and the polydispersity index for the polymers with and without a core and the whole system are calculated (as shown in Appendix A). Furthermore, in order to characterize average dimensions of hyperbranched polymers with and without a core, the first, second and third MSRGs are obtained. In addition, several thermodynamical physical quantities such as the equation of state, the isothermal compressibility and the numbers of four types of structural units in the system are given.

In the present system, hyperbranched polymers can be classified into two types: one with a core and the other without. This is because of the presence of core initiators in the system. To discuss the effect of core initiators on these average physical quantities, the variations of these physical quantities against the conversion x under various molar ratio r and functionality f are presented. In

essence, the above average properties originate from the competition between the two types of hyperbranched polymers in their growth process, while the competition is mainly determined by the molar ratio r and functionality f. For a given r and f, at the initial stage there are enough vinyl groups A capable of reacting with active sites to form polymers such that the two types of polymers grow independently. However, at a higher conversion, the reactions between two types of polymers dominate, and finally the polymers without a core are all connected with those with a core. Such an analysis agrees well with reaction mechanism of the system and has been demonstrated by the relevant results.

Compared with the previous investigations on several SCVP systems, the present study is focused on thermodynamic and statistical properties by the principle of statistical mechanic. As a consequence, the equilibrium free energy, the law of mass action concerning the polymerization is obtained. Along these lines, the average properties of two types of polymers are associated with thermodynamic conditions of interest. This provides a clue of regulating average properties of polymers by controlling the reaction conditions. Therefore the present method and the method of solving kinetic differential equation can be jointly used to investigate various SCVP systems.

Finally, we would like to point out that the proposed statistical model is still a crude one because of the limits mentioned above. From the viewpoints of statistical mechanics and thermodynamics, the relevant studies by taking into account the reactivity difference, cyclization and semibatch process are interesting, which would be performed in future. It is expected that the present methods can provide some useful clues for understanding the SCVP system.

Acknowledgment

This work is supported by the NNSF of P.R. China under Grant Nos. 20873035 and 20574016.

Appendix A. The derivations of the *k*-th moments, the number-, weight-, z-average degrees of polymerization and polysispersity index

In this appendix, the derivations of the k-th moments for hyperbranched polymers with and without a core are detailed. At first, we consider the hyperbranched polymers with a core. Substituting the ESDF of $\mathcal{P}_m^c$ in eq. (12) into the definition of the k-th moment, $M_k^c = \sum_m (m+1)^k \mathcal{P}_m^c$, and then differentiating both sides of the equation with respect to the conversion x, yields

$$M_{k+1}^c = \left(1 + \frac{fx}{\gamma - x}\right) M_k^c + \frac{\gamma x}{\gamma - x} \frac{d}{dx} M_k^c \tag{A1}$$

This is a recursion formula satisfied by M_{k+1}^c and M_k^c, which indicates that once M_k^c is given, M_{k+1}^c can be obtained only by a differential calculation.

According to the growth mechanism, M_0^c denotes the number of hyperbranched polymers with a core such that it equals to the number of core initiators, M (see eq. (11)). Taking the zero-th moment $M_0^c = M$ as the starting point and successively using the recursion formula in eq. (A1), the first, second and third moments can be derived. Finally, we have

$$M_0^c = M, M_1^c = M\left(1 + \frac{fx}{\gamma - x}\right) \tag{A2}$$

$$M_2^c = \frac{M}{(\gamma - x)^2}\left[\frac{f\gamma^2 x}{\gamma - x} + (\gamma - x + fx)^2\right] \tag{A3}$$

$$M_3^c = \frac{Mf\gamma^2 x}{(\gamma - x)^3} S_1^c(\gamma, x) \tag{A4}$$

where the function $S_1^c(\gamma, x)$ is defined as

$$S_1^c(\gamma, x) = \frac{4\gamma + 3fx}{(\gamma - x)} + \frac{3x^2}{(\gamma - x)^2} + \frac{(\gamma - x + fx)^3}{f\gamma^2 x} \tag{A5}$$

The expression of M_1^c indicates that in average, each core initiator has connected with $fx/(\gamma - x)$ inimers. As a matter of fact, for a polymerization system, the zero-th moment stands for the number of molecules and usually depends on the conversion, while the first moment measures the number of structural units and is often independent of the conversion. However, for hyperbranched polymers with a core in the present system, the zero-th moment M_0^c is independent of conversion x, while the first moment M_1^c depends on the conversion x. This is due to the presence of core initiators and reaction mechanism of the SCVP system of interest.

Based on eqs. (A2)–(A5), the number-, weight- and z-average degrees of polymerization, and polydispersity index can be respectively expressed as follows

$$\begin{aligned}
\langle M\rangle_n^c &= 1 + \frac{fx}{\gamma - x}, \\
\langle M\rangle_w^c &= 1 + \frac{fx}{\gamma - x} + \frac{f\gamma^2 x}{(\gamma - x)^2(\gamma - x + fx)}, \\
\langle M\rangle_z^c &= \frac{f\gamma^2 x}{f\gamma^2 x + (\gamma - x)(\gamma - x + fx)^2} S_1^c(\gamma, x), \\
P_I^c &= 1 + \frac{f\gamma^2 x}{(\gamma - x)(\gamma - x + fx)^2}
\end{aligned} \tag{A6}$$

where the relations $\langle M\rangle_n^c = M_1^c/M_0^c$, $\langle M\rangle_w^c = M_2^c/M_1^c$, $\langle M\rangle_z^c = M_3^c/M_2^c$ and $P_1^c = \langle M\rangle_w^c/\langle M\rangle_n^c$ have been used. Notice that $\gamma = 1 + fr$, then the average physical quantities in eq. (A6) can be considered as functions of variable x and parameters r and f. Through these expressions, the effect of core initiators on these average physical quantities can be studied. As an illustration, only are the curves of $\langle M\rangle_n^c$ plotted in Fig. 10. The results of Fig. 10 indicate that up to $x = 1$, the number-average degree of polymerization $\langle M\rangle_n^c$ decreases with an increase in molar ratio r but increases with an increase in functionality f. This is because the more the active sites, the less the mean number of structural units connecting with each of them. At the end of reactions ($x = 1$), the

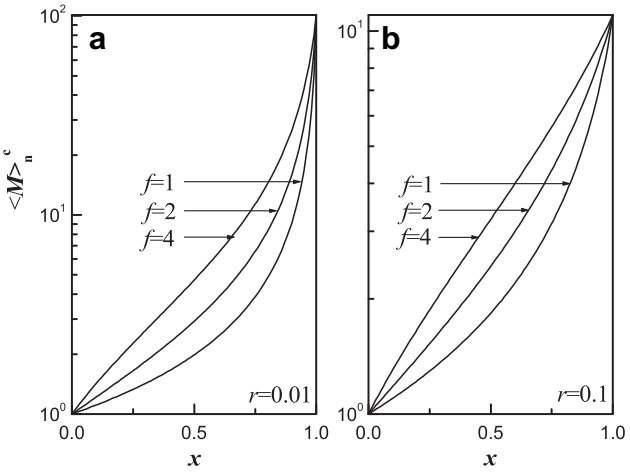

Fig. 10. The plots of $\langle M\rangle_n^c$ against x under the same conditions as those in Fig. 9.

panels a and b in Fig. 10 show that $\langle M\rangle_n^c$ reaches a fixed value that is independent of the functionality f and determined only by the molar ratio r. This agrees well with the expression of $\langle M\rangle_n^c$ in eq. (A6), in which $\langle M\rangle_n^c$ can be expressed as $(1+1/r)$ when $x=1$. Such a result can be applied to explain one of the features for the MSRGs of polymers with a core in Section 4.

Likewise, for hyperbranched polymers without a core, as one substitutes the ESDF of $\mathcal{P}_m$ in eq. (12) into the expression $M_k=\sum_m (m)^k P_m$, and differentiates both sides of this equation with respect to the conversion x, the following relationship between M_k and M_{k+1} can be obtained

$$M_{k+1} = \frac{\gamma x}{\gamma - x}\left[\frac{dM_k}{dx} + \frac{1}{x(1-x)}M_k\right] \tag{A7}$$

Note that, a molecule without a core contains only one vinyl group A such that the number of this type of molecules equals to that of unreacted vinyl groups A. Thus the zero-th moment of polymers without a core is $M_0 = N(1-x)$, which can serve as a starting point to obtain the first, second and third moments as

$$M_0 = N(1-x),\quad M_1 = \frac{N\gamma(1-x)}{\gamma - x} \tag{A8}$$

$$M_2 = \frac{N\gamma^3(1-x)}{(\gamma-x)^3},\quad M_3 = \frac{N\gamma^4(1-x)(\gamma+2x)}{(\gamma-x)^5} \tag{A9}$$

Substituting $\gamma = 1$ into these expressions yields the corresponding results of the SCVP system of pure inimers [23,37]. In comparison with the SCVP system of pure inimers, these polymer moments decrease because of the addition of core initiators. This is simply due to there exists a competition between hyperbranched polymers with and those without a core in consuming inimers.

Accordingly, for hyperbranched polymers without a core, the number-, weight- and z-average degrees of polymerization and the polydispersity index can be given by

$$\begin{aligned}\langle M\rangle_n &= \frac{\gamma}{\gamma - x},\ \langle M\rangle_w = \frac{\gamma^2}{(\gamma-x)^2},\\ \langle M\rangle_z &= \frac{\gamma(\gamma+2x)}{(\gamma-x)^2},\ P_I = \frac{\gamma}{\gamma-x}\end{aligned} \tag{A10}$$

where the relations $\langle M\rangle_n = M_1/M_0$, $\langle M\rangle_w = M_2/M_1$, $\langle M\rangle_z = M_3/M_2$ and $P_I = \langle M\rangle_w/\langle M\rangle_n$ have been used. It should be addressed that the expressions in eq. (A10) only hold true for the cases that the conversion of x is less than 1, and the corresponding physical quantities at $x=1$ should be excluded. This is because when the conversion x equals to 1, there are no polymers without a core in the system at all, and as a consequence the polymer moments M_0, M_1, M_2 and M_3 become zero (see eqs. (A8) and (A9)).

Based on the k-th moments of hyperbranched polymers with and without a core, the k-th moments of the whole system, $\overline{M}_k$, can be expressed as $\overline{M}_k = M_k^c + M_k$. Therefore from eqs. (A2)–(A4), (A8) and (A9), the zero-th, first, second and third moments for the whole system are

$$\begin{aligned}\overline{M}_0 &= M + N(1-x),\qquad \overline{M}_1 = M+N,\\ \overline{M}_2 &= \frac{M(\gamma - x + fx)^2 + N\gamma^2}{(\gamma-x)^2},\quad \overline{M}_3 = \frac{S_2^c(\gamma,x)}{(\gamma-x)^3}\end{aligned} \tag{A11}$$

where the function $S_2^c(\gamma,x)$ has been defined by

$$S_2^c(\gamma,x) = M(\gamma - x + fx)^3 + N\gamma^3(1+3x) + 3\left(f^2M + N\right)\frac{\gamma^2x^2}{\gamma - x} \tag{A12}$$

In terms of the definition of conversion $x(x=\lambda/N)$, the zero-th moment $\overline{M}_0$ can be rewritten as $\overline{M}_0 = M + N - \lambda$. This reflects the fact that with an increase in the number of bonds, the number of molecules in the system will decrease one by one. The first moment $\overline{M}_1$ represents the total number of core initiators and inimers in the initial system and is independent of the conversion x, as it is. Thus the expressions of $\overline{M}_0$ and $\overline{M}_1$ in eq. (A11) accord with their physical interpretations. Furthermore, the number-, weight-, z-average degrees of polymerization and polydispersity index for the whole system can be expressed as

$$\begin{aligned}\langle\overline{M}\rangle_n &= \frac{M+N}{M+N(1-x)},\\ \langle\overline{M}\rangle_w &= \frac{M(\gamma - x + fx)^2 + N\gamma^2}{(M+N)(\gamma-x)^2},\\ \langle\overline{M}\rangle_z &= \frac{S_2^c(\gamma,x)}{(\gamma-x)\left[M(\gamma-x+fx)^2 + N\gamma^2\right]},\\ \overline{P}_I &= \frac{M+N(1-x)}{(M+N)^2(\gamma-x)^2}\left[N\gamma^2 + M(\gamma-x+fx)^2\right]\end{aligned} \tag{A13}$$

In these expressions, if the number of core initiators is partly neglected, these quantities can degenerate to the results of previous works [27,28]. As $\gamma = 1$, all the results in eq. (A13) can degenerate to the corresponding results of SCVP system of pure inimers [23,37].

Appendix B. The k-th mean square radius of gyration

In eq. (19), the definition of the k-th MSRG of polymers with a core is

$$\langle R^2\rangle_k^c = \sum_m (m+1)^k \left\langle R_k^2\right\rangle^c \mathcal{P}_m^c (k = 0,1,2,\ldots) \tag{B1}$$

Upon differentiating both sides of this equation with respect to conversion x, one can find that

$$\langle R^2\rangle_{k+1}^c = \left(1 + \frac{fx}{\gamma - x}\right)\left\langle R_k^2\right\rangle^c + \frac{\gamma x}{\gamma - x}\frac{d}{dx}\left\langle R_k^2\right\rangle^c \tag{B2}$$

Similarly, it is necessary to find a starting point to calculate the k-th MSRG of polymers with a core. For hyperbranched polymers with a core, based on the corresponding kinetic equation given by Zhou and Yan [26], namely

$$\frac{d\mathcal{P}_m^c}{dx} = \frac{\sum_i (f+m-i)\mathcal{P}_i\mathcal{P}_{m-i}^c}{(1-x)(N+fM)} - \frac{(f+m)}{\gamma}\mathcal{P}_m^c \tag{B3}$$

and then substituting the expression of $\mathcal{P}_m^c$ given by eq. (12) into this equation, one can get

$$m\mathcal{P}_m^c = q(T)\sum_i (f+m-i)\mathcal{P}_i\mathcal{P}_{m-i}^c \tag{B4}$$

where $q(T)$ has already been defined by eq. (9). The term on the left hand side of eq. (B4) denotes the number of bonds in $\mathcal{P}_m^c$, while the summation over index i on the right hand side denotes all possible decompositions.

Now we use $D^c(m,i)$ to denote the ways of decomposing an $(m+1)$-mer with a core into an $(m+1-i)$-mer with a core and an i-mer without a core, then $\sum_i D^c(m,i) = m$ holds true according to the physical meaning of $D(m, m_h)$ in eq. (18). Thus we have

$$D^c(m,i) = q(T)(f+m-i)\frac{\mathcal{P}_i\mathcal{P}_{m-i}^c}{\mathcal{P}_m^c} \tag{B5}$$

Substituting this equation into eq. (18) yields

$$\left\langle R_m^2 \right\rangle^c \mathcal{P}_m^c = \frac{q(T)b^2}{(m+1)^2}\sum_{i<m} i(m-i+1)(f+m-i)\mathcal{P}_i\mathcal{P}_{m-i}^c \quad \text{(B6)}$$

When we substitute this equation into eq. (B1), it is ready to find the second MSRG $\langle R^2\rangle_2^c$ as follows

$$\langle R^2\rangle_2^c = \frac{fMb^2\gamma x}{(\gamma-x)^4}\left[\gamma^2+(f-1)(\gamma-x)x\right] \quad \text{(B7)}$$

In the calculation the polymer moments M_1^c, M_2^c and M_1 appeared in Appendix A have been used. As for the third MSRG of polymers with a core, $\langle R^2\rangle_3^c$, it can be obtained by two methods. One is by using the recursion formula in eq. (B2) with the known $\langle R^2\rangle_2^c$, the other is by a direct calculation through eq. (B6) with M_1, M_2, M_2^c and M_3^c being used. The two methods lead to the same result, i.e.

$$\left\langle R^2\right\rangle_3^c = \frac{fMb^2\gamma x}{(\gamma-x)^6}S_3^c(\gamma,x) \quad \text{(B8)}$$

where the function $S_3^c(\gamma,x)$ is expressed as

$$S_3^c(\gamma,x) = \left(\gamma^2+x^2\right)\left[(\gamma-x+fx)^2-f^2x^2\right] + 2x\gamma^2(\gamma+x)+(\gamma-x)^2(\gamma+fx)^2 \quad \text{(B9)}$$

Furthermore, solving the differential equation associated with $\langle R_2^2\rangle^c$ and $\langle R^2\rangle_1^c$ such that $\langle R^2\rangle_1^c$ can be given by the following integral solution

$$\langle R^2\rangle_1^c = fMb^2\gamma\exp\left[-(f-1)\frac{x}{\gamma}\right]\frac{1}{x}\int_0^x B(y)dy \quad \text{(B10)}$$

where the function $B(y)$ is defined as

$$B(y) = \frac{\gamma^2+y(f-1)(\gamma-y)}{(\gamma-y)^3}\frac{y}{\gamma}\exp\left[(f-1)\frac{y}{\gamma}\right] \quad \text{(B11)}$$

Now we turn our attention to the derivation of $\langle R^2\rangle_k$, the k-th MSRG for hyperbranched polymers without a core. For this purpose, one can rewrite the definition of $\langle R^2\rangle_k$ as

$$\langle R^2\rangle_k = \sum_m m^k\left\langle R_m^2\right\rangle\mathcal{P}_m(k=0,1,2,\ldots) \quad \text{(B12)}$$

Differentiating both sides of the equation with respect to the conversion x, we have

$$\langle R^2\rangle_{k+1} = \frac{\gamma x}{\gamma-x}\left[\frac{d}{dx}\langle R^2\rangle_k + \frac{1}{x(1-x)}R^2\right] \quad \text{(B13)}$$

The run of this equation needs a starting point to be determined. To this end, consider the kinetic equation of the size distribution function given by Zhou and Yan [26], one can find that

$$\frac{d\mathcal{P}_m}{dx} = \frac{1}{2}\frac{m\sum_i \mathcal{P}_i\mathcal{P}_{m-i}}{(N+fM)(1-x)} - \left(\frac{m}{\gamma}+\frac{1}{1-x}\right)\mathcal{P}_m \quad \text{(B14)}$$

By using the expression of $\mathcal{P}_m$ in eq. (12), a decomposing formula can be given as follows

$$D(m,i)\mathcal{P}_m = q(T)\frac{m}{2}\mathcal{P}_i\mathcal{P}_{m-i} \quad \text{(B15)}$$

The left hand side of this equation denotes the number of bonds in $\mathcal{P}_m$, while the summation over index i on the right hand side denotes all its decompositions (splitting an m-mer without a core into an i-mer and an $(m-i)$-mer). If one uses the quantity $D(m,i)$ to denote all the decomposition ways, then one gets

$$D(m,i)\mathcal{P}_m = q(T)\frac{m}{2}\mathcal{P}_i\mathcal{P}_{m-i} \quad \text{(B16)}$$

Substituting this equation into eq. (18) yields

$$\left\langle R_m^2\right\rangle\mathcal{P}_m = \frac{q(T)}{2}\frac{b^2}{m}\sum_{i<m} i(m-i)\mathcal{P}_i\mathcal{P}_{m-i} \quad \text{(B17)}$$

This relation is available to calculate the MSRG together with eq. (B12). For example, arranging $k=1$ in eq. (B12) and making use of the ESDF of $\mathcal{P}_i$, we have

$$\langle R^2\rangle_1 = \frac{Nb^2\gamma}{2}\frac{x(1-x)}{(\gamma-x)^2} \quad \text{(B18)}$$

In the calculation, the first moment M_1 has been used. As for $\langle R^2\rangle_2$, it can be obtained by either a direct calculation through its definition or the recursion formula eq. (B13) with $\langle R^2\rangle_1$ as a starting point. Both the two methods lead to the same result, i.e.

$$\langle R^2\rangle_2 = \frac{Nb^2\gamma^3x(1-x)}{(\gamma-x)^4} \quad \text{(B19)}$$

Furthermore, by means of the recursion formula in eq. (B13), the higher MSRG $R_k^2(k\geq 3)$ can be derived in a straightforward manner. For instance, the third MSRG of polymers without a core is

$$\langle R^2\rangle_3 = \frac{2Nb^2\gamma^4x(1-x)(\gamma+x)}{(\gamma-x)^6} \quad \text{(B20)}$$

A list of all symbols and their meanings.

Symbol	Meaning
AB^*, B_f^*	Inimer and core initiator with functionality f.
N, M	The number of inimers and core initiators.
$Q(\Lambda)$, $F(\Lambda)$	The partition function and free energy of the system with Λ bonds.
P,V,T	Pressure, Volume and Temperature.
ε_b, v, $q(T)$	The bond energy, bonding volume and the relative bonding probability.
P_m^c, P_m	The numbers of polymers with and without a core.
F_{eq}	The equilibrium free energy of system.
$\mathcal{P}_m^c$, ω_m^c	The ESDF and combinational factor for $(m+1)$-mer with a core.
$\mathcal{P}_m$, ω_m	The ESDF and combinational factor for m-mer without a core.
λ, $x(x=\lambda/N)$	The equilibrium number of bonds and the conversion of vinyl groups.
r, γ	The molar ratio of core initiators to inimers ($r=M/N$) and $\gamma=1+fr$.
μ_m^c, μ_m	Chemical potentials of an $(m+1)$-mer with a core and an m-mer without a core.
M_k^c, M_k	The k-th moment for polymers with and without a core.
$\left\langle R_m^2\right\rangle$, $D(m,m_h)$	MSRG for m-mers and its decomposition ways.
$\langle R^2\rangle_k^c$, $\langle R^2\rangle_k$	The k-th MSRG of polymers with and without a core.
n, ρ	The number densities of structural units and bonds.
χ_T, χ_T^{id}	Isothermal compressibilities of the system and the ideal state.
$S(\vec{q})$	Static structure factor with wave vector $\vec{q}$.
p	The reacting probability of an active site.
N_m, $N_{t.u.}$	The numbers of monomers and terminal units.
$N_{c.u.}$, $N_{b.u.}$	The numbers of chain units and branched units.
DB, FB	The degree of branching and fraction of branched point.
$\langle M\rangle_n^c$, $\langle M\rangle_w^c$, $\langle M\rangle_z^c$	The number-, weight- and z-average degrees of polymerization of polymers with a core.
$\langle M\rangle_n$, $\langle M\rangle_w$, $\langle M\rangle_z$	The number-, weight- and z-average degrees of polymerization of polymers without a core.
$\langle\overline{M}\rangle_n$, $\langle\overline{M}\rangle_w$, $\langle\overline{M}\rangle_z$	The number-, weight- and z-degrees of polymerization of the system.
P_l^c, P_l, $\overline{P_l}$	Polydispersities for polymers with and without a core and the system.

References

[1] Tomalia DA, Baker H, Dewald J, Hüall M, Kallos G, Martin S, et al. Polym J (Tokyo Jpn) 1985;17:117.
[2] Kim YH, Webster OW. Polym Prepr (Am Chem Soc Div Polym Chem) 1988;29:310.
[3] Kim YH, Webster OW. J Am Chem Soc 1990;112:4592.
[4] Hawker C, Fréchet JMJ. J Am Chem Soc 1990;112:7638.
[5] Fréchet JMJ, Henmi M, Gitsov I, Aoshima S, Leduc MR, Grubbs RB. Science 1995;269:1080.
[6] Hawker CJ, Fréchet JMJ, Grubbs RB, Dao J. J Am Chem Soc 1995;117:10763.
[7] Li X, Hong CY, Pan CY. Polymer 2010;51:92.
[8] Flory PJ. J Am Chem Soc 1952;74:2718.
[9] Miravet JF, Fréchet JMJ. Macromolecules 1998;31:3461.
[10] Yoon K, Son DY. Macromolecules 1999;32:5210.
[11] Sunder A, Hanselmann R, Frey H, Mülhaupt R. Macromolecules 1999;32:4240.
[12] Matyjaszewski K, Gaynor SG, Müller AHE. Macromolecules 1997;30:7034.
[13] Gaynor SG, Matyjaszewski K. Macromolecules 1997;30:4241.
[14] Roos S, Müller AHE, Matyjaszewski K. Macromolecules 1999;32:8331.
[15] Cheng G, Simon P, Hartenstein M, Müller AHE. Macromol Rapid Commun 2000;21:846.
[16] Held D, Ivn B, Müller AHE. Macromolecules 1998;31:7199.
[17] Simon PFW, Müller AHE. Macromolecules 2001;34:6206.
[18] Mori H, Seng DC, Lechner H, Zhang M, Müller AHE. Macromolecules 2002;35:9270.
[19] Mori H, Müller AHE. Polym Prepr (Am Chem Soc Div Polym Chem) 2003;44:435.
[20] Mori H, Walther A, André X, Lanzendörfer MG, Müller AHE. Macromolecules 2004;37:2054.
[21] Muthukrishnan S, Erhard DP, Mori H, Müller AHE. Macromolecules 2006;39:2743.
[22] Yan D, Müller AHE, Matyjaszewski K. Macromolecules 1997;30:7024.
[23] Müller AHE, Yan D, Wulkow M. Macromolecules 1997;30:7015.
[24] Litvinenko GI, Simon PFW, Müller AHE. Macromolecules 1999;32:2410.
[25] Litvinenko GI, Simon PFW, Müller AHE. Macromolecules 2001;34:2418.
[26] Zhou Z, Yan D. Macromolecules 2009;42:4047.
[27] Yan D, Zhou Z, Müller AHE. Macromolecules 1999;32:245.
[28] Radke W, Litvinenko G, Müller AHE. Macromolecules 1998;31:239.
[29] Litvinenko GI, Müller AHE. Macromolecules 2002;35:4577.
[30] Simon PFW, Müller AHE. Macromol Theory Simul 2000;9:621.
[31] He X, Liang H, Pan C. Macromol Theory Simul 2001;10:196.
[32] He X, Liang H, Pan C. Polymer 2003;44:6697.
[33] Cheng KC, Chuang TH, Chang JS, Guo W, Su WF. Macromolecules 2005;38:8252.
[34] Cheng KC. Polymer 2003;44:877.
[35] Zhou Z, Yan D. Macromolecules 2008;41:4429.
[36] Schmaljohann D, Barratt JG, Komber H, Voit BI. Macromolecules 2000;33:6284.
[37] Zhao ZF, Wang HJ, Ba XW. J Chem Phys 2009;131:074101.
[38] Sawada H. Thermodynamics of polymerization. Translated by Yan HK, Jin SJ. Bei Jing. Science Press; 1985. pp. 153–197.
[39] Rubinstein M, Colby RH. Polymer physics. Oxford: Oxford University Press; 2003. pp. 60–66, 224–227.
[40] Dobson GR, Gordon M. J Chem Phys 1964;41:2389.
[41] Li ZS, Ba XW, Sun CC, Tang XY, Tang AC. Macromolecules 1991;24:3696.
[42] Ba XW, Wang HJ, Zhao M, Li MX. Macromolecules 2002;35:3306.
[43] Zimm BH, Stockmayer WH. J Chem Phys 1949;17:1301.
[44] Simon PFW, Müller AHE. Macromolecules 2004;37:7548.
[45] Fu CL, O Wz, Sun ZY, An LJ, Li HF, Tong Z. Polymer 2009;50:5142.
[46] Zhou ZP, Jia ZW, Yan DY. Polymer 2009;50:4464.
[47] Zhou ZP, Jia ZW, Yan DY. Polymer 2010;51:2763.

Polymer 52 (2011) 866–873

Contents lists available at ScienceDirect

Polymer

journal homepage: www.elsevier.com/locate/polymer

Gel time prediction of multifunctional acrylates using a kinetics model

Aparna Boddapati, Santosh B. Rahane, Ryan P. Slopek, Victor Breedveld, Clifford L. Henderson, Martha A. Grover*

School of Chemical & Biomolecular Engineering, Georgia Institute of Technology, Atlanta, GA 30332-0100, United States

ARTICLE INFO

Article history:
Received 5 October 2010
Received in revised form
10 December 2010
Accepted 13 December 2010
Available online 21 December 2010

Keywords:
Photopolymerization
Gel time
Microrheology

ABSTRACT

A kinetics model for prediction of double-bond conversion and gel time in the photopolymerization of multifunctional acrylates is presented. The system consisting of a trifunctional acrylate, trimethylolpropane triacrylate (TMPTA), and a photoinitiator, 2,2-dimethoxy-1,2-diphenylethan-1-one (DMPA), was studied using Fourier-transform infrared spectroscopy (FTIR) measurements to monitor double-bond conversion and microrheology techniques to quantify the gel time for this system. Rate constants for the kinetics model were first estimated by fitting the model only to the FTIR double-bond conversion data, and later to both the FTIR and microrheology data. The measured gel time correlated with both the calculated initial rate of radical generation and a constant value of the predicted double-bond conversion, over a broad range of conditions. The model allows for materials formulation and exposure source intensity variables to be included in stereolithography inverse problem solutions, and could be applied to other cross-linking based photopolymerization systems.

1. Introduction

The photopolymerization kinetics of multifunctional acrylates has been studied extensively. These polymers are used in a wide array of applications ranging from lithography and coatings to biologically related uses such as dental composites and contact lenses [1]. The vinyl bonds on an acrylate react readily in the presence of radicals, and it is this fast rate of radical polymerization that makes acrylates attractive as compared to ionically polymerized monomers such as epoxides. In the case of multifunctional acrylates possessing multiple vinyl groups per monomer, reactions between distinct chains are prevalent. These types of reactions, known as cross-linking, bind different polymer chains in the reaction volume into a network. Cross-linking does not occur during photopolymerization of monofunctional monomers, thus resulting in a soluble collection of linear chains. In contrast, the cross-linked networks formed by multifunctional monomers are insoluble and this is known as the gel state. Polymers formed from the polymerization of pure monomers or mixtures including multifunctional acrylates are used in a wide range of applications. For example, several hydrogels that are used in tissue engineering are non-toxic derivatives of acrylates, and the cross-linking abilities of multifunctional acrylates are often exploited in these scenarios to achieve insolubility, high strength, and rigidity [2,3]. Moving beyond simple bulk multifunctional acrylate polymerization, the spatially controlled photopolymerization of multifunctional acrylates is the foundation on which stereolithography processes were developed. The significant durability of the gel networks formed by multifunctional acrylates is a desirable property in stereolithography applications, where polymer parts of various shapes and sizes are prepared using a computer generated exposure profile to selectively solidify a complex polymer shape in a vat of polymerizable monomer [4–7]. It is important to correctly understand and characterize the point at which gelation occurs (in space and time), because it will determine the geometry of the resulting polymer part.

Relating polymerization kinetics to solid part formation is challenging. To date, models to predict the height of cured parts take the form of analytical solutions to simplified kinetics—for example, deoxygenated systems with radical concentrations at constant steady-state levels [4]. In addition, measurements of the final part shape after removal from the resin vat may be influenced by part shrinkage during washing and drying steps, thus further confounding attempts to quantify the polymerization kinetics by solely measuring part height. This paper uses microrheology to obtain experimental data in support of our efforts to establish the relationship between polymerization kinetics and solid part height through more advanced kinetic models. Of particular importance here is the fact that microrheology can measure the location of the gel front throughout the polymerization process *in situ*, and is

* Corresponding author. Tel.: +1 404 894 2878; fax: +1 404 894 2866.
E-mail address: martha.grover@chbe.gatech.edu (M.A. Grover).

0032-3861/$ – see front matter © 2010 Elsevier Ltd. All rights reserved.
doi:10.1016/j.polymer.2010.12.024

therefore not impacted by shrinkage during washing or drying of the final part. The time point at which a resin transitions from a soluble liquid resin to an insoluble cross-linked network is called the gel time, and this parameter can readily be quantified experimentally through microrheology measurements [8–10].

In this paper, a model based on the kinetics of photopolymerization reactions of multifunctional acrylates is used to compute the gelation time for various cure conditions. First the experimental methods are presented, after which the kinetics model is documented in detail. This kinetics model is initially fit to the FTIR data only, after which the microrheology data are added to obtain a simultaneous fit of the rate constants and thus provide further model validation.

2. Experimental

2.1. Materials

Trimethylolpropane triacrylate (TMPTA, SR® 351) was obtained from Sartomer® and the photoinitiator 2,2-dimethoxy-1,2-diphenylethan-1-one (DMPA, IRGACURE® 651) was obtained from CIBA Specialty Chemicals®. The chemicals were used as received. In particular, the SR® 351 formulation of TMPTA contains 90–120 ppm of MEHQ, and this inhibitor was not removed. Experiments were performed on samples formulated with several different weight fractions of DMPA in TMPTA, and no additional solvent was added to these samples (Fig. 1).

2.2. FTIR procedure

Fourier-transform infrared spectroscopy was used to measure the double-bond conversion of the TMPTA over a range of times throughout the curing process. A sample holder was designed that enabled both UV curing and FTIR characterization on the same sample. This holder was made of two aluminum slabs, each with a 1 cm diameter aperture in the center. The slabs were used to align and contain two sheets of 65 μm thick polypropylene film, separated by a 100 μm thick Teflon® spacer to create a cavity. The cavity between the polypropylene films provides a thin and disposable sample chamber with rigid dimensions due to the Teflon® spacer and aluminum plates. The transmission characteristics of polypropylene enable sample illumination with UV light. Mixtures of initiator and uncured monomer were transferred into the sample chamber by pipetting the liquid samples along an open edge of the cell and allowing capillary action to fill the cavity. No attempts were made to remove oxygen from the TMPTA; rather, the TMPTA was assumed to be in equilibrium with the oxygen in the ambient environment. Three different initiator weight fractions were used for the FTIR measurements: 0.50%, 5.0%, and 10% DMPA. The entire sample holder was exposed to ultraviolet light from a Spectra-Physics

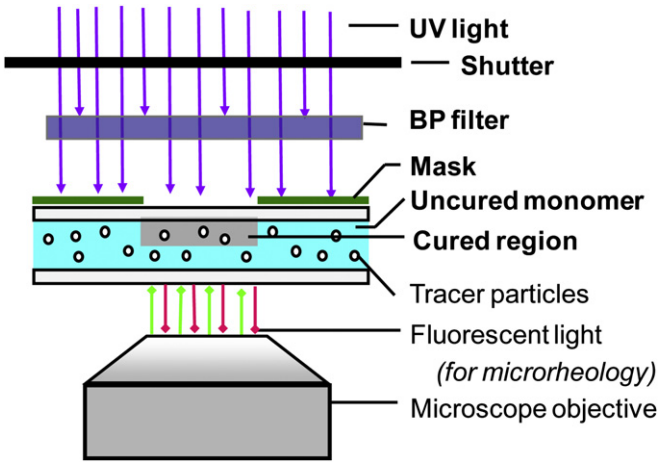

Fig. 2. Schematic of the cure setup used in the experiments and model.

1000 W Hg lamp through an IR water filter and bandpass filter (center wavelength 365 nm, full width at half-maximum 10 nm, peak transmission 55%), resulting in illumination at 365 nm and an intensity of 140 W/m^2. The exposure time of the samples was controlled via an electronic shutter (Uniblitz, Vincent Associates) that was operated through a customized LabView program for precise timing. A schematic of this setup is shown in Fig. 2.

Following UV irradiation for a controlled time period, FTIR measurements on the samples were performed *ex situ* using a Bruker FTIR (Bruker Vertex 80v) instrument operating in transmission mode. A total of 100 scans were collected for each sample at a resolution of 4 cm^{-1} to compile absorbance spectra. The double-bond conversion was calculated using the area under the C=C peak at 1625 cm^{-1}. Because the carbonyl content in the resin does not change during photopolymerization, the peak corresponding to asymmetric carbonyl stretching (C=O peak at 1720 cm^{-1}) was used as an internal standard in the FTIR analysis so that corrections could be made for slight variations in the cell path length. The peak area ratio (PAR) is defined as

$$\mathrm{PAR} = \frac{\mathrm{Area}_{1625\ \mathrm{cm}^{-1}}}{\mathrm{Area}_{1720\ \mathrm{cm}^{-1}}} \tag{1}$$

where $\mathrm{Area}_{1625\ \mathrm{cm}^{-1}}$ is the area under the C=C peak and $\mathrm{Area}_{1720\ \mathrm{cm}^{-1}}$ is the area under the C=O peak. Based on this peak area ratio, the double-bond fractional conversion α is calculated as

$$\alpha = 1 - \frac{\mathrm{PAR}}{\mathrm{PAR}_{t=0}} \tag{2}$$

where $\mathrm{PAR}_{t=0}$ is the initial value of the peak area ratio before any UV exposure.

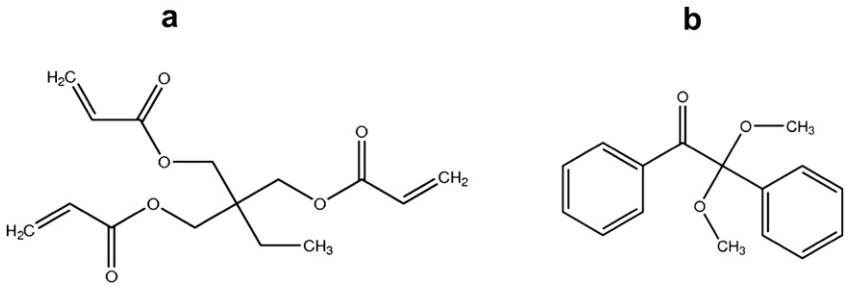

Fig. 1. (a) The trifunctional acrylate monomer SR®351, trimethylolpropane triacrylate (TMPTA); (b) the photoinitiator IrgaCure®651, 2,2-dimethoxy-1,2-diphenylethan-1-one (DMPA).

2.3. Microrheology

The gelation time of the TMPTA was measured via *in situ* particle tracking microrheology using the same optical setup that was used to illuminate samples for the FTIR experiments. Microrheology experiments were carried out under various exposure intensities, initiator concentrations, and with the focal plane of the microscope used to observe particle motion set at varying depths in the sample. The microrheology technique used in this work tracks the Brownian motion of individual 0.50 μm diameter fluorescent silica tracer particles using a high-resolution optical microscope (Leica DM-IRB), a CCD camera (Sentech STC-720) and frame grabber (Imagenation PCX-200AL), and image processing software (IDL, ITT VIS) to extract particle positions and reconstruct particle trajectories. In short, the "gel time" in microrheology experiments refers to the time at which a rapid change in the Brownian mobility of tracer particles is observed, indicating a sudden transition from a viscous liquid to an elastic network due to cross-linking of the trifunctional monomer [8].

Sample chambers of 120 μm thickness for the microrheology experiments were created by placing Parafilm spacers between two glass slides and slightly melting and cooling the Parafilm. A pipette was used to introduce the solution containing TMPTA, DMPA, and silica nanoparticles into the sample chamber. The concentration of tracer particles was extremely low (ca. 0.01 volume%) in order to facilitate tracking of individual tracers without affecting the optical properties of the sample. The sample was then exposed to UV, while simultaneously recording tracer particle motion at a well-defined focal plane in the sample. Further details on the experimental procedures for the microrheology measurements may be found in an earlier publication [8]. The specific experimental data points used in this paper for model comparison are given in Table 1, where I_0 is the incident intensity, [In] is the photoinitiator concentration, z is the depth into the sample from the top illuminated surface, and t_{gel} is the microrheology measured gel time.

3. Model

3.1. Rate equations

In this work, the reaction processes and time-dependent concentrations of various species typical in a radical photopolymerization process are modeled, including the concentrations of photoinitiator [In], radicals present [$R\cdot$], unreacted double bonds [DB], and oxygen [O_2]. The reactions considered in this work are:

$$\mathrm{In} \xrightarrow{k_d} 2R\cdot \tag{R1}$$

$$R\cdot + \mathrm{DB} \xrightarrow{k_p} R\cdot \tag{R2}$$

$$R\cdot + R\cdot \xrightarrow{k_t} R_{dead} \tag{R3}$$

$$R\cdot + \mathrm{O_2} \xrightarrow{k_{t,O_2}} R_{dead} \tag{R4}$$

where R_{dead} is any species produced that destroys one or more radicals.

The decomposition of the initiator is modeled as a first-order reaction with rate constant k_d. Two primary radicals are created per DMPA photoinitiator molecule [11,12], as shown in Reaction (R1). Once radicals have been formed in the system, the other three reactions (R2)–(R4) are assumed to be possible, which are modeled in this work with three additional rate constants: k_p for propagation of a radical through an acrylate double bond, k_t for termination between two radicals, and k_{t,O_2} for termination of a radical with an oxygen molecule. The termination reaction (R3) is a combination reaction, yielding a single species as the product. Vinyl monomers such as acrylates have been shown to terminate mostly via combination, rather than by disproportionation [13]. However, this assumption is not actually relevant for the modeling here, since this work does not involve modeling the molecular weight or concentration of polymer. Instead, the focus of this work is modeling the consumption of vinyl double bonds in the system, and it is this level of double-bond conversion that is used as a predictor of other polymer properties. It should also be noted that chain transfer reactions are not explicitly included here, but again such reactions would be of no consequence in terms of tracking the level of double-bond conversion in the system. In addition to the propagation and termination reactions, oxygen dissolved in the reaction volume can act as a radical scavenger, inhibiting both propagation and termination [14], and is thus explicitly included in the model.

Because we are using a multifunctional monomer, the double-bond conversion in the system is not proportional to the fraction of monomer consumed—the trifunctional monomer in polymer may still have one or two remaining unreacted double bonds. Thus, we model only the concentration of double bonds in the system, and not the concentration of free monomer, as is typical when modeling the reaction of linear polymers.

Given the four chemical reactions above, the following kinetics equations on the four species can be formulated:

$$\frac{d[\mathrm{In}]}{dt} = -k_d I(z)[\mathrm{In}] \tag{3}$$

$$\frac{d[R\cdot]}{dt} = 2k_d I(z)[\mathrm{In}] - 2k_t[R\cdot]^2 - k_{t,O_2}[R\cdot][O_2] \tag{4}$$

$$\frac{d[\mathrm{DB}]}{dt} = -k_p[R\cdot][\mathrm{DB}] \tag{5}$$

$$\frac{\partial[O_2]}{\partial t} = -k_{t,O_2}[R\cdot][O_2] + D_{O_2}\frac{\partial^2[O_2]}{\partial z^2} \tag{6}$$

Table 1
Microrheology data from Slopek [9].

Run	1	2	3	4	5	6	7	8	9	10	11	12
I_0 [W/m^2]	10	10	10	10	10	10	10	10	10	10	10	10
[In] [wt%]	5	5	5	5	5	5	8	6.5	5	4	3	2
z [μm]	112	106	68	44	20	8	60	60	60	60	60	60
t_{gel} [s]	9.0	8.8	7.3	6.0	4.3	3.8	5.3	5.8	6.7	7.5	8.8	11.5
Run	13	14	15	16	17	18	19	20	21	22	23	24
I_0 [W/m^2]	10	10	10	4	8	8	4	6	8	10	12	14
[In] [wt%]	1	0.5	0.25	2	2	1	2	2	2	2	2	2
z [μm]	60	60	60	60	60	60	60	60	60	60	60	60
t_{gel} [s]	17.3	26.7	41.2	22.5	11.7	20.2	22.5	14.0	11.7	9.8	8.1	7.3

Equation (6) is a partial differential equation, in which we explicitly model the diffusion of oxygen within the resin sample in the vertical direction, the only direction in which concentration gradients can develop. Due to its high diffusivity in TMPTA, the oxygen may diffuse from uncured top layers of the sample chamber down to the curing front, competing with double bonds for radicals and significantly slowing down the conversion rate and gel time. The chamber is sealed by the two glass slides, and thus insulating boundary conditions are applied at both the upper and lower ends of the simulation domain. The local illumination intensity is $I(z)$, which deviates from the incident intensity I_0 due to the absorption by the resin.

3.2. Parameterization of the model

There are four unique rate constants in the kinetics model, plus the diffusivity of oxygen in TMPTA. The values of the physical parameters used in the model presented in this work are shown in Table 2.

The decomposition kinetics of a photoinitiator into initiator radicals are typically modeled using the first-order rate constant [19]

$$k_d = \frac{2.3\phi\varepsilon\lambda}{N_A hc} \tag{7}$$

where $0 < \phi < 1$ is the quantum efficiency of the photoinitiator, N_A is Avagadro's number, h is Planck's constant, and c is the speed of light. The molar absorptivity of the resin, ε, depends upon the source wavelength λ. If $\phi = 1$, each photon absorbed triggers a single decomposition reaction to generate the desired initiator radical(s) product. The overall rate of initiator decomposition R_i is modeled by multiplying the rate constant k_d by the initiator concentration [In] and the local intensity (I):

$$R_i = k_d I(z)[\mathrm{In}] \tag{8}$$

$$I(z) = I_0 \exp\{-2.3\varepsilon z[\mathrm{In}]\}$$

The incident intensity at $z = 0$ is I_0, but within the sample at $z > 0$, the intensity will be attenuated, due to absorption of the light in the resin. Beer's law was used along with the molar absorptivity ε to yield the rate of initiator decomposition at depth z.

The TMPTA rate constants for propagation and termination have been estimated at elevated temperatures and lower values of R_i than those considered here [20,21]. The rate constant for oxygen termination k_{t,O_2} is often expected to be faster than k_t, due to some combination of a higher intrinsic reactivity of oxygen with a radical as compared to the vinyl double bond or to a higher diffusivity for oxygen in the resin than the monomer itself [22,23]. In the study here we do not assume specific values of k_p, k_t, and k_{t,O_2} *a priori*, but instead fit them to the experimental data and discuss the values in the context of available estimates in the literature.

The diffusivity of oxygen in TMPTA has been estimated [17], as noted in Table 2. The diffusion length $L = \sqrt{D_{O_2}\tau}$ can be computed as $L = 50$ μm for a time scale $\tau = 30$ s, which is one of the longer gel times recorded in our study. Compared to a cell depth of 100 μm, diffusion of oxygen could therefore be significant over the experimental timescales, although it is not so fast as to create a uniformly well-mixed environment either. Therefore, oxygen diffusion has been explicitly modeled and included in this work. The diffusion of DMPA in TMPTA is expected to be significantly slower due to its higher molecular weight, and thus its diffusion is not included in Equation (4) of the kinetics model.

All calculations were performed using MATLAB®. The resin sample was discretized vertically into slices of thickness $\Delta z = 5$ μm. The spatial second derivative for the oxygen diffusion was approximated using a centered finite difference method, with insulated top and bottom surfaces representing the glass slides sealing the top and bottom surfaces. Integration of the resulting ordinary differential equations was performed using the built-in function `ode23s`. The function minimization to fit the rate constants was implemented using the `patternsearch` function in MATLAB®.

Table 2
Physical parameters used in the kinetics model. Values given are for the initiator DMPA and the monomer TMPTA.

Variable	Description	Value	Units	Reference
ρ_{mon}	Density of monomer	1.1×10^6	g/m^3	
MW_{mon}	Molecular weight of monomer	296	g/mol	
MW_{init}	Molecular weight of initiator	256	g/mol	
λ	Wavelength of light source	365	nm	
ε	Molar absorptivity of initiator at wavelength λ	15	m^2/mol	[15]
ϕ	Quantum efficiency of initiator	0.6	–	[16]
D_{mon,O_2}	Diffusivity of oxygen in monomer	1.0×10^{-10}	m^2/s	[17]
$[O_2]_0$	Initial concentration of oxygen in TMPTA, at equilibrium with ambient air	1.05	mol/m^3	[18]

4. Results

Of the four rate constants used in the model, the initiator dissociation rate constant has been the most thoroughly documented in the literature. Here we use the nominal value for k_d calculated from Eq. (7) using the physical constants reported in Table 2 and fit the remaining three rate constants using several different assumptions.

4.1. Fit to FTIR conversion measurements

A simultaneous fit was made to TMPTA double-bond conversion data from two sources: the measurements of Lee et al. [24] which used *in situ* FTIR under deoxygenated conditions, and the *ex situ* FTIR measurements made in this work in the presence of ambient oxygen levels, as described in Section 2. A subsequent dark reaction following UV irradiation is modeled for the oxygenated data sets collected in this work since it is an *ex situ* measurement that occurs on the time scale of minutes after the initial exposure is completed. In this case, the dark reaction was simulated for 60 s, after which it was found that all radicals in the model have terminated. The diffusion of oxygen within the resin is also included in the model predictions. The conditions used for the deoxygenated data set are similar to the oxygenated experiments, with incident intensity $I_0 = 140$ W/m^2 at the wavelength $\lambda = 365$ nm, and a DMPA concentration of 1.0 wt%. Lee et al. used a sample thickness of 15 μm, much thinner than the 120 μm sample described in Section 2.

The best-fit values for the three rate constants $\{k_p, k_t, k_{t,O_2}\}$ are found by minimizing the sum squared error (SSE) between the FTIR experimental measurements and model-predicted double-bond conversion:

$$\mathrm{SSE}_{\mathrm{FTIR}} = \sum_{i=1}^{2}\left(\frac{1}{n_{t,i}}\sum_{j=1}^{n_{t,i}}\left(\alpha_{j,i}^{\mathrm{meas}} - \alpha_{j,i}^{\mathrm{pred}}(k_p, k_t, k_{t,O_2})\right)^2\right) \tag{9}$$

Here the index j denotes the double-bond conversion α at the jth time point (in experiment i). Since there are two experimental studies used in this fit, the quantity SSE_{FTIR} is thus the sum of the two average sum squared errors. The number of data points in experiment i is $n_{t,i}$.

The motivation for building the kinetics model presented in Equations (3)–(6) is to incorporate more chemical detail relevant for radical polymerization at early conversion, such that the gel time or exposure dose required to form a gel can be predicted as a function of the sample composition and processing conditions. Thus, only the data points at early conversion were used in fitting the rate constants, and consequently the model predictions will only be accurate for early conversion prior to gelation.

The best-fit values for the rate constants are $\{k_p, k_t, k_{t,O_2}\} = \{0.498, 1.30, 2.11\}$ m^3/mol s, and the corresponding predictions are shown in Fig. 3. Only the points marked with 'x's were used in the fit. In the Lee data shown in Fig. 3(a), only points up to 15% conversion were used in the fit, which establishes a clear slope consistent with a constant value of $k_p/\sqrt{k_t}$, as expected for deoxygenated systems with constant values of the rate constants [4]. Beyond this point, the slope of the conversion curve begins to decrease, consistent with increasing viscosity as the polymerization continues to proceed toward imminent gelation. In the oxygenated data set of Fig. 3(b), the data points up to 5 s were included for the lowest weight fraction of initiator (0.5 wt% DMPA). An initial transient is apparent up to 2 s, which is expected due to the presence of oxygen that quenches radicals and prevents significant polymerization until it is consumed. Thus the additional 3 s of data was included in the fit to capture the upturn in the conversion beyond this initial slower startup period. At the higher initiator weight fractions, the *ex situ* measurements did not have the time resolution to capture lower conversions, so the first point was included from the 10% DMPA experiment, and the first two points for 5% DMPA, in order to represent the fast kinetics observed for these high initiator loadings. When the data for 5% or 10% DMPA were not included in the fit, a lower value of $k_p/\sqrt{k_t}$ was computed, and the predictions for 5% and 10% DMPA were significantly slower, inconsistent with the data in Fig. 3(b).

Overall, the model predictions shown in Fig. 3 compare well to the experimental measurements at early conversion, using a single set of rate constants for both data sets. At longer times, the system gels, preventing full conversion to be achieved, while the constant values of the rate constants in the model will allow for predictions of 100% conversion as possible. The constant slope in the deoxygenated data is well predicted by the model ($k_p/\sqrt{k_t} \approx 0.44$). In the oxygenated data set of Fig. 3(b), the conversion rate is slightly overestimated at the low DMPA loading level, while slightly underestimating the high loadings.

We do not argue here that this set of rates is unique. For example, as long as the quantity of $k_p/\sqrt{k_t}$ is maintained constant, k_p and k_t can be varied over a significant range, with little impact on the conversion predictions. However, for values of k_p much less than 0.1, there would not be significant polymerization on the timescales of the experiments, which is inconsistent with the data.

4.2. Joint fit to conversion from FTIR and gel time from microrheology

The objective in this study is not simply to predict conversion, but rather to use a physically realistic model to predict the gelation time at which the liquid monomer is converted into a solid gel. In previous polymerization studies, monomer conversion has frequently been used as a predictor of gelation. For example, Flory provides a criterion for gelation in step condensation polymerization based on the conversion α and monomer functionality f—only beyond a critical conversion α_c can a percolating gel network be formed [25].

$$\alpha_c = \frac{1}{f-1}$$

For our trifunctional monomer, a maximum of $f = 6$ branches can be formed in a radical polymerization, so $\alpha_c = 20\%$. This expression assumes no cycle formation, while a modified version assumes equal probability of cycle formation

$$\tilde{\alpha}_c = \frac{1}{\sqrt{f-1}}$$

and for $f = 6$ yields $\tilde{\alpha}_c = 44\%$. Here we are dealing with a concentrated monomer, so cyclization may be less important than a dilute monomer in solvent. However, the chains are initially growing in isolation, and cycle formation cannot be ruled out either. More significantly, these expressions are derived for step condensation, but the kinetics of radical polymerization incorporates multiple reaction species and events. Critical conversion arguments have also been used for multifunctional acrylate radical polymerization, and the final expressions depend upon the individual rate constants for termination, initiation, and propagation [4]. Similar approaches have recently been developed for living radical polymerization [26]. However, in both cases a steady-state radical concentration is assumed, and neither the oxygen termination nor oxygen diffusion is included. Despite the complexities of

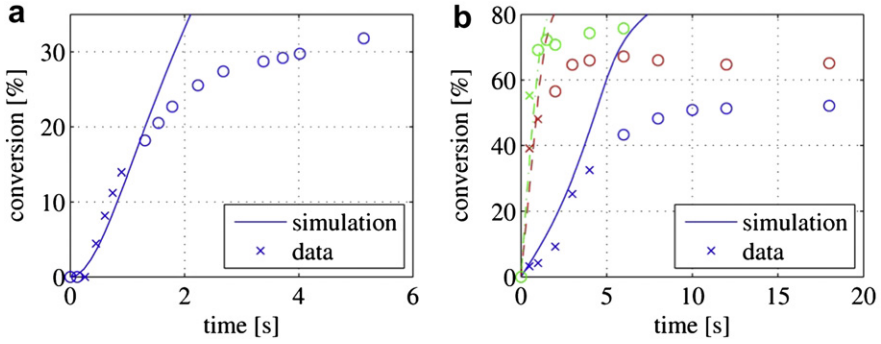

Fig. 3. Conversion data by FTIR, along with the model-predicted conversions α. The three rate constants used here were fit to the FTIR data only: (a) deoxygenated conditions and (b) oxygenated conditions. The 'x's represent data points used in the fit, and the 'o's are data points not used to fit the rate constants. In (b), the blue solid curve and symbols are for 0.5 wt% DMPA, the red dashed curve denotes 5 wt% DMPA, and the green dashed-dot curve is 10 wt% DMPA. (For interpretation of the references to colour in this figure legend, the reader is referred to the web version of this article).

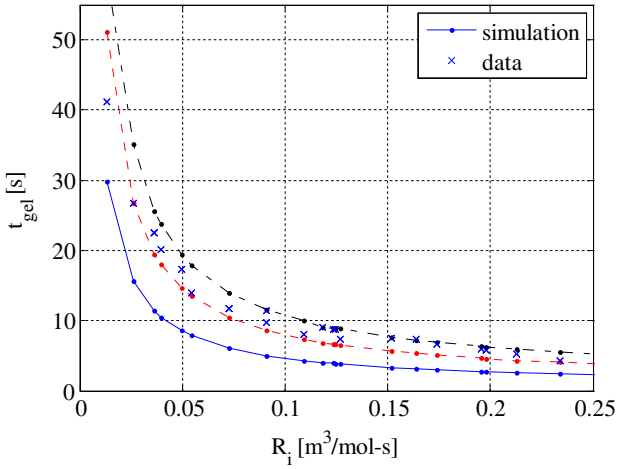

Fig. 4. Plot of microrheology data, and simulated curves with different conversion cutoffs: 10% (blue solid), 20% (red dashed), 30% (black dashed-dot). The rate constants used in the simulation were fit to the FTIR data: $\{k_p, k_t, k_{t,O_2}\} = \{0.498, 1.30, 2.11\}$ m^3/mol s. (For interpretation of the references to colour in this figure legend, the reader is referred to the web version of this article.)

the kinetics, the concept of using a critical conversion for predicting gelation might still be appropriate. Therefore, it was decided to experimentally determine if a single critical conversion criterion could be established for this system.

Here gelation is defined as the time at which the liquid monomer is converted into a solid gel. This transition was measured via microrheology as a sudden drop in the local particle mobility. It was hypothesized in this work that the gel time t_{gel} at a particular position in the vat should depend strongly upon the local initial rate of radical generation R_i. Therefore the rate constants estimated from the FTIR data were used to compute R_i for each of the 24 experimental data points in Table 1. In Fig. 4, the measured gel time t_{gel} is plotted versus R_i, and in fact does fall along a single curve, within an experimental variation of 1 s. Apparently the quantity R_i alone is sufficient to predict the gel time in this system. Of course, R_i depends on many quantities, including the depth in the sample, the initiator weight percent, and the intensity and wavelength of the UV source. This data suggests a simpler design principle, in which any single process setting can be used to vary R_i, and thus the value of t_{gel} at each point in the resin sample. Conversely, to obtain a particular t_{gel} at a desired depth z in the vat, either the intensity I_0 or the initiator concentration [In] may be adjusted to achieve the corresponding value of R_i.

Slopek [9] also reported microrheology measurements for deoxygenated samples, which form gels much more rapidly—at times less than 5 s for all $R_i > 0.05$ mol/m^3 s. It is difficult to draw a definitive conclusion about this deoxygenated data set, due to the limited experimental resolution, but the data did not appear to fall along a single curve on the t_{gel}–R_i plot. Additional unmodeled effects, such as heat release, molecular weight-dependent rate "constants" or residual oxygen levels, might need to be included in the model to accurately predict t_{gel} in such cases. Instead, here we focus on predicting the gel time in the presence of ambient oxygen, which is of more practical relevance for stereolithography.

The goal of this work is to use the kinetics model to predict gel time or gelation dose of illumination so that inverse process design problems like stereolithography might be more accurately solved, even though the kinetics model defined and discussed earlier in this paper only predicts double-bond conversion, as shown in Fig. 3, along with the concentrations of initiator, radical, and oxygen. Viscosity is often modeled as a function of molecular weight, but this dependence was not incorporated into the kinetics model used here for simplicity and to avoid overfitting. Flory predicted a critical value of the double-bond conversion, after which gelation is possible [25], so it was hypothesized in this work that TMPTA double-bond conversion might be correlated with gel time. If such a relationship is valid, then it would provide the connection needed to utilize the kinetic model for predicting the required gelation dose in applications such as stereolithography.

The results of investigating constant double-bond conversion criteria for fitting the microrheology gel time data are shown by the curves in Fig. 4, denoting the times at which 10%, 20%, and 30% conversion was reached, at each of the 24 settings used in the microrheology experiments. Because microrheology is an *in situ* measurement, no dark reaction is included in the simulations, but the effect of oxygen diffusion is included. The lines connecting the 24 modeled points are used only to guide the eye. A strong correlation between the data and the model predictions is evident, and the conversion cutoff of 20% appears to provide the best agreement. The point with the largest disagreement is at the smallest value of R_i, as the curves asymptotically approach infinity.

The rate constants used in the simulations in Fig. 4 were computed using only the FTIR data, and they are not necessarily unique. It might be possible to improve their estimates by performing a simultaneous fit to both the FTIR and microrheology data. This simultaneous fit could add insight into the fundamental rate constants and underlying phenomena; it could also allow for better fitting of the microrheology data for t_{gel} using a conversion cutoff α_{cut}. To perform this simultaneous fit, we defined the average squared error over the set of 24 microrheology measurements as

$$\mathrm{SSE}_{\mu rh} = \frac{1}{24}\sum_{i=1}^{24}\left(t_{gel,i}^{meas} - t_{gel,i}^{pred}\right)^2 \tag{10}$$

and then computed the three rate constants to minimize $\mathrm{SSE}_{FTIR} + \mathrm{SSE}_{\mu rh}$.

The best-fit rate constants are shown in Table 3, for the three different conversion cutoffs shown in Fig. 5 along with two additional intermediate values. The values obtained by fitting only to the FTIR data are shown in the first row for comparison. The numerical values of the sum squared fitting errors are also given in the table. Several observations can be made from Table 3. Including the microrheology data in the fit does not dramatically change k_p or k_t, and thus $k_p/\sqrt{k_t} \sim 0.44$ for all cases in the table. The sum

Table 3
Rate constants and average sum squared error for various fits to the experimental data.

α_{cut} [%]	k_p [m^3/mol s]	k_t [m^3/mol s]	k_{t,O_2} [m^3/mol s]	$k_p/\sqrt{k_t}$	SSE_{FTIR}	$\mathrm{SSE}_{\mu rh}$	$\mathrm{SSE}_{FTIR} + \mathrm{SSE}_{\mu rh}$
–	0.498	1.30	2.11	0.438	106.5	–	–
10	0.535	1.60	3.11	0.423	117.4	22.6	139.9
15	0.533	1.49	2.56	0.437	109.0	10.1	119.1
20	0.504	1.31	2.06	0.440	106.6	6.8	113.4
25	0.493	1.26	1.74	0.439	108.8	7.9	116.7
30	0.502	1.30	1.56	0.441	113.4	12.3	125.7

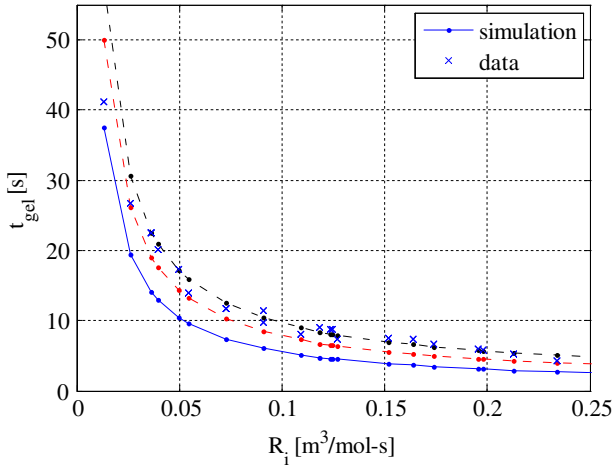

Fig. 5. Plot of fits for three conversion cutoffs: 10% (blue solid), 20% (red dashed), 30% (black dashed-dot). The rate constants used in each fit were optimized for that particular value of the conversion cutoff. (For interpretation of the references to colour in this figure legend, the reader is referred to the web version of this article.)

squared error for the FTIR term is expected to increase when the microrheology data is included in the fit, due to the tradeoff in fitting to more data points. However, this increase is slight, and for the 20% conversion cutoff value there is virtually no loss of accuracy in the FTIR prediction. The conversion cutoff of 20% provides the best overall accuracy among the five cutoff values, having the smallest microrheology fitting error, as can be seen in Fig. 5. The cutoffs of 15% and 25% are nearly as good.

The simulation results shown in Fig. 5 are similar to those in Fig. 4, because the rate constants did not change substantially among the various fits. The three curves in Fig. 5 are somewhat closer together, compared to Fig. 4, since their rate constants are now optimized to fit the gel time data. Note that the value of $k_p/\sqrt{k_t} \sim 0.44$ changed very slightly as the conversion cutoff was changed. The slope on the deoxygenated FTIR data is strongly sensitive only to this quantity, so that it would be difficult to achieve a good overall fit to the FTIR and microrheology data without having $k_p/\sqrt{k_t} \sim 0.44$.

The change in conversion cutoff was compensated in the optimization by a slight change in the value of the oxygen termination rate constant: as the conversion cutoff was raised, the value of k_{t,O_2} decreased by 50%. The effect of this decrease on the kinetics is that fewer radicals are terminated by oxygen early in the cure process, thus prolonging the time during which oxygen is present and ultimately speeding the polymerization. This effect was particularly important for the smallest value of R_i, as can be seen by comparing Figs. 4 and 5.

5. Discussion

As mentioned previously, the rate constants obtained from this fit are not necessary unique. The value of the oxygen termination rate and value of $k_p/\sqrt{k_t}$ are both local minima in the sum square errors indicating a unique fit, while the exact values of k_p and k_t could not be uniquely estimated. Adding the microrheology data to the FTIR data does not provide the additional information needed to better estimate the "true" values of the rate constants, nor does it contradict the values of the rate constants obtained solely from the FTIR data. However, adding the microrheology data to FTIR data does suggest that our FTIR-estimated rate constants are predictive for computing both conversion and gel time.

Constant values were estimated for the three rate constants, even though they are expected to depend on the viscosity. More specifically, the viscosity approaches infinity as the system approaches the gel point. However, Anseth et al. found that $k_p/\sqrt{k_t}$ for TMPTA is approximately constant up to the highest measured value at 14% conversion [21]. This is also consistent with observations in the microrheology experiments. The viscosity is approximately constant, and then increases rapidly when the system approaches gelation. The time of this transition is the gel time as measured by microrheology.

The values of the rate constants for TMPTA can be compared to kinetic parameterizations in previous studies. Anseth et al. determined rate constants for TMPTA using experimental results from a photo differential scanning calorimeter (DSC), including a dependence on free volume [21]. They applied the steady-state analysis for radical concentration during continuous irradiation of the resin to obtain the ratio $k_p/\sqrt{k_t}$ as a function of the propagation rate (measured through the DSC). By turning the UV source on and off, non-steady-state analysis was applied to separately estimate the ratio k_p/k_t, thus enabling independent estimates of k_p and k_t. They estimated $k_p = 0.4\ \mathrm{m^3/mol\ s}$ and $k_t = 100\ \mathrm{m^3/mol\ s}$ at the low conversion limit, yielding a value of $k_p/\sqrt{k_t} = 0.04\ (\mathrm{m^3/mol\ s})^{0.5}$. This value of k_p is consistent with ours in Table 3 ($k_p = 0.5\ \mathrm{m^3/mol\ s}$), while our value of $k_t = 1.3\ \mathrm{m^3/mol\ s}$ is significantly lower. There are two notable differences between our experimental conditions. First, the experiments in Anseth et al. [21] were conducted at 30 °C, while ours were at ambient temperature. Moreover, their value of radical generation rate is $R_i < 0.002\ \mathrm{m^3/mol\ s}$, which is an order of magnitude below our range of $0.02 < R_i < 0.23\ \mathrm{m^3/mol\ s}$ as seen in Figs. 4 and 5. Termination, and even the overall mode of polymerization and cross-linking, may be very different in different R_i regimes. Our model presented here represents a range of R_i that is of practical interest for stereolithography, but it is not necessarily valid outside that range.

Given our estimate of the conversion cutoff of 20%, we can re-evaluate the FTIR conversion data in Fig. 3(a) and (b). At a conversion of 20%, the conversion is still increasing rapidly in both sets of experiments. While this might at first appear inconsistent with gelation, that is not necessarily the case. Conversion will not immediately halt at gelation, but rather the mobility of polymers will cease, hindering both propagation and termination. In fact, termination will slow down first, since two radicals must find each other to terminate, and many radicals will be attached to polymer. Propagation can continue more readily, since the primary radicals and monomer can diffuse through the gel. Thus, Fig. 3 does not contradict our conclusion, since the turn-over in the conversion curves is expected during *or after* gelation. For consistency and completeness we also used Equation (8) to compute the initial rate of radical generation R_i in the FTIR data, which is slightly higher than for the microrheology data. For example, with the Lee conditions [24] at 1 wt% DMPA, we obtain $R_i = 0.38\ \mathrm{mol/m^3\ s}$ at the incident surface, and $R_i = 0.33\ \mathrm{mol/m^3\ s}$ at $z = 100\ \mu\mathrm{m}$, compared to a maximum value of $R_i = 0.23\ \mathrm{mol/m^3\ s}$ in the microrheology data set.

The gel time predictions of the kinetics model presented here are not necessarily more accurate than other alternative modeling approaches. For example, a simpler model can be fit as $R_i\, t_{gel} = 0.95$. Assuming that R_i is approximately constant over the irradiation time, this model implies that the system gels once a fixed number of radicals have been generated. While this is interesting to note, and simple to compute, it is not as accurate as the kinetics model. An alternative approach is to build an E_c–D_p model [27]. While this model is also very simple to evaluate, its two model parameters are

fit to experimental data for a fixed initiator concentration, irradiation intensity, and wavelength, so it is not useful for gaining insight into the underlying chemistry, or for designing a new process and recipe. The kinetics model presented here can be used to design the resin formulation and intensity profile for stereolithography of TMPTA with DMPA, over a wide range of conditions and gel times. It could also be applied to other initiators and multifunctional monomers. Moreover, it could be used to determine the desired properties of a monomer and an initiator, which would then enable the rational selection of the chemical or even enable molecular design of a new monomer with novel chemical reactivity.

6. Conclusions

A kinetics model was presented to predict conversion and gel time as a function of the process conditions and the chemical composition of the resin. The model was validated using the trifunctional monomer TMPTA and the photoinitiator DMPA. Conversion data was obtained from FTIR measurements, and gel time data from microrheology. The gel time could be uniquely predicted using only the initial value of radical generation, as predicted by the kinetics model. The data spanned over gel times from 5 s to 50 s, corresponding to an order of magnitude in both irradiation intensity and initiator concentration. This simple design rule relating R_i to gel time can now be used to select process conditions and sample recipe for applications of TMPTA and DMPA in stereolithography. In addition, the relationship between the radical generation rate and the gel time was correlated with a constant value of the double-bond conversion. It also suggests that these results may have further applicability to other monomer and initiator systems.

Acknowledgments

The authors gratefully acknowledge financial support from CIBA VISION®, and greatly appreciate helpful discussions in their collaboration with David Rosen, Amit Jariwala, and Fei Ding.

References

[1] Bowman CN, Peppas NA. Chemical Engineering Science 1992;47(6):1411–9.
[2] Goodner MD, Bowman CN. Chemical Engineering Science 2002;57(5):887–900.
[3] Nguyen KT, West JL. Biomaterials 2002;23(22):4307–14.
[4] Lee JH, Prud'homme RK, Aksay IA. Journal of Materials Research 2001;16(12):3536–44.
[5] Tang YY, Henderson C, Muzzy J, Rosen DW. International Journal of Materials & Product Technology 2004;21(4):255–72.
[6] Zhang X, Jiang XN, Sun C. Sensors and Actuators A – Physical 1999;77(2):149–56.
[7] Flach L, Chartoff RP. Polymer Engineering and Science 1995;35(6):483–92.
[8] Slopek RP, McKinley HK, Henderson CL, Breedveld V. Polymer 2006;47:2263–8.
[9] Slopek R. In-situ monitoring of the mechanical properties during the photopolymerization of acrylate resins using particle tracking microrheology. Ph.D. thesis. Atlanta, GA: Georgia Institute of Technology; 2008.
[10] Winter HH, Chambon F. Journal of Rheology 1986;30(2):367–82.
[11] Pappas SP, Asmus RA. Journal of Polymer Science. Polymer Chemistry Edition 1982;20(9):2643–53.
[12] Szablan Z, Lovestead TM, Davis TP, Stenzel MH, Barner-Kowollik C. Macromolecules 2007;40:26–39.
[13] Moad G, Solomon DH. Termination. The chemistry of radical polymerization. Oxford: Elsevier; 2006. p. 233–78.
[14] Decker C, Jenkins AD. Macromolecules 1985;18(6):1241–4.
[15] Berchtold KA, Lovestead TM, Bowman CN. Macromolecules 2002;35(21):7968–75.
[16] Goodner MD, Bowman CN. Modeling and experimental investigation of light intensity and initiator effects on solvent-free photopolymerization. In: Long TE, Hunt MO, editors. National meeting of the American chemical society, vol. 713. Las Vegas, Nevada: American Chemical Society; 1998. p. 220–31.
[17] O'Brien AK, Bowman CN. Macromolecules 2006;39(7):2501–6.
[18] Gou LJ, Coretsopoulos CN, Scranton AB. Journal of Polymer Science Part A – Polymer Chemistry 2004;42(5):1285–92.
[19] Odian G. Radical chain polymerization. Principles of polymerization. New York: John Wiley & Sons; 2004. p. 198–349.
[20] Anseth KS, Wang CM, Bowman CN. Macromolecules 1994;27:650–5.
[21] Anseth KS, Wang CM, Bowman CN. Polymer 1994;35(15):3243–50.
[22] Fouassier JP, Merlin A. Journal of Photochemistry 1980;12(1):17–23.
[23] Neta P, Huie RE, Ross AB. Journal of Physical and Chemical Reference Data 1990;19(2):413–513.
[24] Lee TY, Kaung W, Jonsson ES, Lowery K, Guymon CA, Hoyle CE. Journal of Polymer Science Part A – Polymer Chemistry 2004;42(17):4424–36.
[25] Flory PJ. Journal of the American Chemical Society 1941;63:3083–90.
[26] Irzhak TF, Irzhak VI. e-Polymers 2010;118:1–21.
[27] Zissi S, Bertsch A, Jezequel J-Y, Corbel S, Lougnot DJ, Andre JC. Microsystem Technologies 1995;2(1):97–102.

Polymer 52 (2011) 874–880

Contents lists available at ScienceDirect

Polymer

journal homepage: www.elsevier.com/locate/polymer

Modeling shape memory effect in uncrosslinked amorphous biodegradable polymer

Y.S. Wong [a], Z.H. Stachurski [b], S.S. Venkatraman [a,*]

[a] School of Materials Science & Engineering, Nanyang Technological University, N4.1-02-06 Nanyang Avenue, Singapore 639798, Singapore
[b] Department of Engineering, The Australian National University, Canberra, ACT 0200, Australia

ARTICLE INFO

Article history:
Received 6 October 2010
Received in revised form
1 December 2010
Accepted 1 December 2010
Available online 21 December 2010

Keywords:
Shape memory
Biodegradable
Modeling

ABSTRACT

Shape memory effect (SME) is critical for minimally invasive surgical procedures in medicine. In this paper, the shape memory behavior of amorphous biodegradable polymer, poly(D,L-lactide-co-glycolide), is experimentally investigated. Based on the experimental observations and the understanding of the underlying mechanism of SME, a one-dimensional constitutive model is derived to describe the shape memory behavior in the context of (1) the stress-strain behavior in deformation, (2) the isothermal recovery and (3) the recovery at constant heating rate, by using a set of model constants. By fine tuning the model constants, a good agreement between the experimental results and computer predictions was achievable.

1. Introduction

Materials displaying shape memory effect have the capability of changing their shape upon application of an external stimulus. A change in shape may be caused by a change in temperature in which case it is called a thermally induced shape memory effect and has been observed in metals, ceramics, and polymers [1,2]. Perhaps the earliest application of the shape memory effect in polymers has been introduced in the 1960s by the Raychem Corporation as heat-shrink tubing. At approximately the same time Buehler and his co-workers at the U.S. Naval Ordnance Laboratory in USA discovered the shape memory effect in a metallic alloy of nickel and titanium. Since the 1960s many other materials have been found to possess the SME capability [3].

A new development in connection with the design of shape memory materials is biocompatible polymers in which macroscopic properties (for example, mechanical properties) can be controlled by a particular variation of molecular parameters. This makes it possible to tailor the specific combination of the properties of the shape memory polymers that are required for specific applications just by a small variation of the chemical composition [4–6]. The shape memory material presented herein belongs to a family of multiphase polymer networks that are both biocompatible and biodegradable. Such materials which combine shape memory with biodegradability/biocompatibility are highly desirable for applications in the field of minimally invasive surgery, where a compacted device could be passed through a smaller incision and deployed to this full shape once inside the body.

SME in polymers is a consequence of viscoplastic deformation and network elasticity co-existing in the sample/object, and relies on the associated work of deformation being stored in the material as Helmholtz free energy. At some later stage, upon application of an external stimulus, the free energy released provides the driving force to restore the sample/object to its original shape. In this paper we focus on the thermally induced SME behavior of an amorphous polymer used extensively in biomedical applications [7], namely poly(D,L-lactide-co-glycolide), PDLLGA. PDLLGA has been chosen as the model polymer as it has been long used as implant matrices in the commercially available drug-loaded products for human use (e.g., Zoladex®, Eligard®, Atridox®). Minimally invasive procedures, such as percutaneous deployment of stents and valves, require the device material to possess some degree of shape memory, in order to deliver the device in “low profile” or with reduced dimensions. Although an ideal shape memory polymer is a crosslinked polymer, use of such a polymer has some limitations, such as non-degradability or delayed degradability; cytotoxicity of residual crosslinker or additive used for the crosslinking. Generally the use of a crosslinked biodegradable polymer also necessitates more safety testing for the device before approval. Thus if PDLLGA can be made to possess shape memory, the patch to clinical trial becomes easier.

* Corresponding author. Tel.: +65 6790 4259; fax: +65 6790 9081.
E-mail address: assubbu@ntu.edu.sg (S.S. Venkatraman).

0032-3861/$ – see front matter © 2010 Elsevier Ltd. All rights reserved.
doi:10.1016/j.polymer.2010.12.004

Furthermore, potential applications of such shape memory polymer as coronary stents, occluders, ureteral stents have been illustrated [7–9].

A typical cycle in the SME, as shown in Fig. 1, involves the following stages, with the glass transition temperature (T_g) playing a pivotal role:

Stage 1: Viscoelastic or viscoplastic deformation of the polymer object into another shape, carried out at a temperature either above or close to its glass transition temperature (T_g).

a) If it is carried out at a deformation temperature, T_d, sufficiently below T_g, the polymer suffers permanent distortion and can be stored in that form for later use.
b) If it is carried out close to or above T_g, the next stage is necessary to ensure SME.

Stage 2: Cooling of the polymer to a temperature below T_g. The polymer object is stored in that form for later use.

Stage 3: Restoration (without constraints) of the original shape by increase of temperature above the transition temperature, T_{trans}. The temperature, T_{trans}, can be either the glass transition temperature (T_g) or a melting temperature (T_m) in a case of a semi-crystalline polymer. The sample recovers towards its initial macroscopic shape and isotropic structure. In polymer mechanics this is usually referred to as "strain recovery", or simply, recovery.

In stage 1, deformation of the amorphous polymer to large strains below T_g will usually involve yield behavior, followed by increasing stiffness at large deformations due to the limiting chain extensions and increasing preferred molecular orientation [10,11]. After stage 3, one can define deviatoric stress that would be required to keep the previous deformed shape achieved in stage 1. In the development of constitutive equations this stress is usually referred to as the back stress [12].

Over the past decade, extensive studies have been devoted to the experimental characterization of the SME and synthesis of new shape memory polymers. However, only a few attempts have been made to develop models to quantitatively predict the SME, which is important in the practical viewpoint. Two approaches have been explored to describe the SME. The first approach is based on the micromechanics modeling of the material during the change of state [13,14]. Essentially, the material is assumed consisting of two phases, an "active" and a "frozen" phase. During the shape memory process, fraction of the two phases is made varied in order to describe the molecular transition. However, this two mixed phase concept is not in agreement with the physical processes of the glass transition and thus results in nonphysical parameters as highlighted by Nguyen et al. [14]. The second approach is based on the existing linear viscoelastic models to describe the SME [15–19].

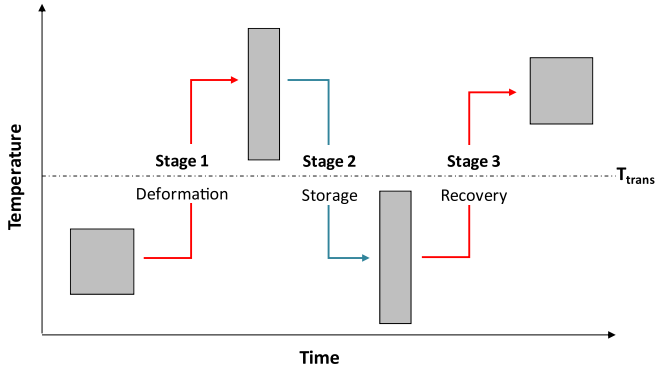

Fig. 1. Schematic diagram of the thermally induced shape memory effect.

Publications describing the modeling of the deformation/recovery response of the shape memory cycle involved complicated models and a number of material parameters to be determined. Furthermore, the models described so far, to author's knowledge, are developed for non-biodegradable polymers such as thermosetting or crosslinked SMPs.

In this paper, we present typical data on the behavior of the amorphous PDLLGA biopolymer during uniaxial stretching (stage 1), during isothermal recovery, and recovery at a constant heating rate (stage 3), and describe a model for the SME behavior based on previously published theories of mechanical behavior of polymers [20–24]. The model described herein shows some interesting features in terms of modeling the shape memory behavior of amorphous polymers, specifically in the simplicity of the model and approach. The experimental results are compared with computations based on the model.

2. Experimental procedure

2.1. Material and sample preparations

Copolymer poly(D,L-lactide-co-glycolide), i.e., 53 mol% of D,L-lactide and 47 mol% of glycolide, ($M_w = 9 \times 10^4$ and $M_w/M_n = 1.6$) was purchased from Purac Biochem and was used as received. Film samples were prepared by casting from a polymeric solution of PDLLGA in dichloromethane. Solution was casted onto glass plates using an automatic film applicator and then dried at vacuum oven for 5 days at 40 °C.

2.2. DMA tests

Dynamic thermal scan was performed using a Dynamic Mechanical Analyzer, DMA (TA Instrument Q800) to determine the basic mechanical response of the specimens. The size of the test specimen was approximately $15 \times 5 \times 1$ mm^3. The test was conducted in tensile mode, at a heating rate of 3 °C/min, an oscillation amplitude of 5 μm and a fixed frequency of 1 Hz. Testing was conducted over the temperature range from 20 to 100 °C.

2.3. Isothermal uniaxial tensile tests

A universal Instron Testing Machine 5548 was used to conduct the isothermal tests of PDLLGA samples. The machine is equipped with a temperature controlled chamber; regulating sample temperature to within ±1 °C. Samples for tensile tests were cut according to ASTM D638-99 Type V. Uniaxial tensile experiments were conducted at two different temperatures of 37 °C and 50 °C with strain rates ranging from 0.0025 s^{-1} to 0.5 s^{-1}.

2.4. Strain recovery tests

Recovery experiments were conducted on two groups of samples: (i) isothermal recovery, and (ii) constant heating rate recovery, respectively. In each case, the sample was first stretched to a certain stretch ratio at the deformation temperature, i.e., 37 or 50 °C, then cooled down to room temperature. In the isothermal recovery experiments, the samples were reheated back to 37 °C, and the change in sample length was measured using an extensometer. In the constant heating rate recovery experiments the samples were reheated to 60 °C at a constant rate of 3 °C/min.

3. Theory and modeling of SME

Three-dimensional development for the viscoplastic mechanics has been described [20] and reviewed [25]. Modeling of stress-

strain behavior of an amorphous polymeric solid as a function of strain rate and temperature is based on a so-called flow rule [20]. For uniaxial deformation the flow rule is reduced to a one-dimensional case, usually expressed as:

$$\sigma_E - \sigma_N = \sigma_v \tag{1}$$

This equation is similar to the one-dimensional model proposed by Sweeney et al. [24] and Morshedian, Khonakdar and Rasouli [19], however with some differences. The model comprises an elastic spring element in series with rubber network and viscoplastic dashpot elements arranged in parallel. The proposed model and the stages involved in SME are shown in Fig. 2. The stress in the elastic spring (σ_E) is equal to the applied stress, ($\sigma = \sigma_E$). The "back" stress caused by the entropic elasticity is σ_N, and the "dissipative" viscoplastic stress is σ_V. It is noted that σ_N is derived from the derivative of internal energy: $(\partial U/\partial L)_{T,V}$, where the change in length is related to atomic interactions as described in detail by Mattice and Suter [26].

The constitutive relation used for the elastic elements is [24]:

$$\sigma_E = E(T)\cdot\ln(\lambda_E) \tag{2}$$

Where: E (T) is the elastic modulus and λ_E is the elastic spring stretch ratio.

In the case of amorphous polymeric materials, the term, σ_N is derived from $T(\partial S/\partial L)_{T,V}$ [27]. For the network element the Arruda-Boyce 8-chain relationship was adopted [20]:

$$\sigma_N = \frac{G}{3}\sqrt{N}\cdot L^{-1}\left\{\frac{\lambda_{chain}}{\sqrt{N}}\right\}\frac{\left(\lambda_N^2-\lambda_N^{-1}\right)}{\lambda_{chain}},\quad \text{and}$$
$$\lambda_{chain} = \left(\lambda^2+\frac{2}{\lambda}\right)\Big/\sqrt{3} \tag{3}$$

Where: G is the modulus of elasticity of the network; N is the number of statistical links between the two crosslinks. In amorphous thermoplastics, which do not have a crosslinked structure, the value of N is related to the number of chain segments between points of physical entanglement in the polymer chain. λ_{chain} is the chain stretch and λ_N is network extension. L^{-1} stands for the inverse Langevin function on the argument.

The viscoplastic element (or viscoelastic, depending on temperature) possesses the property of stress dependent flow, as it is described by the Eyring type relationship [22,24]:

$$\frac{\dot\lambda_V}{\lambda_V} = \frac{\sigma_V}{\eta} = A\cdot\sinh\left(\frac{\sigma_V v}{k_B T}\right) \tag{4}$$

where: η is the apparent viscosity, A is a material constant, v is an activation volume, k_B is Boltzmann constant, and T is the absolute temperature. Solving for stress gives:

$$\sigma_V = \frac{k_B T}{v}\ln\left(\frac{\dot\lambda_V}{A\lambda_V}+\sqrt{\left(\frac{\dot\lambda_V}{A\lambda_V}\right)^2+1}\right) \tag{5}$$

It follows from the series arrangement of the model that: total stretch ratio, $\lambda = \lambda_E\lambda_N$ and from the parallel arrangement of the viscoplastic and rubber network elements that: $\lambda_V = \lambda_N$.

Stage 1: Uniaxial stretch

In the initial stages of very small strains, the deformation occurs mainly within the elastic spring; the viscoplastic element resisting any non-elastic deformation of the molecular chain network. As the magnitude of applied stress rises, the resistance to flow decreases so that eventually, $d\lambda_V/dt$ = machine applied stretch rate, manifesting itself as yield and plastic flow of the material. It is to be noted that σ_V decreases with increasing σ since the flow is stress activated. It is also highly temperature dependent. With further increasing stretch ratio, the effect of the rubber network becomes apparent as strain hardening.

In order to predict the deformation behavior by equation pertinent to the three-element model, a step-by-step method is used to solve the elastic-viscoplastic problem in uniaxial tension. In the experiments a constant stretch rate is applied, $d\lambda/dt = 1.67\times10^{-2}\ s^{-1}$. In computations, the stretch ratio is increased incrementally at the same rate and the corresponding stress, σ, is calculated by numerically solving Eqs. (1)–(5). This was accomplished using the software *Mathematica* to obtain the value of λ_N at each time increment on the basis that the Eq. (1) is satisfied. Terms in this equation are evaluated using relations (2), (3) and (5). By knowing λ and λ_N at each time increment, the λ_E can then be determined and the true stress, σ, can be calculated using Eq. (2). Furthermore, the results are presented in term of tensile nominal stress, which is simply taken as σ/λ assuming incompressibility of the material.

Stage 2: Shape memory retention

Following the deformation, the polymer object is cooled down to room temperature (below glass transition temperature), and the load is removed. On unloading, only the small elastic strain is recovered, $\lambda_E = 1$. The remaining back stress is frozen in, but it is too low compared to the dissipative flow stress to cause flow. At sufficiently low temperature, when the sample is in complete frozen state, the stress is equal to zero, thus Eq. (1) becomes:

$$\sigma_V + \sigma_N = 0 \tag{6}$$

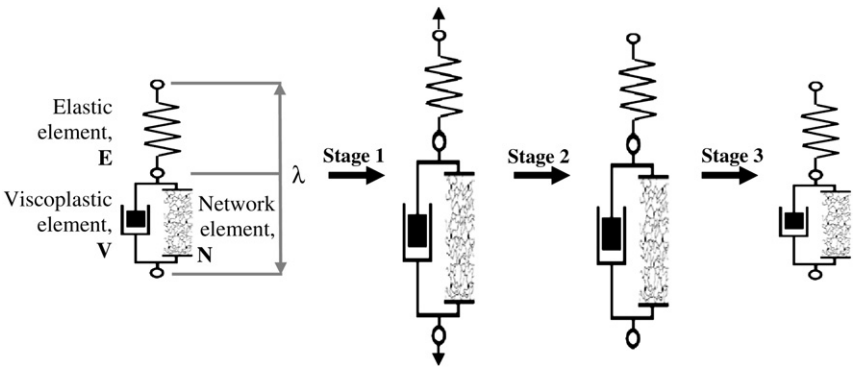

Fig. 2. Proposed mechanical model to describe shape memory process in amorphous PDLGA.

Stage 3: Recovery at $T \geq T_g$

In stage 3 a sudden (or gradual as the case may be) rise in temperature is applied to the sample. Increased temperature lowers the viscoplastic stress resisting flow and the polymer sample responds to the internal back stress to restore the sample towards its original shape. By substituting Eqs. (3) and (4), Eq. (6) can be expressed respectively as:

$$0 = \frac{\eta(T)}{\lambda_V}\frac{d\lambda_V}{dt} + \frac{G}{3}\sqrt{N}\cdot L^{-1}\left\{\frac{\lambda_{chain}}{\sqrt{N}}\right\}\frac{\left(\lambda_N^2 - \lambda_N^{-1}\right)}{\lambda_{chain}} \tag{7}$$

Accordingly, the temperature dependence of viscosity can be expressed as [28]:

$$\eta(T) = B\cdot\exp\left(\frac{Q_p}{RT}\right) \tag{8}$$

Where: B is a constant, Q_p is the activation energy, and R is the gas constant. B and Q_p are used as tuning parameters for the viscosity–temperature dependency.

For isothermal recovery, the solution to the constitutive equation is solved under the condition, $\sigma = 0$ and T = constant, following stage 2. For non-isothermal recovery, the temperature of the sample is made to increase at a finite rate, with strain recovery occurring concurrently. We assume a constant heating rate, $\beta = dT/dt$. Computations again require a step-by-step method to solve the elastic-viscoplastic problem. The temperature is increased incrementally at a constant rate and the corresponding stretch, λ_V, is calculated by numerically solving Eqs. (7)–(8). Here, we define recovery as:

$$R = (1 - \lambda/\lambda_{max}) \times 100\% \tag{9}$$

Where: λ_{max} is the maximum stretch ratio stored in the sample in Stage 2.

4. Results and discussion

4.1. Identification of material parameters

In the model developed in this work, there are 8 material parameters; among with 5 are fitting parameters. In order to identify the material parameters, two types of experiments were conducted. The first experiment is a DMA test to determine the glass transition temperature of PDLLGA and its elastic modulus as a function of temperature. The second experiment is isothermal uniaxial tensile tests at different strain rates and at different temperatures. The material parameters used in the simulation are listed in Table 1. Indeed the material parameters, listed in Table 1, have been either measured by us in the laboratory, or taken from references, and then adjusted by small amounts to obtain best fit.

Fig. 3 shows the experimental DMA results of storage modulus and tan delta as a function of temperature. The PDLLGA polymer exhibits the dynamic mechanical response which is characteristic for a thermoplastic material; at room temperature the storage modulus is relatively high, and with increasing temperature, this modulus gradually reduces. At the glass transition temperature (T_g), a sharp decrease in dynamic modulus is observed, since here the polymer chains acquire full segmental mobility and their state changes from glassy to rubbery. It was determined that the glass transition temperature of the P(DL)GA sample was ~37 °C based on the onset of the modulus drop. Furthermore, the storage modulus of PDLLGA in the glassy state is two orders of magnitude larger than that in the rubbery state and in general, a large modulus ratio of the glassy state to the rubbery state is regarded as favorable to shape memory capacity [13].

Table 1
Material constants used for the simulation of the SME at two temperatures (i.e., 37 and 50 °C).

Material constants	T_d = 37 °C	T_d = 50 °C
Elastic modulus, $E(T)$ [MPa]	1491	170
Rubbery modulus, G [MPa]	0.89	0.89
Number of statistical link, N	13	40
Eyring activation volume, v [Å^3]	1870	1660
Constant, A [s^{-1}]	2.98×10^{-4}	9×10^{-4}
Constant, B [Pa s]	8×10^{-4}	1×10^{-3}
Activation energy, Q_p [kJ mol^{-1}]	73.7	76.4

The tan delta plot in Fig. 3 shows a peak close to T_g, indicating that the contribution of the viscous part to the dynamic response is relatively high in this temperature range. With increasing temperature tan delta decreases again and plateaus, indicating that a more elastic region is reached, the so-called rubbery plateau. In this rubber-elastic region, the polymer chains have full mobility and the properties are determined by the entangled network. Although the rubbery plateau region for thermoplastics is not as extensive as for thermosets, the rubbery modulus is defined in this region. Upon further heating beyond 50 °C, the polymer starts to disentangle and the storage modulus decays further. In this temperature range, the onset of a second 'viscous' peak is observed in tan delta, which indicates that the material becomes liquid-like. Accordingly, the result provides a guide to decide the temperature ranges used in the deformation experiments (i.e., T_d = 37 and 50 °C).

In order to numerically solve the model for varying temperature, the elastic modulus appearing in Eq. (2) must be considered as a function of temperature. This is achieved here by using an empirically defined parameter, x [23]:

$$x = \frac{1}{1 + \exp\left(-\frac{T - T_r}{W}\right)} \tag{10}$$

such that:

$$E(T) = x\cdot E_0 + (1 - x)\cdot G_0 \tag{11}$$

Where: T_r is an adjustable reference temperature, found to be equal to 39.6 °C, and W is an adjustable parameter chosen to fit the expression to the experimental data, and found to be equal to

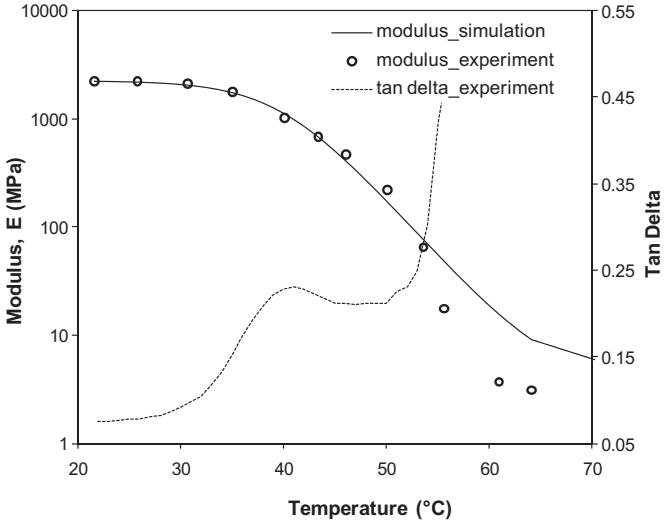

Fig. 3. Variation of the modulus of elasticity on the PDLLGA polymer as a function of temperature.

4.23 °C by a curve fitting procedure. E_0 and G_0 characterize the initial modulus of glassy and rubbery behaviors, respectively. In Eq. (11), the following material constants were obtained based on DMA measurement: $E_0 = 2250$ MPa, and $G_0 = 0.89$ MPa. Substitution of (10) into (11) gives a temperature variation of the modulus as shown in Fig. 3. A reasonable agreement between the experimental and simulated results is achieved between 20 and 52 °C with the parameters as described in the text. However, the simulation results start to divert from the experiment at temperature higher than ~52 °C for the material becomes liquid-like and no longer obeys the rubber-elasticity behavior as described by the simulation equation.

The Eyring activation volume, v, appearing in Eq. (5), was determined by carrying out a series of isothermal tensile experiments on the polymer samples under varying strain rates as shown in Fig. 4. The values of stress at yield and the natural logarithm of the corresponding strain rate are plotted (see Fig. 5). The activation volume is taken as the slope of the linear regression in Fig. 5.

The material parameters that characterize the strain hardening behavior are the rubbery modulus, G, and the number of rigid links between entanglements, N. Those two values can be determined by fitting the isothermal uniaxial tensile stress-strain curve at temperature above T_g.

4.2. Comparisons with the experimental results

In this section, the experimental results obtained in each stage are first discussed, and they are then compared with the computational simulations.

4.2.1. Uniaxial stretch

Fig. 6 shows the stress–stretch ratio curves from uniaxial tensile tests at $T_d = 37$ and 50 °C. PDLLGA exhibits distinct behaviors at temperature near and above its glass transition temperature T_g. At temperature below or near T_g ($T_d = 37$ °C), two features are prominent and are characteristic for glassy amorphous polymer behavior. One is the peak in nominal stress associated with yield followed by strain softening, and the other prominent feature is the pronounced strain hardening at large strains. With increase in temperature, the yield stress fell and strain stiffening is deferred to a later strain. Above T_g ($T_d = 50$ °C), the yielding disappears and it exhibits a hyperelastic behavior, showing remarkably high degree of viscoelastic linearity in tensile tests, which is consistent with Retting's finding [29].

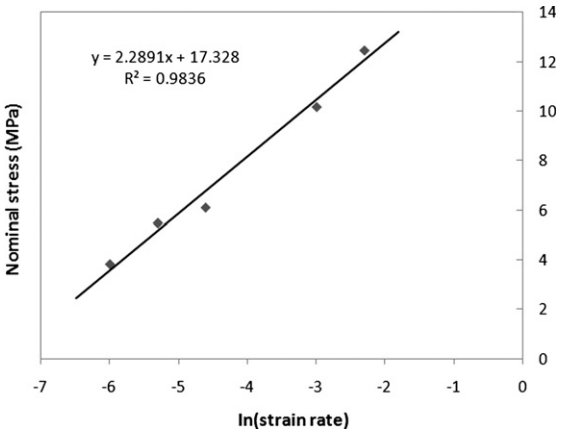

Fig. 5. Linear relationship between the measured yield stress and applied strain rate for the PDLLGA polymer. The constant v in Eq. (5) is derived from the slope of the linear fit.

The comparison between the numerically computed stress–stretch ratio and the experimentally measured responses for two deformation temperatures is shown in Fig. 6. One discrepancy between the experimental and simulation curves, shown in Fig. 6, lies at the significant differences at higher stretch ratio (>3) for $T_d = 37$ °C. The different can be interpreted by the assumption that there is break down of physical entanglement networks at high stretch ratio. Thus N does not remain constant but decreases with deformation [30]. Other network models [30,31] may be used to replace the Arruda-Boyce 8-chain expression to invoke the slippage of entanglements. However, at this stage we are prepared to accept these differences in view of the main aim, which is to use the same model with the same material's parameters to describe both, the stretching and the recovery stages of the SME in this polymer.

4.2.2. Recovery at $T \geq T_g$

The graph in Fig. 7 shows the measured decreasing stretch ratio with time under constant temperature (i.e., isothermal recovery).

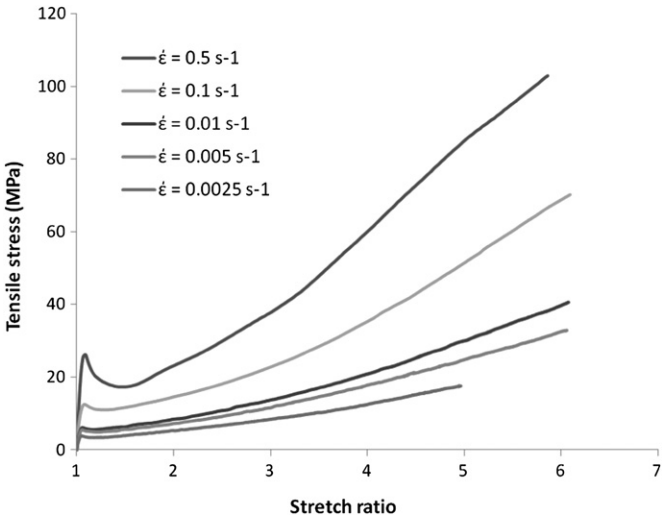

Fig. 4. Tensile stress versus stretch ratio curves for PDLLGA at 37 °C.

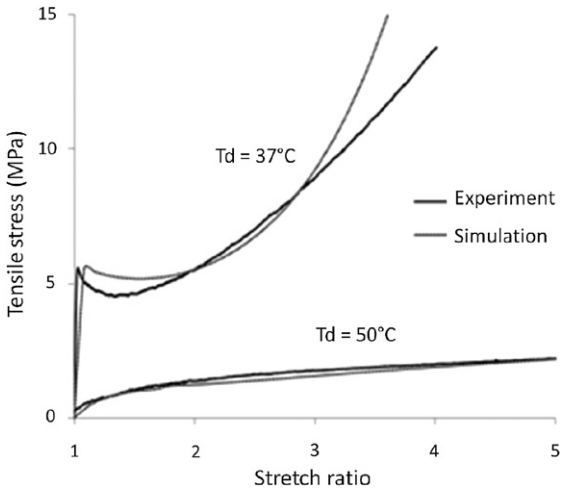

Fig. 6. Stress versus stretch ratio results for uniaxial stretching of PDLLGA sample at deformation temperature, T_d, of 37 °C (upper curve) and 50 °C (lower curves) and strain rate of 1.67×10^{-2} s^{-1}. The simulated stress–stretch ratio results are predicted by the numerical solutions (see Eq. (1)–(5)).

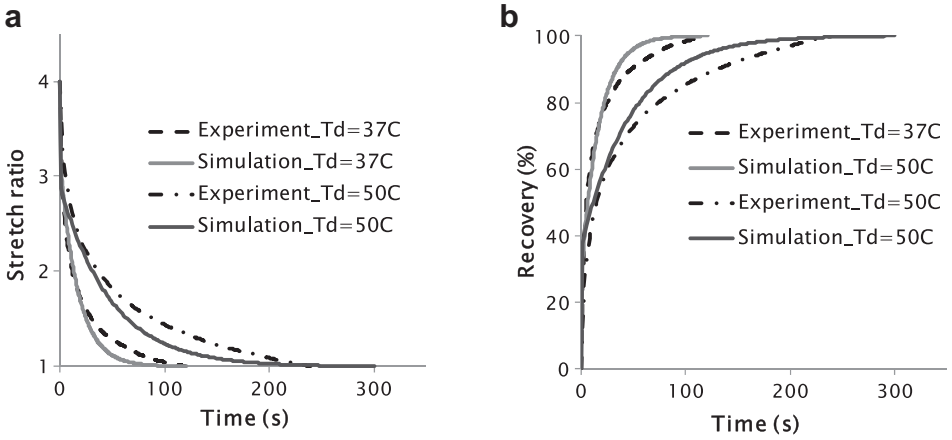

Fig. 7. (a) Stretch ratio decline during recovery of the PDLLGA sample at a temperatures of 37 °C, and (b) the corresponding degree of recovery of the PDLLGA sample at a temperature of 37 °C. The black line shows the experimental result and the solid grey line shows the simulation results as predicted by Eqs. (7)–(9).

As in previous figure, the black line shows the experimentally measured recovery in the sample of PDLLGA, whereas the numerically obtained prediction from the model is shown by the solid grey line. It is observed that the polymer can be completely recovered within 2 min time for the sample stretched at $T_d = 37$ °C. It is critical for the polymer to regain its original dimension in a short time span, especially in the field of minimally invasive surgery. However, sample stretched at $T_d = 50$ °C takes longer time to be fully recovered. It has been reported [16] that sample stretched at higher temperature shows a higher onset of recovery temperature. Both experimental data and simulation results show that the onset of strain recovery occurred instantly upon heating. However, stretch ratio decline occur much slowly in the experiments than the simulations. The discrepancy may be due to stress relaxation of sample during recovery [14]. The agreement between experiment and computation is qualitatively adequate but not sufficient. Rather than fitting a distribution of relaxation times, we have carried out strain recovery at a constant heating rate, as shown in Fig. 8.

For non-isothermal recovery, the temperature of the sample is made to increase at a finite rate; with strain recovery occurring concurrently. Application of a constant heating rate produces recovery in a sigmoidal shape as shown in Fig. 8. As depicted in the figure, there is slow initial recovery followed by high rate of recovery near the glass transition regime. Furthermore, the numerically derived result is also shown in Fig. 8. The agreement between the prediction from the model and the measured behavior of the polymer sample can be taken as satisfactory. When the deformed model is at low temperature, the viscosity of the viscoplastic element is high enough to resist the recoverable elastic entropic force of the network element. Therefore, the recovery is small at temperature below the T_g of the sample. During the recovery process where the sample is being heated up, the viscosity is reduced; the sample is rapidly recovered on the glass transition regime.

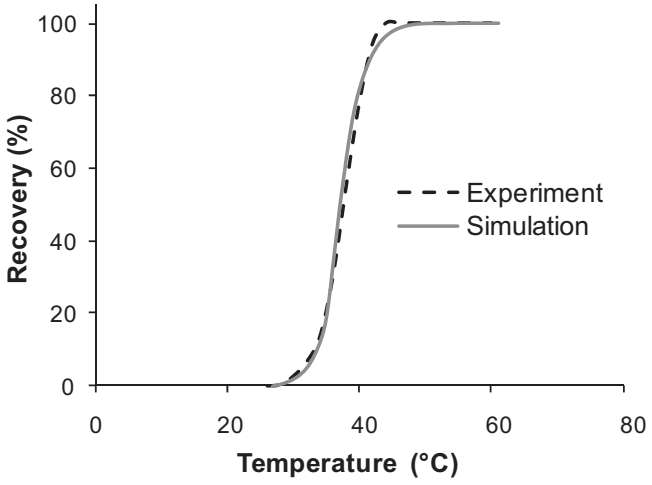

Fig. 8. Percent strain recovery under constant heating rate ($\beta = 3$ °C/min).

In this case, the agreement between the experimentally measured non-isothermal recovery and the computed prediction is good. It remains to be shown whether this agreement is due to the specific choice of the function selected to represent the variation of viscosity with temperature, or to the finite differential calculations that inadvertently performed a time–temperature superposition function. In the first instance we have used the Arrhenius relationship, rather than WLF equation. In order to check the choice of viscosity function, we have carried out these calculations using the WLF equation, with similar results. Therefore, the choice of the viscosity function does not seem to play a significant role in this process.

5. Conclusions

A search of the published literature on viscoplastic behavior of polymers revealed that it is mainly the stage 1 of the deformation that is subjected to modeling. However, in many ways it is the last stage, recovery, which is of practical significance and interest. In biomedical applications, this may involve predicting the extent of shape recovery of an implant, which must occur gradually after insertion, when stimulated by body heat. Therefore, the aim of this work was to experimentally characterize the recovery of the PDLLGA polymer and to tune the model and computations to achieve a reasonable agreement between experimental results and predictions. The graphs presented in Figs. 6–8 show that the viscoplastic models can be applied with good agreement to the experimental results for both the stretching deformation (stage 1), and the time-dependent recovery of the amorphous polymers, as described by the Eqs. (7)–(9). The success of the model in predicting extension and recovery with the same constitutive elements and the same material constants affords some confidence as to the accuracy of the constitutive equations. However, a more critical test will be a comparison of the model predictions in two or three-dimensional deformation schemes of a material with shape memory properties

References

[1] EL Feninat F, Laroche G, Fiset M, Mantovani D. Adv Eng Mater 2002;4:91.
[2] Gandhi MV, Thompson BS. Smart materials and structure. London: Chapman & Hall; 1992.
[3] Otsuka K, Wayman CM. Shape memory materials. New York: Cambridge University Press; 2002.
[4] Lendlein A, Kelch S. Angew Chem Int Ed 2002;41:2034.
[5] Liu CD, Chun SB, Mather PT. Macromolecules 2002;35:9868.
[6] Yakacki CM, Shandas R, Lanning C, Rech B, Eckstein A, Gall K. Biomaterials 2007;28:2255.
[7] Yakacki CM, Gall K. Shape-memory polymers for biomedical applications. In: Advances in Polymer Science. Springer; 2010. p. 148–75.
[8] Venkatraman SS, Tan LP, Joso JFD, Boey YCF, Wang XT. Biomaterials 2006;27:1573.
[9] Yasukawa T, Ogura Y, Sakurai E, Tabata Y, Kimura H. Adv Drug Deliv Rev 2005; 57:2033–46.
[10] Wong YS, Stachurski ZH, Venkatraman SS. Acta Mater 2008;56(18):5083–90.
[11] Stachurski ZH. Polymer 2003;44(19):6067–76.
[12] Beatty MF. Math Mech Solids 2005;10:176.
[13] Liu Y, Gall K, Dunn ML, Greenberg AR, Diani J. Int J Plast 2006;22(2):279–313.
[14] Nguyen TD, Qi HJ, Castro F, Long KH. J Mech Phys Solids 2008;56(9):2792–814.
[15] Lin JR, Chen LW. J Appl Polym Sci 1999;73(7):1305–19.
[16] .Khonakdar HA, Jafari SH, Rasouli S, Morshedian J, Abedini H. Macromol Theory Simul 2007;16(1):43–52.
[17] Bhattacharyya A, Tobushi H. Poly Eng Sci 2000;40(12):2498–510.
[18] Tobushi H, Okumura K, Hayashi S, Ito N. Mech Mater 2001;33(10):545–54.
[19] Morshedian J, Khonakdar HA, Rasouli S. Macromol Theory Simul 2005;14 (7):428–34.
[20] Arruda EM, Boyce MC. J Mech Phys Solids 1993;41:389–412.
[21] Buckley CP, Jones DC. Polymer 1996;37:2403–14.
[22] Haward RN, Thackray G. Proc R Soc A 1968;302:453–72.
[23] Qi HJ, Nguyen TD, Castro F, Yakacki CM, Shandas R. J Mech Phys Solids 2008; 56:1730–51.
[24] Sweeney J, Shirataki H, Unwin AP, Ward IM. J Appl Polym Sci 1999; 74:3331–41.
[25] Beatty MF. J Plast 2003;70:65–86.
[26] Mattice WL, Suter UW. Conformational theory of large molecules and rotational isomeric state model in macromolecular systems. New York: John Wiley & Sons; 1994.
[27] Pellicer J, Manzanares JA, Zúñiga J, Utrillas P, Fernández J. J Chem Educ 2001;78(2):263.
[28] Halsey G, White HJ, Eyring H. Text Res J 1945;15(9):295–311.
[29] Retting W. Colloid Polym Sci 1979;257:689.
[30] Sweeney J, Ward IM. J Mech Phys Solids 1996;44(7):1033–49.
[31] Dooling PJ, Buckley CP, Rostami S, Zahlan N. Polymer 2002;43:2451–65.

Polymer 52 (2011) 881–892

Contents lists available at ScienceDirect

Polymer

journal homepage: www.elsevier.com/locate/polymer

Molecular dynamics simulation of microscopic structure and hydrogen bond network of the pristine and phosphoric acid doped polybenzimidazole

Suhua Zhu [a,b], Liuming Yan [a,*], Dongfang Zhang [a], Qingxia Feng [a]

[a] Department of Chemistry, College of Sciences, Shanghai University, Shanghai 200444, China
[b] College of Material Science, Shanghai University, 99 Shangda Road, Shanghai 200444, China

ARTICLE INFO

Article history:
Received 26 August 2010
Received in revised form
23 November 2010
Accepted 16 December 2010
Available online 23 December 2010

Keywords:
Polybenzimidazole
Phosphoric acid
Hydrogen bonding network

ABSTRACT

The microscopic structure and hydrogen bonding characteristics of the pristine and phosphoric acid (PA) doped polybenzimidazoles (poly[2,2′-(*meta*-phenylene)-5,5′-benzimidazole] or *m*-PBI, and poly [2,2′-(*para*-phenylene)-5,5′-benzimidazole] or *p*-PBI) were studied by molecular dynamics simulations based on a united-atom force field model. In all the simulated systems, a benzimidazole group and an adjacent phenylene group are almost in coplanar configuration, while two adjacent benzimidazole groups are in twisted configuration. In pristine PBIs, the *p*-PBI is more ordered and stretched than the *m*-PBI. In PA doped PBIs, hydrogen bonding network is formed by donating phosphoric acid proton to imine nitrogen, phosphoric acid proton to phosphoric acid oxygen, and amine proton to phosphoric acid oxygen. In addition, the structural transport of proton is attributed to the formation of hydrogen bonding network in PA doped PBIs.

1. Introduction

The proton exchange membrane fuel cells (PEMFCs) are considered to be one of the most promising energy conversion systems in the future society when the conventional fossil fuels are substituted by the green, renewable energies. Although the PEMFC technology has been widely studied almost for a half centuries and a variety of PEMFCs have been developed for applications ranging from small portable devices, to electric vehicles and even to stationary electricity generation; the high cost and relatively short service life have hindered the large scale commercialization of the PEMFC technology. In order to overcome the obstacles for the commercialization of PEMFCs, it is important to develop high temperature proton exchange membrane suitable for PEMFCs operated at elevated temperature well above the boiling point of water (>120 °C). Some of the advantages of high temperature PEMFCs include improved catalyst activity, better tolerance to CO in the fed gas, simplified water and heat management systems. However, the most widely accepted proton exchange membranes nowadays, based on the perfluorosulfonic acid polymer, cannot meet the requirement of the high temperature PEMFCs because the proton conductivity drops too low as water is lost from these membranes at temperatures over 100 °C. Therefore, great efforts have been devoted to the development of proton exchange membranes with good conductivity at high temperatures with little or no hydration of the membrane.

Recently, phosphoric acid doped polybenzimidazole (PBI) membranes have attracted great research interests because of their excellent high temperature proton conductivity at low hydrated or even at anhydrous states and relatively low costs [1,2]. As an aromatic heterocyclic amorphous polymer, the aromatic backbone provides PBI with excellent thermal stability [3], high glass transition temperature (T_g = 425–436 °C) [4–7], good chemical resistance, high retention of stiffness and toughness, but poor processability [1,8,9]. Though the intrinsic conductivity of PBI is only about 10^{-12} S cm^{-1} at 25 °C [10] and cannot meet the requirement of any PEMFCs, great improvement could be achieved if phosphoric acid is doped to PBI. Therefore, the phosphoric acid doped PBI membranes are considered competitive candidates for high temperature PEMFCs. However, one of the greatest obstacles for the commercialization of PEMFCs based on phosphoric acid doped PBI membranes is the relatively short service life owing to the fast drainage of the phosphoric acid at operational environment. Great efforts have been devoted to overcome this obstacle. For example, improved phosphoric acid retention was achieved when inorganic materials which absorb phosphoric acid are incorporated [11,12]; high acid retention was also achievable by doping phosphonic acid with long hydrophobia organic group [13–15]; perfect acid retention has been achieved by bonding the phosphonic acid group to the PBI backbone or by blending a second

* Corresponding author. Tel.: +86 21 66132405; fax: +86 21 66133513.
E-mail address: liuming.yan@shu.edu.cn (L. Yan).

0032-3861/$ – see front matter © 2010 Elsevier Ltd. All rights reserved.
doi:10.1016/j.polymer.2010.12.037

polymer with phosphonic acid groups into PBI [16,17]. It is also plausible to improve the characteristics of PBI by incorporating other moieties into the polymer backbone via copolymerization [18–21], by attaching side groups [22], by changing the acid moiety of polybenzimidazole [23], or by blending with other polymer ingredients [24]. For details of the development of PBI based proton exchange membranes, the readers are referred to the pertinent literatures [1,9,11,25].

Pristine PBI has crystalline domains due to the π–π stacking interactions between the aromatic backbones and hydrogen bonding (H-bonding) between the acidic proton of the amine group and the basic imine nitrogen as revealed by X-ray diffractions [4,7,26]. When doped with phosphoric acid, the crystalline order is completely lost owing to the solvation process. In pristine PBI, the H-bonding is relatively weak since there are still significant amounts of N–H groups not associated with any H-bonding observable from IR spectra [27,28]. In the phosphoric acid doped PBI, the imine nitrogen is supposed to be protonated by the phosphoric acid as a very broad absorption band complex appears in the wave number range from about 2400 to 3000 cm^{-1} [29–32], however, Kawahara argued that phosphoric acid cannot protonate the imine nitrogen [33]. From magic angle spinning NMR, Hughes identified four different ^{31}P environments corresponding to the bound and unbound phosphoric acid molecules and phosphate anions [34]. NMR study also revealed that the proton transport at more than 2 order of magnitude faster than the phosphate anion supporting the proton hopping transport mechanism [35].

Despite the understanding from experimental observations, there still lacks comprehensive understanding of the microscopic structural and H-bonding characteristics and proton transport mechanism of the phosphoric acid doped PBI compared to the enormous knowledge accumulated for the perfluorosulfonic acid membranes by various molecular simulations [36–38]. Some of the molecular simulations which are employed to the study of structure and transport of protons and small molecules of PBIs and related systems include quantum chemistry calculations [39–42], classical molecular dynamics simulations [43], *ab initio* molecular dynamics simulations [44]. However, there are still insufficient *ab initio* calculations and molecular simulations of the phosphoric acid doped PBI. These theoretical studies could provide intuitive understanding of the structural and H-bonding characteristics and proton transport mechanism on molecular scale, which are fundamentally important for the development of new membranes based on PBI with improved properties. In this work, the structural and H-bonding characteristics of both the undoped pristine PBI and the phosphoric acid doped PBI have been studied using molecular dynamics (MD) simulation based on a united-atom force field model. The overall aim is to understand how the hydrogen bond network is formed and how the hydrogen bond network influences the structural diffusion of the proton.

2. The simulation methods

2.1. Molecular models for the PBIs

Two types of PBIs, poly[2,2′-(*m*-phenylene)-5,5′-benzimidazole] (or *m*-PBI) and poly[2,2′-(*p*-phenylene)-5,5′-benzimidazole] (or *p*-PBI), were studied in this work. The *m*-PBI, which is also the commercially available PBI under the trademark Celazole®, is a polymer synthesized by polycondensation of 3,3′,4,4′-tetraaminobiphenyl (TAB) and isophthalic acid (IPA); while the *p*-PBI is synthesized by polycondensation of TAB and terephthalic acid (TPA) [7]. In our MD simulations, both the *m*- and *p*-PBI molecules were modeled by four repeat units and each repeat unit consists of two benzimidazole groups and one phenylene group (Fig. 1). The

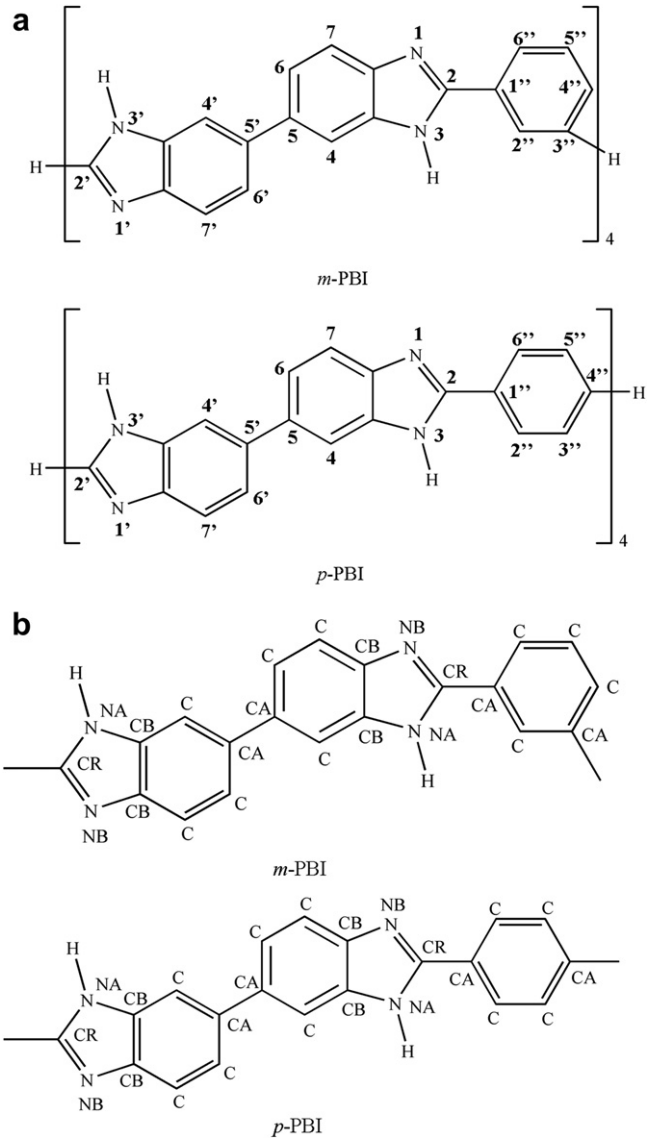

Fig. 1. Molecular models for the *m*- and *p*-PBI molecules, (a) atomic numbering, (b) atomic site names.

model molecules at this size, about 64 Å in length for the stretched *p*-PBI, are suitable for the MD simulations. We noticed that much longer PBI model molecules consisting of 75 repeat units were simulated in literature; however, the overall size (total number of atoms) of the simulated cell is similar to our systems [43]. Considering the rigidity of the PBI backbone, forcing long model molecules into a cubic simulation cell may greatly strain the molecules. On the other hand, if the simulation cell is enlarged to incorporate a long unstrained molecule, the simulation cell will be too large and the computing will take too long. Compared to other simulated oligomers, for example, the typical perfluorosulfonic acid oligomers (which are more flexible than PBIs) are composed of about 160 atoms in the molecular backbone [45,46]; the size of model molecules in this work is suitable.

2.2. The molecular force field model for the PBIs

Most of the published MD simulations are carried out with the all-atom force field model or with the united-atom force field

model. The all-atom force field model is considered more delicate than the united-atom force field model owing to its complexity and the more force field parameters used to model the same molecular system. On the other hand, the united-atom force field model is an approximation respect to the all-atom force field model since it neglects some degrees of freedoms. Despite this approximation, the advantages of a united-atom force field model are also evident: a united-atom force field model consists of less force field parameters and retains less parameterization error; it also speedups the simulations by avoiding nonessential calculations for the systems of interest. Therefore, a united-atom force field model was applied in our MD simulations.

In our united-atom force field model, all the hydrogen atoms that bonded to a carbon atom are not explicitly represented. A carbon atom together with the covalently attached hydrogen atom was modeled by a united-atom locating on the nucleus of the carbon atom. However, the hydrogen atom (referred as amine proton) that bonds to the amine nitrogen is represented explicitly. In this united-atom force field model, each model molecule is represented by 104 atoms or united-atoms.

Considering the rigidity of the aromatic benzimidazole group and phenylene group, both groups are restrained in our MD simulations as rigid bodies according to the geometries optimized at the B3LYP/6-31++G(D, P) level of theory as implemented in the Gaussian 03 program, the widely accepted *ab initio* quantum chemistry program for calculation of molecular structures and energies [47]. The hybrid density functionals, B3LYP, are among the most widely applied functionals by chemists based on the number of citations [48], and a combination of the B3LYP functionals with the 6-31++G(D, P) basis set could reach chemical precision [49].

The bonds connecting the rigid groups are allowed to vibrate near their equilibrium distances by application of the harmonic potential,

$$u_{\mathrm{b}}(r) = \frac{1}{2}k_{\mathrm{r}}(r - r_0)^2 \tag{1}$$

Harmonic potentials are also applied to all the bond angle bendings,

$$u_{\theta}(\theta) = \frac{1}{2}k_{\theta}(\theta - \theta_0)^2 \tag{2}$$

The force field constants for the bond stretching and bond angle bending are based on the DREUDING force field [50], and the equilibrium bond lengths and bond angles are based on the B3LYP/6-311++(D, P) geometries as summarized in Table 1.

During the MD simulations, both the benzimidazole group and the phenylene group are allowed to rotate around the interring bonds that connect these groups. Fig. 2 shows the bond rotational potential profiles for a model molecule, as well as its ground state conformation based on the B3LYP/6-31+G(D) level of theory. It is shown that the rotational potential profile for the dihedral angle ($\varphi_{\mathrm{b-b}}$) between the two benzimidazole groups has a potential barrier of 2.902 kcal/mol and an equilibrium dihedral angle of 41.0°. Two adjacent benzimidazole groups are nonplanar due to the steric repulsion between the hydrogen atoms at C4 and C6′, and at C6 and C4′. This potential profile is approximately fitted to the following cosine function,

$$u_1(\varphi_{\mathrm{b-b}}) = 1.24\cos(4\varphi_{\mathrm{b-b}}) \tag{3}$$

For the dihedral angle ($\varphi_{\mathrm{b-p}}$) between a benzimidazole group and a phenylene group, the rotational potential profile has a potential barrier of 4.972 kcal/mol and an equilibrium dihedral angle of 6.9°. The phenylene group and benzimidazole group are almost coplanar due to the lack of steric repulsion between the benzimidazole group and the phenylene group. This potential profile is fitted to the following cosine function,

$$u_2\left(\varphi_{\mathrm{b-p}}\right) = 2.48\cos\left(2\varphi_{\mathrm{b-p}} - 180\right) \tag{4}$$

Compared to the potential barrier between two benzimidazole groups, the potential barrier between a phenylene group and a benzimidazole group is almost twice of the previous one. This phenomenon could be explained by the fact that the hyperconjugation

Table 1
Force field parameters for the *m*- and *p*-PBI molecules.

Bond stretching		
	r_0 (Å)	k_{r} (kcal mol^{-1} Å^{-2})
C2–C1″, C2′–C3″, C2′–C4″	1.464	700
C5–C5′	1.484	700

Bond angle bending		
	θ_0 (°)	k_θ (kcal mol^{-1} rad^{-2})
C4′–C5′–C5	120.282	100
C6′–C5′–C5	120.284	100
C5′–C5–C4	120.305	100
C5′–C5–C6	120.272	100
N1–C2–C1″	124.878	100
N3–C2–C1″	123.147	100
C2–C1″–C2″	122.218	100
C2–C1″–C6″	119.016	100

Lennard–Jones potential parameters			
Atomic pairs	ε_0 (kcal/mol)	σ_0 (Å)	DREIDING type
H–H	0.000	2.400	H_HB
NA–NA	0.145	3.695	N_3
NB–NB	0.215	3.795	N_R
CR–CR	0.095	3.880	C_R
CA–CA	0.095	3.880	C_R
CB–CB	0.095	3.880	C_R
C–C	0.145	3.980	C_R1

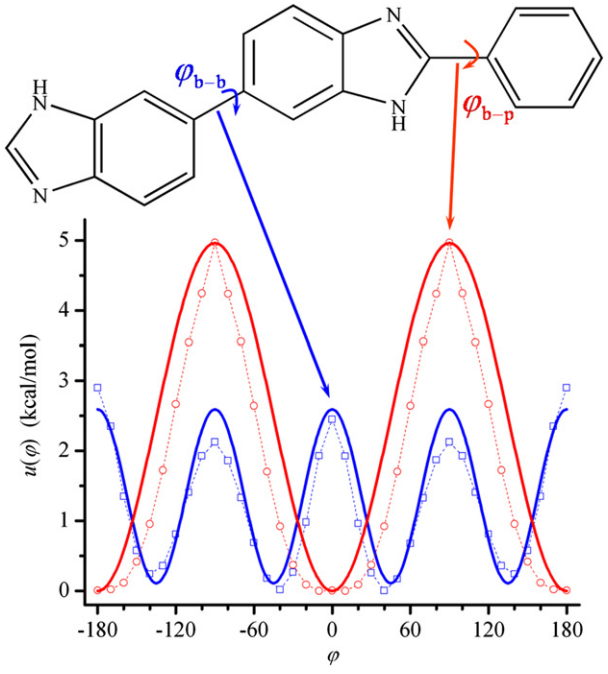

Fig. 2. Bond rotational potential profiles for the model molecule calculated at the B3LYP/6-31+G(D) level of theory. The solid curves are best fits to the calculated potential, and the dotted curves are only guides to the eyes.

interaction between two benzimidazole groups stabilizes the molecule, while the steric repulsion between the hydrogen atoms at C4 and C6′, and at C6 and C4′ destabilize the molecule, the hyperconjugation interaction cancels part of the steric repulsion and lowers the rotational potential barrier. On the other hand, the hyperconjugation interaction is more powerful than the steric repulsion and dominates the rotational potential profile between a phenylene group and a benzimidazole group.

The residual charges for the *m*- and *p*-PBI molecules are also calculated based on model molecules at the B3LYP/6-31+G(D) level of theory by use of the ChelpG method which reproduces the molecular electrostatic potential [51]. The model molecules are optimized first, and then verified to be local minimum by frequency calculation. Based on the optimized geometries, the residual atomic charges are calculated for each of the model molecules, and then the charges of the carbon and the bonded hydrogen are summed to get the residual charge of the united-atom. Finally, the residual charges are averaged and adjusted to get the residual charges for the MD simulation of the PBIs (Fig. 3).

Lennard–Jones potentials are applied to all atomic pairs with force field parameters adopted from DREIDING force field model [50]. The force field parameters between two likely atoms are summarized in Table 1, and that between two unlikely atoms are obtained by use of the Berthelot mixing rules [52].

The united-atom force field model reproduces reliable molecular configurations since the geometrical parameters and interring bond rotational potential profiles are based on density functional theory optimizations at the B3LYP/6-31++G(D, P) level of theory of the specific model molecules. The density functional theory calculation errors for most bond lengths and bond angles, respectively, are within 0.02 Å and 0.6° except a few large errors between 0.02 and 0.04 Å and 0.6°–1.0° [53,54]. The DREIDING force field also leads to accurate geometries and reasonably accurate barriers for various organic systems [50]. By combination of the B3LYP/6-31++G(D, P) geometry, interring bond rotational potential profiles and residual charges, and bonded force constant and non-bonded force field parameters from the DREIDING force field, the united-atom force field model minimizes the number of force field parameters and retains the accuracy for the description of interring rotation and the hydrogen bonding. The united-atom force field model reproduces slightly lower density than the experimental density for *m*-PBI (Table 4).

For comparison, some of the geometrical parameters from our force field model and related systems are summarized in Table 3. It could be seen that the bond length differences between our force field and other similar systems are insignificant; the average bond length difference is zero; the maximum difference is ±0.03 Å. The maximum bond angle difference in these systems is also insignificant at about 1.3°.

2.3. Force field models for the phosphoric acid

The force field model used for the phosphoric acid is a modified version from our previous study [55]. In the modified model, the PO_4 tetrahedron is restrained as a rigid body based on the B3LYP/6-31++G(D, P) geometry, and the hydrogen atoms are not restrained. Harmonic potentials are applied to the OPA–HPA bond stretching and the PA–OPA–HPA bond angle bending, respectively (see Fig. 4 for the atomic site names). The OP–PA–OPA–HPA and OPA–PA–OPA–HPA dihedral angle torsions are represented by two cosine terms. The Lennard–Jones potentials are applied to the non-bonded interactions with the cross-term interactions obtained from the Berthelot mixing rules [52]. All the force field parameters, including the non-bonded interactions and bonded interactions, are summarized in Table 2.

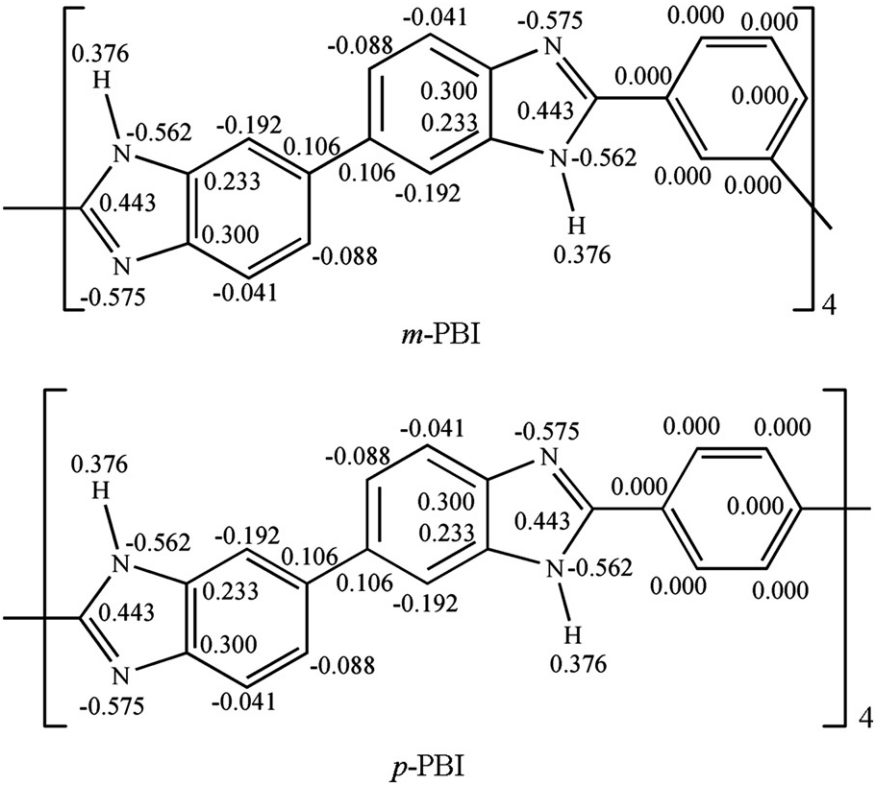

Fig. 3. Residual charges for the *m*- and *p*-PBI molecules.

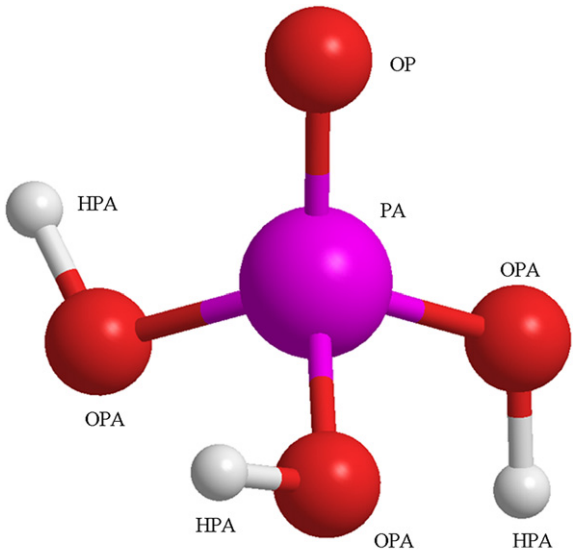

Fig. 4. Molecular model and atomic site names for the phosphoric acid.

This force field for phosphoric acid is similar to that used by Spieser et al. [56]. From the geometrical parameters summarized in Table 3, it could be seen that the three PA–OPA bonds used in this study are nonequivalent; but that used by Spieser et al. are equivalent. However, the average length of three PA–OPA bonds is the same for these two force fields. Furthermore, our bond lengths for PA–OP and OPA–HPA are slightly shorter than that of Spieser's. In solid state of phosphoric acid, the bond length difference between PA–OPA and PA–OP is smaller than that of both force fields (the averaged bond lengths are similar) since the hydrogen atoms are pulled away from OPA atoms by hydrogen bonding and the difference between the protonated oxygen OPA and the non-protonated oxygen OP decreases in solid state [57]. Second, the average of OPA–PA–OPA bond angles is similar for both force fields; however, these bond angles are slightly nonequivalent in our force field, but are equivalent in Spieser's. Third, the bond rotational potentials for dihedral angles are the same for both force fields [56]. Fourth, the electrostatic interaction and the van der Waals interaction parameters are also similar for both force fields. The greatest difference is shown for the OP–PA–OPA angle as our bond angles are about 6.2° larger than that of Spieser's in average. The differences between these two force fields are plausible in the simulation of phosphoric acid in different systems since the intermolecular hydrogen bonding between OP and HPA decreases from solid state to liquid state and then to phosphoric acid doped PBI. The stronger the hydrogen bonding is, the lesser the difference between the PA–OP bond and PA–OPA bond is owing to the decreased hydrogen bonding distance. Our force field is suitable to simulate phosphoric acid doped PBI since it could result slightly weaker hydrogen bonding than Spieser's force field.

Table 2
Force field parameters for the phosphoric acid.

Bond stretching		
	r_0 (Å)	k_r (kcal mol^{-1} Å^{-2})
OPA–HPA	0.966	700
Bond angle bending		
	θ_0 (°)	k_θ (kcal mol^{-1} rad^{-2})
PA–OPA–HPA	111.4	100
Dihedral angle torsion		
OPA–PA–OPA–HPA or OP–PA–OPA–HPA	$u_\varphi = 1 + 0.75\cos 2\varphi + 0.25\cos 3\varphi$	
Lennard–Jones parameters and atomic residual charges		
	σ_0 (Å)	ε_0 (kcal/mol)	q/e
PA–PA	4.595	0.0936	1.093
OPA–OPA	2.955	0.2029	−0.605
OP–OP	3.111	0.1491	−0.601
HPA–HPA	2.500	0.0000	0.441

Table 3
Selected bond lengths and bond angles for the PBIs and phosphoric acid.

Systems	FF[a]	2,6-Diphenyl (1,2-*d*;5,4-*d*′) benzodiimdazole (exp.)[b]	H_3PO_4	PBI[e]	MD results
Bond lengths					
CR–CA	1.464	1.468			1.465 ± 0.029
CA–CA	1.484	–			1.481 ± 0.030
CA–C	1.401	1.378–1.397 (1.386)			1.401 ± 0.001
C–C	1.387	1.374–1.390 (1.380)			1.388 ± 0.001
CR–NA	1.379	1.356–1.359 (1.357)		1.357	1.378 ± 0.001
CR–NB	1.310	1.333		1.339	1.309 ± 0.001
NA–H	1.006	–		0.993	1.006 ± 0.001
NA–CB	1.382	1.399–1.401 (1.400)		1.382	1.382 ± 0.001
CB–CB	1.410	1.425–1.428 (1.427)		1.376	1.410 ± 0.001
CB–C	1.392	1.369–1.383 (1.376)			1.393 ± 0.001
NB–CB	1.382	1.379–1.381 (1.380)		1.372	1.383 ± 0.001
PA–OP	1.471		1.48,[d] 1.52[c]		1.471 ± 0.001
PA–OPA	1.600		1.61,[d] 1.55[c]		1.600 ± 0.001
	1.609		1.61,[d] 1.57[c]		1.609 ± 0.001
	1.620		1.61,[d] 1.59[c]		1.620 ± 0.001
Bond angles					
OPA–HPA	0.966		0.97[d]		0.997 ± 0.046
C4′–C5′–C5	120.282				118.4 ± 5.4
C6′–C5′–C5	120.284				118.8 ± 5.6
C5′–C5–C4	120.305				118.3 ± 5.3
C5′–C5–C6	120.272				118.5 ± 5.2
N1–C2–C1″	124.878	125.4			122.5 ± 4.9
N3–C2–C1″	123.147	123.0			122.4 ± 4.8
C2–C1″–C2″	122.218	121.1			119.5 ± 5.6
C2–C1″–C6″	119.016	120.3			118.9 ± 5.5
OP–PA–OPA	114.2		109.6[d]		114.2 ± 0.1
	119.1		109.6[d]		119.1 ± 0.1
	114.2		109.6[d]		114.2 ± 0.1
OPA–PA–OPA	100.2		103.0[d]		100.2 ± 0.1
	106.2		103.0[d]		106.2 ± 0.2
	101.0		103.0[d]		101.0 ± 0.2
PA–OPA–HPA	111.4		123.0[d]		114.8 ± 0.2

[a] The force field parameters are based on density functional theory calculations at B3LYP/6-31++G(D, P) level of theory. Since each PBI oligomer consists of four repeat units and the corresponding geometrical parameters have slightly different values, the geometrical parameters are averaged over the repeat units.
[b] Experimental values for 2,6-diphenyl(1,2-*d*;5,4-*d*′)benzodiimdazole, if several bond lengths exist for the equivalent bonds, the minimum, maximum and average (in parenthesis) bond lengths are listed [58].
[c] Reference [57].
[d] Reference [56].
[e] Reference [43].

2.4. The molecular dynamics simulation methods

Four systems, the pristine *m*- and *p*-PBI molecules and the phosphoric acid doped *m*- and *p*-PBI molecules, were simulated, and their compositions are summarized in Table 4.

The MD simulations were carried out using the DL_POLY program, a open source molecular dynamics simulation package developed at Daresbury Laboratory [59]. The DL_POLY is a general purpose MD package with a large number of built-in potential functions especially suitable for simulation of molecular systems in materials science. The original package is DL_POLY_2 and the latest

Table 4
Compositions and densities for the simulation cells.

Simulated systems	Number of molecules			Total number of atoms	MD density ρ_{MD} (g/cm^3)	Experimental density ρ_{exp}(g/cm^3)
	m-PBI	*p*-PBI	H_3PO_4			
I	48			4992	1.275	1.296–1.34 [4,5,65]
II	30		720	8880	1.491	
III		48		4992	1.312	
IV		30	720	8880	1.512	

package is DL_POLY_3, each with a serial version and a parallel version. The package used in this study is the parallel version of DL_POLY_3. The advantages of DL_POLY_3 include the excellent scalability, the large number of built-in potential functions easing the simulations of diversified molecular systems, and the variety of algorithms implemented. These are important characteristics making the DL_POLY program suitable for our simulations.

During our MD simulations, 3D periodic boundary conditions were applied to all the simulation cells, and the simulations were carried out in the NPT ensemble with temperature and pressure maintained, respectively, by the Nosé–Hoover thermostat and barostat with the same relaxation time parameters of 0.2 ps [60,61]. The cutoff distance for the calculation of van der Waals interactions is set to 13.0 Å, and coulombic interactions are evaluated using the Ewald algorithm with a convergent criterion of 10^{-8}. The SHAKE algorithm incorporated with the quaternion rotational description for rigid bodies is applied to satisfy the geometrical constraints with tolerance of 10^{-8} [62,63]. The Verlet integration scheme was used to solve the Newtonian equation of motion for atoms in the simulation cell with an integration step time of 1 fs [64]. The neighbor list algorithm is used to speedup simulation with primary cutoff at 11.0 Å and secondary cutoff at 13.0 Å. The initial simulation cells were constructed by insertion of the molecules randomly. During the initial simulations, the loose initial simulation cells were gradually squeezed and reached an equilibrium density (Table 4) in about 1,000,000 steps. After that, another 1,000,000 steps of preparation runs were carried out to guarantee the reach of equilibrium in the NPT ensemble under a pressure of 1 atm and a temperature of 300 K. Finally, the production runs were carried out for the generation of structural characteristics of the systems under the same conditions of the preparation runs. Although no significant difference is observed between short simulations (1,000,000 steps) and long simulations (3,000,000 steps), all the production runs were lasted for 3,000,000 steps, corresponding to a real world evolution time of 3 ns.

3. Calculation results and discussions

3.1. The conformational characteristics of the PBIs

In Fig. 5a, it shows the conformations of the pristine *m*- and *p*-PBI molecules, snapshots from the MD simulation of systems I and III. The equilibrium cell size for *m*-PBI is about $40.0 \times 45.2 \times 46.6$ Å^3 and that for *p*-PBI is about $37.2 \times 27.7 \times 78.6$ Å^3. The reason why the cell size for *p*-PBI in *z*-direction is much larger than that in any other directions is based on the relative dimensions of the simulated molecules and cell size: the cell size in each direction should be larger than the molecular dimension in that direction in order to avoid factitious effects from periodic boundary conditions. Since the *p*-PBI molecules are much longer than the *m*-PBI molecules owing to the difficulties to distort the *p*-PBI molecules, the longer cell size in *z*-direction for *p*-PBI is set than that for *m*-PBI. As the molecular dimensions are smaller than the cell sizes in any corresponding directions; the difference in simulation results caused by cell shape is minimized compared to the use of cubic simulation cells. From the snapshot of MD simulations, it could be seen that both *m*- and *p*-PBI molecules form amorphous conformations, however, the *p*-PBI is slightly more ordered both at short- and long-range compared to the *m*-PBI. These observations are consistent with experimental results by X-ray diffractions [4,7,66] where the diffraction peak at $2\theta \approx 13^\circ$ for *p*-PBI is slightly sharper and higher than that for *m*-PBI [7,26]. Furthermore, the molecular backbones of *p*-PBI are more stretched than that of *m*-PBI. It could also be seen that a phenylene group and a neighboring benzimidazole group are almost in coplanar conformation, while that between two benzimidazole groups are in twisted conformation (a more detailed discussion will be given in Section 3.2.3 based on the dihedral angle distribution functions). In addition to the enhancement of the polymer crystallinity, the introduction of the *p*-phenylene also enhances the flexibility of the polymer chain (the rotational freedom is favored owing to the symmetry) since the experimental glass transition temperature of *p*-PBI is about 59 °C lower than that of *m*-PBI [7].

Despite the conformational differences between the pristine *m*- and *p*-PBI molecules, the conformational differences between the phosphoric acid doped *m*- and *p*-PBI molecules are more limited as shown in Fig. 5b. The cell size for system II is about $46.7 \times 44.3 \times 57.8$ Å^3 and that for system IV is about $46.4 \times 30.1 \times 84.6$ Å^3, and the cell sizes are set according to the same criteria for systems I and III. It could be seen that both the *m*- and *p*-PBI molecules are well separated by the phosphoric acid molecules without agglomeration. In experiments, both *m*- and *p*-PBI molecules could be readily solvated in hot concentrated phosphoric acid, forming phosphoric acid doped *m*-PBI and *p*-PBI. The configurations of the model molecules are similar to that in the pristine *m*- and *p*-PBI molecules. The *p*-PBI model molecules are more stretched than the *m*-PBI model molecules. The dihedral angles between the phenylene group and the benzimidazole group or between two benzimidazole groups are also similar to that in the pristine *m*- and *p*-PBI molecules. The benzimidazole–phenylene–benzimidazole segments are almost coplanar despite the twisting of the oligomer in the phosphoric acid doped *m*- and *p*-PBI molecules (to be detailed in Section 3.2.3). The phosphoric acid molecules form a continuous sub-phase allowing the long-distance transport through the membranes.

3.2. Bond parameter distributions during MD simulations

3.2.1. Bond length vibrations

During MD simulations, the bond length variations are caused by the intrinsic vibrations of covalent bonds and by the numeric errors of the MD algorithms. The last column of Table 3 lists the averaged bond lengths and the standard deviations of the typical covalent bonds of the PBIs and of the phosphoric acid calculated from the trajectories of MD simulations. It could be seen that the averaged bond lengths are very close to the force field equilibrium bond lengths. The standard deviations of interring bonds which are allowed to vibrate in the simulations are about 0.036 Å, much larger than that of bonds in the phenylene rings and in the benzimidazole rings which are constraint during the MD simulations. In the phosphoric acid, the bond lengths in the PO_4 structure are also well conserved to the force field geometry; and the unconstraint O–H bonds vibrate with standard deviations of about 0.044 Å. Therefore, it could be concluded that the bond lengths are well conserved, and variations are low especially for the constraint parts of the model molecules.

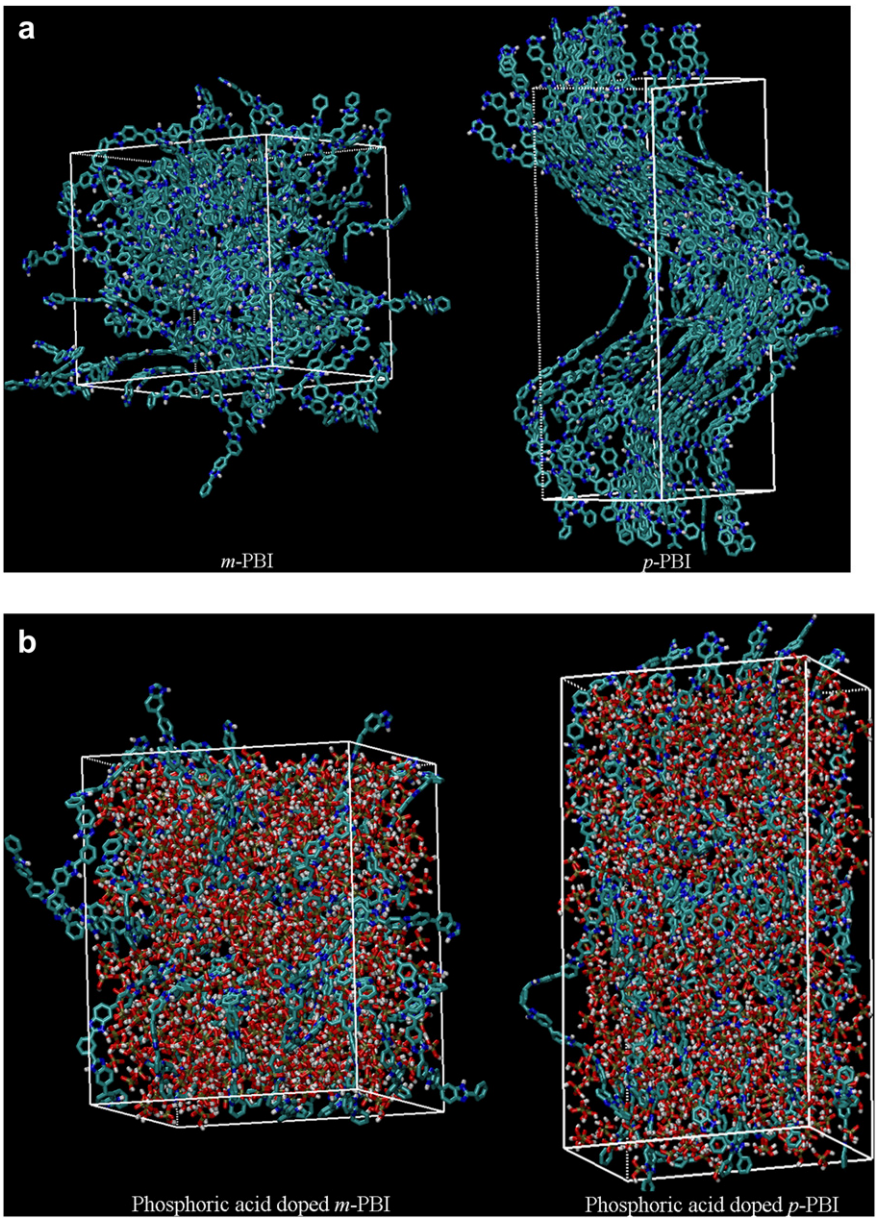

Fig. 5. Conformations of the simulation cells: (a) the pristine *m*- and *p*-PBI molecules, (b) the phosphoric acid doped *m*- and *p*-PBI molecules. Color code: cyan for C, blue for N, white for H, red for O, and tan for P; simulation parameters: NPT ensemble with 3D periodic boundary conditions applied, Verlet algorithm, 1 fs step time.

3.2.2. Bond angle vibrations

Table 3 also summarizes the averaged bond angles and their standard deviations during MD simulations. It could be seen that most of the averaged bond angles are slightly smaller than the equilibrium bond angles for about 1.7° in average. And the standard deviations range from 4.7° to 7.4° with an averaged value of 5.3°. The standard deviations are about 4.4% of the averaged bond angles, similar to that of bond length vibrations (the unconstraint bond length). For the phosphoric acid, the bond angles for the PO_4 tetrahedral structure which is constraint almost conserve during the MD simulations. However, the bond angle HPA–PA–OPA is about 3.4° larger than equilibrium bond angle from the force field.

3.2.3. Dihedral angle distributions

The overall conformation of a PBI oligomer is determined by its dihedral angles (φ_{b-b}) between two benzimidazole rings and that (φ_{b-p}) between a benzimidazole ring and a phenylene ring. During MD simulations, these dihedral angles rotate as the interring bond rotational barriers are low enough to be overcome by the thermal motions of the oligomers. From the dihedral angle distributions g_{b-b} (Fig. 6a), it could be seen that the g_{b-b} at $\varphi_{b-b} = 0°$ is very low corresponding to the bond rotational barrier as shown in Fig. 2. The other four minima of g_{b-b} occur at ±90° and ±180° also corresponding to the other bond rotational barriers. The maxima of g_{b-b} occur at ±45° and ±135° corresponding to the bond rotational potential wells. For the dihedral angle distribution of g_{b-p} (Fig. 6b), the maxima occur at 0° and ±180°, corresponding to the coplanar conformation. For the nonplanar conformations, the g_{b-p} is negligible. These characteristics agree with the bond rotational potential profile since the rotational barrier for the benzimidazole–phenylene interring bonds is almost double of that for the benzimidazole–benzimidazole interring bonds.

The observations of dihedral angle distributions are also consistent with the overall conformation revealed by the snapshots

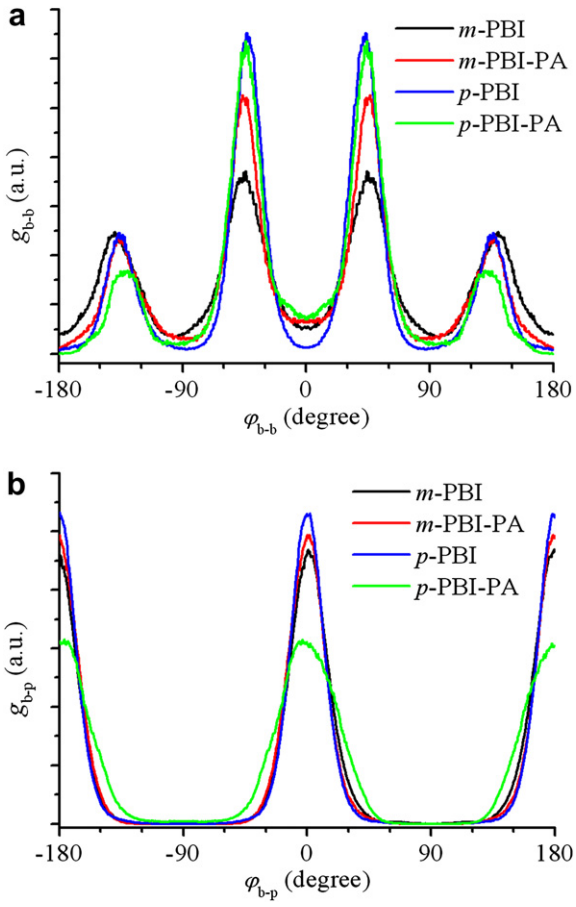

Fig. 6. Dihedral angle distributions (arbitrary units) for the PBI oligomers calculated from the trajectories recorded during the MD simulations, (a) the dihedral angle distribution g_{b-b} between two benzimidazole rings, and (b) the dihedral angle distribution g_{b-p} between a benzimidazole ring and a phenylene ring.

of the simulation cells. For the pristine PBIs, the *p*-PBI is more structured compared to *m*-PBI since the peaks of both g_{b-b} and g_{b-p} for *p*-PBI are higher than that for *m*-PBI. Furthermore, most of the adjacent benzimidazole rings and phenylene rings are in coplanar conformations since the g_{b-p} distributes in a narrow range of dihedral angle φ_{b-p}. On the other hand, most of the adjacent benzimidazole rings are in twisted conformations since the values of g_{b-b} near $\varphi_{b-b} = 0^\circ$ are very low. For the phosphoric acid doped PBIs, the dihedral angle distributions g_{b-b} and g_{b-p} change in opposite direction for the *p*-PBI and for the *m*-PBI. The peaks of g_{b-b} for *p*-PBI are higher than that for *m*-PBI; however, the peaks of g_{b-p} for *p*-PBI are broader than that for *m*-PBI. These characteristics are evident that *para*-configuration of phenylene is more freely to rotate compared to the *meta*-configuration since the rotation of a *para*-phenylene ring will not result in the long distance movement of the other parts of the oligomer, but the rotation of a *meta*-configuration phenylene group will result in the long distance movement of the oligomer.

3.3. The radial distribution functions

The radial distribution function (RDF), $g(r)$, is a measure to determine the correlation between particles, or the probability of finding a particle at a distance of r away from a given reference particle. In non-crystalline condensed materials, such as the ones simulated in this work, the RDFs usually have a small number of peaks at short distances, superimposed on a steady decay to a constant value at longer distances. From the RDF, it is possible to determine how many particles are within a distance of r and $r + dr$ away from a particle, therefore, the local coordination structures, especially the hydrogen bonding or other short-distance orders. In this work, the RDFs were evaluated from the configurations recorded during the production simulations at 0.1 ps intervals. From Figs. 7 and 8, it could be seen that the differences between RDFs of the pristine *m*- and *p*-PBI molecules are significant, however, the differences between RDFs of the phosphoric acid doped *m*- and *p*-PBI molecules are marginal, suggesting that the significant differences in local structure between the pristine *m*- and *p*-PBI molecules are leveled in the phosphoric acid doped *m*- and *p*-PBI molecules.

3.3.1. Hydrogen bonds in the pristine m- and p-PBI molecules

Although the peak sharpness of the RDFs for the pristine *m*- and *p*-PBI molecules (Fig. 7) differs significantly, the corresponding peak positions are almost the same for these two types of PBIs. This characteristic is consistent with the overall conformation revealed by the snapshots of the MD simulations where the *p*-PBI shows more ordered structure compared to the *m*-PBI. From the RDFs for the amine proton (H) and imine nitrogen (NB), it could be seen that hydrogen bonds (H-bonds) are formed between these two types of atoms with the imine nitrogen accepting the amine proton in H-bonding. However, the flat peak shape for RDF of NB—H reveals the weakness of H-bonding consistent with the IR observation [27,28]. Short-range order also exists between the amine nitrogen (NA) and imine nitrogen (NB) with first peak position at about 3.9 Å, slightly shorter than the wide angle X-ray diffraction reported *d*-spacing of 4.05 Å [4]. However, there are no H-bonds formed between the amine nitrogen (NA) and amine proton (H), since the amine nitrogen is in the sp^2 configuration in the aromatic benzimidazole group instead of the sp^3 configuration. For an sp^3 amine nitrogen, the lone electron pair could accept hydrogen in H-bonding, while for the sp^2 amine nitrogen in benzimidazole group, the lone electron pair is in p_z configuration and is part of the π-bond of the conjugated system. This argument could also be rationalized by the optimized geometry based on density functional theory calculations, where the benzimidazole group is almost coplanar.

3.3.2. Hydrogen bonding network in the phosphoric acid doped m- and p-PBI molecules

From the RDFs shown in Fig. 8, it could be concluded that several types H-bonds are formed in both the phosphoric acid doped *m*- and *p*-PBI molecules. First, the strongest H-bonds are formed between the phosphoric acid molecules in terms of peak height of the RDFs; these RDFs show similar structure as that for the pristine phosphoric acid or for the phosphoric acid doped NAFION [55,56,67]. The non-protonated oxygen (OP) is the strongest H-bond acceptor, as it forms the strongest H-bond by accepting the phosphoric acid proton (HPA). And the protonated oxygen (OPA) forms much weaker H-bond also by accepting the phosphoric acid proton (HPA). The H-bond distance between OP and HPA is 1.62 Å, shorter than that between OPA and HPA at 1.72 Å. The difference in H-bonding characteristics between OP and OPA is attributed to the fact that OPA is already covalently bonded to a hydrogen atom (HPA); therefore, it blocks the approaching of other hydrogen in this direction and reduces the overall probability of H-bonding.

Second, the imine nitrogen (NB) could also form strong H-bonds by accepting the phosphoric proton (HPA) from phosphoric acid. The peak position for NB—HPA is about 2.05 Å, almost 0.4 and 0.3 Å farther than that of OP—HPA and OPA—HPA, respectively. However, the peak height for NB—HPA is between that of OP—HPA and

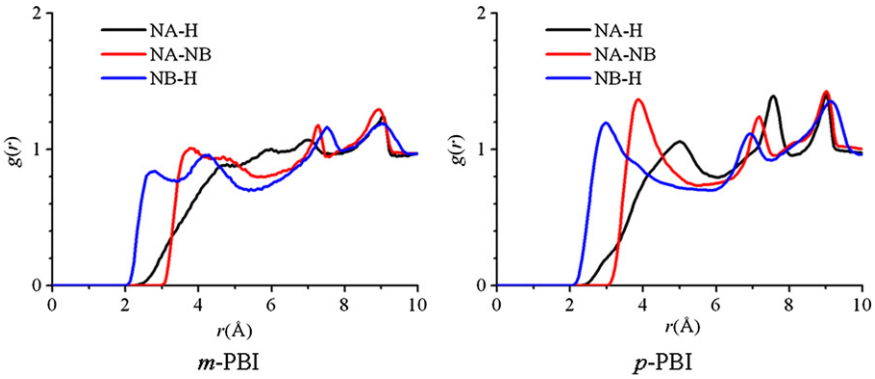

Fig. 7. The RDFs for the pristine *m*- and *p*-PBI molecules showing weak H-bonding between the amine proton (H) and the imine nitrogen (NB), and the more ordered structure for *p*-PBI.

OPA–HPA. The imine nitrogen (NB) is a basic site; for example, the pK_a of a model molecule 2-phenyl benzimidazole (Bz) is 5.07 measured by capillary electrophoresis [68].

$$BzH^+ + H_2O \rightleftarrows Bz + H_3O^+ \quad (5)$$

And H_3PO_4 is an acid, its pK_a is 2.12, 7.21 and 12.32 for the first, second, and third protons, respectively [69]. Therefore, strong H-bond is readily formed between imine nitrogen and phosphoric proton (HPA), or even completely protonation of the imine nitrogen will occur [31,33].

Third, there are also H-bonds formed between the amine proton (H) and phosphoric acid oxygen (OPA and OP), however, these H-bonds are much weaker than those of OP–HPA, OPA–HPA, and NB–HPA. The amine hydrogen (H) is covalently bonded to an aromatic nitrogen atom, and the big aromatic ring prohibits the approaching of any H-bond acceptor from these directions. These characteristics result the poor ability for the amine hydrogen (H) to form H-bond compared to that for the phosphoric proton (HPA).

Finally, similar to the pristine PBIs, the amine nitrogen (NA) cannot accept hydrogen from phosphoric acid (HPA) owing to the steric repulsion between H and HPA which prohibits HPA from approaching to NA.

From all the above information, it could be concluded that hydrogen bond network is formed in phosphoric acid doped PBIs. And the typical geometries of the hydrogen bonds are summarized in Fig. 9a. The hydrogen bond network is composed of three parts: H-bonds in the phosphoric acid sub-phase where phosphoric acid molecules act both as hydrogen acceptors and donors, H-bonds between the phosphoric acid and the imine nitrogen where the imine nitrogen accepts hydrogen from the phosphoric acid, and H-bonds between the phosphoric acid and the amine proton of benzimidazole groups where the phosphoric acid molecules accept hydrogen from the benzimidazole groups. From a few snapshots of the simulated systems as shown in Fig. 9b and c, the types of hydrogen bonds are the same as the ones deduced from the RDFs, and the hydrogen bond network is consistent with the schematic diagram of the hydrogen bonding network in Fig. 9a.

Although the classical MD simulations cannot directly simulate the broken and formation of chemical bonds and thus the proton transport paths, continuous proton transport paths by structural diffusion could be hypothesized. The proton transport path is initiated by the protonation of the imine nitrogen forming a protonated benzimidazole ring and a phosphate anion (proton defect in the phosphoric acid sub-phase) since the imine nitrogen of PBI is a basic site with pK_a of about ~5, and readily reacts with phosphoric acid,

$$(HO)_3P{=}O + Bz \rightleftarrows BzH^+ + (HO)_2PO_2^- \quad (6)$$

On the other hand, the proton transport path in pure phosphoric acid is initiated by the self-dissociation of the phosphoric acid forming pairs of $(HO)_4P^+$and $(HO)_2PO_2$ [70],

$$(HO)_3P{=}O + (HO)_3P{=}O \rightleftarrows (HO)_4P^+ + (HO)_2PO_2^- \quad (7)$$

Proton could hop from a phosphoric acid molecule to the phosphate anion if the conformation is allowed. As the proton

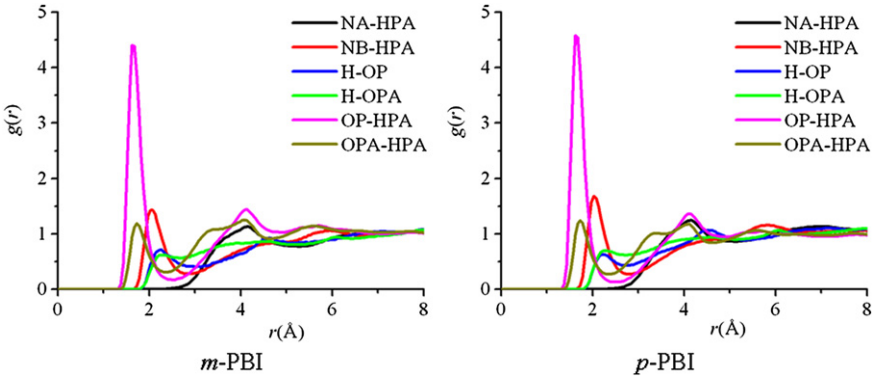

Fig. 8. The RDFs for the phosphoric acid doped *m*- and *p*-PBI molecules reveal the formation of strong H-bonds between phosphoric acid molecules (OP–HPA and OPA–HPA) and between the imine nitrogen and the hydrogen of phosphoric acid (NB–HPA).

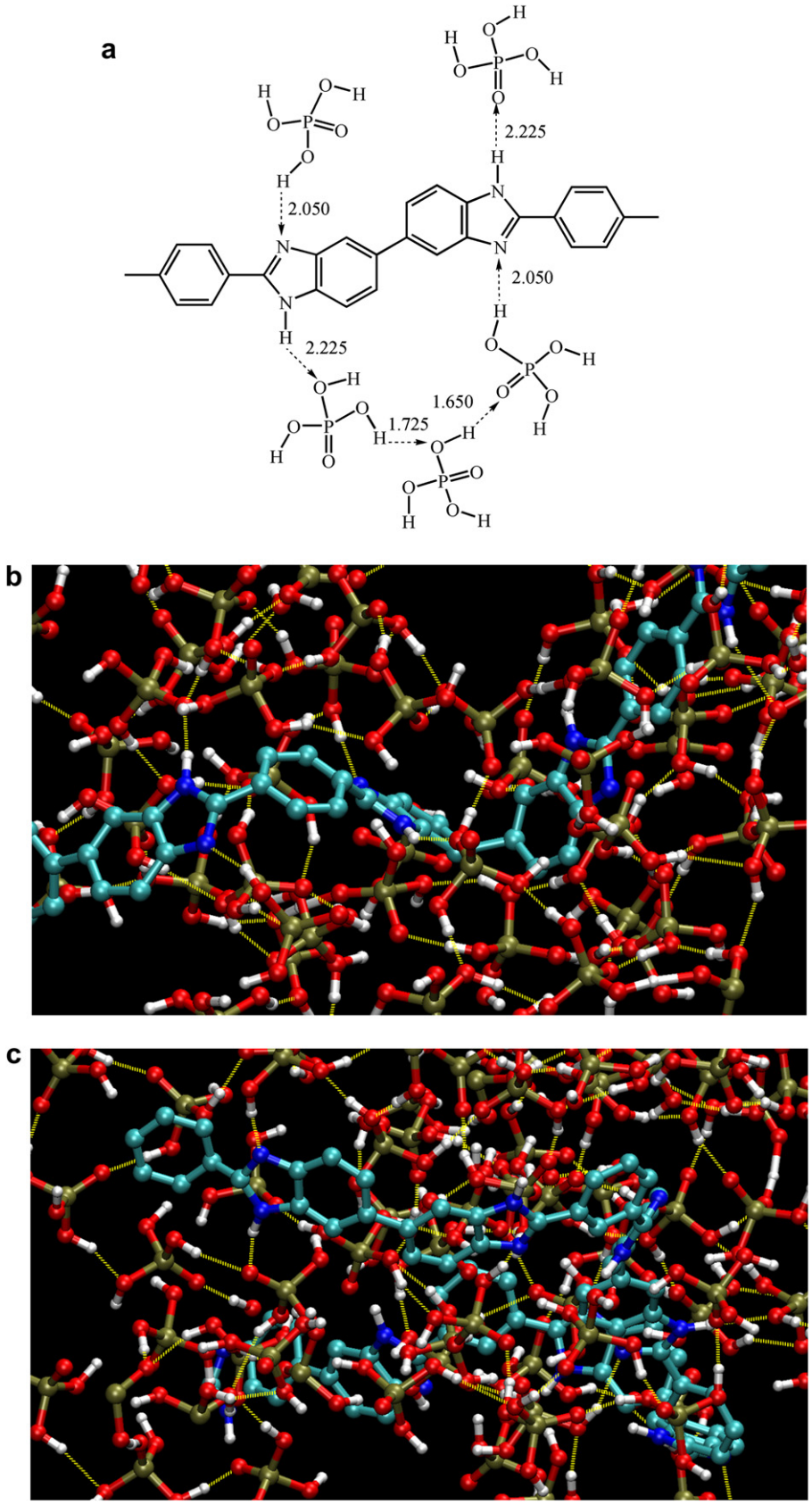

Fig. 9. Typical geometries for the hydrogen bond network formed in the phosphoric acid doped PBIs (a), snapshots from MD simulations showing the H-bonds (dashed lines) zoomed in for *p*-PBI (b), and *m*-PBI (c).

hopping continues, proton transport path develops in the phosphoric acid sub-phase. This proton transport path will terminate if the phosphate anion catches an amine proton and destroying the proton defect. The termination of proton defects is also an important process for the proton transport between the PBI and phosphoric acid sub-phase. In addition, in order to furnish these proton transport steps, bond rotations, local molecular rearrangement is also needed. In this way, continuous proton transport paths by structural diffusion develop in the phosphoric acid sub-phase and at the interface between the phosphoric acid and PBI without interruption.

There are also slight differences in the H-bonding characteristics between phosphoric acid doped *m*- and *p*-PBI molecules. The H-bonds between the phosphoric acid hydrogen (HPA) and imine nitrogen (NB) in *p*-PBI are slight stronger than that in *m*-PBI since the RDFs between NB–HPA in *p*-PBI are slightly sharper and higher than that in *m*-PBI. This reflects the fact that the *p*-PBI molecules are more stretched than the *m*-PBI molecules and the steric hindrance in the *p*-PBI is weaker than that in the *m*-PBI. The H-bonds between the amine proton (H) and phosphoric acid oxygen, the protonated and non-protonated oxygen (OPA and OP), show interesting characteristics. In *m*-PBI, the H-bonds between the amine proton (H) and non-protonated phosphoric acid oxygen (OP) are stronger than that between the amine proton (H) and protonated phosphoric acid oxygen (OPA) since the peak of RDF for H–OP is higher than that for H–OPA, however, the opposite characteristics are observed in the *p*-PBI.

3.4. Diffusion coefficients

The major proton transport mechanism in concentrated phosphoric acid is believed to be structural diffusion, or proton hopping between phosphoric acid molecules, since the molecular diffusion coefficient is as low as 2.3×10^{-11} m^2/s in 93.1% w/w phosphoric acid measured by ^{31}P NMR spectra [56]. In phosphoric acid doped PBI, the high proton conductivity is also contributed by structural diffusion as the diffusion coefficient of ^{1}H is about 2–3 order of magnitude higher than that of ^{31}P by NMR spectra [35]. Our calculated self-diffusion coefficients for the phosphoric acid are about 0.67×10^{-12} m^2/s in phosphoric acid doped *m*-PBI, and 0.47×10^{-12} m^2/s in phosphoric acid doped *p*-PBI. These values are comparable to experimental measurement by ^{31}P NMR spectrum at about 2×10^{-12} m^2/s at 300 K in similar system [35]. In a molecular dynamics simulation of phosphoric acid, the calculated diffusion coefficient is about half of the experimental values [56]. Our calculated diffusion coefficients are reasonable compared to the experimental measurement of the similar system and molecular dynamics simulation calculated value of pure phosphoric acid.

4. Conclusions

From our MD simulations, it was concluded that both of the pristine *m*- and *p*-PBI molecules show essentially amorphous partial crystalline. The *p*-PBI has a more ordered structure. However, no H-bonds are formed between the amine nitrogen (NA) and the amine proton (H). The molecular backbones of the *p*-PBI are more stretched than that of *m*-PBI. The stretched molecular backbones and high symmetry facilitate the rotation of the *p*-phenylene groups, and resulting lowered glass transition temperature compared to the *m*-PBI. The adjacent benzimidazole groups are in twisted configuration, while that a benzimidazole group and an adjacent phenylene group are in coplanar configuration.

The phosphoric acid doped *m*- and *p*-PBI molecules show strong H-bonding interaction between phosphoric acid molecules (OP–HPA and OPA–HPA) and between the imine nitrogen and hydrogen of phosphoric acid (NB–HPA), and weak H-bonding interaction between amine proton of benzimidazole and oxygen of phosphoric acid (OP–H and OPA–H). These H-bonds make a continuous hydrogen bonding network enabling the uninterrupted structural diffusion of proton. It is hypothesized that the interspecies proton transport is initiated by the proton hopping from a phosphoric acid to imine nitrogen forming a phosphate anion (proton defect), followed by its continuous hopping from a phosphoric acid molecule to a phosphate anion, and terminated by its hopping from the protonated benzimidazole ring to the phosphate anion (destroy of proton defect). The termination of proton defects is also essential for the proton transport between the PBI and phosphoric acid sub-phase.

In the design and preparation of similar systems based on acid-base complexes for high temperature PEMFCs, it is essential to balance three processes: the initiation of proton defects, the continuous proton hopping in the acidic sub-phase, and the termination of proton defects. On the one hand, if the base is too weak and cannot be protonated by the acid; the initiation of proton defects will be suppressed and proton hopping could not start. On the other hand, if the base is too strong, the termination of proton defects will be suppressed and interspecies proton transport will be blocked. In addition, the formation of continuous hydrogen bonding network is also essential for the development of proton transport path; and depends on the solvation of the base by the acid during the preparation of the proton exchange membranes.

Acknowledgements

The authors acknowledge the support from the Chinese National Science Foundation (Nos. 20873081, 21073118), and the Nano project (No. 0952nm01300) of Shanghai Municipal Science & Technology Commission.

References

[1] Li Q, Jensen JO, Savinell RF, Bjerrum NJ. Prog Polym Sci 2009;34:449.
[2] He RH, Li QF, Jensen JO, Bjerrum NJ. J Polym Sci Part A Polym Chem 2007;45:2989.
[3] Samms SR, Wasmus S, Savinell RF. J Electrochem Soc 2005;143:1225.
[4] Kumbharkar SC, Karadkar PB, Kharul UK. J Membr Sci 2006;286:161.
[5] Földes E, Fekete E, Karasz FE, Pukánszky B. Polymer 2000;41:975.
[6] He R, Li Q, Bach A, Jensen JO, Bjerrum NJ. J Membr Sci 2006;277:38.
[7] Sannigrahi A, Arunbabu D, Sankar RM, Jana T. J Phys Chem B 2007;111:12124.
[8] Li Q, He R, Jensen JO, Bjerrum NJ. Fuel Cells 2004;4:147.
[9] Li QF, He RH, Jensen JO, Bjerrum NJ. Chem Mater 2003;15:4896.
[10] Pohl HA, Chartoff RP. J Polym Sci Part A 1964;2:2787.
[11] He R, Li Q, Xiao G, Bjerrum NJ. J Membr Sci 2003;226:169.
[12] Li Q, Pan C, Jensen JO, Noyé P, Bjerrum NJ. Chem Mater 2007;19:350.
[13] Roy S, Ataol TM, Müller-Plathe F. J Phys Chem B 2008;112:7403.
[14] Schuster M, Rager T, Noda A, Kreuer KD, Maier J. Fuel Cells 2005;5:355.
[15] Traer JW, Goward GR. Phys Chem Chem Phys 2009;12:263.
[16] Akbey U, Graf R, Chu PP, Spiess HW. Aust J Chem 2009;62:848.
[17] Steininger H, Schuster M, Kreuer KD, Kaltbeitzel A, Bingol B, Meyer WH, et al. Phys Chem Chem Phys 2007;9:1764.
[18] Lee H-S, Roy A, Lane O, McGrath JE. Polymer 2008;49:5387.
[19] Qian G, Smith Jr DW, Benicewicz BC. Polymer 2009;50:3911.
[20] Kim SK, Kim TH, Jung JW, Lee JC. Macromol Mater Eng 2008;293:914.
[21] Kohama S-i, Gong J, Kimura K, Yamazaki S, Uchida T, Shimamura K, et al. Polymer 2008;49:1783.
[22] Kim SK, Kim TH, Jung JW, Lee JC. Polymer 2009;50:3495.
[23] Kumbharkar SC, Islam MN, Potrekar RA, Kharul UK. Polymer 2009;50:1403.
[24] Guan Y, Pu H, Pan H, Chang Z, Jin M. Polymer 2010;51:5473.
[25] Mader J, Xiao L, Schmidt TJ, Benicewicz BC. Polybenzimidazole/acid complexes as high-temperature membranes, Advances in polymer science. In: Fuel cells II, vol. 216. Berlin: Springer-Verlag Berlin; 2008. p. 63.
[26] Carollo A, Quartarone E, Tomasi C, Mustarelli P, Belotti F, Magistris A, et al. J Power Sources 2006;160:175.
[27] Musto P, Karasz FE, MacKnight WJ. Polymer 1993;34:2934.
[28] Musto P, Karasz FE, MacKnight WJ. Polymer 1989;30:1012.
[29] Bouchet R, Siebert E. Solid State Ionics 1999;118:287.
[30] Glipa X, Bonnet B, Mula B, Jones DJ, Rozière J. J Mater Chem 1999;9:3045.
[31] Bouchet R, Miller S, Duclot M, Souquet JL. Solid State Ionics 2001;145:69.

[32] Daletou MK, Kallitsis JK, Voyiatzis G, Neophytides SG. J Membr Sci 2009; 326:76.
[33] Kawahara M, Morita J, Rikukawa M, Sanui K, Ogata N. Electrochim Acta 2000;45:1395.
[34] Hughes CE, Haufe S, Angerstein B, Kalim R, Mahr U, Reiche A, et al. J Phys Chem B 2004;108:13626.
[35] Jayakody JRP, Chung SH, Durantino L, Zhang H, Xiao L, Benicewicz BC, et al. J Electrochem Soc 2007;154:B242.
[36] Devanathan R. Energy Environ Sci 2008;1:101.
[37] Elliott JA, Paddison SJ. Phys Chem Chem Phys 2007;9:2602.
[38] Kreuer K-D, Paddison SJ, Spohr E, Schuster M. Chem Rev 2004;104:4637.
[39] Vilciauskas L, Paddison SJ, Kreuer K-D. J Phys Chem A 2009;113:9193.
[40] Paddison SJ, Kreuer KD, Maier J. Phys Chem Chem Phys 2006;8:4530.
[41] Wang C, Paddison SJ. Phys Chem Chem Phys 2010;12:970.
[42] Zhang D, Yan L. J Phys Chem B 2010;114:12234.
[43] Li S, Fried JR, Colebrook J, Burkhardt J. Polymer 2010;51:5640.
[44] Münch W, Kreuer KD, Silvestri W, Maier J, Seifert G. Solid State Ionics 2001;145:437.
[45] Devanathan R, Venkatnathan A, Rousseau R, Dupuis M, Frigato T, Gu W, et al. J Phys Chem B 2010;114:13681.
[46] Vishnyakov A, Neimark AV. J Phys Chem B 2001;105:9586.
[47] Frisch MJ, Trucks GW, Schlegel HB, Scuseria GE, Robb MA, Cheeseman JR, et al. Gaussian 03, Revision C.2. Wallingford, CT: Gaussian, Inc.; 2003.
[48] John PP, Adrienn R, Jianmin T, Viktor NS, Gustavo ES, Gabor IC. J Chem Phys 2005;123:062201.
[49] Zhang J, Xiao J, Xiao H. Int J Quant Chem 2002;86:305.
[50] Mayo SL, Olafson BD, Goddard III WA. J Phys Chem 1990;94:8897.
[51] Breneman CM, Wiberg KB. J Comp Chem 1990;11:361.
[52] Allen MP, Tildesley DJ. Computer simulation of liquids. Oxford: Clarendon Press; 1990.
[53] Baboul AG, Curtiss LA, Redfern PC, Raghavachari K. J Chem Phys 1999; 110:7650.
[54] El-Azhary AA, Suter HU. J Phys Chem 1996;100:15056.
[55] Yan L, Zhu S, Ji X, Lu W. J Phys Chem B 2007;111:6357.
[56] Spieser SAH, Leeflang BR, Kroon-Batenburg LMJ, Kroon J. J Phys Chem A 2000; 104:7333.
[57] Smith JP, Brown WE, Lehr JR. J Am Chem Soc 1955;77:2728.
[58] Tomlin DW, Fratini AV, Hunsaker M, Wade Adams W. Polymer 2000;41:9003.
[59] Smith W, Leslie M, Forester TR. Computer code DL_POLY_2.14: CCLRC. Daresbury, England: Daresbury Laboratory; 2003.
[60] Nosé S. J Chem Phys 1984;81:511.
[61] Hoover WG. Phys Rev A 1985;31:1695.
[62] Ryckaert J-P, Ciccotti G, Berendsen HJC. J Comput Phys 1977;23:327.
[63] Forester TR, Smith W. J Comput Chem 1998;19:102.
[64] Verlet L. Phys Rev 1967;159:98.
[65] Mecerreyes D, Grande H, Miguel O, Ochoteco E, Marcilla R, Cantero I. Chem Mater 2004;16:604.
[66] Sannigrahi A, Arunbabu D, Jana T. Macromol Rapid Commun 2006;27:1962.
[67] Tsuchida E. J Phys Soc Jpn 2006;75:54801.
[68] Jerez G, Kaufman G, Prystai M, Schenkeveld S, Donkor KK. J Sep Sci 2009; 32:1087.
[69] Kolthoff IM. Treatise on analytical chemistry. New York: Interscience Encyclopedia, Inc.; 1959.
[70] Kerker M, Espenscheid WF. J Am Chem Soc 1958;80:776.

Polymer 52 (2011) 893

Contents lists available at ScienceDirect

Polymer

journal homepage: www.elsevier.com/locate/polymer

Corrigendum

Corrigendum to "In situ fabrication of polyacrylate-silver nanocomposite through photoinduced tandem reactions involving eosin dye" [Polymer 51 (2010), 1363–1369]

Lavinia Balan [a,*], Jean-Pierre Malval [a,*], Raphaël Schneider [b], Didier Le Nouen [c], Daniel-Joseph Lougnot [c]

[a] Département de Photochimie Générale, UMR CNRS 7525, Université de Haute Alsace, ENSCMu, 3 rue Alfred Werner, 68093 Mulhouse, France
[b] Département de Chimie Physique des Réactions, Nancy University, CNRS, 1 rue Grandville, BP 20451, 54001 Nancy Cedex, France
[c] Laboratoire de Chimie Organique et Bioorganique, UMR CNRS Q1 7015, Université de Haute Alsace, ENSCMu, 3 rue Alfred Werner, 68093 Mulhouse, France

The publisher has been notified by the author Jean-Pierre Malval that an error has occurred in the published version of the above paper. The corresponding author indicator was removed from his name by his co-author at proof stage without his knowledge. The indicator has been reinstated on the author details above and footnote below as it should have appeared in the published article. The publisher would like to apologise for any inconvenience caused.

DOI of original article: 10.1016/j.polymer.2009.05.003.
* Corresponding authors.
E-mail addresses: lavinia.balan@uha.fr (L. Balan), jean-pierre.malval@uha.fr (J.-P. Malval).

0032-3861/$ – see front matter
doi:10.1016/j.polymer.2010.12.038

Polymer 52 (2011) 894

Contents lists available at ScienceDirect

Polymer

journal homepage: www.elsevier.com/locate/polymer

Corrigendum

Corrigendum to "Structure–property relations of 55 nm particle-toughened epoxy" [Polymer 51 (2010), 4867–4879]

Quyen-Huyen Le [a], Hsu-Chiang Kuan [b], Jia-Bin Dai [a], Izzuddin Zaman [a], Lee Luong [a], Jun Ma [a,*]

[a] School of Advanced Manufacturing and Mechanical Engineering, University of South Australia, Mawson Lakes, South Australia 5095, Australia
[b] Department of Energy Application Engineering, Far East University, Tainan County 744, Taiwan

ARTICLE INFO

Article history:
Received 15 January 2010
Received in revised form
1 August 2010
Accepted 17 August 2010
Available online 19 November 2010

When first published, equations (3) and (6) were incorrect. The fracture toughness value of the 10 wt% nanocomposite in Table 2 of the original article should be 1.56. The correct equations [39] are shown below.

$$\Delta G_s = 0.5V_f{*}\sigma_{yc}{*}\gamma_f{*}F(r_y){*}\left(1+\mu_m/3^{1/2}\right)^2{*}K_{vm}^2 \quad (3)$$

$$\Delta G_v = \left(1+\frac{\mu_m}{3^{1/2}}\right)^2\left(V_{fv}-V_{fp}\right){*}\sigma_{yc}{*}r_y{*}K_{vm}^2 \quad (6)$$

Young's modulus of DDS-cured epoxy was measured as 3.2 GPa and the rubber's modulus is typically 2.0 MPa. This corresponds to a Max stress concentration factor K_{vm} 3.20, calculated using log (E_{epoxy}/E_{rubber}) [39]; Von Mises pressure sensitivity μ_m is at range 0.175–0.225 [39], and so 0.2 was used; Plane-strain compressive fracture strain of DDS-cured epoxy γ_f was assumed as 0.71 [39]. The explanation of other parameters is shown in the original text. In Fig. 22, the void size of the 5 wt% DDS-cured epoxy/rubber nanocomposite was measured by a software AnalySIS to further examine the model. Using the new equations and parameters as above, the calculated fracture toughness is compared with the experimental result in Table 5. Since the deviation between measure fracture energy values and theoretically calculated values is no more than 20 %, the Kinloch model fits reasonable well into polymer nanocomposites.

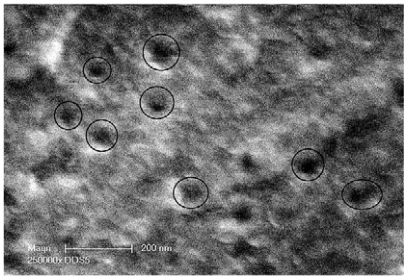

Fig. 22. TEM micrograph of the 5 wt% DDS-cured epoxy/rubber nanocomposite: the circled particles have relatively clear boundary and thus were selected for image analysis.

Table 5
Comparison of theoretical prediction with experimental results.

Materials	Diameter of voids	Shear banding, ΔG_f, kJ/m^2	Void growth ΔG_v, kJ/m^2	Predicted fracture energy, kJ/m^2	Measured fracture energy, kJ/m^2
5 wt% nanocomposite, cured by DDS	76.4 ± 15.2 nm from image analysis of Fig. 22	0.143	0.203	0.419	0.349
10 wt% nanocomposite, cured by DDS	73.5 ± 15.5 nm from image analysis of Fig. 16d	0.195	0.302	0.571	0.696

DOI of original article: 10.1016/j.polymer.2010.08.038.
* Corresponding author.
E-mail address: jun.ma@unisa.edu.au (J. Ma).

0032-3861/$ – see front matter
doi:10.1016/j.polymer.2010.11.002